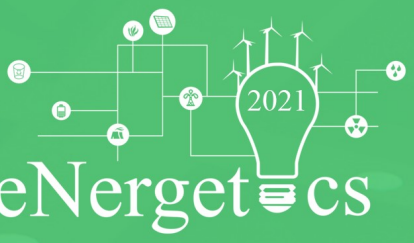

Proceedings of the 7th Virtual International Conference on Science, Technology and Management in Energy

Editor:
Velimirović, L. Z.

Publisher:
Mathematical Institute of the Serbian Academy of Sciences and Arts, Belgrade, Serbia

Serbia, Belgrade, December 16-17, 2021

Editor
Velimirović, L. Z.

eNergetics 2021

7th Virtual International Conference on Science, Technology and Management in Energy

Proceedings

Publisher
Mathematical Institute of the Serbian Academy of Sciences and Arts, Belgrade, Serbia

Serbia, Belgrade, December 16-17, 2021

Proceedings of the
7th Virtual International Conference
on Science Technology and Management in Energy

Serbia, Belgrade, December 16-17, 2021

Editors:
Dr. Lazar Z. Velimirović

Technical Editor:
Dr. Petar Vranić

Published by:
Mathematical Institute of the Serbian Academy of Sciences and Arts, Belgrade, Serbia

Printed by:
Blue Copy, Niš, Serbia

Number of copies printed: 100
The publishing year: 2022

Printing of this edition has been financially supported by
Serbian Ministry of Education, Science and Technological Development

ISBN-978-86-80593-73-9

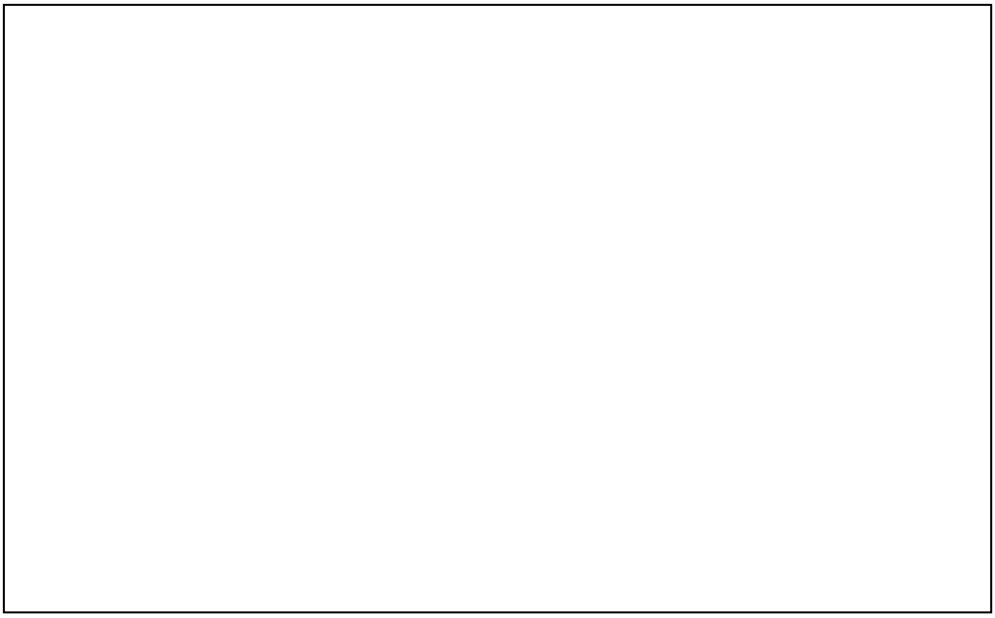

eNergetics 2021

7th Virtual International Conference on Science Technology and Management in Energy

Organizer:
Mathematical Institute of the Serbian Academy of Sciences and Arts, Belgrade, Serbia

Co-organizers:

- Academy of Sciences and Arts of the Republika Srpska
- Faculty of Mining and Geology, University of Belgrade
- Faculty of Technical Sciences, UKLO University St. Climent Ohridski
- Complex System Research Centre COSREC
- National Association of Autonomous and Electric Vehicles of Serbia

Supported by:
Serbian Ministry of Education, Science and Technological Development

Program Committee

Chair:

Prof. Dr. Lazar Z. Velimrović, Mathematical Institute of the Serbian Academy of Sciences and Arts, Belgrade, Serbia

Members:

Prof. Dr. Aleksandar Janjić, Faculty of Electronic Engineering, Serbia

Prof. Dr. Gorazd Stumberger, Faculty of Electrical Engineering and Computer Science, Slovenia

Prof. Dr. Detelin Markov, Faculty of Power Engineering and Power Machines, Bulgaria

Prof. Dr. Marko Serafimov, Faculty of Mechanical Engineering, Macedonia

Prof. Dr. Mileta Janjić, Faculty of Mechanical Engineering, Montenegro

Prof. Dr. Zoran Stajić, Faculty of Electronic Engineering, Serbia

Prof. Dr. Miomir Stanković, Mathematical Institute of the Serbian Academy of Sciences and Arts, Serbia

Prof. Dr. Tomislav Sekara, School of Electrical Engineering, Serbia

Prof. Dr. Enver Agić, Public Enterprise Electric Utility of Bosnia and Herzegovina, Bosnia and Herzegovina

Prof. Dr. Niko Majdandžić, Faculty of Mechanical Engineering, Croatia

Prof. Dr. Serkan Abbasoglu, Cyprus International University, Turkey

Prof. Dr. Bojan Srđević, Faculty of Agriculture, Serbia

Dr. Lenin Kanagasabai, PVP Siddhartha Institute of Technology, India

Prof. Dr. Abdelhak Djoudi, National Polytechnic School, Algeria

Dr. Elson Avallone, Federal Institute of Education, Science and Technology of São Paulo, Brazil

Prof. Dr. Zdravko Milovanović, Faculty of Mechanical Engineering, Bosnia and Herzegovina

Prof. Dr. Miloš Jelić, Research and Development Center Alfatec, Serbia

Prof. Dr. Zoran Markov, Faculty of Mechanical Engineering, Macedonia

Organizing Committee

Chair:

Dr. Petar Vranić, Mathematical Institute of the Serbian Academy of Sciences and Arts, Serbia

Members:

Prof. Dr. Miomir Stanković, Mathematical Institute of the Serbian Academy of Sciences and Arts, Serbia

Prof. Dr. Zoran Stajić, Faculty of Electronic Engineering, Serbia

Dr. Lazar Velimirović, Mathematical Institute of the Serbian Academy of Sciences and Arts, Serbia

Dr. Dusan Tatić, Mathematical Institute of the Serbian Academy of Science and Arts, Serbia

Dr. Radmila Janković, Mathematical Institute of the Serbian Academy of Science and Arts, Serbia

M.Sc. Ljubiša Stajić, Research and Development Center "ALFATEC", Serbia

M.Sc. Danijela Protić, Serbian Armed Force, Serbia

M.Sc. Jelena Velimirović, Mathematical Institute of the Serbian Academy of Sciences and Arts, Serbia

M.Sc. Ivana Veličkovska, Mathematical Institute of the Serbian Academy of Sciences and Arts, Serbia

M.Sc. Vladimir Antic, Serbian Armed Force, Serbia

Table of Contents

Electric Truck Hydropower, an Environmental Friendly and Viable Solution to Hydropower in Mountainous Regions

Julian David Hunt[1], Andreas Nascimento[2]

[1,2]Federal Univeristy of Espírito Santo, Vitória, Brazil, julian.hunt@hotmail.com[1], andreas.nascimento@ufes.br[2]

Abstract—**This paper proposes an innovative solution that consists of catching water from streams at high altitudes to fill storage containers and transport them down a mountain, converting the potential energy of water into electricity and storing it in the truck's battery. The energy stored in the electric truck can be sold to the grid or used by the truck to transport other goods.**

Keywords – hydropower, electric truck, mountains

I. INTRODUCTION

Hydropower is the electricity generation technology that has seen the least innovation in the last century. For instance, the Pelton, Kaplan and Francis turbines, which are the ones most used today, were created in 1876, 1913 and 1920, respectively. Existing facilities can be modernized by applying various approaches such as dam heightening [1], new electrical equipment, digitalization [2], or floating PV [3]. However, currently, hydropower is limited to systems with two set water levels connected via canals, tunnels, and penstocks, and a turbine generation system convert the potential energy of the water into electricity Fig. 1. This approach for hydropower is highly inflexible. In order to guarantee a large installed capacity and capacity factors higher than 30-40%, the catchment area must be high. This significantly reduces the potential of the technology in steep mountainous regions [4]. Additionally, storage reservoirs might also be required to regulate the flow of the river [5] to increase the capacity factor and economic viability of the plant. Furthermore, projected climate change scenarios indicate significant variation in hydropower potential with different regions alternately experiencing decrease and increase in potential [6-10]. This further adds to financial uncertainty of projects. A particular case is in glaciated regions where reduced net glacier mass due to glacial retreat leads to reduced hydro production [11] and may lead to more frequent shut down of run-of-river hydropower [12]. However, despite the above mentioned complexity of hydropower development its role in the power system remains crucial [13] and is an established facilitator of variable renewable energy sources' integration to the grid, as shown for example in the case study of West Africa [14]. Furthermore, in multiple studies the hydropower with reservoir became a foundation for solar-hydro [15, 16], wind-hydro [4, 17] and wind-solar-hydro [18] complementary operation.

II. ELECTRIC TRUCK HYDROPOWER (ETH)

We propose a more flexible alternative for hydropower that features electric trucks. The proposed system consists of using existing road infrastructure that crosses mountain ranges to transport water down the mountain in electricity truck containers, and in this way charge the battery of the truck. The potential energy of the water will be transformed into chemical energy stored in the truck's battery with the regenerative braking of the truck. The ideal configuration of the ETH system is in mountainous regions with steep roads, where the same electrical trucks can be used to generate hydropower from different sites. This increases the chances that there will be water available to generate hydropower and thus increase the capacity factor of the system. Another benefit of

the system is that there is no requirement for dams or reservoirs to regulate the flow of the river. The reservoirs of this system are containers parked close to a river stream on the mountain, which are filled up with water extracted from the river. After the reservoir is filled up, it is ready to be transported down the mountain and to generate hydropower. When the truck reaches the base of the mountain range, the container is parked close to the river, and the water in the container is slowly returned to the river to minimise the impact on the aquatic life. A similar case to ETH happens in the mining industry in Poland, where the extracted minerals are transported down a mountain with electric trucks, and each truck can generate up to 200 kWh per day [19].

The proposed system is divided into four main components, which are: the electric truck, water containers, the charge site and the discharge site, as shown in Fig. 1a. 1) The electric trucks have two main objectives, one of which is to transport water from the charged sites on the mountain to the discharge site. The other is to generate electricity by controlling the descending speed of the truck full of water, charging the battery in the truck. 2) The containers are used to continuously store water from the river in batches on the top of the mountain. It also continuously empties the water back to the river at the discharge site. It is important that the water extraction and release be continuous to reduce the impact of the system on the river flow. 3) The charge sites are the locations where water is extracted from the river and introduced to the containers. They are located in the upper part of the mountain range, on tributary rivers, and/or intermediate locations, to increase the flexibility of the system. The electric truck enters the charge site with an empty container, leaves it to be filled with water, picks a container filled with water, and drives down the mountain. In cold regions, the charge sites on the top of the mountain might not be utilised, as the water in the river might freeze, and icy roads reduce the grip on the tires on the road and the efficiency of the system. 4) The discharge site is where water is removed from the truck and returned to the river. The electric truck enters the discharge site with a container full of water, leaves it to be emptied, collects an empty container, and drives up the mountain. The charged battery is replaced by a discharged battery. The battery is not fully discharged, as the truck requires energy to drive

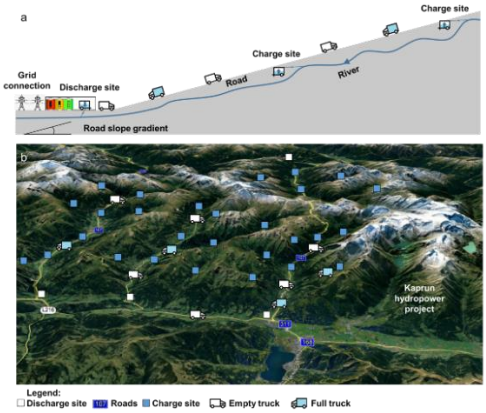

Figure 1. Electric truck hydropower system. (a) axial description of the system where the empty truck moves up the mountain to collect the containers filled with water, and the truck with the full container goes down the mountain generating electricity. (b) aerial view of the ETH system compared with an existing hydropower project, highlighting the flexibility of ETH systems.

up the mountain with an empty container. The discharge site should have a robust connection to the national grid to allow the site to supply electricity to the grid [20]. During periods with low river flow, the battery packs will stop feeding electricity to the grid and will operate as a grid energy storage solution. Alternatively, the electric trucks can be used to transport goods.

III. METHOODOLOGY

The theory behind the electricity truck hydropower concept can be derived from (1), (2) and (3). Equation (1) shows the electric truck hydropower potential (ETH in J). Equation (2) calculates the potential energy that can be extracted from the system (E in J), and Eq. (3) calculates the energy losses in the truck, which is mainly related to the rolling resistance losses of the tires and the aerodynamic friction drag losses in the truck (L in J).

$$ETH = E - L\,, \tag{1}$$

$$E = m \times h \times g \times b \times M\,, \tag{2}$$

where E is the potential energy of the system (in J), m is the mass of water added to the container in the upper water catchment location (in kg), h is the altitude difference between the charge site and the discharge site (in m), g is the acceleration of gravity and equal to $9{,}81\ \ m/s^2$, and b is the battery's energy

storage efficiency cycle, assumed to be 90%. M is the efficiency of electric motor and transmission system, assumed to be 90% [21].

$$L = \frac{\mu \times w \times g \times 0.5 C_p \times \rho \times A \times V^2}{s} \times h \,, \quad (3)$$

where, μ is the rolling resistance coefficient, between the tires and road, assumed to be 0.01 [22]. w is the mass of the truck with or without water, moving down and up a mountain respectively (in kg). C_p is the drag coefficient, assumed to be 0.36 [23], ρ is the air density, assumed to be 1.275 kg/m^3. A is the frontal area of the truck (in m^2). V is the velocity of the truck (in m/s). s is the road slope gradient (in %); for example, a slope gradient of 15% means a 1 m vertical and 6.7 m horizontal distance. The slope gradient is high because the system is designed to operate on existing steep roads.

IV. Results

The efficiency of the ETH system varies from 68% with a road slope of 15% and a speed of 40 km/h, to 35% with a road slope of 5% and speed of 60 km/h, as shown in Fig. 2.

Table I presents the ETH levelized costs of generation in USD/MWh. The truck speed that results in the lower ETH levelized cost varies with each road slope. The levelized costs applied in the paper are the ones highlighted in green. The occasions where the slope is high and electric trucks would not have the power or breaking capacity to drive at high speeds up and down a mountain are highlighted in red. Table I presents the road limits and assumptions used in the model. It assumes that the roads are also used for other purposes and the potential use of the road for ETH is limited to the velocity, number of trucks per hour and water availability.

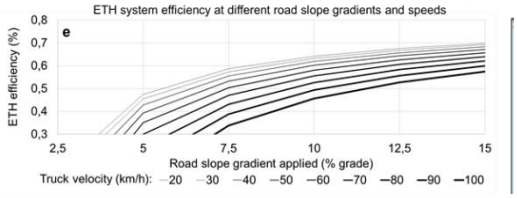

Figure 2. ETH system efficiency at different road slope gradients and speeds.

TABLE I. ETH LEVELIZED COSTS OF GENERATION IN USD/MWH.

Road slope	Trucks speed (km/h)			
	20	40	60	80
5	110.4	**108.5**	127.2	180.3
7.5	59.5	**55.8**	59.0	67.5
10	40.8	**37.5**	38.4	41.5
12.5	31.0	**28.3**	28.5	30.0
15	25.0	22.7	**22.6**	23.4
17.5	21.0	**18.9**	18.8	19.3
20	18.0	**16.3**	16.0	16.3
22.5	**15.8**	14.2	14.0	14.2
25	**14.1**	12.7	12.4	12.5

V. Conclusions

Analysing the results from the ETH system, the lower the truck speed, the fewer are the energy losses, but the least electricity is generated per year. The greater the speed, the greater are the losses, but the generation is greater per year. As the ETH system should achieve a short payback time, the speed of the truck should be as high as possible to maximise the returns in the investment. This system considers that the weight of the empty truck is 30% of the truck filled with water, with its equivalent to the specification of the truck used as the basis for this study. Accordingly, reducing the curb weight of the truck could significantly increase the efficiency of the system and lower the generation costs. Alternatives to reduce the weight of the truck include using aluminum or carbon fiber instead of steel. With trucks being operated autonomously in the future, they could be built without the front section, which could further reduce the curb weight of the truck and the efficiency of ETH systems. The energy storage capacity of the battery should be similar to the amount of energy generated with the ETH system, with the intent of minimising the weight of the truck's battery pack. Another optimized option to further reduce the weight of the truck is to use composite structural batteries (e.g., using modified carbon fibers) which increase the recharge mileage and have potential to substantially to reduce the weight of electric-powered systems. This study assumes that the electric truck is autonomous, which significantly reduces the fixed costs of the system. Even though conventional hydropower systems have long lifetimes (40-100 years) and ETH projects have short ones (3-10), the CAPEX and levelized costs of conventional hydropower projects (1000-5000 USD/kW and 50-200 USD/MWh)

are higher than for ETH projects (200-500 USD/kW and 30-100 USD/MWh). Given that the ETH system is already a competitive electricity generation alternative with existing technology, its cost is expected to further reduce with expected technological improvements in the near future.

ACKNOWLEDGMENT

This research was funded by National Agency of Petroleum, Natural Gas and Biofuels (ANP), the Financier of Studies and Projects (FINEP) and the Ministry of Science, Technology and Innovation (MCTI) through the ANP Human Resources Program for the Oil and Gas Sector Gas – PRH-ANP/MCTI, in particular PRH-ANP 53.1 UFES, for all the financial support received through the grant.

REFERENCES

[1] Hunt, J. D., Byers, E., Prenner, R., & Freitas, M. A. V. de. (2018). Dams with head increaser effect: Harnessing potential and kinetic power from rivers with large head and flow variation. *Energy Conversion and Management*. doi:10.1016/j.enconman.2017.12.034

[2] Quaranta, E., Aggidis, G., Boes, R. M., Comoglio, C., De Michele, C., Ritesh Patro, E., … Pistocchi, A. (2021). Assessing the energy potential of modernizing the European hydropower fleet. *Energy Conversion and Management*, *246*, 114655. doi:10.1016/j.enconman.2021.114655

[3] Silvério, N. M., Barros, R. M., Tiago Filho, G. L., Redón-Santafé, M., Santos, I. F. S. dos, & Valério, V. E. de M. (2018). Use of floating PV plants for coordinated operation with hydropower plants: Case study of the hydroelectric plants of the São Francisco River basin. *Energy Conversion and Management*, *171*, 339–349. doi: 10.1016/j.enconman.2018.05.095

[4] Hunt, J. D., Falchetta, G., Parkinson, S., Vinca, A., Zakeri, B., Byers, E., … Wada, Y. (2021). Hydropower and seasonal pumped hydropower storage in the Indus basin:pros and cons. *Journal of Energy Storage*, *41*, 102916. doi: 10.1016/j.est.2021.102916

[5] Little, J. D. C. (1955). The Use of Storage Water in a Hydroelectric System. *Journal of the Operations Research Society of America*, *3*(2), 187–197. doi:10.1287/opre.3.2.187

[6] Hunt, J. D., & Leal F. W. (2018). Land, Water, and Wind Watershed Cycle: a strategic use of water, land and wind for climate change adaptation. *Climatic Change*, *147*(3–4), 427–439. doi:10.1007/s10584-018-2164-8

[7] Hunt, J. D., Nascimento, A., Caten, C. S. ten, Tomé, F. M. C., Schneider, P. S., Thomazoni, A. L. R., … Senne, R. (2022). Energy crisis in Brazil: Impact of hydropower reservoir level on the river flow. *Energy*, *239*, 121927. doi:10.1016/j.energy.2021.121927

[8] Maran, S., Volonterio, M., & Gaudard, L. (2014). Climate change impacts on hydropower in an alpine catchment. *Environmental Science & Policy*, *43*, 15–25. doi:10.1016/j.envsci.2013.12.001

[9] Tariku, T. B., Gan, K. E., Tan, X., Gan, T. Y., Shi, H., & Tilmant, A. (2021). Global warming impact to River Basin of Blue Nile and the optimum operation of its multi-reservoir system for hydropower production and irrigation. *The Science of the Total Environment*, *767*, 144863. doi:10.1016/j.scitotenv.2020.144863

[10] Turner, S., Hejazi, M., Kim, S., Clarke, L., & Edmonds, J. (2017). Climate impacts on hydropower and consequences for electricity supply investment needs. *Energy*, *141*. doi:10.1016/j.energy.2017.11.089

[11] Schaefli, B., Manso, P., Fischer, M., Huss, M., & Farinotti, D. (2019). The role of glacier retreat for Swiss hydropower production. *Renewable Energy*, *132*, 615–627. doi:10.1016/j.renene.2018.07.104

[12] Puspitarini, H. D., François, B., Zaramella, M., Brown, C., & Borga, M. (2020). The impact of glacier shrinkage on energy production from hydropower-solar complementarity in alpine river basins. *Science of The Total Environment*, *719*, 137488. doi:10.1016/j.scitotenv.2020.137488

[13] IEA. (2021). *Hydropower has a crucial role in accelerating clean energy transitions to achieve countries' climate ambitions securely*. Available at: https://www.iea.org/news/hydropower-has-a-crucial-role-in-accelerating-clean-energy-transitions-to-achieve-countries-climate-ambitions-securely

[14] Sterl, S., Vanderkelen, I., Chawanda, C. J., Russo, D., Brecha, R. J., van Griensven, A., … Thiery, W. (2020). Smart renewable electricity portfolios in West Africa. *Nature Sustainability*, *3*(9), 710–719. doi:10.1038/s41893-020-0539-0

[15] Fang, W., Huang, Q., Huang, S., Yang, J., Meng, E., & Li, Y. (2017). Optimal sizing of utility-scale photovoltaic power generation complementarily operating with hydropower: A case study of the world's largest hydro-photovoltaic plant. *Energy Conversion and Management*, *136*, 161–172. doi:10.1016/j.enconman.2017.01.012

[16] Hunt, J. D., Freitas, M. A. V. D., & Pereira Junior, A. O. (2017). A review of seasonal pumped-storage combined with dams in cascade in Brazil. *Renewable and Sustainable Energy Reviews*, *70*. doi:10.1016/j.rser.2016.11.255

[17] Levieux, L. I., Inthamoussou, F. A., & De Battista, H. (2019). Power dispatch assessment of a wind farm and a hydropower plant: A case study in Argentina. *Energy Conversion and Management*, *180*, 391–400. doi:10.1016/j.enconman.2018.10.101

[18] Liu, B., Lund, J. R., Liao, S., Jin, X., Liu, L., & Cheng, C. (2020). Optimal power peak shaving using hydropower to complement wind and solar power uncertainty. *Energy Conversion and Management*, *209*, 112628. doi:10.1016/j.enconman.2020.112628

[19] Auto Swiat. (2021). Największy pojazd elektryczny świata, który nie wymaga ładowania.

[20] Borlaug, B., Muratori, M., Gilleran, M., Woody, D., Muston, W., Canada, T., … McQueen, C. (2021). Heavy-duty truck electrification and the impacts of depot charging on electricity distribution systems. *Nature Energy*, *6*(6), 673–682. doi:10.1038/s41560-021-00855-0

[21] Xiaozheng, H. (2018). Eco-driving advisory strategies for a platoon of mixed gasoline and electric vehicles in a connected vehicle system. *Transportation Research Part D: Transport and Environment Transport and Environment*, *63*, 907–922.

[22] Mao, Y., Wen, S., Chen, Y., Zhang, F., Panine, P., Chan, T. W., … Liu, L. (2013). High Performance Graphene Oxide Based Rubber Composites. *Scientific Reports*, *3*(1), 2508. doi:10.1038/srep02508

[23] Mohan, A., Sripad, S., Vaishnav, P., & Viswanathan, V. (2020). Trade-offs between automation and light vehicle electrification. *Nature Energy*, *5*(7), 543–549. doi:10.1038/s41560-020-0644-3

Solar Repowering Existing Steam Cycle Power Plants

Erkinjon Matjanov[1], Zarina Akhrorkhujaeva[2]

[1]Scientific-Technical Center with Constructional Bureau and Experimental Production of Uzbekistan Academy of Sciences, Tashkent, Uzbekistan, e.matjanov@gmail.com
[2]Tashkent State Technical University, Tashkent, Uzbekistan, sulaymanovazm8988@mail.ru

Abstract–**Thermal electric power plants on fossil fuel, based on Rankine cycle, are dominated in electricity production worldwide. In recent decades interest in solar power plants is growing up. Particularly, concentrating solar power (CSP) technologies are becoming more attractive. Possibilities of using CSP-technologies in the existing thermal electric power plants are studied in this paper. Steam turbine PVK-150 with electric power output 155 MW of Tashkent thermal electric power plant is chosen for studies. Including parabolic trough collectors parallel to the existing steam generator EP-500/140GM for replacing its economizer and evaporating heating surfaces is proposed. Various values of square of parabolic trough collectors are analyzed for including. Solar-to-electric efficiency and fuel based efficiency in result of solar upgrading are described.**

Keywords - solar upgrading, concentrated solar power, parabolic trough collectors, solar-fossil hybrid power plants, solar-to-electric efficiency

I. INTRODUCTION

Currently, CSP-based power plants, which are applied in industry and investigated by researchers, are mainly: (a) solar gas turbines, (b) solar integrated combined cycle power plants, (c) CSP-based steam cycle power plants, (d) solar-fossil hybrid power plants. Thermal storage can be entered into scheme of all above-mentioned CSP-power plants. The (a) and (b) types are being intensively investigated and improved at the moment by several researchers and companies. The (c) and (d) types are already being implemented in energy generation industry, although they require high capital costs for construction.

Conducted review [1-4] shows following advantages of CSP-based power plants:

- High efficiency (28-30%) in comparison with photovoltaic solar power plants.
- The ability of heat accumulating, which allows operating almost day and night.

Disadvantages of CSP-based power plants are following:

- High capital investments.
- The need for large areas.
- Complex operational processes, which reduces a reliability of the power plants.

Additional advantage of the solar-fossil hybrid power plants will appear when an existing steam cycle power plant is upgraded to the solar-fossil hybrid power plant:

- The possibility of remaining some part of the existing steam cycle equipment, which reduces the capital investments for construction.

Disadvantages of the solar-fossil hybrid power plants are following:

- Lower solar share in comparison with pure CSP-based power plants.
- More complex operational processes in comparison with pure CSP-power plants, which reduces a reliability of the power plants.

Retrofitting the existing thermal electric power plants to the solar-fossil hybrid power plants requires a solution of problems of definition of effective and reliable CSP-technologies, existing in the world market, for

ISBN: 978-86-80593-73-9

intrusion in local climatic conditions. Moreover, technical available and economic optimal point of entering solar heat in schematic diagram of the existing power plant has to be investigated.

This paper deals results of studies on solar-repowering for the existing steam cycle power plants. Obtained results attest about high solar-to-electric efficiency of the solar repowered steam cycle power plants than other types of solar power technologies, when the solar repowering scheme is chosen technical-economical reasonably.

German software EBSILON®Professional was used for the computer modeling and simulations [5].

II. State of The Art

Currently the solar repowering the existing steam cycle power plants are studied by several researchers.

Reference [6] studied seven ways of direct solar heat input to a steam cycle power plant. A solar central receiver was considered as a solar energy collector. Feed water heating, water evaporation, steam super heating, water evaporation and steam super heating, steam reheating, air preheating, pre-air heating and feed water heating were analyzed for integrating solar heat to the steam cycle. Combination of water evaporation and steam super heating was found as the best method.

References [7, 8] analyzed different ways of direct solar generation in power plant. Steam generated in parabolic trough is combined with steam generated in fuel steam generator and enters into steam turbine. Authors concluded that the feed water heating is more economical than using the solar heat in pure solar power plants.

Reference [9] made energy, exergy, economic and environmental analyses of hybrid solar-fossil power plants using CycleTempo software. Parabolic trough concentrators were been used as solar field. According to their conclusion, it is possible to reduce fuel consumption on 5−6% by replacing turbine extract steam.

Reference [10] combined CSP-generation with a 200 MW fossil fuel power plant. Conclusion: the most efficient is using solar heat in low and medium temperature ranges for replacement of turbine steam extractions.

Reference [11] studied using solar heat for preheating feed water in power plants with 200 MW, 300 MW, 600 MW and 1000 MW electric power outputs. Authors found that advantages of using solar heat are different while replacing steam extractions from different points of turbine and in different power plants. Conclusion: the larger the power plant, the more feed water preheating advantages.

Reference [12] analyzed replacing high-pressure feed water heaters with solar heat and concluded, that this increases the net energy and exergy efficiencies of power plant by 18.3% compared to the simple cycle which reaches to 45 % and 43.91 % respectively. Environmental and economic aspects are also had been evaluated.

Reference [13] had made a detailed thermal performance comparison of fifteen power generation technologies including fossil, solar and hybrid options. According to the solar-fossil steam turbine power plants the author had concluded the following: A) the higher the operating temperature of the solar field the higher is the performance of the power plants, however, the use of solar energy for preheating generating-superheating steam is more efficient than when it is used for reheat. B) while operated in fuel saving mode and use solar heat for generating steam is the most efficient option, but the higher share of solar heat input to the cycle the lower is the thermal efficiency.

More attention deserves a paper of [14]. The author had studied three options of solar repowering: A) The existing cycle. B) Low-pressure feed water heaters were replaced by solar field. C) High-pressure feed water heaters were replaced by solar field. D) High-pressure feed water heaters and boiler's economizer (partially) were replaced by solar field. Solar collectors with total net aperture area 81,807 m2 (option B), 64,280 m2 (option C) and 129,656 m2 (option D) were considered to use. Author made a conclusion, that the best option for existing power plants is option C. It needs almost "zero" power plant modification and proposes large solar power generation share, large fossil fuel savings and high power plant efficiency. Option D is most attractive for future power plants, in which the solar power generation share can reach up to 25% of the power plant capacity, having instant efficiency higher than 39% at design point. Author also proposes to reduce steam inlet to the turbine when some feed water

heaters are out of operation owing to solar replacement in order steam volumetric flow in the last turbine stages to be kept at its design point. I.e. steam turbine capacity must be reduced. Nevertheless, eliminating extraction steam to feed water heaters may result in fuel savings as the boiler steam output will be reduced.

Reference [15] investigated a full repowering with merging solar energy in 200 MW units of Montazeri steam cycle power plant (Iran). A 400 MW gas turbine was used for repowering. A part of feed water is saturated in solar field. Conclusion: to increase the efficiency of the considered steam cycle power plant it is expedient to convert to the combined cycles; using solar energy in this power plant can be a rational solution that leads to decrease the investment and eliminate some related limitations.

Analyzing the available publications on solar repowering options for the existing steam cycle power plants, it is impossible to find exact values of the solar-to-electric efficiency, achieved in result of the solar repowering. The solar-to-electric efficiency equation for the solar repowered steam cycle power plants is proposed in the paper. As well as results of a case study for existing 155 MW steam cycle power plant are described.

III. GOVERNING EQUATIONS

Electric efficiency of the power plant is defined by following Eq.:

$$\eta_{PP} = \frac{3600 \times N_e}{Q_f} \ . \qquad (1)$$

where: Q_f – heat input in the steam generator in basic nominal mode, i.e. without solar repowering, kJ/h.

Net electric power output of the power plant is:

$$N_e^{net} = N_e - N_e^{own} \ , \qquad (2)$$

where N_e^{own} - electricity consumption for own needs, kW.

The electricity consumption for own needs N_e^{own} is mainly spent to the feed water pump, condensate pump as well as for circulating water pumps, when a circulating cooling water system is applied. In solar repowering mode electricity charges in circulating pumps for transferring a parabolic trough thermal liquid are also taken into account by N_e^{own}.

Net electric efficiency of the power plant is defined by equation:

$$\eta_{PP}^{net} = \frac{3600 \times N_e^{net}}{Q_f} \ . \qquad (3)$$

In purpose of calculating fuel savings in result of the solar repowering we use a specific fuel: a fuel with heat rate of 7000 kkal/kg. The specific fuel consumption b is measured in g/kwh. The specific fuel consumption for electric energy generation is defined according to Eq.:

$$b = \frac{122.8}{\eta_e^{fuel}} = \frac{122.8 \times Q_f^{sol}}{3600 \times N_e^{sol}} \ , \qquad (4)$$

where: Q_f^{sol} – fuel heat input in the steam generator in solar repowering mode, kW;

N_e^{sol} – electric power output of the power plant in solar repowering mode, kW.

The fuel consumption in the steam generator in basic nominal mode, i.e. without solar repowering, is calculated by Eq.:

$$B_f = 122.8 \times Q_f \ , \qquad (5)$$

and in the solar repowering mode:

$$B_f^{sol} = 122.8 \times Q_f^{sol} \ . \qquad (6)$$

The fuel saving due to the solar repowering is calculated by following Eq.:

$$\Delta B^{sol} = B_f - B_f^{sol} \ . \qquad (7)$$

There are no an exact equation to calculate the solar-to-electric efficiency in the literature. Especially, finding the solar-to-electric efficiency equation concerning the repowered hybrid solar-fossil power plants is impossible. In principle, like the efficiency of any processes, the

solar-to-electric efficiency should be calculated by ratio of work output to work input, i.e. by ratio of the electric power output to the entered solar heat. But for such case, it is impossible to calculate a share of the electric power output, which is earned owing to the solar heat. Steam and feed water is heated partially by the organic fuel and the solar heat: one part of the steam is heated in the feed water heaters and in the steam generator only by organic fuel heat and another part of the steam is heated in low pressure feed water heaters – by organic fuel heat, in high pressure feed water heaters – by the solar heat and in the steam generator superheater – by organic fuel heat. How to calculate a solar share and a fuel share in the electric power output?

It would be correct to calculate the solar-to-electric efficiency as following:

- finding a reduction of the fuel heat input in result of the solar repowering;
- calculating a reduction of the power output by proportionally reducing with the fuel heat input reduction;
- calculating the electric power output, generated due to the solar heat, by subtracting the power output reduction from the nominal mode power output;
- calculating the solar-to-electric efficiency as ratio of the electric power output, generated due to the solar heat, to the solar heat input.

Thus, we derive the following equation for the solar-to-electric efficiency of the solar-fossil hybrid power plants:

$$\eta_e^{sol} = \frac{3600 \times \left(N_e - N_e^{sol} \times \frac{Q_f^{sol}}{Q_f} \right)}{Q_{sol}}, \quad (8)$$

where: Q_{sol} – solar heat input in parabolic trough concentrators, kW.

Electric efficiency of the hybrid solar-fossil power plant is defined by Eq.:

$$\eta_{SPP} = \frac{3600 \times N_e^{sol}}{Q_f^{sol} + Q_{sol}} . \quad (9)$$

IV. Case Study

A. Existing Power Plant Description

Tashkent thermal electric power plant (TPP) consists of 12 steam generators and steam turbines as well as one combined cycle power unit. General electric power output - 2240 MW. Steam turbine PVK-150 with a steam generator EP-500/140GM will be analyzed for the solar repowering. As well, there are two high pressure feed water heaters, feed water deaerator, four low pressure feed water heaters, steam turbine condenser, feed water pump, condensate pump and auxiliaries in a flow diagram of the power unit (Fig. 1). Steam turbine power output is 155 MW.

Steam generator Ep-500/140GM is drum type, product of Taganrog steam generator plant, consists of evaporating heating surfaces, superheater, secondary superheater, economizer and regenerative air heater. Sulfur free natural gas is burned in the steam generator. The steam generator produces a steam with parameters of 14 MPa, 545 ºC and 500 t/h.

Steam turbine PVK-150 – one shaft, two cylinder condensate turbine with two steam outlets into condenser, has eight steam extractions. Inlet steam parameters are 13 MPa

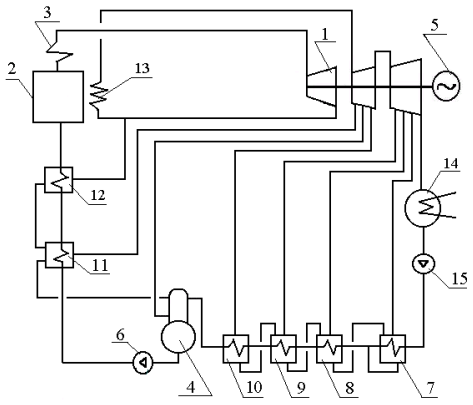

Figure 1. Simplified flow diagram of steam turbine power unit PVK-150. 1 – steam turbine PVK-150; 2 – steam generator Ep-500/140GM; 3 – superheater; 4 – deaerator; 5 – electric generator; 6 – feed water pump; 7 – low pressure heater #1; 8 – low pressure heater #2; 9– low pressure heater #3; 10– low pressure heater #4; 11 – high pressure heater #1; 12 – high pressure heater #2; 13 – secondary superheater; 14 – steam turbine condenser; 15 – condensate pump.

and 540 ºC, secondary steam parameters are 2.75 MPa and 540ºC. Condenser pressure is 0.0035 MPa. Net electrical efficiency of the power unit is 33.1 %.

B. Scheme of Integrating CSP to the Steam Cycle Power Plant

In purpose of remaining the existing equipment in operation we propose to use parabolic trough concentrators and a solar steam generator parallel to the existing fuel steam generator. Some part of feed water behind of high pressure feed water heaters is directed to the solar steam generator (Fig. 2).

Solar part consists of the solar steam generator, parabolic trough concentrators and a circulating pump. The solar steam generator consists of a water economizer and evaporative heating surfaces with a drum. The solar steam generator generates a saturated steam due to the solar, received in parabolic trough concentrators. The generated saturated steam is then returned to the steam turbine cycle and entered into the mixer together with main steam of the fuel steam generator. Then the steam is directed into the superheater and further into the steam turbine.

A rest of the feed water after the high pressure feed water heaters passes via economizer and evaporating heating surfaces of the fuel steam generator, and then joined with saturated steam of the solar steam generator in mixer, then moves via superheater into the steam turbine.

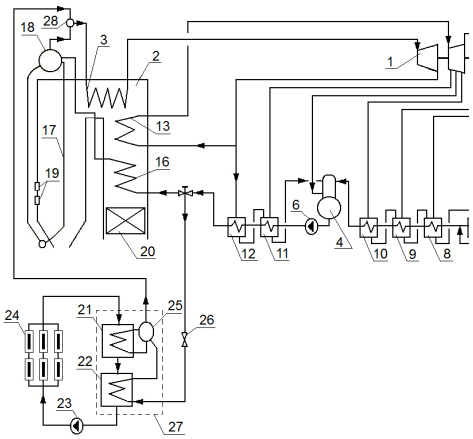

Figure 2. Solar repowering scheme for the steam turbine unit PVK-150. 1÷15 - the same as in fig. 1. 16 – fuel steam generator economizer; 17 - evaporating heating surfaces of the fuel steam generator; 18 – fuel steam generator drum; 19 – torches (burners); 20 - regenerative air heater; 21 - evaporating heating surfaces of the solar steam generator; 22 - solar steam generator economizer; 23 – circulating pump; 24 – parabolic trough concentrators; 25 - solar steam generator drum; 26 - valve; 27 - solar .steam.generator; 28 - mixer.

The following changes are made on the existing steam turbine cycle:

- After the groups of high-pressure feed water heaters a valve is installed on the feed water path to divide the feed water into two streams - into the fuel steam generator economizer and into the solar steam generator economizer.
- A mixer is installed on the steam pipeline between a drum and a superheater of the fuel steam generator to combine saturated steams of the both steam generators.
- An additional pipeline is installed to connect the feed water path after the groups of high-pressure feed water heaters with the solar steam generator economizer;
- An additional steam line is installed, which connects the solar steam generator drum to the mixer between the drum and the superheater of the fuel steam generator.
- Reallocation of torches in the steam generator.

B. Solar Data

Tashkent solar data (DNI) for latitude 41.16 & longitude 69.13 is accepted for June 14, 2016 (Fig. 3). Parabolic trough collectors with 197.5 m length, 5.76 m gross aperture width and 1.71 m focal length have been used while simulations. Number of the parabolic trough collectors – 200 pcs, gross aperture area – 227 520 m^2, total net

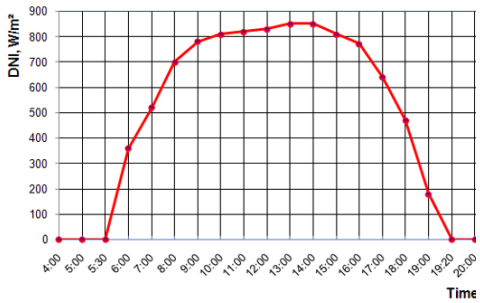

Figure 3. DNI in Tashkent in June 14, 2016.

aperture area – 215 256 m^2. Parabolic trough collectors are able to produce a heat up to 132.2 MW.

V. Results

Calculations were carried out according to the methods and equations, described in the paragraph III. Main results are given in a Table I. In the table where DNI = 0, the data belong to the existing steam cycle power plant without solar repowering.

Simulation results in the computer model show, the proposed solar repowering scheme is able to operate when DNI is not lower than 249 w/m^2. It is worthy to note, solar repowering according to the proposed scheme promotes to reach the solar-to-electric efficiency up to 34.4 %, by other words – the fuel based electric efficiency is improved from 34.9 % up to 49.5 % (when neglecting the solar heat).

TABLE I. Main technical-economic data of the hybrid solar-fossil power plant in June 14, 2016.

Time	DNI, w/m^2	N_e^{sol}, **MW**	$N_e^{sol.net}$, **MW**	Q_f^{sol}, **MW**	Q_{sol}, **MW**	b, **g/kWh**	ΔB^{sol}, **kg/h**	η_e^{sol}, -	η_{SPP}, -
5:00	0	155,00	146.69	443.7	0	351.53	0.0	0	0.349
6:00	360	155.00	146.43	424.6	33.3	336.43	2 340.7	0.200	0.338
7:00	520	155.00	145.67	369.7	82.2	292.90	9 086.8	0.315	0.343
8:00	700	155.00	145.20	335.2	112.9	265.54	13 328.8	0.336	0.346
9:00	780	155.00	145.01	321.1	125.4	254.37	15 059.0	0.342	0.347
10.00	810	155.00	144.97	318.2	128.0	252.06	15 418.1	0.343	0.347
11.00	820	155.00	144.98	319.4	127.0	253.01	15 270.4	0.342	0.347
12.00	830	155.00	144.98	319.5	126.9	253.10	15 257.3	0.342	0.347
13.00	850	155.00	144.93	315.7	130.2	250.15	15 713.4	0.343	0.348
14.00	850	155.00	144.90	313.4	132.2	248.33	15 996.4	0.344	0.348
15.00	810	155.00	144.96	317.4	128.7	251.50	15 505.1	0.343	0.347
16.00	770	155.00	145.03	322.6	124.1	255.55	14 876.8	0.341	0.347
17.00	640	155.00	145.35	346.3	103.0	274.37	11 959.5	0.330	0.345
18.00	470	155.00	145.81	379.4	73.6	300.57	7 898.3	0.305	0.342
19.00	180	155.00	146.69	443.7	0	351.53	0	0	0.349
20:00	0	155.00	146.69	443.7	0	351.53	0	0	0.349

VI. Conclusions

In result of the study we have got the following main conclusions:

- The solar-to-electric efficiency equation for the solar repowered steam cycle power plants is proposed.
- Analyzing the power plant efficiency equations, their components and efficiency improvement options, we have found, the Rankine cycle efficiency is the main candidate to be improved. But however, its improving for the existing power plants is restricted by technical and economic conditions, as well as by original design data.
- It is expedient to enter the solar heat into the existing steam generator. This leads to do some configurations in the steam generator arrangement, which also require capital investments. But this arrangement configuration will be limited with reallocation of torches and resizing some heating surfaces. It may be necessary to replace some parts of the economizer or the evaporating heating surfaces. I.e. in purpose of remaining the existing steam cycle equipment in operation it is possible to use the parabolic trough concentrators and the solar steam generator parallel to the existing

fuel steam generator: the solar part would partially replace the economizer and the evaporating heating surfaces of the existing steam generator.

- In result of the case study it is defined, the solar repowering according to the proposed scheme promotes to reach the solar-to-electric efficiency up to 34.4 %, by other words – the fuel based electric efficiency is improved from 34.9 % up to 49.5 % (when neglecting the solar heat).
- It is worthy to notify, that actually electric efficiency of the considered PVK-150 steam cycle power plant is 34.9 %. If the solar repowering would be applied to steam cycle with electric efficiency 38÷40 %, so the solar-to-electric efficiency could be reached up to ≈38÷39 %.

REFERENCES

[1] Pramanik, S., & Ravikrishna, R. V. (2017). A review of concentrated solar power hybrid technologies. *Applied Thermal Engineering*, *127*, 602-637.

[2] Nathan, G. J., Jafarian, M., Dally, B. B., Saw, W. L., Ashman, P. J., Hu, E., & Steinfeld, A. (2018). Solar thermal hybrids for combustion power plant: A growing opportunity. *Progress in Energy and Combustion Science*, *64*, 4-28.

[3] Qin, J., Hu, E., & Li, X. (2020). Solar aided power generation: A review. *Energy and Built Environment*, *1*(1), 11-26.

[4] Sansaniwal, S. K., Sharma, V., & Mathur, J. (2018). Energy and exergy analyses of various typical solar energy applications: A comprehensive review. *Renewable and Sustainable Energy Reviews*, *82*, 1576-1601.

[5] *As versatile as a planning tool can be EBSILON®Professional for the design of power plants*. Available at: <https://www.steag-systemtechnologies.com/en/products/ebsilon-professional/>

[6] Zoschak, R. J., & Wu, S. F. (1975). Studies of the direct input of solar energy to a fossil-fueled central station steam power plant. *Solar Energy*, *17*(5), 297-305.

[7] Gupta, M. K., & Kaushik, S. C. (2009). Exergetic utilization of solar energy for feed water preheating in a conventional thermal power plant. *International journal of energy research*, *33*(6), 593-604.

[8] Gupta, M. K., & Kaushik, S. C. (2010). Exergy analysis and investigation for various feed water heaters of direct steam generation solar–thermal power plant. *Renewable Energy*, *35*(6), 1228-1235.

[9] Suresh, M. V. J. J., Reddy, K. S., & Kolar, A. K. (2010). 4-E (Energy, Exergy, Environment, and Economic) analysis of solar thermal aided coal-fired power plants. *Energy for sustainable development*, *14*(4), 267-279.

[10] Yang, Y., Yan, Q., Zhai, R., Kouzani, A., & Hu, E. (2011). An efficient way to use medium-or-low temperature solar heat for power generation–integration into conventional power plant. *Applied thermal engineering*, *31*(2-3), 157-162.

[11] Yan, Q., Hu, E., Yang, Y., & Zhai, R. (2011). Evaluation of solar aided thermal power generation with various power plants. *International Journal of Energy Research*, *35*(10), 909-922.

[12] Ahmadi, G., Toghraie, D., & Akbari, O. A. (2017). Solar parallel feed water heating repowering of a steam power plant: A case study in Iran. *Renewable and Sustainable Energy Reviews*, *77*, 474-485.

[13] Behar, O. (2018). Solar thermal power plants–A review of configurations and performance comparison. *Renewable and Sustainable Energy Reviews*, *92*, 608-627.

[14] Popov, D. (2011). An option for solar thermal repowering of fossil fuel fired power plants. *Solar Energy*, *85*(2), 344-349.

[15] Ahmadi, G., Toghraie, D., Azimian, A., & Akbari, O. A. (2017). Evaluation of synchronous execution of full repowering and solar assisting in a 200 MW steam power plant, a case study. *Applied Thermal Engineering*, *112*, 111-123.

Modelling and Simulation of Heat Flow and Pressurization Inside a Batch Reactor for the Hydrothermal Liquefaction of Biomass

Moeen El Bast[1], Nadine Allam[2],Youssef Abou Msallem[3], Sary Awad[4], Khaled Loubar[5]

[1,4,5]IMT Atlantique, Nantes, France, international@imt-atlantique.fr
[2,3]Lebanese International University, Beirut, Lebanon, info@liu.edu.lb

Abstract—**Hydrothermal liquefaction is a thermochemical conversion process used to convert biomass into biocrude under subcritical or supercritical conditions, using suitable solvents and catalysts. This work studies the heat diffusion and medium pressurization inside a hydrothermal liquefaction batch reactor using experiments conducted at lab-scale, and, simulation using COMSOL Multiphysics. Results were satisfactory and errors between the experimental and the numerical results were acceptable. The stabilized pressurization error was less than 3%, and the temperature distribution errors were all averaged below 4%.**

Keywords –- hydrothermal liquefaction – biomass – batch reactor - COMSOL

I. INTRODUCTION

Biomass is an organic matter, involving both flora and fauna. It includes many resources such as wood and wood wastes, animals and agricultural wastes, aquatic plants and energy crops [1]. Normal human activity produces daily huge quantities of biomass, such as cooking wastes, sewage sludge, sawdust, manure, etc. Typical biomass contains mainly carbon, hydrogen, oxygen, sulfur and nitrogen.

In the era of limited energy resources, hydrothermal liquefaction process is established as a processive technique for producing renewable and upgradable fuels. Hydrothermal liquefaction involves thermochemical conversion of biomass into liquid fuels by processing in a hot, pressurized environment, for a sufficient time to decompose biomass polymeric structure to mainly liquid products [2]. Typical conditions for such process involve heating at 523 – 647 Kelvins, and pressurizing the medium between 40 and 220 bars [3]. Liquid bio-fuel, known as biocrude, is the main product of this thermochemical conversion.

Several numerical approaches were adopted to model hydrothermal liquefaction process. Zhongzhong Zhang led a CFD modelling of a continuous tubular hydrothermal liquefaction reactor [4]. A numerical model was built to simulate the process reported in a previous research work. Results were satisfactory and the validated model helped in varying the reaction parameters and conditions for process optimization. Moreover, Alizeb Syed modelled the direct liquefaction of biomass in hydrothermal conditions using ANSYS software [5]. The kinetic model of the reaction, the heat transfer and the fluid flow phenomena were simulated in this model. Validated results helped to determine the optimum conditions for the degradation of cellulose. Xiao Chen simulated numerically the hydrothermal liquefaction of algae in a lab-scale coil reactor using ANSYS CFX software [6]. This work was based on the experimental studies of Valdez et al. for the hydrothermal liquefaction of microalgae [7]. The results of the model were compared to the experimental ones obtained by Valdez et al., and the model was validated, and used to study the effect of heat conductivity, heat capacity, density, and viscosity of biomass on the products yields.

It can be noticed that the majority of numerical studies on hydrothermal liquefaction processes were performed using continuous

ISBN: 978-86-80593-73-9

reactors. Modelling of such reactors can be achieved using steady state conditions for temperature and pressure, whereas in batch reactors, more complex phenomena should be taken into consideration, including the transient heating phase, the phase change of the material inside the reaction zone, etc.

Modelling and simulation of hydrothermal liquefaction process inside a batch reactor is a challenging topic, which deals with different phenomena that need to be modeled and coupled, starting from heat diffusion, passing to the pressurization of the reactor, transitioning to applying chemical reactions in transient phases, and producing new species. Even though it is complicated, the simulation of a batch reactor remains a necessity before designing a continuous one, especially when transient regimes need to be included in the design. Thus, this paper describes the heat diffusion and pressurization phenomena inside a lab-scaled batch reactor. Several experiments were conducted, starting from heating empty reactor, moving to different solvents heating inside the reactor (water, methanol and ethanol). The achieved temperature distribution and pressure increase results were used to validate the suggested numerical model.

II. Materials and Methods

A. Experimental Setup

Experiments were carried out at GEPEA Laboratory in the DSEE Department of IMT Atlantique, Nantes. The hydrothermal reactor used is a 1-L, cylindrical batch reactor, made of stainless steel. The reactor's height is 35.95 cm, with an inner radius of 3 cm, and an outer radius of 8.5 cm

The reactor is insulated using 5.2 cm insulation layer. The top part of the reactor (cover) is fixed, the reactor's body slides relative to the cover, and the insulation slides independently of reactor's body to accelerate the cooling process, as shown in Figure 1.

Heating is provided to the reactor through electric resistance heaters built in the walls of the reactor, capable to deliver up to 20 kW heating power. Temperature is limited to a maximum value of 450°C and the reactor handles a maximum pressure of 190 bars.

The reactor is equipped with a pressure transducer to measure the absolute instantaneous pressure inside the reaction zone. In addition, four thermocouples are installed at different positions to measure four temperatures. T_w at the bottom of the reactor is the temperature of the reactor's metal body. This temperature is used to control the heat power supply. T_{in} placed inside the inner volume of the reactor, measures the temperature of the reaction zone. T_3 is placed on the inner wall of the insulation; between the reactor and the insulation, and thermocouple T_4 is placed on the outer surface of the insulation, at the same horizontal level with T_3. A graphical representation of the thermocouples locations is shown in Fig. 2.

A nitrogen feeding system is connected to the reactor. Nitrogen is used as a washing gas to purge the reactor before starting any experiment.

A data acquisition system is connected to the reactor, to record the pressure, temperatures, and input power during the experiment. The time stepping of this acquisition system can be varied. The most convenient time step for data recording was chosen to be one second. This helps in the comparison with simulation results later on.

Before each experiment, the reactor is purged with nitrogen gas flowing at a rate of 0.09 L/sec (± 0.005) during10 mins. Several experiments were conducted for this work; (1) heating of empty reactor (purged with nitrogen), (2) heating 300 mL of water, (3) heating 750 mL of water, (4) heating 300 mL of ethanol, and (5) heating 300 mL of methanol.

Figure 1. Batch reactor used for the hydrothermal liquefaction in the GEPEA Laboratory of DSEE department in IMT Atlantique.

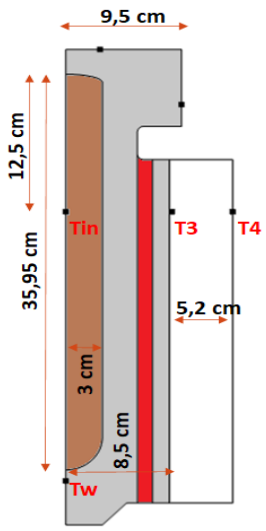

Figure 2. Reactor's axial cross-section as implemented in COMSOL.

B. *Reactor Modelling and Implementation into COMSOL Multipysics*

In this section, the steps for implementing the batch reactor into COMSOL Multiphysics will be listed and discussed. this includes the reactor's geometry, power input method, pressurization of the reaction zone, mesh size influence, boundary conditions, and the calibration of material properties.

1) Reactor's geometry

The dimensions of the reactor taken from the designer's manual are implemented into COMSOL using 2D-axisymmetric coordinates, in which an axial cross-section of the reactor is drawn as shown in Fig. 2. In this figure, the brown zone represents the reaction zone, i.e., the internal volume of the reactor in which the reaction takes place. The grey zone represents the heating zone imbedded in the reactor. Finally, the insulation is represented by the white zone. In addition, the exact locations of the four thermocouples are clearly stated in Fig. 2.

2) Power zone assumption

The reactor is fitted with cylindrical heaters imbedded in its metallic walls. However, modelling these heaters in 2D-axisymmetric coordinates is not possible. For this reason, an assumption was taken transforming the heating zone from separate individual heaters into a volume heating zone. This volume zone emits the same amount of power, and is located at the same radial distance. Fig. 3 shows the transformation from individual heaters to the volume heating zone.

The reactor's acquisition system records the input power (Watts) which is extracted and imported into COMSOL as an interpolation function for the power source. Thus, experimental power is applied accurately to the simulation model. The power was imported in terms of volumetric heat source, the heating volume having a hollow cylindrical shape was calculated and appeared to be equal to 1.6438 L. The experimental power from the acquisition system was divided by this volume to obtain the volumetric power.

3) Isothermal domain interface

To simulate the natural convection phenomenon, in which the velocity, viscosity and density of the matter vary continuously during the heating phase, COMSOL will consume a lot of computational power, and it will take too much time to simulate a single experiment. It took more than an hour to simulate two minutes of natural convection phenomenon using a dual core 16GB RAM machine, which totally makes no sense for trying to simulate tens of experiments of 1800+ seconds. An alternative method is chosen; considering isothermal domain interface in the reaction zone only. This interface is built in COMSOL, where a block is defined to have same properties among its volume; temperature, pressure, density, viscosity, etc. When simulating the batch reactor under study, the isothermal domain model is

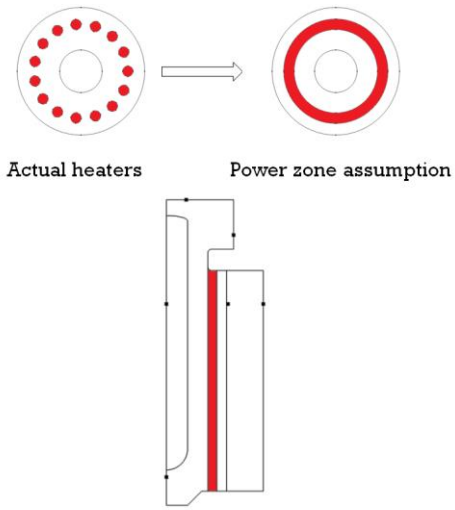

Figure 3. Individual heating to power zone assumption.

applicable since the reaction zone inside the reactor will not have high temperature gradient. Fluid inside the reactor can be treated as one block of uniform properties in case of empty reactor heating, and as two isothermal domains (two blocks) in case of solvent and nitrogen heating. The reaction zone is heated by the inner walls of the reactor through convective heat transfer, which is also included in the isothermal domain assumption. A convective heat transfer coefficient was proposed and calibrated to meet the required performance. This assumption established itself using much less computational resources with satisfying results' accuracy.

4) Pressurizing the reaction medium

Referring to thermodynamics' laws, an increase of temperature in a closed volume yields an increase in pressure. In the case of a batch reactor, the total pressure is the sum of three different pressures; purging gas pressure, solvent vapor's pressure, and pressure obtained from production of new gaseous species. Latter will not be used in this paper due to the fact that our model does not include chemical reactions.

a) Purging gas pressure

Nitrogen gas pressure increase could be modelled following two different laws; ideal gas law and real gas law. Both laws were adapted and compared to know which is most suitable for our study.

Ideal gas law

The ideal gas law states that

$$P_i = \rho RT \ , \qquad (1)$$

where $P_i\left(Pa\right)$ is the partial pressure following the ideal gas law, $\rho\left(kg/m^3\right)$ is the density of gas, $R\left(kJ/\left(kg.K\right)\right)$ is the gas constant and $T\left(K\right)$ is the absolute temperature [8].

Real gas law

Van der Walls Eq. describing the real gas behavior states that

$$\left[P_r + a\left(\frac{n}{V}\right)^2\right]\left(\frac{V}{n} - b\right) = RT \ , \qquad (2)$$

where $P_r\left(Pa\right)$ is the partial pressure following the real gas law, $a\left(Pa.m^6/mol^2\right)$ represents the intermolecular forces correction, $n\left(mol\right)$ is the number of moles, $V\left(m^3\right)$ is the occupied volume, and $b\left(m^3/mol\right)$ represents the correction for the volume occupied by the gas particles [9].

b) Solvents' vapor pressure

When a liquid is heated in a closed volume, it undergoes an isochoric process. In such process under the given conditions, the absolute pressure in the reactor follows the saturation pressure of the liquid throughout the whole experiment [10]. Thus, the solvents' vapor pressure will be the difference between the absolute pressure inside the reactor and the partial pressure of the purging gas.

5) Governing equations

For the analysis of thermochemical conversion of biomass, finite element software adopts four major governing equations, conservation of mass (continuity), conservation of momentum, conservation of energy and mass transport equations.

The continuity Eq. used by COMSOL has the following vector form:

$$\frac{\partial \rho}{\partial t} + \nabla.\vec{u} = 0 \ . \qquad (3)$$

The conservation of momentum equation has the following vector form:

$$\rho\frac{\partial u}{\partial t} + \rho\left(\vec{u}.\nabla\right).\vec{u} = \\ = \nabla.\left[-p.\vec{I} + \mu\left(\nabla\vec{u} + \left(\nabla\vec{u}\right)^T\right)\right] \ , \qquad (4)$$

where μ is the dynamic viscosity *(kg/m.s)*

The conservation of energy Eq. has the following vector form:

$$\rho C_P\left(\frac{\partial T}{\partial t} + \vec{u}.\nabla T\right) = \nabla\left(k\nabla T\right) + \dot{q} \ , \qquad (5)$$

where c_p is the specific heat at constant pressure, and k represents the thermal conductivity of the

material, and $\dot{q}$ represents the amount of generated energy per unit volume.

In this work related to heat diffusion and pressurization only, the mass transport equations will not be used.

6) Material Properties

The reactor is made of stainless steel 316L [11]. Nitrogen, water, methanol and ethanol are chosen from COMSOL's materials' library [12]. The insulation's material was not specified in the reactor's designer's manual, thus, ranges for these properties were taken from previous works [13], and a sensitivity study was performed to fully calibrate them.

III. RESULTS

The results of the experiments conducted on the batch reactor were compared to those obtained by simulation.

A. Nitrogen Heating

Empty reactor heating involves purging it with nitrogen before turning on the heaters, thus, the reactor is not literally empty, it contains only nitrogen gas, which is at atmospheric conditions at the beginning of the experiment. Fig. 4. shows a comparison between the experimental pressure, the simulation pressure following the ideal gas law, and the simulation pressure following the real gas law. It was realized that for the operating temperature range, there is no difference between adapting the real gas law and the ideal gas law for pressurizing the nitrogen; the maximum error between ideal and real values is 0.07%, which is negligible.

It was noticed that the maximum error between the experimental and the simulated pressures reaches a maximum value of 8.88% at

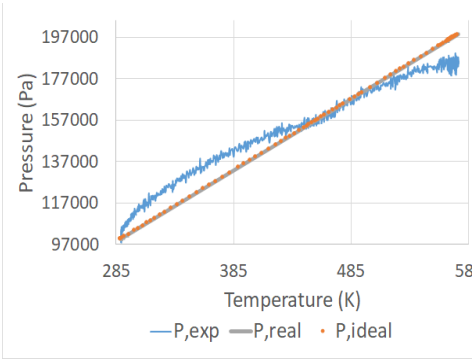

Figure 4. Experimental pressure, real gas pressure and ideal gas pressure plotted versus the inner temperature inside the reactor.

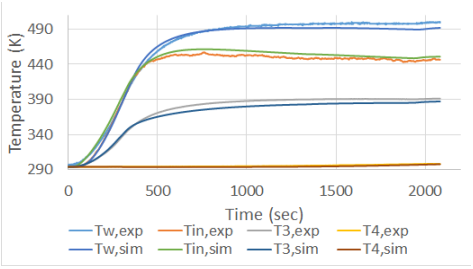

Figure 5. Temperature profiles comparison for nitrogen heating experiments.

the beginning of the heating phase. This can be related to the fact that the temperature measured by the inner thermocouple is not the actual temperature of the gas, it is influenced by the gas temperature and the radiation energy absorbed from the reactor's inner walls. This phenomenon was modelled in COMSOL and the radiation effects were taken into consideration when building the model, but when using the value of the inner temperature to apply gas laws, some errors will take place.

Fig. 5 compares the experimental and the simulated temperatures. Results are satisfactory, the curves behaved in the same manner during the heating phase and the steady state phase, and the maximum error in all the data was less than 4%.

B. Liquid Solvents' Heating

The aim of performing two experiments with different water volumes refers to the fact that in the experiment of 300 mL of water, the liquid level is lower than the thermocouple's tip, whereas when filling the reactor with 750 mL of water, the thermocouple is immersed totally in water. Fig. 6 shows the comparison between experimental and numerical results of temperatures for the heating of 300 mL of water. Results were satisfactory with 6.5% as maximum error between the simulated and experimental results.

Same work was done for all the experiments and Table I shows the maximum and average error percentages between the simulated and experimental temperatures.

Results were satisfactory; the largest temperature error is noticed for the inner thermocouple temperature Tin for all solvents. The maximum error is 12.59% when ethanol was

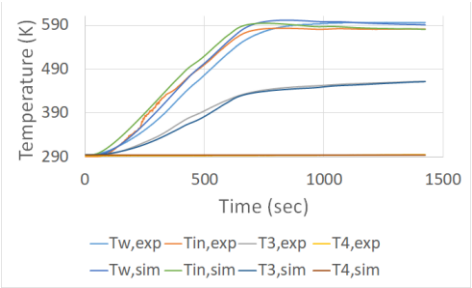

Figure 6. Experimental vs. simulation values of temperature and pressure distribution for 300 mL water heating.

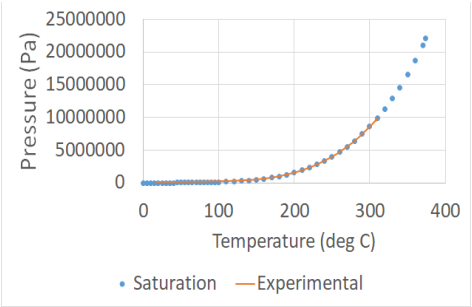

Figure 7. Saturation versus experimental pressure-temperature curves for water heating.

TABLE I. MAXIMUM AND AVERAGE ERROR PERCENTAGES BETWEEN EXPERIMENTAL AND NUMERICAL RESULTS OF TEMPERATURE DISTRIBUTION ACROSS THE REACTOR.

Solvent		Water 300 mL	Water 750 mL	Methanol 300 mL	Ethanol 300 mL
Tw	Max.	6.1	6.79	4.91	4.99
	Avg.	2.57	3.07	2.46	2.57
Tin	Max.	6.55	7.68	8.6	12.59
	Avg.	2.26	3.84	2.71	3.52
T3	Max.	3.61	2.33	4.93	4.53
	Avg.	1.1	0.98	3.46	2.38
T4	Max.	0.62	1.32	2.42	0.98
	Avg.	0.32	0.61	1.9	0.43

TABLE II. MAXIMUM AND AVERAGE ERROR PERCENTAGES BETWEEN EXPERIMENTAL AND NUMERICAL RESULTS OF PRESSURIZATION OF THE REACTOR.

Solvent	**Max. Error %**	**Steady state Error %**
Water 300 mL	79	< 3
Water 750 mL	95	< 2
Methanol 300 mL	72	< 1
Ethanol 300 mL	83	< 2

interval in the heating phase, which may be referred to the fact that when the liquid starts to evaporate in the reactor, the latent heat absorbed used. Whereas all other maximum values in the rest of the thermocouples were below 7%. This relatively high error occurred for a short time affects the inner temperature of the reactor. However, the average error for the inner thermocouple reached 3.84%.

Thus, the COMSOL model reported in this work is assumed validated as long as the maximum averaged error remained below 4%. In another work, Baghli et al. [14] simulated thermal transfer in a batch reactor, and validated the obtained results based on reported experimental data. The maximum error between experimental and numerical results averaged at 2%. Based on the previously reported errors for Zhang and Baghli, as long as our uncertainty ranges between their acceptable and validated reported errors, our model can be assumed as valid for temperature distribution.

C. Solvents' Pressurization

Fig. 7 shows the saturation versus experimental pressure-temperature curves of water. The curves are identical, meaning that assuming that the pressure inside the reactor is always equal to the saturation pressure is an accurate assumption.

The experimental versus simulation results of pressurization of the 300 mL water reactor is shown in Fig. 8, it is noticed that the error reaches a high percentage at t = 400 seconds, then it decreases to below 18% at the beginning of the steady state phase (t = 800 seconds), to reach a value less than 3% during the steady state phase.

The same procedure was followed for simulating the 750 mL water, 300 mL methanol and 300 mL ethanol heating. The results are shown in Table II.

IV. DISCUSSION AND CONCLUSIONS

The aim of this work was to compare the experimental and numerical results of the heat flow and pressurization inside a batch reactor for the hydrothermal liquefaction of biomass. Several experiments were conducted, and a replicating finite element model was built, and the results were satisfactory, and error percentages were acceptable. However, further treatment of the graphical results of the

temperature distribution in solvent heating experiments shows that for the inner thermocouple, where the maximum error occurs, the experimental and simulation results are convergent at the beginning of the heating phase and at the steady state phase. But there exists a transition phase in heating in which the curves diverge, leading to high error values for a short time. This error occurred in all the experiments at the moment where the solvent is supposed to start evaporating inside the reactor, where the experimental temperature curve lags behind the numerical temperature curve for 2-3 minutes, then it makes a jump to match the simulation curve again, and continue with it normally. This can be related to several factors, including, but not limited to:

- The isothermal domain interface used restricts the inner temperature of the liquid to be uniform, and does the same to the gas. But in reality, due to buoyancy forces, the upper part of the reactor should be a little bit hotter than its lower part.
- In the 300 mL setups, the thermocouple is not immersed in the liquid, so it will not measure the actual temperature of the solvent until the evaporated portion of the solvent starts appearing and correcting the thermocouple's reading.

Sharpening the accuracy of the results through future optimizations may include modelling the evaporation phenomenon inside the reactor using mass transport equations in COMSOL. This is supposed to eliminate a huge portion of the remaining difference between experimental and numerical results. A good future approach for continuing this work can be achieved through integrating this model with chemical reactions, in which previous works for hydrothermal liquefaction reactions can be replicated in the reactor experimentally, and modelled in COMSOL.

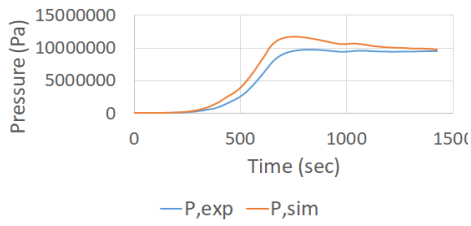

Figure 8. Experimental versus simulation values of the absolute pressure inside the reactor in 300 mL water heating.

REFERENCES

[1] Biomass - an overview. ScienceDirect Topics. Available at: https://www.sciencedirect.com/topics/earth-and-planetary-sciences/biomass (accessed Nov. 17, 2021).

[2] Gollakota, A. R. K., Kishore, N., & Gu, S. (2018). A review on hydrothermal liquefaction of biomass. *Renewable and Sustainable Energy Reviews, 81*, 1378-1392.

[3] *Hydrothermal liquefaction of biomass: Developments from batch to continuous process. Elsevier Enhanced Reader*. Available at: https://reader.elsevier.com/reader/sd/pii/S0960852414013911?token=782793AB73AEC287AC7674C82F6B54731D2836F196F89D5641382F9417EA59FBB596CFC014C86BA33D7E47BE0FDBA190&originRegion=eu-west-1&originCreation=20211117151624 (accessed Nov. 17, 2021).

[4] Zhang, Z. (2013). Computational fluid dynamics modeling of a continuous tubular hydrothermal liquefaction reactor (p. 76).

[5] Syed, A. H. (2013). *CFD modeling for direct liquefaction of biomass in hydrothermal media*. Available at: https://ntnuopen.ntnu.no/ntnu-xmlui/handle/11250/235235. (accessed Nov. 09, 2021).

[6] Chen, X., Tian, Z. F., van Eyk, P. J., Lewis, D., & Nathan, G. G. J. (2021). Numerical simulation of hydrothermal liquefaction of algae in a lab-scale coil reactor. *Experimental and Computational Multiphase Flow*. doi: 10.1007/s42757-020-0104-0.

[7] Valdez, P. J., Tocco, V. J., &.Savage, P. E. (2014). A general kinetic model for the hydrothermal liquefaction of microalgae. *Bioresource Technology, 163*, 123-127.

[8] Ideal Gases. MIT OpenCourseWare. Free Online Course Materials. Available at: https://ocw.mit.edu/high-school/physics/exam-prep/kinetic-theory-thermodynamics/ideal-gases/ (accessed Nov. 09, 2021).

[9] *Real Gases. Introductory Chemistry.* https://courses.lumenlearning.com/suny-introductory-chemistry/chapter/real-gases/ (accessed Nov. 09, 2021).

[10] *Isochoric Process - an overview. ScienceDirect Topics.* Available at: https://www.sciencedirect.com/topics/mathematics/isochoric-process (accessed Nov. 17, 2021).

[11] Harvey, P. D. (1982). Engineering Properties of Steel American. American Society for Metals.

[12] *COMSOL Documentation*. Available at: https://doc.comsol.com/5.6/docserver/#!TOC:/com.comsol.help.matlib/toc.xml:SOURCE:resource_tocfile_-650047560.html (accessed Nov. 17, 2021).

[13] *Thermal Insulation Characteristic - an overview. ScienceDirect Topics.* Available at: https://www.sciencedirect.com/topics/engineering/thermal-insulation-characteristic (accessed Nov. 10, 2021).

[14] Baghli, H., & Benyettou, M. (2006). Modeling and Simulation of Thermal Transfer in Batch Reactor. *Journal of Applied Sciences, 6*(6), 1327-1331.doi: 10.3923/jas.2006.1327.1331.

Mathematical Modelling of Photovoltaic Module in Matlab/Simulink Considering Ambient Conditions

Yacine Bouali[1], Khoukha Imarazene[2], El Madjid Berkouk[3]

[1,2]Power equipments Characterization and Diagnosis Laboratory (of USTHB), Algiers, Algeria, ybouali@usthb.dz[1], imarazen_k@yahoo.fr[2]
[3]Control Process Laboratory (of ENP), Algiers, Algeria, el_madjid.berkouk@g.enp.edu.dz

Abstract—**Modeling of the studied systems is a very important aspect in electrical engineering, which facilities the simulation and shows the different scenarios of the systems. This paper shows a step-by-step single diode photovoltaics model under Matlab/Simulink, where two models are shown for the cell temperature, the first is not affected by the wind speed and ambient temperature, and the second is affected by them.**

Keywords – photovoltaics module, Matlab/Simulink, ambient conditions, modeling

I. INTRODUCTION

In the last decade, renewable energy plays an important role in home and industrial applications. In Micro-Grid, different renewable energy sources are used, especially the photovoltaics (PV) systems, other applications of PV systems in electric vehicles, water pumps, and communication systems are well known. The main component in a PV system is the PV module, which needs an approximate model to the real behavior of PV-panel for simulation purposes.

For a better understanding of PV-module working, different mathematical models are suggested in the literature based on the single or double diode model [1-4]. The output power of a PV panel is affected by two main factors the cell temperature and the irradiation.

In this paper, a step-by-step photovoltaics module Simulation under Matlab/Simulink is carried out, in the second section the single diode mathematical model of the photovoltaics module is presented, and their Simulink simulation in the third section to finish with the results and conclusion.

II. MATHEMATICAL MODELING OF PHOTOVOLTAIC MODULE

The photovoltaic module consists of photovoltaic cells connected in series, these cells are a PN junction. The most used semiconductor for cell fabrication is silicon [5]. The equivalent circuit of the photovoltaic cell is illustrated in Fig. 1.

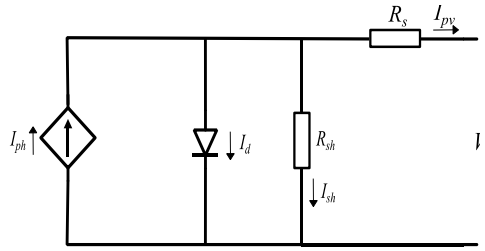

Figure 1. Equivalent circuit of PV cell.

By applying Kirchhoff's law to this circuit, the output current I_{pv} in (1), where the I_{ph} is the photocurrent in (2), I_d is the current pass through the diode in (3) and I_{sh} the current pass through the shunt resistance R_{sh}.

$$I = I_{ph} - I_d - I_{sh} \ . \qquad (1)$$

The I_{pv} in (2), where it's affected by the ratio of illumination and the difference between the cell and reference temperature.

$$I_{ph} = \frac{G}{G_r}\left(I_{sc} + \alpha\left(T_{cell} - T_{ref}\right)\right), \quad (2)$$

where: G is the illumination in (W/m^2), Gr is the reference irradiation equal to 1000 W/m2, I_{sc} is the short current of the PV cell, α is temperature coefficient of I_{sc}, and T_{ref} =25°C.

The Diode formed by a PN junction mathematically expressed in (3), where V_t is thermal voltage, I_0 is the saturation current presented in (5) and I_{rs} the reverse saturation current in (6).

$$I_d = I_0\left(e^{\frac{\left(V_{pv}+I_{pv}R_s\right)}{nV_tN_s}} - 1\right), \quad (3)$$

$$V_t = \frac{kT_{cell}}{q}, \quad (4)$$

$$I_0 = I_{rs}\left(\frac{T_{cell}}{T_{ref}}\right)^3 e^{\left(\frac{qE_{g0}}{kn}\left(\frac{1}{T_{cell}} - \frac{1}{T_{ref}}\right)\right)}, \quad (5)$$

$$I_{rs} = \frac{I_{sc}}{\left(e^{\frac{V_{oc}}{nV_tN_s}} - 1\right)}, \quad (6)$$

where, q: electron charge, $=1.6\times10^{-19}C$, V_{oc}: open circuit voltage (V), N_s: number of cells connected in series, n: the ideality factor of the diode, k : Boltzmann's constant = $1.3805\times10^{-23}\,J/K$, E_{g0}: band gap energy of the semiconductor.

$$I_{sh} = \frac{V + IR_s}{R_{sh}}. \quad (7)$$

In the literature, the previous equations are considered the cell temperature is the same as ambient temperature. However, in this paper, two studies case are presented, where in the first case the cell temperature is equal to the ambient temperature and in the second case the cell temperature effected by the wind speed and the illumination variation, in this case, the T_{cell} is presented in (8) [6].

$$T_{cell} = 1.14\left(T - T_{ref}\right) + \\ +0.0175\left(G - 300\right) - k_r\omega + 30, \quad (8)$$

where ω is the wind speed (m/s), and the coefficient k_r is given in Table I for each PV technology [7].

TABLE I. COEFFICIENT K_R FOR EACH PV TECHNOLOGY.

PV Technology	K_r
Monocrystalline	1.509
Polycrystalline	1.468
Thin-film	1.450

III. SIMULATION OF PV MODULE USING SIMULINK

The equations presented in the previous section are simulated under Matlab/Simulink 2021a using only basic blocks. Each equation is constructed under a subsystem where constant, gain, in, out, product, subsystem, add, divide, math function, ramp, and to workspace blocks, are used. In Fig. 2 the model of the PV module are shown where the addition of three signal I_{ph}, I_d and I_{sh} are carried out to get the output I_{pv} and this output is the same input for diode and shunt current subsystem, which make an algebraic loop error, is one of the most known problems in the PV simulation under Matlab/Simulink. However, to avoid this error one of these solutions can be used: add a Memory Block or Unit Delay Block at the output current I_{pv}. However, in this simulation, to avoid this problem a small value ($\frac{V_{oc}}{N_s}$) is used in the ramp slope which represent the value of V_{pv}.

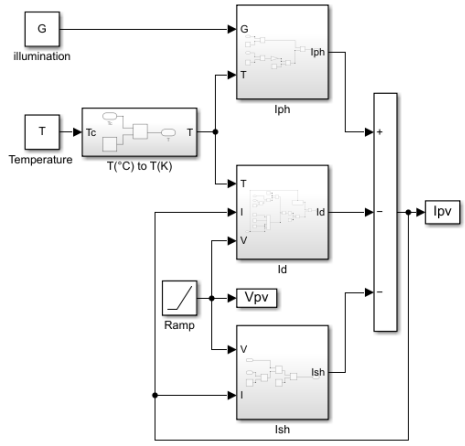

Figure 2. Ipv Simulink model.

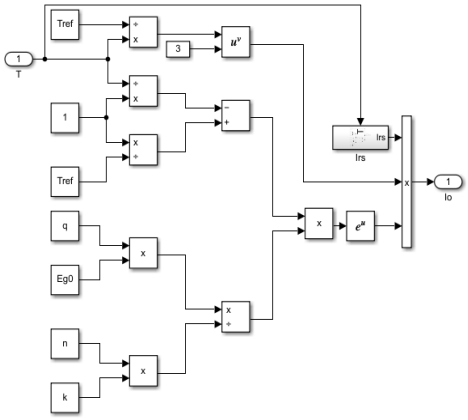

Figure 5. The model under saturation current subsystem.

The Fig. 3, shows the model under the subsystem of I_{ph} . The I_d , I_0 , and I_{rs} subsystems are shown in Figs. 4, 5, and 6 respectively. And the shunt current subsystem in Fig. 7.

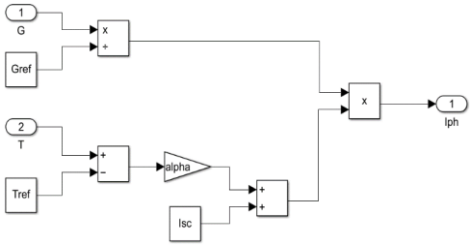

Figure 3. The model of Iph subsystem.

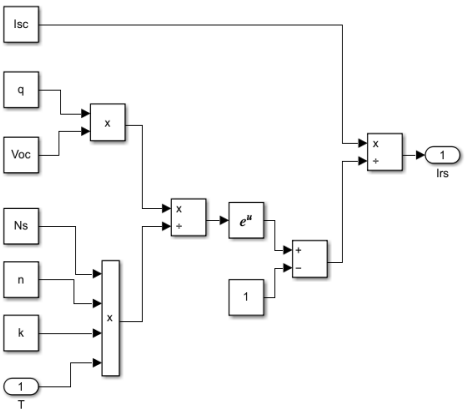

Figure 6. The model under reverse saturation current subsystem.

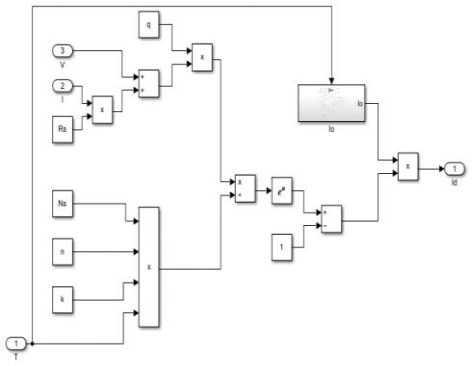

Figure 4. The model of Id subsystem.

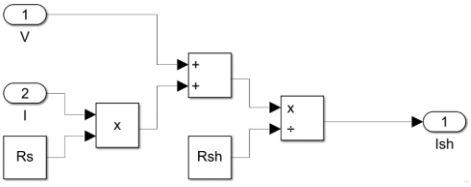

Figure 7. The model under Ish subsystem.

IV. RESUSLTS OF SIMUALTION

The parameters of the PV module used in this simulation are presented in Table II.

TABLE II. THE PARAMETERS OF PV MODULE.

Rated power (Pmp)	100 W
Open circuit voltage (Voc)	13.3 V
Short circuit current (Isc)	9.8 A
Total number of cells in series (Ns)	20
Total number of cells in parallel (Np)	1
Series resistor (Rs)	0.13128 Ω
Shunt resistor (Rsh)	379.3044 Ω
Temperature coefficient of Isc (%/°C)	0.0017
Diode ideality factor (n)	0.95077
Band gap energy of the semiconductor (Eg0)	1.6 eV

In order to simulate the model of this PV, the fixed-step solver ode8 (Dormand-Prince) is chosen with a step size equal to 10^{-4}.

In the first case, the cell temperature is equal to ambient temperature. The results of I-V and P-V for this case are presented in Fig. 8 and Fig. 9 respectively for a constant T=25°C and G variable, and for T variable and G=1000 (W/m^2) are presented in Fig. 10, and Fig. 11.

In the second case, the cell temperature presented in (8) with a monocrystalline PV technology are chosen. The variation of wind speed ω, illumination, and ambient temperature are presented in Table III, the variation of I-V and P-V of the PV panel in this case are shown in Figs. 12 and 13 for the first test, and in Figs.14 and 15 for the second test.

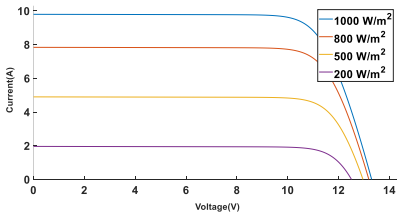

Figure 8. Current-Voltage for different irradiance.

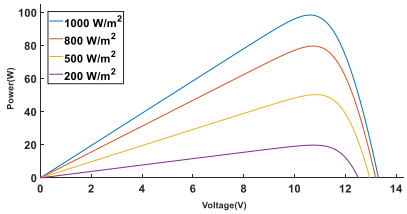

Figure 9. Power-voltage for different irradiance.

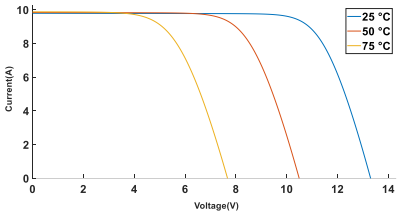

Figure 10. Current-voltage for different temperature.

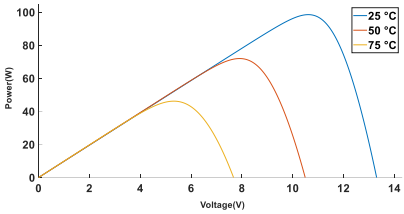

Figure 11. Power-voltage for different temperature.

TABLE III. PARAMETERS FOR EACH TEST.

Test	G(W/m^2)	ω(m/s)	T(°C)
01	1000	11.4314	25
	500		
02	1000	7.5	50
	500		

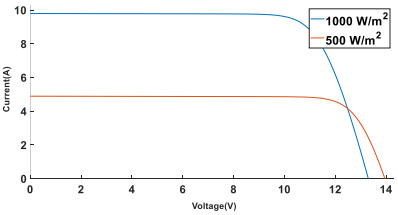

Figure 12. Current-Voltage for the first test.

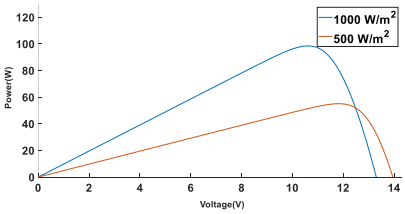

Figure 13. Power-Voltage for the first test.

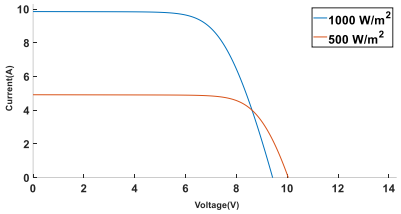

Figure 14. Current-Voltage for the second test.

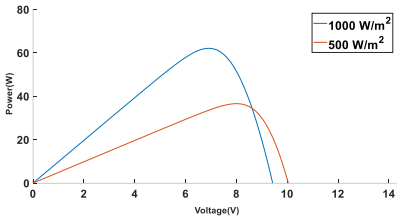

Figure 15. Power-Voltage for the second test.

In the first case, where the cell temperature is equal to the ambient temperature, the short-circuit current is affected by the variation of irradiation with a constant temperature. On the other hand, if the irradiation is constant and the temperature is not fixed, the open-circuit voltage of the PV panel decreased if the temperature increased.

In the second case, where the cell temperature is affected by the wind speed and irradiation. The open-circuit voltage and short circuit current are always affected by the temperature and irradiation, respectively. However, a small variation of open-circuit voltage is remarked compared with the first case when the wind speed and temperature change. This indicates that the second case is more approach to the real PV model where the cell temperature is changed if the wind speed, irradiation, and ambient temperature are changed.

V. CONCLUSION

This study investigated the modeling and simulation of a single diode photovoltaic panel. With the purpose of studying how wind speed, irradiation, and ambient temperature affect cell temperature in a step-by-step simulation under Matlab/Simulink.

The obtained results indicate that the provided model, which takes in consideration wind speed, irradiation, and ambient temperature, is more approach to the real photovoltaic model.

REFERENCE

[1] Pandiarajan, N., & Muthu, R. (2011). Mathematical modeling of photovoltaic module with Simulink. In *2011 1st International Conference on Electrical Energy Systems* (pp. 258-263). IEEE.

[2] Nguyen, X. H., & Nguyen, M. P. (2015). Mathematical modeling of photovoltaic cell/module/arrays with tags in Matlab/Simulink. *Environmental Systems Research*, *4*(1), 1-13.

[3] Singh, O., & Rajput, S. K. (2016). Mathematical modelling and simulation of solar photovoltaic array system. In *2016 International Conference on Research Advances in Integrated Navigation Systems (RAINS)* (pp. 1-5). IEEE.

[4] Yadav, N., & Sambariya, D. K. (2018, July). Mathematical Modelling and Simulation of Photovoltaic Module Using MATLAB/SIMULINK. In *2018 9th International Conference on Computing, Communication and Networking Technologies (ICCCNT)* (pp. 1-6). IEEE.

[5] Luceño-Sánchez, J. A., Díez-Pascual, A. M., & Peña Capilla, R. (2019). Materials for photovoltaics: State of art and recent developments. *International journal of molecular sciences*, *20*(4), 976.

[6] Ayaz, R., Nakir, I., & Tanrioven, M. (2014). An improved Matlab-Simulink model of PV module considering ambient conditions. *International Journal of Photoenergy*, 2014.

[7] TamizhMani, G., Ji, L., Tang, Y., Petacci, L., & Osterwald, C. (2003, June). Photovoltaic module thermal/wind performance: long-term monitoring and model development for energy rating. In *NCPV and Solar Program Review Meeting Proceedings*, (pp. 24-26), Denver, Colorado (CD-ROM).

Experimental Investigation and Heat Transfer Analysis of A Brazed Plate Heat Exchanger

İbrahim Halil Yılmaz[1]

[1]Mechanical Engineering Department, Adana Alparslan Turkes Science and Technology University, Adana, Turkey, iyilmaz@atu.edu.tr

Abstract—**This study involves an experimental study and heat transfer analysis of a brazed plate heat exchanger (BPHE) to propose a procedure for its sizing or selection. The BPHE was selected from the catalog of a manufacturer and an experimental setup was installed to verify the developed thermal model under various operating conditions. Mineral oil was tested in the setup. The model was solved using Engineering Equation Solver. Results were compared with those of the experiments and good agreement was obtained i.e. the deviation <0.7%. The model reported in this study is expected to guide thermal engineers for the selection or design of BPHEs.**

Keywords – brazed plate heat exchanger, heat transfer analysis, experimental study

I. INTRODUCTION

Heat exchangers are widely used devices for mainly heating, cooling, and heat recovery processes in industrial applications from microchannel cooling to nuclear power plants. In recent years, there is has been an increase in the usage of gasketed plate heat exchangers (PHEs) particularly in chemical and food industries due to suitability in hygienic applications, ease of cleaning, and thermal control. Furthermore, PHEs exhibit excellent heat transfer characteristics which allow more compact designs and have flexibility in modifying their size (or capacity) by simply mounting/dismounting the plates used.

Over the past 30 years, it has become possible to manufacture brazed plate heat exchangers (BPHEs). These are manufactured by placing a copper or nickel foil in between each of the stainless steel plates and placing the pile of plates in a furnace just above the melting temperature of copper. The BPHE is in principle constructed as a package of corrugated channel plates between the front and rear cover-plate packages shown in Fig. 1. The cover-plate packages consist of sealing plates, blind rings and cover plates. Certain BPHEs are available with different types of channel plates where the herringbone pattern varies. The benefit of different herringbone patterns is that the hydraulic and thermal characteristics of the BPHE can be modified.

The design of PHEs is highly specialized so that the variety of the designs available for the plates and arrangements must be selected for a specific purpose. Manufacturers have developed their software programs for thermal design, selection and rating the PHEs that they market. Since most of the correlations developed for heat transfer and pressure drop cannot be generalized for every PHE to give a high degree of prediction [1]. The prediction method for analyzing the heat transfer relies on experimental data particular to a specific surface profile. Although some design methods have been reported in the literature [2], there is no rigorous method to be applied to any PHE configuration. However, the sizing of the PHE for a given duty can be predicted by the

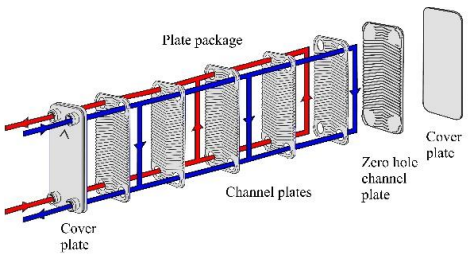

Figure 1. Exploded view of the BPHE.

ISBN: 978-86-80593-73-9

proposed correlations to suit preliminary calculations.

Most experimental investigations of PHEs focused on studying the influence of geometrical parameters regarding the pattern of chevron corrugation including corrugation profile, chevron angle, corrugation pitch, and plate spacing on heat transfer and pressure drop. Most literature studied the effect of the geometrical parameters on PHEs and the correlations for single-phase heat transfer and pressure drop were summarized in [1]. The investigation of chevron angle on the thermal and hydraulic performance of BPHEs depicted that by increasing chevron angle, the thermal performance, heat transfer coefficient, and friction factor increases [3]. The chevron angle is the major parameter influencing the performance of PHE due to the change in flow structure.

Computational fluid dynamics have been adopted by several researchers to describe the flow and heat transfer mechanisms inside corrugation plates for performance improvement. Most of the researchers numerically studied BPHEs by focusing on unitary cell [4], which is repeating part of heat exchanger with two inlets and outlets however the exclusions of the fluid domain exclude geometry around the port, contact points, and brazing joints upon simulation is unable to fully address the actual performance of BPHEs [5].

This study presents a heat transfer model of a BPHE for the determination of the heat transfer rate and outlet temperatures of the hot and cold fluids for prescribed fluid mass flow rates and inlet temperatures. An experimental setup was installed for this purpose and the results of the heat transfer model were compared with those of experiments.

II. Material and Method

A. *Thermal Analysis of The Brazed Plate Heat Exchanger*

A wide variety of corrugation types and flow arrangements is available in practical applications for PHEs. Although many commercial plates have a different surface profile, most modern PHEs are chevron or herringbone in shape as shown in Fig. 2. In the chevron type, one plate is clamped with adjacent which is reversed 180° thus the corrugated pattern maintains numerous contact points between the plates in which the fluid flows. The

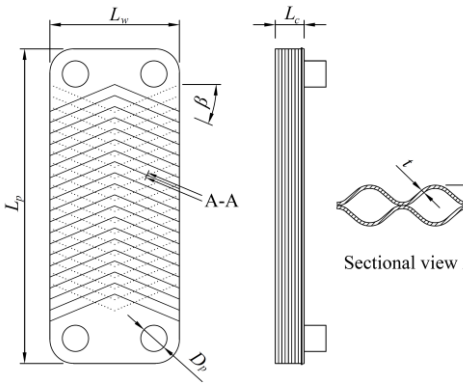

Figure 2. Schematic view of the plate.

effective heat transfer area of the PHE is enlarged by the corrugations. The increase in the surface area is expressed by the enlargement factor, φ which is defined as the ratio of the developed length to the projected length.

The enlargement factor is expressed by the actual effective area specified by the manufacturer, A_1 to the projected plate area, A_{1p}:

$$\varphi = \frac{A_1}{A_{1p}}. \tag{1}$$

A_1 and A_{1p} can be estimated by using the relations below. For the thermal analysis, the constructional data of the proposed BPHE taken from the catalog of SWEP (B10TH model) are provided by the manufacturer [6] as given in Table I.

$$A_1 = \frac{A_e}{N_e}, \tag{2}$$

$$A_{1p} = L_p L_w. \tag{3}$$

The cross-section of a corrugation surface being very complex, flow between two adjacent plates is defined by the mean channel spacing, b shown in Fig. 2.

$$b = p - t, \tag{4}$$

where p is the plate pitch, and t is the plate thickness.

TABLE I. TECHNICAL SPECIFICATIONS OF THE BPHE.

Plate material	AISI 316
Effective flow plate distance, L_p	0.243 m
Effective channel width, L_w	0.119 m
Port diameter, D_p	0.024 m
Plate thickness, t	0.0004 m
Corrugation depth, b	0.00224 m
Total effective area, A_e	0.248 m^2
Enlargement factor, φ	1.19
Chevron angle, β	23°
Number of plates, N_t	10
Effective number of plates, N_e	8
Number of channels on (hot /cold)	4/5
Thermal conductivity of the plate, k_w	15.5 W/m°C

B. Effectiveness-NTU Method

When the inlet or outlet temperatures of the fluid streams are not known, the method of the effectiveness-NTU may be used to avoid a trial-and-error procedure. When the type and size of the heat exchanger are specified, the determination of the heat transfer rate and the outlet temperatures of the hot and cold fluids for prescribed fluid mass flow rates and inlet temperatures can be estimated by using this method. The heat transfer surface area of the heat exchanger, in this case, is known, but the outlet temperatures are not. where the task is to determine the heat transfer performance of a specified heat exchanger. However, in transient system analysis, the heat transfer rate, and the outlet temperatures of the hot and cold fluids will change instantly thus it is necessary to make an iteration to predict them.

The effectiveness-NTU method is based on a dimensionless parameter called the heat transfer effectiveness ε, defined as

$$\varepsilon = \frac{\dot{Q}}{\dot{Q}_{\max}}, \tag{5}$$

which is the ratio of actual heat transfer rate in a heat exchanger $\dot{Q}$ to the thermodynamically limited maximum possible heat transfer rate $\dot{Q}_{\max}$ if an infinite heat transfer surface area were available in a counter flow heat exchanger.

The maximum possible heat transfer rate in a heat exchanger is

$$\dot{Q}_{\max} = C_{\min}\left(T_{h,in} - T_{c,in}\right), \tag{6}$$

where $C_{\min}$ is the smaller of $C_h = \dot{m}_h c_{p,h}$ and $C_c = \dot{m}_c c_{p,c}$. Here, $\dot{m}_h$ and $\dot{m}_c$ are the mass flow rates of hot and cold fluids, and $c_{p,h}$ and $c_{p,c}$ are the specific heats of hot and cold fluids, respectively.

The effectiveness of a heat exchanger depends on the geometry of the heat exchanger as well as the flow arrangement. For counter-flow, ε is expressed as [7]:

$$\varepsilon = \frac{\exp\left[\left(1-c\right)\mathrm{NTU}\right]-1}{\exp\left[\left(1-c\right)\mathrm{NTU}\right]-c}, \tag{7}$$

where c and NTU are the dimensionless quantities called the capacity ratio, the number of transfer units, respectively.

$$c = \frac{C_{\min}}{C_{\max}}, \tag{8}$$

$$\mathrm{NTU} = \frac{UA_e}{C_{\min}}. \tag{9}$$

The overall heat transfer coefficient, U is estimated by using the procedure proposed below:

The flow regime between the plates is characterized by Reynolds number (Re) which is expressed based on channel mass velocity and the hydraulic diameter of the channel.

$$\mathrm{Re} = \frac{G_c D_h}{\mu}. \tag{10}$$

The hydraulic diameter of the channel is defined as:

$$D_h = \frac{4bL_w}{2\left(b + L_w\varphi\right)}. \tag{11}$$

The channel mass velocity is given by

$$G_c = \frac{\dot{m}}{N_{cp} A_c}. \quad (12)$$

N_{cp} is the number of channels per pass and is obtained using:

$$N_{cp} = \frac{N_t - 1}{2N_p}, \quad (13)$$

where N_t is the total number of plates, and N_p is the number of passes. The term "pass" in PHE refers to a group of channels in which the flow is in the same direction. Fig. 1 demonstrates also the flow arrangement of the BPHE (single pass U-type) employed in the experimental setup.

The conventional approach for the estimation of the convection heat transfer coefficient between flow passages is employed by some specific correlations that are used for taking into account the effects of the different geometric parameters of the corrugated profiles. Although generalized correlations for heat transfer and pressure drop predictions are not quite well developed, there are still open questions concerning the choice of the most appropriate models. However, a few researches are proposed for more elaborate calculations [8, 9].

Reference [10] proposed the following Nusselt number correlation for herringbone plates in the range of $1 \le \mathrm{Re} \le 10^4$, $20° \le \beta \le 62°$.

$$\mathrm{Nu} = \left[\mathrm{Nu}_l^3 + \mathrm{Nu}_t^3 \right]^{1/3} \mathrm{Pr}^{1/3} \left(\frac{\mu}{\mu_w} \right)^{0.17}, \quad (14)$$

$$\mathrm{Nu}_l = 3.65 \beta^{-0.455} \varphi^{0.661} \mathrm{Re}^{0.339}, \quad (15)$$

$$\mathrm{Nu}_t = 12.6 \beta^{-1.142} \varphi^{1-m} \mathrm{Re}^{m}, \quad (16)$$

where $m = 0.646 + 0.0011\beta$.

The convection heat transfer coefficient, h can be obtained by using

$$h = \mathrm{Nu} \frac{k}{D_h}. \quad (17)$$

The overall heat transfer coefficient for a clean surface is:

$$\frac{1}{U} = \frac{1}{h_h} + \frac{1}{h_c} + \frac{t}{k_w}, \quad (18)$$

where h and c stand for hot and cold streams, respectively.

The working fluid used in both sides of the BPHE was selected to be Renolin therm 320 [11] as heat transfer fluid (HTF) to easily control the temperature and make the energy analyses precisely. The thermophysical properties as a function of temperature, ρ (density, kg/m^3), c_p (specific heat, J/kg°C), k (thermal conductivity, W/m°C), ν (kinematic viscosity, mm^2/s), are given as :

$$\rho = 880 - 0.6495 T(°C), \quad (19)$$

$$c_p = 1864 + 4.289 T(°C), \quad (20)$$

$$k = 0.1344 - 0.00007235 T(°C), \quad (21)$$

$$\nu = \exp\left(\frac{920}{T(°C) + 102.83} - 2.665 \right). \quad (22)$$

The fluid properties are evaluated at bulk temperatures, $T_{bulk} = (T_{in} + T_{out})/2$ i.e. average of the inlet and outlet temperatures, for the cold side, hot side and the wall of the BPHE.

The outlet temperatures of the hot and the cold fluid streams are determined to be:

$$T_{h,out} = T_{h,in} - \frac{\dot{Q}}{C_h}, \quad (23)$$

$$T_{c,out} = T_{c,in} + \frac{\dot{Q}}{C_c}. \quad (24)$$

The developed equations were coded in Engineering Equation Solver Professional V8.581 using its macro tool and solved simultaneously according to the algorithm given in Fig. 3.

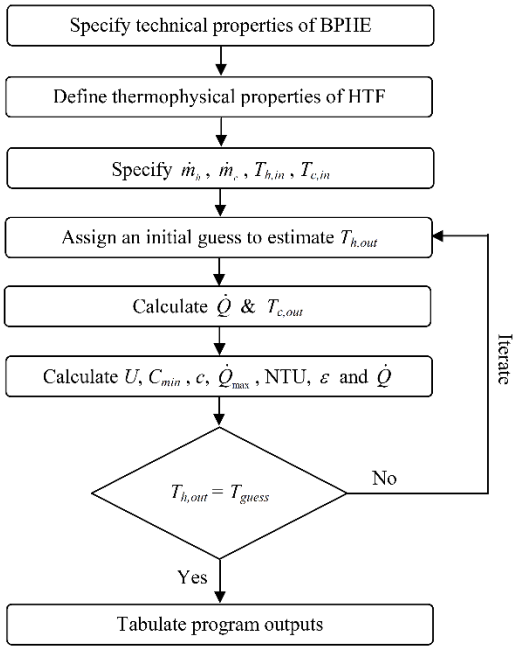

Figure 3. Flowchart for BPHE simulation.

C. Experimental Setup and Measurements

An experimental setup was installed for verifying the presented heat transfer model as shown in Fig. 4. The test setup is composed of two loops for the hot and cold sides where basically consist of a BPHE, temperature-controlled electric heaters (TCEHs), frequency-controlled gear pumps (GPs), thermal expansion tanks (TETs) and measuring instruments for physical quantities. A frequency-controlled gear pump [12] was used to adjust the flow rate of the HTF. The TCEH was controlled by PID (Proportional Integral Derivative) controllers [13,14]. When the operating temperature of the hot or cold side fell below the specified load-temperature, the TCEHs were activated automatically to increase the return-temperature of the HTF to the load-temperature.

The temperature measurements in the experimental setup were performed by the resistance temperature detectors (Pt100, Class A) connected with two leads [15]. The

Figure 4. Experimental setup.

temperature-dependent uncertainty of the detectors was designated by the relation of $\pm(0.15 + 0.002T)$ °C and calibrated according to the standard of IEC751:1983 (BS EN 60751:1996) by the manufacturer. The mass flow rate of the HTF was measured by a Coriolis flowmeter having an accuracy of ±0.1% with a repeatability of less than 0.05% [16]. During the experimental tests, the signal data of the measurement devices were collected by 24-bit USB-2416 [17] and USB-TEMP [18], which are respectively highly-accurate voltage and temperature processing data acquisition devices, and managed by an interface software program (TracerDAQ Pro) to process data by virtual graphing and data logging.

III. Results and Discussion

The model outputs for the BPHE were determined for different mass flow rates and operating temperatures as shown in Table II.

Fig. 5 shows the comparison of model results with experimental results. It is seen that the model results for the outlet temperature of the cold stream agree accurately with those of the given experimental parameters.

This validation is very significant for predicting the outlet temperatures when the BPHE operates different working conditions. This is also crucial in terms of temperature and flow rate control of such systems when the operation parameters are changed. Additionally, it plays an important role in the design stage for the selection of BPHE with proper size and can aid in sizing the capacity of the TCEH or a heating system for system design.

TABLE II. Model prediction for fluid outlet temperatures of the BPHE.

$\dot{m}_h$ **kg/h**	$\dot{m}_c$ **kg/h**	**Experimental data in °C**			
		$T_{h,i}$	$T_{h,out}$	$T_{c,i}$	$T_{c,out}$
1034	328	147.3	143.1	126.4	138.7
1050	496	134.9	131.1	119.7	127.2
1062	501	124.9	120.9	108.9	116.5
1048	652	136.2	132.3	122.7	128.4
1046	807	138.7	134.5	125.9	130.7
1032	1000	150.5	143.3	129.2	136.9

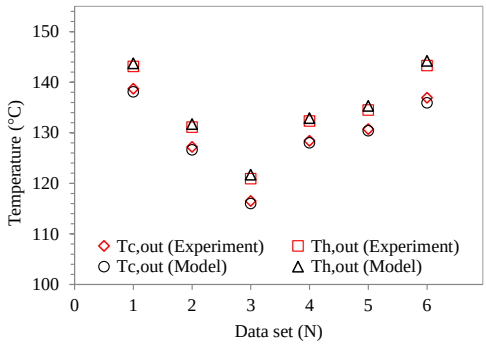

Figure 5. Comparison of results.

IV. CONCLUSIONS

A detailed heat transfer analysis of the BPHE and its benchmark with the experimental results was performed to specify its size or selection under the prescribed thermal load and inlet temperatures. The heat transfer area of the BPHE should be selected properly to meet the thermal load of a process heat application otherwise the system performance would not reach the highest levels or affect the temperature control of the process unfavorably. Researchers should develop generalized correlations for heat transfer and pressure drop predictions of PHEs. There are still open questions concerning the choice of the most appropriate models in the literature. For this reason, manufacturer catalogs or their PHE selection software may not be sufficient to select a PHE for a specific duty due to involving hidden heat transfer analysis and limited HTF library.

REFERENCES

[1] Kakac, S., Liu, H., & Pramuanjaroenkij, A. (2002). Heat exchangers: selection, rating, and thermal design. CRC press.

[2] Palm, B. R., & Claesson, J. (2005, January). Plate Heat Exchangers: Calculation Methods for Single-and Two-Phase Flow (Keynote). In *International Conference on Nanochannels, Microchannels, and Minichannels* (Vol. 41855, pp. 103-113).

[3] Savostin, A. F., & Tikhonov, A. M. (1970). Investigation of the Characteristics of Plate Type Heating Surfaces, Therm.

[4] Ciofalo, M., Stasiek, J., & Collins, M. W. (1996). Investigation of flow and heat transfer in corrugated passages—II. Numerical simulations. *International Journal of Heat and Mass Transfer*, *39*(1), 165-192.

[5] Han, W., Saleh, K., Aute, V., Ding, G., Hwang, Y., & Radermacher, R. (2011). Numerical simulation and optimization of single-phase turbulent flow in chevron-type plate heat exchanger with sinusoidal corrugations. *HVAC&R Research*, *17*(2), 186-197.

[6] Technical datasheet of B10TH. Available at http://www.swep.net/.

[7] Kays, W. M., & London, A. L. (1984). Compact heat exchangers.

[8] Heavner, R. L., Kumar, H., Wanniarachchi AS. (1993). Performance of an Industrial Heat Exchanger: Effect of Chevron Angle. In: *AIChE Symposium Series*, New York.

[9] Muley, A., & Manglik, R. M. (1999). Experimental Study of Turbulent Flow Heat Transfer and Pressure Drop in a Plate Heat Exchanger with Chevron Plates, Journal of Heat Transfer, 121,110–117.

[10] Wanniarachchi, A. S., Ratnam, U., Tilton, B. E., & Dutta-Roy, K. (1995). Approximate Correlations for Chevron-Type Plate Heat Exchangers. In *30th National Heat Transfer Conference*. New York: ASME.

[11] Renolin Therm 320. Available at https://www.fuchs.com/de/en/product/product/127555-renolin-therm-320/.

[12] *Technical properties of YKF-1" internal eccentric gear pump*. Available at: http://www.yildizpompa.com/wp-content/uploads/2017/11/YKF-1%C2%BD.pdf.

[13] Yilmaz, I. H., Hayta, H., Yumrutaş, R., & Söylemez, M. S. (2018). Performance testing of a parabolic trough collector array for a small-scale process heat application. *Journal of Thermal Science and Technology*, *38*(1), 43-53.

[14] Yilmaz, I. H., & Söylemez, M. S. (2020). A novel thermal analysis for cooking process in bulgur production: design considerations, energy efficiency and wastewater diminution for industrial processes. *Journal of Thermal Science and Technology*, *40*(1), 113-129.

[15] *Pt100 Resistance thermometer*. Available at: http://www.ordel.com.tr/en/urun/or60.

[16] Krohne (2019) *Optimass 6000 technical datasheet*. Available at: https://cdn.krohne.com/fileadmin/media-lounge/files-marine/Downloads_pdf/TD_OPTIMASS_6000.pdf.

[17] USB-2416 User's Guide. Available at: https://www.mccdaq.com/pdfs/manuals/USB-2416.pdf.

[18] USB-TEMP User's Guide. Available at: https://www.mccdaq.com/pdfs/manuals/USB-TEMP.pdf.

New Approach to Analyze Homogeneity, Symmetry and Penumbra Quality of Photon Beam Dosimetry

Mohamed Bencheikh[1], Yassine Benkhouya[2]

[1]Physics Department, Faculty of Sciences and Technologies Mohammedia, Hassan II University of Casablanca, Mohammedia, Morocco, bc.mohamed@gmail.com
[2]Department of Radiotherapy, Al Kawtar Clinic, Fez, Morocco, benkhouyassine@gmail.com

Abstract—**The objective of this study is to analyze the homogeneity, symmetry and penumbra of photon beam dosimetry for improving the external photon beam radiotherapy quality. The dose distributions were expressed in dose profiles at a depth of dose maximum. The measurements of dose profiles were done as a function of irradiation field size with an uncertainty of 2% as recommended by IAEA protocols but homogeneity and penumbra was determined with an uncertainty under to 1.5%. Homogeneity, symmetry and penumbra are investigated based on dose profiles measurements for 6 MV photon beam. For small field size, the dose gradient is very high than large field size in homogeneity region but the symmetry is slightly conserved for small field size but for large field size the dose profiles is symmetric by 83% (deviation of 17%). The penumbra is characterized by sharp gradient of dose for small filed size than large field size. For high radiotherapy quality, these parameters should be improved in perspective.**

Keywords - homogeneity, symmetry, radiotherapy, dosimetry, Linac

I. INTRODUCTION

The quality of the photon beam in external radiotherapy treatment of cancer is essential and necessary for enhancing the radiotherapy efficiency in cancer medicine. The penumbra has a major impact on obtaining uniformity of isodose distributions in radiation therapy [1]. The homogeneity represents the flattened region in dose profiles due to flattening filter [2]. Our study is in framework of quality study of radiation therapy. Many researches were done to improve the use of these radiation sources for high radiation therapy efficiency by working on isotopes production [3], by working on beam filtration system quality [4, 5], by working on removing flattening filter from linac head configuration [6,7] and by working on material and geometry of flattening filter [8, 9] with keeping the quality of photon beam as high as possible [10].

The dose profile is a parameter to quantify the quality of photon beam and allows us to check out the beam homogeneity, beam symmetry and beam penumbra. In this study, we focus on homogeny and penumbra of 6 MV photon beam produced by Varian Clinac 2100. The measurements of dose profiles were performed with 2% of uncertainty using a PTW ionization chamber.

This study aims to characterize the beam homogeneity and penumbra by determination of coefficients for quantifying these characterizations. This law allows us to predict the dosimetric behavior of photon beam while dose determination by treatment planning systems. It is a mathematical formula that forms an empiric law for dose evaluation at the skin of patient.

II. MATERIALS AND METHODS

A. Dose Measurements

The dose profiles are measured for 6 MV photon beam produced by Varian Clinac 2100,

all dose profiles were performed using a motorized scanning system (ionization chamber PTW) for many irradiation field sizes at a depth of 1.5 cm in water phantom. The uncertainty of measurements is 2% and it is under the uncertainty recommended by SSRMP [11]. The source to surface distance (SSD) is fixed at 100 cm for all of dose profiles measurements.

The uncertainty of dose profiles measurements includes the uncertainty of experimentation and also the uncertainty of measurement device. The nature of water is pure water that put in a tank of volume of $40\times40\times40$ cm^3.

B. Dose Profile Study

The PDD is a parameter recommended by IAEA for evaluating the quality of radiation beam for clinical usage [12, 13]. The dose profile was determined according to the following formula:

$$Dose\ profile(SSD;d;x)=\frac{D(SSD;d;x)}{D(SSD;d)}\times100\ , \quad (1)$$

where:

D: the measured dose

SSD: the source to surface distance

d: depth in water phantom

x: off-axis distance

The dose profile curve is presented in Fig. 1 as a function of depth for the photon beam energy of 6 MV, for the irradiation field size of 10×10 cm^2 and for the SSD of 100 cm.

Dose profile curve is formed by three regions: homogeneity and symmetry region, penumbra region and umbra region (Fig. 1). In this study, we are interested in homogeneity and symmetry region and penumbra region.

III. RESULTS AND DISCUSSION

This study is based on experimental data measured in radiotherapy department of Al Kawtar clinic center; the photon beam energy of 6 MV produced by Varian Clinac 2100.

A. Dose Profiles

The dose profiles were measured as a function of field size and a depth in water phantom for photon beam energy of 6 MV produced by Varian Clinac 2100. Fig. 2 shows the dose profiles at a depth of 1.5 cm in water phantom for photon beam energy of 6 MV for many irradiation field sizes.

For showing the homogeneity and penumbra beam dependence on irradiation field size, we have expressed beam dose profiles as a function of normalized off-axis distance. This normalization of off-axis distance is introduced as quotient of off-axis distance x to side of irradiation square field a_d. The normalized off-axis distance $N_{off\text{-}axis}$ is determined according to the following formula:

$$N_{Off-axis}=\frac{2x}{a_d}. \quad (2)$$

Fig. 3 shows the dose profiles as a function of normalized off-axis distance $N_{off\text{-}axis}$ for many irradiation field sizes.

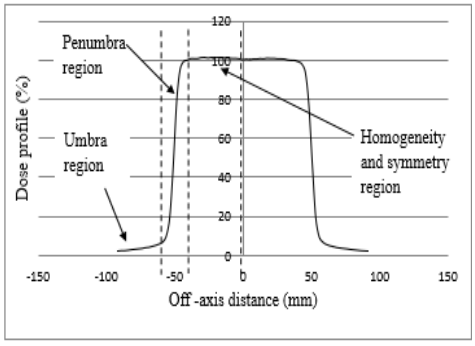

Figure 1. PDD variation as a function of depth in water phantom.

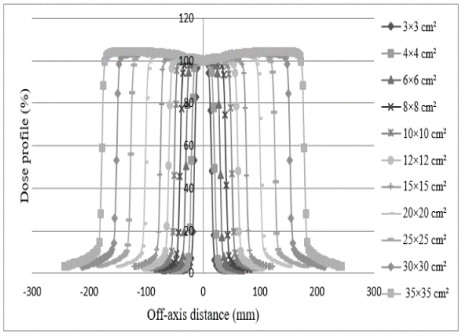

Figure 2. Dose profiles as a function of off-axis distance.

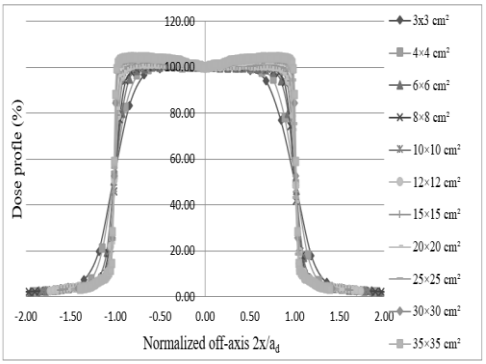

Figure 3. Dose profiles as a function of normalized off-axis distance.

From Fig. 3, it is clear that homogeneity and penumbra depend on the irradiation field size. The question how the homogeneity and penumbra vary with irradiation field size?

B. Homogeneity, Symmetry and Penumbra Study

For studying homogeneity and penumbra of photon beam, we have processed to determine five coefficients: three for homogeneity study, one for symmetry and one for penumbra study. These coefficients are called investigated coefficient IC and it expressed the quotient of relative dose at normalized off-axis distance R_1 to relative dose at normalized off-axis distance R_2 where these coefficients are determined as the following formula:

$$IC = \frac{Dose\ profile(R_1)}{Dose\ profile(R_2)}. \qquad (3)$$

These coefficients are determined on left and right of dose profiles thereafter the averaged value between them was given for each coefficient for five regions on dose profile. The normalized off-axis distance R_1 and R_2 were chosen in the Table I.

TABLE I. NORMALIZED OFF-AXIS DISTANCE FOR HOMOGENEITY, SYMMETRY AND PENUMBRA STUDIES.

Region number	Study objective	R_1	R_2
1	Homogeneity	0.5	0.85
2		0.85	1
3		0.5	1
4	Symmetry	0	1
5	Penumbra	0.85	1.35

The homogeneity is investigated and the results of these investigations are showed on the Figs. 4, 5 and 6 that give the IC variation as a function of side of irradiation square field.

For the region number 1, the IC is big for the small field size because of the high gradient of dose in this region is very important due to smallness of the irradiation field, and the IC decreased with side of square field and it becomes stable and near to 1 for the large field size more than 12×12 cm^2 (Fig. 4).

Fig. 5 gives the IC variation for region number 2 and 3.

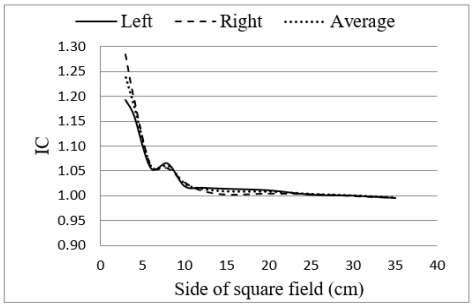

Figure 4. Investigated coefficient IC as a function of side of square field for region number 1.

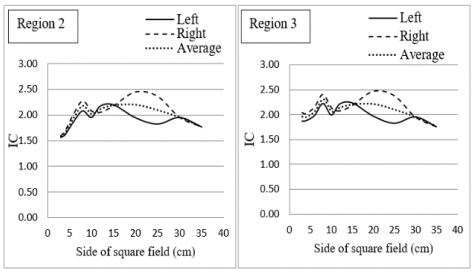

Figure 5. Investigated coefficient IC as a function of side of square field for region number 2 and 3.

Figure 6. Investigated coefficient IC as a function of side of square field for region number 4.

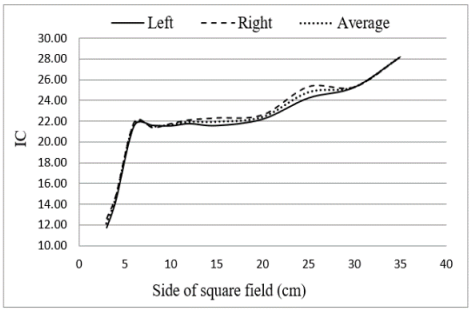

Figure 7. Investigated coefficient IC as a function of side of square field for region number 5.

For small field size, the beam homogeneity is stable in region 3 and it is near to 2 but for region 2 the beam homogeneity is under to 2 and for the large field size the IC on left is different to IC on right of dose profile (Fig. 5). Theoretically the IC=2 for these regions because at normalized off-axis distance of 1 is 50 % for all irradiation field size.

The region 4 allows us to investigate the symmetry of beam dose profile with irradiation field size.

Theoretically, the symmetry of beam dose profile is given by IC=2 for all irradiation field size, but in this study the IC is near to 2 and the IC on left is different to IC on right of the dose profile. The measured beam dose profiles are not ideally symmetric and the deviation of the dose profile symmetry (deviation to 2) is under to 17 % (Fig. 6). For the beam dose profiles are symmetric the IC must be 2 and the deviation must be 0. The reasons behind this asymmetry: the age of linear accelerator, the measurements uncertainty …etc.

The penumbra is investigated by study on the region number 5. Fig. 7 gives the IC variation with side of square field size. It can be seen from Fig. 7; the penumbra is represented by the big values of IC. For small field size, it is very big because it has a big sharp gradient than the field size more than 6×6 cm2. The penumbra on left and on right of dose profile is identical for small field size but it is slightly different for the large field size.

IV. Conclusion

This work is an experimental study of homogeneity, symmetry and penumbra of dose profiles of 6 MV photon beam produced by Varian Clinac 2100. This study was performed inside Al Kawtar clinic center Fez. This study allows us to predict the lifetime effect on beau dose profiles and also the experimentation for dose measurements.

This study can be a basic for increased the radiotherapy quality for cancer treatment by knowing how the dose varied at while patient be treated by radiation [14]. For high radiotherapy quality, these parameters of homogeneity, symmetry and penumbra should be improved in perspective and they must be identical on left as on right of photon beam dose profiles.

Acknowledgment

The authors would like to thank Varian Medical Systems to provide us the Varian Clinac 2100 geometry data and give us this opportunity to study the Varian linear accelerator technology and to participate in its future development.

References

[1] Oh, S. A., Kang, M. K., Yea, J. W., Kim, S. K., & Oh, Y. K. (2012). Study of the penumbra for high-energy photon beams with Gafchromic™ EBT2 films. *Journal of the Korean Physical Society*, *60*(11), 1973-1976.

[2] Bencheikh, M., Maghnouj, A., Tajmouati, J., & Didi, A. (2017). Dosimetry investigation and evaluation for removing flattening filter configuration of Linac: Monte Carlo study. *Moscow University Physics Bulletin*, *72*(6), 640-646.

[3] Didi, A., Dadouch, A., Bencheikh, M., & Jai, O. (2017). Monte Carlo simulation of thermal neutron flux of americium–beryllium source used in neutron activation analysis. *Moscow University Physics Bulletin*, *72*(5), 460-464.

[4] Bencheikh, M., Maghnouj, A., & Tajmouati, J. (2017). Photon beam softening coefficients evaluation for a 6 MeV photon beam for an aluminum slab: Monte Carlo study using BEAMnrc Code, DOSXYZnrc Code, and BEAMDP code. *Moscow University Physics Bulletin*, *72*(3), 263-270.

[5] Bencheikh, M., Maghnouj, A., & Tajmouati, J. (2017). Photon beam softening coefficient determination with slab thickness in small filed size: Monte Carlo study. *Physics of Particles and Nuclei Letters*, *14*(6), 963-970.

[6] Bencheikh, M., Maghnouj, A., Tajmouati, J., Didi, A., & Ezzati, A. O. (2017). Validation of Monte Carlo simulation of 6 MV photon beam produced by Varian Clinac 2100 linear accelerator using BEAMnrc code and DOSXYZnrc code. *Physics of Particles and Nuclei Letters*, *14*(5), 780-787.

[7] Bencheikh, M., Maghnouj, A., & Tajmouati, J. (2017). Energetic properties' investigation of removing flattening filter at phantom surface: Monte Carlo study using BEAMnrc code, DOSXYZnrc code and BEAMDP code. *Physics of Particles and Nuclei Letters*, *14*(6), 953-962.

[8] Bencheikh, M., Maghnouj, A., & Tajmouati, J. (2017). Relative attenuation and beam softening study with

flattening filter volume reduction: Monte Carlo study. *Moscow University Physics Bulletin, 72*(6), 647-652.

[9] Bencheikh, M., Maghnouj, A., Tajmouati, J., Lamrabet, A., & Benkhouy, Y. (2017). Study of possibility to reduce flattening filter volume for increasing energetic photons for high radiotherapy efficiency. *Moscow University Physics Bulletin, 72*(6), 653-657.

[10] Bencheikh M., Maghnouj A., & Tajmouati J. (2017). Study of photon beam dosimetry quality for removing flattening filter linac configuration. *Annals of University of Craiova Physics AUC, 27*, 50-60.

[11] Swiss Society of Radiobiology and Medical Physics SSRMP. (2000). *Dosimétrie des faisceaux de photons de haute énergie l'aide de chambres d'ionisation, Recommandation N° 8*.

[12] International Atomic Energy Agency. (2004). *Commissioning and Quality Assurance of Computerized Planning Systems for Radiation Treatment of Cancer* (Technical Reports Series No. 430).

[13] International Atomic Energy Agency. (2007). *Specification and Acceptance Testing of Radiotherapy Treatment Planning Systems* (IAEA-ECDOC-1540).

[14] Bencheikh M. et al. (2018). Study of 6 MV Photon Beam Dose Profiles, Investigation and Evaluation of Scattered photons and Electrons Contamination Effects on Beam Dose Profiles. *Bulgarian Journal of Physics ((Bulg. J. Phys.), 45*(1), 67- 75.

Parametric Study of Flue Gas Driven Biomass Gasification

Dilini Dharmasiri[1], Dinu Welarathna[2], Praveena Madhubhani[3], Duleeka Sandamali Gunarathne[4]

[1,2,3,4]Department of Chemical and Process Engineering, University of Moratuwa, Moratuwa 10400, Sri Lanka, dilinidharmasiri@gmail.com[1], dswelarathna@gmail.com[2], praveenamadhubhani@gmail.com[3], duleekas@uom.lk[4]

Abstract—**The challenge of global warming can not only be addressed by replacing fossil fuel with renewable sources, but also by increasing energy efficiency and reducing CO_2 emission. In this work, utilization of CO_2, as well as waste heat in the flue gas from the syngas combustor back to the biomass gasifier was investigated, aiming at syngas-fired furnace applications. A system model based on Aspen Plus was developed for the proposed integrated system and the effect of flue gas recycle fraction, flue gas temperature and gasification temperature on syngas composition, syngas yield, lower heating value, cold gas efficiency, effective carbon conversion, CO_2 emission, and equivalence ratio were evaluated. The flue gas recycle fraction should be limited to 0.6 in order to keep the adiabatic flame temperature in the range of that of natural gas. A slight improvement of cold gas efficiency and a considerable improvement of effective carbon conversion from 65% to 86% can be achieved at a gasification temperature of 800 ºC and flue gas recycle temperature of 800 ºC. As a result of improved efficiency, an annual biomass saving of 26 kg/kW can be expected. Approximately, CO_2 emission of 43 kg/kW can be avoided annually.**

Keywords - biomass gasification, CO_2 utilization, waste heat recovery, flue gas recycle, industrial furnaces

I. INTRODUCTION

The energy requirement for human consumption is continuously rising, although there is only a limited amount of fossil fuels available. It takes a long time to reproduce them and they are nonrenewable. Another issue related to consuming fossil fuels is CO_2 emission which is directly connected with global warming. The most promising solution for both declining of fossil fuels and global warming is the usage of renewable energy. When considering renewable energy sources, biomass gasification is one of the most investigated areas as its products can be used in heat and power generation as well as in the production of liquid fuels and chemicals [1]. But to substitute a substantial amount of fossil fuel with a significant profit, efficient utilization of biomass resources is required.

The composition of syngas is influenced by the oxidizer or the gasifying agent that is normally air, O_2, or steam. The CO and H_2 content as well as the heating value of syngas are higher when gasification is made with steam or O_2 than it is made with air [1]. There are some studies done to analyze the feasibility of using CO_2 as a gasifying agent to get higher thermal efficiency. CO yield in the syngas is proportional to the CO_2 fraction in the gasifying medium while H_2 yield is inversely proportional. A positive effect of the CO_2 mixing ratio on the thermal efficiency of the gasifier was observed at a temperature of 850°C and above [2]. The minimum energy requirement for complete carbon conversion has been identified at the operating temperature of 850°C. Further, cold gas efficiency greater than 100% can be obtained by using CO_2 as a gasifying agent due to partial conversion of carbon in CO_2 to CO [3]. Further, studies have been conducted to evaluate the use of steam and CO_2 as co-gasifying agents for CO_2 valorization and production of syngas with a flexible H_2 to CO molar ratio [4].

It is well known that biomass gasification is a carbon-neutral process. This process can be designed as a carbon-negative process by decreasing the amount of CO_2 released from the system to the atmosphere [5]. This concept is already is being practiced by integrating the biomass to energy conversion system with a

ISBN: 978-86-80593-73-9

carbon capture and storage (CCS) system. The issue is the mismatch of feasible scales of the two subsystems. Another interesting option after carbon capture is carbon utilization or reuse either as a storage medium for renewable energy or as a feedstock for various chemicals or as a solvent or working fluid in the processes like food industry [6, 7]. Even though the global warming potential of CCS is significantly lower than of the carbon capture and utilization, other environmental impacts are higher [8]. Therefore, utilization is favored over storage. One such CO_2 utilization application is recycling emitted CO_2 from the combustion process back to the gasifier. In this concept, CO_2 can be used as a heat source for gasifiers as well as a gasifying agent. With the increment of CO_2 recycling ratio, cold gas efficiency is increased since recycled CO_2 acts as an effective heat source supplying some heat demand in the gasifier. The positive effect of CO_2 recycling on cold gas efficiency is more prominent at the lower gasifier temperature of 750ºC when the CO_2 recycling temperature is 1000ºC. At high gasification temperature around 950ºC, the significant progress of the endothermic reactions (Boudouard reaction and the reverse water gas shift reaction) increase the heat demand, and subsequently, more feedstock needs to be oxidized to maintain the gasifier at this target temperature and hence reducing the cold gas efficiency [9].

The studies have been extended to recycling flue gas rather than CO_2, for the gasification process [10-14]. Thermodynamic analysis of the use of coal-fired boiler flue gas as the biomass gasifying medium has been carried out to see the effect of various compositions of biomass and coal, variable fuel/oxidizer ratios, and variable gasification temperatures [10]. Flue gas from coal and coke-oven gas co-fired boiler has also been used as the gasifying medium of a biomass gasifier in laboratory and industrial-scale reactors [11, 12]. The use of recycled flue gas from coal combustion (61% CO_2 and 32% H_2O) as a gasifying agent has also been demonstrated in a fluidized bed gasifier as part of a dry gasification oxy-combustion power cycle [13]. Recycling flue gas from the combustor of a dual bed sewage sludge gasifier has also been investigated under different flue gas compositions [14].

However, according to the studies which have been done so far, analysis of recycling flue gas derived from syngas combustion, as an agent for biomass gasification has not been done yet. This is very important when the growing trend of syngas-fired furnace applications such as steel and ceramic industries are considered [15-18]. Since biomass composition (C, H, O content) is very different from coal composition, syngas-derived flue gas composition (CO_2/H_2O ratio) is also different from that of coal-derived flue gas, requiring dedicated study to understand the feasibility. In this study, flue gas derived from syngas combustion will be recycled to the gasifier as an agent for biomass gasification, and the system will be developed and analyzed using Aspen Plus software. Effect of flue gas recycle fraction, flue gas temperature and gasification temperature on syngas composition, syngas yield, lower heating value, cold gas efficiency, effective carbon conversion, CO_2 emission to the environment, and equivalence ratio will be evaluated.

II. PROCESS DESCRIPTION

As shown in Fig. 1, biomass is gasified with oxygen as the gasification agent. Oxygen is used as a gasifying agent in order to reduce the dilution of syngas with N_2. Synthesis gas from the gasification stage is sent to the oxy-fuel combustion stage. By oxy-fuel combustion, the thermal efficiency of the process is expected to increase [19]. To avoid excessive flame temperatures in the combustor, recycled flue gas is used as a moderator, keeping the temperature equal to the adiabatic temperature of natural gas (2000ºC). In oxy-fuel combustion processes with CO_2 capture, it is a common practice to use a stream of CO_2 for controlling the combustor

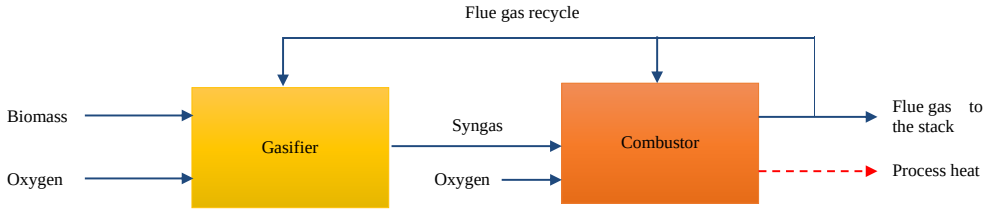

Figure 1. Simple demonstration of the concept.

temperature [19]. Another fraction of the flue gas is recycled back to the gasification process to achieve the following three objectives;

- Provide a heat source for the gasification process due to sensible heat available in the flue gas, reducing O_2 requirement and reducing biomass combustion inside the gasifier (low equivalence ratio and high cold gas efficiency).
- Provide a carbon source to the gasifier increasing the effective carbon conversion.
- Reduce CO_2 emission to the atmosphere per unit of energy production.

III. System modeling

In this work, the simulation is carried out using Aspen Plus software. The basic input specifications and operating conditions are summarized in Table I and Table II.

Fig. 2 shows the Aspen Plus process flow sheet. The gasifier is modeled assuming that equilibrium is achieved which is more realistic for the gasification in fluidized bed and entrained flow reactors. Due to nonconventional feedstock, biomass is first decomposed into the elements in a Yield reactor (BRKDWN) before feeding into the Gibbs reactor (GASIFIER) where Gibbs free energy is minimized to calculate the product composition at a specified gasification temperature. Depending on the recycle fraction a varied amount of oxygen is fed to the GASIFIER so that the total net heat duty of the BRKDWN and GASIFIER reactors become zero to make it a direct gasification process. This is achieved by using the design specification feature in Aspen Plus. Produced syngas is then passed through a cooler (CONDENSR) to condense out the water and fed to another Gibbs reactor (COMBUSTR)

TABLE I. ASPEN PLUS INPUT SPECIFICATIONS.

Input	Specification
Stream class	MIXCINC
Valid phases	Vapor-Liquid
Property method	PR-BM
Enthalpy of NC components	HCOALGEN
Density of NC components	DCOALIGT

TABLE II. OPERATING CONDITIONS.

Item	Value
Feedstock	$CH_{1.4}O_{0.6}$
Moisture content	20%
Inlet temperature of biomass and O_2	25ºC
Flue gas recycle fraction	0-0.6
Temperature of recycled flue gas	750-1000ºC
Gasification temperature	800-1100ºC
Pressure	0.1 MPa

operating at adiabatic conditions. Excess oxygen is supplied to the COMBUSTR by using a calculator block, assuring complete combustion of syngas. Flue gas at adiabatic flame temperature is then passed through another cooler (PROCHEAT) where heat is recovered to the process. A fraction of the flue gas is then recycled back to the GASIFIER with the aid of a splitter (SPLIT) and the remaining flue gas is sent to the stack. Sensitivity Analysis is carried out by varying the flue gas recycle fraction (SPLIT fraction of flue gas recycle) and temperature of recycled flue gas (temperature of PROCHEAT outlet) as specified in Table II. The study was repeated for gasification temperatures 800-1100ºC covering both fluidized bed and entrained flow gasifier operating ranges. These

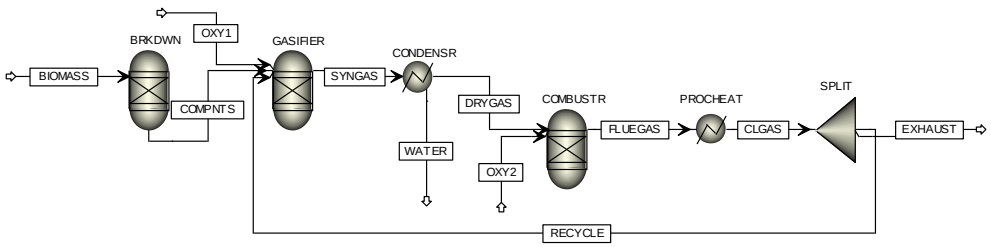

Figure 2. Aspen Plus process flow sheet.

two gasifier types are considered since they are generally used in large-scale applications.

Performance is evaluated in terms of, syngas yield (Y_{syngas}), lower heating value of syngas (LHV_{syngas}), cold gas efficiency (CGE), effective carbon conversion (ECC), specific CO_2 emission (SCE), and equivalence ratio (ER) as defined below.

$$Y_{syngas} = \frac{Syngas\ volume\ flow\ rate\left(Nm^3/h\right)}{Biomass\ mass\ flow\ rate\left(kg/h\right)}, \quad (1)$$

$$LHV_{syngas} = \sum LHV_i \ Y_i \text{ where } i = \text{=} H_2, \text{CO, and } CH_4, \quad (2)$$

$$CGE = (Y_{syngas} LHV_{syngas} / LHV_{biomas}) x100\%, \quad (3)$$

$$ECE = \left(\frac{Rate\ of\ carbon\ output\ with\ syngas\ as\ CO\ and\ CH_4}{Rate\ of\ carbon\ input\ with\ biomass} \right) x100\%, \quad (4)$$

$$SCE = \frac{CO_2\ emission\ through\ the\ exhaust\ (kg)}{Energy\ available\ in\ the\ syngas\ (MJ)}, \quad (5)$$

$$\text{ER} = \frac{\text{Actual } O_2 \text{ supply}}{\text{Stoichiometric } O_2 \text{ requirement}}. \quad (6)$$

III. Results and Discussion

A. Model Validation

As shown in Table III, the model predicts the composition of the syngas fairly well. However, overestimation of CO and H_2 as well as underestimation of CH_4, CO_2, light hydrocarbons, and tar should be expected with equilibrium models. Even though modified equilibrium models improve the model prediction, their major drawback is the loss of generality due to the use of empirical correction factors or correlations that are reactor dependent [22]. Therefore, equilibrium models continue to be important in predicting the thermodynamic limits of the chemical reactions, and hence, the developed equilibrium model is considered suitable for evaluating the flue gas recycling performance.

TABLE III. Comparison of gas composition of biomass gasification with oxygen.

Component	Present study (equilibrium model)	Reference [20] (modified equilibrium model)	Reference [21] (typical experiment)
CO	45.44	45.6	48
H_2	39.86	37.5	32
CH_4	0.11	3.09	2
CO_2	14.60	12.98	15
N_2	0	0.83	3

B. Effect of Flue Gas Recycle Fraction

In order to replace natural gas, the adiabatic flame temperature of resulting syngas combustion should be around 2000ºC. Higher temperatures are acceptable provided that flue gas can be recycled back to the combustor in order to dilute the stream and reduce the temperature. It was found from the study that going beyond 0.6 recycle fraction is not feasible when considering the adiabatic flame temperature and hence results are reported up to 0.6 recycle fraction only.

The CO_2/H_2O molar ratio of coal-derived flue gas is in the range of 0.6 – 2.2 in the case of air combustion where the lower end is from flame coal and the higher end is with anthracite [10]. The CO_2/H_2O molar ratio of oxy-fuel combustion of bituminous coal is 1.9 when 20% of flue gas is recycled back to the gasifier [13]. For different flue gas recycle fractions, the flue gas composition, and the CO_2/H_2O molar ratio is summarized in Table IV for oxy-fuel combustion of biomass. With the increase of flue gas recycle fraction, CO_2/H_2O molar ratio is increasing from 1.5 to 7. This means that recycling can enrich the CO_2 in the flue gas due to increased H_2O in the syngas being condensed out before the combustor. At 20% recycle fraction, a CO_2/H_2O molar ratio of 2.8 which is higher than the case of bituminous coal can be observed. A high CO_2/H_2O molar ratio can result in more CO and less H_2 in the syngas. However, according to the present study, the CO_2 enrichment cannot go beyond 84% due to the violation of the required

TABLE IV. VARIATION OF THE FLUE GAS COMPOSITION AND CO_2/H_2O MOLAR RATIO WITH FLUE GAS RECYCLE FRACTION.

Recycle Fraction	CO_2 (vol%)	H_2O (vol%)	CO_2/H_2O
0	55	37	1.5
0.1	62	31	2
0.2	69	25	2.8
0.3	74	20	3.7
0.4	79	17	4.6
0.5	82	14	5.9
0.6	84	12	7

adiabatic flame temperature. This is a result of increased flue gas recycle which dilutes the syngas, reducing the flame temperature. The flue gas stream containing 84% CO_2 can be further dried to remove the remaining moisture if sequestration is desired.

To study the effect of flue gas recycle fraction, the gasification temperature and the flue gas recycle temperature were kept constant at 800ºC. As can be seen from Fig. 3, with increasing flue gas recycle fraction from 0-0.6, both CO and H_2 molar fractions have decreased, whereas CO_2 and H_2O molar fractions have increased due to dilution with recycled flue gas.

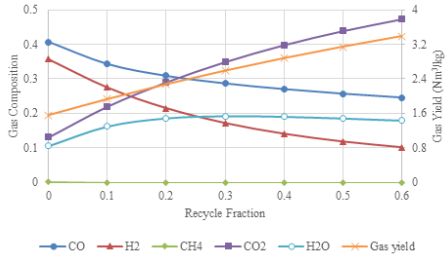

Figure 3. Effect of recycle fraction on gas composition and yield.

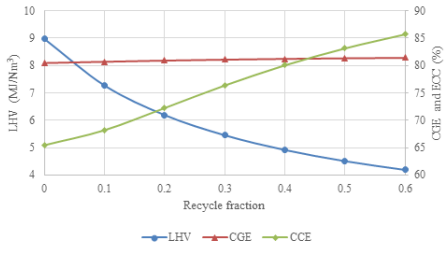

Figure 4. Effect of recycle fraction on LHV, cold gas efficiency, and carbon conversion efficiency.

As a result, the LHV has dropped from 8.97 to 4.19 MJ/Nm^3 as seen from Fig. 4. However, when the gas yield is considered, CO yield has increased from 0.63 to 0.83 Nm^3/kg of biomass whereas H_2 yield has decreased from 0.56 to 0.34 Nm^3/kg of biomass. This trend has been observed by other researchers as well [23-25]. In the presence of CO_2 and H_2O, the Boudouard reaction and water-gas reaction both can happen, producing CO and H_2. However, reverse water gas shift reaction at elevated temperatures will change the gas concentrations of CO and H_2 in the syngas, increasing the CO yield while reducing the H_2 yield. As a result, the effective carbon conversion shows a huge improvement from 65.5% to 85.7% and the cold gas efficiency has slightly increased from 80.5% to 81.4%. According to Fig. 5, both CO_2 emission and ER have been reduced with increased recycle fraction. Recycled flue gas is a heat source for the gasification process, reducing O_2 requirement and ultimately ER and hence CO_2 emissions.

C. Effect of Flue Gas Recycle Temperature

The heat required for the gasification process is supplied by the combustion of biomass and by utilizing the heat available in the recycled flue gas. To achieve CO_2 emission reduction compared to the base case, it is necessary to recycle high-temperature flue gas so that the combustion of biomass inside the gasifier is limited. Depending on the gasification temperature and the recycle fraction, this threshold temperature varies between 755 – 1049ºC as seen from Fig. 6. Below these threshold values, flue gas recycling is not feasible considering the CO_2 emission. This temperature may be lowered by means of an external heat supply. To study the effect of flue gas recycle temperature, the gasification temperature and the flue gas recycle fraction

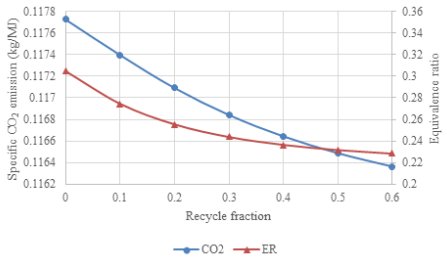

Figure 5. Effect of recycle fraction on specific CO_2 emission and ER.

were kept constant at 800ºC and 0.6 respectively. At this condition, the threshold temperature is 764ºC according to Fig. 6. Therefore, the results of flue gas recycle temperature above 800ºC are reported here. As can be seen from Fig. 7, there's no significant effect of flue gas recycle temperature on the gas composition and hence only a slight increase of LHV from 4.17 to 4.28 MJ/Nm^3 can be seen. However, together with the slight increase of gas yield, cold gas efficiency shows a considerable increase from 80.1 to 87.5% as seen from Fig. 8. The effective carbon conversion also shows a considerable improvement from 84.1% to 93.2%. According to Fig. 9, both CO_2 emission and ER have been reduced with increased recycle temperature. The high temperature of recycled flue gas is a better heat source for the gasification process, reducing O_2 requirement and ultimately ER and hence CO_2 emissions.

D. Effect of Gasification Temperature

To study the effect of gasification temperature, the flue gas recycle temperature and the flue gas recycle fraction were kept constant at 800ºC and 0.6 respectively. As can be seen from Fig. 10, CO_2 and H_2 molar fractions have decreased, whereas CO and H_2O molar fractions have increased due to reverse water gas shift

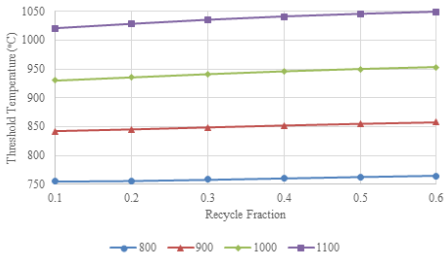

Figure 6. Effect of recycle fraction on threshold temperature.

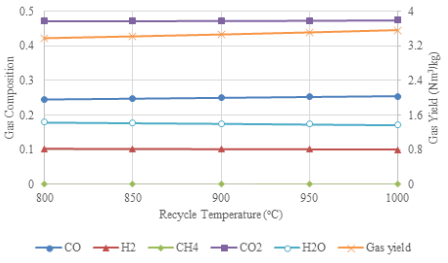

Figure 7. Effect of recycle temperature on gas composition and yield.

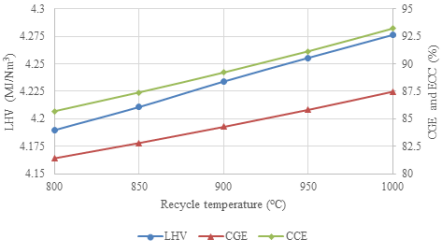

Figure 8. Effect of recycle temperature on LHV, cold gas efficiency, and carbon conversion efficiency.

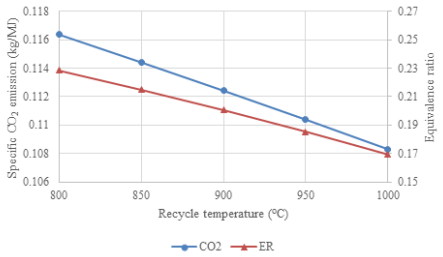

Figure 9. Effect of recycle temperature on specific CO_2 emission and ER.

reaction at elevated temperatures. As a result, the LHV has slightly decreased from 4.19 to 3.94 MJ/Nm^3. However, when the gas yield is considered, CO yield shows a peak around 900ºC whereas H_2 yield is continuously decreasing, considerably de creasing the cold gas efficiency from 81.4 to 70% as seen from Fig. 11. Actually, CO yield should peak somewhere between 800-900ºC since beyond the point, the recycle flue gas temperature of 800ºC is lower than the threshold flue gas recycle temperature required. Due to the same reason, even though there's no significant difference in effective carbon conversion, it shows a peak of around 86.5% at a gasification temperature of 900ºC. According to Fig. 12, both CO_2 emission and ER have been increased with increased gasification temperature. To maintain a high gasification temperature, more O_2 is required, ultimately increasing ER and hence CO_2 emissions.

E. Implications of Flue Gas Recycle

The results obtained with the base case scenario and two flue gas recycle scenarios are summarized in Table V. The base case of oxygen-driven biomass gasification followed by oxy-fuel combustion of syngas was identified as case 1. As observed from Fig. 6, theoretically, flue gas recycle temperature above 764ºC is necessary for gasification at 800ºC with a flue

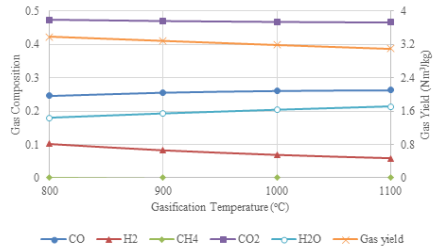

Figure 10. Effect of gasification temperature on gas composition and yield.

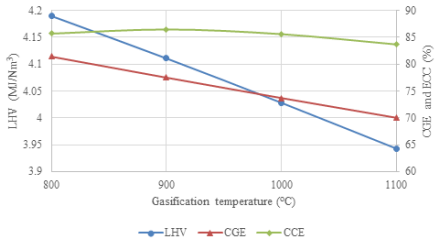

Figure 11. Effect of gasification temperature on LHV, cold gas efficiency, and carbon conversion efficiency.

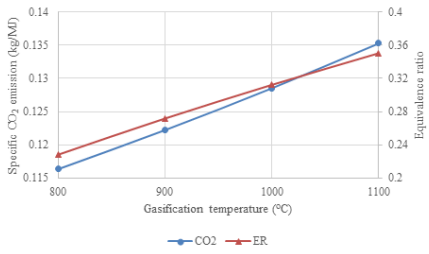

Figure 12. Effect of gasification temperature on specific CO_2 emission and ER.

TABLE V- PERFORMANCE COMPARISON OF DIFFERENT CASES.

Parameter	**Case 1 (Base Case)**	**Case 2 (Recycling at 800^{0}C)**	**Case 3 (Recycling at 1000^{0}C)**
Gas yield	1.56	3.38	3.56
LHV	8.97	4.19	4.28
CGE	80.47	81.42	87.47
ECC	65.46	85.7	93.21
ER	0.3	0.23	0.17
CO_2 (kg/MJ)	0.117725	0.116364	0.108311
CO_2 avoided annually (kg/kW)	-	43	297
Biomass (kg/MJ)	0.071402	0.07059	0.0657
Biomass saved annually (kg/kW)	-	26	180

gas recycle fraction of 0.6. Therefore, recycle temperature of 800ºC was considered as the actual minimum requirement which was identified as case 2. The maximum practical flue gas recycle temperature was considered as 1000ºC which was identified as case 3.

Flue gas recycling results in high gas yield and low calorific syngas compared to the base case. Due to the low calorific value of syngas, burners designed for low calorific gases may be required. In order to obtain the same thermal load as natural gas, the amount of syngas must be over seven times more than natural gas. There are burners designed for such low calorific gases by using combustion techniques such as swirl combustion, staged combustion, or flameless combustion [26].

When flue gas recycling is applied at 800ºC, 43 kg of CO_2 can be avoided, and 26 kg of biomass can be saved annually per kW of thermal output if continuous operation throughout the year is considered. Seven times higher impact can be expected if 1000ºC flue gas derived syngas is used in furnace applications such as steel and ceramic industries [15-18]. The proposed flue gas driven gasification process is a possible alternative integration configuration for such a system. Further, heat recovery from the hot syngas to the gasifier can also be applied either by preheating the low-temperature flue gas, preheating the gasifying agent, or pre-drying the biomass feed. Either a high-temperature conventional plate-type heat exchanger or a special type of radiation recuperative exchanger can be used for air preheating [27].

IV. CONCLUSION

When biomass-derived syngas is used in furnace applications, flue gas recycling for the gasification process is technically feasible in terms of providing a heat source and a carbon source for the gasification process and reducing CO_2 emissions per unit of energy generated. The flue gas recycle fraction should be limited to 0.6 in order to keep the adiabatic flame temperature in the range of that of natural gas. High flue gas recycle temperature is always beneficial and flue gas recycle temperature above 76ºC is necessary for gasification at 800ºC if any other heat source is not available.

Cold gas efficiency around 81% and effective carbon conversion around 86% are achieved with

syngas LHV around 4.2 MJ/Nm^3. This is really beneficial compared to the base case without flue gas recycling having effective carbon conversion of around 65%, though cold gas efficiency is only a slight improvement. Further, the system operates at a lower equivalence ratio and therefore the cost of air separation can be reduced. However, due to the low calorific value of syngas compared to the base case, burners designed for low calorific gases may be required. Approximately CO_2 emission of 43 kg/kW can be avoided and biomass saving of 26 kg/kW can be expected annually.

REFERENCES

[1] Couto, N., Rouboa, A., Silva, V., Monteiro, E., & Bouziane, K. (2013). Influence of the biomass gasification processes on the final composition of syngas. *Energy Procedia*, *36*, 596–606. DOI:10.1016/j.egypro.2013.07.068

[2] Prabowo, B., et al. (2014). CO2-steam mixture for direct and indirect gasification of rice straw in a downdraft gasifier: Laboratory-scale experiments and performance prediction. *Applied Energy*, *113*, 670–679. DOI:10.1016/j.apenergy.2013.08.022

[3] Renganathan, T.,Yadav, M. V.,Pushpavanam, S., Voolapalli, R. K., & Cho, Y.S. (2012). CO 2 utilization for gasification of carbonaceous feedstocks: A thermodynamic analysis. *Chemical Engineering Science*, *83*, 159–170.

[4] Salaudeen, S. A., Acharya, B., Heidari, M., Arku, P., & Dutta, A. (2018). Numerical investigation of CO2 valorization via the steam gasification of biomass for producing syngas with flexible H2 to CO ratio. *Journal of CO2 Utilization*, *27*(July), 32–41. DOI:10.1016/j.jcou.2018.07.003

[5] Xiang, Y., et al. (2019). Study on the biomass-based integrated gasification combined cycle with negative CO2 emissions under different temperatures and pressures. *Energy*, *179*, 571–580. DOI:/10.1016/j.energy.2019.05.011.

[6] Duraccio, V., Gnoni, M. G., & Elia, V. (2015). Carbon capture and reuse in an industrial district: A technical and economic feasibility study. *Journal of CO2 Utilization*, *10*, 23–29. DOI:10.1016/j.jcou.2015.02.004

[7] Billig, E., et al. (2019). Non-fossil CO2 recycling-The technical potential for the present and future utilization for fuels in Germany. *Journal of CO2 Utilization*, *30*(January),130–141.

[8] Cuéllar-Franca, R. M., & Azapagic, A. (2015). Carbon capture, storage and utilisation technologies: A critical analysis and comparison of their life cycle environmental impacts. *Journal of CO2 Utilization*, *9*, 82–102. DOI:10.1016/j.jcou.2014.12.001

[9] Prabowo, B., et al. (2015). Utilization of rice husk in the CO_2-recycling gasification system for the effective implementation of bioenergy with carbon capture and storage (BECCS) technology. In *Proceedings of ACS Symposium Series*. American Chemical Society: (pp. 323–340). DOI:10.1021/bk-2015-1194.ch013

[10] Litka, R., & Kalisz, S. (2012). Thermochemical analysis of a flue gas-driven biomass gasification. *Chemical and Process Engineering*, *33*(3), 487–503. DOI:10.2478/v10176-012-0041-y

[11] Ostrowski, P., Maj, I., Kalisz, S., & Polok, M. (2017). Biomass low-temperature gasification in a rotary reactor prior to cofiring of syngas in power boilers. *Applied Thermal Engineering*. DOI:10.1016/j.applthermaleng.2017.02.120

[12] Prior, G., & Boilers, P. (2017).Testing of an innovative installation for alternative fuel low- temperature gasification prior to co-firing in power boilers. *Procedia Engineering* DOI:10.1016/j.proeng.2017.01.175

[13] Walker, M. E., Abbasian, J., Chmielewski, D. J., & Castaldi, M. J. (2011). Dry gasification Oxy-combustion power cycle. *Energy Fuels*, *25*, 2258–2266.

[14] Weng, Z., et al. (2018). Investigation of Sludge Gasification under Flue Gas. *Energy Procedia*, *152*, 1278–1283.

[15] Sandamali, D., Mellin, P., Yang, W., Pettersson, M., & Ljunggren, R. (2016). Performance of an effectively integrated biomass multi-stage gasification system and a steel industry heat treatment furnace. *Applied Energy*, *170*, 353–361. DOI:10.1016/j.apenergy.2016.03.003

[16] Gomez, H.O., Calleja, M.S., Fernandez, L.A., Kiedrzynska, A., & Lewtak, R. (2019). Application of the CFD simulation to the evaluation of natural gas replacement by syngas in burners of the ceramic sector. *Energy*, *185*. DOI:10.1016/j.energy.2019.06.064

[17] Liu, H., et al. (2014). A thermodynamic study of hot syngas impurities in steel reheating furnaces-Corrosion and interaction with oxide scales. *Energy*, *77*, 352–361. DOI:10.1016/j.energy.2014.08.

[18] Jozwiak, P., Hercog, J., Kiedrzynska, A., & Badyda, K. (2019). CFD analysis of natural gas substitution with syngas in the industrial furnaces. *Energy*, *179*, 593–602. DOI:10.1016/j.energy.2019.04.179

[19] Ahmed, U., Zahid, U., Jeong, Y.S., Lee, C. J., & Han, C. (2015). IGCC process intensification for simultaneous power generation and CO 2 capture. *Chemical Engineering and Processing*. DOI:10.1016/j.cep.2015.12.012

[20] Shayan, E., Zare, V., & Mirzaee, I. (2018). Hydrogen production from biomass gasification ; a theoretical comparison of using different gasification agents. *Energy Conversion and Management*, *159*, 30–41. DOI:10.1016/j.enconman.2017.12.096

[21] Bridgwater, A. V. (1995). The technical and economic feasibility of biomass gasification for power generation. *Fuel*, *14*(5), 631–653.

[22] Ferreira, S., Monteiro, E., Brito, P., & Vilarinho, C. (2019). A holistic review on biomass gasification modified equilibrium models. *Energies*, *12*(160), 1–31.

[23] Freitas, A. C. D., & Guirardello, R. (2015). Use of CO 2 as a co-reactant to promote syngas production in supercritical water gasification of sugarcane bagasse. *Biochemical Pharmacology*, *9*, 66–73.

[24] Valin, S., Bedel, L., Guillaudeau, J., Thiery, S., & Ravel, S. (2016). CO 2 as a substitute of steam or inert transport gas in a fluidised bed for biomass

gasification. *Fuel*, *177*, 288–295. DOI:10.1016/j.fuel.2016.03.020

[25] Parvez, A. M., Mujtaba, I. M., & Wu, T. (2016). Energy, exergy and environmental analyses of conventional, steam and CO 2 -enhanced rice straw gasification. *Energy*, *94*, 579–588. DOI:10.1016/j.energy.2015.11.022

[26] Chanphavong, L., & Zainal, Z. A. (2018). Characterization and challenge of development of producer gas fuel combustor: A review. *Journal of the Energy Institute.*

[27] Kilkovsky, B., et al.(2014). Heat exchangers for energy recovery in waste and biomass to energy technologies-I. Energy recovery from flue gas. *Applied Thermal Engineering*, 64, 213–223.

Advanced MOS Structures Design for Low-Power Devices – Review and Future Challenges

Lidia Dobrescu[1], Cristian Stancu[2], Dragoș Dobrescu[3]

[1,2,3]University POLITEHNICA of Bucharest, Bucharest, Romania,
lidia.dobrescu@electronica.pub.ro[1]

Abstract—**From classical MOS transistor build on silicon to its modified version, FINFET, semiconductor devices technological processes evolved from planar architectures to vertical ones. Other major steps included new materials searching, with significant improvements in power performances. The next 5 nm prototype transistor, reported to the previous 10 nm generation chips, improved performances by 40 percent, or 75 percent power savings at same performances, using a new architecture with innovative elements, silicon nanosheets. The 2 nm chips are already announced as a major next step, with 45 percent improving in performance, but also a decreasing of 75 percent in energy, these expected achievements are related to 7nm node, the most advanced existing node. These evolution steps from classical planar MOS transistor to contemporary devices with 3D architectures including new materials will be analyzed and described in this paper. Although FINFETs are intended to be scaled down towards 3nm, the new multibridge-channel FET will replace the fin from the FINFETs with a stack of nanosheets, each of them fully surrounded by the gate, as basic support of the 3nm node of the next generation process as an ambitious target. Following this rapid development low-power and energy efficiency will be focused.**

Keywords - MOSFET, FINFET, GAA

I. INTRODUCTION

Complementary Metal Oxide Semiconductor (CMOS) technologies continuously progressed due to their many advantages regarding low static power dissipation, high density of integration, ideal switching, high input impedance. Mohamed M. Atalla (engineer, entrepreneur, physical chemist, cryptographer and inventor) and Dawon Kahng (engineer in solid-state electronic) were the creators of Metal Oxide Semiconductor (MOS) transistor, in 1959, at Bell Laboratories. After this original step, by means of symmetrical pairs of complementary types of MOS transistors (p-channel and n-channel), in a planar architecture, the CMOS technology and fabrication process was imposed in 1963 by Fairchild Semiconductors for digital logic circuits as memories, but also for analog circuits as shown in Fig. 1 [1]. CMOS process, reported to nMOS, with the feature of low power consumption had initially a greater production cost, a lower-speed and an increased time of fabrication [1], but soon it was imposed as a standard process for memories, with continuous improvements such as twin-well, this circuit used a 3μm node and a 15mA current instead of 110mA for older versions of nMOS SRAM (Static Random-Access Memory) [1]. As an example of integrated circuit [2], from 1967, a memory cell, in CMOS technology, consisted in seven n-channel and nine p-channel transistors, with 8.4μW standby power, using 12V supply voltage. The power dissipation of 600μW for 100kHz frequency repetition rate was the power performance of this circuit**.** The real revolution in electronics was possible based on the Metal Oxide Semiconductor Field Effect Transistor (MOSFET) process development. Two opposite research and design directions acted since then, a

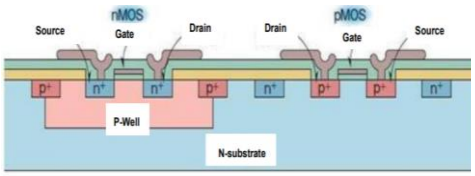

Figure 1. CMOS transistors cross-sectional areas. Source: [1].

continuously effort for diminishing the power consumption by lowering the supply voltage and the threshold voltage, and on the contrary, an increasing of power dissipation for a higher integration. Other further improvements were based on a modified MOS concept, the Floating Gate MOS transistor (FGMOS), consisting in a floating gate not connected to the external circuit, electrically isolated and placed between other multiple gates and the substrate [3]. Combining FGMOS transistors with innovative circuits design, as shown in Fig. 2, this new architecture lowered the threshold voltage (using a circuit design with two supplementary inputs biased with 2 fixed bias voltages) and decreased the power with 30%, preserving the conventional CMOS inverter speed [4]. Nowadays using new technologies and techniques on silicon, MOSFET threshold voltage can be lowered, having typical 300-400mV values. By using them in integrated circuits, the minimum supply voltage can be decreased, and the total power dissipation can be reduced. But an important disadvantage is that when the transistor is in the subthreshold region, at high temperatures (150˚C) the leakage current will increase. In CMOS logic gates used in memory cells, the average power dissipation is the sum of two types of power. The first one, the static power:

$$P_{static} = I_{leak} * V_{dd} \ , \qquad (1)$$

is generated by the residual (leakage) current when the transistor is off, I_{leak} , that also depends on the supply voltage, V_{dd} , so the static power depends on the square of the supply voltage. The second one, the dynamic power, is a result of the load capacitor charging and discharging process. The equation of the dynamic power was mentioned first in 1995 by [5]:

$$Pdynamic = \frac{1}{2} C * {V_{dd}}^2 * f \ , \qquad (2)$$

where C is the circuit total capacitance and f is the logic gate frequency. The dynamic power depends on the clock frequency of the circuit and for the first memory circuits, only the dynamic power was important. By lowering the supply voltage, using state-of-the-art CMOS transistors, both can be reduced, but scaling down the transistor dimensions, the static power increases.

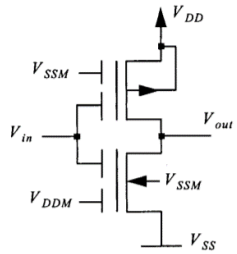

Figure 2. Logic gate with FGMOSFETs. Source: [4].

Limiting the clock frequency is another general way to limit the dynamic power. In modern microprocessors, the dynamic voltage scaling [5] represents an interdependent process between the supply voltage and the clock frequency.

II. SOI TRANSISTORS

Using a layered silicon–insulator–silicon substrate, as shown in Fig. 3, a new Silicon On Insulator (SOI) transistor was produced usually in 0.1µm technology with many advantages regarding an increased speed, reduced leakage currents, diminished interference between high and low voltage components [6]. These transistors can be classified in two categories: Fully Depleted transistors (FD) and Partially Depleted transistors (PD), differing on substrate thickness t_{sub} dimensions. If the substrate is very thin, t_{sub} under 20 nm, the space-charge region under the channel will be fully depleted, if the substrate is thicker, more than 50 nm, then a PD SOI can be obtained as the space charge region under the gate is limited by the buried oxide. Improved SOI MOSFETs can include Ultra Thin Body and Buried Oxide (UTBB) or Double Gate SOI topologies (DGSOI), the second architecture can reduce the length of the channel up to 30% versus a normal FD SOI having a single gate. With the threshold voltage in such a double gate transistor dynamically controlled, the supply

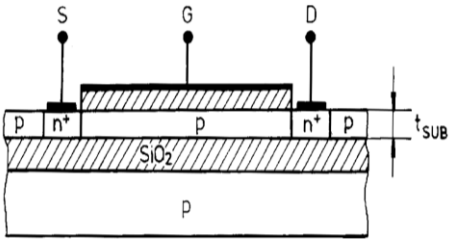

Figure 3. SOI Transistor structure.

voltage can be scaled down and improved performances for low power and low voltages circuits can be obtained [7]. Because the oxide isolation is buried in SOI technology, the drain-source capacitance is usually between 20-25% lower than the standard CMOS technology. That means the dynamic power is smaller. Furthermore, SOI devices have a lower threshold voltage and the leakage current in weak inversion region is significantly reduced compared to MOS. Thus, the static power is smaller. The disadvantages of the SOI transistors must be considered. At the boundary between strong and weak inversion a hysteresis in gate can occur for high V_{DS} voltages and, in some cases, because of the bipolar parasitic transistor the drain current in the subthreshold region can be significant. Moreover, the body of the transistors is left unconnected. That means the body is floating and could affect the threshold voltage and other parameters [8].

III. FINFETs 3D Spatial Architecture

Although DGSOI was considered as a promising candidate for replacing planar MOSFET under 50 nm [9], the true real revolution in MOS architecture begun with a fin -shaped gate transistor, (FINFET) spatial development, avoiding 20 nm technology limit [10]. Their fabrication was constantly scaled down under 28-nm. As the FINFET channel length gradually descended from 22-nm to16-nm and then to 14-nm process, an improvement of 30% in performance was reported [11], and it is still continuously decreasing. FINFET operation principle is the same as the conventional MOSFET transistor and its static characteristics (current- voltages) dependences are similar. The FINFET current between source and drain is better controlled by the new gate terminal, also called *FIN*, its new channel has three dimensions,

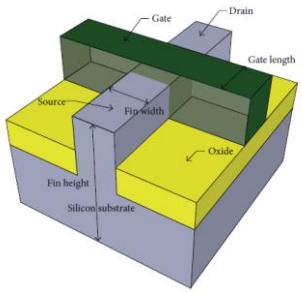

Figure 4. FINFET channel dimensions
Source: [10].

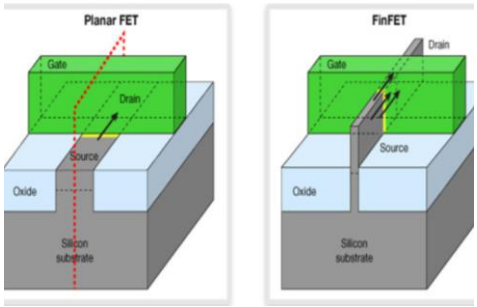

Figure 5. MOSFET and FINFET architectures.
Source: [12].

as shown in Fig. 4 [10]. The new transistor has a new spatial structure, evolving from the planar channel of a traditional MOSFET, as shown in Fig. 5 [12], the new channel is raised above the silicon substrate, as a block, using a 3D design. The FINFET gate wraps the channel, improving drain current using a better control of the channel. FINFETs have significantly less static leakage current, smaller switching voltages, faster switching times, but they also offer the possibility to scale down the channel length. There are 3 channel dimensions: length, width, and height, usually twice than the width. As FINFETs design uses a spatial assembly, the gate envelops the conducting channel, and the drain current will not be allowed to increase in OFF state (I_{OFF}). The better control of the channel in FINFETs results in lower threshold and supply voltages [13].

The ratio between the currents in ON state and OFF state (I_{ON}/I_{OFF}) for a 7nm FINFET process is on average 9 to 10 times higher in the saturation region than a 14nm bulk CMOS process in subthreshold region (with the same supply voltage) [14]. This demonstrates the benefits of using FINFETs to reduce the static power of a circuit. Even if the total power dissipation in 3D transistor is expected to have lower values than in CMOS or SOI devices, the power density is still a challenge nowadays. FINFETs have a higher pin capacitance compared to planar transistors (SOI or CMOS) and that can lead to a higher dynamic power. A study done by Cavium Networks states that the normalized gate capacitance per micron in FINFETs in a 14/16nm process is the same as in a 130nm planar process and 66% higher compared to a 28nm process [15]. Power optimizations must be done in the early stages of a design project. The increased cost of FINFET technology is recovered by high volume

products, area reduction, extreme power reduction and performance increase. Although FINFET concept was announced since 2012 by Liu from University of California, Berkeley [16], significant drawbacks were observed such as the technology cost due to significant changes, corner effects, quantum effects, layout dependences, width quantization. Additional parasitic were initial challenges in 2013 [17]. The FINFET drain current can be increased by increasing the height of the Fin. Another major improvement in current increasing is to build parallel multiple fins connected as shown in Fig. 6, but these fins introduce many parasitic elements, mostly capacitances that can be modeled and extracted from FINFET-based designs [18].

IV. GATE ALL AROUND FETS OR NANOWIRES

The first Gate All Around Field effect Transistor (GAAFET) was showcased in 1988 by Toshiba. It was a vertical nanowire GAAFET. The difference between FINFETs and GAAFETs is that the last one uses layers of silicon one over the other with a controlled spacing between them in contrast to the first one, where the fin is expanding from the substrate. The first nanowires were based on silicon materials, but new generations use high-mobility channel materials [19]. Below 7 nm, GAA FETs can be regarded as modified FINFETs, where the gate material fully envelops the channel region as in Fig. 7 [20]. The all-around gate offers an improved control of the channel. If the process descends under 7nm the GAA transistors have a better control on channel region, lower leakage current and higher current drive capability than FINFETs [19]. That means the static power of GAA transistor is lower compared to FINFETs. Generally, the short-channel MOSFETs drain

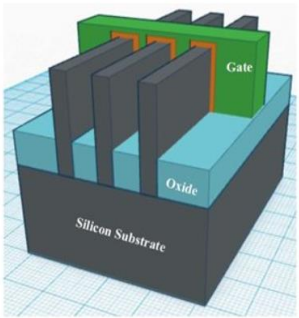

Figure 6. Multiple fins structure. Source: [8].

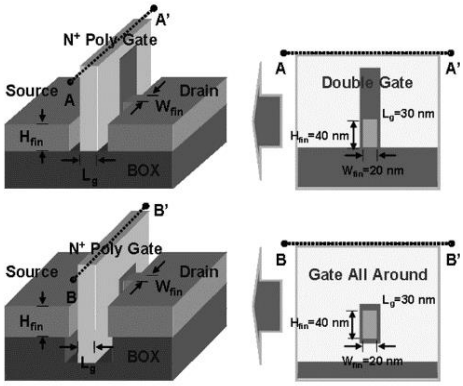

Figure 7. GAA structure versus Double Gate FET. Source:[20].

currents increase with drain-source voltages, becoming critical in some applications. One of the most important characteristics of GAA is the decrease of short channel effects due to a superior electrostatic control on the channel [21]. In GAA the number and width of the nanowires can be modified by the engineers and offers more control on the parameters of the device compared to FINFETs. The technology behind GAA has helped to reduce the supply voltage even further which was limited in FINFET. They are also named surrounding-gate transistor (SGT). Two important companies, Samsung and Intel, have declared their strategies to produce GAAFET transistors (using a new spatial structure arrangement called Multi-Bridge Channel FET) while Taiwan Semiconductor Manufacturing Company Limited (TSMC) has announced an own strategy to use FINFETs, by scaling down to 3nm node [22] Fig. 8.

V. MULTI-BRIDGE CHANNEL FETS

Using a CMOS process, the new 3D multi-bridge transistor was announced since 2003 in a prestigious scientific journal with an amazing subthreshold swing of 61mV/decade [23], high performances and low power dissipation. The new structures were fabricated on a bulk silicone

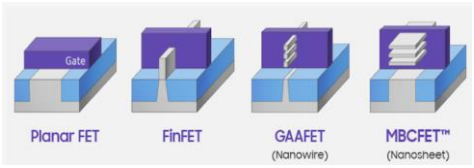

Figure 8. Advanced MOS structures design evolution Source: [22].

substrate using an epitaxial growth of a new multilayer from SiGe/Si. An ion implantation was used before the epitaxial growth of multiple nanosheets and silicone layers for a superior channel isolation, to avoid parasitic effects at the bulk substrate. The number of channels was defined by controlling the SiGe/Si alternating epitaxial sheets number. Such a device threshold voltage decreased (around 0.1 V) compared to a normal MOSFET (0.45V), the new Multi-Bridge Channel Field Effect Transistor (MBCFET) current drivability was 4.6 times higher than a normal MOSFET with an equal threshold voltage because of the new vertically structure. The possibility to increase the number of stacked nanosheets recommend these transistors for a future integration, thus increasing device speed. FINFETs needs fins to be laterally added, while nanosheets can be vertically stacked. One of the most important aspects is that the new MBCFETs are compatible with existing FINFETs design, permitting to keep the existing footprint without any area increase. New improvement can be acquired by using additional advanced fabrication techniques, for example an elevated flat source/drain, or replacing silicon with new materials. Using as insulator a TiN-gate [24], or an ultrathin high-k oxide, (i-oxide) sheet, for a better electrostatic integrity [25], low operating power devices can be obtained. Niobium pentoxide (Nb_2O_5), Transition Metal Dichalcogenide (TMD), or Tungsten Ditelluride (WTe_2) are new explored materials as high-k dielectrics [26] used for MBCFETs developing.

The International Technology Roadmap for Semiconductors (ITRS) determines research directions and timelines established by experts from Taiwan, United States of America, South Korea, Europe, Japan, China for electronic domain. The International Roadmap for Devices and Systems (IRDS), as ITRS successor [27] also set the next research directions for electronic devices and systems." Beyond CMOS" is the name of a chapter of IRDS [28] that focuses cryogenic and low-temperature electronics, devices based on magnetic tunnel junctions and quantum computing but also hardware security. In 2020 IRDS established the microprocessors power dissipation limits at 120-130 W and the maximum operation frequency at 5-6 GHz.

All over the world, there are research efforts for new technologies focusing germanium again or new materials such as SnO_2 (Tin oxide) [29], a new stable p-type semiconductor, in 2D form (in sheet form) for future power-saving complementary circuits using new methods to synthesize nanoparticles, or thin-films with superior electrical and thermal properties [30]. Other materials are also investigated, such as high-power gallium nitride, antimonide or molybdenum or bismuth-based materials.

VI. Conclusions

Every new advanced electronic structure design enabled a better control of electrostatic effects, but new requirements were also introduced. The transistors device design was changed from 2D classical MOSFET towards FINFET, nanowire and nanosheet structures, with a vertically 3D architecture, using also new materials. At system level, the architecture increased the number of transistors on chip, at a limited operating frequency, implementing the new concept of "3D power scaling" for low-power devices.

References

[1] Semiconductor History Museum of Japan (2019). *Double-well fast CMOS SRAM (Hitachi)*. Available at: https://www.shmj.or.jp/english /pdf/ic/exhibi727E.pdf

[2] Tsai, J. C., Van Beek, H. W., Roe, C. C., & Schliesing, F. (1967). Integrated complementary MOS circuit. *Proceedings of the IEEE*, *55*(6), 1121-1122.

[3] Kahng, D., & Sze, S. M. (1967). A floating gate and its application to memory devices. *The Bell System Technical Journal*, *46*(6), 1288-1295.

[4] Rodriguez-Villegas, E., Quintana, J. M., Avedillo, M. J., & Rueda, A. (2002, May). High-speed low-power logic gates using floating gates. In *2002 IEEE International Symposium on Circuits and Systems. Proceedings (Cat. No. 02CH37353)* (Vol. 5, pp. V-V). IEEE.

[5] Jacob, B., Wang, D., & Ng, S. (2010). *Memory systems: cache, DRAM, disk*. Morgan Kaufmann.

[6] Udrea, F., Popescu, A., & Milne, W. (1997, October). Breakdown analysis in JI, SOI and partial SOI power structures. In *1997 IEEE International SOI Conference Proceedings* (pp. 102-103). IEEE.

[7] Wei, L., Chen, Z., & Roy, K. (1998, October). Design and optimization of double-gate SOI MOSFETs for low voltage low power circuits. In *1998 IEEE International SOI Conference Proceedings (Cat No. 98CH36199)* (pp. 69-70). IEEE.

[8] Vandana, B. (2013). A theoretical study of low power soi technology. *IOSR J VLSI Signal Process (IOSR-JVSP)*, *2*(5), 30-37.

[9] Gupta, S. K., Pathak, G. G., Das, D., & Sharma, C. (2011, April). Double Gate MOSFET and its application for efficient digital circuits. In *2011 3rd International Conference on Electronics Computer Technology* (Vol. 2, pp. 33-36). IEEE.

[10] Tahrim, A., Chin, H. C., Lim, C. S., & Tan, M. L. P. (2015). Design and performance analysis of 1-bit FinFET full adder cells for subthreshold region at 16 nm process technology. *Journal of Nanomaterials*, 2015.

[11] Saggurti, P. (2021). *Is a FinFET Process the Right Choice for Your Next SoC?* Available at: https://www.synopsys.com/designware-ip/technical-bulletin/finfet-process.html

[12] Kawa, J. (2021). *FinFET Design, Manufacturability, and Reliability*. Available at: https://www.synopsys.com/designware-ip/technical-bulletin/finfet-design.html

[13] Kushwah, R. S., & Sikarwar, V. (2015). Analysis of leakage current and power reduction techniques in FinFET based SRAM cell. *Radioelectronics and Communications Systems*, *58*(7), 312-321.

[14] Xie, Q., Lin, X., Wang, Y., Chen, S., Dousti, M. J., & Pedram, M. (2015). Performance comparisons between 7-nm FinFET and conventional bulk CMOS standard cell libraries. *IEEE Transactions on Circuits and Systems II: Express Briefs*, *62*(8), 761-765.

[15] Narayanan, A. (2015). *FinFET impact on dynamic power.* Available at: https://www.edn.com/finfet-impact-on-dynamic-power/

[16] Liu, T. J. K. (2012, June). FinFET history, fundamentals and future. In *Proceedings of the Symposium on VLSI Technology Short Course*. University of California.

[17] Bhole, M., Kurude, A., & Pawar, S. (2013). Finfet-benefits, drawbacks and challenges. *Int. J. of Engineering, Sciences and Research Technology*, *2*, 3219-3222.

[18] Vora, P. H., & Lad, R.. (2017). *Review Paper on CMOS, SOI and FinFET Technology*. Available at: https://www.design-reuse.com/articles/41330/cmos-soi-finfet-technology-review-paper.html

[19] Lapedus, M. (2021). *New Transistors structures at 3nm/2nm*, Available at: https://semiengineering.com/new-transistor-structures-at-3nm-2nm/

[20] Song, J. Y., Choi, W. Y., Park, J. H., Lee, J. D., & Park, B. G. (2006). Design optimization of gate-all-around (GAA) MOSFETs. *IEEE Transactions on Nanotechnology*, *5*(3), 186-191.

[21] Neelam, A.K. (2021), *Performance Evaluation of GAA Nanosheet FETwith Varied Geometrical and Process Parameters.* Available at: https://www.researchsquare.com/article/rs-965209/v1

[22] Cutress, I. (2020) *Where are my GAA-FETs? TSMC to Stay with FinFET for 3nm*. Available at: https://www.anandtech.com /show/16041/where-are-my-gaafets-tsmc-to-stay-with-finfet-for-3nm

[23] Lee, S. Y., Kim, S. M., Yoon, E. J., Oh, C. W., Chung, I., Park, D., & Kim, K. (2003). A novel multibridge-channel MOSFET (MBCFET): Fabrication technologies and characteristics. *IEEE transactions on nanotechnology*, *2*(4), 253-257.

[24] Lee, S. Y., et al. (2005, June). Sub-25nm single-metal gate CMOS multi-bridge-channel MOSFET (MBCFET) for high performance and low power application. In *Digest of Technical Papers. 2005 Symposium on VLSI Technology* (pp. 154-155). IEEE.

[25] Wu, Y. T., Chiang, M. H., Chen, J. F., & Liu, T. J. K. (2021). Simulation-Based Study of High-Permittivity Inserted-Oxide FinFET With Low-Permittivity Inner Spacers. *IEEE Transactions on Electron Devices*, *68*(11), 5529-5534.

[26] Ahmed, F., Paul, R., & Saha, J. K. (2020, November). Comparative Performance Analysis of TMD based Multi-Bridge Channel Field Effect Transistor. In *2020 IEEE 10th International Conference Nanomaterials: Applications & Properties (NAP)* (pp. 01TPNS04-1). IEEE.

[27] Gargini, P. (2017). *Radmap Evolution: Fron NTRS to ITRS, From ITRS 2.0 to IRDS*. Available at: https://e3s-center.berkeley.edu/wp-content/uploads/2017/12/1-1-1_Gargini.pdf

[28] *Beyond CMS: the future of Semiconductors.* Available at:https://irds.ieee.org/home/what-is-beyond-cmos

[29] Johnson, D. (2016). *Tin Oxide: The First Stable p-type 2-D Semiconductor Material*. *New material promises to lead to 2-D complementary logic circuits.* Available at: https://spectrum.ieee.org/the-first-stable-ptype-2d-semiconductor-material-has-been-developed

[30] Orlandi, M.O. (2020). *Tin Oxide Materials, Synthesis, Properties, and Applications.* Available at: https://www.sciencedirect.com/science/article/pii/B9780128159248

Experimental Evaluation of Explicit and Implicit Models in Prediction of PV Module Temperature

Abdelhak Keddouda[1], Razika Ihaddadene[2], Guerrira Belhi[3], Nabila Ihaddadene[4], Hamza Ahmed[5], Tettahi Nedhirou[6], Sofian Belabbes[7]

[1,2,4,5,6]Mechanical Engineering Department, Med Boudiaf University,M'sila, Algeria, abdelhak.keddouda@univ-msila.dz[1], razika.ihaddadene@univ-msila.dz[2], nabila.ihaddadene@univ-msila.dz[4], welhamza@gmail.com[5], nedhiroutth@gmail.com[6]
[3,7]Mechanical Engineering Department, Mohamed Khider University, Biskra, Algeria, b.guerira@univ-biskra.dz[3], belabbessofian66@gmail.com[7]

Abstract—**The present study is aiming to evaluate the performance of some of the well-known models provided in the literature for module temperature evaluation. Different explicit and implicit modèles, with and without wind consideration were used. Experimental results were performed at the University of Biskra (Algeria). According to obtained results, different degrees of agreement with experimental data was established, implementing wind effects and parameters that depends on cell temperature does provide more accuracy in general, it was also found that wind must be accurately and carefully implemented in the correlations for a precise cell temperature estimation.**

Keywords - PV modules, temperature prediction, explicit models, implicit models, wind

I. INTRODUCTION

It is well established in the literature that ambient conditions, material properties, and PV module temperature play a significant role in their performance, and generally, the efficiency of a solar cell is related to its temperature through a linear Eqs. [1-6]. Therefore, the accurate prediction of the operating temperature of a PV module is essential to assess its performance, which may be a quite complex process, bearing in mind that different heat transfer mechanisms must be taken into account when performing the energy balance for the non-converted heat, a process involving in particular convection, radiation, and conduction. Although the latter (at steady state) is simply transporting heat to the surfaces, which is then released into the environment via convective and radiative heat transfer [3]. Many correlations over the years have been providedin the literature to estimate the operating temperature as a function of ambient conditions, material and system properties, and mounting configurations. An earlier simple, linear and straightforward expression for the cells temperature was provided by Ross [7] is given in (1), which was presented for no load and open-air field to the solar cells:

$$T_c = T_a + k.G\,, \tag{1}$$

where T_a and G are the ambient temperature and the incident solar radiation, respectively, k is known as the Ross coefficient, which represents the slop of $T_c - T_a$ versus G plot. Earlier values of k were reported to be in the range of 0.02-0.04, however, more recent studies indicated an extend in the range upwards [8].

Another methodology that is widely used for a quick estimation of the PV module temperature is the so-called nominal operating cell temperature (NOCT) approach [6]. It is defined as the temperature of the module at the nominal terrestrial environment (NTE): irradiation of 800 W/m^2, average wind velocity of 1 m/s, ambient temperature of 20°C. The temperature of the cell/module using this approach is given by:

$$T_c = T_a + \frac{G}{G_{NOCT}}(T_{NOCT} - T_{a,NOCT})\,. \tag{2}$$

Based on those models, a variety of models were presented in the literature [9-14]. Reference [15] presented an equation based on the Ross

model, it was obtained based on a regression analysis for an air temperature between 0 and 35°C and a wind speed of 1 to 1.5 *m/s*. Reference [16] developed a simple linear model to predict PV module temperature requiring 3 input parameters (G, T_a and V) only. Their study indicated that ambient temperature mainly dictates the module temperature; the irradiance sets its increment by 0.028°C per W/m^2. More involved models that account for the fact that –as mentioned above– the efficiency of PV module is a function of the temperature itself, and different heat transfer mechanisms occur as the module exchanges heat with its surroundings, are also available in the literature. Reference [17] indicated that the energy balance for an array can be written as:

$$\tau\alpha G = \eta G + U_L(T_c - T_a), \quad (3)$$

where $\tau\alpha$ is the transmittance absorbance coefficient and U_L is the heat loss coefficient to the ambient. From (3), estimating η to be 0.1 $\tau\alpha$ an Eq. for T_c can be derived as:

$$T_c = T_a + 0.9(\tau\alpha / U_L)G, \quad (4)$$

where the term $\tau\alpha / U_L$ can be determined at NOCT conditions as: $\tau\alpha / U_L = (T_{c,NOCT} - T_{a,\mathrm{NOCT}})G_{NOCT}$. Reference [18] presented an equation for the estimation of the PV module temperature based on the environmental parameters measured in the field (T_a, G and V), three coefficients were calculated for each type of the panels using a least mean square method, the study results were in the order of ∓4℃.

Given the fact that numerous correlations and equations for estimating the operating temperature of PV modules are presented in the literature [19-22], this work was proposed to assess the performance of some of the well-known models in an arid climate. It is structured as follows: a quick review and classification of PV temperature correlations proposed in the literature is established in Section 2. In section 3, the experimental Set-up and data measurements were presented, then, the results and discussion were presented in Section 4, and finally, a conclusion was reported.

II. Theoretical Models In Predicting Module Temperature

A. Explicit Models

Involving parameters independent of T_c , explicit methods generally use empirical means to find and fit coefficients for the variables in the cell temperature equation. The explicit equations for T_c used in this study are listed in Table I, with and without wind effects in consideration.

B. Implicit Models

On the other hand, implicit equations for T_c involve parameters that depend on the cell temperature and processing climate parameters, with heat transfer equations that depend on T_c usually more complex and require iterative procedures for the solution. Table II lists the used implicit equations; they are classified based on wind effects.

TABLE I. Explicit equations for cell temperature.

Group	Correlation	Comments	Ref.
No wind effect	$T_c = T_a + kG$	Ross model	[7, 23-25]
	$T_c = 30.006 + 0.0175(G - 300) + 1.14(T_a - 25)$	Lasnier model	[22, 26]
	$T_c = T_a - 1 + 0.028G$	Schott model 01	[4, 22, 27]
With wind effect	$T_c = T_a + G\left(e^{a+bV} + \frac{\Delta T_{ref}}{G_{ref}}\right)$	King model a=-3.47 b=-0.0549	[6, 19, 28]
	$T_c = 0.943T_a + 0.028G - 1.528V + 4.3$	TamizhMani model	[16, 29]
	$T_c = \frac{U_{PV}T_a + G\left[(\tau\alpha) - \eta_{ref}(1 + \beta T_{ref})\right]}{U_{PV} - \beta\eta_{ref}G}$	Mattei model $U_{PV} = 26.6 + 2.3V$	[20, 30]

TABLE II. IMPLICIT EQUATIONS FOR CELL TEMPERATURE.

Group	Correlation	Comments	Ref.
No wind effect	$T_c = T_a + \frac{G}{G_{NOCT}}\left(T_{c,NOCT} - T_a\right)\left(1 - \frac{\eta}{\tau\alpha}\right)$	Duffie model 01	[31]
	$T_c = T_a + \frac{G}{G_{NOCT}}\left(T_{c,NOCT} - T_{a,NOCT}\right)\left(1 - \frac{\eta}{\tau\alpha}\right)$	Duffie model 02	[32, 33]
	$T_c = T_a + \frac{(\tau\alpha - \eta)}{U_L}G$	Hove model	[17, 19]
With wind effect	$T_c = T_a + \left(\frac{G}{G_{NOCT}}\right)\left(T_{NOCT} - T_{a,NOCT}\right)\left[1 - \left(\frac{\eta}{\tau\alpha}\right)\right]\left(\frac{9.5}{5.7 + 3.8V}\right)$	Duffie model 03	[33]
	$T_c = T_a + \alpha G(1 - \beta T_a)(1 - \gamma V)(1 - 1.0553\eta)$	Servant model	[18]
	$T_c = T_a + \frac{\left[(\alpha - \eta)G(a + bT_a)\right]}{(17.8 + 2.1V)}$	Schott model 02	[15]

III. MATERIALS AND METHODS

A. Experimental Set Up

The experiments were conducted on a PV panel (ALPV85-125M-36 type) located at Biskra University in Algeria (34°.48'N (latitude), 5°44'E (longitude) and 85 m of altitude) during the 11-01-2021 day. The module electrical characteristics are presented in Table III. The values of ambient and panel temperatures, solar irradiation, and wind speed were carried out from 09:53 to 16:06 with a time interval of one minute.

TABLE III. ELECTRICAL CHARACTERISTICS OF THE PV MODULE USED IN THIS STUDY.

Parameters	Values
Nominal power	85 W
Short-circuit current (Isc)	5.33 A
Open circuit voltage (Voc)	21.83 V
Maximum Power current (I_{max})	4.93 A
Maximum Power tension (V_{max})	17.27 V
Cells number (N)	36 (9x4)
Temperature coefficient of Isc	+0.069%/°C
Temperature coefficient of Voc	-0.39%/° C
Temperature coefficient of Pmp	-0.46%/°C

B. Error Analysis

To assess the results of the twelve models a statistical indicators were used, they involves the RMSE, RRMSE and MAE. These metrics equations are given in (5), (6) and (7):

$$RMSE = \sqrt{\frac{1}{N}\sum_{i=1}^{N}\left(T_{Measured} - T_{predicted}\right)^2}, \quad (5)$$

$$RRMSE = \sqrt{\frac{1}{N}\sum_{i=1}^{N}\left(\frac{T_{Measured} - T_{predicted}}{T_{Measured}}\right)^2}, \quad (6)$$

$$MAE = \frac{1}{N}\sum_{i=1}^{N}\left|T_{Measured} - T_{predicted}\right|. \quad (7)$$

IV. RESULTS AND DISCUSSION

In the present work, twelve models for the temperature prediction in PV modules were examined. Some of them were as simple as linear equations, while others were more complicated, as some of them may involve wind effects and parameters that depend on the cell temperature.

A. Explicit Models

Fig. 1 represents the results of explicit models that does not include wind effects, it is evident that those models are under-estimating the PV module temperature, this comes at the expanse of being quick and easy to implement and, hence they may be used as a first approximation for T_c. The error analysis for this group of models, as presented in Fig. 2, reveals that at an average, the temperature gap between that resulted in by the three models and the measured one, is

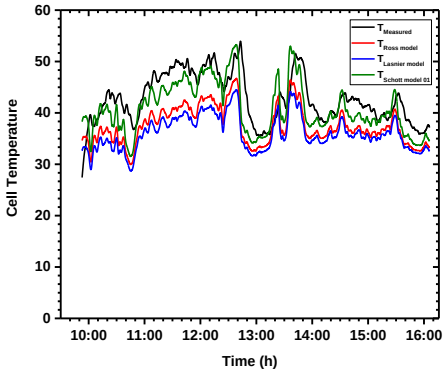

Figure 1. Measured and estimated cell temperature for explicit models without wind consideration.

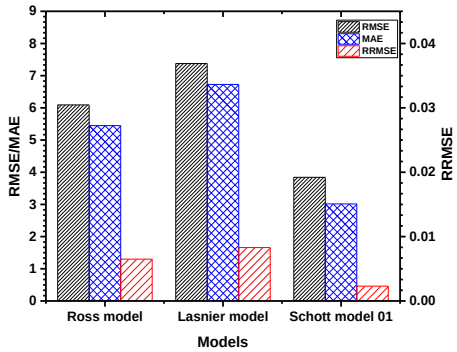

Figure 2. RMSE, MAE and RRMSE for explicit models results without wind considerations.

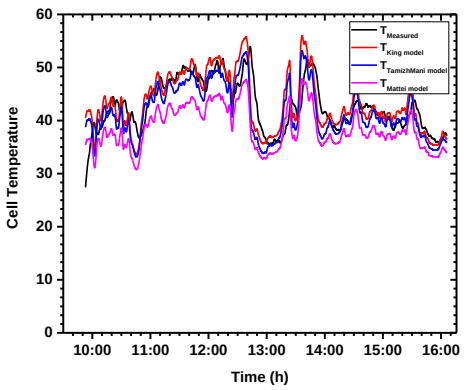

Figure 3. Measured and estimated cell temperature for explicit models with wind consideration.

ranging from 6.7°C by Lasnier model, to 3°C by the Schott model.

The latter tends to have the best accuracy among the three models with a RRMSE of 0.0023.

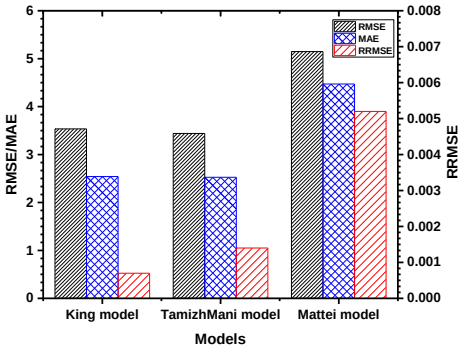

Figure 4. RMSE, MAE and RRMSE for explicit models results with wind considerations.

Including the wind effect into the equation of T_c was proposed by several authors to account for the module's thermal losses to the ambient due to convection heat transfer induced by the wind. Results of temperature estimation by such models from present study are presented in Fig. 3, as it is obvious, generally, accounting for the wind effects does provide more accuracy to the prediction of the cell operating temperature and reduces the error to the average of 4.7°C at maximum by Mattei model. Fig. 4 shows that the average temperature difference is reduced even further to values of 3.5 and 3.4°C using King and TamizhMani models respectively.

B. Implicit Models

A closer to reality approach in predicting the PV module temperature is to comprise for parameters that depend on the operating temperature itself, a process accomplished through generating implicit correlation for the

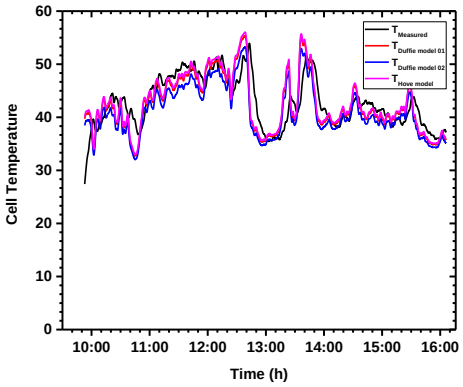

Figure 5. Measured and estimated cell temperature for implicit models without wind consideration.

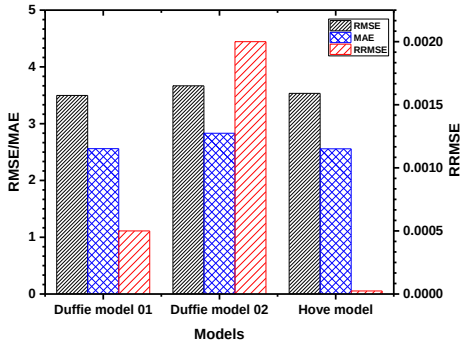

Figure 6. RMSE, MAE and RRMSE for implicit models results without wind considerations.

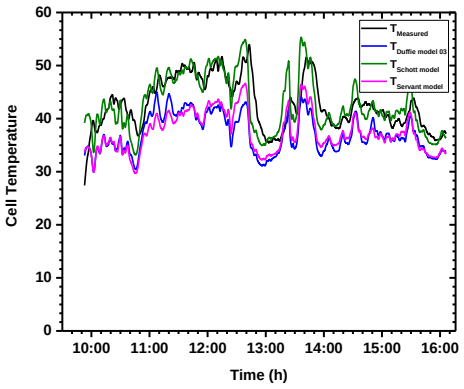

Figure 7. Measured and estimated cell temperature. for implicit models with wind consideration.

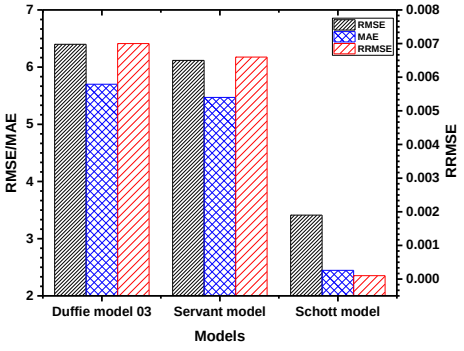

Figure 8. RMSE, MAE and RRMSE for implicit models results with wind considerations.

calculation of T_c some of the well-known, implicit models are examined in present work.

An illustration of estimated temperature of implicit models that does not include wind effects is shown in Fig. 5, a good agreement between measured and estimated temperature is observed throughout the figure, comparing this result with the explicit models indicates that accounting for the temperature dependent parameters does improve the accuracy of the models significantly. Applying the different metrics to the models results is shown in Fig. 6, which reveals that the approach by Hove based on the energy balance equation and taking the thermal loss coefficient at NOCT conditions, tends to be the most accurate with a RRMSE of the order of 2.10^{-5}, other models are not far behind, with an average temperature difference between the measured and that calculated by the models at the limit of 2.8°C.

Further improvement to the implicit models is to consider the wind effects, as it accounts for the cooling of module provoked by the wind, which generally augment the heat removal from module. Three models were tested in this study to assess the wind effects, the results are quite unexpected as Fig. 7 shows, a good performance by Schott model with a great agreement with experimental data, while other models are underestimating the operating temperature with a difference as much as 5°C.

The difference of accuracy in the calculation of T_c using different models is represent in Fig. 8, the latter indicates that values of RRMSE, RMSE and MAE are favoring Schott model, and revealing that much less accurate results are obtained by other models. This reflects not only the importance of the wind effects, but also the importance of accuracy when representing that effect in the models constants, which in turn, explains the verity of equations and correlations for the wind heat transfer coefficient present in the literature [34]. All those reasons combined, are motivating the authors to perform an extended version of this study in the future to improve the performance of the models by modifying constants such as the ones appearing the wind heat transfer coefficient.

V. CONCLUSION

The performance of a number of twelve explicit and implicit models (with and without wind considerations) for estimating the operating temperature of the PV module was investigated. The experiments were carried out on a PV panel at the University of Biskra (Algeria). The main results of the study are as follows:

- Among tested models, implicit ones tend to have the best agreement with experimental field data.

- In implicit models, wind has significant and different effects on the estimation process of T_c. It could produce errors if not represented well by the equations.
- The Schott model is the most suitable and accurate explicit model, while Hove's model is the best implicit one.
- Wind effects need to be as accurate as possible to have the best estimation of the cell's operating temperature.

REFERENCES

[1] Evans, D. L., & Florschuetz, L. W. (1978). Terrestrial concentrating photovoltaic power system studies. *Solar Energy*, *20*(1), 37-43.

[2] Garg, H. P., Agarwal, R. K., & Joshi, J. C. (1994). Experimental study on a hybrid photovoltaic-thermal solar water heater and its performance predictions. *Energy Conversion and Management*, *35*(7), 621-633.

[3] Skoplaki, E., Boudouvis, A. G., & Palyvos, J. A. (2008). A simple correlation for the operating temperature of photovoltaic modules of arbitrary mounting. *Solar energy materials and solar cells*, *92*(11), 1393-1402.

[4] Skoplaki, E., & Palyvos, J. A. (2009). On the temperature dependence of photovoltaic module electrical performance: A review of efficiency/power correlations. *Solar energy*, *83*(5), 614-624.

[5] Dubey, S., Sarvaiya, J. N., & Seshadri, B. (2013). Temperature dependent photovoltaic (PV) efficiency and its effect on PV production in the world–a review. *Energy Procedia*, *33*, 311-321.

[6] Aly, S. P., Ahzi, S., Barth, N., & Abdallah, A. (2018). Using energy balance method to study the thermal behavior of PV panels under time-varying field conditions. *Energy Conversion and Management*, *175*, 246-262.

[7] Ross Jr, R. G. (1976). Interface design considerations for terrestrial solar cell modules. In *12th Photovoltaic Specialists Conference* (pp. 801-806).

[8] Nordmann, T., & Clavadetscher, L. (2003, May). Understanding temperature effects on PV system performance. In *3rd World Conference onPhotovoltaic Energy Conversion, 2003. Proceedings of* (Vol. 3, pp. 2243-2246). IEEE.

[9] Mora Segado, P., Carretero, J., & Sidrach-de-Cardona, M. (2015). Models to predict the operating temperature of different photovoltaic modules in outdoor conditions. *Progress in Photovoltaics: Research and Applications*, *23*(10), 1267-1282.

[10] Sandnes, B., & Rekstad, J. (2002). A photovoltaic/thermal (PV/T) collector with a polymer absorber plate. Experimental study and analytical model. *Solar Energy*, *72*(1), 63-73.

[11] Mondol, J. D., Yohanis, Y. G., & Norton, B. (2007). The effect of low insolation conditions and inverter oversizing on the long-term performance of a grid-connected photovoltaic system. *Progress in Photovoltaics: Research and Applications*, *15*(4), 353-368.

[12] Mondol, J. D., Yohanis, Y. G., Smyth, M., & Norton, B. (2005). Long-term validated simulation of a building integrated photovoltaic system. *Solar energy*, *78*(2), 163-176.

[13] Mondol, J. D., Yohanis, Y. G., & Norton, B. (2007). Comparison of measured and predicted long term performance of grid a connected photovoltaic system. *Energy conversion and management*, *48*(4), 1065-1080.

[14] Irodionov, A. E., Kurenkova, V. A., Potapov, V. N., & Strebkov, D. S. (1989). Choice of resistance for elements of photovoltaic system's external switching. *Geliotechnika*, *25*, 18-21.

[15] Schott, T. (1985). Operation temperatures of pv modules: a theoretical and experimental approach. In *EC Photovoltaic solar energy conference* (pp. 392-396).

[16] TamizhMani, G., Ji, L., Tang, Y., Petacci, L., & Osterwald, C. (2003, June). Photovoltaic module thermal/wind performance: long-term monitoring and model development for energy rating. In *NCPV and Solar Program Review Meeting Proceedings, 24-26 March 2003, Denver, Colorado (CD-ROM)* (No. NREL/CP-520-35645). National Renewable Energy Lab., Golden, CO.(US).

[17] Hove, T. (2000). A method for predicting long-term average performance of photovoltaic systems. *Renewable Energy*, *21*(2), 207-229.

[18] Servant, J. M. (1986). Calculation of the cell temperature for photovoltaic modules from climatic data. In *Intersol Eighty Five* (pp. 1640-1643). Pergamon.

[19] Skoplaki, E. P. J. A., & Palyvos, J. A. (2009). Operating temperature of photovoltaic modules: A survey of pertinent correlations. *Renewable energy*, *34*(1), 23-29.

[20] Rawat, R., Kaushik, S. C., & Lamba, R. (2016). A review on modeling, design methodology and size optimization of photovoltaic based water pumping, standalone and grid connected system. *Renewable and Sustainable Energy Reviews*, *57*, 1506-1519.

[21] Coskun, C., Toygar, U., Sarpdag, O., & Oktay, Z. (2017). Sensitivity analysis of implicit correlations for photovoltaic module temperature: A review. *Journal of Cleaner Production*, *164*, 1474-1485.

[22] Sohani, A., & Sayyaadi, H. (2020). Employing genetic programming to find the best correlation to predict temperature of solar photovoltaic panels. *Energy Conversion and Management*, *224*, 113291.

[23] Notton, G., Lazarov, V., & Stoyanov, L. (2010). Optimal sizing of a grid-connected PV system for various PV module technologies and inclinations, inverter efficiency characteristics and locations. *Renewable Energy*, *35*(2), 541-554.

[24] Livera, A., et al. (2021). Data processing and quality verification for improved photovoltaic performance and reliability analytics. *Progress in Photovoltaics: Research and Applications*, *29*(2), 143-158.

[25] Durisch, W., Bitnar, B., Mayor, J. C., Kiess, H., Lam, K. H., & Close, J. (2007). Efficiency model for photovoltaic modules and demonstration of its

application to energy yield estimation. *Solar energy materials and solar cells*, *91*(1), 79-84.

[26] Lasnier, F., & Ang, T. G. (2017). *Photovoltaic engineering handbook.* Routledge.

[27] Bailek, N., Bouchouicha, K., Hassan, M. A., Slimani, A., & Jamil, B. (2020). Implicit regression-based correlations to predict the back temperature of PV modules in the arid region of south Algeria. *Renewable Energy*, *156*, 57-67.

[28] King, D. L., Kratochvil, J. A., & Boyson, W. E. (2004). *Photovoltaic array performance model* (pp. 1-43). United States. Department of Energy.

[29] Chenni, R., Makhlouf, M., Kerbache, T., & Bouzid, A. (2007). A detailed modeling method for photovoltaic cells. *Energy*, *32*(9), 1724-1730.

[30] Mattei, M., Notton, G., Cristofari, C., Muselli, M., & Poggi, P. (2006). Calculation of the polycrystalline PV module temperature using a simple method of energy balance. *Renewable energy*, *31*(4), 553-567.

[31] Kou, Q., Klein, S. A., & Beckman, W. A. (1998). A method for estimating the long-term performance of direct-coupled PV pumping systems. *Solar Energy*, *64*(1-3), 33-40.

[32] Davis, M. W., Fanney, A. H., & Dougherty, B. P. (2001). Prediction of building integrated photovoltaic cell temperatures. *J. Sol. Energy Eng.*, *123*(3), 200-210.

[33] Duffie, J. A., Beckman, W. A., & Blair, N. (2020). *Solar engineering of thermal processes, photovoltaics and wind*. John Wiley & Sons.

[34] Palyvos, J. A. (2008). A survey of wind convection coefficient correlations for building envelope energy systems' modeling. *Applied thermal engineering*, *28*(8-9), 801-808.

Voltage Profile Improvement of the Distribution Line with Distributed Generation Using Energy Storage System

Nikola Krstić[1], Dragan Tasić[2]

[1,2]University of Niš, Faculty of Electronic Engineering, Niš, Serbia,
nikola.krstic@elfak.ni.ac.rs[1]; dragan.tasic@elfak.ni.ac.rs[2]

Abstract—**This paper considers the improvement of voltage profile of the distribution line with distributed generation (DG) using energy storage system (ESS). For this purpose, optimal location on the distribution line and optimal charging and discharging powers of ESS during the day, considering voltage profile, are determined using metaheuristic optimization method of genetic algorithm. Before presentation of the main results, theory behind proposed solution and simple example on that how ESS can improve voltage profile are given. Optimal values for location and power of ESS, and voltage profile improvement obtained by their use, are determined for different types of load diagrams and different locations of DG on the distribution line.**

Keywords – energy storage system (ESS), distribution line, genetic algorithm, load diagram, distributed generation (DG)

I. INTRODUCTION

Voltage profile of the distribution line is greatly affected by the active and reactive power flows [1]. Power flows along the distribution line create voltage deviations, that could be positive or negative depending on the power directions, which in some cases can create overvoltage or undervoltage conditions to some consumers connected to the distribution line. Significant voltage deviations usually appear when high load power is present or in the case of large DG on the distribution line [2, 3]. One of the solutions to in some measure overcome this problem and provide the consumers a higher level of power quality is the use of ESS. The main characteristic of ESS from the power grid perception is that they operate as loads in the period of charging and as generators in the period of discharging. This gives flexibility and better power flow control of the distribution line on which ESS is connected [4].

Having that in mind, in this paper ESS is used to mitigate power peaks and load oscillations and thus improve the voltage profile of the distribution line [5]. This is generally achieved by charging ESS in the low load periods and discharging it in the periods of high load. Distribution line with DG is considered in this paper, because DG often can have negative affect on the voltage profile, especially when it comes from the renewable intermittent energy sources [6, 7]. Also for this reason, consumers connected to the distribution line are of constant power load type. To find optimal charging and discharging powers, and optimal location of ESS [8, 10] on the distribution line considering voltage profile improvement, metaheuristic optimization method of genetic algorithm [11] is used. Two different load diagrams are considered, where in both cases DG is located at the end or in the middle of the distribution line. Also, theory behind the proposed solution and simple example on that how ESS can improve voltage profile are given before the main results presentation. Sum of the squared voltage deviations from the referent value over the distribution line is used as the indicator of voltage profile quality.

II. OPTIMIZATION PROBLEM DEFINITION

Improvement of the distribution line voltage profile using ESS is the nonlinear optimization problem with constraints. Nonlinearity arises

ISBN: 978-86-80593-73-9

from the nonlinear dependency of the distribution line voltage profile quality on the power flows and the nonlinear constraints for ESS. Considering the complexity of the optimization problem, especially because of constraints which appear in it, metaheuristic optimization method of genetic algorithm is used to find the solution. Advantage of genetic algorithm and metaheuristic optimization methods in general, is their flexibility and easy implementation on the wide range of complex optimization problems [11].

Control variables in this optimization problem are powers of ESS and its location on the distribution line. Constraints of the control variables are given by (1) and (2):

$$P_{ESS_{\min}} < P_{ESS} < P_{ESS_{\max}} \ , \qquad (1)$$

where are: P_{ESS} - power of *ESS*, $P_{ESS_{\max}}$ - maximum charging power of *ESS*, $P_{ESS_{\max}}$ - maximum discharging power of *ESS*.

$$i \in \{i_1, i_2, \ldots, i_n\} \ , \qquad (2)$$

where are: i - index of the location on the distribution line in which *ESS* is located, $i \in \{i_1, i_2, \ldots, i_n\}$ – set of indexes of the locations on the distribution line in which *ESS* can be located.

Depended variables are current and voltage along the distribution line and the state of charge of ESS. Considering that in this paper load and ESS powers are constant in one-hour time period (ΔT), state of charge of *ESS* at the end of *k*-th hour of the day is determined by (3) in the case of charging, and by (4) in the case of discharging:

$$SOC_k = SOC_0 + \frac{1}{Q_{ESS}} \sum_{i=1}^{k} P_{ESS}(i) \eta \Delta T \ , \ (3)$$

$$SOC_k = SOC_0 + \frac{1}{Q_{ESS}} \sum_{i=1}^{k} P_{ESS}(i) \frac{1}{\eta} \Delta T \ , (4)$$

where are: SOC_0 – state of charge of *ESS* at the beginning of the day, SOC_k – state of charge of *ESS* at the end of the *k*-th hour, P_{ESS_i} – power of *ESS*, Q_{ESS} – total energy capacity of *ESS*, η – efficiency of the charge/discharge process.

Constraints of the depended variables are determined by the current limits of the distribution line and the range in which consumer voltage and the state of charge of *ESS* must be.

$$I < I_{\max} \ , \qquad (5)$$

$$V_{\min} < V < V_{\max} \ , \qquad (6)$$

$$SOC_{\min} < SOC < SOC_{\max} \ , \qquad (7)$$

where I and V are the current and voltage of some point on the distribution line.

To make the solution of the optimization problem sustainable over time, additional constraint for the state of charge of *ESS* is applied:

$$SOC_{24} = SOC_0 \ . \qquad (8)$$

Constraint (8) provides the operation of *ESS* so that the state of charge at the end and at the beginning of the day are equal.

Criterium function used for finding the solution of the optimization problem is one parameter criterium function equal to the voltage profile quality indicator.

$$F = \frac{1}{24N} \sum_{i=1}^{N} \sum_{j=1}^{24} \left(V_{i,j} - V_{ref} \right)^2 \ , \qquad (9)$$

where: F is the criterium function, $V_{i,j}$ is the voltage of *j*-th hour and *i*-th location on the distribution line and V_{ref} is the referent voltage.

III. THEORY BEHIND THE PROPOSED SOLUTION

Basic idea behind the distribution line voltage profile improvement using ESS can be analytically shown starting with the expression for voltage profile quality indicator:

$$Q = \frac{1}{24N} \sum_{i=1}^{N} \sum_{j=1}^{24} \left(\bar{V}_i + \Delta V_{i,j} - V_{ref} \right)^2 \ , \ (10)$$

where are: Q – voltage profile quality indicator, V_i – mean voltage of the i-th location on the distribution line, $\Delta V_{i,j}$ – j-th hour voltage difference from the mean value of the i-th location on the distribution line.

Using (10) and the fact that the sum of the voltage differences from the average value is equal to zero $\left(\sum_{j=1}^{24}\Delta V_j = 0\right)$, voltage profile quality indicator can be expressed as:

$$Q = \frac{1}{N}\sum_{i=1}^{N}\left(\bar{V}_i - V_{ref}\right)^2 + \sigma_i^2 \ , \qquad (11)$$

where σ_i is the daily voltage standard deviation of the i-th location on the distribution line.

From (11) it is clear that voltage profile can be improved in two ways. First is to get the mean voltage value close to its referent value, and the second is to lower the voltage deviation. Connection between the voltage and the load is given by voltage drop formula (12):

$$V = V_0 - \frac{PR+QX}{V} - j\frac{PX-QR}{V} \ , \quad (12)$$

where are: $P-$ active load power, $Q-$ reactive load power, $R-$ resistance of the distribution line, $X-$ reactance of the distribution line, V_0- voltage at the beginning of the distribution line.

Considering (12) it can be concluded that the mean voltage corresponds to the average load. Based on (3) and (4), it is clear that for ideal charge/discharge process average load cannot be changed by ESS operation if its state of charge at the beginning and at the end of the day are equal. This means, that in this paper for voltage profile improvement *ESS* are mostly used to even the load diagram and according to (12) reduce the voltage deviations from the mean value. This can be achieved by charging *ESS* in the low load periods and discharging it in the high load periods.

In order to confirm these theoretical assumptions, voltage profile improvement using *ESS*, is determined on a simple example of the uniformly loaded distribution line, before main results presentation. Power distribution along the distribution line in time of maximum (first half of the day) and minimum load (second half of the day), used in this example, is illustrated on Figs. 1 and 2, respectively. To simplify the procedure, only the real part in voltage drop formula (12) is taken into account for voltage calculation. Considering this and the fact that ESS is connected on the distance d from the end of the distribution line, voltage along the distribution line, before (13) and after (14) the point of *ESS* connection, is determined as:

$$V(l) = V_0 - \frac{1}{V_0}\int_l^L \left(\frac{P_r + Q_x}{L}\lambda + P_{ESS}r\right)d\lambda \ , \ (13)$$

$$V(l) = V(d) - \frac{1}{V_0}\int_l^d \frac{P_r + Q_x}{L}d\lambda \ , \qquad (14)$$

where are: $V(l)-$ voltage on the distance l from the end of the distribution line, $V(d)-$ voltage at the point of connection of *ESS* (calculated from (13) for $l = d$), $P-$total active power of the load, $Q-$total reactive power of the load, $P_{ESS}-$ active power of *ESS*, $L-$ the total length of the distribution line, $r-$resistance per unit of length of the distribution line, $x-$ reactance per unit of length of the distribution line.

In (13) active power of *ESS* can have positive or negative values depending on the operating mode of *ESS*.

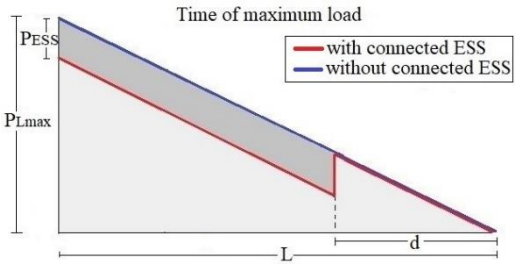

Figure 1. Power distribution along the distribution line in time of maximum load (ESS is discharging).

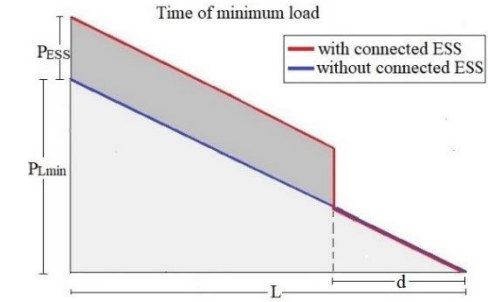

Figure 2. Power distribution along the distribution line in time of minimum load (ESS is charging).

In this case voltage profile quality indicator is determined as:

$$Q = \frac{1}{2L}\int_0^L \left(V_1(l) - V_r\right)^2 + \left(V_2(l) - V_r\right)^2 dl \,, \quad (15)$$

where V_1 is voltage in the first and V_2 in the second half of the day, while V_r is the referent voltage.

To find the optimal location and optimal power of *ESS* first derivative of voltage profile quality indicator over location and power of *ESS* is equalized with zero.

$$\frac{dQ}{dd} = 0 \,, \quad (16)$$

$$\frac{dQ}{dP_{ESS}} = 0 \,. \quad (17)$$

After replacing (13) and (14) in (15), for the case where maximum load is twice the minimum, (16) and (17) become:

$$\frac{P_r + Q_x}{L_r}\left(\frac{L^2 - 3d^2}{12}\right) = P_{ESS}\left(L - d\right), \quad (18)$$

$$\frac{P_r + Q_x}{L_r}\left(\frac{5L^4 + d^4 - 6L^2d^2}{48}\right) = P_{ESS}\frac{L^3 + 2d^3 - 3Ld^2}{3} \,, (19)$$

where P and Q are active and reactive power in the period of minimum load.

By numerically solving (18) and (19) optimal location d (distance from the end of the distribution line) and optimal power of *ESS* P_{ESS} (charge/discharge power) are found:

$$d = 0.38L \,, \quad (20)$$

$$P_{ESS} = 0.345\left(P + Q\frac{x}{r}\right). \quad (21)$$

Using optimal values for the location and the power of *ESS*, for the case where maximum load has the same duration and twice the size of the minimum load, voltage profile quality indicator has 10.15% improvement in relation to the case where no *ESS* is used.

IV. Results and Discussion

For finding the optimal solutions to the optimization problem of distribution line voltage profile improvement using *ESS*, computer simulations that use optimization method of genetic algorithm are performed.

Results are generated for the case of uniformly loaded 10 kV distribution line with the total length of 4 km. Resistance and reactance of the distribution line per unit of length are $r = 0.648\Omega/km$ and $x = 0,352\Omega/km$. Two types of load diagrams are considered, both with the same average load power $(P_m = 2679\,\text{kW})$, but with different load factors $(m_1 = 0.788, m_2 = 0.788)$. Both load diagrams have equal power factors $(\cos\varphi = 0.97)$, and are shown on Figs. 3 and 4. Also, two different locations of the DG on the distribution line are considered. First is in the middle, and the second location is at the end of the distribution line. Power generation diagram of the DG is given in Fig. 5 with power factor $(\cos\varphi = 1)$. For poorer voltage conditions, generated power from the DG is not in time with the majority of the power demand on the distribution line. In order to see how efficiency of the charge/discharge process of ESS affects the optimal solution and voltage profile improvement, different values for efficiency are considered. It is assumed that efficiencies of charging and discharging process of ESS are equal. In all considered cases voltage at the beginning of the distribution line is equal to the referent voltage $(10kV)$ and the state of charge of ESS is equal at the beginning and at the end of the day.

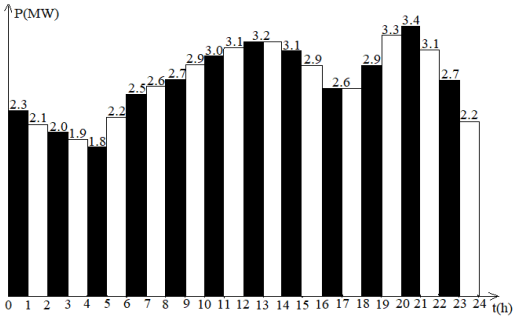

Figure 3. First load diagram with load factor m_1=0.788.

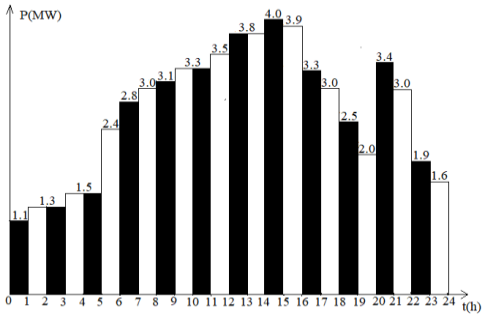

Figure 4. Second load diagram with load factor m_2=0.669.

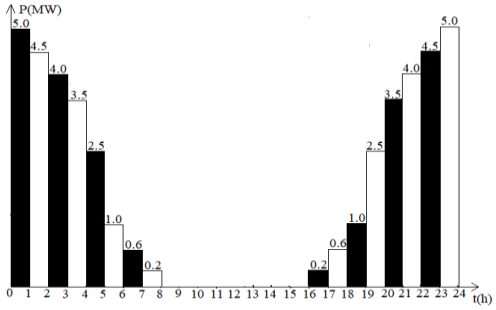

Figure 5. Power generation diagram of the DG.

In optimization method implementation population of 200 individuals is used and the solution is generated after 100 iterations (generations). Every individual is described with 25-dimensional vector, in which first dimension contains the value of the location index of *ESS* and the next 24 dimensions are related to the appropriate one-hour powers of *ESS* during the day. For location determination 10 m accuracy is used.

To make a comparison, Table I. contains results, for the cases where DG is located in the middle and at the end of the distribution line, for both load diagrams, before *ESS* connection. In the second column are values for voltage profile quality indicator (criterium function), third and fourth column refer to locations (*loc*) (distance from the beginning of the distribution line) and time (*t*) (hour in the day) with lowest voltage profile quality, respectively.

Table I. shows that before ESS connection voltage profile has been better in the case of first, more even load diagram. Lowest voltage profile quality has been measured at the end of the distribution line for both load diagrams.

Critical hours have been periods of high load for the cases where DG was in the middle of the distribution line (low voltage along the distribution line), and periods of low load when DG was at the end of the distribution line (high voltage along the distribution line).

Powers of ESS during the day, obtained by the optimization method of genetic algorithm as the part of the optimization problem solution, are given in Figs 6 and 7. Fig. 6 refers to the case where DG is in the middle and Fig. 7. to the case where DG is at the end of the distribution line. By comparing Figs. 6 and 7 with the load diagrams and power of distributed generation it is obvious that power of *ESS* is positive (charging mode) in periods of low load and high DG and negative in the periods of high load and low DG.

TABLE I. RESULTS BEFORE ESS CONNECTION.

Case	$Q[(kV)^2]$	$loc[m]$	$t[h]$
Dis. gen. in the middle of dis. line (1. load diag.)	0.06373	4000	13
Dis. gen. at the end of the dis. line (1. load diag.)	0.09702	4000	24
Dis. gen. in the middle of dis. line (2. load diag.)	0.09479	4000	15
Dis. gen. at the end of the dis. line (2. load diag.)	0.13629	4000	1

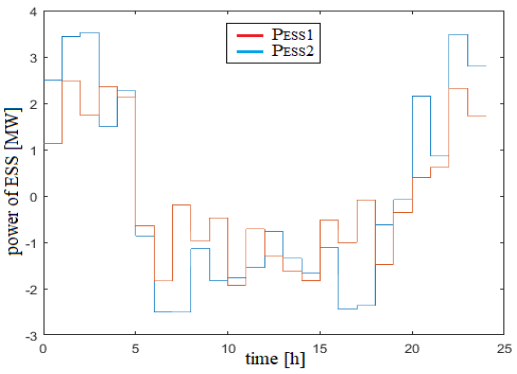

Figure 6. Power of ESS for the case where DG is in the middle of the distribution line.

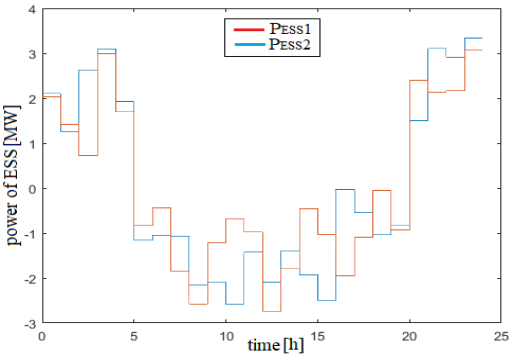

Figure 7. Power of ESS for the case where DG is at the end of distribution line.

Figs. 8-11 refer to the case where DG is placed in the middle of the distribution line. Figs 8 and 9 show voltage along the distribution line in the time of lowest voltage quality during the day, with and without ESS, for the first and second load diagram, respectively.

Figs. 10 and 11 show voltage during the day in the point with lowest voltage quality on the distribution line, with and without *ESS*, for the first and second load diagram, respectively.

Based on Figs. 8-11 it can be seen that distribution line voltage in the presence of *ESS* is changing in the smaller range with approximately the same average value as in the case without *ESS*.

This confirms previously given theoretical predictions about the impact of *ESS* with ideal efficiency and the equal state of charge at the beginning and at the end of the operation cycle on the voltage of the distribution line.

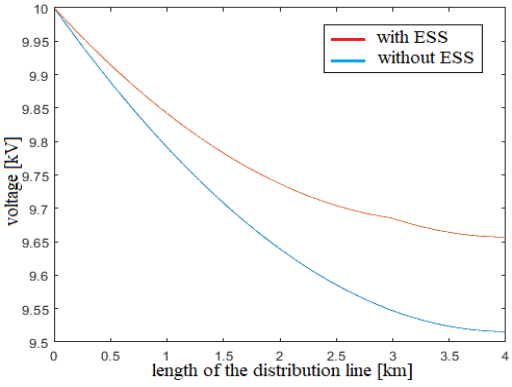

Figure 8. Voltage with and without ESS for the first load diagram and DG in the middle of the distribution line.

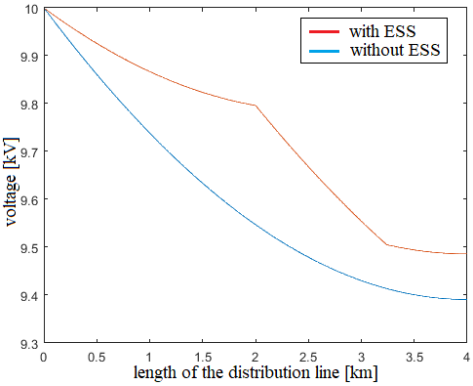

Figure 9. Voltage with and without ESS for the second load diagram and DG in the middle of the distribution line.

Figs. 12-15 refer to the case where DG is placed at the end of distribution line. Figs. 12 and 13 show voltage along the distribution line in the time of lowest voltage quality during the day, with and without ESS, for the first and second load diagram, respectively.

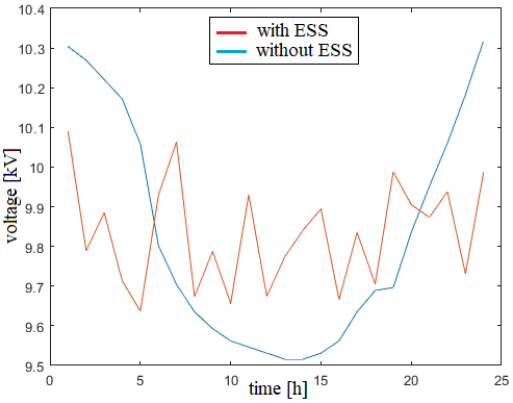

Figure 10. Voltage with and without ESS for the first load diagram and DG in the middle of the distribution line.

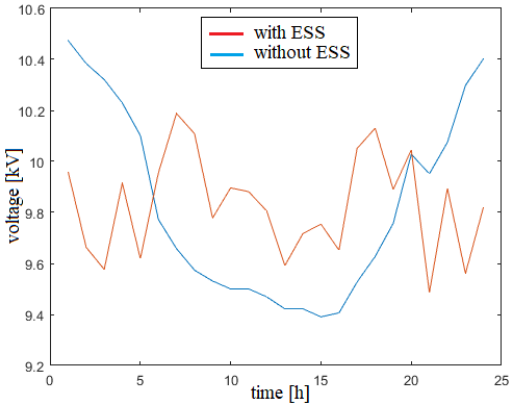

Figure 11. Voltage with and without ESS for the second load diagram and DG in the middle of the distribution line.

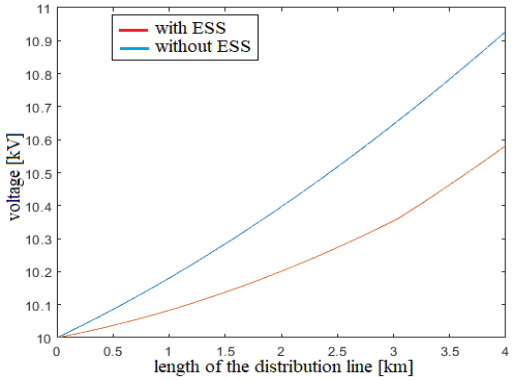

Figure 12. Voltage with and without ESS for the first load diagram and DG at the end of distribution line.

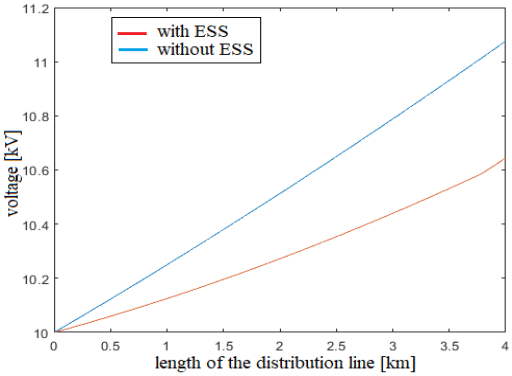

Figure 13. Voltage with and without ESS for the second load diagram and DG at the end of distribution line.

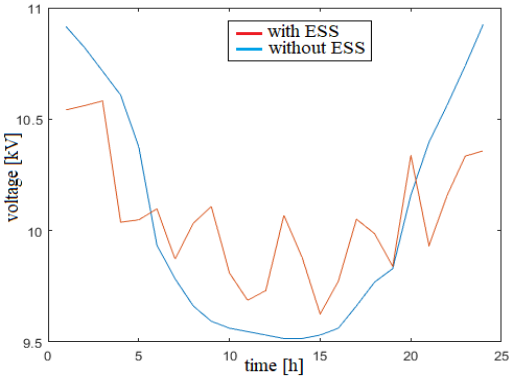

Figure 14. Voltage with and without ESS for the first load diagram and DG at the end of distribution line.

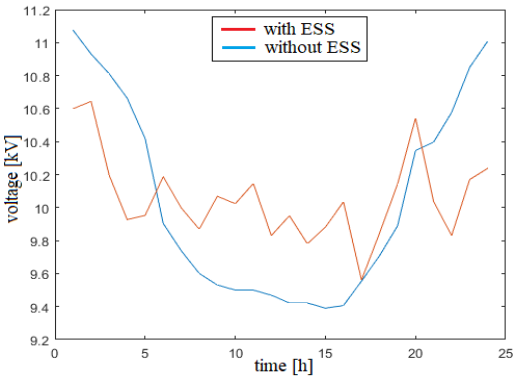

Figure 15. Voltage with and without ESS for the second load diagram and DG at the end of distribution line.

Figs. 14 and 15 show voltage during the day in the point with lowest voltage quality on the distribution line, with and without ESS, for the first and second load diagram, respectively.

Based on Figs. 12-15 a similar conclusion can be made as in the case where DG is placed in the middle of the distribution line (Figs. 8-11). Only difference is that now critical situations for voltage quality appear for voltage above the referent.

Table II contains results generated after *ESS* connection. Results refer to voltage profile quality indicator (*Q*), location of ESS (*locESS*) (length from the beginning of the distribution line), location on the distribution line with the lowest voltage quality (*loc*) (length from the beginning of the distribution line), time with lowest voltage quality along the distribution line (*t*) (hour in the day). By comparing values for voltage profile quality indicator from Tables I and II it can be concluded that *ESS* can significantly improve voltage profile of the distribution line with DG. This is true for both considered locations of DG and both load diagrams.

Also, obtained results in Table II suggest that location of DG, does not have significant impact on the value of the voltage profile quality indicator after *ESS* connection, as the load diagram itself.

In the presence of *ESS* more uneven load diagram (second load diagram) has again lower voltage profile quality, but in this case that difference is relatively small compared to the case before *ESS* connection. Also, from table II it can be seen that optimal locations of *ESS* are closer to the end of the distribution line for the

second load diagram and the case where DG is placed at the end of the distribution line. Although critical time considering voltage quality has changed after ESS connection, location with the lowest voltage quality is again at the end of the distribution line.

TABLE II. RESULTS AFTER ESS CONNECTION

Case	$Q[(kV)^2]$	$locESS[m]$	$loc[m]$	$t[h]$
DG in the middle of dis. line (1. load diag.)	0.02254	2990	4000	10
DG at the end of the dis. line (1. load diag.)	0.02482	3040	4000	3
DG in the middle of dis. line (2. load diag.)	0.02939	3240	4000	21
DG at the end of the dis. line (2. load diag.)	0.02759	3790	4000	2

TABLE III. VOLTAGE PROFILE QUALITY INDICATOR FOR DIFFERENT EFFICIENCIES OF ESS

η	Case 1 $Q[(kV)^2]$	Case 2 $Q[(kV)^2]$	Case 3 $Q[(kV)^2]$	Case 4 $Q[(kV)^2]$
1	0.02254	0.02482	0.02939	0.02759
0.95	0.02693	0.02848	0.03391	0.03332
0.9	0.02885	0.03265	0.04115	0.03967
0.85	0.03145	0.03472	0.05339	0.04881
0.8	0.03287	0.03668	0.05524	0.05403
0.7	0.03756	0.03793	0.05694	0.05553
0.6	0.04214	0.04174	0.05933	0.05717
0.5	0.04756	0.04737	0.06372	0.05967
0.3	0.04960	0.05040	0.07135	0.07030
0.1	0.05711	0.05554	0.07945	0.08297

All results so far are obtained for the efficiency of *ESS* equal to one.

Voltage profile quality indicator values for different efficiencies of charging/discharging process of ESS are given in Table III. As in Tables I and II four different cases are considered. Case 1 and 3 (DG in the middle of the distribution line), Case 2 and 4 (DG at the end of distribution line). Case 1 and 2 (first load diagram) Case 3 and 4 (second load diagram).

Table III shows, as predicted, that in all considered cases better voltage profile quality is obtained for higher efficiency values of ESS. Although for efficiencies below one ESS increase average load power and decrease mean daily voltage, Table III shows that has not been a problem considering voltage quality. This is possible because of high DG power periods, when it is desirable to increase load considering voltage quality. Specifically, this can be seen on the example $\eta = 0.1$ for where *ESS* is practically controlled load but still voltage profile quality is better than the case without *ESS* (Table I). Also, results in Table III show that *ESS* is making higher voltage profile improvement in the case of the second, more uneven load diagram.

V. CONCLUSION

In this paper optimization problem of voltage profile improvement of the distribution line with DG using *ESS*, is successfully solved with optimization method of genetic algorithm. Obtained results have shown that voltage profile of the distribution line with DG can significantly be improved using *ESS*. This is especially true for more uneven load diagrams and cases where power from DG does not match in time the load power. Optimal power and location of ESS depend on the shape of load diagram, power of DG and its location on the distribution line. Also, it can be concluded that greater efficiency of *ESS* gives better voltage profile improvement.

REFERENCES

[1] Rajaković, N., Tasić, D., & Savanović, G. (2004). Distribution and Industrial Networks, *Academic mind, Belgrade, in Serbian*.

[2] Wong, L., Shareef, H., Mohamed, A., & Ibrahim, A. (2017). Optimal Placement and Sizing of Energy Storage System in Distributed Network with Photovoltaic Based Distributed Generation Using Improved Firefly Algorithms. *International Journal of Energy and Power Engineering 11*(7), 895-903.

[3] Nick, M., Hohmann, M., Cherkaoui, R., & Paolone, M. (2013, June). Optimal location and sizing of distributed storage systems in active distribution networks. In *2013 IEEE grenoble conference* (pp. 1-6). IEEE.

[4] Stecca, M., Elizondo, L. R., Soeiro, T. B., Bauer, P., & Palensky, P. (2020). A comprehensive review of the integration of battery energy storage systems into distribution networks. *IEEE Open Journal of the Industrial Electronics Society*, *1*, 46-65.

[5] Jin, R., Song, J., Liu, J., Li, W., & Lu, C. (2020). Location and capacity optimization of distributed energy storage system in peak-shaving. *Energies*, *13*(3), 513.

[6] Home-Ortiz, J. M., Pourakbari-Kasmaei, M., Lehtonen, M., & Mantovani, J. R. S. (2019). Optimal location-allocation of storage devices and renewable-based DG in distribution systems. *Electric Power Systems Research*, *172*, 11-21.

[7] Karanki, S. B., & Xu, D. (2016, December). Optimal capacity and placement of battery energy storage systems for integrating renewable energy sources in distribution system. In *2016 National Power Systems Conference (NPSC)* (pp. 1-6). IEEE.

[8] Das, C. K., Bass, O., Kothapalli, G., Mahmoud, T. S., & Habibi, D. (2018). Optimal placement of distributed energy storage systems in distribution networks using artificial bee colony algorithm. *Applied energy*, *232*, 212-228.

[9] Das, C. K., Bass, O., Kothapalli, G., Mahmoud, T. S., & Habibi, D. (2018). Overview of energy storage systems in distribution networks: Placement, sizing, operation, and power quality. *Renewable and Sustainable Energy Reviews*, *91*, 1205-1230.

[10] Tang, X., Deng, K., Wu, Q., & Feng, Y. (2020). Optimal location and capacity of the distributed energy storage system in a distribution network. *IEEE Access*, *8*, 15576-15585.

[11] Radosavljević, J. (2018), Metaheuristic Optimization in Power Engineering. *Institution of Engineering and Technology, London*.

Solar Photovoltaic Prediction of Power Output Using Artificial Neural Network

Khadija Lmesri[1], Samira Chabaa[2], Abdelouhab Zeroual[3]

[1,3]Physics department Faculty of Sciences Semlalia, Cadi Ayyad, Marrakesh, Morocco, khadija.lmesri@ced.uca.ma[1]

[2]LISAD Laboratory National School of Applied Sciences, Ibn Zohr University Agadir, Morocco, s.chabaa@uiz.ac.ma

Abstract—**Photovoltaic (PV) output power inherently exhibits an intermittent property depending on the variation of weather conditions. Since PV power producers may be charged to large penalties in forthcoming energy markets due to the uncertainty of PV power generation, they need a more accurate PV power prediction model in energy market operation. In this study, we propose a model based on Artificial Neural Network (ANN) to predict the output power of a PV system installed in Agadir city (320°25'39"N 9°35'53"W), Morocco. In order, to integrate efficiently this PV system into a smart grid, it primordial to predict accurately the PV power output over the next hours or days. The developed model estimate the PV power output values based on meteorological data. The obtained results demonstrate the reliability and the precision of our developed model to predict the hourly PV power output in case of missing real values. Consequently, electrical power engineers can adopt this prediction model to design and supervise the PV systems and integrated it into the power grid.**

Keywords - photovoltaic, artificial neural network, pv power, prediction

I. INTRODUCTION

In recent years, the world has faced an urgent climate change problem and a depletion problem of fossil fuels. The portion of renewable energy sources (RESs) has gradually increased instead of fossil fuel based generators in many countries. We expect that worldwide penetration of solar power rapidly increase until 2030 since it is manageable to build, operate, and maintain PV systems. In order to successfully integrate these power plants into the system, power output predictions need to be more accurate. Several approaches to predicting have been developed throughout previous years, from physical methods using weather forecasts and satellite images to purely statistical, numerical methods and lately even artificial intelligence.

When adopted for PV power systems, prediction techniques can be divided into two categories, direct methods applied directly to the produced power and indirect methods, applied indirectly to the solar irradiation, which is the main factor related to the output power that is calculated in the next step [1].

Indeed, there are two commonly employed estimating approaches for PV power prediction. Statistical techniques based time series regression and data driven based artificial intelligence (AI) algorithms [2]. The AI approaches used some advanced models, such as artificial neural network ANN, and fuzzy logic inference systems [3].

Artificial neural network (ANN) is the most common artificial intelligent (AI) technique that has been utilized in the last two decades. It can model nonlinear and complex systems due to its capability to regulate the weights and the biases [4]. The ANNs were widely used in the prediction of PV power production during the last years. In [5], the ANN is applied to estimate the power output based on the past power measurements and meteorological forecasts of solar irradiance. Additionally, F. Barbieri et al. [6] are used the ANN in conjunction with numerical weather prediction models, which is based on satellite and land-based sky imaging. The efficacy of the ANN approaches depends on

ISBN: 978-86-80593-73-9

various factors as well as initial weight values, network architecture, type of training algorithm, and training data set [7].

This search study aims to predict the PV power with the ANN. The ANN can be effectively employed in various prediction problems successfully. It can also be used to solve the issues related to field of PV power production prediction.

The remaining of this paper is written as follows: in section 2, the materials and methods are detailed. In Section 3, the PV power production prediction results of the proposed model are presented and discussed. Finally, in Section 4 conclusions are given.

II. MATERIALS AND METHODS

A. *Artificial Neural Network*

Artificial neural network (ANN) is a theoretical simulation of a real nervous system that consists of a set of neural units connected to each other through axon connections which are very similar to the dendrites and the axons in biological nervous systems [8-10].

ANN consists of three layers including input, output, and intermediate hidden layers, with their corresponding neurons. ANN has a huge number of connections, because the neurons of each layer are connected to the next layer's neurons. Each connection is associated with a weight. The role of the hidden layer is that to learn the relationship existing between the inputs and the outputs [11].

When, the neuron received the inputs variables, the output of each neuron is calculated by applying an activation function to the weighted sum as shown Fig. 1.

An artificial neuron receives external inputs $(x_1, x_2, ..., x_n)$ and produces a result y at the output [11]. Hence, it can be considered as an element of information processing.

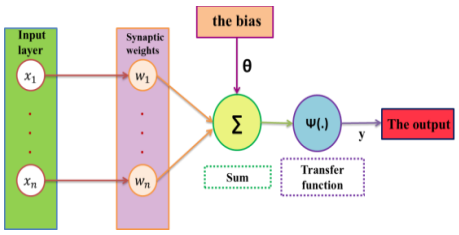

Figure 1. Typical architecture of Artificial Neural Network.

$$Y = \Psi\left(u\left(w,x\right)\right), \quad (1)$$

$$u\left(w,x\right) = \sum w_j x_j + \theta = W'X + \theta, \quad (2)$$

where:

- $w_1, w_2, \ldots, w_n$ are the synaptic weights associated with each connection,
- $W = \left[w_1, w_2, \ldots, w_n\right]'$ is the vector of synaptic weights,
- $X = \left(x_1, x_2, \ldots, x_n\right)$ is the vector of inputs,
- θ is the bias or threshold vector,
- $\psi(.)$ is the nonlinear activation function.

The choice of the activation function type depends on the application. Various activation functions types can be used, with linear activation function, logistic sigmoid function, hyperbolic tangent sigmoid function and Gaussian radial basic function [10].

Various optimizers can be adopted to train ANN prediction models. In this paper, the Levenberg-Marquardt (LM) optimizer was used [12]. Because LM optimizer is the efficient and the robust one and it has demonstrated a high efficiency to train several ANN architectures.

The performance function, $f_p(w)$, of LM algorithm has the form of the error vector sum of squares, which is defined as follows:

$$f_p(w) = \frac{1}{2} e^T(w) e(w) = \frac{1}{2} \sum_{i=1}^{k} \sum_{j=1}^{p} \left(0_{ij} - 0_{ij}\right)^2, \quad (3)$$

where:

- $W = \left[w_1, w_2, \ldots, w_n\right]'$ is the vector of all the network's weights.

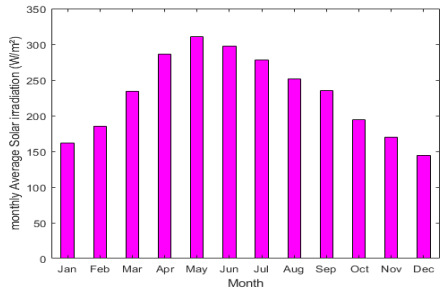

Figure 2. Monthly Average Solar irradiance evolution.

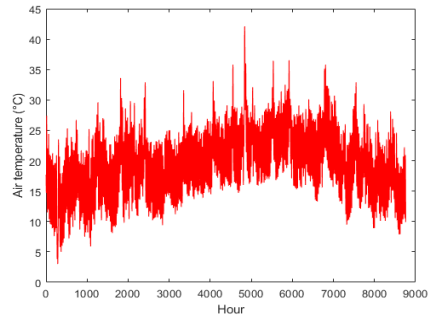

Figure 3. Hourly Air temperature evolution.

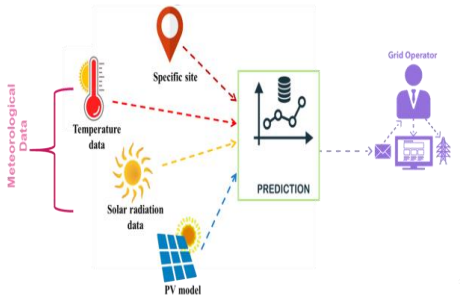

Figure 4. Proposed predictive model's scheme.

Oij, *tij*, *i* and *j* are, respectively, the observed output, the desired output, the iteration number, and the number of samples.

B. *Data Description*

In this research study, the typical year of solar irradiation and air temperature measurements of hourly meteorological measurements of Agadir city, Morocco (320°25'39"N 9°35'53"W), are adopted to train and evaluate the proposed prediction model. The high correlation between PV power production and these meteorological data demonstrate the pertinence of the choice of these variables as an input.

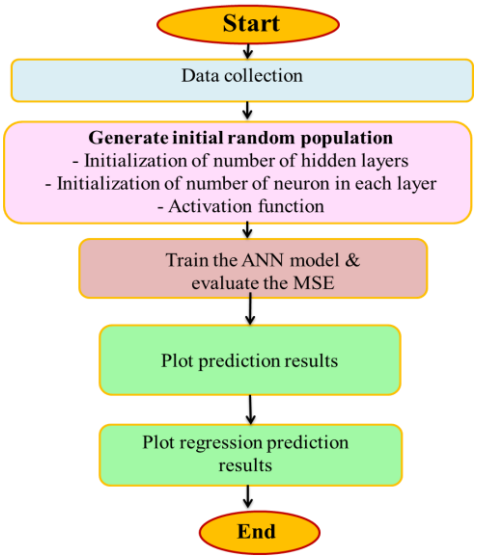

Figure 5. Steps to develop the ANN.

Figs. 2 and 3 show the hourly solar irradiation and the air temperature time series, respectively.

III. PREDICTION RESULTS AND DISCUSSION

A. *Proposed Prediction Scheme*

In this case, the optimization problem is to find the optimal number of weights with the minimization of performance function of ANN. For modeling the non-linear PV power production, ANN model structure with 2 inputs and 20 hidden neurons is used. In Fig. 5 the proposed model's scheme is presented. Indeed, the proposed prediction model is trained using the LM optimizer; where 70% of the whole database is used for training the model's parameters and the remaining 30% of the database is used for validation (15%) and testing (15%) in order to evaluate the performance and the accuracy of the developed model.

In Fig. 5, the different steps to develop the proposed predictive model are presented.

To evaluate the reliability of the developed predictive model, two performance factors are used, which are the mean square error (MSE) and the correlation coefficient (R). They are defined by the following formulas [16]:

$$MSE = \frac{1}{N}\sum_{i=1}^{N}(d_i - p_i)^2 \ , \qquad (5)$$

$$R = \sqrt{\sum_{i=1}^{N}(p_i - d_{mi})^2 / \sum_{i=1}^{N}(d_i - d_{mi})^2} \ , \quad (6)$$

where:

- YPi : YPi The predicted output,
- Yi : The desired output,
- Ymi : The average value of Yi ,
- N : The number of samples.

B. *Results Discussion*

This study aimed to predict PV power production values from other independent meteorological variables (Solar radiation and air temperature) using the Artificial Neural Networks. The results of the presented model are shown in the Table I.

The obtained results of test data for 180 hours of a week period, are presented in Fig. 6. The graph shows clearly the similarity between real and predicted PV power values during the testing process. Furthermore, Fig. 7 presents the scattering diagram, which demonstrates the height relationship between the prediction and real PV power.

From the obtained results, the developed model is able to accurately perform the prediction of PV power. Consequently, this model is adequate and robust to predict efficiently the production of the PV systems using metrological data. Hence, it is reliable to be adopted by electrical engineers, to design or supervise the PV systems, in case of missing values measurement.

IV. CONCLUSION

The main goal of this search study was to offer an intelligent and accurate model to predict the PV power production values ahead from two parameters (solar irradiation, air temperature). For this reason, the artificial neural network is used for the predicting the PV power. In this work, we are used indirectly prediction method. The first step was modeling PV module, which is able to calculate PV power based on metrological data. Then, setting the parameters of the ANN model. Finally, to provide the reliability and accuracy of the elaborated model, the used database is divided into two parts: the first one is used for training and validating the model, and the second one is used for testing the efficiency of the model. The performance and the precision of the model were evaluated using the statistical indicator Mean Square Error (MSE). In terms of this indicator, the predictive model can accurately forecast the PV power output of a solar panel. The obtained results showed that MSE=2.3091% and R= 99.976% in the testing process. The achieved results confirm the

TABLE I. ARTIFICIAL NEURAL NETWORK MODEL RESULTS.

Training algorithm	*Number of layers*	*R (%)*	*MSE (%)*
ANN model	16	99.99976	2.3091

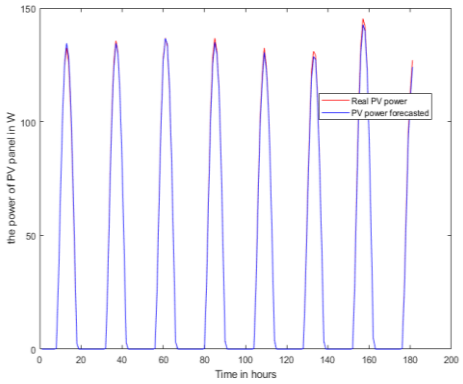

Figure 6. Real PV power and predicted PV power for hours of the week during the testing process.

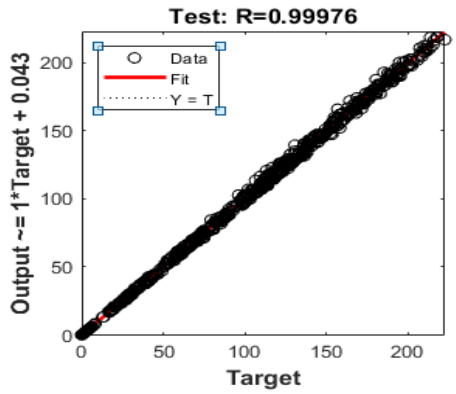

Figure 7. The scattering diagram of PV power production in testing process.

model's effectiveness to accurately predict the PV power production time series. Consequently, it was adequate to be adopted in case of absence of real measurements.

ACKNOWLEDGMENT

This research was financially supported by the National Center for Scientific and Research (CNRST) of Morocco.

REFERENCES

[1] Rosato, A., Altilio, R., Araneo, R., & Panella, M. (2017). Prediction in Photovoltaic Power by Neural Networks. *Energies*, *10*, 1003; doi:10.3390.

[2] Voyant, C., Notton, G., Kalogirou, S., Nivet, M.L., Paoli,C., Motte, F., & Fouilloy, A. (2017). Machine learningmethods for solar radiation forecasting: A review. *Renewable Energy, 105*, 569-582.

[3] Jallal, M. A., Chabaa, S., Zeroual, A., El Yassini, A., Ibnyaich, S., & Raoufi, M. (2019). Elman Neural Network for Solar Radiation Components Forecasting based on the desired tilt angle. In *7th International Renewableand Sustainable Energy Conference (IRSEC), Agadir, Morocco* (pp. 1-5).

[4] Jallal, M. A., Chabaa, S., & Zeroual, A. (2019). A new artificial multi-neural approach to estimate the hourly global solar radiation in a semi-arid climate site. *Theoretical and Applied Climatology*, 03033-1.

[5] Chen, C., Duan, S., Cai, T., & Liu, B. (2011). Online 24-h solar power forecasting based on weather type classification using artificial neural network. *Sol. Energy, 85*, 2856–2870.

[6] Barbieri, F., Rajakaruna, S., & Ghosh, A. (2017). Very short-term photovoltaic power forecasting with cloud modeling: A review. *Sustain. Energy Rev. 75*, 242–263.

[7] Islam, Z. Baharudin, M. Q., & Nallagownden, R. P. (2014). Optimization of Neural Network Architecture Using Genetic Algorithm for Load Forecasting. IEEE 978-1-4799-4653-2/14/31.00 2014.

[8] Chiteka, K., & Enweremadu, C. C. (2016). Prediction of global horizontal solar irradiance in Zimbabwe using artificial neural networks. *J Clean Prod 135*, 701–711. doi:10.1016/j.jclepro.2016.06.128

[9] El Badaoui, H., Abdallaoui, A., & Chabaa, S. (2017). Optimization numerical the neural architectures by performance indicator with LM learning algorithms. *J Mater Environ Sci 8*, 169–179.

[10] Idrissi, M. A. J., Ramchoun, H., Ghanou, Y. & Ettaouil, M. (2016). Genetic algorithm for neural network architecture optimization. In *3rd International Conference on Logistics Operations Management (GOL)* (pp. 1-4). doi: 10.1109/GOL.2016.7731699.

[11] Jallal, M. A., Chabaa, S., & Zeroual, A. (2021). Half-hour global solar radiation forecasting based on static and dynamic multivariate neural networks. *Journal of Engg. Research., 9*(2), 203-217.

[12] Chabaa, S., Zeroual, A., & Antari, V. (n.a). Identification and prediction of internet traffic using artificial neural networks. *Journal of Intelligent Learning Systems and Applications, 02*(03), 147-55.

[13] Burney, S., Jilani, T., & Ardil, C. (2008). Levenberg-Marquardt algorithm for Karachi stock exchange sharerates forecasting. *International Journal of Computer andInformation Engineering, 2*(4), 1330-1335.

[14] Luo, X. J., Lukumon, O., Oyedele, A. O., Ajayi, O. O., Akinade, Delgado, J. M. D., Owolabi, H. A., & Ahmed, A. (2020). Genetic algorithm-determined deep feedforward neural network architecture for predicting electricity consumption in real buildings. *Energy and AI 2*, 100015.

[15] Nayak, S. C., Misra, B. B., & Behera, H. S. (2012). Index prediction with neuro-genetic hybrid network: A comparative analysis of performance. *In Computing, Communication and Applications (ICCCA), 2012 International Conference* (pp. 1-6).

[16] Abbes, D., Martinez, A., & Champenois, G. (2012). Eco-design optimisation of an autonomoushybrid wind-photovoltaic system with battery storage. *IETRenew Power Gener, 6*(5), 358–71.

[17] Jallal, M. A., González-Vidal, A., Skarmeta, A. F., Chabaa, S., & Zeroual, A. (2020). A hybrid neuro-fuzzyinference system-based algorithm for time seriesforecasting applied to energy consumption prediction. *Applied Energy, 268*,114977.

The Improvement of the Heating, Cooling and Air Conditioning (HVAC) Units in Existing Buildings After Covid 19 Pandemic: A Case Study

Ayşe Fidan Altun[1]

[1]Bursa Uludag University, Orhangazi Yenikoy Asil Celik Vocational School, Bursa, Turkey, aysealtun@uludag.edu.tr

Abstract—**During the pandemic, heating, cooling and air conditioning systems (HVAC) needs to be controlled for the risk of airborne transmission of the SARS-CoV-2 virus. It is possible for the CoV-2 virus to be carried by air movements, more precisely by the suspended particles. This transmission and spread of the disease can occur quickly to the people in the same volume if there is no proper ventilation system. For this reason, the suitable measures to be taken for the operation of HVAC systems can reduce the causes of airborne contamination. Additional steps to be taken in HVAC systems do not entirely eliminate the risk of contamination but play an essential role in reducing the rate of spread in closed spaces. In this study, various improvements were proposed for HVAC systems for currently used buildings. A case study was conducted for an existing building to minimize the risks of COVID-19.**

Keywords – indoor air quality, HVAC systems, COVID-19

I. INTRODUCTION

COVID-19 disease has been affecting the whole world since the end of 2019. Many studies have shown that most of the outbreaks occurred in indoor spaces [1]. There is a great risk of airborne transmission of the SARS-CoV-2 virus. Therefore, airborne transmission of the virus must be controlled with engineering tools. The transmission of the virus is caused by the transmission of the aerosols emitted by the sick person from the mouth, nose, and eyes due to sneezing, coughing, and breathing at a close distance (within 2 m) or from the surfaces on which these droplets were suspended. Many researchers have shown that airborne transmission is the number one transmission reason, specifically in closed volumes. Ventilation in indoor spaces is highly associated with the risk of infection [2].

Heating, ventilation and air-conditioning (HVAC) systems are mainly used in buildings to control temperature, relative humidity and many other characteristics of indoor air. So, before the pandemic, HVAC systems only conditioned indoor air and provided fresh air when needed. After the COVID-19 pandemic, HVAC systems were also used to destroy the virus and reduce the spread rate of the disease. However, the infrastructure of the HVAC systems in currently used buildings are not designed to control infection of the biological contaminants. After the COVID-19 pandemic, significant transformations and new requirements are occurring in HVAC systems [3].

In Fig. 1, infection control hierarchy was provided which was taken from REHVA standard [4]. According to the figure, engineering control mechanisms come prior to the personal protective equipment and administrative control. This figure emphasizes the importance of ventilation, air filtering and other engineering tools that separate people and pathogens.

To minimize risks of the virus, a detailed investigation should be conducted for existing buildings considering the purpose of use, physical conditions, and HVAC systems. The proper measures to be taken for the operation of

ISBN: 978-86-80593-73-9

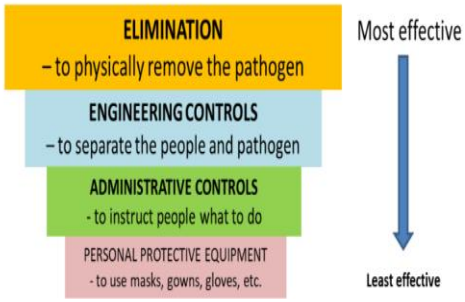

Figure 1. The infection control hierarchy pyramid [4].

HVAC systems can reduce the causes of airborne contamination.

In this paper, a comprehensive review was provided regarding COVID-19 countermeasures on the operation of HVAC systems. Also, a currently used school building was examined in terms of HVAC systems, and various guidelines were recommended.

II. HVAC System Guidelines During the Pandemic

Many organizations worldwide, such as ASHRAE, REHVA etc., proposed operation guidelines for HVAC systems during the pandemic. The main guidelines were summarized as below:

- The spread of the virus is mainly realised in enclosed volumes. Well-designed HVAC systems with high-efficiency air filters may eliminate aerosols that carry the SARS-CoV-2 virus. Therefore, HVAC systems have a crucial role in decreasing the spread rate of the virus. The HVAC system is also beneficial in terms of thermal comfort.

- It is not recommended to have a specific heating cooling or relative humidity setpoint to inactivate the virus as there is not enough scientific evidence. Despite, some works support low relative humidity may increase the survival of COVID-19, most of the organizations recommend to maintain relative humidity around 40-60% only to keep thermal comfort without targeting virus disinfection.

- Air movement is associated with the transmission of the virus from sick people to other occupants. Air currents and movements created by fans and air conditioners should be directed upwards instead of directing to the people's breathing zones [5].

- As stated in the REHVA document [4], COVID-19 aerosols may spread through the recirculated air by the HVAC systems. During the pandemic, indoor air quality should be the primary target. Therefore, air handling units should be switched to 100% outdoor air without recirculation mode. It is recommended to disable demand-controlled ventilation [1]. All of the standards prioritize indoor air quality and occupant health over energy efficiency and consumption. Operate exhaust fans in toilets, bathrooms and kitchens at full capacity. In addition to mechanical ventilation, natural ventilation should be recommended to the occupants. Before using a room, occupants should ventilate the room by opening the windows for at least 15 minutes. Increasing the air change rate, increasing the use of fresh outdoor air, and decreasing the use of recirculation air are essential concerns.

- Using appropriate air filters is also recommended by many organizations [4, 6]. An essential consideration is to improve the central air filter to the highest compatible filter type (at least MERV14 or F8 is recommended by [7]) and seal the filter's edges to decrease bypass air. In addition, using portable air purifiers with HEPA filters is another vital consideration. However, regular surface disinfection should also keep done as the air purifiers do not disinfect surfaces.

- UVC technology is the most accessible method to eliminate biological contaminants as viruses [8]. UV radiation is divided into three different categories, which are UV-A (from 315 to 400 nm), UV-B (from 280 to 315 nm), and UV-C (from 100 to 280 nm). UV-C radiation is recognized as the most influential category for disinfection. UVC was recommended by many organizations, especially in high population density volumes like prisons, shelters, etc.

- Also, most of the standards recommended increasing the working hours of the HVAC systems to improve indoor air quality. Ventilation systems should start to operate at least two hours before the building using time and finish operating at least two more hours after the building usage time. It is also recommended to run the ventilation system at the weekend and at night at a lower speed [1].
- It is also recommended to install indoor air quality monitoring systems, especially for high population density areas like classrooms Fig. 2. CO2 sensors are advantageous for identifying underventilated locations.

III. Case Study: A School Building

The selected building is an educational building located in Ozluce, Bursa. The school building can be considered as a campus that serves as kindergarten - primary school - secondary school, and high school. The total number of classes in the school is 68. Forty-eight of them are actively used. Each class has 24 student capacity. In terms of occupant density, capacity is around 50%. The usage area of the classrooms is 50 m^2.

Primary data of the HVAC system of the building were summarized below:

- Underfloor heating systems were used in the building.
- The mechanical ventilation system works with 100% fresh air, and fresh air systems are available in all classrooms.
- There is a conference and multi-purpose hall for 500 people capacity. A rooftop air conditioner is used in that room, and it works with 40% fresh air.
- VRF air conditioning systems infrastructure is available in administrative offices.
- All toilets have exhaust ventilation.
- Floor heights in classrooms and public areas is 3.5 m.

Based on the investigations, areas of the school building were ranked according to infection risk, and results were enumerated below:

Figure 2. A picture of the classrooms.

1. Level risk areas:

- Cafeteria
- Multi-Purpose Hall
- Gym – Changing Rooms
- Entrance Turnstiles
- Level risk areas:
- Classrooms
- Laboratories
- Toilets

After determining the current situation of the school building, measures to be taken in the building were recommended based on the international guidelines. Recommendations were divided into four groups as given below:

2. Physical measures to be taken
3. Daily, weekly and monthly maintenance measures
4. Educational measures
5. Precautions to be considered in building operation, considering global health risks.

In terms of physical measures, HVAC system was considered first.

- The fact that 100% outdoor (fresh) air is used in the ventilation system of the classrooms without mixing with the indoor (exhaust) air has been evaluated positively. This was recommended by numerous standards during the

pandemic [4–6].

- The fresh air capacity of the air handling unit should be checked and, if possible, more fresh air should be given to the interior spaces.
- The exhaust air which is sucked from the indoor spaces should not be mixed with the fresh air. The return air must be closed completely, or the leak-proof test of the plate heat exchanger in the heat recovery unit must be carried out. The leakage risk of plate type heat recovery units is very low. However, leakage control should be done, and its use should be decided accordingly.
- There should be at least 10 m distance between the air handling unit exhaust discharge fans and fresh air intake fans and/or it should be arranged in such a way that there is no risk of interference. Fresh air intake and exhaust fans should be removed from the environments of people/students.
- In ventilation installations, solutions should be used to minimize air turbulence as much as possible. If possible, blowing from the top, suction from places close to the ground level will prevent air turbulence.
- Fixed or portable fan-coil, VRV-VRF, heat pump indoor units that results in indoor air recirculation in classrooms, halls and/or corridors should be turned off or used in a controlled manner. These devices can be used in existing systems by using HEPA filters and/or UV, controlling the air circulation directions and keeping the risk of contamination at a minimum level.
- Attention should be paid to other possible bacterial and fungal risks in systems that have not been operated for a long time during the pandemic. Appropriate precautions should be taken in areas such as water tanks and reservoirs.
- For places that cannot be mechanically ventilated or insufficiently ventilated, windows must be opened at regular intervals to ensure fresh air intake. However, it should not be forgotten that irregular air currents and dust, allergens and other pathogens that can be taken inside will increase other health risks.
- The operating times of indoor ventilation systems can be extended and the systems can be continued to operate at low speed (flow rate) even when the buildings are not in use. Energy efficiency is not the priority during the pandemic.
- The ventilation device should be operated at least 2 hours before the cafeteria starts to be used, and the ventilation system should be turned off at least 2 hours after the work in the cafeteria is completed (Fig. 3).
- In general, it is appropriate to operate the ventilation systems 24 hours a day, seven days a week during the epidemic period.
- Toilets:
- Toilet aspirators (negative exhaust ventilation) should be operated 24/7

Figure 3. The picture of the cafeteria.

Figure 4. Picture of the toilets.

without interruption. Negative pressure must be maintained in the toilets. At least 80% of the exhaust air should be given as fresh air to the bathrooms.

- In toilet exhausts, return flaps that will not take the return air should be used.
- Toilet exhaust vents should never be mixed with fresh air intake and should not be brought close (Fig. 4).

Daily, weekly and monthly maintenance measures:

- Every occupant in the school should be ensured to pay attention to social distance.
- Cleaning of frequently touched surfaces [door handles, handrails, frequently touched buttons (elevator, lighting, etc.), toilets and sinks in common areas should be done at least twice a day.
- Arrangements should be made so that the distance between tables and chairs is at least 1 meter (preferably 2 meters) in the cafeteria. For easy contact tracking; mealtimes should be determined according to the groups, and if possible, the same people should eat at the same table.

Educational measures:

- Relevant training should be given to the occupants, students, teachers, administrators, and officers.

Precautions to be considered in building operation, considering global health risks:

- It is appropriate to operate the ventilation systems 24 hours a day, seven days a week during the epidemic period.
- Air curtains should not be operated during the epidemic period.
- During the epidemic, it is vital for students to carry their own drinking water containers or prefer disposable bottled water.

IV. Conclusions

Heating, Ventilation and Air Conditioning systems mainly provide occupants conditioned and clean air and maintain indoor air at desirable temperature and humidity levels. However, during the time of the COVID-19 pandemic, the importance of the HVAC systems was emphasized by many organizations around the globe in terms of eliminating the droplets containing the SARS-COV2 virus.

In general, both mechanical and natural ventilation were recommended by the health and vocational organizations. Ventilation systems were recommended to operate with 100% outdoor air. Recirculation of the indoor air is not desirable if it is possible. Enhancing the air filters with higher efficiency ones and using HEPA and UVC filter in ventilation systems is adviced by many organizations.

Increasing the operation times of the HVAC system is another important concern. The operation of the HVAC system should start at least two hours before and stop at least two hours after the occupancy schedule. During the pandemic, the main concern is occupant health and comfort; therefore, energy consumption comes after.

In the light of the guidelines of the well-known organizations, a case study was conducted. A school building was investigated in terms of COVID-19 safety. Based on the investigations, locations with high population density, such as cafeteria (Fig. 3), multi-purpose hall, gym, and entrance turnstiles, were found to be the riskiest locations. Classrooms were ventilated with 100% fresh air. For other indoor spaces, the fresh air intake of the air handling unit was recommended to increase. For heat recovery systems, it was recommended to control leakage to not to mix fresh air with the exhaust air. Also, it was recommended to have at least 10 m distance between the air handling unit exhaust discharge fans and fresh air intake fans. Since air movement is undesirable and can transmit the virus from person to person, ventilation solutions should be used as minimizing air turbulence. For places without mechanical ventilation, natural ventilation should be used to ensure fresh air intake.

Despite the fact that there is no guarantee of elimination of the virus, application of the guidelines might decrease the spread rate of the virus and help to control the pandemic. The importance of the engineering tools comes prior to administrative controls or personal protective equipment.

ACKNOWLEDGMENT

This study is supported by Scientific and Technology Research Council of Turkey (TÜBİTAK), under project number 218M604. The author would like to thank TÜBİTAK for its support.

REFERENCES

[1] Guo, M., Xu, P., Xiao, T., He, R., Dai, M., & Zhang, Y. (2020). Review and comparison of HVAC operation guidelines in different countries during the COVID-19 pandemic. *Building and Environment*, 107368.

[2] Sun, C., & Zhai, Z. (2020). The efficacy of social distance and ventilation effectiveness in preventing COVID-19 transmission. *Sustainable cities and society*, *62*, 102390.

[3] Zheng, W., Hu, J., Wang, Z., Li, J., Fu, Z., Li, H., ... & Yan, J. (2021). COVID-19 Impact on Operation and Energy Consumption of Heating, Ventilation and Air-Conditioning (HVAC) Systems. *Advances in Applied Energy*, 100040.

[4] REHVA. (2020). How to operate HVAC and other building service systems to prevent the spread of the coronavirus (SARS-CoV-2) disease (COVID-19) in workplaces.

[5] Health Ontario P. Heating, Ventilation and Air Conditioning (HVAC) Systems in Buildings and COVID-19 FOCUS ON Heating, Ventilation and Air Conditioning (HVAC) Systems in Buildings and COVID-19. n.d.

[6] ASHRAE. (2020). *Guidance for Building Operations During the COVID-19 Pandemic*.

[7] Agency N. E. (2021). ACMV systems include air handling units and fan coil units such as cassette- or wall-mounted types. Specialised premises refer to those with ACMV systems that fall outside the scope of SS553: Code of Practice for Air Conditioning and Mechanical Ventilatio.

[8] Brincat, J. P., Sardella, D., Muscat, A., Decelis, S., Grima, J. N., Valdramidis, V., & Gatt, R. (2016). A review of the state-of-the-art in air filtration technologies as may be applied to cold storage warehouses. *Trends in Food Science & Technology*, *50*, 175-185.

Applications of "Intersection" Multi-Objective Optimization in Scheme Selection of Energy Engineering

Maosheng Zheng[1], Yi Wang[2], Haipeng Teng[3]

[1,2,3]School of Chemical Engineering, Northwest University, Xi'an, 710069, China, mszhengok@aliyun.com[1]

Abstract—**The newly developed "intersection" multi – objective optimization is utilized to conduct the scheme selections of energy engineering in this paper, which include the site selection of nuclear power plants (NPP) in considering the surrounding factors, the dispatching decision of reservoir flood control (RFC), and the comprehensive evaluation of design schemes for long–distance natural gas pipelines (LDNGP). Accordingly, the utility of each performance attribute is equivalently and conformably treated, which contributes a partial favorable probability linearly to its scheme. The total favorable probability of each scheme is the product of its all possible partial favorable probabilities, which is the uniquely decisive index for the selection excluding any artificial or subjective scaling factors. The result of this study indicates the applicability of the newly developed "intersection" multi–objective optimization in scheme selection of energy engineering.**

Keywords - energy engineering; multi–objective optimization, scheme selection, probability theory, favorable probability

I. INTRODUCTION

In this paper, the newly developed "intersection" multi – objective optimization is utilized to conduct the scheme selections of energy engineering, the site selection of NPP in considering the surrounding factors, the dispatching decision of RFC, and the comprehensive evaluation of design schemes for LDNGP are taken as examples.

As a clean and new energy resource, nuclear power generation has become an important developing direction in China's new energy exploration. As a relatively scarce resource, NPP sites are becoming more and more complex, and the potential sources of external incidents surrounding the site are becoming more and more diversified. For the safety, the sources of potential external incidents around the site should be fully considered during the site selection phase of the NPP.

According to the "Safety Regulations on Site Selection for NPP" and the related requirements for site selection of NPP, there are three basic contents that need to be evaluated in the site selection of NPP. The first is the possible impact of the external environment around the site on the safety of NPP, including man–made and external natural events. Therefore, when selecting a NPP site, it is necessary to quantitatively evaluate various possible potential external events around the NPP in detail in order to get a reliable consequence of the safety [1].

In China, in order to fully consider the potential impact of the external events around the site on NPP during the site selection phase, it has issued the specific document of "Potential External Events for the Site Selection of HAF0105 Nuclear Power Plants", which defines the potential external incidents and proposes corresponding strategies for investigation and evaluation. According to the document, the potential aircraft crashes, explosions, and dangerous liquid releases are all included in the item, so the fundamental conditions for the quantitative evaluation are met for NPP site selection in principle [2].

Dispatching decision of RFC is our second example. There are several approaches for the

ISBN: 978-86-80593-73-9

plan selection, including vague set, grey relational analysis method, set pair analysis method and fuzzy clustering iteration method mainly. However, in the actual application process of the priority ranking of decision – making schemes, quite often the decision – makers cannot always guarantee absolute rationality due to the influence of flood control and benefit, flood season and post–flood, local and overall factors, and they are often subjective in the decision – making process. It shows a clear risk preference subjectively, and this subjective preference directly affects the reliability and applicability of the decision - making results. Therefore, in considering the risk factors of decision makers and the risk attitude of decision makers facing in the evaluation process, the quantitative target flood control dispatching decision is of great significance to the raise of the behavioral factors and psychological perception characteristics of the decision makers [3].

The third example is the scheme selection of long – distance natural gas pipeline project. It has the characteristics of high technology, high investment and high risk. It is very important to make scientific decisions on various engineering schemes. Since 1990s, a set of comprehensive multi – scheme evaluation methods for oil and gas pipeline design has been formed on basis of fuzzy set theory, gray theory and matter – element analysis. The gray correlation analysis method, gray matter–element analysis method, fuzzy matter – element analysis method, gray multi - objective situation decision – making method, fuzzy matter – element situation decision-making method, and analytic hierarchy process (AHP) are the main approaches. For multi – objective situation decision – making, there is a certain improvement in the algorithm, but the calculation of the method itself is more complicated. The calculation process of AHP is also more complicated. Gas pipeline engineering is complex and changeable system engineering. The evaluation result is very important to practice of the actual engineering, though many factors need to be considered, so the quantitative evaluation must be appropriate without any query [4].

Since the early work in Multi–Objective problem (MOOP), it has been more than 60 years [5, 6], a series of methods have been developed to analyze the big amount of data involved in scheme selection process so as to obtain a systematic result, such as the methods of Pareto solution, Technique for Order Preference by Similarity to Ideal Solution (TOPSIS), Vlse Kriterijumska Optimizacija Kompromisno Resenje (VIKOR), Multi Attribute Decision Making (MADM), Analytical Hierarchy Process (AHP) and Multi – Objective Optimization on the basis of Ratio Analysis (MOORA), etc [5, 6]. However, there exist inherent problems of personal and subjective factors in the above mentioned multi – object optimizations.

In fact, MOOP involves the simultaneous satisfaction of multi attributes involved. Practically, many actual problems are composed of multiple objects in daily life, which conflict and influence each other. It often encounters the optimization problem of arranging multiple tasks as best as possible simultaneously in a given condition. That is, a multi-objective optimization problem. For example, when a factory manufactures a product, it requires not only less investment, fewer workers, and lower costs, but requires high work efficiency and high profits al well. In viewpoint of probability theory, the general approach for "simultaneous optimization of multiple objects" needs to take the form of "joint probability" of the multiple evaluated attributes, or "intersection" of above multiple attributes in the eyes of set theory [7]. Early in 1980s, Derringer et al and Jorge et al once developed a desirability function to transfer each response variable into a desirability value [8, 9], and all the desirability are combined by employing the geometric mean method to obtain a single desirability to reflect the full assessment for the combined responses. Unfortunately, their approach is not fully consistent with the intention of probability theory with respect of simultaneous optimization of multi – objects.

Currently, a new multi – object optimization approach named "intersection" method for MOOP was proposed in the viewpoints of probability theory and set theory [5], it attempts to solve the inherent problems of personal and subjective factors in the previous multi – object optimizations. The new

concept of favourable probability was proposed to reflect the favourable degree of the candidate in the optimization. All performance utility indicators of all candidates are divided into beneficial or unbeneficial types due to their function and preference of decision maker, each performance utility indicator of the candidate contributes a partial favourable probability in linear type quantitatively, and the total favourable probability of a candidate is the product of all partial favourable probabilities in the viewpoints of probability theory and "intersection" of set theory, which is an uniquely decisive index in the overall selection process competitively. The new multi – object optimization method was also extended in application of multi – objective orthogonal test design method (OTDM) and uniform test design method (UTDM) successfully as well [5].

In this paper the newly developed multi – object optimization method is used to perform the overall scheme selections in energy engineering, which involves the site selection of nuclear power plants (NPP) in considering the potential external events, the dispatching decision of reservoir flood control (RFC), and the comprehensive evaluation of design schemes for long–distance natural gas pipelines (LDNGP).

II. Application of the "Intersection" Multi–Objective Optimization in Energy Engineering for Scheme Selection

A. Brief Introduction of the "Intersection" Multi–Objective Optimization

In the newly developed multi – object optimization method [5], all performance utility indices of all candidates are divided into both beneficial or unbeneficial types due to their function and preference of decision maker; a performance utility index of the beneficial indicator contributes to a partial favorable probability in the selection process in linear manner positively, i.e.,

$$\begin{aligned} &P_{ij} \propto X_{ij}, \\ &P_{ij} = \alpha_j X_{ij}, \end{aligned} \quad i = 1, 2, ..., n;\ j = 1, 2, ..., m. \quad (1)$$

In (1), X_{ij} is the j^{th} performance utility index of the i^{th} candidate scheme; P_{ij} represents the partial favorable probability of the beneficial performance utility indicator X_{jj} ; n is the total number of candidate schemes in the scheme group involved; m is the total number of performance utility indicators of each candidate scheme in the group; α_j is the normalized factor of the j^{th} performance indicator.

Furthermore, the summation of each P_{ij} for the index i in j^{th} scheme factor is normalized equaling to 1 according to the general principle of probability theory [5], i.e., $\sum_{i=1}^{n} P_{ij} = 1$, which naturally results in

$$\alpha_j = 1/(n\bar{X}_j), \quad (2)$$

$\bar{X}_j$ is the arithmetic mean value of the scheme performance indicator in the scheme group involved.

Equivalently, for a unbeneficial (cost) scheme performance utility indicator X_{ij} , its partial favorable probability is negatively correlative to this scheme performance indicator linearly, i.e.,

$$\begin{aligned} &P_{ij}\mu\left(X_{jmax} + X_{jmin} - X_{ij}\right), \\ &P_{ij} = b_j\left(X_{jmax} + X_{jmin} - X_{ij}\right), \\ &i = 1, 2, \ldots, n;\ j = 1, 2, \ldots, m. \end{aligned} \quad (3)$$

In (3), X_{jmax} and $X_{j\min}$ represent the maximum and minimum values of the performance utility index X_j in the scheme group, respectively. Moreover, the normalized factor β_j of the j^{th} scheme performance indicator is

$$\beta_j = 1/[n(X_{j\min} + X_{j\max}) - n\bar{X}_j]\ . \quad (4)$$

Furthermore, according to basic probability theory [5], the total /

comprehensive favorable probability of the i^{th} candidate scheme is the product of its partial favorable probability P_{ij} of each scheme performance utility indicator in the overall selection, i.e.,

$$P_i = P_{i1} \cdot P_{i2} \cdots P_{im} = \prod_{j=1}^{m} P_{ij} \quad . \qquad (5)$$

The total favourable probability P_i of a candidate is the unique decisive index in the overall selection process competitively. The main characteristic of the new "intersection" method for MOOP is that the treatment for both beneficial performance utility index and unbeneficial performance utility index is equivalent and conformable without any artificial or subjective scaling factors.

By employing above procedure and Eqs. (1) through (5), the MOOP now becomes a single object optimization one automatically with the help of the total favourable probability in the viewpoint of probability theory.

B. Application in Site Selection of Nuclear Power Plants (NPP) in Considering External Human Events

Under the guidance of China's specific document of "Potential External Events for the Site Selection of HAF0105 Nuclear Power Plants", the on–site investigation was conducted for the three plant sites, the multiple indicator values of external surrounding events related to the site selection of NPP were obtained, as shown in Table I [2]. The schemes of the three plant sites are signed by A_1, A_2 and A_3.

The meanings of each performance index in Table I are as follow: ma — the actual distance between the airport and the nuclear power plant with unit of km; mb — the actual distance between the explosion source and the nuclear power plant with unit of km; mc — the actual distance between the dangerous liquid source and the nuclear power plant with unit of km; md — the actual distance between the source of the dangerous gas cloud and the nuclear power plant with unit of km; V_1 (m^3) – – the amount of storage in the facility; P_1 — the probability of any leakage or container rupture in the evaluation facility warehouse; V_2 (m^3) – – the maximum amount that can be released in the evaluation facility; P_2 — the probability of the release amount. M — the mass of TNT or TNT equivalent of the explosive source with unit of kg [2].

Subsequently, the survey value in Table I was transformed into the performance utility value for decision–making according the procedure in [2], which is shown in Table II. The objects C and D are the beneficial indices, and the objects Q, W, C_b(m) and D_{an} are the unbeneficial indices.

Table III shows the partial and total favorable probabilities for each performance utility indicator and scheme.

From Table III, it can be seen that scheme A3 is the optimal decision in the ranking, that is, the environment of the potential external surrounding factors of scheme A_3 is the best choice.

C. Application in Site Selection of Dispatching Decision of Reservoir Flood control (RFC)

Taking the decision – making and optimization problem of the multi – objective dispatching plan of Yanwangbizi RFC in Chaoyang City, Liaoning Province of China as an example, the set of flood control dispatching plans is shown in Table IV [3]. Combining the actual status of the reservoir and the basic characteristics of the flood control plan, the representative evaluation indicators are selected

TABLE I. SURVEY VALUES RELATED TO DECISION-MAKING TARGET FACTORS OF NPP.

Plan	**Survey value**								
	ma (km)	mb (km)	mc (km)	md (km)	V_1 (m^3)	V_2 (m^3)	P_1(%) $\times 10^3$	P_2(%) $\times 10^3$	M (kg)
A_1	8	15	20	7	500	90	3	2.4	58
A_2	7	9	8.5	16	100	200	0.9	3.5	45
A_3	11	12	6	20	350	30	1.2	0.9	20

in this paper, mainly including the amount of abandoned water of the reservoir W, the amount of power generation E, the degree of closeness between the ideal water level and the flood level, Z_Δ, the maximum discharge flow q_{max}, and the use flood control storage capacity V_F.

According to [3], the power generation amount E is a beneficial index, and all other indicators are unbeneficial indexes. Table V shows the partial and total favorable probabilities for each performance utility indicator and scheme. Table V indicates that scheme 1 is on the top of the ranking, which is the optimal decision in this selection.

TABLE II UTILITY VALUE FOR DECISION-MAKING OF NPP.

Plan	**Object**					
	C	D	Q	W	C_b(m)	D_{an}
A_1	0.8	1	0.7	1	14930	0.1522
A_2	0.7	0.9	1	0.85	8936	0.0079
A_3	1	1	1	0.6	11951	0.0045

TABLE III PARTIAL AND TOTAL FAVORABLE PROBABILITIES FOR EACH UTILITY PERFORMANCE INDICATOR AND SCHEME.

Probability	**Plan**		
	A_1	A_2	A_3
P_C	0.32	0.28	0.4
P_D	0.3448	0.3104	0.3448
P_Q	0.4167	0.2917	0.2916
P_W	0.2553	0.3192	0.4255
P_{Cb}	0.2497	0.4173	0.3330
P_{Dan}	0.1049	0.4435	0.4516
$Pt\times10^3$	0.3076	1.4969	2.5742
Rank	3	2	1

TABLE IV. DISPATCHING PLAN OF YANWANGBIZI RFC IN CHAOYANG CITY, LIAONING PROVINCE OF CHINA.

Plan	**Object**				
	E(10^4 kW/h)	W (10^8m^3)	Z_Δ(m)	VF (10^8m^3)	q_{max} (m^3/s)
1	5452.86	3.51	0.080	1.49	2996
2	5445.43	3.62	0.180	1.41	3004
3	5387.64	3.84	0.310	1.33	3185
4	5443.61	5.56	0.260	1.43	1937
5	5448.27	3.57	0.180	1.41	3005
6	5422.05	3.70	0.230	1.37	3108

TABLE V PARTIAL AND TOTAL FAVORABLE PROBABILITIES FOR EACH UTILITY PERFORMANCE INDICATOR AND SCHEME.

Plan	**P_E**	**P_W**	**P_Z**	**P_V**	**P_q**	**$P_i\times10^4$**	**Rank**
1	0.1673	0.1816	0.2818	0.1568	0.1575	2.1146	1
2	0.1670	0.1780	0.1909	0.1663	0.1569	1.4810	3
3	0.1653	0.1708	0.0727	0.1757	0.1435	0.5177	6
4	0.1670	0.1146	0.1182	0.1639	0.2360	0.8750	5
5	0.1671	0.1796	0.1909	0.1663	0.1568	1.4946	2
6	0.1663	0.1754	0.1455	0.1710	0.1492	1.0825	4

D. Application in Comprehensive Evaluation of Design Schemes for Long–distance Natural Gas Pipelines (LDNGP)

Since long – distance natural gas pipeline project is with high technology, high investment and high risk, the evaluation of its design scheme must be reliable and serious.

In the optimization of the long–distance gas pipeline design scheme, it should solve the following main problems: 1) to get the proper design of the diameter and wall thickness of pipeline, the location and the number of compressor stations along the line, the type of compressor and its unit combination mode, the compression ratio of the compressor station and the inlet and outlet pressures, the length of the end section under conditions of the topography along the line being undulating, involving several gas inlet and gas distribution points along the line, and knowing the gas inlet and gas volume; 2) to get the proper technical and economic indicators (pipeline investment costs, station construction investment costs, power fees, annual equivalent fees, etc.).

As the process parameters and economic indicators of multiple pre–selected schemes are obtained, the pre–selected schemes should be prioritized and sorted according to the thinking method of system theory.

Table VI shows a set of gas pipeline engineering design plan [4]. All the objects belong to unbeneficial index type.

Table VII shows the partial and total favorable probabilities of each performance utility indicator and scheme of this gas pipeline engineering design plan selection.

Table VII shows that scheme 6 is the optimal decision in this selection.

III. CONCLUSION

By using the newly developed multi – object optimization method, the appropriate selections of optimal scheme of energy engineering are successfully conducted. Three examples are involved, which include the site selection of NPP in considering the potential external events, the dispatching decision of RFC, and the comprehensive evaluation of design schemes for LDNGP. The main features of the new "intersection" method for MOOP are that: the treatment for both beneficial performance utility index and unbeneficial performance utility index being equivalent and conformable; no artificial or subjective scaling factors involved in the assessment process.

Some uncertainty factors would be involved in the multi – object optimization method to extend its usage in more disciplines and fields.

TABLE VI. A SET OF GAS PIPELINE ENGINEERING DESIGN PLAN.

Plan	Annual equiv. fee A (M Yuan / year)	Station invest. B (M Yuan)	Invest. C (M Yuan)	Power fee D (M Yuan / year)	Number of compr. stations E
1	358.1	2007.3	4115.8	213.6	8
2	443.9	2488.0	3908.2	264.8	10
3	270.9	1518.3	4463.5	161.6	6
4	422.6	2367.9	3973.8	252.2	6
5	494.3	2769.1	4039.9	294.9	7
6	285.1	1597.3	4932.3	170.1	4

TABLE VII. PARTIAL AND TOTAL FAVORABLE PROBABILITIES FOR EACH UTILITY PERFORMANCE INDICATOR AND SCHEME OF THIS GAS PIPELINE ENGINEERING DESIGN PLAN SELECTION.

Plan	P_A	P_B	P_C	P_D	P_E	$P_i \times 10^4$	Rank
1	0.1757	0.1757	0.1711	0.1758	0.1395	1.2960	3
2	0.1387	0.1387	0.1786	0.1387	0.0930	0.4435	6
3	0.2134	0.2134	0.1585	0.2134	0.1860	2.8668	2
4	0.1479	0.1479	0.1763	0.1479	0.1860	1.0608	4
5	0.1170	0.1170	0.1739	0.1169	0.1628	0.4510	5
6	0.2073	0.2073	0.1416	0.2073	0.2326	2.9316	1

REFERENCES

[1] Wang, W., & Tan, C. (2017). Studies of Investigation Content and Method of External Human-induced Events around Nuclear Power Plants. *Environmental Impact Assessment*, *39* (4), 82-84. DOI: 10.14068/j.ceia.2017.04.018.

[2] Wang, X., Zou, S., & Pang, B. (2009). The Assessing Method on Site-choosing of NPP about Outside Artificial Event Based on Fuzzy Optimal Selection. *Value Engineering*, *4*, 8-10. DOI:10.14018/ j.cnki.cn13-1085/n.2009.04.002.

[3] Qu, X. (2018). Research on Multi-Objective Flood Control Operation Decision Method of Reservoir Based on Cumulative Prospect Theory and Maximum Entropy Theory. *Water conservancy technical supervision*, *3*, 124-127. DOI: 10.3969/j.issn. 1008-1305.2018.03.038.

[4] Wang, Y., Zhao, S., Chen, J., et al. (2003). Long Gas Pipeline Design Optimization System. *Natural Gas Ind.*, *23* (6), 136-140.

[5] Zheng, M., Wang, Y., & Teng, H. (2021). A New "Intersection" Method for Multi - Objective Optimization in Material Selection. *Tehnicki Glasnik*, 15 (4), 562-568. DOI:10.31803/tg- 20210901142449.

[6] Liu, W., & Yang, Y. (2008). Multi-objective optimization of sheet metal forming process using Pareto-based genetic algorithm, *Journal of Materials Processing Technology*, 208, 499–506.

[7] Brémaud, P. (2020). *Probability Theory and Stochastic Processes*, Universitext Series. Springer, (pp.7-11).

[8] Derringer, G., & Suich, R. (1980). Simultaneous optimization of several response variables, *J. of Quality Technology*, 12, 214-219. DOI:10.1080/ 00224065.1980.11980968.

[9] Jorge, L. R., Yolanda, B. L., Diego, T., Mitzy P. L., & Ivan, R. B. (2017). Optimization of multiple response variables using the desirability function and a Bayesian predictive distribution, *Research in Computing Science*, 13, 85-95.

Performance and Degradation Assessment of Three Silicon Photovoltaic Technologies

Mustapha Adar[1], Youssef Najih[2], Ahmed Chebak[3], Mustapha Mabrouki[4], Amin Bennouna[5]

[1,2,4]Laboratory of Industrial Engineering, University of Sultan Moulay Slimane, Beni Mellal, Morocco, adar.mustpha@gmail.com
[3]Innovation Lab for Operations, Mohammed VI Polytechnic University, Benguerir, Morocco, ahmed.chebak@um6p.ma
[5]Faculty of Sciences Semlalia, Cadi Ayyad University, Marrakech, Morocco, sindibad@uca.ac.ma

Abstract—**This study investigates seasonal performance and assesses the annual degradation rates (R_D), of three types of silicon-based PV module technologies, using four statistical methods, namely Linear Regression (LR), Classical Seasonal Decomposition (CSD), on a five-year Performance Ratio time series. The lowest performance degradation rates being exhibited are found for the pc-si system with a R_D value confined between 0.14%/year and 0.15%/year. The R_D values provided by the two statistical methods to the mc-si PV modules range from 0.41%/year to 0.57%/year. The values attributed to the annual performance degradation rate of PV modules of amorphous Silicon technology typically range from 0.46%/year to 0.51%/year. The average performance ratio value over the 5-year period for the pc-si, mc-si, and a-si technologies was 85.2%, 83.23%, and 83.28%, respectively.**

Keywords – perfermance ratio, degradation rate, silicon PV technology

I. INTRODUCTION

Renewable energies have become a key driver of socioeconomic development in a number of countries. Solar energy is one of the renewable energy sources that is now undergoing rapid development. Photovoltaic energy presently holds a significant position in the renewable energy sector, with an annual growth rate of 45% projected between 2019 and 2020 [1]. By 2022, solar photovoltaics is predicted to be the fastest growing renewable energy source. The PV modules must be monitored and maintained in order for all of these PV installations to match the demands of the power producers in terms of cost-efficiency and dependability. Monitoring allows for the analysis of PV installation performance, and the research of reliability and longevity allows for the prediction and avoidance of faults in the production process. Consumers, in particular, are continuously looking for less expensive items with a high level of dependability and a lengthy life lifetime. PV module manufacturers include a warranty on the data sheet to reassure customers.

They promise that the performance does not fall below 80% over the first 20 years of operation [2]. However, real-world operating conditions differ from normal test conditions (STC). Because of the varying behavior of PV modules based on weather conditions, quantifying degradation rates allows for the circumvention of certain budgetary and technological obstacles. Financial risks are involved with long-term energy efficiency estimation, notably due to assessments of the rate of deterioration and volatility of solar resources, as represented in levelized electricity cost (LCOE) calculations for PV systems [3].

Several degradation determinants and mechanisms are described and investigated in the literature. Temperature, humidity, precipitation, dust, snow, and sun irradiation are the most common elements associated with PV module performance degradation during field operation [4, 5]. The presence of broken cells, glass breakage, and mechanical stress damage to

ISBN: 978-86-80593-73-9

the frame causes moisture to permeate the interior of the PV module, resulting in deterioration processes such as corrosion. When PV modules are exposed to UV light, the encapsulant discolors and experiences photochemical deterioration [6]. Environmental factors frequently lead to encapsulant delamination. Front glass encapsulant delamination, cells, interconnecting ribbons, and backsheet are all examples of encapsulant delamination. All of these types of delamination contribute to various types of PV module degradation [7]. All these types of delamination contribute to different types of degradation of the PV module. Potential-induced degradation (PID) [8-12] and light-induced degradation (LID) [13] are others degradation mechanisms for which the encapsulant is responsible.

In this work, we will analyze the performance and adopt the Performance Ratio to evaluate the performance degradation rate experienced in the field by PV modules based on three silicon technologies (mc-si, pc-si, and a-si). The performance of the three PV plants has been monitored from January 2015 until the end of December 2019. Monthly time series have been constructed using the 60 Performance Ratio values. These time series have undergone seasonal adjustment operations to extract performance trends for each technology using Classical Seasonal Decomposition (CSD).

II. MATERIALS AND METHODS

A. PV Grid-Connected Description

The first PV grid-connected system is based on 8 monocrystalline silicon PV modules of the Sunmodule Plus SW brand from Solar World. The nominal power of each module is 255 Wp. The modules are connected in series, making a peak power of 2K Wp injected into the grid through an SMA 2000 inverter. The second installation, based on eight polycrystalline silicon PV modules from Sunmodule Plus SW 255 Wp, has the same structure as the first and is connected to the grid through an SMA 2000 inverter. The third PV plant consists of 12 amorphous silicon modules of the brand NEXPOWER NT_155AF with an output of 155 Wp per module. The modules form two strings connected in parallel. Each string consists of 6 PV modules. Both strings are grid-connected through an SMA 2000 inverter. PV modules are cleaned regularly. Table I summarizes some technical and electrical characteristics of PV systems. For the measurement of solar irradiance, we used two 20 Wp polycrystalline silicon PV modules calibrated by a Kipp and Zonen pyranometer. Four PT100 temperature sensors are used to measure the temperature of the three photovoltaic technologies and the ambient temperature. The studies [14-18] describe and present more information about the installed technologies, meteorological data acquisition, and some preliminary results regarding the analysis of the performance of these PV systems.

TABLE I. SYSTEMS ELECTRICAL CHARACTERISTICS.

PV System	mc-si	pc-si	a-si
Nominal installed power (KWp)	2.04	2.04	1,86
Module nominal power (W)	255	255	155
Module nominal open circuit voltage (V)	37.8	38	85.5
Module nominal voltage at maximum power (V)	31.4	30.9	65.2
Module nominal short circuit current (A)	8.66	8.88	2.56
Module nominal current at maximum power (A)	8.15	8.32	2.38
Temperature coefficient of power (per K)	-0.45%	-0.41%	-0.28%
Temperature coefficient open circuit voltage (per K)	-0.30%	-0.31%	-0.32%
Temperature coefficient short circuit current	0.004%	0.051%	0.07%

B. PV Performance Metrics

Reference Yield (Yr): The reference yield is the ratio of the total solar radiation H(kWh/m^2) arriving at the surface of PV solar panels and the reference radiation quantity G (1 kW/m^2). The Reference Yield is given by 1):

$$Y_r = \frac{H}{G} \ . \qquad (1)$$

Final Yield (Y_f): The final yield is the total energy produced by the PV system, E_{AC} (kWh)

with respect to the nominal installed power P (kWp). This quantity, which represents the number of hours during which the PV field operates at its nominal power. The Final Yield is given by (2):

$$Y_r = \frac{E_{AC}}{P} \ . \qquad (2)$$

Performance Ratio (PR): The performance ratio PR indicates the overall effect of losses on the energy production of the PV system. The PR values indicate how a PV system approaches its ideal performance under actual operating conditions. PR, which is a dimensionless quantity, is defined as the ratio between the final yield and the reference yield as shown in (3):

$$Y_r = \frac{Y_f}{Y_r} \ . \qquad (3)$$

C. Classical Seasonal Decomposition (CSD)

This technique consists of decomposing the time series into three components: the trend, seasonal and remaining random components. The trend is obtained from the time series using a moving average centered on two steps. For a moving average of 2k, where k is the order of the moving average (k = 12 due to the number of months in a year), the centered average at time t is calculated using the (4)[19-22]:

$$T_t = \frac{1}{2}\left(\frac{1}{k} \sum_{i=t-m}^{t+m-1} Y_i + \frac{1}{k} \sum_{i=t-m+1}^{t+m} Y_i \right) , \qquad (4)$$

where T_t represents the trend at time t, ($t > m$), and m is defined as half the width of a moving average, $m = k/2$. As a result, the trend for each time series is constructed by the calculated moving averages. Thereafter, the seasonal component is calculated by subtracting the trend from the initial time series data. The gross seasonal component was extracted using (5) [23]:

$$S_t = Y_t - T_t \ , \qquad (5)$$

where seasonality St is defined as the difference between the original data T_t and the trend at time t. After extracting the trend for each technology, the linear regression is reapplied to calculate the performance degradation rate (R_D). The degradation rate is calculated using (6):

$$R_D = 12a \ , \qquad (6)$$

where a is the slope of the linear regression curve.

III. Results and Discussions

A. Performance Analysis

The performance of any photovoltaic system depends on the weather conditions at the location of the PV plant. to provide insight into the weather conditions under which the PV system performance evolves. Fig. 1 illustrates the total monthly insolation measured in the PV module plane between January 2015 and December 2019. The monthly insolation varied from 139 kWh/m^2 in November 2016 to 205.6 kWh/m^2 in May 2019, averaging 173.3 kWh/m^2/m over 60 months. The total annual solar radiation measured is 2051.7 kWh/m^2, 2091.3 kWh/m^2, 2125.5 kWh/m^2, 1659.5 kWh/m^2 and 2157.6 kWh/m^2 for the years 2015, 2016, 2017, 2018 and 2019, respectively, making an average of 2017.14 kWh/m^2/year.

The same figure shows the average monthly ambient temperature measured over the same monitoring period. The average monthly ambient temperature ranged from 12.06°C in November 2016 to 34.22°C in May 2019, while the average value was 23.5°C/m. 2019 was the warmest year with an average of 25.63°C, and 2018 was the coldest with an average of 20.41°C.

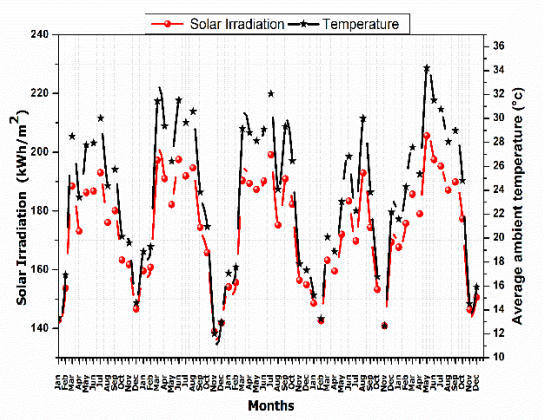

Figure 1. Solar irradiation and ambient temperature.

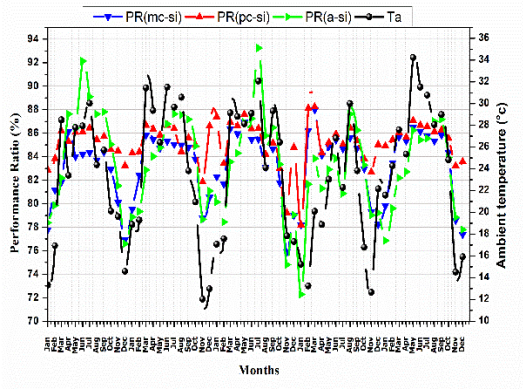

Figure 2. Performance ratio and ambient temperature.

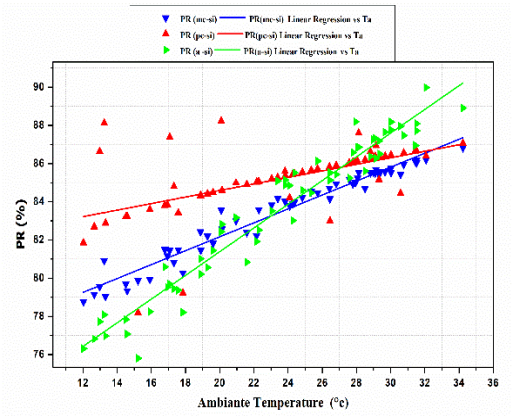

Figure 3. The linear regression of performance against temperature.

The same figure shows the average monthly ambient temperature measured over the same monitoring period. The average monthly ambient temperature ranged from 12.06°C in November 2016 to 34.22°C in May 2019, while the average value was 23.5°C/m. 2019 was the warmest year with an average of 25.63°C, and 2018 was the coldest with an average of 20.41°C.

The performance ratio represents the overall losses (system losses and conversion losses) on the nominal power of the PV installation that can result from the effects of module temperature, wiring, inverter inefficiencies, component failures, etc. Fig. 2 depicts the average monthly ambient temperature and the performance ratio of the three PV technologies tested during the monitoring period. The PR of the PV modules consisting of pc-si cells undergoes the smallest fluctuations during the monitoring period, with a deviation of 10.05%. It ranges from 78.19% in January 2018 to 88.94% in March 2018. The fluctuations in the monthly performance of mc-si technology are slightly higher, quantified at 12.1% and ranging from 75.89% in November 2017, to 87.99% in March 2018. The PR of a-si modules fluctuated more widely, ranging from 72.28% in January 2018 to 93.24% in July 2017, a difference of around 21%.

During five years of operation, the average monthly performance ratio of the pc-si, mc-si, and a-si technologies was obtained at 85.2%, 83.23%, and 83.28%, respectively. According to the power temperature coefficients of each photovoltaic module technology, the PR of pc-si, mc-si, and a-si modules should all decrease as the ambient temperature increases. As a result, and taking solar irradiation into account, the performance of the mc-si and pc-si technologies reaches its maximum values during the period from February to May each year. This period is characterized by an almost constant low temperature and good solar irradiation. On the contrary, the performance of a-si modules increases during the warmer months, exceeding the performance of crystalline technology and reaching high performance during the period between May and September. This is logical because amorphous silicon (a-si) cells can improve electrical performance in high temperature conditions. This effect is called thermal annealing. It allows the recovery of some of the nominal power initially lost due to light-induced degradation (LID) caused by prolonged exposure to high temperatures [24, 26].

In Fig.3, it can be clearly seen that the effect of thermal annealing became more evident for a-si technology from average temperatures above 23°C which correspond to average temperature values recorded in the period between May and September of each year. Another reason is the larger size of the amorphous modules which allows for greater heat dissipation and therefore the amorphous solar modules are cooler than the c-si solar modules [27]. As a result, it achieves a better performance than other technologies during the warmer months. In January and February, when the temperature reaches the lowest values, the c-si technologies, unlike the amorphous silicon technology, operate with high performance, the pc-si shows higher performance than the mc-si.

B. *Annual Degradation Rate Assessment Using Classical Seasonal Decomposition (Csd) Method*

A five-year time series of monthly average performance ratio (PR) values, comprising 60 data sets, was prepared for the period June 2015 to December 2019. The graphs in Fig.4, Fig.5, and Fig.6 illustrate the monthly PR time series constructed for the mc-si, pc-si, and a-si PV technologies, respectively. From these graphs, it can be seen that all technologies show seasonal behavior, while a trend of gradual loss of performance is most evident in all silicon PV technologies. The trend of decreasing performance is visible from the end of the first year (2015) of field operation. This is attributed to potential induced degradation (PID) for crystalline silicon (c-si) technologies [8, 10, 28, 29] and to the Staebler-Wronski effect and thermal annealing cycles that are generally attributed to amorphous silicon PV technology [17, 30-32].

The linear regression of the PR values is used to quantify this decreasing trend. The rate of performance degradation for mc-si is around 0.57%/year; for a-si, the degradation reaches 0.46%/year. The pc-si has the lowest degradation rate, with an R_D of 0.15% per year.

The degradation rates were also evaluated using another statistical technique, the Classical Seasonal Decomposition (CSD), which was used to decompose the time series by extracting the trend and seasonality for each PV technology. In this section, CSD the degradation rates were also evaluated using another statistical technique, the classical seasonal decomposition, which was used to decompose the time series by extracting the trend and seasonality for each PV technology. In this section, CSD was selected as it is one of the most commonly used decomposition procedures to extract the trend, seasonality, and remaining irregularity of the input signal with minimum effort and computational simplicity, and it also forms the basis of most modern decomposition methods.

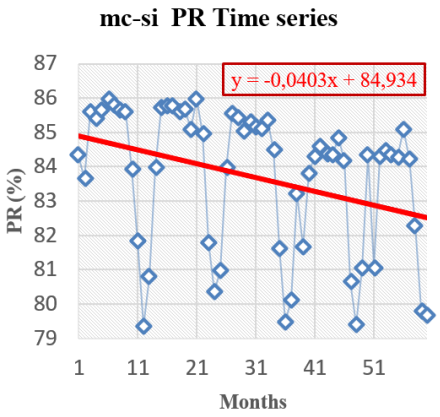

Figure 4. Time series of mc-si PR values.

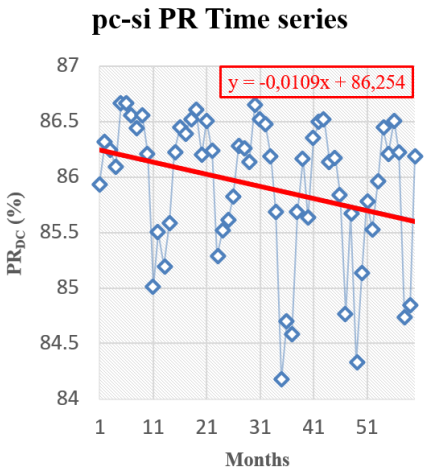

Figure 5. Time series of pc-si PR values.

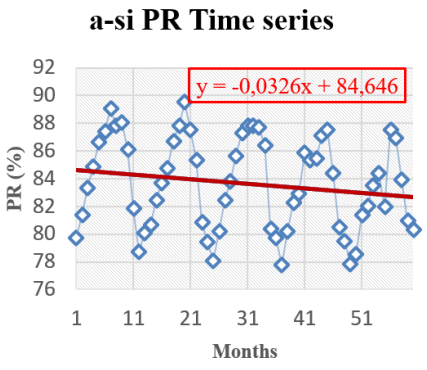

Figure 6. Time series of a-si PR.

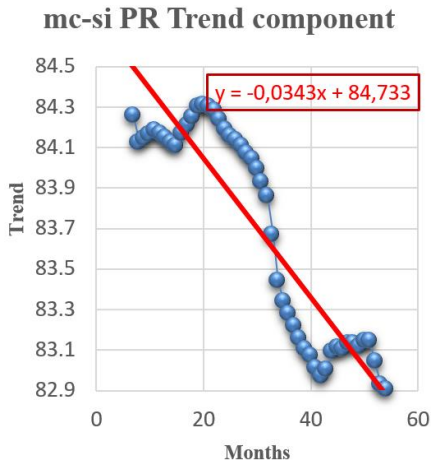

Figure 7. mc-si trend component.

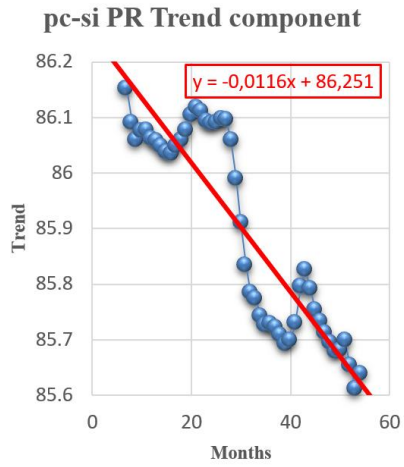

Figure 8. pc-si trend component.

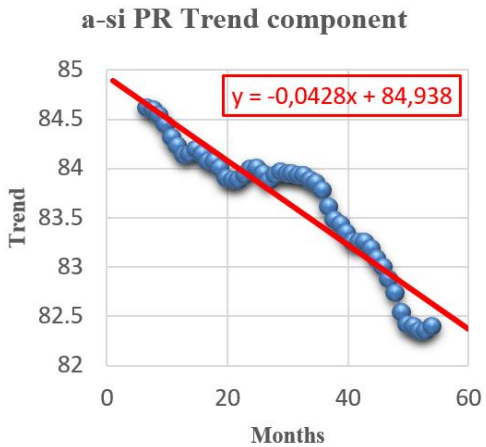

Figure 9. a-si trend component.

CSD was applied to the monthly average of the PR time series of all three Silicon PV technologies to extract the trend, seasonality, and random component over the five-year period. It was selected as it is one of the most commonly used decomposition procedures to extract the trend, seasonality, and remaining irregularity of the input signal with minimum effort and computational simplicity, and it also forms the basis of most modern decomposition methods. CSD was applied to the monthly average of the PR time series of all three Silicon PV technologies to extract the trend, seasonality, and random component over the five-year period.

Figs .7-9 represent the trend components of the three PV systems, extracted from their performance time series. The linear regression applied to the trend components shows that the degradation rate of the a-si PV system is the highest, at 0.51%/year, while the mc-si system shows a quantified annual performance degradation rate of 0.41%/year. The pc-si technology showed a lower annual performance degradation rate of about 0.14%/year over the same five-year period.

REFERENCES

[1] I. Energy and Agency, "Renewable Energy Market Update," 2020.

[2] Schlothauer, J., Jungwirth, S., Köhl, M., & Röder, B. (2012). Degradation of the encapsulant polymer in outdoor weathered photovoltaic modules: Spatially resolved inspection of EVA ageing by fluorescence and correlation to electroluminescence. *Solar Energy Materials and Solar Cells*, *102*, 75-85.

[3] Ascencio-Vásquez, J., Kaaya, I., Brecl, K., Weiss, K. A., & Topič, M. (2019). Global climate data processing and mapping of degradation mechanisms and degradation rates of PV modules. *Energies*, *12*(24), 4749.

[4] Phinikarides, A., Kindyni, N., Makrides, G., & Georghiou, G. E. (2014). Review of photovoltaic degradation rate methodologies. *Renewable and Sustainable Energy Reviews*, *40*, 143-152.

[5] Park, N. C., Oh, W. W., & Kim, D. H. (2013). Effect of temperature and humidity on the degradation rate of multicrystalline silicon photovoltaic module. *International Journal of Photoenergy*, *2013*.

[6] Badiee, A., Wildman, R., & Ashcroft, I. (2014, October). Effect of UV aging on degradation of Ethylene-vinyl Acetate (EVA) as encapsulant in photovoltaic (PV) modules. In *Reliability of Photovoltaic Cells, Modules, Components, and Systems VII* (Vol. 9179, p. 91790O). International Society for Optics and Photonics.

[7] Wohlgemuth, J. H., Hacke, P., Bosco, N., Miller, D. C., Kempe, M. D., & Kurtz, S. R. (2017). Assessing the causes of encapsulant delamination in PV modules. In 2017 *IEEE 44th Photovoltaic Specialist Conference, (PVSC)* (pp. 1–6). IEEE.

[8] Pingel, S., Frank, O., Winkler, M., Daryan, S., Geipel, T., Hoehne, H., & Berghold, J. (2010, June). Potential induced degradation of solar cells and panels. In *2010 35th IEEE Photovoltaic Specialists Conference* (pp. 002817-002822). IEEE.

[9] Luo, W., Khoo, Y. S., Hacke, P., Naumann, V., Lausch, D., Harvey, S. P., ... & Ramakrishna, S. (2017). Potential-induced degradation in photovoltaic modules: a critical review. *Energy & environmental science*, *10*(1), 43-68.

[10] Naumann, V., Lausch, D., Hähnel, A., Bauer, J., Breitenstein, O., Graff, A., ... & Hagendorf, C. (2014). Explanation of potential-induced degradation of the shunting type by Na decoration of stacking faults in Si solar cells. *Solar Energy Materials and Solar Cells*, *120*, 383-389.

[11] Papargyri, L., Theristis, M., Kubicek, B., Krametz, T., Mayr, C., Papanastasiou, P., & Georghiou, G. E. (2020). Modelling and experimental investigations of microcracks in crystalline silicon photovoltaics: A review. *Renewable Energy*, *145*, 2387-2408.

[12] Schwark, M., Berger, K., Ebner, R., Ujvari, G., Hirschl, C., Neumaier, L., & Mühleisen, W. (2013, November). Investigation of potential induced degradation (PID) of solar modules from different manufacturers. In *IECON 2013-39th Annual Conference of the IEEE Industrial Electronics Society* (pp. 8090-8097). IEEE.

[13] Lindroos, J., & Savin, H. (2016). Review of light-induced degradation in crystalline silicon solar cells. *Solar Energy Materials and Solar Cells*, *147*, 115-126.

[14] Adar, M., Mabrouki, M., Bennouna, A., & Chebak, A. (2016, November). Production study of a grid connected PV plant. In *2016 International Renewable and Sustainable Energy Conference (IRSEC)* (pp. 116-120). IEEE.

[15] Adar, M., Khaouch, Z., Mabrouki, M., Benouna, A., & Chebak, A. (2017, December). Performance analysis of PV grid-connected in fours special months of the year. In *2017 International Renewable and Sustainable Energy*

Conference (IRSEC) (pp. 1-5). IEEE.

[16] Adar, M., Bazine, H., Najih, Y., Bahanni, C., Mabrouki, M., & Chebak, A. (2018, December). Simulation Study of three PV Systems. In *2018 6th International Renewable and Sustainable Energy Conference (IRSEC)* (pp. 1-5). IEEE.

[17] Adar, M., Najih, Y., Gouskir, M., Chebak, A., Mabrouki, M., & Bennouna, A. (2020). Three PV plants performance analysis using the principal component analysis method. *Energy*, *207*, 118315.

[18] Bahanni, C., Adar, M., Boulmrharj, S., Khaidar, M., & Mabrouki, M. (2020, June). Analysis of weather impact on the yield of PV plants installed in two antagonists cities in Morocco. In *2020 5th International Conference on Renewable Energies for Developing Countries (REDEC)* (pp. 1-6). IEEE.

[19] Malvoni, M., Kumar, N. M., Chopra, S. S., & Hatziargyriou, N. (2020). Performance and degradation assessment of large-scale grid-connected solar photovoltaic power plant in tropical semi-arid environment of India. *Solar Energy*, *203*, 101-113.

[20] Singh, R., Sharma, M., Rawat, R., & Banerjee, C. (2020). Field Analysis of three different silicon-based Technologies in Composite Climate Condition–Part II–Seasonal assessment and performance degradation rates using statistical tools. *Renewable Energy*,

147, 2102-2117.

[21] Solís-Alemán, E. M., de la Casa, J., Romero-Fiances, I., Silva, J. P., & Nofuentes, G. (2019). A study on the degradation rates and the linearity of the performance decline of various thin film PV technologies. *Solar Energy*, *188*, 813-824.

[22] Makrides, G., Zinsser, B., Schubert, M., & Georghiou, G. E. (2014). Performance loss rate of twelve photovoltaic technologies under field conditions using statistical techniques. *Solar Energy*, *103*, 28-42.

[23] Lindig, S., Kaaya, I., Weiß, K. A., Moser, D., & Topic, M. (2018). Review of statistical and analytical degradation models for photovoltaic modules and systems as well as related improvements. *IEEE Journal of Photovoltaics*, *8*(6), 1773-1786.

[24] Raugei, M., Bargigli, S., & Ulgiati, S. (2007). Life cycle assessment and energy pay-back time of advanced photovoltaic modules: CdTe and CIS compared to poly-Si. *Energy*, *32*(8), 1310-1318.

[25] Makrides, G., Zinsser, B., Phinikarides, A., Schubert, M., & Georghiou, G. E. (2012). Temperature and thermal annealing effects on different photovoltaic technologies. *Renewable Energy*, *43*, 407-417.

[26] Adar, M., Najih, Y., Gouskir, M., Chebak, A., Mabrouki, M., & Bennouna, A. (2020). Three PV plants performance analysis using the principal component analysis method. *Energy*, *207*, 118315.

[27] Amin, N., Lung, C. W., & Sopian, K. (2009). A practical field study of various solar cells on their performance in Malaysia. *Renewable Energy*,

34(8), 1939-1946.

[28] Wohlgemuth, J. H. (2020). *Photovoltaic module reliability*. John Wiley & Sons.

[29] Yamaguchi, S., Yamamoto, C., Ohshita, Y., Ohdaira, K., & Masuda, A. (2020). Influence of emitter position of silicon heterojunction photovoltaic solar cell modules on their potential-induced degradation behaviors. *Solar Energy Materials and Solar Cells*, *216*, 110716.

[30] Silvestre, S., Kichou, S., Guglielminotti, L., Nofuentes, G., & Alonso-Abella, M. (2016). Degradation analysis of thin film photovoltaic modules under outdoor long term exposure in Spanish continental climate conditions. *Solar Energy*, *139*, 599-607.

[31] Tahri, A., Silvestre, S., Tahri, F., Benlebna, S., & Chouder, A. (2017). Analysis of thin film photovoltaic modules under outdoor long term exposure in semi-arid climate conditions. *Solar Energy*, *157*, 587-595.

[32] Nofuentes, G., de la Casa, J., Solís-Alemán, E. M., & Fernández, E. F. (2017). Spectral impact on PV performance in mid-latitude sunny inland sites: Experimental vs. modelled results. *Energy*,

141, 1857-1868.

A Literature Review of The Evaluation of Combined Energy Systems

José Luciano Batista Moreira[1], Carlos Marlon Santos[2], Adriano da Silva Marques[3]

[1,3]Federal Rural University of Pernambuco, Cabo de Sto Agostinho, Brazil,
lucianomoreirab7@gmail.com[1], adriano.marques@ufrpe.br[3]
[2]Paulist Foundation for Technology and Education, Lins, Brazil,
carlos.marlon@unilins.edu.br

Abstract—**Polygeneration energy systems seek to meet demands related to electrical energy, cooling, and heat. Based on these types of systems, a systematic bibliographic review evaluating articles associated with the following themes: trigeneration, polygeneration, CCHP, distributed generation, combined generation, thermoeconomics, exergy destruction, energy efficiency, and energy optimization. From selected studies were evaluated, industrial plants and thermal cycles proposal that uses waste heat, seeking to increase energy efficiency. It was proposed a discussion about the energy conversion systems, the fuels used, the primary sources of exergy destruction, and the systems that use wasted heat as a source of energy recovery. As a main result, it was observed that CCHP systems have a high degree of versatility and can be applied in the most diverse industrial plants or domestic installations, contributing to the sustainable development of energy conversion systems.**

Keywords - CCHP, energy efficiency, distributed generation, energy optimization, polygeneration

Nomenclature

CCHP: combined cooling, heat power

ASME: American Society of Mechanical Engineers

MDPI: Multidisciplinary Digital Publishing Institute

ORC: Organic Rankine Cycle

ICE: Internal Combustion Engine

I. INTRODUCTION

The exploitation of renewable energy sources and the use of primary energy-saving techniques have been recognized as the leading solutions to face climate change [1]. In the context of the energy economy, there is a growing development of policies to encourage the transition from a centralized energy generation system to a distributed polygeneration system, capable of meeting the simultaneous demand for heating, cooling, and electricity [2].

CCHP systems are widely accepted as more efficient [3] and ecologically friendly, with them a traditional separate energy generation [4]. CCHP systems utilize fuel energy to a greater extent [5] because the heat can be used for heating in winter and cooling in summer with an absorption cooler [6].

Distributed generation systems can use waste heat from sources with high exergy destruction potential [7]. Exergy can be defined as a qualitative perspective of energy use [8]. The exergy analysis identifies the inefficiencies of an energy system and can be an essential tool for identifying and controlling the energy losses of a thermodynamic system [9]. In addition, the concept of exergy analysis is applied to identify the main irreversibility and the optimal operating conditions to achieve efficiency improvement [10].

With the exergy study, the exergoeconomic analysis is often required [11], which is described as an approach that combines exergy analysis with economic evaluation [12], seeking to explore the constitution of the cost of capital for different equipment in an integrated system [13]. Thus the exergetic analysis is used when the objective is to optimize the energy use.

The main objective of this work is to present a systematic review of the literature through the results of articles that deal with energy

optimization for polygeneration energy systems, from the use of waste heat from processes.

II. METHODOLOGY

The reviewed articles were selected in the following databases: Elsevier, Springer, ASME, and MDPI. Research articles published in the last ten years (2011 to 2021) were analyzed. The keywords used in the research were: trigeneration, polygeneration, CCHP, distributed generation, combined generation, thermoeconomics, exergy destruction, exergeconomics, energy efficiency, and energy optimization. Through the search, 70 articles associated with the keywords and their respective fields of study were selected. The selected studies include practical systems, where a plant or bench is evaluated, and theorical systems, where studies propose simulations or alternatives applied in existing systems.

With the articles, a systematic literature review was performed. This type of review aims to provide a comprehensive and contemporary evaluation of the research [14]. The review is conducted through three steps. Initially, the data entry is done, which is characterized by selecting the object of study. The second step is related to data processing, where the searches and the analysis of the results are done. Finally, the synthesis of the results is conducted, indicating the primary information gathered in the study [15].

A systematic review was applied to this study based on systems that increase exergetic and energetic efficiency from utilizing heat from sources with high exergy destruction potential by implementing a CCHP system. The evaluation of the articles for review followed the approach of the items listed below.

- What was a system for converting thermal energy into electrical energy used?
- What were fuels and energy sources used?
- What is the energy potential used and wasted by thermal machines?
- What is the waste heat availability associated with thermal machines?
- What is the exergetic efficiency associated with CCHP systems?

The evaluation of the indicated items was applied to the 70 articles reviewed, providing a helpful database that quantifies the systems in terms of energy conversion methods, fuels used, energy potential used and wasted, and the types of systems that use waste heat as an energy source.

III. FINDINGS

Of the 70 evaluated articles related to the keywords used in the review, most were published in the journal Energy Conversion and Management, followed by the journal Energy, equivalent to 34.2% and 21.4% of the studies, respectively, the other studies evaluated (44.4% of the articles) were published in other journals, such as Journal of Thermal Analysis and Calorimetry, Renewable Energy, Journal of Thermal Engineering, among others.

A. Evaluated Thermal Machinery

The evaluated thermal machines are shown in the Fig. 1; altogether, 81 waste heat sources were studied. This number is higher than the number of articles because some works consider more than one thermal machine in the trigeneration or polygeneration system.

The gas turbine represents the most used thermal machine, followed by boilers and steam turbines, approximately 26.0% and 23.4%. Thermal machines that use low-temperature heat sources, such as the ORC cycle, account for approximately 19.8% of the total equipment evaluated.

B. Rated Fuels

The fuels and energy sources employed in the evaluated distributed generation systems are presented in the Fig. 2.

Natural gas represents the most widely used fuel, while solar energy is the second most present energy source in the evaluated studies,

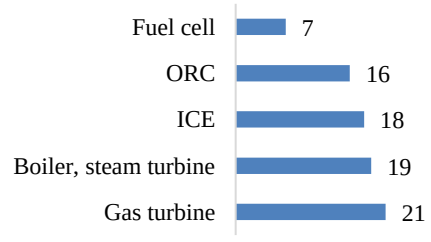

Figure 1. Evaluated thermal machines.

approximately 32.4% and 23.0%, respectively. Fuels such as biomass, hydrogen, and geothermal heat sources are listed in the other field and account for about 18.9% of thermal energy sources. Fossil fuels are used in 33 thermal machines, while renewable fuels are present in 41 thermal cycles.

C. Waste Heat Utilization

The use of residual heat from distributed generation systems is indicated in the Fig.3.

Absorption refrigeration systems represent the most used equipment in the evaluated studies, followed by thermal energy storage systems for industrial processes, corresponding to approximately 32.0% and 21.8%, respectively. Heat storage systems for use in domestic operations, modified steam compression refrigeration, fuel treatment units, among other systems, are indicated in the field other and correspond to about 19.0% of the cycles evaluated.

D. Presentation of Articles

Next were presented the summaries of the review of 10 articles that represent the researched models. The approach describes the constitution of the combined generation cycles and the studies' main results; the works are organized according to the alphabetical order of the authors' names.

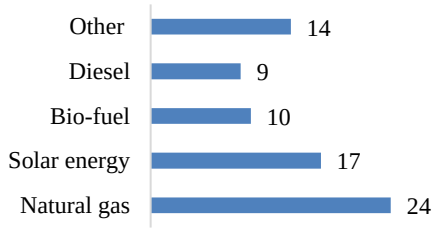

Figure 2. Fuels and energy sources.

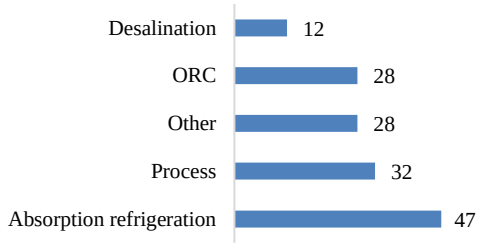

Figure 3. Systems that use waste heat as an energy source.

Reference [16] proposes a trigeneration unit composed of an internal combustion engine with natural gas. The exhaust gases from the engine provide thermal energy to an absorption refrigeration unit, which uses a mixture of lithium bromide and water as working fluids, and for steam production in the boiler. The study applies the proposal of the CCHP plant for operation in an ice cream factory, considering the electric and thermal energy demand of this kind of industry. According to the work results, considering the engine full-load operation, the overall trigeneration system presented an energy utilization factor of 74%, with average electricity production, refrigeration, and heating of 214.1 kW;35.7 kW and 162.1 kW, respectively.

Reference [17] proposes a solar energy harvesting plant using parabolic channel collectors with a total area of 100 square meters. The heat generated by the plant is used in a Rankine cycle, in a cooling system with an ejector device, and in a hot water production unit for domestic use. The cooling load is produced at ten °C and the heating load at 50°C, typical temperature levels for applications in buildings such as hotels. As a result, the study indicates the equivalent electricity, cooling, and heating productions of 4.6 kW, 7.1 kW, and 59.4 kW, respectively. Another significant effect is that the ideal system has 11.2% exergetic efficiency and 87.3% energy efficiency.

Reference [18] proposes using a gas turbine with biofuel derived from the wastewater of the textile industry, which has organic compounds in its composition. The exhaust gases from the turbine's combustion chamber provide power to an electric power generator, based on a Rankine cycle, a cooling system, based on the Kalina cycle and modified steam compression, and a water heating unit for use in industrial processes. The study concluded that the proposed trigeneration system provided 88 kW of electrical energy, the COP (coefficient of performance) of the cooling system was approximately 6, and the energy efficiency considering all plant components was 62.0%.

Reference [19] uses the waste heat from the combustion chamber of a gas turbine, which operates as biogas fuel. The exhaust gases are used in a water desalination unit and a refrigeration cycle based on an ORC system. For this refrigeration cycle, five working fluids were

tested, the results concluded that the toluene was the fluid with the highest cooling load (249.8 kW). In addition, the study showed that the combustion chamber and the element with the most increased exergetic destruction of 771.6 kW, followed by the desalination unit 221.4 kW.

The article models a trigeneration system in a gas turbine, operating according to a Brayton cycle. The turbine uses a mixture of ammonia and hydrogen, a zero-carbon fuel. The exhaust gases of the combustion chamber are used in a second turbine, with a lower working generation potential compared to the first. When passing through the second turbine, the gases are still a high-temperature fluid. Therefore, they are used in thermal energy reservoirs and a cooling system through the expansion of ammonia. As a result of the numerical and analytical analysis of the proposed system, it was found that the operation of the plant depends on strict control of the ammonia and hydrogen fractions in the combustion chamber. Another significant result is that the proposed plant achieves an efficiency of approximately 59.0% without any carbon emissions.

Reference [21], the object of its study is a bench of a micro trigeneration system, consisting of an internal combustion engine with diesel fuel, an absorption cooling system, and a heat reservoir for industrial processes. The cooling system and the heat reservoir use thermal energy from the engine exhaust system. As the main result, the practical study observed a slight reduction in engine efficiency, around 2.0%, comparing the integrated and disintegrated operating regimes of the CCHP unit. In addition, it was observed that the maximum percentage of energy saved was 15.3%, obtained with an engine load equivalent to 4.4 kW.

Reference [22] studies presents exergoeconomic and exergoenvironmental assessments applied to an internal combustion engine that uses diesel or biodiesel as fuel, integrated to this engine, a heat recovery unit based on a Rankine cycle and a reverse osmosis system, for desalination of seawater using waste heat from the engine exhaust gases. Thus, the proposed plant configures a combined cycle where work and drinking water are obtained from a thermal machine. As main results, the study cites that the most significant exergy destruction occurs in the engine, and the second corresponds to the reverse osmosis system. The exergetic efficiency of the plant is 6.9% and 6.7%, considering the use of fossil diesel and soybean-based biodiesel, respectively.

Reference [23] studies the exergoenvironment evaluation of a trigeneration plant used in a university laboratory. The plant consists of an internal combustion engine that uses as a natural gas fuel. The engine's exhaust gases are used in an absorption refrigeration with water and ammonia as working fluids, together with a heat recovery unit that pumps hot water to a biodiesel production plant. From the exergoeconomic evaluation of the trigeneration unit, it was observed that the highest environmental impact rates are related to the flows of the internal combustion engine and the heat recovery unit of the biodiesel plant. Based on that fact, it was suggested improvements regarding the type of material that constitutes the internal combustion engine and the geometry of the heat exchanger of the biodiesel production unit was.

Reference [4] proposes a plant with a boiler and an internal combustion engine, with spark ignition, both using natural gas as fuel, the heat rejected by the combustion chambers of the two thermal machines is used in an absorption refrigeration system, and in a thermal energy reservoir, which can be used in industrial processes. Based on this object of study, an energy optimization model was proposed, aiming to improve the system's cost-benefit ratio, accounting for comprehensive scenarios of energy demands and prices (fuels and electricity). As the top result, the study innovates with a variable modeling approach, which allows obtaining more economical trigeneration systems operation regimes capable of operating under fluctuating energy demands and prices.

Reference [24] proposes a trigeneration system with an internal combustion engine (diesel). According to an ORC, the engine's exhaust gases are used for both steam compression and absorption refrigeration system. Additionally, part of the engine waste heat is used for domestic water. As a result, the study indicates a 12.86% exergetic efficiency, comparing the studied system with an internal combustion system only or with an OCR.

.

TABLE I. SUMMARY OF THE STUDIES EVALUATED.

Reference	Thermal machine	Fuel	Use of Residual Heat
[16]	ICE	Natural gas	Cooling system, heat for industrial processes
[17]	Boiler	Solar energy	Rankine cycle, cooling system, heat for domestic applications
[18]	Gas turbine	Biofuel	Rankine cycle, cooling system, heat for industrial processes
[19]	Gas turbine	Biogas	Water desalination, cooling system
[20]	Gas turbine	Ammonia and hydrogen mixture	Cooling system, heat for industrial processes
[21]	ICE	Diesel	Cooling system, heat for industrial processes
[22]	ICE	Diesel or biodiesel	Rankine Cycle, Water Desalination
[23]	ICE	Natural gas	Cooling system, heat for industrial processes
[4]	Boiler and internal combustion engine	Natural gas	Cooling system, heat for industrial processes
[24]	ICE	Diesel	Rankine cycle, cooling system, heat for domestic applications

TABLE II. SUMMARY OF STUDIES OPERATING WITH ALTERNATIVE THERMAL MACHINES.

Reference	Thermal machine	Fuel	Use of Residual Heat
[25]	ORC	Solar energy	Cooling system, heat for domestic applications
[26]	Solid oxide fuel cell	Natural gas	Cooling system, ORC
[27]	Nuclear power plant	Solid and liquid Sodium Hydroxide	Hydrogen production, water desalination
[28]	Steam turbine	Solar and geothermal energy	Hydrogen production, cooling system
[29]	Steam turbine	Geothermal energy	Hydrogen production, Kalina cycle, water desalination
[30]	ORC	Biomass	Cooling system, heat for domestic processes
[31]	Phosphoric acid fuel cell	Natural gas and solar energy	Cooling system, heat for industrial processes
[32]	ORC	Solar energy	Cooling system, heat for domestic processes

A summary of the studies and a synthesis of the main information evaluated in the literature review is presented in the Table I. Highlights for the type of thermal machine evaluated, the fuel used, and the system that uses the residual heat.

E. Presentation of Systems with Alternative Heat Sources

A summary of the investigation of the innovative systems CCHP which uses alternative thermal machines is shown tin the Table II. It highlights eight evaluated studies or unusual applications of (gas turbines, internal combustion engines, boilers, among others).

F. Exergoeconomic Analysis

As the last analysis of the review, this section presents a summary of exergoeconomics studies, indicating the energy efficiency and economic evaluation of 5 distributed generation systems.

The study [33] points out that the storage tank has the highest exergy destruction cost, 35.3 $/h. Among all components, the turbine has the highest investment cost rate 0.65837 $/h;

The study [34] presents a specific exergogoeconomic cost of electricity and hot water, $0.12/kWh and 0.31 $/kWh, respectively, while the economic payback time for the implementation of the trigeneration system is 3.5 years.

TABLE III. SUMMARY OF THE STUDIES FROM AN EXERGOECONOMIC APPROACH.

Reference	Power source	Exergergetic Efficiency	Highest exergy destruction
[33]	Solar energy	27.9%	Energy storage tank
[34]	Solar and geothermal energy	9,6%	Absorption refrigeration system
[35]	ICE and solar power	11.7%	ORC Unit
[36]	Solar energy	14.4%	Solar energy capture tower
[37]	Natural gas and solar energy turbine	56,0%	Turbine combustion chamber

In considering the distributed generation system, the capital cost rate and the exergy destruction cost rate are calculated as equivalent to $37.98/h and $122.25/h, respectively.

The study [36] presents a cost related to electricity production of $0.2341/kWh, while the total cost rate of the product at a maximum efficiency operation regime is equivalent to $0.11/kWh.

Finally, article [37] presents the exergoeconomic optimization that resulted in a reduction in the exergy destruction up to 28.3% (58.5 $/h), it was possible with a 21.9% (2.5 $/h) capital cost investment

The studies indicated in this section present at least one sustainable energy source, which operates individually or assists in assisting some system that uses fossil entire as the heat source. It is possible to verify a high degree of variation in the exergetic efficiency of the systems (a discrepancy of 46.4%), comparing the study [37], which operates with a high-efficiency turbine with the study [34] that works with thermal energy storage tanks.

A summary of the results discussed from the exergoeconomics approach for combined generation systems is presented in the Table III. Conclusion

This study evaluated 70 articles related to distributed generation systems. This analysis separated and quantified different types of thermal machines, the types of fuels used, and the sources of utilization for each of the studies. In addition, abstracts and tables with information related to energy and exergetic evaluation of thermal cycles were presented. From the systematic review, it was concluded that:

- Thermal machines, such as gas turbines and boilers, represent most of the equipment present in CCHP systems (approximately 49.4%), being two pieces of equipment with high potential for exergy destruction, which can increase their energy efficiency implementing a combined heat and power system.
- Both fossil and renewable fuels are used in the CCHP units. Although renewable fuels are present in more significant numbers in this study (they account for 55.5% of the studies), Natural gas alone is the most widely used energy source.
- Industrial processes' absorption cooling and heat storage processes represent the most used systems in distributed generation plants. The two added together are equivalent to approximately 53.7% of the thermal cycles that use waste heat as an energy source.
- Through exergoeconomic analysis, we observed a high variation in exergetic efficiency (46.4%) when comparing studies operating with turbines (Brayton cycle)

The evaluated studies demonstrate that distributed generation systems can be applied in different thermal machines that operate with the most diverse types of fuels to produce variable energy. Thus, from the points explored, the versatility and applicability of CCHP systems is verified.

This study suggests that thermal cycles that operate solely converting thermal energy into work can be better exploited by implementing distributed generation systems, increasing the energy and exergetic efficiency of the thermodynamic cycle. In addition, it contributes to the sustainable and economic development of energy sources.

REFERENCES

[1] Vera, Y., Dufo-López, R., & Bernal-Agustín, J. L. (2019). Energy management in microgrids with renewable energy sources: A literature review. *Applied Sciences* (9).

[2] Gimelli, A., & Muccillo, M. (2019). Performance assessment of a 15 kW Micro-CHCP plant through the 0D/1D thermo-fluid dynamic characterization of a double water circuit waste heat recovery system. *Energy*, *181*, 803-814.

[3] Qian, J., Wu, J., Yao, L., Mahmut, S., & Zhang, Q. (2021). Comprehensive performance evaluation of Wind-Solar-CCHP system based on emergy analysis and multi-objective decision method. *Energy*, (230).

[4] Onishi, V. C., Antunes, C. H., Fraga, E. S., Cabezas, H. (2019). Stochastic optimization of trigeneration systems for decision-making under long-term uncertainty in energy demands and prices. *Energy*,*175*, 781-797.

[5] Yamano, S., Nakaya, T., Ikegami, T., Nakayama, M., & Akisawa, A. (2021). Optimization modeling of mixed gas engine types with different maintenance spans and costs: Case study OF CCHP to evaluate optimal gas engine operations and combination of the types. *Energy*, (222).

[6] Lozano, M. A., Jc, Branches., & Saw, L. M. (2010). Cost optimization of the design of CHCP (combined heat, cooling and power) systems under legal constraints. *Energy*, *35*,794–805.

[7] Asgari, N., Khoshbakhti Saray, R., & Mirmasoumi, S. (2020). Energy and exergy analyses of a novel seasonal CCHP system driven by a gas turbine integrated with a biomass gasification unit and a LiBr-water absorption chiller. *Energy Conversion and Management*, *220*, 96-113.

[8] Abusoglu, A., & Kanoglu, M. (2009). Exergoeconomic analysis and optimization of combined heat and power production: A review. *Renewable and Sustainable Energy Reviews*, *13*, 295–308.

[9] Mustafa, I., Al Ghamdi, A. (2018). Exergy Analysis of Thermal Seawater Desalination-A Case Study. *Renewable Energy Powered Desalination:*2-5.

[10] Authayanun, S., Hacker, V. (2018). Energy and exergy analyses of a stand-alone HT-PEMFC based trigeneration system for residential applications. *Energy Conversion and Management*, *160*, 230-242.

[11] Bejan, A., Tsatsaronis, G., & Moran, M. (1999) Thermal Design and Optimization-John Wiley & Sons (pp. 111–115).

[12] Wang, S., Liu, C., Li, J., Sun, Z., Chen, X., & Wang, X. (2020). Exergoeconomic analysis of a novel trigeneration system containing supercritical CO2 Brayton cycle, organic Rankine cycle and refrigeration absorption cycle for gas turbine waste heat recovery. *Energy Conversion and Management*, (221).

[13] Sahoo, P. K. (2008). Exergoeconomic analysis and optimization of a cogeneration system using evolutionary programming. *Applied Thermal Engineering*, (28).

[14] Needleman, I. G. (2002). A guide to systematic reviews. *National Center For Biotechnology Information*, *29*, 6–9.

[15] Comfort, E. C., Amaral, D. C., Silva, S. L. Da. (2011). Script for systematic literature review: application in product development and project management. *8th Brazilian Congress on Product Management and Development*, 1–12.

[16] Alcântara, S. C. S., Ochoa, A. A. V., da Costa, J. A. P., Michima, P. S. A., Silva, H. C. N. (2019). Natural gas based trigeneration system proposal to an ice cream factory: An energetic and economic assessment. *Energy Conversion and Management*, (197).

[17] Bellos, E., Tzivanidis, C. (2018). Multi-objective optimization of a solar driven trigeneration system. *Energy*, 149, 47–62.

[18] Dehghani, M. J., Kyoo Yoo, C. (2020). Modeling and extensive analysis of the energy and economics of cooling, heat, and power trigeneration (CCHP) from textile wastewater for industrial low-grade heat recovery. *Energy Conversion and Management*, (205).

[19] Gholizadeh, T., Vajdi, M. (n.a) Rostamzadeh H2020. Exergoeconomic optimization of a new trigeneration system driven by biogas for power, cooling, and freshwater production. *Energy Conversion and Management*, (205).

[20] Guteša Božo, M., Mashruk. S., Zitouni, S., Valera-Medina, A. (2021). Humidified ammonia/hydrogen RQL combustion in a trigeneration gas turbine cycle. *Energy Conversion and Management*, *227*, 1–14.

[21] Johar, D. K., Sharma, D., Soni, S. L., Goyal, R., Gupta, P. K. (2017). Experimental investigation of thermal storage integrated micro trigeneration system. *Energy Conversion and Management*, *146*, 87–95.

[22] Lourenço, A. B., Carvalho, M. (2020). Exergoeconomic and exergoenvironmental analyses of an off-grid reverse osmosis system with internal combustion engine and waste heat recovery. *Chemical Engineering Journal Advances*, (4).

[23] Marques, A. S., Carvalho, M., Ochoa, A. A. V., Abrahão, R., & Santos, C. A. C. (2021). Life cycle assessment and comparative exergoenvironmental evaluation of a micro-trigeneration system. *Energy*, (216).

[24] Zoghi, M., Habibi, H., Chitsaz, A., Javaherdeh, K., & Ayazpour, M. (2019). Exergoeconomic analysis of a novel trigeneration system based on organic quadrilateral cycle integrated with cascade absorption-compression system for waste heat recovery. *Energy Conversion and Management*, (198).

[25] Cioccolanti, L., Tascioni, R., Bocci, E., & Villarini, M. (2018). Parametric analysis of a solar Organic Rankine Cycle trigeneration system for residential applications. *Energy Conversion and Management*, *163*, 407-419.

[26] Tian, M., Yu, Z., Zhao, H., & Yin. J. (2018). Thermodynamic analysis of an integrated solid oxide fuel cell, Organic Rankine Cycle and absorption chiller trigeneration system with CO2 capture. *Energy Conversion and Management*, 171, 350-360.

[27] Marques, J. G. O., Costa, A. L., Pereira, C. (2020). Thermodynamic study of a novel trigeneration process of hydrogen, electricity and desalinated water: The case of Na-O-H thermochemical cycle, SCWR nuclear power plant and MED desalination installation. *Energy Conversion and Managemen*, 209,112-118.

[28] Siddiqui, O., Ishaq, H., & Dincer, I. (2019). A novel solar and geothermal-based trigeneration system for electricity generation, hydrogen production and cooling. *Energy Conversion and Management*. *198*, 111-118.

[29] Cao, Y., Xu, D., Togun, H., Dhahad, H. A., Azariyan, H., & Farouk, N. (2021). Feasibility analysis and

capability characterization of a novel hybrid flash-binary geothermal power plant and trigeneration system through a case study. *International Journal of Hydrogen Energy*, (46).

[30] Nasir, M. T., Ekwonu, M. C., Esfahani, J. A., Kim, K. C. (2021). Performance assessment and multi-objective optimization of an organic Rankine cycles and vapor compression cycle based combined cooling, heating, and power system. *Sustainable Energy Technologies and Assessments*, (47).

[31] Wang, J., Wu, J., Xu, Z., & Li, M. (2017). Thermodynamic performance analysis of a fuel cell trigeneration system integrated with solar-assisted methanol reforming. *Energy Conversion and Management*, (150), 81-89.

[32] Sebastián, A., Abbas, R., Valdés, M., & Rovira, A. (2021). Modular micro-trigeneration system for a novel rotatory solar Fresnel collector: A design space analysis. *Energy Conversion and Management*, (227).

[33] Montazerinejad, H., Ahmadi, P., & Montazerinejad, Z. (2019). Advanced exergy, exergo-economic and exergo-environmental analyses of a solar based trigeneration energy system. *Applied Thermal Engineering*, (152).

[34] Chen, Y., Xu, J., Zhao, D., Wang, J., & Lund, P. D. (2021). Exergo-economic assessment and sensitivity analysis of a solar-driven combined cooling, heating and power system with organic Rankine cycle and absorption heat pump. *Energy*, *Energy*, (230).

[35] Noorpoor, A. R., & Heidararabi, S. (2016). Exergoeconomic assessment, parametric study and optimization of a novel solar trigeneration system. *International Journal of Renewable Energy Research*. *6*, 795–816.

[36] Abbasi, H. R., & Pourrahmani, H. (2020). Multi-objective optimization and exergoeconomic analysis of a continuous solar-driven system with PCM for power, cooling and freshwater production. *Energy Conversion and Management*, (211).

[37] Baghernejad, A., Yaghoubi, M., & Jafarpur, K. (2016). Exergoeconomic optimization and environmental analysis of a novel solar-trigeneration system for heating, cooling and power production purpose. *Solar Energy*, *134*, 165-179.

Fractional-order MRAC Adaptive Control of Doubly Fed Induction Generator in a Variying Parameters Wind Energy System

Samir Ladaci[1], Sihem Djebbri[2], Horst Schulte[3]

[1]Electrical Engineering Department, University of 20th August 1955, Skikda, 21000 Algeria, djebbri.sihem@gmail.com
[2]Automatics Department, National Polytechnic School of Algiers, Algiers, 16200 Algeria, samir.ladaci@gmail.com
[3]Hochschule für Technik und Wirtschaft Berlin, Berlin, Germany, horst.schulte@htw-berlin.de

Abstract—**The purpose of this paper is to improve the performances of the fractional order model reference adaptive control (FOMRAC) design for the control of doubly fed induction generator (DFIG) for active and reactive power in wind energy systems. In the beginning, we recall the modeling of doubly fed induction generator in wind energy systems. Then, we introduce classical adaptive MRAC controller design to regulate the active and reactive power provided by DFIG. After that, a fractional order adaptive FO-MRAC controller is designed in order to improve the energy system performance. The objective is to realize a comparative study using the quadratic error criterion, calculating this last for integer MRAC and fractional order model reference FOMRAC in each case for active and reactive powers. Finally, a robustness test with parameters fluctuation by rotor resistance change is study. Numerical simulations are given to validate this performance enhancement.**

Keywords - doubly fed induction generator (DFIG), renewable energy, fractional order integral, MRAC, FOMRAC, robustness

I. INTRODUCTION

One way of addressing the rising energy demands and growing environmental concerns, is to harness green sources of power. Among these, wind energy using a doubly-fed induction generator (DFIG) are the more used for production of the electric energy [1-4]. Nowadays, wind generation system based on a doubly fed induction generator (DFIG) are employed widely in large wind farms fat has its many advantages: a very good energy efficiency, robust sensorless operation [5, 6]. In addition, the power converter is usually rated at 25-30% of the generator power rating [7-10], For such several advantages, this machine has generated a lot of curiosity on the part of researchers have tried to develop strategies to best exploit its strong points [11].

The problematic studied in this paper is to find a type of control independent to the parametric variations of the machine, that is realized by adaptive control with integer order model reference MRAC and fractional order model reference FOMRAC.

Many fractional order control works have been developed in literature, beginning with the earlier works of [12] and [13-15]. This popularity is mainly due to its simple principle and easiness to implement on one hand and its improved performance and robustness comparatively to classical adaptive control schemes on the other [16]. Various applications of fractional-order model reference adaptive control schemes are also available in literature, in different science and engineering fields like: in electric vehicle using a fractional order model reference adaptive strategy [17], Voltage control of DC/DC converter in multi sources renewable [18], and a

ISBN: 978-86-80593-73-9

multi-source renewable energy system using fractional-Order Integrals [19], etc.

We will show that the proposed adaptive control with fractional model reference strategy is more powerful than the classical MRAC control in regards of error, response time and overshoot.

To arrive at the previous objectives, this paper is organized as follows: Section I, recalls the modeling of the system with the different equations of active and reactive power. Then fractional order MRAC control theory will be presented in section II. The results of simulations obtained are presented and discussed for validating the proposed controller in Section III, with a study on robustness test with parameters fluctuation by rotor resistance change. Finally, the conclusion is presented in the last section.

II. DFIG System Modeling

Doubly fed induction machine, is a kind of wound rotor machine has to be fed both from stator and rotor sides, as sketched in Fig. 1. Normally, the stator is directly connected to the grid and the rotor is interfaced through a variable frequency power converters. In order to cover a wide operation range from sub-synchronous to synchronous speeds, the power converter placed on the rotor side bas to able to operate with power flowing in both directions [4].

The mathematical model can be expressed as in [5]. The stator and rotor voltage Eqs. are given by:

$$\begin{cases} V_{sd} = R_s I_{sd} + \dfrac{d}{dt}(\varphi_{sd}) - \omega_s \varphi_{sq} \\ V_{sq} = R_s I_{sq} + \dfrac{d}{dt}(\varphi_{sq}) + \omega_s \varphi_{sd} \end{cases} . \quad (1)$$

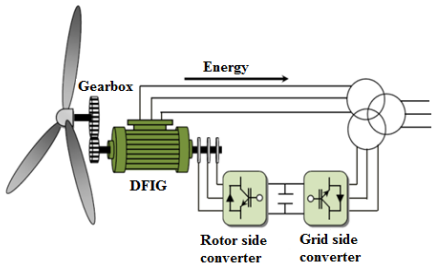

Figure 1. Doubly fed induction machine basic configuration for wind turbine.

$$\begin{cases} V_{rd} = R_r I_{rd} + \dfrac{d}{dt}(\varphi_{rd}) - (\omega_s - \omega_r)\varphi_{rq} \\ V_{rq} = R_r I_{rq} + \dfrac{d}{dt}(\varphi_{rq}) + (\omega_s - \omega_r)\varphi_{rd} \end{cases} . \quad (2)$$

The stator and rotor flux linkage Eqs. are given by:

$$\begin{cases} \varphi_{sd} = L_s I_{sd} + M I_{rd} \\ \varphi_{sq} = L_s I_{sq} + M I_{rq} \end{cases} , \quad (3)$$

$$\{\varphi_{rq} = L_r I_{rq} + M I_{sq} \ . \quad (4)$$

Electromagnetic torque Eqs.:

$$J\frac{d\Omega}{dt} = \left(\frac{J}{p}\frac{d\omega_r}{dt}\right) = - \\ -\frac{3}{2} p \frac{M}{L_s}\left(\varphi_{rd} I_{sq} - \varphi_{rd} I_{sd}\right) - C_r - f_r \Omega \quad . \quad (5)$$

A. Reference-frame

By choosing a reference frame linked to the stator flux, rotor currents will be related directly to the stator active and reactive power. If the stator flux is linked to the d-axis of the frame we have [8]:

$$\psi_{ds} = \psi_s \quad and \quad \psi_{qs} = 0 \ . \quad (6)$$

B. Control Strategy

The torque and consequently the active power only depend on the q-axis rotor current component. If the per phase stator resistance is neglected, the stator voltage vector is in quadrature advance in comparison with the stator flux vector [9].

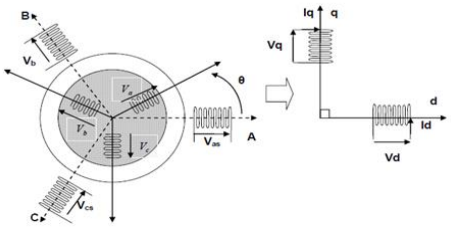

Figure 2. PARK's model of DFIG

$$V_{ds} = 0 \quad and \quad V_{qs} = V_s = \omega_s \psi_s \ . \qquad (7)$$

The stator active and reactive power can be expressed only versus these rotor currents as:

$$\begin{cases} P = -V_s \dfrac{M}{L_s} i_{qr} \\ Q = \dfrac{V_s \varphi_s}{L_s} - \dfrac{V_s M}{L_s} i_{dr} \end{cases}, \qquad (8)$$

$$\begin{cases} V_{rd} = R_r I_{rd} + \left(L_r - \dfrac{M^2}{L_s} \right) \dfrac{di_{dr}}{dt} - \\ -g\omega_s \left(L_r - \dfrac{M^2}{L_s} \right) i_{qr} \\ V_{rq} = R_r I_{rq} + \left(L_r - \dfrac{M^2}{L_s} \right) \dfrac{di_{qr}}{dt} + \\ +g\omega_s \left(L_r - \dfrac{M^2}{L_s} \right) i_{qr} + g\omega_s \dfrac{MV_s}{\omega_s L_s} \end{cases} . \qquad (9)$$

III. FRACTIONAL ORDER MRAC CONTROL

Adaptive control is the control method used by a controller which must adapt to a controlled system with parameters which vary, or are initially uncertain.

A. *Linear Approximation of Fractional Order Transfer Function*

In order to approximate the fractional order model reference we use the so-called singularity function method proposed by [13-14]. For fractional second order system with m a positive real number such that 0<m<1,

$$H(s) = \frac{1}{\left(\dfrac{s^2}{\omega^2} + 2\xi \dfrac{s}{\omega} + 1 \right)^m} , \qquad (10)$$

can be expressed as:

$$H(s) = \frac{\left(\dfrac{s}{\omega} + 1 \right) \left(\dfrac{s}{\omega + 1} \right)^{\beta}}{\left(\dfrac{s^2}{\omega^2} + 2\alpha \dfrac{s}{\omega} + 1 \right)} , \qquad (11)$$

with $\alpha = \xi^m$ and $\beta = 1 - 2m$, which can also be approximated by the function:

$$H(s) = \frac{\left(\dfrac{s}{\omega} + 1 \right)}{\left(\dfrac{s^2}{\omega^2} + 2\alpha \dfrac{s}{\omega} + 1 \right)} \frac{\prod_{i=1}^{N-1} (1 + \dfrac{s}{z_i})}{\prod_{i=1}^{N} (1 + \dfrac{s}{p_i})} . \qquad (12)$$

Model Reference Adaptive Control

The controller parameter adjustment is achieved by mean of the error between the output of the plant and the model reference output. This can be represented in Fig. 3.

The control signal is computed using the following relation.

$$u = \phi^T . \theta \ , \qquad (13)$$

where φ is the regression vector containing the measured input signals u and output signals y and the input reference signal u_c.

B. *M.I.T Rule*

We consider a closed loop system where the controller has an adjustable parameter vector θ. A model which output is y_m specifies the desired closed loop response. Let e be the error between the closed loop system output y and the model one y_m, one possibility is to adjust the parameters such that the cost function:

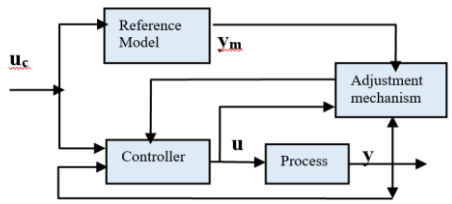

Figure 3. Direct MRAC control.

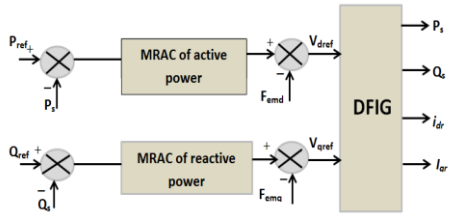

Figure 4. Model reference adaptive control MRAC of active and reactive power of DFIG in wind system.

$$J(\theta) = \frac{1}{2}e^2 \ , \qquad (14)$$

be minimized. In order to make J small it is reasonable to change parameters in the direction of negative gradient J, so:

$$\frac{d\theta}{dt} = -\gamma \frac{\partial J}{\partial \theta} = -\gamma e \frac{\partial e}{\partial \theta} \ . \qquad (15)$$

Which leads to the following bloc's scheme of Fig. 3.

C. *Application of Model Reference Adaptive Control to DFIG Active and Reactive Power Control In Wind Energy Conversion*

The block diagram of the MRAC control of active and reactive power of DFIG is shown in Fig. 4. by adding the parameters of the DFIG system presented in Table I.

IV. RESULTS AND DISCUSSION

In this section, we will present the operating characteristics of DFIG, then we will have the results of simulation of the uncoupled control from the active and reactive powers of doubly fed induction generator DFIG in wind energy system, using integer model reference control MRAC and fractional order model reference adaptive control FO-MRAC, whose objective is to compare the responses of active and reactive powers compared to the references desire.

TABLE I. CHARACTERISTIC PARAMETERS OF THE DFIG.

Parameter	Meanings	Values
V_{seff}	Effective value of the stator voltage	*230 V*
p	Number of pairs of poles	2 pairs of pôles.
R_s	Stator resistance	0.455 Ω
R_r	Rotor resistance	0.19 Ω
L_s	Stator leakage inductance	0.07 H
L_r	Rotor leakage inductance	0.0213 H
M_{sr}	Magnetizing inductance	0.034 H
f	Gird frequency	50 Hz

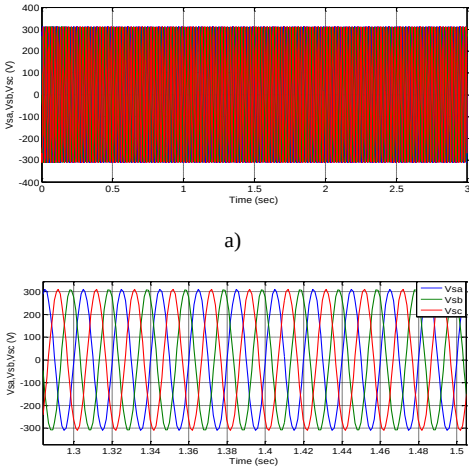

a)

b)

Figure 5. (a) DFIG supply voltage, (b) Zoom.

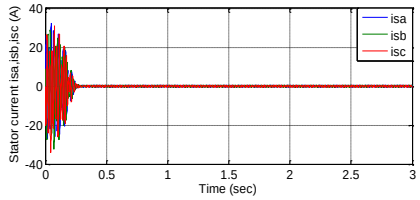

a)

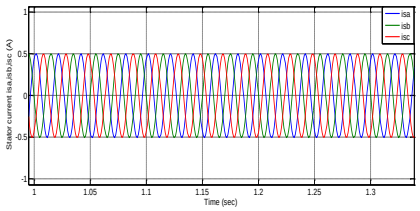

b)

Figure 6. (a) DFIG stator current, (b) Zoom.

A. *DFIG Characteristics*

The system is described using the following Eq.:

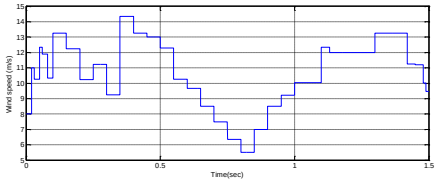

Figure 7. Wind speed profile

$$H(\mathrm{S}) = \frac{M.V_s}{L_s.R_r + S.L_s\left(L_r - \frac{M^2}{L_s}\right)} \quad . \quad (16)$$

The numerical replacement gives the following transfer function:

$$H(\mathrm{S}) = \frac{Y(s)}{U(S)} = \frac{2.334e04}{S + 39.7} = \frac{B}{A} \quad , \quad (17)$$

$$H(S) = \frac{2.334.10^4}{S + 39.7} \quad . \quad (18)$$

B. MRAC Controller

According to the characteristics of the system studies, the reference model is chosen as:

$$\mathrm{G}_M = \frac{6.4\ 10^7}{(S^2 + 15200s + 6.4\ \ 10^7)^m} \quad . \quad (19)$$

The RST control structure is characterized by the Diophantine Eq.,

$$A.\mathrm{R} + \mathrm{B}.\mathrm{S} = \mathrm{A}_r = A_0.A_m \quad . \quad (20)$$

The objective is to minimize the error:

$$e = y - y_m \, .$$

Let k, l and m be respectively the degree of the polynomials R; S and T, such that:

$$A.\mathrm{R} + \mathrm{B}.\mathrm{S} = \mathrm{A}_r = A_0.A_m \, .$$

A=1st order, B=0 order, R=order 1, A_o=constant, A_m=2nd order.

We take degS = degR, so: k=degR=1, l=degS=1, m=degT=1, where R, S and T are polynomial called the "observer" polynomial. Therefore, the regulation parameters vector is given as:

$$\theta = \left[r_o \ \ s_0 \ \ s_1 \ \ t_o \ \ t_1\right], \quad (21)$$

and the regression vector,

$$\varphi^T = \frac{b_0}{A_0 A_m}\left[U \ \ S_y \ \ y \ \ -Suc \ \ -uc\right], \quad (22)$$

s: Laplace operator. the recurrence Eq. of φ^T obtained after the discretization (T=0.001s) is given by :

$$\varphi(t+1) = -0.0008007 * \varphi(t) - \\ -2.2505e-7 * \varphi(t+1) + \alpha(\mathrm{t}) \quad . \quad (23)$$

C. FOMRAC Controllers

The reference model is a fractional order system of second order-like of the from (10) with m = 0,4. Using Charef's approximation method, we obtain the approximating rational transfer function given by:

$$\mathrm{G}_M = \frac{6.4\ 10^7}{(S^2 + 15200s + 6.4\ \ 10^7)^{0.4}} \quad . \quad (24)$$

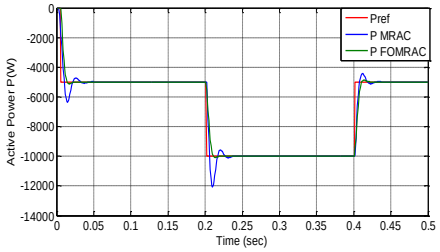

Figure 8. Active power output comparison between integer reference model (blue) and Fractional order reference models (green) with m=0.4.

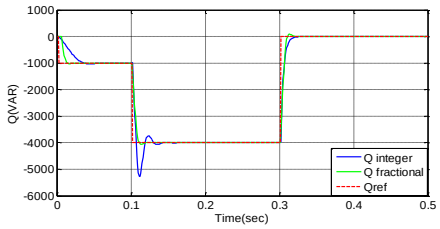

Figure 9. Reactive power output comparison between integer reference model (blue) and Fractional order reference model (green) with m=0.4.

The approximation function is of order 5:

$$\mathrm{G}_{ap} = \frac{7.308\ 10^{-9}\ s^2 + 0.0001806\,s + 1}{6.376\ 10^{-22}\ s^5 + 7.412\ 10^{-17}\ s^4 + 2.909\ 10^{-12}\ s^3 + 4.893\ 10^{-08}\ s^2 + 0.0003641\,s + 1} \quad . \quad (25)$$

Then deg (A_m) = 5 and from the Diophantine (19), we obtain:

$$deg(S) = deg(R) = deg(S) = 4$$

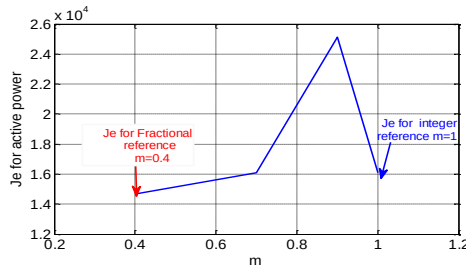

Figure 10. Variation of error *Je* for different values of *m* for active power.

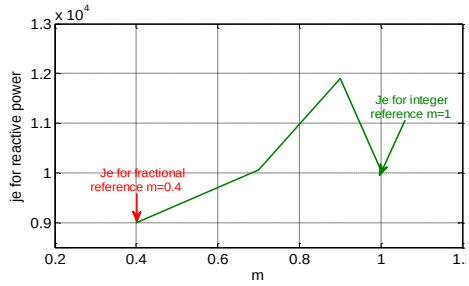

Figure 11. Variation of error *Je* for different values of *m* for reactive power.

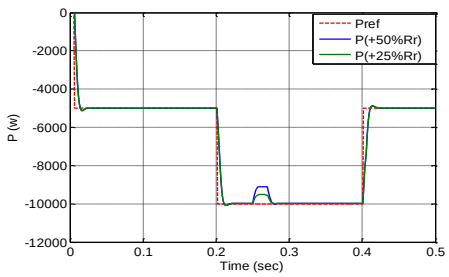

Figure 12. Active power P(W) output with fractional reference model FO-MRAC with different increases in rotor resistance Rr (+25% and +50%).

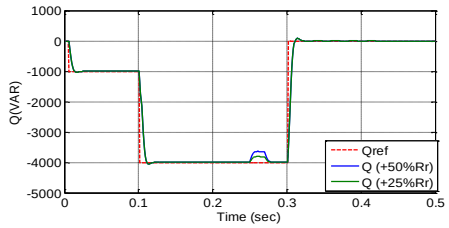

Figure 13. Reactive power Q(VAR) output with FO-MRAC with different R_r (+25% and +50%).

Therefore, the regulation parameters vector is given as:

$$\theta = \left[r_1\, r_2\, r_3\, r_0\, s_0\, s_1 \quad s_2\, s_3\, s_4\, t_0\, t_1\, t_2\, t_3\, t_4 \right], \quad (26)$$

and the regression vector,

$$\phi^t = \frac{b_0}{A_0 A_m} \begin{bmatrix} s^{k-1}u \ldots . u & s^l y \ldots . y - \\ -s^m u_c \ldots . - u_c \end{bmatrix}. \quad (27)$$

Figs. 8 and 9 show comparative results for active and reactive power control respectively using integer and fractional order MRAC.

And let us define the quadratic cost function criteria for the tracking error J_e and the input energy J_u as follows:

$$J_e = \sqrt{\sum_{n=0}^{N_{max}} (u_c(n) - y(n))^2}\,, \quad (28)$$

$$J_u = \sqrt{\sum_{n=0}^{N_{max}} u(n)^2}\,. \quad (29)$$

Computing these criteria for different values of then fractional order m and the integer case, we obtain:

TABLE II. J_E AND J_U CRITERIA FOR ACTIVE POWER WITH FO-MRAC (M = 0.4, 0.7, 0.9, 1).

m	Je (P)	Ju (P)
0.4	**14667.7**	312.66
0.7	16109.7	309.19
0.9	25115.1	349.02
1	16088.0	337.80

TABLE III. J_E AND J_U CRITERIA FOR REACTIVE POWER WITH FRACTIONAL ORDER REFERENCE MODELS FO-MRAC (M = 0.4, 0.7, 0.9, 1).

m	Je(Q)	Ju(Q)
0.4	**8995.1**	122.58
0.7	10054.3	120.14
0.9	11895.9	135.48
1	10044.8	135.67

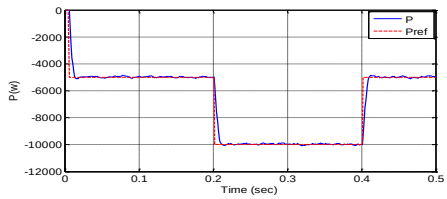

Figure 14. Active power with FO-MRAC with random output noise of 30% of the reference signal amplitude.

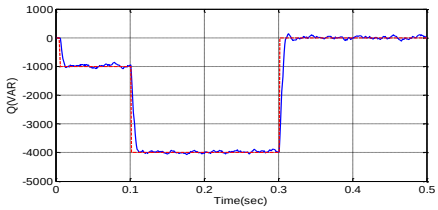

Figure 15. Reactive power with FO-MRAC with random output noise of 30% of the reference signal amplitude.

Whereas Figs. 8 and 9 prove that the FOMRAC control with fractional order reference gives better performance than the integer order MRAC because the responses of active and reactive power follow perfectly the suggested references, besides, Tables II and III which confirm that the tracking error obtained for FO-MRAC (m=0.4) is smaller than that obtained for the MRAC for active and reactive power control.

D. Parametric Robustness Test

The test consists in varying the parameters of the DFIG model (test of robustness) with the maintenance of the first test conditions. We suppose that the rotor resistance of the doubly fed induction generator DFIG increases by +25% and 50% between t=[0.25-0.27] s, as represented in Table IV.

G{P,Q} (s) present the transfer function of active (P) and reactive (Q) powers, in initial case (0%), with 25 and 50 % increase of rotor resistance of DFIG.

TABLE IV. SYSTEM TF WITH ROTOR RESISTANCE VARIATION.

Rr increase	G{P,Q} (s)
0%	$\frac{23340}{S+39.7}$
25%	$\frac{23340}{S+45.63}$
50%	$\frac{23340}{S+59.55}$

E. FOMRAC with Random Output Noise

Let us consider the proposed FOMRAC controller for m = 0,4 in presence of random output noises of 30% of the reference signal amplitude.

The simulation results are given in Fig. 14 for active power and Fig. 15 for reactive power respectively.

V. CONCLUSION

In this paper, a Fractional Model Reference Adaptive Control scheme (FOMRAC) was presented that can guarantee the stability with a satisfying level of performances for a wind energy system.

First, a FOMRAC controller is designed to supervise the active and reactive powers of a doubly fed induction generator (DFIG) for wind energy conversion. Simulation results show that the proposed adaptive control strategy is more powerful than classical MRAC controls in regards of error, response time and overshoot. Simulation results illustrate the reliability and robustness of FO-MRAC control towards this change of parameters, in our case the rotor resistance variation, where the active and reactive powers follow perfectly the proposed references.

This research work is a first step in the study of the adaptive control MRAC with fractional order regulators and its application to power generation processes. It will be interesting to continue this work by improving the controls performed by introducing fractional order filters [20] to the control systems with the aim of improving the performance of renewable energy systems, in particular solar and wind power.

REFERENCES

[1] Shen, B., Mwinyiwiwa, B., Zhang, Y., & Oo, B.T. (2009). Sensorless Maximum Power Point Tracking of Wind by DFIG Using Rotor Position Phase Lock Loop (PLL). *IEEE Transactions on Power Electronics*, *24*(4), 942 - 951.

[2] Mihet-Popa, L., Blaabjerg, F., & Boldea, I. (2004). Wind Turbine Generator Modeling and Simulation Where Rotational Speed is the Controlled Variable. *IEEE Transactions on industry applications*, *40*(1), 3-10.

[3] Tapia, G., Tapia, A., & Séenz, J. R. (2002). A new simple and robust control strategy for wind power farm re active power regulation. In *Proceedings of the International IEEE Conference on Control Applications, Glasgow, UK* .

[4] Melício, R., Mendes, V. M. F., & Catalão, J. P. D. S. (2010). Power converter topologies for wind energy

conversion systems: Integrated modeling, control strategy and performance simulation. *Renewable Energy, 35*(10), 2165-2174.

[5] Cardenas, R., Pena, R., Proboste, J., Asher, G. & Clare, J. (2005). MRAS observer for sensorless control of standalone doubly fed induction generators. *IEEE Transaction on Energy Convertion 20,* 710–718.

[6] Karimi, S., Gaillard, A., Poure, P. & Saadate, S. (2008). FPGA-Based Real-Time Power Converter Failure Diagnosis for Wind Energy Conversion Systems. *IEEE Transactions on Industrial Electronics 55*(12), 4299 - 4308.

[7] Anaya-Lara, O., Jenkins, N., Ekanayake, J., Cartwright, P., & Hughes, M. (2009). *Wind energy generation: Modelling and control.* Chichester, UK: John Wiley & Sons.

[8] Chakib, M., Essadki, A., & Nasser, T. (2018). Robust ADRC Control of a Doubly Fed Induction Generator Based Wind Energy Conversion System. In *International Conference on Electronic Engineering and Renewable Energy, ICEERE.*

[9] Taveiros, F.E.V., Barros, L.S., & Costa, F.B. (2015). Back-to-back converter state-feedback control of DFIG (doubly-fed induction generator)-based wind turbines. *Energy, 89*(C), 896-906.

[10] Oliveira, R.V., Zamadei, J.A., & Hossi, C.H. (2011). Robust Tuning of the Control Loops of DFIG Wind Turbine Systems. In *IEEE International Conference on Control Applications (CCA), Part of 2011 IEEE Multi-Conference on Systems and Control Denver, CO, USA*.

[11] Kalantar, M., & Mousavi, G. S. M. (2010). Dynamic behavior of a stand-alone hybrid power generation system of wind turbine, microturbine, solar array and battery storage. *Applied Energy, 87,* 3051–3064.

[12] Vinagre, B.M., Petras, I., Podlubny, I., & Chen, Y.Q. (2002). Using fractional order adjustment rules and fractional order reference models in model-reference adaptive control. *Nonlinear Dynamics, 29*(1–4), 269–279.

[13] Ladaci, S., & Charef, A. (2002). Fractional order model reference adaptive control of a robot arm (in French). *Revue Communication Sciences and Technologie, 1,* 20–52.

[14] Ladaci, S., & Charef, A. (2006). On fractional adaptive control. *Nonlinear Dynamics. 43*(4), 365–378.

[15] Ladaci, S., & Charef, A. (2012). Fractional order adaptive control systems: a survey. In E.W. Mitchell, & S.R. Murray (eds.). *Classification and Application of Fractals* (pp. 261–275). USA: Nova Science Publishers.

[16] Hotzel, R. (1998). *Contribution à la théorie structurelle de la commande des systèmes linéaires fractionnaires* (Doctoral Thesis). France : Université de Paris-Sud, Centre d'Orsay.

[17] Balaska, H., Ladaci, S., Schulte, H., & Djouambi, A. (2019). Adaptive Cruise Control System for an Electric Vehicle Using a Fractional Order Model Reference Adaptive Strategy. In *9th IFAC Conference on Manufacturing Modelling, Management and Control, MIM'2019, Berlin, Germany*.

[18] Djebbri, S., Ladaci, S., Metatla, A. & Balaska, H. (2018). Robust MRAC Supervision of a Multi-source Renewable Energy System Using Fractional-Order Integrals. In *International Conference on Electrical Sciences and Technologies in Maghreb (CISTEM), IEEE, Algeria*.

[19] Djebbri, S., Ladaci, S., Metatla, A. & Balaska, H. (2020). Fractional-order model reference adaptive control of a multi-source renewable energy system with coupled DC/DC converters power compensation. *Energy Systems, 11,* 315–355.

[20] Ladaci, S., Loiseau, J.J. & Charef A. (2006). Using Fractional order Filter in Adaptive Control of Noisy plants. In *The 3rd International Conference on Advances in Mechanical Engineering And Mechanics, ICAMEM 2006 Hammamet, Tunisia* (pp. 1-6).

Emulation, MPPT Control for Integration of the Photovoltaic Energy into the Grid under Partial Shading Conditions

Mustapha Alaoui[1], Hattab Maker[2], Azeddine Mouhsen[3]

[1,2]Interdisciplinary Laboratory of Applied Sciences, ENSA, Hassan First University, Morocco, mu.alaoui@uhp.ac.ma

[2]Laboratory of Radiation-Matter & Instrumentation, FST, Hassan First University, Morocco

Abstract— **For the sake of minimizing greenhouse gas emissions and contributing strongly to climate change mitigation, many researchers and scientists endeavored to improve the research and development in renewable energies as an inevitable alternative to reduce the use of conventional power generation resources. Solar photovoltaic (PV) energy has known an increased interest in the last years. However, its dependence on climatic conditions hinders PV researchers to carry out their tests and experiences at the desired weather parameters of temperature (T) and solar insolation (G), beside the expensive cost of actual PV panels and the required large area. Furthermore, due to the nonlinearity of the PV characteristic curve, the optimizing algorithms commonly known as Maximum Power Point Tracking (MPPT) algorithms are used to harvest the maximum power from the PV source to be injected into the grid, especially under non uniform weather conditions. Therefore, The proposed system has been invented to cover three main functions: to reproduce faithfully similar PV characteristics and mimic the behavior of actual PV modules and arrays irrespective of environmental conditions change, to maximize the energy fed from the PV modules, and to synchronize the PV source with the gird and inject thus the peak power by the means of controlling the active and reactive power quantities. Simulation Results using Matlab Simulink Software are proposed in order to evaluate the performance of the proposed system and verify its robustness and efficiency.**

Keywords - current-voltage characteristic, partial shading conditions, photovoltaic emulator, MPPT algorithm, PLL, grid synchronization.

I. INTRODUCTION

This Renewable and sustainable energies have become an important issue that interests many researchers and scientists nowadays aiming to mitigate the drawbacks of conventional energy resources and fight climate change. For this reason, photovoltaic solar energy is being continuously developed and widely used in many countries. However, this energy suffers from less efficiency beside its dependence on environmental conditions. Therefore, many authors have focused on the development of different optimization techniques and control strategies so-called Maximum Power Point Tracking (MPPT) algorithms in order to extract the maximum power from the solar panel and improve thereby its efficiency. Among these techniques, there are for instance Perturb and Observe method, Incremental conductance technique, Fractional Open circuit voltage technique… Nevertheless, most of existing MPPT algorithms do not guaranty good dynamic and static tracking performances under rapid variation of atmospheric conditions and especially under partial shading conditions.

On the other hand, PV source emulator is a nonlinear power supply that reproduces nearly the same current and voltage as a real PV generator. It consists essentially of a power electronic converter such as buck converter,

boost converter and a reference generator where the PV characteristics are implemented, beside the control part which determines the operating point of the system and tracks the current and voltage of the actual PV source. DC-DC buck converter with the Look-Up-Tables (LUT) technique have been used in this application in order to have a simple structure of the system as well as ensure high dynamic performances and good accuracy [1, 2]. The Artificial Neural Network controller has been utilized to follow accurately the current-voltage (I-V) characteristic of the PV array. Unlike many PV emulator researchers [2-4], the proposed PV emulator is not only able to replicate the electrical behavior of PV array under uniform solar conditions but also under partially shaded conditions.

The proposed paper suggests thus the use of an Artificial Neural Network controller trained by a feed-forward back propagation technique in order to control the PV emulator and to inject the maximum power into the Grid at any operational conditions. Phased Locked Loop (PLL) has been used to synchronize the PV system with the Grid since it is well-known with its efficiency and widely used [5-7]. Double Stage Three Phase connected solar inverter is used in this application in order to separate the MPPT controller dynamics with the inverter ones. Simulations results using Matlab Simulink software are presented and deeply discussed so as to highlight the performances of this innovative system.

Fig. 1 describes the overall architecture of the proposed system.

II. EASE METHODS AND PARAMETERS

The PV array parameters are extracted from the technical datasheet, and the I-V curve is generated offline using Matlab Simulink software and implemented in the LUT. A comparison is made between the generated I-V curve and the datasheet one to validate the accuracy of the PV characteristic. The reference generator finds the corresponding operating point of the system taking into consideration the given weather conditions and generates, as a result, the current reference. The latter is used by the ANN controller to regulate the system and deliver with the pulse width modulation (PWM) system the control signal of the buck converter.

The following Fig. 2 describes the control strategy used for emulation and MPPT

A. Artificial Neural Network Controller

The ANN controller is used in this system in order to find the optimized parameters of the PID controller so that the system can achieve rapidly and accurately the Global Maximum Power Point (GMPP). Feed-forward back propagation method has been used in this application, while the training algorithm is the Levenberg Marquardt Nntool has been used in Matlab Simulink to train the algorithm offline and to adapt continuously the parameters of the PVE and GMPPT (Fig. 3)

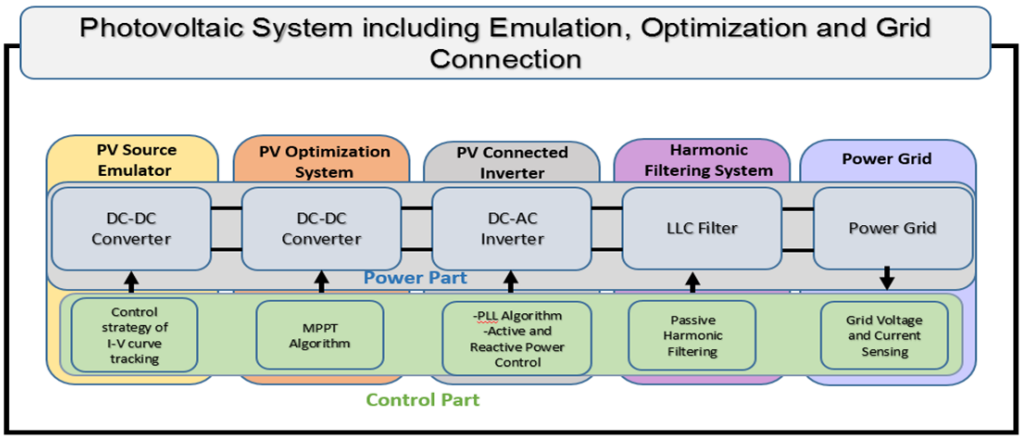

Figure 1. Overall synoptic system of the proposed photovoltaic solar emulator.

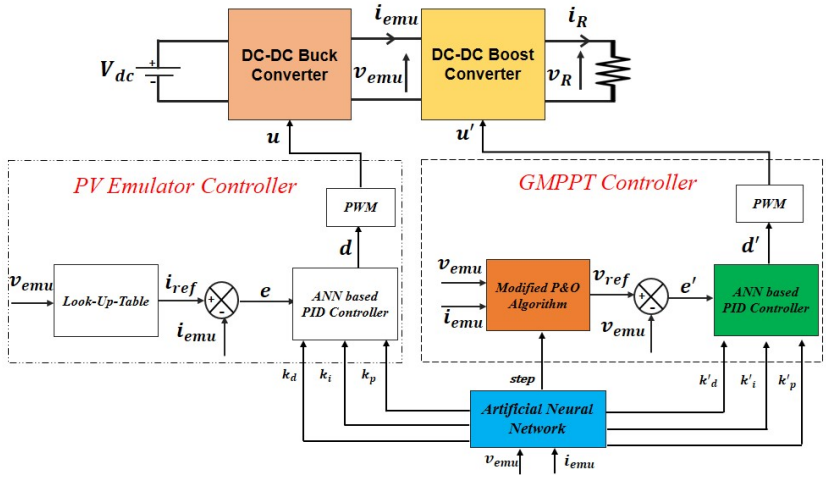

Figure 2. Control technique used for the PV emulation and MPPT control.

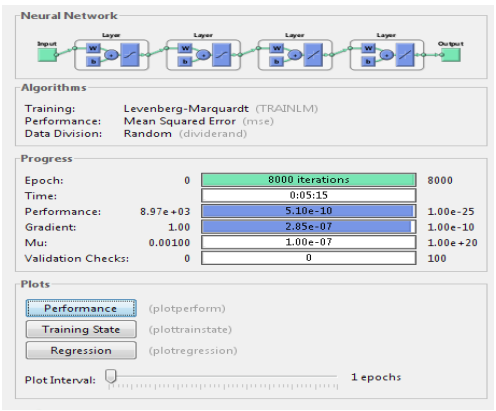

Figure 3. ANN training using Nntool of Matlab Simulink.

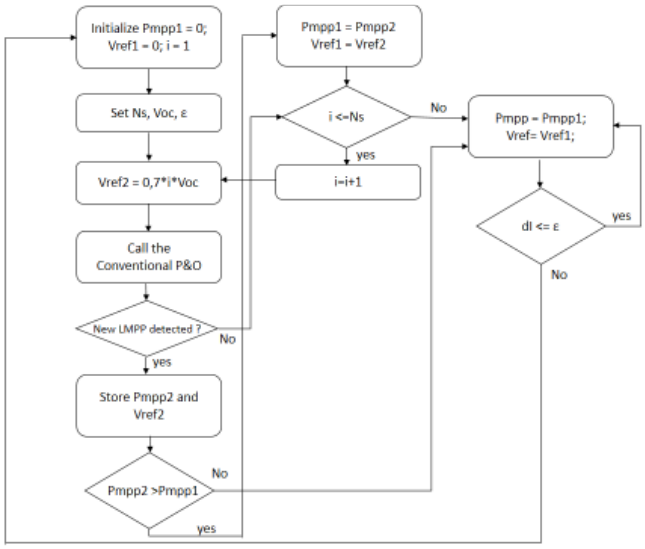

Figure 4. Modified P&O technique for GMPPT under Partial Shading Conditions.

The following table describes the electrical parameters of the system (Table I).

TABLE I. PV ARRAY AND PV EMULATOR PARAMETERS.

Parameter	Value
Input voltage Vdc	200 V
Inductors L	10 mH
Capacitor C	10 µF
Switching frequency f	10 kHz
Grid frequency	50 Hz
Phase to phase voltage	380 V
Peak rated power	285 W
Short circuit current Isc	9.64 A
Open circuit voltage Voc	38.3V
Maximum power point current Imp	9.06 A
Maximum power point voltage Vmp	31.4 V
Temperature coefficient of power kp	-0.39
Temperature coefficient of Voc kv	-0.29
Temperature coefficient of Isc ki	0.05
Cell number Ns	60
PI proportional gain Kp	[0.1,5.6]
PI integrator gain Ki	[155,232]
PI integrator gain Ki	$[1e\text{-}5\ 1e\text{-}^{3}]$

Under the Partial Shading Conditions, and in order to track the Global maximum Power Point , a new modified Perturb and Observe (P&O) has been used, since the conventional P&O technique fails to find the GMPP and sticks only in the local one, which leads to energy losses in the PV system[8-11]. The modified P&O is presented in the flow chart (Fig. 4).

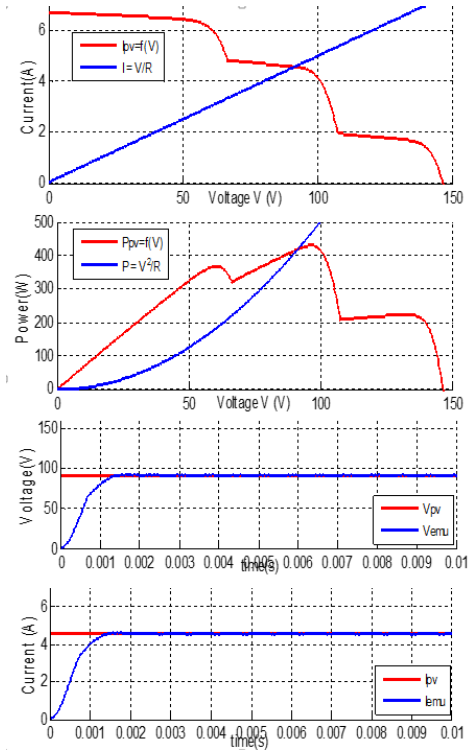

Figure 5. PV emulator under partial shading conditions (G=700 W/m2, G=500 W/m2, G=700 W/m2, G=200 W/m2) for R=20 Ω.

III. RESULTS

In order to validate the functioning of the PV emulator under partial shading conditions, four series PV module have been connected and their I-V and PV characteristic is depicted in Fig. 5. The Fig. 5 chows the operating point of the system and compares then the current and voltage outputs of the PV emulator with the PV field ones.

The following figure (Fig. 6) shows the P-V characteristics and the PV power extracted from the solar field using Matlab Simulink under partial shading conditions connected to the PV emulator.

So as to highlight the performance of the proposed system compared to the existing techniques, a comparison has been made between the proposed control strategy based on Modified ANN P&O, the Scanning P&O and the Conventional P&O as illustrated in Fig. 7.

IV. DISCUSSION

As depicted in the figures above, the designed PV array emulator is able to track the current and voltage of actual PV source under uniform irradiance and partial shadow conditions. Two operating points have been presented and the simulation results show the dynamic performances of the system. The proposed circuit has good accuracy and speed since the static error does not exceed 5 % and the settling time is about 1,5 ms.

The simulation results using Matlab Simulink software proofs that:

- The PV array emulator based on ANN technique acts as an actual PV source
- The developed ANN based GMPPT algorithm circumvents the problem from which many existing MPPT techniques suffer.
- Allow extracting the maximum power from the PV modules even under partial shading conditions.

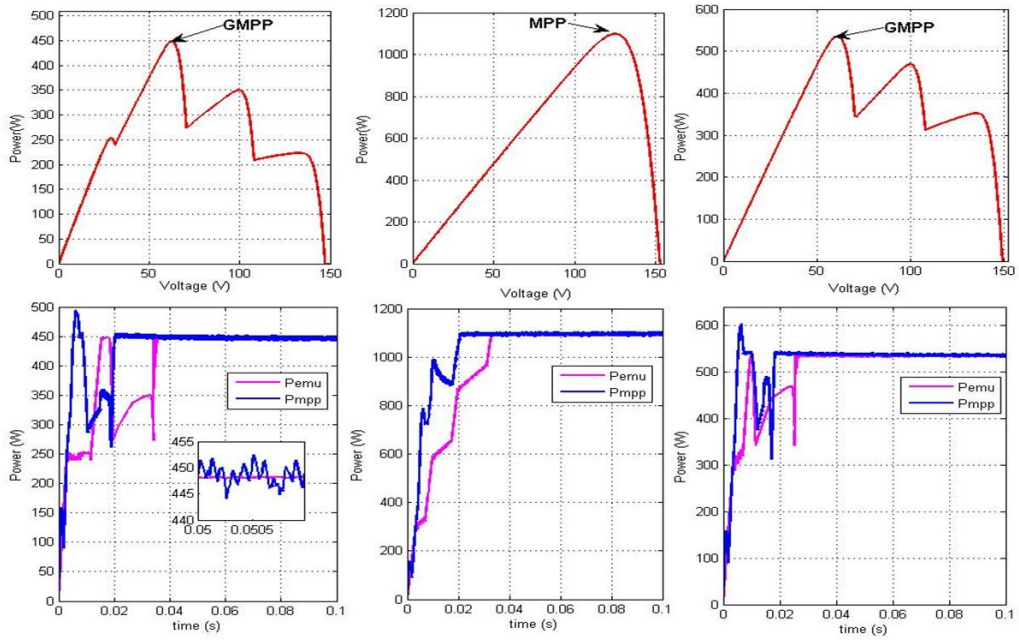

Figure 6. P-V characteristics and the PV power extracted from the solar field using Matlab Simulink under partial shading conditions using the developed modified GMPPT.

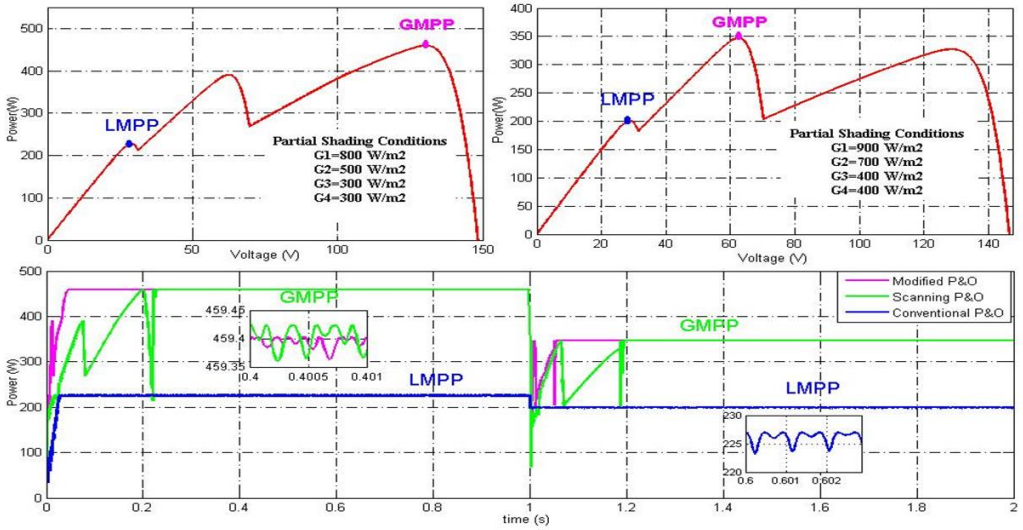

Figure 7. Simulation comparison between the proposed Modified ANN P&O, the Scanning P&O and the Conventional P&O using Matlab Simulink software.

- Improve the performances of existing algorithms in terms of accuracy and tracking speed.

V. Conclussion

The present paper proposes a nonlinear power system able to behave similarly as an actual PV source irrespective of environmental parameters variation, it can track the PV characteristics under uniform solar insolation as well as partially shaded conditions. Further work will be dedicated to the experimental validation of the proposed solar emulator.

References

[1] Di Piazza, M. C., & Vitale, G. (2013). Photovoltaic sources: modeling and emulation. Springer: London.

[2] Ayop, R. & Tan, C. W. (2017). A comprehensive review on photovoltaic emulator. *Renewable and Sustainable Energy Reviews*, *80*(430–452). doi: 10.1016/j.rser.2017.05.217.

[3] Ram, J. P., Manghani, H., Pillai, D. S., Babu, T. S., Miyatake, M., & Rajasekar, N. (2018). Analysis on solar PV emulators: A review. *Renewable and Sustainable Energy Reviews*, *81*(149–160). doi:10.1016/j.rser.2017.07.039.

[4] Piazza, M. C. D., Pucci, M., Ragusa, A. & Vitale, G. (2010). Analytical Versus Neural Real-Time Simulation of a Photovoltaic Generator Based on a DC–DC Converter. *IEEE Transactions on Industry Applications*, *46*(6)2501–2510. doi:10.1109/TIA.2010.2072975.

[5] Jamil, M., Rizwan, M., & Kothari, D. P. (n.a). Grid Integration of Solar Photovoltaic Systems. Routledge, p. 273.

[6] Mohamed Hariri, M. H., Mat Desa, M. K., Masri, S., & Mohd Zainuri, M. A. A. (2020). Grid-Connected PV Generation System—Components and Challenges: A Review. *Energies*, *13*(17), 4279. doi:10.3390/en13174279.

[7] Advances in Grid-Connected Photovoltaic Power Conversion Systems (2019). Elsevier.

[8] Gosumbonggot, J., & Fujita, G. (2019). Partial Shading Detection and Global Maximum Power Point Tracking Algorithm for Photovoltaic with the Variation of Irradiation and Temperature. *Energies*, *12*(2), p202, doi:10.3390/en12020202.

[9] Department of Electrical Engineering. Federal University of Technology – UTFPR-CP, Cornélio Procópio – PR - Brazil, Rocha, M. V., Sampaio, L. P., & Silva, S. A. O. (2018). Maximum Power Point Extraction in PV Array Under Partial Shading Conditions Using GWO-Assisted Beta Method. *Renewable Energy and Power Quality Journal*, *1*, 450–455. doi:10.24084/repqj16.346.

[10] Nguyen, T. L. & Low, K.-S. (2010). A Global Maximum Power Point Tracking Scheme Employing DIRECT Search Algorithm for Photovoltaic Systems. *IEEE Transactions on Industrial Electronics*, 57(10), 3456–3467. doi10.1109/TIE.2009.2039450.

[11] Liu, Y.-H., Chen, J.-H., & Huang, J.-W. (2015). A review of maximum power point tracking techniques for use in partially shaded conditions. *Renewable and Sustainable Energy Reviews*, *41*, 436–453, doi:10.1016/j.rser.2014.08.038.

Multivariate Statistics of Location And Socioeconomic Status of A Rural Household in the Energy Consumption Dynamics-Nepal as a Case Study

Jyoti U. Devkota[1]

[1]Department of Mathematics, Kathmandu University, Dhulikhel, Nepal,
drjdevkota@ku.edu.np

Abstract—**This study is based on data collected from survey of 300 households of national grid electricity users and 400 households of biogas users. The responses to questions in the questionnaire, developed for these surveys, were classified into multiple choice options. This resulted in categorical data; and it reduced ambiguity and confusion between interviewee and interviewer. The data generated were classified into ordinal scale and modeled. As the dependent variable had more than two categories, polytomous and not dichotomous models were developed and fitted. Ten different hypotheses assessing and measuring the energy consumption dynamics were tested. Values of parameters of these model and odds ratio, quantified the change with respect to energy consumption. The variables considered were namely time spent in the collection of firewood, type of house, amount of firewood saved, time saved, employer and school located within 15 min distance. Countries like Nepal have knowledge gap due to the lack of official data. This paper tries to fill the gap. Such results can be generalized to other countries of Asia and Africa. They can provide guidelines to policy makers and planners regarding formulation of realistic energy policies.**

Keywords - categorical data, biogas, hydropower, odds ratio

I. INTRODUCTION

Data based study is evidence based study. But countries from the developing world have a knowledge gap due to limited and scarce official records. In such countries, factors playing a critical role in energy consumption dynamics need to be identified, quantified and measured. Their interplay and interdependence needs to be analyzed and predicted. There are several intangible advantages of energy use especially in rural areas. These outweigh directly attributable advantages and benefits. These benefits need to be quantified and measured. Further, what get's measured through carefully generated good quality data, also gets done. Sustainable development goals can also be achieved through this motto, in such countries.

According to 2011 Census of Nepal, 64% of the households use fire wood for meeting their energy needs [1]. The contribution of biomass in fulfilling energy consumption needs of households is 80%. The contribution of fuel wood is 87.1%. The involvement of grid electricity is only 7%. Hydropower projects are the major sources of grid electricity in Nepal. In such agriculture based economy, cattle are also kept for their draft power and milk. Biogas generates energy from the dung produced by farm animals and also from agricultural wastes. Thus biogas as an alternative energy source is very suitable for Nepal. Biogas plants were promoted by Government of Nepal in agriculture year 1974/75 as a part of special program.

In the modern world of big data, development of new methods of statistics and application of existing statistical techniques, in diverse fields hold a great significance. The role of techniques such as Multivariate Statistics, Categorical Data Analysis, Structural Equation Modeling and Cluster Analysis in the evidence based study of energy consumption dynamics of rural households are discussed in detail by Devkota [2-6]. The importance of use of statistical methods

ISBN: 978-86-80593-73-9

in interdisciplinary studies ranging from public health issues to active forest fires are also highlighted by [5-8].

In this paper categorical data are analyzed and polytomous models are developed. The work is novel, unlike other papers; statistical methods are used in in-depth analyses. Here categorical data are generated and classified in ordinal scale. This method is useful in situations where we have lack of accurate measurement instruments. It can also be useful in situations where due to lack of awareness, exact answers cannot be furnished, but a multiple choice option can be chosen correctly. Thus the dynamics of change of variables related to energy consumption of 700 households such as time spent in the collection of firewood, type of house, amount of firewood saved, time saved, employer and school located within 15 min distance are minutely analyzed and predicted. The data used here is based on sample survey of 300 households of normal users which are national grid energy users and 400 households of biogas users.

II. Materials and Methods

Data: This study is based on data collected from 400 households of Biogas users and 300 households of national grid electricity users. The electricity in the national grid comes from hydropower projects. This survey generated more than 350 multivariate data. In these surveys, the base questionnaire is the same. It is a structured questionnaire with answers given as multiple choices that resulted in categorical data. This categorical data could be analyzed on ordinal scale. Because of large sample size this could be treated as a continuous data by the application of central limit theorem. The questionnaire was pretested. Multivariate statistics is used here to quantify and explain the relationship between these variables. Consumer profile databases were constructed. The details of the variables are given in Table I.

Polytomous Models: When the response variable is not dichotomous that is it has more than two options, then it is called polytomous. So polytomous response models have more than two categories, say more than two categories in row or column or both. This can be explained by multinomial probability density function. Here:

$$\log\left(\dot{\pi}_j\right) = \frac{1}{I}\sum_i \log\left(\pi_{i|j}\right) , \qquad (1)$$

where i=1, 2, …I; j=1, 2, …J.

Here $\pi_{i|j}$ is the conditional probability of i given j $\dot{\pi}_j$ is the value of the probability obtained in this way for the jth category of the explanatory variables. This value is called the geometric mean. Back-transformation, eliminating the logarithm, shows its definition:

$$\dot{\pi}_j = \left(\prod_i \pi_{i|j}\right)^{\frac{1}{I}} . \qquad (2)$$

So, polytomous logistic models with one explanatory variable can be written as:

$$\log\left(\frac{\pi_{i|j}}{\dot{\pi}_j}\right) = \mu_i + \alpha_{ij} \;\; i = 1, 2, \ldots I; \quad j = 1,\ 2,\ \ldots J \qquad (3)$$

III. Results and Discussion

Main Hypothesis: There is dependence between the location and socio-economic status of the house on energy consumption dynamics.

- Hypothesis 1: For household living within 15 minutes to the school the dependence on firewood is less (normal users).
- Hypothesis 2: For household living within 15 minutes to the employer the dependence on firewood is less (normal users).
- Hypothesis 3: Low socio economic status (indicated by the type of house) implies more time spent on the collection of firewood (normal users).
- Hypothesis 4: Low socio economic status (indicated by the type of house) implies more kilograms of firewood consumed (normal users).
- Hypothesis 5: Low socio economic status (indicated by the type of house) implies less litters of kerosene consumed (normal users).
- Hypothesis 6: Low socio economic status of biogas owners (indicated by

the type of house) implies more time spent on the collection of firewood before the installation of plant.

- *Hypothesis 7:* Low socio economic status of biogas owners (indicated by the type of house) implies more time spent on the collection of firewood after the installation of plant.
- *Hypothesis 8*: Low socioeconomic status (indicated by type of house) implies more time saved after construction of biogas plant.
- Hypothesis 9: Low socioeconomic status (indicated by type of house) implies more firewood saved after a switch over to biogas plant for cooking.
- Hypothesis 10 : More time spent on collection of firewood before the construction of biogas plant implies "relatively" more time spent in after the construction of biogas plant.

We see from Table I, the 'time spent in the collection of firewood' for biogas users is classified into six categories. According to the amount of time devoted for the collection of firewood, these categories are labelled as 0, 1, 2, 3, 4, 5. Here 0 stands for no time spent whereas 5 denote maximum time of 1-2 hours spent. These numbers are on ordinal scale as these values signify the amount of time spent. As seen from Table I, this holds true for national grid energy users. Same is true for the attribute 'type of house' labelled as 1, 2, 3 and 4 for both biogas users and grid energy users. Here household with concrete house with label 1 is highest in the socioeconomic status whereas the mud house labelled 4 ranks lowest in the socioeconomic status. For the attributes 'amount of firewood saved and amount of time saved', the values labels are 0, 1, 2 and 3, 1, 2, 3 and 4 respectively. These numbers are also classified on ordinal scale going from smallest to highest as the amount of firewood saved and amount of time saved increases. Similarly, 'distance from employer'and 'distance from school' are also classified on ordinal scale of 1, 2 proportional to the closeness from these places.

The attributes mentioned above in ten hypotheses are tested for independence using Chi square test of independence of attributes in Table II. Table II shows these ten hypotheses under the assumption of a true null hypothesis. G^2 is a maximum likelihood estimate of the degree of association between these variables. It is useful when the cell frequency is 0. As seen from Table II, both chi square and G^2 give same results. The results are highly significant for eight out of ten hypotheses shown in Table II. As seen from Table II, for national grid energy users, there is a highly significant dependence between times spent in the collection of firewood and distance of the household from the school. Similarly there is a dependence between time spent in the collection of firewood and distance of the household from the employer. The dependence between socio-economic status (indicated by type of house) and time taken to collect the firewood is highly significant. As seen from Table II, the dependence between socio-economic status and amount of firewood used is also highly significant. The details of parameters obtained fitting polytomous models are given in Table III. The impact of interrelationship between these variables given in Table III, is summarized in terms of odds ratio in Table IV.

TABLE I. DETAILS OF CATEGORICAL DATA.

User/Sample size	Variable name	Values on ordinal scale	Frequency
Biogas (400 household)	Time spent in the collection of firewood before		
	No time spent	0	33
	<15 minutes	1	15
	15-30 minutes	2	21
	30-45 minutes	3	18
	45-60 minutes	4	53
	1 hour-2 hours	5	260
	Time spent in the collection of firewood after		
	No time spent	0	153
	<15 minutes	1	137
	15-30 minutes	2	67
	30-45 minutes	3	24
	45-60 minutes	4	7
	1 hour-2 hours	5	12
	Type of house		
	Concrete	1	166
	Tile/asbestos	2	17
	Modern light roof	3	77
	Mud house	4	140
	Amount of firewood saved after biogas		
	Up to 30 Kg	1	39
	30-50 Kg	2	115
	Above 50 Kg	3	246
	Time saved		
	No change	0	13
	Less than 60 minutes	1	132
	1 hour to 3 hours	2	195
	3-5 hours	3	23
	More than 5 hours	4	37
Normal (300 household)	Time for the collection of firewood		
	Not applicable	0	13
	<15 minutes	1	29
	15-30 minutes	2	176
	30-45 minutes	3	78
	45 min-1 hour	4	04
	Type of house		
	Concrete house	1	4
	Tiled/asbestos	2	89
	Modern light roof	3	185
	Mud house	4	22
	Employer within 15 minutes		
	Yes	1	17
	No	2	283
	School within 15 minutes		
	Yes	1	86
	No	2	214

TABLE II. RESULTS OF HYPOTHESIS TESTING AT 5% LEVEL OF SIGNIFICANCE.

User	Null hypothesis	Chi square	G^2	P value (chi Square)	Conclusion
National grid	There is no dependence between the location of school and time taken to collect firewood	19.545	21.311	0.031	There is a dependence
	There is no dependence between the location of employer and time taken to collect firewood	10.611	9.021	0.001	There is a dependence
	There is no dependence between socioeconomic status (indicated by type of house) and time take to collect firewood	56.320	53.607	0.000	There is a dependence
	There is no dependence between socioeconomic status and kilograms of firewood consumed per month	30.823	19.359	0.005	There is a dependence
	There is no dependence between socioeconomic status and litters of Kerosene consumed per month	15.343	11.878	0.08	There is no dependence
Biogas	There is no dependence between socioeconomic status and time take to collect firewood before the plant construction	57.566	49.425	0.00	There is a dependence
	There is no dependence between socioeconomic status and time take to collect firewood after the plant construction	20.174	20.947	0.165	There is no dependence
	There is no dependence between socioeconomic status and amount of time saved after the construction of biogas plant	29.759	35.478	0.003	There is a dependence
	There is no dependence between socioeconomic status and amount of time saved after the construction of biogas plant	29.788	27.504	0.00	There is a dependence
	There is no dependence between the time take to collect the firewood before the plant and time taken to collect the firewood after the plant	128.374	139.804	0.00	There is a dependence

TABLE III. DETAILS OF POLYTOMOUS MODELS.

User/ Sample size	Adjective	Variable	Time taken (minutes)				
			No time	**<15**	**15-30**	**30-45**	**45-60**
Normal (300 households)	Time taken to collect firewood versus school within 15 min of home	School					
		μ_i (average)	-1.1492	-0.2133	2.0535	1.0074	-1.6985
		α_{i1} (yes)	-0.57495	0.4123	0.4121	-0.0924	0.6675
		α_{i2} (no)	0.57495	-0.4123	-0.4121	0.0924	-0.6675
		αi1 (concrete house	0.5922	0.7949	-1.8184	-0.5754	1.0068
		αi2 (tiled/asbestos)	-0.5002	0.1474	0.657	0.8741	-1.1812
		αi3 (modern light roof)	0.4367	-1.4867	0.5912	1.2204	0.1114
		αi4 (mud house)	0.3417	0.5445	0.5701	-1.5191	0.06301
	Time taken to collect firewood versus employer within 15 min of employer	Employer					
		μ_i (average)	-0.2925	0.001395	1.7588	0.1788	-1.6466
		α_{i1} (yes)	0.6918	0.00755	-0.0602	-0.8781	0.2541
		α_{i2} (no)	-0.6918	-0.00755	0.0602	0.8781	-0.2541
	Time taken to collect firewood versus type of house	Type of house					
		μi (average)	-0.3960	0.4999	1.3215	0.0785	-1.5037
		αi1 (concrete house)	0.5922	0.7949	-1.8184	-0.5754	1.0068
		αi2 (tiled/asbestos)	-0.5002	0.1474	0.657	0.8741	-1.1812
		αi3(modern light roof)	-0.4367	-1.4867	0.5912	1.2204	0.1114
		αi4 (mud house)	0.3417	0.5445	0.5701	-1.5191	0.06301
			Firewood used (kg/month)				
			0	100	200	300	
	Type of house versus amount of firewood used	Type of house					
		μi (average)	-1.5663	-1.0466	2.2235	0.389	
		αi1 (concrete house)	0.8733	1.0466	-1.53	-0.389	
		αi2 (tiled/asbestos)	-0.3207	-.14744	0.179	0.239	
		αi3(modern light roof)	-0.6897	-1.2096	1.356	0.533	
		αi4 (mud house)	0.1373	0.31045	-0.0156	-0.432	
			Kerosene used (liters/month)				
			0	1	2	3	
	Type of house versus amount of kerosene used	Type of house					
		μi (average)	2.03	-0.386	-0.28	1.364	
		αi1 (concrete house)	0.471	-0.1341	-0.24	0.844	
		αi2 (tiled/asbestos)	0.43	0.1374	0.619	-1.187	
		αi3(modern light roof)	0.077	-0.506	+0.237	-0.819	
		αi4 (mud house)	-0.036	0.51	-0.616	1.61	
			Time taken (minutes)				
			No time	<15	15-30	30-45	45-60
Biogas (400 households)	Type of house versus time spent in the collection of firewood before biogas installation	Type of house					
		μi (average)	-0.1115	-0.8868	-0.7948	-0.4581	0.6576
		αi1 (concrete house)	0.4212	0.3978	-0.09942	-0.63101	-0.51035
		αi2 (tiled/asbestos)	0.1896	0.2718	-0.51333	0.5237	1.030026
		αi3(modern light roof)	-0.169	0.0954	-0.40203	0.39731	-0.35033
		αi4 (mud house)	-0.4417	-0.765	1.01477	-0.29001	-0.16935

TABLE III. DETAILS OF POLYTOMOUS MODELS (COUNTINUES).

User/ Sample size	Adjective	Variable	Time taken (minutes)				
			No time	**<15**	**15-30**	**30-45**	**45-60**
Biogas (400 households)	Type of house versus time spent in the collection of firewood after biogas installation	Type of house					
		µi (average)	1.619992	1.239025	0.4277	-0.6344	-1.4128
		αi1 (concrete house)	-0.31207	-0.0346	-0.0118	0.5395	-0.697
		αi2 (tiled/asbestos)	0.680932	-0.4044	-0.6919	-0.3228	0.4556
		αi3(modern light roof)	-0.1788	0.3076	0.3567	-0.1216	0.2513
		αi4 (mud house)	-0.1899	0.1315	0.3468	-0.0952	-0.0099
			Time saved				
			30 min	1-3 h	3-5 h	>5 h	no time
	Type of house versus time saved after biogas installation	Type of house					
		µi (average)	0.821712	1.74324	-0.68261	-0.73179	-1.15056
		αi1 (concrete house)	-0.15683	-0.56319	0.083797	0.70352	-0.06729
		αi2 (tiled/asbestos)	-1.08606	0.700459	0.418257	-0.22571	0.19306
		αi3(modern light roof)	0.842625	0.315002	-0.3272	-0.97117	0.140748
		αi4 (mud house)	0.400269	-0.45227	-0.17485	0.493365	-0.26652
			Amount of firewood saved in (kg/month)				
			<=30 kg	30-50 kg	>50 kg		
	Type of house versus amount of firewood	Type of house					
		µi (average)	-1.0805	0.39897	0.68160		
		αi1 (concrete house)	-0.0997	-0.2355	0.3352		
		αi2 (tiled/asbestos)	-0.627	1.225	-0.598		
		αi3(modern light roof)	0.479	-0.541	0.0610		
		αi4 (mud house)	0.248	-0.449	0.202		
	Time spent after versus time spent in the collection of firewood before biogas installation	Time spent after biogas installation					
		µi (average)	-0.58287	-0.94764	-0.51339	-0.46169	0.286038
		αi1 (no time)	1.378904	-0.93047	0.021568	-0.72327	0.753621
		αi2 (<15 min)	-0.74252	1.494059	0.892749	-0.45823	-1.61142
		αi3 (15-30 min)	-1.36678	-1.00201	-0.04997	1.507774	0.536899
		αi4 (30-45 min)	-0.4461	-0.08132	-0.51558	0.125876	0.476757
		αi5 (45-60 min)	-0.06233	0.302441	-0.13181	-0.18351	0.860521
		αi6 (>60 min)	1.238825	0.217304	-0.21695	-0.26864	-1.01638

TABLE IV. IMPACTS OF FACTORS GOVERNING ENERGY CONSUMPTION IN TERMS OF ODDS RATIO.

Hypo.	User	Factors	Odds ratio	Conclusion
1	Normal grid energy (300 households)	Distance of the households from the School Versus Time taken to collect Firewood	12 times more in favor of households with schools far way for <15 min of firewood collection per day than 45-60 min per day.	Odds in favor tilted towards households far away from school for spending less time in firewood collection
2		Distance of the households from the Employer Versus Time taken to collect Firewood	3 time more in favor of households with employers close to the household for no times spent in the collection of firewood than 30-45 min spent per day.	Odds in favor tilted towards households close to the employer for spending less time in firewood collection
3		Socioeconomic status (indicated by type of house) Versus Time spent in the collection of firewood	14 time more in favor of households with mud houses than households with concrete houses for spending 15-30 minutes in collection of firewood than no time spent	Odds in favor tilted towards households living in mud houses -Indicator of energy poverty
4		Socioeconomic status (indicated by type of house) Versus Kilograms of firewood consumed per month	1.69 time more in favor of people with mud houses than households with concrete houses for spending 200 kg of firewood per month than 300 kg of firewood	Odds in favor tilted towards households living in mud houses-Indicator of energy poverty
5		Socioeconomic status (indicated by type of house) Versus liters of Kerosene consumed per month	2.59 time more in favor of people with mud houses than households with concrete houses for spending 0 liters of Kerosene per month than 2 liters of Kerosene	Odds in favor tilted towards households living in mud houses-Indicator of energy poverty
6		Socioeconomic status (indicated by type of house) Versus time taken to collect the firewood per day before biogas plant	3 times more in favor of people with mud houses than households with concrete houses for spending more than 60 minutes in the collection of firewood than no time in the collection of firewood	Odds in favor tilted towards households living in mud houses-this is indicator of energy poverty
7		Socioeconomic status (indicated by type of house) Versus time taken to collect the firewood per day after biogas plant	More than 2 times for people with mud houses than people with concrete houses for spending more than 60 minutes in the collection of firewood than no time in the collection of firewood	Odds in favor tilted towards households living in mud houses-this is indicator of reduction in energy poverty
8		Time saved from firewood collection Versus Socioeconomic status (indicated by type of house) after the construction of biogas plant	1.55 times more for people in concrete houses than people in mud houses	Odds in favor tilted towards people in concrete houses. This indicated the benefit of biogas in terms of time saved per day is substantial not only in low socioeconomic groups but also in high socioeconomic groups.
9	Biogas (400 households)	Amount of firewood saved from biogas plant Versus Socioeconomic status (indicated by type of house) after the construction of biogas plant	1.67 times more for people in concrete houses than people in mud houses.	Odds in favor tilted towards people in concrete houses. This indicated the benefit of biogas in terms of firewood saved per day is substantial not only in low socioeconomic groups but also in high socioeconomic groups.
10		Time spent in the collection of firewood before Versus time taken to collect the firewood after biogas construction	More than 1.28 times for households with no time in the collection of firewood after than less than 15 minutes after to spend more than 60 minutes before the plant than no time before the plant.	Odds in favor tilted towards households spending no time in the collection of firewood after the plant-this is indicator of immensity of positive impact in terms of time saved after biogas construction.

IV. CONCLUSIONS

Benefits of use of energy are not only direct but permeate in an intangible manner to several sectors. Ten different hypotheses related to energy consumption pattern of normal users and biogas users are tested with the help of this data. In eight of these ten hypotheses the null hypothesis of no dependence is rejected. It is found that location of school, location of employer and socioeconomic status of a household, plays a critical role in the energy consumption dynamics for both types of users. Energy poverty is assessed with the help of socioeconomic poverty in these hypotheses. The use of odds ratio has been used in quantifying the impact. The summary of the impact in terms of odds ratio is provided in Table IV. It is seen that the positive effects of biogas are substantial. The immensity of positive impact is shown here with the help of odds ratio. The results obtained here can be generalized to other countries in Asia and Africa.

ACKNOWLEDGMENT

This work is funded by NORAD, SINTEF under Renewable Nepal Project grant number RENP-10-06-PID-379. Jyoti U. Devkota thanks the partner industry in this project, Rapti Renewable energy services and all the students of the data collection team

REFERENCES

[1] CBS (2012). National report on national population and housing census 2011. National Planning Commission Sectariat, Central Bureau of Statistics, Kathmandu, Nepal (vol. 1, pp. 25-29).

[2] Devkota, J. U. (2019). Multivariate statistics of biogas and national grid energy consumers for countries with limited and scarce data – Nepal as a Case Study. *SN Applied Sciences, 1*(4). doi:10.1007/s42452-019-0367-x

[3] Devkota, J. U. (2020). Role of location of a household and its socio-economic status on energy consumption dynamics of rural Nepal: A categorical data analysis, *International Journal of Applied Power titute of Advanced Engineering and Science*.

[4] Devkota, J. U. (2020). Structural Equation Modeling in Forecasting Satisfaction of Biogas to a Rural Household - Examples from Nepal. *Biophysical Economics and Sustainability 5*(16). doi:10.1007/s41247-020-00082-3

[5] Devkota, J. U. (2020). Time Series Analysis of Radiant Heat Using 74 hours VIIRS Satellite Day and Night Band Nightfire Data. *e-Journal of Analysis and Applied Mathematics, 2020*(1), 98-117.doi:10.2478/ejaam-2020-0008

[6] Devkota, J. U. (2021). Forecasting Satisfaction of Grid Electricity to a Rural Household - Examples from Nepal. *SN Business & Economics, 1*(30). doi:10.1007/s43546-020-00036-3

[7] Devkota, J. U. (2021). Multivariate Analysis of COVID - 19 for Countries with Limited and Scarce Data - Examples From Nepal. *Journal of Environmental and Public Health*, Article ID 8813505. doi: 10.1155/2021/8813505

[8] Devkota J. U. (2021), Statistical Analysis of Active Fire Remote Sensing Data - Examples from South Asia, Environmental Monitoring and Assessment, Springer Nature, Vol. 193, Article No, 608, 2021. doi: 10.1007/s10661-021-09354-x

Energy Management System as a Big Data Generator in Smart Grid

Miodrag Forcan[1], Jovana Forcan[2]

[1]University of East Sarajevo, Faculty of Electrical Engineering, East Sarajevo, BiH, miodrag.forcan@etf.ues.rs.ba

[2]University of East Sarajevo, Faculty of Philosophy, Department of Mathematics, and Informatics, East Sarajevo, BiH, jovana.forcan@ffuis.edu.ba

Abstract—**Energy Management System of Smart Grid is capable to generate a Big Data. This paper considers sources of Big Data in electric utilities, underlining analytics and processing tools. The volume of Big Data and utility-related application barriers are analyzed. Hadoop and Berkeley Data Analytics Stack are identified as open source Big Data processing tools worth considering for Energy Management System applications. The conceptual Big Data range of Europe-level Energy Management System is revealed. Big Data is divided into three levels according to its range in power systems. The case study of Finland's transmission system operator Fingrid is identified as a good example of state-level data managing authority.**

Keywords – energy management system, big data, smart grid

I. INTRODUCTION

As power systems are rapidly evolving towards Smart Grid (SG) concept, information technologies are being used more than ever before. The consequence is the creation of various information systems producing the vast amounts of data often called Big Data. Big Data needs to be handled and examined appropriately to draw valuable information and take business decisions. Big data applications can help companies to make better business decisions by analyzing large volumes of data and discovering hidden patterns, unknown correlations, market trends, consumer preferences, and other valuable business information [1]. Utility companies simultaneously manage energy and data using Energy Management Systems (EMS). EMS software is designed to reduce energy consumption, improve the utilization of the system, increase reliability, and predict electrical system performance as well as optimize energy usage to reduce cost [2].

State-of-the-art, challenges, opportunities, and future directions Big data analytics in SG are considered in [3]. A quantitative and qualitative literature review on data analytics in the electricity sector is presented in [4]. A review on Big data issues in SG is presented in [5]. Big data driven smart energy management is considered in [6]. An example of Big data energy management, analytics and visualization for residential areas is given in [7]. Big data applications that are novel and have demonstrated value to the electricity industry are considered in [8]. In [9], an overview and key issues of EMS for SG are elaborated. State-of-the-art and future trends of EMS for SG are identified in [10].

According to literature review, EMS and Big Data are interconnected terms. EMS could be considered as a Big Data generator in SG. The main goal of this paper is to further reveal the interconnection of EMS and Big Data. Big Data range and the available Big Data processing tools are considered as an assistance to Independent/Transmission System Operators (ISO/TSO) and Distribution System Operators (DSO) in managing the SG.

The rest of this paper is organized as follows. Section II introduces EMS main functions, enabling technologies, and commercial software solutions. Defining properties of SG's Big Data (5V's of Big Data) are explained in Section III with emphasis on volume and application barriers. Big Data processing tools Hadoop and Berkeley Data Analytics Stack are considered in

ISBN: 978-86-80593-73-9

Section IV. Section V presents the conceptual Big Data range of Europe-level Energy Management System with emphasis on the example of Finland's transmission system operator Datahub. The paper is concluded in Section VI.

II. Energy Management System

EMSs are automation systems that collect energy measurement data from the field and making it available to users through graphics, online monitoring tools, and energy quality analyzers, thus enabling the management of energy resources [11]. EMS assists energy utilities to analyze, forecast, supervise, and optimize energy to decrease the costs of production, transmission, distribution, and consumption. Apart from the basic objectives of EMS, such as ensuring safe, reliable, stable, efficient, and flexible operation of the power grid, nowadays there are additional objectives related to SG [12]:

- Enable the proportional distribution of active/reactive power output of distributed resources and realize the desired power exchange with the external power grid.
- Compensate for the fluctuations of the distributed energy generators output and the dynamic load power demand.
- Be adaptive to the plug-and-play feature and the system topology changes.
- Participate in the regulation of the electricity market.

A. Technologies Enabling EMS in SG

The key technologies enabling EMS in SG can be roughly divided into communication and information systems.

The communication systems used in the SG could be classified into wired and wireless. Most commonly used wired technologies are Power Line Communications (PLC) and Optical communications. Wireless technologies are more diverse depending on the specific application requirements. ZigBee, Wi-Fi, Bluetooth, Worldwide Interoperability for Microwave Access (WiMAX), Cellular communications, and Satellite communications are among the mostly considered for SG [13]. The selection of communication system requires the corresponding application-specific techno-economic analysis. Communication system using Cloud-Fog computing approach seems to be an efficient solution for some applications in SG [14].

Utility information systems could contain several components: Supervisory Control and Data Acquisition System (SCADA), Customer Information System (CIS), Geographic Information System (GIS), Meter Data Management System (MDMS), Demand Response Management System (DRMS) and Outage Management System (OMS) [12]. SCADA has been effectively used by utilities in the past for monitoring and control of power systems. To enable new advanced information systems in SG Advanced Metering Infrastructure (AMI) deployment is required. Continuous, reliable and near real-time two-way communication should be enabled between different information systems. It is certain that the future EMSs will be driven by Big Data generated by information systems deployed in SG.

B. Commercial Software Solutions for EMS

Commercial software solutions for EMS could be divided into consumer-oriented and utility-oriented.

Consumer-oriented software is engineered specifically for electricity consumers with main goal to optimally manage their energy consumption. Typical examples are Energy Hippo EEM Suite and Wattics. They provide business intelligence to customers by creating efficient billing practices and operations. XClarity Energy Manager is an example of energy management software specifically engineered for data centers.

Utility-oriented software is engineered for grid-level EMS. Typical examples are Advanced Distribution Management System (ADMS) by Schneider Electric and Wide-Area Distributed Supervisory Control System for Power Grids by Hitachi. ADMS is used by 75 utility companies around the world. Its applications could be divided into: Distribution Management System (DMS), Outage Management System (OMS), and EMS for transmission and subtransmission networks. Hitachi's software solution could be used at the total system level, at each regional level, and at each station level. These grid-level software platforms for EMS work with Big Data.

III. BIG DATA IN ELECTRIC UTILITIES

Volume, velocity, variety, value, and veracity are five defining properties of Big Data - the so-called the 5V's of Big Data [15]. Volume is the size of big data, the quantity of collected and stored data. Velocity measures how fast data are coming into the system, it is speed at which data is generated collected, analyzed. Variety refers to the diversity of data types. Value refers on data importance, ability to derive business values from data. Veracity refers on data quality and accuracy, the truth and authenticity of the data.

A. 5V's of Big Data Applied to Smart Grid

The universal 5 V big data model is applied to SG in [16]:

- Volume – the widespread application of smart meter and advanced sensor technology provide huge amount of data.
- Velocity – with a sampling rate of 4 times per hour, 1 million smart meters installed in the smart grid would result in 35.04 billion records, equivalent to 2920 TB data in quantification [17].
- Variety – according to the extensive data sources in smart grid the formats and dimensions of data are diverse in structure.
- Veracity – errors of measurements in smart grid may exist due to the imperfections in devices or mistakes in data transmission.
- Value – with the improvement of intelligent devices adopted in smart grid, more and more value of big data analytics is revealed according to the various applications.

B. Big Data Analytics

Big data analytics is more than just data management; it is rather an operational integration of big data analytics into power system decision-making frameworks [18]. Big data analytics will play a critical role not only for the efficient operation of future electric grids but also for the development of proper business models for the key stakeholders (e.g., electric utilities, system operators, consumers, aggregators).

Three biggest areas for Big Data analytics in EMS are: Visualization, Situational Awareness and Predictive Forecasting [19]. Accurate information on distribution grid connectivity, Meters, Distributed Generation and Energy Storage should be visualized. Real-time monitoring of SG topology is an important function [20]. Situation Awareness enables Demand Response and Distributed Generation contributions, Grid Management in terms of reliability and resiliency, and Grid Efficiency in terms of optimal capital and O&M costs. Predictive Forecasting enables wide-area situational awareness, system protection & restoration and grid security [19].

C. Big Data Volume in Electric Utilities

As electric utilities are heavily regulated organizations, they are more focused on system reliability rather than trying a new technology including big data analytics [3]. Big Data storage and management are already successfully implemented in other industries, such as banking. However, electric utilities are faced with many specific constraints, such as a real-time operation efficiency and reliability. There are simultaneous power and information flows to be managed.

A typical pattern of Big Data volume in electric utilities is given in Fig. 1. The starting point in transition from traditional power system to SG is AMI deployment [21]. It is estimated that a moderately sized city with 2 million homes could generate 22 GB of meter data every day [22]. According to pattern of big data volume in electric utilities (Fig. 1), electricity consumption data volume is the lowest. However, in the case of the application of Demand Response (DSM) programs, data volume from SMs surpasses 100 TB annually. The biggest data volume is expected to originate from Home Energy Management systems, 600-800 TB annually.

Application of Big Data analytics in utilities has been facing different barriers. Identified barriers are given in Table I. Data management has been identified as a major barrier for Big Data implementation in EMS. The complexity of data managing proved to be a leading limitation among the others.

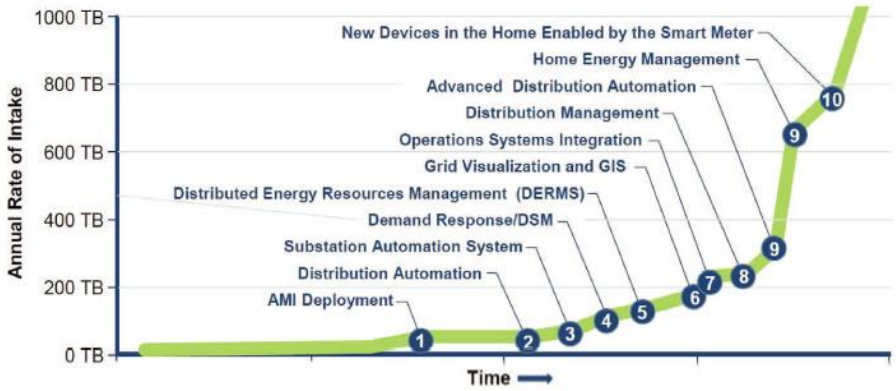

Figure 1. Pattern of big data volume in electric utilities [19, 3].

TABLE I. IDENTIFIED BARRIERS FOR BIG DATA IMPLEMENTATIONS [24]

High data storage and manipulation costs	**Data management**			**Skill shortage**	**Lack of management support**
26 %	***Complexity***	***Access issues***	***Privacy issues***	13 %	8 %
	23 %	18 %	13 %		

IV. BIG DATA PROCESSING TOOLS

To handle massive data processing needs that Google was facing in early 2000, Google designed and implemented Google File System (GFS). The architecture of GFS is considered to be the pioneer example in Big Data processing area. A GFS clusters consists of single master and multiple chunk servers also called slave servers. It is accessed by multiple clients. If any server crashes, data can be found on another server. The master server stores metadata associated with the chunks.

As data is growing at rapid rate, the main challenges of Big Data are storing, processing, and securing this incredible amount of data. The traditional approaches are not efficient in doing that. To deal with Big Data challenges, Hadoop and Berkeley Data Analytics Stack open source tools are used as a benchmark in computer engineering, thus they are worth considering for EMS applications. They can be divided into the following categories: data storage and management, data cleaning, data mining, data visualization, data reporting, data ingestion, data analyst, and data acquisition.

A. Hadoop

Hadoop is an Apache open source framework written in java for storing big data sets distributed across clusters of computers with commodity hardware and process it parallelly [23]. Two basic components of Hadoop are Hadoop Distributed File System (HDFS) which is storage unit of Hadoop based on GFS and MapReduce which is processing, computation unit of Hadoop. HDFS provides a distributed file system for storing huge datasets in commodity hardware. HDFS has highly fault-tolerance and throughput, it is designed to be deployed on low-cost hardware and provides data security [23].

HDFS has master-slave architecture. It consists of master server called *NameNode* and number of *DataNodes* called slave servers that form HDFS cluster. HDFS exposes a file system namespace and allows user data to be stored in files. Large files are divided into small blocks each of size 128 MB, by default, that are stored in a set of *DataNodes*. Multiple copies of blocks are distributed across different nodes. *NameNode* manages and maintain *DataNodes*, stores the metadata, and executes file system namespace operations. *DataNodes* store the actual data, it performs read and write request. *NameNode* and *DataNode* communicate through the *HeartBeat*, a signal that each *DataNode* sends to NameNode periodically to show its status.

Hadoop MapReduce is a software framework for easily writing applications which process

huge data sets in a parallel and distributed fashion on large clusters of commodity hardware in a reliable, fault-tolerant manner. It is introduced by Google [24]. MapReduce programming model is a representation model of the divide and concur processing model [25]. In the Map phase the input data is split into small blocks over cluster's slave nodes. In the Reduce phase the results are filtered and aggregated, and the result is obtained and sent to master node. Hadoop ecosystem, the framework of various type of complex and evolving tools and techniques, contains the following components [26]: Common, Yarn, Ambari, Cassandra, HBase, Apache Spark, Hive, Pig, Oozie, Zookeeper. Some of Hadoop Vendors are Amazon Elastic MapReduce, Hortonworks Data Platform (HDP), IBM Open Platform, Microsoft Azure's HDInsight-Cloud based Hadoop Distribution etc.

Hadoop application in AMI proved its efficiency for managing data from one million electricity meters. A 4-nodes cluster was constructed and used to store the generated one million meters' data in a distributed fashion and perform parallel processing across nodes [7].

B. Berkeley Data Analytics Stack

An alternative of the Hadoop framework to deal with the Big Data in a fastest way is proposed by AMPLab, University of California, Berkeley [27]. The Berkeley Data Analytics Stack (BDAS) contains the following layers: Resource Visualization, Storage, Processing Engine, Access, and Interface.

Visualization layer contains two components: Mesos and Yarn. Mesos provides features such as scalability, fault tolerance, and scheduling of multiple resources such as ports, memory, disk, and the CPU [28]. In the Storage layer, the base is the File System. It should be any file systems like HDFS, Amazon's S3 or Ceph [27]. The processing layer contains the Spark core. Spark is an open source cluster computing system that aims to make data analytics fast - both fast to run and fast to write [29]. Spark overcomes the Hadoop's problem of the disk data access by managing the data in cache and process data faster than Hadoop. The top layer consists of many different components such as [28]: Spark streaming, MLBase, MLib, SparkSQL, SparkR, GrapX and BlikDB.

V. EUROPE-LEVEL EMS BIG DATA

European Network of Transmission System Operators for Electricity (ENTSO-E) developed a Transparency platform (TP) to serve market participants. It is meant to provide open data related to electricity market. The goal is to reduce insider trading and level the playing field between small and large actors [30]. At the moment TP cannot be considered as Big Data analytics platform for EMS, since it only publishes limited (regulated) data on electricity market. However, it is meant to become the most important data source of European power systems [31].

A. Big Data Levels in European Power Systems

It is meaningful to divide Big Data related to European power systems into following levels:

- DSO-level: data on particular intra-state distribution network, distributed energy sources, medium and low voltage electricity consumers, etc.
- ISO/TSO: data on transmission network of particular European state, Independent power producers (IPP), intra-state DSOs, state-level electricity market, etc.
- ENTSO-E: data on European transmission network, ISO/TSO participants, European electricity market.

The main data sources can be divided into: SCADA – monitoring and control (DSO and ISO/TSO levels), AMI – electricity consumption (DSO level), and electricity market (ENTSO-E and ISO/TSO levels: data on generators, retailers, traders, etc.).

B. Conceptual Big Data of Europe-level EMS

The conceptual Big Data range for Europe-level EMS, Finland state-level EMS case study, is presented in Fig. 2. DSO-level is a starting point in considering solutions for Big Data Analytics. DSO-level Big Data is used as a basis for DSO-level EMS. By collecting the selected and filtered DSO-level Big Data sets the ISO/TSO-level Big Data is created. It is used for ISO/TSO-level EMS, which is usually a state-level EMS. Finland's TSO Fingrid is a good example of an advanced state-level operator enabling EMS. Fingrid collects data from DSOs, IPPs, and other electricity market participants.

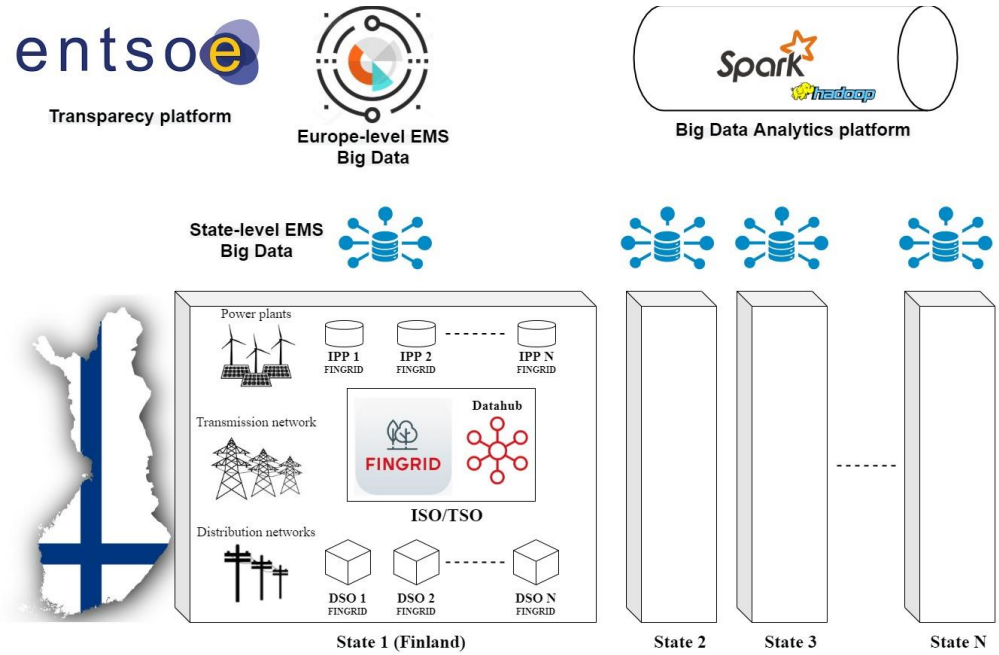

Figure 2. Big Data range for Europe-level EMS – Finland state-level EMS case study

It provides a shared system called Datahub enabling up-to-date and equally available information for all eligible parties. ISO/TSOs of European states provide EMSs and generate state-level Big Data. By collecting state-level Big Data sets ENTSO-E TP has potential to become Europe-level EMS, thus requiring advanced Big Data processing tools.

VI. CONCLUSION

The Big Data processing tools are expected to be used in EMS of SG in the near future. Although there are many barriers imposed by utility companies, the usage of Big Data Analytics could bring higher efficiency to EMS. Hadoop and Berkeley Data Analytics Stack have potential to be integrated in EMS with aim to store and process the Big Data. This paper identifies the range of Big Data at Europe-level EMS. Finland state-level EMS case study is presented as a benchmark example for managing Big Data using Datahub. EMS is identified as a Big Data generator of constantly increasing data volume that should be efficiently processed.

REFERENCES

[1] Sunagar, P., Hanumantharaju, R., Siddesh, G. M., Kanavalli, A. & Srinivasa, K. G. (2020). Influence of big data in smart tourism. In S. Bhattacharyya, V. Snášel, D. Gupta, & A. Khanna (eds). *Hybrid Computational Intelligence for Pattern Analysis and Understanding*, *Hybrid Computational Intelligence*. Academic Press.

[2] *Nptel. EMS lecture 1: introduction.* Available at: https://nptel.ac.in/content/storage2/courses/108106022/LECTURE%201.pdf

[3] Bhattarai, B. P., et al. (2019). Big data analytics in smart grids: state-of-the-art, challenges, opportunities, and future directions. *IET Smart Grid*, *2*(2), 141-154.

[4] Scheidt, F., et al. (2020). Data analytics in the electricity sector – A quantitative and qualitative literature review. *Energy and AI*, *1*, 100009.

[5] Tu, C., He, X., Shuai, Z. & Jiang, F. (2017). Big data issues in smart grid – A review. *Renewable and Sustainable Energy Reviews*, *79*, 1099-1107.

[6] Zhou, K., Fu, C., & Yang, S. (2016). Big data driven smart energy management: From big data to big insights. *Renewable and Sustainable Energy Reviews*, *56*, 215-225.

[7] Gupta, R., Al-Ali, A. R., Zualkernan, I. A., & Das, S. K. (2020). Big Data Energy Management, Analytics and Visualization for Residential Areas. *IEEE Access*, *8*, 156153-156164.

[8] Kezunovic, M., et al. (2020). Big data analytics for future electricity grids. *Electric Power Systems Research*, *189*, 106788.

[9] Rathor, S. K., Saxena, D. (2020). Energy management system for smart grid: An overview and key issues. *Int J Energy Res.*, *44*, 4067– 4109.

[10] Meliani, M., Barkany, A. E., Abbassi, I. E., Darcherif, A. M., & Mahmoudi, M. (2021). Energy management in the smart grid: State-of-the-art and future trends. *International Journal of Engineering Business Management*.

[11] Segatto, M. E. V., Rocha, H. R. O., Silva, J. A. L., Paiva, M. H. M., & Cruz, M. A. R. S. (2018).

Telecommunication Technologies for Smart Grids: Total Cost Optimization. In I. Yahyaoui, (ed.). *Advances in Renewable Energies and Power Technologies* (451-478). Elsevier.

[12] Xu, Y., Zhang, W., Liu, W., & Yu, W. (2021). *Distributed Energy Management of Electrical Power Systems*. Wiley-IEEE Press.

[13] Alam, S., Sohail, M. F., Ghauri, S. A., Qureshi, I. M., & Aqdas, N. (2017). Cognitive radio based Smart Grid communication network. *Renewable and Sustainable Energy Reviews*, *72*, 535–548.

[14] Forcan, M., & Maksimović, M. (2020). Cloud-Fog-based approach for Smart Grid monitoring, *Simulation Modelling Practice and Theory*, *101*, 101988.

[15] Troester, M. (2012). *Big Data meets Big data Analytics*. SAS Institute Inc.

[16] Zhu, T., Xiao, S., Zhang, Q., Gu, Y., Yi, P., & Li, Y. (2015). Emergent Technologies in Big Data Sensing: A Survey. *International Journal of Distributed Sensor Networks*.

[17] Sagiroglu, S., Terzi, R., Canbay, Y., & Colak, I. (2016). Big Data Issues in Smart Grid Systems. In *2016 IEEE International Conference on Renewable Energy Research and Applications* (pp. 20–23).

[18] Dong, Z., & Zhang, P. (2010). *Emerging techniques in power system analysis*. Springer.

[19] Pancholi, S. (2014). Solving big data challenges us electric utility industry. In *PES General Meeting*.

[20] Forcan, M., Maksimović, M., & Forcan, J. (2019) Cloud-based approach for real-time monitoring of Smart Grid topology. In *5th Jubilee Virtual International Conference on Science, Technology and Management in Energy - eNergetics* (pp. 47-54).

[21] Forcan, M. (2021). A Novel Technologies Empowering the Transition from Traditional Distribution Network to Smart Grid. In *6th International Conference on New Energy and Future Energy Systems*.

[22] Rusitschka, S., Eger, K., & Gerdes, C. (2010). Smart Grid Data Cloud A Model for Utilizing Cloud Computing in the Smart Grid Domain. In *First IEEE International Conference on Smart Grid Communications* (pp. 483 – 488).

[23] Borthakur, D. (2008). *HDFS architecture guide.*

[24] Dean, J., & Ghemawat, S. (2008). MapReduce: simplified data processing on large clusters. *Commun. ACM*, *51*(1), 107–113.

[25] Abedallah, A. (2019). Hadoop and Big Data challenges. *Journal of Theoretical and Applied Information Technology*, *97*, 3488.

[26] Nagdive, A. S. & Tugnayat, R. M. (2018). A Review of Hadoop Ecosystem for BigData. *International Journal of Computer Applications*, *180*, 35-40.

[27] Manoharan, P., Pradeep, D. & Sundar, C. (2017). An overview of big data: concept, frameworks and research issues. *Advances in Natural and Applied Sciences*, *11*(3), 146.

[28] Arfat Y., Usman S., Mehmood R. & Katib I. (2020). Big Data Tools, Technologies, and Applications: A Survey. In R. Mehmood, S. See, I. Katib, I. Chlamtac (eds). *Smart Infrastructure and Applications. EAI/Springer Innovations in Communication and Computing*. Cham: Springer.

[29] *Apache Spark™—unified analytics engine for big data. Apache Software Foundation*. Available at: https://spark.apache.org/.

[30] European Commission (2017). *A review of the ENTSO-E Transparency Platform. Study on the quality of electricity market data.* Available at: https://ec.europa.eu/energy/sites/ener/files/documents/review_of_the_entso_e_plattform.pdf

[31] Hirth, L., Mühlenpfordt, J. & Bulkeley, M. (2018). The ENTSO-E Transparency Platform – A review of Europe's most ambitious electricity data platform. *Applied Energy*, *225*, 1054-1067.

Study of the Behavior of Co-Combustion of Coffee Waste and Sugarcane Bagasse

Dalila Medeiros de Araújo[1], Isabel Alves Pimenta Gabriel[2], Sahyonara Estrela Lacerda Hussein Melo[3], Silvia Layara Floriani Andersen[4]

[1,2,3]Federal University of Paraíba, João Pessoa, dalilaamedeiros@gmail.com[1], isabelpimenta@cear.ufpb.br[2], sahyonarahussein@gmail.com[3]
[4]Department of Renewable Energy Engineering, Federal University of Paraíba, João Pessoa, Brazil, silvia@cear.ufpb.br

Abstract—**With the uncontrolled increase in energy demand, the use based on fossil fuels, has become a global problem. However, the search for sources that are less harmful to the environment began to increase, and the use of renewable sources, especially biomass, was an alternative that has been adopted. This work aimed to study the co-combustion behavior of coffee grounds waste (BCF) and sugarcane bagasse (BCC) for energy purposes. The methodology applied for the analysis of BCF and BCC was through the physicochemical characterization and thermogravimetric analysis (TG). The results obtained in the study showed that the levels of volatile matter found for the samples indicated that there is a large amount of compounds that can be devolatilized, in addition, the values found for the BCF (18.34 MJ.kg^{-1}) and BCC (18.05 MJ.kg^{-1}) (PCS) are comparable to traditional biomass fuels that have already been used for energy purposes. Through TG it was found that with the co-combustion process the greatest mass loss happens around 150 ºC to 350 ºC in all mixtures, and the mixture of 25% BCF with 75% BCC was the most reactive either by ignition temperature (Tig) around 175 °C and by the highest rate of mass loss at a low temperature (25%.min^{-1}at 402°C). Through this work, it was possible to note that it is plausible to use mixtures of BCF and BCC for energy purposes through co- combustion process.**

Keywords - solid waste, thermogravimetric analysis, renewable energy

I. INTRODUCTION

In recent times, due to the accelerated growth in energy demand, there has been an inability to maintain the standard of living based only on the use of fossil fuels, due to the depletion of reserves, air pollution and price instability. Thus, there was an increase in the demand for public policies aimed at expanding the supply of renewable energy and energy efficiency [1].

In this context, there was the search for sources less harmful to the environment, and one of the possibilities are renewable energy sources. An option that has proven viable among these sources is biomass, because it has great energy potential, whether on a global and national scale, being, a low-cost raw material [2].

Among biomasses, coffee grounds waste (BCF) and sugarcane bagasse (BCC), can be good alternatives, both of which are highlighted, due to Brazil being one of the largest producer of coffee and sugarcane in the world [3]. Furthermore, the use of them for energy purposes would reduce the problem of their destination and could replace other sources in the energy application used on the site.

Brazil is the world's largest producer of sugarcane, obtaining a production of around 654.5 million tons in the 2020/2021 harvest. In addition, for ethanol production it reached approximately 29.7 billion liters, and in sugar production it was 41.2 million tons [4]. In 2018 Brazil was the country that most produced the coffee with a production in the range of 51 million bags, with exports of 33.5 million bags [5].

Among the thermochemical conversion processes of biomass, co-combustion have received much attention in recent years, due to its

ISBN: 978-86-80593-73-9

flexibility, besides being, a promising short- term alternative for waste disposal and its exploitation as an energy source, as it improves the efficiency of the combustion process and helps to minimize CO_2 emissions into the atmosphere. Biomass can be burned together with waste materials, reducing the consumption of fossil fuels for energy generation [6].

Thus, the objective of this work is to contribute to the research agenda in the area of materials applied to renewable energies, verifying the co-combustion process of BCF and BCC characterizing the physicochemical properties of these residues for energy purposes.

II. MATHERIALS AND METHODS

A. Preparation of Raw Material

For this study, two solid wastes were selected: Coffee ground wastes (BCF) from the industrial processing for the production of soluble coffee, and sugarcane bagasse (BCC) obtained from a cachaça mill. BCF was obtained in a coffe e industry located in João Pessoa, Paraíba, Brazil, and BCC was obtained in a cachaça mill factory located in Santa Cruz do Espírito Santo, Paraíba, Brazil. The analysis of moisture was performed using a moisture analyzer AND, MF50. Then, samples were dried in an oven with air circulating at 105 ºC during 3 hours. After dried, samples were crushed and sieved (<100 mesh) in order to homogenize particle size.

B. Proximate Analysis

The proximate analyses were carried out in accordance with the methodologies exposed by ASTM E872-82 (2019) [7] and ASTM E1755-01 (2001) [8] to determine the contents of volatile matter and ash.

Moisture content was determined using an AND moisture balance (Moisture Analyzer, MF-50), volatile material content and ash content were obtained using a muffle furnace (Zezimaq, 2000 F). To obtain the volatiles, the samples were submitted to a muffle furnace (without the presence of oxygen) at a temperature of 950 ºC for 7 (seven) minutes, in order to release all the organic matter, leaving only the biochar.

And to carry out the ash, the samples were exposed in the muffle mold at 575 ºC, with a residence time of approximately 2 (two) hours, to carry out the total burning of the organic compounds present in the sample. All analyzes were performed in triplicate.

The fixed carbon content of biomass was obtained using (1) on a dry basis.

$$TFC = 100 - (TVM + TA), \quad (1)$$

where: T_{FC} – Fixed carbon (%, m/m), T_{VM} – Volatile matter (%, m/m), T_A – Ashes content (%, m/m).

C. Superior Calorific Value Analysis (PCS)

The calculation of the PCS used the proximate analysis, using the correlation recommended by Nhuchhen & Salam (2012), in which the equation depends on the fixed carbon content (FC), the volatile material content (VM) and the ash content (A) (2).

$$PCS(\mathrm{MJ.kg^{-1}}) = 19,2880 - 0,2135\left(\frac{VM}{FC}\right) + \\ + 0,0234\left(\frac{FA}{A}\right) - 1.9584\left(\frac{A}{VM}\right) \quad (2)$$

D. Co-Combustion Behavior of BCF and BCC

Firstly, to investigate the behavior of the BCF and the BCC, thermogravimetric analyzes (TG) and differential thermogravimetry (DTG) were performed. These analyzes were performed at LabMaQ, using the SDT 650, TA equipment. For these analyses, an inert atmosphere (N_2, purity of 99.99%) was applied with a temperature program from room temperature to 900 ºC, at a heating rate of 10 ºC/min and flow rate of 100 mL/min.

Subsequently, the BCF and BCC co-combustion process was verified using TGA and DTG. The BCC and BCF samples were dried on a moisture balance and then the proportions of mixtures of 25% BCF with 75% BCC, 50% BCF with 50% BCC and finally 75% BCF with 25% of BCC. In this analysis, an oxidizing atmosphere of synthetic air will be used (synthetic air, 99.99%) 21% v/v of O_2 and 79% v/v of N_2) from room temperature to 1200 ºC, with heating rate of 10 °C/min and flow rate of 100 mL/min. The mass of each sample will be approximately 10 mg in an alumina crucible. And for each trial, duplicates were made.

III. RESULTS AND DISCUSSION

A. Proximate Analysis of BCF and BCC

Table I below shows the data obtained regarding the proximate analysis of BCF.

TABLE I. PROXIMATE ANALYSIS OF BCF.

Proximate analysis (%, m/m)	
Moisture	11.72 ± 0.23
Volatile matter (VM)	69.25 ± 0.15
Ash (A)	10.05 ± 0.32
Fixed carbon (FC)	20.70

Table I shows that the moisture content of BCF was 11.72%, in which it was above 10%, which may have been due to the removal of liquid that was not as efficient during the industrial processing of coffee beans for the production of soluble coffee. However, there are few studies in the literature that have made this type of analysis for BCF, but compared with pieces of work [9], [3] and [10] that resulted in the moisture content 11.78%, 9.76% and 9.79%, respectively, it is seen that the result obtained is in the range of the values presented.

Table II presents the contents of volatile material, fixed carbon and ash reported in the literature for BCF. From Table II, it is noted that the levels of volatile matter (69.25%) and fixed carbon (20.70%) obtained for BCF are within the range found in the literature. However, taking into account the ash content, it is noted that the obtained value is much higher than the values reported in other studies. High levels of ash are not desired, as they contribute to low PCS values, besides that, they can cause problems with fouling in the equipment [13].

TABLE II. VOLATILE MATERIAL, FIXED CARBON AND ASH REPORTED IN THE LITERATURE FOR BCF.

VM (%)	FC (%)	A (%)	Author
68.94	17.46	1.82	9
77.06	10.18	3.00	3
74.82	21.93	0.56	11
76.02	15.59	1.75	12

TABLE III. PROXIMATE ANALYSIS OF BCC.

Proximate analysis (%, m/m)	
Moisture	8.58 ± 0.18
Volatile matter	76.92 ± 0.19
Ash	7.90 ± 0.04
Fixed carbon	15.18

TABLE IV. VOLATILE MATERIAL, FIXED CARBON AND ASH REPORTED IN THE LITERATURE FOR BCC.

VM (%)	FC (%)	A (%)	Author
76.10	6.90	9.60	15
66.40	14.80	18.80	19
77.50	13.10	9.50	20
80.90	14.00	5.10	21

Table III shows the BCC proximate analysis results obtained by da Silva [14]. It can be seen in Table III that the moisture content of the BCC was below 10%, which may have been due to the efficiency of liquid removal during the grinding of sugarcane. According to other studies [15], [16] and [17] a moisture content of 6.70%, 5.25% and 4.80%, respectively was obtained. The content found by Silva work [14] is considered high, however, according to [18], the result achieved is acceptable and has good applicability for thermochemical process.

Table IV shows the contents of volatile material, fixed carbon and ash reported for BCC in the literature.

The values obtained by Silva work [14] is within a considerable range compared to the pieces of work presented in Table IV, the ends up generating greater reliability to the data obtained. The levels of VM (76.92%) and FC (15.18%) for BCC by Silva work [14] shows the large number of compounds that can be devolatilized, since high levels of VM makes the solid fuel more reactive [18].

In the same way, it was observed that the moisture content of BCF is higher than that of BCC that both samples have a large number of volatile materials, and BCC (76.92%) had a higher content than BCF (69.25%). The fixed carbon content of BCF (20.70%) is higher than BCC (15.18%).

B. PCS Analysis

Table V reports the PCS values found for BCF and BCC through (2), and its comparison with data from other biomasses reported in the literature.

Table V shows that the PCS contents obtained for BCF and BCC were 18.34 $MJ.kg^{-1}$ and 18.05 $MJ.kg^{-1}$, respectively. Where BCF has higher PCS than BCC, this may be due to the FC and VM content found in the proximate analysis, since the higher the FC contents and the lower the VM content, the higher the PCS [24].

TABLE V. PCS VALUES FOUND FOR BCF AND BCC THROUGH EQUATION 2, AND ITS COMPARISON WITH DATA FROM OTHER BIOMASSES REPORTED IN THE LITERATURE.

Biomass	PCS (MJ.kg^{-1})	Author
BCF	18.34	This study
BCC	18.05	This study
Pine bark	21.78	22
Yerba mate residue	18.30	23
Corn husk	17.80	22
Rice husk	14.50	22

And with regard to the values reported by other authors in Table V, it is perceived that the BCF and BCC presented higher levels when compared with the other biomasses, except for the shell of pine and yerba mate residue that obtained 21.78 MJ.kg^{-1} and 18.30 MJ.kg^{-1}, respectively. Therefore, through the results it is inferable that BCF and BCC may have a good applicability in its use for energy purposes.

C. Study of the Co-Combustion Behavior of BCF and BCC

Fig. 1 below describes the co-combustion process, in which it is possible to verify the overlap of the TG and DTG curves of the mixtures of 25% BCF with 75% BCC as a function of temperature.

From Fig. 1, it is noted that the drying process takes place at temperatures below 150 ºC, with moisture loss of 3.96%. Between the range around 150 ºC to 350 ºC there is the decomposition of the volatile material, which according to the TG curve had a loss of 56.21% at this stage and mass loss velocity (10.62%.min^{-1}) in the DTG curve is maximum when it reaches 308 ºC, since, according to [25] volatile material can ignite and burn at lower temperatures, in which it will favor ignition and combustion.

The ignition temperature (Tig) is around 175 ºC as can be seen in the DTG curve, as it is at this temperature that there is no moisture and the sample starts to burn [26]. Through the TG curve in the range of 350 ºC to 480 ºC, the thermal decomposition of the heavier volatile materials and the residual fixed carbon occurs, with a mass loss of 28.12%, in which, according to [27], the peaks in higher temperatures (above 400 ºC) are possibly related to the burning of volatile materials with higher molecular weight and fixed carbon. And according to the DTG curve, at 402 °C there is a high rate of mass loss of 25.61%.min^{-1}.

From the temperature of 480 ºC until the end of the process, the sample of 25% BCF with 75% BCC had a thermal stability, in which it produced 10.73% of ash.

In relation to the mixture to the co-combustion process of 50% BCF with 50% BCC, it can be seen in Fig. 2, where it presents the overlap of the TG and DTG curves as a function of temperature.

Through the TG curve (Fig. 2) it was verified that up to the temperature of 150 ºC the sample had residual moisture loss of 3.87% and Tig started around 180 ºC.

The release of volatile material occurred at approximately 150 ºC to 350 ºC (TG Curve) with mass loss of 52.82% and a peak is formed with high mass loss velocity (7.76%.min^{-1}) when it reaches 305 ºC (DTG Curve).

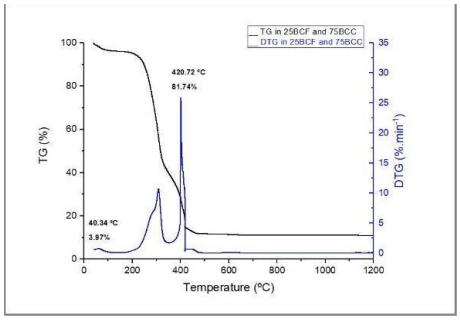

Figure 1. Overlapping of the TG and DTG curves of the mixtures of 25% BCF with 75% BCC as a function of temperature.

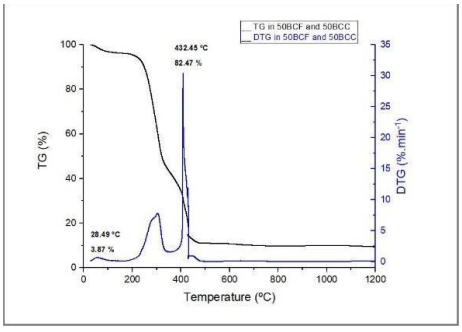

Figure 2. Overlapping of the TG and DTG curves of the mixtures of 50% BCF with 50% BCC as a function of temperature.

At around 350 ºC to 480 ºC, there is a mass loss of 32.32% in this region, which can be characterized as the decomposition of the heaviest volatiles and fixed carbon. In addition, a second peak of thermal decomposition in the DTG curve is generated at the temperature of 409 ºC, with a high speed of mass loss (30.38%.min^{-1}).

When it reached approximately the temperature of 480 ºC up to 1200 ºC the mixture of 50% BCF with 50% BCC occurred no further reaction in the sample and produced 9.31% of ash at the end of the process.

Finally, Fig. 3 presents the co-combustion process of 75% BCF with 25% BCC, where the TG and DTG curves are overlapped as a function of temperature.

In the TG curve (Fig. 3) the sample of 75% BCF with 25% BCC lost 4.87% of residual moisture, at a temperature below 150 ºC. Between 150 ºC to 350 ºC there was thermal degradation of 48.68 ºC of volatile material and from the DTG curve the high speed of mass loss (6.83%.min^{-1}) happens at 289 ºC. Tig started at about 200 ºC (DTG Curve).

It is noted that between the range of 350 ºC to 480 ºC it may have occurred both the degradation of the heaviest volatile matter and the residual fixed carbon, which according to the TG curve the loss it was 36.25%. And through the DTG curve at the temperature of 413 ºC a new peak is formed with high mass loss velocity (33.40%.min^{-1}).

It is also observed that the sample of 75% BCF with 25% BCC submitted to the oxidizing atmosphere was fully gradated to 480 ºC, when

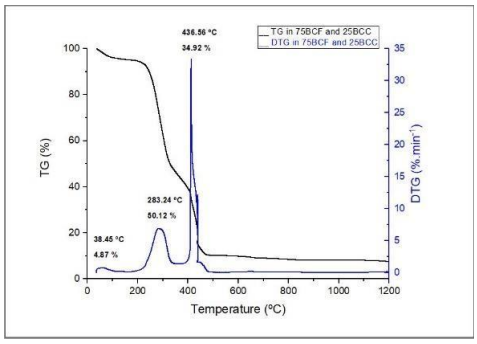

Figure 3. Overlapping of the TG and DTG curves of the mixtures of 75% BCF with 25% BCC as a function of temperature.

the thermal stability was, leaving it only ashes, percentage of 7.43% (TG Curve).

Thus, after the analyses of Figs. 1-3 it can be understood that both proportions of BCF mixtures with BCC present distinct values of Tig ranging from 175 ºC to 200 ºC, and the mixture of 25% of BCF with 75% BCC is easier to ignite in relation to the other mixtures. In addition, the greatest mass loss occurs in both samples at the range of 150 ºC to 350 ºC. The mixture of 25% BCF with 75% BCC is pointed out as the most reactive, had the highest rate of mass loss at a lower temperature with 25%.min^{-1} to 402 ºC. And mixing 75% of BCF with 25% of BCC generated the lowest percentage of ash (7.43%), which can be an indicator that there was a great oxidation of the material during the process.

IV. CONCLUSION

The results of the proximate analysis showed that the volatile material contents found for both BCF and BCC samples were 69.25% and 76.92%, respectively, as well as the fixed carbon of BCF (20.70%) and BCC (15.18%) have a large number of compounds that can be devolatilized, which makes solid fuel more reactive.

Regarding the values obtained from the PCS through the correlation proposed by Nhuchhen & Salam (2012) of BCF (18.34 MJ.kg^{-1}) and BCC (18.05 MJ.kg^{-1}), it was found that the values found are comparable to those of traditional biomass fuels that have already been used for energy purposes.

In addition, regarding the co-combustion process, it was noted that the greatest mass loss occurs in the temperature range from 150 ºC to 350 ºC in all mixtures, and the mixture of 25% of BCF with 75% BCC was the most reactive either by Tig (175 ºC) to be the lowest among them and having had the highest rate of mass loss at a lower temperature with 25%.min^{-1} to 402 ºC. The mixture of 75% BCF with 25% BCC was the one that generated the least ash (7.43%).

Therefore, through these results it is noticed that BCF and BCC biomasses and mixtures of 25% BCF with 75% BCC, 50% BCF with 50%

BCC and 75% BCF with 25% BCC, may have a good applicability in its use for energy purposes in combustion processes. In addition, the co-combustion process is a promising alternative, since it contributes to the reduction of the use of fossil fuels, and there is a great

availability of wastes (biomass) to be used simultaneously.

REFERENCES

[1] Herbert, G. J., & Krishnan, A. U. (2016). Quantifying environmental performance of biomass energy. *Renewable and Sustainable Energy Reviews*, *59*, 292-308.

[2] Philippi Jr., A., & Reis, L. B. (2016). *Energy and Sustainability*. Barueri: Manole.

[3] Batista Jr. (2017). *R. Pyrolysis of Coffee Ground: Chemical Kinetics and Fixed Bed Operation* [Masters Dissertation, Federal University of Triângulo Mineiro].

[4] CONAB. (2021). *Historical Series of Harvests*. Available at: https://www.conab.gov.br/info-agro/safras/serie-historica-das-safras. Accessed on: Jul 2021.

[5] ICO. (2018). *Total production by all exporting countries 2018*. Available at: http://www.ico.org/prices/po- production.pdf.

[6] Hu, S., Ma, X., Lin, Y., Yu, Z., & Fang, S. (2015). Thermogravimetric analysis of the co-combustion of paper mill sludge and municipal solid waste. *Energy conversion and Management*, *99*, 112-118.

[7] ASTM. (2019). *Standard Test Method for Volatile Matter in the Analysis of Particulate Wood Fuels (E872-82)*. ASTM International.

[8] ASTM. (2001). *Standard Test Method for Ash in Biomass (E1755-01)*. ASTM International.

[9] Jeguirim, M., Limousy, L., & Dutournie, P. (2014). Pyrolysis kinetics and physicochemical properties of agropellets produced from spent ground coffee blended with conventional biomass. *Chemical Engineering Research and Design*, *92*(10), 1876-1882.

[10] Magnago, R.F. et al. (2019). Solid Fuel From Residual Biomass Of Coffee Grounds, Rice Husks And Potato Skins. *Sustainable Mix*, *5*(2), 43–53.

[11] Chen, J. et al. (2017). Investigation of co-combustion characteristics of sewage sludge and coffee grounds mixtures using thermogravimetric analysis coupled to artificial neural networks modeling. *Bioresource Technology*, *225*, 234–245.

[12] Ruan, M. et al. (2021). Co-combustion kinetics and synergistic characteristics of sewage sludge and spent coffee grounds. *Heat Transfer Research*, *52*(5), 79–94.

[13] Borges, A. C. P. (2015). *Energetic characterization of "in natura" and roasted eucalyptus grandis chips* [Masters Dissertation, Federal University of Bahia].

[14] Silva, J. C. G. (2017). *Study of the kinetic parameters of sugarcane bagasse pyrolysis* [Masters Dissertation, Federal University of Paraíba].

[15] Carrier, M., Joubert, J. E., Danje, S., Hugo, T., Görgens, J., & Knoetze, J. H. (2013). Impact of the lignocellulosic material on fast pyrolysis yields and product quality. *Bioresource technology*, *150*, 129-138.

[16] Montoya, J. I. et al. (2015). Bio-oil production from Colombian bagasse by fast pyrolysis in a fluidized bed: An experimental study. *Journal of Analytical and Applied Pyrolysis*, *112*, 379–387.

[17] Ribeiro, N. S. (2017). *Thermogravimetric study of combustion and oxycombustion of coal-biomass mixtures* [Masters Dissertation, Universidade Estadual Paulista].

[18] McKendry, P. (2002). Energy production from biomass (part 1): overview of biomass. *Bioresource technology*, *83*(1), 37-46.

[19] Cieslinski, J. E. F. (2014). *Study of the emission and control of gases and particulates from biomass burning* [Doctoral Thesis, Universidade Estadual Paulista].

[20] Marchese, L., Souza, F. B., Soares, D., & Domenico, M. D. (2018). Evaluation of the fuel potential of residual biomass by thermogravimetry. In 6th *International Congress on Technologies for the Environment*.

[21] Spadim, E. R. (2020). *Development of an automatic device to determine the combustion rate of briquettes. 2020* [Masters Dissertation, Universidade Estadual Paulista].

[22] Nhuchhen, D. R., & Salam, P. A. (2012). Estimation of higher heating value of biomass from proximate analysis: A new approach. *Fuel*, *99*, 55-63.

[23] Marchese, L. (2019). *Pyrolysis of malt bagasse and mate residue: characterization and kinetic study by isoconversional methods.* [Completion of course work, Federal Technological University of Paraná].

[24] Silva, F. T. M. (2019). *Valorization of eucalyptus sp. via pyrolysis: characterization and yields of the products* [Doctoral Thesis, Federal University of Uberlândia].

[25] Fang, X., Jia, L., & Yin, L. (2013). A weighted average global process model based on two− stage kinetic scheme for biomass combustion. *Biomass and Bioenergy*, *48*, 43-50.

[26] Demirbas, A. (2005). Potential applications of renewable energy sources, biomass combustion problems in boiler power systems and combustion related environmental issues. *Progress in Energy and Combustion Science*, *31*, 171-192.

[27] Lira, J. O. B., Silva, K. C. G. D. A. (2015). Study of Solid Waste Combustion Characteristics of the Northeast Region Using Thermogravimetric Analysis. 8661–8669.

Impact of Solar Power Injection on Performance of OIP Transformer

Aprajita Kumari[1], Nitai Pal[2]

[1]MITS Gwalior, EED, Gwalior,474005,aprajita.iitdhn@gmail.com
[2]IIT (ISM) Dhanbad, EED, Dhanbad, 826004, nitai@iitism.ac.in

Abstract—**The paper presents the case study regarding the impact of solar plant on transformers loss of life. The analysis has been done on 20MW power plant installed in India. The plant has installed the both inverter transformer as well as the auxiliary transformer of the rating of 20kVA and 5 kVA respectively. The loss of life of transformer has been calculated using various parameters and the impact of solar plant has been discussed. The sample of transformer insulating system is created in lab and the analysis of PDC curve has been done with the level of harmonics generated by the solar inverters through with the OIP transformer is connected. Through the analysis of PDC curve various parameters such as percentage moisture value, HST, and dissipation factor have measured through which the loss of life of transformer can be calculated. The life of the transformer is based on its insulation condition. There are few parameters of OIP transformer insulation, which shows its condition whether it is in healthier condition or deteriorating. So, through the study of these parameters in the presence of solar, we can estimate the impact of solar on transformer insulation and the life of the transformer. In every country, the solar plant has gained its popularity in such conditions. It becomes vital to check the impact of solar on our conventional equipment such as transformers, etc. The deteriorating rate of transformer is overall high in presence of solar plant.**

Keywords - hotspot-temperature, polarization depolarization curve(PDC), percentage moisture, dissipation factor, solar injection, loss of life, rooftop solar plant, oil impregnated paper (oip) transformer, degree of polarization(DP), percentage moisture (%pm)

I. INTRODUCTION

The paper is divided into five sections, in the first section, the primary insulation system of the transformer and its properties has been discussed. The impact of various factors on the transformer insulation system has been addressed in the second section. There are some key factors that decide the transformer insulation system: the degree of polarization, HST, percentage moisture, and dissipation factor. These factors can influence the life of transformer insulation in certain instances. We can find the intensity of these factors on transformer insulation health. The presence of a solar plant is also a factor which enhances the deteriorating condition of transformer insulation day by day [1]. The solar plant has some constructional and featured requirements, which may influence the other equipment in the transmission systems such as the transformer. The presence of moisture is harmful for transformer insulation, which acts as the catalyst for enhancing the chemical reaction in the solid insulation and, consequently, the decrease in the DP value of transformer insulation [2]. In the presence of solar, the rate of decrease of DP value is more than that of without solar plant. Similarly, the value of the HST is calculated in the two conditions that are with solar, and the without solar and comparative study has been presented, which solar the impact of solar on transformer insulation HST variations [3]. The high value of the dissipation factor of transformer insulation is undesirable, and it shows the decorating conditions of the insulation system. In the presence of the solar plant, the rate of increase of dissipation factor is more in comparison to the without the solar plant.

There are various conventional methods for transformer insulation assessment, such as PDC and FDS. In this paper, the FDS method is taken as the base method to get the conclusion of the dependence of the dissipation factor on harmonics generated by the solar inverters [4]. As in the solar power plant, solar inverters play an impotent role. On the other side, the harmonics generated by it harm the transformer

insulation system. The value dissipation factor means the contribution of resistive loss increases in the dielectric system in the presence of solar. This led to the decaying of the insulation system of OIP transformer [5].

Some real-time data have been taken from various plants, and the result has been established, which may lead the formula of the real-life assessment of transformer in the presence of solar. Few works in the literature presented the detailed study of the transformer insulation system and life assessment in various conditions [6]. In the presence of solar, few factors may get affected, but which has changed the most is described in the paper. The paper has also presented an assessment rule for transformer insulation system in presence solar so that transformer insulation system can be saved before getting deteriorating. The paper divided in three sections the II section describe about the system of study for which the real time data is obtained and analysis has been done, III section provide insights about the impact of solar injections on various factor of transformer insulation system and through which the loss of life of transformer is calculated and analysis has been done in IV section.

II. Literature Survey

Reference [7] established the relation between increase in hotspot temperature due to solar irradiation and its impact on the transformer insulation. The region in which the case study is done has variation in temperature rise during summer and winter seasons according to the solar irradiation capacity in the whole year. The result described in the paper have influence of the irradiation of solar on the effective top side area of the transformer as well as the cooling capacity of the transformer. The effect of the increased hot-spot temperature on the paper's DP-value can be significant (a difference of 100 units compared with the paper's DP-value without solar irradiation effect). The transformer remaining lifetime may be reduced by up to 40%, in situation with a load of 70% and ambient temperature of 30ºC due to solar irradiation.

Reference [8] addresses key concerns from electrical utilities with respect to operation of auxiliary transformers under conditions of injection of solar plant in respect of reverse flow and harmonic distortion. Voltage THD maintains acceptable values below standard limits, whereas current THD is high at light loads and decreases with loading. Waveform distortion increases with the increase in solar penetration level as well as on the rating of solar plant, in reference to system capacity. Different sources of harmonics affecting the performance of distribution networks and transformers as a result of integrating SP generators [8].

Reference [9] paper describe about the impact of PEV charging on distribution transformer hot-spot temperature and LOL in the presence of rooftop solar PVs. The paper concluded the level of penetration of PEV and its impact on the transformer. In the case of 0% PEV and 50% PV, the transformer may experience reverse power flow, reaching almost 50% of its loading which may have negative impact on the protection devices. The results have shown that a 50% PEV penetration may result in significant reduction in LOL [9].

Ali Asghar Taheri described about the novel method of calculation of the impact of solar on transformer HST by considering the concept of thermal resistance of the insulation in presence of solar injection. Monitoring the insulation status of a transformer requires the availability of accurate information of the oil temperature at any moment. Considering the importance of oil temperature prediction in oil-immersed transformers and its direct relation with the life of transformer. The heat transfer in distribution transformers in presence of solar is calculated using standard thermal model of transformer. These results show that in the studied transformer and rated loading, solar radiation can increase the oil temperature by about 3.7°C.

III. The System for Study

As the Fig. 1 shows the industry uses two types of transformers one is inverter transformer and other is the auxiliary transformer. The inverter transformer is directly connecting with the solar inverter and the study has more focus on the inverter transformer than the auxiliary transformer. The inverter transformer is of three phase transformer having rating of 20 Kva. All

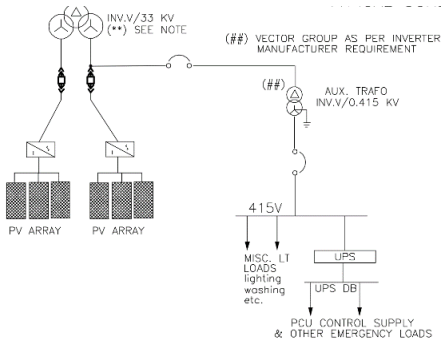

Figure 1. Line diagram of system for study in industry.

the analysis in the paper has concentrated pn the inverter transformer only. The auxiliary transformer has not been affected by the solar system use in the plant as the transformer is not directly connected with any component of the solar plant and it is use for the load in the substation only. Various data have been collected for the analysis pf solar injection on the transformer, and through which the analysis has done which shows the loss of life of transformer due to solar injection.

The geographical condition of the plant has also shown in Table I. Through which it becomes easy to analysis the impact of solar on

TABLE I. GEOGRAPHYCAL ASPECT.

	Global Horizontal Irradiation	***Horizontal Diffuse Irradiation***	***Temperature***	***Wind velocity***	***Realtive humadity***
JAN	137.6	36.6	16.7	1.30	57.8
FEB	149	40.9	20.1	1.50	52
MARCH	190	61.1	25.2	1.60	42.1
APRIL	199	74.5	29.5	1.90	37.7
MAY	211.8	88.9	30.5	2.11	48.2
JUNE	171.1	92.9	28.4	2.30	70.1
JULY	138.5	89.0	26.4	2.21	83.6
AUGUST	145.7	89.4	26.5	2.00	85.1
SEPT	142.5	71.1	25.8	1.79	85.3
OCT	147.9	65.5	24.4	0.99	73.3
NOV	136.7	43.6	20.1	0.81	67.4
DEC	136.9	31.0	16.9	0.91	63.5

TABLE II. PERMISSIBLE RANGE OF OIL USED IN OIP TRANSFORMER.

	A. Property	*B. Permissible range*
1.	Kinematic viscosity,mm^2/s	<12 at 40 °C < 1800 at 30°C
2	Flash point	>140 °C
3	Pour point	<(-) 40°C
4	Appearance	Clear, free from sediment and suspended matter
5	Density kg/dm^3 at 20 °C	< 0.895
6	Interfacial tension N/m at 25°C	>0.04
7	Neutralization value, mgKOH/g	<0.01
8	Corrosive Sulphur	Non corrosive
9	Water content mg/kg	<30 in bulk supply < 40 in drum supply
10	Oxidation stability -Neutralization value, mgKOH/g -Sludge,% by mass	<1.2 <0.8
11	BDV	60kV(min)

transformer on annual basis.

The Table II. Shows the permissible range of oil used in oil immersed power transformer for the solar plant. Through which it becomes easy to analyze the property of oil used in transformer and the effect which alter the properties to certain extent due to solar injection.

TABLE III. SPECIFICATION OF TRANSFORMER USED IN THE PLANT.

1.	Rating	2.5MVA
2	Winding	TWO
3	Nos of phase	Three
4	Permissible temperature rises Top oil	35
5	Winding Temperature	40
6	Cooling	ONAN
7	Frequency	50HZ
8	Max Daily avg ambient air temperature	45

TABLE IV. INVERTER SPECIFICATION.

1	Maximum ac power	4.20kW
2	Maximum ac current	16.00A
3	Maximum input current	21.8A
4	Maximum efficiency	97.00%
5	Maximum MPP voltage	500V

TABLE V. SOLAR MODULE SPECIFICATION.

No of module in series	18
type	Si-monochromatic
Nominal power	230Wp

IV. IMPACT OF SOLAR ON TRANSFORMER INSULATION PARAMETERS

A. Harmonics and Hotspot temperature

The overheating of the transformer has been recorded due to the harmonics caused by solar inverters. The variation in harmonic may lead to a rise in transformer losses and so that the overheating of the transformer has occurred. If the insulating system of the transformer is not able to withstand the rise of transformer overheating it may lead to deterioration of transformer insulation and the loss of life of the transformer. If we measure the HST and top oil temperature using Oti (Oil temperature instrument) and Wti (Winding temperature instrument), it is found that due increase in harmonics, these two temperature increases and may sone time went beyond the safe limits [11, 12]. If the harmonics level is 22%, the HST and the top oil temperature reach 110℃ and 85℃, respectively, which is beyond the safe limit for transformer working [13]. Thus, the variation in harmonics due to solar plants may lead to the overheating of transformer oil and thus lead to the gradual degradation of the transformer insulation system and also the reduction in the life of the transformer.

As discussed above, the current THD may go up to a value of 20%. This may lead to an increase of HST to beyond the safe limit.

There is a relation between the %pm and HST once the value of %pm is measured using IDAX300 the value of HST is also calculated using the (1). The loss of life of the transformer may also be calculated using the value of HST [14].

The loss of life of the transformer may increase to 0.5% in the presence of solar as compared to the condition without solar Figs. 2 and 3.

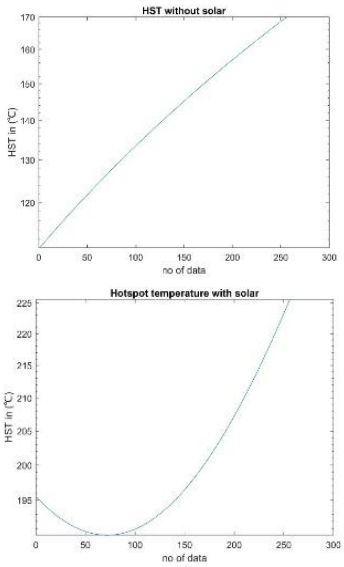

Figure.2. Variation of transformer HST with and without solar.

$$HST = 127.6 \times e^{-1.334 \times \%pm} + 136.7 \times e^{-0.0423 \times \%pm} \text{ , (1)}$$

$$RLA = \frac{365 \times 24 \times AVG\ insulation\ life}{F_{AA}} \text{ . (2)}$$

B. Dissipation Factor Due to Solar Injection

The dissipation factor is one of the most important properties of the transformer insulation system. It gives quick analysis and overall conditions of the health of the insulation system. Higher the value of the dissipation factor poor is the condition of transformer insulation. There is an existence of harmonics due to solar inverter used for the solar plant. The voltage THD is in the limit of IEEE, but there is an alarming range of current THD due to solar plants. It is known that the dissipation factor is a function of harmonics. The imaginary part of the dielectric constant of insulation has a variation with the frequency it has high value at a higher frequency so as there is variation in frequency waveform due to harmonics the value of the dissipation factor get changed and at the THD value more the 10% the value of dissipation factor is of 3.903, which is undesirable [15]. The acceptable limit of the dissipation factor is 0.002, and as the value of tanδ increases, the rate of decaying of insulation increases day by day. It becomes necessary to analyze the value of tanδ from time to time so that the condition of transformer insulation can be analyzed easily.

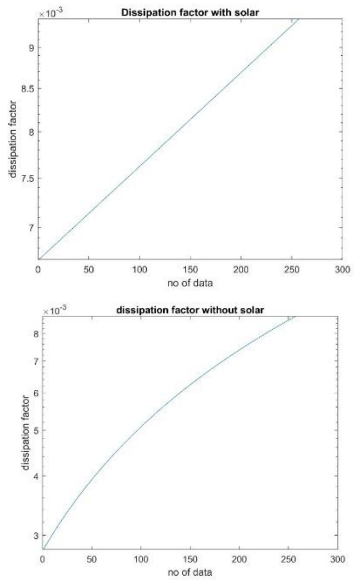

Figure 3. Variation of transformer HST with and without solar.

In the ac field, the dielectric constant of insulation has divided real and imaginary parts and given as εr = εr'- j εr''. The dissipation factor is the ratio of εr'' and εr'. The two-part of the εr has where the different response with respect to frequency variations [16]. The real part of dielectric constant decreases with the frequency and the imaginary part of the dielectric constant first increase with the frequency and then decreases with frequency. Thus due to harmonics, the value of dielectric constant also varied in a different form and have shown variation in the value of the dissipation factor. This is the reason behind the variation dissipation factor with the solar plant harmonics effect [17]. The harmonics are the main problem of the solar plant; it has a negative impact on the transformer insulation system. Also, if the insulation withstands the high harmonics to a long time, the rate of decaying of insulation may go high in comparison to the condition without the solar plant. The value of tanδ can be calculated if the value of %pm is known using (4), and it can be directly calculated using the IDAX300. If the value of tanδ is known, the loss of life of the transformer can be easily calculated by (5) [18]. The dissipation factor measurement is one of the key factors for the calculation of transformer loss of life. If the value of tanδ goes beyond the 1unit, the loss of life of the transformer maybe 0.4%.Due to a solar plant, there is a chance of huge variation in the value of tanδ due to higher range of THD, so it becomes important to continuous assessment of the value of tanδ [19].

$$LOL\ of\ transformer = 45 - 7 \times e^{51.26 tan\delta} \text{ . (3)}$$

The Table II shows the measured value of %pm and tanδ of transformers shown in Table III in two conditions with and without solar.

C. Moisture Content due to Solar Injection

The degree of polarization is the primary parameter for getting information about the transformer insulation conditions. This is the basic factor that determines the aging of the transformer. The decaying of transformer insulation is ongoing with the time, but in the presence of the solar, its decaying rate has

enhanced. There is an established formula for the DP value and the percentage moisture present in the insulation system [20]. Through that formula, the DP value can be calculated for the transformer insulation system from time to time. The presence of moisture in the insulation system is due to various factors in which temperature is one of them. The DP value of transformer depends on the category of transformer for the new transformer the value of DP is more than 1500 and the maximum permissible water content in insulation system mainly in oil is 10 mg/Kg [8].

The rate of increase of moisture in the transformer insulation system very much depends upon the environmental conditions and type of insulation used for insulation. The reason behind the increase in moisture may be due to both internal and external causes. The one of the main reason for the rise in the moisture in transformer insulation system is an increase in the rate of chemical reactions, due to which the chemical bonds breaks and water molecules and acids forms, farther the rate of increase of acid enhance the solubility of water in transformer oil [21]. The balance between the concentration of water in solid and liquid insulation of the transformer depends on various factors, and may these factors get enhanced due to the presence of solar plant working and requirements. The main factors which decide the concentration of water in the insulation system are influenced by both the factor i.e, the temperature and the load profile of the power transformer. As the temperature rises, the rate of migration of water from papers to liquid insulation enhances, and the temperature drops the reverse action is observed [10]. Due to the effect of the solar plant, the temperature is lower than the condition of without solar, so the result is that the concentration of moisture in more in solid insulation in case of the presence of solar plants. Consequently, the decaying rate of solid insulation is high in the presence of a solar plant. Through the equipment IDAX 300, the value of percentage moisture is obtained for the transformer insulation, and through (1), (2), and (3), the DP value and life of the transformer is estimated [22].

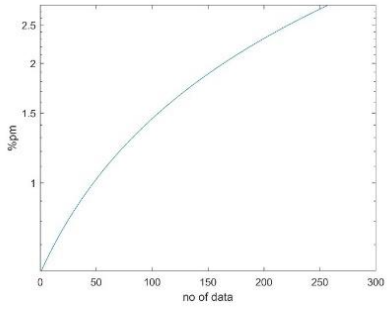

Figure 4. Variation of %pm of transformer insulation without solar.

Once the elapsed life of the transformer is calculated, it is found that life on the transformer is reduced almost by 40%.So the life of the transformer is getting reduce at a faster r rate in the presence of a solar plant. By estimating the elapsed life and deteriorating condition of transformer insulation one take the proper remedial action to reduce the rate of decaying of transformer.

$$elasped\ life = 20.5 \times in\left(\frac{1100}{DP}\right), \quad (4)$$

$$Tensile\ strength = 84.78 \times e^{0.0256 \times \%pm}, \quad (5)$$

$$DP = 21.71 \times Tensile\ strength - 491.5\ . \quad (6)$$

D. Polarization and Depolarization Curve

The PDC-Analyzer is an instrument for on-site measuring and analyzing of the dielectric behaviors of electrical insulation materials and insulation systems. All kinds of insulation materials are subjected ageing effects or degradation processes, when stressed with electric fields, temperature, partial discharges and/or mechanical load.

Due to the behaviors of transformer insulation as the capacitor the PDC curve analysis become popular for analysis of transformer insulation condition by calculating the various parameters using the PDC curve [23]. Any distortion in the curve may reflects the degradation in the transformer insulation system. As in the Fig, 5. It is clear that in presence of solar injection the distortion in the curve of transformer insulation can be found. By injecting the HST and harmonics as per the range of the data obtained from the plant in the sample of insulation system and then the curve

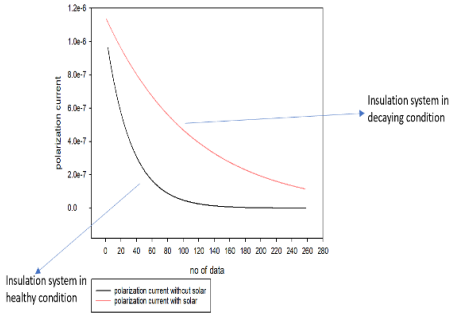

Figire 5. Polarization curve of transformer insulation system.

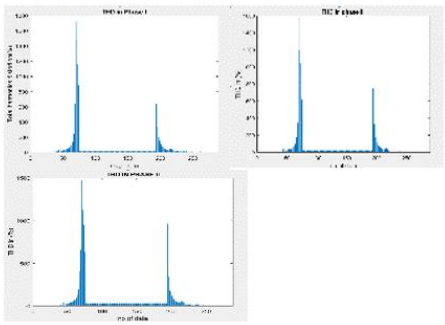

Figure 6. Harmonics injection in three phases of transformer.

is obtained and it is found as distorted due to solar injection condition.

The steepness of the curve shows the characteristics and condition of the transformer insulation as it get distorted the steepness of the curve decreases as shown in Fig 5.

The PDC curve of the insulation in decaying condition is not perfect as of the healthier insulation system [24]. The distortion may be due to harmonics or temperature rise during sudden effect of solar power plant. When the values of the essential parameters of the insulation is calculated it reflects different values then the normal insulation system.

V. Simulation Result and Real Time Data

With reference to the data obtained from the solar plant of 20MW on annual basis the simulation has been performed using the COMSOL software and the MATLAB on the sample of transformer insulation and obtained the PDC curve. The values of the different parameters of the transformer insulation are obtained with solar and without solar. Table VI represents the various parameters which get influences from the solar injection and which may lead to degradation of transformer insulation system.

VI. Loss of Life of Transformer

Loss of life of transformer is calculated using (2), (3) and (4) in which the various parameters of the transformer insulation system is consider. The impact of solar injection on the transformer insulation parameters are discussed above and as it is proved by the various equations that the life of transformer insulation is affected by the condition of the insulation. Better the condition of the insulation system better will be the life of the transformer. The various parameters of the transformer are diagnosis in presence of solar injection and then the loss of life of transformer is calculated both in with and without solar injection condition. Fig. 6 shows the comparison between the loss of life of transformer with and without solar.

The loss of life of auxiliary transformer is calculated on annual basis and it is shown in Fig. 7. From Fig. 7 it is shown as the month in which the irradiation level of solar is high the loss of life of transformer is also high due to impact on various parameters. The calculation is concluded with considering the solar up to 15-20 years. The impact of solar on transformer parameters are not the frequent effect but it is a gradual effect.

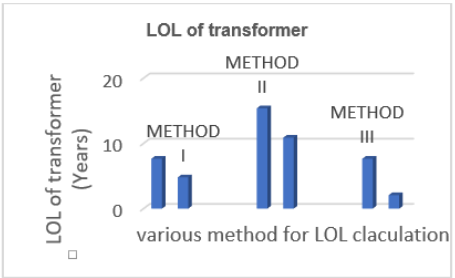

Figure 7. Loss of life of transformer calculated from above three methods.

TABLE VI. DIFFENET INSULATION PARAMETERS WITH AND WITHOUT SOLAR.

S.No	*%Pm Without Solar*	*%Pm With Solar*	*Tanδ Without Solar*	*Tanδ With Solar*	*Hst Withouts Solar*	**HST WITH SOLAR**
1	0.694531	1.676464	2.80E-03	6.16E-03	110	191.0414
2	0.703125	1.681405	2.82E-03	6.17E-03	110.2344	190.9797
3	0.711719	1.686345	2.85E-03	6.19E-03	110.4688	192.0343
4	0.694531	1.676464	2.80E-03	6.16E-03	111.875	191.9454
5	0.797656	1.735749	3.03E-03	6.30E-03	112.1094	194.1217
6	0.80625	1.74069	3.05E-03	6.31E-03	112.3438	193.993
7	0.814844	1.74563	3.08E-03	6.32E-03	111.875	195.0812
8	0.797656	1.735749	3.10E-03	6.34E-03	113.75	194.9379
9	0.883594	1.785154	3.21E-03	6.41E-03	113.9844	196.9646
10	0.892187	1.790094	3.24E-03	6.42E-03	114.2188	197.1351
11	0.900781	1.795034	3.26E-03	6.44E-03	114.4531	198.9557
12	0.952344	1.824677	3.28E-03	6.45E-03	115.625	199.1493
13	0.960937	1.829617	3.79E-03	6.76E-03	115.8594	205.9294
14	0.969531	1.834558	3.81E-03	6.77E-03	116.0938	206.1879
15	0.995312	1.849379	3.84E-03	6.79E-03	117.0313	207.7825
16	1.003906	1.854319	3.86E-03	6.80E-03	117.2656	208.0555
17	1.0125	1.85926	4.07E-03	6.93E-03	117.5	210.9015
18	1.055469	1.883962	4.09E-03	6.94E-03	118.9063	211.1976
19	1.064062	1.888902	4.11E-03	6.95E-03	119.1406	212.7096
20	1.072656	1.893843	4.14E-03	6.97E-03	120.7813	213.0182
21	1.124219	1.923485	4.76E-03	7.34E-03	121.0156	214.9142
22	1.132812	1.928426	4.78E-03	7.36E-03	122.8906	215.2375
23	1.141406	1.933366	4.81E-03	7.37E-03	123.125	216.8854
24	1.407812	2.086519	4.83E-03	7.39E-03	124.7656	217.2213
26	1.425	2.0964	5.36E-03	7.71E-03	125.4688	219.2804
27	1.751562	2.284136	5.38E-03	7.72E-03	130.3906	220.6951
29	1.76875	2.294016	5.98E-03	8.09E-03	150.7813	222.8798
30	1.777344	2.298957	6.00E-03	8.10E-03	161.5625 167.98	223.2512
31	2.000781	2.427408	6.26E-03	8.25E-03	168.3594	224.7579
32	2.009375	2.432348	6.28E-03	8.27E-03	169.7656	225.1398

One more observation is found that the impact of solar on transformer is based on the installation capacity as well as purpose of solar plant. If it is a rooftop solar plant the impact of solar on transformer is somehow positive but on commercial level is not supportive to the transformer.

As we can see that the transformer is not directly connected to the rooftop solar plant so it does not affect the transformer in large extent. The transformer is connected to the grid directly but not with solar so when the solar plant is not producing power as per the requirement of the household then only the transformer come into the existence of the distribution circuit. Thus, in case of the rooftop solar plant the solar may have some positive impact on transformer performance. There are three methods from which the LOL of the transformer can be obtained the first method is by using (1) and (2), the second method by using (3) and the third method is by using (4). As the basic parameters are obtained by the PDC curve by MATLAB curve fitting so the calculation of LOL of transformer become easier.

VII. CONCLUSION

The loss of life of auxiliary transformer in the 20MW solar plant is calculated by measuring various data regrading transformer insulation system on the annual basis. The life of the transformer in presence of the solar is detreating at the faster pace than without solar. The detrition rate is also vary during the various seasons according to the level of solar irradiation penetration in the plant. The prediction has been done for the 20MW is that the transformer may lost its life 4-5 years due to solar injection. The

conclusion is validated by the simulating the real time data of transformer in the plant and also by diagnosis the sample in the lab in different penetration level of solar irradiation. The decaying rate of the sample is faster in presence of solar than without solar. The decaying rate of transformer is 0.02-0.56% faster in presence of solar. The experimental result of decaying of life of transformer is validated by the case study of the 20MW solar plant.

REFERENCES

[1] Kumari, A., et.al. (2017). Comparison Of Different Method Available For Evaluating Remaining Life Of OIP Insulation Used In Power Transformer. *IEEE* (pp. 5090- 4874).

[2] Uçar, B. et. al. (2017). Influence of PV penetration on distribution transformer aging." *Journal of Clean Energy Technologies*, *5*(2),131.

[3] Supramaniam, K. G. et. al. (2008). Application of frequency domain spectroscopy (FDS) in assessing dryness and ageing state of transformer insulation systems. In *2008 IEEE 2nd International Power and Energy Conference*, (pp. 55-61).

[4] Pezeshki, H. et. al. (2018). Impact of high PV penetration on distribution transformer insulation life. *IEEE Transactions on Power Delivery 29*, 1212-1220.

[5] Lazari, L. A. et. al. (2015). Life-cycle loss evaluation of power transformers serving large photovoltaic plants in vertically integrated and decentralised systems. *IET Generation, Transmission & Distribution*, *9*, 759-766.

[6] Gorgan, B. et. al. (2012). Influence of solar irradiation on power transformer thermal balance. *IEEE Transactions on Dielectrics and Electrical Insulation*, *19*,1843-1850.

[7] Krpal, O. et. al. (2012). Influence of renewable energy on power transformer insulating system. *Annals of DAAAM for 2012*.

[8] Abdelsamad, F. S. et. al. (2015). Probabilistic impact of transportation electrification on the loss-of-life of distribution transformers in the presence of rooftop solar photovoltaic. *IEEE Transactions on Sustainable Energy*, 6, 1565-1573.

[9] Elmoudi, A. et. al. (2006). Effect of harmonics on transformers loss of life. In *Conference Record of the 2006 IEEE International Symposium on Electrical Insulation* (pp. 408-411). IEEE.

[10] El-Bataway et. al. (2018). Distribution Transformer's Loss of Life Considering Residential Prosumers Owning Solar Shingles, High-Power Fast Chargers and Second-Generation Battery Energy Storage. *IEEE Transactions on Industrial Informatics*, *15*, 1287-1297.

[11] El-Gasseir et. al (1993). Enhancing transformer dynamic rating through grid application of photovoltaic arrays. In *Conference Record of the Twenty Third IEEE Photovoltaic Specialists Conference-1993 (Cat. No. 93CH3283-9*, pp. 1279-1284). IEEE.

[12] Islam, Md R. et. al. (2018). State-of-the-art of the medium-voltage power converter technologies for grid integration of solar photovoltaic power plants. *IEEE Transactions on Energy Conversion*, *34*,372-384.

[13] Kumari, A. et. al. (2019). Impact of Solar Panel on the Transformer Performance: A Case Study. *Iranian Journal of Science and Technology, Transactions of Electrical Engineering*, pp.1-10.

[14] Overett, J. et. al. (2017). Quality assessment of harmonic measurement data from a utility-scale PV plant. In *2017 IEEE AFRICON*, (pp. 1189-1194). IEEE.

[15] Brncal, P. et. al. (2019). Analysis of insulation properties of transformer materials at different ambient temperatures. *Transportation Research Procedia*, *40*, 12-15.

[16] El-Gasseir et. al. (1993). Enhancing transformer dynamic rating through grid application of photovoltaic arrays." In *Conference Record of the Twenty Third IEEE Photovoltaic Specialists Conference-1993 (Cat. No. 93CH3283-9*, pp. 1279-1284). IEEE.

[17] Chen, Q. et. al. (2019). The Probabilistic Assessment of Outgoing Transformer Operation Risk Considering the Correlation Between Wind Power and Photovoltaic. In *2019 IEEE Sustainable Power and Energy Conference (iSPEC)*, (pp. 1785-1790). IEEE.

[18] Thango et. al. (2020). Effects of Current Harmonics on Maximum Loading Capability for Solar Power Plant Transformers." In *2020 International SAUPEC/RobMech/PRASA Conference*, (pp. 1-5). IEEE.

[19] Khanali, M. et. al. (2015). Effectiveness of electrostatic shielding in suppressing the impact of fast transients on transformer insulation. In *2015 IEEE Conference on Electrical Insulation and Dielectric Phenomena (CEIDP)*, (pp. 652-655). IEEE.

[20] Srinivasan, M. et. al. Prediction of transformer insulation life with an effect of environmental variables. *International Journal of Computer Applications*, *55*(5).

[21] Behi, B. et. al. (2017). Distribution transformer lifetime analysis in the presence of demand response and rooftop PV integration. In *World Renewable Energy Congress XVI*. World Renewable Energy Congress, 2017.

[22] Lazari, A. et. al. (2015). Life-cycle loss evaluation of power transformers serving large photovoltaic plants in vertically integrated and decentralised systems. *IET Generation, Transmission & Distribution* 9(8), 759-766.

[23] Irtaza, S. M., Ullah, M., Aziz Ikram, A., & Muhammad Naveed Aman, M., (2020). Selecting and sizing transformer and AC cable for PV system's safe and reliable operation. *International Transactions on Electrical Energy Systems* 30(2).

[24] Kumar, A., Verma, H. C., Baral, A., Pradhan, A. K. & Chakravorti, S. (2018). Estimation of paper-moisture in transformer insulation employing dielectric spectroscopy data. *IET Science, Measurement & Technology*, *12*(4), pp.536-541.

Fixed-Boundary Grad Shafranov Solver Using Finite Element Method with FreeFem++Tools

Amina Djellouli[1], Assia Rachida Senoudi[2]

[1]Theoretical laboratory, Abu bekrbelkaid university, Tlemcen, Algeria, djellouliamina13@gmail.com
[2]Department of Physics, Abu bekrbelkaid university, Tlemcen, Algeria, arsenoudi@gmail.com

Abstract—**Numerical solver based on the Finite Element Method (FEM) is applied to solve the Grad-Shafranov (GS) equation for the fixed boundary plasma's equilibrium. The proposed numerical tool FEM is a powerful solver for non linear partial differential equations; however it generally requires the knowledge of the border of computational domain. GS equation is solved numerically using FreeFEM++ software and its solution is validated and compared to the analytical result for the Soloviev's equilibrium case.**

Keywords-Grad-Shafranov plasma equilibrium equation, fixed boundary Solver, finite element method.

I. INTRODUCTION

The source of energy from thermonuclear reactor tokamak is very powerful, just one gram of Deuterium or Tritium is necessary to produce energy to a big city. Moreover it is a clean energy source without nuclear waste. Fusion plasma is created and controlled inside toric shape vacuum chamber and it is confined by intense magnetic fields. Fusion plasma is of high temperature and very high pressure forces. Magnetic and pressure forces must be balanced in vacuum chamber [1, 2].

Plasma equilibrium is a very essential state for understanding various phenomena such the MagnetoHydroDynamic (MHD) instabilities [3]. Assuming azimuthal symmetry for the plasma geometry, ideal and stationary MHD leads to the GS equation which is an elliptical and nonlinear partial differential equation established in cylindrical system and having as unknown scalar function representing the poloidal magnetic flux noted Ψ [4]. The second member of GS equation represents the term of current source which depends strongly on ψ. Spatial configurations of equilibrium plasma is given by isofluxes of Ψ. Several analytical and numerical methods have been carried out for computing equilibrium plasma [5-8]; generally in these studies, the term of toroidal rotation is not considered in the formalism [9]. Soloviev's plasma equilibrium is a particular case where the second member of GS equation doesn't depend on Ψ [10].

In the present paper, we use a computational GS equation solver based on the finite element method to determine the plasma equilibrium. In order to deal with fixed boundary FEM solver, the plasma border is computed from the analytical solution in Soloviev's equilibrium case [11, 12]. We also compute the expression of the constant found in the analytical solution, to satisfy the boundary conditions. For our numerical computation, we performed code in C++ language using FreeFem++ software; this solver is highly adaptative, has automatic mesh generator based on the Delaunay-Voronoi algorithm, and has also large variety of linear direct and iterative matrix solvers [13].

We present our computational results for the Soloviev's equilibrium and theses FEM results are compared to the analytical solution where, the error calculation has been performed.

ISBN: 978-86-80593-73-9

II. THEORETICAL STUDY

A. Grad-Shafranov Equation

Ideal magnetohydrodynamic is the simplest form of MHD formulation where the plasma is considered as a perfect conductor fluid moving in electromagnetic field. In static and stationary equilibrium, ideal MHD is representing by the following fundamental equations [14]:

$$\vec{J} \wedge \vec{B} = \vec{\nabla} P,\ \vec{\nabla}.\vec{B} = 0,\ \ \mu_0 \vec{J} = \vec{\nabla} \wedge \vec{B} \quad , (1)$$

with, μ_0, B, J and P being the magnetic permeability of free space, the magnetic field, current density and the plasma's pressure, respectively.

Assuming axisymmetry in the plasma geometry, we introduce the magnetic vector potential A in cylindrical coordinates (R, Z, ϕ), and we define the following functions:

$$\psi = \frac{1}{2\pi} \iint_{S_P} \vec{B}.\vec{n} dS_P = RA_\phi \quad , \qquad (2)$$

$$F = R.B_\phi = R\left(\frac{\partial A_R}{\partial Z} - \frac{\partial A_Z}{\partial R} \right) , \qquad (3)$$

where, Ψ, F, $\vec{n}$, S_p represent poloidal flux function, toroidal field function depending on Ψ, normal vector to surface element dS_p and plasma poloidal surface, respectively.

Thus, magnetic field can be written as:

$$\vec{B} = \vec{\nabla} \wedge \left(\psi . \vec{\nabla} \phi \right) + F \vec{\nabla} \phi \ . \qquad (4)$$

Components (B_R, B_Z, B_ϕ) of the total magnetic field vector are computed from the function Ψ, as:

$$B_R = -\frac{1}{R}\frac{\partial \psi}{\partial Z},\ B_Z = \frac{1}{R}\frac{\partial \psi}{\partial R},\quad B_\phi = \frac{F}{R} \quad .(5)$$

where (B_R, B_Z) represent components of the poloïdal magnetic field B_P and B_ϕ is the toroidal magnetic field.

Combining (4), (3) and (2) in (1), mathematical derivation leads to GS Eq.:

$$-\frac{\partial^2 \psi}{\partial R^2} + \frac{1}{R}\frac{\partial \psi}{\partial R} - \frac{\partial^2 \psi}{\partial Z^2} = F\frac{\partial F}{\partial \psi} + R^2 \mu_0 \frac{\partial P}{\partial \psi} \quad .(6)$$

$P(\Psi)$ is the plasma isotropic pressure, and the second member of (6) is the source term noted $J\phi$ (R, Z) and representing the toroidal current density of the plasma. Equation (6) is a nonlinear partial differential equation in (R, Z) plane and the quantity $\Psi = \Psi$ (R, Z) gives the equilibrium plasma configuration. In general the current density $J\phi$ (R, Z) depends on Ψ.

B. Analytical Solution of GS equation

Soloviev equilibrium of plasma is a particular case when the second member of (6) doesn't depend on the unknown Ψ, this means that:

$$\mu_0 \frac{\partial P}{\partial \psi} = -A1,\ F\frac{\partial F}{\partial \psi} = -A_2 R_0^2 \ . \qquad (7)$$

Thus, analytical soloviev's solution is the sum of homogeneous Ψ_h and particular Ψ_P solutions [12]:

$$\psi(\mathrm{R}, \mathrm{Z}) = \psi_\mathrm{h} + \psi_p \ . \qquad (8)$$

$$\psi(R,Z) = C\left(\frac{1}{2}R^2 Z^2 - \frac{1}{8}\left(R^2 - R_0^2 \right)^2 \right) + \frac{1}{2}A_2 R_0^2 Z^2 + \frac{1}{8}A_1 \left(R^2 - R_0^2 \right)^2 \quad . \qquad (9)$$

where, R_0 represents plasma major radius.

The constant C in (9) is determined to satisfy the boundary conditions whereas, the two constants A1 and A2 are adjusted to meet the equilibrium constraints namely, the total plasma poloidal current and as well as the poloidal beta [9].

The previous analytical solution is valid only if the pressure is written as $P(\Psi) = A_1(\Psi b - \Psi)/\mu_0$ where Ψb is the value of magnetic flux on the plasma border and corresponding to the last closed magnetic surface.

The safety factor on magnetic axis is defined as follows [2]:

$$q_0 = \frac{a}{R_0}\frac{B_\phi}{B_P}\bigg|_{R=R_0} = \frac{a}{R_0}\frac{B_{\phi 0}}{B_{P0}} \quad . \qquad (10)$$

with *a* being the plasma minor radius and $B_{\phi 0}$, B_{P0} being toroidal and poloidal magnetic field at magnetic axis $R = R_0$, respectively.

At the magnetic axis, the condition 1/R $\partial\Psi / \partial R = 0$ is satisfied, this implies that magnetic component $B_Z = 0$ and $B_P\,|_{R=R0} = B_R\,|_{R=R0}$.

Using the definition of the component B_R in (5), it is easy to show that:

$$B_P\big|_{R=R_0} = (A_2 + C) R_0 Z \quad . \qquad (11)$$

The definition of the function *F* in (3) and the integration of the term *FF'* in (7) between two plasma positions M(R, Z) and M'(R=R_0, Z=0), lead to the following relation:

$$F^2(R,Z) = F^2(R_0, Z=0) - \\ -2A_2 R_0^2 \psi(R,Z) \quad . \qquad (12)$$

Setting $F^2(R_0, Z=0)$ as F^2 and plugging (10) in (5), this yields:

$$B_\phi\big|_{R=R_0} = \sqrt{\frac{F_0^2}{R_0^2} - 2A_2\psi(R_0,Z)} \quad . \qquad (13)$$

Ellipticity of plasma is defined by the factor $\kappa_0 = Z_b / a$; where *Zb* represents the vertical elongation of plasma (b denotes plasma border).

At $Z = Z_b$, the expression of constant *C* is determinate from (11) and (13) and it found:

$$C = \frac{\sqrt{B_0^2 - 2A_2\psi_b}}{q_0 \kappa_0 R_0^2} - A_2 \quad . \qquad (14)$$

For usual tokamak devices, the constant $A1 = B_0\left(\kappa_0^{\,2} + 1\right) / R_0^{\,2}\kappa_0 q_0$ [15].

C. Computation of Plasma Boundary

From (7), it is easy to show that plasma boundary $\partial\Omega$ for Soloviev equilibrium can be analytically described by:

$$\partial\Omega = \left\{ \begin{array}{l} Z = \pm\sqrt{\dfrac{2\psi_b - \frac{1}{4}(A_1 - C)\left(R^2 - R_0^2\right)^2}{A_2 R_0^2 + CR^2}}, \\ R \epsilon \left[R_1, R_2\right] > 0 \end{array} \right\} \qquad (15)$$

The values of R_1 and R_2 are computed from the relation $Z = 0$ given by (15):

$$R_{1,2} = \sqrt{R_0^2 \mp \sqrt{\frac{8\psi_b}{(A_1 - C)}}} \quad . \qquad (16)$$

The last closed isoflux Ψb must satisfy the following inequality:

$$\psi_b < \frac{R_0^4}{8}(A_1 - C) \quad . \qquad (17)$$

III. Finite Element Method

From variational principle, finite element method transforms (6) into an integral form as:

$$\int\int_\Omega \vec{\nabla}\psi . \vec{\nabla} v \, dS + \int\int_\Omega \frac{1}{R}\frac{\partial\psi}{\partial R} v \, dS = \\ = \int\int_\Omega \left(F \frac{\partial F}{\partial \psi} + \mu_0 \frac{\partial P}{\partial \psi} R^2 \right) v \, dS \quad . \qquad (18)$$

∇ is the gradient operator in (R, Z) coordinates system, v is arbitrary test function, Ω is domain of delimited plasma and dS is the surface element of Ω.

The Dirichlet boundary condition on the border $\partial\Omega$ is chosen as $\Psi = \Psi b$.

Global relative error in Hilbert space is defined as [13]:

$$E = \sqrt{\frac{\int_\Omega (\psi_{exact} - \psi)^2 d\Omega}{\int_\Omega \psi_{exact}^2 d\Omega}} \quad . \qquad (19)$$

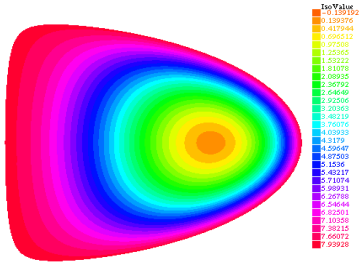

a)

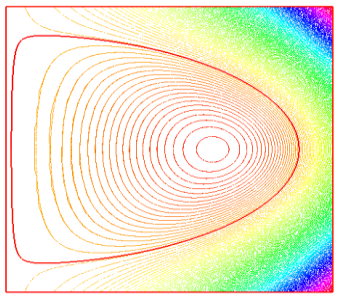

b)

Figure 1. Numerical FEM isofluxes of poloïdal magnetic function Ψ of ITER plasma equilibrium having Dshape profile (a). Both analytical and FEM solutions (b).

IV. RESULTS AND DISCUSSION

A. *Case, A2=0*

Using FreeFem++ tools, we performed a code in C++ language, where the domain of the plasma delimited by the border $\partial\Omega$ is well defined and the integral form in (18) is programmed and transformed into a matrix system of unknown Ψ. For testing, we choose the next data of international thermonuclear experimental reactor (ITER) [16]: $R_0 = 6.2m$, $a = 2m$, $B_0 = 5.3T$, $\kappa_0 = 0.85$, $q_0 = 3$, $\Psi b = 7.8T/m2$ (Ψb is computed from (17)). Fig. 1a shows isofluxes of poloidal function Ψ in the (R, Z) plane, obtained from numerical FEM. We can see that the ITER plasma is D-shaped. To check the proposed FEM fixed boundary solver, we compare the obtained results with those obtained from the Soloviev's analytical solution (9). We report in the same graph (Fig. 1b) both the solutions of analytical and FEM results. Theses graphics shows an excellent agreement. Relative global error computed from (19) is of value= 6.10^{-5} and corresponding to number of triangular mesh elements= 1.410^{6}. We can see that Ψb

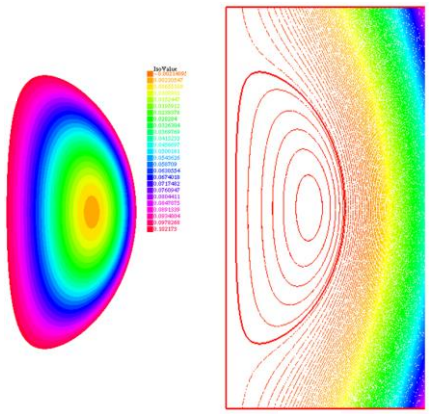

a) b)

Figure 2. Numerical FEM poloidal magnetic function Ψ of plasma equilibrium Dshape configuration [15] (a). Both analytical and FEM solutions (b).

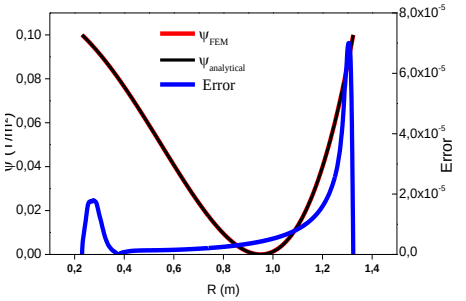

Figure 3. Numerical FEM, analytical isofluxes of Ψ and computed error, upon radial distance R (m), along the R-axis (R,Z=0) for plasma equilibrium configuration [15].

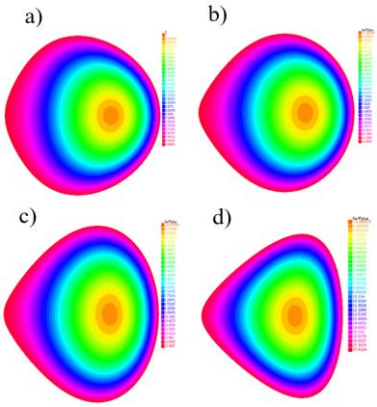

Figure 4. Effect of factor A2 on ITER plasma equilibrium configurations, for: A2= 0.01 (a), A2= 0.02 (b), A2= 0.03 (c), A2= 0.06 (d).

computed from (17) corresponds exactly to the last closed boundary plasma.

A second test has been done and we chose for testing, the next parameters from [15]: $R_0 = 0.95m$, $a = 0.6m$, $B_0 = 0.5T$, $\kappa_0 = 2.2$, $q_0 = 1.1$, $\Psi b = 0.1T / m2$. Fig. 2 shows both in the same graph, analytical and numerical FEM solutions of Ψ. Excellent agreement is obtained with relative global error= 10^{-5} (number of triangular mesh elements= 4810^4). Fig. 3 shows the variation of Ψ as function of the radial position R, along the R-axis (R, Z=0) and the absolute error does not exceed the value of 10^{-5}.

B. Case, A2≠0

In this section, we are interesting to see whether the parameter A2 affects the equilibrium configuration of ITER or not, we performed a computational calculation of the boundary plasma flux for different values of A2. Figures (4a-d) illustrate the obtained results where Ψb= 9.5, 11.4, 13.2 and 17.5T/m2 correspond to A2= 0.01, 0.02, 0.03 and 0.06, respectively. The function F through the parameter A2 has the significant effect on the plasma equilibrium shape.

V. CONCLUSION

In this paper, we carried out a computational solution of the GS equation by using the FEM fixed boundary solver of the plasma equilibrium and FreeFem++ software. The isofluxes of the poloïdal magnetic flux function gives the spatial configuration of the plasma equilibrium. Numerical results have been validated by using comparative analysis with the analytical solution. A global relative error of the order of 10^{-5} demonstrated a very good agreement. We study also the effect of parameter A1 which is related to toroidal function F and we have shown that a slight increase in A1 from 0, the plasma can lose its equilibrium configuration initially Dshape.

REFERENCES

[1] Ariola, M. & Alfredo, P. (2008). Magnetic control of tokamak plasmas. London: Springer-Verlag.

[2] Miyamoto, K., (2005) Plasma Physics and Controlled Nuclear Fusion. Springer Series on atomic, optical, and plasma physics. Berlin Heidelberg N.Y.

[3] Schnack, D.D., (2009). Lectures in Magnetohydro dynamics: With an Appendix on Extended MHD. Lect. Notes Phys. 780, Springer, Berlin Heidelberg.

[4] Zheng, L., (2015). Advanced Tokamak Stability Theory. Chapter 1. In *IOP Concise Physics.* Morgan & Claypool Publishers.

[5] Jardin, S., (2010). Computational Methods in Plasma Physics. Boca Rayton, Taylor & Francis.

[6] Chance, M. Greene, J. Grimm R. & al., (1978). Comparative numerical studies of ideal magnetohydrodynamic instabilities. *Journal of Comput. Phys.28:*1.

[7] Atanasiu, C.V., Guntern S., Lackner, K., & al., (2004). Analytical solutions to the Grad- Shafranov equation. *Physics of Plasmas, 11*(7):3510.

[8] Nath, D., Kalra, M.S., & Munshi, P., (2015). Computation of fixed boundary tokamak equilibria using a method based on approximate particular solutions. *Elsevier , Computers and Mathematics with Applications. 70,*1220–1233.

[9] Jeon, Y. M., (2015) Development of free-boundary tokamak equilibrium solver for advanced study of tokama equilibria. *J. Korean Phys. Soc. 5,* 843-853.

[10] Solov'ev, L.S., (1967). The theory of hydromagnetic stability of toroidal plasma configurations. *Sov. Phys. JETP 26,*400.

[11] Zheng, S.B., Wootton, A.J. & Solano, E. R., (1996). Analytical tokamak equilibrium for shaped plasma. *Phys plasma, 1176.*

[12] Deriaz, E., Despresy, B., Faccanoniz, G. & al., (2011). Magnetic Equations with freefem: the Grad-Shafranov equation and The Current Hole. ESAIM Proceedings (pp.1-10).

[13] Hecht, F., *FreeFem++. Third Edition, Version 3.56-2.Laboratoire Jacques-Louis Lions, University of Pierre et Marie Curie, Paris*. Available at: http://www.freefem.org/ff++

[14] Takeda, T. & Tokudas S. (1991). Computation of MHD Equilibrium of Tokamak Plasma. *J. of Comp.physics 93,*1-107.

[15] Lopez, J. E. & al, (2019). Fixed boundary Grad-Shafranov solver using finite difference method in nonhomogeneous meshgrid. *J. Phys., conf. Ser. 1159* 012017.

[16] Lecture 1 (2011). *Introduction to ITER AP 4990y Seminar Columbia University Spring*. Available at: http://sites.apam.columbia.edu/courses/apph4990y_ITER/ITER-Lecture-1.pdf

Strategies Selection in a Coal Mining Company by a Hybrid MCDM Method

Ivana Petkovski[1]

[1]Mathematical Institute SANU, Knez Mihailova 36, Belgrade, Serbia,
ivana993@turing.mi.sanu.ac.rs

Abstract—**The aim of this paper is to propose and prioritize future strategies for the economic development of a company for underground coal exploitation located in Serbia. Although there are strong tendencies towards the use of renewable energy sources, coal remains the most important source for electricity generation in Serbia and beyond. Considering complex business environment involving a number of influential factors, both internal and external are taken into account when creating a company's strategy. For defining influencing factors, a very useful tool called SWOT (Strengths, Weaknesses, Opportunities, and Threats) analysis is used. Four criteria and nineteen sub-criteria are identified. By considering the criteria and sub-criteria of SWOT analysis, six business strategies are proposed. Using the Analytical Hierarchy Process (AHP) method of multi-criteria decision-making, prioritization is carried out and the obtained results show that the most important proposed strategy that has priority in implementation is the strategy of diversification.**

Keywords - coal mining, strategy prioritization, SWOT, AHP

I. INTRODUCTION

Energy is an important indicator of economic development and its availability points to the strengthening of economic activities [1, 2]. Coal has a significant share in the energy supply. One of the most important energy sources in the world, according to the IEA data in 2019 [3] is coal with its share of 38% in electricity production. As stated by the IEA data, observing period from 1990 to 2019, coal is also very important source for electricity production in Serbia, over 90% of total coal consumption is used for electricity production and this is the main reason for considering coal as an important national energy supply source.

According to the Energy development strategy of the Republic of Serbia for the period until 2025 with projections until 2030 [4], energy resources and potentials consist of fossil, conventional (coal, oil and natural gas) and non-conventional fuels (oil shale) as well as renewable energy sources. Reserves of oil and gas are less than 1%, while the rest 99% of reserves consist of different types of coal, which shows the importance of coal as a national source of energy. As reported in the strategy, geological coal reserves are mostly comprised of lignite that has approximately 4 billion tons, then brown coal of over 500 million tons, 111 thousand tons of brown coal and pit coal has at least 8 million tons.

Results of a recent survey report that the world's coal reserves are provided for the next 153 years, which is far more than the supply of natural gas and oil [5]. IEA report [3] indicates the fluctuation in demand for coal, where the US and EU move towards reducing demand while Asian countries are going towards increasing demand while China remains the largest producer and consumer but with a decreasing trend in both.

Of the total domestic coal production in 2019 in Serbia, it is planned to use 94% for the production of electricity in thermal power plants [6]. Therefore, it is necessary to find a balance between the interests of companies engaged in the exploitation of coal and interests of other stakeholders that these companies have an impact. There has been much controversy about the impact of coal production on the environment. Developed countries plan to reduce the use of coal in electricity generation and direct their production to exports in developing countries where there is still no initiative to reduce coal use for the purpose of electricity production [5, 7].

ISBN: 978-86-80593-73-9

Enterprises for coal exploitation must be vigilant as to energy policy and environmental standards [8]. On the contrary, raising awareness on the conservation of ecology encourages the reduction of the level of coal production thus affect the reduction in the number of employees in the industry [7, 9]. According to a recent study, the way in which producers can protect themselves from a global initiative to reduce the use of coal is by creating an integrated market that can be resisted by external pressures [10].

Examining literature it can be concluded that the use of the Multiple Criteria Decision Making (MCDM) methods in solving real world problems is great [11-16]. In this paper, we use SWOT tool for defining influencing factors and AHP method for prioritizing the factors and strategies that are obtained when conducting the SWOT analysis. The importance of each element is determined with the help of experts in this field. This methodology is used for proposing strategies for business improvement.

The expected scientific contribution of the study is related to filling the existing literature gap in researches related to coal mining industry in Serbia that involve MCDM problem solving. Another contribution is found in proposing contemporary directions of future development plans of mines that can be applied to other mines as well. It is expected to highlight major challenges of the coal mine industry and take in consideration current state in the industry and government's initiative in natural resource management.

The paper is organized in the following sections. Section 2 discusses the literature review. Section 3 consists of the methodological framework used in the paper. The practical part of applying the SWOT-AHP model is given in Section 4. Subsequently, Section 5 with description of results and Sections 6 with final considerations is followed.

II. LITERATURE REVIEW

The use of AHP, as a method of MCDM, in solving organizational problems in different sectors is very broad.

In this paper, SWOT analysis provides initial data for the application of the AHP method in the form of criteria and sub-criterion. For this purpose, it is necessary to apply the AHP method to determine the weight values for each criteria and sub-criterion of the SWOT analysis. Based

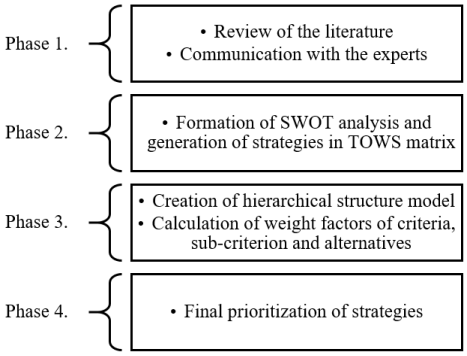

Figure 1. Phrases of conducting SWOT-AHP.

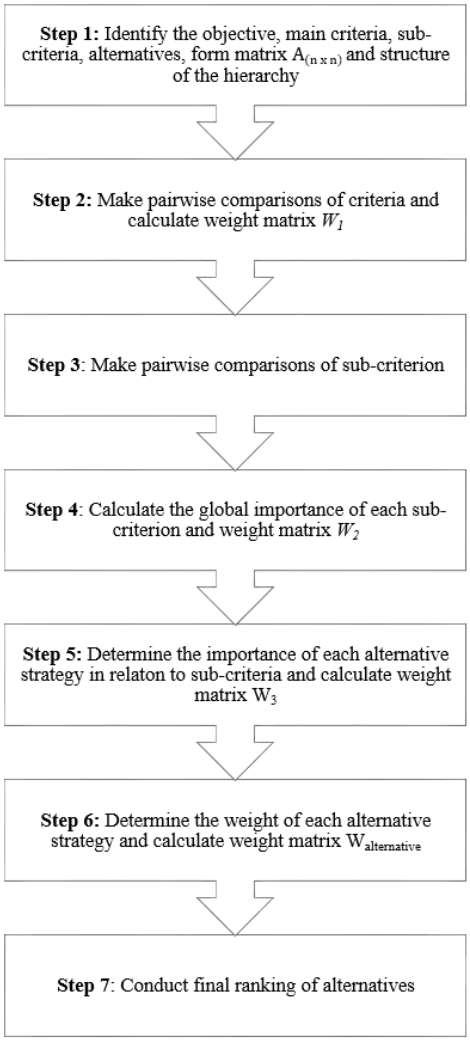

Figure 2. Analytical Hierarchy Process methodology.

on [17] research, SWOT analysis is criticized for equating all criteria that are obtained as a result, but they are not always the same relevance for the company but also SWOT analysis is seen as a great tool for strategies generation [18].

The process of development of a model for strategy prioritization in the research consists of several phases and it is given in Fig. 1.

A more detailed explanation of application of the AHP method can be seen in Fig. 2. Similar research conducted on the subject of prioritization strategy in mining and implementation of SWOT analysis are done in many countries such as China, India, Iran, Turkey and others. Reference [19] introduced AHP method and the procedure of AHP method is presented in the Fig. 2.

When implementing AHP method it is important to define decision making problem which is the top level of the hierarchy, next level of the hierarchy consists of criteria and sub-criteria (n criteria) and the bottom level of the hierarchy comprises n alternatives that are seen as possible solutions for the decision-making problem [20].

Examples of researches in the domain of mining and the use of SWOT and AHP methodology are shown in Table I.

A recent survey conducted by [30] shows that the most used multi-criteria decision-making method in mining and mineral processing is AHP. They also analyzed the progressive use of MCDM methods from 1999 to 2017 in mining sector. The authors [1] use the AHP method to prioritize energy policy alternatives in order to select the best source of energy. Reference [31] propose the use of AHP method in decision making for sustainable energy systems. In the business world the AHP methodology can find application in the evaluation and selection of energy projects for investment [32]. AHP method also found its application in evaluation of different types of power plants [33]. In this research, using the AHP it is found that renewable energy power plants are the best choice for the future. Coal power plants are not high ranked because of their impact on the environment but they are very important because of their high reserve levels and stability of energy supply. Hybrid models for multi-criteria decision-making find their application in the selection of renewable energy sources [34]. AHP approach is used in evaluating coal-based power generation in Bangladesh on the basis of economic, technological and social aspects [22]. The final ranking has shown that it is necessary to turn to more sustainable energy sources in the future.

An integrated VIKOR-AHP approach is showed for the purpose of choosing the best energy alternative and energy production site selection [1]. A lot of research is done in fuzzy environment taking into consideration the vagueness and ambiguity of information that are an integral part of the decision-making process [35]. In their research, [23] use Balanced Scorecard and FAHP to evaluate performance of outsourcing decision of an Indian coal mining organization. They find this model as a guiding mechanism for any strategic decision making and policy measures developing. When choosing a technology for the production of electricity, it is

TABLE I. LITERATURE REVIEW OF PREVIOUS RESEARCHES RELATED TO THE USED METHODOLOGY.

Authors	**Method**	**Aim**	**Year**	**Location**
Balusa and Gorai [21]	Fuzzy AHP	Selection of the appropriate underground metal mining method	2019	India
Zaman et al. [22]	AHP	Analysis of predominant factors related to coal-based power generation	2018	Bangladesh
Modak et al. [23]	BSC - Fuzzy AHP	Performance evaluation of outsourcing decision in coal mining enterprise	2017	India
Niu et al. [24]	SWOT	Analysis of system competitiveness in coal production	2017	China
Zhang et al. [25]	AHP	Sustainable development of coal cities	2017	China
Shi [26]	SWOT	Analysis of challenges to more cleaner energy mix	2016	Singapore
Shahabi et al. [27]	SWOT-AHP-ANP	Strategy prioritization in steel industry	2014	Iran
Esmaeili et al. [28]	SWOT-AHP-TOPSIS	Formulation of organizational strategies	2014	Iran
Fouladgar et al. [29]	SWOT-ANP-VIKOR	Strategy prioritization in mining industry	2011	Iran

possible to apply the AHP method [36]. Reference [37] carried out a survey in which he ranked technologies for the production of electricity using renewable and non-renewable energy sources. Using the AHP method, ranking of technologies based on financial, technical, environmental, socio-economic-political criteria was performed. The results show that the top-ranked technology for the production of electricity using renewable energy sources such as wind, solar, hydro and geothermal.

The reasons for using AHP method include its possibility to break a major problem into several levels that makes the analysis much easier. It is used in solving many problems in strategic management. However, many researchers are trying to compare larger number of methods for calculating criteria weights such as Best Worst Method (BWM), Full Consistency Method (FUCOM), Level Based Weight Assessment (LBWA), Weighted Product Method (WPM), Weighted Sum Method (WSM) and other emerging methods in order to find optimal solution [38, 39]. Some of these methods offer better solution in regard to a number of comparison or consistency issues solution [38, 39].

III. RESULTS OF SWOT-AHP MODEL

Step 1. Experts identify the most important elements of conducted SWOT analysis and they represent criteria and sub-criterion used for the purpose of AHP method. Using the results obtained by SWOT analysis a TOWS matrix is generated. The results of creating the TOWS matrix are presented in the Table II. The result obtained by the TOWS matrix is presented in the form of strategies generated as S-O strategies, W-O strategies, S-T strategies and W-T

TABLE II. TOWS MATRIX.

Internal factors **External factors**	**Strengths (S)** S_1 Explored reserves of exploitable coal S_2 Good quality coal S_3 Regional mine allocation S_4 History and Personnel Potential	**Weaknesses (W)** W_1 Insufficiently explored and utilized reserves W_2 Old technologies W_3 Poor overall economic picture of the company W_4 Long-term investment processes in the mining sector W_5 Part of the public sector W_6 Very sensitive demographic and social character
Opportunities (O) O_1 Real market for commercial and energy coal O_2 Coal needs in the energy balance of Serbia; the basic energy potential of Serbia (66% of electricity and thermal energy from thermal power plants) O_3 Interest of strategic partners O_4 Importance and impact of company's survival and development on economic, demographic and social regional policy O_5 Positive impact on Serbia's foreign trade balance	**SO strategy** **S_1O_5** Diversification **S_2O_2** Implementation of systematic geological exploration of oil shale as one of the potential energy raw material	**WO strategy** **W_1O_3** Finding a strategic partner for increased efficiency and production volume **W_2O_1** Business optimization
Threats (T) T_1 The economic situation - the budget deficit in Serbia and the necessity of short-term measures T_2 Potential withdrawal of strategic partners T_3 Problems and waves of transition T_4 Gasification	**ST strategy** **S_1T_1** Increase in productivity due to the strengthening of economic growth and regional development	**WT strategy** **W_2T_1** Inflow of foreign investment to modernize equipment

strategies ranked according to the priority of the implementation in the next part of the research.

Step 2. The next step in conducting the research is the application of the AHP method for multi-criteria decision-making for determining the importance of each group defined by the SWOT analysis with the help of experts using Saaty's scale [19] for determining relative importance. Consistency level in comparison with the goal of the prioritization is calculated for each criteria and is less than 10%.

Step 3. After defining the importance of each SWOT group (criteria), the next step in implementing AHP method is defining the importance of each sub-criterion. Consistency level in comparison with the goal of the prioritization is calculated for each sub-criterion and is less than 10%.

Step 4. Multiplying the obtained weights calculated in previous steps, the global importance of the sub-criterion is calculated and presented in Table III.

Normalized data indicate the impact of each sub-criterion on the main objective. Sub-criterion with the greatest influence in each group are marked in the table.

Positive sub-criteria are S_1 (0.431) and O_1 (0.378). Negative sub-criteria are W_2 (0.344) and T_4 (0.508). The influence of the SWOT factors is given in the descending sequence of S→W→O→T. The values of the most important sub-criterion in relation to the group of criteria are also given in the descending sequence $S_1 \rightarrow W_2 \rightarrow O_1 \rightarrow T_4$.

Step 5. The next step is to determine the importance of each alternative strategy in relation to each sub-criterion.

Step 6. Multiplying the results of matrix W_2 and matrix W_3 final weight of each strategy is determined.

Final ranking of proposed alternative strategies obtained by AHP methodology is shown in Table IV.

Step 7. Considering the result of the W alternative matrix, a sequence of priorities for the proposed strategies can be created in the following descending sequence: $S_1O_5 \rightarrow W_2T_1 \rightarrow W_1O_3 \rightarrow W_2O_1 \rightarrow S_2O_2 \rightarrow S_1T_1$.

TABLE III. THE IMPORTANCE OF THE CRITERIA AND SUB-CRITERION OF THE SWOT ANALYSIS.

SWOT groups - criteria	The importance of the SWOT criteria	SWOT sub-criterion	Global importance of SWOT sub-criterion
(S)	0.467	S_1	0.202
		S_2	0.152
		S_3	0.080
		S_4	0.034
(W)	0.277	W_1	0.066
		W_2	0.095
		W_3	0.050
		W_4	0.035
		W_5	0.018
		W_6	0.013
(O)	0.160	O_1	0.060
		O_2	0.044
		O_3	0.029
		O_4	0.010
		O_5	0.017
(T)	0.095	T_1	0.009
		T_2	0.023
		T_3	0.015
		T_4	0.048

TABLE IV. FINAL RANKING OF ALTERNATIVES BASED ON AHP METHODOLOGY.

Strategy	Final weight (w_j)	Rank
S_1O_5	0.249	1
S_2O_2	0.142	5
W_1O_3	0.176	3
W_2O_1	0.152	4
S_1T_1	0.099	6
W_2T_1	0.183	2

IV. DISCUSSION OF RESULTS

According to the final results of SWOT-AHP methodology, strategy that has the greatest impact on future business and implementation priority is S_1O_5 - diversification. The most common approach used in situation of long-term bad business results is diversification, yet the latest research on the diversification of coal exploitation enterprises concludes that a great deal of caution is needed in this process [40]. This strategy relies on the strengths and uses opportunities arising from the environment to influence the improvement of business operations of the company. The strategy proposes the activation of coal resources that the

company has and focuses on new markets and the possibility of selling coal to new thermal power plants that are planned to be build and who support environmental policy. In support of the strategy is good quality coal that is characteristic for the company and that is needed for thermal power plants production. Although many countries want to reduce the use of coal, it remains one of the most important energy sources. In particular, its importance and necessity of exploitation is reflected in those countries with large coal reserves, such as China, India [3] and among them Serbia.

Internal analysis of the weaknesses of the company identified the bad condition of the technology, and in order to respond promptly to threats that could come from the environment where competitors use advanced technology, it is necessary to define a strategy that would be a response to the threat. In order to maintain the level of coal production that would be sufficient to meet domestic and foreign market needs and to modernize technology, W_2T_1 strategy - Foreign direct investment (FDI) for equipment modernization needs to be implemented. The mechanization used in the mines in Serbia is obsolete and depreciated [4]. The reason for the bad condition is the lack of adequate investments for the purchase of new and maintenance of old mechanization for many years. The inflow of foreign investments will provide solution for the most important technological problems. Along with solving the problems of modernizing technology, the problem of low productivity can be improved [41]. Using clean technologies positive influence is achieved on preservation of the environment [25].

Taking into account weaknesses of the company and the opportunities that environment provides further growth and development is reflected in finding a strategic partner in order to increase efficiency and production volume, which is the W_1O_3 strategy. This strategy is based on the fact that the company has large coal reserves that are not currently used because of the lack of funds to increase production. Coal supply in the domestic market depends partly on the import of this energy source [42], which indicates the need to increase coal production in order to reduce imports and supply the market. Strategic partner would provide an inflow of investments that would be used to increase production capacity.

Business optimization - W_2O_1 strategy is the next strategy that needs to be implemented. Some of the known methods that could be applied in this case, and are examples of best practices are Lean production [43], Kaizen [44], establishing stronger relationships with suppliers and customers [45]. Reducing production costs is a basic prerequisite for gaining competitive advantage on the market [46]. Reducing all activities that do not contribute to the creation of added value positively influence on the value chain [47].

By implementing all of the aforementioned strategies, the conditions for the implementation of the S_2O_2 strategy are created. Implementation of systematic geological exploration of oil shale as one of the potential energy raw material is very important for discovering a new energy source that will be produced. According to the Energy development strategy of the Republic of Serbia [4], oil shales have a share of 9% in total geological reserves of the country. The reserves are significant, but the conditions for their exploitation and the technologies of their use have yet to be defined, since this is an unconventional fuel. Reducing oil reserves leads to the need for other energy sources and oil shales can be used for this purpose. The company has explored reserves of oil shales on the territory of the one part of the basin and this site is for now the largest deposit of oil shale in the country. However, the vast majority of the territory is unexplored and there is no accurate data on the reserves of oil shales.

Another strategy that is important for the company, knowing that is a part of the public sector is the S_1T_1 strategy in terms of increasing productivity for the purpose of strengthening economic growth and regional development. This strategy uses the strength of the company to the best way to address current threats from the environment. Coal enterprises are usually large employers [10, 48] so achieving positive financial results of the company leads to economic and social stability of the region. Regions where the company does business are undeveloped, population's living standards are low, and it has the means to stimulate economic activities in the regions where it operates. The survival and development of the company prevents further departure of people from these areas that affects demographics.

V. Discussion of Results

Competitiveness on the global market is reflected in the struggle for natural resources, amongst the most important ones are oil, natural gas and coal. Serbia is a country rich in coal reserves and based on the resource the majority of electricity generation is obtained thereby coal supplying is a critical factor for the functioning of the energy system in Serbia. Further production and use of coal are directly associated with the production of electricity. Given the overall development of society, it can be concluded that demand for energy will have an upward trend.

According to the International Energy Agency (IEA), in the period from 2005 to 2025, primary energy consumption is expected to increase by 40% [49]. However, coal is a conventional energy source and as such is non-renewable and it is necessary to devise a sustainable development plan for its use so that future generations can achieve their growth and development. Such a strategic approach can be achieved by meeting the needs of the market with a higher living standard of the population and reducing pollution of the environment.

The current state of the coal mine production in Serbia is such that production is unprofitable and depends on state aid as they are part of the public sector. Investments in mines are insufficient and the equipment used is obsolete. Investments are needed to revitalize this sector. The same case is with the company that we are discussing about in this research. This paper is an example of how the economic development of the company can be achieved through detailed analysis of the environment, identification of influencing factors and the development of future business strategies. Based on determined strengths, weaknesses, opportunities and threats, strategies have been defined, their importance has been assessed, and implementation prioritized through the implementation of the SWOT situational analysis and AHP multi-criteria decision making.

The result points to the significance of the strategy of diversification as a strategy that has priority in implementation. Followed by the strategy of FDI in this sector. The research is important for filling the gap in the literature addressing the coal mines problems in Serbia. Another contribution of the study reflects multidisciplinary problem solving by tackling several questions at once such as organizational, operational, governmental, environmental and social. It triggers many questions that are essential for the future development of mining industry such as importance of foreign trade and allocation of foreign investments into the country.

The company represents the potential pillar of development of the region in which the mine is located. The development of the mine follows the improvement of the living standards of the population, development of small and medium-sized enterprises and concentration of educated population of different educational profiles to the region. Development of the mine should be followed by the development of appropriate legislative frameworks, institutions and bodies that are responsible for the Energy and mining sector in Serbia. In the future, the company must be connected to the Energy sector of the country to ensure the placement of coal and provide energy stability of the country in the foreseeable future. The expected trend of increase in electricity consumption justifies the cost-effectiveness of investing in this business.

Some of the main limitations of the study are seen in spatial scope of the research since it does not question all coal mines in Serbia to have a complete insight into the needs and challenges of mine industry. Another limitation may regard the used methodology of AHP, since it requires a large number of pairwise comparison compared to other MCDM methods for determining criteria weights.

Future research direction should be focused towards investigating long-term electricity consumption across different sectors and the feasibility of realizing diversification strategy due to efforts of economies to switch to renewable energy sources. In addition, author will compare AHP results with several MCDM methods for prioritizing strategies in order to investigate their results and differentiate the procedures.

Acknowledgment

This work was supported by the Serbian Ministry of Education, Science and Technological Development through Mathematical Institute of the Serbian Academy of Sciences and Arts National Institute of the Republic of Serbia.

REFERENCES

[1] Kahraman, C., & Kaya, İ. (2010). A fuzzy multicriteria methodology for selection among energy alternatives. *Expert Systems with Applications*, *37*(9), 6270-6281.

[2] Wu, Y., & Zhang, W. (2016). The driving factors behind coal demand in China from 1997 to 2012: An empirical study of input-output structural decomposition analysis. *Energy Policy*, *95*, 126-134.

[3] International Energy Agency. *Key world statistics*. Available at: https://www.iea.org/topics/coal/. Accessed: 28.03.2021.

[4] *Energy development strategy of the Republic of Serbia for the period until 2025 with projections until 2030. „Official Gazette RS", No. 101*. Available at: http://www.pravno-informacioni-sistem.rs/SlGlasnikPortal/eli/rep/sgrs/skupstina/ostalo/2015/101/1/reg Accessed: 01.04.2021.

[5] Song, Y., & Wang, N. (2019). Exploring temporal and spatial evolution of global coal supply-demand and flow structure. *Energy*, *168*, 1073-1080.

[6] *Energy Balance of Republic of Serbia for 2019, „Official Gazette RS", No. 105-18*. Available at: http://mre.gov.rs/doc/efikasnost-izvori/ENERGETSKI-BILANS-REPUBLIKE-SRBIJE-ZA-2019-Sluzbeni-glasnik-RS-broj-105-18.pdf Accessed: 01.04.2021.

[7] Riker, D.A. (2012). International coal trade and restrictions on coal consumption. *Energy Economics*, *34*(4), 1244-1249.

[8] Jonek-Kowalska, I. (2019). Consolidation as a risk management method in the lifecycle of a mining company: A novel methodological approach and evidence from the coal industry in Poland. *Resources Policy*, *60*, 169-177.

[9] Bianco, V., Cascetta, F., Marino, A., & Nardini, S. (2019). Understanding energy consumption and carbon emissions in Europe: A focus on inequality issues. *Energy*, *170*, 120-130.

[10] Zhao, S., & Alexandroff, A. (2019). Current and future struggles to eliminate coal. *Energy Policy*, *129*, 511-520.

[11] Nassereddine, M., & Eskandari, H. (2017). An integrated MCDM approach to evaluate public transportation systems in Tehran. *Transportation Research Part A: Policy and Practice*, *106*, 427-439.

[12] Pineda, P.J.G., Liou, J.J., Hsu, C.C., & Chuang, Y.C. (2018). An integrated MCDM model for improving airline operational and financial performance. *Journal of Air Transport Management*, *68*, 103-117.

[13] Lee, H.C., & Chang, C.T. (2018). Comparative analysis of MCDM methods for ranking renewable energy sources in Taiwan. *Renewable and Sustainable Energy Reviews*, *92*, 883-896.

[14] Arsić, S., Nikolić, D., Mihajlović, I., Fedajev, A., & Živković, Ž. (2018). A new approach within ANP-SWOT framework for prioritization of ecosystem management and case study of National Park Djerdap, Serbia. *Ecological Economics*, *146*, 85-95.

[15] Wang, H., Jiang, Z., Zhang, H., Wang, Y., Yang, Y., & Li, Y. (2019). An integrated MCDM approach considering demands-matching for reverse logistics. *Journal of Cleaner Production*, *208*, 199-210.

[16] Nikolić, I.P., Milošević, I.M., Milijić, N.N., & Mihajlović, I.N. (2019). Cleaner production and technical effectiveness: Multi-criteria analysis of copper smelting facilities. *Journal of Cleaner Production*, *215*, 423-432.

[17] Phadermrod, B., Crowder, R.M., & Wills, G.B. (2019). Importance-performance analysis based SWOT analysis. International *Journal of Information Management*, *44*, 194-203.

[18] Khaba, S., & Bhar, C. (2017). Quantifying SWOT analysis for the Indian coal mining industry using Fuzzy DEMATEL. *Benchmarking: An International Journal*, *24*(4), 882-902.

[19] Saaty T. (1980). *The analytic hierarchy process: planning, priority setting, resource allocation*. McGraw-Hill.

[20] Aragonés-Beltrán, P., Chaparro-González, F., Pastor-Ferrando, J.P., & Pla-Rubio, A. (2014). An AHP (Analytic Hierarchy Process)/ANP (Analytic Network Process)-based multi-criteria decision approach for the selection of solar-thermal power plant investment projects. *Energy*, *66*, 222-238.

[21] Balusa, B.C., & Gorai, A.K. (2019). Sensitivity analysis of fuzzy-analytic hierarchical process (FAHP) decision-making model in selection of underground metal mining method. *Journal of Sustainable Mining*, *18*(1), 8-17.

[22] Zaman, R., Brudermann, T., Kumar, S., & Islam, N. (2018). A multi-criteria analysis of coal-based power generation in Bangladesh. *Energy Policy*, *116*, 182-192.

[23] Modak, M., Pathak, K., & Ghosh, K.K. (2017). Performance evaluation of outsourcing decision using a BSC and Fuzzy AHP approach: A case of the Indian coal mining organization. *Resources Policy*, *52*, 181-191.

[24] Niu, D.X., Song, Z.Y., & Xiao, X.L. (2017). Electric power substitution for coal in China: Status quo and SWOT analysis. *Renewable and Sustainable Energy Reviews*, *70*, 610-622.

[25] Zhang, X., Winchester, N., & Zhang, X. (2017). The future of coal in China. *Energy Policy*, *110*, 644-652.

[26] Shi, X. (2016). The future of ASEAN energy mix: A SWOT analysis. *Renewable and sustainable energy reviews*, *53*, 672-680.

[27] Shahabi, R.S., Basiri, M.H., Kahag, M.R., & Zonouzi, S.A. (2014). An ANP–SWOT approach for interdependency analysis and prioritizing the Iran′ s steel scrap industry strategies. *Resources Policy*, *42*, 18-26.

[28] Esmaeili, A., Kahnali, R.A., Rostamzadeh, R., Zavadskas, E.K., & Sepahvand, A. (2014). The formulation of organizational strategies through integration of freeman model, SWOT, and fuzzy MCDM methods: A case study of oil industry. *Transformations in business & economics*, *13*(3C), 602-627.

[29] Fouladgar, M.M., Yakhchali, S.H., Yazdani-Chamzini, A., & Basiri, M.H. (2011). Evaluating the strategies of Iranian mining sector using an integrated model. In *2011 International Conference on Financial Management and Economics Proceedings* (pp.58-63).

[30] Sitorus, F., Cilliers, J. J., & Brito-Parada, P. R. (2019). Multi-criteria decision making for the choice problem

in mining and mineral processing: Applications and trends. *Expert systems with applications*, *121*, 393-417.

[31] Wang, J. J., Jing, Y. Y., Zhang, C. F., & Zhao, J. H. (2009). Review on multi-criteria decision analysis aid in sustainable energy decision-making. *Renewable and sustainable energy reviews*, *13*(9), 2263-2278.

[32] Büyüközkan, G., & Karabulut, Y. (2017). Energy project performance evaluation with sustainability perspective. *Energy*, *119*, 549-560.

[33] Chatzimouratidis, A. I., & Pilavachi, P. A. (2009). Technological, economic and sustainability evaluation of power plants using the Analytic Hierarchy Process. *Energy policy*, *37*(3), 778-787.

[34] Kabak, M., & Dağdeviren, M. (2014). Prioritization of renewable energy sources for Turkey by using a hybrid MCDM methodology. *Energy conversion and management*, *79*, 25-33.

[35] Jayawickrama, H. M. M. M., Kulatunga, A. K., & Mathavan, S. J. P. M. (2017). Fuzzy AHP based plant sustainability evaluation method. *Procedia Manufacturing*, *8*, 571-578.

[36] Štreimikienė, D., Šliogerienė, J., & Turskis, Z. (2016). Multi-criteria analysis of electricity generation technologies in Lithuania. *Renewable energy*, *85*, 148-156.

[37] Stein, E. W. (2013). A comprehensive multi-criteria model to rank electric energy production technologies. *Renewable and Sustainable Energy Reviews*, *22*, 640-654.

[38] Pamučar, D., Stević, Ž., & Sremac, S. (2018). A new model for determining weight coefficients of criteria in mcdm models: Full consistency method (fucom). *Symmetry*, *10*(9), 393.

[39] Song, B., & Kang, S. (2016). A Method of Assigning Weights Using a Ranking and Nonhierarchy Comparison. *Advances in Decision Sciences*.

[40] Li, C.M., Cui, T., Nie, R., Lin, H., & Shan, Y. (2019). Does diversification help improve the performance of coal companies? Evidence from China's listed coal companies. *Resources Policy*, *61*, 88-98.

[41] Mishra, D.P., Sugla, M., & Singha, P. (2013). Productivity improvement in underground coal mines-a case study. *Journal of Sustainable Mining*, *12*(3), 48-53.

[42] IEA. *World Energy Balances 2018*. Available at: https://webstore.iea.org/world-energy-balances-2018 Accessed: 02.04.2021.

[43] Vilkas, M., Koreckaja, I., Katiliūtė, E., & Bagdonienė, D. (2015). Adoption of Lean production: preliminary evidence from Lithuania. *Procedia-Social and Behavioral Sciences*, *213*, 884-889.

[44] Maarof, M.G., & Mahmud, F. (2016). A review of contributing factors and challenges in implementing kaizen in small and medium enterprises. *Procedia Economics and Finance*, *35*, 522-531.

[45] Kowalska-Styczeń, A., & Sznajd-Weron, K. (2016). From Consumer Decision to Market Share–Unanimity of Majority? *Journal of Artificial Societies and Social Simulation*, *19*(4).

[46] Manowska, A., Osadnik, K.T., & Wyganowska, M. (2017). Economic and social aspects of restructuring Polish coal mining: Focusing on Poland and the EU. *Resources Policy*, *52*, 192-200.

[47] Thompson, A., Strickland, A.J., & Gamble, J. (2015). *Crafting and executing strategy: Concepts and readings*. McGraw-Hill Education.

[48] Jonek-Kowalska, I. (2018). How do turbulent sectoral conditions sector influence the value of coal mining enterprises? Perspectives from the Central-Eastern Europe coal mining industry. *Resources Policy*, *55*, 103-112.

[49] IEA. *Today in Energy*. Available at: https://www.eia.gov/todayinenergy/detail.php?id=41433 Accessed: 25.04.2021.

Improvement of Heptane Recovery Process in Polypropylene Plant: A Case Study

Ozben Kutlu[1]

[1]Ege University Solar Energy Institute, Izmir, Turkey, ozben.kutlu@ege.edu.tr

Abstract—**The petrochemical industry is a capital-intensive industry consuming much energy and material, and their costs effect significantly the sustainability of production. Heptane is the most critical component to reduce production cost of polypropylene. Based on process management phenomenon, remaining heptane is enriched with the solvent recovery unit, and it is recycled to the polymerization unit again. During this process, the desired amount of heptane is not separated from heavy compounds at one distillation column. The aim of this case study is to reduce the heptane composition of the bottom stream of the related-distillation column. The real-time data are collected from the plant in operation for reducing the unused waste heptane amount. In this case, the related-distillation column is simulated by using a comprehensive process simulation package, and sensitivity analysis of the column is performed. Six scenarios are created to retrofit the process, compared with real-time data, and suggestions are presented.**

Keywords – process management, energy, simulation, solvent recovery, polypropylene, sensitivity analysis

I. INTRODUCTION

Process integration is a family of methodology for combining several processes to reduce consumption of resources or harmful emissions to the environment [1]. Considering the impact of the imbalance in oil prices and poor process management on Refineries and Petrochemical Companies, efficient material and energy usage becomes a key factor to be considered [2]. Especially energy saving is the most important issue in the petrochemical industry associated with cost. There are literally hundreds of different energy conservation techniques that fall into the following categories:

- efficiency improvement of equipment and specific systems
- heat recovery
- power recovery
- recovery and reuse/recycling of waste materials/waste minimization
- utilization of cryogenics

While recovery and reuse of energy includes recovery of heat of compression from high-pressure and -temperature systems, reuse of waste materials covers recovery of useful products from feedstocks, by-products, and products [3].

The petrochemical industry is a capital-intensive industry consuming much energy and material, and their costs effect significantly the sustainability of production [4]. Polypropylene is a semi-crystalline polymer widely used in packaging, textile and automobile industries due to its good processability and properties [5]. Classification can be done according to the polymerization method into solvent processes, bulk polymerization processes and vapor phase polymerization processes. Solvent polymerization is carried out in the presence of hexane, heptane or another inert hydrocarbon solvent where polymerization inhibitors have been eliminated [6]. For the reason, solvent recovery quite affects the operating cost beside energy saving.

Nowadays, with the increasing importance of process integration and digitization, it is seen that the number of process simulation and digital twin applications are also increasing. However, there are limited number of simulation studies on polypropylene production. Most of the studies are conducted by a type of polypropylene

ISBN: 978-86-80593-73-9

membrane to filter specific compounds like heavy metals or CO_2 [7–10]. In one of them, two industrial-scale pressure swing adsorption processes were designed [11]. The recovery of only nitrogen and recovery of both nitrogen and propylene from purge gas stream in a polypropylene production were optimized by simulations.

There are also limited number of simulation studies on heptane recovery even though the studies regarding to solvent recovery systems are also present. In one of the solvent recovery studies, a recovery process of a quaternary waste solvent was simulated [12]. In other study, a separation process of propylene oxide from direct propylene epoxidation was aimed via solvent screening followed by process optimization [13]. Even though they focused on different solvents such as ethers, ketones, esters, aromatics, none of them did have a heptane solvent-specific modeling. On the other hand, to separate heptane from compounds, such as toluene, acetone and butanone, extractive distillation and pressure swing distillation methods were modeled [14–17], but the studies covered mostly the processes of pharmaceutical industry.

Different from all these studies, the present work is conducted to improve the heptane recovery process as a critical solvent for production of polypropylene. The real-time data are collected from the plant in operation for reducing the unused waste heptane amount. This case study describes the modeling, simulation, and sensitivity analysis of the column by using a comprehensive process simulation package. Six scenarios are created, and the results are compared to the real-time conditions. Some suggestions about the operation conditions, design of reboiler and heat duty are presented for improvement.

II. PROCESS DESCRIPTION

In the polypropylene plant, there are many sections which include special processes. The solvent recovery section consists of steam stripping, film evaporation, solvent purification, storage, vent gas recovery and hot oil systems. In the solvent purification process, heptane is recovered step-by-step from the solvent mixtures that also include butanol and water.

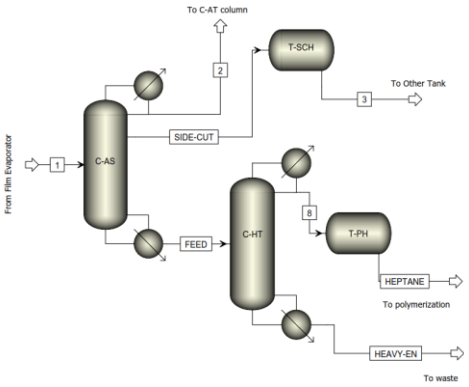

Figure 1. The Flowsheet of solvent purification process.

Flowsheet of the solvent purification process simulated in Aspen PLUS is shown in Fig. 1. Due to azeotrope binary properties, solvent mixture is firstly fed to the Azeotrope Stripper (C-AS). From the top stream, the azeotrope mixture of heptane, butanol and water is distilled out after the condenser and fed to the other azeotrope tower (C-AT) to recover butanol. From middle stage of C-AS, the heptane with some heavy compounds is separated and stored in the side cut heptane tank (T-SCH). From the bottom stream of C-AS, the solvent mixture that consists of more concentrated heptane, is fed to the Heptane Tower (C-HT). Purified heptane is distilled out from the top stream, and it is stored in the purified heptane tank (T-PH). Finally, the heavy-end is sent to the storage tank as waste.

In this study, the C-HT column is modified with suitable conditions and required constraints of company to increase the composition of heptane in distillate in other words the decrease in operating cost. The column specifications at the base case are shown in Table I.

The feed stream contains approximately fifty compound clarified by various measurements carrying out periodically by the company. The compounds are ordered according to their boiling points, and summarized in a way that would not distort the results. Thus, the model used in this study divides the feed composition into thirty-nine compound listed Table II.

TABLE I. COLUMN SPECIFICATIONS AT BASE CASE.

Setup option	***Data***
Feed flow rate (kg/h)	23000
Feed temperature (°C)	113.8
Feed pressure (kg/cm^{2}g)	2.2
No of Stage	32
Reflux Ratio	1.4
Distillate flow rate (kg/h)	15750
Heptane composition in feed stream (%w)	36.2
Heptane composition in distillate (%w)	40.3
Reboiler heat capacity (kcal/h)	2240000

TABLE II. FEED COMPOSITION (COMP.) AND THE BOILING POINTS (BP) OF COMPOUNDS.

Compound	**Group**	**Comp. (% w/w)**	**BP (°C)**
n-hexane	nP6	0.03029	68.7
Methylcyclopentane	N6	0.02392	71.8
2,2-Dimethylpentane	iP7	0.05249	79.2
2,4-Dimethylpentane	iP7	0.12134	80.5
Cyclohexane	N6	0.35609	80.7
3,3-Dimethylpentane	iP7	0.36184	86.0
1,1-Dimethylcyclopentane	N7	0.18037	87.8
2,3-Dimethylpentane	iP7	2.92398	89.7
2-Methylhexane	iP7	8.66579	90.0
Cis-1,3-Dimethylcyclopentane	N7	0.93123	90.77
Trans-1,3-Dimethylcyclopentane	N7	0.77589	91.73
3-methylhexane	iP7	15.31967	91.85
Trans-1,2-Dimethylcyclopentane	N7	1.55207	91.87
3-ethylpentane	iP7	2.04661	93.47
n-heptane	nP7	36.24461	98.4
2,2,4-trimethylpentane	iP8	0.03659	99.2
Methylcyclohexane	N7	9.75913	100.9
1,1,3-Trimethylcyclopentane	N8	0.38441	104.8
2,2-Dimethylhexane	iP8	0.30822	106.8
2,5-Dimethylhexane	iP8	2.28616	109.1
2,2,3-Trimethylpentane	iP8	0.59085	109.8
3,3-Dimethylhexane	iP8	0.06975	111.97
2,3,4-Trimethylpentane	iP8	0.02659	113.4
1,1,2-Trimethylcyclopentane	N8	0.3567	113.7
2,3,3-Trimethylpentane	iP8	0.01995	114.77
2-Methylheptane	iP8	0.13195	117.6
3,4-Dimethylhexane	iP8	0.01769	117.7
3-Methyl-3-ethylpentane	iP8	0.06223	118.2
3-Ethylhexane	iP8	0.01897	118.5
3-Methylheptane	iP8	0.3166	118.9
Cis-1,4-Dimethylcyclohexane	N8	0.01526	124.3
2,4,4-Trimethylhexane	iP9	0.24417	130.66
Ethylcyclohexane	N8	0.01551	131.79
3,3-Dimethylheptane	iP9	0.16279	132.69
2,4-Dimethylheptane	iP9	1.78375	133.65
4-Methyloctane	iP9	0.73464	142.4
2-Methyloctane	iP9	1.27976	143.28
Trans-Decalin	N10	0.38319	187.31
Cis-Decalin	N10	11.73356	195.82

III. METHOD

The cascaded units are simulated in Aspen Plus software package. The sequential simulation is performed, and UNIQUAC property method as the most suitable model is chosen due to the binary interaction parameters of azeotrope mixture at low pressure.

The base case of unit is created by the real-time plant data at certain time considering some appropriate changes in operating conditions. The process is assumed at steady state conditions and does not include a reaction. A rigorous distillation model as the C-HT column is chosen for the simulation. Total condenser and thermosyphon reboiler types are assumed as the suitable designs for actual plant, and the bottom stream and reboiler feed are both drawn from the column sump with the same composition.

An algorithm is generated to propose a solution to the issue, and it comprises the following steps:

a) The content of solvent mixture is collected from company based on various analysis results.

b) Considering privacy policies, some regulations are applied to modeling.

c) The suitable compounds and property method are selected from ASPEN database.

d) The real-time process (i.e. base case) is simulated as Scenario 1.

e) The issue is investigated by changing the product stream stage. In the Scenario 2, the product is distilled out from intermediate stage (No of Stage: 11) instead of top stream.

f) In the Scenario 3, the issue is investigated by dividing the feed to three streams. The feed is given to column from three different stages (No of Stage: 10 / 13 / 16).

g) In the Scenario 4, the change in the feed stage is investigated according to heptane composition in distillate by using sensitivity analysis in Aspen Plus.

h) Despite of the requirement of investment cost, the aim is to change the number of column stage in the Scenario 5. Its effect on heptane composition is observed by using sensitivity analysis.

i) As being other crucial parameter for distillation, the effect of reflux ratio on the heptane composition in distillate is analyzed during the Scenario 6.

j) According to results, the heat duty of the column reboiler is investigated and re-designed finally.

IV. Results and Discussion

The critical intention of this study is to reduce the heptane composition in bottom product, in other words, to increase in heptane content in the distillate. For this purpose, six scenarios were created. If the heptane composition in the distillate is greater than 41%, the results could be acceptable when comparing the real-time process conditions.

A. *Scenario 1: The Base Case*

In this case, the real-time condition was simulated. As shown in Table III, the simulated model is fitted to the real-time process.

B. *Scenario 2 and Scenario 3: Product from Intermediate Stage and Multi-feed options*

The redrawn flowsheets of column for each scenario are given in Fig. 2. In the Scenario 2, The placement of intermediate stage and its amount are studied with different variations. Consequently, it is assumed that the product was taken from the eleventh stage at a flow rate of 4000 kg/h, and the optimum values of heptane concentration in the distillate and bottom stream were calculated as 42.2% and 2.9%, respectively.

On the other hand, the desired retrofitting was not observed in this Scenario 3, and hence it is decided that the multi-feed did not an alternative option for real-time process.

TABLE III. STREAM RESULTS OF SIMULATION.

Stream Name	Feed	Heptane	Heavy-End
Temperature (°C)	113.8	104.3	130.3
Pressure (bar)	3.170	1.307	1.543
Mass Flow (kg/h)	23000	15750	7250
Mass Fractions			
n-hexane	303 ppm	442 ppm	2 ppb
n-heptane	0.362	0.401	0.278
Cis-Decalin	0.117	0.003	0.366

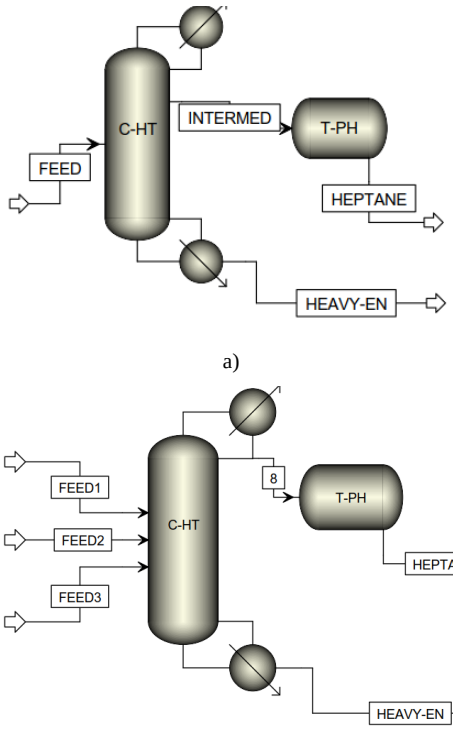

Figure 2. The alternative flowsheets for Scenario 2 (a) and Scenario 3 (b) .

C. Scenario 4: Change in Feed Stage

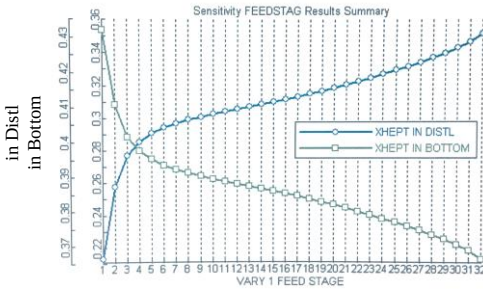

Figure 3. The distribution of heptane composition in the distillate and bottom stream based on various feed stages.

In this case, the sensitivity analysis tool is used for the investigation of the effect of different feed stage. As shown in Fig. 3, the feeding between eighteenth and twenty-seventh stages could increase the heptane composition in the distillate to 41.1% and 42.3%, respectively. At this point, the cost of recovered material should be higher than any repair cost in distillation in order to be acceptable case. Hence, it should be economically investigated whether the existing column design could be in accordance with this case.

D. Scenario 5: Change in Number of Stage

The heptane composition could be increase to 42.9% in case the maximum number of stages of 10. According to sensitivity analysis, the fractionation increases up to the tenth stage of the column. After that stage, the separation is affected negatively by the increase in the stage of column. Considering that the column consists of 32 stages in the base case, it can be understood that it is designed at the redundant height for heptane recovery (Fig. 4).

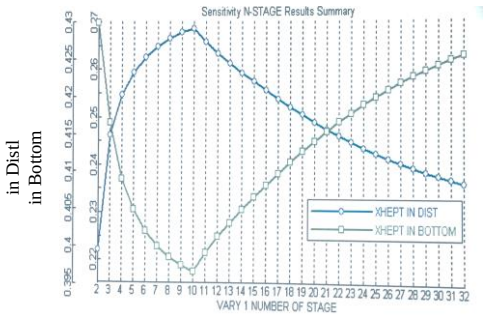

Figure 4. The distribution of heptane composition in the distillate and bottom stream based on the number of column stages.

E. Scenario 6: Change in Reflux Ratio

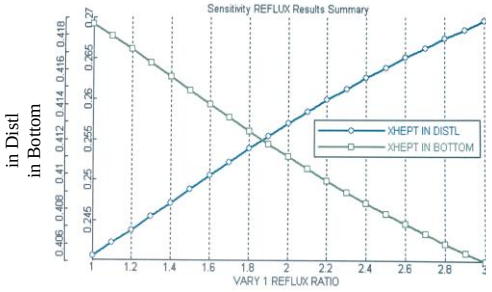

Figure 5. The distribution of heptane composition in the distillate and bottom stream based on the reflux ratio.

In the Scenario 6, the effect is investigated by the reflux ratios between 1 and 3. The composition of heptane in the distillate is increasing with increasing of reflux ratio as expected. At reflux ratios between 2.1 and 3, the heptane composition in the distillate can reach up to 41.8% (Fig. 5). If the reflux ratio has high, heat duty of system increases, and hence this case is not acceptable for a plant operating economically. At this point, the operating cost should be determined before the decision as observed in Scenario 4.

F. Effect of Reboiler Heat Duty

According to results, the maximum improvement at the composition (42.9%) was observed by the change in column stage. On the other hand, one difference between simulation result and real-time heat duty in the column reboiler was defined. Whereas heat duty is found as 2823849.91 kcal/h at the current mass flow rate in the reboiler model, the existing reboiler heat duty capacity is 2240000 kcal/h.

By sensitivity analysis, required total mass flow rate of feed was calculated based on the heat duty in the existing reboiler design. At this analysis, manipulated variable is selected as mass flow rate of feed and overall change in mass flow rate is adjusted between 1000 kg/h and 23000 kg/h with increment of 1000. While the nearest reboiler heat duty is calculated as 2239826.57 kcal/h, the appropriate mass flow rate is found as 18500 kg/h. Hence, the energy consumption also reduces by approximately 20% by changing the flow rate.

V. CONCLUSION

The aim of this case study is to reduce the heptane composition of the bottom stream of the

related-distillation column. The real-time data were collected from the plant in operation for reducing the unused waste heptane amount. The C-HT column was modified with suitable conditions and required constraints of company in the six cases, which includes the effect of change in feed type and stage, intermediate product, reflux ratio and number of column stage. In case of taking the product from intermediate stage on column, heptane composition in distillate was increased to 42.2% and that composition in bottom stream was decreased up to 2.9%. Although more effective results were also obtained from many scenarios, the maximum heptane composition in distillate was calculated as 42.9%. More suitable alternative was observed the renovate of distillation. Furthermore, the repairing and operating cost calculations must require for deciding. The most applicable retrofit was found at the column reboiler design. It was seen that the heat duty capacity of existing design was not enough for this column. As a result of the calculation of new feed flow rate, it was foreseen that it could be decreased from 23000 kg/h to 18500 kg/h. Thus, the energy consumption also reduces by approximately 20% by changing the flow rate.

REFERENCES

[1] Hohmann, E.C. (1971). *Optimization networks for heat exchange* [PhD thesis, University of Southern California].

[2] Agbo, A. F., Aboje, A. A., & Obayomi, K. S. (2019). Exergy analysis of Naphtha Hydrotreating Unit (NHU). *Journal of Physics: Conf. Ser. 3rd International Conference on Science and Sustainable Development (ICSSD 2019)*, *1299*, 012025.

[3] Rajan, G.G. (2006). *Practical Energy Efficiency Optimization*. USA: PennWell Coperation.

[4] Yoon, S.G., Lee, J., & Park, S. (2007). Heat integration analysis for an industrial ethylbenzene plant using pinch analysis. *Applied Thermal Engineering*, *27*, 886-893.

[5] Lu, X., Yi, J., Chen, S., Zu, F., & Li, R. (2012). Characterization of Impact Polypropylene Copolymers by Solvent Fractionation. *Chinese Journal of Polymer Science*, *30*(1), 122-129.

[6] Sato, H., & Ogawa, H. (2009). *Review on Development of Polypropylene Manufacturing Process*. Translated from R&D Report, "SUMITOMO KAGAKU", 2009-II.

[7] Liu, Y., Zhang, B., Fu, Z., & Fan, Z. (2017). Synthesis of polyethylene/poly(ethylene-co-propylene) in-reactor alloys by periodic switching polymerization process: Effects of switching frequency on polymer structure and properties. *Macromolecular Research volume 25*, 534–541.

[8] Cai, J. J., Hawboldt, K., & Abdi, M. A. (2016), Improving gas absorption efficiency using a novel dual membrane contactor. *Journal of Membrane Science 510*, 249-258

[9] Agne, A., & Barriere, T. (2017). Modelling and numerical simulation of Supercritical CO2 debinding of Inconel 718 components elaborated by Metal Injection Molding. *Applied Science 7*(10), 1024.

[10] Zhang, X., Liu, C., Yang, J., Zhu, C. Y., Zhang, L., & Xu, Z. K. (2020). Nanofiltration membranes with hydrophobic microfiltration substrates for robust structure stability and high water permeation flux. *Journal of Membrane Science, 593*, 117444.

[11] Narin, G., Ribeiro, A. M., Ferreira, A., Hwang, Y. K., Lee, U-H., Loureiro, J. M., Chang, J. S., & Rodrigues A. E. (2014). Propylene/Nitrogen Separation in a By-Stream of the Polypropylene Production: From Pilot Test and Model Validation to Industrial Scale Process Design and Optimization. *Industrial & Engineering Chemistry Research, 53*, 9199−9213.

[12] Chaniago, Y. D., Lee, M. (2018). Distillation design and optimization of quaternary azeotropic mixtures for waste solvent recovery. *Journal of Industrial and Engineering Chemistry 67*, 255–265.

[13] Lu, M., Zhao, X., Zhou, J., Qian, G., Duan, X., Yuan, W., & Zhou, X. (2019). Solvent Screening and Process Optimization for Separating Propylene Oxide from Direct Propylene Epoxidation with H2 and O2. *Ind. Eng. Chem. Res., 58*, 395−402.

[14] Pekar, T., Choksi, N., & Joshipura, M. (2020). Simulation Studies of n-Heptane/Toluene Separation by Extractive Distillation Using Sulfolane, Phenol and NMP. In *Proceedings of the International Conference on Advances in Chemical Engineering (AdChE)*. Available at: https://ssrn.com/abstract=3679379

[15] Kianinia, M., & Abdoli, S. M., (2021). The Design and Optimization of Extractive Distillation for Separating the Acetone/n-Heptane Binary Azeotrope Mixture. *ACS Omega, 6*, 22447−22453.

[16] Zhang, F., Sun, D., Li, Y., Shan, B., Ma, Y., & Wang, Y. (2022). Heat integration and dynamic control for separating the ternary azeotrope of butanone/isopropanol/n-heptane via pressure-swing distillation. *Chemical Engineering & Processing: Process Intensification, 170*, 108657.

[17] Hou, W., Zhang, Q., & Zeng, A. (2021). Separation of n-heptane/isobutanol via eco-efficient vapor recompression-assisted distillation: process optimization and control strategy, *Front. Chem. Sci. Eng., 15(5)*, 1169–1184.

Structural, Microstructural and Optical Propreties of ZnO/MgO Thin Films Prepared by Spray Pyrolysis Method

Sabrina Roguai[1], Abdelkader Djelloul[2]

[1,2]Department of Science of the Matter, Abbes Laghrour University, Khenchela, Algeria, rog.sabrina@yahoo.fr[1], djelloulabdelkader@yahoo[2] tr

Abstract—**The thin layers of ZnOx%/MgO [x=30, 40 and 50 at%], were prepared by the spray pyrolysis method on glass substrates at 450°C, then tested for methyl blue (MB) degradation under visible irradiations. The ZnOx%/MgO [x=30,40 and 50 at%] thin films were analysed by X-ray diffraction (XRD), scanning electron microscopy (SEM), and UV–Vis spectroscopy. X-ray diffraction analysis revealed that the layers have a polycrystalline nature of hexagonal (wurtzite) and cubic structure. Microstructures the films were also analyzed using scanning electron. The films show a radical change in the surface morphology in accordance with the XRD results. The above analyses confirm the co-existence of a mixture of the wurtzite (ZnO) structure and cubic phase of MgO. For optical properties It was confirmed that the ZnO50%/MgO had a profound effect on reduction of band gap.**

Keywords - ZnOx%/MgO thinfilms, structural, microstructural, and optical properties

I. INTRODUCTION

Oxides semiconductor in the form of thin-film, and in particular zinc oxide (ZnO), have been the subject of a great deal of research work. The development of these materials is linked to their interesting physical properties. ZnO is a semiconductor exhibiting an attractive electrical and optical properties. The importance of its exciton binding energy (60 meV), and the width of its forbidden band (3.37 eV) [1].

This diversity means that ZnO could find many applications in different fields such as optoelectronics, acousto-optics, piezoelectric and as a gas detector photocatalysts and light emitting diodes (LEDs) [2]. In addition, ZnO has attracted a lot of interest as a semiconductor photocatalyst, as a powder [3], nanoparticle [4] or thin film [5]. It should be noted that the photocatalytic properties of ZnO are directly linked to its structure, morphology and crystallite size, which in turn depend on the ZnO preparation method. In addition, doping ZnO with metallic elements can also improve its photo-catalytic properties.

The objective of this work is the development of ZnOx%/MgO [x=30, 40 and 50 at%] thin layers diluted by the technique of ultrasonic spray pyrolysis, on glass substrates. The structural, morphological, and optical characterization of the samples were performed.

II. EXPERIMENTAL METHODS

A. Film Preparation

The ultrasonic pyrolysis spray method is used as a main method to develop ZnOx%/ MgO [x=30, 40 and 50 at%] thin layers [6–8]. In this work, we will change the quantities of solvents, the deposition time as well as the fow rate in order to obtain very homogeneous layers. We have used the following precursors: Zinc acetate ($C4H_6O_4Zn{\cdot}2H_2O$) (Fulka 99.9%); and magnesium acetate Mg (CH_3COO) (Fulka 99.9%); as the source material for Zn and Mg, which were dissolved in5 ml of methanol (Merck 99.5%) and 7.5 ml ethanol (Merck 99.5%) mixed with12.5 ml of deionized water (resistivity 18.2 MO cm). The solution is mixed for 1 h using a heating magnetic stirrer. Thin films were deposited onto microscope cover glass substrates ($30\times10\times1.2$ mm^3), with solution fow rate

ISBN: 978-86-80593-73-9

0.25 ml/min, at temperature of 450°C and the testimony time was fixed at 1 h.

B. Characterization Techniques

For the structural properties X-ray diffraction was performed using X-ray difractometer (MiniFlex600) with Cu Kα radiation, 0.15418 nm). The morphology of the films was examined by scanning electron microscopy (TESCAN_VEGA3) equipped with energy dispersive X-ray spectroscopy (EDS) for chemical analysis. The optical properties are determined by measuring the transmittance of the films using a SpectroScan 80D spectrophotometer UV–Vis in the 190–1100 nm spectral range.

III. Results and Discussion

A. Structure Analysis

Fig. 1 shows the typical XRD patterns of all prepared samples in the 2θ range of 10–80°. The data show the presence of phase mixtures characterized by the following peaks, related to (100) (002) (101) characteristic of the wurtzite phase of ZnO according to the map (00-036-1451) [9–11], while the peak around 2θ=29° can be assigned to the MgO phase according to the map (00-030-0794). Therefore, no preferential orientation was observed, yet three directions, with varying intensities were detected because of the Mg content (x=0.3, 0.4 and 0.5) which is clearly higher than the thermodynamic solubility limit (x=0.04) [12]. The intensity of the peaks varies according to the rate of Mg in the films is due to the insertion of Mg in the ZnO network, we notice that the most intense characteristic peak of the wurtzite phase (002) at 34°, gradually decrease to a minimum intensity at a concentration of (50%), and the same chosen for the peak (100) is that this indicates that the wurtzite structure is degraded at this concentration, the fact that the position of the peak relative to the plane (002) is greater than the position of the reference peak (undoped ZnO), thus, indicating the presence of internal stresses in the material when the foreign atoms are inserted into the crystal lattice. The other part of the peak intensity of the MgO phase increases with the level of Mg in the films and takes a maximum intensity at a rate of 40%.

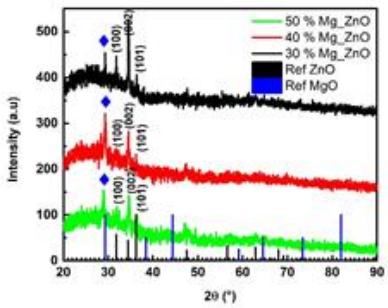

Figure 1. XRD patterns of ZnO/MgO thin films.

B. Microstructural Observations

Fig. 2a–c show the top view SEM images of the MZO thin layers obtained on glass substrates by polarysis spray. In these fgures, the surface of the MZO thin films are completely covered by aggregates. For $Zn_{0.70}Mg_{0.30}O$ films, it is characterized by the presence of grains in the form of nano-dots and nanotubes (nanopetals) distributed over the entire surface of the substrate. While, in the case of the $Zn_{0.60}Mg_{0.40}O$ and $Zn_{0.50}Mg_{0.50}O$ layers it is well illustrated that the surface is made of aggregates between grains in the form of nanoderms, between them other

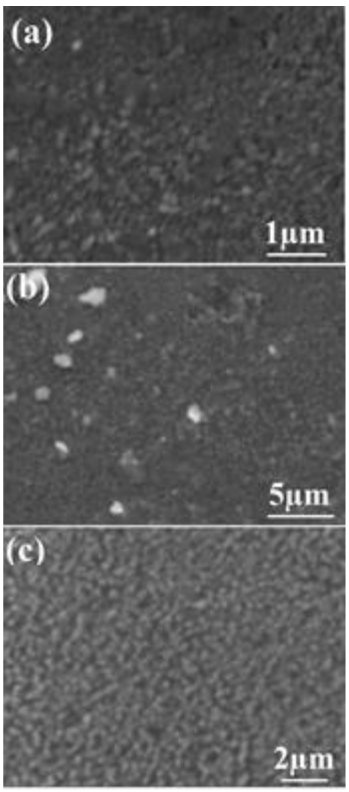

Figure 2. SEM images of (a–c) ZnOx%/MgO thin films. The images a, b and c correspond to the Mg atomic content of 30%, 40% and 50%, respectively.

morphology of the MgO phase which appears in the form of black pores through these nano-grains. These increase with the level of Mg which explains by the difference between the ionic rays Zn^{2+}(0.083 nm) and Mg^{2+}(0.078 nm) and which confirms the insertion of Mg into the ZnO network which induces a stress causing pores in the thin flm leading to increase with the rate of dilution [13]. It is important to note that the porosity of the films increases the surface accessibility of the material, which is suitable for catalytic applications as will be shown hereafter.

C. Energy Dispersive Spectroscopy (EDS) Analysis

The chemical compositions of ZnOx%/MgO [x=30, 40, 50 at%] were determined from EDS analysis. The elemental analysis spectrum represented in Fig. 3, clearly indicates the presence of the emission lines of zinc, oxygen and magnesium. However, two additional emission lines that are attributed to silicon and calcium were also observed. The presence of this chemical element originates from the glass substrates, and the high intensity of these two peaks explained by the low thickness of the thin films [6–8]

D. Optical Absorption

Fig. 4 shows the transmission spectra of MZO thin films as a function of wavelength in the range 190–1100 nm. The appearance of all the transmission spectra measured in our samples is the same. In the visible region, the samples exhibit an average T transmission varying between 76 and 78% over a wide wavelength range from 400 to 1100 nm, which gives MZO films the character of thin transparent layers that can be used as optical windows for solar cells.

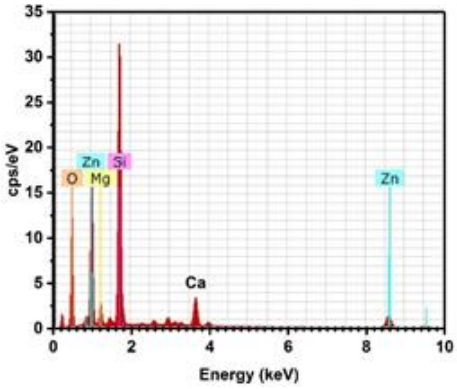

Figure 3. Example of EDS spectrum recorded for $Zn_{0.70}Mg_{0.30}O$ thin.

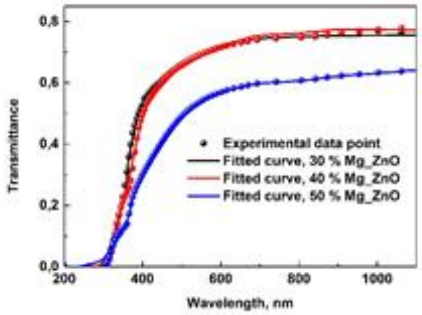

Figure 4. Transmission spectra of ZnOx%/MgO thin films deposited on glass substrate at 450 °C. Measured (full circles) and calculated (solid lines) transmittance spectra of films.

TABLE I. DISPERSION PARAMETERS OF THE ZNOX%/MGO THIN FILMS EXTRACTED BY FITTING THE EXPERIMENTAL DATA.

Samples	**Thickness (nm)**	**Eg (eV) ZnO**	**Eg (eV) MgO**
30%Mg_ZnO	196	3.62	3.84
40%Mg_ZnO	204	3.28	3.82
50%Mg_ZnO	219	3.23	3.84

The dispersion parameters of the films were evaluated using a single-effective-oscillator ft, proposed by Wemple et al. [6–8, 14]. The solid line in Fig. 4 correspond to the curve fitting and the symbols represent the experimental data, the experimental data are listed in Table I.

We observed that the gap energy of diluted ZnO is greater than that of pure ZnO [6–8]. This has been attributed to the disorder generated by the defects in the ZnO matrix.

IV. CONCLUSION

During this study, we developed by spray pyrolysis, thin films of ZnOx%/MgO [x=30,40, and 50 at%] deposited on glass substrates at 450 °C. We have also studied the infuence of the Mg on structural, microstructural, and optical properties of MZO thin films. Magnesium dilution was found to introduce pores on the surface of the films and deteriorate the crystallinity movies with mixture structure

wurtzite and cubic (ZnO + MgO). The transmission spectra of MZO thin films indicate that the films is transparent in the visible and opaque in the UV. The optical bandgap calculation of films increases with increasing dilution concentration with Mg.

ACKNOWLEDGMENT

The authors would like to thank the National Project Research (PNR) and LASPI2A Laboratory of Khenchela University (Algeria) for their financial support of this research project.

REFERENCES

[1] Li, Y., Liu, X., & Li, J. (2010). Preparation and characterization of CeO2 doped ZnO nano–tubes fluorescent composite. *Journal of Rare Earths, 28*, 571-575.

[2] Huang, Z. et al. (2017). Modified bentonite adsorption of organic pollutants of dye wastewater. *Mater. Chem. Phys*, *202*, 266-276.

[3] Hosseini–Sarvari, M., Ataee–Kachouei, T., & Moeini, F. (2015). A novel and active catalystAg/ZnO for oxidant–free dehydrogenation of alcohols. *Materials Research Bulletin, 72*, 98-105.

[4] Hariharan, C. (2006). Photocatalytic degradation of organic contaminants in water by ZnO nanoparticles. *Revisited. Applied Catalysis A: General*, *304*, 55-61.

[5] Lv, J. et al. (2011). Effect of annealing temperature on photocatalytic activity of ZnO thin films prepared by sol–gel method. *Superlattices and Microstructures, 50*, 98-106.

[6] Roguai, S., & Djelloul, A., (2019). Synthesis and evaluation of the structural, microstructural, optical and magnetic properties of Zn1−xCoxO thin films grown onto glass substrate by ultrasonic spray pyrolysis. *Appl Phys A, 125*, 816.

[7] Roguai, S., & Djelloul, A., (2020). A structural and optical properties of Cu–doped ZnO films prepared by spray pyrolysis. *Appl Phys A, 126*, 122.

[8] Segnit, E.R., & Holland, A.E. (1965). The System MgO-ZnO-SiO2. *Ceram Soc*, *48*, 412.

[9] Jiao, S.J. et al. (2007). Donor–acceptor pair luminescence of nitrogen doping p–type ZnO by plasma–assisted molecular beam epitaxy. *J Lumines, 122*, 368–370.

[10] Savchuk, A.I., Fediv, V.I., Savchuk, S.A., & Perrone, A. (2005). Growth and characterization of ZnMnO thin films. *Superlattices Microstruct*, *38*, 421-427.

[11] Tsay, C.T., Fan, K.S., & Lei, C.M. (2012). Synthesis and characterization of sol–gel derived gallium– doped zinc oxide thin films. *J Alloys Compds, 512*, 216–222.

[12] Choopun, S., Vispute, R.D., Yang, W., Sharma, R.P., Venkatesan, T., & Shen, H.(2002). Realization of band gap above 5.0 eV in metastable cubic- phase MgxZn1−xOMgxZn1−xO alloy films. *Appl Phys Lett, 80*, 1529.

[13] Wemple, S.H., & DiDomenico, M. (1971). Behavior of the electronic dielectric constant in covalent and ionic materials. *Phys Rev B, 3*, 1338-2135.

[14] Xin, M. (2019). Optical properties of nanostructured ZnO: Eu flm by sol–gel method. *Surf Eng, 35*, 947-953.

The MCDM Approach for Evaluation of the Projects in the Energy Sector

Gabrijela Popović[1], Dragiša Stanujkić[2], Darjan Karabašević[3]

[1,3]Faculty of Applied Management, Economics and Finance, Belgrade, Serbia, gabrijela.popovic@mef.edu.rs[1], darjan.karabasevic@mef.edu.rs[3]
[2]Technical Faculty, Bor, Serbia, dstanujkic@tfbor.bg.ac.rs

Abstract—**The main objective of this paper is to emphasize the possibilities of the application of the *Multiple-Criteria Decision-Making – MCDM* methods in the facilitation of the decision-making process in the electric energy sector. For that matter, an objective-subjective approach is proposed. For determination of the criteria weights, the objective weighting method named the *MEthod based on the Removal Effects of Criteria – MEREC* and subjective weighting method named the *PIvot Pairwise RElative Criteria Importance Assessment – PIPRECIA* are used. The final ranking of the alternatives is performed by using the *Simple Weighted Sum Product – WISP* method. The applicability of the proposed approach is demonstrated through a real case study regarding the projects for new production capacities development in the electric energy sector. Thirteen alternative projects are evaluated against four criteria, and the evaluation process is performed in the group decision environment. The obtained results are reliable and adequate, and confirm the adequacy of the application of the MCDM methods in the decision process in the energy sector.**

Keywords – MEREC method, PIPRECIA method, WISP method, projects, electric energy sector

I. INTRODUCTION

Making a decision is a very complex task despite the type of problem which should be resolved, as well as the business field. A final decision is influenced by many different and often conflicting criteria. To obtain the best possible solution and make the optimal decision it is necessary to involve each of the influential criteria in the decision process. In that sense, the Multiple-Criteria Decision-Making (MCDM) methods is very useful. Until now many decision-making methods have been proposed [1-10]. Also, these methods were used for facilitation the decision process in various business areas which is proved by following research studies [11-17]. As in the other business fields, the MCDM techniques could be useful as decision-making assistance in the energy sector as well.

This paper proposes the approach based on the objective and subjective MCDM methods as an aid for performing the decision-making process in the electric energy sector. Namely, the Ministry of the Mining and Energy of the Republic of Serbia prepared a document named *Energy Sector Development Strategy of the Republic of Serbia for the period by 2025 with projections by 2030* [18]. which contains the list of projects and their main performances directed to the construction of new production capacities of the electric energy sector. To define the most appropriate project from the given list which should have the priority for investment, the objective-subjective MCDM approach is proposed. The MEthod based on the Removal Effects of Criteria – MEREC [19] and PIvot Pairwise RElative Criteria Importance Assessment – PIPRECIA [20] are used for defining the criteria significance, while the alternatives are evaluated and ranking with help of the Simple Weighted Sum Product – WISP method [21]. All the proposed methods are relatively recently introduced and their potentials are not fully examined yet. The main scientific intention is to highlight the potential that MCDM methods have, as well as to present the possibilities of the methods on which the proposed approach in this paper is based.

II. THE METHODOLOGY

A. The MEREC Method

The first method used for defining the criteria significance is the recently proposed MEREC

method [19]. This method belongs to the objective type of weighting methods whose application is based on the input data. Considering that the MEREC method is relatively new, there is not much research paper that provides insight into its potential and possibilities [22-23].

The calculation procedure of the MEREC method could be precisely illustrated by using the following steps.

Step 1. Creation of a decision-making matrix:

$$X = \begin{bmatrix} x_{11} & x_{12} & \cdots & x_{1j} & \cdots & x_{1m} \\ x_{21} & x_{22} & \cdots & x_{2j} & \cdots & x_{2m} \\ \vdots & \vdots & \ddots & \vdots & \ddots & \vdots \\ x_{i1} & x_{i2} & \cdots & x_{ij} & \cdots & x_{im} \\ \vdots & \vdots & \ddots & \vdots & \ddots & \vdots \\ x_{n1} & x_{n2} & \cdots & x_{nj} & \cdots & x_{nm} \end{bmatrix}, \quad (1)$$

where x_{ij} denotes the performance rating of alternative i in relation to criterion j ($x_{ij} > 0$), n are alternatives and m are criteria.

Step 2. Normalization of the decision-making matrix in the following way:

$$n_{ij}^{x} = \begin{cases} \dfrac{\min\limits_{k} x_{kj}}{x_{ij}} \; if \; j \in B \\ \dfrac{x_{ij}}{\max\limits_{k} x_{kj}} \; if \in C \end{cases}, \quad (2)$$

where n_{ij}^{x} denotes elements of the normalized matrix N, B is the set of benefit criteria, and C is the set of cost criteria.

Step 3. Calculation of the overall performance of the alternatives as is shown:

$$S_i = \ln\left(1 + \left(\frac{1}{m}\sum\nolimits_{j} \left|\ln(n_{ik}^{x})\right| ij\right)\right), \quad (3)$$

where S_i denotes the overall performance of the alternatives.

Step 4. Calculation of the alternatives` performances by removing each criterion as follows:

$$S_{ij} = \ln\left(1 + \left(\frac{1}{m}\sum\nolimits_{k,k\neq j} \left|\ln(n_{ik}^{x}\right| ij\right)\right), \quad (4)$$

where $S_{ij}^{'}$ represents the overall performance of alternative i regarding the removal of criterion j.

Step 5. Calculation of the total of the absolute deviations. The removal effect of the criterion j is calculated by using Eq. (5):

$$E_j = \sum\nolimits_{i} \left|S^{'}_{ij} - S_i\right|, \quad (5)$$

where E_j denots the effect of removing criterion j.

Step 6. Determination of the overall criteria weights. The final value of the criteria significance is determined in the following way:

$$W_j = \frac{E_j}{\sum_k E_k}, \quad (6)$$

where w_j denotes the weight of the criterion j.

B. The PIPRECIA Method

The second method used for defining the criteria significance is the PIPRECIA method [20]. This method belongs to the group of subjective weighting methods. To avoid the subjectivization of the results, three decision-makers will be involved in the evaluation procedure of the considered criteria. Until now, the PIPRECIA method is used for defining the criteria weights of various criteria [24-30].

The calculation procedure of the PIPRECIA method could be presented by following a series of steps.

Step 1. Evaluation criteria selection. Pre-sorting of the criteria according to the expected significance is not obligatory.

Step 2. Determination of the relative importance s_j, starting from the second criterion, in the following way:

$$s_j = \begin{cases} >1 \; when \; C_j \succ C_{j-1} \\ 1 \; when \; C_j = C_{j-1} \\ <1 \; when \; C_j \prec C_{j-1} \end{cases}. \quad (7)$$

Step 3. Determination of the coefficient k_j as follows:

$$k_j = \begin{cases} 1 & j = 1 \\ 2 - s_j & j > 1 \end{cases}. \quad (8)$$

Step 4. Calculation of the recalculated value q_j, in the following manner:

$$q_j = \begin{cases} 1 & j = 1 \\ \dfrac{q_{j-1}}{k_j} & j > 1 \end{cases}. \quad (9)$$

Step 5. Determination of the relative criteria weights as follows:

$$w_j = \frac{q_j}{\sum_{k=1}^{n} q_k}, \quad (10)$$

where w_j indicates the relative weight of the criterion j.

Step 6. When more decision-makers are engaged in the decision process, then the overall criteria significances are determined as follows:

$$w_j^* = \left(\prod_{r=1}^{R} w_j^{nr}\right)^{1/R}, \quad (11)$$

$$w_j = \frac{w_j^*}{\sum_{j=1}^{n} w_j^*}, \quad (12)$$

where w_j^{nr} signifies the significance of the criterion j that is defined by the respondent r, R denotes the total number of the respondents, w_j^* is group weight of criterion j before its adjusting in order to fulfill the condition $\sum_{j=1}^{n} w_j = 1$, and w_j depicts the overall significance of criterion j.

C. The WISP Method

For the final ranking of the considered projects regarding the construction of an appropriate type of power plant, the WISP method is applied [21]. This method is recently proposed and its capabilities and applicability have not been tested yet.

The calculation procedure of the WISP method could be illustrated by using the following series of steps.

Step 1. Formation of the normalized decision-making matrix in the following way:

$$r_{ij} = \frac{x_{ij}}{\max_i x_{ij}}, \quad (13)$$

where r_{ij} signifies a dimensionless number that denotes a normalized rating of alternative i regarding the criterion j.

Step 2. Calculation of the four utility measures values in the following way:

$$u_i^{wsd} = \sum_{j\in\Omega_{\max}} r_{ij} w_j - \sum_{j\in\Omega_{\min}} r_{ij} w_j, \quad (14)$$

$$u_i^{wpd} = \prod_{j\Omega_{\max}} r_{ij} w_j - \prod_{j\Omega_{\min}} r_{ij} w_j, \quad (15)$$

$$u_i^{wsr} = \frac{\sum_{j\in\Omega_{\max}} r_{ij} w_j}{\sum_{j\in\Omega_{\min}} r_{ij} w_j}, \quad (16)$$

$$u_i^{wpr} = \frac{\prod_{j\in\Omega_{\max}} r_{ij} w_j}{\prod_{j\in\Omega_{\min}} r_{ij} w_j}, \quad (17)$$

where: u_i^{wsd} and u_i^{wpd} ilustrate differences between the weighted sum and weighted product of normalized ratings of alternative i, respectively. As in the previous case, u_i^{wsr} and u_i^{wpr} denotes ratios between weighted sum and weighted product of normalized ratings of alternative i, respectively.

Step 3. Recalculation of the four utility measures values as follows:

$$\bar{u}_i^{wsd} = \frac{1 + u_i^{wsd}}{\left(1 + u_{\max_i}^{wsd}\right)}, \quad (18)$$

$$\bar{u}_i^{wsd} = \frac{1 + u_i^{wpd}}{\left(1 + u_{\max_i}^{wpd}\right)}, \quad (19)$$

$$\bar{u}_i^{wsr} = \frac{1 + u_i^{wsr}}{\left(1 + u_{\max_i}^{wsr}\right)}, \quad (20)$$

$$\bar{u}_i^{wpr} = \frac{1 + u_i^{wpr}}{\left(1 + u_{\max_i}^{wpr}\right)}, \quad (21)$$

where: $\bar{u}_i^{wsd}$, $\bar{u}_i^{wpd}$ $\bar{u}_i^{wsr}$ and $\bar{u}_i^{wpr}$ ilustrate recalculated values of u_i^{sd}, u_i^{pd}, u_i^{sr} and u_i^{pr}.

Step 4. Definition of the overall utility u_i of each alternative in the following manner:

$$u_i = \frac{1}{4}\left(\bar{u}_i^{wsd} + \bar{u}_i^{wpd} + \bar{u}_i^{wsr} + \bar{u}_i^{wpr}\right). \quad (22)$$

Step 5. Ranking of the alternatives in descending order and selecting the optimal one. The optimal alternative is the one that has the highest value of u_i.

III. A CASE STUDY

With the aim of presenting the possibilities of using the MCDM techniques in the field of energetics, the real case study is utilized. This case study is pointed to the construction of the new capacities for power production. More precisely, the case study is directed to ranking and isolating the optimal alternative type of power plant which includes: thermal power plant (TPP), combined heat and power plants (CHP), hydropower plant (HPP), and pumped storage hydropower plants (PSHP). Data about the considered projects for construction of these power plants as well as their characteristics are taken over from the *Energy Sector Development Strategy of the Republic of Serbia for the period by 2025 with projections by 2030* [18]. Alternative projects submitted under evaluation are:

- A_1 – TENT B3
- A_2 – TPP Kolubara B
- A_3 – TPP Kostolac
- A_4 – TPP Novi Kovin
- A_5 – TPP Štavalj
- A_6 – CHP Novi Sad
- A_7 – Natural gas fired CHP
- A_8 – HPP Velika Morava
- A_9 – HPP Ibar
- A_{10} – HPP Middle Drina
- A_{11} – PSHP Bistrica
- A_{12} – PSHP Djerdap 3
- A_{13} – Mini HPP

Criteria on which the evaluation procedure is based are as follows:

- C_1 – Installed capacity (MW)
- C_2 – The estimated time necessary for project implementation (years)
- C_3 – Approximate investment value (€)
- C_4 – The impact on the environment (points form 1 – the smallest impact to 10 – the greatest impact)

Criterion C_4 is not anticipated in the mentioned *Strategy* and represents the estimation of involved decision-makers in the light of the current situation regarding the impact on the environment.

The data about the considered alternative projects are presented in Table I.

First, the objective weighting MEREC method is applied for the determination of the criteria significance. The normalized performance ratings of alternatives are calculated by using (2) and they are presented in Table II.

TABLE I. INPUT DATA.

	C_1	C_2	C_3	C_4
	MW	***years***	***bil. €***	***points***
	max	***min***	***min***	***min***
A_1	750	5	1.6	9.9
A_2	375	6	1.5	9.9
A_3	350	4	0.45	9.8
A_4	350	6	1.33	8.8
A_5	300	5	0.75	8.6
A_6	340	2.5	0.4	7.5
A_7	860	4	1.5	4.5
A_8	147.7	5	0.36	5.9
A_9	117	4.5	0.3	5.1
A_{10}	321	7	0.819	5.8
A_{11}	170	5	0.56	5.7
A_{12}	300	5	0.4	5.4
A_{13}	387	3	0.5	7.9

TABLE II. THE NORMALIZED DECISION MATRIX.

	C_1	C_2	C_3	C_4
A_1	0.156	0.714	1.000	1.000
A_2	0.312	0.857	0.938	1.000
A_3	0.334	0.571	0.281	0.999
A_4	0.334	0.857	0.831	0.889
A_5	0.39	0.714	0.469	0.869
A_6	0.344	0.357	0.25	0.758
A_7	0.136	0.571	0.938	0.455
A_8	0.792	0.714	0.225	0.596
A_9	1.000	0.643	0.188	0.515
A_{10}	0.364	1.000	0.512	0.586
A_{11}	0.688	0.714	0.35	0.576
A_{12}	0.39	0.714	0.25	0.545
A_{13}	0.302	0.857	0.313	0.780

The overall performance ratings of alternatives are defined by using (3). The obtained results are presented in Table III.

The overall performances of alternatives that implies removing each criterion (S'_{ij}) are obtained by using (4). Table IV presents all defined S'_{ij} values.

TABLE III. THE OVERALL PERFORMANCES OF ALTERNATIVES.

	S_i
A_1	0.44
A_2	0.30
A_3	0.55
A_4	0.33
A_5	0.43
A_6	0.66
A_7	0.62
A_8	0.50
A_9	0.53
A_{10}	0.44
A_{11}	0.46
A_{12}	0.60
A_{13}	0.52

TABLE IV. S'_{ij} VALUES.

	C_1	C_2	C_3	C_4
A_1	0.08	0.38	0.44	0.44
A_2	0.05	0.27	0.28	0.30
A_3	0.38	0.47	0.35	0.55
A_4	0.11	0.30	0.29	0.31
A_5	0.27	0.38	0.30	0.41
A_6	0.51	0.52	0.47	0.63
A_7	0.30	0.54	0.61	0.50
A_8	0.46	0.45	0.24	0.42
A_9	0.53	0.46	0.24	0.42
A_{10}	0.27	0.45	0.33	0.36
A_{11}	0.40	0.40	0.27	0.36
A_{12}	0.50	0.55	0.39	0.51
A_{13}	0.33	0.50	0.34	0.49

Decision-makers calculate the removal effect of each criterion on the overall performance of the alternatives by using (5). Table V contains the results regarding mentioned removal effect of each criterion on the overall performance of alternatives (E_j).

The final weights of criteria are obtained by using (6), and they are presented in Table VI.

TABLE V. E_j VALUES.

	E_j
C_1	2.19
C_2	0.73
C_3	1.83
C_4	0.68

TABLE VI. THE CRITERIA WEIGHTS.

	w_j^1
C_1	0.40
C_2	0.13
C_3	0.35
C_4	0.13

As Table VI shows, the obtained results gained by using the MEREC method emphasize the criterion C_1 – *Installed capacity*, which is followed by the C_3 – *Approximate investment value.* The same significance is assigned to the criteria C_2 – *The estimated time necessary for project implementation* and C_4 – *The impact on the environment.*

Now, the subjective criteria weights are defined by using the PIPRECIA method in the group decision environment. In this case, three decision-makers familiar with the considered topic were involved in the evaluation process.

Table VII presents the criteria significance obtained from the first decision-maker, which is determined by using (7)-(10). As can be seen from Table VII, the criterion that has the greatest significance according to the first decision-maker is C_3 – *Approximate investment value*. The least significance has the criterion C_1 – *Installed capacity*.

Table VIII shows the criteria significances determined by the second decision-maker. In this case, (7)-(10) are again used for obtaining the weights. According to the second decision-maker, all the considered criteria have the same significance.

Table IX presents the evaluation results obtained from the third decision-maker. Once again, (7)-(10) are applied for defining the criteria weights.

TABLE VII. THE CRITERIA WEIGHTS OBTAINED BY THE FIRST DECISION-MAKER.

Criteria	s_j	k_j	q_j	w_j^2
C_1		1	1	0.21
C_2	1.15	0.85	1.18	0.24
C_3	1.15	0.85	1.38	0.29
C_4	0.90	1.10	1.26	0.26
			4.82	1.00

TABLE VIII. THE CRITERIA WEIGHTS OBTAINED BY THE SECOND DECISION-MAKER.

Criteria	s_j	k_j	q_j	w_j^3
C_1		1	1	0.25
C_2	1.00	1.00	1.00	0.25
C_3	1.00	1.00	1.00	0.25
C_4	1.00	1.00	1.00	0.25
			4.00	1.00

TABLE IX. THE CRITERIA WEIGHTS OBTAINED BY THE THIRD DECISION-MAKER.

Criteria	s_j	k_j	q_j	w_j^4
C_1		1	1	0.24
C_2	1.00	1.00	1.00	0.24
C_3	1.05	0.95	1.05	0.26
C_4	1.00	1.00	1.05	0.26
			4.11	1.00

Third decision-maker assigned equal significance to the first placed criteria which are as follows: C_3 – *Approximate investment value* and C_4 – *The impact on the environment*. Criteria C_1 – *Installed capacity* and C_2 – *The estimated time necessary for project implementation* are slightly less significant according to the opinion of the third decision-maker.

As can be concluded, the objective weighting method – MEREC gives different results from the subjective weighting method – PIPRECIA. Besides, each of the decision-makers has a different perspective on the significance of the criteria. Because of all said, the overall criteria weights are determined by the help of (11) and (12), and presented in Table X.

Since the criteria significances are determined, now the WISP method for final evaluation of the alternative projects could be applied.

Table XI presents the recalculated values of four utility measures obtained by using (18)-(21).

TABLE X. THE OVERALL CRITERIA WEIGHTS.

	MEREC	**PIPRECIA**			w_j
	w_j^1	w_j^2	w_j^3	w_j^4	
C_1	0.40	0.21	0.25	0.24	**0.27**
C_2	0.13	0.24	0.25	0.24	**0.22**
C_3	0.35	0.29	0.25	0.26	**0.29**
C_4	0.13	0.26	0.25	0.26	**0.22**

By (22) the final ranking of the considered projects is performed and it is presented in Table XII.

According to the results presented in Table XII, the most suitable alternative project is A_6 – *CHP Novi Sad*. That means that this project should have priority for investing, according to the given conditions. The evaluation procedure points to the alternative A_2 – *TPP Kolubara B* as

the least desirable. This result probably caused the highest amount of approximate investment and a very high negative impact on the environment.

TABLE XI. RECALCULATED VALUES OF FOUR UTILITYMEASURES.

	$\bar{u}_i^{wsd}$	$\bar{u}_i^{wpd}$	$\bar{u}_i^{wsr}$	$\bar{u}_i^{wsd}$
A_1	-0.5382	0.1802	0.2313	0.2071
A_2	-0.7052	0.0853	0.1135	0.0920
A_3	-0.3950	0.0860	0.1692	0.4339
A_4	-0.6453	0.0808	0.1154	0.1090
A_5	-0.4885	0.0720	0.1276	0.2034
A_6	-0.2641	0.0845	0.2197	0.9915
A_7	-0.2792	0.2129	0.3563	0.6966
A_8	-0.3843	0.0360	0.0862	0.3042
A_9	-0.3409	0.0287	0.0781	0.3717
A_{10}	-0.4943	0.0772	0.1334	0.2111
A_{11}	-0.4153	0.0410	0.0911	0.2330
A_{12}	-0.3180	0.0741	0.1772	0.6075
A_{13}	-0.2988	0.0958	0.2206	0.7142

TABLE XII. THE FINAL RANKING ORDER OF THE ALTERNATIVES.

	u_i	*Rank*
A_1	0.0201	7
A_2	-0.1036	13
A_3	0.0735	5
A_4	-0.0850	12
A_5	-0.0214	11
A_6	0.2579	1
A_7	0.2467	2
A_8	0.0105	8
A_9	0.0344	6
A_{10}	-0.0181	10
A_{11}	-0.0126	9
A_{12}	0.1352	4
A_{13}	0.1830	3

IV. CONCLUSION

The main goal of this paper was to emphasize the suitability and applicability of the MCDM methods for the facilitation of the decision process in the area of energetics. In this particular case, by applying a multiple-criteria approach, the projects that point to the improvement of the current production capacities of the electric energy sector were evaluated and ranked. For that matter, the approach based on the objective-subjective weighting methods is proposed. More precisely, the criteria weights were obtained by using the MEREC method that belongs to the objective weighting methods, and the PIPRECIA method that belongs to the subjective weighting methods. Besides, three decision-makers were involved in the application of the PIPRECIA method. The intention was to obtain as realistic criteria weights as possible. Finally, for the evaluation and ranking of the alternative projects recently proposed the WISP method is used. Applied multiple-criteria framework enabled obtaining of the reliable and adequate results and proved its efficiency and reliability in the decision-making process in the field of energetics.

As in other research studies, this one has certain limitations, too. First, only four criteria are involved in the decision-making procedure. It would be better if the evaluation is based on a greater number of criteria. To obtain the real picture of the environment and performances of the projects it is necessary to include technical, economic, and environmental aspects important for this kind of project. Second, the evaluation will be more accurate if the fuzzy, grey, or neutrosophic numbers are involved. In that way, the vagueness of the environment would be better expressed. Then, it would be desirable to involve a greater number of decision-makers from the energy sector in the decision-process. But, besides mentioned limitations, it is proved that the application of the multiple-criteria techniques in the energy sector is justified and adequate.

REFERENCES

[1] Churchman, C. W., & Ackoff, R. L. (1954). An approximate measure of value. *Journal of the Operations Research Society of America*, *2*(2), 172-187.

[2] Fishburn, P. C. (1967). Letter to the editor—additive utilities with incomplete product sets: application to priorities and assignments. *Operations Research*, *15*(3), 537-542.

[3] Saaty, T. L. (1980). *The Analytic Hierarchy Process: planning, priority setting, resource allocation*. New York: McGraw-Hill.

[4] Hwang, C. L., & Yoon, K. (1981). Methods for multiple attribute decision making. In *Multiple attribute decision making* (pp. 58-191). Springer.

[5] Brans, J. P., & Vincke, P. (1985). Note—A Preference Ranking Organisation Method: (The PROMETHEE Method for Multiple Criteria Decision-Making). *Management science*, *31*(6), 647-656.

[6] Roy, B. (1991). The outranking approach and the foundation of ELECTRE methods. *Theory and Decision*, *31*(1), 49-73.

[7] Opricovic, S. (1998). *Multicriteria optimization of civil engineering systems.* Belgrade: Faculty of Civil Engineering (In Serbian).

[8] Stanujkic, D., & Zavadskas, E. K. (2015). A modified weighted sum method based on the decision-maker's preferred levels of performances. *Studies in Informatics and Control*, *24*(4), 461-470.

[9] Pamučar, D., Stević, Ž., & Sremac, S. (2018). A new model for determining weight coefficients of criteria in mcdm models: Full consistency method (fucom). *Symmetry*, *10*(9), 393.

[10] Stević, Ž., Pamučar, D., Puška, A., & Chatterjee, P. (2020). Sustainable supplier selection in healthcare industries using a new MCDM method: Measurement of alternatives and ranking according to COmpromise solution (MARCOS). *Computers & Industrial Engineering*, *140*, 106231.

[11] Alptekin, G. I., & Büyüközkan, G. (2011). An integrated case-based reasoning and MCDM system for Web based tourism destination planning. *Expert Systems with Applications*, *38*(3), 2125-2132.

[12] Anojkumar, L., Ilangkumaran, M., & Sasirekha, V. (2014). Comparative analysis of MCDM methods for pipe material selection in sugar industry. *Expert systems with applications*, *41*(6), 2964-2980.

[13] Stojčić, M., Zavadskas, E. K., Pamučar, D., Stević, Ž., & Mardani, A. (2019). Application of MCDM methods in sustainability engineering: A literature review 2008–2018. *Symmetry*, *11*(3), 350.

[14] Çolak, M., & Kaya, İ. (2017). Prioritization of renewable energy alternatives by using an integrated fuzzy MCDM model: A real case application for Turkey. *Renewable and sustainable energy reviews*, *80*, 840-853.

[15] Kumar, A., et al. (2017). A review of multi criteria decision making (MCDM) towards sustainable renewable energy development. *Renewable and Sustainable Energy Reviews*, *69*, 596-609.

[16] Muravev, D., Hu, H., Zhou, H., & Pamucar, D. (2020). Location optimization of CR express international logistics centers. *Symmetry*, *12*(1), 143.

[17] Li, Y. L., Ying, C. S., Chin, K. S., Yang, H. T., & Xu, J. (2018). Third-party reverse logistics provider selection approach based on hybrid-information MCDM and cumulative prospect theory. *Journal of Cleaner Production*, *195*, 573-584.

[18] Republic of Serbia, Ministry of Mining and Energy. (2016). *Energy Sector Development Strategy of the Republic of Serbia for the period by 2025 with projections by 2030*. Belgrade.

[19] Keshavarz-Ghorabaee, M., Amiri, M., Zavadskas, E. K., Turskis, Z., & Antucheviciene, J. (2021). Determination of Objective Weights Using a New Method Based on the Removal Effects of Criteria (MEREC). *Symmetry*, *13*(4), 525.

[20] Stanujkic, D., Zavadskas, E. K., Karabasevic, D., Smarandache, F., & Turskis, Z. (2017). The use of the pivot pairwise relative criteria importance assessment method for determining the weights of criteria. *Journal of Economic Forecasting*, *4*, 116-133.

[21] Stanujkic, D., Popovic, G., Karabasevic, D., Meidute-Kavaliauskiene, I., & Ulutaș, A. (2021). An Integrated Simple Weighted Sum Product Method—WISP. *IEEE Transactions on Engineering Management*.

[22] Keshavarz-Ghorabaee, M. (2021). Assessment of distribution center locations using a multi-expert subjective–objective decision-making approach. *Scientific Reports*, *11*(1), 1-19.

[23] Gül, S., & Aydoğdu, A. (2021). Novel Entropy Measure Definitions and Their Uses in a Modified Combinative Distance-Based Assessment (CODAS) Method Under Picture Fuzzy Environment. *Informatica*, 1-36.

[24] Tomašević, M., Lapuh, L., Stević, Ž., Stanujkić, D., & Karabašević, D. (2020). Evaluation of criteria for the implementation of high-performance computing (HPC) in Danube Region countries using fuzzy PIPRECIA method. *Sustainability*, *12*(7), 3017.

[25] Jauković-Jocić, K., Karabašević, D., & Jocić, G. (2020). The use of the PIPRECIA method for assessing the quality of e-learning materials. *Ekonomika*, *66*(3), 37-45.

[26] Stanujkic, D., Karabasevic, D., & Sava, C. (2018). An application of the PIPRECIA and WS PLP methods for evaluating website quality in hotel industry. *Quaestus*, *12*, 190-198.

[27] Ulutaș, A., Popovic, G., Radanov, P., Stanujkic, D., & Karabasevic, D. (2021). A new hybrid fuzzy PSI-PIPRECIA-CoCoSo MCDM based approach to solving the transportation company selection problem. *Technological and Economic Development of Economy*, *27*(5), 1227-1249.

[28] Popović, G., et al. (2021). An integrated SWOT–extended PIPRECIA model for identifying key determinants of tourism development: The case of Serbia. *Acta geographica Slovenica*, *61*(2), 23-40.

[29] Stanujkić, D., et al. (2021). A New Grey Approach for Using SWARA and PIPRECIA Methods in a Group Decision-Making Environment. *Mathematics*, *9*(13), 1554.

[30] Blagojević, A., Stević, Ž., Marinković, D., Kasalica, S., & Rajilić, S. (2020). A novel entropy-fuzzy PIPRECIA-DEA model for safety evaluation of railway traffic. *Symmetry*, *12*(9), 1479.

Control of Post Combustion to Stabilize Power Generation in a Sponge Iron Plant

Brahma Deo[1], Puneet Choudhary[2], Sourava Saran Bose[3]

[1,2]School of Minerals, Meta llurgical, and Materials Engineering, IIT Bhubaneswar, Jatni, Odisha, India, bdeo@iitbbs.ac.in[1]

[3]Tata Steel Long Products Limited, Beliapda, Joda, Odisha, India

Abstract—**The product gases from coal-fired sponge iron kilns exit at a high temperature (800-950°C) and contain some unburnt carbon and carbon monoxide along with nitrogen, carbon dioxide and entrained dust. The sensible heat of gas as well as the heat generated from the combustion of unburnt carbon and CO in gases is used to raise the exit gas temperature within a specified window inside the Post Combustion Chamber (PCC). The exit gas is then used in the waste-heat recovery boiler for steam and electricity generation. Temperature and combustion control of product gas in the PCC is done by regulating the supply of additional air needed for completing the combustion. When the exit gas temperature exceeds the maximum allowed value, the same is brought under control by spraying cold water. Due to continuous variation in input parameters in PCC, a chaotic situation prevails inside. To control the air and water flow inside the PCC, a cascade based control logic has been developed in this work to regulate the water and air control valves using PID controllers. Lyapunov exponent is used as a guide to assess the chaos present in different parameters of the system (both in the kiln and in PCC). The analytical tools used include multiple linear regression (MLR) and artificial neural network (ANN) to develop the models for predicting the exit gas temperature and steam generation rate. The models are dynamically updated to take care of the continuous changes in the conditions inside the rotary kiln and PCC.**

Keywords - Post-combustion chamber, chaos monitoring, Lyapunov exponent, PID control, cascade logic

I. INTRODUCTION

Tata Steel Long Products Limited (TSLPL), Joda, India, uses coal-fired rotary kilns to make high-grade sponge iron. The coal used in the kiln is of low grade and contains up to 50% fines. The product gases from the kiln are passed through the post-combustion chamber followed by a boiler for steam generation. The generated steam is used to drive the turbines and generate electric power which is sold to the grid. The schematic of the TSLPL plant layout is shown in Fig. 1.

Rotary kiln is a countercurrent reactor with a slight inclination to the horizontal and rotating so that the gravity aids the material to flow in the forward direction. Coal, iron ore and dolomite are fed as raw materials into the kiln where reduction reaction takes place resulting in the formation of pure sponge iron. The coal enters from both ends of the rotary kiln: one end is known as the feed side (kiln inlet hood), and another end is called the injection side (kiln outlet hood). In the current plant set up, the iron

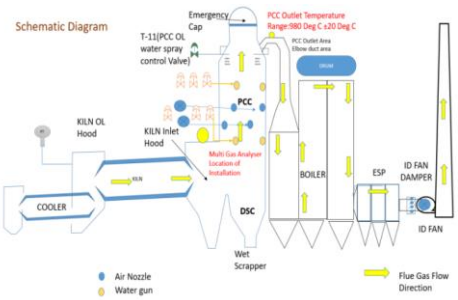

Figure 1. Schematic diagram of the gas flow in sponge iron plant.

ore, dolomite, and coal enter from the feed end of the rotary kiln, and only coal enters from the injection side (coal combustion end). The coal is combusted with the aid of air blown from the primary air blower (PAB), root air blower (RB) and eight secondary air blowers (SABs) inside the kiln. Part of the coal fines particles are entrained in the flowinggas due to fine particle size and less weight. The gases such as CO, CO_2, O_2, and N_2 are required for heating and reduction of the iron ore. The cause for the direction of flow of the gases from the injection side towards the feed side is due to an induced draft (ID) fan which sucks the gases and maintains the flow of gases inside the kiln. For better combustion efficiency, the gas is made to flow in the opposite direction of movement of the charge. ID fan is fitted with a damper to regulate both pressure and flow of gases.

The post-combustion chamber (PCC) is installed on the feed side of the rotary kiln. The gases generated inside the kiln flow from the injection side to the feed side of the kiln and then enter the post-combustion chamber at a high temperature. The waste gas thus enters the PCC within a temperature range between 860 – 950°C, consisting unburnt carbon and CO gas, along with nitrogen and entrained dust particles and carbon. The waste gases along with other particulates enter the post-combustion chamber wherein the un-burnt carbon and CO are burnt to complete the combustion resulting in formation of $CO_2$and heat, by supplying extra air. The sensible heat thus generated further increases the waste gas temperature. However, to restrict temperature in the desired window, the amount of additional supply of air directed to the PCC needs to be controlled. In case the product gas temperature is more than the desired range, the same is brought under control by spraying cold water automatically through a closed-loop control. In order to achieve this control of product gas temperature, three actions are needed: (a) firstly, to predict the waste gas flow and temperature from the kiln, (b) use of PID controllers to control air inflow and water spray in PCC, simultaneously, and (c) to control exit gas temperature from the post-combustion chamber. Cascade logic is used for control of airflow and water flow in the PCC. The logic is applied to control the amount of steam subsequently produced from boilers, and thereby the power generation from steam turbines. The efficacy of control of PCC decides the power generation rate and hence the supply to the power grid which, again, needs to be in the predictable window. Huge penalties are imposed by the customer (in this case the central power grid management which is purchasing power) if the window is exceeded, both in upper and lower bounds. The thermocouple (PCC T-11) is placed to measure the temperature of the product gases from PCC for monitoring purpose. The place where this temperature is measured is known as the elbow-duct, the piping through which the hot gases move towards the boiler for steam generation.

As explained earlier, the input parameters in PCC are chaotic, and they can be measured using the magnitude and fluctuation in the Lyapunov exponent. Chaos in the kiln which also affects the PCC is controlled by adjusting the air supply from primary and secondary air blowers through several dynamic models at regular intervals.

In the present study, Lyapunov exponent (LE) is calculated by following a standard procedure: the first step is to find the time delay, which is then followed by finding the embedding dimension, and correlation dimension. From the knowledge of these, the Lyapunov Exponent can be calculated. A sudden change in LE indicates the combined effect of change in feed material properties, accretions and reduction processes inside the kiln. These affect the pressure and temperature of exit gas from the kiln. For example, sudden changes in LE are caused when accretions inside the kiln get dislodged. The technology of predicting and controlling accretion formation is explained in detail in [1-6]. Prior to the present work, adjustments at all the sections in the plant under consideration were made manually. In the present work, the results of automatic regulation through PID controllers in cascade logic are presented. Data analysis tools like multiple linear regression (MLR) and artificial neural network (ANN) are used for making advance prediction models which are included in the PCC control model.

II. Prediction of Exit Gas Temperature, T-11, from PCC

A large number of process parameters affect the PCC T-11 temperature, that include: airflow rate in any (or all) of the eight secondary air blowers (SAB 1-8), primary air blower (PAB), root air blower (RAB), volume of CO, CO_2 and O_2 in the exit gas at PCC inlet, at various sections of PCC, % fines in feed and injected

coal, kiln inlet hood temperature and amount of water injected inside the PCC for cooling purpose.

For multiple input system, it is required to identifythe most effective parameters at the time of prediction of PCC T-11 temperature. In order to make an accurate prediction, data were collected for all the input variables averaged through eight hours, followed by5-point running average. The 5-point median was then taken for smoothing the data. A correlation matrix was created to determine the relationship between input variables with each other. High value of correlation coefficient (≥ 0.4) was used as a limit for dropping parameters, following which, the most effective parameters were identified. However, the number of effective parameters are dynamic due tothe dynamic nature of kiln (as discussed in section 1). The prediction of PCC T-11 (for a single set of data) by these effective parameters givesa root-mean squared error of ± 3.69; and a correlation coefficient of 0.575, and adjusted R^2 0.526. However, as the kiln life increase, the above values will change. Old data are replaced with newer ones according to a particular scheme as explained in Shah et al. (2019). In actual practice, the data file is updated continuously. When the first value (topmost input data in the table) is dropped a new pattern enters for the next prediction such that the total number of data points remains the same. For example, if 100 sets of data points are considered, then 101st data point, i.e., the expected value of PCC exit gas temperature in the next 101st step is predicted. After the same is observed, the first data point from the table is removed such that only 100 data points are considered at any given time. In continuous analysis, prediction error is found to be around ±2^{o}C. The effect of the kiln input variables on PCC exit gas temperature is changing continuously due to dynamic and non-linear input conditions inside the kiln. One has to make a judicious selection (several combinations were tested) of the data period and "averaging interval," depending upon the data collection and measurement system in place.

III. Prediction of Steam Flow Rate

The variation in coal fines and moisture affects volumetric flow rate and temperature of gas produced in the kiln and entering the PCC. Temperature is controlled in the PCC to regulate the steam generation in the boiler. To predict the next day steam flow rate, both ANN and MLR models were considered in the present study. The input parameters to the ANN model include PCC T11 temperature, the volumetric flow rate of gas, and multi-level damper (MLD or ID) opening. The output parameter is the steam flow rate. The prediction is done for the next day by taking data onthe previous three days. The correlation coefficient (R^2) of predicted steam flow is 0.6, with a standard error of 47.7±1.17 tons/day. The prediction by using MLR model for the same data set was slightly inferior with R^2 of predicted steam flow as 0.58, and standard error of 47.7±1.19 tons/day. Both the models were evaluated each day. Several ANN architectures were tried as the database used for analysis changes dynamically. The plot of actual versus predicted steam flow by using the ANN model (with ten middle layer neurons) is shown in Fig. 2.

IV. Automatic Control of Air and Water Flow Inside the PCC Through the Auto-Cascade Logic of PIDs

The predictions of steam flow rate and exit gas temperature, as discussed in sections 2 and 3 earlier, are used for the control of post-combustion in (PCC). To complete the combustion of partially combusted gas, the PCC is equipped with four blowers to supply necessary air, as shown in Fig. 3.

Blowers-1, 2 and 3 have a capacity of 17,000 Nm^3/hr, subject to existing pressure in PCC. The

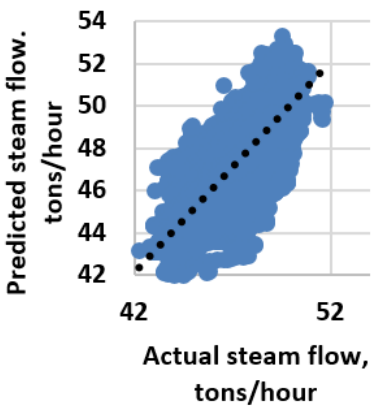

Figure 2. Steam flow (SF, in tons per day) prediction by the artificial neural network (10 neurons).

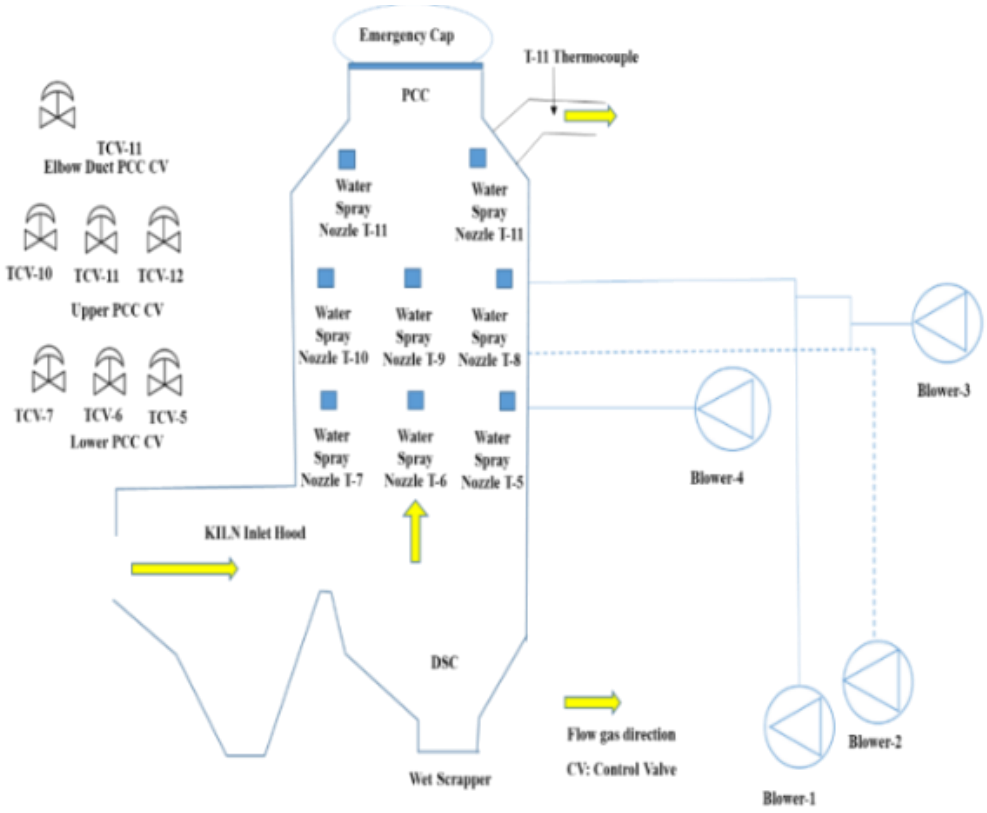

Figure 3. Schematic diagram of the post-combustion chamber (PCC); water spray locations and air blower locations are also shown; T11 thermocouple is at the elbow (top).

pressure in PCC varies between 5-25 mm of the water column. As a result, blower-1 discharges a maximum of 13,500 Nm^3/hr air quantity, blower-2 discharges a maximum of 12,700 Nm^3/hr of the air; while blower-3 acts as a substitute blower in case any of the two blowers, 1 and 2,fails. Blower-4 can provide a maximum discharge of 6000 Nm^3/hr of air. PCC is also equipped with seven PID operated water control valves (CV-5 toCV-11) to injectwater when the PCC T-11 temperature goes beyond the set point. If the PCC T-11 temperature stays higher than 1050°C for more than 40 seconds, the emergency cap on the head of the PCC gets opened, and the gases inside the PCC are released to the environment as a safety measure. However, this situation is to be used very infrequently due to environmental regulations that the plant have adhered too.The control model should be fast, smooth and dynamic to adhere to regular and emergency situations.The primary objective of the control model aims to keep the variation in the steam generation as low as possible to minimize fluctuation in the power generation. The steam generation primarily depends on two factors:

- Boiler inlet gas temperature: this temperature is linearly affected by PCC exit gas temperature (PCC T-11). In fact, the boiler inlet temperature is only slightly less than PCC T-11 temperature.
- Total gas flow volume at the PCC outlet: the total gas volume consists of both gases and steam (steam formed due to injection of water in PCC). The temperature shown by the thermocouple T-11 is the equivalent to the temperature of the mixture (gases and steam). The steam generation occurs in the boiler.

The steam generation in boiler follows the pattern of PCC T-11 temperature. However, the total gas volume shows high fluctuation. Regression value (R^2) which determines the strength of the linear relationship between the dependent and independent variables for the steam generation with PCC T-11 temperature

and total flow volume is around 0.77 and the root means squared error of steam generation prediction is ± 0.77, with the adjusted R-squared value of 0.761. The value of t_{stat}(greater t_{stat} value indicate higher chance against null hypothesis or fewer points will act abnormally) for PCC T-11 temperature is three times higher than the t_{stat} value of total flow volume, i.e., here temperature plays a more dominant role in determining steam generation pattern. So, the control on PCC T-11 is more effective on the steam generation rate rather than the control of total flow volume.

The observed pattern of PCC T-11 temperature under normal conditions is shown in Fig. 4. It can be seen that the PCC T-11 temperature and steam generation have the same shape of the curve, with a time lag between both of these curves: when the PCC T-11 temperature goes down then after few seconds, steam generation also goes down. Similarly, when the PCC T-11 suddenly goes up, then, after few seconds, steam generation also goes up, i.e., a sudden change in PCC T-11 temperature takes a finite time to show an effect in the steam generation rate.

V. PD Tuning of Water Control Valves

Initially, an effort was made to control the PCC exit gas temperature with only one PD (PID, I = 0) operated control valve (CV-11) with optimum tuning. However, it was found that a single control valve was not able to maintain the PCC T-11 temperature within the range. It was also found after performing several experiments that since the system is dynamically changing its condition, the 'I' term in PID [7] gain parameters was giving additional water even when the temperature was below the set point. To avoid this situation, more than one control valves were placed in auto mode with PD control.

Currently, the following cascade logic is applied to five PD operated water control valves in order to control the upper limit of the PCC exit gas temperature, i.e., the temperature should not exceed 1050°C, irrespective of the set point of PCC T-11 temperature. Separate PID Loop set points are made for the high-temperature window, 980 to 1010°C, and for low-temperature window: 950 to 980°C. Fig. 5 shows the logic for the water spray control system for exit gas temperature, while Fig. 6 shows the PCC logic for regulating air input for

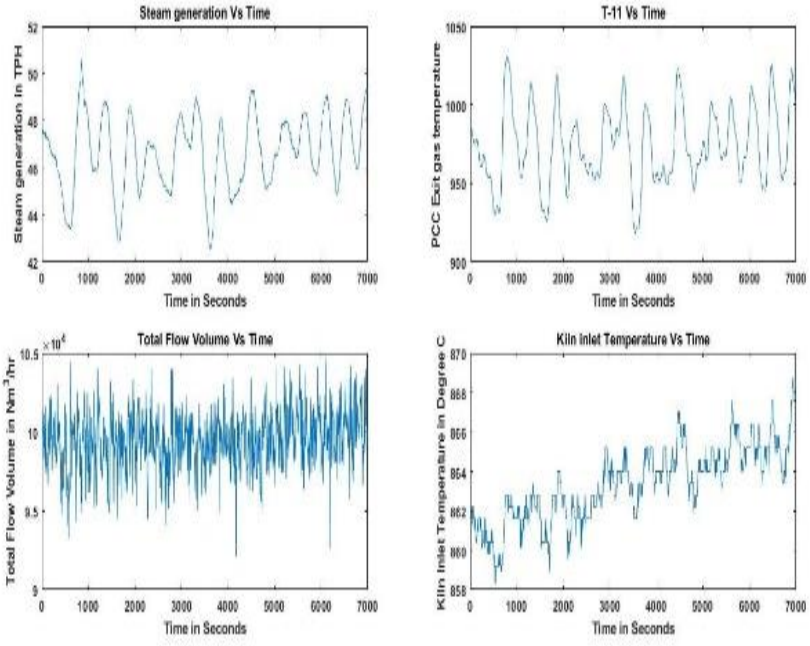

Figure 4. Pattern of PCC T-11, Steam generation, kiln inlet temperature, and total flow volume.

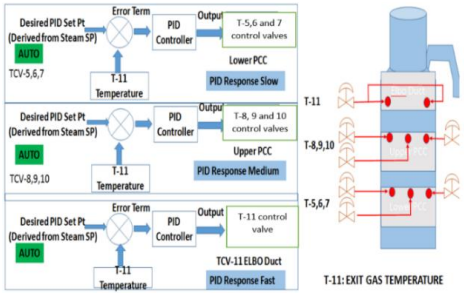

Figure 5. New cascade closed-loop water spray control system for exit gas temperature.

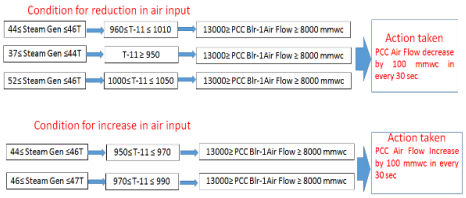

Figur 6. PCC air cascade control logic for regulating air input for combustion in PCC.

combustion in PCC. These two logics are combined into a cascade.

VI. RESULTS

The average and standard deviation of the 7 seconds steam data for 24 hours is taken. Test runs on the same data showed that when the steam set point was kept at 47 TPH, then the average steam generation was significantly improved as compared to earlier results. Results obtained over an extended period are compared in Fig. 7, which shows the efficacy of the control method implemented. Presently, the control system is in continuous operation at the plant.

Chaos fluctuation (standard deviation in LE) significantly decreased after implementing the

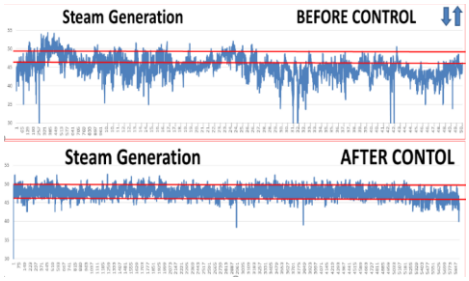

Figure 7. Comparison of the stability of steam generation at TSIL with and without auto-cascade control.

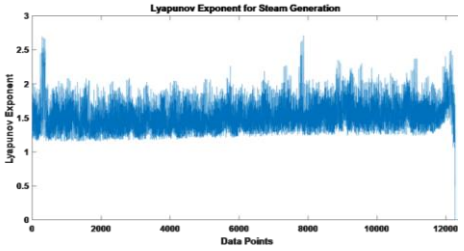

a)

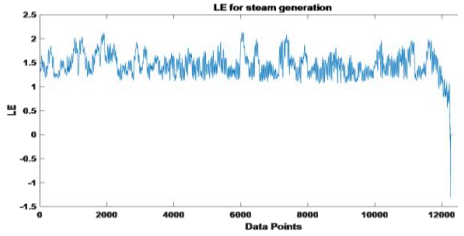

b)

Figur 8. (a) Chaos (Lyapunov Exponent) in the steam generation before control; (b) Chaos (Lyapunov exponent) in the steam generation after control.

new control system as shown by the comparison of chaos in the steam generation before and after control in Figs. 8a and 8b.

VII. CONCLUSION

Actual plant data is used to make models based on ANN and MLR for predicting the product gas flow, product gas temperature, and steam generation rate. These models provide input to the PCC control model or deciding and regulating the airflow rate for combustion. Water flow rate is regulated for the cooling of gases to limit the product gas temperature within the desired window. A controlled and predictable steam generation has led to the regulation of power produced from steam turbines in a predefined window. This has been done to optimize the use of energy and steam production as well as to avoid penalty imposed if the specified window of power supply to the grid is violated.

A controlled and predictable steam generation has led to the regulation of power produced from steam turbines in a predefined window. This has been done to optimize the use of energy and steam production as well as to avoid penalty imposed if the specified window of power supply to the grid is violated.

The auto-cascade control system has been designed by conducting controlled experiments on the shop floor of an actual plant. The respective PIDs of water control valves and drive operated air blower-1 are tuned to minimize the variation in Lyapunov Exponent (LE). LE is analyzed for the various parameters of the system and is used to assess the effectiveness of manual control versus and auto control. This is the first time that such an approach has been used for control of PCC. The variation in a steam generation, and hence in the power generation, has been reduced significantly at the Tata Steel Long Products Limited (TSLPL) after applying auto-cascade logic to PID operated water control valves and air blower-1. The developed system of control is now in continuous operation bringing significant technical and financial benefits to the plant. Lyapunov exponents (LE) are monitored continuously to ensure that on-line adjustments in none of the operational parameters cause a sudden or significant change in their LE values. However, process instability becomes unavoidable for 8-48 hours (depending on the size of broken accretion) when accretions unexpectedly get dislodged from the lining inside the kiln. Uncertainty always prevails about the rate of dislodging process of accretion. This affects kiln and PCC response during that period, even though the accretion height is dynamically predicted by a separate model.

ACKNOWLEDGMENT

This work is a result of collaborative R&D project between Tata Steel Long Products Limited (TSLPL), Joda, India, and IIT Bhubaneswar, Jatni, Odisha India.

REFERENCES

[1] Choudhary, P., Deo, B., Sahoo, S. K., Malakar, P., Pothal, G., and Chattopadhyay, P. (2018). Prediction of Accretion Growth from Dynamic Analysis of Heat Transfer in Coal Fired Sponge Iron Rotary Kiln at TATA Sponge, Joda, India. In *AISTech Proceedings* (pp. 691-696).

[2] Vishal, G., et al. (2018). On Optimal control of production rate, accretion growth and quality of sponge Iron in a coal fired rotary kiln at TATA Sponge, India. In *AISTech Proceedings* (pp. 773-780).

[3] Shah, C., et al. (2019). Conventional and AI models for operational guidance and control of sponge iron rotary kilns at TATA sponge. In *Soft Computing for Problem Solving* (pp. 461-469).

[4] Srivastava, M. P., Bandyopadhyay, A., Prasad, K. K., & Chowdhury, B. R. (1988). Operating Experiences of Sponge Iron Pilot Plant--Some Aspects. *Trans. Indian Inst. Met.*, *41*(2), 177-187.

[5] Garikayi, T., Nyanga, L., Mushiri, T., Mhlanga, S., & Kuipa, P. K. (2013). Designing of an Intelligent Fuzzy Logic System for Accretion prevention in sponge iron SL/RN rotary kiln based 100TPD DRI process. In *SAIIE25 Proceedings* (pp. 523_1-523_14).

[6] Runkana, V. (2015). Model-based optimization of industrial gas-solid reactors. *KONA Powder and Particle Journal*, *32*, 115-130.

[7] Astrom, K.J., & Hagglund, T. (1955). *PID controllers, theory design and tuning 2nd ed*. Research Triangle Park, NC: Instrument Society of America.

Effect of Partial Shading on Polycristallin Silicon Photovoltaic Modules Connected in Series and in Parallel

Inchirah Sari-Ali[1], Bachir Chikh-Bled[2], Boumedienne Benyoucef[3]

[1,2,3]Unit of Research on Materials and Renewable Energies, Department of Physics, Faculty of Sciences, Abou Bekr Belkaid University, Tlemcen, Algeria, sinchirah@yahoo.fr[1], bachikhbled@yahoo.fr[2]

Abstract—**Solar cells allow the energy from the sun to be converted into electrical energy; this makes solar energy much more environmentally friendly than fossil fuel energy sources. These solar cells are connected in series and in parallel to gather in a photovoltaic (PV) module to provide the higher current, voltage and power outputs necessary for electrical applications. Cell mismatch occurs when some cells are damaged or shaded and produce lower current output than the other cells in the series connected string. The cell mismatch lowers the module performance and can result in further damage as the weak cells are reverse biased and dissipate heat. The aim of this study is to investigate the harmful effects of partial shading of series and parallel connected Solar PV modules and compare their performance. In the first Bypass diodes must be connected into the module to increase the module current output and prevent further damage. A PVSYST simulation model that represents 60 cells PV module under partial shaded conditions has been used to test several shading profiles and results are presented.**

Keywords - partial shading, simulation, poly-cristallin silicon, maximum power point

I. INTRODUCTION

Solar cells are able to produce energy from the abundant resource of sunlight. The photo-electric effect was first observed by Becquerel in 1839 when a light-dependent voltage was measured from an electrolyte solution [1]. Further developments in solar cell production and design in recent years has made solar energy a viable and sustainable option to traditional fossil fuel energy. The radiant power per unit area emitted by the sun outside the earth's atmosphere is known as the solar constant. The solar constant used in PV research is 1.353 kW/m^2 [1] however, the earth's atmosphere reduces the solar constant through scattering and absorption processes. But even with these losses the daily irradiance on a sunny day can be in the region of 700- 1000 W/m^2 [2]. Photovoltaics (PV) is the renewable energy technology with the highest potential in the urban context, it is versatile and does not produce any noise or pollution. Photovoltaics is ready for introduction into urban areas in several applications like multi-functional building elements, energy supply systems for public information boards, traffic control, telecommunications systems and other infrastructures [3].

There are various types of solar cells with different properties. Monocrystalline silicon modules are the most efficient (16%-21%) and long life ones, polycrystalline are the most common used and thin-film PV that are the cheapest but less efficient ones (7%) [4].Several solar cells connected in series to produce higher voltage or in parallel to increase current create a module. Standard modules are made of 60 cells [4]. One or more PV modules assembled together form a PV panel and various panels together complete a PV array which is the complete power generating unit as it can be observed in Fig. 1.

With a physical Solar PV module it is difficult to study the effects of partial shading

ISBN: 978-86-80593-73-9

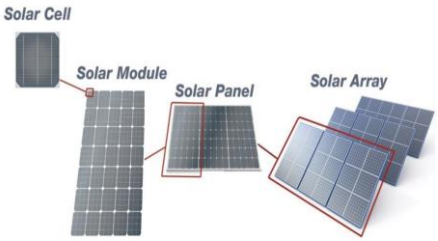

Figure 1. PV cell, module, panel and array [5].

since the field testing is costly, time consuming and depends heavily on the prevailing weather condition. Moreover it is difficult to maintain the same shade under varying numbers of shaded and fully illuminated cells throughout the experiment [6]. However it is convenient to carry out the simulation study with the help of a computer model.

This work is mainly concentrated to study the harmful effects of the shading patterns in series and parallel connected modules. A PVSYSTEM model to simulate V-I (Voltage-Current) and V-P (Voltage-Power) characteristics of a PV module consisting of 60 cells in series has been developed. One of the modules in the combination is considered to be with uniform illumination and other module is partially shaded.

It is used to study the effect of shade on varying number of cells on the power output of the shaded module and stresses on the shaded illuminated cells under various illumination levels.

II. Equivalent Circuit for Solar Photovoltaic Module

The electrical behaviour of a PV module can be successfully modelled by a diode equation based on an equivalent electrical circuit.

A. One-Diode Model

In dark conditions the one-diode PV module can be represented by the circuit shown in Fig. 2 [7]. The solar cell is non-ideal and the performance is limited by parasitic resistances. The dark current-voltage behaviour of the solar cell is modified for non-ideal cells, equation 1, by the inclusion of the ideality factor, n. In an ideal solar cell n is equal to one but in reality n is typically between 1 and 2.

$$I = \frac{V + R_s I}{R_p} + I_0 \left[\exp\left(\frac{q\left(V - R_s I\right)}{nKT} \right) - 1 \right]. \quad (1)$$

In illuminated conditions the photogenerated current is represented by a current source as seen in Fig. 3. The equation for the illuminated current-voltage behaviour is given in (2) [8].

$$I = -I_{ph} + \frac{V + R_s I}{R_p} + I_0 \left[\exp\left(\frac{q\left(V + R_s I\right)}{nKT} \right) - 1 \right]. \quad (2)$$

The photogenerated current flows in the opposite direction to the dark current. Since the photogenerated current is greater than the dark current the equation can be rearranged to (3).

$$I = I_{ph} - \frac{V + R_s I}{Rp} - I_0 \left[\exp\left(\frac{q\left(V + R_s I\right)}{nKT} \right) - 1 \right], \quad (3)$$

where:

I_{ph}: the light-generated current of the solar cell,

V: the solar cell terminal voltage,

Rs: the equivalent series resistance

Rp: the equivalent parallel resistance.

T: cell's operating temperature in degree Kelvin

k: the Boltzman constant,

q: the electron charge

n: ideality factor of the diode,

I: the output current of PV module,

The two forms of the one-diode equation are equivalent but the convention in photovoltaics is such that the photocurrent is positive and thus (3) is used.

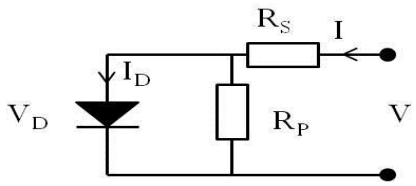

Figure 2. The equivalent circuit of a PV module in a dark.

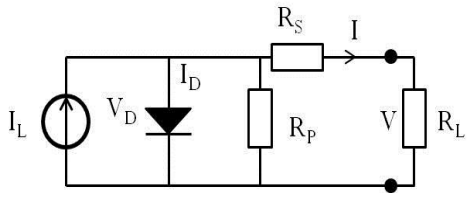

Figure 3. The equivalent circuit of a PV module in a illuminated.

III. Effect of Shadow on the Module and Bypass Diode

Since PV cells electricity production depends on the sun radiation they receive, when shading is produced, some negative consequences are derived. The main problem found is that the output power of the PV cell is reduced because of a decreasing current. Furthermore, shading can produce thermal stress on the module which means that the PV circuit might reverse and if the system is not well protected, damage could happen in terms of hot spots. In the case that one cell is partially shaded, it works as a resistive load which means that it consumes electricity. In order to solve shading problems, by-pass diodes are placed connecting the cell strings in parallel. When a solar cell is reverse biased the bypass diode conducts, allowing the current from the good solar cells to flow in the external circuit rather than forward biasing each good cell [9].

The interconnection of the strings can be varied depending on the voltage output required, 12 or 24 V. For this study we used the 24V connection with 3 bypass diodes placed in parallel over the three strings as seen in Fig. 4[10].

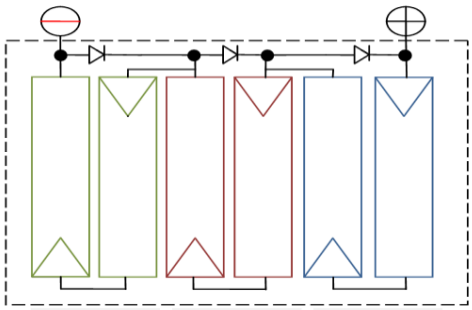

Figure 4. PV module connected in series strings with the bypass diodes.

This module has a specified power output of 250 W with an Isc of 8,63 A and Voc of 37,40V. The effects of the damage on the module's I-V characteristics are investigated using PVSystem software.

IV. Simulation Results

In this article, a photovoltaic module based on polycrystalline silicon comprising 60 solar cells connected in series from two groups is studied. Each group is connected in anti-parallel to a bypass diode. The simulation results of the effect of the bypass diode on the I-V characteristic of the PV panel are shown in the following figures.

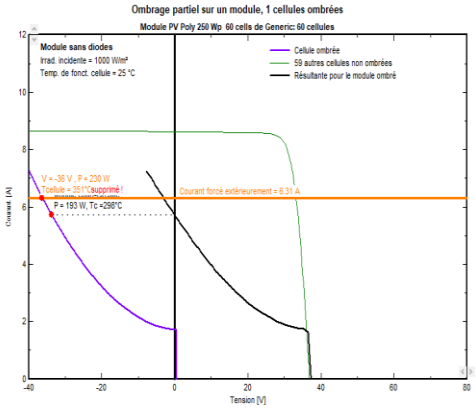

Figure 5. Characteristics I-V of PV module without bypass diode.

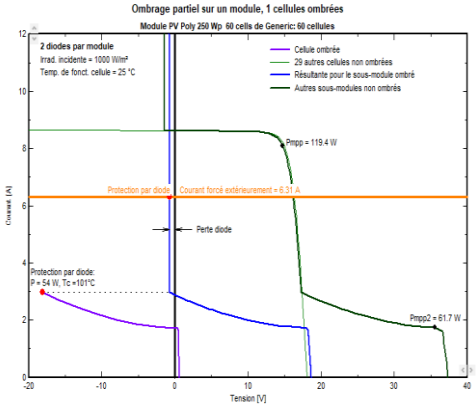

Figure 6. Characteristics I-V of PV module with 2 bypass diode.

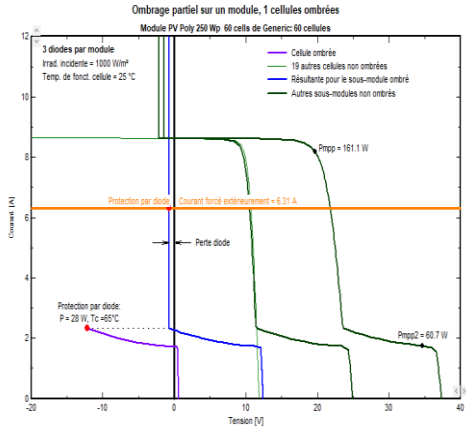

Figure 7. Characteristics I-V of PV module with 3 bypass diode.

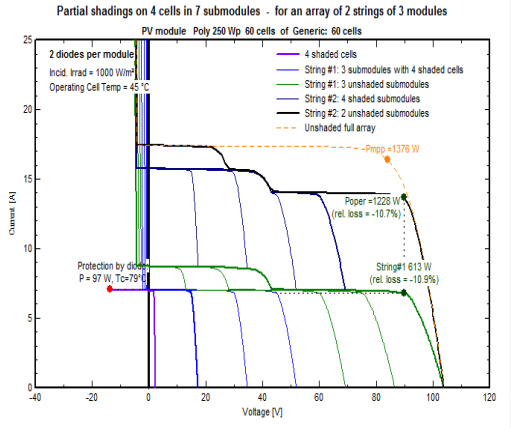

Figure 8. I-V characteristic of poly-Si PV module where four cell shaded at 30%.

Figs. 5-7 show the current-voltage characteristics before and after integration of the bypass diode in the photovoltaic module. We notice that this characteristic of the shaded panel has been improved. It has also been found that, with respect to each diode, the addition of three diodes per module can achieve ideal characteristics.

In this part in order to increase the point of maximum power (MPP) and improve efficiency, we have associated three modules (Poly 250 WP 60 cells) in series and two in parallel. For this we performed partial shading on the I-V characteristics for different shading rates.

We realized a scenario of for shaded cells of 30%, 50% and 90% on the panel of seven submodules.

The results obtained for the I-V characteristics by our simulation are shown in the Figs. 7-10.

From the previous figures, it was found that the appearance of the characteristics (I-V) of the photovoltaic panel causes significant deformations with the increase in the shading rate.

We have noticed for Fig. 8 the 20% shading does not have a significant effect on the power generated by the photovoltaic panel, because its loss is about 10.7%, which is a small percentage.

In Fig. 9 when the cell is not shaded, the maximum power point is around 1376W; for a shading rate of 50%, we observed for the first

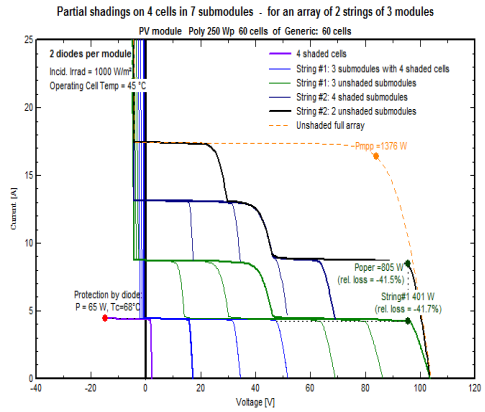

Figure 9. I-V characteristic of poly-Si PV module where four cell shaded at 50%.

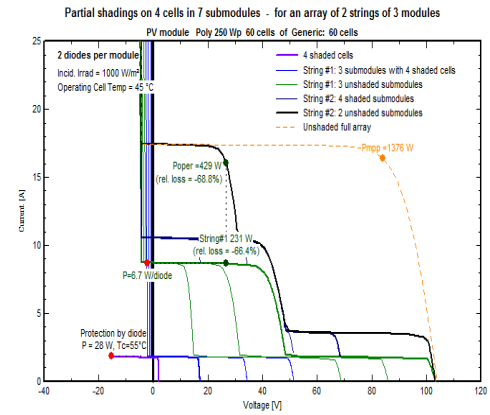

Figure 10. I-V characteristic of poly-Si PV module where four cell shaded at 90%.

case the maximum power is of the order of 805W, so the power loss is about 41.5%, while the maximum power in the second case is 401W, the power loss is about 41.7%. This indicates that the increase in shade is negatively affecting the energy produced by solar panels.

We have noticed from Fig. 10 that the effect of shading on the solar panel reduces the open circuit voltage but the short circuit current is not influenced. We noticed for in this case the maximum power point is around 231W, so the power loss is significant is about 66.4%.

V. CONCLUSION

This article presented the impact of shading on the I-V curves of a solar panel based on silicon polycristalline. The results obtained show that the behavior of the module is degraded when it operates in shaded conditions. Increasing the shading rate on a cell produces multiple peaks of the I-V characteristic of the modules. The point of maximum power MPP shifts to lower voltage values. The power loss can reach 68.8% for the shading of 90% of seven submodules.

REFERENCES

[1] Green M.A. (1992). In *Solar Cells*, pp. 91-92. University of New South Wa les, Kensington.

[2] Teo, J. C., Tan, R. H., Mok, V. H., Ramachandaramurthy, V. K., & Tan, C. K. (2017). Effects of bypass diode configurations to the maximum power of photovoltaic module.

[3] Barker, M., Blewett-Silcock, T., Eising, K., Gutschner, M., Kjellsson, E., Lutter, E., & Tondi, G. (2001). Solar ElectriCity Guide. *European Commission. Institut Cerdà, Spain*.

[4] Parida, B., Iniyan, S., & Goic, R. (2011). A review of solar photovoltaic technologies. *Renewable and sustainable energy reviews*, *15*(3), 1625-1636.

[5] Etap, Photovoltaic array fundamentals. Operation technologies, 216.

[6] Honsenberg, C., & Bowden, S. (2011). Photovoltaic CDRom. *Accessed on*, *8*(09).

[7] Alonso-García, M. C., & Ruíz, J. M. (2006). Analysis and modelling the reverse characteristic of photovoltaic cells. *Solar Energy Materials and Solar Cells*, *90*(7-8), 1105-1120.

[8] Sari-Ali, I., Rahmoun, K., Chikh-Bled, B., Benyoucef, B., Menni, Y., Ghazvini, M., & Ahmadi, M. H. (2020). Mono-crystalline silicon photovoltaic cells under different solar irradiation levels. *Optik*, *223*, 165653.

[9] Hanitsch, R. E., Schulz, D., & Siegfried, U. (2001). Shading effects on output power of grid connected photovoltaic generator systems. *Rev. Energ. Ren.: Power Engineering*, 93-99.

[10] Crozier, J. L. (2012). *Characterization of cell mismatch in photovoltaic modules using electroluminescence and associated electro-optic techniques* (Doctoral dissertation, Nelson Mandela Metropolitan University)

Application of Machine Learning for Cyber Security Risk Assessment in Industrial IoT Systems: A Review

Mirjana D. Stojanović[1], Jasna D. Marković-Petrović[2]

[1]University of Belgrade, Faculty of Transport and Traffic Engineering, Belgrade, Serbia
m.stojanovic@sf.bg.ac.rs
[2]Public Enterprise Electric Power Industry of Serbia, Belgrade, Serbia,
jasna.markovic-petrovic@eps.rs

Abstract—**This review paper describes application of machine learning for cyber security risk assessment in the Industrial Internet of Things (IIoT) environment. First, we briefly explain IIoT cyber security risks, threats and attacks. Next, the architectural view of continuous security risk assessment is presented. State-of-the-art is discussed through review of research papers that utilize machine learning algorithms for IIoT cyber security risk assessment. The paper ends with recommendations for future research.**

Keywords - cyber security, industrial control system, internet of things, machine learning, risk assessment

I. INTRODUCTION

Industrial Internet of Things (IIoT) is the extension of the Internet of Things (IoT) concept intended for industrial sectors and applications. As an essential building block of the Industry 4.0 model, the IIoT encompasses interconnected sensors, actuators, and other devices networked together with computers' industrial applications.

An important characteristic of IIoT is the convergence of the office information technology (IT) and operational technology (OT), which refers to the networking of operational processes and industrial control systems (ICSs). IIoT assumes complete digitalization of industrial production lines, greater system integration in terms of automation and optimization, and better visibility of the supply chains and logistics. Examples of IIoT applications can be found but are not limited to the following sectors: energy and utilities, transportation, food and farming, healthcare, public safety and military, finance and banking, and government.

Although IIoT concept brings substantial benefits for the industry regarding information and economic efficiency, cyber security seems to be a predominant risk factor for its implementation and deployment. An IIoT network can be characterized by high-speed and long-distance connectivity, with hundreds of thousands of data points, as well as by the requirement to carry a wide variety of network services and traffic types. A vulnerability of one device can jeopardize operation of many other devices and increase the risk of process interruptions, unauthorized manipulation and industrial espionage. For those reasons, IIoT needs robust security and privacy mechanisms, such as encrypted and agile system architectures, authentication, specialized chip sets, as well as real-time intrusion detection and prevention [1].

According to the U.S. National Institute of Standards and Technology (NIST), risk assessment is defined as "the process of identifying risks to operations, assets, or individuals by determining the probability of occurrence, the resulting impact, and additional security controls that would mitigate this impact" [2]. While security risk assessment methods in ICSs using traditional Internet technologies have reached a high level of maturity [3–5], introducing the same approach to IIoT systems is not straightforward, and in many cases new solutions are needed that are tailored to this new environment. A highly dynamic environment such as IIoT needs continuous cyber security risk assessment in its operational phase [6, 7].

ISBN: 978-86-80593-73-9

Artificial intelligence (AI) and machine learning (ML) offer a strong potential to achieve this goal because of capabilities for data processing, improved efficiency, real-time and predictive risk management, and better decision making [8].

The aim of this work is to present the state-of-the-art and to identify directions for the future research in the area. Although ML techniques have been utilized as a powerful mechanism for anomaly detection tools in ICSs [9, 10], cyber security risk assessment methods based on machine learning are still in the early stage of development. For example, the work [11] provides a structured review of publications utilizing ML methods for engineering risk assessment in different industries; only one out of 130 papers dealt with the cyber security risk. Reference [12] present an overview of security risk assessment approaches that use AI; only three out of 33 papers addressed IoT environment.

The rest of the paper is structured as follows. Section II briefly describes IIoT cyber security risks, threats and attacks. Section III presents frameworks for cyber security risk assessment in IIoT, with an emphasis on continuous risk assessment. Section IV provides a review of seven works that utilize machine learning for risk assessment in the IIoT environment. Section V contains conclusions and future research directions.

II. IIoT Cyber Security Risks, Threats and Attacks

In addition to performance degradation, cyber attacks on IIoT system can endanger human lives, the environment and assets. Also, data collected during manufacturing process are usually strictly confidential. The main security risks include the lack of authentication and security in sensors and other cyber-physical devices; insecure gateways through which data is transmitted to the cloud; cloud security issues and insecure communication protocols. The consequences of successful attack reflect in a number of operational issues such as: equipment damage, unforeseen operational concerns, endangered personal safety and regulatory issues [1].

Several recent studies have provided classification and description of the cyber security threats and attacks against IIoT systems [13–15]. The most specific threats include advanced persistent threats (APT), lack of data integrity protection, man-in-the-middle (MITM) attacks, identity theft, eavesdropping, replay attacks, as well as different forms of denial of service (DoS) attacks. Berger et al. [14] propose a multi-layer taxonomy of attacks on the IIoT, which consists of the three layers, eight dimensions, and 19 characteristics, as illustrated in Fig. 1.

The method of operation layer identifies the entry points and methods used to perform an attack. This layer classifies attacks according to the technique, mechanism, executability and focus. *The attack technique* is characterized as physical or logical, depending on whether the physical access to devices is required or not. *The attack mechanism* can be active or passive depending on whether the attack performs changes on the targeted system or not. *The executability* distinguishes between stand-alone and coupled attacks. Stand-alone attacks usually act as “door openers” to further attacks. Coupled attacks are initiated after successful previous attacks. *The focus* determines the attacker’s information about the target. Attacks are undirected if they are not focused on particular target, e.g., network scanning. On the contrary, directed attacks exactly know the victim or target, e.g., MITM attack.

The target layer classifies attacks according to the vulnerability and IIoT level. *Vulnerabilities* can be technical and social. Technical vulnerabilities refer to hardware and software components, while social vulnerabilities are caused by human errors, including unintentional errors, absence of security awareness or even naivety of employees, e.g., phishing and social engineering. Attacks on IIoT can be targeted to different *IIoT levels*, including physical level, network level and application level.

Finally, the impact layer characterizes effects of the successful attack in the sense of consequence and scope. *The consequence* describes how the attack compromises the victim and jeopardizes security goals. Thus, disclosure directly affects confidentiality, e.g., due to eavesdropping or password attacks.

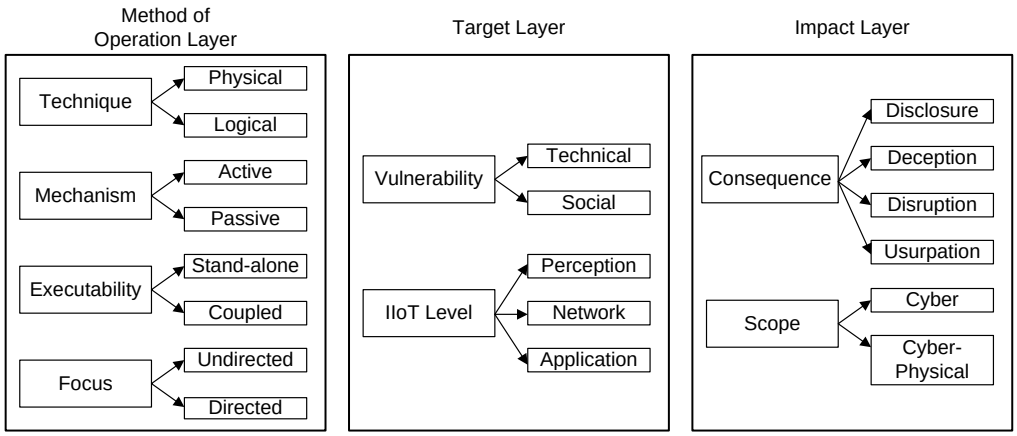

Figure 1. Classification of attacks on IIoT systems (according to [14]).

Deception influences integrity, typically by replacing correct data with false, e.g., malware or physical manipulation. Disruption mainly affects system availability, and typical examples of attacks are different forms of DoS. Usurpation influences system authenticity by allowing unauthorized entities to control services and functions, e.g., privilege escalation and hardware Trojan. *The scope* dimension makes a distinction between cyber and cyber-physical attacks.

III. Continuous Security Risk Assessment in IIoT

The Industrial Internet Consortium (IIC) addresses risk assessment in the context of overall security measures and highlights the need to adapt to continually changing threats and system configurations, provide responses that will minimize the impact on the IIoT system, and enable different organizations work together to ensure the early identification of security threats [16].

Nakamura and Ribeiro propose a general IIoT risk assessment methodology that starts from the use case point of view for the IIoT system to provide an integrated security view that determines the actions to be taken by the different actors [17]. In other words, risk assessment in IIoT can be performed in different contexts, depending on the risk view and the involved actors. Risk views may refer to sensors and actuators manufacturers, platform tier, application and ICS developers, industrial sector, integrators, service providers and users. In each context, the participating entities should be identified, e.g., human, hardware, software, communication and cloud. The entities are the basis for determining the data flow.

Continuous risk assessment will probably become an imperative in highly dynamic and heterogeneous IIoT environment. This means that the risk assessment is performed on an ongoing basis and relies on data that are collected and processed in the run-time. A conceptual model of continuous cyber security risk assessment in IIoT is proposed in [6] and illustrated in Fig. 2.

Various detection tools are distributed throughout the IIoT system and they include logs monitoring, intrusion detection and prevention systems, malware detection tools, tools for network traffic monitoring and analysis, etc. These tools capture inputs from the IIoT system in a real time and generate the information about anomalies and other suspicious events. The security information and event management (SIEM) software imports information from detection tools and performs correlation of the corresponding events. The preprocessing module takes data from the SIEM and prepares appropriate dynamic inputs (indicators) for the risk assessment tool. The risk assessment tool takes into account these dynamic inputs as well as some static inputs from the knowledge repository to calculate the risk measure. The knowledge repository stores some data that are not changed frequently (e.g., asset register, asset values, definition of normal and abnormal states of operation), as well as the initial and current risk measures, and the risk mitigation plan.

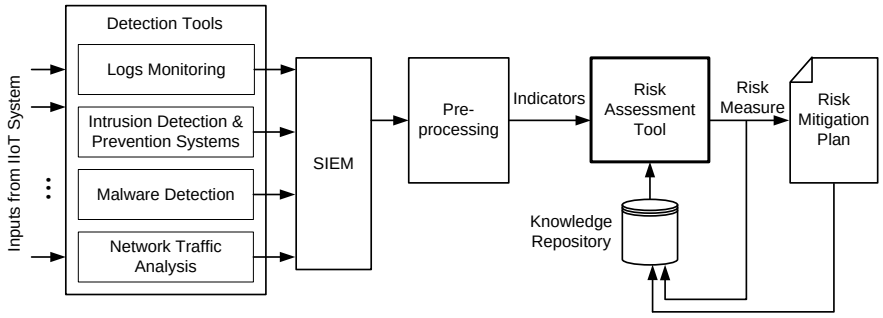

Figure 2. A model for continuous IIoT risk assessment (adapted from [6]).

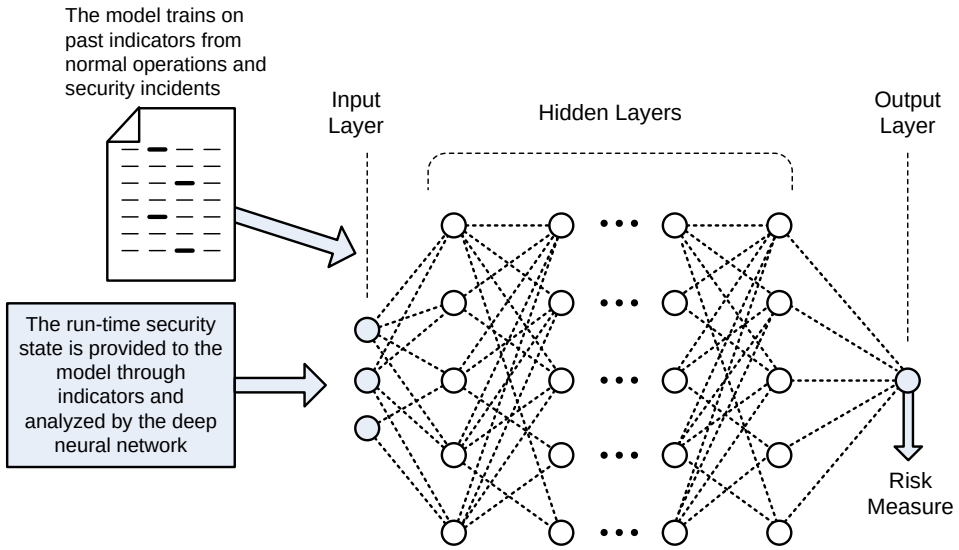

Figure 3. An example of risk assessment tool implemented using deep neural network.

In the context of the described model, risk assessment tool can be implemented using some of ML algorithms. Comprehensive surveys of ML approaches, algorithms and applications can be found in the literature, e.g., [18, 19].

In [20], the mainstream ML-based approaches for multi-access edge computing have been surveyed and compared, including supervised and unsupervised learning, deep learning, reinforcement learning and deep reinforcement learning. Implementation of risk assessment tool using deep learning approach is illustrated in Fig. 3.

IV. A Review of Research Works

Our study focuses on research journal articles, conference papers and book chapters found by searching the IEEE Xplore, Web of Science (WoS) and SCOPUS databases, with the following keywords: “Industrial IoT”, “Risk assessment” and “Machine learning”. After manual inspection and exclusion of the replicated papers, we selected papers that contained original proposals for ML-based risk assessment methods. The set consists of seven papers, which are briefly summarized in Table I.

The first three papers are based on supervised learning techniques [21–23].

An evolutionary algorithm is proposed in [21] and based on cuckoo search (inspired by behavior of cuckoo species who lay their eggs in the nests of other host birds) to pre-train a back propagation neural network (BPNN).

TABLE I. A BRIEF OVERVIEW OF SELECTED PAPERS.

Authors, year & reference	**ML approach & algorithm**	**Implementation**	**Validation**	**Application domain**
Li et al., 2018, [21]	Supervised learning: BPNN	MATLAB	Simulation (MATLAB)	Cyber-physical-social systems
Zhang et al., 2018 [22]	Supervised learning: FPBN	MS Visual Studio 2015 (C++)	Simulation (chemical reactor control system)	Industrial control systems
Kalinin et al., 2021 [23]	Supervised learning: ANN	TensorFlow and Keras	Simulation (NS3)	Smart cities
Abbas et al., 2018, [24]	Deep learning: CNN	PyTorch (Anaconda)	Simulation (cloud client and server)	IIoT network layer
Baldini et al., 2020 [25]	Deep learning: GNN	Not published	Not published	Smart transport, Industry 4.0, food supply chain
Zakaria et al., 2020 [26]	Deep learning: CNN	Not published	Not published	Healthcare
Liu et al., 2020, [27]	Deep reinforcement learning: DQN	Julia	Numerical analysis and real-time simulation	Wind power system

Using this pre-training process, the BPNN can improve the accuracy and stability. Such a neural network is used as a part of information security risk assessment for a miniature IoT system. Risk factors have been analyzed from the three aspects: assets, information flow control and human factors. Simulation experiments were conducted using MATLAB tools.

An approach for dynamic cyber security risk assessment in ICSs based on fuzzy probability Bayesian network (FPBN) is presented in [22]. Fuzzy probabilities are used to overcome the problem of limited amount of historical data. The FPBN is designed with multi-domain knowledge about attacks, system functions, hazardous incidents, and system assets. The noise evidence filter helps in distinguishing cyber attacks from system faults. The FPBN inference engine calculates posterior probabilities that assets are damaged and dynamically assesses the cyber security risk with the losses of assets, i.e., the risk value is equal to the product of asset losses and the corresponding probabilities. Simulation studies were conducted on a simplified chemical reactor control system to verify the effectiveness of the approach, the effectiveness of the noise filter, the execution time performance and the scalability.

A cyber security risk assessment method in a smart city infrastructure is described in [23]. This work relies on object typing, data mining, and quantitative risk assessment based on the artificial neural network (ANN). The method consists of the following four stages: (1) preparatory stage; (2) generation of training samples to create the base of scenarios of the dynamic device-to-device networks operation modes; (3) classification and (4) cyber security risk assessment. The asset types were identified (e.g., vehicle, smart phone, traffic light, road-side unit, various sensors, etc.) and the threshold for unacceptable risk was associated with each asset type. The environment of a smart city was simulated by the NS-3 simulator; log files were generated during simulation and converted to appropriate vectors that were used to feed neural network. Training datasets were synthesized by means of the NS-3 simulator, while TensorFlow and Keras frameworks were used for developing a three-layer ANN. Results of the simulation study have clearly indicated that the ANN approach outperforms the traditional probabilistic approach.

The next three papers are based on deep learning techniques [24–26].

The use of deep learning for classifying IoT security risks is proposed in [24]. A convolutional neural network (CNN) algorithm is applied, which consists of the two stages, namely the extraction and classification. Extraction is used to automatically extract and learn features from raw data, and it comprises two layers: (1) convolution layer, which collects the input data and (2) max-pooling layer, which classifies the collected data into sub-samples. The learning is performed through back-propagation, assuming several iterations of the convolution and max-pooling. In the second

stage, classification is performed at the fully connected layer that is responsible for connecting the neurons to a single final output that corresponds to an appropriate risk level. After training, the output is saved to be used as an input for further calculations, thus resulting in a fully dynamic approach. The PyTorch framework was used to implement the proposed model. Simulation study assumed an interconnection between a cloud client and the Dropbox tool for three weeks, with the raw data consisted of 14 simulated attacks such as illegal access network, malware intrusion, probe attacks, integrity loss, DoS, MITM, etc. As the authors state, the classification accuracy strongly depends on the available computational capacity.

A policy-based system is proposed in [25] to address several aspects of risk management in IoT scenarios. The system consists of the device authenticator, profile manager, profile builder, profile publisher and policy enforcer. It reduces the potential security risks associated to IoT devices by enforcing traffic profiles to be defined either by the device's manufacturer or automatically. The system integrates a distributed mechanism based on multiple agents for risk monitoring. To enable automatic feature extraction and anomaly detection by the agents, the system utilizes the deep learning approach that deals with graph structured datasets, i.e., graph neural networks (GNNs).

Deep learning based on CNN is proposed in [26] to assess cyber security risk in healthcare domain. The model relies on the U.S. NIST Guide for Conducting Risk Assessments (NIST SP 800-30) and comprises definition of services, service models, attack's surface, impact of attacks, risk mitigation and priority. Similarly to the work [24], CNN is used for classification of security risks. A brief discussion on deployment possibilities based on open source libraries such as Keras, TensorFlow, and PyTorch is also provided.

Finally, the work [27] presents deep reinforcement learning and an adapted common vulnerability scoring system tailored to assess vulnerabilities in wind integrated power systems. This approach considers adversaries that make use of open source intelligence (OSINT) modeling techniques to construct power system models. Such models are then coupled with contingency analysis that takes into account wind intermittent generation to identify the critical cyber and physical vulnerabilities of the electric power system. The state of the power system is modeled as a partially observable Markov decision process that is solved using deep Q-network (DQN). The algorithm is implemented in programming language Julia. The proposal is validated via numerical analysis and real-time simulation, using realistic data from various actual wind energy systems, and various test case power systems. The results indicate that the proposed method based on deep Q-network performs closely to a graph-search approach in terms of the number of transitions needed to find the optimal attack policy, without the need for full observation of the system.

V. Discussion

The observed set of papers is not too large; hence, it is difficult or even impossible to draw general conclusions. However, our findings slightly differ from the results of studies [11] and [12] that addressed engineering and security risk assessment, respectively, but did not encompass IIoT security risk. In those studies, supervised learning with ANN is the prevalent method in the reviewed papers, probably because it is a nonlinear calculating apparatus by nature; ANNs require less formal statistical training and are capable of detecting all possible interactions between the input and output variables.

Our study confirms benefits of ANNs, but also indicates a trend towards deep learning and deep reinforcement learning approaches. Deep learning can be integrated into edge-computing-based systems and used for feature extraction and risk classification. Some disadvantages include very long training time, massive training data and the need for high-performance computational capacity. On the other side, deep reinforcement learning brings together function approximation and target optimization by mapping state-action pairs to expected rewards, which makes it suitable for feature extraction and decision making.

Regarding implementation, open source ML platforms such as TensorFlow, Keras and PyTorch seem quite appropriate, as well as self-developed software based on some general-purpose programming language. Validation of proposals (if published) is mostly performed using simulation and synthetic datasets.

VI. Conclusions and Future Research Directions

ML-based algorithms are powerful tools for meeting challenges that continuous IIoT risk assessment, as a multidisciplinary area, poses to cyber security, industry and business experts. They can be very efficient in dynamic processing of big data, risk classification and decision making. Although the research in the field is still relatively underdeveloped, its importance has been recognized and will probably gain a strong momentum in the next few years.

The main future research directions are as follows.

- Equal emphasis should be placed upon the architectural view of continuous risk assessment, specific ML-based algorithms, development of appropriate testbeds, and the standardization efforts in the field.
- Development of distributed and decentralized architectural frameworks, based on multiple cooperative agents, should be enforced in order to cover risk assessment at different IIoT layers, ranging from edge through cloud to the application layer.
- Development of ML-based algorithms for risk assessment should be focused on deep learning and deep reinforcement learning due to their end-to-end learning capabilities and suitability for decision making.
- To enable development of superior performance risk assessment engines, attempts to build open-source platforms dedicated to industrial environment should be enforced.
- Realistic and comprehensive cyber physical system testbeds are needed to allow for experimentation with different solutions. In this regard, there is a need to use datasets from real networks, which is a limiting factor at the initial stage of IIoT deployment. Alternative strategy is to reuse datasets, either publicly available or obtained from testbeds.
- Finally, we strongly encourage investigation of hybrid approaches, which combine experts' assessment with some of ML algorithms, in order to mitigate shortcomings of ML approaches, primary regarding high error susceptibility and possibly wrong interpretation of results.

Acknowledgment

This work was supported by the Ministry of Education, Science and Technological Development of Serbia.

References

[1] Stojanović, M., & Boštjančič Rakas, S. (2020). Challenges in securing industrial control systems using future Internet technologies. In M. Stojanović, & S. Boštjančič Rakas (Eds.) *Cyber Security of Industrial Control Systems in the Future Internet Environment* (pp. 1-26). IGI Global, Hershey, PA.

[2] Stouffer, K., Pillitteri, V., Lightman, S., Abrams, M., & Hahn, A. (2015). *Guide to industrial control systems (ICS) security (NIST Special Publication 800-82 Rev. 2)*. Gaithersburg, MD: U.S. National Institute of Standards and Technology. Available at: https://nvlpubs.nist.gov/nistpubs/SpecialPublications/NIST.SP.800-82r2.pdf

[3] Cherdantseva, Y., Burnap, P., Blyth, A., Eden, P., Jones, K., Soulsby, H. et al. (2016). A review of cyber security risk assessment methods for SCADA systems. *Computers & Security*, *56*, 1-27.

[4] Qassim, Q. S., Jamil, N., Daud, M., Patel, A., & Ja'affar, N. (2019). A review of security assessment methodologies in industrial control systems. *Information and Computer Security*, *27*(1), 47-61.

[5] Markovic-Petrovic, J. D., Stojanovic, M. D., & Bostjancic Rakas, S. V. (2019). A fuzzy AHP approach for security risk assessment in SCADA networks. *Advances in Electrical and Computer Engineering*, *19*(3), 69–74.

[6] Adaros Boye, C., Kearney, P., & Josephs, M. (2018). Cyber-risks in the Industrial Internet of Things (IIoT): Towards a method for continuous assessment. In L. Chen, M. Manulis, & S. Schneider (Eds.), *Information Security. ISC 2018. Lecture Notes in Computer Science*, (vol. 11060, pp. 502-519). Springer, Cham.

[7] Radanliev, P., De Roure, D., Walton, R.,Van Kleek, M., Montalvo, R. M., Maddox, L. et al. (2020). Artificial intelligence and machine learning in dynamic cyber risk analytics at the edge. *SN Applied Sciences*, *2*(11), 1773.

[8] Federation of European Risk Management Associations (FERMA). (2019). *Artificial Intelligence Applied to Risk Management.* Available at: https://www.eciia.eu/wp-content/uploads/2019/11/FERMA-AI-applied-to-RM-FINAL.pdf

[9] Boštjančič Rakas, S., Stojanović, M., & Marković-Petrović, J. (2020). A review of research work on network-based SCADA intrusion detection systems. *IEEE Access*, *8*, 93083-93108.

[10] Radoglou-Grammatikis, P. I., & Sarigiannidis, P. G. (2019). Securing the smart grid: A comprehensive compilation of intrusion detection and prevention systems. *IEEE Access*, *7*, 46595-46620.

[11] Hegde, J., & Rokseth, B. (2020). Applications of machine learning methods for engineering risk assessment – A review. *Safety Science*, *122*, 104492.

[12] Erdogan, G., Garcia-Ceja, E., Hugo, A., Nguyen, P. H., & Sen, S. (2021, June). A systematic mapping study on approaches for AI-supported security risk assessment. In *COMPSAC 2021: Intelligent and Resilient Computing for a Collaborative World 45th Anniversary Conference* (pp. 1-7).

[13] Leander, B., Čaušević, A., & Hansson, H. (2019, Sept.). Cybersecurity challenges in large industrial IoT systems. In *24th IEEE International Conference on Emerging Technologies and Factory Automation (ETFA)* (pp. 1035-1042).

[14] Berger, S., Burger, O., & Roglinger, M. (2020). Attacks on the Industrial Internet of Things – Development of a multi-layer taxonomy. *Computers & Security*, *93*, 101790.

[15] Tsiknas, K., Taketzis, D., Demertzis, K., & Skianis, C. (2021). Cyber threats to industrial IoT: A survey on attacks and countermeasures. *IoT*, *2*(1), 163-186.

[16] Industrial Internet Consortium (IIC). (2016). *Industrial Internet of Things Volume G4: Security Framework*. IIC:PUB:G4:V1.0:PB:20160919. Available at: https://www.iiconsortium.org/pdf/ IIC_ PUB_G4_ V1.00_PB-3.pdf

[17] Nakamura, E. T., & Ribeiro, S. L. (2018, June). A privacy, security, safety, resilience and reliability focused risk assessment methodology for IIoT systems steps to build and use secure IIoT systems. In *Global Internet of Things Summit (GIoTS)* (pp. 1-6).

[18] Sarker, I. H. (2021). Machine learning: Algorithms, real-world applications and research directions. *SN Computer Science*, *2*, 160.

[19] Cui, L., Yang, S., Chen, F., Ming, Z., Lu, N., & Qin, J. (2018). A survey on application of machine learning for Internet of Things. *International Journal of Machine Learning and Cybernetics*, *9*, 1399-1417.

[20] Cao, B., Zhang, L., Li, Y., Feng, D., & Cao, W. (2019). Intelligent offloading in multi-access edge computing: A state-of-the-art review and framework. *IEEE Communications Magazine*, *57*(3), 56-62.

[21] Li, S., Bi, F., Chen, W., Miao, X., Liu, V., & Tang, C. (2018). An improved information security risk assessments method for cyber-physical-social computing and networking. *IEEE Access*, *6*, 10311-10319.

[22] Zhang, Q., Zhou, C., Tian, Y., Xiong, N. , Qin, Y., & Hu, B. (2018). A fuzzy probability Bayesian network approach for dynamic cybersecurity risk assessment in industrial control systems. *IEEE Transactions on Industrial Informatics*, *14*(6), 2497-2506.

[23] Kalinin, M., Krundyshev, V., & Zegzhda, P. (2021). Cybersecurity risk assessment in smart city infrastructures. *Machines*, *9*(4),78.

[24] Abbass, W., Bakraouy, Z., Baina, A., & Bellafkih, M. (2018, October). Classifying IoT security risks using deep learning algorithms. In *6th International Conference on Wireless Networks and Mobile Communications (WINCOM)* (pp. 1-6).

[25] Baldini, G., Fröhlich, P., Gelenbe, E., Hernandez-Ramos, J. L., Nowak, M., Nowak, S. et al. (2020). IoT network risk assessment and mitigation: The SerIoT approach. In J. Soldatos (Ed.), *Security Risk Management for the Internet of Things: Technologies and Techniques for IoT Security, Privacy and Data Protection* (pp. 88-104). Now Publishers, Boston-Delft.

[26] Zakaria, M. N., Bakar, N. A. A., Abas, H., & Hassan, N. H. (2020). A conceptual model for Internet of Things risk assessment in healthcare domain with deep learning approach. *International Journal of Innovative Computing*, *10*(2), 7-19.

[27] Liu, X., Ospina, J., & Konstantinou, C. (2020). Deep reinforcement learning for cybersecurity assessment of wind integrated power systems. *IEEE Access*, *8*, 208378-208394.

Significant Reduction of Lattice Thermal Conductivity of $SrTiO_3$: A Potential Material for Heat to Electricity Generation

Al Jumlat Ahmed[1]

[1]Institute for Superconducting and Electronic Materials, University of Wollongong, Wollongong, Australia, jumlat@gmail.com

Abstract—**$SrTiO_3$ is promising oxide thermoelectric (TE) material for waste heat to electricity generation especially for high temperature applications. However, its thermoelectric performance still inferior compared to telluride TE materials mainly due to high lattice thermal conductivity. In this study, nanoscale pores were introduced into bulk sample of $SrTiO_3$ by polymeric micelle self-assemble method followed by rapid solidification technique called spark plasma sintering. The sintering condition, holding time was optimized to maintain the nano structure of the bulk sample. The X-ray diffraction (XRD) analysis confirms that the samples are bare $SrTiO_3$ and there is no presence of any secondary phase in the bulk samples and scanning electron microscopic (SEM) analysis confirms the presence on nanoscale pores in sample and number of pores increases with the amount of pore format (surfactant F127). There is significant reduction in lattice thermal conductivity in the sample due to anisotropic scattering of phonon by the nano pores. The lowest thermal conductivity of 0.88 $W m^{-1} k^{-1}$ at 900 K was achieved for the sample with 400mg of F127 surfactant and sintered for 5 min. The nanoscale pores in the bulk $SrTiO_3$ shows a new pave of improving performance of thermoelectric materials.**

Keywords - thermoelectric, $SrTiO_3$, nanoscale porosity, lattice thermal conductivity, spark plasma sintering (SPS)

I. INTRODUCTION

The thermal energy which is being wasted enormously from different sources can be directly converted into valuable electrical energy using thermoelectric (TE) device [1-4]. Theoretical calculation shows that more than 60 percent of energy produced worldwide has been wasting in the form of heat continuously. This waste heat from different sources for instance: exhaust system of vehicle, industrial boilers and chimneys, thermal power plant and even waste heat from the cooking stove can be directly converted into useful electrical energy by thermoelectric generator [1, 2, 5]. The thermoelectric generator was integrated with the exhaust system of BMW 530i concept car to improve the fuel efficiency [6]. The radioisotope thermoelectric generator (RTG) is used in deep spaceship to generate electricity from heat of radioactive decomposition [7]. However, the energy conversion efficiency and lifetime of thermoelectric device are not enough for widely usage. Energy scientists around the globe are working on different thermoelectric materials and device configurations to overcome these hurdles.

Strontium titanate ($SrTiO_3$) is a well-known thermoelectric material with the cubic perovskite ABO_3 crystal structure. The melting temperature of $SrTiO_3$ is 2080ºC which gives it chemical as well as thermal stability at high temperature [8]. The lattice thermal conductivity of $SrTiO_3$ is high, 12 $Wm^{-1}K^{-1}$ at room temperature which is the main challenge to become a usable thermoelectric material [9]. $SrTiO_3$ with appropriate stoichiometry is an insulator having a band gap of 3.2 eV. However, the electrical conductivity can be changed from insulating to metallic by substitutional doping of $SrTiO_3$ with La^{3+} or Nb^{5+} [10, 11]. There are different synthesis techniques were used to

improve thermoelectric performance of the material. It was reported that the high performance $SrTiO_3$ with La-Nb co-doping, was prepared by a combination of hydrothermal method and high-efficiency sintering. Nano-scale co-doping is successfully modulated by hydrothermal method, and nano-inclusions precipitate during sintering process, to form complex microstructures [12]. The Nb-doped $SrTiO_3$ ceramics doped with the surface modification of nanosized titania was prepared via liquid phase deposition approach and subsequent sintered in an Ar atmosphere [13]. In another study, high density $Sr_{0.8}La_{0.067}Ti_{0.8}Nb_{0.2}O_{3-\delta}$ ceramics containing of Cu or Fe were prepared by the mixed oxide route and sintered under reducing conditions at 1700 K [14]. $Sr_{1-x}La_xTiO_3$ (x=0, 0.02, 0.05, 0.08) nanoparticles were directly prepared by mechanical alloying, followed by carbon burial sintering to produce the bulk thermoelectric sample. The purpose is to obtain pure phase and fine microstructures [15]. Sr-deficient $SrTiO_3$ with La and Dy co-doped powders were synthesized via the sol-gel method, followed by sintering at 1550ºC under a reducing atmosphere [16-18]. A rapid synthesis process at a low temperature of thermoelectric Y-doped $SrTiO_3$ was tried by using the polymerized complex process and the spark plasma sintering method with addition of TiB_2 powder [19]. Although different approaches were carried out to improve performance of $SrTiO_3$, still its performance hinder due to large lattice thermal conductivity.

Optimizing conditions of solidification of nano structured powder samples could be a possible way of reducing lattice thermal conductivity of $SrTiO_3$. Conditions of solidification process (Spark Plasma Sintering, SPS) like sintering temperature, pressure, holding time, heating and cooling rate of metal oxide thermoelectric materials were reported in different literatures. Sintering conditions for preparing bulk sample of $SrTiO_3$ are summarized in the Table I. Bulk material with nanostructure sintered in SPS can reduce the thermal conductivity of the material dramatically [20]. Sol-gel process followed by SPS significantly decreased the thermal conductivity of $SrTiO_3$. The lowest value of thermal conductivity was reported 1.19 $Wm^{-1}K^{-1}$ of the sample sintered at 1203K in SPS [21].

In this study, nanoscale pores were introduced in into bare $SrTiO_3$ samples using chemical process called polymeric micelle self-assembly method, followed by quick densification method called spark plasma sintering (SPS) at reducing atmosphere. The effect of nano structure and sintering condition like holding time on thermal conductivity of bare $SrTiO_3$ has been examined in this study.

II. Experiment

A. Sample Preparation

There are two main steps of nano structured bulk sample preparation. At first, powder samples with nano porosity preparation using chemical process called polymeric micelle assemble method. Secondly, bulk samples preparation from the powder using the Spark plasma sintering (SPS) technique. The details of the synthesis process were discussed in our previous reports[11, 18].

B. Powder Preparation by Polymeric Micelle Assembly Method

$SrTiO_3$ powder with nano scale porosity were prepared by polymeric micelle assembly method. The commercially available poly (ethylene oxide)-*block*-poly(propylene oxide)-*block*-poly(ethylene oxide) symmetry triblock copolymer commonly known as Pluronic F127 ($PEO_{100}PPO_{65}PEO_{100}$) were used as template to form nano scale pores into the material [27]. At a concentration higher than the critical micelle concentration (CMC), the block copolymers start to aggregate for forming micelles [28]. The

TABLE I. Conditions of spark plasma sintering of pure and doped $SrTiO_3$ samples.

Doping	Temp (ºC)	Pressure (MPa)	Holding time (min)	Ref
$SrTiO_3$	875	200	5	[22]
	900		3	
	950		0	
$SrTi_{0.8}Nb_{0.2}O_3$	1300	50	1	[23]
$La_{0.08}Sr_{0.92}TiO_3$	930	40	5	[21]
	1000			
	1100			
	1200			
$Sr_{1-x}Gd_xTiO_3$ X = 0 to 0.12	1375	40	5	[24]
$Sr_{1-x}La_xTiO_3$, x = 0:08	1240-1390	34	15	[25]
$Sr_{0.92}La_{0.08}TiO_3$	1573	34	30	[26]

shape of the micelles depends on length of propylene oxide (PO) and ethylene oxide (EO) group, concentration of block copolymer and temperature. The micelle has hydrophobic core created by PPO chains and hydrophilic shell created by PEO chains. The temperature at which the micelles are formed is called critical micelle temperature (CMT) and most of the Pluronic copolymers, the CMT is range between 25ºC to 40ºC [28]. The powder samples with different amount of F127 surfactant were prepared to examine the effect of amount of pore former in the nanostructure of the samples. The samples are denoted based on amount of F127 surfactant in the sample. The samples STO 0F127, STO 100F127, STO 200F127, STO 300F127 and STO 400F127 has 0 mg, 100 mg, 200 mg, 300 mg, and 400 mg of F127 surfactant respectively.

C. Bulk Sample Preparation Using Spark Plasma Sintering

The spark plasma sintering (SPS) is also known as field-assisted sintering technique (FAST)[20]. It is a low voltage, pulsed high DC current and pressure assisted sintering and synthesis technique. In this technique, pulsed high DC current directly passes through the graphite die as well as the powder within the die. A very fast heating and cooling rate and very short sintering time in SPS, lead to a rapid densification of powder and prevent grain growth and nano structure. The calcinated nano scale porous powder were packed into a graphite die (20mm diameter) with protecting graphite foil for spark plasma sintering. The sintering process has been carried out under vacuum condition (10^{-3} bar). Sintering parameters such as sintering temperature, pressure were carefully chosen based on literature review and sintering time was optimized to prepare bulk sample with nano structure. The powder sample with 400mg F127 surfactant (STO 400F127) was used to prepared bulk sample. The samples were heated at 1173K under a uniaxial pressure of 40 MPa for different sintering time 5, 8, 15 and 30 min. The bulk samples were denoted based on their sintering time. The temperature and pressure were increased with a rate of 25K per min and 10 MPa per min respectively.

D. Sample Characterization

The powder XRD patterns were determined by the X-ray diffractometry (Cu Kα, GBC MMA, λ = 1.5418 Å) with a step size of 0.02° and speed of 2° per min. The nanostructures of samples have been studied using field emission scanning electron microscopy (FE-SEM, JEOL 7500F) with a maximum magnification of x1,000,000 and highest resolution of 1nm. The thermal diffusivity of the samples was measured under vacuum conditions using the instrument, LINSEIS LFA 1000, and the specific was measured under argon atmosphere by DSC-204F1 Phoenix. The results of the samples were confirmed by repeating all the measurements several times.

III. RESULTS AND DISCUSSION

The Fig. 1 shows XRD patterns of $SrTiO_3$ powder samples with different amount of F127 surfactant for pore formation in the samples. For all the samples, the XRD peaks match with card number 00-001-1018 which confirms that the main phase is Strontium titanium oxide ($SrTiO_3$). There is a presence of some minor peaks corresponded to other phases such as TiO_2 and $SrTi_{12}O_{19}$ [29] at 2θ range of 25º – 35º in the XRD patterns. And there is no presence of any peak which is indicating the presence of F127 surfactant. It is implied that the F127 organic compound were removed completely during the calcination process and the process would help to from nano structure in the powder samples.

The Fig. 2 shows SEM images of calcinated $SrTiO_3$ powder samples with different amount of F127 surfactant (0, 100, 200, 300 and 400mg).

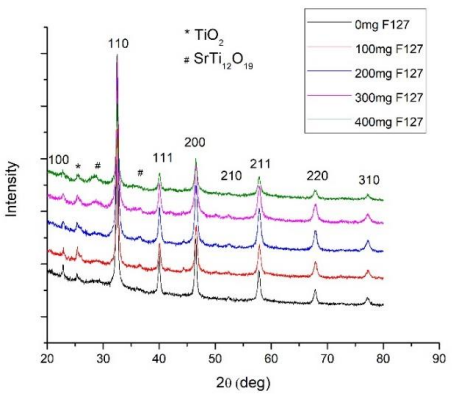

Figure 1. XRD patterns of $SrTiO_3$ powder samples with different amount of F127 Surfactant.

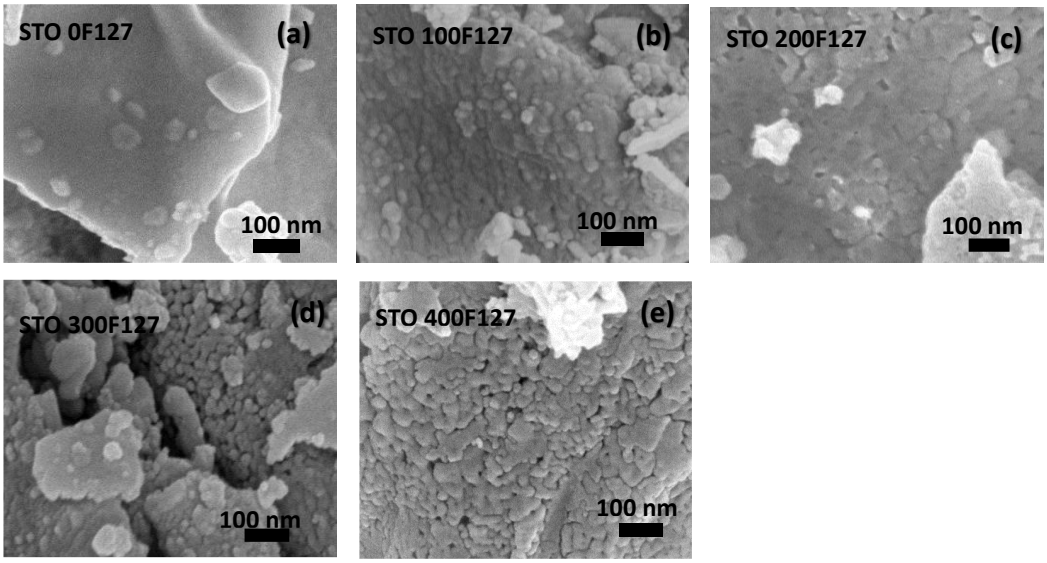

Figure 2. SEM image of $SrTiO_3$ powder samples with different amount of F-127 surfactant (a) 0mg, (b) 100 mg, (c) 200 mg, (d) 300 mg, and (e) 400 mg of F-127.

The images reveal that number of pores increases with the amount of F127 in the samples. The Fig. 2(c, d) clearly shows that the size of particles is few ten nanometre and there are nano scale pores in between of particles which makes the particles loosely connected to each other. The images also show that some pores start to agglomerate due to high calcination temperature.

The powder samples STO 400F127 was chosen for further experiments to prepare bulk sample using SPS technique because of nano structure of the sample. The sintering time of SPS was varied from 5 to 30 min. The XRD patterns of bulk samples with different sintering time (5, 8,15 and 30 min) are shown in the Fig. 3. The figure shows that the XRD peaks of all the bulk samples match with card number 00-001-1018 which confirms the main phase is Strontium titanium oxide ($SrTiO_3$) and there are no secondary phases in the XRD patterns. The sharp peaks of XRD indicate that the bulk samples are well crystalline.

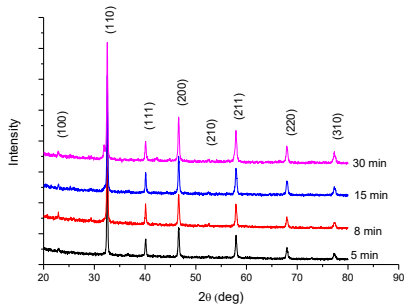

Figure 3. XRD patterns of $SrTiO_3$ bulk samples sintered in SPS for different times.

The Fig. 4 shows the SEM image of the bulk sample STO 400F127 which was sintered for 15 min in SPS. The average grain size of the sample is around 50 nm and most of them are around in shape. It is clear from the figure that there are nano pores in between of grains which separate grain boundaries from each other. It can be anticipated that the nano scale grains and pores

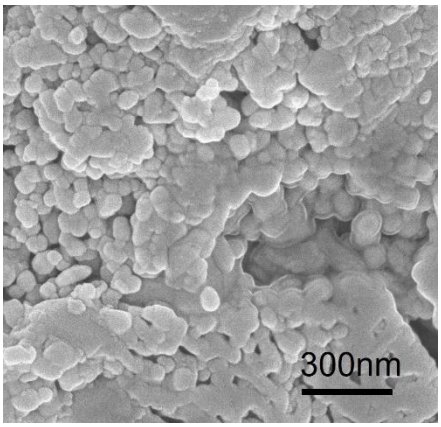

Figure 4. SEM image of the $SrTiO_3$ bulk sample with 400mg of F127 Surfactant and Sintering for 15 min.

will help to reduce the thermal conductivity of the sample.

The thermal conductivity of bulk $SrTiO_3$ samples is calculated from the thermal diffusivity, specific heat capacity, and density of the material, $\kappa = \alpha\, C_p\, \rho$, where α, C_p, and ρ are the thermal diffusivity, heat capacity at constant pressure, and the material density, respectively. The thermal diffusivity, the specific heat capacity, and the thermal conductivity of bulk $SrTiO_3$ samples are shown in Figs. 5 (a-c). The Fig. 5a shows that the thermal diffusivity of the samples slightly decreases with temperature. Most importantly, the figure shows that the thermal diffusivity increases significantly with the increment of sintering time. This may be due to growing of grains with longer sintering time and growth of grain reduces nano pores in the samples. The value of specific heat capacity of the samples as shown in Fig. 5b is close to the theoretical value and there is no significant change in specific heat capacity with temperature.

It can be observed in the Fig. 5c that the thermal conductivity of the samples follows the trend of the thermal diffusivity. The sample sintered for 5 min shows the lowest thermal conductivity however, the sample has low density due to very low holding time and the sample with lower density is not suitable for thermoelectric application because it will not show enough electrical conductivity. The sample with 30 min sintering time shows high thermal conductivity due to growth of grains which is also not suitable for thermoelectric application. The samples with 8 and 15 min sintering time show moderate thermal conductivity which would be suitable for heat to electricity generation application of the material. All the samples have significantly lower thermal conductivity compared to the reference sample. This could be due to the phonon boundary scattering by the nanostructured pores of the sample [30, 31]. Theoretical studies shows that pores in the range of a few nanometres to few ten of nanometres can effectively scatter phonons of different wavelengths [32]. The thermal conductivity has two parts, electronic thermal conductivity, and lattice thermal conductivity. Since bare $SrTiO_3$ is electrically insulator, the lattice thermal conductivity is mainly contributing to the thermal conductivity of the samples and there is a significant reduction in the lattice thermal conductivity due to presence of nano structure in the samples.

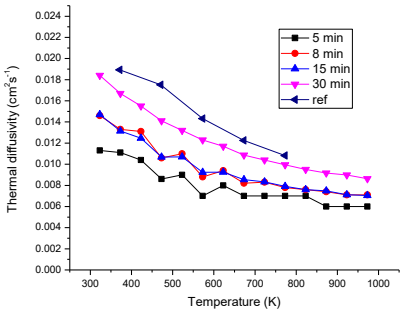

a)

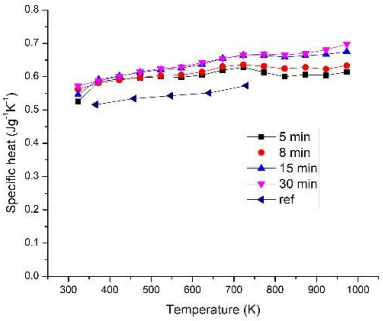

b)

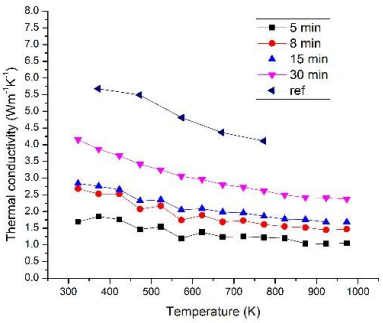

c)

Figure 5. (a) Thermal diffusivity, α (cm2/s), (b) Specific heat, Cp (J/gk) and (c) Thermal conductivity, K (W/mK) of $SrTiO_3$ bulk samples sintered for different time.

IV. CONCLUSION

The nanoscale pores were introduced successfully into bulk sample of $SrTiO_3$ by polymeric micelle self-assemble method followed by rapid solidification technique called spark plasma sintering. The sintering condition, holding time was optimized to maintain the nano structure of the bulk sample. The X-ray diffraction (XRD) analysis confirms that the samples are bare $SrTiO_3$ and there is no presence of any secondary phase in the bulk samples and scanning electron microscopic (SEM) analysis confirms the presence on nanoscale pores in sample and number of pores increases with the amount of pore format (surfactant F127). There is significant reduction in lattice thermal conductivity in the sample due to anisotropic scattering of phonon by the nano pores. The lowest thermal conductivity of 0.88 $W\ m^{-1}\ k^{-1}$ at 900 K was achieved for the sample with 400mg of F127 surfactant and sintered for 5 min. The nanoscale pores in the bulk $SrTiO_3$ shows a new pave of improving performance of thermoelectric materials.

REFERENCES

[1] Ohta, H. (2007). Thermoelectrics based on strontium titanate. *Materials today*, *10*(10), 44-49.

[2] Zhang, Y., et al. (2018). Double thermoelectric power factor of a 2D electron system. *Nature communications*, *9*(1), 1-7.

[3] Zhu, F. F., et al. (2015). Epitaxial growth of two-dimensional stanene. *Nature materials*, *14*(10), 1020-1025.

[4] Islam, S. M. K. N., et al. (2018). Giant enhancement of the figure-of-merit over a broad temperature range in nano-boron incorporated Cu 2 Se. *Journal of Materials Chemistry A*, *6*(38), 18409-18416.

[5] Zhang, X., & Zhao, L. D. (2015). Thermoelectric materials: Energy conversion between heat and electricity. *Journal of Materiomics*, *1*(2), 92-105.

[6] Vining, C. B. (2009). An inconvenient truth about thermoelectrics. *Nature materials*, *8*(2), 83-85.

[7] He, J., & Tritt, T. M. (2017). Advances in thermoelectric materials research: Looking back and moving forward. *Science*, *357*(6358).

[8] Ahmed, A. J. (2021). *Development of Nano-engineered Perovskite-based Thermoelectric Material for Waste Heat Recovery* [Doctoral dissertation, Institute for Superconducting and Electronic Materials, University of Wollongong].

[9] Zhang, L., et al. (2017). Tuning the thermal conductivity of strontium titanate through annealing treatments. *Chinese Physics B*, *26*(1), 016602.

[10] Ahmed, A. J., et al. (2020). Significant Improvement in Electrical Conductivity and Figure of Merit of Nanoarchitectured Porous SrTiO3 by La Doping Optimization. *ACS applied materials & interfaces*, *12*(25), 28057-28064.

[11] Ahmed, A. J., et al. (2019). Enhancement of thermoelectric properties of La-doped SrTiO3 bulk by introducing nanoscale porosity. *Royal Society open science*, *6*(10), 190870.

[12] Wang, J., et al. (2017). Record high thermoelectric performance in bulk SrTiO3 via nano-scale modulation doping. *Nano Energy*, *35*, 387-395.

[13] Li, E., Wang, N., He, H., & Chen, H. (2016). Improved thermoelectric performances of SrTiO 3 ceramic doped with Nb by surface modification of nanosized titania. *Nanoscale research letters*, *11*(1), 1-5.

[14] Srivastava, D., Norman, C., Azough, F., Schäfer, M. C., Guilmeau, E., & Freer, R. (2018). Improving the thermoelectric properties of SrTiO3-based ceramics with metallic inclusions. *Journal of Alloys and Compounds*, *731*, 723-730.

[15] Liu, D., Zhang, Y., Kang, H., Li, J., Chen, Z., & Wang, T. (2018). Direct preparation of La-doped SrTiO3 thermoelectric materials by mechanical alloying with carbon burial sintering. *Journal of the European Ceramic Society*, *38*(2), 807-811.

[16] Han, J., Sun, Q., & Song, Y. (2017). Enhanced thermoelectric properties of La and Dy co-doped, Sr-deficient SrTiO3 ceramics. *Journal of Alloys and Compounds*, *705*, 22-27.

[17] Han, J., Sun, Q., Li, W., & Song, Y. (2017). Microstructure and thermoelectric properties of La0. 1Dy0. 1SrxTiO3 ceramics. *Ceramics International*, *43*(7), 5557-5563.

[18] Ahmed, A. J., et al. (2021). Significant Reduction in Thermal Conductivity and Improved Thermopower of Electron-Doped Ba1–xLaxTiO3 with Nanostructured Rectangular Pores. *Advanced Electronic Materials*, *7*(4), 2001044.

[19] Ito, M., & Ohira, N. (2010, June). Transport properties of thermoelectric SrTiO3 synthesized by polymerized complex method and spark plasma sintering. In *Journal of Physics: Conference Series* (Vol. 232, No. 1, p. 012005). IOP Publishing.

[20] Guillon, O., et al. (2014). Field-assisted sintering technology/spark plasma sintering: mechanisms, materials, and technology developments. *Advanced Engineering Materials*, *16*(7), 830-849.

[21] Shang, P. P., Zhang, B. P., Li, J. F., & Ma, N. (2010). Effect of sintering temperature on thermoelectric properties of La-doped SrTiO3 ceramics prepared by sol–gel process and spark plasma sintering. *Solid State Sciences*, *12*(8), 1341-1346.

[22] Maca, K., Pouchly, V., & Shen, Z. (2008). Two-step sintering and spark plasma sintering of Al2O3, ZrO2 and SrTiO3 ceramics. *Integrated Ferroelectrics*, *99*(1), 114-124.

[23] Sonne, M., Van Nong, N., He, Z., Pryds, N., & Linderoth, S. (2010, September). Improvement of Niobium Doped SrTiO3 by Nanostructuring. In *8th European Conference on Thermoelectrics* (pp. 22-24).

[24] Li, L., Liu, Y., Qin, X., Li, D., Zhang, J., Song, C., & Wang, L. (2014). Enhanced thermoelectric performance of highly dense and fine-grained (Sr1− xGdx) TiO3− δ ceramics synthesized by sol–gel process and spark plasma sintering. *Journal of alloys and compounds*, *588*, 562-567.

[25] Kikuchi, A., Zhang, L., Okinaka, N., Tosho, T., & Akiyama, T. (2010). Optimization of sintering

temperature for maximizing dimensionless figure of merit of La-doped strontium titanate thermoelectric material in the combination of combustion synthesis with post spark plasma sintering. *Materials transactions*, *51*(10), 1919-1922.

[26] Okinaka, N., Zhang, L., & Akiyama, T. (2010). Thermoelectric properties of rare earth-doped SrTiO3 using combination of combustion synthesis (CS) and spark plasma sintering (SPS). *ISIJ international*, *50*(9), 1300-1304.

[27] Wang, L., & Yamauchi, Y. (2009). Block copolymer mediated synthesis of dendritic platinum nanoparticles. *Journal of the American Chemical Society*, *131*(26), 9152-9153.

[28] Kabanov, A. V., Batrakova, E. V., & Alakhov, V. Y. (2002). Pluronic® block copolymers as novel polymer therapeutics for drug and gene delivery. *Journal of controlled release*, *82*(2-3), 189-212.

[29] Shen, H., Lu, Y., Wang, Y., Pan, Z., Cao, G., Yan, X., & Fang, G. (2016). Low temperature hydrothermal synthesis of SrTiO 3 nanoparticles without alkali and their effective photocatalytic activity. *Journal of Advanced Ceramics*, *5*(4), 298-307.

[30] Hudiono, Y., Greenstein, A., Saha-Kuete, C., Olson, B., Graham, S., & Nair, S. (2007). Effects of composition and phonon scattering mechanisms on thermal transport in MFI zeolite films. *Journal of Applied Physics*, *102*(5), 053523.

[31] Parrish, K. D., Abel, J. R., Jain, A., Malen, J. A., & McGaughey, A. J. (2017). Phonon-boundary scattering in nanoporous silicon films: Comparison of Monte Carlo techniques. *Journal of Applied Physics*, *122*(12), 125101.

[32] Lee, H., Vashaee, D., Wang, D. Z., Dresselhaus, M. S., Ren, Z. F., & Chen, G. (2010). Effects of nanoscale porosity on thermoelectric properties of SiGe. *Journal of Applied Physics*, *107*(9), 094308.

Eco-Friendly and Environmentally Absorbent Materials for Solar Energy Applications

Faten Belarbi[1], Utku canci.C.Matur[2], Nulgun Baydogan[3],Mohamed Adnane[4]

[1,4]Laboratoire de Microscopie Electronique et Sciences des Matériaux. University of Sciences and Technology Mohamed Boudiaf Oran, Algeria, belarbifaten84@gmail.com[1], mohamed67adnane@gmail.com[4]

[2]Istanbul Gedik University, Energy Technologies Application and Research Center, Istanbul, Turkey

[2,3]Energy Institute, Istanbul Technical University, 34469, Istanbul, Turkey

Abstract—**In this paper are have interested to the most lowest-cost and stable materials, such as Cu2ZnSnS4(CZTS) and Cu2SnS3(CTS), because this materials are non-toxic, economical and have the elements which are abundant in nature these two materials represent absorbent layers for thin-film solar cells, with a direct band gap and a high absorption coefficient (~105cm−1). In this study we have prepared CZTS and CTS thin films by low cost technique which is sol-gel technique and we have made a different characterization for this films.**

Keywords - thin films, CZTS, CTS, solgel

I. INTRODUCTION

This main challenge of photovoltaic solar technology is to reduce the cost and using elements which they are abundant in the earth to make reliable PV devices and efficient for clean energy needs. A promising way to reduce the cost of PV is the use of technological thin films in which thin layers of photoactive materials abundant in the earth. One of the most promising thin-film photovoltaic technologies is that which is based on CZTS and CTS materials.

Despite the fact that Si-based solar cells have a high conversion efficiency 26.7% [1]. But, it suffers from a high cost, so it cannot satisfy the world energy markets [2]. On the other hand, CIGS and CdTe offer high returns (around 23.4%, 22.1% respectively) [3] for which they attracted researchers these lately but the main problem with these two materials is the toxicity of constituent materials of cadmium and selenium as well as the reduced availability of tellurium and indium on earth. The same problem occurs in CXS-type chalcopyrites (CIS, CGS, ex) although they have attracted a lot of attention due to their applications significant potential in photovoltaic cells [4, 5] but their commercialization the pilot scale is limited because of In and Ga which they are expensive.

Therefore for this reason that most research in recent years has focused on alternative thin layered materials for photovoltaic cells like CZTS and CTS, which they have attracted a lot of attention because they made up of abundant and non-toxic earth elements and they have properties optoelectronics that make them favorable candidates for solar cell development.

CZTS and CTS are semiconductor absorbent materials with P-type conductivity. These semiconducting compounds have an optical band gap of 1.4–1.5 for CZTS and 0,8 à 1,77eV for CTS and have they also a large absorption coefficient i.e. $\geqslant$104 cm−1 [6, 7].

A number of different techniques are employed in the elaboration of CZTS and CTS solar cells, as thermal evaporation [8], magnetron sputtering [9, 10], screen printing [11, 12], chemical bath deposition [13], electro-deposition [14], and sol-gel method [15].

In this work we have elaborated CZTS and CTS thin films using sol-gel method by dip-coating technique. The structural and optical properties have been carried out by Scanning

ISBN: 978-86-80593-73-9

Electron Microscopy (SEM) and UV/Visible spectroscopy.

II. Experimental Details

A. Elaboration of CZTS Thin Films

CZTS thin films were produced by the sol-gel dip-coating method from these precursors: copper chloride dehydrates (CuCl2·2H2O) (2M), zinc chloride dehydrates (ZnCl2·2H2O) (1M), tin chloride dehydrates (SnCl2·2H2O) (1M), thiourea (CH4N2S) (4M) dissolved into a mixture of 50ml of absolute ethanol-deionized water. The mixtures of absolute ethanol/DIW (30%/70%) were used as solvent and the Diethanolamine was used as the stabilizer. The sol-gel solution was stirred for 2h at 50°C. A clear and transparent yellow sol-gel solution Fig. 1 has been obtained after a perfect dissolution of all the chemical compounds.

CZTS thin films were have been coated onto a glass substrate, using the method of sol-gel dip-coating method, and they were deposited layer by layer. So in this technique the cleaned substrates were first dipped in the CZTS solution for 8s. Following this step, the thin film was drying on a hot plate at 200° C for 10 min. The deposition and drying cycles have been repeated 6 times to get a thin film of 2.5 µm thick Fig. 2.

B. Elaboration of CTS Thin Films

For the CTS layer, follow the same protocol except the difference is in the production temperature where it is 65°C. In the end, a yellow and transparent solution is obtained Fig. 3.

So after the deposition by the dip-coatig technique we get a layer of CTS (Cu2SnS3) which has a dark brown color Fig. 4.

III. Results and Discussion

A. SEM Characterization

In this work, the JEOL brand scanning electron microscope (JSM-6610LA) within the electron microscopy and Materials science laboratory (LMESM) from U.S.T.O.MB University was used to analyze our samples.

Fig. 5 shows the SEM image of CZTS thin film prepared with Sol-gel dipcoating. We can see grains evenly distributed and covering the surface of the substrate.

Fig. 6 shows the characterization of the SEM layer of CTS. The morphology of the deposit surface is homogeneous, it reveals semi-complete crystal growth over the entire surface of the substrate and fewer ports are found.

B. Optical Properties

For the optical properties the measurements have been made by using Avantes spectrometer (AvaSpec 2048). The energy band gap was calculated based on a plot estimate $(\alpha h\upsilon)^2$ over $h\upsilon$. The energy band gap was calculated from an

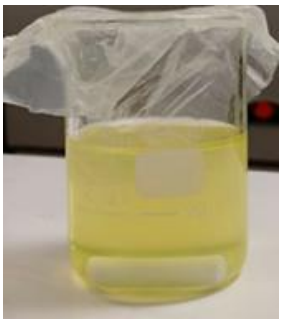

Figure 1. CZTS sol–gel solution.

Figure 2. CZTS thin film.

Figure 3. CTS sol–gel solution.

Figure 4. CTS thin film.

- *CZTS*

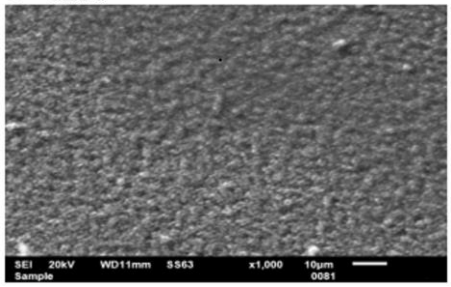

Figure 5. SEM characterization of the CZTS sample.

- *CTS*

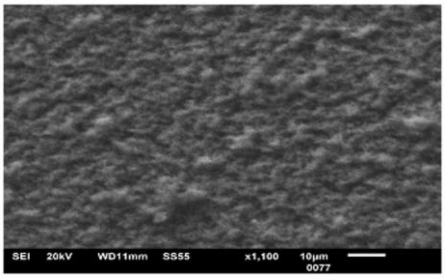

Figure 6. SEM characterization of the CTS sample.

- CZTS

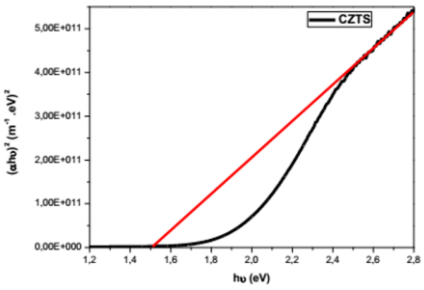

Figure 7. The transmittance and the Variation of $(\alpha h\nu)^2$ as a function of $(h\nu)$ for CZTS.

- CTS

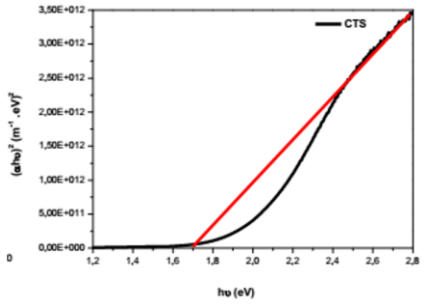

Figure 8. The transmittance and the Variation of $(\alpha h\nu)^2$ as a function of $(h\nu)$ for CTS.

estimate of the trace $(\alpha h\upsilon)$ 2 with respect to $h\upsilon$ [16].

From the optical analysis we found that the CZTS has a gap of 1.5eV and the CTS has a gap of 1.71eV.

IV. Conclusion

In this study, the gap and the thickness of thin films derived from sol-gel technique with a cost effective way were determined from the experiments at novel non-toxic solar cells manufacturing.so so according to this work we have concluded that the application of sol-gel technique (avoiding the sulfurization) was supported to obtain non-toxic and non-complex solar cells.

References

[1] Anwar, H. E. S. Q. S. (2012). *Handbook of Research on Solar Energy Systems and Tech Engeineering Science Refrences*. IGI Global.

[2] Barreto, A.K. (2003). The hydrogen economy in the21st century: a sustainable development scenario. *Int. J. Hydrogen Energy*, (p. 267).

[3] Dickson, M. M.H .(2005). *Geothermal Energy, Utilization and Technology*. Routledge.

[4] Ford, K.F. (1975). *Studies on the more efficient use of enery*. APS.

[5] Sorensen, B. (1997). *Renewable enrgy*. Academic Press.

[6] Miyamoto, Y., Tanaka, K., Oonuki, M., Moritake, N., & Uchiki, H.(2008). Optical Properties of Cu 2 ZnSnS 4Thin Films Prepared by Sol–Gel and Sulfurization Method, *Jpn. J. Appl. Phys. 47*, 596–597. DOI:10.1143/JJAP.47.596.

[7] Katagiri, H., Saitoh, K., Washio, T., Shinohara, H., Kurumadani, T., & Miyajima, S. (2001). Development of thinfilm solar cell based on Cu2ZnSnS4 thin films, *Sol. Energy Mater. Sol. Cells. 65*, 141– 148. DOI:10.1016/S0927-0248(00)00088-X.

[8] Shin, B., Gunawan, O., Zhu, Y., Bojarczuk, N. A., Chey, S. J., & Guha, S., (2013). Thin film solar cell with 8.4% power conversion efficiency using an earth-abundant Cu2ZnSnS4 absorber. *Progress in Photovoltaics: Research and Applications, 21*(1), 72–76. DOI: 10.1002/pip.1174.

[9] Jiang, F., Shen, H., & Wang,W. (2012). Optical and electrical properties of Cu 2ZnSnS4 film prepared by sulfurization method. *Journal of Electronic Materials*, 41(8), 2204–2209. DOI:10.1007/s11664-012-2112-8.

[10] Muhunthan, N., Singh, O. P., Singh, S., & Singh, V. N. (2013). Growth of CZTS thin films by cosputtering of metal targets and sulfurization in H 2S. *International Journal of Photoenergy*, 752012, DOI:10.1155/2013/752012.

[11] Sheng, X., Wang, L., Tian,Y., Luo,Y., Chang, L., & Yang,D. (2013). Lowcost fabrication of Cu2ZnSnS4 thin films for solar cell absorber layers. *Journal of Materials Science: Materials in Electronics, 24*(2), 548–552. DOI: 10.1007/s10854-012-0824-4.

[12] Wang,W., Shen, H., Jiang, F., He, X., & Yue, Z. (2013). Low-cost chemical fabrication of Cu 2ZnSnS4 microparticles and film. *Journalof Materials Science: Materials in Electronics, 24*(6), 1813–1817 DOI: 10.1007/s10854-012-1017-x.

[13] Shinde, N. M., Lokhande, C. D., Kim, J. H., & Moon, J. H. (2012). Low cost and large area novel chemical synthesis of Cu2ZnSnS4(CZTS) thin films. *Journal of Photochemistry and Photobiology A: Chemistry, 235*, 14–20. DOI:10.1016/j.jphotochem.2012.02.006.

[14] Jeon, M., Shimizu, T., & Shingubara, S. (2011). Cu2ZnSnS4 thin films and nanowires prepared by different single-step electrodeposition method in quaternary electrolyte. *Materials Letters, 65*(15-16), 2364–2367. DOI:10.1016/j.matlet.2011.05.003.

[15] Maeda, K., Tanaka, K., Nakano, Y., & Uchiki, H. (2011). Annealing temperature dependence prepared by sol-gel sulfurization method. *Japanese Journal of Applied Physics, 50*(5), Article ID 05FB08. DOI:10.1143/JJAP.50.05FB08.

[16] Matur, U.C., & Baydogan, N. (2017). Changes in gamma attenuation behaviour of sol-gel derived CIGS thin film irradiated using Co-60 radioisotope. *Journal of Alloys and Compounds, 695*, 1405-1413. DOI:10.1016/j.jallcom.2016.10.265

Waste Materials From Biofuel Manufacture as a Promising Substrate for Antibiotics Production

Jovan Ćirić[1], Nikola Stanković[2], Marko Živković[3], Đorđe Lazarević[4], Dušan Sadiković[5]

[1]Faculty of Technology, University of Niš, Leskovac, Serbia

[1,2,3,4] Faculty of Electronic Engineering, University of Niš, Niš, Serbia,
joca.ciric@gmail.com[1]

[5]Faculty of Sciences and Mathematics, University of Niš, Niš, Serbia

Abstract—**During the process of biodiesel production, by-product waste glycerol is obtained at approximately 10 % of the total input quantities. Glycerol obtained in this way, usually in alkali-catalyzed transesterification, can be considered as waste fraction due to the content of impurities such as traces of soap, dirt from the oil, residues of catalyst, and others. Waste glycerol, obtained in that way can be used as a promising microbial substrate and can be starting material for the production of valuable industrial products. It is well known that most species from the actinomycete genus *Streptomyces* can produce antibiotics, and grow on media with a different source of carbon and nitrogen. The study of the potential production of antibiotics by *S. hygroscopicus* CH-7 strain on the media that contains waste glycerol obtained in the biodiesel production from the sunflower and rapeseed oil as a carbon source.**

Keywords – biodiesel, *Streptomyces*, waste glycerol, antibiotics

I. INTRODUCTION

A large amount of waste glycerol is generated as a by-product during the process of biodiesel production where various raw materials such as crude oil and fat, vegetable oil, waste cooking oils, animal fats, or microalgae oil are used. Approximately 10 % of the starting materials go to waste glycerol in the biodiesel production process [1]. The production of biofuels, especially biodiesel, has rapidly increased during recent years. The growth of biodiesel production increases the generation of waste glycerol, which consequently causes significant decreases in the pure and waste glycerol prices. Depending on the purity degree, the glycerol price ranges between 0.27–0.41 US$/kg for the pharmaceutical grade (99.9 %), and between 0.09–0.20 US$/kg for the technical grade (80 %) [1, 2]. A prediction for the global production of waste glycerol in 2020 was 41.9 billion liters [1]. Huge amounts of waste glycerol obtained during biodiesel production do not only significantly lower its price, but also cause great concern for the environment due to the impurities it contains [3]. The cost of biodiesel production increases by 0.021 $/l for every 0.22 $/kg reduction in glycerol selling price [4]. Consequently, the economic utilization of glycerol for industrially significant products is of great importance for the sustainability of commercial biodiesel production and in that manner, crude glycerol could be considered as a desirable by-product, not as a waste product [1].

Waste glycerol obtained during biodiesel production contains impurities such as water, methanol, soaps, catalysts, salts, and non-glycerol organic matter, predominantly free fatty acids. Because of these reasons, it is necessary to purify waste glycerol as it would be suitable for existing and new usage but the conventional purification techniques are too expensive and complex. Therefore, the direct utilization of waste glycerol has become very important for the biodiesel industry. The major applications of waste glycerol are in many chemical processes as a reactant or a solvent or in diverse biotechnological processes for the production of value-added products such as chemicals and certain biofuels [5].

ISBN: 978-86-80593-73-9

It is well known that glycerol is a great substrate for the cultivation of different microorganisms [4], whereby the carbon content in the waste glycerol is 24-58 % that depending on the raw material used for biodiesel production [6]. Waste glycerol is used as the only carbon source in many fermentation processes for microbial growth and production of various products, such as 1,3-PD, 2,3-butanediol, ethanol, succinate, propionic acid, glyceric acid, citric acid, microbial oil, and others [7]. The impurities present in waste glycerol such as methanol, ethanol, salts, metals, and soaps can inhibit the growth of some microorganisms and the biochemical conversion of glycerol. Hence, it is necessary to use microorganisms with a high tolerance to impurities in waste glycerol.

On the other side, a large number of bacteria and molds can produce secondary metabolites. The microorganisms are the main producers of bioactive compounds, of which over 60 % are produced by actinomycetes, 28 % by molds, and around 11 % by non-filamentous bacteria. Antibiotics are among the most important secondary metabolites. Actinomycetes produce near three-quarters of the known antibiotics of various chemical structures [8]. Species of the genus *Streptomyces* are among the most prolific microorganisms, with certain *Streptomyces* spp. producing more than 180 different secondary metabolites [9]. In recent years, intensive research has been conducted in the field of improving the production of secondary metabolites with different activities and applications in biotechnology [8, 10].

II. EXPERIMENTAL

The *Streptomyces hygroscopicus* CH-7 (NCAIM (P) B-001336) strain from the Microbial collection of the Faculty of Chemistry and Institute of Chemistry, Technology, and Metallurgy in Belgrade, Serbia [11, 12] was stored at 4 °C at soybean medium with the following content (g/l): glucose 15; soybean 10; $CaCO_3$ 3; NaCl 3; agar 2 (pH 7.2) (Fig. 1). The experimental fermentation media were inoculated with 5 % (v/v) of a 48 hours old inoculum and incubated at 30 °C for 168hourswith shaking at 180 rpm. The content of the fermentative media was: (glucose, pure or waste glycerol 15 g/l; soybean 10 g/l; $CaCO_3$ 3 g/l; NaCl 3 g/l; $MgSO_4$ x 7 H_2O 0.5 g/l; $(NH_4)_2HPO_4$ 0.5 g/l; K_2HPO_4 1 g/l. The results were obtained by spectrophotometrically measuring of absorbance (Perkin-Elmer Lambda 15 UV/VIS) at λ_{max} = 364 nm for Hexaene H-85 and λ_{max} = 252 nm for Azalomycine B [11, 12]. Microbial growth was determined by measuring the dry weights of cells [12].

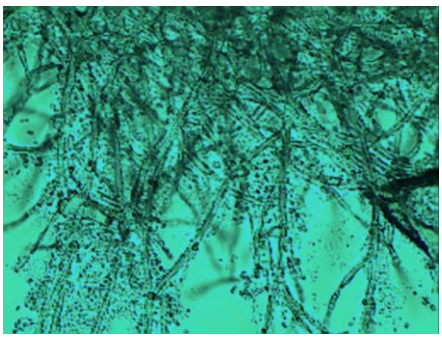

Figure 1. A microscopic preparation of strain *Streptomyces hygroscopicus* CH-7 (foto – Jovan Ćirić, Mikro Lab – TFL, 60X).

The concentrations of glycerol were determined using the HPLC method by Agilent 1100 Series chromatograph with Aminex HPX-87H column.

III. RESULTS AND DISCUSSION

To study the possibility of exploiting the waste glycerol obtained from biodiesel production, the bacterium *S. hygroscopicus* CH-7 was cultivated on the Basal Soy Medium (BSM) with pure and waste glycerol as a carbon source (15 g/l). A standard glucose medium was used as the comparative control. During the fermentation, microbial growth (defined as the change in dry biomass), consumption of carbon sources (glucose and glycerol), and the production of antibiotics hexaene-H-85 and azalomycin B were monitored. Fermentation was monitored for 168 hours (eight consecutive days), with sampling performed every 24 hours. Fig. 2–5 show the changes in the monitored parameters during fermentation, while Table I shows the achieved maximum values of dry biomass, carbon source consumption as well as maximal concentrations of produced antibiotics.

The highest maximal concentration of dry biomass of *S. hygroscopicus* CH-7 and the highest consumption rate of carbon source, which is often the limiting growth substrate with most microorganisms [13], were observed in the medium with glucose. This effect is expected due to modest glucose metabolism and the achieved values are in a line with the published results [14]. The maximal

concentration of dry biomass was observed in the glucose medium after 72 hours of fermentation at 10.18 g/l (Table I). The highest glucose consumption was achieved in 72–96 hours of fermentation (86 % of the available amount). During further fermentation, the total glucose content decreases, and by the end of the fermentation, the consumption of 98 % of the total available amount was achieved. In the medium with pure glycerol, the maximal concentration of dry biomass was slightly higher than the growth in the medium with waste glycerol obtained during biodiesel production from sunflower oil (SFO). The maximum values (9.04 g/l and 8.88 g/l) were achieved at 48 hours of fermentation. These values were lower by 12 % and 13 % compared to the glucose medium (Fig. 2), while the glycerol consumption was almost twice lower (47 and 42 %) (Fig. 3).

The lowest growth, with the achieved maximum concentration of dry biomass of 6.52 g/l after 96 hours of fermentation, was observed in the substrate with waste glycerol obtained from biodiesel production from rapeseed oil (RSO), and 36 % of available glycerol was consumed, which is also the lowest consumption. The maximum concentrations of antibiotics during the fermentation process by *S. hygroscopicus* CH-7 depend on the carbon source. In all cases, after reaching the maximum value, the concentration of antibiotics decreased during the further course of fermentation. The increase in the concentration of antibiotics and the time to reach the maximum value is not related to the consumption of the substrate, which is typical for antibiotic biosynthesis. This indicates the independence of antibiotic production, respectively secondary metabolites, from substrate utilization and microbial growth.

In the medium with SFO waste glycerol, the maximum concentration of hexaene H-85 was reached after 72 hours of fermentation and it was 162 μg/ml. This was 10 % more than the maximum achieved concentration in the glucose media (146 μg/ml), achieved after 96 hours of fermentation (Fig. 4). In the medium with pure glycerol, an 18 % lower maximum concentration of hexaene H-85 (121 μg/ml) was achieved compared to the medium with glucose, while the lowest concentration (94 μg/ml) was achieved in the medium with RSO waste glycerol.

Unlike hexaene H-85, the maximum concentration of azalomycine B (38.7 μg/ml) was achieved after 72 hours of fermentation in the glucose medium, and lower concentrations were achieved after 96 hours of fermentation in the media with pure glycerol (33.1 μg/ml) and RSO waste glycerol (24.4 μg/ml) (Fig. 5). In the SFO waste glycerol medium, *S. higroscopicus* CH-7 produced the lowest amount of azalomycine B, with a maximum concentration of 11.0 μg/ml reached after 48 hours of fermentation.

The achieved maximum concentrations of hexaene H-85 were nearly 20 % lower than the achieved concentrations in previously published studies with various carbon sources [14], while the maximum concentrations of azalomycine B were almost twice lower. However, the achieved results during the present study are important because, in the aforementioned research, significantly more expensive carbon sources were used.

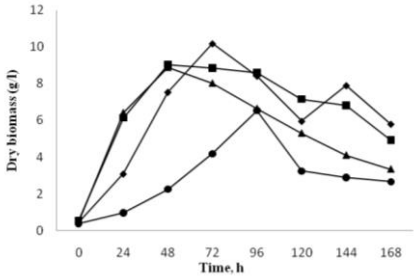

Figure 2. The change in concentration of dry biomass of bacteria *S. higroscopicus* CH-7 3 during the fermentation on basal medium with glucose (♦), pure glycerol (■), SFO waste glycerol (▲) and RSO waste glycerol (●).

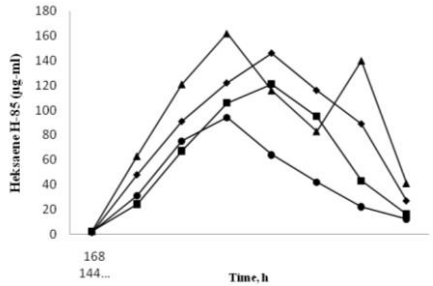

Figure 4. The change in concentration of antibiotic hexaene H-85 during the fermentation on basal medium with glucose (♦), pure glycerol (■), SFO waste glycerol (▲) and RSO waste glycerol (●).

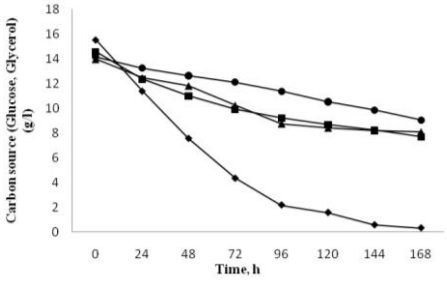

Figure 3. The change in concentration of carbon source during the fermentation on basal medium with glucose (♦), pure glycerol (■), SFO waste glycerol (▲) and RSO waste glycerol (●).

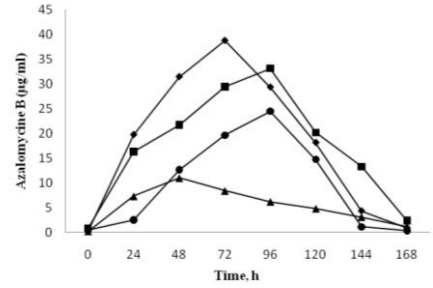

Figure 5. The change in concentration of antibiotic azalomycine B during the fermentation on basal medium with glucose (♦), pure glycerol (■), SFO waste glycerol (▲) and RSO waste glycerol (●).

TABLE I. THE MAXIMUM VALUES OF CONCENTRATION OF DRY BIOMASS (DBM), CONSUMPTION OF GLUCOSE AND GLYCEROL (ΔGLUC, ΔGLIC) AND MAXIMUM CONCENTRATION VALUES OF HEXAENE H-85 AND AZALOMYCINE B (C_{MAX}) AS WELL AS THE SPECIFIC RATE OF THEIR SYNTHESIS (Q_P) BY CULTIVATING THE BACTERIUM STREPTOMYCES HIGROSCOPICUS CH-7 ON MEDIA WITH GLUCOSE AND GLYCEROL.

Carbon source (g/l)				**Characteristics of bioprocess**								
Glucose	**Glycerol**			**DBM**	**Δ_{gluk}**		**Δ_{glic}**		**Hexsaene H-85**		**Azalomycine B**	
	Pure	Waste SFO[a]	Waste, RSO[b]	X_{max} (g/l)	(g/l)	(%)	(g/l)	(%)	C_{max} (μg/ml)	q_p (mg/g/d)	C_{max} (μg/ml)	q_p (mg/g/d)
15	-	-	-	10.18	15.24	98	-	-	146	2	38.7	0.5
-	15	-	-	9.04	-	-	6.85	47	121	1.8	33.1	0.5
-	-	15	-	8.88	-	-	5.87	42	162	2.6	11.0	0.2
-	-	-	15	6.52	-	-	5.10	36	94	2	24.4	0.5

[a] Waste glycerol obtained in biodiesel production from sunflower oil.
[b] Waste glycerol obtained in biodiesel production from rapeseed oil.

IV. CONCLUSIONS

Based on the study of the potential of *S. higroscopicus* CH-7 strain antibiotics production cultivated on glycerol waste substrates, obtained from biodiesel production, it can be concluded that the studied strain produces different maximum amounts of hexaene and azalomycine, depending on the carbon source. The highest concentration of hexaene was achieved on a substrate with waste glycerol obtained from sunflower oil biodiesel production (162 μg/ml), 10 % higher than it was obtained in a medium with glucose as a conventional carbon source. In contrast to hexaene, azalomycine production was the highest on conventional medium (38.7 μg/ml) and 37 % lower on medium with rapeseed oil waste glycerol while that was higher than it was obtained on pure and sunflower oil glycerol media. On media with pure substances as a carbon source, bacterial cells produced higher amounts of azalomycine, whereas culturing the bacterium on waste glycerol directs cell metabolism to produce higher amounts of hexaene. Certainly, waste glycerol obtained in biodiesel production can be a useful and inexpensive feedstock for cultivating bacteria antibiotics producers. Also, the remaining amount of used media could be suitable for further biogas production.

ACKNOWLEDGMENT

This work has been funded by the Ministry of Education, Science and Technological Development of the Republic of Serbia (Projects III 45001 and III 44006).

REFERENCES

[1] Konstantinović, S., Danilović, B., Ćirić, J., Ilić, S., Savić, D., & Veljković, V. (2016). Valorization of crude glycerol from biodiesel production. *Chemical Industry and Chemical Engineering Quarterly, 22*(4), 461-489.

[2] Nanda, M. R., Yuan, Z., Qin, W., Ghaziaskar, H. S., Poirier, M., & Xu, C. (2014). Thermodynamic and kinetic studies of a catalytic process to convert glycerol into solketal as an oxygenated fuel additive. *Fuel, 117*, 470-477.

[3] Yazdani, S. S., & Gonzalez, R. (2007). Anaerobic fermentation of glycerol: a path to economic viability for the biofuels industry. *Current Opinion in Biotechnology, 18*, 213–219.

[4] Da Silva, G. P., Mack, M., & Contiero, J. (2009). Glycerol: a promising and abundant carbon source for industrial microbiology. *Biotechnology Advances, 27*, 30–39.

[5] Quispe, C., Coronado, C., & Carvalho Jr, J. (2013). Glycerol: Production, consumption, prices, characterization and new trends in combustion. *Renewable and Sustainable Energy Review, 27*, 475–493.

[6] You, Y. D., Shie, J. L., Chang, C. Y., Huang, S. H., Pai, C. Y., Yu, Y. H., & Chang, C. H. (2008). Economic Cost Analysis of Biodiesel Production: Case in Soybean Oil. *Energy & Fuels, 22*, 182–189.

[7] Chatzifragkou, A., Makri, A., Belka, A., Bellou, S., Mavrou, M., Mastoridou, M., Mystriot, P., Onjaro, G., Aggelis, G., & Papanikolaou, S. (2011). γ-decalactone Production by *Yarrowia Lipolytica* and *Lindnera Saturnus* in Crude Glycerol. *Energy, 36*, 1097-1108.

[8] Ćirić, J., Ilić, S., Konstantinović, S., Veljković, V., Gojgić-Cvijović, G., & Savić, D. (2012). The fermentation of glycerol by *Streptomyces hygroscopicus* CH-7. *Advanced Technologies, 1*(2), 20-25.

[9] Demain, A. L. (1999). Pharmaceutically active secondary metabolites of microorganisms. *Applied Microbiology and Biotechnology, 52*, 455-463.

[10] Ćirić, J., Konstantinović, S., Ilić, S., Gojgić-Cvijović, G., Savić, D., & Veljković, V. (2016). The impact of isatin derivatives on antibiotic production by *Streptomyces hygroscopicus* CH-7. *Chemical Industry, 70*(2), 123-128.

[11] Vučetić, J., Karadžić, I., Gojgić-Cvijović, & G., Radovanović, E. (1994). Improving hexaene H-85 production by *Streptomyces hygroscopicus*. *Journal of Serbian Chemical Society, 59*, 973–980.

[12] Karadžić, I., Gojgić-Cvijović, G., & Vučetić, J. (1991). Hexaene H-85, A hexaene H-85 macrolide complex. *Journal of Antibiotics, 12*, 1452–1453.

[13] Baras, J., Veljković, V., Popov, S., Povrenović, D., Lazić, M., & Zlatković, B. (2009). Osnovi Bioprocesnog Inženjerstva. Univerzitet u Nišu, Leskovac, 69-137.

[14] Ilić, S. B., Konstantinović, S. S., Veljković, V. B., Savić, D. S., & Gojgić-Cvijović, G. (2010). The impact of different carbon and nitrogen sources on antibiotic production by *Streptomyces hygroscopicus* CH-7. Current Research: *Technology and Education Topics in Applied Microbiology and Microbial Biotechnology*, Formatex, Spain.

Exploring Quality Dimensions in Construction Perspective

Abdurrahman Salihu Abubakar[1], Nuzul Azam Haron[2], Aidi Hizami Alias[3], Law Teik Hua[4], Raja Ahmad Azmeer Raja Ahamad Effendi[5],

[1,2,3,4,5]Universiti Putra Malaysia, Serdang, Selangor, Malaysia, abdulss06@gmail.com[1]

Abstract—**The quality of products and services is fundamental to organizational performance and reputation. The focus on continuous improvement through constructive enhancements that match the client's expectations is the unifying aspect of any quality plan. Construction project entails meeting the specification criteria and standards, finishing the task on time, and within the specified budget. An exploratory research method was used to examine the qualitative data using the inductive research approach to explore the eight quality dimensions within the construction industry's perspective by exploring the quality issues within the Malaysian construction industry. The findings indicate that a related quality dimension is conformance or the degree to which a product's design and operating characteristics meet established standards. Thus, the study's significant contribution is the exploration of the eight quality dimensions from the construction industry's perspective. In conclusion, for many clients, quality is less about the availability of specific features but is more about the overall aesthetic appearances of the building.**

Keywords - construction, dimensions, quality

I. INTRODUCTION

The quality of products and services is fundamental to organizational performance. The company should emphasize the importance of quality in all its management and operational activities [1].

The focus on continuous improvement through constructive enhancements that match the client's expectation of quality is the fundamental unifying aspect of any quality plan [2]. A company's desire to satisfy the perceived quality of product and services of clients are increasingly challenging to satisfy. Through quality improvement, products and resources can be efficiently and effectively managed, resulting in quicker, cheaper, and more quality workmanship [3]. Quality challenges vary from company to company, and companies tend to resolve their quality problems differently. Construction quality and success entails finishing the task on time, according to the quality specifications, and staying within the specified budget [4].

Quality standards, management commitment, coordination, planning, design, and relationships among building stakeholders are critical factors that play a vital role in addressing quality concerns [1].

II. METHODOLOGY

An exploratory research method was used to examine the qualitative data using the inductive research approach. The eight quality dimensions were explored within the construction industry's perspective based on quality issues within the Malaysian construction industry. The dimensions were further analyzed using narrative description and interpretation of the quality dimensions in the construction industry's context. There was no existing research exploring the quality dimensions within the construction industry's perspective at the time of this study. As a result, this study will act as a context study. Exploring quality dimensions in the construction perspective was undertaken using qualitative research methods. The exploratory nature of the study issue impacted the general research approach, using the inductive approach [5]. The research topic explores the current quality dimension from the construction perspective, focusing on Malaysia. Qualitative data was studied using the action research strategy within the construction perspective by exploring the quality issues within the Malaysian construction industry.

ISBN: 978-86-80593-73-9

III. Definition of Quality

Quality is a broad term that is difficult to describe. There is no one definition of quality that is universal. The three most influential quality management gurus define quality in the following ways; Juran defined it as "fitness to use" [6, 7] while Deming defined it as "the predictable degree of uniformity and reliability at low cost and appropriate for use [8]" and Crosby defined it as "Compliance with requirements [9]." Other quality experts' defined it based on their distinct views as the "fitness for use, doing it right the first time, clients need to adhere to specified standards, recognize the value for money, doing it right at the right time and so on [10-12]." Reference [13] categorizes quality definitions into five categories to provide a solution for the range of quality definitions: transcendental, product-based, user-based, manufacturing-based, and value-based.

More broadly, quality is defined as the greatness of a product or service in terms of meeting or exceeding customers' expectations [14]. These expectations are primarily determined by the product's or service's intended usage and the price. When a product or service meets or exceeds expectations, it is considered high quality. As a result, the concept is primarily intangible and perception-based.

Reference [15] expresses quality as an equation:

$$\textit{Where} \quad \begin{aligned} Q &= P / E \\ Q &= \textit{Quality} \\ P &= \textit{Price} \\ E &= \textit{Expectations} \end{aligned} \qquad (1)$$

"If Q is greater than 1.0, then the customer has a good feeling about the quality of the product or services. Of course, the determination of P and E will most likely be based on perception, with the organization determining the price and the customer determining the expectations [15]."

IV. Eight Dimensions of Quality

Understanding the critical factors or dimensions of quality in the construction perspective is essential for improving construction quality. The primary objective of this study is to explore the dimensions of quality from the construction perspective. Therefore, it is necessary to ascertain the perception dimension of quality in a construction context. Additionally, Garvin established eight quality dimensions for products and services. Quality has eight dimensions. The eight dimensions of quality are listed in Table I, together with their associated definitions and explanations [16].

Since these dimensions are partly independent, a product can be good in one dimension and medium or bad in another. Very few items can be said to satisfy all the eight dimensions. For instance, in the 1970s, the Japanese were recognized for their high-quality automobiles only based on their reliability, conformance, and aesthetics. As a result, some of the quality dimensions could be used to judge whether or not a product or service is of high quality or not. Hence, it is necessary to determine the relative value of each quality dimension in construction work. The identified dimensions can then be used to define the requirements for improving the quality of construction work.

A. Performance

This dimension is primarily concerned with the question, "Does the construction work satisfy the client specified performance standards; does it meet the aesthetic quality as specified in the 3D model?" Performance is frequently cited as a point of concern between workers and clients, especially when project quality is not explicitly and adequately stated within the quality standards [14]. Even though this quality dimension contains quantitative features,

TABLE I. Summary and Definition of Eight Dimensions of Quality as Proposed by Garvin (1987).

Eight dimensions of quality	
Dimensions	***Definitions***
Performance	A product's primary operational characteristics
Features	Additional features of a product.
Reliability	The probability that a product will fail within a specific period
Conformance	The extent to which a product's design adheres to set standards, i.e., workmanship
Durability	Product's useful life
Serviceability	After-sale service for the product like the ease of repair
Aesthetics	The product's appearance and characteristics, such as exterior finishing
Perceived Quality	Indirect assessment of product quality

companies typically rate the performance objectively and based on specific performance elements [13, 17].

B. Features

This aspect pertains to the characteristics that make a building function as designed. Reference [13] asserts that "features are the bells and whistles of high-quality service, the qualities that augment their fundamental functionality." As a result, it is critical for companies to describe the performance characteristics, features explicitly, and the intended processes to achieve high quality in implementing their projects [14]. Furthermore, for many clients, better quality is less about the availability of specific features but more about the overall aesthetic appearances of the building [14, 18].

C. Reliability

Reliability is inextricably linked to performance and continues to be a significant driver to a company's image and organizational reputation. The underlying question remains, "Will companies continue to meet standard quality specifications? "This dimension represents the likelihood of a product or services failure or degradation of the technology over a specific period. The mean time to the first failure, the mean time between failures, and the failure rate per unit time are among the most frequently used dependability metrics [13]." Additionally, clients want reliability more as mechanical problems and management costs increase.

D. Conformance

Reference [13] defines quality conformance as the degree to which a product's design and operating characteristics meet established standards." The central question under this dimension is, "Does the construction work conform to the design specifications in the 3D model?" When the workmanship quality met the specified performance specifications, it is said to have conformed with the quality standards set in the design model [14].

E. Durability

Reference [13] defined durability as "the lifespan of a product," which has economic and technological implications. Durability is a technical word that measures the duration of use that a thing may withstand before deteriorating. Clients often evaluate the anticipated operating and maintenance costs against the initial investment cost, both in economic terms and personal discomfort [13]. Thus, this dimension covers the critical question of how long can the building withstand the adverse effect of weather and other environmental hazards? As a result, it is intertwined with the principle of contractual terms. More significantly, clients frequently incorporate quality durability criteria in procurement contracts. Reference [13] states that "the durability dimension has two direct implications. Firstly, it implies that "durability and reliability" are inextricably related. Second, it implies that details relating to durability must be evaluated critically through new technological tools like BIM. The quality of workmanship can be improved by using more quality materials. Hence, new technologies capable of improving quality need to be adopted throughout the construction process [19].

F. Serviceability

This dimension is concerned with the serviceability and maintainability of the building. According to [13] and [17], "Clients are worried not just about the issues of rework, defects, but also about the quality of workmanship, the regularity of future maintenance work and other quality issues.

G. Aesthetics

This dimension, which refers to the final appearance of the building, is centered on the viewer's opinion whether the building is precisely the same as in the 3D model and pertains to the structure's construction precision [19]. Additionally, it is concerned with the aesthetic qualities of the building and their relationship to the company's overall corporate image and quality adherence reputation. Thus, this is one of the primary focuses of this research. Clients here are more concerned with the extent to which the physical aesthetics conforms to the 3D model and the overall appearance of the building.

Reference [13] asserts that "aesthetics appearance of a building is a subjective matter, but with the advent of new technologies, it possible to measure or identify the quality problems easily. Additionally, [19] mentioned that "quality issues that impair on the aesthetic characteristics of a building do not necessarily mean altering the quality dimensions or lack of conformance to a quality specification, but the aesthetic appearance that significantly affects the building design which leads to rejection [16].

H. Perceived Quality

Perceived service quality evaluation is done at the end of the project completion to rate the client's satisfaction. The perceived quality is obtained from customer satisfaction feedback based on the quality inspector's evaluation after a complete project evaluation [20]. Reference [13] summarizes the link between reputation and perceived quality succinctly when he states, "Reputation is the primary stuff of perceived quality." More precisely, reputation relates to how the quality of service is perceived. Its strength stems from an implicit "analogy: that the quality of products today was similar to yesterday's products, or the quality of goods in a new product line is similar to the quality of a company's established products [16]. " Thus, the basic premise remains that perception is reality. The use of high-quality materials in construction work is not just the element that impacts the overall quality reputation of the construction project. Because a project may be labelled as low-quality due to poor workmanship or poor construction service even though the materials used are qualitative. If the building is not correctly constructed and fails to meet the aesthetic appearance, the failure is frequently attributed to service quality rather than the material quality [21].

Quality should be embedded in the construction process, decision-making, design, maintenance, and operation [22]. Construction experts should prioritize quality as their topmost priority in the project's execution to maintain their competitive edge among other industries. Reference [23] suggests that construction work's quality should be suppliers' and consultants' primary attitude and focus. However, the good's standard is negatively affected if the stakeholders are not committed to quality standards. Then, quality culture becomes more challenging to execute [24]. It is essential to have strong collaborative team players to meet the project's desired goal. Continuous improvement in all aspects of the project can lead to a high-quality culture.

The construction sector can compete with other industries worldwide where quality is still in high demand [25]. Additionally, applying the quality culture concept on site is a significant problem in the construction industry because construction projects are unique in terms of the project's location, design, workers, materials, cost, and time. Project quality is influenced by quality standards, materials, quality of workmanship, and future maintenance costs [26]. The structure's safety depends on the construction quality and stakeholders' satisfaction. The quality establishment is the target of every construction company to maintain its fame and recognition among its competitors. The truth is that most companies are still left behind in understanding the true potentials of adhering to quality standards. Quality is critical for organizational efficiency, performance improvement, client satisfaction, and business success [27].

In Malaysia, the quality challenge is mainly with the on-site and off-site workers. It also includes; the whole construction process, management process, team players, suppliers, training and education, and policies [28]. The primary challenge in developing a quality model include contractors' roles in the construction process, resource optimization to achieve the intended outcome, meeting design standards, and fully implementing a structured quality framework [29, 30]. Additionally, other factors to consider in ascertaining the perceived quality of goods and services are; Clarity and applicability of design, compliance with quality specifications, construction environment, energy efficiency, and ease of operation and maintenance. Other quality activities in the construction environment include; management commitment, suppliers' relationships, information analysis, and human resource management [31]. The quality of construction work is affected by three key factors; Lack of management commitment, lack of adherence to standard specifications and training policies [32].

Nevertheless, several benefits have been identified by attributing the quality issues to a specific dimension in the construction industry. They are; continuous quality improvement, client satisfaction, the company's image and reputation, enhancement of its growth and efficiency, and documentation establishment [33].

V. Problems of Quality in Malaysian Construction Industry

In recent times, quality improvement has gained much attention. The importance of quality in construction has equal importance as in other industries [34]. On the other hand, the construction industry is faced with discontinuous, uncoordinated, complicated, and different construction operations compared to

other sectors [34]. The project's quality level represents the technology used in its execution and is key to its success [35, 36]. The above gave us some insight into some of the quality issues being faced by the construction industry. In another effort to address quality in construction work, the Malaysian government also mandated the use of a Quality Management System (QMS) in construction work [37]. QMS, as defined by the International Organization for Standardization (ISO), "is the management system used to direct and control an organization regarding quality [38]" QMS models are being used effectively by different industries, in particular the manufacturing and construction industries, because of the wide range of models it contains, such as Total Quality Management (TQM), Malcolm Baldrige National Quality Award, Six Sigma, Lean, and the ISO 9000 quality standards which are among the most recognized quality models in the world [39]. In addition, [39] stated that many companies strive for quality certification for different reasons, and other potential benefits are gained in return. The whole idea of implementing QMS is to resolve quality issues by satisfying the client's demands [40]. It is, however, worthy of mentioning that the successful adoption of QMS in the manufacturing industry prompted the integration of QMS into the construction industry more than 20 years ago [41]. According to research done by [42], the utmost and most apparent benefit of QMS is that it reduces rework if adequately implemented. Furthermore, other factors should be considered in developing a new quality approach such as conformance to quality and design specifications, constructability and design analysis, life cycle cost analysis, and sustainability issues to enhance construction output and develop a good quality reputation in the construction industry [30].

VI. CONCLUSION

In Malaysia, the quality challenges can be attributed to any of the aforementioned dimensions. The quality issues also include; the whole construction process and management process. As such, knowing the right quality dimension could ease quality assessment in the construction process, decision-making, design, maintenance, and operation. The explored quality dimensions could be used to categorize quality issues into a specific quality dimension. Furthermore, it can be used to attribute each quality issue to a dimension for a more

Figure 1. Showing the 8 dimensions of quality.

straightforward assessment. The attributed dimension can then be used to define the requirements for improving the quality of construction work. Construction quality entails finishing the task on time, meeting the specification criteria, and completing the project within the budget. A related quality dimension is conformance or the degree to which a product's design and operating characteristics adhere to established standards. For many clients, better quality is less about the availability of specific features and more about the overall aesthetic appearances of the building. The aesthetic quality of a building is a subjective matter. As Aristotle said, " Quality is not just a habit, but an act." Therefore, construction experts should make quality a habit and prioritize it in executing construction projects.

ACKNOWLEDGMENT

The present research has been developed within a broad research interest to explore the eight quality dimensions based on the construction industry's perspective. The authors are grateful to Universiti Putra Malaysia for its support and contribution to the Research project

REFERENCES

[1] Janipha, N. A. I., & Ismail, F. (2013). Conceptualization of Quality Issues in Malaysian Construction Environment. *Procedia - Soc. Behav. Sci.*, *101*, 53–61, doi: 10.1016/j.sbspro.2013.07.178.

[2] Doumbouya, L., Gao, G., & Guan, C. (2016). Adoption of the Building Information Modeling (BIM) for Construction Project Effectiveness : The Review of BIM Benefits. *Am. J. Civ. Eng. Archit.*, *4*,(3), 74–79, doi: 10.12691/ajcea-4-3-1.

[3] Olugboyega, O. (2016). Quality management practices among construction firms in Lagos State, Nigeria. *PM World J.*, *V*, (VI), 1–14.

[4] Eynon, J. & Emmitt, S. (2016). BIM and the Future of Design Management. *Constr. Manag. BIM Handb.*, 123–126. doi: 10.1002/9781119163404.ch18.

[5] Golafshani, N. (2015). Understanding Reliability and Validity in Qualitative Research. *Qual. Rep.*, *8*(4), 597–606. doi: 10.46743/2160-3715/2003.1870.

[6] Khan, F. (2010). Developing a Total Quality Management Framework for Public National University of Modern Languages.

[7] Saleh, R. A., Sweis, R. J., & Mahmoud Saleh, F. I. (2018). Investigating the impact of hard total quality management practices on operational performance in manufacturing organizations: Evidence from Jordan. *Benchmarking*, *25*(7), 2040–2064. doi: 10.1108/BIJ-05-2016-0074.

[8] Chen, R., Lee, Y. D. & Wang, C. H. (2010). Total quality management and sustainable competitive advantage: serial mediation of transformational leadership and executive ability. *Total Qual. Manag. Bus. Excell.*, *31*, (5–6), 451–468. doi: 10.1080/14783363.2018.1476132.

[9] Sim, Y. L. & Putuhena, F. J. (2015). Green building technology initiatives to achieve construction quality and environmental sustainability in the construction industry in Malaysia," *Manag. Environ. Qual. An Int. J.*, *26*(2)233–249. doi: 10.1108/MEQ-08-2013-0093.

[10] Dung, T. M., & Pham (2020). On the relationship between total quality management practices and firm performance in Vietnam : The mediating role of non-financial performance. *Manag. Sci. Lett.*, 10, 1743–1754. doi: 10.5267/j.msl.2020.1.005.

[11] Zairi, M. (1993). Competitive Manufacturing Combining Total Quality with Advanced Technolocrv," *Long Range Plann.*, 26(3),123–132.

[12] Sreenivasan, J., & Boon, L.I.M.P. (2006). Critical Success Factors of Total Quality Management. *Qual. Quant.*, 40(2), 675–695. doi:10.1007/s11135-005-10972.

[13] Garvin, D. A. (1987). Competing on the Eight Dimensions of Quality. *Harvard Business Review*.

[14] Nasereddin, M. (2015). An investigation into the importance of Total Quality Management in construction field projects : Quality Control.

[15] Xiang, Y. P. (2007). *Total Quality Management approach, a case study in manufacturing industry*. *Univ. Malaysia Pahang*, Available: http://digilib.unila.ac.id/4949/15/BAB II.pdf.

[16] Alotaibi, F. (2016). Perceived Dimensions Of Quality In Higher Education. *PhD diss Wichita State Univ.*

[17] G. N & K. C. (2005). Customer' s Perceptions and the Dimensions of Quality Abstract. In *Proceedings of Western Decision Sciences* (pp. 1–6). doi:10.13140/2.1.4738.4326.

[18] Tey, L. S. & Ooi, T. L. (2014). Exploring the barriers and the level of TQM implementation in Malaysian construction industry. *Res. J. Appl. Sci. Eng. Technol.*, 7(16), 3419–3424. doi: 10.19026/rjaset.7.692.

[19] Pereira, R. (2008). Dimensions of Quality – Gemba Academy. *Gemba Acad.*, p. 1, , [Online]. Available: https://blog.gembaacademy.com/2008/05/28/8-dimensions-of-quality/.

[20] Rehman, M. A. U., Hussain, Z., &. Gafoor, M. M. (2020). The Impact of Service Quality Dimensions on Customers' Trust. *J. Bus. Soc. Rev. Emerg. Econ.*, *6*(2), 557–563. doi: 10.26710/jbsee.v6i2.1181.

[21] Williams, L. (2014). Briefly discuss the eight dimensions of quality. Does this improve our understanding of quality ? *Dimension Qual.*, (5–6), [Online]. Available: http://www.learnmanagement2.com/dimensionsofqualitygarvin.htm.

[22] Magd, H. & Karyamsetty, H. (2020). Organizational Performance and Sustainability in Manufacturing and Service through TQM Implementation. *Open J. Bus. Manag.*, 08(06), 2775–2804. doi: 10.4236/ojbm.2020.86172.

[23] Yee, J. C. (2018). The Influence of Total Quality Management on Project Performance: The Case of Construction Organizations in Malaysia.

[24] Ding, L., Zhou, Y., & Akinci, B. (2014). Automation in Construction Building Information Modeling (BIM) application framework : The process of expanding from 3D to computable nD. *Autom. Constr.*, *46*, 82–93. doi: 10.1016/j.autcon.2014.04.009.

[25] Chai, C. S., Yusof, A. M., & Habil, H. (2015). Delay mitigation in the Malaysian housing industry: A structural equation modelling approach. *J. Constr. Dev. Ctries.*, 20(1), 65–83.

[26] Santos, R., Costa, A. A., Silvestre, J. D., & Pyl, L. (2019. Informetric analysis and review of literature on the role of BIM in sustainable construction. *Autom. Constr.*, *103*(February), 221–234. doi: 10.1016/j.autcon.2019.02.022.

[27] Ali, A. S. (2010). The performance measurement of construction projects managed by ISO-certified contractors in Malaysia. *J. Retail Leis. Prop.*, 9,(1), 25–35. doi: 10.1057/rlp.2009.20.

[28] Ting, T. Y., & Taib, M. (2018). The awareness of building information modelling in Malaysia construction industry from contractor perspective," *Malaysian Constr. Res. J.*, 3(*Special Issue 1*), 75–81.

[29] Ali, M. C., Bin Ismail, R., Kam, K. J., & Dzulkalnine, N. (2014). Preliminary findings on potential areas of improvement in QLASSIC Preliminary findings on potential areas of improvement in QLASSIC. *Elixir Proj. Qual.*, *76*(December), 1–10.

[30] Janipha, N. A. I., Ismail, F., Afida, N., Janipha, I., & Ismail, F. (2013). Conceptualization of Quality Issues in Malaysian Construction Environment. *Procedia - Soc. Behav. Sci.*, *101*, 53–61. doi:10.1016/j.sbspro.2013.07.178.

[31] Haruna, A., Shafiq, N., & Montasir, O. A. (2020). Building information modelling application for developing sustainable building (Multi-criteria decision-making approach). *Ain Shams Eng. J.* doi:10.1016/j.asej.2020.06.006.

[32] Petri, I., Kubicki, S., Rezgui, Y., Guerriero, A., & Li, H. (2017). Optimizing energy efficiency in operating built environment assets through building information modelling: A case study. *Energies*, *10*(8),1–17. doi:10.3390/en10081167.

[33] Ilias Said, T. K. K., Abd Rahman Ayub, Arman Abd Razaki. (2005). Factor Affecting Construction Organization Quality Management In The Malaysian Construction Industry.

[34] Leighton, E., Martin, H., & Charles, M. (2020). BIM implementation in the practice of architecture in

Trinidad. In *The International Conference on Emerging Trends in Engineering and Technology* (pp. 453–463).

[35] Succar, B., Sher, W., Aranda-mena, G., & Williams, T. (2007). A proposed framework to investigate Building Information Modelling through knowledge elicitation and visual models. In *Conf. Australas. Univ. Build. Educ. Assoc.*, no. July, (pp. 1–18). Available: https://s3.amazonaws.com/academia.edu.documents/31438743/A_Proposed_Framework_To_Investigate_Building_Information_Modelling_Through_Knowledge_Elicitation_And_Visual_Models.pdf?AWSAccessKeyId=AKIAIWOWYYGZ2Y53UL3A&Expires=1556635407&Signature=cjDOwjjcYp1V8m.

[36] Ghaffarianhoseini, A. *et al.* (2016). Building Information Modelling (BIM) uptake: Clear benefits, understanding its implementation, risks and challenges. *Renew. Sustain. Energy Rev.*, 75(September), 1046–1053, doi: 10.1016/j.rser.2016.11.083.

[37] Samsudin, N. S., Ayop, S. M., Sahab, S., & Ismail, Z. (2012). Problems And Issues On The Implementation Of Quality Management System In Construction Projects. In *2012 IEEE Symposium on Business, Engineering and Industrial Applications*, 2012, no. 600, (pp. 684–689).

[38] Tan & Syazwan, "Implementation of Iso Quality Management System in Construction Companies of Malaysia. *J. Technol. Manag. Bus.*, *3*(1).

[39] Kiew, P. N., Ismail, S., & Yusof, A. M. (2016). Integration of Quality Management System in the Malaysian Construction Industry. *J. Organ. Manag. Stud.*, *2016*, 1–9. doi: 10.5171/2016.117211.

[40] Alotaibi, F. Yusoff, R. Z., & Islam, R. (2013). Assessing the Impact of Total Quality Management Practices and Quality Culture with Competitiveness of Saudi Contractors. *Am. J. Appl. Sci.*, *10*(6), 638–645. doi: 10.3844/ajassp.2013.638.645.

[41] Benzaquen, J., Carlos, M., Norero, G., Armas, H. & Pacheco, H. (2021). Quality in private health companies in Peru: The relation of QMS & ISO 9000 principles on TQM factor. *Int. J. Healthc. Manag.*, *14*(2),311–319, 2021, doi: 10.1080/20479700.2019.1644472.

[42] McIntyre, C., & Kirschenman, M. (2000). Survey of TQM in construction industry in upper Midwest. *J. Manag. Eng.*, *16*(October), 67–70.

Online Fault Detection, Classification and Localization in Power System using PMUs Measurements Units

Toufik Tarif[1], Ahmed Amine Ladjici[2], Ahmed Tiguercha[3]

[1,2,3]LSEI Lab. Dept. Electrical Engineering, University of Sciences and Technology Houari-Boumediene, Cité Alia, Bab Ezzouar, Algiers, Algeria, toufik.tarif@usthb.dz[1], aladjici@usthb.dz[2], atiguercha@usthb.dz[3] tr

Abstract—**The current paper proposes a methodology for fault classification and localization in a power system using voltage synchro-phasor from PMUs Measurement Units. The proposed methodology is performed in three steps: 1) optimal PMU placement for full power system observability. 2) Data and feature selection, and 3) classifier training and testing. In this work an SVM classifier is trained for the classification and localization of faults in a power system based on the energy of voltage signals measured form optimally located PMUs. Simulations are carried out on IEEE 39-bus system, and the results show the efficiency of the proposed methodology in the classification and localization of various faults occurring in the power system, highlighting its potential for real-world applications.**

Keywords - faults classification, faults localization, optimal PMUs' placement, support vector machines classifier

I. INTRODUCTION

Modern power systems may function closer to its stability limit due to increasing uncertainties and greater complexity, which has caused many disastrous accidents, such as the large scale blackouts. New monitoring, communication and protection technologies [1] are needed to improve the security of the present power systems.

The phasor measurement units (PMUs) is a device has the ability to measure the magnitude and phase angle of power system components, in real time [2]. PMUs take these synchronized measurements with 30-60 samples/s; compared with the traditional 2-4 second SCADA measurements [3].

In recent years, there has been a significant application of PMUs in power systems have been reported in the literature. Important topics such as: Voltage security monitoring [4, 5], transient stability [6] and small-signal stability assessment [7], and event detection and location that is the heart of this work [8, 9].

A number of papers are proposed in the literature for events location and classification in power networks. Different features are mainly extracted from the disturbance signals in order to identify the feature vectors, methods such as artificial neural network (ANN) [10, 11] and support vector machine (SVM) [12] have largely been used in the field.

Fault identification and classification methodology based PMU measurements were proposed in [13]. In [14], a SVM is utilized for security evaluation and classification, and transient stability analysis [15, 16]. A PSO method based multi-layer perceptron neural network has been proposed to classify events in transmission lines [17].

A fault location for N-terminal lines of transmission is presented in [18]. However, these studies did not consider the optimal location of the PMU to make a power network observable, i.e., many buses are not monitored. In addition, the advantage of the proposed algorithm is that the monitoring of the complete power system because of the optimal PMU placement and high classification accuracy. In addition, the advantage of the proposed algorithm is that the monitoring of the complete power system because of the optimal PMU placement and high classification accuracy.

ISBN: 978-86-80593-73-9

In this paper, a method for online fault detection, classification and localization using PMUs' voltage synchro-phasor signal is proposed. In order to minimize the number of PMUs used, the Differential evolution (DE) technique is employed for optimal PMUs placement. Secondly, after optimal placement of PMU the energy of voltage signal of each PMU is used for the training the SVM classifier for fault identification and localization. The simulations are carried out using time domain simulation of the power system considering several events: line disconnections, short-circuit and load switching.

II. PROPOSED METHODOLOGY FOR FAULT LOCATION AND CLASSIFICATION

The basic idea of the proposed methodology is that a fault perturbs the voltage signal translated in a variation of its amplitude and phase. A synchronized measurement of voltage modules and phases of each bus of the system can gives a good indication on the nature and the location of the event.

Placing a PMU in each bus of large power system for the purpose of fault detection is not interesting. Thus, and in order to reduce the number of PMUs needed and to reduce the problem complexity, the PMUs location in the system has to be optimized. Solving the optimal PMUs placement problem can reduce the number of PMUs needed while preserving the measurement quality [19].

The proposed methodology involves three major stages: optimal PMU placement, feature extraction, classifier training and testing, Fig.1.

- Optimal PMUs placement in the system: in this work a Differential Evolution (DE) algorithm is used to find the optimal buses where the PMUs have to be placed [19], in order to make the network N-1 observable.
- Feature extraction: the energy of each voltage signal is calculated for each fault type and fault location. This is done by first running a time domain simulation considering the fault nature and location. With a system with *n* Buses, *m* PMUs and *k* Fault types, a dataset, as shown in Table I, is produced.
- Classifier Training and testing: The data set obtained from the previous step is used for the training and testing of the classifiers, and thus the best classifier in terms of accuracy can be chosen.

TABLE I. TRAINING AND TESTING DATA SET.

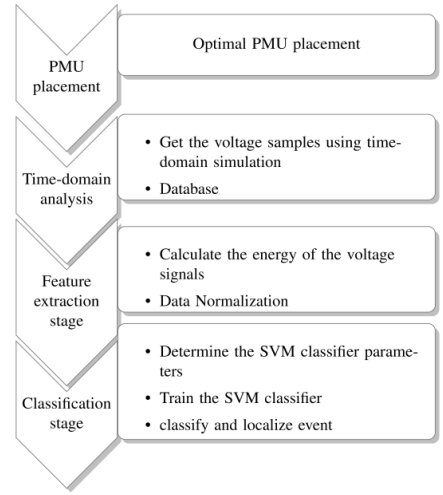

Figure 1. Flow chart of proposed methodology.

PMU1	*PMU2*	...	*PMU_m*	*Bus*	*Type*
E1	*E2*	...	*E3*	*1*	*1*
E1	*E2*	...	*E3*	*2*	*1*
...	...	...	...	...	...
E1	*E2*	...	*E3*	*N*	*k*

III. OPTIMAL PMUS PLACEMENT

The objective of the PMUs placement problem is to identify the number and suitable placement of PMUs to ensure complete observability of the power grid [19]. The problem is formulated as follow:

$$min \sum_{i=1}^{N_{bus}} x_i \ , \qquad (1)$$

$$L = C.X \geq e \ , \qquad (2)$$

where N_{bus} is the number of buses X is an array of binary decision variables. X_i equal to "1" when a PMU is present on bus i and vice-versa.

The matrix A_{n*n} is described as: $a_{i,j} = 1$ if $i = j$ or i and j are connected, $a_{i,j} = 0$ else. The vector e is a vector of two of size n, 1. Ensuring that every bus is observed by at least two PMUs.

$$L = \left[L_1 L_2 \ldots L_n \right] . \quad (3)$$

In addition, the impact of zero injection bus (ZIB) is taken into account in the model [20].

A. Differential Evolution Algorithm

Differential Evolution Algorithm is an efficient, effective intelligent optimization algorithm initially proposed by R. Storn and K. Price [21] designed to optimize problems over continuous space. Similar to *GA*, *DE* algorithm is based in evolutionary operators: crossover, mutation and selection operators. Then, the optimization procedure is summarized in algorithm 1.

Algorithm1: Differential Evolution Algorithm

```
t = 0;
initialize(P(t = 0));
evaluate(P(t = 0));
while !termination criteria do
        P (t) = P(t):select Parents();
        Pc(t) = reproduction(PP );
        mutate(Pc(t));
        evaluate(Pc(t));
        P(t + 1) =NextGenerationFrom(Pc(t); P(t));
        t = t + 1;
end
```

At the algorithm convergence, the optimal number and location of the PMUs needed for full observability is obtained. In the rest of the paper all the voltage synchro-phasor signals are supposed to be measured from PMUs with optimal location.

IV. Data and Feature Selection

A. Data Preparation

The voltage signals at the PMU locations are obtained using a time domain simulation, performed under different scenarios of fault nature and location. For each scenario (type, location) a set of voltage signals $V(i; j)$; $i = 1, \ldots, N_S \quad j = 1, \ldots, N_{PMU}$, is obtained.

B. Feature extraction

In this work, the energy of the voltage signal is used as a feature, instead of the voltage signal itself. The energy of the voltage signal is determined as follow:

$$E_i = \sum_{j=1}^{N_S} \left| V_{ij} \right|^2 , i = 1, \ldots, N_{PMU} \quad , \quad (4)$$

where: N_S is the number of sample of the signal V_i, N_{PMU} is the number of PMUs in the system.

The Energy data have to be normalized and scaled in a standard range of [0-1] to avoid over-fitting and enhance the classifier performance [22].

V. Classification

In this work a support vector machine (SVM) is used as a classifier for fault classification and localization, based on the energy of voltage signals measured at PMUs locations.

A. Support Vector Machine

SVM was originally introduced by Vapnik [23] in 1960 based on theoretical results from the machine learning theory. The SVMs are based on the notion of minimizing structural risk, which minimizes the error of generalization [24].

Supposing that a training set $(x_1; y_1) \ldots (x_l; y_l)$ belonged to two different classes y_i {-1; +1}, the linear hyper-planes can be given as:

$$w \cdot \varnothing(x) + 1 = 0, \; w \in \Re^n, b \in \Re \quad . \quad (5)$$

SVM constructs the primary quadratic constraint optimization problem that minimizes the error of training and generalization by:

$$min_{w,b} \frac{1}{2} \|w\|^2 + C \sum_{j=1}^{m} \xi_i \quad . \quad (6)$$

Also can be determined in terms of Lagrange multipliers, α [25]:

$$maxL(\alpha) = \sum_{j=1}^{m} \alpha_i + 2^{-1} \sum_{i=1}^{m} \sum_{j=1}^{m} \alpha_i \alpha_j y_i y_j \left\langle x_i, x_j \right\rangle , \quad (7)$$

$$w = sgn \sum_{i=1}^{m} y_i \alpha_i \varnothing(x_i), \; \sum_{\substack{i=1 \\ \leq C, \forall_i}}^{m} y_i \alpha_i = 0, 0 \leq \alpha_i \quad . \quad (8)$$

The SVM method can be applied to a non-linear space using a kernel trick. The kernel is how the dot product $< x_i; x_j >$ is calculated in high dimensional feature space. There are several kernel functions used in SVMs, including linear, Gaussian RBF and polynomial functions, Gaussian RBF kernel is generally the most dependable. [26].

After choosing the kernel *k(*,*)*, and by solving the optimization problem, we obtain the coefficients α_i that are necessary to express the *w* to solve Eq. (7). The optimal function is given by [25]:

$$f(x) = sgn\left(\sum_{i=1}^{m} y_i \alpha_i k(x_i, x_i) + b\right). \qquad (9)$$

B. Fault Classification

Faults are classified into categories according to their nature. In this study three types of faults are considered: short circuit, line disconnection and Load Switching.

The SVM classifier is trained to predict the fault type using the energies of the PMUs voltage signals at the PMUs location as inputs. The outputs are labeled "1" for "short circuit", "2" for "line disconnection" and "3" for "Load Switching", as shown in the Fig. 2.

C. Fault Localization

The SVM classifier is trained for the fault location. The inputs are the energy of the voltage signal measured by the PMUs, while the output is the bus number where the fault occurs, Fig. 3.

VI. Case Study

In order to test the effectiveness of the proposed methodology for fault classification and localization, The IEEE 39-bus system is used. In this work, three classes of events are considered: short circuit, line disconnection and load switching.

The proposed methodology is implemented in MATLAB, time domain simulations are done using PSAT toolbox, and SVM are from MATLAB classification toolbox.

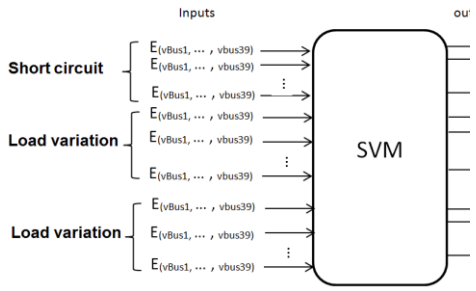

Figure 2. SVM based fault classification.

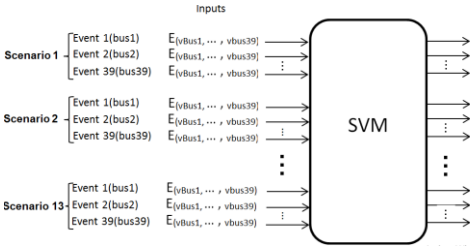

Figure 3. SVM based fault location.

A. Optimal PMUs Placement

In order to find the optimal location of the PMUs in the IEEE 39-bus system, the proposed DE algorithm is used with the following parameters: Population size = 100; crossover = 0.7; mutation = 0.01; generations' number = 300.

The optimal solution found by the algorithm is shown in Table II; this solution provides both a complete observability with a minimum number of PMUs.

B. Feature Extraction and Training Data Sets

The Voltage signal at PMUs location is obtained by performing a time domain simulation [Fig] given the location and the fault type:

- The total time of the simulation is fixed as 10s, and each event is applied at *t = 1s*.
- Since voltage synchro-phasors are measured at up to 50 samples per second as specified by the PMU, thus *n = 500* samples are simulated.
- The energy of each voltage signal is calculated using (5).

Fig. 4 show the signals of voltage from the time domain simulation for three faults: a) short-circuit at bus 22, b) line disconnection and c) load switching at bus 12. Fig. 5 shows the energy values of voltage signal measured at the PMUs locations.

TABLE II. Optimal PMUs location in IEEE 39-bus system.

System	nbr PMUs	Location
IEEE 30-bus	18	1,5,9,10,14,16,18, 20,21,23,25,26,29, 34,36,37,38,39

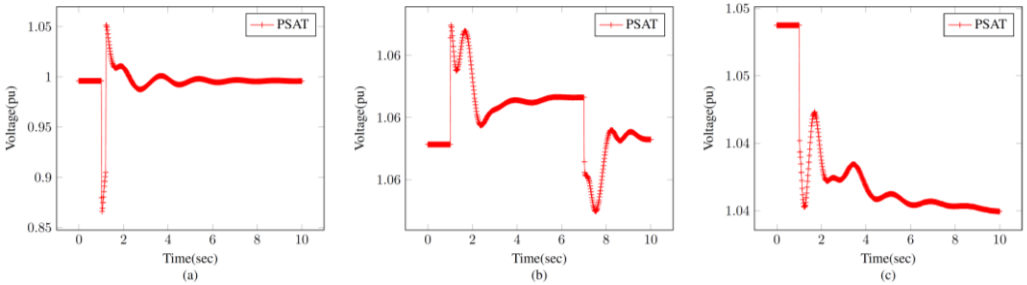

Figure 4 Voltage signal. (a) short circuit at bus 22. (b) line 7-6 disconnection. (c) load switching at bus 12.

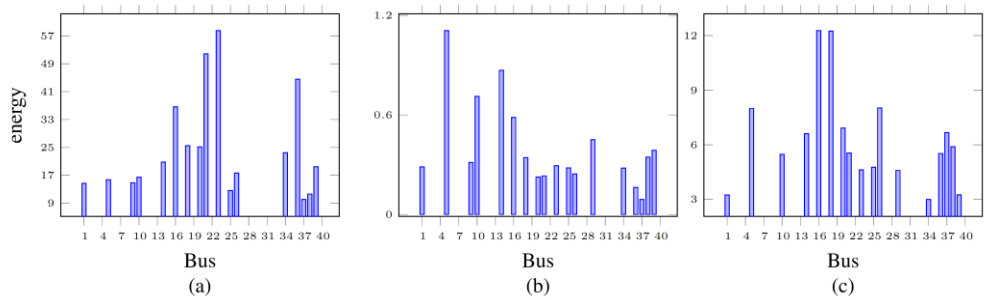

Figure 5 Voltage signal. (a) short circuit at bus 22. (b) line 7-6 disconnection. (c) load switching at bus 12.

From Figs. 4 and 5, one can see that each fault has its unique signature in terms of energy values and distribution:

- Short-circuits had the higher energy values followed by load switching and line disconnection.
- The signal from PMUs in the vicinity of the fault has higher energy compared to more distant PMUs.
- By training a classifier to learn the unique signature of each fault and its location.

C. *Training*

MATLAB classification toolbox is used for the training and testing of SVM and KNN classifiers using the obtained classification and localization data sets.

1) *Fault classification*

According to the results shown in Table III, two conclusions can be made:

- Compared KNN algorithms, SVM classifier in this case study, is significantly more accurate.
- The results show that is Medium Gaussian kernel gives better results with an accuracy of 92.9%.

TABLE III. COMPARISON BETWEEN THE ACCURACY OF SVM AND KNN CLASSIFIERS FOR FAULT CLASSIFICATION.

Classifier	Kernel	Accuracy
SVM	Linear SVM	73.20%
	Quadratic SVM	90.20%
	Cubic SVM	87.50%
	Fine Gaussian SVM	81.30%
	Medium Gaussian	92.90%
	Coarse Gaussian	71.40%
KNN	Fine KNN	82.10%
	Coarse KNN	80.20%
	Cosine KNN	83.00%
	Cubic KNN	81.30%
	Medium KNN	82.10%
	Weighted KNN	79.50%

Table IV shows the standardized confusion matrix for the median Gaussian SVM classifier. The results show that short-circuits (class 1) faults is the easiest to classify with a positive predictive values (PPV) of 97% and false discovery rates (FDR) of 3%. This result is expected because it is the most severe fault in the system. Line disconnection (class 2) and load switching (class 2) are classified with an accuracy of 91% and 90% respectively

TABLE IV. CONFUSION MATRIX FOR FAULT CLASSIFICATION.

		Predicted 92.9%				
		class 1	**class 2**	**class 3**	PPV	FDR
Actual	**class1**	38	1	0	97%	3%
	class 2	3	31	0	91%	9%
	class 3	0	4	35	90%	10%

2) *Fault localization*

As for the classification, the localization results, Fig. 5, confirm that SVM classifiers give better results than KNNs, and that the SVM with a medium Gaussian kernel is the one that gives the best accuracy (95.3%).

TABLE V. COMPARISON BETWEEN THE ACCURACY OF SVM AND KNN CLASSIFIERS FOR FAULT LOCALIZATION.

Classifier	***Kernel***	***Accuracy***
SVM	Linear SVM	88.80%
	Quadratic SVM	91.30%
	Cubic SVM	92.10%
	Fine Gaussian SVM	88.80%
	Medium Gaussian	95.30%
	Coarse Gaussian	88.20%
KNN	Fine KNN	86.90%
	Coarse KNN	76.40%
	Cosine KNN	88.20%
	Cubic KNN	92.30%
	Medium KNN	82.10%
	Weighted KNN	83.40%

Fig. 6 shows the confusion matrix of medium Gaussian SVM classifier for fault localization problem.

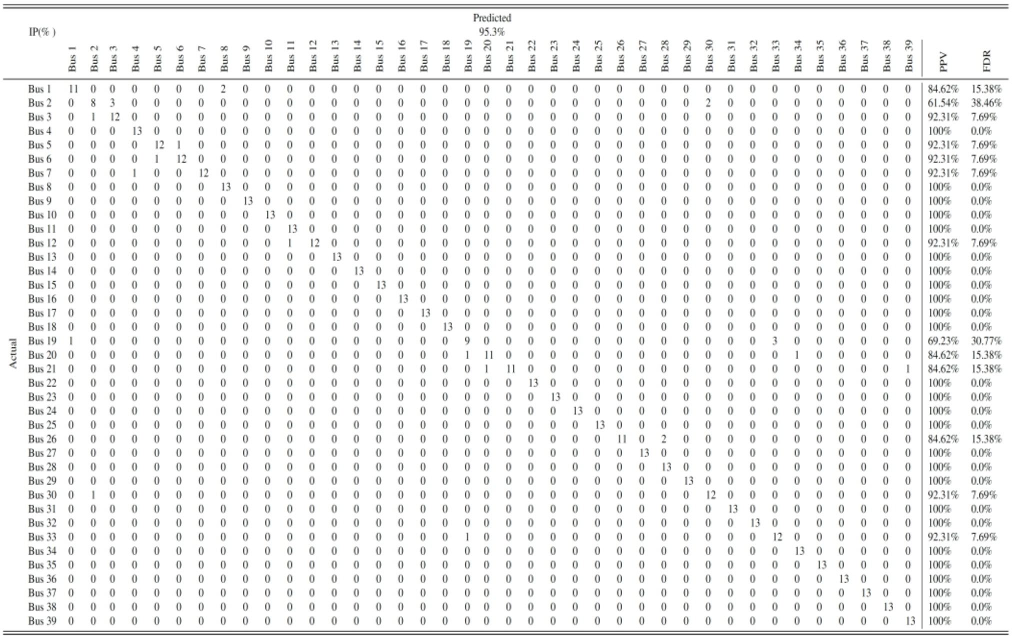

	IP(%)	Predicted 95.3%																																								
		Bus 1	Bus 2	Bus 3	Bus 4	Bus 5	Bus 6	Bus 7	Bus 8	Bus 9	Bus 10	Bus 11	Bus 12	Bus 13	Bus 14	Bus 15	Bus 16	Bus 17	Bus 18	Bus 19	Bus 20	Bus 21	Bus 22	Bus 23	Bus 24	Bus 25	Bus 26	Bus 27	Bus 28	Bus 29	Bus 30	Bus 31	Bus 32	Bus 33	Bus 34	Bus 35	Bus 36	Bus 37	Bus 38	Bus 39	PPV	FDR
Actual	Bus 1	11	0	0	0	0	0	0	2	0	0	0	0	0	0	0	0	0	0	0	0	0	0	0	0	0	0	0	0	0	0	0	0	0	0	0	0	0	0	0	84.62%	15.38%
	Bus 2	0	8	3	0	0	0	0	0	0	0	0	0	0	0	0	0	0	0	0	0	0	0	0	0	0	0	0	0	0	2	0	0	0	0	0	0	0	0	0	61.54%	38.46%
	Bus 3	0	1	12	0	0	0	0	0	0	0	0	0	0	0	0	0	0	0	0	0	0	0	0	0	0	0	0	0	0	0	0	0	0	0	0	0	0	0	0	92.31%	7.69%
	Bus 4	0	0	0	13	0	0	0	0	0	0	0	0	0	0	0	0	0	0	0	0	0	0	0	0	0	0	0	0	0	0	0	0	0	0	0	0	0	0	0	100%	0.0%
	Bus 5	0	0	0	0	12	1	0	0	0	0	0	0	0	0	0	0	0	0	0	0	0	0	0	0	0	0	0	0	0	0	0	0	0	0	0	0	0	0	0	92.31%	7.69%
	Bus 6	0	0	0	0	1	12	0	0	0	0	0	0	0	0	0	0	0	0	0	0	0	0	0	0	0	0	0	0	0	0	0	0	0	0	0	0	0	0	0	92.31%	7.69%
	Bus 7	0	0	0	1	0	0	12	0	0	0	0	0	0	0	0	0	0	0	0	0	0	0	0	0	0	0	0	0	0	0	0	0	0	0	0	0	0	0	0	92.31%	7.69%
	Bus 8	0	0	0	0	0	0	0	13	0	0	0	0	0	0	0	0	0	0	0	0	0	0	0	0	0	0	0	0	0	0	0	0	0	0	0	0	0	0	0	100%	0.0%
	Bus 9	0	0	0	0	0	0	0	0	13	0	0	0	0	0	0	0	0	0	0	0	0	0	0	0	0	0	0	0	0	0	0	0	0	0	0	0	0	0	0	100%	0.0%
	Bus 10	0	0	0	0	0	0	0	0	0	13	0	0	0	0	0	0	0	0	0	0	0	0	0	0	0	0	0	0	0	0	0	0	0	0	0	0	0	0	0	100%	0.0%
	Bus 11	0	0	0	0	0	0	0	0	0	0	13	0	0	0	0	0	0	0	0	0	0	0	0	0	0	0	0	0	0	0	0	0	0	0	0	0	0	0	0	100%	0.0%
	Bus 12	0	0	0	0	0	0	0	0	0	0	1	12	0	0	0	0	0	0	0	0	0	0	0	0	0	0	0	0	0	0	0	0	0	0	0	0	0	0	0	92.31%	7.69%
	Bus 13	0	0	0	0	0	0	0	0	0	0	0	0	13	0	0	0	0	0	0	0	0	0	0	0	0	0	0	0	0	0	0	0	0	0	0	0	0	0	0	100%	0.0%
	Bus 14	0	0	0	0	0	0	0	0	0	0	0	0	0	13	0	0	0	0	0	0	0	0	0	0	0	0	0	0	0	0	0	0	0	0	0	0	0	0	0	100%	0.0%
	Bus 15	0	0	0	0	0	0	0	0	0	0	0	0	0	0	13	0	0	0	0	0	0	0	0	0	0	0	0	0	0	0	0	0	0	0	0	0	0	0	0	100%	0.0%
	Bus 16	0	0	0	0	0	0	0	0	0	0	0	0	0	0	0	13	0	0	0	0	0	0	0	0	0	0	0	0	0	0	0	0	0	0	0	0	0	0	0	100%	0.0%
	Bus 17	0	0	0	0	0	0	0	0	0	0	0	0	0	0	0	0	13	0	0	0	0	0	0	0	0	0	0	0	0	0	0	0	0	0	0	0	0	0	0	100%	0.0%
	Bus 18	0	0	0	0	0	0	0	0	0	0	0	0	0	0	0	0	0	13	0	0	0	0	0	0	0	0	0	0	0	0	0	0	0	0	0	0	0	0	0	100%	0.0%
	Bus 19	1	0	0	0	0	0	0	0	0	0	0	0	0	0	0	0	0	0	9	0	0	0	0	0	0	0	0	0	0	0	0	0	3	0	0	0	0	0	0	69.23%	30.77%
	Bus 20	0	0	0	0	0	0	0	0	0	0	0	0	0	0	0	0	0	0	1	11	0	0	0	0	0	0	0	0	0	0	0	0	0	1	0	0	0	0	0	84.62%	15.38%
	Bus 21	0	0	0	0	0	0	0	0	0	0	0	0	0	0	0	0	0	0	0	1	11	0	0	0	0	0	0	0	0	0	0	0	0	0	0	0	0	0	1	84.62%	15.38%
	Bus 22	0	0	0	0	0	0	0	0	0	0	0	0	0	0	0	0	0	0	0	0	0	13	0	0	0	0	0	0	0	0	0	0	0	0	0	0	0	0	0	100%	0.0%
	Bus 23	0	0	0	0	0	0	0	0	0	0	0	0	0	0	0	0	0	0	0	0	0	0	13	0	0	0	0	0	0	0	0	0	0	0	0	0	0	0	0	100%	0.0%
	Bus 24	0	0	0	0	0	0	0	0	0	0	0	0	0	0	0	0	0	0	0	0	0	0	0	13	0	0	0	0	0	0	0	0	0	0	0	0	0	0	0	100%	0.0%
	Bus 25	0	0	0	0	0	0	0	0	0	0	0	0	0	0	0	0	0	0	0	0	0	0	0	0	13	0	0	0	0	0	0	0	0	0	0	0	0	0	0	100%	0.0%
	Bus 26	0	0	0	0	0	0	0	0	0	0	0	0	0	0	0	0	0	0	0	0	0	0	0	0	0	11	0	2	0	0	0	0	0	0	0	0	0	0	0	84.62%	15.38%
	Bus 27	0	0	0	0	0	0	0	0	0	0	0	0	0	0	0	0	0	0	0	0	0	0	0	0	0	0	13	0	0	0	0	0	0	0	0	0	0	0	0	100%	0.0%
	Bus 28	0	0	0	0	0	0	0	0	0	0	0	0	0	0	0	0	0	0	0	0	0	0	0	0	0	0	0	13	0	0	0	0	0	0	0	0	0	0	0	100%	0.0%
	Bus 29	0	0	0	0	0	0	0	0	0	0	0	0	0	0	0	0	0	0	0	0	0	0	0	0	0	0	0	0	13	0	0	0	0	0	0	0	0	0	0	100%	0.0%
	Bus 30	0	1	0	0	0	0	0	0	0	0	0	0	0	0	0	0	0	0	0	0	0	0	0	0	0	0	0	0	0	12	0	0	0	0	0	0	0	0	0	92.31%	7.69%
	Bus 31	0	0	0	0	0	0	0	0	0	0	0	0	0	0	0	0	0	0	0	0	0	0	0	0	0	0	0	0	0	0	13	0	0	0	0	0	0	0	0	100%	0.0%
	Bus 32	0	0	0	0	0	0	0	0	0	0	0	0	0	0	0	0	0	0	0	0	0	0	0	0	0	0	0	0	0	0	0	13	0	0	0	0	0	0	0	100%	0.0%
	Bus 33	0	0	0	0	0	0	0	0	0	0	0	0	0	0	0	0	0	0	1	0	0	0	0	0	0	0	0	0	0	0	0	0	12	0	0	0	0	0	0	92.31%	7.69%
	Bus 34	0	0	0	0	0	0	0	0	0	0	0	0	0	0	0	0	0	0	0	0	0	0	0	0	0	0	0	0	0	0	0	0	0	13	0	0	0	0	0	100%	0.0%
	Bus 35	0	0	0	0	0	0	0	0	0	0	0	0	0	0	0	0	0	0	0	0	0	0	0	0	0	0	0	0	0	0	0	0	0	0	13	0	0	0	0	100%	0.0%
	Bus 36	0	0	0	0	0	0	0	0	0	0	0	0	0	0	0	0	0	0	0	0	0	0	0	0	0	0	0	0	0	0	0	0	0	0	0	13	0	0	0	100%	0.0%
	Bus 37	0	0	0	0	0	0	0	0	0	0	0	0	0	0	0	0	0	0	0	0	0	0	0	0	0	0	0	0	0	0	0	0	0	0	0	0	13	0	0	100%	0.0%
	Bus 38	0	0	0	0	0	0	0	0	0	0	0	0	0	0	0	0	0	0	0	0	0	0	0	0	0	0	0	0	0	0	0	0	0	0	0	0	0	13	0	100%	0.0%
	Bus 39	0	0	0	0	0	0	0	0	0	0	0	0	0	0	0	0	0	0	0	0	0	0	0	0	0	0	0	0	0	0	0	0	0	0	0	0	0	0	13	100%	0.0%

Figure 6 Confusion matrix of fault localization with medium gaussian SVM classifier

The result shows that, for the majority of buses, even those where a PMU is not installed, all tested faults are correctly detected with accuracy from 92.3% (one misclassified fault) to 100%.

For buses 2 and 19, where the classification error is highest, these errors are mainly due to the network topology. In bus 2, some faults are misclassified to adjacent buses 3, and 30, this is mainly due to the low impedance of branches 2-3 and 2-30. Similarly for bus 19 where some faults are misclassified to the adjacent bus 33 due to the low impedance of branch 19-33.

D. Testing

In order to validate and test the methodology, a new dataset is used to test the medium Gaussian SVM classifier.

Table VI shows that the SVM classifier succeeds in correctly classifying the nature and location of most faults. However, it remains that some faults are not correctly identified or localized.

TABLE VI. FAULT IDENTIFICATION AND LOCALIZATION TESTING.

Fault Location	Fault type	Estimated location	Estimated type	Error location	Error classif.
5	1	5	1		
12	2	12	2		
15	3	15	3		
16	3	**17**	3	**error**	
38	**1**	38	**2**		**error**
25	2	25	2		
15	3	15	3		
19	3	**33**	3	**error**	
9	2	9	2		
36	**3**	36	**2**		**error**

VII. CONCLUSION

This paper presents a methodology for fault classification and localization using PMUs measurements and SVM classifier. The optimal PMUs placement problem is resolved using the DE algorithm, to identify the optimal PMU locations in the network. The energy of voltage signals measured by the PMUs is then used as features to identify the nature and location of faults.

The obtained results show the efficiency of the proposed methodology. With a minimum of PMUs installed in the system, the trained SVM classifiers give an accuracy of 95.3%, for fault localization, and 92.9% for fault classification. SVM with a medium Gaussian kernel proves to be more accurate than other SVMs and KNN classifiers.

Classification with optimal placement of PMUs proves to be quite effective. With 18 PMUs after optimal placement, nearly 95% of the contingencies are correctly identified. The results of the event classification indicate that the proposed algorithm is robust and can be applied on real systems provided that there is enough measurement history to allow training of the classifiers.

The results obtained are interesting but still perfectible, deep learning can be a better alternative to classic SVM. It is also interesting to consider the use of more features: ROCOF and ROCOV are the most interesting.

REFERENCES

[1] Zhang, N., & Kezunovic, M. (2007). A real time fault analysis tool for monitoring operation of transmission line protective relay. *Electric Power Systems Research*, *77*(3-4), 361-370.

[2] Mohammadi, M. B., Hooshmand, R. A., & Fesharaki, F. H. (2015). A new approach for optimal placement of PMUs and their required communication infrastructure in order to minimize the cost of the WAMS. *IEEE Transactions on smart grid*, *7*(1), 84-93.

[3] Terzija, V., Valverde, G., Cai, D., Regulski, P., Madani, V., Fitch, J., ... & Phadke, A. (2010). Wide-area monitoring, protection, and control of future electric power networks. *Proceedings of the IEEE*, *99*(1), 80-93.

[4] Diao, R., Sun, K., Vittal, V., O'Keefe, R. J., Richardson, M. R., Bhatt, N., ... & Sarawgi, S. K. (2009). Decision tree-based online voltage security assessment using PMU measurements. *IEEE Transactions on Power systems*, *24*(2), 832-839.

[5] Chavez, J. J., Kumar, N. V., Azizi, S., Guardado, J. L., Rueda, J., Palensky, P., ... & Popov, M. (2021). PMU-voltage drop based fault locator for transmission backup protection. *Electric Power Systems Research*, *196*, 107188.

[6] Rashidi, M., & Farjah, E. (2016). LEs based framework for transient instability prediction and mitigation using PMU data. *IET Generation, Transmission & Distribution*, *10*(14), 3431-3440.

[7] Jia, H., Yu, X., Yu, Y., & Wang, C. (2008). Power system small signal stability region with time delay. *International Journal of Electrical Power & Energy Systems*, *30*(1), 16-22.

[8] Niazazari, I., & Livani, H. (2018). A PMU-data-driven disruptive event classification in distribution systems. *Electric Power Systems Research*, *157*, 251-260.

[9] Wang, C., Dou, C. X., Li, X. B., & Jia, Q. Q. (2007). A WAMS/PMU-based fault location technique. *Electric Power Systems Research*, *77*(8), 936-945.

[10] Rajakarunakaran, S., Venkumar, P., Devaraj, D., & Rao, K. S. P. (2008). Artificial neural network approach for fault detection in rotary system. *Applied Soft Computing*, *8*(1), 740-748.

[11] Jain, A. (2013). Artificial neural network-based fault distance locator for double-circuit transmission lines. *Advances in Artificial Intelligence*, *2013*.

[12] Zhang, Y., Wang, L., Sun, W., Green II, R. C., & Alam, M. (2011). Distributed intrusion detection system in a multi-layer network architecture of smart grids. *IEEE Transactions on Smart Grid*, *2*(4), 796-808.

[13] Gopakumar, P., Reddy, M. J. B., & Mohanta, D. K. (2015). Adaptive fault identification and classification methodology for smart power grids using synchronous phasor angle measurements. *IET Generation, Transmission & Distribution*, *9*(2), 133-145.

[14] Kalyani, S., & Swarup, K. S. (2010). Classification and assessment of power system security using multiclass SVM. *IEEE Transactions on Systems, Man, and Cybernetics, Part C (Applications and Reviews)*, *41*(5), 753-758.

[15] Moulin, L. S., Da Silva, A. A., El-Sharkawi, M. A., & Marks, R. J. (2004). Support vector machines for transient stability analysis of large-scale power systems. *IEEE Transactions on Power Systems*, *19*(2), 818-825.

[16] Jafarzadeh, S., & Genc, V. I. (2021). Real-time transient stability prediction of power systems based on the energy of signals obtained from PMUs. *Electric Power Systems Research*, *192*, 107005.

[17] Upendar, J., Gupta, C. P., Singh, G. K., & Ramakrishna, G. (2010). PSO and ANN-based fault classification for protective relaying. *IET generation, transmission & distribution*, *4*(10), 1197-1212.

[18] Liu, C. W., Lien, K. P., Chen, C. S., & Jiang, J. A. (2008). A Universal Fault Location Technique for N-Terminal (n>_3) Transmission Lines. *IEEE Transactions on Power Delivery*, *23*(3), 1366-1373.

[19] Tarif, T., Ladjici, A. A., Amrane, Y., & Chabane, Y. (2019). Multi-objective optimal PMUs placement for online assessment of small-signal stability. *International Transactions on Electrical Energy Systems*, *29*(11), e12117.

[20] Abiri, E., Rashidi, F., Niknam, T., & Salehi, M. R. (2014). Optimal PMU placement method for complete topological observability of power system under various contingencies. *International Journal of Electrical Power & Energy Systems*, *61*, 585-593.

[21] Storn, R., & Price, K. (1997). Differential evolution–a simple and efficient heuristic for global optimization over continuous spaces. *Journal of global optimization*, *11*(4), 341-359.

[22] Saitta, S. (2007). Standardization vs. normalization. *Data Mining Research blog*.

[23] Naumovich, V. V., & Vlamimir, V. (1998). Statistical learning theory. Wiley, New York.

[24] Vapnik Vladimir, N. (1995). The nature of statistical learning theory. Berlin, Springer

[25] Cristianini, N., & Shawe-Taylor, J. (2000). *An introduction to support vector machines and other kernel-based learning methods*. Cambridge university press.

[26] Guo, Y., Li, C., Li, Y., & Gao, S. (2013). Research on the power system fault classification based on HHT and SVM using wide-area information. *Energy and Power Engineering*, *5*(4), 138-142.

[27] Saboune, S., Ladjici, A. A., & Tiguercha, A. (2021). Adaptive decentralized fuzzy logic-based underfrequency load shedding to enhance power system stability. *International Transactions on Electrical Energy Systems*, *31*(11), e13087.

Sustainable Concrete in Energy Efficient Buildings

Danica Goleš[1], Arpad Čeh[2]

[1,2]University of Novi Sad, Faculty of Civil Engineering, Subotica, Serbia,
dgoles@gmail.com[1], ceh@gf.uns.ac.rs[2]

Abstract—**Concrete production, construction and use of buildings significantly contribute to the total greenhouse gas emissions and energy consumption in the world. Critical elements of the concrete production and the construction process are cement manufacture, transport and depletion of non-renewable natural resources. An additional problem is the disposal of waste generated by the demolition of buildings after the end of their service life. The sustainability of concrete as a building material can be improved by optimizing its use and strength class, maximizing the service life of buildings, designing according to performance, using local resources, optimizing the composition of the concrete mix, etc. The paper shows how the changes in a concrete mix - substitution of the part of cement and aggregates by by-products, recycled or waste materials, as well as the use of seawater or brine, affect the strength and durability of hardened concrete and contribute to the reduction of CO_2 emissions. It is also shown how these composition changes affect the thermal properties of concrete (thermal conductivity), which can be used to significantly improve the energy efficiency of buildings, primarily by reducing the heat losses through the thermal bridges in concrete parts of buildings.**

Keywords – concrete, constituent material substitution, carbon emission, thermal conductivity, energy efficiency

I. INTRODUCTION

Concrete is a widely used and versatile building material. It can be found in road pavements, agricultural, industrial, residential and public buildings, but also in more demanding engineering structures, such as bridges, dams, nuclear power plants, etc. Concrete has many advantages compared to other building materials. It is natural, mainly locally sourced, low-cost, easy-to-shape, durable, low-maintenance, resistant to some chemicals, resilient to fire, recyclable material, with high thermal mass and good acoustic performance. On the other hand, conventional concrete also has some disadvantages. Beside its low tensile strength which imposes the use of steel reinforcement with issues concerning corrosion protection, its time-dependent behavior (creep and shrinkage) and change of properties with age, concrete manufacture is energy and carbon-intensive, mainly due to the cement production.

According to the projections, demand for concrete is expected to increase by 12-23% by 2050 compared to 2014 [1]. The growing concrete production has a significant environmental impact. Uncontrolled aggregate extraction, especially of the river gravel, may cause erosion, river flow change, and endanger its flora and fauna. Extraction of aggregate far from the concrete manufacture site leads to the higher energy consumption and higher CO_2 emission due to the transportation. Concrete production is water demanding. To obtain the adequate resistance of reinforced concrete (RC) structures to corrosion of steel reinforcement, water used in concrete mix must meet rigorous demands, thus drinking water is often used, contributing to the depletion of this valuable and vital resource. Cement production is one of the largest greenhouse gas (GHG) emitters in the world. Cement industry is responsible for about 7% of the CO_2 emissions globally [1]. In 2016 it was the third-largest industrial energy consumer, with around 40% of all energy use in the non-metallic mineral sector [2].

According to [3] buildings are the single largest energy consumer in Europe and are responsible for approximately 40% of total EU energy consumption and 36% of GHG emissions. In 2019 about 21% of total final energy consumption globally was used in residential sector [4]. Thus, improving the energy efficiency of buildings is one of the priorities of

ISBN: 978-86-80593-73-9

sustainable development. CO_2 emission in construction process (including material production) accounts for about 20% of CO_2 produced during the whole lifetime of building [5]. This amount can be reduced by the proper design of concrete mix.

According to studies [6, 7] up to 30% of the heat loss can occur through thermal bridges in well-insulated residential buildings. Thus, concrete with lower thermal conductivity coefficient can contribute to the reduction of heat loss through the concrete parts of buildings (subterranean parts, floors and ceilings).

This paper concerns the possible ways of improvement of concrete sustainability through the replacement of its conventional constituents by by-products, waste and recycled materials. The benefits of these replacements are many. Beside the most important - to decarbonize the concrete production, to preserve the natural raw materials, to preserve the environment from waste materials, to reduce the energy consumption, this material substitution can result in more durable concrete, but also improve its thermal properties with positive impact on the energy efficiency of buildings.

II. Concrete – Performance Requirements

In the broadest sense, concrete is a mixture of cementing medium (binder), filler, water and admixtures [8]. Traditional, or conventional concrete mix consists about 15% or more of cement as a binder and about 75% of natural aggregate (river or seashore gravel, or crushed rocks) as a filler, by mass. The water content varies depending on desired properties of fresh and hardened concrete. Admixtures are chemical components added to the concrete mix, usually in very small amount up to 5% of the cement mass, to improve some properties of fresh or hardened concrete.

Concrete properties are mainly determined by properties and quantity of the constituent materials, but also by transporting, placing, compacting and curing of fresh concrete. These properties must ensure the compliance of concrete with all the requirements for its application in specific structure.

A. Basic Requirements

All concretes must have the required ***strength*** in compression, which may vary depending on its purpose, from very low - less than 10 MPa (e.g. for pedestrian pavements), "normal" – from about 20 to 50 MPa (e.g. for residential and some industrial buildings), to "high" – even above 100 MPa, for demanding engineering structures. Higher strength of conventional concrete is usually achieved by higher cement content, lower water-to-cement ratio (i.e. lower water content) and higher strength of aggregate.

Durability is the property which, generally, plain concrete naturally possesses. It becomes a serious issue when a steel reinforcement is used in RC structure. In that case, concrete plays the main role in corrosion protection, and must fulfil more rigorous demands than the plain concrete.

Fire resistance. Concrete is a non-flammable material. Significant change of its compressive strength and deformation is recorded at temperatures above 200^0 C. The fire resistance of RC members and structures is highly dependent on quality and depth of the concrete cover to reinforcement.

B. Specific Requirements

Depending on a method of transportation, placing, compacting, and on the use in structure, specific performance requirements may be prescribed. Some of them are higher workability, pumpability, self-compacting, high early strength, low shrinkage, watertightness, frost-thaw resistance, resistance to some chemicals, resistance to wear, etc.

III. Guidance for Low-Carbon, Energy Efficient Conrete

Since the cement production is the most energy demanding stage in concrete manufacture, with the highest CO_2 emission, a great number of research is focused on achieving all the desired concrete properties with ***reduced ordinary Portland cement (OPC) content***, by using the low-carbon and less energy consuming materials, preferably substituting part of the OPC by secondary or waste material. This could deliver 37% of the cumulative CO_2 emissions saving by 2050 globally. Effort is made to improve the energy efficiency and to switch to alternative (waste) fuels, which could jointly provide about 15% of the cumulative CO_2 emissions saving by 2050 globally. At present, coal, oil and natural gas still cover more than 90% of the global cement industry thermal energy consumption. [1]

Other pathways for decarbonization and reduction of energy consumption of concrete are listed below [1, 9, 10]:

- Construction and material efficiency - Optimizing the use of concrete in construction and the concrete mix design, concerning the purpose and the required material properties (performance-based design).
- Maximizing design life and reuse of concrete structure.
- Use of admixtures, which modify physical properties of concrete, but also may enhance its sustainability credentials and reduce the embodied CO_2 (ECO_2).
- Resource efficient manufacture and waste reduction - use of recycled and secondary aggregates; recycling of concrete.
- Optimization of concrete strength class. Required concrete strength should be in accordance with its application. For example, a reduction in compressive strength from 70 to 32 MPa may reduce ECO_2 for around 185 kg per m^3 of concrete [9].
- Responsible sourcing of materials.
- Use of recovered, waste, sea, or combined water wherever appropriate.
- Use of local sources, thus minimizing the transportation distance.

IV. Effect of Alternative Mix Components on Properties and Sustainability of Concrete

Replacing certain constituents of concrete mixture can improve one group of properties, but at the same time worsen another. The key points in choosing the right mix are:

- Good knowledge of the influence of a certain mix composition on all relevant properties of concrete, over a sufficiently long time. This requires comprehensive testing and the establishment of a broad database, with clearly defined testing and data processing conditions.
- Clear specification of the requirements to be met by concrete for the specific application and the mix design according to these requirements.

In the following text, some of the research results of the influence of replacement materials (binders, aggregates, water) on the properties of hardened concrete and its ecological footprint will be presented.

A. Binder

The significant amount of OPC in binder can be replaced by supplementary cementitious materials (SCMs), such as ground granulated blast-furnace slag (GGBS), fly ash or silica fume. Most important and most widely used SCMs can be found in abundance as industrial waste materials or by-products. The benefits of using SCMs from the point of view of environmental concern are multiple, but the quantities of SCM materials in the binder are often limited by the requirements for durability of concrete to only 10-20%. Consequently, CEM I and CEM II types of cements (without or with very low SCM content, respectively) are still dominantly in use.

Residential and public buildings usually are not exposed to severe, highly aggressive environment, thus the requirements for concrete resistance to environmental actions are milder. Thus, the concrete with significantly higher SCM content in binder, and notably reduced amount of OPC can be used. These buildings are also expected to be energy efficient. It is shown that the SCMs in binder can improve disadvantageous high thermal conductivity of concrete (Figs. 1-5).

However, the influence of SCM on other concrete properties should be also considered. They can cause the need for longer moist-cure of concrete, lower its early-age strengths and increase demand for chemical admixtures [11].

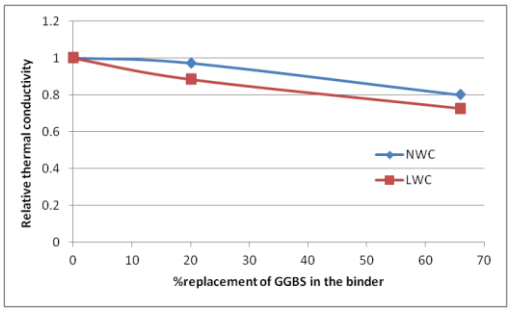

Figure 1. Effect of partial replacement of OPC by GGBS on the thermal conductivity of NWC and LWC.

1) GGBS – ground granulated blast-furnace slag

GGBS is a by-product from the production of iron. It is a material with hydraulic properties which hydrates in the presence of water and can even fully replace cement in the binder. Its cementitious properties can be accelerated in alkaline environment created by the clinker component in OPC. Considering the durability requirements of concrete, the rate of the Portland cement replacement by GGBS in binder is usually between 20 and 70%. As an industrial by-product with such properties, GGBS is one of the most commonly used SCM and has an important role in circular economy and sustainable development.

Beside the above-mentioned benefits, the replacement of OPC by GGBS in the binder also influences the concrete thermal properties.

In our experimental research three normal-weight concrete (NWC) mixes were composed with 0, 20 and 66% of GGBS replacement. The aggregate was riverbed quartz sand and gravel with maximum aggregate size of 16 mm. The water-binder ratio of 0.4 was kept constant in all mixes. Tests were also performed on three lightweight aggregate concrete (LWC) mixes with the same composition as the NWC samples, except the coarse aggregate which was replaced by expanded clay aggregate. The tests of thermal conductivity were carried out at the age of 28 days in oven-dried state.

Experiments have shown that the partial replacement of OPC by GGBS in binder reduces the thermal conductivity of NWC up to 20% and of LWC up to 30% (Fig. 1). Huge difference in the coefficient of thermal conductivity of NWC and LWC is shown in Fig. 2.

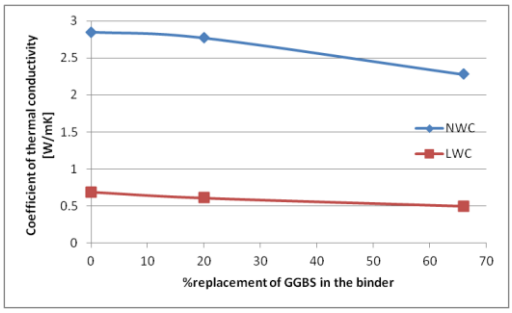

Figure 2. Effect of partial replacement of OPC by GGBS on the coefficient of thermal conductivity of NWC and LWC.

2) Fly ash

Fly ash is a coal combustion product, whose chemical, physical and morphological properties can vary in a wide range, making it difficult to be a universal, all-purpose SCM in concrete. Nevertheless, as a porous material, in the binder, it can beneficially lower the thermal conductivity of concrete. To improve unsatisfying properties of this industrial by-product as a SCM, various methods for its activation are used, among which the mechanical activation by grinding is most common. Although the primary goal of mechanical activation of the fly ash is to improve the mechanical properties and durability of concrete, grinding process simultaneously affects its thermal conductivity.

The mortar mix applied in this research was designed with a relatively high volume of fly ash in the binder, to demonstrate the effect of grinding time on the thermal conductivity. The aggregate in the experiment was riverbed quartz sand with maximum aggregate size of 4 mm with applied binder to aggregate ratio of 1:3. The water-binder ratio of 0.5 by volume was kept constant in all mixes.

The fly ash originating from power plant "Morava" was mechanically activated by grinding in a laboratory ball mill for 0, 30, 60, 120, 240 and 480 minutes. The replacement rate of cement with fly ash was 40% by volume in all mixes.

The results of experiment are shown in Fig. 3. Although the volumetric quantity of fly ash in the mortar mix is less than 9%, it can reduce the thermal conductivity of the mortar up to 30% compared to the OPC mortar without fly ash (reference sample, labeled "0" in Fig. 3).

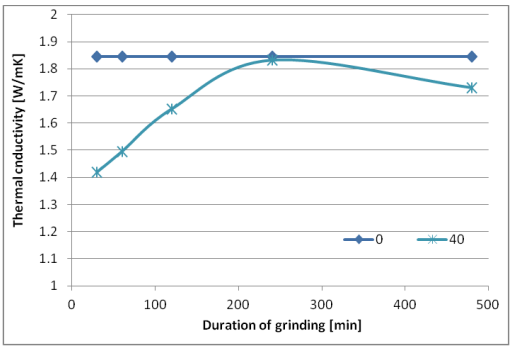

Figure 3. Effect of grinding time of fly ash on the thermal conductivity of mortar.

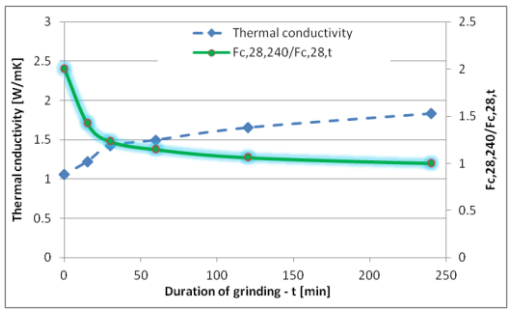

Figure 4. Optimization of thermal conductivity and compressive strength of mortar by the grinding time of fly ash.

Fig. 4 shows the influence of grinding time on thermal conductivity and compressive strength of mortar made with 40% fly ash in binder. Relative mortar strength is expressed as a ratio of the 28-day compressive strengths of mixtures with fly ash grinded 240 (Fc,28,240) and *t* minutes (Fc,28,t). Both thermal conductivity and compressive strength rise by the increase of grinding time up to 240 min. Optimal duration of grinding, which gives the best strength-thermal conductivity relation can be found at the intersection of these two curves.

3) Silica fume

Micro-silica or silica fume is an exceptional SCM. It is an industrial by-product of the silicon and ferrosilicon alloy production which, due to its pozzolanic properties, can remarkably enhance the mechanical properties and durability of concrete. At the same time, as silica fume consists of very small spherical particles (average size of 100nm), it can greatly reduce the concrete thermal conductivity (Fig. 5).

Addition of SCMs can significantly reduce the ECO_2 of concrete. The ECO_2 of three concrete mixes, with binder containing 0, 20 and 66% of GGBS was calculated using the Circular

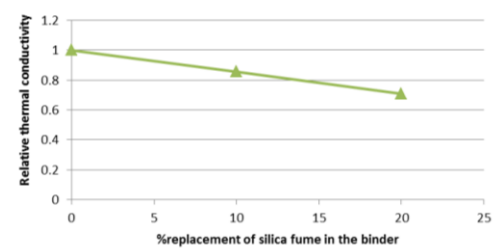

Figure 5. Effect of cement replacement with silica fume on thermal conductivity of concrete.

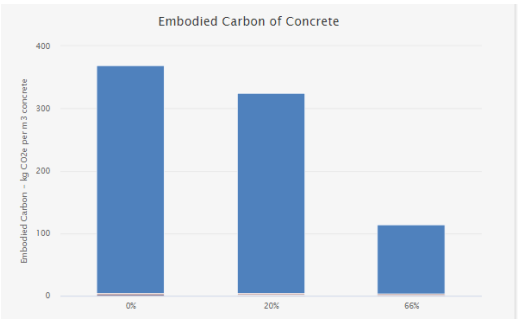

Figure 6. Contribution of binder containing GGBS to embodied carbon of concrete [12].

Ecology's Embodied Carbon Footprint Database [12]. With the highest replacement rate, binder contribution to ECO_2 of concrete is reduced by about 65% (Fig. 6), compared to the binder with 100% OPC.

The contribution of binder containing 0, 20 and 40% of fly ash to ECO_2 of concrete is shown in Fig. 7. With the highest fly ash content, savings of about 39% in binder ECO_2 contribution can be achieved.

B. Aggregate

Aggregates usually represent 60-80% of the fresh concrete volume; hence they have a significant impact on the environment. While riverbed gravel and sand are still the most common choice for aggregate, due to environmental concern and in order to protect affected ecosystems, the number of riverbed mining bans are rising. Although the production of crushed aggregate is more energy demanding and simultaneously have increased GHG emissions, crushed aggregate can provide other, long-term benefits on the residential or public building energy efficiency, when used in concrete which is a part of the building envelope. Namely, concrete made with riverbed gravel and

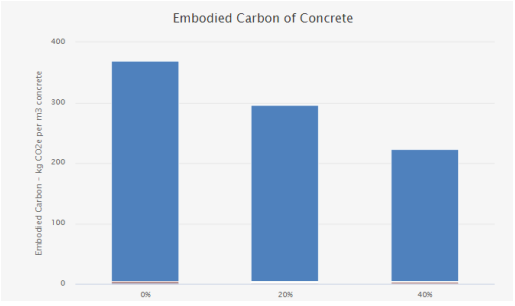

Figure 7. Contribution of binder containing fly ash to embodied carbon of concrete [12].

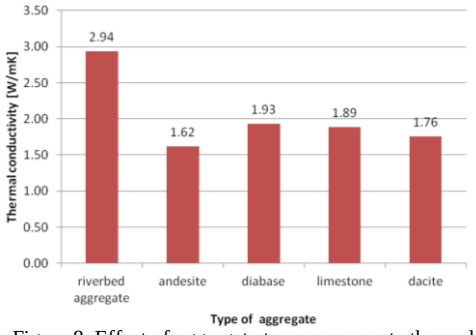

Figure 8. Effect of aggregate type on concrete thermal conductivity.

sand will have inherently higher coefficient of thermal conductivity, due to the dominant presence of quartzite whose thermal conductivity ranges from 5.2 to 8.2 W/mK. Most often used types of crushed aggregates (limestone, dolomite, granite, basalt, etc...) have approximately 2-3 times lower value of thermal conductivity coefficient [11].

Results of our tests in Fig. 8 demonstrate the influence of aggregate type on the thermal properties of resulting NWC mix. All concrete mixtures were made with the same cement content (400 kg/m^3), water to cement ratio of 0.4, the aggregate grading and the maximum grain size of 16 mm. The varying types of aggregates were riverbed aggregate, andesite, diabase, limestone and dacite. Concrete specimen with andesite had the lowest thermal conductivity.

In extensive study published in [13] the results of tests on light-weight aggregate concrete (LWAC) mixtures also showed the significant effect of lowering the thermal conductivity of concrete by using dacite sand instead of quartzite. The LWAC mixes with dacite sand had approximately 20% lower thermal conductivity compared to identical LWAC mixtures with quartzite sand.

From the aspect of sustainable development and circular economy a more beneficial alternative for aggregate is the use of construction and demolition waste (CDW) materials especially recycled concrete aggregate (Fig. 9).

Since CDW is accountable for almost 1/3 of all generated solid waste [14], the potential benefits of its reuse are significant. Especially in residential and public buildings these materials as aggregates can fully replace the commonly


Figure 9. Separated ground recycled concrete aggregate.

used, natural materials. Although there is a potential risk concerning the durability requirements of concrete made with recycled concrete aggregate, in low-story residential and public buildings the environmental exposure conditions can allow the use of these recycled aggregates without limitations. Additionally, concrete made with recycled concrete aggregate can have a lower thermal conductivity.

As explained above the thermal conductivity of concrete is dominantly determined by the type of aggregate. Concerning the fact that ground recycled concrete aggregate (RCA) has a considerable porosity and only 60-80% of its volume is represented by natural stone materials (the rest is bound mortar), the lower density of recycled aggregate will also result in lower thermal conductivity.

The effect of recycled concrete aggregate in four concrete mixes, in which the natural riverbed aggregate is replaced by 0, 25, 50, and 100% RCA, was analyzed. In all concrete mixes the amount of cement was 400 kg/m^3, water to cement ratio was kept 0.35 (excluding the amount of absorbed water by RCA), the maximum grain size was 31.5 mm, and the aggregate grading was kept constant. The results presented in Fig. 10 show that the replacement of

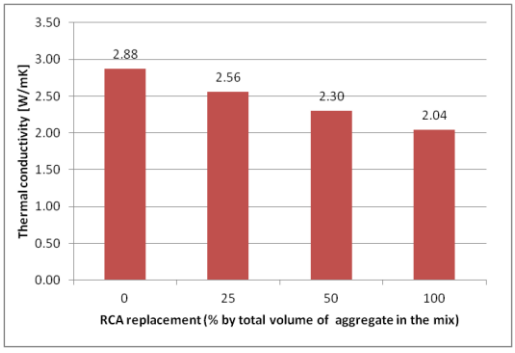

Figure 10. Effect of RCA content on concrete thermal conductivity.

natural aggregate by the RCA may reduce the thermal conductivity of concrete up to 30%.

C. Water

Although 71% of the Earth's surface is water-covered, only approximately 1.2% is the accessible freshwater. Considering the importance and the ever-growing demand for water affected by population growth, industrial, social and economic developments, the amount of water used for concrete production can be declared considerable, in some situations even crucial. In a lack of fresh water, the use of salt water can be considered, but having in mind that this also implies accelerated hardening (due to the presence of chloride), and a reduction of the 28-day strength of concrete by 10-20% [15]. These concretes are not suitable for use in structures with steel reinforcement or steel fibers, due to the corrosive effect of chlorides on steel.

Studies [16] conducted on green concretes containing high volume of SCMs have shown that ternary binder systems composed of fly ash, GGBS and cement can have a synergy with water containing chlorides. These binder systems provide better mechanical properties when salt water or brine are used as mixing water, especially at ambient temperatures above 20°C. The amount of SCMs in these binder compositions is above 80%, which also provides reduced thermal conductivity of the resulting green concrete.

V. CONCLUSION

As the most widely used building material, concrete makes a significant ecological footprint. In a life-cycle assessment of buildings the influence of concrete properties on carbon emissions and energy consumption is evident not only in production and construction phase, and finally in the waste disposure at the end of the service life of buildings. Concrete properties also have a great influence on energy efficiency of buildings in use, mostly its high thermal mass, which can be used in the passive control of interior temperature. Concerning the energy efficiency of buildings, due to its relatively high thermal conductivity concrete plays an important role in the heat loss through the “thermal bridges”, which commonly occur in the concrete parts of buildings.

The most energy and carbon intense stage of concrete production is the manufacture of cement. To lower its footprint, effort is made to switch from the use of fossil fuels to renewable energy sources, but also to replace cement clinker in binder by other by-product or waste material, such as ground granulated blast-furnace slag, fly ash or silica fume. It is shown that this replacement also has a beneficial influence on the thermal conductivity of concrete, lowering it even up to 30%.

Improvement of the thermal properties of hardened concrete can be also achieved by the careful choice of aggregate. Concrete with andesite or dacite may have about 20% lower thermal conductivity than the same mixture with quartzite aggregate. Use of recycled aggregates in concrete mixes means not only the safe disposal of the construction and demolition waste, but also may lower the thermal conductivity of concrete. However, caution is needed concerning other concrete properties, such as porosity, durability, freeze-thaw resistance etc., which can be significantly modified using recycled concrete as aggregate.

Sea water and brine are not suitable for concrete mixes which are to be used in structural members containing steel reinforcement or steel fibers. Nevertheless, they can be used for the production of plain concrete or concrete elements with fiber-reinforced polymer reinforcement or with carbon or glass fibers, which are not prone to the chloride induced corrosion. The use of salt water in combination with the right amount of secondary cementitious materials in binder may also improve mechanical properties of hardened concrete.

The way we produce concrete can lower its carbon emission and energy consumption. Its proper design and application significantly influence the energy efficiency of buildings. Concrete structure should be designed concerning the optimal use of concrete, relaying on local sources and producers, maximizing the building’s service life, and providing its adaptability to other purposes.

REFERENCES

[1] *Technology roadmap: Low-carbon transition in the Cement Industry*. (2018). International Energy Agency & Cement Sustainability Initiative.

[2] Chan, Y., Petithuguenin, L., Fleiter, T., Herbst, A., Arens, M. & Stevenson, P. (2019). *Industrial innovation: Pathways to deep decarbonisation of Industry. Part 1: Technology analysis*. ICF Consulting Services Limited. Fraunhofer.

[3] *EU Energy performance of building directive*. Available at: https://ec.europa.eu/energy/topics/energy-efficiency/energy-efficient-buildings/energy-performance-buildings-directive_en#facts-and-figures

[4] *IEA Energy and carbon tracker*. (2020). Available at: https://www.iea.org/data-and-statistics/data-browser?country=WORLD&fuel=Energy%20consumption&indicator=TFCbySector

[5] *Concrete buildings scheme design manual*. (2009). The Concrete Centre.

[6] Theodosiou, T.G. & Papadopoulos, A.M. (2008). The impact of thermal bridges on the energy demand of buildings with double brick wall constructions. *Energy and Buildings, 40*(11), 2083-2089.

[7] Erhorn, H., Erhorn-Kluttig, H., Thomsen, K.E., Rose, J. & Aggerholm, S. (2010). *An effective handling of thermal bridges in the EPBD context: Final report of the IEE ASIEPI work on thermal bridges*. ASIEPI.

[8] Neville, A.M. & Brooks, J.J. (2010). *Concrete Technology*. Pearson Education Limited.

[9] *Specifying sustainable concrete*. (2020). The Concrete Centre.

[10] *In-depth analysis in support of the commission comunication COM(2018) 773: A clean planet for all – A European long-term strategic vision for a prosperous, modern, competitive and climate neutral economy*. (2018). European Commission.

[11] Balázs, G.L., Nehme, S. Nemes, R. Ceh, A. & Kopecskó, K. (2016, June 13-15). *Engineering the way for sustainability* [Paper presentation]. Second International Conference on Concrete Sustainabilitz, Madrid.

[12] Jones, C. (2019). *ICE Database – The Inventory of Carbon and Energy*. Circular Ecology. Available at: https://circularecology.com/embodied-carbon-footprint-database.html

[13] Cseh, Á., Balázs, G.L., Kekanović, M. & Miličić, I. (2021). Effect of SCMs on heat transfer properties of LWAC. *Journal of Thermal Analysis and Calorimetry, 144*, 1095-1108.

[14] Mália, M., de Brito, J., Pinheiro, M.D. & Bravo, M. (2013). Construction and demolition waste indicators. *Waste Management & Research, 31*(3), 241-255.

[15] Mindess, S., Young, F.J., Darwin, D. (2003). *Concrete: 2nd Edition.* PrenticeHall, Upper Saddle River, New Jersey.

[16] Čeh, A. (2020). *Zeleni betoni visokih performansi sa velikim sadržajem letećeg pepela*. PhD thesis, Faculty of Civil Engineering, University of Novi Sad, Serbia.

Study of Efficiency of a Coupled Thermoacoustic MHD Generator Channel

Yassine Laghouati[1], Ahcène Bouabdallah[2], Antoine Alemany[3]

[1]Laboratory LAMOSI, University USTO, Oran, Algeria, laghouatiy@yahoo.fr
[2]Laboratory LTSE, University USTHB, Alger, Algeria, abouab2002@yahoo.fr
[3]Laboratory SIMAP-EMP, INPG, Grenoble, France,
antoine.alemany@simap.grenoble-inp.fr

Abstract—**The present work is concerned with the study of thermos-acoustic effect coupled to an MHD generator duct with non-conducting walls. In this flow system, the pulsed flow of magnetic fluid in channel is submitted to an applied magnetic field B_0. The pulsed axial velocity field u and the oscillating pressure are caused by the thermos-acoustic effect. In these conditions, we attempt to resolve this problem from the magneto-hydrodynamic MHD equations and boundary conditions. By manipulating the induction equations, we lead to the second order equation of the induced magnetic field b_b with respect of the coordinate z, where b_b is a function of I_0. The pressure value p_0 and the current intensity I_0 are obtained respectively from the momentum and Ohm equations. The results are analyzed and discussed, it is confirmed that the thermos-acoustic process allows producing electricity with moderate efficient.**

Keywords – magneto-hydrodynamic, thermo-acoustic, electrical generator, electrical efficiency

I. INTRODUCTION

The researches in energetic systems and particularly the studies about the thermos-acoustic systems coupled to MHD generator have attracted the intention of many authors. Due to their simplicity and the absence of moving solid components, thermos-acoustic engine connected to MHD produce electricity energy and they are convenient used indeed in space field applications [1].

The MHD generator based on the interaction of magnetic field with an oscillating velocity flow, produce a current and induced magnetic field generating by coils connected with the load [2-4]. The process is much simpler than the previous MHD power generator based on the use of a double liquid/gas loop [5].

Among the experimental investigations on MHD generator considering the dynamic behavior and the effect of various MHD parameters on the velocity and induced magnetic field, we can cite the work done by [6-7].

In this paper, we are concerned about the study of thermo-acoustic engine connected to an MHD generator with non-conducting walls. The pulsed flow of the MHD channel is submitted to an applied uniform magnetic field B_0. The pulsed hydrodynamic is caused by the thermo-acoustic effect generated by temperature gradient across a stack device compounded of thin superposed parallel plates.

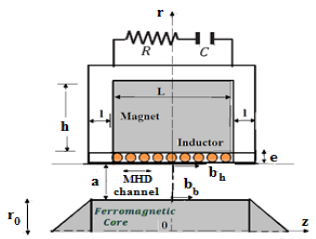

Figure 1 Schematic of Thermoacoustic MHD Generator.

TABLE I. GEOMETRICAL DIMENSIONS.

Scales	Explanation
r_0	inner radius of the MHD Chanel
r_t	outer radius of the MHD Chanel
a	channel gap
h	height of the yoke
L	length of the active part
l	length of the yoke pole
e	thickness of the coils

II. DESCRIPTION OF THE MODEL

The geometrical configuration of the MHD generator is illustrated in Fig. 1.

The active part of the generator with length $L1 = L + 2l$, is supposed to be larger than the MHD channel gap a, the channel is considered as infinitely long.

The MHD channel contains a liquid metal with mass density ρ, kinetic viscosity ν, magnetic permeability μ_0 and electrical conductivity σ_f. The pressure has the amplitude p_0, causes a velocity value V_0. The pulsation in the fluid metal is ω.

The uniform magnetic field $B = -B_0$ is acted in radially direction. The induced current in azimuthal direction produces an induced magnetic field in the ferromagnetic core (permeability μ_f) of the generator. The magnetic fluxes induce an electric current in the external coil connected to the load. The inductor has N coils is connected in series with the load circuit, including a correction capacitor C and a resistive load R.

III. FORMULATION OF THE PROBLEM

A. Governing Equations

- Continuity,

$$\vec{\nabla}.\vec{V} = 0 \ . \tag{1}$$

- Navier-Stokes Eq.,

$$\frac{d\vec{V}}{dt} = -\frac{1}{\rho}\vec{\nabla}\, p + \nu\Delta\vec{V} + \frac{1}{\rho}\vec{j}\times\vec{V} \ . \tag{2}$$

- Maxwell Eqs.,

$$\vec{\nabla}\times\vec{B} = \mu_0\,\vec{j} \ . \tag{3}$$

$$\vec{\nabla}.\vec{E} = 0 \ , \tag{4}$$

$$\vec{\nabla}\times\vec{E} = -\frac{\partial\vec{B}}{\partial t} \ , \tag{5}$$

- Ohm law,

$$\vec{J} = \sigma\left(\vec{E} + \vec{V}\times\vec{B}\right) . \tag{6}$$

B. Work Conditions

The perturbed flow has an axial velocity field $\vec{V}\left(0,0,V_0\exp\left(i\omega t\right)\right)$. We consider an electrical tangential field $\vec{E}\left(0,E_\theta\exp\left(i\omega t\right),0\right)$. The magnetic perturbed field is represented by $\vec{B}\left(b_r\exp\left(i\omega t\right),B_0,b_z\exp\left(i\omega t\right)\right)$. Where b_r and b_z designed respectively the radial and vertical components of the induced magnetic field. The induced magnetic field is small compared to the external magnetic field $(b << B_0)$.

Equation of the Perturbed Magnetic Field

By manipulating the (1) to (6) expressed in cylindrical coordinates (r,θ,z) and by considering the work conditions, we lead to the differential equation of the induced magnetic field at the bottom of the MHD channel:

$$\left(\left(\frac{\mu_f}{\mu_0}\right)\frac{r}{2}\right)\frac{d^2b}{dz^2} + \left[\left(\frac{\mu_f}{\mu_0}\right)\frac{r}{2\alpha a} - \left(\frac{1}{a}\right) - \frac{r}{2}\left(i\omega\sigma\mu_0\right)\right]b + \left(\frac{\mu_0 nI_0}{a}\right) - \left(\sigma\mu_0 V_0 B_0\right) = 0 \tag{7}$$

The associated boundary conditions are:

$$1) - \frac{db}{dz} = 0 \ \textit{for}\ z = 0 \ , \tag{8}$$

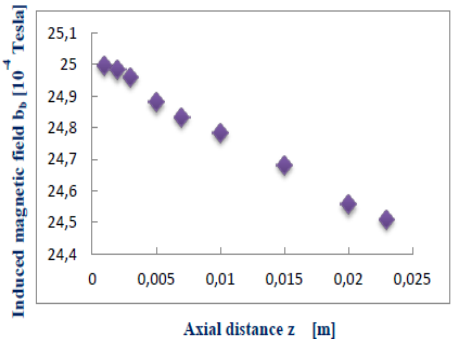

Figure 2. Variation of induced magnetic field in the bottom of channel versus axial distance.

$$2)\ b_{core} = b_b\left(\frac{\mu_f}{\mu_0}\right)\ for\ z=0 \quad . \qquad (9)$$

IV. Results and Discussions

By resolving the (7) with boundaries layer (8) and (9), we obtain the evolution versus respect the axial distance of the induced magnetic field at channel's bottom (Fig. 2). The induced magnetic field varies linearly slightly from the value $b_b = 0.0025$ Tesla at $z=0$ to $b_b = 0.002442$ for $z = 0.025\,m$.

We can access to value of the induced magnetic field b_T near the inductor by mean of Ampere's law.

The Fig. 3 illustrates the evolution of the induced magnetic field b with the radial distance.

The variation of the induced magnetic field b and the current density versus the radial distance is exhibited in Fig. 3. The induced magnetic field

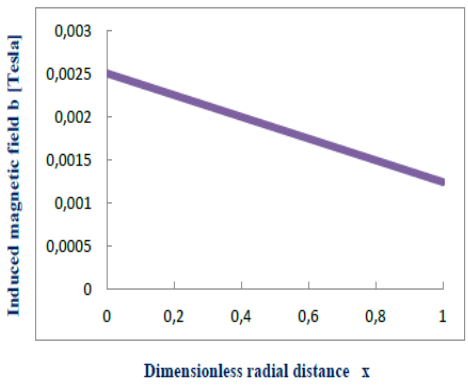

Figure 3. Variation of induced magnetic field in the mhd channel versus the dimensionless radial distance.

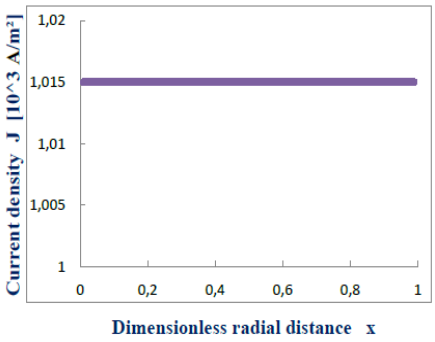

Figure 4. Variation of the current density in the mhd channel versus the dimensionless radial distance.

varies linearly from the value $b = 0.0025$ Tesla $(x=0)$ to $b = 0.0012$ Tesla for $(x=1)$.

The distribution of the current density (Fig. 4) is uniform $(J = 1.015103\,A/m^2)$.

From the working conditions, the analytical resolution leads to the results of the MHD generator presented in the Table II.

The electrical efficiency is given by,

$$\eta = P_{out} \Big/ \left(P_{out} + P_{j_{fluide}}\right). \qquad (10)$$

$P_{out} = RI_0^2 \Big/ 2$, is the Ohmic power loss in the resistance.

TABLE II. The parameters values of the MHD generator.

Parameter	Notation	Value
Frequency	f	50 Hz
Melt Velocity	V_0	8.41 m/s
Load current	I_0	2.05 A
Number of wires	N	200
Load resistance	R	200 Ω
Load capacitance	C	20 µF
Load Power	P_0	422 W
Total Power	P_{in}	645 W
Efficiency	η	0.65

$P_{j_{fluide}} = \left(L\mu_0^2 \Big/ aB_0^2 \right)(r_0 + a/2) \int_{r_0}^{r_0+a} J_\theta{}^2 dr$, is the Ohmic power loss in the fluid.

We attain the value output power Pout =422 W, and the corresponding efficiency $\eta = 0,65$.

The values of the physical parameters of the mhd generator are presented in the Table II.

V. CONCLUSION

This study is focused on characterization of the MHD generator coupled to thermo-acoustic engine. In the work conditions, we neglected the viscosity and the effect of the wall conductivity.

We have presented the evolution of the induced magnetic field and the current density in the MHD channel.

By optimizing the parameters of the load circuit, we can obtain higher values of output power and efficiency of the system.

It is important to control essentially the output power and the efficiency for producing electricity.

REFERENCES

[1] Castrejón-Pita, A. A. & Huelsz, G. (2007). Heat to electricityo-magnetohydrodynamic conversion. *Applied Physics Letters, 90(7).*174110.

[2] Vogin, C & Alemany, A. (2007) .Analysis of the flow in a thermo-acoustic mhd generator with conducting wall. *European Journal of Mechanics B/Fluids, 26*(4), 479–493.

[3] Mirhoseini, T. & Alemany, A. (2014, June). Analytical Calculation of Thermoacoustic Magneto-hydrodynamic (TA-MHD) Generator. *In Intern. Conf. Fund . Appl MHD* (pp.479-483).

[4] Schreppl, S.C. & Busch-Vishni, I.J. (1991). A magneto-hydrodynamic underwater acoustic transducer. *The Journal of the Acoustical Society of America*, *89*(2).

[5] Rosa, R.J. (1987). *Magnetohydrodynamic Energy Conversion*. Hemisphere Publishing Corporation.

[6] Fabris G. & Pierson, E. S. (1979). The role of interfacial heat and mechanical energy transfer in a liquid-metal mhd generator. *Journal of Energy Conversion, 19*, 111–118.

[7] Jousselin, F. Marty, P. Alemany, A. & Werkoff, F. (1989). Mhd induction generator at weak magnetic Reynolds number, part I . self-excitation criterion and efficiency. *European Journal of Mechanics B/Fluids*, *8*, 23-35.

Optimal Coal Supplier Selection for Thermal Power Plant Based on Mcrat Method

Miloš Gligorić[1], Katarina Urošević[2], Suzana Lutovac[3], Dževdet Halilović[4]

[1,2,3,4]University of Belgrade – Faculty of Mining and Geology, Belgrade, Serbia,
milos.gligoric@rgf.bg.ac.rs[1], katarina.urosevic@rgf.bg.ac.rs[2],
suzana.lutovac@rgf.bg.ac.rs[3], dzevdet.halilovic@rgf.bg.ac.rs[4]

Abstract—**The growing demand for electricity energy requires expansion and improvement of the appropriate capacities of thermal power plants. In order to provide the stable and sustainable electricity production as well as to improve the sustainable development of each mining company, optimal coal supplier selection for thermal power plant has a great significance and represents the core of this study. There are many reasons for coal supplier selection for thermal power plant. Some of them are related to decreasing the cost of electricity production, enhancing market competitiveness, establishing a balanced quantity and quality of ore delivery to power plant etc. In this paper, we have developed a new model of optimal coal supplier selection for thermal power plant based on MCRAT method. The model was tested as hypothetical example related to coal supplier selection for thermal power plant.**

Keywords - coal supplier selection, multi – criteria decision – making, MCRAT method, objective criteria weights

I. INTRODUCTION

Coal represents one of the strategically most important energy raw material, both in the world and in our country. Coal plays a vital role in electricity production. The economy and energy development of each country largely depends on stable electricity production. In Serbia, coal is primary applied for electricity production and represents a crucial factor in sustainable development of the country. In the world, about 40% of electricity is produced by coal combustion, while in Serbia, even 70% of electricity is produced by coal combustion in thermal power plants.

Thermal power plant is a key facility at each coal mine. The main role of each thermal power plant is referred on electricity production obtained by coal combustion. The type of coal that used for burning can vary from lignite to brown coal depending on target attribute value required by thermal power plant. Coal, used for combustion in thermal power plant, is characterized by the following attribute values (criteria) such as: calorific value, ash, sulphur and moisture content. In addition to the above coal quality attributes, we should not forget the economic attribute of coal such as the coal price on the market. Based on these main attributes (criteria) that characterize each coal types, coal supplier can be selected for sustainable delivery to thermal power plant.

Several authors in mining industry have dealt with multi – criteria decision – making optimization and applied different mathematical methods and new approaches for coal supplier selection for thermal power plant [1-4].

In this paper, multi – criteria decision – making method called MCRAT method is applied for optimal coal supplier selection for thermal power plant. Also, we have applied a novel objective method for criteria weights determination, Method based on the Removal Effects of Criteria (MEREC) and compare results with a traditional Shannon's entropy method. The rest of this paper is organized as follows. In Section 2, detailed description of the multi – criteria decision – making method (MCRAT method) is represented including description of methods for objective criteria weights determination (Shannon's entropy method and MEREC method). Section 3 is referred on

numerical example where hypothetical situation is tested. Finally, conclusions about the developed model and obtained results are discussed in Section 4.

II. Multi – Criteria Decision – Making Model

The most suitable way to describe the problem of alternative ranking is the decision-making matrix, abbreviated decision matrix:

$$D = \left[x_{ij} \right]_{m \times n} = \begin{bmatrix} A/C & C_1 & C_2 & \dots & C_n \\ A_1 & x_{11} & x_{12} & \dots & x_{1j} \\ A_2 & x_{21} & x_{22} & \dots & x_{2j} \\ \vdots & \vdots & \vdots & \ddots & \vdots \\ A_m & x_{m1} & x_{m2} & \dots & x_{mn} \end{bmatrix}, \quad (1)$$

where:

$A = \left[A_1, A_2, \dots, A_m \right]$ – a given set of alternatives,

$C = \left[C_1, C_2, \dots, C_n \right]$ – a given set of criteria,

m – the total number of alternatives

n – the total number of criteria

$\left[x_{ij} \right]_{m \times n}$ – an assessment of alternative Ai with respect to a set of criteria.

The procedure of the multiple criteria ranking by alternative trace (MCRAT) method [5] is composed of the following steps:

Step 1: Normalization of input data

Normalization is a process of transforming different dimensions of input data into compatible scale i.e., unity interval [0,1]. For that purpose, we applied a simple linear normalization technique, and it is described as follows:

For the benefit criteria:

$$r_{ij} = \frac{x_{ij}}{max_i \left(x_{ij} \right)}, \ \forall i \in \left[1, 2, \dots, m \right] \wedge j \in S_{max} \ , \quad (2)$$

For the cost criteria:

$$r_{ij} = \frac{min_i \left(x_{ij} \right)}{x_{ij}}, \ \forall i \in \left[1, 2, \dots, m \right] \wedge j \in S_{min} \ , \quad (3)$$

where:

S_{max} – a set of benefit criteria

S_{min} – a set of cost criteria

The normalized decision matrix R is formed as:

$$R = \left[r_{ij} \right]_{m \times n} = \begin{bmatrix} A/C & C_1 & C_2 & \dots & C_n \\ A_1 & r_{11} & r_{12} & \dots & r_{1j} \\ A_2 & r_{21} & r_{22} & \dots & r_{2j} \\ \vdots & \vdots & \vdots & \ddots & \vdots \\ A_m & r_{m1} & r_{m2} & \dots & r_{mn} \end{bmatrix} \frac{1}{2} . \quad (4)$$

Step 2: Weighted normalization

For each normalized assessment r_{ij} do the weighted normalization as follows:

$$u_{ij} = w_j r_{ij}, \forall i \in \left[1, 2, \dots, m \right], \forall j \in \left[1, 2, \dots, n \right] . \quad (5)$$

The outcome of weighted normalization is weighted normalized matrix:

$$U = \left[u_{ij} \right]_{m \times n} = \begin{bmatrix} A/C & C_1 & C_2 & \dots & C_n \\ A_1 & u_{11} & u_{12} & \dots & u_{1j} \\ A_2 & u_{21} & u_{22} & \dots & u_{2j} \\ \vdots & \vdots & \vdots & \ddots & \vdots \\ A_m & u_{m1} & u_{m2} & \dots & u_{mn} \end{bmatrix} . \quad (6)$$

Step 2.1: Shannon's entropy method

One of the most used methods for determining the criteria weights is Shannon's entropy method. Entropy is a measure of uncertainty in the information formulated using probability theory. This method provides a help the decision maker to reduce subjectivity during criterion weight assignment. Shannon and Weaver [6] proposed the entropy concept and this concept has been upgraded by Zeleny [7] for deciding the objective criteria weights. Entropy contains the following steps:

Step 2.1.1: Construct the initial decision-making matrix as follows:

$$(A/C) = \left[x_{ij}\right]_{mxn} = \begin{bmatrix} A/C & C_1 & C_2 & \cdots & C_n \\ A_1 & x_{11} & x_{12} & \cdots & x_{1n} \\ A_2 & x_{21} & x_{22} & \cdots & x_{2n} \\ \vdots & \vdots & \vdots & \ddots & \vdots \\ A_m & x_{m1} & x_{m2} & \cdots & x_{mn} \end{bmatrix}, \quad (7)$$

where:

x_{ij} – represents the evaluation of the alternative i with respect to criterion j,

m – the number of alternatives,

n – the number of criteria.

Step 2.1.2: Construct the normalized matrix r_{ij} using following Eq.:

$$r_{ij} = \frac{x_{ij}}{\sum_{i=1}^{m} x_{ij}} . \quad (8)$$

Step 2.1.3: Value of the entropy e_j is calculated as follows:

$$e_j = -k\sum_{i=1}^{m} r_{ij} ln\ a_{ij} , \quad (9)$$

where:

$k = \frac{1}{lnm}$ – a constant that guarantees $0 \le e_j \le 1$.

m – a total number of alternatives.

Step 2.1.4: The degree of divergence d_j is determined using following Eq.:

$$d_j = 1 - e_j . \quad (10)$$

Step 2.1.5: The objective weight for each criterion w_j is calculated as follows:

$$w_j = \frac{d_j}{\sum_{j=1}^{n} d_j} . \quad (11)$$

Step 2.2: MEREC method

This method was developed by [8] for obtaining the objective criteria weights determination in multi – criteria decision – making problems. This novel idea for criteria weights determination represents the Method based on the Removal Effects of Criteria (MEREC). MEREC is created by the following steps:

Step 2.2.1: Construct the initial decision – making matrix with input data

$$X = \left[x_{ij}\right]_{nxm} = \begin{bmatrix} x_{11} & x_{12} & \cdots & x_{1m} \\ x_{21} & x_{22} & \cdots & x_{2m} \\ \vdots & \vdots & \ddots & \vdots \\ x_{n1} & x_{n2} & \cdots & x_{nm} \end{bmatrix}, \quad (12)$$

where are:

n – the number of alternatives,

m – the number of criteria.

Step 2.2.2: Normalization of the initial decision – making matrix

for beneficial (maximization) criteria:

$$r_{ij} = \frac{\min\limits_{i=1,2,\ldots,n} x_{ij}}{x_{ij}} . \quad (13)$$

for non – beneficial (minimization) criteria:

$$r_{ij} = \frac{x_{ij}}{\max\limits_{i=1,2,\ldots,n} x_{ij}} . \quad (14)$$

Step 2.2.3: Calculation the overall performance of the alternative S_i:

$$S_i = \ln\left(1 + \left(\frac{1}{m}\sum_j \left|\ln\left(r_{ij}\right)\right|\right)\right) . \quad (15)$$

Step 2.2.4: Calculate the performance of the alternatives by removing each criterion S_{ij}':

$$S_{ij}^{'} = \ln\left(1+\left(\frac{1}{m}\sum_{k,k\neq j}\left|\ln\left(r_{ik}\right)\right|\right)\right), \quad . \quad (16)$$
$$k = 1,2,\ldots,m$$

Step 2.2.5: Compute the summation of absolute deviations E_j :

$$E_j = \sum_i \left|S_{ij}^{'} - S_i\right| \ . \quad (17)$$

Step 2.2.6: Final criteria weights determination w_j:

$$w_j = \frac{E_j}{\sum_k E_j},\ k = 1,2,\ldots,m \ . \quad (18)$$

Step 3: Optimal alternative determination

Determine each element of the optimal alternative as follows:

$$q_j = max\left(u_{ij} | 1 \le j \le n\right),\ \forall i \in \left[1,2,\ldots,m\right] \ . \quad (19)$$

Optimal alternative is represented by the following set:

$$Q = \left\{q_1, q_2, \ldots, q_j\right\}, j = 1,2,\ldots,n \ . \quad (20)$$

Step 4: Decomposition of the optimal alternative

This step implies decomposition of the optimal alternative in the two subsets or two components. The set Q can be represented as the union of the two subsets:

$$Q = Q^{max} \bigcup Q^{min} \ . \quad (21)$$

If the k represents the total number of benefit criteria, then $h = n - k$ represents the total number of cost criteria. Hence, the optimal alternative is defined as:

$$Q = \left\{q_1, q_2, \ldots, q_k\right\} \bigcup \left\{q_1, q_2, \ldots, q_h\right\}; \quad . \quad (22)$$
$$k + h = j$$

Step 5: Decomposition of the alternative

Similarly, to the Step 4 we perform decomposition of each alternative:

$$U_i = U_i^{max} \bigcup U_i^{min}, \forall i \in \left[1,2,\ldots,m\right] \ , \quad (23)$$

$$U_i = \left\{u_{i1}, u_{i2}, \ldots, u_{ik}\right\} \bigcup \left\{u_{i1}, u_{i2}, \ldots, u_{ih}\right\}, \quad . \quad (24)$$
$$\forall i \in \left[1,2,\ldots,m\right]$$

Step 6: Magnitude of component

For each component of the optimal alternative, calculate the magnitude defined by:

$$Q_k = \sqrt{q_1^2 + q_2^2 + .. + q_k^2} \ , \quad (25)$$

$$Q_h = \sqrt{q_1^2 + q_2^2 + .. + q_h^2} \ . \quad (26)$$

The same approach is applied for each alternative.

$$U_{ik} = \sqrt{u_{i1}^2 + u_{i2}^2 + \ldots + u_{ik}^2}, \forall i \in \left[1,2,..,m\right] \ , \quad (27)$$

$$U_{ih} = \sqrt{u_{i1}^2 + u_{i2}^2 + \ldots + u_{ih}^2}, \forall i \in \left[1,2,..,m\right] \ . \quad (28)$$

Step 7: Multiple-Criteria Ranking by Alternative Trace (MCRAT) [5]

Create the matrix F composed of optimal alternative components:

$$F = \begin{bmatrix} Q_k & 0 \\ 0 & Q_h \end{bmatrix} . \quad (29)$$

Also, create the matrix G_i composed of alternative components:

$$G_i = \begin{bmatrix} U_{ik} & 0 \\ 0 & U_{ih} \end{bmatrix}, \forall i \in \left[1,2,\ldots,m\right] \ . \quad (30)$$

If T_i is a matrix obtained by the product of matrix F and G_i :

$$T_i = F \times G_i = \begin{bmatrix} t_{11;i} & 0 \\ 0 & t_{22;i} \end{bmatrix}, \forall i \in \left[1,2,\ldots,m\right] \ . (31)$$

Then, trace of the matrix T_i is as follows:

$$tr\left(T_i\right) = t_{11;i} + t_{22;i}, \forall i \in \left[1,2,\ldots,m\right] . \quad (32)$$

Alternatives are now ranked according to the descending order of $tr(T_i)$.

III. NUMERICAL EXAMPLE

Management of the coal mining company is faced with a problem of coal supplier selection for thermal power plant. The thermal power plant was built 35 years ago, with total power capacity of about 400 MW and an annual coal delivery of nearly 3.5 million tons of coal. As currently coal reserves near thermal power plant are almost exhausted, there is a need to find a new coal supplier for existing thermal power plant. In order to provide the stable and sustainable electricity production as well as to improve the sustainable development of the company, optimal coal supplier must be selected for the thermal power plant. Note that the example is hypothetical. Detailed description of the input parameters of alternatives and criteria is represented in Table I. Coal supplier 1, coal supplier 2…, coal supplier 7 are represented as a set of alternatives $A_1, A_2, \ldots, A_7$. Calorific value, ash content, sulphur content, moisture content and price are represented as a set of criteria $C_1, C_2, \ldots, C_5$.

Calorific value is one of the most important criteria of each coal type that indicates the fuel quality. It is mainly used to select the coal type based on quality. Calorific value can be defined as the amount of heat released during the complete combustion of 1 kg of coal. It can be defined in kJ/kg or MJ/kg units. This criterion, as the rest of criteria, is quantitative. It is the only positive attribute of coal and should be maximized.

Ash content also has important role in coal type selection based on quality. If the percentage of ash in coal sample is high, it means that it will cause the larger amounts of slag and dust during combustion. Since this is a negative characteristic of coal, this criterion should be minimized. It can be shown in % units.

Sulphur content, as well as ash content, represents the parameter that has a significant impact on coal quality. High percentage of sulphur in coal sample implies high emissions of air pollutants and concentrations of harmful substances in the air, primarily sulphur oxides. Due to the unfavorable impact on environment, this criterion should be minimized. It can be shown in % units.

Moisture content represents important criterion that affects the coal quality. When the percentage of moisture content in coal sample increases, then calorific value decreases and vice versa. The presence of moisture in coal sample requires his drying which increases the total costs and additional negative consequences. It can be shown in % units. Due to all negative characteristics, this criterion should be minimized.

Price, such as calorific value, is one of the key attributes that influence the coal type selection as well as coal supplier selection for thermal power plant. Electricity price directly depends on coal price. Large variations and fluctuations of coal price on the market have an extremely negative impact on stable electricity production. Price is defined in EUR/t units. It is tendency for the lowest possible price, so this criterion should be minimized.

The procedure for criteria weights determination by Shannon's entropy method is well – known and often used while detailed calculation process of MEREC method is shown in the following Equations and Tables.

Based on Step 2.2 using (13) – (14), normalization of the input data is performed and obtained values are shown in Table II.

TABLE I. DETAILED DESCRIPTION OF THE INPUT PARAMETERS OF ALTERNATIVES AND CRITERIA.

A/C	C_1 (MJ/kg)	C_2 (%)	C_3 (%)	C_4 (%)	C_5 (EUR/t)
	max	*min*	*min*	*min*	*min*
A_1	7.90	17.75	0.96	46.13	70.00
A_2	8.40	18.83	1.03	43.41	80.00
A_3	7.40	19.40	0.45	46.20	50.00
A_4	14.20	17.12	1.25	28.00	130.00
A_5	13.80	13.21	1.00	30.21	120.00
A_6	6.00	19.28	0.88	44.33	105.00
A_7	7.80	17.40	1.02	45.00	110.00

TABLE II. NORMALIZED DECISION – MAKING MATRIX.

A/C	C_1	C_2	C_3	C_4	C_5
	max	*min*	*min*	*min*	*min*
A_1	0.7595	0.9149	0.7680	0.9985	0.5385
A_2	0.7143	0.9706	0.8240	0.9396	0.6154
A_3	0.8108	1.0000	0.3600	1.0000	0.3846
A_4	0.4225	0.8825	1.0000	0.6061	1.0000
A_5	0.4348	0.6809	0.8000	0.6539	0.9231
A_6	1.0000	0.9938	0.7040	0.9595	0.8077
A_7	0.7692	0.8969	0.8160	0.9740	0.8462

The overall performance of the alternative S_i is calculated by 15. Detailed calculation process for the alternative S_1 is shown in (33). The same procedure is valid for other alternatives from S_2 to S_7.

$$S_1 = \ln\left(1+\left(\frac{1}{5}\left(\begin{array}{l}\left|\ln(0.7595)\right|+\\ +\left|\ln(0.9149)\right|+\\ +\left|\ln(0.7680)\right|+\\ +\left|\ln(0.9985)\right|+\\ +\left|\ln(0.5385)\right|\end{array}\right)\right)\right) = \quad .(33)$$
$$= 0.2229$$

The performance of the alternatives by removing each criterion $S_{ij}{}'$ is calculated by (16). Two detailed numerical examples (for $S_{12}{}'$ and $S_{64}{}'$) are represented in (34) and (35) to describe this step of calculation process. $S_{12}{}'$ is the overall performance of the A_1 related to the removal of C_2 , while $S_{64}{}'$ is the overall performance of the A_6 related to the removal of C_4. The same calculation process is valid for other alternatives and obtained values are shown in Table III.

$$S_{12}{}' = \ln\left(1+\left(\frac{1}{5}\left(\begin{array}{l}\left|\ln(0.2751)\right|+\\ +\left|\ln(0.2640)\right|\\ +\left|\ln(0.0015)\right|\\ +\left|\ln(0.6190)\right|\end{array}\right)\right)\right) = , \quad (34)$$
$$= 0.2086$$

$$S_{64}{}' = \ln\left(1+\left(\frac{1}{5}\left(\begin{array}{l}\left|\ln(0.0000)\right|+\\ +\left|\ln(0.0062)\right|+\\ +\left|\ln(0.3510)\right|+\\ +\left|\ln(0.2136)\right|\end{array}\right)\right)\right) = . \quad (35)$$
$$= 0.1081$$

TABLE III. VALUES OF PERFORMANCE OF THE ALTERNATIVES BY REMOVING EACH CRITERION $S_{ij}{}'$.

A/C	C_1	C_2	C_3	C_4	C_5
A_1	0.1779	0.2086	0.1797	0.2227	0.1186
A_2	0.1434	0.1952	0.1679	0.1899	0.1173
A_3	0.3332	0.3628	0.2095	0.3628	0.2202
A_4	0.1179	0.2409	0.2604	0.1801	0.2604
A_5	0.2009	0.2717	0.2960	0.2655	0.3170
A_6	0.1155	0.1144	0.0509	0.1081	0.0767
A_7	0.0963	0.1238	0.1070	0.1383	0.1135

The summation of absolute deviations E_j is computed by (17). Detailed calculation process for E_1 is represented in (36). The same calculation process is valid for each corresponding criteria from E_2 to E_5.

$$\begin{aligned} E_1 &= \left|0.1779-0.2229\right|+\\ &+\left|0.1434-0.2001\right|+\left|0.3332-0.3628\right|+\\ &+\left|0.1179-0.2604\right|+\left|0.2009-0.3286\right|+ .\\ &+\left|0.1155-0.1155\right|+\left|0.0963-0.1429\right| = \end{aligned} \quad (36)$$
$$= 0.4481$$

Finally, criteria weights are determined by (18), and obtained values are shown in Table IV.

Graphical review of obtained criteria weights is represented in Fig. 1. Spearman's rank correlation coefficient between criteria weights obtained by Shannon's entropy and MEREC is $r = 0.9862$. The high level of correlation shows that both methods can be successfully used for criteria weights determination.

TABLE IV. CRITERIA WEIGHTS OBTAINED BY SHANNON'S ENTROPY AND MEREC METHOD.

	C_1	C_2	C_3	C_4	C_5
Shannon entropy	0.3314	0.0448	0.2214	0.1161	0.2863
MEREC	0.2985	0.0771	0.2410	0.1105	0.2729

Using (5) we obtained weighted normalized decision – making matrix for both methods for criteria weights determination. The values are shown in Table V and Table VI.

By applying (19), optimal alternative is determined for both methods for criteria weights determination. Results are shown in Table VII and Table VIII.

TABLE V. WEIGHTED NORMALIZED DECISION MATRIX USING SHANNON'S ENTROPY METHOD.

A/C	C_1	C_2	C_3	C_4	C_5
	max	*min*	*min*	*min*	*min*
A_1	0.1844	0.0333	0.1038	0.0705	0.2045
A_2	0.1960	0.0314	0.0967	0.0749	0.1789
A_3	0.1727	0.0305	0.2214	0.0704	0.2863
A_4	0.3314	0.0346	0.0797	0.1161	0.1101
A_5	0.3221	0.0448	0.0996	0.1076	0.1193
A_6	0.1400	0.0307	0.1132	0.0733	0.1363
A_7	0.1820	0.0340	0.0977	0.0722	0.1301

TABLE VI. WEIGHTED NORMALIZED DECISION MATRIX USING MEREC METHOD.

A/C	C_1	C_2	C_3	C_4	C_5
	max	*min*	*min*	*min*	*min*
A_1	0.1661	0.0574	0.1130	0.0671	0.1949
A_2	0.1766	0.0541	0.1053	0.0713	0.1705
A_3	0.1556	0.0525	0.2410	0.0670	0.2729
A_4	0.2985	0.0595	0.0868	0.1105	0.1049
A_5	0.2901	0.0771	0.1085	0.1024	0.1137
A_6	0.1261	0.0528	0.1233	0.0698	0.1299
A_7	0.1640	0.0585	0.1063	0.0688	0.1240

TABLE VII. OPTIMAL ALTERNATIVE USING SHANNON'S ENTROPY METHOD.

Opt. A/C	C_1	C_2	C_3	C_4	C_5
	max	*min*	*min*	*min*	*min*
Q	0.3314	0.0448	0.2214	0.1161	0.2863

TABLE VIII. OPTIMAL ALTERNATIVE USING MEREC METHOD.

Opt. A/C	C_1	C_2	C_3	C_4	C_5
	max	*min*	*min*	*min*	*min*
Q	0.2985	0.0771	0.2410	0.1105	0.2729

TABLE IX. DECOMPOSITION OF THE OPTIMAL ALTERNATIVE USING SHANNON'S ENTROPY METHOD.

Opt. A/C	C_1	C_2	C_3	C_4	C_5
	max	*min*	*min*	*min*	*min*
Q^{max}	0.3314	-	-	-	-
Q^{min}	-	0.0448	0.2214	0.1161	0.2863

TABLE X. DECOMPOSITION OF THE OPTIMAL ALTERNATIVE USING MEREC METHOD.

Opt. A/C	C_1	C_2	C_3	C_4	C_5
	max	*min*	*min*	*min*	*min*
Q^{max}	0.2985	-	-	-	-
Q^{min}	-	0.0771	0.2410	0.1105	0.2729

Using (21), decomposition of the optimal alternative is obtained for both methods for criteria weights determination. The values are shown in Table IX and Table X.

By applying (23), decomposition of alternatives is represented for both methods for

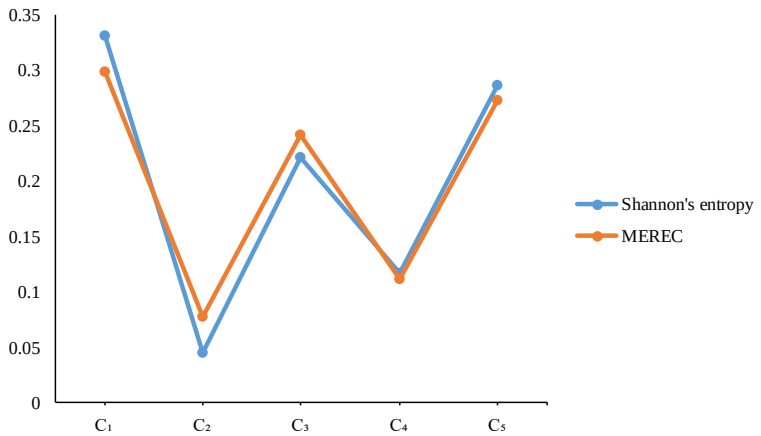

Figure 1. Graphical review of criteria weights obtained by Shannon's entropy and MEREC method.

criteria weights determination. Results are shown in Table XI and Table XII.

Based on (25) – (28), magnitude of optimal alternative and alternatives is calculated for both methods for criteria weights determination. The values are shown in Table XIII.

Using (29) - (32), Multiple-Criteria Ranking by Alternative Trace (MCRAT) method is applied and trace of the matrix $tr(T_1), tr(T_2), \ldots, tr(T_7)$ such as final rank by descending order is represented in Table XIV

TABLE XI. DECOMPOSITION OF ALTERNATIVES USING SHANNON'S ENTROPY METHOD.

A/C		C_1	C_2	C_3	C_4	C_5
		max	*min*	*min*	*min*	*min*
A_1	U^{max}	0.1844	-	-	-	-
	U^{min}	-	0.0333	0.1038	0.0705	0.2045
A_2	U^{max}	0.1960	-	-	-	-
	U^{min}	-	0.0314	0.0967	0.0749	0.1789
A_3	U^{max}	0.1727	-	-	-	-
	U^{min}	-	0.0305	0.2214	0.0704	0.2863
A_4	U^{max}	0.3314	-	-	-	-
	U^{min}	-	0.0346	0.0797	0.1161	0.1101
A_5	U^{max}	0.3221	-	-	-	-
	U^{min}	-	0.0448	0.0996	0.1076	0.1193
A_6	U^{max}	0.1400	-	-	-	-
	U^{min}	-	0.0307	0.1132	0.0733	0.1363
A_7	U^{max}	0.1820	-	-	-	-
	U^{min}	-	0.0340	0.0977	0.0722	0.1301

TABLE XII. DECOMPOSITION OF ALTERNATIVES USING MEREC METHOD.

A/C		C_1	C_2	C_3	C_4	C_5
		max	*min*	*min*	*min*	*min*
A_1	U^{max}	0.1661	-	-	-	-
	U^{min}	-	0.0574	0.1130	0.0671	0.1949
A_2	U^{max}	0.1766	-	-	-	-
	U^{min}	-	0.0541	0.1053	0.0713	0.1705
A_3	U^{max}	0.1556	-	-	-	-
	U^{min}	-	0.0525	0.2410	0.0670	0.2729
A_4	U^{max}	0.2985	-	-	-	-
	U^{min}	-	0.0595	0.0868	0.1105	0.1049
A_5	U^{max}	0.2901	-	-	-	-
	U^{min}	-	0.0771	0.1085	0.1024	0.1137
A_6	U^{max}	0.1261	-	-	-	-
	U^{min}	-	0.0528	0.1233	0.0698	0.1299
A_7	U^{max}	0.1640	-	-	-	-
	U^{min}	-	0.0585	0.1063	0.0688	0.1240

and Table XV for both methods for criteria weights determination.

TABLE XIII. MAGNITUDE OF OPTIMAL ALTERNATIVE AND ALTERNATIVES USING SHANNON'S ENTROPY AND MEREC METHOD.

A	MCRAT with Shannon's entropy		MCRAT with MEREC	
	max	*min*	*max*	*min*
	Q_k U_{ik}	Q_h U_{ik}	Q_k U_{ik}	Q_h U_{ik}
Q	0.3314	0.3827	0.2985	0.3882
cc	0.1844	0.2422	0.1661	0.2420
A_2	0.1960	0.2190	0.1766	0.2195
A_3	0.1727	0.3700	0.1556	0.3739
A_4	0.3314	0.1821	0.2985	0.1852
A_5	0.3221	0.1943	0.2901	0.2028
A_6	0.1400	0.1942	0.1261	0.1993
A_7	0.1820	0.1812	0.1640	0.1867

TABLE XIV. TRACE OF THE MATRIX AND FINAL RANK OF ALTERNATIVES USING SHANNON'S ENTROPY METHOD FOR CRITERIA WEIGHTS DETERMINATION.

A	MCRAT with Shannon's entropy		
	Trace tr(T_i)	*Value*	*Rank*
A_1	$tr(T_1)$	0.4266	4
A_2	$tr(T_2)$	0.4151	5
A_3	$tr(T_3)$	0.5427	1
A_4	$tr(T_4)$	0.5135	3
A_5	$tr(T_5)$	0.5163	2
A_6	$tr(T_6)$	0.3343	7
A_7	$tr(T_7)$	0.3633	6

TABLE XV. TRACE OF THE MATRIX AND FINAL RANK OF ALTERNATIVES USING MEREC METHOD FOR CRITERIA WEIGHTS DETERMINATION.

A	MCRAT with MEREC		
	Trace tr(T_i)	*Value*	*Rank*
A_1	$tr(T_1)$	0.4080	4
A_2	$tr(T_2)$	0.3961	5
A_3	$tr(T_3)$	0.5294	1
A_4	$tr(T_4)$	0.4837	3
A_5	$tr(T_5)$	0.4929	2
A_6	$tr(T_6)$	0.3255	7
A_7	$tr(T_7)$	0.3506	6

IV. CONCLUSION

Having ability to select the best coal supplier for thermal power plant is recognized as a major activity to provide stable and sustainable electricity production as well as to improve the sustainable development of each mining company. This paper proposed a newly multi – criteria decision – making model based on MCRAT method with two approaches for objective criteria weights determination (Shannon's entropy and MEREC method) for optimal coal supplier selection for thermal power plant. The high level of correlation between these two methods for criteria weights determination leads to equal rank of alternatives by using MCRAT method. Having in mind the values of rank of alternatives in both approaches, our developed model is absolutely acceptable and capable to solve such complex problem.

The model is not closed and can be upgraded by increasing the uncertainty of input data using fuzzy or interval numbers. Also, there is possibility to create dynamic model by integrating the stochastic differential equations to describe the behavior of some criterion.

REFERENCES

[1] Zhongfu, T., Liwei, J., Xiaobao, Y., Huijuan, Z., & Chao, Y. (2014). Selection Ideal Coal Suppliers of Thermal Power Plants Using the Matter-Element Extension Model with Integrated Empowerment Method for Sustainability. *Mathematical Problems in Engineering, 2014*.

[2] Dong, F. (2015). Coal suppliers Evaluation Model Based on AHP and PROMETHEE. *International Conference on Education Reform and Modern Management* (pp. 359-362).

[3] Firoz, F., Biswal, J. N., & Satapathy, S. (2018). Supplier selection criteria for sustainable supply chain management in thermal power plant. *In IOP Conference Series: Materials Science and Engineering* (Vol. 310, p. 012016). Bristol: IOP Publishing.

[4] Rao, C., Wang, C., Hu, Z., Meng, Y., & Liu, M. (2019). Sustainable procurement decision of electric coal under fuzzy information environment. *Sci. Iran., 26,* 1039–1048.

[5] Urošević, K., Gligorić, Z., Miljanović, I., Beljić, Č., & Gligorić, M. (2021). Novel Methods in Multiple Criteria Decision-Making Process (MCRAT and RAPS)—Application in the Mining Industry. *Mathematics*, 9 (16).

[6] Shannon, C.E. (1948). A mathematical theory of communication. *Bell Syst. Tech. J*., 27, 379–423.

[7] Zeleny, M. (1982). *Multiple Criteria Decision Making*. McGraw Hill, New York.

[8] Keshavarz-Ghorabaee, M., et al. (2021). Determination of Objective Weights Using a New Method Based on the Removal Effects of Criteria (MEREC). *Symmetry, 13*, 525.

Influence of Metal Foam Insertion in Heat and Mass Transfers inside Steam Reforming Reactor of Dimethyl Ether

Abaidi Abou Houraira[1]

[1]LTPMP/USTHB, Algiers, Algeria, abaidiadel@yahoo.com

Abstract—**This study presents a numerical simulation by using COMSOL Multiphysics of Dimethyl Ether steam reforming (DME-SR). This micro-reactor with fixed bed CuO/ZnO/Al2O3 + ZSM-5 is designed to produce hydrogen. The aim of this work is to see the insertion of metal foam inside this reformer. The results indicate that; the insertion of metal foam inside the reactor, it has an excess effect on heat and mass transfer phenomena, consequently that is mean more hydrogen production for fuel cell battery.**

Keywords - dimethyl ether steam reforming, hydrogen production, heat and mass transfers, metal foam insertion.

I. INTRODUCTION

A fuel cell is an electrochemical device that produces direct current electricity as long as fuel and oxidant are supplied to the anode and cathode respectively. A fuel cell is more simply described as an un-rechargeable battery. Practical fuel cells today operate with hydrogen fuel, generating only power and drinking water.

Hydrogen production through dimethyl ether steam reforming is an attractive choice for mobile applications of hydrogen fuel cells. Hydrogen is a major trend in the future of clan energy development. It is not only pollution-free, but also has a high energy density. Therefore, research on hydrogen fuel cells is particularly important. Therefore, the study [1] presents a computational fluid dynamic (CFD) study of Dimethyl Ether steam reforming (DME-SR) in a large scale Circulating Fluidized Bed (CFB) reactor. The DME-SR reactions occurs in the presence of a bifunctional catalyst of CuO/ZnO/Al2O3 + ZSM-5. The results show that The DME conversion and hydrogen yield were found to be 87% and 59% respectively, resulting in a product gas consisting of 72 % mol hydrogen. The second paper [2], which the effect of the reactor inlet configuration, gas residence time, inlet temperature and steam to DME ratio on the overall reactor performance and products have all been investigated. According to the parametric analysis, the inlet temperature 300 °C, steam to DME molar ratio 5.5, 4 s gas residence time and 37,104 (ml /gcat h) space velocity. The results give; the DME conversion and hydrogen molar concentration in the product gas were both found to be around 80%. In [3], a 180-h stability evaluation was carried out and the results show that the optimized Cu/Ni/c-Al2O3/Al catalyst has an excellent stability under critical conditions with 400 °C, and gives a 100% DME conversion. Moreover, temperature initially decreased because of the endothermic reformation reactions and then increased along the reaction bed when the reaction rate was reduced as a function of lower temperature and DME content [4]. The volume content of H2 and CO2 increased rapidly while DME and steam decreased dramatically along the reaction bed. DME conversion and hydrogen production were increased with increasing exhaust gas velocity. A reduction in the value of the DME to steam mass ratio increased the conversion of DME conversion and hydrogen production. Furthermore, the simulation results of [5] showed the temperature distribution, mass distribution, DME conversion and hydrogen production in DME steam reforming process. These simulation results will provide useful data for the design and operation of small-scale catalytic reforming bed reactors. Another a three-dimensional reactor [6] model developed by the commercial software COMSOL (version 5.2a) was used to simulate the reaction characteristics by modifying reforming conditions. The simulation results indicate the temperature distribution, mass distribution, and reveal the

dependency of dimethyl ether reforming reaction rate on temperature, pressure, the length of the reactor. The yield of H2 and conversion of dimethyl ether with different mass ratios and inlet temperature (200°C, 300°C 400°C, 500°C) were examined. Besides, thermodynamic equilibrium calculations [7] of DME steam reforming indicate complete conversion of dimethyl ether to hydrogen, carbon monoxide and carbon dioxide at temperatures greater than 200 °C and steam-to-carbon ratios greater than 1.25 at atmospheric pressure (P = 1 atm). Increasing the operating pressure shifts the equilibrium toward the reactants; increasing the pressure from 1 to 5 atm decreases the conversion of dimethyl ether from 99.5 to 76.2%. The optimal processing conditions for dimethyl ether steam reforming occur at a steam-to-carbon ratio of 1.50, a pressure of 1 atm, and a temperature of 200 °C. These thermodynamic equilibrium calculations show dimethyl ether processed with steam will produce hydrogen-rich fuel-cell feeds—with hydrogen concentrations exceeding 70%.

The aim of this work is to see the influence of metal foam insertion on heat and mass transfers, inside the reformer of DME-SR, which is designed to produce hydrogen for fuel cells.

II. DME Steam Reforming

Usually, the catalytic reaction of DME-SR involves two major reactions [1, 2, 8, 9]. This includes a hydrolysis reaction converting the DME to methanol and a steam reforming reaction converting the methanol to hydrogen and carbon dioxide. The proposed reactions now have all been extracted from various literature sources. The studies [10, 11] have shown that within the temperature range of 200-300 °C the DME undergoes catalytic steam reforming (hydrolysis) in the presence of the acid-based catalyst ZSM-5 to produce methanol according to the following reaction:

$$CH_3OCH_3 + H_2O \rightarrow 2\ CH_3OH \ . \quad (1)$$

$$\Delta H_r^0 = +24.5 kJ / mol$$

The methanol then undergoes steam reforming to generate carbon dioxide and hydrogen enhanced by the presence of the metal-based catalysts $CuO/ZnO/Al_2O_3$ according to the following reaction:

$$CH3OH + H_2O \rightarrow 3H_2 + CO_2 \ . \quad (2)$$

$$\Delta H_r^0 = +49.1 kJ / mol$$

Some studies suggested that without the $CuO/ZnO/Al_2O_3$ catalyst the DME reforming process produces methanol only, whereas with the catalyst, hydrogen and carbon dioxide are the major products along with some portion of unreacted methanol and carbon monoxide [11, 12]. The generally reported side reactions are associated with the methanol decomposition and the WGSR [16] and these reactions are as follows:

$$CH_3OH \rightarrow 2\ H_2 + CO \ . \quad (3)$$

$$\Delta H_r^0 = +90 kJ / mol$$

$$CO + H_2O \rightarrow H_2 + CO_2 \ . \quad (4)$$

$$\Delta H_r^0 = -41.17 kJ / mol$$

Reference [12] suggested that the WGSR is the only side reaction that may occur in the overall process. It is also understood that the carbon monoxide production is favoured at higher temperature as the WGSR shifts to the left, which means reduction of hydrogen produced.

Kenitics law of DME-SR

The kinetics laws of DME steam reforming reaction are summarized below:

Firstly, DME hydrolysis reaction is [10, 11]:

$$r_{DME} = r_{DMO^+} = k'_{F,DMO^+} C_{R_1^+ P_{MeOH}} - \\ -k'_{C,DMO^+} C_{DMO^-} \ . \quad (5)$$

Secondly, methanol steam reforming reaction is [13, 14]:

$$r_R = (1-\varepsilon)\rho_s k_R C_{MeOH} \ , \quad (6)$$

where:

$$k_R = C_R \left[A_1 + B_1 \ln\phi\right] exp\left(\frac{-E_R}{RT}\right) \ . \quad (7)$$

CR= 5.5 is the reforming rate constant, ϕ is the steam to methanol ratio, A1 and B1 are

constant (A1= 1.15 x 106 [m3 s-1 kg-1], B1 = 9.41 x 105 [m3 s-1 kg-1]) and ER= -84100 J mol-1 is the activation energy.

Thirdly, MeOH decomposition reaction is [13-15]:

$$r_D = (1-\varepsilon)\rho_s k_D , \quad (8)$$

where:

$$k_D = C_D A_2 exp\left(-E_D / RT\right) . \quad (9)$$

CD= 5.5 is the decomposition rate constant A2= 7.09 x 107 mol s-1 kg-1 is the constants and ED= -111200 J mol-1 is the activation energy

Finally, water gas shift reaction is [15,16]:

$$r_{WGS} = C_{WGS} K_{WGS} \cdot \cdot\left(P_{CO}P_{H2O} - P_{CO}P_{H2} / K_{eq}\right) , \quad (10)$$

where:

$$K_{eq} = exp\left(4577.8/T - 4.33\right) , \quad (11)$$

$$K_{WGS} = 1.74\times10^{17} \cdot \cdot\left(1 - 0.1540\delta + 0.008\delta^2\right)\cdot . \cdot T^{-8.5} exp\left(-35000/RT\right) \quad (10)$$

CWGS = 11.2 is a constant, and δ steam to CO molar ratio.

The most important performance indexes of dimethyl ether reforming reaction mainly include dimethyl ether conversion rate, production rate of hydrogen. The DME conversion is defined as follows:

DME conversion is presents the percentage of DME consumption

$$X_{DME} = \frac{F_{DME_{in}} - F_{DME_{out}}}{F_{DME_{in}}} \cdot 100\% . \quad (13)$$

The hydrogen yield is a parameter used for the activity, was defined as the ratio of the molar amount of DME converted to hydrogen to the total molar amount of DME fed to the reactor. This was calculated by the following formula:

$$Y_{H2} = \frac{F_{H2}}{F_{DME_{in}}} \cdot \frac{1}{6} \cdot 100\% , \quad (14)$$

where F_{H2} was the molar flow rate of H_2, and the number 1/6, which means if 1 mol DME is consumed, 6 mols of hydrogen would be produced theoretically.

Similarly, the methanol conversion (C_{MeOH}) was given by:

$$X_{DME} = \frac{F_{MeOH_{Prod}} - F_{MeOH_{out}}}{F_{MeOH_{prod}}} \cdot 100\% , \quad (15)$$

where $n_{MeOH,prod}$ and $n_{MeOH,out}$ are the molar flow of methanol produced from the DME pyrolysis reaction and the unreacted methanol leaving with the product gas respectively.

The selectivity of carbon dioxide was defined in terms of the molar flow ratio of carbon dioxide produced to the total moles of the carbon present in the product as follows:

$$S_{CO_2} = \frac{n_{CO_2}}{n_{CO_2} + n_{CO}} , \quad (16)$$

where n_{CO} and n_{CO2} are the molar flow rate of carbon monoxide and carbon dioxide at the reactor outlet respectively.

The simulation assumptions:

- Reaction flows are laminar and steady;
- All fluids are incompressible;
- six species—DME, H_2O, CO_2, CO, MeOH and H_2 are taken into account as ideal gas [10]
- The pressure drop is supposed equal zero and is equal 1 atm.

A. Physics Model:

The physics model is defined as a rectangle with 50 mm of length and 06 mm of high Fig. 1, and the catalyst layer is situated in the middle of the lower wall, which has a 38 mm length. The boundary conditions are; at the inlet, the velocity and the temperatures are 0.1 m/s and 400 K,

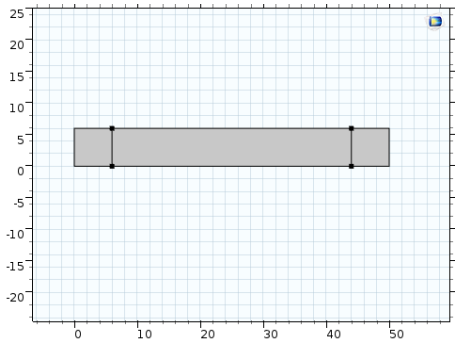

Figure 1. Physic Model of reformer.

respectively, also the pressure is assumed to be constant and equal to the atmospheric pressure, in addition, the temperature of the wall is assumed 500 K.

B. Mesh Sensitivity:

Table I presents the influence of meshes configuration in DME consumption. After this table it is seen for the three first configurations (1, 2 and 3); the DME consumptions are not constant (86, 85, and 84.5%), then the three-second configurations (4, 5 and 6); it has clearly seen the stabilization of DME consumption 84 %, whatever the configuration. As result, the fourth configuration (coarser) is adopted the optimal mesh for those simulations.

TABLE I. MESH CONFIGURATIONS INFLUENCE IN DME CONSUMPTION %.

Mesh configurations	**1**	**2**	**3**	**4**	**5**	**6**
DME consumption %	86	85	84.5	84	84	84

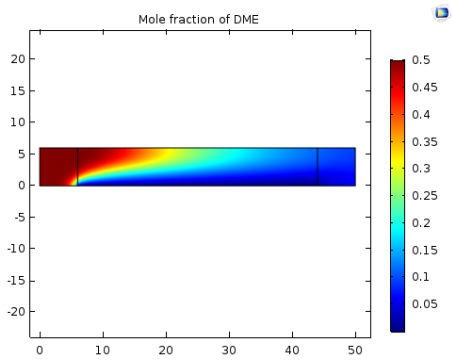

Figure 2. Mole fraction of DME.

C. Smouth Channel:

The flowing Fig. 2 and Fig. 3 present a reactor of DME steam reforming with simply a catalyst layer situated in the bottom. As noted, there are logical consumption of DME and Water and the production of H_2, CO_2, and CO. The next Fig. 4 presents the evolution of all species along the rector side; this last picture can explain the reaction process. Concerning the reactor efficiency is dependent on the DME consumption, which near 80%, in the other side the hydrogen yield is 20%, also it noted an important quantity of MeOH inside the reactor assumed by the value 25%. Fig. 5 presents the heat field inside the reactor.

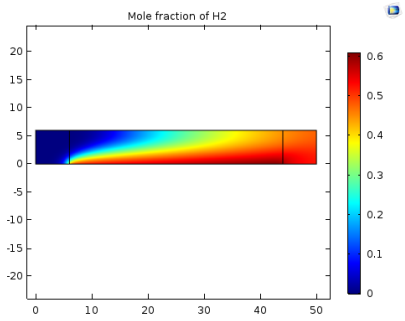

Figure 3. Mole fraction of H_2.

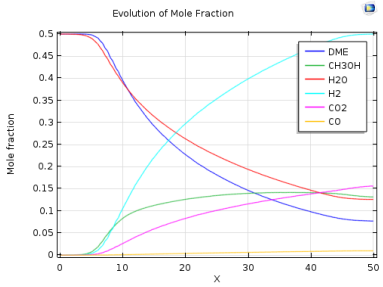

Figure 4. Evolution of species mole fractions.

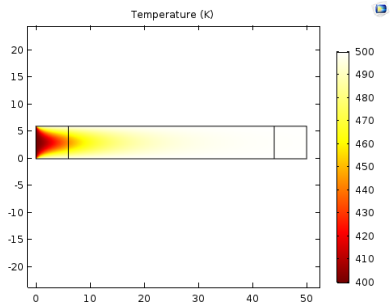

Figure 5. Heat filed.

TABLE II. PHYSICAL CHARACTERISTICS OF USED METAL FOAM.

ε	PPI	d_f [m]	d_p [m]	C_f[J.kg^{-1}.K^{-1}]	K_p [m^2]	ρ_s[kg/m^3]	λ_s [W.m^{-1}.K^{-1}]	Cp_s [J.kg^{-1}.K^{-1}]
0.8991	10	0.00043	0.0032	0.0068	0.94 10^{-7}	850	400	385

D. Insertion of Metal Foam inside the Reformer

Figs. 6 and 7 display the reactor of DME steam reforming occupied with a metal foam, this metal foam resumed in Table II. After thus pictures is can see the enormous mass transfer near the catalyst because the reaction has occurred, consequently, there are consumption of DME and Water and production of H_2, CO_2 and a small quantity of CO. Fig. 8 shows the evolution of all species in the same picture, also Fig. 9 presents the heat field inside the reactor full of metal foam. Well, the efficiency of the reactor is equal to 86%. The comparison between two cases; smooth reactor and with insertion of metal foam can give an advantage in heat and mass transfers in Fig. 10.

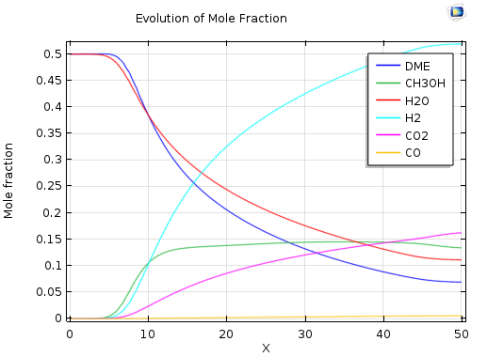

Figure 8. Evolution of species mole fractions.

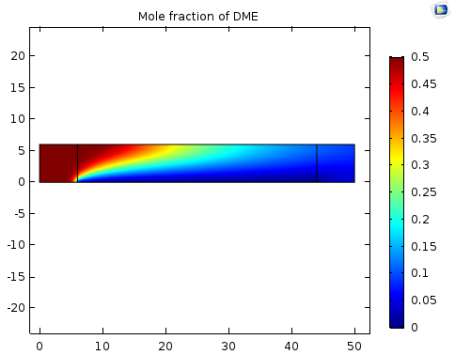

Figure 6. Mole fraction of DME.

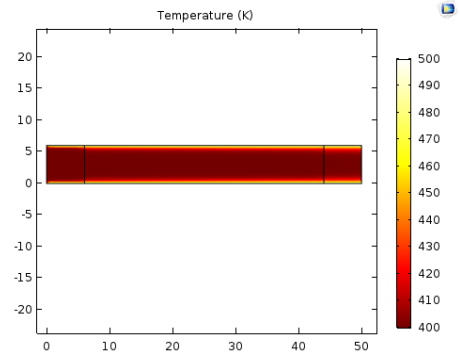

Figure 9. Heat field.

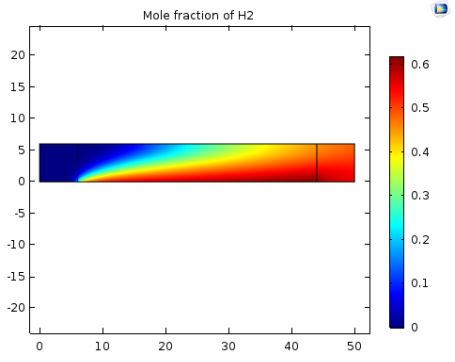

Figure 7. Mole fraction of H_2.

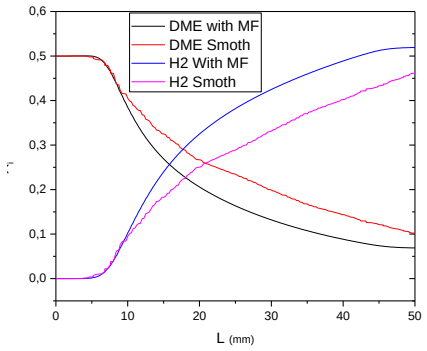

Figure 10. Comparison between two cases.

III. CONCLUSION

In the current work, we have presented a numerical study for hydrogen production from dimethyl ether steam reforming. The aim of this work is to see the influence of the insertion of metal foam inside the reactor. The results indicate that; the insertion of metal foam inside the reactor, it has an excess impact in heat and mass transfer's phenomena.

REFERENCES

[1] [Elewuwa, F. A., & Makkawi, Y. T. (2015). Hydrogen production by steam reforming of DME in a large scale CFB reactor. Part I: Computational model and predictions. *International journal of hydrogen energy*, *40*(46), 15865-15876. doi:10.1016/j.ijhydene.2015.10.050.

[2] Elewuwa, F. A., & Makkawi, Y. T. (2016). A computational model of hydrogen production by steam reforming of dimethyl ether in a large scale CFB reactor. Part II: Parametric analysis. *International Journal of Hydrogen Energy*, *41*(44), 19819-19828. doi: 10.1016/j.ijhydene.2016.08.072.

[3] Fan, F., Zhang, Q., Wang, X., Ni, Y., Wu, Y., & Zhu, Z. (2016). A structured Cu-based/γ-Al2O3/Al plate-type catalyst for steam reforming of dimethyl ether: self-activation behavior investigation and stability improvement. *Fuel*, *186*, 11-19. doi: 10.1016%2Fj.fuel.2016.08.036.

[4] Li, C., Gao, Y., & Wu, C. (2015). Modeling and simulation of hydrogen production from dimethyl ether steam reforming using exhaust gas. *International Journal of Energy Research*, *39*(9), 1272-1279. doi:10.1002/er.3330.

[5] Guo, L. (2018). Modeling and Numerical Simulation of Hydrogen Production from Dimethyl Ether Steam Reforming. *Open Access Library Journal*, 5(05), 1. doi: 10.4236/oalib.1104531.

[6] Guo, L., & Li, C. (2018). Parameter Analysis and Numerical Simulation of Hydrogen Production by Steam Reforming of Dimethyl Ether. *Journal of Power and Energy Engineering*, *6*(11), 1-11. doi:10.4236/jpee.2018.611001.

[7] Semelsberger, T. A., & Borup, R. L. (2005). Thermodynamic equilibrium calculations of dimethyl ether steam reforming and dimethyl ether hydrolysis. *Journal of Power Sources*, *152*, 87-96. doi:10.1016/j.jpowsour.2005.01.056/

[8] Zhang, T., Ou, K., Jung, S., Choi, B., & Kim, Y. B. (2018). Dynamic analysis of a PEM fuel cell hybrid system with an on-board dimethyl ether (DME) steam reformer (SR). *International Journal of Hydrogen Energy*, *43*(29), 13521-13531. doi:10.1016/j.ijhydene.2018.05.098

[9] Zhang, T. Q., Choi, B., & Kim, Y. B. (2020). Numerical and experimental study on hydrogen production via dimethyl ether steam reforming. *International Journal of Hydrogen Energy*, *45*(20), 11438-11448.doi :10.1016/j.ijhydene.2020.02.091

[10] Yan, C. F., Ye, W., Guo, C. Q., Huang, S. L., Li, W. B., & Luo, W. M. (2014). Numerical simulation and experimental study of hydrogen production from dimethyl ether steam reforming in a micro-reactor. *International Journal of Hydrogen Energy*, *39*(32), 18642-18649. doi:10.1016/ j.ijhydene.2014.02.133.

[11] Feng, D., Wang, Y., Wang, D., & Wang, J. (2009). Steam reforming of dimethyl ether over CuO–ZnO–Al2O3–ZrO2+ ZSM-5: A kinetic study. *Chemical Engineering Journal*, *146*(3), 477-485. doi:10.1016/j.cej.2008.11.005.

[12] Li, C., Wang, Y., & Fan, P. (2012). Numerical analysis and experimental study of hydrogen production from dimethyl ether steam reforming. *Science China Chemistry*, *55*(9), 1982-1987. doi:10.1007/s11426-012-4603-0

[13] Suh, J. S., Lee, M. T., Greif, R., & Grigoropoulos, C. P. (2007). A study of steam methanol reforming in a microreactor. *Journal of Power Sources*, *173*(1), 458-466. doi:10.1016/ j.jpowsour.2007.04.038

[14] Amphlett J, Creber KA, Davies J, Mann R, Peppley B, Stokes D. Hydrogen production by steam reforming of methanol for polymer electrolyte fuel cells. Int J Hydrogen Energy (1994);19:131-7. doi :10.1016/0360-3199(94)90117-1.

[15] Chein, R., Chen, Y. C., & Chung, J. N. (2013). Numerical study of methanol–steam reforming and methanol–air catalytic combustion in annulus reactors for hydrogen production. *Applied Energy*, *102*, 1022-1034. doi:10.1016/ j. apenergy.2012.06.010.

[16] Chen, W. H., Lin, M. R., Jiang, T. L., & Chen, M. H. (2008). Modeling and simulation of hydrogen generation from high-temperature and low-temperature water gas shift reactions. *International journal of hydrogen energy*, *33*(22), 6644-6656. doi:10.1016/ j. ijhydene.2008.08.039.

Real Power Loss Reduction by Opposition based Krill Herd Algorithm

Lenin Kanagasabai[1]

[1] Prasad V.Potluri Siddhartha Institute of Technology, Kanuru, Vijayawada, Andhra Pradesh -520007, India, gklenin@gmail.com

Abstract—**In this paper Opposition based Krill Herd (OKH) algorithm is utilized to solve the real power loss reduction problem. Krill Herd performance performances are imitated to formulate the algorithm. Important mission for the Krill movement is the least distance of each individual Krill from food to the supreme deliberation of the herd. Based on the swayed movement of other Krill's, foraging drive and substantial propagation the position of every krill in a time period is depended. Opposition based learning is one of the influential optimization tools to boost the convergence speed of different optimization techniques. The thriving implementation of the Opposition based learning engages evaluation of opposite population and existing population in the similar generation to discover the superior candidate solution of the given problem. In order to improve the convergence speed and precision - Krill Herd algorithm is integrated with the Opposition based learning. Proposed Opposition based Krill Herd (OKH) algorithm has been validated in IEEE 30 bus test systems. Real Power Loss is reduced significantly when compared to other regular procedures.**

Keywords - optimization, reactive power, transmission loss, optimization, Krill Herd, opposition

I. INTRODUCTION

Reduction of power loss plays the important role in secure and economic operation of the power system. Several conventional methods [1-6] already solved the problem. But many disadvantages have been found in the conventional methods and principally trouble in handling the inequality constraints. Because of this difficulty attaining the best solution is complicated in the conventional methods. Many evolutionary algorithms [7-17] are applied these years to solve the problem. In this work Opposition based Krill Herd (OKH) algorithm is utilized to solve the real power loss reduction problem. Herd activities of the Krill individuals are imitated to articulate the algorithm. Important task for the Krill movement is the least distance of each individual Krill from food to the supreme concentration of the herd. Grounded on the persuaded movement of other Krill's, foraging movement and substantial propagation the location of every krill in a time period is to be contingent. The symphony of the krill herd after predation depends on many parameters. The herding of the krill individuals has two key goals: swelling of krill concentration, and accomplishment of food. Depth of grouping the krill and finding food (are used as objectives which eventually direct the krill herd approximately the global minimum. In this process, an individual krill budge toward the most excellent solution when it explore for the uppermost concentration and food. Development persuaded by other krill individuals by Foraging action and arbitrary propagation. Opposition based learning is one of the influential optimization tools to boost the convergence speed of different optimization techniques. The thriving implementation of the Opposition based learning engages evaluation of opposite population and existing population in the similar generation to discover the superior candidate solution of the given problem. In order to improve the convergence speed and precision - Krill Herd algorithm is integrated with the Opposition based learning. Proposed Opposition based Krill Herd (OKH) algorithm has been validated in IEEE 30 bus test systems. Real Power Loss is reduced significantly when compared to other regular procedures. Section II presents the problem formulation, Section III presents the proposed

Opposition based Krill Herd (OKH) algorithm. Section IV narrates about the simulation stud and Section V presents the conclusion.

II. PROBLEM FORMULATION

Foremost goal is to minimize the system real power loss:

$$P_{loss}= \sum_{\substack{k=1 \\ k=(i,j)}}^{n} g_{k\left(V_i^2+V_j^2-2V_i\ V_{j\cos\theta_{ij}}\right)} \ . \qquad (1)$$

PL – power loss, *gk* – conductance of branch, *Vi* and *Vj* are voltages at buses i, j, *Nbr* – total number of transmission lines in power systems.

Voltage deviation magnitudes (VD) is:

$$Min(VD) = \sum_{k=1}^{nl} |V_k - 1.00| \ . \qquad (2)$$

Load flow equality constraints:

$$P_{Gi} - P_{Di} - V_{i_j \sum_{j=1}^{nb} V_j} \begin{bmatrix} G_{ij} & \cos\theta_{ij} \\ +B_{ij} & \sin\theta_{ij} \end{bmatrix} = \\ = 0,\ i = 1,2\ldots.,nb \qquad (3)$$

$$Q_{Gi} - Q_{Di} - V_{i_j \sum_{j=1}^{nb} V_j} \begin{bmatrix} G_{ij} & \cos\theta_{ij} \\ +B_{ij} & \sin\theta_{ij} \end{bmatrix} = \\ = 0,\ i = 1,2\ldots.,nb \qquad (4)$$

active power of slack bus is symbolized by PG and reactive power of generators symbolized by QG.

Inequality constraints are:

Upper and lower bounds on the bus voltage magnitudes (Vi) is given by:

$$V_{Gi}^{min} \le V_{Gi} \le V_{Gi}^{max}, i \in ng \ , \qquad (5)$$

$$V_{Li}^{min} \le V_{Li} \le V_{Li}^{max}, i \in nl \ . \qquad (6)$$

Upper and lower bounds on the compensators (Qc) is given by:

$$Q_{Ci}^{min} \le Q_{Ci} \le Q_{Ci}^{max}, i \in nc \ , \qquad (7)$$

$$Q_{Gi}^{min} \le Q_{Gi} \le Q_{Gi}^{max}, i \in ng \ . \qquad (8)$$

Upper and lower bounds on the transformers tap ratios (Ti) are given by:

$$T_i^{min} \le T_i \le T_i^{max}, i \in nt \ , \qquad (9)$$

$$S_{Li}^{min} \le S_{Li}^{max}, i \in nl \ . \qquad (10)$$

III. OPPOSITION BASED KRILL HERD ALGORITHM

Opposition based Krill Herd (OKH) algorithm is designed based on the krill herd activities. Krill has capability of creating huge swarms. Systematic deeds of krill have been imitated to form the procedure. The krill individuals try to preserve an elevated concentration and budge due to their shared effects [18]. Itinerary of motion persuade, α_i , and is computed from the local swarm concentration (narrowed outcome), a target swarm concentration (bout outcome), and a repulsive swarm concentration (repugnant outcome).

Krill's individual movement can be demarcated as:

$$P_i^{new} = P^{max}\alpha_i + \omega_n P_i^{old} \ , \qquad (11)$$

where

$$\alpha_i = \alpha_i^{confined} + \alpha_i^{attack} \ , \qquad (12)$$

p_i^{new} - new movement of krill,

$p_i^{\max}$ - maximum movement of krill,

ω_n - inertia weight,

$\alpha_i^{confined}$ - effect provided by neighbours,

α_i^{attack} - direction provided by best krill

Individual krill movement grounded on the consequence of the neighbours is demarcated by:

$$\alpha_i^{confined} = \sum_{j=1}^{PP} KH_{ij}\hat{Z}_{ij} \ , \qquad (13)$$

$$\hat{Z}_{i,j} = \frac{Z_j - Z_i}{\left\| Z_j - Z_i + \varepsilon \right\|} \ , \qquad (14)$$

$$\hat{K}H_{i,j} = \frac{KH_i - KH_j}{KH^{poor} - KH^{good}} \quad . \qquad (15)$$

$\hat{Z}_{i,j}$ - relative positions, $\hat{K}H_{i,j}$ - fitness of the krill herd.

$$DS_{s,i} = \frac{1}{EN}\sum_{j=1}^{N}\left\|Z_i - Z_j\right\| \quad . \qquad (16)$$

$DS_{s,i}$ - sensing distance of the krill.

Most excellent fitness of individual krill is taken into account by:

$$\alpha_i^{attack} = CF^{good} KH_{i,good}\hat{Z}_{i,good} \quad . \qquad (17)$$

CF^{good} - effect of the coefficient of the krill

CF^{good} is defined as:

$$CF^{good} = 2\left(random + \frac{I}{I_{maximum}}\right) . \qquad (18)$$

For the i[th] krill individual the Foraging motion can be articulated by:

$$Fg_i = vl_f\beta_i + \omega_f Fg_i^{old} \quad , \qquad (19)$$

where:

$$\beta_i = \beta_i^{food} + \beta_i^{good} \quad . \qquad (20)$$

vl_f foraging speed, ω_f - inertia weight, Fg_i - last foraging motion, β_i^{food} - food attractive

In iterations the centre of food is created by:

$$Z^{food} = \frac{\sum_{i=1}^{P}\frac{1}{K_i}Z_i}{\sum_{i=1}^{P}\frac{1}{KH_i}} \quad . \qquad (21)$$

For the i[th] krill individual food attraction is given as:

$$\beta_i^{food} = CF^{food} KH_{i,food}\hat{Z}_{i,food} \quad . \qquad (22)$$

The food coefficient is defined by:

$$CF^{food} = 2\left(1 - \frac{I}{I_{maximum}}\right) . \qquad (23)$$

Premium fitness of the i[th] krill individual is found by:

$$\beta_i^{best} = KH_{i,igood}\hat{Z}_{i,igood} \quad . \qquad (24)$$

The corporeal dissemination, greatest dissemination speed is articulated as follows:

$$DS_i = DS^{maximum}\delta \quad . \qquad (25)$$

On the foundation of a geometrical annealing sketch out, it can be formulated as:

$$DS_i = D^{maximum}\left(1 - \frac{I}{I_{maximum}}\right)\delta \quad . \qquad (26)$$

Position vector of a krill individual during the interval t to $t + \Delta t$ is given by:

$$Z_i(t + \Delta t) = Z_i(t) + \Delta t\frac{dZ_i}{dt} \quad . \qquad (27)$$

Δt Entirely depends on the search space and it obtained from the following:

$$\Delta t = CF_t\sum_{(j=1)}^{PV}(UB_j - LB_j) \quad . \qquad (28)$$

Genetic reproduction mechanisms are integrated into the Krill herd algorithm to improve the performance of the algorithm.

a. Crossover

$$Z_{i,m} = \begin{cases} Z_{r,m} & random_{i,m} < Cr \\ Z_{i,m} & else \end{cases} \quad . \qquad (29)$$

$$C_r = 0.210KH_{i,best} \quad . \qquad (30)$$

b. Mutation

$$Z_{i,m} = \begin{cases} Z_{gbes,m} + \mu\left(Z_{p,m} - Z_{q,m}\right) random_{i,m} < Mu \\ Z_{i,m} \qquad\qquad\qquad\qquad\qquad else \end{cases} \tag{31}$$

$$Mu = 0.0475 / KH_{i,best} . \tag{32}$$

Opposition based learning (OBL) is one of the influential optimization tools to boost the convergence speed of different optimization techniques [19]. The thriving implementation of the OBL engages evaluation of opposite population and existing population in the similar generation to discover the superior candidate solution of the given problem. The conception of opposite number requirements is to be defined to explain OBL.

Let $N\left(N \in [x, y]\right)$ be a real number and the N^o (opposite number) can be defined as follows:

$$N^o = x + y - N \ . \tag{33}$$

In the exploration space it has been extended as:

$$N_i^o = x_i + y_i - N_i \ , \tag{34}$$

where $(N\_1, N\_2, .., N\_d)$ is a point in the dimensional search space, $N\_i \in [x\_i, y\_i]$, $i \rightarrow \{1, 2, 3, ..d\}$

In all oppositional based optimization; the conception of OBL is used in the initialization procedure and as well as in each iteration using the generation jumping rate, Jr.

a. Start

b. Create oppositional based population

c. Fitness assessment of each krill individual based on its location.

d. Motion calculation:

Motion induced by the attendance of other individuals,

Foraging movement

Physical propagation

e. Applying the genetic operators

f. Updating krill individual location in the search space.

g. Based on a jumping rate jr (jumping probability), oppositional based variables is engendered and fitness value of the oppositional based variables is computed

h. Until the end conditions is reached; Repeat: go to step fitness evaluation

i. End

IV. Simulation Results

Validity of the proposed Opposition based Krill Herd (OKH) algorithm has been verified by testing in standard IEEE 30 Bus [20] without considering Voltage stability evaluation. In Table I Control variables limits are given. Obtained Real power loss by proposed Opposition based Krill Herd algorithm has been compared with SGA [21], PSO [22], LP [23], EP [23], CGA [23], AGA [23], CLPSO [23], HSA [24], BB-BC [25] and MCS [26]. Real power loss reduction achieved and proposed algorithms performed well when compared to other reported algorithms.

In Table II gives the power limits of generator buses.Table III shows the values of control variables. Table IV narrates the performance of the proposed algorithm. Overall comparison of real power loss is given in Table V.

TABLE I. Primary Variable Limits (PU).

Parameters	lowest limit	utmost limit
Value of Generator Bus	0.9500	1.100
Value of Load Bus	0.9500	1.0500
Value of Transformer-Tap	0.9000	1.1000
Value of Shunt Reactive Compensator	-0.1100	0.3100

TABLE II. Power Limits of the Generator Buses.

Bus No.	Pgmin	Pgmax	Qgmin	Qgmax
1	49.000	200.000	0.000	10.00
2	18.000	79.000	-40.000	50.000
5	14.000	49.000	-40.000	40.000
8	11.000	31.000	-10.000	40.000
11	11.000	28.000	-6.0000	24.000
13	11.000	39.000	-6.0000	24.000

TABLE III. AFTER OPTIMIZATION VALUES OF CONTROL VARIABLES.

List of Control Variables	OKH
Value of V1	1.04139
Value of V2	1.04120
Value of V5	1.01524
Value of V8	1.02631
Value of V11	1.06712
Value of V13	1.04119
Value of T4,12	0.00000
Value of T6,9	0.01000
Value of T6,10	0.90000
Value of T28,27	0.91000
Value of Q10	0.10000
Value of Q24	0.10000
Value of Real power loss in MW	4.10960
Value of Voltage deviation	0.90790

TABLE IV. PERFORMANCE OF OPPOSITION BASED KRILL HERD (OKH).

Total Number of Iterations	29
Time taken in seconds	12.98
Value of Real power loss in MW	4.10960

TABLE V. COMPARISON OF RESULTS.

Methods	Real power loss in MW
SGA [21]	4.980
PSO [22]	4.92620
LP [23]	5.9880
EP [23]	4.9630
CGA [23]	4.9800
AGA [23]	4.9260
CLPSO [23]	4.72080
HSA [24]	4.76240
BB-BC [25]	4.690 0
MCS [26]	4.872310
Proposed OKH	4.10960

V. CONCLUSION

In this paper Opposition based Krill Herd (OKH) successfully solved the optimal reactive power problem. Real Power Loss is reduced considerably when compared to other standard algorithms. Based on the swayed movement of other Krill's, foraging drive and substantial propagation the position of every krill in a time period is depended. Opposition based learning is one of the influential optimization tools to boost the convergence speed of different optimization techniques. The thriving implementation of the Opposition based learning engages evaluation of opposite population and existing population in the similar generation to discover the superior candidate solution of the given problem. In order to improve the convergence speed and precision - Krill Herd algorithm is integrated with the Opposition based learning. Proposed Opposition based Krill Herd (OKH) algorithm has been validated in IEEE 30 bus test systems. Real Power Loss is reduced significantly when compared to other regular procedures.

REFERENCES

[1] Lee, K. Y. (1984). Fuel-cost minimisation for both real and reactive-power dispatches," *Proceedings Generation, Transmission and Distribution Conference 131*(3), 85-93.

[2] Deeb, N. I. (1998). An efficient technique for reactive power dispatch using a revised linear programming approach. *Electric Power System Research, 15*(2), 121–134.

[3] Bjelogrlic, M. R., Calovic, M. S., & Babic, V (1990). Application of Newton's optimal power flow in voltage/reactive power control. *IEEE Trans Power System, 5*(4), 1447-1454.

[4] Granville, S. (1994). Optimal reactive dispatch through interior point methods. *IEEE Transactions on Power System, 9*(1), 136–146. doi:10.1109/59.317548

[5] Grudinin, N. (1998). Reactive power optimization using successive quadratic programming method. *IEEE Transactions on Power System, 13*(4), 1219–1225. doi: 10.1109/59.736232.

[6] Shin Mei, Ng., Sulaiman, R., Mustaffa, M.H., Daniyal, Z.H. (2017). Optimal reactive power dispatch solution by loss minimization using moth-flame optimization technique. *Appl. Soft Comput*. *59*, 210–222.

[7] Chen, G., Liu, L.m Zhang, Z., & Huang, S. (2017) Optimal reactive power dispatch by improved GSA-based algorithm with the novel strategies to handle constraints. *Appl. Soft Comput*. *50*, 58–70.

[8] Naderi, E., Narimani, H., Fathi, M., & Narimani, M.R, (2017). A novel fuzzy adaptive configuration of particle swarm optimization to solve large-scale optimal reactive power dispatch. *Appl. Soft Comput. 53*, 441–456.

[9] Heidari, A.A., Ali Abbaspour, R., & Rezaee Jordehi, A. (2017). Gaussian bare-bones water cycle algorithm for optimal reactive power dispatch in electrical power systems. *Appl. Soft Comput*., *57*, 657–671.

[10] Mahaletchumi M., Abdullah, N.R.H., Sulaiman, M., Mahfuzah M., & Samad. R. (2016). Benchmark Studies on Optimal Reactive Power Dispatch (ORPD) Based Multi-objective Evolutionary Programming (MOEP) Using Mutation Based on Adaptive Mutation Adapter (AMO) and Polynomial Mutation Operator (PMO). *Journal of Electrical Systems*, 12-1.

[11] Rebecca N. S. M., Sulaiman, M. H., & Zuriani M,. (2016). Ant Lion Optimizer for Optimal Reactive Power Dispatch Solution. *Journal of Electrical Systems*, (Special Issue AMPE2015), 68-74.

[12] Anbarasan, P., & Jayabarathi, T. (2017). Optimal reactive power dispatch problem solved by symbiotic

organism search algorithm. *Innovations in Power and Advanced Computing Technologies*. doi: 10.1109/IPACT.2017.8244970

[13] Gagliano A., Nocera F. (2017). Analysis of the performances of electric energy storage in residential applications, International Journal of Heat and Technology , Vol. 35, Special Issue 1, pp. S41-S48. doi: 10.18280/ijht.35Sp0106.

[14] Caldera M., Ungaro P., Cammarata G., & Puglisi G. (2018). Survey-based analysis of the electrical energy demand in Italian households. *Mathematical Modelling of Engineering Problems, 5*(3), 217-224. doi: 10.18280/mmep.050313

[15] M. Basu (2016). Quasi-oppositional differential evolution for optimal reactive power dispatch. *Electrical Power and Energy Systems, 78*(29-40).

[16] Lenin K., (2021). Reduction of power loss by Henry's law-based soluble gas, mobula alfredi and balanced condition optimization algorithms. *COMPEL - The international journal for computation and mathematics in electrical and electronic engineering*, *40*(3), 689-721. doi:10.1108/COMPEL-02-2021-0031

[17] Lenin, K. (2021). Real Power Loss Reduction by Extreme Learning Machine Based Leontodon Algorithm. *Technology and Economics of Smart Grids and Sustainable Energy*, *6*,16 doi:10.1007/s40866-021-00110-1

[18] Gai-gewang, W., Suash, D., Amir H. G., & Alavi, A. H. (2016). Opposition-based krill herd algorithm with Cauchy mutation and position clamping. *Journal Neurocomputing, 177*, 147-157. doi:10.1016/j.neucom.2015.11.018.

[19] Tizhoosh H. R. Opposition-based learning: a new scheme for machinei ntelligence. In*: Proceeding of the international conference on computational intelligence for modeling, control and automation, Austria*. 695–701.

[20] IEEE (1993). The IEEE-test systems, http://www.ee.washington.edu/trsearch/pstca/.

[21] Wu.Q.H., Cao Y.J., & Wen J.Y. (1998). Optimal reactive power dispatch using an adaptive genetic algorithm. *Int. J. Elect. Power Energy Syst. 20*, 563-569. doi: 10.1016/S0142-0615(98)00016-7

[22] Zhao B, Guo C. X., & Cao Y.J. (2005). Multiagent-based particle swarm optimization approach for optimal reactive power dispatch. *IEEE Trans. Power Syst. 20*(2), 1070-1078. doi:10.1109/TPWRS.2005.846064

[23] Mahadevan K, & Kannan P. S. (2010). Comprehensive learning particle swarm optimization for reactive power dispatch. *Applied Soft Computing 10*(2) 641–52. doi:10.1016/j.asoc.2009.08.038

[24] Khazali, A. H., & Kalantar, M. (2011). Optimal reactive power dispatch based on harmony search algorithm. *Electrical Power and Energy Systems 33*(3),684–692. doi:10.1016/j.ijepes.2010.11.018

[25] Sakthivel, S., Gayathri, M., & Manimozhi, V. (2013). A Nature inspired optimization algorithm for reactive power control in a power system. International *Journal of Recent Technology and Engineering 2*(1), 29-33.

[26] Tejaswini Sharma,Laxmi Srivastava,Shishir Dixit (2016). Modified Cuckoo Search Algorithm For Optimal Reactive Power Dispatch. *Proceedings of 38 th IRF International Conference*, (pp. 4-8). 20th March, Chennai, India.

European Green Deal: Serbian Path Towards Renewable Energy

Milos Dobrojevic[1]

[1]Singidunum University, Belgrade, Serbia, mdobrojevic@singidunum.ac.rs

Abstract—**In June 2021, the European Union adopted European climate law within the current European Green Deal, aiming to incrementally reduce greenhouse gas emissions in the EU, first by 2030 to 55% of total 1990 emissions, and then to a neutral level by 2050. However, in the last quarter of 2021, there was a crisis in the global energy market, caused by the COVID-19 pandemic and labor shortages in the transport industry, a severe winter in 2020 that has exhausted previously accumulated fuel reserves, as well as abandonment of traditional energy sources, primarily coal and oil, in favor of renewable energy sources. The Republic of Serbia largely depends on fossil fuels, primarily in the production of electricity and heat. Given the EU candidate status and the recently adopted national law on climate change, Republic of Serbia must prepare different strategies for tectonic changes towards reduction the carbon footprint and the transition to renewable energy sources.**

Keywords - power production in Serbia, green transition, CO_2 emissions reduction

I. INTRODUCTION

According to data from 2017, the global emission of greenhouse gases (GHG) caused by the combustion of fossil fuels was by 63% higher in comparison to the level of 1990 emissions. The five largest polluters, which at the time accounted for 48.70% of the world's population and 61.08% of global Gross Domestic Product (GDP), caused 64.06% of CO_2 emissions in the same year, Table I [1-4].

Regarding the global CO_2 and GHG emissions, energy production was the largest cause of pollution with a share of 73.2% according to 2016 data, Fig. 1. [5] By sector, 24.2% of emissions were caused by industry, 18.4% by agriculture, 16.2% by transport, 17.5% by commercial and residential real estate, while as much as 7.8% were caused by fugitive emissions.

TABLE I. TOP 5 GLOBAL FOSSIL CO_2 EMITTERS (2017).

Rank	Country	Fossil CO_2 emission [mt]	[%] of global emission	[%] of global population
	World	37.077.404		
1	China	10.877.218	29.34	18.83
2	U.S.A.	5.107.393	13.77	4.31
3	E.U.	3.548.345	9.57	5.91
4	India	2.454.774	6.62	17.74
5	Russia	1.764.866	4.76	1.93

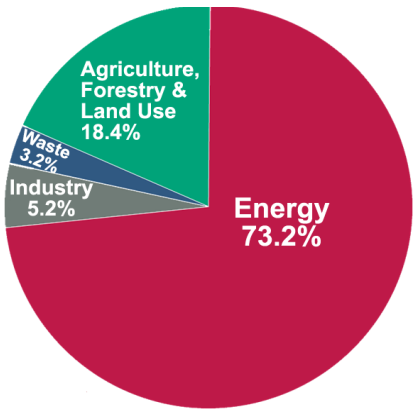

Figure 1. Global CO_2 and GHG emission by sector.

A. The European Green Deal

The *European Green Deal* is a set of European Commission policy initiatives with the overall goal of making the European Union (EU) climate-neutral by 2050 [6-7], with greenhouse gas emissions expected to be

f

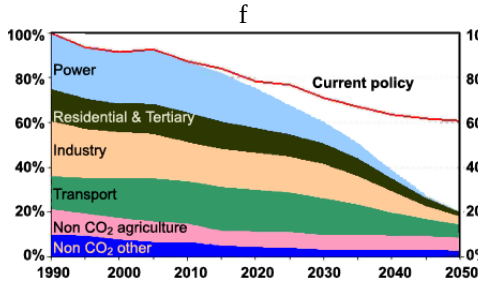

Figure 2. EU GHG emissions reduction plan.

reduced by 2030 to 50%-55% of 1990 emissions, Fig. 2 [8].

The *Paris Agreement* is an international agreement on climate change, adopted in 2015, which targets actions aimed at mitigating climate change. As of November 2021, 193 members of the *United Nations Framework Convention on Climate Change* (UNFCCC) have signed this agreement.

The long-term goal of this agreement is to keep the increase of the global average temperature below 2° C, preferably around 1.5° C above pre-industrial levels, which would significantly reduce the impact of climate change and reduce emissions to zero by the middle of the 21st century [9].

According to the report by *United Nations Environment Program* (UNEP), meeting the targeted increase of global temperatures to 1.5° C from the Paris Agreement requires a global emissions reduction of 57% by 2030, compared to 2019 levels, Table II [10].

TABLE II. ESTIMATED GHG REDUCTION COMP. TO 1990.

GHG reduction comp. to 1990	**2005 [%]**	**2030 [%]**	**2050 [%]**
Total	7	40-44	79-82
Power	7	54-68	93-99
Industry	20	34-40	83-87
Transport incl. aviation, excl. maritime	30	9-20	54-67
Residential & Services	12	37-53	88-91
Agriculture	20	36-37	42-49
Other non CO_2	30	72-73	70-78

The goal set represents an average global reduction, with developed economies expected to make a greater contribution [11].

The plan is to revise every existing law in the context of given climate values, as well as to introduce new laws on the circular economy, construction industry, biodiversity, agriculture and innovation [6]. The circular economy, unlike the traditional linear economy, is a model of production and consumption, which includes sharing, leasing, reusing, repairing, renovating and recycling existing materials and products for as long as possible [12] in order to reduce impact on environment.

One of the EU's important instruments aimed on control of the amount of absolute emissions, including non-EU countries, is the introduction of a cross-border carbon taxation mechanism (CBAM) or CO_2 tax, with implementation starting by 2023.

The European Green Deal also includes mechanisms to ensure that nations relying on fossil fuels not to be left out in the process of transitioning to renewable energy [13-15].

B. Law on Climate Change and Low Carbon Strategy in Republic of Serbia

In 2001, the Republic of Serbia ratified the UNFCCC, committing itself to deliver national reports on the Convention implementation. Being a developing country [16], Serbia has no obligation to reduce GHG emissions, but is expected to integrate climate change issues into planning processes and provide relevant information on GHG emissions. Accordingly, Serbia is required to submit National Reports every four years, and biennial updates every other year.

Serbia ratified the Paris Agreement in 2017. Developing country members are obligated to provide information on the provided financial support, along with information on technology development and transfer and capacity building, in accordance with Article 13, paragraph 9, of this Agreement [17].

In accordance with the signed international agreements, the *Law on Climate Change* was adopted in 2021 as a base for establishing a system for limiting GHG emissions, in a cost-effective manner [18].

The law will introduce the obligation to develop a *low-carbon development strategy* (LCS) and an action plan for its implementation,

as well as a program of adaptation to changed climatic conditions, the so-called *national adaptation plan*. The law stipulates that policy documents must contain a quantitative assessment of the level of GHG emissions, and bodies and organizations, including local governments, must assess the effects of policies on the level of emissions and report to the ministry.

Based on the strategy and action plan, the government will set permitted emission levels per sector, and the Ministry of Environmental Protection will prepare annual reports and propose measures by November 15 each year. It is obliged to inform the public about the strategy, action plan and adjustment program, as well to take into account given feedback and remarks.

Following the experience of other countries, the law establishes a national climate change council consisting of representatives of the Ministry of Environmental Protection, other ministries and bodies, the scientific and professional public and civil society and a representative of the Office of the Commissioner for Equality of the Serbian Government.

The law will introduce an obligation to have data available at points of sale on fuel economy and carbon dioxide emissions from vehicles. The main goal of this section is to raise awareness of CO_2 emissions when buying passenger or leasing passenger cars. In other words, the law prescribes the publication of data already provided by vehicle manufacturers.

A special segment refers to the issuance of permits for the release of GHG to certain industrial facilities and power plants and airline operators, being a mandatory document to establish operations. Existing facilities are subject to licensing too. The emissions of each plant in Serbia will become transparent, and the ministry is obliged to make the reports publicly available. The law will introduce monitoring and reporting on emissions at the annual base, and on the facility level as well, which is the base for more precise long-term planning of the transition of industry and energy to low-carbon or climate-neutral GHG emissions, and thus increase in competitiveness on the international market.

The Law on Climate Change defines the administrative fees for applying for a permit, issuing a permit, amending a permit and amending a monitoring plan. So, this is an additional environmental levy targeted to be additional budget revenue.

Having a candidate status for EU membership, but also due to the dominant share of the EU in Serbian exports, the goals of the EU are certainly of the greatest importance, especially having in mind the already set EU goal to achieve climate neutrality by 2050.

By introducing the CBAM, the EU plans to indirectly reduce emission of GHG in the countries from which it imports goods, but also to ensure the competitiveness of its economy. Although aimed to all products, the tax will be first applied to energy-intensive sectors, such as the production of steel, cement, chemicals and artificial fertilizers. In other words, basing Serbia's energy system on coal is becoming a matter of economic survival from 2023 [19].

It is expected that the future Law on Climate Change contains postulates that will make economy more robust, but also ensure the resilience of the entire society to increasingly intense climate change. Therefore, it is surprising that the law is misaligned with the decision of the Paris Agreement (Decision 18 / CMA.1 - Modalities, procedures and guidelines for the transparency framework for action and support referred to in Article 13 of the Paris Agreement) and current EU legislation. Moreover, the law transposes EU legislation that already expired. Since the adoption of the law was announced in 2018, there was enough time to comply with the new requirements.

II. ENERGY STRATEGY OF REPUBLIC OF SERBIA

The Republic of Serbia is on turning point regarding the future of its energy system. Although there is no current obligation to reduce GHG emissions, being a developing country and a non-EU country, there is a possibility that this issue will be integrated into the requirements of the future EU accession process.

According to data from 2016, the energy sector in the Republic of Serbia is responsible for 67% of CO_2 emissions, Fig. 3 [20] The country's strategic commitment is to base electricity production on coal, due to the significant amounts of coal reserves estimated at 7.5-8.3 billion tons, the 14th largest in the world and with the 16th largest annual production [21-23].

Although the given data may lead to conclusion that the Republic of Serbia is a major

polluter, annual CO_2 emissions account for 16.12% of total emissions in the Balkans, Table III. According to data from 2017, 70% of electricity was obtained by burning coal, while approximately 30% was obtained from renewable sources, primarily hydropower plants, Table IV [24-25] and Figs. 4 and 5 [26-28].

TABLE III. FOSSIL CO_2 EMITTERS IN BALKANS.

Rank	Country	Fossil CO_2 emission [mt]	[%] of global fCO_2 emission	[%] of Balkans fCO_2 emission	Rank fCO_2 em. per capita
	Balkans	387.555	1.05	-	
1	Romania	81.131	0.22	20.93	8
2	Greece	72.145	0.19	18.62	5
3	Serbia[a]	62.487	0.17	16.12	3
4	Hungary	50.856	0.14	13.12	6
5	Bulgaria	49.568	0.13	12.79	4
6	B&H	25.618	0.07	6.61	1
7	Croatia	17.466	0.05	4.51	7
8	Slovenia	15.209	0.04	3.92	2
9	N. Macedonia	8.049	0.02	2.08	9
10	Albania	5.026	0.01	1.30	10

[a)] Cumulative data for Serbia, including Montenegro and Kosovo

TABLE IV. ELECTRIC PRODUCTION IN SERBIA.

Rank	Source	2017		2020	
		GWh	%	GWh	%
1	Coal	23.864	72.10	23.935	70.34
2	Hydro	8.740	26.41	8.609	25.30
3	Wind	48	0.15	963	2.83
4	Gas	351	1.05	317	0.93
5	Biomass	72	0.22	189	0.56
6	Solar	13	0.04	13	0.04
7	Unspecified fossil	11	0.03	0.6	0.00
	SUM	**33.100**		**34.028**	

This data is also significant because the population of the Republic of Serbia makes up about 12.5% of the population of the Balkans, while the GDP of the Republic of Serbia is only 4.78% of the cumulative GDP of the countries on the Balkan Peninsula.

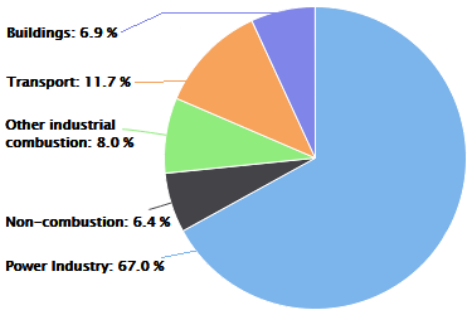

Figure 3. Republic of Serbia, CO2 emissions per sector.

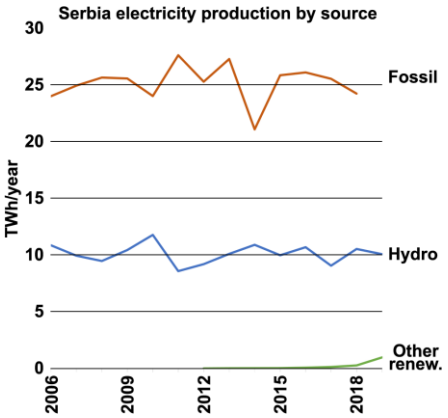

Figure 4. . Republic of Serbia, energy production.

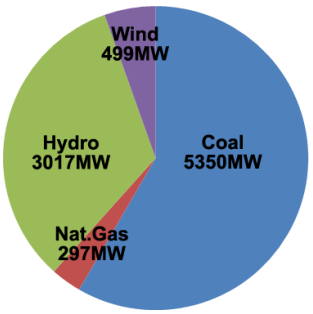

Figure 5. Installed power generation capacity in Serbia.

Despite the significant potential for increasing the share of renewable energy and improving energy efficiency, the Republic of Serbia in the near future plans significant investments in coal and water based electricity production, primarily through the construction of new or replacement thermal and hydro power plants, giving the impression that there is no strategic commitment to the so-called. "green transition", neither in Serbia, nor in the region of Western Balkan.

III. TECHNOLOGY IN GREEN TRANSITION

The low-carbon economy will have a much greater need for renewable energy production, energy-efficient building materials, hybrid and electric vehicles, and carbon capture and storage technologies, as well as energy storage technologies.

To make the transition, the EU will have to invest additional 270 billion euros annually, over the next four decades. Additional investment would spur growth across a wide range of manufacturing sectors and environmental services, if governments properly use CO_2 tax revenues [29].

A. Dealing With Media Pressure

In the last quarter of 2021, the hot topic in Serbian media was the green transition and reduction of GHG emissions, which was presented as an obligation towards the EU.

Although the reduction in use of nuclear power plants in electricity production regarding security and environmental reasons is a global trend, the construction of a nuclear power plant in Serbian media was presented as inevitable, as a project that should be implemented as soon as possible. Such an endeavor would require the lifting of the moratorium on the construction of nuclear power plants introduced in 1989 after the Chernobyl accident, which was also advocated by the director of the Public Utility Company "Belgrade Power Plants" by sending an open letter to the Serbian Prime Minister and Minister of Mining and Energy. [30] The approximate cost of such a project was estimated to be between 5 and 15 billion euros. As an alternative, the possibility of buying a stake in a nuclear power plant in neighboring countries such as Hungary or Bulgaria was mentioned too. Such option would be more attractive in terms of finance, providing the necessary amounts of electricity, but would jeopardize the country's energy security [31]. As an alternative to the construction of a traditional nuclear power plant, the procurement of modular nuclear power plants was mentioned as well [32-33].

B. Electricity Generation

At the moment, the Kostolac B3 thermal power plant (350MW) is under construction in Serbia, and the construction of the Kolubara B thermal power plant (350MW) is currently suspended [34], which has been interpreted as Serbia's first concrete step towards a green transition. The construction of two large hydropower plants, Đerdap 3 (reversible, 2,400MW) and Bistrica (680MW) is also planned.

An alternative, yet efficient mean of electricity generation could be the Stirling engine. Although known for more than 200 years, this highly efficient heat engine (40% thermal efficiency vs. 25% in OTTO or 35% in Diesel engines [35]) is among devices believed to be able to contribute improving the efficiency of the process of electricity production. It is suitable for electric power generation from abundant energy sources that are incompatible with the internal combustion engines (ICE), such as solar, biomass, nuclear, or even from waste heat generated in thermal power and heating plants. Compared to ICE, Stirling engines use more efficiently renewable heat sources, reduce noise pollution, have higher work reliability and easier maintenance. Being economically competitive up to a power of 100 kW [36], they are suitable for micro combined heat and power (mCHP) cogeneration.

C. Energy Storage

Energy storage is the process of storing energy produced for later use [37] in order to reduce or resolve the imbalance between production and consumption. A device that stores energy is usually called an accumulator or battery, while the type of stored energy can difere. Energy storage can be short-term or long-term, and involves converting energy from forms that are difficult to store into more convenient forms.

Electricity produced by wind turbines or solar panels can be stored in the form of potential or kinetic energy.

Figure 6. Energy Vault prototype, 60m.

Pumped-storage hydroelectricity (PSH), or reversible hydropower plants, can be regarded as energy storage, the so-called water batteries. They can help addressing the inconsistency of the production of wind and solar power plants, but require appropriate terrain that allows large amounts of water to be stored above the main water source. Excess electricity produced by the sun or wind can be used to pump water up into the reservoir, and afterwards, during the periods of energy deficit, PSH can make up for that deficit. The round-trip energy efficiency of PSH is in the range of 70%-80% [38].

Storing electricity can be obtained by so-called gravity batteries, actually machines similar to tower cranes, Fig. 6. Excess electricity in the network is used to lift the concrete blocks to a certain height. At night, the ballast can be slowly released to produce electricity in a controlled descent. A 120 meter high unit can store about 20 MWh of energy, quantity enough to power electricity to circa 2,000 households throughout the day, with round trip energy efficiency of 80-90% [39]. The machines are scalable, and do not require significant logistics during assembly and operation. The estimated lifespan of such machines is about 50 years.

The electricity produced can also be stored in the form of kinetic energy using a flywheel, a mechanical device that has been known in its basic form for more than 1,000 years. The Flywheel Energy Storage (FES) method has been evolving for many years, and is already being used in real-world conditions in the United States to equalize fluctuations in electricity supply. The flywheel floats in vacuum vessels by means of a magnetic field. Electricity initiates rotational motion, thereby converting it into kinetic energy that can subsequently be used to generate electricity with efficiency of 90-95% and rated power ranges of 0-50 MW [40].

Large battery packs can be used to store large amounts of electricity produced. The current lithium-ion batteries, being an old technology originating from the early 1970s, will probably be replaced in the foreseeable future by more efficient technologies such as Lithium-sulfur batteries (40% higher energy density), Redox flow batteries (70% higher energy density), Aluminum-graphite batteries (fully charged smartphone in less than a minute, an EV could charge in minutes) and Solid-state batteries (much safer, insensitive to weather conditions, could last a lifetime), etc.

IV. CONCLUSION

In the production of electricity, the Republic of Serbia relies on two, the most abundant resources - coal (70%) and water (~30%). Other renewable sources, such as wind, solar or geothermal energy, are used in electricity production in a negligible percentage. Although it is the 16th largest coal producer in the world, it is only the third largest emitter of CO_2 on the Balkan Peninsula, both in terms of total quantity and quantity per capita. Compared to global fossil CO_2 emissions, the pollution that Serbia creates is negligible, being at the level of statistical error (0.17%). However, it should be borne in mind that the current level of industrial activity is still significantly below the record level of 1989, and that if that level is reached, Serbia would need twice the amount of energy per year compared to its current production.

The energy transition to renewable energy and reduced GHG emissions implies long-term planning, as well as large investments in new energy capacities, which will lead to the creation of new jobs for the construction and management of new power plants and energy collection, storage and redistribution plants. The whole process will take decades, and requires careful development and evaluation of the strategy at the state level.

Although as a developing country is not obliged to reduce GHG emissions, the Republic of Serbia has already taken the first steps in that direction with the recent adoption of the Law on Climate Change. This law will enable the

creation of a more accurate awareness of GHG emissions, which will afterwards provide means of easier tracking, control and taxation of the polluters. However, the fear remains that the cost of GHG taxation will be passed on to the end consumer.

It is very likely that the future of coal use in the energy sector will be dictated by the prices of certificates for CO_2 emissions and supply, i.e. the demand for electricity on the regional market.

Unfortunately, these trends are not recognized in the national energy policies of the Western Balkan countries, including Serbia, which at some point may lead to a belated and campaign reduction of coal use for electricity production, which will cause incomparably higher costs compared to the gradual decades-long transition.

When planning the state energy strategy in this area, regardless of whether Serbia will become a full member of the EU or not, we must not neglect the intention of the EU to control imports (CBAM, CO_2 tax) from 2023.

The transition to a low-carbon society requires technical innovation, a change in the way society thinks and organizes. As these are large investments, the activities of certain energy lobbies are already noticeable, which are trying to gain public opinion through the media.

Although in the context of the transition to renewable energy sources, investments in the so-called clean technologies and the production of electricity with low or zero carbon emissions, accidentally or intentionally, neglects the energy storage systems.

Finally, this paper gives a brief overview of alternative technologies, some of which have been known to our civilization for hundreds and thousands of years, which combined with modern technology could provide the ability to produce and store energy in an accessible, cost effective and simple manner.

Analytics presented in this paper is based on data from 2017. Although it would be ideal to draw conclusions on more timely data, 2017 data was the most recent comprehensive data set publically available at the time of writing of this paper.

REFERENCES

[1] Wikipedia. (2021). *List of countries by carbon dioxide emissions*. Available at: https://en.wikipedia.org/wiki/List_of_countries_by_carbon_dioxide_emissions

[2] Worldometers. (2021). *Population: World*. Available at: https://www.worldometers.info/population/world/

[3] Worldometers. (2021). *Gross Domestic Product (GDP)*. Available at: https://www.worldometers.info/gdp/

[4] Eurostat press office. (2021). *EU population up to almost 512million at 1 January 2017*. Available at: https://ec.europa.eu/eurostat/documents/2995521/10722195/3-10072017-AP-EN.pdf/a61ce1ca-1efd-41df-86a2-bb495daabdab

[5] Ritchie, H., & Roser, M., (2021). *Emissions by sector, GCDL*. Available at: https://ourworldindata.org/emissions-by-sector

[6] Tamma, P., Schaart, E., & Gurzu, A. (2019). *Europe's Green Deal plan unveiled, POLITICO*. Available at: https://www.politico.eu/article/the-commissions-green-deal-plan-unveiled/

[7] Simon, F. (2019). *EU Commission unveils 'European Green Deal': The key points*. Available at: https://www.euractiv.com/section/energy-environment/news/eu-commission-unveils-european-green-deal-the-key-points/

[8] European commission Memo/11/150. (2021). *Climate change: Questions and Answers on a Roadmap for moving to a low carbon economy in 2050*. Available at: https://ec.europa.eu/commission/presscorner/detail/en/MEMO_11_150

[9] UNFCCC. (2021). *The Paris Agreement*. Available at: https://unfccc.int/process-and-meetings/the-paris-agreement/the-paris-agreement

[10] RPS Group. (2011). *Common Carbon Metric*. Available at: https://www.rpsgroup.com/company/news/common-carbon-metric/

[11] Heil, M. T., & Wodon, Q. T. (1997). Inequality in CO_2 Emissions Between Poor and Rich Countries. *The Journal of Environment & Development*, *6*(4): 426–452.

[12] European Parliament. (2015). *Circular economy: definition, importance and benefits | News | European Parliament*. Available at: https://www.europarl.europa.eu/news/en/headlines/economy/20151201STO05603/circular-economy-definition-importance-and-benefits

[13] European Investment Bank. (2021). *International investors enter Poland renewable energy market after rule change*. Available at: https://www.eib.org/en/stories/poland-renewable-energy

[14] Geden, O., Schenuit, F., & Stiftung W. U. P. (2020). *Unconventional Mitigation*. SWP Research Paper. doi:10.18449/2020RP08.

[15] IIGCC. (2021). *€33 trillion investor group: strong EU climate targets key to economic recovery & future growth*. Available at: https://www.iigcc.org/news/e33-trillion-investor-group-strong-eu-climate-targets-key-to-economic-recovery-future-growth/

[16] World Economic Outlook. (2018). *World Economic Outlook, Database - WEO Groups and Aggregates Information, October 2018*. Available at: https://www.imf.org/external/pubs/ft/weo/2018/02/weodata/groups.htm

[17] Markovic, M., (2021). *Climate financing in Serbia*. *United Nations Development Programme*, ISBN-978-86-7728-297-4, Available at: https://www.klimatskepromene.rs/wp-content/uploads/2021/07/ClimateFinancingStudy.pdf

[18] Vlada Republike Srbije. (2021). *Usvojen Zakon o klimatskim promenama*. Available at: https://www.srbija.gov.rs/vest/529078/usvojen-zakon-o-klimatskim-promenama.php

[19] Božanić, D. (2021). *Zakon o klimatskim promenama - forma ili suština*. Available at: https://balkangreenenergynews.com/rs/zakon-o-klimatskim-promenama-forma-ili-sustina/

[20] Worldometers. (2021). *Serbia CO2 Emissions*. Available at: https://www.worldometers.info/co2-emissions/serbia-co2-emissions/

[21] Wikipedia. (2021). *List of countries by coal reserves*. Available at: https://en.wikipedia.org/wiki/List_of_countries_by_coal_reserves

[22] Worldometers. (2021). *Coal Reserves by Country*. Available at: https://www.worldometers.info/coal/coal-reserves-by-country/

[23] Worldometers. (2021). *Coal Production by Country*. Available at: https://www.worldometers.info/coal/coal-production-by-country/

[24] Elektromreža Srbije a.d. (2018). *Godišnji izveštaj o nacionalnom rezidualnom miksu za Srbiju za 2017. godinu*. Available at: https://archive.org/details/godisnjiizvestajonacionalnom/Godisnji_izvestaj_o_nacionalnom_rezidualnom_miksu_2017/page/n9/mode/2up

[25] Elektromreža Srbije a.d. (2021). *Godišnji izveštaj o nacionalnom rezidualnom miksu za Srbiju za 2020. godinu*. Available at: https://ems.rs/media/uploads/2021/Garancije%20porekla/Godisnji%20izve%C5%A1taj%20o%20nacionalnom%20rezidualnom%20miksu%20-%202020.pdf

[26] CEE Bankwatch Network. (2021). *The energy sector in Serbia*. Available at: https://bankwatch.org/beyond-coal/the-energy-sector-in-serbia

[27] Tallungs, K. *Serbia electricity production by source*. U.S. Energy Information Administration.

[28] Public Enterprize Electric Power Industry of Serbia. (2021). *Production Capacity*. Available at: http://www.eps.rs/eng/Pages/Kapaciteti-ElEn.aspx

[29] European Comission. (2011). *A Roadmap for moving to a competitive low carbon economy in 2050*. Available at: https://eur-lex.europa.eu/resource.html?uri=cellar:5db26ecc-ba4e-4de2-ae08-dba649109d18.0002.03/DOC_1&format=PDF

[30] Beogradske elektrane. (2021). *Ukinite moratorijum na izgradnju nuklearnih elektrana*. Available at: https://www.slobodnaevropa.org/a/nuklearne-elektrane-srbija-moratorijum-beogradske-elektrane/31569560.html

[31] Blic. (2021). *SRBIJA DOBIJA NUKLEARKU?! Imamo dve mogućnosti, a čista je matematika koliko nam je važno da takav projekat VIDIMO ŠTO PRE*. Available at: https://www.blic.rs/biznis/privreda-i-finansije/srbija-dobija-nuklearku-imamo-dve-mogucnosti-a-cista-je-matematika-koliko-nam-je/s6zm3ks

[32] Blic. (2021). *ŠTA SU ZAPRAVO MODULARNE NUKLEARKE Opcija su i za Srbiju, imamo još jednu mogućnost i svaka nosi svoje prednosti*. Available at: https://www.blic.rs/biznis/privreda-i-finansije/sta-su-zapravo-modularne-nuklearke-opcija-su-i-za-srbiju-imamo-jos-jednu-mogucnost-i/z8x7t0n

[33] Vujić, J., Bergmann, R. M., Škoda, R., & Miletić, M. (2012). Small modular reactors: Simpler, safer, cheaper. *Energy*, *45*(1), 288-295.

[34] Balkan Green Energy News. (2021). *Srbija obustavlja gradnju elektrane na ugalj Kolubara B*. Available at: https://balkangreenenergynews.com/rs/srbija-obustavlja-gradnju-elektrane-na-ugalj-kolubara-b/

[35] Ahmadi, M. H., Ahmadi, M. A., & Mehrpooya, M. (2016). Investigation of the effect of design parameters on power output and thermal efficiency of a Stirling engine by thermodynamic analysis. *International Journal of Low-Carbon Technologies*, *11*(2), 141-156. Available at: https://academic.oup.com/ijlct/article/11/2/141/2198425

[36] McConnico, J. B., & Moore, P. W. (2006). *Stirling Engines. World Alliance for Decentralized Energy*. Available at: https://www.localpower.org/deb_tech_se.html

[37] Clarke Energy. (2021). *Energy Storage*. Available at: https://www.clarke-energy.com/energy-storage/

[38] Yang, C. J. (2016). *Pumped Hydroelectric Storage, Storing Energy with Special Reference to Renewable Energy Sources*, Chapter 2, Elsevier Science, ISBN 9780128034408.

[39] Hodari, D. (2020). *The Pull of Gravity, The Wall Street Journal*. Available at: https://helena.org/projects/energy-vault

[40] Moradzadeh, A., & Asadi, S. (2021). Energy storage fundamentals and components. *Energy Storage in Energy Markets*, 2, 23-39.

Modeling of a Photovoltaic Module Under Physical and Environmental Effects

Nasima El Assri[1], Samira Chabaa[2], Khadija Lmesri[3], Mohammed Ali Jallal[4], Abdelouhab Zeroual[5], Saida Ibnyaich[6]

[1,3,4,5,6]Faculty of Sciences Semlalia, Physics department, Cadi Ayyad University, Marrakesh, Morocco, nasima.elassri@gmail.com[1], khadija.lmesri@ced.uca.ma[3], mohammedali.jallal@edu.uca.ac.ma[4], zeroual@uca.ac.ma[5], s.ibnyaich@uca.ac.ma[6]
[2]National School of Applied Sciences, Industrial Engineering Departmnet, Ibn Zohr University, Agadir, Morocco, s.chabaa@uiz.ac.ma

Abstract—**A photovoltaic (PV) module is an assembly of photovoltaic cells that converts light into electricity using semiconducting materials. A single diode equivalent circuit model is chosen for a good complexity-accuracy ratio. Modeling and simulating this device is an essential step for any performance optimization or diagnosis process. This paper presents a method to ensure a closer understanding of I-V and P-V characteristics of a PV module to predict simply and accurately the electrical behavior including physical and climate parameters changes such as temperature and solar irradiation. The simulated result of the BP MSX-60 PV module is then verified and shows a good agreement with the manufacturer datasheet.**

Keywords – photovoltaic module, solar cell, modeling, simulation, I(V)/P(V) characteristic

I. INTRODUCTION

Energy is one of the most critical problem facing humanity in the next 100 years. Global energy demand is increasing due to the world population growth. Fossil fuel energy sources such as oil, coal, and gas are highly used, which release large amounts of carbon dioxide to the atmosphere, causing global warming [1].

Renewable energies are efficient, free and much cleaner to use than fossil fuels because they not produce harmful gases that cause pollution and climate change. Among renewable energy sources, photovoltaic (PV) energy is the most important for generating electricity by using solar cells to convert energy of light directly into electricity by the photovoltaic effect.

The modeling of solar module is imperative for describing both the I-V and P-V characteristics curves, for having one optimal operating point corresponding to maximum power point tracking (MPPT) [2] and for optimizing the design of the solar PV system [3].

This paper presents a model for the solar PV module taking into account different parameters variations effects as a function of ambient temperature, solar irradiation, series resistor, shunt resistor, etc. The result is then validated with the manufacturer datasheet of the PV module BP MSX-60.

II. MATHEMATICAL DESCRIPTION OF SOLAR CELL MODULE

A. Solar Cell

Solar cells are the basic building blocks of PV modules that produce direct current electricity from sunlight which can be used to power equipment or to recharge a battery. They are made of semiconducting materials, typically silicon, doped with special additives.

The amount of current produced is directly proportional to the cell's size, conversion efficiency, and the intensity of light.

Currently, solar panels that are used for domestic purposes are only able to take around 20% of the sunlight that they receive and turn it into electricity [4].

The chosen solar cell model as shown in Fig.1 is known as five-parameter model. it

includes a current source which models the conversion of the light flux into electrical energy, a single diode which models the PN junction, a series resistor Rs representing various contacts and connections and a shunt resistor Rsh is the consequence of the state along the periphery of the surface of the cell [4, 5].

This model is the best known for moderate complexity and acceptable accuracy [3, 6].

The five parameters are: photo-current Iph, saturation current Id, diode quality factor n, series resistance Rs and shunt resistance Rsh [4, 7].

The characteristic of photovoltaic cell can be modeled as follows:

$$I_{ph} = \left[I_{sc} + K_i * (T - 298)\right] * \frac{G}{1000}. \quad (1)$$

Module saturation current I_d:

$$I_d = I_{rs} * \left(\frac{T}{T_n}\right)^3 * \exp\left(\frac{q * E_{g0} * \left(\frac{1}{T_n} - \frac{1}{T}\right)}{n * K}\right). \quad (2)$$

Module reverse saturation current I_{rs}:

$$I_{rs} = \frac{I_{sc}}{\exp\left(\frac{q * V_{oc}}{n * N_s * K * T}\right) - 1}. \quad (3)$$

Module shunt current I_{sh}:

$$I_{sh} = \frac{V_{gv} + I_{gv} * R_s}{R_{sh}}. \quad (4)$$

The current output of PV cell is:

$$I_{pv} = I_{ph} - I_d * \left[\exp\left(\frac{(V_{gv} + I_{gv} * R_s) * q}{n * K * T * N_s}\right) - 1\right] - I_{sh}. \quad (5)$$

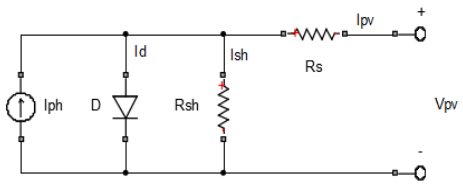

Figure 1. Single diode model of solar cell.

The nomenclatures used in this study are presented in Table I.

B. PV Module

A group of PV cells connected electrically and placed into a frame is called a photovoltaic module is shown in Fig 2.

The equivalent circuit of PV module connected in series with a number Ns of cells to achieve a desired output voltage or in parallel with a number Np of cells to provide a desired current capability (amperes) [8, 9].

The current output of a PV module is:

$$I = N_p * I_{ph} - N_p * I_d * \left[\exp\left(\frac{\left(\frac{V}{N_s} + \frac{s * R_s}{N_g}\right) * q}{n * K * T * N_s}\right) - 1\right] - \frac{\frac{N_g}{N_s} * V + I * R_s}{R_{sh}}. \quad (6)$$

TABLE I. NOMENCLATURE USED IN THIS STUDY.

I_{ph}	Photo-current (A)
I_{sc}	Short circuit current (A)
K_i	Temperature coefficient of Isc at STC
T	Operating temperature (K)
T_n	Nominal temperature (K)
G	Solar irradiation (W/m²)
q	Electron charge $electon\,charge\,q = 1.6 * 10^{-19}\,C$
V_{oc}	Open circuit voltage (V)
n	The ideality factor of the diode
K	Boltzmann's constant $K = 1.38 * 10^{-23}\,J/K$
E_{g0}	Band gap energy of the semiconductor (eV)
N_s	Number of cells connected in series
N_p	Number of PV modules connected in parallel
R_s	Series resistance (Ω)
R_{sh}	Shunt resistance (Ω)
V_t	Diode thermal voltage (V)

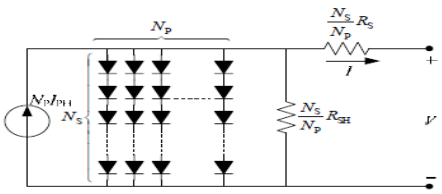

Figure 2. General model of a PV module.

III. MODELING AND SIMULATION OF SOLAR MODULE

BP MSX-60 PV module has been chosen for modeling and analysis in this work. The MSX 60 provides 60 watts of nominal maximum power, and is well adapted to traditional applications of photovoltaics. The electrical characteristics of the PV module are presented in Table II.

PV module specifications are under standard test conditions (STC): irradiance of 1kW/m², spectrum of 1.5 air mass, and cell temperature of 25°C.

I-V & P-V characteristics of the PV module are shown in Figs. 3 and 4.

TABLE II. ELECTRICAL CHARACTERISTICS OF BP MSX-60 PV MODULE.

Maximum power, Pmax	60W
Voltage at Pmax, Vmp	17.1V
Current at Pmax, Imp	3.5A
Short-circuit current, Isc	3.8A
Open-circuit voltage, Voc	21.1V
Temperature coefficient of Isc, Ki	0.065%/°C
Temperature coefficient of Voc, Kv	-80mV/°C
Number of cells	36

IV. EFFECT OF PARAMETERS ON THE MODEL

A. *Effects of Varying Solar Irradiation*

PV module photocurrent depends on the solar irradiation variation and temperature according to (1).

The I-V & P-V characteristics under varying irradiation (1000W/m², 800W/m², 600W/m², 400W/m²) with constant temperature (25°C) are shown in Figs. 5 and 6.

The output current and power of the PV module increase with higher solar irradiation

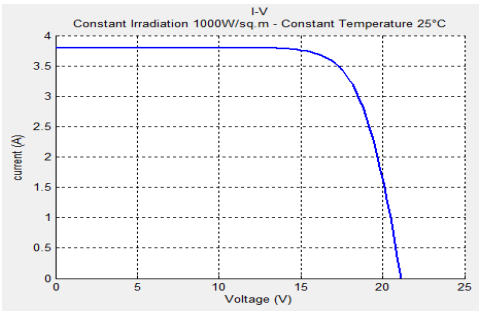

Figure 3. I-V characteristic of PV module at constant irrandiation & constant temperature.

and depend strongly on the solar irradiation. However, the voltage increases by 1V when the solar irradiation has increased from 400 W/m² to 1000 W/m².

B. *Effect of Varying Temperature*

The inverse saturation current relies on the temperature effect and varies as a cubic function of the temperature as expressed in the previous Eq. (2). I-V & P-V curves are shown in Figs. 7

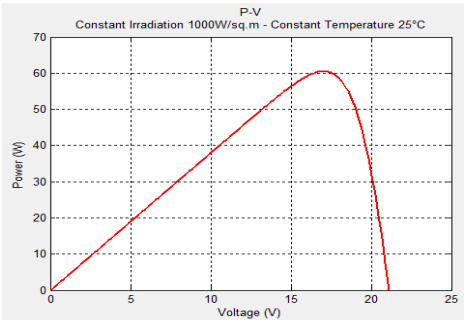

Figure 4. P-V characteristic of PV module at constant irrandiation & constant temperature.

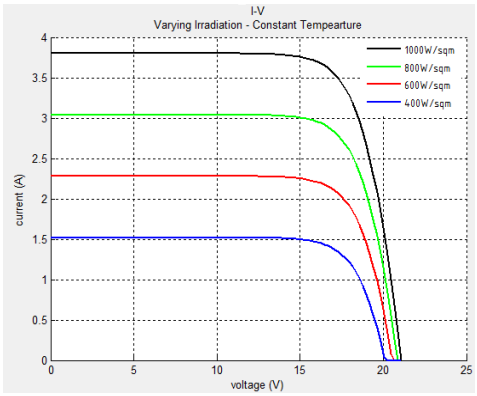

Figure 5. I-V characteristics of PV module at varying irrandiation & constant temperature.

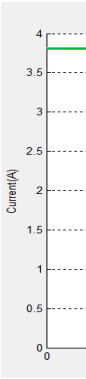

Figure 7.

and 8 under constant irradiation (1000W/m²) and various values of temperature (25°C, 40°C, 50°C).

The curves show the effect of the temperature on the voltage and the current. For a constant irradiation, when the temperature increases, the short circuit current Isc increases and the open circuit voltage Voc decreases.

C. Effect of Varying Series Resistance Rs

Series resistors in solar cells are parasitic parameters that represent various contacts and connections [4]. Rs is very small [3], and in some cases it can be neglected, it affects the current-voltage (I-V) characteristics and the efficiency of the cells.

I-V & P-V curves are presented in Figs. 9 and 10 under different values of series resistance.

Series resistances affect the efficiency of PV module. The increasing of Rs results an influence on the angle of I-V & P-V curves and reduces the power output of the PV module, Rs does not affect the solar module at open-circuit voltage and short circuit current.

D. Effect of Varying Shunt Resistance Rsh

Shunt resistance Rsh is another important parasitic resistance caused by the junction region of the semiconductor features and impurities within the PN junction.

Rsh must be high enough for a better output power [5, 10], low Values of Rsh can affect Isc, Voc, and the output power [11].

The effects of shunt resistance Rsh are illustrated in Figs 11 and 12.

The short circuit current Isc are not affected by shunt resistance but it reduces the open circuit voltage Voc. Hence, the significant effects of Rsh are on the output power.

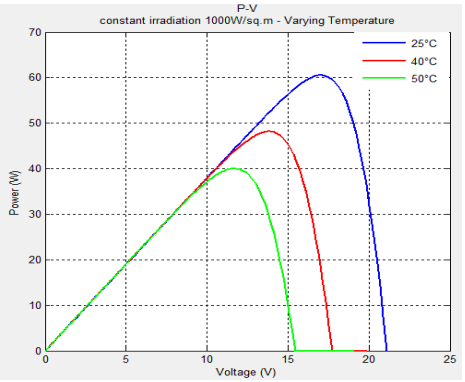

Figure 8. P-V characteristics of PV module at constant irrandiation & varying temperature.

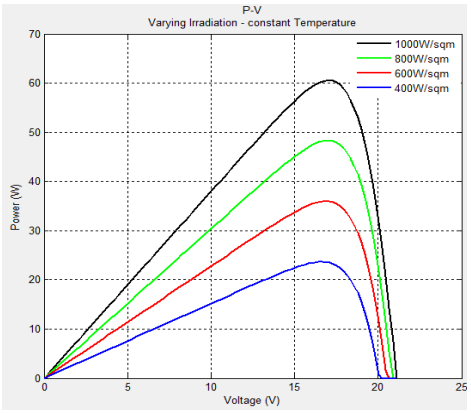

Figure 6. P-V characteristics of PV module at varying irrandiation & constant temperature.

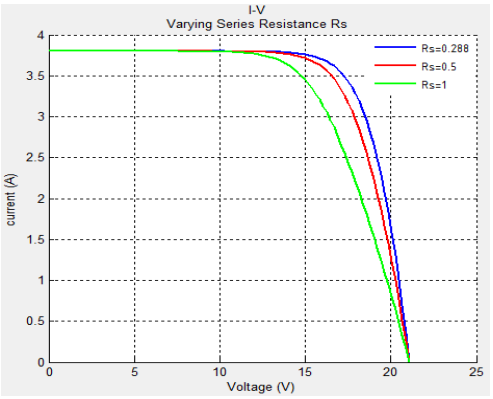

Figure 9. I-V characteristics of PV module at varying series resistance Rs.

E. Effect of Varying the Ideality Factor n

The ideality factor n is an indicator which affects the characteristics of solar cells. It defines the quality of the junction between two semiconductors (PN junction) [12].

The model gives the possibility to know the behavior of the photovoltaic module for different ideality factor n. The characteristics I-V & P-V in Fig 13 and 14 have been drawn for three different values of n (n=1.2, 1.5 and 2).

In general, the influence of an increase in n is obviously considered as the decrease of the power.

V. VALIDATION OF THE OBTAINED RESULTS

In order to validate the results, we compare the manufacturer specifications of the solar module BP MSX-60 at Standard test conditions (STC) with our model presented in section III.

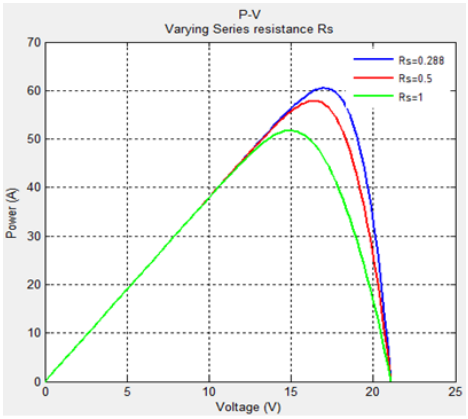

Fig. 10. P-V characteristics of PV module at varying series resistance Rs

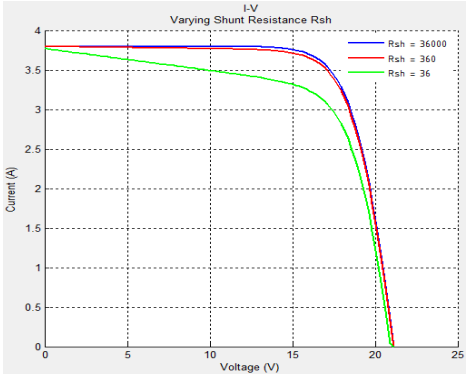

Figure 11. I-V characteristics of PV module at varying shunt resistance Rsh.

The characteristics obtained by the manufacturer datasheet are shown in Figs. 15 and 16 [13, 14].

The I-V & P-V characteristics obtained by our modeling (Figs. 3 and 4) are in line with the manufacturer's datasheet (Figs. 15 and 16).

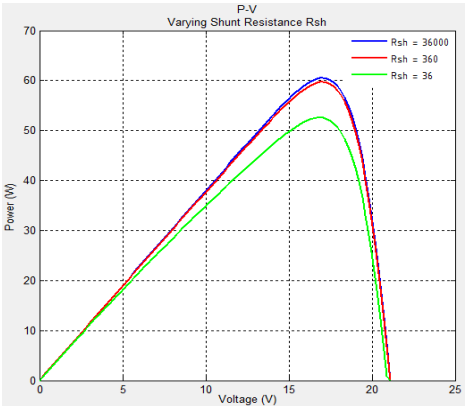

Figure 12. P-V characteristics of PV module at varying shunt resistance Rsh.

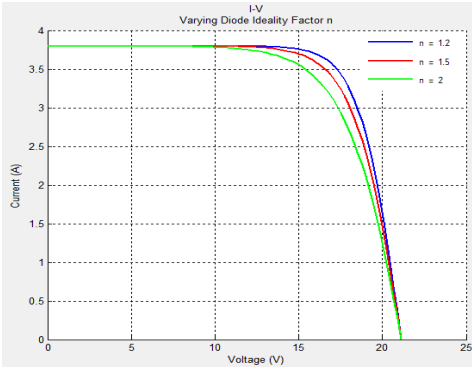

Figure 13. I-V characteristics of PV module at varying ideality factor n.

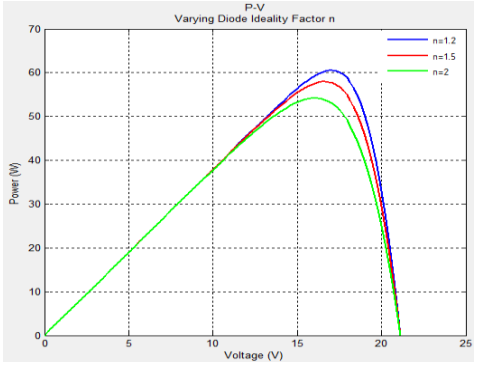

Figure 14. P-V characteristics of PV module at varying ideality factor n.

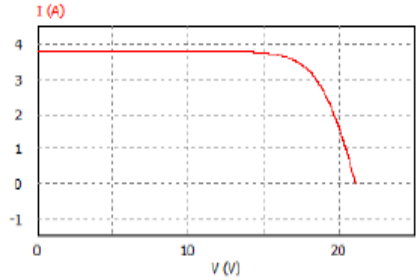

Figure 15. I-V curve obtained by the manufacturer datasheet.

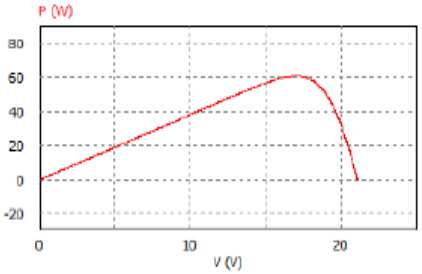

Figure 16. P-V curve obtained by the manufacturer datasheet.

Besides, the maximum power value result is similar (Pmax = 60.53W).

VI. Conclusions

The paper presents a model capable of predicting the behavior of the photovoltaic module BP MSX-60 under different effects. The chosen solar cell to our PV module is known as a five-parameter due to its intermediate complexity and reasonable accuracy. As a result of the study, I-V & P-V characteristics of a PV module change under various climate and physical parameters such as irradiation and temperature which affect the maximum power point. Furthermore, the obtained results are matching with the manufacturer's datasheet.

The future objective will expand on modeling a hybrid photovoltaic (PV) and thermal system for more efficiency (production of electricity and heat), to generate domestic hot water or to contribute to space heating.

References

[1] Arent, D. J., Wise, A., & Gelman, R. (2011). The status and prospects of renewable energy for combating global warming. *Energy Economics*, *33*(4), 584-593.

[2] Pandiarajan, N., & Muthu, R. (2011, January). Mathematical modeling of photovoltaic module with Simulink. In *2011 1st International Conference on Electrical Energy Systems* (pp. 258-263). IEEE.

[3] Bhuvaneswari, G., & Annamalai, R. (2011, December). Development of a solar cell model in MATLAB for PV based generation system. In *2011 Annual IEEE India Conference* (pp. 1-5). IEEE.

[4] Zina, B., Mouna, B. H., & Lassad, S. (2017). Photovoltaic cell Mathematical Modeling. *IJERT*, *6*(06).

[5] Salmi, T., Bouzguenda, M., Gastli, A., & Masmoudi, A. (2012). Matlab/simulink based modeling of photovoltaic cell. *International Journal of Renewable Energy Research (IJRER)*, *2*(2), 213-218.

[6] Lyden, S., Haque, M. E., Gargoom, A., & Negnevitsky, M. (2012, January). Modelling photovoltaic cell: Issues and operational constraints. In *2012 IEEE International Conference on Power System Technology (POWERCON)* (pp. 1-6). IEEE.

[7] Rusirawan, D., & Farkas, I. (2014). Identification of model parameters of the photovoltaic solar cells. *Energy Procedia*, *57*, 39-46

[8] Mesri, K., Chabaa, S., Jallal, M. A., & Zeroual, A. (2020, September). Modeling and simulation of the electrical behaviors of a photovoltaic module. In *National PhD students Days "3rd Edition"*.

[9] Jiang, Y., Qahouq, J. A. A., & Orabi, M. (2011, March). Matlab/Pspice hybrid simulation modeling of solar PV cell/module. In *2011 Twenty-Sixth Annual IEEE Applied Power Electronics Conference and Exposition (APEC)* (pp. 1244-1250). IEEE.

[10] Rajkanan, K., & Shewchun, J. (1979). A better approach to the evaluation of the series resistance of solar cells. *Solid-State Electronics*, *22*(2), 193-197.

[11] Rageh, M., & Soliman, F. (1990). Radiation damage in silicon solar cells by helium ions. In *Energy and the Environment* (pp. 351-356). Pergamon.

[12] Zekry, A., Shaker, A., & Salem, M. (2018). Solar cells and arrays: principles, analysis, and design. In *Advances in renewable energies and power technologies* (pp. 3-56). Elsevier.

[13] Motahhir, S., El Ghzizal, A., & Derouich, A. (2015). Modélisation et commande d'un panneau photovoltaïque dans l'environnement PSIM (Modeling and Control of a Photovoltaic Panel in the PSIM Environment). In *CIGIMS 2015*.

[14] *BP MSX 60 manufacturer datasheet*. Available at: https://pdf.dzsc.com/autoupload/41ea4270-37f9-44fb-bfd6-1bcb1678c121.pdf

Model-Driven Approach to Smart Grid Stability Prediction in Neo4j

Nenad Petrović[1], Issam Al-Azzoni[2], Abdullah Alqahtani[3]

[1]University of Niš, Faculty of Electronic Engineering, Niš, Serbia, nenad.petrovic@elfak.ni,ac.rs
[2]College of Engineering, Al Ain University, Al Ain, UAE, issam.alazzoni@aau.ac.ae
[3]College of Computer Engineering and Science, Prince Sattam bin Abduulaziz University, Alkharj, KSA, aq.alqahtani@psau.edu.sa

Abstract—**Stability is of utmost importance when it comes to smart grid infrastructures. Dramatic parameter variations and fluctuations can lead to wrong decisions, which could lead to fatal consequences. In this paper, we propose a model-driven methodology for highly automated machine learning approach to smart grid stability prediction. Stability prediction is treated as binary classification problem and implemented relying on Neo4j graph database's Graph Data Science Library (GDS). The proposed framework is evaluated on open, publicly available dataset. According to the achieved results, the predictive model shows better performance in terms of accuracy and execution time compared to other solutions based on deep learning. On the other side, the adoption of model-driven approach is beneficial when it comes to reusability and convenient experimentation compared to manual, non-automated design.**

Keywords – stability, smart grid, machine learning, model-driven enginnering, Neo4j

I. INTRODUCTION

Smart grids represent critical infrastructure and have utmost strategical importance for development worldwide [1, 2]. They support exploiting combinations of alternative sources like wind and solar power for clean and affordable energy. Unlike traditional power grids, here we have participant nodes (either households or enterprises) which are both energy consumers and producers at the same time, the so-called prosumers [2]. Therefore, the flow of energy in smart grids is considered bidirectional, as the participants which produce more energy than needed can offer and sell it to others for some specific price. However, unexpected fluctuations and changes as consequences of anomalies, failures or malicious attacks that alter the measured data about supply and demand within them could have fatal consequences to the environment. Therefore, smart grid stability determination in dynamic environment is crucial for their successful adoption. The goal is to detect disturbances and fluctuations, considering not only technical aspects, but taking into account the way the participants respond to the changes when it comes associated economic aspects, such as energy price.

In this paper, we focus on adoption of machine learning classification algorithm within Neo4j graph database for purpose of smart grid stability prediction. Moreover, we develop model-driven methodology leveraging code generation on top of it, in order to automatize data importing and writing complex queries, while enabling better reusability.

II. BACKGROUND AND RELATED WORKS

A. Smart Grid Stability Model: 4-Node Star

The stability model assumed in this paper is built upon the works from [2-4]. In what follows, the 4-node star architecture adopted in this paper will be introduced (depicted in Fig. 1).

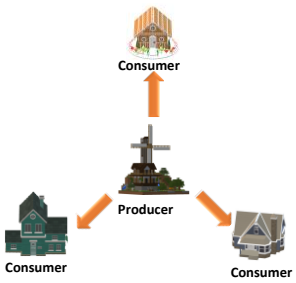

Figure 1. 4-node star smart grid architecture.

ISBN: 978-86-80593-73-9

The mathematical model based on differential equations aiming to identify instability of smart grid in case of 4-node star architecture was presented in [3, 4]. This kind of architecture assumes one power generation node that supplies energy to three other nodes which act as consumers. The following features are considered within the model: 1) total power balance – energy produced or consumed for each of the participant nodes; 2) reaction time – the time required to adjust energy production/consumption as response to changes of price 3) elasticity of energy price. Furthermore, in [2], a simulated, augmented dataset based on this model for purpose of evaluating deep learning-based approach to smart grid stability prediction using classification was created.

B. Neo4j

The template is used to format your paper and style the text. All margins, column widths, line spaces, and text fonts are prescribed; please do not alter them.

Neo4j [5] is graph-based database management system. The underlying model consists of three main concepts [6]: 1) nodes – represent entities form the domain of interest 2) connections between the nodes 3) properties – refers to key-value pair whose role is to provide further description of characteristics relevant to entities and their relations. It includes Cypher [7], which is a declarative query language used for retrieval of desired data from graph.

However, since the end of the last year, Graph Data Science (GDS) Library [8, 9] was added to Neo4j in order to enable functionalities executed over the data stores as graph. As for now, it covers only two machine learning techniques – link prediction and classification. While Community Edition of GDS is free, additional license is required in order to leverage more than 4 cores for further acceleration of calculations. Despite the fact that its set of machine learning-related capabilities is not so wide, it was shown that GDS outperforms several other solutions, especially when it comes to efficiency [9]. In [10], it was shown that classification in Neo4j can be used for hotel cancellation prediction relying on binary classification, while the execution time was superior to other data mining and deep learning-based solutions.

C. Classification and Graph Data Science Library

In this paper, classification capabilities offered by Graph Data Science Library within Neo4j for purpose of smart grid stability prediction are leveraged. The problem is treated as binary classification with two possible categorical outcomes (1 – stable, 0 – not stable).

Classification problem, in general, represents assignment of the correct label to the sample from collection of observations. For this purpose, a set of input variables known as feature properties is considered, while the output itself produced as outcome of this process is denoted as target property.

However, when it comes to supervised learning (as in this case), predictive model is trained by adjusting its parameters iteratively based on estimations obtained within dataset containing only samples with correct labels (train set). The distance from the correct value is estimated using error function, while the amount of weight parameter modification as a response depends on learning rate (also called penalty in Neo4j). After finishing the training phase, it is possible to evaluate model on either the same training data or dataset with previously unseen samples (test set). Neo4j supports two commonly used metrics in case of classification task:

$$Accurancy = \frac{TP + TN}{TP + TN + FP + FN}\ , \quad (1)$$

$$F - score = \frac{TP}{TP + \frac{1}{2}(FP + FN)}\ . \quad (2)$$

In these Eqs., variables represent different types of observation counts: true positive (TP), true negative (TN), false positive (FP) and false negative (FN).

In order to train a classification model using Neo4j's GDS Library, the method `gds.alpha.ml.nodeClassification.train` [11] is used. Before training, a set of algorithm parameters has to be set, while the most important ones are mentioned: `modelName` – how the model will be stored in catalog; `featureProperties` - names of independent variables; `targetPropery` – class label, the dependent variable name; holdoutFraction – percentage of dataset used for

evaluation; `metrics` – evaluation metric, either f1-score (two variants - `F1_WEIGHTED` and `F1_M ACRO`) or accuracy. Furthermore, it is required to set the model parameter, while GDS gives the ability to define multiple candidate models within `params`.

For each of the candidate models, the following values are adjustable: `penalty` – learning rate; `batchSize` – number of samples processed within one training iteration; `minEpochs` – minimum number iteration through the training set; `maxEpochs` – maximum number of training iterations; patience – maximum number of training iterations without performance improvement before stopping; `tolerance` – minimum acceptable error function value before stopping.

D. Model-Driven Engineering using Eclipse Modelling Framework (EMF)

Model-driven software engineering makes use of domain or system model-based representations with synergy of code generation in order to automatize or speed-up certain phases related to development of software assets. software development phases and usage scenarios [12]. Therefore, models can be used in many different ways and for various purposes, ranging from generation of documentation executable code to system verification and validation.

Reference [13] within Eclipse Modelling Framework (EMF) [14] for Java programming language provides the capabilities for construction of metamodels that can be further used as templates for user-specified instances, which are structured in a way that complies with the definition provided by the underlying metamodel. Moreover, it gives the ability to generate adapter classes that aid the manipulation of model instances, enabling parsing and traversal, which are crucial steps for retrieval of parameters and code generation. On the other side, we make use of PyEcore [15], which allows handling of EMF/Ecore metamodels and models in Python. It provides an API that is compatible with the original EMF implementation in Java. Using pyecore, the network planning problems can be represented as Ecore model instances. Furthermore, the instance of a model can be verified and imported in form of Python objects, which is suitable for automated solving of network planning problems

In this paper, model-driven approach is leveraged for automatization of two aspects relevant to classification in Neo4j: graph construction and classification query generation.

III. IMPLEMENTATION

A. Classification Workflow in Neo4j

In the first step, data is loaded from CSV file within Neo4j environment by executing `LOAD CSV WITH HEADERS FROM file` query, as it can be seen in Listing 1. We import the dataset under consideration in form of a collection of data rows labelled as “Stability”. Within the query, file: parameters is used to specify the corresponding path. On the other side, `MERGE` serves to choose the desired columns from the CSV file and set user-defined node label (“Stability” in this case).

```
LOAD CSV WITH HEADERS FROM
'file:///sg_stability.csv' AS row
WITH row WHERE row.stabf IS NOT NULL
MERGE (s:Stability {tau1: row.tau1,
...
stabf : row.stabf});
```

Listing 1. Loading CSV file into Neo4j as set of nodes.

Furthermore, a graph must be constructed from the loaded rows before classification model is trained. Method `gds.graph.create.cypher` is used for that purpose with corresponding parameters, as it can be seen in Listing 2. There are three mandatory parameters: 1) name of graph 2) Cypher query for node retrieval 3) Cypher query filtering the edges between nodes. However, in

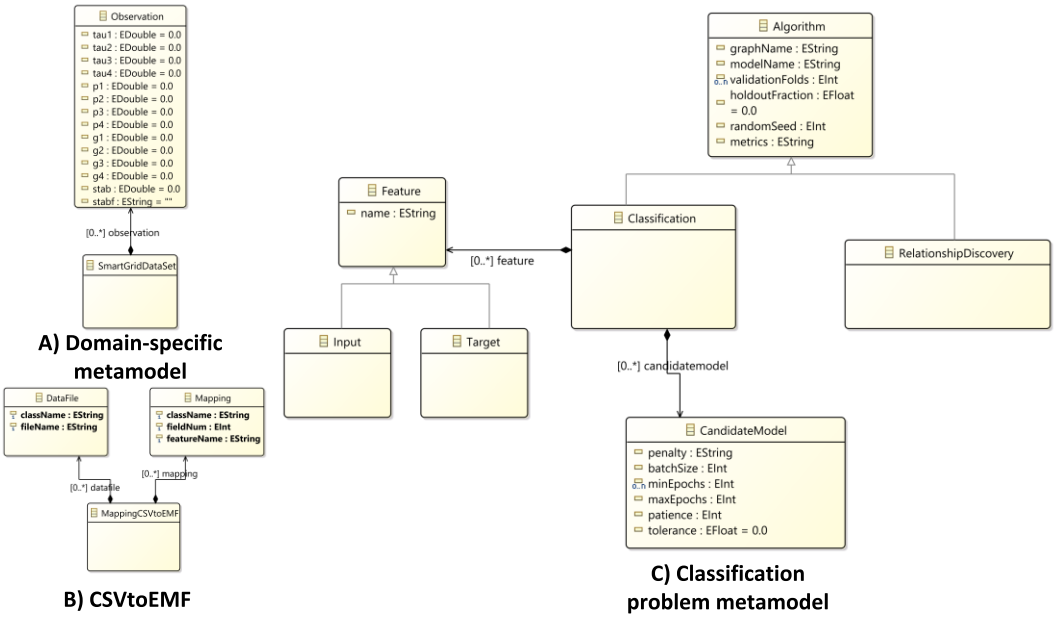

Figure 2. Metamodels: a) Smart grid stability dataset metamodel b) Data import metamodel - CSVtoEMF c) Prediction problem metamodel.

this paper we rely only on node properties for classification, while edges between nodes are not leveraged.

```
CALL gds.graph.create.cypher(
  'StabilityGraph',
  'MATCH (s:Stability) WHERE s.stabf is
NOT NULL RETURN id(s) as id,
   toFloat(s.tau1) as tau1,
   ...
   toInteger(s.stabf) as stabf',
  'MATCH (start:Stability)-[link]-
>(end:Stability)
RETURN ID(link) as link, ID(start) as
source, ID(end) as target'
)
```

Listing 2. Graph construction starting from collection of imported rows in Neo4j.

Once graph is constructed, we train the predictor based on classifier by executing `gds.alpha.ml.nodeClassification.train` procedure from Graph Data Science Library, in a way which is illustrated in Listing 3. The invocation command contains three main parts: 1) specification of classification algorithm's inputs and output – name of the input graph, name of classification model, set of independent variables, dependent variables and desired evaluation metric 2) setting the candidate model parameters 3) best model selection criteria – defining how the candidate models are compared and which one should be selected as the best and stored into Neo4j catalog under `modelName`.

```
CALL
gds.alpha.ml.nodeClassification.train('S
tabilityGraph', {
  modelName: 'stability_prediction',
  featureProperties:
        ['tau1', 'tau2',
          . . .
        'g4'],
  targetProperty: 'stabf',
  randomSeed: 3,
  holdoutFraction: 0.25,
  validationFolds: 5,
  metrics: [ 'ACCURACY'],
  params: [
        {
                penalty: 0.01,
                maxEpochs: 10,
                batchSize: 100
        },
        . . .
        {       penalty: 0.1 }
]
}) YIELD modelInfo
```

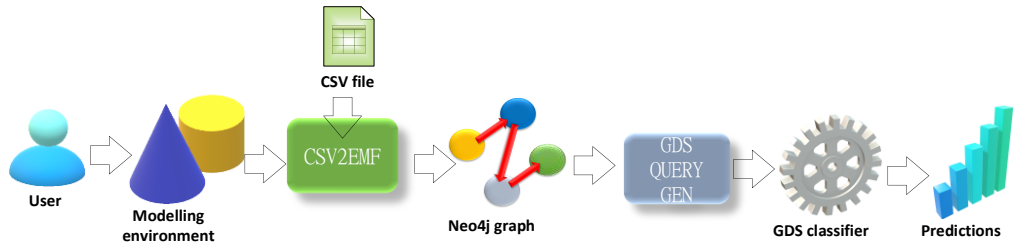

Figure 3. Model-driven framework for machine learning in Neo4j.

```
RETURN
  {penalty:
modelInfo.bestParameters.penalty} AS
winningModel,
  modelInfo.metrics.ACCURACY.outerTrain
AS trainGraphScore,
      modelInfo.metrics.ACCURACY.test AS
testGraphScore
```

Listing 3. Graph-based classifcator training command.in Neo4j.

B. *Model-Driven Framework*

The proposed model-driven framework covers two aspects – efficient data import [16] and Neo4j query generation. It consists of metamodels and code generation procedures.

Metamodels aiming the automated import of CSV data into Neo4j as depicted in Fig. 2a and 2b. Two of them are relevant for this task: domain-specific metamodel (2a) and CSVtoEMF [16] (2b). The first one describes the data of interest from a particular domain, which is smart grid stability in our case. The second gives the ability to define mapping between the corresponding CSV file rows and domain-specific features. Based on these two metamodels, the final outcome is to import the raw CSV file into Neo4j by generating the corresponding loading and graph construction queries based on model instances. The output of mapping are Neo4j queries for data import and graph creation, similar to code from Listings 1 and 2.

On the other side, another metamodel describing the classification problems (shown in Fig. 2c) is used for automated generation of machine learning-related queries executable by GDS in Neo4j. For that purpose, user has to provide corresponding parameters relevant to the specific machine-learning task, such as input and target variable or hyperparameters. At the moment, it covers the aspects related to classification-alike problems and relevant parameters. The generated output based on this metamodel is classification train function invocation, structured as shown in code within Listing 3.

In Fig. 3, the model-driven workflow leveraging metamodels and automated code generation is depicted. In the first step, user sets the desired CSV file path and selects which columns from the table to include. Additionally, for purpose of classification, it is also required to distinguish which columns represent input features and which one is the target output. The modeling is done within automatically generated GUI-enabled environment within Eclipse, provided by EMF. After that, the user-created model instance about CSV column mapping is leveraged to construct Cypher queries for data import and graph construction in Neo4j. Moreover, once the data is imported, classification training method invocation code is parametrized. Finally, user can input the generated queries into Neo4j, execute them and functional classifier for smart grid stability prediction will be created and stored into Neo4j catalog. The classifier is ready after that for predictions on previously unseen data.

IV. Experiments and Evaluation

For evaluation of the proposed approach, we used publicly available online dataset from [17]. It contains 60 000 observations from the simulated smart grid environment with the features described in Table I. It was split into training (75%) and test set (25%). Independent variables are in white fields, while the dependent variables are gray. The experiments were executed on a laptop with given capabilities: Intel i7 7700HQ 2.8GHz quad-core CPU, 16GB of DDR4 RAM and M1 SSD.

Moreover, an overview of experiment results for the proposed approach is shown in Table II. Several different aspects were taken into account, regarding different steps and components: classification model prediction

TABLE I. STABILITY PREDICTION DATASET OVERVIEW.

Variable	*Type*	*Description*
τ_1-τ_4	Real [0.5, 10]	Reaction time for each of the participant nodes. The first one (τ_1) is for the supplier node, while the others represent consumers.
p_1-p_4	Real consumers [-2.0, 0.5]	Nominal power which is consumed (negative) or produced (positive) by participant nodes. Here, p1 denotes producer, while the others are consumers, so the following Eq. holds: $p_1 = -(p_2 + p_3 + p_4)$
γ_1- γ_4	Real [0.05-1.00]	Coefficient of price elasticity for smart grid nodes.
stab	Real	Characteristic differential Eq. maximum real part of the root.
stabf	Categorical	if (stab>0) then stabf=1 else stabf=0

TABLE II. EXPERIMENT RESULTS OVERVIEW.

Aspect	*Component*	*Condition*	*Result*
Classification perfoamance	Predictive model	Learning rate 0.01 75% train 25% test	F1: 0.98 Acc.: 0.97
Execution time	Import CSV	60 000 records, 12 features	*4 min*
	Training		*8 s*
	ML query generation	5 candidate models	*0.57 s*
		10 candidate models	*0.68 s*
Speed-up	Model creation	User-created in Eclipse tool	283 s
	Auto. query	Code generation algorithm	1.32 s
	Manual query	Medium skill	1149 s
	Speed-up	Manual/ Auto	4.04 [times]

performance, execution time for various steps and speed-up achieved as outcome of adopting model-driven approach. The first column denotes the considered aspect of interest for evaluation. Furthermore, the second column denotes to which component experiment refers to. Moreover, the next column holds the description of relevant conditions for experiment related to the observed aspect. Finally, the last column shows the values obtained as a metric for the considered aspect.

Observing the obtained values, we can notice that classification model gives performance comparable, but slightly worse than approach presented in [3], but outperforms several other solutions based on deep learning discussed in [3]. On the other side, the execution time for training is faster than most of the methods relying on neural networks, confirming the efficiency of Neo4j, when it comes to classification task. Additionally, query execution time increases with the number of candidate models included. On the other side, the benefits of model-driven code generation were measured by comparing the sum of user-defined model instance creation and code generation to manual query construction by medium-skilled professional The speed-up in our case was a bit more than 4 times.

V. CONCLUSION AND FUTURE WORK

According to the experimentally obtained results on publicly available dataset, our approach to model-driven smart grid stability prediction seems promising. Classification model created as outcome of the experiments outperforms several deep learning-based solutions when it comes to both accuracy and execution time. On the other side, the adoption of model-driven code generation is highly beneficial, as it reduces the time necessary for manual query construction by about 4 times.

In future, it is planned to extend the approach for more machine learning tasks applicable in smart grid use cases (such as load forecast using regression), apart from classification and also for other data science frameworks, as well. Moreover, adopting similar approach to smart grid observability is also considered.

ACKNOWLEDGMENT

This work has been supported by the Ministry of Education, Science and Technological Development of the Republic of Serbia.

REFERENCES

[1] Bashir, A. K. et al. (2021). Comparative analysis of machine learning algorithms for prediction of smart grid stability. *International Transactions on Electrical Energy Systems, 31*(9), 1-23. DOI:10.1002/2050-7038.12706

[2] Breviglieri, P., Erdem, T. & Eken, S. (2021). Predicting Smart Grid Stability with Optimized Deep Models. *SN Computer Science. 2*(73), 1-12. DOI:10.1007/s42979-021-00463-5

[3] Schäfer, B. et al (2016). Taming instabilities in power grid networks by decentralized control. *Eur. Phys. J. Spec. Top. 225*, 569–582. DOI:10.1140/epjst/e2015-50136-y

[4] Arzamasov, V., Böhm, K. & Jochem, P. (2018). Towards Concise Models of Grid Stability. In *2018 IEEE International Conference on Communications, Control, and Computing Technologies for Smart Grids (SmartGridComm)* (pp.1-6). DOI:10.1109/SmartGridComm.2018.8587498

[5] *Neo4j*. Available on: https://neo4j.com/, last accessed: 01/11/2021.

[6] *Graph database concepts*. Available on: https://neo4j.com/docs/getting-started/current/graphdb-concepts/,last accessed: 30/11/2021.

[7] *The Neo4j Graph Data Science Library Manual v1.7*. Available on: https://neo4j.com/docs/graph-data-science/current/, last accessed: 30/11/2021.

[8] *Cypher Query Language*. Available on: https://neo4j.com/developer/cypher/, last accessed: 01/11/2021.

[9] *Announcing: Graph-Native Machine Learning in Neo4j!*. Available on: https://neo4j.com/blog/announcing-graph-native-machine-learning-in-neo4j/, last accessed: 01/11/2021.

[10] Petrović, N. (2021). Booking Cancellation Prediction Relying on Graph Database in Neo4j. In *IEEESTEC – 14th Student Projects Conference* (pp.209-212).

[11] *Node Classification*. Available on: https://neo4j.com/docs/graph-data-science/current/algorithms/ml-models/node-classification/, last accessed: 01/11/2021.

[12] Brambilla, M., Cabot, J. & Wimmer, M. (2017). Model-Driven Software Engineering in Practice, 2nd Edition. Morgan & Claypool Publishers.

[13] *Eclipse Modeling Framework*. Available on: https://www.eclipse.org/modeling/emf/, last accessed: 30/11/2021.

[14] *Ecore*. Available on: https://wiki.eclipse.org/Ecore , last accessed: 30/11/2021.

[15] *PyEcore: A Pythonic Implementation of the Eclipse Modeling Framework*. Available on: https://github.com/pyecore/pyecore, last accessed: 30/11/2021.

[16] Al-Azzoni, I., Petrovic, N., & Alqahtani, A. (2021). A Utility to Transform CSV Data into EMF. In *International Conference on Software Defined Systems (SDS 2021)* (pp.1-6).

[17] *Predicting Smart Grid Stability with Deep Learning*. Available on: https://www.kaggle.com/pcbreviglieri/predicting-smart-grid-stability-with-deep-learning , last accessed: 30/11/2021.

Biochemical Methane Potential and Biogas Yield Prediction for Diversified Biomass

Divya Wadekar[1], Somnath Nandi[2]

[1,2]Department of Technology, Savitribai Phule Pune University, Pune, India,
divyawadekar123@gmail.com[1], somnath.nand11@gmail.com[2]

Abstract—**There is an increasing need of renewable energy sources due to growing energy consumption and depleting fossil supplies. It is essential to develop energy source which offers considerable environmental benefits and also are economical. Biogas is being used as renewable source of energy since more than 100 years and biogas production has attracted interest of many industries and researchers in recent time. A well maintained and highly efficient biogas plant follows optimal procedure and biogas potential of the feed stock must be known. This is accomplished through Biochemical Methane Potential (BMP) tests, which are expensive and time-consuming processes. This study reports development of multiple linear regression models (MLR) for prediction of biochemical methane potential (BMP), Biogas yield (Yb) and methane yield (Ym) from diversified biomasses including energy crops, animal manures and grassland specific plants, using dataset available in open literature. Systematic studies regarding influence of chemical components on biogas yield from different biomass are reported, subsequently developed models were validated using unseen data-set.**

Keywords - biogas yield, methane yield, multiple linear regression model, biochemical methane potential

I. INTRODUCTION

Ever increasing global demand of energy resulting to energy crisis, depletion of fossil fuels and environmental pollution. Hence, it is need of the hour to focus on renewable and sustainable resources. Renewable sources of energy not only produce energy, heat and transport fuel but they also offer environmental benefits over the conventional energy resources. The increasing demand of sustainable energy could be met by effective use of biomass for biogas production. Biogas is being used as a renewable source of energy for more than 100 years [1]. Production of 'green energy' from biogas offers environmental and economic benefits, and grabbed attention of researchers. Consequently, many new plants of biogas production are established across the globe.

Biogas production is the process of conversion or degradation of organic substrates or wastes in absence of oxygen [1, 2]. The end product of anaerobic digestion is biogas: a mixture of methane, carbon dioxide majorly. The typical biogas composition in an anaerobic co-digestion consists of 55-80% of methane, 20-45% of carbon dioxide and some other gases [2, 3]. The biogas production using anaerobic digestion depends primarily on the potential of biomass to produce biogas. In order to achieve successful plant operation biogas potential of a feedstock must be known beforehand. This is accomplished by various methods, one of them is Biochemical Methane Potential (BMP) test, [2, 3] determining maximum methane production from organic matter of the biomass. However, BMP measurements are very costly and time consuming. They take up to 90 days for standard incubation process [4, 6]. To evaluate BMP quickly and reliably theoretical methods of prediction of BMP have been assessed by different researchers and institutes [3-7].

This work reports development of multiple linear regression models (MLR) to predict biochemical methane potential (BMP), biogas yield (Y_b) and methane yield (Y_m) using different biomasses. Reference [8] were used to develop BMP prediction models and dataset from [9] is used for validation of BMP prediction model.

ISBN: 978-86-80593-73-9

Impact of different chemical components were also observed on ultimate biogas yield. Subsequently, suitable MLR models were also developed for effective prediction of Y_b and Y_m utilizing available open datasets from [10].

II. METHODOLOGY

A. Selection of the Data

Datasets from [8] and [10] are selected for the development of MLR model. A simple regression model was developed to predict BMP using chemical components of different biomass using data from [8]. Chemical composition of ten energy crops and ten animal manures were taken and their influence on BMP was examined. Chemical composition of these energy crops and animal manures were utilized to develop MLR model for predicting BMP. The second dataset is taken from [10] which includes values of chemical components of fifty-five different grassland specific plants. In their work, they have performed field experiments under defined conditions and have created a dataset with grassland plant species. Six typical agricultural grassland plant species were selected: four grass species namely *Lolium perenne, dactylis glomerata, Poa pratensis. Festuca pratesis* and two legume species titled *Trifolium pratense, Trifolium repen* were studied [10]. The complete dataset is used to develop the MLR model for Y_b and Y_m prediction.

TABLE I. BMP AND OTHER CHEMICAL COMPONENTS OF ENERGY ANIMAL MANURE FROM TRIOLO ET AL.(2011)[8].

Biomass	**DM**	**VS**	**TKN**	**Lignocellulose**	**Hemicellulose**	**Cellulose**	**Lignin**	**BMP**
	(g/kg w/w)	(g/kg w/w)	(g/kg w/w)	% of DM	% of DM	% of DM	% of DM	NL/(kg/ VS)
Perennial grass	288.2	77.2	5.53	60.79	25.99	29.05	5.75	271
Perennial grass	235	52	6.54	58.33	28.25	26.86	3.22	410.5
Dried wild grass	934.1	880.2	10.82	64.85	22.89	35.99	5.98	306.3
Grass	187.4	32.3	4.8	59.54	27.30	29.97	2.27	373.5
Grass	180.2	28.9	3.55	47.72	20.93	25.56	1.23	420.8
Grass	175.3	27.7	3.53	51.73	24.39	25.38	1.96	438.9
Maize	387.5	145.5	4.84	63.82	37.68	23.74	2.40	399.4
Maize	299.2	85.6	2.96	65.77	35.92	26.86	2.98	405.3
Maize	278.9	74.5	5.62	60.86	36.73	22.31	1.81	360.5
Straw	936.9	906.3	3.45	83.76	28.38	47.97	6.41	289.5

(DM:Dry Matter, VS:Volatile Solid, TKN:Total Kjeldahl Nitrogen)

TABLE II. BMP AND OTHER CHEMICAL COMPONENTS OF ENERGY ANIMAL MANURE FROM TRIOLO ET AL.(2011)[8].

(DM: dry matter, VS:Volatile Solid,TKN:Total Kjeldahl Nitrogen, man:manure, fatt:fatteners)

Biomass	**DM**	**VS**	**TKN**	**Lignocellulose**	**Hemicellulose**	**Cellulose**	**Lignin**	**BMP**
	(g/kg w/w)	(g/kg w/w)	(g/kg w/w)	% of DM	% of DM	% of DM	% of DM	NL/(kg/ VS)
Piglet man.	16.2	11.8	1.13	5.11	0.97	3.76	0.38	417.2
Sow man.	49.0	38.2	3.71	47.11	15.36	21.41	10.34	213.8
Sow man.	109.4	90.2	3.56	47.59	14.79	23.22	9.58	248.8
Pig fatt.	119.6	100.6	5.63	47.10	15.65	24.16	7.30	284.8
Pig fatt.	9.4	5.2	1.51	NA	NA	1.15	0.51	345.3
Calf man.	154.6	142.3	1.65	71.18	17.74	42.78	10.65	198.7
Calf man.	322.6	295.2	2.19	72.92	22.24	42.97	7.76	237.0
Cattle man.	115.6	94.3	1.90	36.46	7.97	16.58	11.91	197.0
Cattle man.	173.6	96.8	1.82	25.63	3.56	15.58	6.49	223.6
Inoculum	34.7	22.9	3.90	25.27	3.41	10.65	11.21	142.1

TABLE III. CHEMICAL COMPOSITION, BIOGAS AND METHANE YIELD OF 55 SAMPLE FROM DANDIKAS ET AT. (2018)[10].

Sr. No.	Sample	XP	XF	NfE	XL	ST	RS	HC	CL	ADL	OR	NFC	Y_b	Y_m
1	G-1	138	189	643	30	ND	263	213	235	26	95	358	676	356
2	G-2	129	179	660	31	ND	292	198	216	14	120	412	645	345
3	G-3	108	205	657	30	ND	275	226	247	21	93	368	637	333
4	G-4	125	236	602	37	ND	146	277	259	62	94	240	547	291
5	G-5	144	213	629	14	ND	215	272	246	22	86	301	572	308
6	G-6	152	192	617	39	ND	198	197	261	36	118	315	655	354
7	G-7	170	178	611	40	ND	198	194	242	36	120	318	708	385
8	G-8	121	239	617	23	ND	162	191	296	36	171	333	698	374
9	G-9	220	245	499	36	ND	63	319	286	18	53	121	584	316
10	G-10	191	251	523	35	ND	57	299	296	26	92	153	577	313
11	G-11	163	231	571	34	ND	109	291	271	25	107	216	597	322
12	G-12	152	242	592	14	ND	160	295	267	28	83	243	606	328
13	G-13	161	185	619	35	ND	217	207	242	25	113	330	629	346
14	G-14	127	226	623	24	ND	162	166	288	37	192	357	652	349
15	G-15	149	243	580	28	ND	130	296	289	18	909	220	642	345
16	G-16	97	265	605	33	ND	108	310	315	25	112	220	594	306
17	G-17	175	240	543	41	ND	76	300	267	39	90	178	547	298
18	G-18	158	247	582	13	ND	135	343	270	25	57	192	549	302
19	G-19	169	176	618	37	ND	225	194	231	22	122	346	663	357
20	G20	123	201	649	27	ND	252	206	251	17	125	376	651	342
21	G-21	130	179	659	32	ND	263	206	228	14	128	391	663	353
22	G-22	90	214	671	24	ND	261	243	265	16	101	361	662	352
23	G-23	79	267	630	23	ND	164	282	310	28	114	278	599	319
24	G-24	192	243	525	40	ND	89	289	274	37	79	168	612	362
25	G-25	155	204	626	15	ND	224	271	238	22	76	300	620	335
26	G-26	183	196	577	43	ND	182	215	240	37	101	282	679	377
27	G-27	164	221	574	41	ND	165	246	253	26	105	270	620	338
28	G-28	159	193	604	44	ND	187	219	245	36	109	297	696	379
29	G-29	124	222	619	35	ND	173	219	274	38	137	310	614	330
30	G-30	108	301	555	36	ND	87	305	321	37	107	194	570	308
31	G-31	109	327	527	37	ND	24	304	352	39	130	158	536	290
32	G-32	167	259	557	18	ND	86	304	306	36	83	169	524	288
33	G-33	182	208	576	33	ND	154	223	258	31	119	273	636	345
34	G-34	129	248	596	27	ND	141	244	294	39	126	267	603	329
35	G-35	108	274	594	24	ND	136	322	303	43	64	200	588	319
36	G-36	120	319	548	13	ND	51	401	358	39	16	68	488	269
37	G-37	152	264	572	12	ND	123	361	297	28	27	150	572	310
38	G-38	139	197	631	33	ND	224	222	251	24	108	332	621	336
39	G-39	134	225	612	29	ND	179	236	274	20	128	307	652	352
40	G-40	122	227	622	30	ND	172	254	279	21	121	294	662	359
41	G-41	109	243	621	28	ND	163	254	294	21	132	295	655	351
42	G-42	131	273	558	38	ND	105	295	282	50	99	204	574	305
43	G-43	157	251	579	13	ND	122	305	298	22	84	206	545	297
44	L-1	162	185	631	21	74	116	64	245	51	266	456	577	318
45	L-2	157	198	627	19	70	109	76	256	55	258	437	540	297
46	L-3	174	195	609	22	88	99	88	228	52	248	435	524	287
47	L-4	209	196	570	25	88	78	147	225	59	169	336	539	292
48	L-5	178	219	581	21	70	99	137	258	51	184	354	537	292
49	L-6	178	241	557	24	73	79	129	293	64	161	313	535	290
50	L-7	227	154	588	31	53	95	104	212	51	227	375	639	352
51	L-8	191	182	602	25	52	132	99	215	41	246	429	585	319
52	L-9	207	178	590	25	71	98	77	235	53	235	404	586	325
53	L-10	163	182	629	26	71	90	62	247	53	289	449	538	289
54	L-11	223	195	540	42	99	55	183	260	52	88	241	578	286
55	L-12	285	183	503	30	79	60	140	198	74	135	275	506	277

(XP: Crude protein, XF: Crude fibre, NfE: nitrogen-free extract, XL: Crude lipid, ST: starch, RS: reducing sugar, HC: Hemicellulose, CL: cellulose, ADL: Acid detergent Lignin, OR: Organic residue, NFC: Non-fiber carbohydrates)

B. Data Segregation and Preparation

Selected datasets are divided into two categories, training dataset and testing datasets. Training datasets are used for development of MLR models whereas testing datasets are used for validation of developed models. As mentioned earlier, dataset from [8], consisting of energy crops and animal manure is used for prediction of BMP and dataset from [10], consisting of grassland specific plants, are used for prediction of Y_b and Y_m . Validation of developed models for prediction of BMP is carried out using unseen dataset from [9]. Dataset includes chemical composition of six dairy cow manures and ten maize varieties and their respective methane yields. Similarly, validation of developed models for prediction of Y_b and Y_m is carried out using dataset from [10], where dataset includes chemical composition, methane and biogas yields of average values of nine cultivars.

C. Development of Multiple Regression Model

Multiple linear regression (MLR) analysis is used to asses relationship between one dependent variable and two or more independent variables. Here, BMP, Y_m or Y_b are considered as dependent variables and chemical compounds of given biomass are considered as independent variables. To define a relationship between BMP and chemical components of particular biomass, with one dependent and multiple number of independent variables,

$$Y_{(model_i)} = B_0 + B_1X_1 + B_2X_2 + \\ +B_3X_3 \ldots..B_nX_n \quad , \qquad (1)$$

where, X_1, X_2 ,X_3 ,and X_n are chemical components of biomass and B_0, B_1, B_2, B_3 and B_n are constants to be determined.

There might be some mismatch of the model with the actual field data and hence the error is defined as,

$$E^2 = \sum[Y(model_i) - Y(actual_i)]^2 , \qquad (2)$$

where, E is error, $Y(\text{model}_i)$ is modeling equation for BMP and $Y(\text{actual}_i)$ is observed or measured value of BMP.

Substituting (1) in (2)

$$E^2 = \sum[\, B_0 + B_1X_1 + B_2X_2 + \\ +B_3X_3 \ldots..B_nX_n - Y(actual_i)]^2 . \qquad (3)$$

Solving (3) with conventional method of partial differentiation, we get,

$$\begin{bmatrix} N & \sum x_{i1} & \sum x_{i2} & \cdots & \sum x_{in} \\ \sum x_{i1} & \sum x_{i1}^2 & \sum x_{i1}x_{12} & \cdots & \sum x_{i1}x_{in} \\ \sum x_{i2} & \sum x_{i1}x_{i2} & \sum x_{i1}^2 & \cdots & \sum x_{i2}x_{in} \\ \vdots & \vdots & \vdots & \ddots & \vdots \\ \sum x_{in} & \sum x_{i1}x_{in} & \sum x_{i2}x_{in} & \cdots & \sum x_{in}^2 \end{bmatrix} \cdot \begin{bmatrix} B \\ B_1 \\ B_2 \\ \vdots \\ B \end{bmatrix} = \begin{bmatrix} y_i \\ x_{i1}y_i \\ x_{i2}y_i \\ \vdots \\ x_{in}y_i \end{bmatrix}$$

The defined matrices are then solved in MATLAB environment to obtain the model coefficients B_0, B_1, B_2, B_3 and B_n and to formulate the overall expression of the desired multiple linear regression models.

D. Statistical Analysis

All the values of Lignin cellulose and hemicellulose, crude fiber, crude protein and crude lipid are taken in g/(Kg VS). BMP, Y_m and Y_b values are taken in NL/(Kg VS). Relationship is obtained between BMP/ Y_b / Y_m and independent variables using multiple linear regression analysis performed in MATLAB. Statistical analysis is performed using Excel the model and model is further improved by adding more regressors in the equation for more accuracy and better prediction of the parameters. R^2 and Relative Root Mean Square Error (RRMSE) for each model is calculated using Excel. The formula used to calculate RRMSE is,

$$RRMSE = 1/O \left[\sqrt{\sum (P_i - O_i)^2 / n}\right], \qquad (4)$$

where P_i is predicted value, O_i is observed value and O is mean of observed values and n is number of data points.

III. Results and Discussion

A. Prediction of BMP using Energy Crops and Animal Manure

Multiple regression models are developed to predict BMP for both of the biomasses combined (Energy crops and Animal manure). Lignin and cellulose values from chemical composition are taken as independent variable in g/(kg VS) and BMP is taken as dependent variable in NL/Kg VS. Relationship is obtained between Lignin, cellulose and BMP using Excel and MATLAB. Developed relationships are shown in Table IV.

Statistical regression analysis is performed in Excel using regression in data analysis tool. R-square values for relationships obtained between BMP and Lignin, cellulose are observed and compared. Relative root mean square error is calculated for all developed models. As given in the Table V, R^2 value for model 2 is 0.823 which is the highest among three. R^2 value for model 1 is found to be 0.8077.

TABLE IV. Developed models for BMP prediction using multiple regression.

Model 1	BMP = 358.13 - 2.175Lignin + 0.2111Cellulose + 0.0047Lignin² - 0.00003812cellulose²
Model 2	BMP = 370.322- 1.8263 Lignin + 0.1222 Celluose + 0.00121 Lignin² - 0.0000376 Cellulose² + 0.0007372 Lignin.Cellulose
Model 3	Log BMP = 2.1856 - 0.321 Log Lignin + 0.3358 Log Cellulose

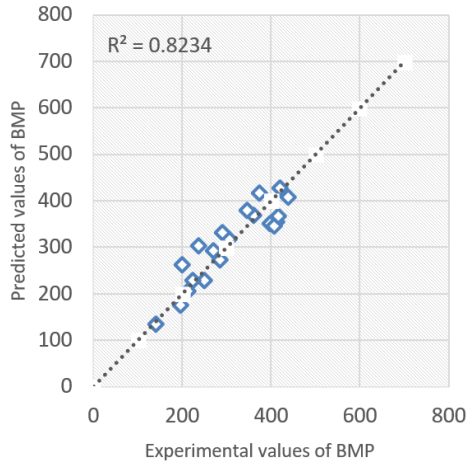

Figure 1. Predicted values of BMP by Model 2 versus experimental Values of BMP in NL/kg VS.

To improve R^2 value and accuracy of the model, square of lignin and cellulose and combination of their multiplication is applied as regressor in model 2. Model 2 is seen to be slightly improved by this addition. As model 3 shows least R^2 value and increased RMSE % it could not be used significantly for the prediction of the BMP. Fig.1. shows the plot between predicted values of BMP by model 2 and experimental values from the dataset.

B. Prediction of Y_b using Grassland Specific Plants

Dataset from [10] is used to obtain a relationship between Y_b and chemical components of different biomasses using Excel and MATLAB. All the values of chemical components are taken in g/(kg VS) and values of Y_b are taken in L/(kg VS). Developed models for prediction of the Y_b are shown in Table VI.

Statistical regression analysis is performed for above models in Excel using regression in data analysis tool. Relative root mean square error is calculated for all the developed models for Y_b prediction.

TABLE V. Regression statistics for BMP prediction models.

Statistics	Model 1	Model 2	Model 3
Multiple R	0.898	0.907	0.887
R square	0.8077	0.823	0.787
Adjusted R	0.756	0.760	0.762
Observations	20	20	20
RRMSE %	12.56	12.04	15.20

TABLE VI. Developed models for prediction of *Yb*.

Model 1	*Yb* = 809.41 - 2.2771 ADL - 0.222 CL - 0.2263 HC
Model 2	*Yb* = 572.2429 + 2.5936 ADL - 0.30377 CL + 1.246 HC - 0.05954 ADL² + 0.000271 CL² - 0.00342 HC²
Model 3	*Yb* = 528.519 + 3.6073 ADL + 0.3864 CL + 0.6951 HC - 0.00103 ADL² + 0.003338 CL²- 0.04316 HC² - 0.02841 ADL.CL - 0.00529 CL.HC + 0.021557 ADL.HC
Model 4	*Yb* = 773.3899 - 1.3577 ADL + 0.7574 CL + 0.0827 HC - 0.45121 XP - 1.5039 XF + 2.078 XL
Model 5	*Yb* = 587.56 + 2.7546 ADL + 2.698 CL + 1.0268 HC - 1.3269 XP - 2.7399 XF + 0.7363 XL - 0.0518 ADL² - 0.00382 CL² - 0.00229 HC² + 0.003166 XP² + 0.003143 XF² + 0.000879 XL²

TABLE VII. TABLE VII. REGRESSION STATISTICS FOR PREDICTION OF Y_B.

Statistics	Model 1	Model 2	Model 3	Model 4	Model 5
Multiple R	0.677	0.823	0.841	0.835	0.877
R square	0.458	0.678	0.707	0.698	0.769
Adjusted R	0.426	0.638	0.649	0.660	0.703
Observat.	55	55	55	55	55
RRMSE (%)	7.21	5.01	4.77	4.85	4.24

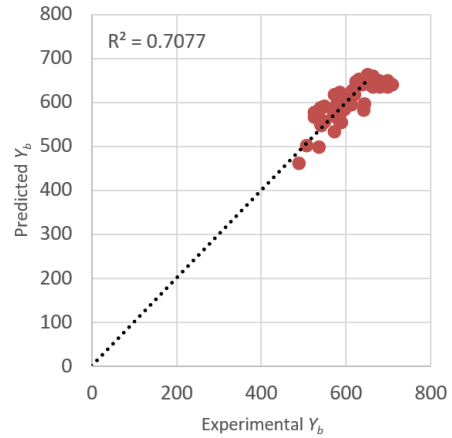

a)

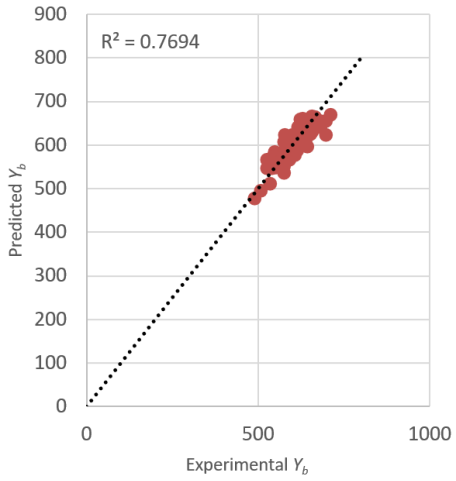

b)

Figure 2. Predicted values of Y_b by (a) Model 3 and (b) Model 5 versus Experimental Values of Y_b in L/kg VS.

As shown in the Table VII., Model 5 is giving the highest R^2 of 0.769, as compared to other models. Model 1, 2 and 3 predicts the effect of lignin, cellulose and hemicellulose on yield of biogas. Addition of crude protein (XP), crude fibre (XF) and crude lipid (XL) and their squares as regressors shows significant improvement in R^2 value. Predicted values of Y_b by model 3 and model 5 models are plotted against experimental values of Y_b As shown in Fig.2.

C. Prediction of Y_m using Grassland Specific Plants

Similarly, a relationship is obtained between Y_m and chemical components using multiple regression in Excel and in MATLAB. All the values of chemical components are taken in g/(kg VS) and values of Y_m are taken in L/(kg/VS). Table VIII. Shows developed of Y_m models using multiple regression for prediction Statistical analysis is performed to estimate the R^2 values. Table IX. Shows the statistical analysis for all the developed models. Model 1,2 and 3 give the relation between Y_m and Lignin, cellulose and hemicellulose. Addition of crude protein (XP), crude fiber (XF) and crude lipid (XL) to the modeling equation gives slightly improved R^2. RMSE % has also observed to be decreasing from Model 1 to Model 5. Fig. 3 shows the trend line obtained by predicted values of Y_m by model 3 and 5.

TABLE VIII. DEVELOPED MODELS FOR PREDICTION OF $Y_{M.}$.

Model 1	Y_m = 437.1518 - 1.3728 ADL - 0.14903 CL - 0.106 HC
Model 2	Y_m = 326.6828 + 2.148 ADL - 0.279 CL + 0.5824 HC - 0.04075 ADL² + 0.000214 CL² - 0.00158 HC²
Model 3	Y_m =320.11 + 3.696 ADL - 0.399 CL + 0.568 HC - 0.036 ADL² + 0.0033 CL² - 0.00021 HC² - 0.0169 ADL.CL - 0.00387 CL.HC + 0.0105 HC.ADL
Model 4	Y_m =404.05 - 0.788 ADL + 0.343 CL + 0.0283 HC - 0.162 XP - 0.694 XF + 1.064 XL
Model 5	Y_m =322.412 + 2.08 ADL + 0.862 CL + 0.47 HC - 0.439 XP - 1.067 XF + 0.6214 XL- 0.036 ADL²- 0.0012 CL² - 0.00106 HC² + 0.00109 XP² + 0.0011 XF² - 0.00325 XL²

TABLE IX. REGRESSION STATISTICS FOR YM PREDICTION MODEL.

Statistics	Model 1	Model 2	Model 3	Model 4	Model 5
Multiple R	0.637	0.781	0.797	0.770	0.817
R square	0.406	0.610	0.635	0.593	0.667
Adjusted R	0.371	0.561	0.562	0.542	0.572
Observat.	55	55	55	55	55
RRMSE (%)	6.78	5.50	5.34	5.62	5.08

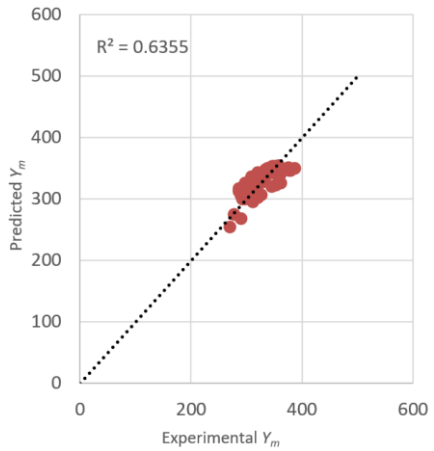

a)

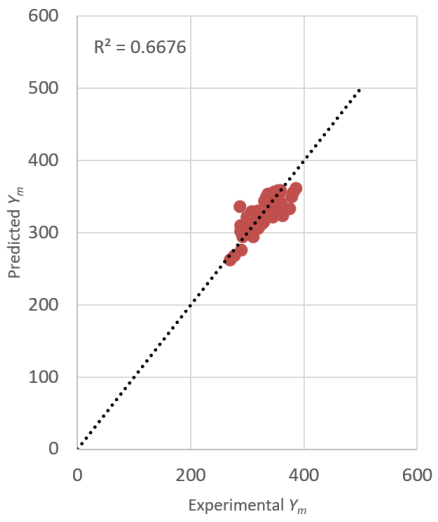

b)

Figure 3. Predicted values of Y_m by (a) Model 3 and (b) Model 5 versus Experimental Values of Y_m in L/kg VS.

D. *Validation of Developed MLR Models*

We have tested 16 data points from [9] to validate developed models for BMP. It included chemical composition of 10 manures used as a biomass and Methane yield. Methane yield is given in NL/(Kg VS) whereas Lignin and cellulose are converted into g/(kg VS). R^2 is found to be higher in model 3 (R^2 = 0.859) as compared to model 2 (R^2=0.788) and model 1 (R^2 = 0.820) from Table X. However, RMSE % is also high in model 3, which indicates the low accuracy, therefore model 3 cannot be prominently a significant model. Considering a least value of RMSE % for model 2, a trend line is obtained between predicted values of methane yield Experimental values as shown in Fig. 4.

For validation of Y_m and Y_b prediction model, we tested 9 data points from [10]. Chemical composition of average values of 9 cultivars is given in the dataset (N = 9). All the values of chemical components are taken in g/(Kg VS) and Y_b and Y_m are taken in L/(Kg VS). Statistical and regression analysis is done using Excel and RMSE % is calculated for all the models using chemical composition of 9 cultivars (Table XI.). R^2 values for prediction of Y_b ranged between 0.584 and 0.902, whereas R^2 values for prediction of Y_m ranged.

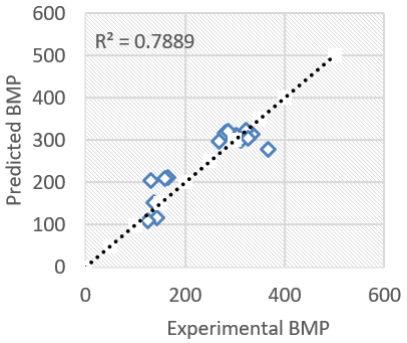

Figure 4. Validation of BMP prediction model: Predicted values of BMP by Model 2 versus Experimental Values of BMP in NL/kg VS

TABLE X. VALIDATION OF BMP PREDICTION MODEL.

	R^2	RMSE %	Intercept
Model 1	0.8201	16.903%	92.253
Model 2	0.7889	15.909%	60.466
Model 3	0.8592	17.773%	111.81

TABLE XI. VALIDATION OF Y_B AND Y_M PREDICTION MODEL.

	Statistical analysis for Y_b prediction		Statistical analysis or Y_m prediction	
	R^2	RRMSE %	R^2	RRMSE %
Model 1	0.584	4.53 %	0.607	2.96 %
Model 2	0.875	2.63 %	0.751	3.20 %
Model 3	0.902	1.91 %	0.774	2.84 %
Model 4	0.879	1.17 %	0.778	2.21%
Model 5	0.885	2.01 %	0.756	2.8%

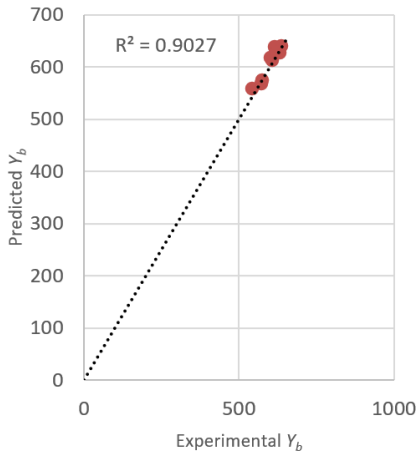

Figure 5. Validation of Yb prediction model: Predicted values of Yb by Model 3 versus Experimental Values of Yb in L/kg VS.

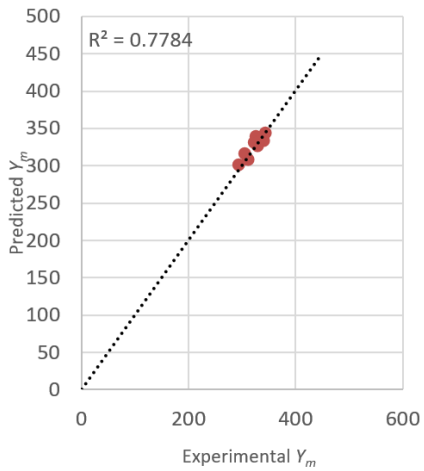

Figure 6. Validation of Ym prediction model: Predicted values of Ym by Model 4 versus Experimental Values of Ym in L/kg VS.

between 0.607 and 0.778. For prediction of Y_b, highest value of R^2 is given by Model 3 as shown in Fig. 5. However, RMSE is observed to be least in the model 4. In case of Y_m prediction models addition of XP, XF and XL in model 4 has slightly increased the accuracy. However, R^2 values of model 3 and 4 are almost equal (R^2 = 0.774 and R^2 = 0.778). Fig. 6 shows the graph of predicted values of Y_m by model 4.

IV. CONCLUSION

BMP prediction model was observed to be improved when a term, lignin and cellulose combined was added. Validation of BMP models show that there is a scope of improvement in accuracy of the model.

Study of Y_b and Y_m models confirms that crude protein, crude fiber and crude lipid has great influence on prediction of Y_b as well as Y_m. Model could explain up to 76 % of data for Y_b model within 95% accuracy, when crude protein, crude fiber and crude lipid was included in model. However, some more parameters or a more complex Y_m model could be targeted as there is scope of improvement for the presently developed model predicting Y_m of the data.

ACKNOWLEDGMENT

Support rendered by administrative and technical staff members of Department of Technology, Savitribai Phule Pune University are gratefully acknowledged.

REFERENCES

[1] Møller, H. B., Sommer, S. G., & Ahring, B. K. (2004). Methane productivity of manure, straw and solid fractions of manure. *Biomass and bioenergy*, *26*(5), 485-495.

[2] Oslaj, M., Mursec, B., & Vindis, P. (2010). Biogas production from maize hybrids. *Biomass and bioenergy*, *34*(11), 1538-1545.

[3] Hagos, K., Zong, J., Li, D., Liu, C., & Lu, X. (2017). Anaerobic co-digestion process for biogas production: Progress, challenges and perspectives. *Renewable and Sustainable Energy Reviews*, *76*, 1485-1496.

[4] Gunaseelan, V. N. (2007). Regression models of ultimate methane yields of fruits and vegetable solid wastes, sorghum and napiergrass on chemical composition. *Bioresource technology*, *98*(6), 1270-1277.

[5] Thomsen, S. T., Spliid, H., & Østergård, H. (2014). Statistical prediction of biomethane potentials based on the composition of lignocellulosic biomass. *Bioresource technology*, *154*, 80-86.

[6] Bartocci, Pietro, Sara Massoli, Mauro Zampilli, Federia Liberti, Yan Yunjun, Qing Yang, Haiping Yang et al. (2021). Substrate Characterization in the Anaerobic Digestion Process. In *Bioenergy Research: Basic and Advanced Concepts* (pp. 307-342). Springer, Singapore.

[7] Achinas, S., & Euverink, G. J. W. (2016). Theoretical analysis of biogas potential prediction from agricultural waste. *Resource-Efficient Technologies*, *2*(3), 143-147.

[8] Triolo, J. M., Sommer, S. G., Møller, H. B., Weisbjerg, M. R., & Jiang, X. Y. (2011). A new algorithm to characterize biodegradability of biomass during anaerobic digestion: influence of lignin concentration on methane production potential. *Bioresource technology*, *102*(20), 9395-9402.

[9] Amon, T., Amon, B., Kryvoruchko, V., Zollitsch, W., Mayer, K., & Gruber, L. (2007). Biogas production from maize and dairy cattle manure—influence of biomass composition on the methane yield. *Agriculture, Ecosystems & Environment*, *118* (1-4), 173-182.

[10] Dandikas, V., Heuwinkel, H., Lichti, F., Drewes, J. E., & Koch, K. (2018). Predicting methane yield by linear regression models: a validation study for grassland biomass. *Bioresource technology*, *265*, 372-379.

Effects of Phone Covers on the Thermal Behaviour of a Smartphone when Performing Common Tasks

Chibuoke T.Eneh[1], Howard O. Njoku[2], Mtamabari S.Torbira[3]

[1]Sustainable Energy Engineering Research Group, Department of Mechanical Engineering, University of Nigeria, Nsukka, Nigeria. chibuokeeneh@gmail.com
[2]Department of Mechanical Engineering Science, University of Johannesburg, Johannesburg, South Africa. howard.njoku@unn.edu.ng
[3]Department of Mechanical Engineering, University of Port Harcourt, Choba, Nigeria.

Abstract—**Smartphones integrate functionalities that enable users to process information in numerous formats, incorporating power-intensive capabilities that create heating scenarios that are detrimental to phone components and users' comfort. As dissipation of this heat is obviously impeded when phone covers are present, the widespread adoption of phone covers necessitates studies on their contributions to thermal issues in smartphones. In this study, we monitored thermal behaviours of two identical smartphones — one bare and the other encased in a cover, obtaining their skin temperatures with k-type thermocouples, processor and battery temperatures from inbuilt sensors and infrared thermograms using a thermal imager, as they simultaneously performed voice call, online gaming, music playing and video streaming tasks. The risein skin temperatures during the tasks was greater in the covered phone, and the increase in back surface temperatures relative to front surface temperatures was intensified by the presence of covers except during gaming tasks. Hence, though the covers could protect users in the non power-intensive tasks by retaining or impeding the heat generated, the power-intensive gaming task which actively utilized the LCD emitted additional heat from screens. User comfort threshold temperatures were not exceeded in this study unlike in earlier studies on bare phones. We, therefore, recommend further investigations on covered phones during high power-intensive tasks.**

Keywords - mobile phone, smartphone temperature, phone covers, thermal imaging, thermal management

I. INTRODUCTION AND BACKGROUND

Smartphones have become a necessary part of contemporary living, and their usage have become ubiquitous in recent years. As users have increasingly relied on their smartphones for the generation, communication and consumption of various forms of information (text, audio, video, etc.), manufacturers have been propelled to integrate greater functionalities. However, this has been accompanied by concurrent reductions in form factors, so that as smartphone power densities have grown, their effective areas for heat dissipation have shrunken simultaneously.

Several phone components, including the Wi-Fi chipset, battery, camera, big core, LITTLE core, GPU, codec and liquid crystal display (LCD), generate heat when in operation. Previously, the ensuing thermal problems resulted from reductions in device size, which increased device power densities. Currently, however, increased computing capabilities in the form of multiprocessor system on chip (MPSoC) devices, parallel processing and power-intensive processes such as gaming, high bandwidth internet, etc., are the new drivers of thermal issues in mobile phones. The rapid increase in smartphone functionality has occurred as form factors have reduced simultaneously, bringing mobile phone technology to the limits of thermal enhancements at the package level [1]. The future of mobile device development may thus be confronted with thermal constraints to improvements in performance and functionality rather than power constraints [2, 3], creating situations in which smartphones operate for

extended periods below their real capabilities and negating the ab initio incorporation of high performance features in such phones.

Heating in smartphones presents a serious challenge for smartphone designers. If left unmanaged, the eventual overheating will result in the damage of internal components on the circuit board, acceleration of thermal fatigue in solders, thermal runaway in batteries, etc. Elevations in phone surface temperatures also degrade user experience due to reduced battery life, reduced frame rates (as a result of process throttling), low-temperature skin burn injury, anxiety, and other discomforts during usage [4].

Phone surface temperatures need to be maintained below the 45°C threshold temperature for pain [5, 6] since they are usually in contact with users' skins. To achieve this, several power and thermal management techniques have been proposed, developed and implemented, which seek to optimize the power consumption and thermal behaviour of the mobile devices [7]. At the kernel level, these goals are achieved by any of [7, 8] 1) *the Dynamic Power Management* (DPM) technique, which suspends idle processing elements (PEs) or other idle components of the system if required to reduce energy consumption; 2) *the Dynamic Voltage Frequency Scaling* (DVFS) technique that allows processors to operate at variable voltage-frequency levels; 3) the customization of processors to match the processing needs of tasks on an MPSoC; 4) the customizing of cache-based memory access; and 5) the mapping of application tasks to the processors to improve utilisation and reduce energy consumption of PEs by balancing workload across all processors in an MPSoC.

On the hardware side, [9] demonstrated the cooling of mobile electronic devices with a phase change material (PCM), n-eicosane, with which the temperature of a simulated electronic unit was successfully maintained below a set threshold under moderate heating conditions. Reference [10] (using Gallium PCM), [11] (using a microencapsulated PCM) and [12] (using the n-eicosane and dodecanoic acid PCMs) also obtained similar results as the PCMs introduced a delay effect in the dissipation of the heat generated by the device [11, 12].

The heat generated within mobile devices travels along heat transfer paths to their surfaces and raises the skin temperatures [13]. From the surfaces, the heat is ultimately lost to the environment by thermal convection and radiation. While users' safety is more closely linked to device skin temperatures, traditional thermal management techniques focus on throttling processes on the application processors to maintain their temperatures beneath acceptable thresholds [4, 14]. Mobile phone thermal management approaches are however advancing to incorporate skin temperature considerations [13, 15]. For the effective design of such, an understanding of how the processes being performed by a smartphone influence its skin temperature is required, and this may be obtained experimentally or by modelling. Reference [16] studied the correlation between smartphone tasks and the measured temperatures of the phone's surfaces. They analyzed infrared (IR) thermograms and phone surfaces temperatures obtained during some common phone tasks and found that processes that intensively used the application processor, power management circuit and camera chip caused major heating of the smartphones. Reference [17] performed a tear-down analysis of a popular smartphone and measured temperature rises in the phone to develop a smartphone thermal model, which was implemented while varying the thermal conductivities of the back- and middle-plates (stiffener within the tablet). The obtained results showed that metallic spreaders and gap filler pads helped in establishing contact between surfaces within the mobile phone, facilitating heat conduction to the phone's outer surfaces for dissipation to the atmosphere. This cooled the phone's internal parts, preventing any deteriorations.

Phone covers have been available since the advent of mobile phones themselves, and a large number of smartphone owners utilize them for a wide variety of functions. They initially offered protection from shocks and cracks resulting from falls, normal wear and tear resulting from routine use, and other forms of physical damage that mobile devices could experience. With the emergence of multi-purpose smartphones, phone covers now offer additional services like aesthetics, abrasion/scratch resistance, and waterproof and dust-proof abilities. Multi-functional phone covers are also available, which provide overall phone protection and also offer battery charging abilities, additional data storage capacity, wallet space (for holding small notes, cash, and cards), signal boosting, etc. The use of phone covers, irrespective of their varied material properties, introduces additional

barriers in the heat dissipation routes of the devices.

Notwithstanding the widespread use of phone covers — more than three quarters of smartphone owners in the US were estimated to use phone covers by 2013 [19], while the estimated worth of the global market for protective phone covers was USD 21.4 billion in 2018 [20] — their contributions to the thermal characteristics of smartphones have been largely excluded from existing studies. For example, in the studies of [21] and [22], skin temperatures were measured and IR thermograms obtained and analyzed for different smartphone models to determine their characteristic temperatures in normal use scenarios but the effects of phone covers were not considered. Furthermore, the models theoretical models of [4, 13, 17, 18] did not consider scenarios that involved the use of phone covers. Reference [16] presented a comparison of steady-state skin temperatures in the presence and absence of a cover, which showed that the covered phone took a longer time to reach its steady-state temperature, which was also lower than the temperature of the bare phone. However, the phone cover tests weren't comprehensive, being only for *Skype* video calls.

The present paper investigates the impact of phone covers on the thermal behaviours of smartphones. Skin temperatures, processor and battery temperatures and infrared (IR) thermograms of two identical smartphones — one in a cover and the other bare — were monitored as they simultaneously performed common tasks, to evaluate the influence of the phone covers. The results show that the skin and battery temperatures of the smartphones were elevated by the presence of phone covers, while the processor temperatures were minimally affected. This initial study highlights the need for further studies to further investigate the thermal response of smartphones, especially when their processing abilities are fully exploited.

II. MATERIALS AND METHODS

Test were performed on two identical (Samsung J6+) phones — a control phone without a cover and a test phone encased in a cover — to simultaneously monitor their front and back surface temperatures. The temperatures were used to evaluate the influence of the phone covers on the range of temperatures experienced by users when performing typical phone operations, and the heat flow directions in the phones, i.e., towards either the front or back faces of the phones. The phones were operating on the Android 9 OS and were equipped with the Qualcomm MSM8917 Snapdragon 425 mobile AP, which has a Quad-core and various peripheral components. Each phone also had a 6 inch 720 × 1480 resolution LCD screen, 802.11 b/g/n Wi-Fi interfaces, a 13MP rear camera and a 3300 mAh battery.

A test chamber was built to enclose the phones during the tests (Fig. 1a). In order to prevent heat exchange between the phones and the external environment, five of the chamber's inner surfaces were lined with a reflective aluminium foil to diminish radiant heat exchange between the phones and the chamber's walls, while the sixth wall was made of a glass sheet which is opaque to low frequency thermal radiation. Temperature distributions on the phone screens during the tests, in the form of infrared (IR) thermograms were captured by means of an infrared thermal imaging camera (Seek Thermal CompactPRO ™). This was attached to one of the test chamber's walls to ensure a fixed distance between the imaging camera and the phones during the tests.

a)

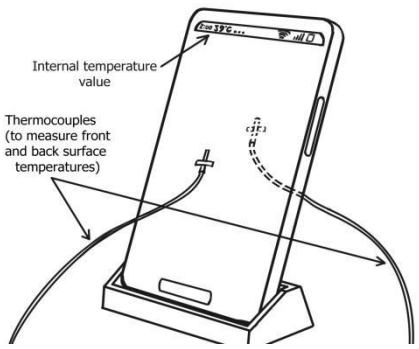

b)

Figure 1. (a) Test chamber with the mobile phone setup; (b) Thermocouple locations on the phones.

The temperatures within the test chamber and at identical positions on the surfaces of both control and test phones were measured using k-type thermocouples (Fig. 1 b). The temperatures were recorded using an Applent AT4208 eight-channel temperature data logger (having accuracy of 0.2C ± 2 digits a resolution of 0.1°C). Furthermore, the CPU Monitor mobile phone app was also used to record the phones' processor and battery temperatures that were measured by in-built sensors and displayed the phone screens. The phone casings investigated represented the phone casing designs in commonest use, and included those made of carbon fibre, leather, plastic and silicone materials (Fig. 2).

Tests were performed as the phones simultaneously performed four common tasks, including audio voice calling using the default app, online gaming using the *PUBG MOBILE* online gaming application, musing playing using the *Deezer* music streaming app, and online video streaming using the *YouTube* video streaming app. In order to ensure identical operations in both (test and control) phones and minimize thermal measurement errors, the batteries of both phones were fully charged before the start of each test; all background applications, including auto-update, adaptive screen brightness and battery saving features, were disabled; Wi-Fi was used for all processes that required internet access; and each test lasted for 30 minutes to ensure that the phones had reached steady state.

III. Results and Discussion

A. *Effects of Covers on Skin Temperatures*

Fig. 3a shows the time-varying temperatures of the front and back surfaces of the control and test phones during an audio call test with the test phone encased in a carbon fibre cover. The test enclosure's ambient temperatures during the test are plotted alongside. The corresponding temperatures recorded during the online gaming, audio music playing and online video streaming tests are presented in Figs. 4a, 5a and 6a, respectively. For both phones, the front and back surface temperatures recorded were all within the phone user comfort rage (<45°C).

Increments in the measured skin temperatures above their initial values, i.e., ($T_{front} - T_{front,0}$) and ($T_{back} - T_{back,0}$), are presented in Figs. 3b, 4b, 5b and 6b, for the audio calling, online gaming, audio music playing and online video streaming tests, respectively.

The plots show that the temperatures rose rapidly within the ~10 minutes of the tests. Subsequently, the gains in temperature diminished as steady-state conditions were approached.

a) Carbon fibre b) Leather c) Plastic d) Silicone

Figure 2. Casings for the test phones.

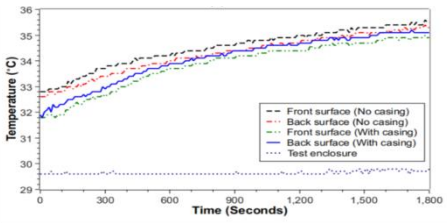

a)

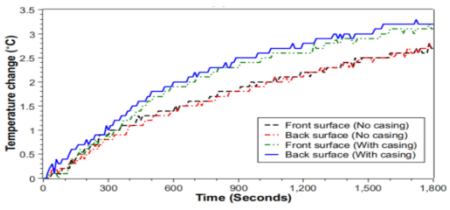

b)

Figure 3. (a) Temperature responses of the phone surfaces (with test phone enclosed in carbon fibre casing) during audio calls; (b) Transient changes in the phone surface temperatures above their initial temperatures.

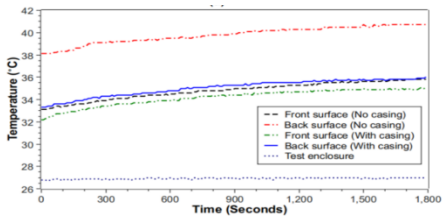

a)

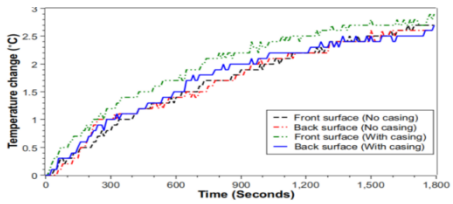

b)

Figure 4. (a) Temperature responses of the phone surfaces (with test phone enclosed in carbon fibre casing) during an online gaming session; (b) Transient changes in the phone surface temperatures above their initial temperatures.

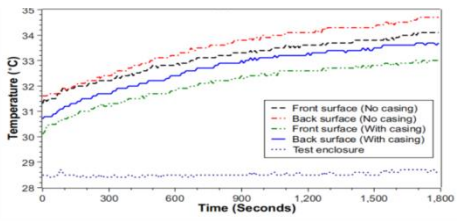

a)

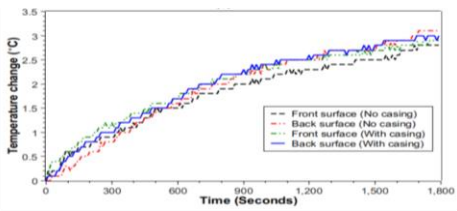

b)

Figure 5. (a) Temperature responses of the phone surfaces (with test phone enclosed in carbon fibre casing) during an audio music session; (b) Transient changes in the phone surface temperatures above their initial temperatures.

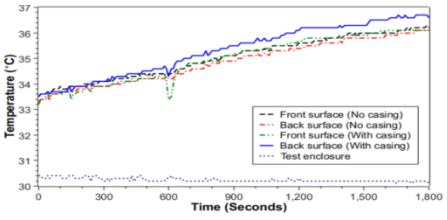

a)

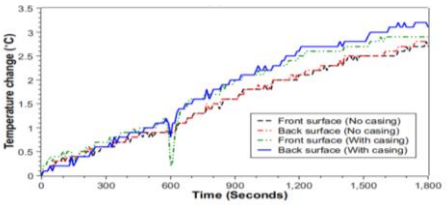

b)

Figure 6. (a) Temperature responses of the phone surfaces (with test phone enclosed in carbon fibre casing) during video session; (b) Transient changes in the phone surface temperatures above their initial temperatures.

The increments in the phone surface temperature were between 2.5 – 3°C, depending on the phone task being undertaken, although the extent to which the phone tasks affected the skin temperature gains could not be fully determined. This was because, as the phones had to be fully charged before the start of the tests, their initial skin temperatures weren't the same at the start of the different tests.

The (b) plots show that increments in the test (encased) phone's skin temperatures were more than those of the control (bare) phone during all the tests, indicating that the covers had an inhibitory effect on heat dissipation from the encased phone.

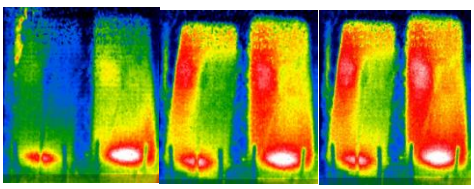

(a) 0 min. (b) 15 min. (c) 30min.

Figure 7. Infrared thermograms of the phones in 15 minute intervals of an audio call session with the test phone in a carbon fibre cover. (Control (bare) phone the left and test (covered) phone on the right).

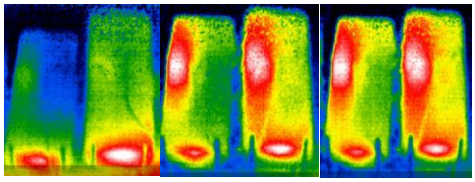

a) 0 min. b) 15 min. c) 30min.

Figure 8. Infrared thermograms of the phones in 15 minute intervals of a video streaming session with the test phone in a carbon fibre cover. (Control (bare) phone the left and test (covered) phone on the right).

Infrared thermograms of the phones that were obtained in 15 minute intervals are shown in Fig. 7 for the voice call test and in Fig. 8 for the video streaming test (with the test phone in a carbon fibre cover). The thermograms showed that the skin temperature of the covered phone (on the right) is slightly elevated beyond the skin temperature of the bare phone (on the left).

Furthermore, we observe that for the covered phones, the temperature increments on the back surface were generally higher than the temperature increments on the front surface except during the gaming test. For the bare phones, the temperature increments for both surfaces were comparable, again except during the gaming test, when the front surface temperature recorded higher increments.

B. Effects of Covers on Heat Flow Directions

Because the phone covers possess lower thermal conductivities than the shells of the phones, the covers introduce an additional barrier to heat dissipation by the phones. This most likely explains why increments in the surface temperatures of the encased phone were higher in comparison to the bare phone — the larger heat capacities of the casings caused them to accumulate more heat, leading to the higher temperature increments in the encased phones. For both bare and encased phones, the back surface temperatures rose higher than the front surface temperatures (b plots), and since the heat loss $\dot{Q}_{loss} \alpha T_{surface} - T_{ambient}$, there will be more heat flow through the phone's rear than its front surface. This will be beneficial during audio calls when the front surface of a phone is in contact with the skin of the user's face and the back surface is in contact with the user's palm, since the face is more sensitive than the palm. The question however arises on how the respective heat flows through the phone's rear and front surfaces compare in the presence of casings.

$$r_Q \quad \overline{\int dt \int dt^{test}} \,. \qquad (1)$$

In Figs. 9 a– d, the ratios of cumulative rear surface temperature rise to front surface temperature rise for different tasks are compared for the control and test phones, i.e., where $\Delta T_{back} = T_{back} - T_{back,0}$ and $\Delta T_{f\ ront} = T_{front} - T_{f\ ront,0}$ are the temperature increments above the initial temperatures. During the tests, r_Q was higher in the encased phone than in the bare phone, except during the online gaming task (Fig. 9)).

Fig. 4b indicated this, with front surface temperature increments in the encased phone that were remarkably higher than the rear surface temperature increments, although both

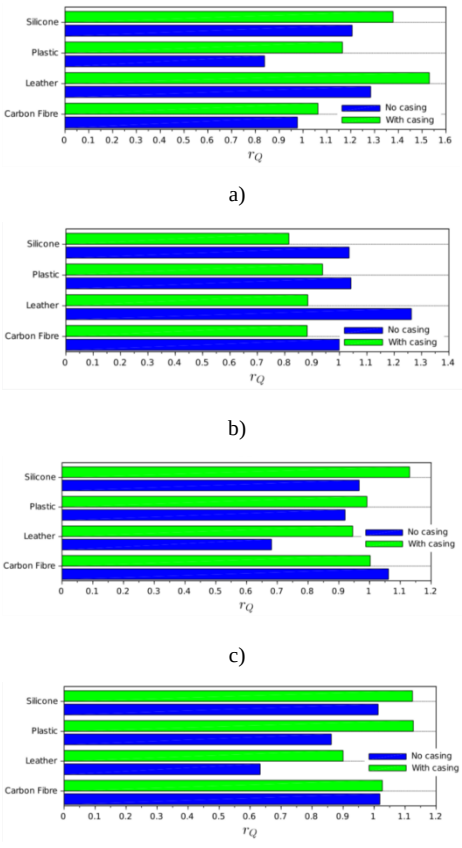

Figure 9. Evaluation of the influence of casing material on the heat flows through the front and back surfaces of the uncovered and encased phones during (a) audio call (b) gaming (c) audio music and (d) video sessions.

temperature increments were comparable in the bare phone. The online gaming task, in addition to the application processor and Wi-Fi chipset, also actively utilizes display resources in the LCD. Hence, heat generation in the LCD, which is ultimately dissipated on the phone's front surface, is greater for this task than for the rest. With a cover, the increased barrier to heat dissipation on the phone's rear will further increase r_Q as seen from Fig. 9b.

C. *Processor and Battery Temperature Responses*

The phone processor and battery temperatures that were measured by inbuilt sensors in the phones are present in Figs. 10 – 13. These were recorded during the phone tasks with the test phones encased in the different covers. The temperatures recorded during the music playing tests were excluded to improve clarity since they roughly coincided with the temperatures obtained during the video playing test. For both bare and encased phones, the highest processor and battery temperatures generally occurred during the online gaming tests, while the lowest temperatures occurred during the audio call tests. The processor temperatures recorded during the gaming tasks exceeded those recorded during the call tasks by up to 20°C, and differences in battery temperatures were up to almost 10°C.

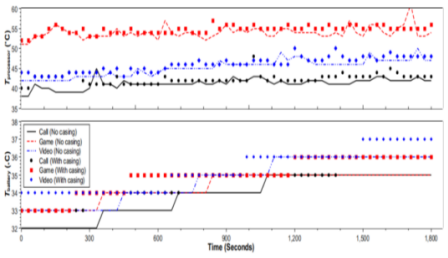

Figure 10. Variation of processor and battery temperatures during audio call, gaming, and video sessions with the test phone placed in a carbon fibre casing.

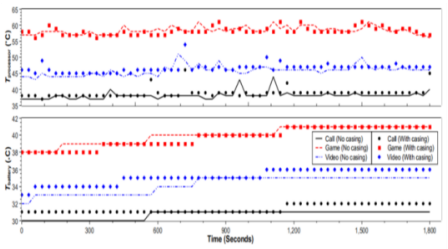

Figure 11. Variation of processor and battery temperatures during audio call, gaming, and video sessions with the test phone placed in a leather casing.

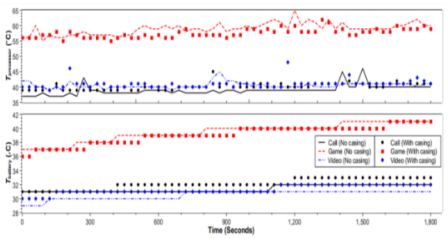

Figure 12. Variation of processor and battery temperatures during audio call, gaming, and video sessions with the test phone placed in a plastic casing.

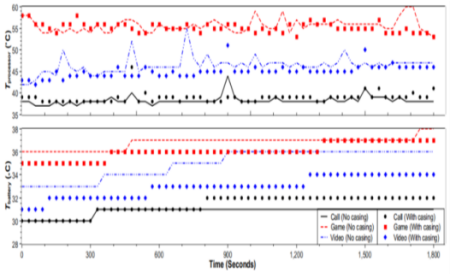

Figure 13. Variation of processor and battery temperatures during audio call, gaming, and video sessions with the test phone placed in a silicone casing.

The presence of casings didn't significantly alter the processor and battery temperatures. In some cases, the control phone had slightly higher processor temperature than the test phone, suggesting that the tasks undertaken were well within the limits of the phones' thermal management algorithms. Further investigations are needed to assess their performance under more severe conditions (e.g. more power-intensive processes and multiple concurrent processes). As expected, higher battery temperatures (by ~ 1°C) consistently occurred in the encased phone, since the battery is positioned at the phone's rear (where temperature increments had been early found to be higher).

IV. CONCLUSION

Mobile handheld devices dissipate the heat generated during processes through passive convection and radiation from their surfaces and this determines their skin temperatures and, in turn, user experience. As the presence of covers introduces barriers to this heat dissipation, this study investigated the influence of covers on the thermal behaviour of a smartphone. Temperature histories, temperature rises and IR thermograms of a covered smartphone were compared to those

of an identical bare phone while both simultaneously performed common tasks. Elevations in the skin temperatures were observed in the presence of the covers, though they could offer some protection to users during low power consuming tasks. The test phone tasks were performed under conditions of well controlled ambient conditions although the tested phones had unequal initial temperatures. This limited the extent to which the influence of the phone covers was determined. Further tests with better-controlled phone temperatures, which will also investigate thermal behaviors during power-intensive or multiple concurrent tasks, are needed to provide further clarity on the phone covers' thermal influence.

REFERENCES

[1] Nelson, C., & Galloway, J. (2018, March). Package thermal challenges due to changing mobile system form factors. In *2018 34th Thermal Measurement, Modeling & Management Symposium (SEMI-THERM)* (pp. 98-106). IEEE.

[2] Sekar, K. (2013, September). Power and thermal challenges in mobile devices. In *Proceedings of the 19th annual international conference on Mobile computing & networking* (pp. 363-368).

[3] Huang, Z., Zhang, X., Zhou, M., Xu, X., Zhang, X., & Hu, X. (2012). Bio-inspired passive skin cooling for handheld microelectronics devices. *Journal of Electronic Packaging*. *134*(*1*).

[4] Park, J., Lee, S., & Cha, H. (2018, March). Accurate prediction of smartphones' skin temperature by considering exothermic components. In *2018 Design, Automation & Test in Europe Conference & Exhibition (DATE)* (pp. 1500-1503). IEEE.

[5] Berhe, M. K. (2007, January). Ergonomic temperature limits for handheld electronic devices. In *International Electronic Packaging Technical Conference and Exhibition* (Vol. 42789, pp. 1041-1047).

[6] Bernard, T. E., & Foley, M. F. (1993). Upper acceptable surface temperature for prolonged hand contact. *International journal of industrial ergonomics*, *11*(1), 29-36.

[7] Singh, A. K., Dey, S., McDonald-Maier, K., Basireddy, K. R., Merrett, G. V., & Al-Hashimi, B. M. (2020). Dynamic energy and thermal management of multi-core mobile platforms: A survey. *IEEE Design & Test*, *37*(5), 25-33.

[8] Dey, S., Singh, A. K., Saha, S., Wang, X., & McDonald-Maier K. D. (2019). Rewardprofifiler: A reward based design space profifiler on DVFS enabled MPSoCs, in: *2019 6th IEEE International Conference on Cyber Security and Cloud Computing (CSCloud)/2019 5th IEEE International Conference on Edge Computing and Scalable Cloud (EdgeCom)*, (pp. 210–220).

[9] Tan, F. L., & Tso, C. P. (2004). Cooling of mobile electronic devices using phase change materials. *Applied thermal engineering*, *24*(2-3), 159-169.

[10] Ge, H., & Liu, J. (2013). Keeping smartphones cool with gallium phase change material. *Journal of Heat Transfer*, *135*(5).

[11] Tomizawa, Y., Sasaki, K., Kuroda, A., Takeda, R., & Kaito, Y. (2016). Experimental and numerical study on phase change material (PCM) for thermal management of mobile devices. *Applied Thermal Engineering*, *98*, 320-329.

[12] Maranda, S., Sponagle, B., Worlitschek, J., & Groulx, D. (2019). Experimental investigation of thin PCM packages and thermal spreader for thermal management of portable electronic devices. *Applied Sciences*, *9*(21), 4613.

[13] Luo, Z., Cho, H., Luo, X., & Cho, K. I. (2008). System thermal analysis for mobile phone. *Applied Thermal Engineering*, *28*(14-15), 1889-1895.

[14] Park, J., Lee, S., & Cha, H. (2018, July). App-oriented thermal management of mobile devices. In *Proceedings of the International Symposium on Low Power Electronics and Design* (pp. 1-6).

[15] Yim, M. K., Lee, K. M., & Han, T. H. (2014). Surface temperature-aware thermal management technique for mobile devices. *IEICE Electronics Express*, *11*(23), 20140944-20140944.

[16] Kang, S., Choi, H., Park, S., Park, C., Lee, J., Lee, U., & Lee, S. J. (2019, August). Fire in your hands: Understanding thermal behavior of smartphones. In *The 25th Annual International Conference on Mobile Computing and Networking* (pp. 1-16).

[17] Gurrum, S. P., Edwards, D. R., Marchand-Golder, T., Akiyama, J., Yokoya, S., Drouard, J. F., & Dahan, F. (2012, May). Generic thermal analysis for phone and tablet systems. In *2012 IEEE 62nd Electronic Components and Technology Conference* (pp. 1488-1492). IEEE.

[18] Xie, Q., Dousti, M. J., & Pedram, M. (2014, August). Therminator: A thermal simulator for smartphones producing accurate chip and skin temperature maps. In *Proceedings of the 2014 international symposium on Low power electronics and design* (pp. 117-122).

[19] The NPD Group, One-in-four smartphone owners don't use a case to protect their phone according to NPD, https://www.npd.com/wps/portal/npd/us/news/press-releases/one-in-four-smartphone-owners-dont-use-a-case-to-protect-their-phone according-to-npd/, Last accessed on 2020-06-03 (2013).

[20] Grand View Research, Mobile phone protective cover market size, share &trends analysis report by product (body glove, pouch, phone skin, hybrid case), by distribution channel, by region, and segment forecasts, 2019 - 2025, https://www.grandviewresearch.com/industry-analysis/mobilephone-protective-cover-market, Last accessed on 2020-06-03 (2019).

[21] Varga, P. J., Kalecz, A., & Illesi, Z. (2018, May). Thermal Test of Mobile Devices in Normal Use. In *2018 IEEE 12th International Symposium on Applied Computational Intelligence and Informatics (SACI)* (pp. 000267-000272). IEEE.

[22] Hell, P. M., Varga, P. J., & Illési, Z. (2018, September). Mobile phones thermo-ergonomic analysis. In *2018 IEEE 16th International Symposium on Intelligent Systems and Informatics (SISY)* (pp. 000249-000254). IEEE

Advanced Electric Vehicle Technologies

Milan Prokin[1], Dragana Prokin[2]

[1]University of Belgrade – School of Electrical Engineering, Belgrade, Serbia
National Association of Autonomous and Electric Vehicles, Belgrade, Serbia
[2]Academy of Technical and Art Applied Studies, School of Electrical and Computer Engineering, Belgrade, Serbia

Abstract—**The major technical problems with electric vehicles (EVs) are range, fast charging, regenerative braking, explosions and fires. All these problems can be solved cost effectively with lithium purification in combination with hybrid supercapacitors instead of state-of-the-art lithium ion batteries with or without ultracapacitors.**

Keywords – lithium purification, regenerative braking, hybrid supercapacitors

I. INTRODUCTION

Lithium dendrites are inherent to lithium ion batteries due to lithium electrodeposition on impurities (Fig. 1), since battery grade lithium hydroxide or lithium carbonate is typically 99.7% pure in average (99.5%-99.9%) [1-6].

Lithium dendrites grow (buildup themselves) over time during cycling (charging & discharging) (Fig. 2) [7].

Grown lithium dendrites can punch trough a separator between electrodes (an anode & a cathode) (Fig. 3), short circuit electrodes, pass high short circuit current, overheat themselves, electrodes and surrounding electrolyte, and finally produce explosion and fire (Fig. 4) [8].

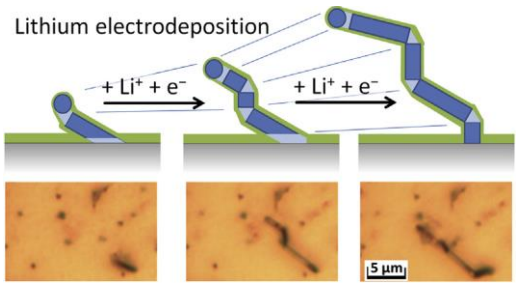

Figure 1. Lithium dendrites buildup due to lithium electrodeposition on impurities.

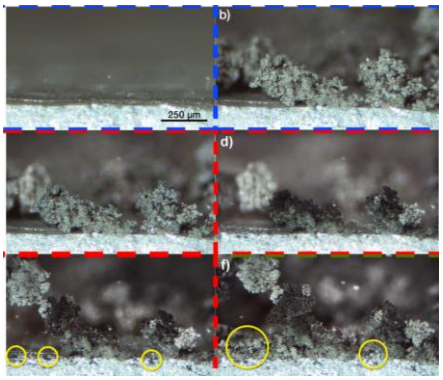

Figure 2. Lithium dendrites buildup during cycling.

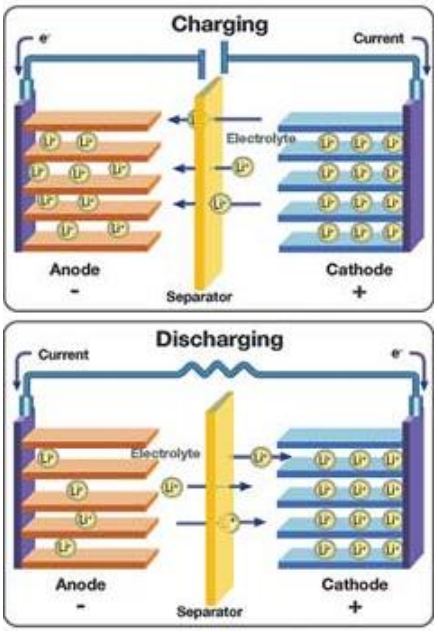

Figure 3. Lithium dendrites can grow over time and cause internal battery shorting through the separator, explosion and fire.

ISBN: 978-86-80593-73-9

Figure 4. EV fires due to lithium dendrites.

II. Lithium Purification

Lithium dendrites grow on impurities in an anode and a electrolyte. The state-of-the-art solution is to coat anode with graphite or graphene, which decreases lithium ion battery capacity and EV range in almost half. The other solution is lithium purification in order to remove impurities providing the following benefits [9-12]:

- Lithium carbonate purification to 99.99% and 99.999%.
- Lithium hydroxide purification to 99.99% and 99.999%.
- Lithium chloride purification to 99.99% and 99.999%.
- Production time is one hour from start to finish, much faster than pond evaporation process that takes many months to finish.
- Production generates other useful chemicals for sale, such as HCl (Fig. 5).
- Production can operate as an extension of state-of-the-art lithium mining operation, especially in case of lithium brine from geothermal sources (Fig. 6).

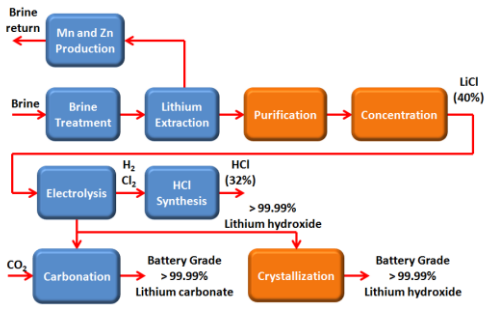

Figure 5. Proven lithium purification process.

Figure 6. Lithium purification manufacturing facility.

III. Energy Storage Variants

These three energy storage variants are used in EVs (from the most used to the least used):

- Lithium batteries have good specific energy (can store a lot of energy), but have relatively low Specific power, which translates to long charge and discharge cycles.
- Supercapacitors have high specific power (can charge and discharge at much greater rates than chemical batteries), longer lifetime without deteoration and wide operational temperature range (both freezeing and hot), but have lower specific energy, which translates to larger units than lithium ion batteries.
- Hybrid supercapacitors are half way between lithium batteries and supercapacitors. They can also utilize lithium chemistry.

IV. Regenerative Braking Energy

EVs in ideal case can return most of braking energy into lithium ion batteries, thus extremely increasing the efficiency in city driving via regenerative braking:

- Regenerative braking is the process of deceleration with energy return to energy storage instead of heating brakes.
- Batteries are too slow to be charged from regenerative braking, rendering the complete regenerative braking inefficient.
- High surge currents during regenerative braking decrease battery lifetime.
- Supercapacitors are sufficiently fast to be charged from regenerative braking, making the complete regenerative braking highly efficient.

- City driving with frequent acceleration and deceleration will be highly efficient due to regenerative braking.

Major components for regenerative braking energy systems are batteries, ultracapacitors and DC/DC converters [13-18].

There are several electrical schematics for combining supercapacitors/ultracapacitors with lithium ion batteries and DC/DC converters [19-24], spanning two decades of the continuous research and development interest.

An ultracapacitor can be simply connected in parallel with a battery, which essentially inhibits quick ultracapacitor charging to voltage higher than battery voltage, while the power distribution between the ultracapacitor and the battery is uncontrollable (Fig. 7) [25-29].

Decoupling an ultracapacitor and a battery from an inverter by a bi-directional DC/DC converter doesn't help much in resolving the previous problem, but it stabilizes inverter voltage at the expense of high surge current rating of the DC/DC converter (Fig. 8) [27].

Decoupling an ultracapacitor from a battery by a bidirectional DC/DC converter enables ultracapacitor voltage to be different from battery voltage, at the expense of high surge current rating of the DC/DC converter and decreased battery lifetime due to high charging and discharging currents (Fig. 9) [30-40].

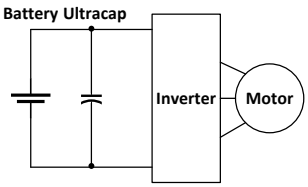

Figure 7. An ultracapacitor in parallel with a battery.

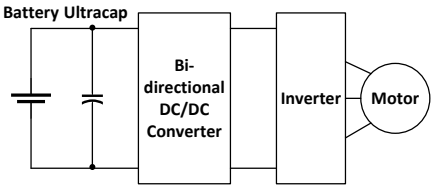

Figure 8. Decooupling an ultracapacitor and a battery from an inverter by a DC/DC converter.

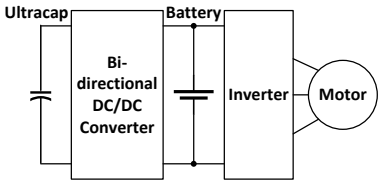

Figure 9. Decoupling an ultracapacitor from a battery by a DC/DC converter.

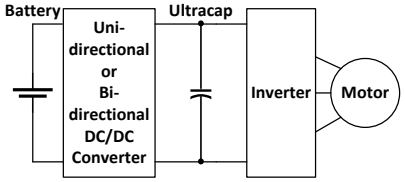

Figure 10. Decoupling a battery from an ultracapacitor by a DC/DC converter.

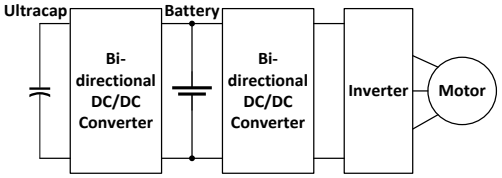

Figure 11. Decoupling an ultracapacitor, a battery and an inverter by two serial DC/DC converters.

Decoupling a battery from an ultracapacitor by an unidirectional or a bidirectional DC/DC converter decreases surge currents through the DC/DC converter and increases battery lifetime, but enables ultracapacitor voltage to be too much different from battery voltage, thus increasing breakthrough voltage rating of an inverter (Fig. 10) [26, 41-43].

Decoupling an ultracapacitor, a battery and an inverter can be performed by two serial DC/DC converters in order to provide different ultracapacitor and battery voltages, but stable inverter voltage at the same time (Fig. 11) [44, 45].

Decoupling a battery, an ultracapacitor and an inverter can be performed by two serial DC/DC converters in order to provide different battery and ultracapacitor voltages, but stable inverter voltage at the same time (Fig. 12) [27, 46].

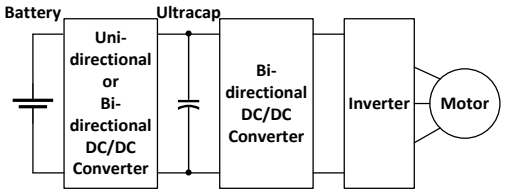

Figure 12. Decoupling a battery, an ultracapacitor and an inverter by two serial DC/DC converters.

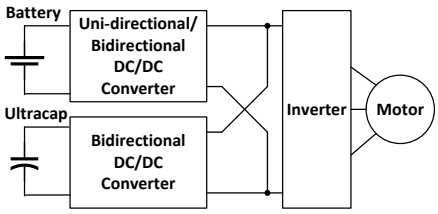

Figure 13. Decoupling a battery, an ultracapacitor and an inverter by two parallel DC/DC converters.

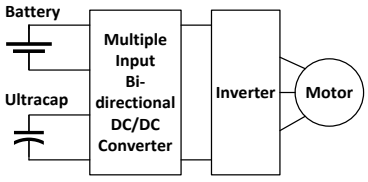

Figure 14. Decoupling a battery, an ultracapacitor and an inverter by one multiple input DC/DC converter.

The problem with the configurations in Figs. 11 and 12 is lower efficiency due to currents passing through two serial DC/DC converters. This problem is solved by decoupling a battery, an ultracapacitor and an inverter by two parallel DC/DC converters enabling different ultracapacitor and battery voltages (Fig. 13) [27, 47-53].

The configuration in Fig. 11 can be improved by using a multiple input bidirectional DC/DC converter instead of two parallel DC/DC converters (Fig. 14) [24, 47, 54-62].

V. HYBRID SUPERCAPACITORS

Hybrid supercapacitors (Fig. 15) are halfway between lithium batteries (Fig. 16) and carbon supercapacitors (Fig. 17) [63-71].

Hybrid supercapacitor feates are:

- One lithium compound electrode.
- The other graphen electrode.
- There is no chemical reaction.
- There is no free flow of lithium ions floating in the battery that can form potentially dangerous lithium dendrites shortcircuiting electrodes, producing explosion and fire.
- They are inherently fire safe.
- The charges are stored statically, like in a supercapacitor.
- There is some electrolyte involved, but as a filler that allows the charges to move.
- The electrolyte is soaked up by the nano-carbon electrode material, so if the cells are ruptured, very little or none will leak out.
- Operating temperatures are from -40°C to +80°C.
- No active thermal management is needed.
- The same assembling and packaging process already used for state-of-the-art lithium batteries and carbon supercapacitors can be also used for hybrid supercapacitors (Fig. 18).

A. Power Type Version of Hybrid Supercapacitors (Fig. 19) [71-73]

- Specific energy of 80-100 Wh/kg.
- Specific power of 1,000-1,500 W/kg.
- Lifetime 20,000-50,000 cycles (or 2 million – 5 million km).

B. Energy Type Version of Hybrid Supercapacitors (Fig. 19) [71-73]

- Specific energy of 200-230 Wh/kg.
- Specific power of 300-500 W/kg.
- Lifetime over 10,000 cycles (or more than 1 million km).

C. Lithium Ion Battery for Comparison (Fig. 19) [72-73]

- Specific energy of 180-250 Wh/kg.
- Specific power of 100-500 W/kg.
- Lifetime over 2,000 cycles (or more than 200,000 km).

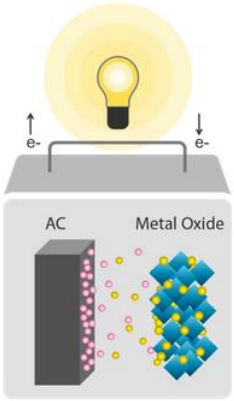

Figure 15. Hybrid supercapacitor.

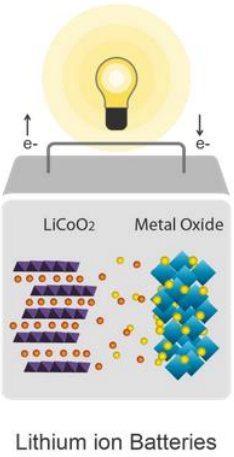

Figure 16. Typical lithium ion battery.

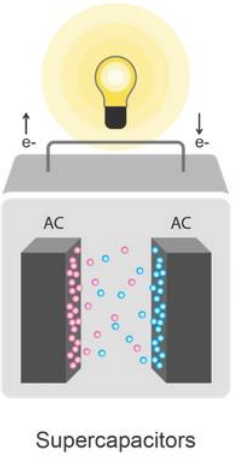

Figure 17. Typical supercapacitor.

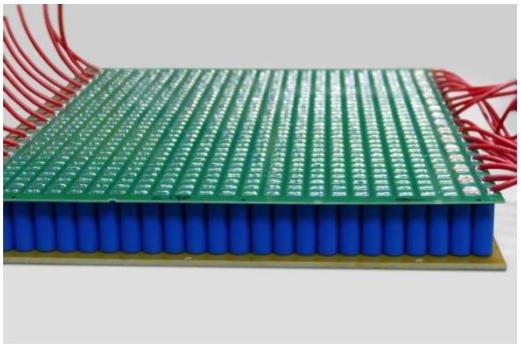

Figure 18. Hybrid supercapacitor pack.

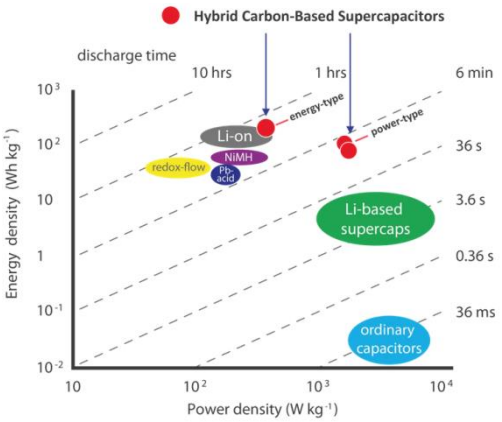

Figure 19. Battery comparison.

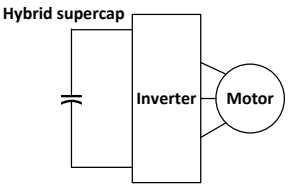

Figure 20. A hybrid supercapacitor instead of an ultracapacitor, a battery and DC/DC converter(s).

A hybrid supercapacitor can be used instead of an ultracapacitor, a battery and DC/DC converters in all configurations in Figs. 7-14 (Fig. 20).

VI. Superfast Chargers

Hybrid supercapacitors or supercapacitors or can be also used for superfast chargers [74]:

- Each superfast charger has a hybrid supercapacitor or a supercapacitor before water cooled charging cable.
- Charging the hybrid supercapacitor or the supercapacitor in the superfast

charger at slow rate from existing power grid.

- No need for upgrading existing power grid since surge current originates from the hybrid supercapacitor or the supercapacitor in the superfast charger.
- Discharge quickly from the hybrid supercapacitor or the supercapacitor in the superfast charger to a hybrid supercapacitor or a supercapacitor in an EV.
- No need to wait several tenths of minutes for charging an EV.
- Smaller queue of EVs waiting for charging.
- Bigger satisfaction of EV drivers.

VII. CONSCLUSIONS

Explosions and fires resulting from lithium dendrites can be solved by lithium purification and/or hybrid supercapacitors. The later additionally inherently solve regenerative braking efficiency problem without any additional components: ultracapacitors/ supercapacitors and DC/DC converter(s), thus increasing the reliability and decreasing size and weight of electric vehicle subsystems.

ACKNOWLEDGMENT

This work was partially supported by European Institute of Innovation & Technology Urban Mobility (EIT UM) under grant no. SGA21 21342, as well as Ministry of Education, Science and Technological Development of Republic of Serbia under grant nos. TR32039 and TR32047.

REFERENCES

[1] Jow, T. R., Xu, K., Borodin, O., & Ue, M. (2014) Electrolytes for lithium and lithium-ion batteries. Springer.

[2] Santhanagopalan, S., Smith, K., Neubauer, J., Kim, G.-H., Keyser, M., & Pesaran, A. (2015). Design and analysis of large lithium-ion battery systems. Artech House.

[3] Jiang, J., & Zhang, C. (2015). Fundamentals and applications of lithium-ion batteries in electric drive vehicles. John Wiley & Sons Singapore.

[4] Chagnes, A., & Swiatowska, J. (ed.) (2015). Lithium process chemistry: Resources, exctraction, batteries, and recycling. Elsevier.

[5] Blum, A. F., & Long Jr., R. T. (2016). Fire hazard assessment of lithium ikon battery energy storage systems. Springer.

[6] Lin, D., Liu, Y., & Cui, Y. (2017, Mar. 1). Reviving the lithium metal anode for high-energy batteries. *Nature nanotechnology*, 12, 194-206.

[7] Wood, K. N., Kazyak, E., Chadwick, A. F., Chen, K.-H., Zhang, J.-G., Thornton, K., & Dasgupta, N. P. (2016, Sep. 1). Dendrites and pits: Untangling the complex behavior of lithium metal anodes through operando video microscopy. *ACS Central Science*, *2*, 790-801.

[8] Maslyn, J. A., Loo, W. S., McEntush, K. D., Oh, H. J., Harry, K. J., Parkinson, D. Y., & Balsara, N. P. (2018). Growth of lithium dendrites and globules through a solid block copolymer electrolyte as a function of current density. *J. Physical Chemistry*, 122, 26797-26804.

[9] Paranthaman, M. P., Li, L., Luo, J., Hoke, T., Ucar, H., Moyer, B. A., & Harrison, S. (2017, Nov. 9). Recovery of lithium from geothermal brine with lithium-aluminum layered double hydroxide chloride sorbents. *Environmental Science and Technology*, 51(22), 13481-13486.

[10] Luo, Q., Dong, M., Nie, G., Liu, Z., Wu, Z., & Li, J. (2021, Nov. 5). Extraction of lithium from salt lake brines by granulated adsorbents. *Colloids and Surfaces A: Physicochemical and Engineering Aspects*, 628, 127256.

[11] Harrison, S., Blanchet, R. (2013, May 7, 2013, Nov. 5, 2015, Jul. 7). Process for preparing highly pure lithium carbonate and other highly pure lithium containing compounds. *U.S. Patent nos. 8435468*, *8574519*, and *9074265*.

[12] Harrison, S. (2014, Jun. 3, 2015, May 19, 2015, Dec. 29). Preparation of lithium carbonate from lithium chloride containing brines. *U.S. Patent nos. 8741256*, *9034295*, and *9222149*.

[13] Liu, D., & Li, H. (2006, Nov. 6-10). A three-port three-phase DC-DC converter for hybrid low voltage fuel cell and ultracapacitor. In *IECON 2006 - 32nd Annual Conference on IEEE Industrial* Electronics (pp. 2258-2563).

[14] Lukic, S. M., Cao, J., Bansal, R. C., Rodriguez, F., Emadi A. (2008, June). Energy storage systems for automotive applications. *IEEE Transactions on Industrial Electronics*, 55(6), 2258-2267.

[15] Alireza, K., & Li, Z. (2010, July). Battery, ultracapacitor, fuel cell, and hybrid energy storage systems for electric, hybrid electric, fuel cell, and plug-in hybrid electric vehicles: State of the art. *IEEE Transactions on Vehicular Technology*, *59*(6), 2806–2814.

[16] Siang, F. T., Chee, W. T. (2013, April). A review of energy sources and energy management system in electric vehicles. *Renewable and Sustainable Energy Reviews*, 20, 82–102.

[17] Ding, N., Prasad, K., & Lie, T. T. (2017, Jan.). The electric vehicle: a review. *Int. Journal of Electric and Hybrid Vehicles*, *9* (1), 49-66.

[18] Un-Noor, F., Padmanaban, S., Mihet-Popa, L., Mollah, M. N., Hossain, E. (2017, Aug. 17). Comprehensive study of key electric vehicle (EV) components, technologies, challenges, impacts, and future direction of development. *Energies*, 10, 1217-1301.

[19] Cao, J., Emadi, A. (2009, Sep. 7-10). A new battery/ultra-capacitor hybrid energy storage system

for electric, hybrid and plug-in hybrid electric vehicles. In *2009 IEEE Vehicle Power and Propulsion Conference*, Dearborn, MI, USA.

[20] Cao, J., Emadi, A. (2012, Jan. 1). A new battery/ultra-capacitor hybrid energy storage system for electric, hybrid and plug-in hybrid electric vehicles. *IEEE Transactions on Power Electronics, 27*(1), 122-132.

[21] Bobba, P. B., Rajagopal, K. R. (2012, Dec. 16-19). Modeling and analysis of hybrid energy storage systems used in electric vehicles. In *2012 IEEE Int. Conference on Power Electronics, Drives and Energy Systems*, Bengaluru, India.

[22] Xiang, C., Wang, Y., Hu, S., Wang, W. (2014, Apr. 29). A new topology and control strategy for a hybrid battery-ultracapacitor energy storage system. *Energies*, 7(5), 2874-2896.

[23] Chakraborty, S., Vu, H.-N., Hasan, M. M., Tran, D.-D., Baghdadi, M. E., Hegazy, O. (2019, Apr. 25). DC-DC converter topologies for electric vehicles, plug-in hybrid electric vehicles and fast charging stations: State of the art and future trends. *Energies*, *12*(8), 1569-1612.

[24] Lai, C.-M., Teh, J., Lin, Y.-C., & Liu, Y. (2020, Mar. 6). Study of a bidirectional power converter integrated with battery/ultracapacitor dual-energy storage. *Energies*, 13(5), 1234-1257.

[25] Pay, S., & Baghzouz, Y. (2003, June 23-26) Effectiveness of battery-supercapacitor combination in electric vehicles. In *2003 IEEE Bologna Power Tech Conference*, Bologna, Italy.

[26] Gao, L., Dougal, R. A., Liu, S. (2005, Jan. 10). Power enhancement of an actively controlled battery/ultracapacitor hybrid. *IEEE Transactions on Power Electronics*, *20*(1), 236-243.

[27] Lukic, S. M., Wirasingha, S. G., Rodriguez, F., Cao, J., & Emadi A. (2006, Sep. 6-8). Power management of an ultracapacitor/battery hybrid energy storage system in an HEV. In *2006 IEEE Vehicle Power and Propulsion Conference*, Windsor, UK.

[28] He, H.-W., Xiong, R., Chang, Y.-H. (2010, Nov. 22). Dynamic modeling and simulation on a hybrid power system for electric vehicle applications. *Energies*, *3*(11), 1821–1830.

[29] Ding, S., Wei, B., Hang, J., Zhang, P., Ding, M. (2017, Aug. 11-14). A multifunctional interface circuit for battery-ultracapacitor hybrid energy storage system. In *2017 20th Int. Conference on Electrical Machines and Systems (ICEMS)*, Sydney, NSW, Australia.

[30] Dixon J., Ortuzar M., & Wiechmann E. (2000, Oct. 15-18). Regenerative braking for an electric vehicle using ultracapacitors and a buck-boost converter. In *The 17. International Electric Vehicle Symposium and Exposition: Driving New Visions*, Montreal, PQ (Canada).

[31] Ortuzar M., Moreno J., & Dixon J. (2007, Aug.). Ultracapacitor-based auxiliary energy system for an electric vehicle: implementation and evaluation. *IEEE Transactions on Industrial Electronics*, *54*(4), 2147-2156.

[32] Niemoeller, B. A., & Krein, P. T. (2010, Feb. 12-13). Battery-ultracapacitor active parallel interface with indirect control of battery current. In *2010 Power and Energy Conference*, Urbana-Champaign, IL, USA (pp. 12-19).

[33] Miller, J. M., & Sartorelli, G. (2010, Sep. 1-3). Battery and ultracapacitor combinations - Where should the converter go? In *2010 IEEE Vehicle Power and Propulsion Conference*, Lille, France.

[34] Pan, C., Chen, L., Chen, L., Chen H., Xie M. (2013, Jan.). Research on energy management of dual energy storage system based on the simulation of urban driving schedules. *Int. Journal of Electrical Power and Energy Systems*,. *44*(1), 37-42.

[35] Machado, F., Antunes, C. H., Dubois, M. R., & Trovao, J. P. (2015, Oct. 19-22). Semi-active hybrid topology with three-level DC-DC converter for electric vehicle application. In *2015 IEEE Vehicle Power and Propulsion Conference (VPPC)*, Montreal, QC, Canada (pp. 1-6).

[36] Shen, J., Khaligh, A. (2015, Oct.). A supervisory energy management control strategy in a battery/ultracapacitor hybrid energy storage system. *IEEE Transactions on Transportation Electrification*, *1*(3), 223-231.

[37] Hinov, N. L., Penev, D. N., Vacheva, G. I. (2016, Sep. 12-14). Ultra capacitors charging by regenerative braking in electric vehicles. In *2016 XXV International Scientific Conference Electronics (ET)*, Sozopol, Bulgaria.

[38] Castaings, A., Lhomme, W., Trigui, R., Bouscayrol, A. (2016). Practical control schemes of a battery/supercapacitor system for electric vehicle. *IET Electrical Systems in Transportation*, *6*(1), 20-26.

[39] Naseri, F., Farjah, E., & Ghanbari, T. (2017, May). An efficient regenerative braking system based on battery/supercapacitor for electric, hybrid and plug-in hybrid electric vehicles with BLDC motor. *IEEE Transactions on Vehicular Technology*, *66*(5), 3724-3738.

[40] Adib, A., & Dhaouadi, R. (2018). Performance analysis of regenerative braking in permannt magnet synchronous motor drives. *Advances in Science, Technology and Engineering Systems Journal*, *3*(1), 460-466.

[41] Lhomme, W., Delarue, P., Barrade, P., Bouscayrol, A., & Rufer, A. (2005, Oct. 2-6). Design and control of a supercapacitor storage system for traction applications. In *2005 Industry Applications Conference* (pp. 2013-2020).

[42] Liu, X., Zhang, Q., & Zhu, C. (2009, Sep. 7–10). Design of battery and ultracapacitor multiple energy storage in hybrid electric vehicle. In *2009 IEEE Vehicle Power and Propulsion Conference*, Dearborn, MI, USA.

[43] Kuperman, A., Aharon, I., Malki, S., & Kara, A. (2013, Feb.). Design of a semiactive battery-ultracapacitor hybrid energy source. *IEEE Transactions on Power Electrononics*, 28(2), 806-815.

[44] Miller, J. M., McCleer, P. J., Everett, M., & Strangas, E. G. (2005, June 20-23). Ultracapacitor plus battery energy storage system sizing methodology for HEV power split electric CVT's. In *2005 IEEE International Symposium on Industrial Electronics*, Dubrovnik, Croatia.

[45] Jing, W., Lai, C. H., Wong, S. H. W., & Wong, M. L. D. (2017). Battery-supercapacitor hybrid energy storage system in standalone DC microgrids: A review. *IET Renewable Power Generation*, 11(4), 461–469.

[46] Onar, O., & Khaligh, A. (2008, Sep. 3-5). Dynamic modeling and control of a cascaded active battery/ultra-capacitor based vehicular power system. In *2008 IEEE Vehicle Power and Propulsion Conference (VPPC)*, Harbin, China.

[47] Di Napoli, A., Crescimbini, F., Capponi, F. G., & Solero, L. (2002, July 8-11). Control strategy for multiple input DC-DC power converters devoted to hybrid vehicle propulsion systems. In *2002 IEEE International Symposium on Industrial Electronics*, L'Ayuila, Italy (pp. 1036-1041).

[48] Li, Z., Onar, O., Khaligh, A., & Schaltz, E. (2009-01-1387). Design, control, and power management of a battery/ultra-capacitor hybrid system for small electric vehicles. In *SAE World Congress & Exhibition*, Detroit, MI, USA.

[49] Dixon, J., Nakashima, I., Arcos, E. F., & Ortuzar, M., 2010, Mar.). Electric vehicle using a combination of ultracapacitors and ZEBRA battery. *IEEE Transactions on Industrial Electronics*, 57(3), 943-949.

[50] Allegre, A. L., Bouscayrol, A., & Trigui, R. (2013). Flexible real-time control of a hybrid energy storage system for electric vehicles. *IET Electrical Systems in Transportation*, 3(3), 79-85.

[51] Trovão, J. P. F., & Pereirinha, P. G. (2015). Control scheme for hybridised electric vehicles with an online power follower management strategy. *IET Electrical Systems in Transportation*, 5(1), 12-23.

[52] Trovão, J. P., Silva, M. A., & Dubois, M. R. (2017). Coupled energy management algorithm for MESS in urban EV. *IET Electrical Systems in Transportation*, 7(2), 125-134.

[53] Livreri, P., Castiglia, V., Pellitteri, F., & Miceli, R. (2018, Sep. 10-13). Design of a battery/ultracapacitor energy storage system for electric vehicle applications. In *2018 IEEE 4th International Forum on Research and Technologies for Society and Industry (RTSI)*, Palermo, Italy (pp. 1-5).

[54] Napoli, A., Crescimbini, F., Rodo, S., & Solero, L. (2002, June 23-27.). Multiple input DC-DC power converter for fuel-cell powered hybrid vehicles. In *2002 IEEE 33rd Annual Power Electronics Specialists Conference*, Cairns, QLD, Australia (pp. 1685-1690).

[55] Gummi, K., & Ferdowsi, M. (2010, Feb.). Double-input DC–DC power electronic converters for electric-drive vehicles - Topology exploration and synthesis using a single-pole triple-throw switch. *IEEE Transactions on Industrial Electronics*, 57(2), 617-623.

[56] De Castro, R., Pinto, C., Araujo, R. E., & Melo, P., Freitas, D. (2012, Oct. 9-12). Optimal sizing and energy management of hybrid storage system. In *2012 IEEE Vehicle Power and Propulsion Conference (VPPC)*, Seoul, Korea.

[57] Kumar, L., & Jain, S. (2013). Multiple-input DC/DC converter topology for hybrid energy system. *IET Power Electronics*, 6(8), 1483-1501.

[58] Lai, C.-M., & Yang, M.-J. (2016). A high-gain three-port power converter with fuel cell, battery sources and stacked output for hybrid electric vehicles and DC-microgrids. *Energies*, 9(3), 180-195.

[59] Hintz, A., Prasanna, U. R., & Rajashekara, K. (2015, May). Novel modular multiple-input bidirectional DC-DC power converter (MIPC) for HEV/FCV application. *IEEE Transactions on Industrial Electronics*, 62(5), 3163-3172.

[60] Momayyezan, M., Hredzak, B., & Agelidis, V. G. (2015, Nov. 9-12). A new multiple converter topology for battery/ultracapacitor hybrid energy system. In *IECON 2015 - 41st Annual Conference of the IEEE Industrial Electronics Society*, Yokohama, Japan (pp. 464-468).

[61] Lai, C.-M., Cheng, Y.-H., Hsieh, M.-H., & Lin, Y.-C. (2018, Feb.). Development of a bidirectional DC/DC converter with dual-battery energy storage for hybrid electric vehicle system. *IEEE Transactions on Vehicular Technology*, 67(2), 1036-1052.

[62] Lai, C.-M., Yang, C.-Y., & Cheng, Y.-H. (2018, Dec. 1). Power supply system and power supply method for electric vehicle including a supercapacitor to receive power from a motor and capable of extending the battery life. *Taiwan Patent no. I642575*.

[63] Scrosati, B., Abraham, K. M., Van Schalkwijk, W. & Hassoun, J. (ed.) (2013). Lithium batteries: Advanced technologies and applications. ECS-The Electrochemical Society.

[64] Pistoia, G. (ed.) (2014). Lithium-ion batteries: Advances and applications. Elsevier.

[65] Gulbinska, M. K. (ed.) (2014). Lithium-ion battery materials and engineering: Current topics and problems from the manufacturing perspective. Springer.

[66] Julien, C., Mauger, A., Vijh, A., & Zaghib, K. (2015). Lithium batteries. Science and technology. Springer.

[67] Wu, Y. (2015). Lithium-ion batteries: Fundamentals and applications. CRC Press.

[68] Warner, J. (2015). The handbook of lithium-ion battery pack design: Chemistry, components, types and terminology. Elsevier.

[69] Korthauer, R. (ed.) (2018). Lithium-ion batteries: Basics and applications. Springer.

[70] Eftekhari, A. (ed.) (2019). Future lithium-ion.batteries. The Royal Society of Chemistry.

[71] Liu, S., Ouyang, X., & Zheng, Y. (2016, Aug. 24). Carbon back capacity battery and carbon back capacity battery group. *China Patent No. 205751881*.

[72] *Batteries are dead, long live Carbon based Power Capacitors!* Available at: https://kurt.energy/wp-content/uploads/2019/04/WHITE-PAPER-Carbon-based-power-caps.pdf

[73] *Hybrid carbon-based supercapacitor cell specifications*. Available at: https://kurt.energy/wp-content/uploads/2020/01/Hybrid-C-Supercaps-Datasheet08012020.pdf

[74] Zheng, Y., & Zheng. D. (2017, Jul. 11). New energy automobile charging station based on carbon back capacity battery group. *China Patent No. 206323188*.

Wind Energy Scenario and Challenges in India

Sunil Kumar[1], Nishant Mishra[2], Debi Prasad Mishra[3]

[1,2]Shiv Nadar University, Delhi-NCR, India, sk300@snu.edu.in[1], nishant.mishra@snu.edu.in[2]

[3]NITTR Kolkata, Kolkata, India, dpmishraiitk@gmail.com

Abstract— **India is the second-largest country in terms of population which is about to gallop on the path of giant economy. Hence its energy consumption is spiraling at alarming rate and has already emerged as the world's 3rd largest energy consumer in world. It is interesting to note that energy consumption in this country has almost doubled since 2000 and the potential for further rapid growth is enormous. According to Energy Outlook magazine published in India January 2019, India's energy consumption set to grow by 165% and become the fastest among all major economies by 2040. India's share of global demand rises to 11% in 2040 from 5% in 2017. Fig. 1 shows that total power generation in India still mainly depends on the thermal sources. The share of thermal energy (coal, diesel, gas) is around 63% of the total energy supply of the country. In current scenario to fulfill the ongoing energy demands, we need to look other alternative energy resources because the carbon-based convention sources are limited and have hazardous impact on environment and living beings. Solar energy and wind energy are two most potential energy areas under renewable energy category which can adopted in India.**

Keywords – renewable energy, India energy policy, wind energy

I. INTRODUCTION

India is 4th largest wind energy producer. If we talk about other countries, in last 2 decades china reached at top of wind energy producers in world. India's speed of growth in wind energy was enormous in last 2 decades still we need to accelerate it further to utilize the maximum of available wind potential in nation. Fig. 2 shows that India's renewable sector has two major contributors as solar and wind energy sector. As a part of its contribution to the Paris Agreement on Climate Change, India has set a target of achieving 175 GW installed capacity of renewable energy of which 100 GW would be from solar and 60 GW from wind energy [1].

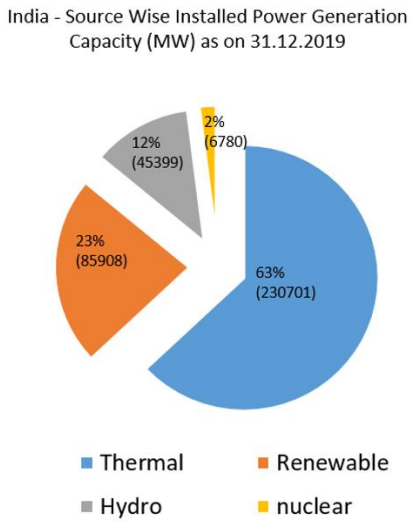

Figure 1. India Energy Scenario.

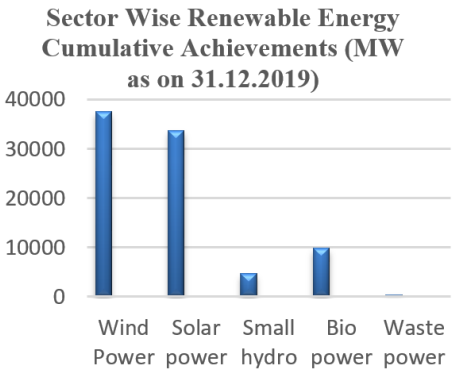

Figure 2. Sector-wise renewable energy.

ISBN: 978-86-80593-73-9

Figure 3. Betz limit.

II. WORKING OF THE WIND TURBINES

Before going to discuss about the government's initiatives and challenges in wind energy sector let's see how a wind turbine works. Wind turbine extract energy from wind by slowing it down. The power carried by a flowing mass of air is the product of the cross-sectional area of the mass and the wind, the density of the wind, ρ, and the wind speed, v. Wind Power, where,

$$P = \frac{1}{2}\rho A v^3, \qquad (1)$$

$$\rho = Air \quad density \quad (kg/m^3), \qquad (2)$$

$$v = wind \quad speed \quad (m/s). \qquad (3)$$

The power in wind cannot be converted in to mechanical energy completely as it will create a congestion at rotor. Betz limit [2] put a theoretical constrain on maximum power gain from a wind rotor. This limit says at max 59% of energy can be extracted as shown in Fig. 3. Further if we include unavoidable swirl losses it reduces to 42%.

So, wind energy depends on many factors such as wind velocity, density of air, area of wind turbine, there other factors also those affects the gain of wind energy like the surface is plain or mountain terrain, wind farm layout, fluctuation of wind velocity, atmospheric boundary layer. Wind velocity when approaches 3.5 to 4 m/s, some energy gain starts and around 14 to 25 m/s, turbines work at rated power. So for any location setting of wind most necessary thing is that average wind velocity there should be more than 10 m/s.

Blade hub height is one of the important factor as the hub height increases, wind velocity also increases (to the 1/7th power) and same time cost of hub also increases, so it is significant cost-benefit trade-off. Second is a turbines output could be reduced if the spacing between them is not enough. So, layout of a wind farm should be such that land area could be utilized for maximum power output.

India has wind potential up to 302 GW at height of 100m and 102 GW at height of 80m as shown in Fig. 4. More than 95% of the wind potential is concentrated in five states in southern and western India. These states are Andhra Pradesh, Gujarat, Karnataka, Maharashtra, Rajasthan and Tamil Nadu. Among these, 40% are concentrated in Tamil Nadu and Gujarat, reflecting that these states have crafted the wind energy policy efficiently, while other states have started developing

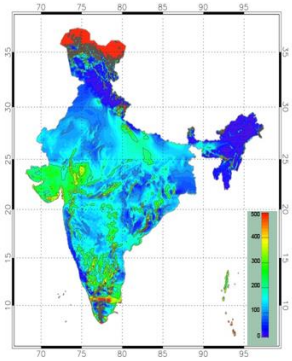

Figure 4. India wind potential at 80 m height in MW [3].

Figure 5 India's largest wind farm Muppandal (Tamilnadu) Photo: CC-by-sa PlaneMad/Wikimedia.

policies progressively for wind turbine installations. This scenario made it possible to identify the suitable areas for harnessing wind power for electricity generation.

III. Programs by Government for the Development of the Wind Power

Government of India launched various wind power support programs and schemes on different times. In 2013 generation-based incentive scheme was launched which provides wind electricity producers INR 0.50 per unit of electricity fed into the grid for a period of not less than four years [4]. In 2014 Accelerated Depreciation (AD) was reinstated for wind power plants established on or after April1 2014 at the rate of 80%. AD does not provide any direct monetary assistance ship but it helps investors in tax reduction in initial premature period. This attracted different private sector investors in the wind energy. Tariff Design for Wind Power provides no inter-state transmission charges and the charges generated due to the loss of wind power during selling of wind power to facilitate the inter-state transmission are also waived of under certain condition. Renewable Energy Certificate (REC) mechanism to relieve states with high share of wind power in their grid as it's a market-based instrument to promote renewable energy and facilitate compliance of Renewable Purchase Obligations (RPO). REC mechanism has encouraged the windy states to deploy additional capacity by reducing the procurement cost of wind. One REC equivalent to the 1MWh. REC would be traded in power exchange within the forbearance price and floor price determined by CERC from time to time. In July 2020 CERC reduced the cost of the forbearance price and floor price for both solar and non-solar REC to zero [5].

Renewable purchase obligation (RPO) was important programme in which states must purchase or produce some share of energy from renewable means. Forecasting and scheduling mechanism helped to evacuate higher units in 2016-17 compare to previous years. MNRE drafted wind solar hybrid policy for large grid connected wind –solar PV system for optimal use of transmission infrastructure, land and for better grid stability. Wind bidding schemes was launched in 2016 for non-windy states to fulfill their non-solar renewable energy purchase obligation through purchase of wind power at a tariff determined by transparent bidding process. The Green Energy Corridors Project plays a significant role in setting up transmission requirement for renewable power capacity addition.

IV. Challenges

Despite such supportive programs wind energy growth still need to accelerate as PM Modi has vison of 40% share of renewable energy by 2030. There are some barriers to wind energy development in India.

Major barrier is lack of evacuation and transmission infrastructure that causes large waste of generated electricity [6]. Grid connectivity development includes focus on sub-stations, transformers, transmission links and communication networks in remote areas. Grid structure reformation must be done on urgent basis. Green energy corridors can play a significant role in the improvement of transmission lines. Technical issues are because of wind turbine technology in India is based on the European technology. The Indian market lacks local standards in turbine manufacturing and thus, a mismatch in the self-manufactured items and imported components is likely to occur [7]. As the Government gave the slogan for Aatmanirbhar Bharat, we need to set our local wind industry standards.

Modern wind turbines are quite efficient, but when a wind farm is concerned, the performance of individual turbine is adversely affected by the other turbines so the wind farm layout optimization need to be adopted. Proper forecasting and scheduling techniques would help to harness more wind energy. For accurate forecasting and scheduling, it is essential to put in a metering and communication infrastructure at every pooling station for real time generation of data.

Initial capital investment is very high and risk factor is always involved questioning the confirmed profitability of the project. This

makes it important to have access to credit at cheap rates of interest [8].

Land availability puts a challenge to wind farm developments as the process of conversion of usable land like agricultural to the non-agriculture is a time taking process. India needs wind power development friendly land policy.

Renewable energy purchase obligation (RPO) needs to make stricter as many a state failed to fulfill the required level of RPO. Different states have different tariff that causes uncertainty among investors.

India lacks R&D in major area of wind energy, India's wind energy market mainly depends on foreign companies for components and wind turbines technology. We need to increase manufacturing in wind turbine technology and innovation in big data analytics to reduce the operating cost and to meet the current requirement of the wind industry. Professional base needs to cultivate to fulfil the skilled human capital for wind energy industry.

Offshore wind power development: India has an estimated offshore wind energy potential to generate around 70,000 MW power, most of that identified in coastal Gujrat and Tamilnadu. It is needed to focus upon this offshore wind energy.

It's a fact that India is a major energy importer and consumer of energy, so it is strongly recommended that we must move on the non-conventional sources of energy, wind energy can play a big role in coming decades. India needs more investments in wind power research and development, wind component manufacturing industry, wind project installation, distribution, and evacuation, grid integration, and more importantly skilled manpower development. Country is expected to reach Grid Parity in 2022 [1], which means production cost of energy from renewable energy resources will be same as of conventional sources.

V. CONCLUSION

Wind energy is sustainable and clean source of energy. Fossil fuels sources increase environment pollution and also these are limited in India and it has the maximum share of total imports by it. Wind energy provides a solution for India's energy growth requirement as well environment concern. India has abundant wind energy potential and certain government schemes increased the development of this sector. But still there are many things to be done on ground of governance and technological requirement especially remote sensing technique for resource assessment and better logistic services.

REFERENCES

[1] Chaurasiya, P. K., Warudkar, V., & Ahmed, S. (2019). Wind energy development and policy in India: A review. *Energy Strategy Reviews*, *24*, 342-357.

[2] Betz, A. (2014). Introduction to the theory of flow machines. Elsevier.

[3] NIWE, India ' s Wind Potential Atlas at 120m agl, no. October, 2019.

[4] Kar, S. K., & Sharma, A. (2015). Wind power developments in India. *Renewable and Sustainable Energy Reviews*, *48*, 264-275.

[5] Sharma, S., & Sinha, S. (2019). Indian wind energy & its development-policies-barriers: An overview. *Environmental and Sustainability Indicators*, *1*, 100003.

[6] Thapar, S., Sharma, S., & Verma, A. (2018). Key determinants of wind energy growth in India: Analysis of policy and non-policy factors. *Energy Policy*, *122*, 622-638.

[7] Irfan, M., Zhao, Z. Y., Ahmad, M., & Mukeshimana, M. C. (2019). Critical factors influencing wind power industry: A diamond model based study of India. *Energy Reports*, *5*, 1222-1235.

[8] Diógenes, J. R. F., Claro, J., Rodrigues, J. C., & Loureiro, M. V. (2020). Barriers to onshore wind energy implementation: A systematic review. *Energy Research & Social Science*, *60*, 101337.

Experimental-data-based Mathematical Modeling for the Purpose of Optimizing Energy Generation from a Municipal Landfill Site

Mehrdad Adl[1], Mohammad-Reza Vahid-Estakhri[2], Hossein Ghadamian[3]

[1,2,3]Materials and Energy Research Center, Karaj, Iran, adl.mehrdad@gmail.com[1], mohammadrezavahid@yahoo.com[2], hghadamian@gmail.com[3]

Abstract—**Biogas as a renewable energy carrier is achievable from municipal landfill sites while needs a suitable and efficient extraction network. Designing such extraction system for biogas from landfills has to taking multiple variables including indigenous potential of landfill gas (LFG) generation in the dumped solid wastes, environmental circumstances, gas flow characteristics within the pipelines and accessories, economical aspects of LFG extraction system and spatial configuration of the system components into account. Simple traditional methods in design of LFG extraction wells and headers might provide inappropriate paths and impose extra costs to the LFG management entities. Cost minimization in LFG collections might be accessible by selecting suitable path and proper sizing for pipes, valves and other system components as well as by considering constraints in pressure losses and flow-rates. This goal can be formulated as an optimization challenge. A mathematical model has been established in this research in which, the most suitable path is adopted for header pipes at the first step in order to collect LFG from the extraction wellheads and at the next steps various sizes of high-density poly-ethylene (HDPE) pipes are selected in a manner to minimize the system costs meanwhile considering the technical restraints and obligated standards. Finally the model solution was implemented using Genetic algorithm by MATLAB® software.**

Keywords- landfill gas, optimization, energy

I. INTRODUCTION

Following the increasing consumption of fossil energy reserves the crises of global warming and global environmental degradation have been emerged as vital threats to the world's life and civilization. The facts such as limited fossil fuel reservoirs and their non-renewable nature have captured the attention of worldwide governments and state authorities to the renewable resources of energy among which, biomass is considered as one of the most diverse and multi-way applicable resource of various energy carriers [1]. Biogas is known as a valuable energy carrier with suitable energy content that is generated from biomass through a chain of biological reactions that make a process named as anaerobic digestion [1]. The main constituents of biogas are methane (CH_4), carbon dioxide (CO_2), hydrogen sulfide(H_2S), water vapor (H_2O), ammonia(NH_3), along with a few percentage of other possible gases such as oxygen (O_2) and nitrogen (N_2) as a consequence of air presence in the process medium as well as trace amounts of other chemical compounds such as non-methane hydrocarbons and volatile organic compounds (VOCs) [2]. Taking the landfill gas (LFG) as a sort of biogas into account, the potential of energy generation from the solid wastes landfilling sites has somehow been neglected and virgin in Iran due to a couple of reasons such as variable and slow biogas flow rate, deficient LFG extraction systems, gas leakage in the

ISBN: 978-86-80593-73-9

transfer pipeline, unsuitable infrastructures and improper dumping procedures. LFG collection and transfer to a central station for the further landfill gas to energy (LFGTE) purposes requires designing an optimal collection network with certain specifications to guarantee the minimum pressure losses during the gas transfer [3]. The increased pressure losses within a collection network will pursue the biogas blower to consume more energy in order to provide sufficient negative pressure in the network for the enough suction on the LFG extraction wellheads. Hence one of the main objectives for LFG extraction network design is to minimize pressure losses in biogas flow [3]. On the other hand since the network investment cost will significantly be increased with the increase in size and length of pipes and connectors therefore, the LFG collection network should optimally be designed in order to minimize the costs while maximizing the net energy gain from the landfill.

Estimation models for LFG generation are employed to predict the methane flow rate from the landfill sites [4].Optimizing the LFG transfer process from the gas extraction wellheads to the central station of LFGTE is highly prioritized for maximizing the energy uptake from a landfill site.

II. Methodology

The landfill site in Barmshur area as shown in Figure.1, located south-east to Shiraz city in Iran has been investigated in the current research. The site contains 4 zones as the main landfilling cells from which, the zone #4 that is the newest solid wastes accepting cell has been under the focus of investigation in this study work. The number and the exact location of pre-fabricated LFG extraction wells were determined in this methodology and the LFG flow rate for each well was estimated considering a zone of influence for the well. The effective space of the aforementioned zone of influence and the characteristics of the dumped solid wastes within that space were taken into account for estimating the biogas and methane flow rate.

Figure.1. Geographical location and aerial image of the landfill site in Barmshur, Shiraz

A couple of different geometries were considered on the next steps for LFG collection design and the calculations for pressure losses and system costs were compiled afterwards.

A. Mathematical Modeling

The mixed-integer programming was adopted as the main procedure for the objective optimization in this research. This is a powerful tool for solving the highly data intensive and sophisticated problems [5].

The mixed-integer programming was adopted as the main procedure for the objective optimization in this research. This is a powerful tool for solving the highly data intensive and sophisticated problems [5].

The methane flow rate from every extraction well could be estimated using the (1) adopted from USEPA LandGEM model [4].

$$\bar{Q}_{CH_4} = \frac{1}{8760}\sum_{t=1}^{n} kL_0M_i(e^{-kt_i}), \qquad (1)$$

Q is the average flow rate of methane in *m*^3/*h*, *k* is the biodegradation rate coefficient of organic wastes in 1/*y*, L_0 is the methane yield potential for the buried wastes in *m*^3/ton, *M* is the quantity of buried wastes in the i_{th} layer within the zone of influence for the extraction well under study in metric ton, and t is the time after landfilling of the i_{th} layer in years.

The pressure loss in the suggested model is estimated using Darcy-Weisbach equation assuming the LFG flow rate is known for each header or pipeline branch from the estimations in the LFG modeling section for every LFG extraction well.

$$\Delta P = f\left(\frac{L}{d}\right)\left(\frac{\rho_g}{\rho_w}\right)\left(\frac{v^2}{2g}\right), \qquad (2)$$

where, f is the dimensionless coefficient of friction that can in turn be estimated from Blasius formula (3) as follows [6]:

$$f = \frac{0.3164}{R_e^{0.25}}. \qquad (3)$$

L and *d* are the pipe length and diameter in meter respectively, *v* is the gas velocity in m/s and g is the gravity acceleration (*m*/*s*^2).

The model for LFG collection was developed on the graph concept basis in which, the collection points are assumed as the nodes and the headers for LFG flow are considered as the edges [6]. The following assumptions were established for the applied model:

(a) The distance between the nodes is known and determined from the geometrical layout. (b) The distance between the biogas blower/compressor and collection points is determined by the same manner. (c) The supply (LFG flow rate) in every node is known and determined using (1) and landfill site management data. (d) The demand by the central station (blower/compressor) is known and equal to the sum of the flow rates from the LFG wellheads. (e) The cost of each header branch is known and estimated from the unit cost of pipes and connectors thereby applied, their length and types, and market data for the applied equipment's and materials. (f) The diameter of each pipe is specified. (g) The range of gas transfer velocity is specified.

The model input parameters were defined at the beginning of mathematical computation as follows:

Distances between all nodes and the central station, unit cost of each pipe type, and the quantity of LFG that inflows to each node.

Symbols and definitions in the model

The symbols and parameters in the mathematical model are defined in the form of a directional graph problem G(N,S) as follows:

N = [1,2,3,…,*n*] is the set of nodes (collection and distribution points).

S = [1,2,3,…,*s*] is the set of available pipes in various sizes.

The parameters include: *L*; the pipe length (*m*), *D*; the pipe diameter (*m*), $d_{i,j}$; the distance between node "*i*" and node "*j*" (*m*), C_K; the cost per unit length of pipe from type "*K*" in the market (US$/m), $Q_{i,j}$; the gas transfer flow rate from node "*i*" to node "*j*" (*m*3/*h*), H_i; the LFG inflow in the node "*i*" (*m*3/*h*).

- *Decision variables*

X_{ijk}: is a binary decision variable equal to 1 if the pipe type "*K*" is applied for gas transfer from node "*i*" to node "*j*" and otherwise is zero. Z_{ij}: is a binary decision variable equal to 1 if the gas transfer operates from node "*i*" to node "*j*" and otherwise is zero. Vm_{ij}: is gas transfer velocity from node "*i*" to node "*j*". Y_{ijk}: the length of pipe type *K* in the edge from node "*i*" to node "*j*". Pm_{ij}: the pressure loss along the gas transfer from node "*i*" to node "*j*" [5].

The objective of modeling was to minimize the collection system costs and simultaneously minimizing the pressure losses. These objectives will consequently provide the selection of appropriate configuration and pipe size for each part of the system. The target function has been defined as a cost function in which the unit cost of pipe per meter of length is the variable that in turn has a direct relationship with the pipe size. Four standard internal diameters of high-density poly-ethylene (HDPE) pipes were considered in design works including 0.075m, 0.09m, 0.11m and 0.125m. The unit cost per length for each of those pipes is known from the market data.

The objective function and the model's limitations were as follows [5].

$$min\ F = \sum_{i\in N}\sum_{j\in N}\sum_{k\in S} y_{i,j,k}C_k, \forall i,j\in N, k\in S, \quad (4)$$

$$\sum_{i\in N}\sum_{j\in N} Z_{i,j} \le n-1, \forall i,j\in N\frac{1}{2}, \quad (5)$$

$$\sum_{i\in N} Z_{i,j} = 1, \forall j\in N, \quad (6)$$

$$Z_{ii} = 0, \forall i\in N, \quad (7)$$

$$Y_{i,j,k} = d_{i,j}, \ \forall i,j\in N, \ \forall k\in S, \quad (8)$$

$$\sum_{k\in S} X_{i,j,k} = 1, \ \forall i,j\in N, \ i<j, \quad (9)$$

$$\bar{v}_{i,j} \le 3X_{i,j,k}, \ \forall i,j\in N, \ \forall k\in S, i<j, \quad (10)$$

$$\bar{v}_{i,j} = \frac{Q_{gas_{i,j}}}{3600*0.785*D_k^2}, \ \forall i,j\in N, \ \forall k\in S, \quad (11)$$

$$Q_{gas_{i,t}} = Q_{gas_{i,j}} + H_j, \forall i,j,t\in N, i<j<t, \quad (12)$$

$$X_{i,j,k} \le Z_{i,j}, \forall i,j\in N, i<j, \forall k\in S, \quad (13)$$

$$X_{i,j,k} \in \{0,1\}, \ \forall i,j\in N, i<j, \ \forall k\in S, \quad (14)$$

$$Z_{i,j} \in \{0,1\}, \forall i,j\in N, i<j, \quad (15)$$

$$j = i+1, \ t = j+1, \ \forall i,j,t\in N, \quad (16)$$

$$\begin{gathered} 0.075m \le D_k \le 0.125m \\ \forall k\in S, \quad D_k \in \{0.075, 0.090, 0.110, 0.125\} \end{gathered}, \quad (17)$$

$$\frac{P_{m_{i,j}}}{d_{i,j}} \le 0.0002, \ \forall i,j\in N, \quad (18)$$

$$P_{m_{i,j}} = (12.62)\left(\frac{0.3164}{105042 D_k \bar{v}_{i,j}}\right)^{0.25}\left(\frac{Y_{i,j,k}}{D_k}\right)\left(\frac{\bar{v}_{i,j}^2}{2g}\right), \quad (19)$$

$$\begin{gathered} 0.626US\$/m \le C_k \le 1.715US\$/m \\ \forall k\in S, \quad C_k \in \{0.626, 0.899, 1.329, 1.715\} \end{gathered} \quad (20)$$

Obviously with increasing the size of headers and collection pipes, the collection network cost will be increased therefore, appropriate pipe sizes should be selected in order to fulfill the requirements and limitations in the system while minimizing the costs. The (4) has been considered in order to minimize the cumulative costs of collection network as the objective function [5].

The constraints (5) through (7) in fact establish a tree algorithm. According to the problem's circumstance the LFG collection network should follow a tree algorithm in which all nodes connected together. The constraint (5) demonstrates that the total number of edges might be at most equal to the number of nodes minus one. This is essential for a tree-graph. The right part of the equation has been divided by 2 since every edge is considered twice in this equation. The constraint (6) ensures the entrance to every node from only one adjacent node hence, it prevents from formation a ring. The constraint (7) prevents self-entrance for each node. The constraints (8) and (9) encompass the distance between two nodes and limitation of one pipe-size for every edge. The gas velocity limitation has been considered in the constraints (10) and (11). The limit on average gas flow rate in every pipe has been determined in (12). The constraint (13) defines that a pipeline might be

established between the nodes “i" and “j” only if gas transfer exists from “i" to “j”. The specification of decision variables has been defined in constraints (14) to (17). The constraints (18) and (19) obligate that the head loss per meter of pipe length should not exceed 0.0002m of water column [8]. The constraint (20) concerns the unit cost of pipe per meter for various sizes from HDPE type PE-100 as instance, a pipe of this type with internal diameter of 75mm (0.075m) costs 0.626US$ per meter.

B. Optimization Procedure

As mentioned before the main objective of the research was to select the best route for LFG transfer following the requirements, limitations and constraints of the problem. Since the model was non-linear with several complexities, the solution with the conventional linear optimization software is not recommended therefore, the Genetic Algorithm was adopted to solve the optimization problem. In this manner the initial data for LFG collection from the gas extraction wells and transfer to the central station were acquired and introduced to the mathematical model within the framework of Genetic Algorithm. The best routes for collection and transfer of LFG along with the size and length of the header pipes, LFG flow rates, gas velocities and pressure losses inside the pipes, and pipeline costs were afterwards extracted from the optimization algorithm. The Genetic Algorithm as a powerful approach for search in extra-large data-spaces acts on the basis of natural genetic mechanism at the end of which, leads to finding the optimal answer that might be unattainable by the other methods even after long durations. This Darwin’s evolution theory inspired algorithm reflects the natural selection process by which, the fittest individuals from a population will survive for reproducing the next generation. Every generation if have the better fitness characteristics than the parents will have more chance for survival and the iteration process will be continued until a generation with the fittest individuals will be found at the end. The main advantage of the Genetic Algorithm comparing the older optimization procedures is the capability to work with a population or a complex of points at each moment not a certain single point [7].

C. The Case Study

The Zone 4 in Barmshur landfill site near Shriaz as mentioned before contains the most recent landfilled solid wastes and has been equipped to 38 LFG extraction wells each one by a particular geographical coordination. Two configuration geometries were appraised for the collection system in order to collect and transfer the LFG from the extraction wells to the central station adjacent to the power plant. The first configuration was in form of branch or open loop as shown in the aerial image of 0.

The second configuration was considered in the form of matrix or closed loop in which, some header branches pass through the loops and connect some of the nodes together. This configuration has the advantage of facilitating the gas collection from the wells in the middle of the network [8]. The matrix configuration has been shown in 0.

According to the proposed model the code was developed in MATLAB® environment. This software optimized the cost function by the help of Genetic Algorithm and calculated the minimum value of this function. The number of function evaluation (NFE) is calculated from (21) shown below,

$$NFE = n_{pop}.(t+1)\,, \qquad (21)$$

where, n_{pop} is the quantity of population and “t” is the number of iterations.

III. Results and Discussion

The cost of the LFG collection and transfer system has been considered as the objective function in this study (Figs. 2 and 3). The optimization process for this function was carried out by MATLAB software using mixed-integer programming procedure and Genetic Algorithm. The costs values for the system versus the numbers of function evaluation have been demonstrated in 0 in which the vertical axis shows the total cost for piping system and horizontal axis represents NFE. This graph implies that the algorithm has obtained the final solution or minimal cost at an NFE equal to around 5800. This cost has been estimated as 1071US$ to which the total cost of connector pipes is added to finish the final cost at around 1550US$. The details of pipe lengths, pressure

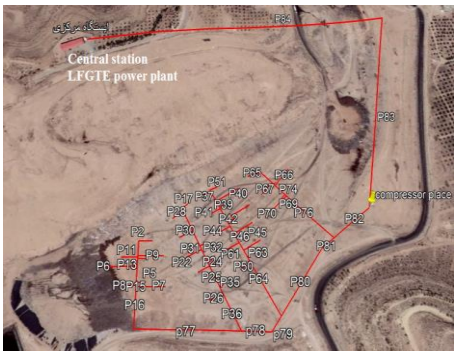

Figure 2. The locations for LFG collection network, transfer pipeline and central station.

Figure 3. The matrix type configuration for LFG collection system.

losses and pipe costs have been presented in Table I as the output from the software.

The total pressure loss that mainly influences the working power consumed by the LFG compressor, was calculated for both geometrical configurations. As might be seen in, the matrix collection system provided smaller pressure drop and consequently this configuration was accepted as the proper network for collecting the LFG from Zone 4 and transfer to the central station.

Various options for the utilization of LFG were appraised in terms of overall system efficiency and finalized energy cost (Fig. 4.). The considered options included: Power generation from LFG using IC-engine-generator sets, Upgrading of LFG to biomethane for Bio-CNG generation. Combined heat and power (CHP) generation, and combined cooling-heating and power (CCHP) generation.

The evaluations implied that CCHP was the most appropriate utilization option for LFG having an overall energy efficiency of 84.1%,

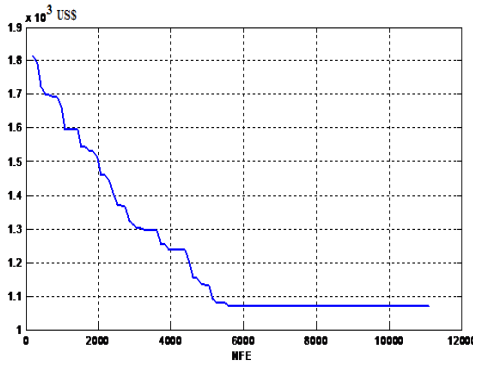

Figure 4. Optimization graph for cost function regarding the LFG collection and transfer system.

TABLE I. THE INFLUENCE OF COLLECTION SYSTEM CONFIGURATION ON THE TOTAL PRESSURE DROP AND WORKING POWER OF COMPRESSOR.

Configuration type	**Cumulative pressure drop (m-water)**	**Compressor's working power (kW)**
Branch	0.0241	0.105
Matrix	0.020	0.103

total useful thermal-electrical power of 619.3kW, and finalized cost of energy equal to 0.0134US$/kWh.

ACKNOWLEDGEMENTS

The current research was jointly supported by the Materials and Energy Research Center under the grant No. 571396062 and THN Consulting Engineers. The authors should warmly appreciate the supports by Mr. Iraj Pournasiri, the CEO of THN company during the field works in Barmshur landfill site in Shiraz.

REFERENCES

[1] Biosantech, T. A. S., Rutz, D., Janssen, R., & Drosg, B. (2013). Biomass resources for biogas production. In *The Biogas Handbook* (pp. 19-51). Woodhead Publishing.

[2] Gomez, C. D. C. (2013). Biogas as an energy option: an overview. *The biogas handbook*, 1-16.

[3] SA, L. C., & Denmark, S. AHEF TASK GE96" Capacity strengthening of the SWMCG by introducing applicable methods for assessing landfill gas potential at the existing dumpsites in Georgia".

[4] Fei, X., Zekkos, D., & Raskin, L. (2016). Quantification of parameters influencing methane generation due to biodegradation of municipal solid waste in landfills and laboratory experiments. *Waste management*, *55*, 276-287.

[5] Drouven, M. G., & Grossmann, I. E. (2017). Mixed-integer programming models for line pressure optimization in shale gas gathering systems. *Journal of Petroleum Science and Engineering*, *157*, 1021-1032.

[6] Dranchuk, P. M., & Abou-Kassem, H. (1975). Calculation of Z factors for natural gases using equations of state. *Journal of Canadian Petroleum Technology*, *14*(03).

[7] Burhaneddin Sandikci. (2004). Genetic Algorithms. Bilkent University, Department of Industrial Engineering, Ankara-TURKEY.

[8] United States Army. (2008). Landfill off-gas collection and treatment systems, Report EM 1110-1-4016 30 MAY 2008.

Appendix A
Table A-1

Pipe code	L(m)	D(m)	V(m/s)	Q(m^3/h)	$h_f(m_{water})$	h_f/l	pipe cost (US$)
p1	20.44	0.075	0.922	-14.65	5.06E-04	2.48E-05	1.41E+01
p2	2.06	0.075	0.703	-11.17	3.17E-05	1.54E-05	1.42E+00
p3	1.68	0.075	0.484	-7.69	1.35E-05	8.01E-06	1.16E+00
p4	11.5	0.075	0.265	-4.21	3.21E-05	2.79E-06	7.92E+00
p5	22.22	0.075	0.047	-0.74	2.96E-06	1.33E-07	1.53E+01
p6	4	0.075	0.172	2.73	5.23E-06	1.31E-06	2.75E+00
p7	1.75	0.075	0.391	6.21	9.65E-06	5.51E-06	1.21E+00
p8	209.74	0.075	0.61	9.69	2.52E-03	1.20E-05	1.44E+02
p9	50.06	0.075	0.647	-10.29	6.68E-04	1.33E-05	3.45E+01
p10	10.66	0.075	0.427	-6.78	6.85E-05	6.43E-06	7.34E+00
p11	31.63	0.075	0.209	-3.33	5.86E-05	1.85E-06	2.18E+01
p12	5.54	0.075	0.008	0.132	3.61E-08	6.52E-09	3.82E+00
p13	20.55	0.075	0.221	3.52	4.19E-05	2.04E-06	1.42E+01
p14	5.4	0.075	0.446	7.09	3.75E-05	6.95E-06	3.72E+00
p15	24.2	0.075	0.665	10.57	3.38E-04	1.40E-05	1.67E+01
p16	6.21	0.075	0.884	14.05	1.43E-04	2.30E-05	4.28E+00
p17	23.03	0.075	1.103	17.53	7.80E-04	3.39E-05	1.59E+01
p18	8.31	0.075	1.322	21.01	3.87E-04	4.65E-05	5.72E+00
p19	81	0.075	1.141	-18.13	2.91E-03	3.60E-05	5.58E+01
p20	67	0.075	1.257	19.98	2.85E-03	4.26E-05	4.61E+01
p21	52	0.075	2.681	42.62	8.34E-03	1.60E-04	3.58E+01
p22	2.21	0.075	0.087	-1.38	8.76E-07	3.97E-07	1.52E+00
p23	18.6	0.075	0.132	2.1	1.54E-05	8.27E-07	1.28E+01
p24	10.62	0.075	0.351	5.58	4.86E-05	4.57E-06	7.31E+00
p25	2.21	0.075	0.57	9.06	2.36E-05	1.07E-05	1.52E+00
p26	17.57	0.075	0.789	12.54	3.31E-04	1.89E-05	1.21E+01
p27	4.97	0.075	1.008	16.02	1.44E-04	2.90E-05	3.42E+00
p28	7.55	0.075	1.227	19.5	3.08E-04	4.08E-05	5.20E+00
p29	12.31	0.075	1.446	22.98	6.70E-04	5.44E-05	8.48E+00
p30	7.43	0.075	1.665	26.46	5.18E-04	6.97E-05	5.12E+00
p31	6.65	0.075	1.883	29.94	5.75E-04	8.65E-05	4.58E+00
p32	12.57	0.075	2.102	33.42	1.32E-03	1.05E-04	8.66E+00
p33	10.91	0.075	2.321	36.9	1.36E-03	1.25E-04	7.51E+00
p34	11	0.075	2.54	40.38	1.61E-03	1.46E-04	7.58E+00
p35	81	0.075	2.759	43.86	1.37E-02	1.69E-04	5.58E+01
p36	136	0.09	2.793	63.94	1.87E-02	1.37E-04	1.34E+02
p37	83.72	0.075	2.987	-47.48	1.62E-02	1.94E-04	5.77E+01
p38	28.8	0.09	2.226	-50.96	2.66E-03	9.23E-05	2.85E+01
p39	3.53	0.09	2.378	-54.44	3.66E-04	1.04E-04	3.49E+00
p40	2.33	0.09	2.53	-57.92	2.69E-04	1.15E-04	2.30E+00
p41	20.26	0.09	2.682	-61.4	2.59E-03	1.28E-04	2.00E+01
p42	3.16	0.09	2.834	-64.88	4.45E-04	1.41E-04	3.12E+00
p43	91.42	0.09	2.986	-68.36	1.41E-02	1.54E-04	9.04E+01
p44	72	0.125	2.995	132.23	7.40E-03	1.03E-04	1.36E+02
						Total cost	**1.07E+03**

Automotive electric retrofit: A model for circular economy and pollution reduction in Serbia

Dalibor Ignjatović[1], Radovan Jevtić[2]

[1,2]NAAEV, Belgrade, Serbia

Abstract—**The automotive electric retrofit, or more commonly called e-retrofit, aims to respond favorably to the worldwide forced march of electric mobility and at the same time to allow the resolution of environmental issues of design, production, use and recycling of the automotive sector. The objective of this paper is to review the pollution problems identified in Serbia, to present the advantages of the innovative model that is the automotive e-retrofit in terms of reducing these pollution problems and finally to show how it is part of the circular economy movement.**

Keywords - e-retrofit, automotive, circular economy, pollution

I. INTRODUCTION

In Serbia, there are today more than 2.4 million Internal Combustion (IC) vehicles with dominance of vehicle categories visible in Fig. 1 [1]. These vehicles are mainly imported from Western countries (more than 100,000 vehicles per year).

Mostly second-hand, already aged and worn, they enter into use for an uncertain duration and end their days in scrap-yards without consideration for recycling. From their use to their end-of-life vehicle status, they are sources of various pollution with a considerable impact on the entire territory of the Republic of Serbia.

Between the use phase and until the end of the vehicle's life, there are environmental repercussions of air, soil, groundwater, but also noise pollution.

Also, with a restricted purchasing capacity or severe vehicle regulations, buyers are forced to seek new solutions forcing them to tend towards recent or new models often far from being accessible for their wallet.

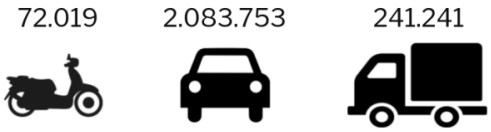

Figure 1. Registered mopeds, motorcycles, passengers cars and trucks in Serbia (2020)

If we add European directives implying the end of Internal Combustion Engines (ICE) by 2035, the task only becomes more complex.

It is in this perspective of environmental and economic consideration that the automotive e-retrofit provides an answer in line with the needs and requirements of each. It presents itself as a useful, albeit ephemeral, solution and is also part of the circular economy movement.

II. DIFFERENT KIND OF POLLUTION

In Europe, the average age of a vehicle is 11.5 years, while as presented in Fig. 2 in Serbia it is 17 years [2, 3]. This difference is mainly explained by a large import of used vehicles from Western Europe.

If we add to this that combustion vehicles are responsible on a global scale for nearly 20% of total CO2 emissions and almost 39% of total NOx emissions, i.e. almost 10% of particles (PM10, PM2,5) and that the majority of vehicle engines in Serbia are Euro 3 engines (released in 2004) we are witnessing catastrophic air pollution having a consequent impact on the health of the population. These engines, compared to Euro 6 engines (released in 2014), exhibit CO_2 emissions levels of around 22% to 26% higher and CO emission levels approximately 4 times higher [4].

ISBN: 978-86-80593-73-9

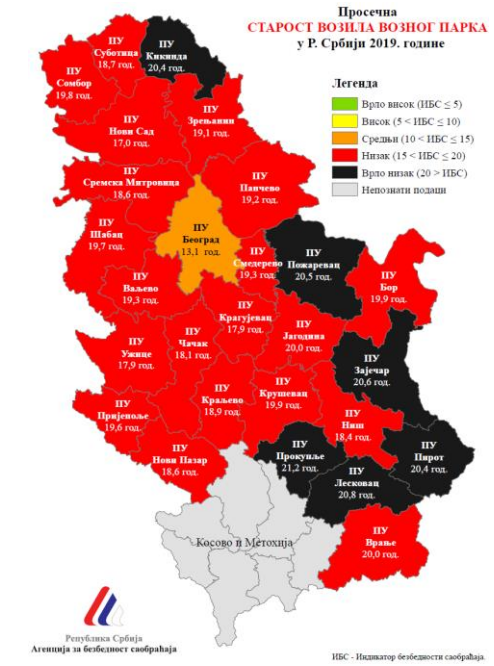

Figure 2. Map of the average age of vehicle fleet in Serbia (2019) [2].

We can see in Fig. 3 that the levels of NOx between Euro 3 and Euro 6 are between 6 to 10 times higher.

An Internal Combustion vehicle is responsible for almost 80% of noise pollution as shown in Fig. 4 [6]. The World Health Organization informs that noise is the second source of pollution having significant repercussions on population.

In Belgrade (Serbia) a study aimed to find out the level of noise pollution (dB) in the city by placing 35 measurement points [7]. Out of all these measurement points, 30 of them were found to be above the authorized thresholds.

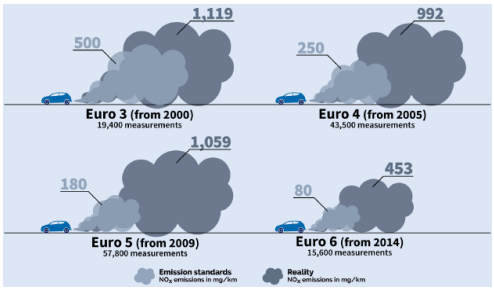

Figure 3. Comparison of Euro standards with actual emissions observed [5].

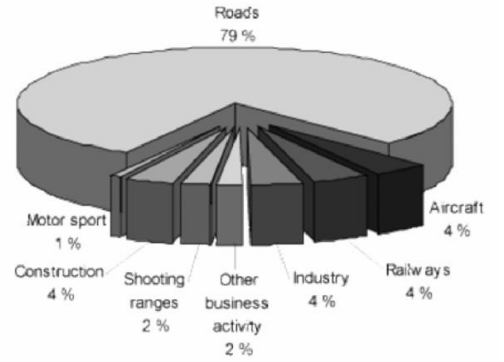

Figure 4. Distribution of noise annoyance.

Moreover, when we take into consideration the fact that vehicles registered in Serbia are around 17 years old and that they end up being scrapped without being treated, or partially, due to a lack of recycling means, this results in catastrophic repercussions on soil and water pollution.

III. ECONOMICAL IMPACT

In Serbia, older vehicle users are particularly disadvantaged economically. The restriction of older vehicles, considering among others those using a Euro 3 engine or more, obliges users to invest in the maintenance of their vehicle or to buy newer and more expensive cars despite their limited purchasing capacity.

Rising fuel prices, which has multiple consequences, both financial and psychological for users, makes the economic toll of car use more complicated. Fig. 5 presents a forecast of the price of the barrel for 2050 around $175 [8].

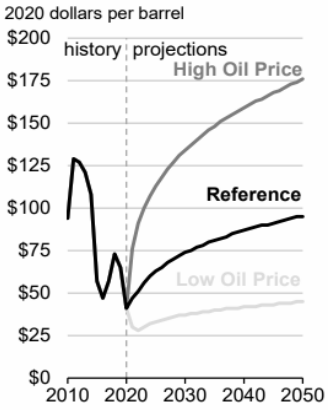

Figure 5. World oil prices [8].

IV. THE E-RETROFIT

Retrofitting generally consists of adding, modifying or restoring technological functions in aging systems. This involves replacing obsolete or worn parts with new ones while maintaining the configuration and operation of the device.

In the field of transport, e-retrofit is the replacement of an Internal Combustion Engine by an electric motor using a battery or a fuel cell as a source of energy. It includes the possibility of conversion for two-wheelers, motorcycles, vintage and modern cars, light commercial vehicles, trucks, buses, boats and others.

The e-retrofit is present in 13 countries of the European Union but there is currently no common European regulation, and the e-retrofit can have completely different standards and security criteria.

Major benefits of the e-retrofit is low operating costs, high level of customization, flexible integration and the consideration that the vehicle can be designed to satisfy individual needs.

V. ENVIRONNEMENTAL BENEFITS OF E-RETROFIT

The e-retrofit solves the challenges of sustainable development through the principles of circular economy.

Thus, in the context of the e-retrofit of a diesel-powered IC vehicle, we can see in Fig. 6 achievement of 66% less Green Houses Gases (GHG) emissions. This vehicle will have driven 10 years (on a basis of 10,000 km per year) in Internal Combustion configuration then will have completed the following 10 years having been converted to electric [9].

The e-retrofit allows a reduction of industrial waste by reusing the carcass of the vehicle. By converting the Internal Combustion vehicle to electric, we avoid the production of a new vehicle and we also avoid greenhouse gas emissions associated with this same production (Fig. 7).

The results of a Japanese study, giving the comparison in terms of noise between a hybrid vehicle (in electric mode) and a vehicle with Internal Combustion Engine (ICE), are presented in Fig. 8 [10]. We note a significant difference in the starting phase of the vehicle with values equivalent to 20 dB. This difference up to 30 km/h, although decreasing with increasing

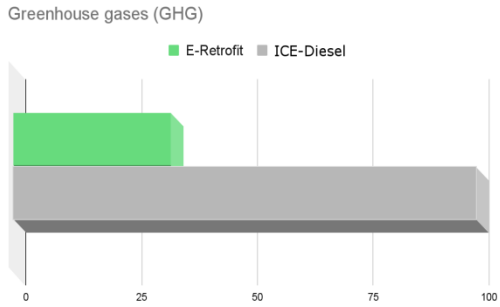

Figure 6. Comparison between a 20-year-old internal combustion vehicle and an internal combustion vehicle used for 10 years and then converted to electric for the remaining 10 years [9].

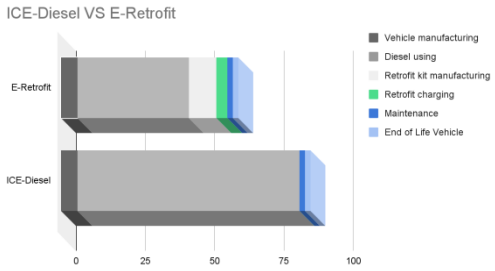

Figure 7. Comparison of GHG emissions between a diesel ICE vehicle and an electric retrofitted vehicle [9].

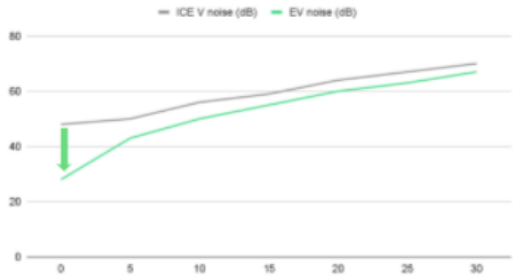

Figure 8. Noise levels from an HEV (electric mode) compared to an ICE vehicle [10].

vehicle speed, remains lower for electric vehicles.

A similar study considers values of 15 dB at 10 km/h. This is explained by the consideration of different measurement methods [11].

VI. E-RETROFIT OPPORTUNITIES

The e-retrofit is also a vector of technological opportunities with development, research and innovation in the electric mobility sector. Opportunities for new jobs exist in battery manufacturing, the production of powertrain

assemblies and the manufacture of power electronic components.

The trend in major European cities is to restrict access to certain parts of the city to vehicles with Internal Combustion Engines. As examples, when entering London, it costs £12.5 per day for ICE vehicles, upon entering Rome, the hypercentre is strictly off-limits to ICE vehicles at certain times of the day, and for Paris in 2030, only zero emission vehicles will be authorized. The advantage for e-retrofit is that in these kinds of situations it is not impacted.

VII. Economical Benefits of E-Retrofit

The starting price for new electric cars is today around 20,000-25,000 euros. Fig. 9 shows that the production of electric vehicles is about 45% more expensive compared to ICE vehicles. This difference is expected to narrow by 2030 to 9% [12]. For the e-retrofit the prices start between 8,000-11,000 euros.

As in the subsidy process for the purchase of a new electric vehicle, there are a large number of European countries that offer grants for the e-retrofit, the latter being part of the electric mobility process and of the European climate plan.

If we consider an ICE vehicle X whose consumption is 5.7 liters per 100 km, with use for 5 years and a distance of 40 km per day (i.e. 75,000 km over 5 years), we arrive at a consumption of fuel of 4,275 liters. If we consider a fuel price of 170 Serbian dinars per liter, we arrive at a total amount of 726,750 Serbian dinars (or about 6,210 euros for 5 years of use).

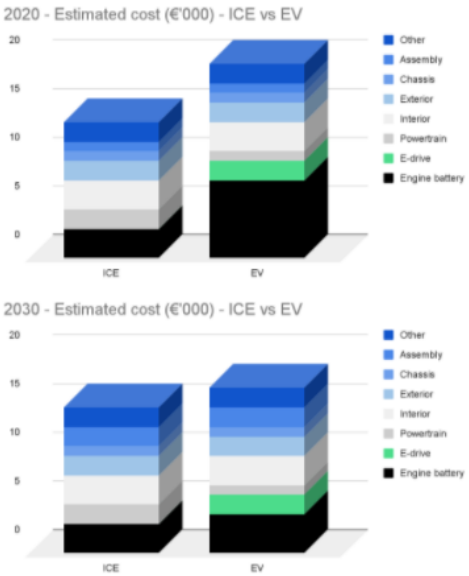

Figure 9. Comparison of direct costs ICE vs. BEV - European compact class vehicle [12].

If we compare this consumption with the electric consumption of a retrofitted vehicle we have a total electricity consumption of about 61,500 Serbian dinars (or about 525 euros).

Table I shows a savings of 5,685 euros for the use of the same vehicle considering e-retrofit.

As part of the e-retrofit analysis it is important to take into consideration the impact of vehicle maintenance. The number of parts in the maintenance of an ICE vehicle is much higher than an electric vehicle.

Table II shows the case of a bus, where the maintenance savings for an electric bus are estimated at an average of 40% compared to a standard diesel bus [13].

TABLE I. Consumption comparison between an ICE vehicle and his electrical equivalent (e-retrofit).

	ICE	**E-RETROFIT**
Consumption (kW/km)	0.60	0.14
Gasoil (RSD/l)	170	-
Electricity (RSD/kWh)	-	6
Distance (km)	75.000	75.000
Cost (RSD)	726.750	61.500
Cost (EUR)	6.210	525
Difference (EUR)	-	**-5,685**

TABLE II. Range of relative maintenance costs per mile to a diesel bus by fuel type [13].

-% Difference $/mile relative to diesel			
	Low	**Mid**	**High**
CNG	-10%	0%	12%
Diesel hybrid	4%	13%	27%
Battery electric	21%	**40%**	59%

VIII. CHALLENGES

From a technological point of view, in Serbia there are all the elements necessary for the development of e-retrofit solutions. It is possible to develop motors, electronic devices, EV chargers, software solutions and other systems. However, a lot of work lies on the level of regulation and standardization insofar as today in Serbia it is very complicated if not impossible to carry out any conversions whatsoever to electric.

As with the purchase of a new electric vehicle, economic incentives and clear government support for e-retrofit is more than necessary to enable the people of Serbia to access electric mobility.

The increase in energy consumption linked to the entry into the electric vehicle market will most certainly have an impact on the price of electricity due to the limitation of the infrastructure and the electricity network, hence the need to work in parallel on the reflection of adequate solutions.

ACKNOWLEDGMENT

This work was partially supported by European Institute of Innovation & Technology Urban Mobility (EIT UM) under grant no. SGA21 21342.

REFERENCES

[1] (2020). Registered road motor vehicles and trailers and road traffic accidents. *The Statistical Office of the Republic of Serbia*. Available at: https://publikacije.stat.gov.rs/G2021/Pdf/G20211072.pdf

[2] (2021) Vehicles in use Europe. *ACEA Report.* Available at: https://www.acea.auto/publication/report-vehicles-in-use-europe-january-2021

[3] (2020). Average age of vehicle fleet 2019 / Prosečna starost vozila voznog parka 2019. *Safety Road Agency*. Available at: https://www.abs.gov.rs/admin/upload/documents/20200723053848--starost-vozila-voznog-parka-2019.pdf

[4] Jaworski, A., Lejda, K., Lubas, J., & Mądziel, M. (2019). Comparison of exhaust emission from Euro 3 and Euro 6 motor vehicles fueled with petrol and LPG based on real driving conditions. *Combustion Engines, 178*(4), 106-111.

[5] Grelier, F. (2018, Sep. 18). *Car with engines: can they ever be clean? Transport & Environment*. Available at: https://www.transportenvironment.org/wp-content/uploads/2021/07/2018_09_TE_Dieselgate_report_final.pdf

[6] Amundsen, H. A., & Klæboe, R. (2005). *A Nordic perspective on noise reduction at the source*. The Institute of Transport Economics, Norway. Available at: *https://www.researchgate.net/profile/Astrid-Amundsen/publication/265434216_A_Nordic_perspective_on_noise_reduction_at_the_source/links/54b78ea30cf24eb34f6eb546/A-Nordic-perspective-on-noise-reduction-at-the-source.pdf*

[7] (2017). *Nivoi buke prema mernim mestima u Beogradu*. City Institute for Public Health. Available at: https://www.zdravlje.org.rs/

[8] Nalley, S., & LaRose, A. (2021). Annual Energy Outlook 2021. *U.S. Energy Information Administration*. Available at: https://www.eia.gov/outlooks/aeo/pdf/AEO_Narrative_2021.pdf

[9] (2021). Retrofit study - Necessary conditions for an economical, safe and beneficial retrofit for the environment / Etude retrofit - Conditions nécessaires à un rétrofit économe, sûr et bénéfique pour l'environnement. *ADEME*. Available at: https://librairie.ademe.fr/mobilite-et-transport/4590-etude-retrofit.html

[10] (2009). *A study on approaching warning systems for hybrid vehicle in motor mode. Japanese Automobile Standards International Centre, Informal document No GRB-49-10*. Available at: https://unece.org/fileadmin/DAM/trans/doc/2009/wp29grb/ECE-TRANS-WP29-GRB-49-inf10e.pdf

[11] Lelong, J., Michelet, R. (2001, Aug. 27-30). Passenger cars. Power unit and tyre-road noise, driving behaviour: what are the stakes? *Inter-noise 2001 – Int. Congress and Exhibition on Noise Control Engineering*, The Hague, Netherlands, pp. 562-565.

[12] Wyman, O. (2020). *Vehicle cost development*. Available at: https://www.oliverwyman.com

[13] Blynn, K. (2018, Feb.). *Accelerating bus electrification: Enabling a sustainable transition to low carbon transportation systems. Middlebury College. Massachusets Institue of Technology*. Available at: https://dspace.mit.edu/bitstream/handle/1721.1/115600/1036985839-MIT.pdf?sequence=1

Providing Thermal Correlation for the Tube-Bundles with Linear and Staggered Arrangements using CFD

Masoud Darbandi[1], Mohammad-Saleh Abdollahpour[2], Kazem Mashayekh[3]

[1,2,3]Sharif University of Technology, Tehran, Iran, darbandi@sharif.edu[1], ka_abdollahpour@sharif.edu[2], kazem.mashayekh2016@student.sharif.edu[3]

Abstract—**Heat transfer is an important phenomenon occurring in almost in all industries. Accurate identification of the heat transfer phenomenon saves energy consumption. Among various equipment to control the heat transfer processes is the shell and tube heat exchanger (STHEs). The high reliability and good performance in different working conditions have led to the widespread use of STHEs in so many industries. The STHEs consist of several tubes that determine the tube bundle's thermal performance. Their accurate analysis can provide optimal design of STHEs. The present study uses the numerical method to calculate the thermal correlation of the tube bank with linear and staggered arrangements. The numerical results are compared with experimental data, with a good agreement in the studied ranges. The thermal performance of tube banks with staggered arrangement is higher than that of the linear arrangement in similar Reynolds and Prandtl numbers. The comparison between the achieved correlated results and experimental data is less than 8%, indicating that the derived correlations provide high accuracy. These correlations help to calculate the performance of STHEs more accurately. So, they can be readily used for the thermal design of extra compact STHEs.**

Keywords – heat transfer, shell and tube heat changer, numerical simulation, tube bank, thermal performance

I. INTRODUCTION

One of the vital and commonly used equipment in various industries is heat exchangers. The equipment's primary function is to transfer heat between one or more fluids to perform a process. Shell and tube heat exchanger (STHE) is a heat exchanger that is widely used due to proper performance in different working conditions. Due to the widespread use of STHEs, a large part of the energy will be wasted in the case of improper operation. Due to the very high importance of energy saving, the study of the thermal performance of the STHE has attracted the attention of many researchers.

The STHEs actually consist of a set of tube bundles, which are called tube banks. If the thermal function of the tube bank is accurately known, the performance of the STHE can be easily identified. Therefore, in this regard, extensive research activities have been carried out so far. An example is the work of [1] used experimental studies to investigate heat transfer and flow behavior on a tube bank with a staggered arrangement. Their experimental results showed that the heat transfer in the rear rows would be reduced due to the stagnation flow in the wake region. Reference [2] experimentally and numerically investigated the heat transfer and pressure drop of air passing through the finned tube bank with the staggered arrangement. They extracted the Nusselt number finned tube bank in different Reynolds numbers and compared the results with the non-finned one. Reference [3] experimentally studied the heat transfer and pressure drop in a conical finned tube bank. They compared the experimental results with the analytical method and concluded that using a tube bank with conical fins would increase the heat transfer rate by 58%. Reference [4] experimentally investigated the heat transfer and friction on finned tube banks considering various finned arrangements. They proposed the correlations for the Nusselt number and the friction coefficient as a function of Reynolds number.

In addition to experimental work, analytical work can be mentioned. This method is much

less expensive than the experimental method, and the results obtained from the method are based on several hypotheses. Reference [5] analytically investigated the cross-flow heat transfer within a tube bank. They considered the temperature on the wall of the tubes would be constant and presented a calculating heat transfer mathematical model for tube banks with the linear and staggered arrangement. Reference [6] theoretically investigated the heat transfer for parallel flow inside a tube bundle. The flow on the tube bundles was turbulent and fully developed, and they also used the constant heat flux boundary condition on the tube walls. They also theoretically predicted the Nusselt number of the flow.

Due to the characteristics of the numerical method, including low cost and high accuracy, in recent years, many researchers have started to use numerical-based approaches to derive the correlations. Reference [7] numerically studied the hydraulic and thermal performance of the flow on a trapezoidal tube bank. They obtained the Nusselt number and the pressure drop based on the trapezoidal arrangement factors of the tube bank. They provide a correlation for the Nusselt number with a trapezoidal tube bank arrangement. Reference [8] numerically studied the flow and heat transfer in a tube bank with a linear arrangement in the range of Reynolds number 100 to 1000. They obtained the average heat transfer value and Nusselt number on the tubes, and the results were in good agreement with the experimental data. Reference [9] numerically investigated the effect of longitudinal conical fines on a tube bank. Their numerical results showed that the types of fines would have a perfect impact on the hydraulic and thermal performance of the flow. In addition, they observed that the Nusselt number increased significantly with increasing fin length. Using the computational fluid dynamics method, Reference [10] investigated the exergy and energy characteristics for the airflow through the tube bank in two linear and staggered arrangements. They also introduced a new arrangement called the twisted tube bank.

In the present study, the primary purpose is to extract correlation to calculate the thermal performance of the tube bank to design the extra compact STHE. In this regard, first, the Nusselt number is calculated for 5, 10, and 20 tube rows with different tube lengths (B). Then, the coefficients obtained from the numerical method for the different rows are compared with experiment. Then, for the Prandtl number from 0.7 to 70 and the Reynolds number from 300 to 10,000, the Nusselt number for the flow on the tube bank is extracted considering both linear and staggered arrangements. Finally, the extracted correlations are compared with each other. The correlations can be used to design the flow of the shell part of the STHE to calculate the thermal performance.

II. COMPUTATIONAL METHOD

In this section, the numerical method used to simulate flow and heat transfer is summarized. In this regard, first, the geometry, grid generated, and boundary conditions are described. The governing equations and the experimental correlation used is then expressed. Finally, the numerical method and the convergence conditions are presented.

A. Geometry

In general, two geometries with linear and staggered tube arrangements are considered. In both arrangements, the tube outer diameter (d) is 2 mm. Fig. 1a shows the staggered arrangement in which the longitudinal and transverse distances are 1.5 times larger than the diameter of the tube with five rows. Fig. 1b shows a tube bank with a linear arrangement. In both geometries, the distance between the first tube to the inlet and the last tube to the outlet equals 5 mm. Also, the intended length for each tube (B) is equal to 10 mm. The distance between the

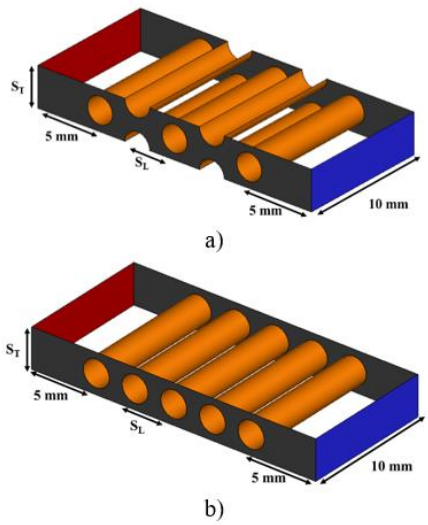

Figure 1. Geometry intended to simulate the flow on a tube bank with five rows and arrangements of (a) staggered, (b) linear.

center and the center of the two side tubes is 1.5 times of the tube outer diameter. In both arrangements, the number of tube rows is 5, 10, and 20 rows.

B. Grid

Fig. 2 the grid generated for both staggered and linear arrangements is shown, respectively. As shown in the figures, in both arrangements, an unstructured grid is used, in addition, a boundary layer is used near the wall. After examining the solution independence from the computational grid, the number of computational cells given in TABLE I has been used for simulation.

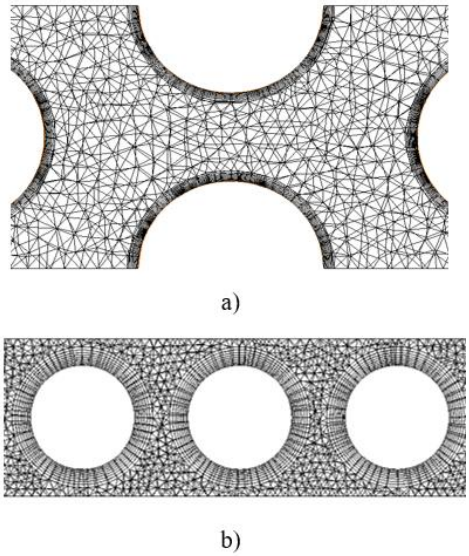

Figure 2. Computational grid generated with boundary layer mesh for both arrangements (a) staggered, (b) linear.

TABLE I. NUMBER OF COMPUTATIONAL CELLS GENERATED FOR ARRANGEMENT AND NUMBER OF DIFFERENT ROWS WITH TUBE LENGTH 10 MM

No. Row	Staggered	Linear
5	880.000	779.000
10	1.820.000	1.289.000
20	3.300.000	2. 331.000

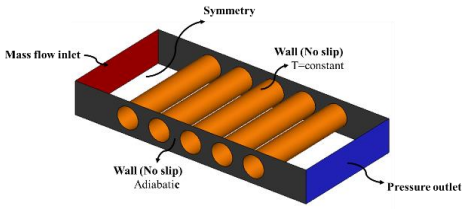

Figure 3. Boundary conditions applied to simulate the flow and heat transfer on the tube bank with a linear arrangement.

C. Bondary Condition

One of the most important parts of numerical simulation is defining boundary conditions. The boundary conditions for the two arrangements are the same, so only the boundary conditions for the linear arrangement are shown in Fig. 3. The figure shows that the mass flow inlet and pressure outlet are considered for the input and output section, respectively. The boundary conditions considered for the tube walls are constant temperature and non-slip. The beginning and end of the tubes, which are baffles, are regarded as adiabatic walls. The upper and lower levels of the solution domain are considered symmetrically.

D. Equation

The Navier-Stokes equations are solved in three dimensions, steady-state, and incompressible conditions, to identify the flow and heat transfer behavior for the defined domain. These Eqs. are as follows.

$$\frac{\partial u_i}{\partial x_i} = 0 \ , \tag{1}$$

$$\frac{\partial (u_i u_j)}{\partial x_j} = -\frac{1}{\rho}\frac{\partial p}{\partial x_i} + \frac{\partial}{\partial x_j}\left[(\nu + \nu_t)\left(\frac{\partial u_j}{\partial x_i} + \frac{\partial u_i}{\partial x_j} \right) \right] , \tag{2}$$

$$\frac{\partial (u_i T)}{\partial x_j} = -\frac{1}{\rho}\frac{\partial p}{\partial x_i} + \rho \frac{\partial}{\partial x_i}\left[\left(\frac{\nu}{\mathrm{Pr}} + \frac{\nu_t}{\mathrm{Pr}_t} \right) \frac{\partial T}{\partial x_i} \right] . \tag{3}$$

In the above Eqs., u, ρ, and P represent the fluid velocity, the fluid density, and the pressure, respectively. In addition, ν is the kinematic viscosity of the fluid, and T is the temperature. The subscript t also indicates the turbulence property.

The k-ε model is used to simulate the turbulence flow, which are as follows:

$$\frac{\partial(ku_i)}{\partial x_i} = \frac{\partial}{\partial x_i}\left[\left(\nu + \frac{\nu_t}{\sigma_k}\right)\frac{\partial k}{\partial x_i}\right] + \Gamma - \varepsilon \quad , \quad (4)$$

$$\frac{\partial(\varepsilon u_i)}{\partial x_i} = \frac{\partial}{\partial x_i}\left[\left(\nu + \frac{\nu_t}{\sigma_\varepsilon}\right)\frac{\partial \varepsilon}{\partial x_j}\right] + \quad , \quad (5)$$
$$+C_1\Gamma\varepsilon - C_2\frac{\varepsilon^2}{k+\sqrt{\nu\varepsilon}}$$

where the turbulence model constants are σ_k=1, C_2=1.9, and σ_ε=1.2. Furthermore, $\nu t=C_\mu(k^2/\varepsilon)$, $C_1=\max[0.43,(\mu/(\mu_t+5)]$, Γ is the generation of turbulence kinetic energy due to the mean velocity gradients.

E. Non-Dimensional Number and Experimental Correlation

Three dimensionless Reynolds, Prandtl, and Nusselt numbers were used in this study. They are

$$\mathrm{Re} = \frac{uD_h}{\nu} \quad , \quad (6)$$

$$\mathrm{Pr} = \frac{\mu c_p}{k} \quad , \quad (7)$$

$$Nu = \frac{hD_h}{k} \quad . \quad (8)$$

In the above Eqs., D_h is the hydraulic diameter in m, μ is the dynamic viscosity in N.S/m^2, C_P is the specific heat in J/kgK, k is the thermal conductivity in terms of W/mK, and h is the heat transfer coefficient in terms of W/m^{2}K.

One of the empirical equations, which are widely used to calculate the tube banks, have been provided by [11]. It is given by

$$Nu_D = \frac{h\,D_h}{k_f} = C\,\mathrm{Re}^{m}_{D,\max}\,\mathrm{Pr}^{0.36}\left(\frac{\mathrm{Pr}}{\mathrm{Pr}_s}\right)^{1/4} \quad , \quad (9)$$
$$\begin{bmatrix} N_L \geq 20 \\ 0.7 < \mathrm{Pr} < 500 \\ 10 < \mathrm{Re}_{D,\max} < 2\times10^6 \end{bmatrix}$$

where N_L and Re_{Dmax} are the number of tube rows and the maximum Reynolds number, respectively. If the number of rows becomes less than 20, a correlation should be considered, see Ref. [11].

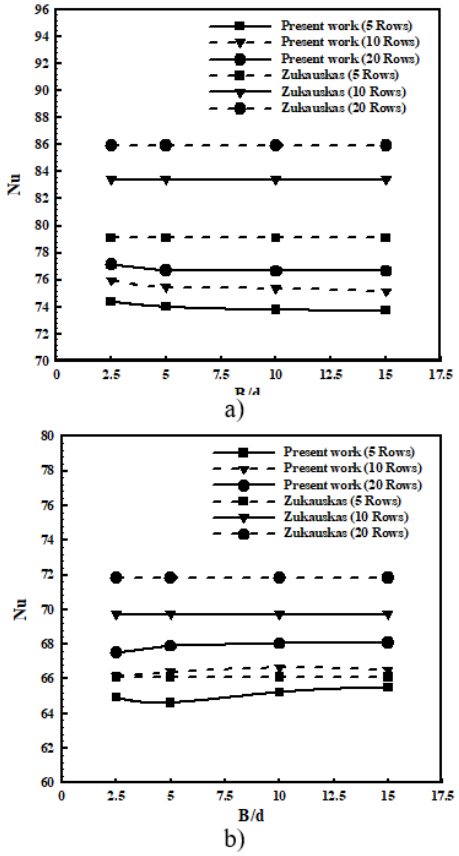

Figure 4. Comparison of Nusselt number obtained from the present study and Zukauskas relation for different length-to-diameter ratios and rows; Re=1500 and Pr=7; with (a) staggered and (b) linear arrangements.

F. Numerical Method

The finite-volume-based finite-element (FVBFE) method is used to discretize the governing equations. The simple algorithm is used for the pressure and velocity coupling. The second-order central approximate is used for the pressure, and the convection fluxes are approximated using the second-order upwind scheme. The flow is turbulent with steady-state condition. The effects of gravity have also been ignored. The convergence criterion of 10^{-6} is considered for the residuals. More details on the solution method can be found in [12].

III. Results

The Nusselt number obtained from the numerical method for different tube rows is

primarily compared with the experimental data. Fig. 4 shows a comparison between the results of the present study and experimental data considering different length-to-diameter ratios and rows. They are provided for Reynolds number of 1,500 and Prandtl Number of 7. In all numerical results, the diameter of the tube is constant, and its length is changed. The horizontal and vertical axes indicate the length-to-diameter ratio and the Nusselt numbers, respectively. As can be seen in the figure, the difference between the Nusselt numbers calculated numerically and experimentally is less than 8%. In addition, the [11] predicts a larger magnitude in all cases.

According to the obtained results, the correlations for staggered and linear arrangement are as follows:

$$Nu_{St} = 0.7174\, Re^{0.5704}\, Pr^{0.2961} \left(\frac{S_L}{D}\right)^{-0.0406} \left(\frac{S_T}{D}\right)^{-2.38} \quad , \quad (10)$$
$$\begin{bmatrix} 0.7 < Pr < 70 \\ 300 < Re < 10^4 \end{bmatrix}$$

$$Nu = 0.2338\, Re^{0.6902}\, Pr^{0.2630} \left(\frac{S_L}{D}\right)^{0.5975} \left(\frac{S_T}{D}\right)^{-2.1367} \quad , \quad (11)$$
$$\begin{bmatrix} 0.7 < Pr < 70 \\ 300 < Re < 10^4 \end{bmatrix}$$

Fig. 5 shows the Nusselt number versus Reynolds number for three different Prandtl numbers considering two staggered and linear tube bundle arrangements, where longitudinal and transversal ratios are 1.5. In Fig. 5 the Prandtl numbers are 8.2, 45.3, and 70, respectively. The figure shows that the difference between the linear and staggered arrangements increases as the Reynolds number increases. In addition, with increasing the Prandtl number, the difference between Nusselt numbers in different Reynolds is more observable.

IV. CONCLUSION

In the present study, the thermal correlation were extracted for the staggered and linear arrangements of tubes to design high compact STHE using the numerical method. In this regard, first, the effects of row number and tube

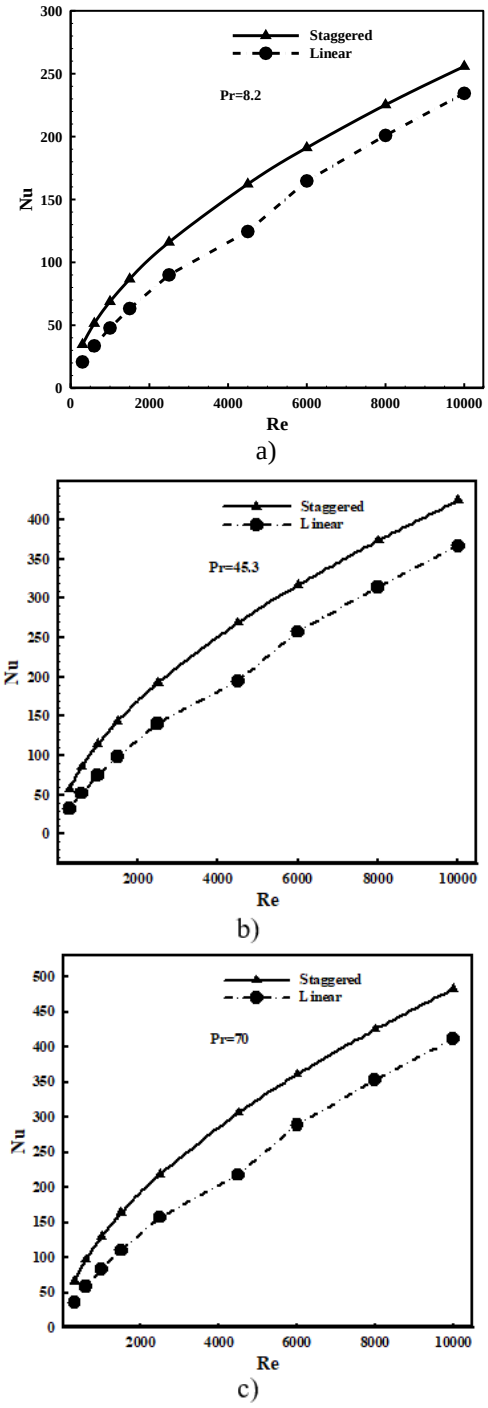

Figure 5. Comparison of Nusselt number in different Reynolds numbers for two linear and staggered arrangements for Prantel number (a) 8.2; (0b) 45.3; (c) 70.

length were investigated, and then the correlations were extracted for both staggered and linear arrangements. Finally, the derived Nusselt numbers were compared for the two tube arrangements at different Prandtl and Reynolds numbers. According to the results, the staggered arrangement performs better in more significant Reynolds and Prandtl numbers. Also, the difference between the obtained numerical results and experimental data is less than 8%, which indicates great agreement of the numerical-based results with the experiment.

ACKNOWLEDGMENT

The authors would like to acknowledge the financial support (Award Number: SUT-1397-00125) received from the Deputy of Research and Technology in Sharif University of Technology.

REFERENCES

[1] Ebihara, Y., Katsuta, A., Koizumi, Y., & Ohtake, H. (2009). Heat Transfer Experiments of Mini-Tube Bank. *International Conference on Nuclear Engineering*, *43543*, 321–325.

[2] Hofmann, R., & Walter, H. (2012). Comparison between numerical and experimental gas side heat transfer and pressure drop of a tube bank with solid and segmented circular I-fins. *Engineering Systems Design and Analysis*, *44854*, 709–720.

[3] Carvajal-Mariscal, I., Sanchez-Silva, F., & Polupan, G. (2010). Tube banks heat transfer enhancement using conical fins. *Fluids Engineering Division Summer Meeting*, *49484*, 1745–1750.

[4] Zheng, F.-C. *et al.* (2018) 'Experimental Study on Heat Transfer Performances of Flat Tube Bank Fin Heat Exchanger Using Four Different Fin Patterns', *Journal of Heat Transfer*, 140(4).

[5] Yovanovich, M. M., Khan, W. A., & Culham, J. R. (2005). Convection Heat Transfer From Tube Banks in Crossflow: Analytical Approach. *43rd Aerospace Sciences Meeting & Exhibit*, 10–12.

[6] Friedland, A. J., & Bonilla, C. F. (1961). Analytical study of heat transfer rates for parallel flow of liquid metals through tube bundles: II. *AIChE Journal*, *7*(1), 107–112.

[7] Bender, A. *et al.* (2018) 'A numerical study of forced convection in a new trapezoidal tube bank arrangement', *International Communications in Heat and Mass Transfer*, 91, pp. 117–124.

[8] Gorman, J. M., Sparrow, E. M., & Ahn, J. (2019). In-line tube-bank heat exchangers: Arrays with various numbers of thermally participating tubes. *International Journal of Heat and Mass Transfer*, *132*, 837–847.

[9] Abraham, J. D., Dhoble, A. S. and Mangrulkar, C. K. (2020) 'Numerical analysis for thermo-hydraulic performance of staggered cross flow tube bank with longitudinal tapered fins', *International Communications in Heat and Mass Transfer*, 118, p. 104905.

[10] Rawa, M. J. H. *et al.* (2021) 'Multi-objective optimization of heat transfer through the various types of tube banks arrangements', *Alexandria Engineering Journal*, 60(3), pp. 2905–2919.

[11] Žukauskas, A. (1972) 'Heat transfer from tubes in crossflow', in *Advances in heat transfer*. Elsevier, pp. 93–160.

[12] Darbandi, M., Abdollahpour, M.-S. and Hasanpour-Matkolaei, M. (2021) 'A new developed semi-full-scale approach to facilitate the CFD simulation of shell and tube heat exchangers', *Chemical Engineering Science*, p. 116836

Performances of a 2by2 Heller Dry Cooling Tower Array in Various Wind Conditions Using the CFD

Masoud Darbandi[1], Kazem Mashayekh[2], Pooya Javadpour-Langroodi[3], Fakhereh Seyedi[4], Shahram Iranpak[5], Javad Farhadi[6]

[1,2,3]Sharif University of Technology, Tehran, Iran, darbandi@sharif.edu[1], kazem.mashayekh2016@student.sharif.edu[2], javadpoor.pooya@ae.sharif.ir[3]
[4]Shahid Beheshti University, Tehran, Iran, fakhereh.Seyyedi@gmail.com
[5,6]Shazand Thermal Power Plant, Shazand, Arak, Iran, iranpak@shazandtpp.ir[5], j-farhadi@shazandtpp.ir[6] tr

Abstract—**Natural Draft Dry (HELLER) Cooling Towers are among the efficient heat dissipation systems in steam cycles with abundant applications in dry and arid areas. One of the main issues of these systems is that their performance is greatly affected by environmental conditions, especially wind conditions of the region. Past research indicates that increasing the wind speed reduces the thermal temperature of these systems and thus declines the overall efficiency of the power plant. The purpose of the present study is to investigate the thermal performance of the Heller cooling towers of Shazand thermal power plant by numerical simulation based on flow physics. The prevailing wind in Shazand power plant site blows from geographical north-east and south-west directions, which according to the available wide range of wind speeds at site, the thermal performance of cooling towers is studied based on flow field physics at wind speeds of 6, 10 and 14 m/s and the two above directions.**

Keywords - thermal power plant, heller cooling towers, internal and external wind screens, thermal performance and numerical simulation

I. INTRODUCTION

As it is known, variations in climatic conditions such as air temperature, wind speed and direction, can affect the operating conditions and efficiency range of power plant equipment [1]. Heller cooling tower is one type of various dry cooling systems. The variations in wind speed and its direction are accounted among the parameters with negative impact on the operation of a dry cooling tower. Studies show that an increase in the wind speed leads to a reduction in the performance of these systems. The reason for this phenomenon is the disruption in distribution of the ideal suction pressure of the tower. Precisely, creating choking conditions for plume deflection at the tower outlet, which is somehow reducing the cross-sectional area of the outlet flow, increases the pressure inside the tower and ultimately reduces the suction pressure and inlet flow rate of the tower. In recent years, many researchers conducted experimental studies as well as numerical simulations on Heller cooling towers to improve their performance in different weather conditions.

Among the experimental works, the study by Reference [2] could be mentioned. In their research, they used a cooling tower of 20 meters high as an experimental test system in different environmental conditions. They investigated the effect of exhaust air plume at different wind speed and wind direction on the performance of the cooling tower. Reference [3] applied theoretical analysis to optimize a Heller cooling tower. Parameters such as the shape of the tower, the arrangement of the radiators, the wind speed and flow, and the mass flow rate of the circulating water were considered as important optimization factors. Reference [4] studied the behavior of Heller towers in different environmental conditions using mathematical models. Reference [5] utilized the numerical method to investigate the hydraulic and thermal

performance of a cooling tower at different wind speeds and proposed a new model of cooling tower. Reference [6] by the use of numerical simulations as well as experimental work, proposed a cylindrical cooling tower instead of a hyperbolic cooling tower. Reference [7] applied numerical simulations of three different designs of Sugarloaf-type, Swirl-type and Impeller-type internal wind barriers inside the cooling tower to improve the thermal performance of the cooling tower. They examined the flow field inside and outside the cooling tower for three different designs of windscreens in different wind conditions. Reference [8] investigated the performance of a cooling tower in different environmental conditions through numerical simulations. They developed a three-dimensional model to predict the thermal performance of three cooling towers arranged in a linear arrangement relative to each other.

The purpose of this study is to physically investigate the thermal performance of cooling towers of Shazand Arak power plant in summer, during peak hours of electricity consumption by the use of computational fluid dynamics. According to the studies performed in the reference [9], the prevailing wind direction in Shazand power plant site is geographical north-east as well as south-west with the wind speeds of 6, 10 and 14 meters per second. Therefore, these two directions and mentioned wind speeds are applied here for physical performance analysis of the cooling towers of Shazand power plant.

II. Modeling Steps

A. Governing Equations

In this research, the differential equations of continuity, momentum and energy for an incompressible and viscous flow will be solved in steady state. The turbulent flow regime and the turbulence model are also used to model the turbulent flow. The equations of continuity, momentum, energy and equations related to the turbulence model are as follows [5]:

$$\frac{\partial\left(\rho u_j\right)}{\partial x_j}=0 \ , \qquad (1)$$

$$\frac{\partial\left(\rho u_j u_i\right)}{\partial x_j}=-\frac{\partial p}{\partial x_i}+\frac{\partial T_{ij}}{\partial x_i}-\rho\beta\left(T-T_r\right)g_i+R_i \qquad (2)$$

$$\frac{\partial\left(u_j T\right)}{\partial x_j}=-\frac{\partial}{\partial x_i}\left[\left(\alpha+\alpha_t\right)\frac{\partial T}{\partial x_j}\right]+q_h \ , \qquad (3)$$

$$\frac{\partial\left(\rho u_j k\right)}{\partial x_j}=-\frac{\partial}{\partial x_i}\left[\left(\nu+\frac{\nu_t}{\sigma_k}\right)\frac{\partial k}{\partial x_j}\right]+P+G-\varepsilon \qquad (4)$$

$$\frac{\partial\left(\rho u_j \varepsilon\right)}{\partial x_j}=-\frac{\partial}{\partial x_i}\left[\left(\nu+\frac{\nu_t}{\sigma_z}\right)\frac{\partial \varepsilon}{\partial x_j}\right]+ \ , \qquad (5)$$
$$+C_{1z}\frac{\varepsilon}{k}\left(P+G\right)-C_{2z}\frac{\varepsilon^2}{k}$$

in which we have $\tau_{ij}=\left(\mu+\mu_t\right)S_{ij}$ and $P=\nu_t S_{ij}S_{ji}$ and $G=-g\beta\frac{\nu_t}{\alpha_t}\frac{\partial T}{\partial z}$ and $S_{ij}=\left(\frac{\partial u_i}{\partial x_j}+\frac{\partial u_j}{\partial x_i}\right)$. In the above equations, u_i is the velocity in x_i direction. Additionally, ρ, g, T, p and β are air density, gravity acceleration, air temperature and pressure, and air compressibility coefficient, respectively. Also, ν and μ are kinematic and dynamic viscosities. α is the molecular heat dissipation of air, as well. S_{ij} is the strain rate tensor, while k and ε represent the turbulence kinetic energy and the turbulence dissipation rate, respectively. To change the pressure and temperature of the radiators, the term of moment source (Ri) and term of energy source (q_h) are considered, respectively. Turbulence viscosity and turbulence heat dissipation are calculated through $\nu_t=C_\mu\frac{k^2}{\varepsilon}$ and $\alpha_t=\frac{\nu_t}{Pr_t}$. C_μ, $C_{1\sigma}$, $C_{2\sigma}$, σ_k, σ_ε and σ_t are the constants of the k-ε turbulence model.

B. Geometric Modelling

In this section, the geometric modeling of the cooling towers of Shazand power plant is comprehensively presented along with its boundary conditions. Fig. 1 demonstrates the details of the geometric model for the cooling towers with the corresponding dimensions and size. Also in this figure, the number of each tower is specified on each of them. Considering that Shazand cooling towers are numerically studied in the conditions of northeast and southwest wind

blows, so in Fig. 2, the geographical direction and also the wind blow from the top view of the cooling towers are shown.

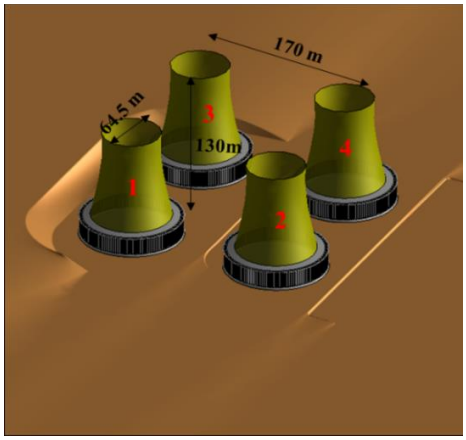

Figure 1. Size and dimensions of cooling towers.

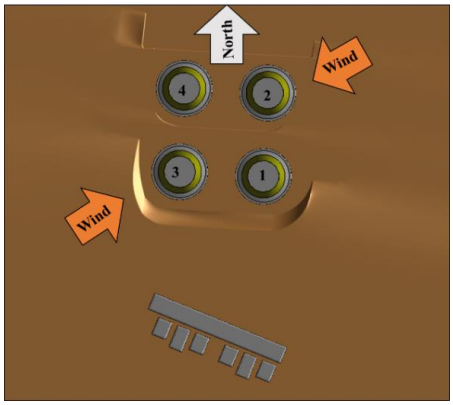

Figure 2. Top view of cooling towers and prevailing wind direction in site.

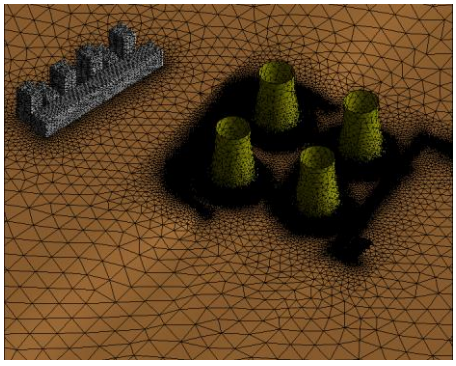

Figure 3. Generated grid around the Heller towers with 13 million cells.

C. Grid Generation and Results of Grid Independency

TABLE I. HEAT RELEASED FROM ONE OF THE COOLING TOWERS AT AN AMBIENT TEMPERATURE OF 31°C AND WIND-FREE CONDITIONS IN DIFFERENT SIZES OF THE DEVELOPED GRID MESH.

Grid	Heat Released of Towers (MW)
9.5 million	449.7
13 million	455
16 million	455.4

In this section, the grid generation and grid independence results are introduced. For this purpose, the structured grid have been used for meshing as far as possible. Therefore, a grid of about 13 million high quality cells is created for meshing the Shazand power plant site. Fig. 3 illustrates the meshing performed over the entire domain. As can be seen, very fine grids are generated near and around Heller towers, which are of great computational importance.

To investigate the independence of the results from the produced mesh in this study, the amount of heat released from one of the cooling towers in design conditions, i.e. temperature of 31°C and wind-free conditions, is considered as a measure of the grid independence of the results. The obtained results for the three generated grids of 9.5 million, 13 million and 16 million meshed cells are shown in Table I. Regarding the close results for the grids of 13 million and 16 million cells, the grid of 13 million cells is selected to solve numerical simulations.

D. Simulation Details

In simulations of this study, the Simple algorithm is applied to correct the pressure and the coupling between pressure and velocity in discretization equations. The turbulent steady flow and the $k-\varepsilon$ turbulence model of the RNG mode are considered. The only factor causing any change in density is the ambient temperature variation, which in this simulation, the temperature increase acts as a varying factor of air density in the system and air is assumed as ideal gas. In discretization of governing equations, the first-order upwind method is utilized. The convergence criterion of the results is 10^{-4} for the continuity and momentum equations and 10^{-6} for the energy equation.

III. Numerical Simulation Results and Discussion

A. *Validation of Numerical Results*

In this section, the validation assessment for simulation results of thermal performance of one of the Shazand power plant cooling towers are presented at design conditions.at considered design conditions the air temperature is 31°C, the temperature of hot water entering the Forgo radiators is equal to 62°C and wind-free conditions are assumed. Table II compares the values for the heat released by one of the cooling towers in numerical simulation, with the empirical values in the documents received from Shazand power plant at design conditions. The small value of error observed here, ensures the accuracy of the numerical solution of present simulation.

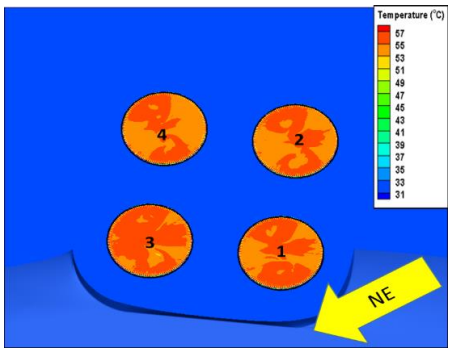

Figure 4. Ambient temperature contour, northeast wind with 6 m/s speed.

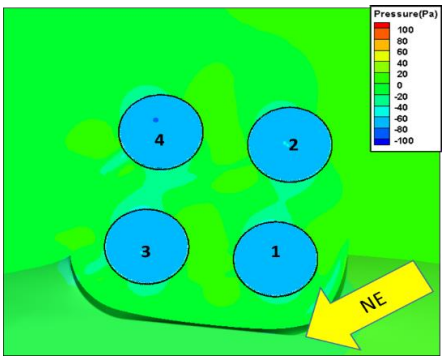

Figure 5. Relative pressure contour, northeast wind with 6 m/s speed.

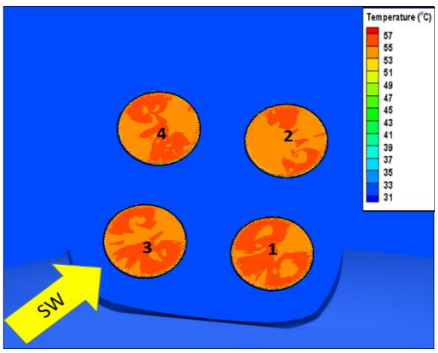

Figure 6. Ambient temperature contour, southwest wind with 6 m/s speed.

To depict the physical effects of wind blow on the thermal performance of Heller towers of Shazand power plant in each section, the contours are drawn on a horizontal plane passed through the radiators of the Heller towers along with air flow lines.

Figs. 4 and 5 show the temperature and relative pressure contours at a wind speed of 6 m/s from the north-east, respectively. As can be seen from Fig. 4, the windscreens at the front of the tower radiators show better performance. The pressure drop between the towers and thus the flow reduction of the towers is quite obvious in Fig. 5. The Heller Tower of Unit 4 with 351 MW heat release, shows the best performance and the Heller Tower of Unit 3 with 313.2 MW accounts for the worst performance.

Fig. 6 and 7 demonstrate the temperature and relative pressure contours at a wind speed of 6 m/s respectively, from the southwest direction. According to Fig. 6 and 7, Towers 2 and 4 have their own natural trend. However, since Towers 1 and 3 are located just below the hill and the hill caused a pressure drop around Towers 1 and 3, where this pressure reduction has reduced the performance of these towers. Heller Tower of Unit 2 with 350.3 MW heat release exhibits the best performance and Heller Tower of Unit 1 with 305.3 MW released heat shows the worst performance among all.

Figs. 8 and 9 depict the contours of temperature and relative pressure at a wind speed of 10 meters per second from the northeast

TABLE II. Numerical Simulation Results and Empirical Data for Heat Released from One of the Cooling Towers of Shazand Power Plant at Design Conditions.

	Numerical result	**Experimental value**
Heat released from tower (MW)	457	455

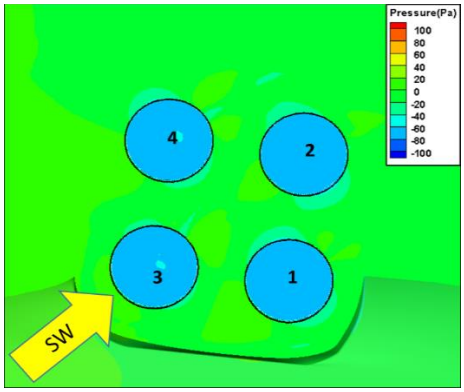

Figure 7. Relative pressure contour, southwest wind with 6 m/s speed.

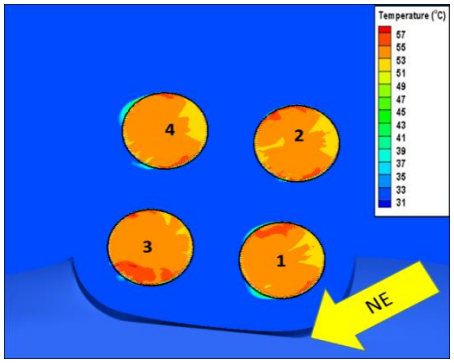

Figure 8. Ambient temperature contour, northeast wind with 10 m/s speed.

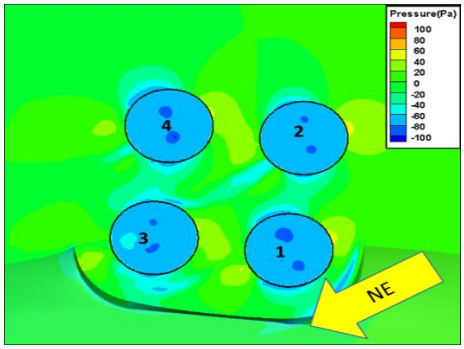

Figure 9. Relative pressure contour, northeast wind with 10 m/s speed.

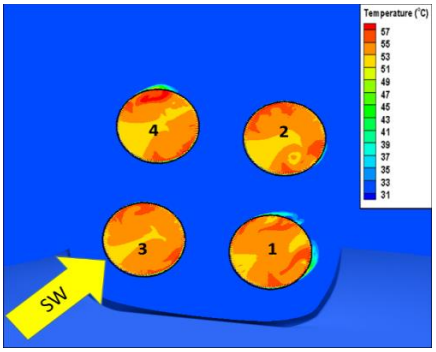

Figure 10. Ambient temperature contour, southwest wind with 10 m/s speed.

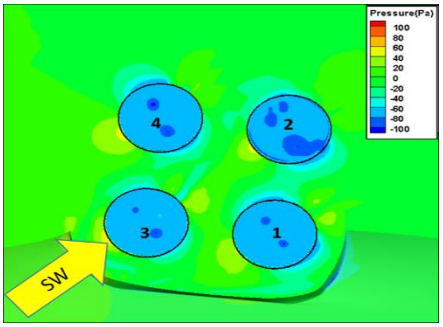

Figure 11. Relative pressure contour, southwest wind with 10 m/s speed.

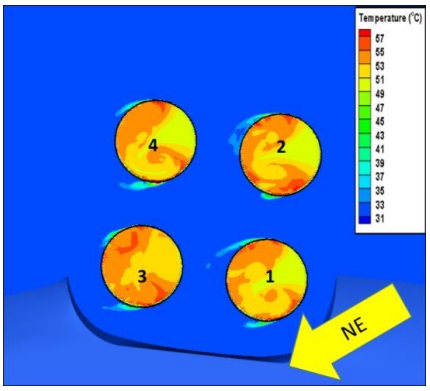

Figure 12. Ambient temperature contour, northeast wind with 14 m/s speed.

direction, respectively. As can be seen from Fig. 8, the radiators at the front of the towers that are in the wind path, reveals better performance. Additionally, in towers 1 and 4, hot air returns and exits in the radiators, which causes a decrease in the performance of radiators. In Fig. 9, illustrating pressure contour, the side radiators of the Heller towers cause a functional drop in the side radiators due to the acceleration of the flow around the towers and consequently the reduction of pressure. Also, due to the increase in flow velocity between the hill and towers 1 and 3, a pressure drop has occurred in this area. Another point that can be seen from the pressure contour is that a pressure drop has been generated behind Tower 2 and continued to Tower 3, which may have originated from the flow rotation behind Tower 2. The Heller Tower of Unit 2 with 272.3 MW heat release has the best performance among all and the Heller Tower of Unit 1 with 254.1 MW shows the worst.

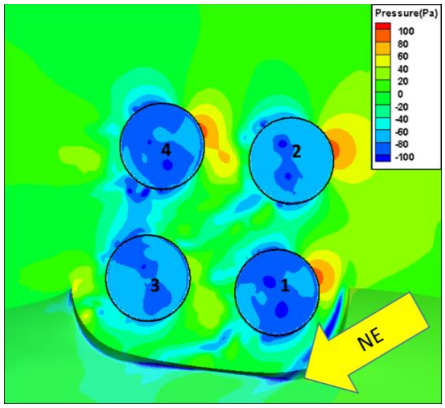

Figure 13. Relative pressure contour, northeast wind with 14 m/s speed.

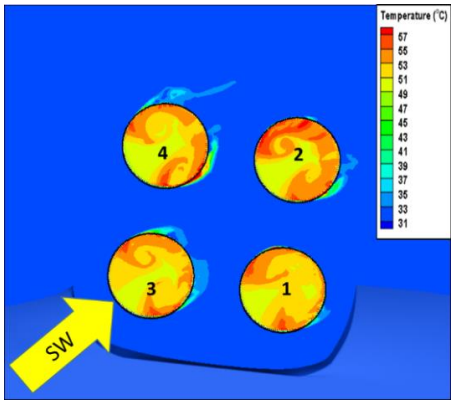

Figure 14. Ambient temperature contour, southwest wind with 14 m/s speed.

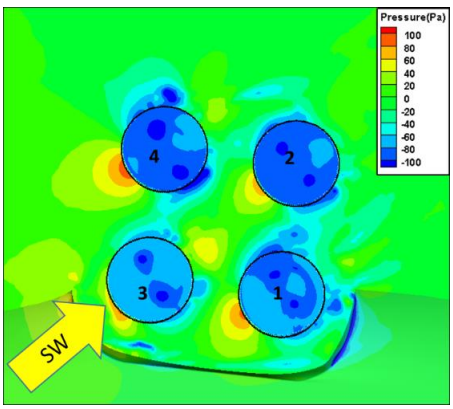

Figure 15. Relative pressure contour, southwest wind with 14 m/s speed.

Figs. 10 and 11 display the temperature and relative pressure contours respectively at wind speed of 10 m/s, respectively, from the south-west. According to Figs. 10 and 11, radiators located in the wind direction show better performance. There is also a pressure drop

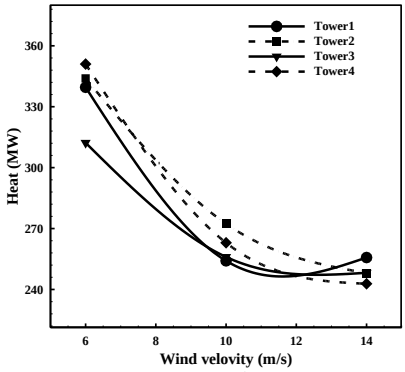

Figure 16. Heat release value from cooling towers at different wind speeds and northeast direction.

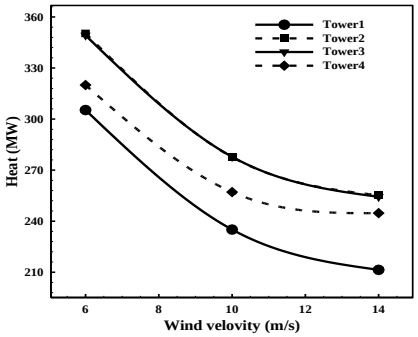

Figure 17. Heat release value from cooling towers at different wind speeds and southwest direction.

between and around the towers which reduces the performance of the radiators. The hot air return and exit on the radiators of towers 1 and 4 in the southwest direction is also observed. The Heller Tower of Unit 3 with 277.8 MW released heat contains the best performance and the Heller Tower of Unit 1 with 235.1 MW has the worst performance among all.

Figs. 12 and 13 illustrate the temperature and relative pressure contours respectively at a wind speed of 14 m/s from the north-east. According to the drawn contours, the return and exit of hot air from the radiators is quite obvious. The increase in pressure is clearly seen in the towers facing the wind. Also, the pressure drop between the towers is visible in the pressure contour. The Heller Tower of Unit 1 with 255.7 MW heat release shows the best performance among all and the Heller Tower of Unit 4 with 242.8 MW shows the worst case.

Figs. 14 and 15 show the temperature and relative pressure contours, respectively. At a wind speed of 14 meters per second from the

south-west, the Heller Tower of Unit 2 with 255.2 MW of released heat demonstrates the best performance and the Heller Tower of Unit 1 with 211.4 MW shows the worst performance.

B. Calculation of Heat Released from Each Tower at Different Wind Speeds

Fig. 16 shows a diagram of the heat released from each tower at wind speeds of 6, 10 and 14 meters per second in a northeast direction. The horizontal axis in this diagram describes the wind speed and the vertical axis denotes the heat released from each tower. As expected, as the wind speed increases, the thermal performance of the cooling towers declines. Also at this situation, Tower 4 at the wind speed of 6 meters per second exhibits the highest performance with 351 MW heat released whereas Tower 4 at 14 m/s wind speed shows the lowest thermal performance with heat release of 243 MW compared to other towers.

Similar to the previous diagram, Fig. 17 demonstrates the thermal performance of cooling towers at wind speeds of 6, 10 and 14 m/s in a southwest wind blow direction. Under these conditions, Tower 2 has the best performance compared to other towers at a wind speed of 6 meters per second with a heat release of 350 MW. In addition, Tower 1 shows the lowest performance at a wind speed of 14 meters per second with the amount of 211 MW heat released. Also, according to the results, the thermal performance of Tower 2 and Tower 3 are very close to each other.

IV. CONCLUSION

This study was performed to numerically investigate the thermal performance of cooling towers of Shazand power plant in summer and during peak hours for wind speeds of 6, 10 and 14 m/s in the northeast and southwest, using simulation approaches. The wind reduces the air flow through the radiators by increasing the pressure drop and disrupting the distribution of inlet air into the radiators. Reducing the air flow through the towers severely reduces the performance of the plant's cooling systems. The results show that at peak hours of electricity consumption, the wind blow at 14 m/s speed in the southwest direction leads the cooling towers of Shazand power plant to have the worst performance. Further observations indicate that the cooling towers perform best at a wind speed of 6 m /s in the northeast direction.

ACKNOWLEDGMENT

The authors would like to acknowledge the financial grant received from the Shazand Thermal Power Plant. It is highly appreciated. The authors also would like to appreciate the help received from the Department of Research and Technology of Sharif University of Technology.

REFERENCES

[1] Kröger, & Detlev, G. (2004). Air-cooled heat exchangers and cooling towers. Penwell Corporation. Oklahoma Vol. 1.

[2] Li, X., Hal, G., Zhiqiang, G., & Yubiao, S. (2018). Experimental study of cold inflow effect on a small natural draft dry cooling tower. *Applied Thermal Engineering, 128*, 762-771.

[3] Ge, W., Jun, F., Chuan Xiao, L., Wendong, L., Guangan, C., & Yuanbin, Z. (2019). Critical impact factors on the cooling performance design of natural draft dry cooling tower and relevant optimization strategies. *Applied Thermal Engineering, 154*, 614-627.

[4] Khodakaram-Tafti, A., & Golneshan, A.A. (2020). A general mathematical model for predicting the thermal performance of natural draft dry cooling towers and extending it to three aligned towers. *Energy Sources, Part A: Recovery, Utilization, and Environmental Effects*, 1-23.

[5] Goodarzi, M., & Moradi Maryamnegari., S. (2018). A new natural draft dry cooling tower with improved thermal performance during windy condition. *Applied Thermal Engineering, 139*, 341-351.

[6] Song, G., Xudong Z., Feng F., Wei W., & Peng W. (2020). Cooling performance of cylinder-frustum natural draft dry cooling tower. *Applied Thermal Engineering 180*, 115797.

[7] Shirazi, M., & Jahangiri, A. (2021). 3D Numerical study using three novel windbreak walls in natural draft dry cooling towers for performance enhancement under various crosswind conditions. *Thermal Science and Engineering Progress* 100971.

[8] Ghafari, S., & Golneshan. A.A. (2018). Wind effects and the challenge to enhance thermal performance of three aligned natural draft dry cooling towers. *Iranian Journal of Science and Technology, Transactions of Mechanical Engineering 42*(4), 347-354.

[9] The Center for Developing Modern Energy Systems, Sharif High Tech Park, Sharif university of Technology. (2021). *Technical and economic feasibility studies on hybrid implementations of wind guides and TOSAN auxialary cooling system to improve the thermal performance of Heller towers in Shazand power plant*, Report Phase 1.

Lean & Kaizen Concepts for Better Environmental Management System

Bratimir Nešić[1], Jelena Malenović Nikolić[2]

[1]Academy of Technical and Vocational Studies Niš, Serbia, bratimir@gmail.com
[2]Faculty of Occupational Safety, Niš, Serbia, jelena.malenovic@znrfak.ni.ac.rs

Abstract—**The objective of this paper was to provide an analysis of lean & kaizen concepts application for better environmental management system. The basic idea is to provide useful improvement strategies based on lean & kaizen concepts with the purpose of achieving more sustainable solutions for various environmental management system problems, green strategies, sustainable waste management and costs reduction.**

Keywords - lean, kaizen, concept, environment, management

I. INTRODUCTION

Lean & Kaizen philosophy has been growing during the last decade, because increasingly, clients are demanding it. For that reason companies have implemented lean & kaizen processes improvement as part of their business. The implementation of lean & kaizen strategies focuses on getting the right things, to the right place, at the right time, in the right quantity, to achieve perfect work flow while minimizing waste and being flexible and able to change. These strategies aim to make the work simple enough to understand, to do and manage [1, 2].

Today, markets are changing continuously and organizations are under tremendous pressure to improve productivity and quality while reducing costs. This has led many organizations to implement the Toyota Production System, otherwise known as lean manufacturing [3-5]. Implementation of green practices in waste management such as recycling and composting is a powerful tool to increase sustainability. The implementations of these strategies have been completed to reduce environmental issues and improve customer satisfaction regarding waste management.

Lean and green manufacturing can have a more significant, positive impact on multiple measures of operational performance when implemented concurrently rather than separately. The link between lean production and environmental improvement is strong. The main objective of lean process improvement is the systematic elimination of waste by focusing on production costs, product quality and delivery, and worker involvement. This means that the implementation of lean methods continually seeks to reduce the materials, energy, water, space, and equipment needed per unit of production [1].

II. MATERIAL AND METHOD

A. Lean Origins

The term lean goes back to the 1990s when a book called *The Machine That Changed the World: The Story of Lean Production* introduced the term lean production [6]. The book follows the transfer of manufacturing ideas from craft production to mass production to lean production. The origins of lean manufacturing processes came from the Toyota Production System (TPS) and were initiated by Ohno and Shingo at Toyota, with the aim of efficient use of resource through level scheduling. Ohno and Shingo used the Japanese word “muda”, which were defined as any human activity that absorbs resources but creates no value [7].

B. Lean Concepts

Recent studies have determined that due to the intensive competitive environment of the global economy, the survival of many companies depends on the ability to continuously improve their processes while reducing costs. These studies have determined that many organizations have been adopting lean thinking in order to improve performance and allow for competitive advantage.

According to [8], lean is about servicing the customer better with less staff, less inventory and

less capital expenditure. Based on the author's statement, lean has been developed to improve inventory management to avoid waste of material and reduce costs. Toyota has used this tactic as a philosophy to improve their manufacturing process, reduce waste, and implement changes among others. Excess raw material, work in process, or finished goods cause longer lead time, obsolescence, damaged goods, transportation and storage costs, and delay [3]. To decrease amount of excess material, companies have to keep an accurate inventory in order to avoid chemical spoilage and obsolescence. The elimination of waste by applying sustainable waste management leads to improved quality, and decreased production time and cost.

According to Seth and Gupta [9] the goal of lean manufacturing is to reduce waste in human effort, inventory, time to market and manufacturing space to become highly responsive to customer demand while producing quality products in the most efficient and economical manner. There is a common interchangeable usage between the terms lean thinking, lean production, lean manufacturing and TPS. The principles behind lean production aim at minimization of resources, and by this minimization of waste in the context of mass production, i.e. less human effort, less manufacturing space, less inventory, less defects [10, 11]. Accordingly, lean production aims at meeting customers' expectations by delivering quality products and services at the right time and at the right cost [12, 13].

C. Lean and Green Connection

The relationship between lean and green manufacturing has been well documented in recent literature. Green, or sustainable, manufacturing is defined by [14] as a method to develop technologies to transform materials without emission of greenhouse gases, use of nonrenewable or toxic materials or generation of waste. Markedly, the green wastes are different from the lean wastes. Lean seeks to eliminate traditional production objectives like cost or time [15] while green is generally concerned with wastes that impact the environment [13, 16].

According to [17] the connection between lean manufacturing and the environmental movement with its inherent value-stream view and focus on the systematic elimination of waste, makes it natural that the lean concept fits with the overall strategy of protecting the environment, which the authors call Environmental Lean (En-Lean). Due to research conducted by Teresko [18] the connection between green manufacturing and the Lean movement was made. The author stated in his research that the main goal of lean process improvements, when applied within a manufacturing facilities layout, is to involve a structure around an optimized process including the entire external commercial environment in the optimized process, integrating all the manufacturing flows from global to national to submicroscopic levels.

D. Lean and Green Strategies

Traditionally, the implementation of lean process improvements have been accomplished through analysis of the shortcomings of an existing process, implementation of a revised process, and subsequent Plan-Do-Check-Act (PDCA) cycles [19]. Much like lean, green manufacturing implementation is largely dependent on PDCA for deployment and assessment [20].

According to [21] the implementation of an environmental management system (EMS) is a process where organization's management identifies environmental aspects either regulated or unregulated and the impacts of its operations, assesses current performance, and develops targets and plans to achieve both significant and incremental environmental improvements. In a 1997 study, Briscoe, Marcus, Maxwell, and Rothenberg identified that 80% of Fortune 500 firms had written environmental statements, or the "Plan" in Plan, Do, Check and Act (PDCA). The mid-1990's is identified as the start of the green manufacturing movement [22].

While lean and green strategies share similar implementation strategies, they differ in the standards to which implementation is evaluated. According to The International Organization of Standardization, 14001 is a standard for environmental management systems to be implemented in any business, regardless of size, location or income. The purpose of this standard is to reduce the environmental track of a business and to decrease the pollution and waste a business produces.

The main topic areas of the ISO 14001 standard are as follows [20]:

1. Scope
2. Normative References
3. Definitions

4. Environmental Management System Requirements
5. General Requirements
6. Environmental Policy
7. Planning
8. Implementation & Operation
9. Checking/Corrective Action
10. Management Review

Lean manufacturing does not have any accepted standardization for assessments. Lean's fundamental principles developed by Toyota are universally accepted but commonly adapted to each organization or industry. Lean and green manufacturing have similar implementation strategies but distinctly different methods by which their respective implementations are evaluated.

E. Environmental Benefits of 5S Tools

5S tools are systems created to reduce waste and optimize productivity through maintaining an orderly workplace and using visual cues to achieve more consistent operational results. The implementation of 5S methods [2, 5] within the workplace specifically in its existing process is typically the first lean method which organizations implement.

According with The United States Environmental Protection Agency [23], a typical 5S implementation would result in significant reductions in the square footage of space needed for existing operations. Also this agency states that the implementation of 5S strategies would result in the organization of tools and materials into labeled and color coded storage locations, as well as "kits" that contain just what is needed to perform a task [23].

The United States Environmental Protection Agency [23], identified that the most important benefits of implementing 5S strategies, especially in inventory systems are:

1. The removal of obstacles and the marking of main thoroughfares decrease the potential of accidents that could lead to spills and associated hazardous waste generation (e.g., spilled material, absorbent pads and clean up materials).
2. Regular cleaning, as part of the Shine pillar, decreases the accumulation of cuttings, shavings, dirt, and other substances that can contaminate production processes and result in defects. Reduction in defects has significant environmental benefits.
3. Organizing equipment, parts, and materials so they are easy to find can significantly reduce unneeded consumption.
4. 5S visual cues (e.g., signs, placards, scoreboards, laminated procedures in workstations) can be used to raise employee understanding of proper waste handling and management procedures, as well as workplace hazards and appropriate emergency response procedures.
5. 5S techniques can be used to improve labeling of hazardous materials and wastes. According with agency, the integration of 5S visual cues and operating procedures will improve employee environmental management.

Many companies have reached a superficial implementation of lean and that is due to the fact that they are concentrated on some of the lean tools like 5S or Just in Time, rather than grasping the concept and apply it as a cultural change throughout the whole organization [3]. According with [3] previous research has demonstrated that companies can just implement three of the five S and fail in the standardization of processes and even more difficult of a task is to keep the sustainability of the results of the project, therefore the completeness of the 5S tool is essential to achieve a complete process improvement.

F. Lean Manufacturing Relationship with Compost and Recycling Systems

According to The United States Environmental Protection Agency [24], some lean experts indicate that between 30% and 40% of all United States manufacturers report having begun implementing lean methods, with approximately 5% well down the road of implementing multiple advanced manufacturing tools. Some opportunity areas that the EPA might consider to advance environmental improvement through lean manufacturing efforts are compost and recycling systems.

According with the U.S. Composting Council [25] compost manufacturing is an

environmentally sound, cost-effective, and decentralized method for processing organic materials into an environmentally beneficial product, thereby avoiding the long-term negative impacts associated with disposal. Due to this organization, composting is part of the recycling industry that directly or indirectly employs more than 450,000 Americans throughout the United States. These jobs account for more than $90 billion in economic output [25].

Recycling turns materials that would otherwise become waste into valuable resources. Collecting used bottles, cans, and newspapers and taking them to the curb or to a collection facility is just the first in a series of steps that generates a host of financial, environmental, and social returns [13].

The United States Environmental Protection Agency [24] states that lean manufacturing network has a shared goal - elimination of waste from business - with the environmental management network promoting environmental improvement, waste minimization, pollution prevention, design for environment, and sustainability.

G. Sustainability

In this changing world sustainability has become a fundamental requirement for human development. Sustainability has been defined in different ways. According to The World Commission on Environment and Development sustainability is [26]: "In essence, sustainable development is a process of change in which the exploitation of resources, the direction of investments, the orientation of technological development and institutional change are all in harmony and enhance both current and future potential to meet human needs and aspirations".

Sustainability strategies have been implemented by companies in order to fight against environmental issues and reach efficiency and effectiveness in their business. According to [27] however sustainability focuses on not only economic growth and production but also human condition in this generation as well the future generation.

Reference [27] illustrate that the implementation of lean strategies are vital to achieve sustainability within companies. The integration and collaboration of all staff involved with this project was also vital. In another perspective, [28] argue that sustainability requires balanced, complex interactions involving cooperation and competition among all subsystems on the planet.

One of the goals in the process to achieve sustainability is to work hand in hand with local companies in order to pursue a common goal [28]. For that reason we can say that implementation of lean process improvement in the compost and recycling systems is a win-win solution.

H. Corporate Sustainability

Corporate sustainability is commonly used to define sustainable development on a corporate level. This term was brought up to address the change of value system in companies driven by sustainability requirements [29]. Based on this definition, companies are seeking to create multiple benefits for stakeholders, including not just shareholders but also employees, customers and community. According to [30] most companies accepted corporate sustainability as a precondition for their business activities.

Corporate sustainability identifies a realization in companies that economic sustainability alone is insufficient for overall sustainability in a corporation [31]. From [30] definition, corporate sustainability contains three key elements: economic, social and environmental. These important elements involve three kinds of capital for the company: environmental, social and economic capital. Understanding types of capitals is important for a company to understand what they are aiming to sustain. The three capitals definitions based on [30] are:

- **Economic capital** means debts, stocks, machinery, inventions, and reputation.
- **Natural capital** consists of both natural resources (e.g. fossil fuel, wood) and ecosystem services (e.g. climate stabilization, water purification). This way, corporations will not degrade ecosystem but sustain its service ability.
- **Social capital** can be both human capital and societal capital. Human capital concerns people's skills, motivations and growth while societal capital concerns public service, community health and so on.

Recently studies conducted by the Harvard Business School have revealed that corporate sustainability is a key driver for company's

innovation that also yields real financial rewards rather than extra cost. A new study in the Harvard Business Review has found that by treating sustainability as a goal today, early movers will develop competencies that rivals will be hard-pressed to match [32].

I. Serbian Experiences

Japan Tobacco International (JTI) in Senta, is the first company in Serbia to fully implement Lean & Kaizen concepts that are responsible for the success of Japanese companies. By applying the Lean & Kaizen concepts, productivity was increased by 50% and production scrap was reduced by 46% [2]. Visual management is a technique that ensures that all workers in the company, through the information presented in a visual form, can understand the state of the process. It creates an environment where things are obvious from the moment of entry. Visual information should be relevant, useful and timely. In JTI in Senta, visual management is ubiquitous: in production, warehousing and offices. Changes in the work environment lead to changes in the attitude of employees, which together affect the change and improvement of the business culture and environment. Employees develop themselves, teamwork is established, which improves the atmosphere in the company and increases the motivation of employees. Good organization of work environment reduces unnecessary work, increases employee safety and productivity which all leads to lower costs. A number of activities are organized for employees at JTI. Lean & Kaizen concepts apply to every employee of the company, every day and in every place. Only in this way permanent and long-term progress is possible. Satisfied employees are important for the success of the company. JTI has this because 88% of employees would recommend them as an employer and as many as 94% would make the extra effort for the company to succeed. It is also important for employees to move forward, so job positions are always first advertised internally to evaluate potential candidates within the company [2].

The implementation of Lean & Kaizen concepts at Strauss Adriatic began in 2010, when the first trainings began and the application of the specific principles began after a visit to Japan Tobacco International in Romania in 2011. Like any innovation and application, initially encountered resistance and concern among employees and it took an extraordinary amount of effort to get all employees involved. That accepting the application of Lean & Kaizen concepts though progress is the fact that in 2011, there were 58 proposals for improvement, one of which 31 was adopted. Although anonymously making proposals helped to overcome the feeling of insecurity because of the opinion that their proposal is not good, thanks to the provision of public proposals that are followed by specific people, the most valuable and creative proposers were rewarded for their efforts. The idea behind the introduction of Lean & Kaizen concepts in Strauss was to improve working conditions, increase productivity and safety, arrange space, but also to improve communication among employees as well as solving environmental problems. For the time being, application of these concepts is represented in production and most proposals relate to modification of working methods or certain procedures that employees have identified as a barrier to work. The equipment that was damaged was repaired and brought back into serviceable condition, and the one that was destroyed was replaced with a new one. For ease of reference, numerous instructions and panels have been put in place that clearly indicate how some piece of equipment is used, where it stands and who is in charge of a particular sector. The use of coffee weed as biomass for heating is a proposal that came from one employee is an outstanding example of Lean & Kaizen application, which solves the problem of waste disposal and finds its new purpose. Although this proposal also required some investment, one year after the implementation of this heating system, the investment was fully paid off, so it can be said that the company now has drastically lower costs [2].

Tetra Pak also uses Lean & Kaizen tools. At different stages of implementation they faced different challenges. The first challenge of any organization looking to implement a new business process is how to ensure that all employees embrace change in the right way. Top management plays a key role here. If top management has a 1% doubt about success then manufacturing employees will have 50% doubt and the program will not be successful. The second challenge was how to keep the program active and further improve in conditions of production growth, increase in production complexity and increase in the number of employees. The proper set up of the process improvement system, the quality of the achieved standards and, above all, the quality of training

of newly hired colleagues in order to enable them to get involved in the program as quickly as possible and to contribute, played a major role here [2]. Lean & Kaizen also have an impact on the financial perspective and innovation, which are two very important aspects of business. By increasing productivity and efficiency of production and business processes, as well as by reducing waste, it directly influences profits, partly through savings generated in manufacturing processes and partly through innovations in the field of new products and services, as well as innovations in improving the quality of existing products and services and significant contribution to environmental problems solving [2].

III. DISCUSSION

According to [33] Lean & Kaizen concept development trends and directions indicate that the highest lean production practices with application in the ISO 14001 certified companies include Continuous Improvement (Kaizen) - 93,8% of companies have adopted Continuous Improvement (Kaizen). This is followed by Just-In-Time that is 89,6%. 5S' and General Visual Management and Standardized Work have the same value that is 87,5%. It follows by Zero Defect that is 81,3%. Other than that, 79,2% have adopted Total Preventive Maintenance (TPM) in the companies. It is followed by Pull Production and Kanban that is 68,8%. The last lean production practice is Cellular Manufacturing that is 62,5%.

Reference [34], did the research about application of Lean & Kaizen concept in energy sector in order to protect environment and concluded that following lean concepts, the management of environmental aspects should be focused in improving material and energy flows that can cause significant environmental impacts. One of the keys to lean thinking is simplification. Applied in the context of the whole process or plant, it has the added benefit of simultaneously saving such resources such as space, materials, energy, transportation and time. The logic of lean thinking, with the emphasis on eliminating the seven classic wastes can be redesigned and integrated to the sustainability systemic concept. By minimizing the amount of waste that is produced in manufacturing, reducing energy use, and using the materials and resources in a more efficient way, can lead to financial cost savings and reduction of environmental impacts. Therefore, integrating this concept offers the foundation for a new business logic, where the pillars of sustainability, social, economic and environmental, can support business goals, requirements and needs.

IV. CONCLUSION

The classical deployment of lean's tools such as standardized work, visual control, and Kaizen, are ways to identify problems and solve them. The main purpose of lean is to highlight the underlying root cause of many types of problems to find the correct process to solve it. Each organization should have its own detailed definition of sustainability based on their specific concerns and intentions. This means that there is not a specific definition or strategy to achieve sustainability in organizations. The purpose of this paper was to gain insight on the approach and application of lean strategies and apply this knowledge in solving the general environmental problems.

REFERENCES

[1] Chacon, W. (2012). Implementation of lean process improvement strategies to the compost and recycling systems in the Memorial Student Center at the University of Wisconsin-Stout, Research report, University of Wisconsin-Stout, Graduate School, Wisconsin, USA.

[2] Nešić, B., Vasović, D., Nešić, L., & Stajić, Lj. (2019). Processes, Examples and Experiences in Applying Kaizen Management Concept in Serbia. In *Proceedings of the 1st Virtual International Conference: Path to a Knowledge Society-Managing Risks and Innovation PaKSoM 2019* (pp. 3-10), Alfatec & Complex System Research Centre, Niš, Serbia.

[3] Liker, J. K. (2004). *The Toyota way*. McGraw-Hill, New York, USA.

[4] Womack, J., Jones, D. (2003). *Lean thinking*. Free Press, New York, USA.

[5] Nesic, B., Vasovic, D., Tanovic, P., Nesic, N., & Nesic, L. (2020). Environmental improvements via lean manufacturing. In *Proceedings of the 6th International Conference on Knowledge Management and Informatics* (pp. 296-304), The Higher Education Technical School of Professional Studies in Novi Sad, Novi Sad, Serbia.

[6] Holweg, M. (2007). The genealogy of lean production, *Journal of Operational Management*, USA.

[7] Demeter, K., & Matyusz, Z. (2008). The impact of Lean practices on inventory turnover. *International Journal of Production Economics*.

[8] Balle, M. B. (2011). *The Lean manager*. Lean Enterprise Institute, Cambridge, UK.

[9] Seth, D., & Gupta, V. (2005). Application of value stream mapping for Lean operations: An Indian case study. *Production Planning & Control*, 44-59.

[10] NSPR, ASE. (2004). The national shipbuilding research program and the Lean shipbuilding initiative.

Reference Package developed for Students at the Defense Acquisition University, USA.

[11] Nesic, B., Vasovic, D., Tanovic, P., Nesic, N., & Nesic, L. (2020). Lean implementation and OHS. In *Proceedings of the 15th International Conference Risk and Safety Engineering* (pp. 232-240), The Higher Education Technical School of Professional Studies in Novi Sad, Novi Sad, Serbia.

[12] Ross & Associates Environmental Consulting, Ltd., (2004). *Findings and Recommendations on Lean Production and Environmental Management Systems in the Shipbuilding and Ship Repair Sector*. U.S. Environmental Protection Agency National Center for Environmental Innovation, USA.

[13] US EPA, (2012). Available at: http://www.epa.gov/Lean/environment/methods/fives.htm.

[14] Allwood, J. (2005). *Sustainable manufacturing seminar series.* Available at:retrieved from: http://www.ifm.eng.cam.ac.uk/sustainability/seminar/documents/050216lo.pdf.

[15] Bergman, L., Hermann, C., Stehr, J., Sebastian, T. (2008). An environmental perspective on Lean production. In *41st CIRP Conference on manufacturing Systems*.

[16] Bergmiller, G., & McWright P. (2009). Lean manufacturers' transcendence to green manufacturing. In *Proceedings of the Industrial Engineering Research Conference*, Miami, FL, USA.

[17] Sawhney, R., Teparakul, P., Aruna, B., Li, B., & X. (2007). En-Lean: A framework to align Lean and green manufacturing in the metal cutting supply chain. *Society for Modeling and Simulation International*.

[18] Teresko, J. (2004). Lean, green and smart. Industry Week, 2004.

[19] Dennis, P. (2007). *Getting the right things done*. The Lean Enterprise Institute Brookline, MA, USA.

[20] Maynard, H. (2007). *Industrial engineering handbook* [5th edition]. McGraw-Hill.

[21] Bergmiller, G., & McWright, P. (2009). Lean manufacturers' transcendence to green manufacturing. *Proceedings of the Industrial Engineering Research Conference*, Miami, FL, USA.

[22] Haworth, D. (2009). Sustainability, Forest Products Society, Great Lakes Region, Seminar presentation, Crowne Plaza, Grand Rapids, MI, USA.

[23] US EPA, (1996). Available at: http://www.epa.gov/Lean/environment/methods/fives.htm.

[24] US EPA, (2003). Lean manufacturing and the environment.

[25] U.S. Composting Council (2012). Position statement: 2012 farm bill.

[26] The World Commission on Environment and Development, (2011). Available at: http://www.un-documents.net/wced-ocf.htm.

[27] Bell, S., & Morse, S. (2003). *Measuring sustainability: Learning by doing*. Earthscan Publications, UK.

[28] Stead, W. E., & Stead, J. G. (2004). *Sustainable strategic management.* M.E. Sharpe, New York, USA.

[29] Salzmann, O., Ionescu-Somers, A., & Steger, U. (2005). The Business Case for Corporate Sustainability: Literature Review and Research Options. *European Management Journal*, *23*(1), 27–36.

[30] Dyllick, T., & Hockerts, K. (2002). Beyond the business case for corporate sustainability. *Business Strategy and the Environment*, *11*, 130–141.

[31] Gladwin, T. N., Kennelly, J. J., & Krause, T-S, (1995). Shifting Paradigms for Sustainable Development: Implications for Management Theory and Research, *Academy of Management Review*, *20*(4), 874-907.

[32] Eccles, R. G., Ioannou, I., & Serafeim, G., (2011). Available at: http://www.hbs.edu/faculty/Publication%20Files/12-035.pdf.

[33] Puvanasvaran, P., et al., (2013). Lean principles adoption in environmental management system (EMS) - ISO 14001. *Journal of Industrial Engineering and Management*, *5*(2), 406-430.

[34] Pampanelli, A. B., Found, P., & Bernardes, A. M. (2011, April). A lean and green Kaizen model. In *POMS annual conference* (p. 29).

A Numerical Simulation of HTL Free Pb based Perovskite Solar Cell Using SCAPS-1D

Muhammad Aamir Shafi[1], Shafi Ullah[2], Hanif Ullah[3], Laiq Khan[4], Bernabé Mari[5]

[1,2,5]Instituto de diseño y Fabricación (IDF)-Universitat Politécnica de València (UPV) Camino de Vera, s/n 46022 Valencia, Spain. Shafi399@yahoo.com[2], bmari@fis.upv.es[5]

[1,3]Department of Electrical Engineering, Federal Urdu University of Arts, Science and Technology, Islamabad, Pakistan. hanifuet@yahoo.com[3]

[1,4]COMSATS University Islamabad, Abbottabad Campus (CUI), Pakistan. aamirshafi@ymail.com[1], laiqkhan@comsats.edu.pk[4]

Abstract—**The HTL free perovskite based solar cell has been suggested in this simulation work, with CH3NH3PbI3 as the active layer and TiO2 as the electron transport layer (ETL). To construct the suggested HTL-free CH3NH3PbI3-based PSC and simulate its performance at 300K under A.M 1.5 G 1 Sun irradiation, the solar cell capacitance simulator in one dimension software was used. By altering the physical characteristics of various layers, the proposed PSC's output parameters, such as open circuit voltage (Voc), short-circuit current density (Jsc), fill factor (FF), power conversion efficiency, and quantum efficiency, are analysed. The suggested cell's thermal stability has also been investigated. The ETL and absorber thicknesses have been tuned to be 0.025 and 0.50 um, respectively. The active and ETL layers' acceptor and donor concentrations were tuned to be 1.00E+17 and 5.00E+21 cm-3, respectively. The suggested HTL-free CH3NH3PbI3-based PSC has a conversion efficiency of 18.61%, a Voc of 1.07 V, a Jsc of 20.73 mA/cm2, and an FF of 83.78%. These simulation results might aid in the development of highly efficient and low-cost perovskite solar cells.**

Keywords - HTL Free Perovskite, simulation, efficiency, SCAPS-1D

I. INTRODUCTION

Photovoltaic (PV) technology has advanced in recent years as a result of the introduction of numerous solar device architectures [1-12]. Due to its cost effectiveness and enhanced performance, the perovskite absorber-based solar structure has become one of the most developing PV technologies [13-21]. Perovskite materials have good PV output characteristics because to their high absorption coefficient, favorable band gap, and long charge-carrier diffusion lengths. Many researchers have attempted to improve perovskite solar cells (PSCs) based on the $CH_3NH_3PbI_3$ absorber material's PV performance [22-26]. Because of its outstanding characteristics, such as optimal band gap, broad absorption spectrum, good cartrier transport mechanism, simplicity of production on a flexible substrate, variable band gap, and long diffusion length, $CH_3NH_3PbI_3$ becomes a superb light harvester [27-32]. The aforementioned characteristics of lead halide perovskite material encourage its usage in the manufacture of perovskite solar cells, making it a viable alternative to standard silicon [33-36]. The maximal PCE of these $CH_3NH_3PbI_3$ based perovskite solar cells is 3.8% at first [37]. The PCE of perovskite solar cells has now reached 22.1%, thanks to innovative production processes and careful architectural choices [38]. The ETL and HTL's primary objectives are to transport electrons and holes created by light intensity within the perovskite layer from the absorber to the front and rear metallic contacts, as well as to prevent electrons and holes from flowing from the absorber to the back or front contact. However, fabricating defect-free multi-layered PV devices remains a difficulty. Furthermore, flaws at the ETL or HTL/perovskite interface encourage carrier

ISBN: 978-86-80593-73-9

recombination and reduce the overall stability of the solar cell design [39, 40]. To address these issues, the PV community was recently exposed to a novel idea of HTL-free solar device configuration, which would minimise manufacturing costs and interface flaws without compromising cell performance [41-44]. In addition, numerous electron transport layer (ETL) materials, such as ZnO, TiO_2, CdS, and CeO_2, have been employed in PSCs to boost output performance [45-48]. The basic knowledge for developing this model came from the literature and associated simulation efforts [49-53]. The earth's abundance of methylammonium lead halide perovskite materials, which are solution processable, allows for a cost-effective production procedure. To increase the device's performance, a clear knowledge of the underlying relationship between the material characteristics and the device design is required. An HTL-free PSC with $CH_3NH_3PbI_3$ as an absorber layer and TiO_2 as an ETL is examined in this study to better understand the characteristics of a $CH_3NH_3PbI_3$-based PSC. Using the solar cell capacitance simulator in the one dimension (SCAPS-1D) simulation tool, the output performance of the developed HTL-free $CH_3NH_3PbI_3$-based PSC was investigated.

II. Solar Cell Model and Numerical Parameters

Fig. 1 shows the solar model that was utilised for the simulation in this study work. A one-dimensional programme called SCAPS-1D is used to examine the solar cell's performance. The simulations of the SCAPS-1D simulator are based on the answers of three basic semiconductor equations: Poisson's equation, electron continuity equation, and hole continuity equation. For the electrostatic potentials of electrons and hole concentrations as a function of locations x, SCAPS-1D software solves these three coupled partial differential equations numerically [54]. The solar model under investigation consists of a $CH_3NH_3PbI_3$ absorber layer and a TiO_2 electron transport layer. Academic literature, theories, and experiment-based results were used to choose solar cell properties for our simulation as shown in Table I [55]. The lighting spectrum is adjusted to AM1.5 G 1 sun, whereas working temperature is set to 300 K [56]. Time and money can be saved by using computer-based simulation software. It's a powerful method for predicting and evaluating the impact of a variety of model parameters and

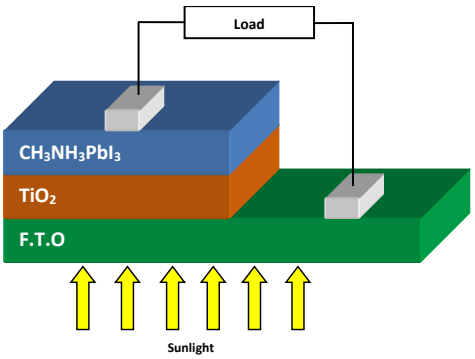

Figure 1. Solar cell model used in Simulation.

material properties on a solar cell's output performance. SCAPS software, created by Marc Bargeman and colleagues at the University of Gent, is used in this investigation [57].

The influence of active layer and ETL layer thickness on sun cell performance, as well as acceptor and donor concentration changes, was investigated. The effect of different operating temperatures on solar cell performance was then simulated. The solar cell parameters that were utilized in the simulation are provided in the Table I below. The Table II, on the other hand, shows parameters for both front and rear contacts.

TABLE I. Numerical parameters used for simulation [58-60].

Parameters	**$CH_3NH_3PbI_3$**	**ETL (TiO_2)**
$W\ (\mu m)$	2.00	0.05
$E_g(eV)$	1.55	3.20
$\chi\ (eV)$	3.7500	4.0
ε_r	6.500	100
$N_C(cm^{-3})$	2.20E+15	1.0E+21
$N_V(cm^{-3})$	2.20E+17	2.0E+20
$V_e\ (cm/s)$	1.000E+7	1.000E+7
$V_P\ (cm/s)$	1.000E+7	1.000E+7
$\mu_e(cm^2/(Vs))$	2.000E+0	6.000E-3
$\mu_p(cm^2/(Vs))$	2.000E+0	6.000E-3
$N_D(cm^{-3})$	0.000E+0	5.000E+19
$N_A(cm^{-3})$	1.000E+13	0.000E+0
α	Scaps Value	Scaps Value

TABLE II. CC USED FOR BACK AND FRONT CONTACT FROM SCAP-1D.

Parameters	Front Contact	Back Contact
Surface recombination velocity of electrons (cm/s)	1.00E+7	1.00E+5
Surface recombination velocity of holes (cm/s)	1.00E+5	1.00E+7
Metal work function (eV)	4.6039	5.8973
Majority carrier barrier height relative to Ef (eV)	0.0539	0.1527
Majority carrier barrier height relative to Ev (eV	0.0000	0.0000

A. *Study as a Function of Dark and Sun Illuminated*

To observe the validity of the solar cell, the simulation of proposed solar cell model "Glass/Back.Contact/$CH_3NH_3PbI_3$/TiO_2/Front.Contact" was executed both under dark and sun. The thickness of active layer and ETL layer was kept 2.0 um and 0.05 um respectively. Whereas the series and shunt resistance were kept by default as they are in SCAPS-1D simulation tool. The simulation was carried out at 300K temperature under A.M 1.5 G 1 Sun illumination.

B. *Study as a Function of $CH_3NH_3PbI_3$ Absorber Layer Thickness and Acceptor Density*

To observe the effect of $CH_3NH_3PbI_3$ active layer thickness and acceptor concentration was changed from 0.50 to 3.0 um and 1.00E+12 to 1.00E+17 cm^{-3} respectively, the simulation of proposed solar cell model "Glass/Back.Contact/$CH_3NH_3PbI_3$/TiO_2/Front.Contact" was executed at 300K temperature under A.M 1.5 G 1 Sun illumination. Whereas the series and shunt resistance were kept by default as they are in SCAPS-1D simulation tool.

C. *Study as a Function of ETL Layer Thickness and Donor Density*

To observe the effect of TiO2 ETL layer thickness and donor concentration was changed from 0.025 to 0.150 um and 5.00E+16 to 5.00E+21 cm-3 respectively, the simulation of proposed solar cell model "Glass/Back.Contact/$CH_3NH_3PbI_3$/TiO_2/Front.Contact" was executed at 300K temperature under A.M 1.5 G 1 Sun illumination. Whereas the series and shunt resistance were kept by default as they are in SCAPS-1D simulation tool.

D. *Study as a Function of Series and Shunt Resistances*

To observe the effect of series and shunt resistances, the simulation of proposed solar cell model "Glass/Back.Contact/$CH_3NH_3PbI_3$/TiO_2/Front.Contact" was executed at 300K temperature under A.M 1.5 G 1 Sun illumination. Series and shunt resistances were varied from 0.0 to 5.0 ohm.cm-2 and 100 to 100E+5 ohm.cm-2 respectively.

E. *Study as a Function of Working Temperature*

To observe the effect of working temperature on the performance of solar cell, the simulation of proposed solar cell model "Glass/Back Contact/$CH_3NH_3PbI_3$/ TiO_2/Front Contact" was executed under A.M 1.5 G 1 Sun illumination. Whereas the series and shunt resistance were kept by default as they are in SCAPS-1D simulation tool. The working temperature was varied from 300 to 425 K.

III. RESULTS AND DISCUSSIONS:

A. *Energy Band Diagram*

The energy band diagram of our suggested solar model "Glass/Back.Contact/CH3NH3PbI3/TiO2/Front Contact" generated from the SCAPS-1D simulation programme is given below (Fig. 2). The purpose of this energy band diagram is to aid in the discussion of solar cell optical characteristics [61]. The visible light is absorbed not just at the junction, but also throughout the absorber. More or equal to 1.55 eV is the bandgap value for incident light photons that is suitable for most of the light to be absorbed for effective power conversion efficiency [62].

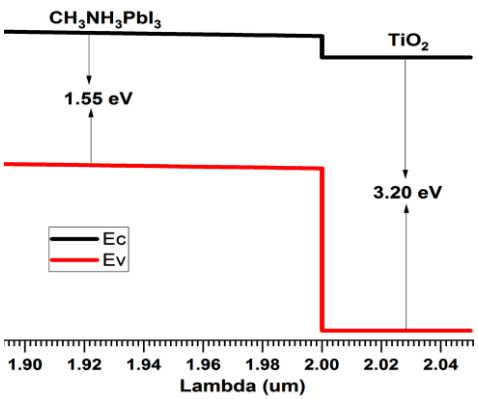

Figure 2. Energy band diagram.

B. *I-V Curve Under Dark and Sun*

To observe the validation of the proposed solar cell, the simulation was run at first under dark condition and then at AM1.5 G 1 sun was executed. During dark condition the SCAPS-1D don't show the values of Voc, Jsc, FF and eta because the solar cell acts as a diode only, as a result no generation is carried out. But when illuminated then as a result Voc of 0.96 V, Jsc of 21.55 mA/cm^2 , FF of 43.13% and eta of 8.94% was recorded as shown in Table III.

The I-V characteristics curve under dark and sun is shown below in Fig. 3.

C. *Effect of $CH_3NH_3PbI_3$ Absorber Layer Thickness and Acceptor Concentration Density*

The simulation was run initially at the 0.50 um thickness of active layer and at this layer Voc of 0.96 V, Jsc of 23.5 mA/cm^2, FF of 61.4% and efficiency of 13.8% was recorded. The thickness was increased upto 3.0 um with the step increase of 0.50 um, so total 6 calculations were recorded and here we note that with increase in thickness, the characteristics parameters decreased gradually because of recombination factor as shown in the Fig. 4. When the thickness was put 3.0 um, the Voc of 0.963 V, Jsc of 19.0 mA/cm^2, and FF of 35.2% and efficiency of 6.44% was recorded.

TABLE III. .J-V CHARACTERISTICS CURVE UNDER DARK AND SUN.

Initial Characteristics Parameters under sun	Voc	Jsc	FF	Eta
	V	mA/cm^2	%	%
	0.96	21.55	43.13	8.94

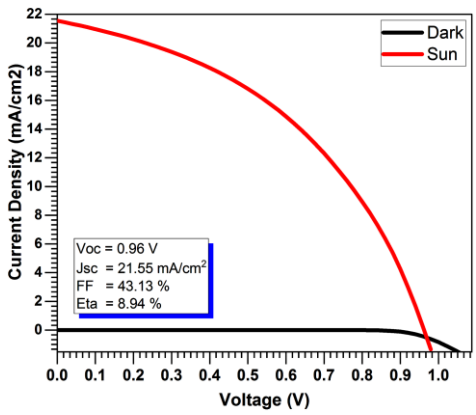

Figure 3. Initial J-V Characterisitic Curves under sun and dark.

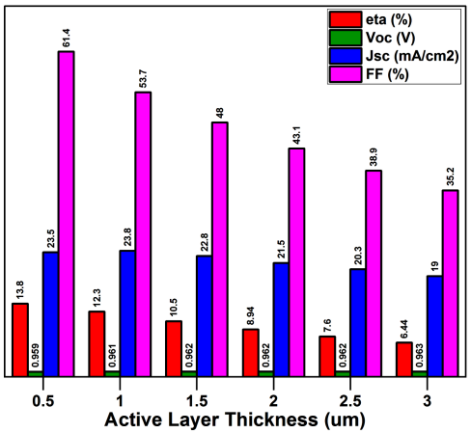

Figure 4. Effect of absorber layer thickness on characteristics parameters of solar cell.

Fig. 5 shows the effect of acceptor density variation. Here we observed that the acceptor density has a major effect on the performance of solar cell. As the acceptor density was varied from 1.00E+12 to 1.00E+17 cm^{-3}, the efficiency was improved from 7.68% to 20.5% gradually. Similarly the other characteristics parameters were also improved as Voc from 0.907 to 0.957 V, Jsc from 21.0 to 24.8 mA/cm^2, and FF from 40.4 to 86.4%.

D. *Effect of TiO_2 (ETL) Layer Thickness and Donor Concentration Density*

To observe the effect of ETL layer thickness on the performance of solar cell, the thickness was varied from 0.025 um to 0.150 um. By this variation we observe that there was no effect on the Voc of the cell due to this variation, where as a minor effect was observed on short circuit current density. There in the case of efficiency

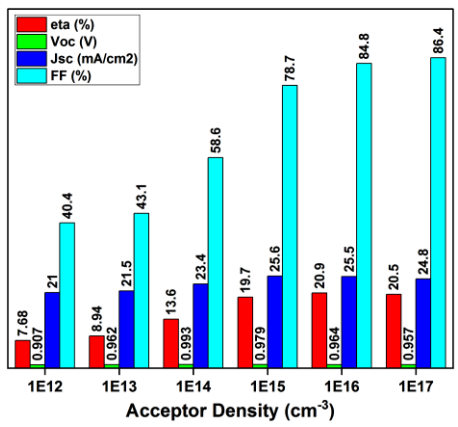

Figure 5. Effect of acceptor concentration density on characteristics parameters of solar cell.

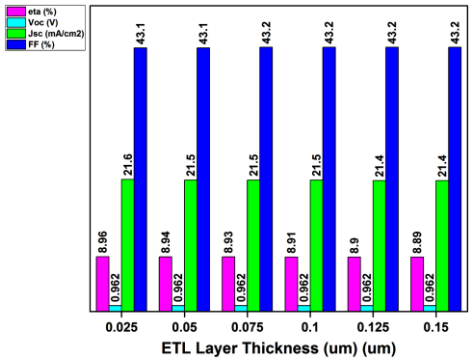

Figure 6. Effect of ETL layer thickness on characteristics parameters of solar cell.

and fill factor, the effect of ETL layer thickness is very minor, but here it was observed that even there was a minor effect, but efficiency was decreased by increasing the thickness of ETL layer, whereas the fill factor was improved lightly. The effect of ETL layer thickness is shown in the following Fig. 6.

With the effect of ETL layer thickness, we also change the concentration of donor density form 5.00E+16 to 5.00E+21 cm^{-3}. So by varying the donor concentration, the characteristics parameters were improved significantly as shown in the Fig. 7.

At 5.00E+16 cm-3 donor densities, the Voc of 0.783 V, Jsc of 20.4 mA/cm2, FF of 40.4% and eta of 6.46% was observed. By increasing the donor concentration upto 5.00E+21 cm-3, the characteristics parameters were increased as Voc of 1.08 V, Jsc of 22.1 mA/cm2, FF of 44.8% and eta of 10.7% increased.

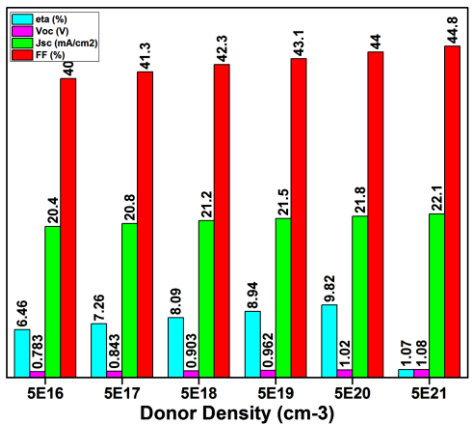

Figure 7. Effect of donor concentration density on characteristics parameters of solar cell.

E. Effect of Series and Shunt Resistances

The proposed solar cell was simulated to observe the effect of series and shunt resistances on the performance of solar cells. For this purpose the series resistance was varied from 0.0 to 5.0 ohm.cm-2. In case of series resistance, there was no effect on the Voc of the solar cell, but short circuit current was varied accordingly. Here it is important to mention that the 0.0 ohm of series resistance is an ideal case, because in practical it is not zero as there are many factors or parameters that are caused to increase the series resistance of solar cell i.e layers of solar cells etc. The effect of series resistance is shown in the Fig. 8.

To observe the effect of shunt resistance, it was varied from 100 to 1.00E+7 ohm.cm-2. As the shunt resistance was increased the

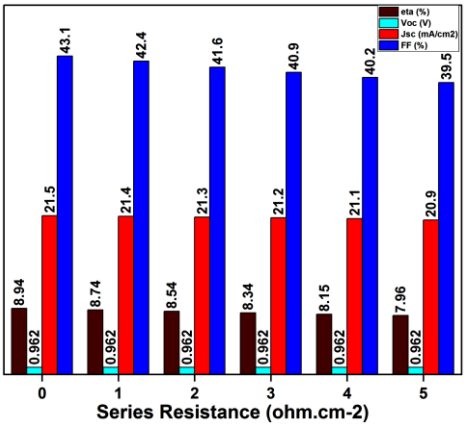

Figure 8. Effect of series resistance on characteristics parameters of solar cell.

performance of the solar cell was also improved.

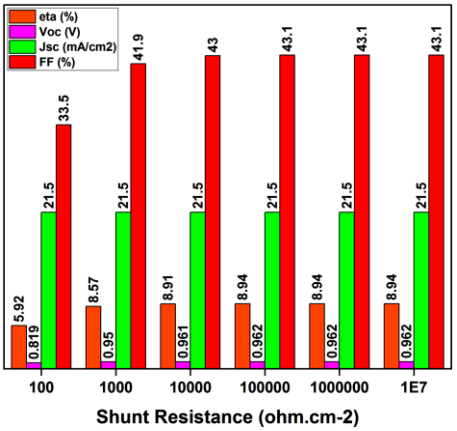

Figure 9. Effect of shunt resistance on characteristics parameters of solar cell.

Because by increasing the shunt resistance, basically we are stopping the leakage current, hence the performance increased as shown in the Fig. 9.

F. Effect of Working Temperature

The working temperature of the solar cell plays an important role on the performance of the solar cell. By varying the temperature from 300K to 425K, the Voc varied from 0.962 to 0.781 V, Jsc decreased from 21.5 to 19.1 mA/cm^2, hence the case with FF which also decreased from 43.1% to 39% and eta (efficiency) 8.94 to 5.83%. As the temperature increased the performance of the solar cell decreased because the collision of the ions increased hence their movement decreased causing the negative effect on the performance.

IV. Conclusion

The SCAPS-1D simulation programme was used to construct and analyse a new HTL-free PSC with the structure of FTO/TiO2/CH3NH3PbI3/glass. By varying the thickness, doping concentration, series and shunt resistances, and operating temperature, a numerical simulation is run to better understand the performance of the proposed PSC. According to the simulation findings, the suggested HTL-free PSC structure may achieve high photovoltaic performance. Furthermore, analysis reveals that the output performance of the suggested device structure may be improved by varying the acceptor and donor concentrations, as well as the thicknesses of both layers. As a result, our simulation research points in a new route for an HTL-free CH3NH3PbI3-based PSC that is more simple, low-cost, highly efficient, and stable.

Acknowledgement

The work was supported by Higher Education Commission of Pakistan, International Research Support Initiative Program (IRSIP) under grant No: 1-8/HEC/HRD/2020/10744 PIN: IRSIP 45 Engg 17. One of the Author Shafi Ullah acknowledged the post-doctoral contract supported by the, RRHH, postdoctoral contract (PAID-10-20), and Ministerio de Economía y Competitividad (Grant Number PID2019-107137RB-C21), Universitat Politécnica de València (UPV) Spain. Authors also acknowledge Dr. Marc Burgelman for providing the software SCAPS-1D.

References

[1] Kosyachenko, L. A., et al. (2014). Optical and recombination losses in thin-film Cu (In, Ga) Se2 solar cells. *Solar energy materials and solar cells*, *130*, 291-302.

[2] Chatzisideris, M. D.,et al. (2016). Ecodesign perspectives of thin-film photovoltaic technologies: A review of life cycle assessment studies. *Solar Energy Materials and Solar Cells*, *156*, 2-10.

[3] Xu, M., et al. (2017). Silicon heterojunction interdigitated back-contact solar cells bonded to glass with efficiency> 21%. S*olar Energy Materials and Solar Cells*, *165*, 82-87.

[4] Medina-Montes, M. I.,et al. (2018). Development of sputtered CuSbS2 thin films grown by sequential deposition of binary sulfides. *Semiconductor Science and Technology*, *33*(5), 055004.

[5] Powalla, M., et al. (2018). Thin - film solar cells exceeding 22% solar cell efficiency: An overview on CdTe-, Cu (In, Ga) Se2-, and perovskite-based materials. *Applied Physics Reviews*, *5*(4), 041602.

[6] Xu, M., et al (2018). Simple emitter patterning of silicon heterojunction interdigitated back-contact solar cells using damage-free laser ablation. *Solar Energy Materials and Solar Cells*, *186*, 78-83.

[7] Xu, M., et al. (2018). Dry passivation process for silicon heterojunction solar cells using hydrogen plasma treatment followed by in situ a-Si: H deposition. *IEEE Journal of Photovoltaics*, *8*(6), 1539-1545.

[8] Cho, J., et al. (2018). Passivating electron - selective contacts for silicon solar cells based on an a - Si: H/TiOx stack and a low work function metal. *Progress in Photovoltaics: Research and Applications*, *26*(10), 835-845.

[9] Bouich, A., et al. (2019). Experimental, theoretical, and numerical simulation of the performance of CuInxGa (1-x) S2-based solar cells. *Optik*, *183*, 137-147.

[10] Abderrezek, M., et al. (2021). Numerical study of CZTS/CZTSSe Tandem thin film solar cell using SCAPS-1D. *Optik*, *167320*.

[11] Ahmad, F., et al. (2020). Corrigendum: Towards highly efficient thin-film solar cells with a graded-bandgap CZTSSe layer (2020 J. Phys. Energy 2 025004). *JPhys Energy*, *2*(3).

[12] Baig, F., et al. (2020). Performance investigation of Sb2Se3 based solar cell by device optimization, band offset engineering and Hole Transport Layer in SCAPS-1D. *Current Applied Physics*, *20*(8), 973-981.

[13] Wang, Y., et al. (2015). Towards printed perovskite solar cells with cuprous oxide hole transporting layers: a theoretical design. *Semiconductor Science and Technology*, *30*(5), 054004.

[14] Huang, L., et al. (2016). Electron transport layer-free planar perovskite solar cells: further performance enhancement perspective from device simulation. *Solar Energy Materials and Solar Cells*, *157*, 1038-1047.

[15] Kung, P. K., et al. (2018). A review of inorganic hole transport materials for perovskite solar cells. *Advanced Materials Interfaces*, *5*(22), 1800882.

[16] Lin, L., et al. (2019). Simulation of optimum band structure of HTM-free perovskite solar cells based on ZnO electron transporting layer. *Materials Science in Semiconductor Processing, 90*, 1-6.

[17] Syafiq, U., Ataollahi, N., & Scardi, P. (2020). Progress in CZTS as hole transport layer in perovskite solar cell. *Solar Energy, 196*, 399-408.

[18] Ahmed, S., et al. (2019). Simulation studies of non-toxic tin-based perovskites: Critical insights into solar performance kinetics through comparison with standard lead-based devices. *Superlattices and Microstructures, 130*, 20-27.

[19] Abdelaziz, S., Zekry, A., Shaker, A., & Abouelatta, M. (2020). Investigating the performance of formamidinium tin-based perovskite solar cell by SCAPS device simulation. *Optical Materials, 101*, 109738.

[20] Islam, M. T.,et al. (2020). Numerical simulation studies of a fully inorganic Cs2AgBiBr6 perovskite solar device. *Optical Materials, 105*, 109957.

[21] Haider, S. Z., et al. (2020). A theoretical study for high-performance inverted pin architecture perovskite solar cells with cuprous iodide as hole transport material. *Current Applied Physics, 20*(9), 1080-1089.

[22] Cui, J., et al. (2014). CH3NH3PbI3-based planar solar cells with magnetron-sputtered nickel oxide. *ACS applied materials & interfaces, 6*(24), 22862-22870.

[23] Singh, P. K., et al. (2017). Effect of crystal and powder of CH3NH3I on the CH3NH3PbI3 based perovskite sensitized solar cell. *Materials Research Bulletin, 89*, 292-296.

[24] Moyez, S. A., & Roy, S. (2018). Dual-step thermal engineering technique: a new approach for fabrication of efficient CH3NH3PbI3-based perovskite solar cell in open air condition. *Solar Energy Materials and Solar Cells, 185*, 145-152.

[25] Jamal, M. S., et al. (2019). Effect of defect density and energy level mismatch on the performance of perovskite solar cells by numerical simulation. *Optik, 182*, 1204-1210.

[26] Rai, S., Pandey, B. K., & Dwivedi, D. K. (2020). Modeling of highly efficient and low cost CH3NH3Pb (I1-xClx) 3 based perovskite solar cell by numerical simulation. *Optical Materials, 100*, 109631.

[27] Dong, Q., et al. (2015). Electron-hole diffusion lengths> 175 μm in solution-grown CH3NH3PbI3 single crystals. *Science, 347*(6225), 967-970.

[28] Chen, Y., Peng, J., Su, D., Chen, X., & Liang, Z. (2015). Efficient and balanced charge transport revealed in planar perovskite solar cells. *ACS applied materials & interfaces, 7*(8), 4471-4475.

[29] Hsiao, Y. C., et al. (2015). Fundamental physics behind high-efficiency organo-metal halide perovskite solar cells. *Journal of Materials Chemistry A, 3*(30), 15372-15385.

[30] Luo, S., & Daoud, W. A. (2015). Recent progress in organic–inorganic halide perovskite solar cells: mechanisms and material design. *Journal of Materials Chemistry A, 3*(17), 8992-9010.

[31] Mola, G. T. (2015). Enhanced photon harvesting in OPV using optical reflective surface. *Applied Physics A, 118*(2), 425-429.

[32] Tessema, G. (2012). Charge transport across bulk heterojunction organic thin film. *Applied Physics A, 106*(1), 53-57.

[33] Kazim, S., Nazeeruddin, M. K., Grätzel, M., & Ahmad, S. (2014). Perovskite as light harvester: a game changer in photovoltaics. *Angewandte Chemie International Edition, 53*(11), 2812-2824.

[34] Qarony, W., et al. (2015). Optical analysis in CH3NH3PbI3 and CH3NH3PbI2Cl based thin-film perovskite solar cell. *Am. J. Energy Res, 3*(2), 19-24.

[35] Mandadapu, U., et al. (2017). Simulation and analysis of lead based perovskite solar cell using SCAPS-1D. *Indian Journal of Science and Technology, 10*(11), 65-72.

[36] Yin, W. J., Shi, T., & Yan, Y. (2014). Unusual defect physics in CH3NH3PbI3 perovskite solar cell absorber. *Applied Physics Letters, 104*(6), 063903.

[37] Kojima, A., Teshima, K., Shirai, Y., & Miyasaka, T. (2009). Organometal halide perovskites as visible-light sensitizers for photovoltaic cells. Journal of the *American Chemical Society, 131*(17), 6050-6051.

[38] NREL. Available at : https://www.nrel.gov/pv/cell-efficiency.html

[39] Qin, P., et al. (2014). Inorganic hole conductor-based lead halide perovskite solar cells with 12.4% conversion efficiency. *Nature communications, 5*(1), 1-6.

[40] Xiang, J., Li, Y., et al. (2019). Effect of interfacial recombination, bulk recombination and carrier mobility on the J–V hysteresis behaviors of perovskite solar cells: a drift-diffusion simulation study. *Physical Chemistry Chemical Physics, 21*(32), 17836-17845.

[41] Etgar, L., et al. (2012). Mesoscopic CH3NH3PbI3/TiO2 heterojunction solar cells. *Journal of the American Chemical Society, 134*(42), 17396-17399.

[42] Lin, L., et al. (2017). Modeling and analysis of HTM-free perovskite solar cells based on ZnO electron transport layer. *Superlattices and Microstructures, 104*, 167-177.

[43] Rai, S., et al. (2020, May). Device simulation of low cost HTM free perovskite solar cell based on TiO2 electron transport layer. In *AIP Conference Proceedings* (Vol. 2220, No. 1, p. 140022). AIP Publishing LLC.

[44] Pal, D., & Das, S. (2021). Numerical modeling and simulation for augmenting the photovoltaic response of HTL free perovskite solar cells. *Materials Today: Proceedings, 46*, 6367-6373.

[45] Gan, Y., et al. (2020). Numerical investigation energy conversion performance of tin-based perovskite solar cells using cell capacitance simulator. *Energies, 13*(22), 5907.

[46] Lakhdar, N., & Hima, A. (2020). Electron transport material effect on performance of perovskite solar cells based on CH3NH3GeI3. *Optical Materials, 99*, 109517.

[47] Salah, M. M.,et al. (2019). A comparative study of different ETMs in perovskite solar cell with inorganic copper iodide as HTM. *Optik, 178*, 958-963.

[48] Rai, N., et al. (2020). Analysis of various ETL materials for an efficient perovskite solar cell by

numerical simulation. *Journal of Materials Science: Materials in Electronics*, *31*(19), 16269-16280.

[49] Mahani, N. (2016). Pseudo-System-Level Network-on-Chip Design and Simulation with VHDL: A Comparative Case Study on Simulation Time Trade-Offs. *Indian Journal of Science and Technology*, *9*(7).

[50] Gorgani, H. H. (2016). Innovative conceptual design on a tracked robot using TRIZ method for passing narrow obstacles. *Indian Journal of Science and Technology*, *9*(7).

[51] Malathi, M., Ramar, K., & Paramasivam, C. (2016). Obtaining feasible paths with obstacle avoidance using watershed algorithm through simulation. *Indian Journal of Science and Technology*, *9*(8), 1-9.

[52] Allagui, H., Mzoughi, D., Bouaicha, A., & Mami, A. (2016). Modeling and simulation of 1.2 kW Nexa PEM fuel cell system. *Indian Journal of Science and Technology*, *9*(9), 1-8.

[53] Mezaal, Y. S. (2016). New compact microstrip patch antennas*: Design and simulation results. Indian Journal of Science and Technology*, *9*(12), 1-6.

[54] Bello, I. T., et al. (2018). Modeling and simulation of CZTS-perovskite sandwiched tandem solar cell. *Turkish Journal of Physics*, *42*(3), 321-328.

[55] Bibi, B., Farhadi, B., ur Rahman, W., & Liu, A. (2021). A novel design of CTZS/Si tandem solar cell: A numerical approach.

[56] Elbar, M., Tobbeche, S., & Merazga, A. (2015). Effect of top-cell CGS thickness on the performance of CGS/CIGS tandem solar cell. *Solar energy*, *122*, 104-112.

[57] Cherouana, A., & Labbani, R. (2018). Numerical simulation of CZTS solar cell with silicon back surface field. Materials Today: *Proceedings*, *5*(5), 13795-13799.

[58] Sunny, A., et al. (2021). Numerical study of high performance HTL-free CH3NH3SnI3-based perovskite solar cell by SCAPS-1D. *AIP Advances*, *11*(6), 065102.

[59] Du, H. J., Wang, W. C., & Gu, Y. F. (2017). Simulation design of P–I–N-type all-perovskite solar cells with high efficiency. *Chinese Physics B*, *26*(2), 028803.

[60] Mandadapu, U., et al. (2017). Simulation and analysis of lead based perovskite solar cell using SCAPS-1D. *Indian Journal of Science and Technology*, *10*(11), 65-72.

[61] Hamakawa, Y., Okamoto, H., & Nitta, Y. (1979). A new type of amorphous silicon photovoltaic cell generating more than 2.0 V. *Applied Physics Letters*, *35*(2), 187-189.

[62] Moon, M. M. A., et al. (2020). Design and Simulation of FeSi2 - Based Novel Heterojunction Solar Cells for Harnessing Visible and Near - Infrared Light. *Physica status solidi (a)*, *217(6)*, 1900921.

Modelling of an End of Pipe Filteration System Technology for Processing Petroleum Oily Sludge in Hydrocarbon Crude Distillation Tank

Kingsley E. Abhulimen[1], Ngozi Eze[2], Tope Akintola[3]

[1,2]Chemical Engineeering University of Lagos, Lagos, Nigeria, kabulimen@unilag.edu.ng[1]
[3]University Technology System Limited, TX, United States, syntexacad@gmail.com

Abstract—**This paper presents a Science filter treatment system technology to process petroleum oily sludge in a process Hydrocarbon crude tank. Thus the end of pipe solution design proposed was based on characterization of physical and chemical data of spent sludge obtained from a national refinery in Portharcourt, Nigeria analyzed in a central research laboratory in the University of Lagos in Nigeria. The ChemCad software was used to process data obtained from laboratory results to simulate design the unmanned end of pipe process solution that integrates a hybrid of separation physical unit equipment, bioremediation methods, HMI based control process automation methodologies and filter technologies for sludge treatment requirements up to 97% optimal oil recovery at close-loop personnel safety requirements and environment low carbon foot print.**

Keywords- end of pipe, filter system technology, petroleum oily sludge

I. INTRODUCTION

Petroleum extraction and refining are connected with many engineering and environmental problems. Accumulation of oil sludge in tanks is one of such problems. Disposal and treatment of sludge waste streams presents a major challenge for refinery operators [1-3]. Several technologies exist [2, 4] for disposal of sludge in tanks and saver pits of refinery petroleum products production. Green technology is a continuously evolving to reverse environmental pollution from process systems [5, 6] Thus technologies for oil sludge treatment is based on physical, chemical and thermal methods. Physical methods are centrifuging, storage, land filling, lime stabilization, stabilization and solidification are temporary solution [2, 7-14] whereas chemical method such as extraction, oxidative thermal treatment, treatment with fly-ash, solvent extraction, pyrolysis could lead to denaturing the sludge oil products [2, 15-17]. Thermal treatment such as desorption, combustion and incineration could permanently impairs sludge to the end that products from sludge treatment are not easily reusable. This alternatives technology solution has been reported that optimizes sludge processing and treatment have not been found to be optimal. Therefore the end of pipe technology solution scheme we had proposed uses a filter system based on extensive data selection pre-trial studies, sludge data characterization and model applications to design an applicable end of pipe technology for processing and treatment of oily sludge from a crude oil tank from refinery processes. The multifaceted end of pipe solution for sludge treatment approach recorded was derived from the characterization of oil sludge samples with scientific measuring and analytical equipment at the University of Lagos Central Research Laboratory using Gas chromatography, atomic association spectrometer and Rheometer. Another milestone recorded by our research work is the simulation using ChemCad software to design the end of pipe equipment specifications based on field work collated and measured data obtained from a Laboratory. The end result is the design of a hybrid solution for the End of Pipe technology for tank cleaning, oil sludge handling with inputs to scientific observations. Therefore the un-manned flexible

ISBN: 978-86-80593-73-9

end of Pipe Solution developed could provide oil sludge and soil decontamination solution petroleum oily sludge treatment that optimize recovery and cost up to 97% 2) ensures maximum return on environment and personnel safety. Most oily sludge in the petroleum industry is generated during crude oil exploration, production, transportation, and storage and refining processes [18, 19]. The compositions of the various amounts of the sludge generated from these processes are not the same but they contain a high concentration of petroleum hydrocarbons (PHCs) ranging from 5% to 86.2% by mass, and solid particles 5–46%, of which metals heavy metals are usually within the ranges 7–80 mg/kg for zinc (Zn), 0.001–0.12 mg/kg for lead (Pb), 32–120 mg/kg for copper (Cu), 17–25 mg/kg for nickel (Ni), and 27–80 mg/kg for chromium(Cr) and water in the range of 30–85% [4]. Concentration by mass of nitrogen, sulphur and oxygen in oily sludge is usually less than 3%, 0.3–10% less than 4.8% respectively.

II. Technology Methods an Design

The existing technologies for sludge treatment are based on one or a combination of more of the following conventional methods 1) Physical methods such as centrifuging, storage, landfilling, lime stabilization, stabilization and solidification [2,-12, 14, 15]; 2) Chemical method such as extraction, oxidative thermal treatment, treatment with fly-ash, solvent extraction, pyrolysis [2, 15, 17]; 3) Thermal treatment such as desorption, combustion and incineration. Biological methods such as land farming, bio-reactor treatment, composting [2, 15-22]; 4) these methods can be classified as oil recovery methods, and sludge disposal methods [4] (Fig. 1).

A. Description of the Science Filter System

- SFS

The SFS system relies on the performance of the Science absorber material and its properties. The Science absorber material is at present a heat treated Scandinavian Pit material which is hydrophobic and therefore capable for absorbing oil and oil contaminated water. It can also work as an Ion exchange and thus capable of binding ionized metals in solution. This property can lead to a reduced leakage of unwanted soluble metal ions without any previous treatment.

The Metal catching ability of the system is further increased by adding flocculating and pH increasing agents. Flocculation makes unwanted metals to precipitate as hydroxides. The floc can be sequestered by sedimentation (require tank reservoirs), filtration through bag filters (requires continues changes) or band filters. The use of sand filters with backwashing abilities is also an alternative that help in the water cleaning. To further decrease the impact of offensive material leaking into the environment the system is equipped with active carbon filters (amount depending on the load). The carbon will bind organic particles. An oxidation system (ozone or UV/TiO2 based) may also help to decrease COD (Chemical Oxygen Demand = organic load) particles in the water.

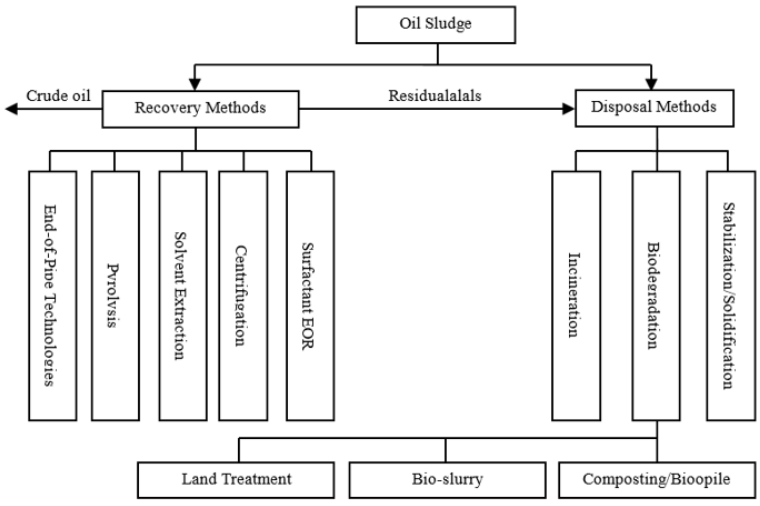

Figure 1. Oil recovery methods, and sludge disposal methods [4].

The water was analyzed for Conductivity (ORP), clarity (turbidometry) and also oil content. If the water does not complain with limits values then the system is stopped and the water eventually returned to the origin instead of been disposed of.

- The System design and developed in Sweden at Öckerö Shipyard is composed of the following (See accompanying picture).

Pump into system (provided by the customer):

2 containers (can be constructed as one 40 foot container)

3 sedimentation tanks

3 level detectors for the sedimentation tanks

2 chemical tanks with detectors

1 Oil separator with oil detection and level alarm system

1 Reservoir middle tank and pump

1 level sensor and programmed pump operation under PLC

3 7-bag filters with the Science absorber (15 liters absorber/ bag -> 105 liters absorber per item and 315 liters in total)

1 Flocculation tank with automatic pH dependent dispenser of flocculation chemicals.

1 IR levels sensor in flocculation tank that operate screw pump activity

1 Screw pump

1 Pressure sensor to monitor the status of filters (bag filters, sand and active carbon))

3 1-bag filters (alternative: band filter)

1 Sand filter

2 Active carbon filters

1 Conductivity sensor

1 oil detection system.

The system is controlled by a Siemens PLC controller using own code with menu system.

Power is supported by a 340V 3-phase system

- Capacity of the Öckerö system

Flow capacity 4-10m^3 per hour

Sedimentation tanks total capacity of up to 2500 liters.

Absorber capacity of SFS system:

Oil: At half the volume it implies a maximum capacity of about 150 liters oil can be trapped by the system. This implies that OiW (Oil in Water) at 5ppm in the water will saturate the filter material after a total flow of about 30000 m^3 of water flow before a change of filter material is needed. At a flow of 10m3/h saturation is reached after 125 days (approx. 4 months). At 10ppm OiW the filters will need change after approx. 60 days (2 months)

Metal absorption: The Science absorber material has a capacity to bind ionized metals. The absorption rate varies depending on the conditions for example: 6-40g Cu or Zn /kg absorber or 20-120g Pb /kg absorber.

- The Sludge collecting system: Adding a centrifuge to the Science Filter System

In cases were a high amount of sludge is expected the use of a centrifuge system may be required.

The centrifuge system can be chosen dependent on the flow and sludge characteristics. To determine the most optimal solution it is important to have samples of the water to be processed. The samples are analyzed and a suggestion of a proper system is made. The centrifuge models available and their characteristics are specified below. The proposed model for the application at 10m^3 per hour is the DC10 model.

Other ways to effectively reduce the space needed is to alter the filtration system (Fig. 2). For example the flocculation may be done

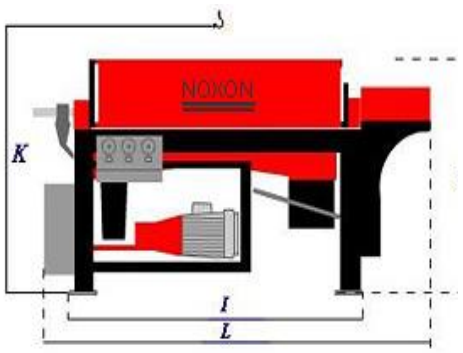

Figure 2. Space considerations.

previous to the centrifuge dependent filtration steps. This will take away the need of sedimentation tanks. Such a preliminary system is depicted in the attached figures for the system.

- Additional Items

The following items are not included in the base offer and are specified only for information. A special quote for these items may be requested if the there is a specific need.

1. - External power generator: To power the filter system in remote areas

2. - Insulated container and air condition system to keep constant temperature. Most electronic systems may work poorly at temperatures below 0ºCand above 50ºC.

Pre-treatment:

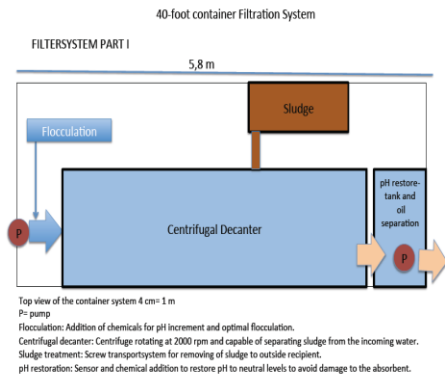

Figure 3. End of Pipe SFS Pretreatment System reproduced from Scandinavian Green Export (SGE).

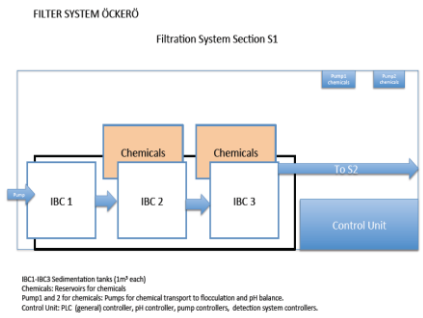

Figure 4. End of Pipe SFS Desludging System reproduced from Scandinavian Green Export (SGE).

Fig. 3 is an end of pipe SFS pretreatment system reproduced from Scandinavian Green export pre-treatment system incorporated to avoid risk of explosion, an inert gas, typically nitrogen is injected into the tank before the cleaning process is started to reduce the oxygen level to below 8 per cent. This level is maintained throughout the entire tank cleaning process. The hydrocarbon phase of the sludge is fluidized by injecting petroleum cuts example Kerosene, Naphtha, or Diesel cuts, compatible with the sludge to be cleaned., the petroleum fractions naphtha and kerosene cuts are preferred for the process of hydrocarbon recovery in sludge treatment, reaching 83.99% using volume 7 ml only, while kerosene cut gives a higher hydrocarbon recovery of 97.2% using a sludge-solvent ratio of 1:4 (sludge in gram: solvent in ml). These conditions are for the sludge for separation in the hydro cyclone by reducing the viscosity of the sludge and breaking the emulsion. This technology ensures close to 100% hydrocarbon recovery from crude oil sludge [23]. Sludge fluidization is determined by the chemical action of the heated kerosene cut, and by the mechanical action of jet washers that are installed on the tank roof. The nozzles of these jet washers eject the kerosene stream at a pressure of 6 bars approximately. Generally Jet Washers are assembled in the center of some roof supports, therefore avoiding the need to cut through the roof. The kerosene solution is ejected through Jet Washers toward the sludge deposited within the Tank in order to break, dissolve, disperse and fluidize the sludge.

Desludging:

Fig. 4 is an end of pipe SFS desludging system reproduced from Scandinavian Green export is the first process of tank cleaning and it is also where most of the oily sludge from the tank is removed. The fluidized sludge is flushed out of the tank by the use of a suction pump. This pump is used to suction oil from the tank being cleaned It then passes through Heat exchangers to raise the temperature of the sludge kerosene mixture to about 70°C in order to enhance oil separation and improve flow of the sludge (Naggar et al., 2010). The oil is pumped on to the recirculation module through hydro cyclones to separate heavy solid particles from the liquids. The oil from the bottom of the hydro cyclones matches the tank owner's specifications pumped directly to the pipeline. Further treatment is carried out in the separation module, comprising of a decanter and an oil/water separator, is used.

Fig. 5 is End of Pipe SFS Separation System I reproduced from Scandinavian Green Export (SGE). Fig. 6 is End of Pipe SFS Separation System II reproduced from Scandinavian Green Export (SGE). Separation of the sludge takes place simultaneously with desludging and is separated into clean oil, solids and water [23].

There are two steps in the separation module. First a liquid/solids separation takes place in the decanter, where solids are removed from the oil. The solids are deposited in containers for disposal or treatment, if required.

If the recovered oil still contains water, a further oil/water separation is performed via the high-speed separator. The clean oil is pumped to the pipeline while the water can be pumped directly to a local waste water treatment facility. Heat exchangers are used to facilitate the separation process. Regular laboratory tests make sure the separated oil conforms to the tank owner's specifications. The oil/water separator tank is also used to separate oil from water during water-washing operation.

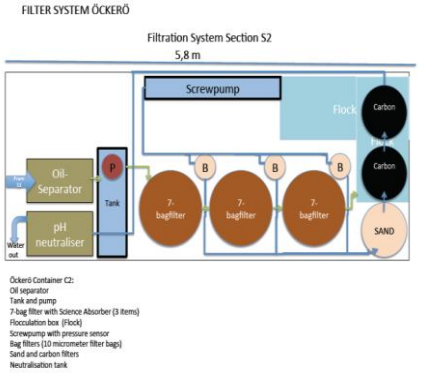

Figure 5. End of Pipe SFS Separation System I reproduced from Scandinavian Green Export (SGE).

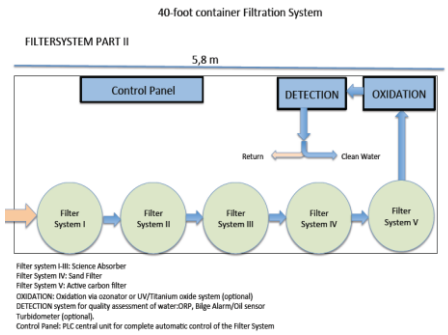

Figure 6. End of Pipe SFS Separation System II reproduced from Scandinavian Green Export (SGE).

Efficiency:

The end of pipe SFS solution offers several benefits 1) This technology enables the recovery of about 98% valuable, saleable hydrocarbons from the sludge 2) The fluidizing oil is a petroleum cutter stock, the recovered oil needs no further treatment before it is carried to the production 3) The non-manned concept of this technology means that nobody needs to enter the tank during cleaning operations ensuring this way the utmost personnel safety. During the washing the atmosphere within the tank is continuously monitored to guarantee that it does not become flammable, and nitrogen is used to control it. To this end the unit is equipped with O_2 monitoring system and alarm. 4) This technology is environmentally-friendly: during operations no chemicals are used, the process minimizes hydrocarbon emissions due to closed-loop cleaning and substantially reduces liquids and solid waste 5) The treatment is efficient; offering desludging, tank cleaning and oil recovery in one integrated process 6) Cost Savings,

The technology recovers more than 98% of the hydrocarbon phase contained within the sludge, which is returned to the client together with the fresh oil used to fluidize it. Such result generates a significant cost saving that is evidenced only by evaluating the entire cleaning project. Sometimes comparing the offer for manual cleaning with the offer for recovery operations, it might appear that using this technology is more expensive 7). The operation during the washing phase of the sludge is treated at a speed of approximately 230.000kg/day depending on the type of sludge. There is therefore a significant reduction of Tank Down-Time. 8) Thus the recovery method is very flexible since utilities such as power, steam and nitrogen are on site in order to minimize the cost to the operator [23].

III. Description of the Science Filter System-Field Data Collation System and Refinery Location

The Port Harcourt refinery located at Alesa-Eleme, Rivers state, like other refineries around

the world, has the problem of oil sludge generation in their crude oil storage tanks. The six 64,000 millimeters diameter crude oil storage tanks in the refinery contain oily sludge of an average height of 0.6 meters each, giving an estimated total volume of sludge in the storage tanks to be approximately 11,581 cubic meters. The sample used for this research work was collected from the Port Harcourt refinery's crude oil tank 50-TK01F, the tank is a floating roof tank of networking capacity 60,000 cubic meters, 64,000 millimetres diameter, and 21,000 millimetres height, design temperature: 25°C, and design pressure: Atmospheric Pressure. The crude oil processed in the refinery is Bonny light crude, the oily sludge formed is flowable sludge, of height 0.8 meters, giving a total sludge volume of 2570 cubic meters in the tank. Technologies to handle sludge should not disrupt the refinery processes. The oil sludge mischaracterized for its chemical and physical properties before a design of the end of pipe sludge process. This is because the chemical compositions of oily sludge vary depending on crude oil source, processing scheme, and equipment and reagents used in refining process. The result of this difference in chemical compositions of the oily sludge, its physical properties such as density, viscosity, and heat value equally vary significantly [4].

B. Laboratory Results

Table I shows the physico-chemical analysis of Port Harcourt refinery petroleum oil sludge. Table I shows the physico-chemical properties of the crude oil sludge sample. The results of laboratory analysis of the sludge sample (Figs. 7 and 8) fell close of the ranges: total petroleum hydrocarbon (TPH) contents in oily sludge from 5% to 86.2% by mass, contents of water from 30–85% and solids from 5–46%, as reported by [4]. The metal content of the crude oil sludge also fall within the range given by American Petroleum Institute (API, 1989), as the average metals composition of crude oil sludge from petroleum refineries around the world.

Table I is Physico-Chemical Analysis of Port Harcourt Refinery Petroleum Oil Sludge.

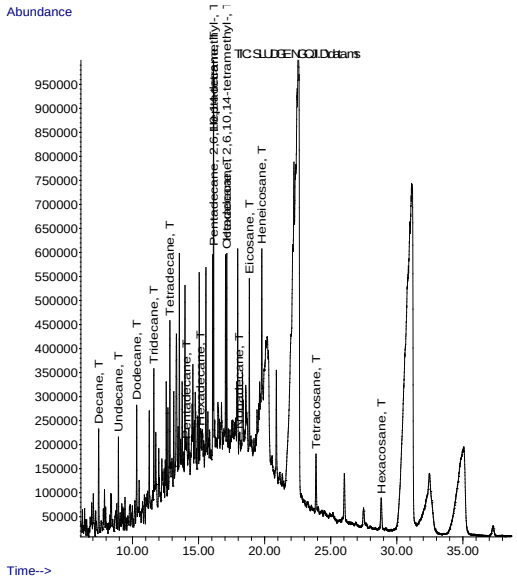

Figure 7. Gas Chromatography results for the Aliphatic Hydrocarbons in the Sludge Sample.

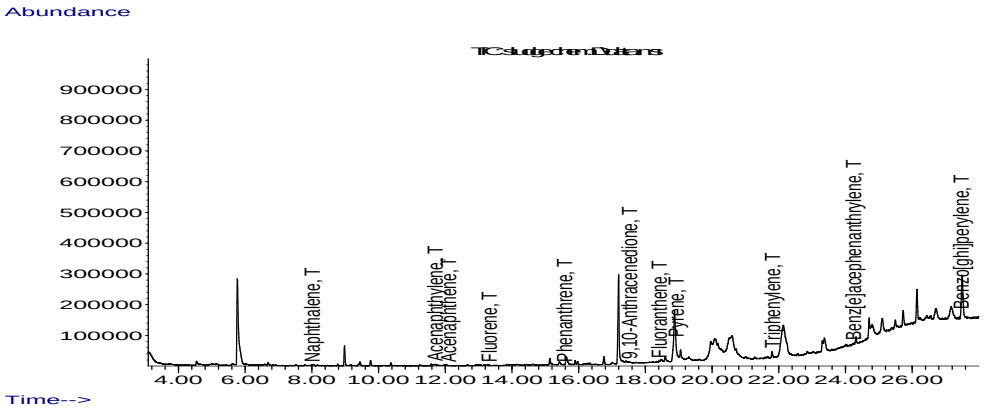

Figure 8. Gas Chromatography Result for the Aromatic hydrocarbons in the Sludge Sample.

TABLE I. PHYSICO-CHEMICAL ANALYSIS CRUDE OIL SLUDGE.

S/N	Compound	R.T.	QIon	Response	Conc Units $\times 10^4$	Dev(Min)
1)	Decane	7.443	57	97964	2.62 PPM	95
2)	Undecane	8.931	57	113066	2.82 PPM	94
3)	Dodecane	10.315	57	116440	2.74 PPM	94
4)	Tridecane	11.614	57	150500	3.42 PPM	94
5)	Tetradecane	12.827	57	161492	3.58 PPM	88
6)	Pentadecane	14.063	57	11792	0.25 PPM	75
7)	Hexadecane	15.145	57	23879	0.54 PPM	85
8)	Heptadecane	16.135	57	413355	10.78 PPM	82
9)	Pentadecane 2,6,10,14...	16.135	57	413355	9.51 PPM	83
10)	Octadecane	17.136	57	165609	3.60 PPM	89
11)	Hexadecane, 2,6,10,14-...	17.136	57	165609	4.13 PPM	95
12)	Nonadecane	18.063	57	5536	0.12 PPM	# 16
13)	Eicosane	18.841	57	153182	3.69 PPM	94
14)	Heneicosane	19.785	57	172127	3.72 PPM	96
15)	Heptadecane	20.878	57	123647	No Calib	
16)	Eicosane	0		0	N.D.	
17)	Tetracosane	23.882	57	97820	4.16 PPM	95
18)	Heptadecane	26.034	57	100303	No Calib	
19)	Hexacosane	28.832	57	83852	2.36 PPM	95
20)	Heptacosane	0		0	N.D.	
21)	Tetracosane	37.289	57	41741	No Calib	#

TABLE II. COMPOSITION OF PRODUCT AND EFFLUENTS FROM END-OF-PIPE SIMULATION.

Results Summation				
	Composition/Mass Flow Kg/h			
Streams	**Hydrocarbons**	**Water**	**Solids**	**Total Flow (Kg/h)**
Sludge Feed	5028.2841	2397.46	2574.255	10000.00
Kerosene Feed	30119.9579	0	0	30119.9579
Hydro cyclone Underflow	104.2221	111.587	2530.122	2745.9308
Hydro cyclone Overflow	35044.0187	2285.873	44.1337	37374.0257
Component Separator Top Stream	0.023626132	2217.297	0	2217.320726
Component Separator Bottom Stream	35043.99507	68.5762	44.1337	35156.70497

B. Computer Simulation Results and Design Specifications

The results show a hydrocarbon recovery rate up to 97% by the applied end-of-pipe technology. Tables II are the design specifications of the equipment. Table III, Table IV and Table V are the results obtained from simulating the design end-of-pipe technology with the results obtainable using a similar end-of-pipe technology using centrifugation. Table II is a summary of the simulation result showing the product streams compositions. The recovery rate of the crude oil is. The hydrocyclone underflow is the solids separated from the sludge. The results show that the solids in the

TABLE III. COMPUTER MODEL SIMULATION BASIS.

CHEMCAD	6.1.4	Page		1					
Job name:	NG2	Date:		1/10/2014	Time:	18:33:06			
STREAM PROPERTIES									
Stream No.	1	2	3	4	5	6	7	8	9
Name	Sludge	kerosene	Sludge+Kerosene	Heated Mix	Pump Outlet	Cyclone OH	Solids	Water	Recvrd Oil
- - Overall - -									
Molar flow kmol/h	160.9803	176.8247	337.8049	337.8049	337.8049	268.673	69.132	102.8896	165.7833
Mass flow kg/h	10000.0002	30119.9579	40119.9581	40119.9581	40119.9581	30241.3577	9878.5933	1853.5692	28387.7914
Temp C	25	25	24.9791	70	70.0722	70.0722	70.0722	100.2242	70
Pres psia	14.7	14.7	14.7	14.7	24.7	14.9717	14.9717	14.9717	14.9717
Vapor mole fraction	0.003744	0	0.0007049	0.001528	0.0003312	0	0	0	0.002411
Enth MMBtu/h	-41.322	-58.887	-100.21	-96.543	-96.54	-76.949	-19.594	-27.338	-49.388
Tc C	442.8315	385.1	395.3885	395.3885	395.3885	395.3885	395.3885	374.1964	396.5759
Pc psia	4431.3018	263.0573	1581.535	1581.535	1581.535	1581.537	1581.5359	3207.9219	335.4297
Std. sp gr. wtr = 1	0.946	0.753	0.793	0.793	0.793	0.777	0.849	1	0.765
Std. sp gr. air = 1	2.145	5.881	4.101	4.101	4.101	3.886	4.934	0.622	5.912
Degree API	18.0972	56.415	46.8642	46.8642	46.8642	50.7173	35.0687	10.0005	53.3759
Average mol wt	62.1194	170.338	118.7667	118.7667	118.7667	112.5582	142.8947	18.0151	171.2343
Actual dens kg/m3	400.2402	745.028	708.4881	595.7042	732.1279	740.6068	815.742	957.6345	568.916
Actual vol m3/h	24.985	40.428	56.6276	67.3488	54.7991	40.8332	12.1099	1.9356	49.898
Std liq liter/hr	10572.2573	40000	50572.253	50572.253	50572.253	38943.5141	11628.7363	1853.578	37089.9359
Std vap 0 C m3/h	3608.1552	3963.2856	7571.4399	7571.4399	7571.4399	6021.9411	1549.5001	2306.1322	3715.8078
- - Vapor only - -									
Molar flow kmol/h	0.5978		0.2372	0.5141	0.1114				0.3985
Mass flow kg/h	16.5667		6.5759	13.1046	2.9545				10.1752
Average mol wt	27.7149		27.7253	25.488	26.511				25.5357
Actual dens kg/m3	1.1336		1.1341	0.9072	1.5846				0.9257
Actual vol m3/h	14.6144		5.7984	14.4444	1.8646				10.9915
Std liq liter/hr	20.4213		8.1063	15.5688	3.5724				12.0986
Std vap 0 C m3/h	13.3978		5.3161	11.524	2.4979				8.9311
Cp kJ/kg-K	1.0605		1.0608	1.2662	1.1719				1.2618
Z factor	0.9997		0.9997	0.9981	0.9986				0.9982
Visc cP	0.01745		0.01744	0.01667	0.01789				0.01672
Th cond W/m-K	0.0252		0.0252	0.0269	0.0277				0.0269
- - Liquid only - -									
Molar flow kmol/h	159.0658	176.8247	336.251	335.974	336.3767	268.1948	68.2934	102.8896	164.9067
Mass flow kg/h	7409.178	30119.9579	37539.1238	37532.5963	37542.749	29925.4483	7620.2517	1853.5693	28061.701
Average mol wt	46.5793	170.338	111.6402	111.7128	111.6092	111.581	111.581	18.0151	170.1672
Actual dens kg/m3	887.1738	745.028	769.0861	737.5937	737.356	737.2894	737.2894	957.6345	725.8248
Actual vol liter/hr	8351.4398	40427.9536	48810.0444	50885.1901	50915.3632	40588.4699	10335.496	1935.5707	38661.8113
Std liq liter/hr	8532.7029	40000	48545.0095	48537.5535	48549.5515	38698.8043	9854.3101	1853.578	36833.1278
Std vap 0 C m3/h	3565.2452	3963.2856	7536.611	7530.4034	7539.4294	6011.2241	1530.7051	2306.1322	3696.1595
Cp kJ/kg-K	2.5985	2.098	2.1964	2.3728	2.3729	2.3732	2.3731	4.2253	2.2522
Z factor	0.003	0.0118	0.0078	0.007	0.0118	0.0071	0.0071	0.0008	0.0106
Visc cP	1.943	1.407	1.498	0.7549	0.7548	0.7535	0.7535	0.2799	0.7859
Th cond W/m-K	0.2154	0.1354	0.1451	0.1348	0.1348	0.1347	0.1347	0.6761	0.126
Surf. tens. N/m	0.04	0.0249	0.0271	0.0228	0.0228	0.0228	0.0228	0.0586	0.0215

TABLE IV. COMPUTER SIMULATION FLOW SUMMARIES (KG/H).

FLOW SUMMARIES

Stream No.	1	2	3	4	5	6	7	8	9
Stream Name	Sludge	kerosene	Sludge+Kerosene	Heated Mix	Pump Outlet	Cyclone Ovflow	Cyclone Undflw	Sep top	Sep bottom
Temp C	25	25	24.9791	70	70.0722	70.0722	70.0722	100.2242	70
Pres psia	14.7	14.7	14.7	14.7	24.7	14.9717	14.9717	14.9717	14.9717
Enth MMBtu/h	-41.322	-58.887	-100.21	-96.543	-96.54	-76.949	-19.594	-27.338	-49.388
Vapor mass fraction	0.002231	0	0.00017514	0.00034903	7.87E-05	0	0	0	0.00036247
Total kg/h	10000.0002	30119.9579	40119.9581	40119.9581	40119.9581	37374.0257	2745.9308	2217.320726	35156.70497
Component kg/h									
Iron	0.0622	0	0.0622	0.0622	0.0622	0.0066	0.0556	0	0.0066
Nitrogen	17.3729	0	17.3729	17.3729	17.3729	13.8469	3.526	0.0138	13.8331
Sulphur	21.4607	0	21.4607	21.4607	21.4607	3.854	17.6067	0	3.854
Water	2397.4603	0	2397.4603	2397.4603	2397.4603	2285.8733	111.587	2217.2971	68.5762002
N-Undecane	148.5885	0	148.5885	148.5885	148.5885	138.4311	10.1574	0.009701659	138.4213983
N-Tridecane	180.2032	0	180.2032	180.2032	180.2032	173.6293	6.5739	0	173.6293
N-Tetradecane	188.6337	0	188.6337	188.6337	188.6337	180.3487	8.285	0	180.3487
N-Pentadecane	514.2641	0	514.2641	514.2641	514.2641	512.8893	1.3747	0	512.8893
N-Hexadecane	246.0668	0	246.0668	246.0668	246.0668	231.1252	14.9416	0	231.1252
N-Heptadecane	568.0083	0	568.0083	568.0083	568.0083	562.7257	5.2826	0	562.7257
N-Octadecane	189.6875	0	189.6875	189.6875	189.6875	188.1886	1.4989	0.000124473	188.1884755
N-Nonadecane	6.3229	0	6.3229	6.3229	6.3229	6.2396	0.0833	0	6.2396
N-Eicosane	194.4298	0	194.4298	194.4298	194.4298	189.9684	4.4614	0	189.9684
n-heneicosane	196.0106	0	196.0106	196.0106	196.0106	191.9284	4.0822	0	191.9284
n-Tetracosane	219.1945	0	219.1945	219.1945	219.1945	215.1069	4.0876	0	215.1069
hexacosane	124.3507	0	124.3507	124.3507	124.3507	114.1126	10.2381	0	114.1126
N-Dodecane	143.3195	30119.9579	30263.2754	30263.2754	30263.2754	30261.0606	2.2157	0	30261.0606
N-Decane	138.0504	0	138.0504	138.0504	138.0504	138.0318	0.0186	0	138.0318
napthalene- 2-et	531.1249	0	531.1249	531.1249	531.1249	531.0281	0.0968	0	531.0281
Copper	0.0553	0	0.0553	0.0553	0.0553	0.001	0.0543	0	0.001
Cadmium	0.0344	0	0.0344	0.0344	0.0344	0.0042	0.0303	0	0.0042
Lead	0.0271	0	0.0271	0.0271	0.0271	0.001	0.0261	0	0.001
Silica	2552.0542	0	2552.0542	2552.0542	2552.0542	40.2553	2511.799	0	40.2553
Nickel	0.314	0	0.314	0.314	0.314	0.0016	0.3124	0	0.0016
Vanadium	0.0094	0	0.0094	0.0094	0.0094	0.0036	0.0058	0	0.0036
Chromium	0.2379	0	0.2379	0.2379	0.2379	0.0064	0.2315	0	0.0064
Biphenyl	486.8643	0	486.8643	486.8643	486.8643	475.8537	11.0107	0	475.8537
Phenanthrene	422.5815	0	422.5815	422.5815	422.5815	411.8146	10.7669	0	411.8146
Acenaphthalene	510.0485	0	510.0485	510.0485	510.0485	504.5294	5.5191	0	504.5294
1-Dodecene	3.1615	0	3.1615	3.1615	3.1615	3.1598	0.0016	0	3.1598
Total kg/h	9999.9996	30119.9579	40119.9555	40119.9555	40119.9555	37374.0257	2745.9308	2217.320726	35156.70497

TABLE V. COMPUTER SIMULATION FLOW SUMMARIES ((MASS) %).

FLOW SUMMARIES

Stream No.	1	2	3	4	5	6	7	8	9
Stream Name	Sludge	kerosene	Sludge+Kero	Heated Mix	Pump out	Cyclone Ovflow	Cyclone Undflow	Sep top	Sep bottom
Temp C	25	25	24.9791	70	70.0722	70.0722	70.0722	100.2242	70
Pres psia	14.7	14.7	14.7	14.7	24.7	14.9717	14.9717	14.9717	14.9717
Enth MMBtu/h	-41.322	-58.887	-100.21	-96.543	-96.54	-76.949	-19.594	-27.338	-49.388
Vapor mass fraction	0.002231	0	0.00017514	0.00034903	7.87E-05	0	0	0	0.00036247
Total kg/h	10000.0002	30119.9579	40119.9581	40119.9581	40119.9581	37374.0257	2745.9308	2217.320726	35156.70497
Component mass %									
Iron	0.000622	0	0.000155	0.000155	0.000155	1.76593E-05	0.002024814	0	1.87731E-05
Nitrogen	0.173729	0	0.043302	0.043302	0.043302	0.037049528	0.128408189	0.000622373	0.039346975
Sulphur	0.214607	0	0.053491	0.053491	0.053491	0.010311975	0.641192415	0	0.010962347
Water	23.974602	0	5.97573	5.97573	5.97573	6.116208402	4.063722218	99.99893447	0.195058667
N-Undecane	1.485885	0	0.370361	0.370361	0.370361	0.37039387	0.369907355	0.00043754	0.393726882
N-Tridecane	1.802032	0	0.449161	0.449161	0.449161	0.464572111	0.239405159	0	0.493872506
N-Tetradecane	1.886337	0	0.470174	0.470174	0.470174	0.482550907	0.301719184	0	0.512985219
N-Pentadecane	5.14264	0	1.281816	1.281816	1.281816	1.372314837	0.05006317	0	1.45886624
N-Hexadecane	2.460668	0	0.613328	0.613328	0.613328	0.618411305	0.544136072	0	0.657414283
N-Heptadecane	5.680083	0	1.415775	1.415775	1.415775	1.505659852	0.192379211	0	1.600621277
N-Octadecane	1.896875	0	0.472801	0.472801	0.472801	0.503527775	0.054586226	5.61366E-06	0.535284736
N-Nonadecane	0.063229	0	0.01576	0.01576	0.01576	0.016695017	0.00303358	0	0.017747966
N-Eicosane	1.944298	0	0.484621	0.484621	0.484621	0.508289906	0.16247314	0	0.540347567
n-heneicosane	1.960106	0	0.488561	0.488561	0.488561	0.51353419	0.148663615	0	0.545922606
n-Tetracosane	2.191945	0	0.546348	0.546348	0.546348	0.57555186	0.14886027	0	0.611851708
hexacosane	1.243507	0	0.309947	0.309947	0.309947	0.305325953	0.372846249	0	0.324582751
N-Dodecane	1.433195	100	75.431973	75.431973	75.431973	80.96815912	0.080690307	0	86.07479177
N-Decane	1.380504	0	0.344094	0.344094	0.344094	0.369325481	0.000677366	0	0.392618706
napthalene- 2-et	5.311249	0	1.323842	1.323842	1.323842	1.420848009	0.003525216	0	1.510460381
Copper	0.000553	0	0.000138	0.000138	0.000138	2.67566E-06	0.001977472	0	2.84441E-06
Cadmium	0.000344	0	0.000086	0.000086	0.000086	1.12378E-05	0.001103451	0	1.19465E-05
Lead	0.000271	0	0.000067	0.000067	0.000067	2.67566E-06	0.000950497	0	2.84441E-06
Silica	25.520542	0	6.361059	6.361059	6.361059	0.107709296	91.47349962	0	0.114502483
Nickel	0.00314	0	0.000783	0.000783	0.000783	4.28105E-06	0.011376834	0	4.55105E-06
Vanadium	0.000094	0	0.000023	0.000023	0.000023	9.63236E-06	0.000211222	0	1.02399E-05
Chromium	0.002379	0	0.000593	0.000593	0.000593	1.71242E-05	0.008430657	0	1.82042E-05
Biphenyl	4.868643	0	1.213522	1.213522	1.213522	1.273220348	0.400982428	0	1.353521897
Phenanthrene	4.225814	0	1.053295	1.053295	1.053295	1.101873808	0.392103836	0	1.171368592
Acenaphthalene	5.100485	0	1.271309	1.271309	1.271309	1.349946629	0.200991955	0	1.435087277
1-Dodecene	0.031615	0	0.00788	0.00788	0.00788	0.008454535	5.8268E-05	0	0.008987759
Total kg/h	99.999993	100	99.999995	99.999995	99.999995	100	100	100	100

underflow from the cyclone contain about 3.8% by mass hydrocarbons and 4.06% water by mass. Therefore solids need is treated using bioremediation techniques. The hydrocarbon content of the hydrocyclone overhead recovered via the component separator bottoms contains 97% mass of hydrocarbon, 1.5% mass of water and 0.9% mass of solids. The component separator top is the water stream separated from the hydrocarbon. The results show that this stream contains a negligible amount, less than 1%, of hydrocarbons. Thus, the stream is sent to a waste water filter system for further treatment.

IV. CONCLUSIONS

The design end-of-pipe SFS technology deployed for crude oil sludge treatment in this research work meets the requirements for high quality oil recovery, environmental and personnel safety, economic viability and applicability. The results of the close-loop nature of the process ensures a high environmental and personnel safety. The volume of solid waste to be disposed of is drastically reduced to 27.45%. From the simulation results we demonstrate using the end-of-pipe SFS technology offers a very attractive cost/benefits ratio. Furthermore, after returning the recovered hydrocarbon phase contained within the sludge together with the fresh oil used to fluidize it, the volume of solid waste to be disposed of was reduced to about 24 %, thereby saving the costs disposal. The technology has the capacity to handle large volume of crude oil sludge, thus reducing the overall storage tank down time during tank cleaning processes.

The processes involved in the end-of-pipe technology applied to treat crude oil sludge in this work do not address the problem of heavy metals contained in the sludge cake to be disposed of. It is recommended that further work be done to find an appropriate bioremediation solution to handle the heavy metals prior to the solid waste disposal. The bioremediation can then be an additional module to complete this end-of-pipe technology.

ACKNOWLEDGMENT

The contribution of the Laboratory assistants and technicians of the central research laboratory and Department of the Chemical Engineering of the University of Lagos is greatly acknowledged. We also acknowledged the Port Harcourt Refinery for their contribution to the quality of the research work by providing access to data. The contribution of Scandinavia Green Export in Goteborg, Sweden, Sigma Technology USA and Syntechsys Global Network in collaboration with University Technology System Limited is also appreciated for supporting, sponsoring this work and providing the technical rights for publishing some of the field works through the Department of Petroleum Resources approvals.

REFERENCES

[1] Srinivasarao Naik, B., Mishra, I. M., & Bhattacharya, S. D. (2011). Biodegradation of total petroleum hydrocarbons from oily sludge. *Bioremediation journal*, *15*(3), 140-147.

[2] Kam, E. K. (2001). Assessment of sludges and tank bottoms treatment processes. In *The 8th International Petroleum Environmental Conference. November* (pp. 6-9).

[3] Ling, C. C., & Isa, M. H. (2006). Bioremediation of oil sludge contaminated soil by co-composting with sewage sludge.

[4] Hu, G., Li, J., & Zeng, G. (2013). Recent development in the treatment of oily sludge from petroleum industry: a review. *Journal of hazardous materials*, *261*, 470-490.

[5] *Green Technology*. (2006) Available at: http://www.green-hnology.org/what.htm

[6] *Green Technology*. (2006, 2010) Available at: http://www.green-hnology.org/what.htm

[7] Ubani, O., Atagana, H. I., & Thantsha, M. S. (2013). Biological degradation of oil sludge: A review of the current state of development. *African Journal of Biotechnology*, *12*(47), 6544-6567.

[8] Wright, R., & Noordhius. (1991). The treatment and disposal of oil solids. Part 2. In *Proceedings of the first international conference on health, safety and environment, In oil and gas exploration and production*, (pp. 521-526).

[9] Karamalidis, A. K., & Voudrias, E. A. (2001). Stabilization/Solidification of oil refinery sludge: immobilization of heavy metals. In *7th conference of environmental Science and Technology Ermonpolis, Syros Island, Greece*.

[10] Bhattacharyya, J. K., & Shekdar, A. V. (2003). Treatment and disposal of refinery sludges: Indian scenario. *Waste management & research*, *21*(3), … 249-261.

[11] Mater, L., Sperb, R. M., Madureira, L. A. S., Rosin, A. P., Correa, A. X. R., & Radetski, C. M. (2006). Proposal of a sequential treatment methodology for the safe reuse of oil sludge-contaminated soil. *Journal of hazardous materials*, *136*(3), 967-971.

[12] Beech, J. F., Elder, S., & Weeks, N. (2009). Case-study: Use of circulating fluidized bed boiler by-product to solidify oil sludge. World of coal ash (WOCA) conference may 4-7. *Lexington, KY, USA*.

[13] Liu, J., Jiang, X., Zhou, L., Wang, H., & Han, X. (2009). Co-firing of oil sludge with coal–water slurry in an industrial internal circulating fluidized bed boiler. *Journal of Hazardous Materials*, *167*(1-3), 817-823.

[14] Liu, W., Luo, Y., Teng, Y., Li, Z., & Ma, L. Q. (2010). Bioremediation of oily sludge-contaminated soil by stimulating indigenous microbes. *Environmental geochemistry and health*, *32*(1), 23-29.

[15] Ubani, O., Atagana, H. I., & Thantsha, M. S. (2013). Biological degradation of oil sludge: A review of the current state of development. *African Journal of Biotechnology*, *12*(47), 6544-6567.

[16] Jenkins, S. H. (1980). Sludge farming: A technique for the disposal of oil refinery wastes.: Report No. 3/80, March 1980, Concawe, The Hague, Netherlands, pp. 94. *Water Research*, *14*(9), 1367.

[17] Taiwo, E. A., & Otolorin, J. A. (2009). Oil recovery from petroleum sludge by solvent extraction. *Petroleum Science and Technology*, *27*(8), 836-844.

[18] Xu, N., Wang, W., Han, P., & Lu, X. (2009). Effects of ultrasound on oily sludge deoiling. *Journal of hazardous materials*, *171*(1-3), 914-917.

[19] Mrayyan, B., & Battikhi, M. N. (2005). Biodegradation of total organic carbons (TOC) in Jordanian petroleum sludge. *Journal of hazardous materials*, *120*(1-3), 127-134.

[20] Pereira-Neta, J. (1987). *On the treatment of municipal refuse and savage sludge using aerated static pile composting- A low cost technology approach. PhD. Dissertation.* U.K: Leeds University.

[21] Piotrowski, M. R. (1991). Bioremediation of hydrocarbon contaminated surface water, groundwater, and soils. In *Proceedings of hydrocarbon contaminated soils and groundwater*.

[22] Lees, Z. M. (1996). *Bioremediation of oil-contaminated soil: a South African case study* (Doctoral dissertation).

[23] Oreco. (2010). *BLABO-Oil Tank Cleaning System for Crude Oil, HFO and Other Black Oil Tanks by Oreco A/S.* Available at: Oreco A/S Web site: http:// www.envrironmental-experts.com/products/blabo-oil-tank-cleaning-systems-for-crude-oil-hfo-and-other-black-oil-tanks-89454

Influence of Zn Contents on Optical and Electrochemical Properties Doped with CdS for Thin Film Application

Shafi Ullah[1], Muhammad Aamir Shafi[2], Hanif Ullah[3], Bernabé Mari[4]

[1,4]Instituto de diseño y Fabricación (IDF)-Universitat Politécnica de València (UPV) Camino de Vera, s/n 46022 Valencia, Spain. Shafi399@yahoo.com[1], bmari@fis.upv.es[4]
[2]COMSATS University Islamabad, Abbottabad Campus (CUI), Pakistan, aamirshafi@ymail.com
[3]Department of Electrical Engineering, Federal Urdu University of Arts, Science and Technology, Islamabad, Pakistan. hanifuet@yahoo.com

Abstract—**Binary cadmium sulfide (CdS) is an n-type semiconductor material which conventionally used as a buffer layer for CZTS and CIGS devices. The CdS has a tunable bandgap around 2.40 eV where the window layer of the complete device ZnO has a wide bandgap in the range of 3.20 to 3.50 eV. In this work, the Zn contents were electrochemically incorporated into the CdS thin film to decrease the energy losses between the mismatching of the bandgap. The obtained thin films were characterized by different techniques such as X-ray diffraction XRD, Scanning electron microscopy SEM, Energy dispersive spectroscopy EDS, and Optical and photocurrent response PC analysis. The crystallography of the film was confirmed by XRD with polycrystalline nature. The morphology and the elemental composition of the film investigated by SEM, it observed that the film is stoichiometry with a small variation of the grain size by increasing the Zn content. The optical analysis was studied in the visible range with a direct bandgap of 2.45 eV for CdS and 3.03 eV for 5% Zn contents. The photocurrent response of the film confirmed that the incorporation of Zn content high energy photons was captured to enhance the photocurrent of the film and decrease the bandgap mismatching between the CdS buffer and ZnO window layer. The obtained results could be the better choice to improve the device performance.**

Keywords - CdS buffer layer, Zn doping and electrochemical analysis

I. INTRODUCTION

Cadmium sulfide (CdS) known as a suitable material for photovoltaic applications. A variety of methods has been used to synthesis CdS thin films such as spray pyrolysis, electrodeposition [1], vapor deposition, and chemical bath deposition. Among the above-mentioned methods we used the chemical bath deposition CBD technique due to easily available, not expansive, adherent to the substrate, and uniform deposition [2]. Copper indium gallium sulfide ($CIGS_2$) device achieved high efficiency recently by using $Cd_{1-x}Zn_xS$ window layer to improve the collection of short-wavelength photons [3]. $Cd_{1-x}Zn_xS$ layer is a wide bandgap material from 2.45 to 3.50 eV depending on Cd/Zn ratio using as heterojunction for device application [4-7]. CdS doped Zn using as a window layer for device fabrication need to optimize the controlling the bath parameters during the deposition. Furthermore, the optical properties of the thin film could be enhanced like transmission to capture the high energy wavelength for device performance. CBD is a simple and suitable method to obtained low cast with easily controlled deposition parameters for thin film application [8].

In this work, we doped Zn a wide bandgap material with a CdS buffer layer to decrease the mismatching between the buffer layer and window layer, which is a significant bandgap difference from 2.45 to 3.03 eV. The Zn doped CdS significantly increase the optical and electrochemical performance of the thin film which could be a good choice to use as a buffer window layer for CIGS/CZTS photovoltaic device.

ISBN: 978-86-80593-73-9

II. EXPERIMENTAL SETUP

Zn doped CdS thin films were successfully deposition by CBD method with slightly modified parameter as used elsewhere [9, 10]. All the chemicals were purchased from Sigma Aldrich without any further purification. The $CdSO_4$ as Cd^{2+} ion source, $ZnSO_4$ as Zn^{2+} ion source, and triethanolamine (TEA) as a complexing agent in the bath solution. The solution ph was adjusted around 10 with different ammonia concentrations at various deposition times. The bath temperature was maintained at 75 ºC with a temperature controller and the solution was continuously stirred throughout the deposition process. The Indium Tin Oxide (ITO) was used as a substrate after completion of the deposition the film was washed with distilled water to remove the loosely bonded deposition. The structure, morphological and elemental composition of the prepared samples were performed using, X-Ray Diffraction (XRD) using a Rigaku Ultima IV diffractometer Cu-Kα radiation (λ = 1.54060 Å), Scanning Electron Microscopy (SEM) of model Zeiss ULTRA 55 equipped with In-Lens and secondary electrons detectors, The chemical composition analysis, surface morphology, elemental composition using energy dispersive spectroscopy (EDS) respectively. The optical properties of the thin films were measured by using IR-VIS-UV spectrophotometer at a wavelength within the range (300 - 1050) nm. The electrochemical performance of the samples was analyzed with a slight modification and reported elsewhere [11, 12]. The PEC measurements were performed in a quartz cell with a Pt rod counter electrode and Ag/AgCl saturated in 3 M KCl reference electrode potentiostat PGSTAT302N [13].

III. RESULTS AND DISCUSSIONS

Fig. 1 illustrates the XRD patterns of CdS and doped Zn at 3% and 5% respectively. The CdS doped Zn thin films are polycrystalline with multiple diffraction peaks located at 2θ angle 25.10º, 26.5º, 37.5º, 43.6º, 45.3º, and 50.5º corresponding to (100), (002), (102), (110), (103) and (004) lattice planes, respectively. The Zn doped CdS XRD patterns were observed to shift slightly to the lower 2θ angles, which represent that the Zn atoms were successfully incorporated into the Cd atoms. Furthermore, it was founded that the peak intensities gradually decreased with the incorporation of Zn contents from 0 to 5%. The decreasing of the intensities with increasing Zn contents are suggesting that Cd^{2+} ions (109 pm) are being replaced by smaller in size Zn^{2+} ions (88 pm).

Furthermore, the thin films were analysed to find out the topography of the obtained films CdS and Zn doped at different concentrations. Fig. 2 (a-c) represents the Cd, Zn 3%, and Zn 5%, respectively. The fine fragments with a white Cd dots and homogeneous morphology were observed as we incorporated the Zn contents the grain size 249.3 to 173.2 nm which is in good agreement with the XRD results.

The elemental composition and optical bandgap of CdS, Zn 3%, and Zn 5% are summarized in Table I. However, when the Zn percentage increases the Cd content seems to decrease according to the incorporation of Zn content into the solution. Therefore, the obtained thin films have exhibited a shortfall of sulfur.

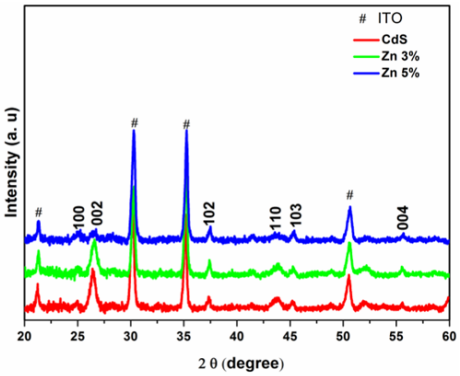

Figure 1. X-ray diffraction pattern of CdS with different Zn content 3%, and 5% respectively.

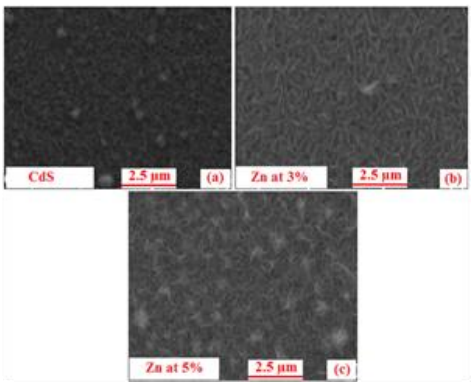

Figure 2. Surface morphology of CdS thin films doped Zn 3% and 5%.

TABLE I. EDS ANALYSIS OF CDS THIN FILMS WITH DIFFERENT ZN 3% AND ZN 5% CONCENTRATION.

Samples	Cd%	S%	Zn%	Optical band gap (eV)
CdS	58.0	42.0	0.0	2.45
Zn 3%	56.6	40.8	2.6	2.84
Zn 5%	54.6	40.6	4.8	3.03

IV. OPTICAL ANALYSIS

Optical properties absorption of CdS and different Zn contents are illustrated in Fig. 3. The absorption of the films was measured with UV-Vis spectroscopy at the range of 300 to 800 nm. The absorption spectrum was observed to shift the high energy wavelength by the incorporation of Zn contents. We can conclude the incorporation of Zn content into CdS strongly affect the optical absorbance of the films to increase the transmission, which is a good sign for a window layer to use for the photovoltaic device.

Fig. 4 shows the optical bandgap of CdS doped Zn 3% and 5 %. The direct optical bandgap was calculated from the touc plot, plotting the absorbance time photons energy $(Ahv)^2$ versus the photon energy (hv) then a linear line was drawn where intercept the x-axis is the optical bandgap value. The obtained results confirmed that incorporation of Zn content shifts the bandgap to the lower energy wavelength. The bandgap energy for CdS is 2.45 eV, Zn 3% 2.84 eV and for Zn 5% 3.03 eV. This is a good indication that Zn doped CdS could be used as a window layer for photovoltaic application.

Photoelectrochemical response of CdS doped Zn concentration was performed in a conventional three electrode setup. Fig. 5 shows the photo electrode current versus time curve the black curve represent the CdS photocurrent show 0.04 mA. Furthermore, when we introduced Zn contents to a significant increase were found in the photocurrent, 0.05 mA for Zn 3% and 0.14 mA for Zn 5%. The Zn content increase the donor concentration and enhanced the charge carrier carriage by boosting the electric field within the space charge layer.

V. CONCLUSION

The Zn doped CdS thin films successfully deposited on ITO substrate by CBD technique. XRD analysis confirmed the polycrystalline nature of CdS and doped Zn with a hexagonal structure. The SEM analysis shows the uniform, homogenous and pin-hole-free surface. The incorporation of Zn was confirmed by the EDS

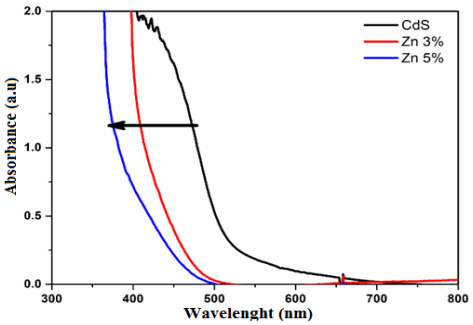

Figure 3. Optical absorbance of CdS doped Zn 3% and 5% concentration.

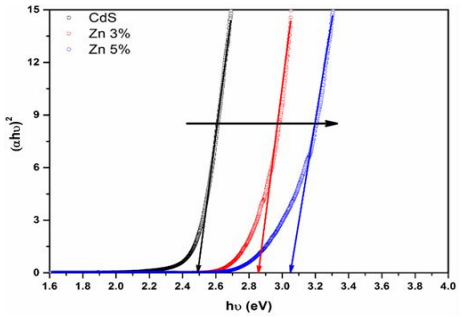

Figure 4. Optical bandgap of CdS and different Zn concentration.

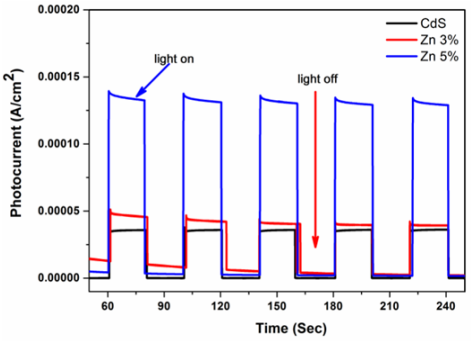

Figure 5. Photoelectrochemical response of CdS doped Zn concentration.

analysis. The optical absorbance and the energy bandgap show a significant shift to the high energy wavelength by incorporation of Zn contents. Furthermore, the photoelectrochemical response has good evidence that the incorporation of Zn content play a key role in the photocurrent response, which is boosted from 0.04 for CdS to 0.14 mA for Zn 5%. It's to conclude that CdS doped Zn could be a good choice to use as a window layer for photovoltaic solar cells.

ACKNOWLEDGMENT

This work was supported by the, RRHH, postdoctoral contract (PAID-10-20), UNIVERSIDAD POLITECNICA DE VALENCIA and Ministerio de Economía y Competitividad (Grant Number PID2019-107137RB-C21), Valencia (Spain). One of the author Aamir Shafi acknowledged Higher Education Commission of Pakistan, International Research Support Initiative Program (IRSIP) under grant No:1-8/HEC/HRD/2020/10744 PIN:IRSIP 45 Engg 17.

REFERENCES

[1] Ullah, S., Mollar, M., & Marí, B. (2016). Electrodeposition of CuGaSe 2 and CuGaS 2 thin films for photovoltaic applications. *Journal of Solid State Electrochemistry*, *20*(8), 2251-2257.

[2] Kumar, T. P., Saravanakumar, S., & Sankaranarayanan, K. (2011). Effect of annealing on the surface and band gap alignment of CdZnS thin films. *Applied Surface Science*, *257*(6), 1923-1927.

[3] Bouich, A., Ullah, S., Ullah, H., Mollar, M., Marí, B., & Touhami, M. E. (2020). Electrodeposited CdZnS/CdS/CIGS/Mo: characterization and solar cell performance. *JOM*, *72*(2), 615-620.

[4] Baig, F., Khattak, Y. H., Ullah, S., Marí, B., Beg, S., & Khan, K. (2018). Effect of MAPbBr3 HTL and CBD Deposited Cd1–x Zn x S ETL Band Offset on Lead Halide Perovskite Solar Cell. *Materials Focus*, *7*(5), 610-616.

[5] Liu, H. J., & Zhu, Y. C. (2008). Synthesis and characterization of ternary chalcogenide ZnCdS 1D nanostructures. *Materials Letters*, *62*(2), 255-257.

[6] Kumar, B., Vasekar, P., Pethe, S. A., Dhere, N. G., & Koishiyev, G. T. (2009). ZnxCd1− xS as a heterojunction partner for CuIn1− xGaxS2 thin film solar cells. *Thin Solid Films*, *517*(7), 2295-2299.

[7] Kuhaimi, S. A., & Tulbah, Z. (2000). Electrochemical/Chemical Deposition and Etching-Structural, Compositional, Optical, and Electrical Properties of Solution-Grown ZnxCd1-xS Films. *Journal of the Electrochemical Society*, *147*(1), 214-218.

[8] X.Wu, J. C. Keane, R. G. Dhere, C. Dehart, A. Duda, T. A. Gessert, and P. Shelton, (2001). Proceedings of the 17th European Photovoltaic Solar Energy Conference, 995-1000.

[9] Bhattacharya, R. N., Ramanathan, K., Gedvilas, L., & Keyes, B. (2005). Cu (In, Ga) Se2 thin-film solar cells with ZnS (O, OH), Zn–Cd–S (O, OH), and CdS buffer layers. *Journal of Physics and Chemistry of Solids*, *66*(11), 1862-1864.

[10] Sanap, V. B., & Pawar, B. H. (2010). Optical study of effect of cadmium sources on nanocrystalline CdS thin films. *Chalcogenide Lett*, *7*, 227-231.

[11] Jaramillo, T. F., Baeck, S. H., Kleiman-Shwarsctein, A., Choi, K. S., Stucky, G. D., & McFarland, E. W. (2005). Automated Electrochemical Synthesis and Photoelectrochemical Characterization of Zn1-x Co x O Thin Films for Solar Hydrogen Production. *Journal of combinatorial chemistry*, *7*(2), 264-271.

[12] Jaramillo, T. F., Baeck, S. H., Kleiman-Shwarsctein, A., & McFarland, E. W. (2004). Combinatorial electrochemical synthesis and screening of mesoporous ZnO for photocatalysis. *Macromolecular rapid communications*, *25*(1), 297-301.

[13] Phuana, Y. W. Ibrahima, E. M. Chong, N. Zhua, T. B. Leec, K. Ocond, J. D. (2017). Eng Seng Chana, *Applied Surface Science*, *392*, 144–152.

Transient Analysis at Short Circuit and Start of Induction Motor

Enver Agić[1], Damir Šljivac[2], Bakir Agić[3]

[1]PIM University Banja Luka, Ulica D.S. Lazarevića bb, 78000 Banjaluka, Bosnia and Herzegovina, enveragic99@gmail.com
[2]Electrical Faculty, The University J.J. Strossmayer of Osiijek, Kneza Trpimira 28, 31 000 Osijek, Croatia, damir.sljivac@etfos.hraddress
[3]Faculty of Elecrtical Engineering, The University of Tuzla, Franjevačka 2., 75 000 Tuzla, Bosnia and Herzegovina, bakir.agic@outlook.com

Abstract— **The paper considers transients at short circuit and start of induction motor. Using electrical equipment: power analyzer MI 7111, control transformer (220/400 V, 1.25 kVA, 5 A), resistor R1 (220 V, 10 Ω, 4.1 A), resistor R2 (220 V, 5 Ω and 7 (4.1 A) and the MATLAB software tool, the waveforms of the voltage drop at the short circuit and the start of the induction motor on the transformer during the transient will be determined. The value of the starting torque and current are the basic issues when starting an asynchronous machine.**

Keywords - insert induction motor, transients, rated current, starting torque,starting current

I. INTRODUCTION

Used equipment for transient short-circuit and start of induction motor analysis:

Electric circuit 1:

1. MI 7111 power analyser
2. Control transformer (220/400 V, 1.25 kVA, 5 A)
3. Resistor R1 (220 V, 10 Ω, 4.1 A)
4. Resistor R2 (220 V, 5Ω and 7Ω, 4.1 A)

Electric circuit 2:

1. MI 7111 power analyzer
2. Three-phase control transformer (380 V, 5.46 kVA, 7 A)
3. Current measuring transformer (50/5 A)
4. Induction motor (380 V, 5.59 kW, cosφ = 0.89, connection: Δ)

For the realization of these activities, electric circuits were made of electrical equipment as in Figs.1 and 2 [1].

The beginning of the short circuit according to Fig. 1 is modeled by turning on the switch at time t = T1. The short-circuit elimination according to Fig. 2 is modeled by switching off the switch at the moment t = T2. It is necessary to record the waveforms and the rms value of the voltage drop during a laboratory-simulated short circuit with the MI 7111 instrument.

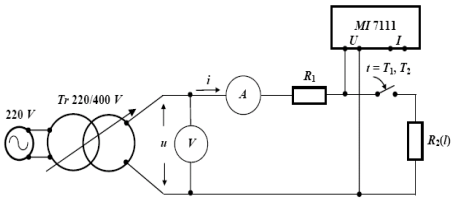

Figure 1. Failure analysis scheme.

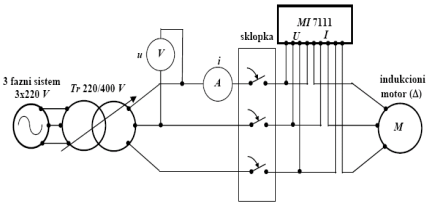

Figure 2. Start of the induction motor.

ISBN: 978-86-80593-73-9

Check of the validity of the analytical relation for the rms value of the voltage drop is done by comparing it with the measured rms value. Fault impedance together with faulty line impedance represented by resistor R2 vary by at least two different values of resistor R2.

It is important to show that the farther the fault location is from the measuring point, the higher the value of the collapse magnitude (the depth of the failure is smaller), i.e. the collapse is less serious [2].

$$z_f = z\,l\ . \qquad (1)$$

II. MEASUREMENT ANALYSIS

A. *Analysis of Voltage Drop Measurement at Induction Motor Short Circuit*

One of the most inconvenient quality disturbances is voltage drop. Failure is defined as a short-term decrease in the rms value of the voltage between 0.1 and 0.9 nominal for a period of 0.5 period to 1 minute. Voltage dips are measured by observing a time diagram of the change in the rms value of the voltage during a disturbance. Voltage failure occurs due to the inclusion of power transformers, powerful induction motors or due to faults in the electrical network, distribution or transmission.

Transmission network failures affect many more consumers and at greater distances [3]. Consumers up to 100 km from the fault location may experience a voltage drop. A large number of these failures originate from earth faults, which occur due to weather disasters (lightning, wind, ice, etc.). Most often, single-phase failures occur, i.e. earth faults. Three-phase failures are much rarer but more serious, with a higher intensity of the fault current.

A typical fault elimination time range is three to thirty periods depending on the amplitude of the fault current and the type of overcurrent protection [4]. Although certain measures are being taken to prevent these breakdowns in the electricity network, they cannot be completely eliminated.

After connecting the elements of the electrical circuit as in Fig. 1 and using the power analyzer MI 7111, the following characteristics were obtained.

The simplest voltage drop can be analyzed in Fig. 3c where a short circuit occurs in a line

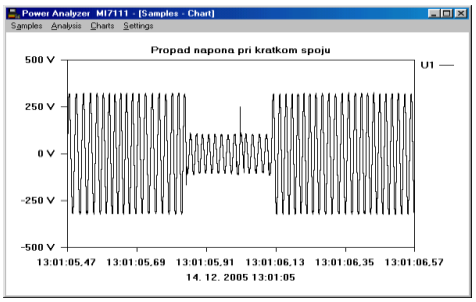

a)

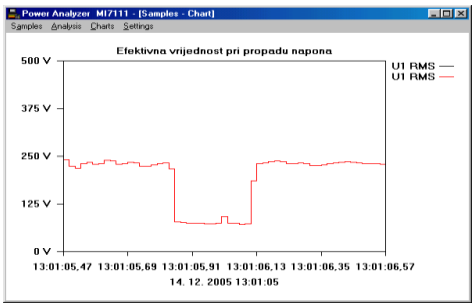

b)

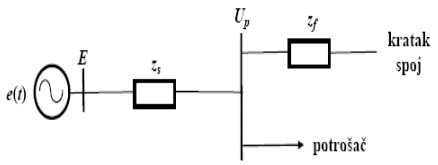

c)

Figure 3. (a) Voltage drop on short circuit; (b) Effective value on voltage drop; (c) Simplified model for voltage drop calculation.

parallel to the consumer [5]. This is a simplified model for a three-pole short circuit to ground.

Fig. 2c shows the labels:

Zs - system impedance

Zf - serial impedance of the line impedance on which the fault occurred and the fault impedance

E - system voltage

Up - magnitude of voltage drop

The assumption is that all the current will flow along the faulty line, so you can easily calculate the voltage at the busbars, consumer voltage as:

$$U_p = \frac{z_f}{z_f + z_s} \cdot E < E, z_f \neq 0 \ . \qquad (2)$$

Changing the last relation by taking the impedance on the faulting line as directly proportional to the length of the line $zf = zl$, where z is the unit resistance of the line, the Eq. is:

$$U_p(l) = \frac{z \cdot l}{z \cdot l + z_s} \cdot E \ . \qquad (3)$$

The magnitude of the voltage drop given with the last equation is an increasing function, i.e. with increasing length l, the magnitude of voltage drop increases, i.e. the voltage drop is less serious, which was expected. The closer the fault is to the busses, the smaller the magnitude of the collapse will be, i.e. the deeper the failure will be, so the failure is more serious [6].

Let the rms value of the connected voltage be 230 (V). The short circuit simulation is performed by turning on the switch at time t = T1 (corresponds to the time from Figure 1b, 13: 01: 05, 84) or by turning off the switch at time t = T2 (Figs. 1b, 13: 01: 06, 09). For the system impedance (Zs) value of the resistance of R1 = 10 (Ω) is used and for the resistance of the serial impedance of the line (Zf) in which the fault occurred and the fault impedance, the resistance value of R2 = 5 (Ω), Fig. 1.

Equation for the magnitude of the voltage drop:

$$U_p = \frac{R_2}{R_1 + R_2} \cdot E = \\ = \frac{5\Omega}{(10+5)\Omega} \cdot 230V = 76,66V \ . \qquad (4)$$

Assuming that the fault location is farther from the measurement location, then the interest is in how much the magnitude or depth of the voltage drop will be in that case [7].

Let the impedance resistance of the line (Zf) be the fault and the fault impedance be R2 = 3 (Ω).

The magnitude value is now:

$$U_p = \frac{R_2}{R_1 + R_2} \cdot E = \\ = \frac{5\Omega}{(10+3)\Omega} \cdot 230V = 88,46V \ . \qquad (5)$$

TABLE I. RELATION BETWEEN MAGNITUDE AND DEPTH OF THE VOLTAGE DROP.

R_2 (Ω)	**The magnitude of the voltage drop** (V)	Depth of voltage drop (V)
5	76.66	153.34
3	88.46	141.54

This shows that the farther the fault location is from the measuring point, the higher the value of the failure magnitude is, i.e. the smaller the failure depth then the less serious the failure, or in other words, the farther we are from the short-circuit location, the smaller the failure is [8]. The read (measured) value of the voltage drop magnitude from Figure 1b is approximately one third of the rms voltage (230 V) and it's value is 76.66 (V) which corresponds exactly to the analytically calculated under (4).

According to the diagram in Figure 2, it is necessary to record the starting current of the three-phase induction motor as well as the corresponding phase voltages when starting the motor [9]. In addition, it is necessary to determine the maximum value of the current electricity of the motor, compare it with the nominal one. Also, determination of how long the starting current is higher than the rated motor current is needed, and to analyze the voltage when starting the motor. We should come to conclusion is there a voltage drop when the engine is switched on and what is its magnitude (monitor the rms value over time on the RMS instrument on MI 71711) [10]. Finally, it is necessary to propose measures to reduce the starting current of the induction motor.

III. VOLTAGE DROP ANALYSIS AT THE START OF AN INDUCTION MOTOR

The value of the starting torque and current are the basic issues when starting an asynchronous machine [11]. When the motor is connected to the mains, its rotor is mechanically immobile and electrically short-circuited (regardless of the type of asynchronous machine), and with the maximum induced electromotive force in the rotor winding (rotating field intersects

conductors at synchronous speed), this condition is accompanied by the appearance of large currents. These currents can cause high heating of the motor windings as well as large voltage drops and this can negatively affect other receivers in the network. In order for the rotor to start working during start-up, the starting torque developed by the motor must be greater than the resistance torque produced on the shaft by the working machine [12].

The hazards that can occur when switching on or off high-voltage drive motors are very important from the aspect of the safety of the motors themselves. Motors are damaged due to excessive currents that occur in these phenomena. The forces on the winding are proportional to the square of the current, and the winding deformations due to the force depend on the geometric configuration of the winding heads (longer heads with a lower moment of resistance are exposed to larger deformations) [13].

Non-sinusoidal voltages applied to the motor cause non-sinusoidal currents to flow through the motor windings.

The losses in the windings are proportional to the square of the current flowing through the winding, and the following applies to the current:

$$I = \sqrt{I_1^2 + I_2^2 + I_3^2 + ... + I_n^2} \quad . \qquad (6)$$

where:

I - the rms value of the current flowing through the winding

In - rms value of the nth current harmonic

Using the power analyzer MI 7111, the following characteristics were obtained, and after connecting the elements of the electrical circuit as in Fig. 4:

When a three-phase induction motor is connected to the mains, the motor draws a current of 4 ... 8. In and a smaller (larger) voltage drop occurs, depending on the motor power [14].

In Fig. 3a the waveform of three-phase motor switching currents is shown. It can be concluded that the maximum value of current is 48 A, when the motor is turned on and compared to the nominal (in the amount of 5.5 A, calculated on the basis of the given nominal values of the three-phase motor) is 8.7 times higher. This switch-on

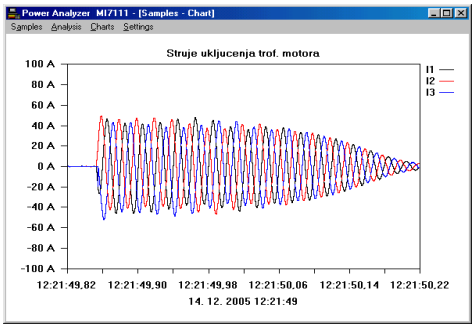

a)

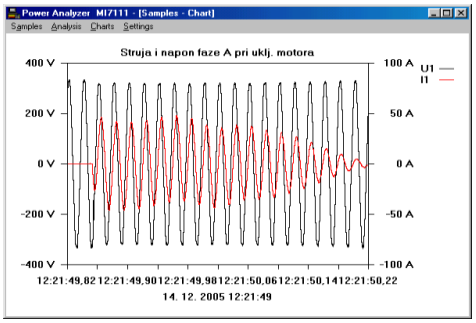

b)

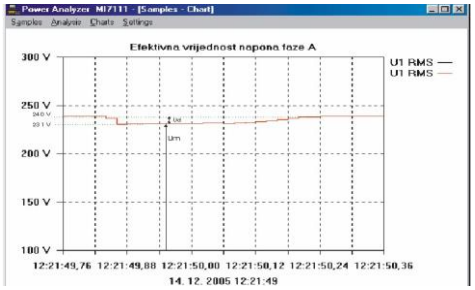

c)

Figure 4. a) Waveform of three-phase motor switching currents; b) Voltage and current in phase A when switching on the motor; c) Effective voltage value in phase A.

current is greater than the rated motor current for the time of 00: 00: 00, 38 (h).

In Fig. 3b on which the current and voltage of phase A are recorded when the motor is switched on, it is visible that there is a change in the waveform of the voltage, i.e., to voltage drop as long as the motor takes a large current from the mains [15].

From Fig. 4c., we see that the value of the magnitude of that decay is 231 (V) i.e. 96% of Un = 240 (V).

IV. MEASURES TO REDUCE TOHE STARTING CURRENT OF THE INDUCTION MOTOR

The following methods are used to start the motor and to reduce the starting current.

- Direct connection to the network, which is associated with minor or major electric shocks. Depending on the quality and power of their distribution network, they prescribe the highest power of asynchronous machines with a short-circuited rotor that can be put into operation in this way. These are lower power motors (up to approximately 3 kW).

According to regulations, the output current of motors must not exceed 60 (A), and motors over 3 (kW) must be started with:

- by applying additional devices that are connected to the stator circuit (in the line between the network and the terminals of the stator windings). The star connection is three times smaller than triangle connection, however, the starting torque is three times smaller) or the power supply is done via a block transformer or by regulating the voltage using power electronics devices (frequency converters).
- by applying a special design of the rotor and its windings, which consists in the construction of the rotor with deep and double grooves. This construction improves the initial characteristics, because it increases the ohmic resistance and reduces the phase shift between ems and current during start-up.
- by means of an additional resistance (resistor for commissioning) connected to the rotor circuit, it is possible to develop large starting moments at low starting current. Namely, when the total resistance of the rotor circuit increases, with the unchanged torque, the slip and the starting torque increase, and the starting current decreases.

REFERENCES

[1] A.Tokić (n.a.). Introduction, Definitions, Transition CEFES-3. In *Quality of el. Energy*.

[2] Dugan, R., McGranaghan, M., & Beaty, W. (1996): Electric Power System Quality. McGraw Hill, New York. (pp. 34-36).

[3] Katic, V. (2005). Standards, Harmonics, Fail Voltage CEFES. In *Quality of electrical energy*. (p. 66).

[4] Tokić, A. (2005). Electricity Quality CEFES Novemberr. (p. 23).

[5] MATLAB Simulink Power System Blockset 7 - software package for simulation and analysis of EE dynamic systems within the MATLAB tool

[6] Agić, E. (2006). Power quality–CEFES. (p. 7).

[7] WG on Modelling and Analysis of System Transients Using Digital Programs. (2000). Modelling and Analysis Guidelines for Slow Transients – Part III: The Study of Ferroresonance. *IEEE Trans. on Power Delivery, 15*(1), 255-265.

[8] K. Miličević, Ferroresonance: "Systems, Analysis and Modeling", Wiley Encyclopedia of Electrical and Electronics Engineering, pp. 1-8,2014.

[9] Vinkovic, A., & Mihalic, R. (2008). A current- based model of the static synchronous series compensator (SSSC) for Newton– Raphson power flow. *Electr. Power Syst. Res., 78*(10), 1806–1813.

[10] SimPowerSystems (2013). User's Guide, Mathworks.

[11] Katić, V. Standards, harmonics, Voltage Disruptions CEFES. In *Electricity Quality*.

[12] Carpinelli, G. et all. (n.a). Probabilistic Evaluation of the Economical Damage due to Harmonic Losses in Industrial energy system.

[13] Energy System (1996). *IEEE Transaction on Power Delivery, 11*(2), 1021-1030.

[14] Piasecki, W., Florkowski, M., Fulczyk, M., Mahonen, P., & Nowak, W. (2007). Mitigating Ferroresonance in Voltage Transformers in Ungrounded MV Networks. *IEEE Trans. on Power Delivery, 22* (4), 2362-2369.

[15] WG C-5 (2000). Mathematical Models for Current, Voltage, and Coupling Capacitor Voltage Transformers. *IEEE Trans. on Power Delivery, 15* (1), 62-72.

Investigation of the Effect of Semiconductors (ZnO and TiO_2) on Efficiency of DSSCs Based on Celosia Cristata

Mozhgan Hosseinnezhad[1], Kamaladin Gharanjig[2], Shoheh Rouhani[3]

[1,2,3]Department of Organic Colorants, Institute for Color Science and Technology, Tehran, Iran

[1,2,3]Center of Excellence for Color Science and Technology, Institute for Color Science and Technology, Tehran, Iran, hosseinnezhad-mo@icrc.ac.ir[1]

Abstract—**This natural extraction of Celosia Cristata was used as green photosensitiser in TiO_2 and ZnO dye sensitized solar cells. Ultraviolet–visible spectrophotometry of the natural dye in solution and on TiO_2 and ZnO substrate were carried out in order to assess changes in the status of the dyes. The wavelength of maximum absorption (λ_{max}) and the molar extinction coefficients (ε_{max}) for the natural dye in solution are 467 nm and 1723 $M^{-1}cm^{-1}$. The results show that the dyes from J type aggregate on the ZnO substrate. Finally, the DSSCs devices were prepared based on synthesized dyes and ZnO or TiO_2. Overall, the results show that the efficiency of the DSSCs-based on ZnO is lower than that TiO_2.**

Keywords – dye-sensitized solar cells, natural dyes, ZnO, efficiency

I. INTRODUCTION

Dye sensitized solar cells or Gratzel cells (DSSC) have attracted more and more attention as renewable energy source. TiO_2 nanocrystalline material has been utilized as photoelectrode in DSSC. Other n-type metal oxide semiconductors, such as ZnO, SnO_2, In_2O_3 and Nb_2O_5 can be utilized in dye-sensitized solar cells due to studies phtoelectro chemically active thin semiconductor films [1]. ZnO is the well Known metal oxide to replace TiO_2 due to similar bandgap and its higher electronic mobility as TiO_2. Few studies have been focused on ZnO-based dye-sensitized solar cells and commonly used inorganic dye molecules in this studies [2]. However, dye-sensitized solar cells based on organic dyes have attracted more attention due to low cost, environmentally friendly and easily synthesized characteristic of organic dye molecules [3]. However, dye aggregation on nanocrystals substrate in DSSCs is a limitation of metal-free organic dyes since, dye aggregation inhibits electron transfer from the exited dye to nanocrystals substrate [4].

In this study, we prepared natural extraction as photosevsitizer and disclosed the high efficiency of DSSCs based on ZnO. Then investigated influence of use of anti-aggregation agent on performamce of dye-sensitized solar cells based on ZnO. The spectrophotometric properties of the organic dyes in solution and on a ZnO substrate also examined.

II. EXPERIMENTAL

A. Materials

Natural resources used in this study was Celosia Cristata, obtained from underbrush grown in the north of Iran. All chemical reagents and solvents were analytical grades provided by Merck Co. and used without further purification. Transparent conducting oxide, FTO (F-doped SnO2, DyeSol), ZnO and TiO_2 pastes, scattering layer and Di-tetrabutylammonium Cis-bis(isothiocyanato)bis(2,2′-bipyridyl-4,4′-dicarboxylato)-Ruthenium(II) (N719 Grade) were purchased from Sharif Solar Co.

ISBN: 978-86-80593-73-9

B. *Preparation of Green Sensitizers*

The alcohol extracts of Celosia Cristata was obtained via a continuous procedure. The dye extracted with ethanol as solvent were prepared by the following step: (i) Celosia Cristata was drained with water and vacuum dried at 45°C; (ii) Approximately 4 g of dried natural sources of the previous step was put into a 95% wt.% ethanol solution and kept for two days at room temperature without exposing to direct sunlight; (iii) The resulting solid residues were washed, filtered and the resulting solutions were concentrated with rotatory evaporator at 40 °C to obtain green sensitizers.

C. *Dye-sensitized Solar Cells Fabrication*

A nanocrystalline ZnO and TiO_2 film was coated on a transparent glass support. Naturaldye was adsorbed by dipping a separate coated glass in extraction solution in the absence and presence of anti-aggregation agent such as 3α,7α-dihydroxy-5β-cholanic acid (cheno) for several hours. Finally, the film was washed with a 1:1 acetonitrile:ethanol mixed solution. Acenonitrile : ethylenecarbonate (v/v=1:4) containing tetrabutyl ammonium iodide (0.5 mol dm^{-3}) was used as an electrolyte. Each dye-adsorbed ZnO and TiO_2 electrode, together with a Pt counter electrode and the mentioned electrolyte solution were separately assembled into a sealed sandwich type solar cell. For each solar cell an action spectrum was measured under monochromatic light with a constant photon number (5×10^{15} photon cm^{-2} s^{-1}). J-V characteristics were measured under illumination with AM 1.5 simulated sun light (100 mW cm^{-2}) through a shading mast (5.0 mm×4 mm) by using a Bunko-Keiki CEP-2000 system.

III. Results and Discussion

Natural dye as sensitizer is directly effective on the conversion efficiency of dye-sensitized solar cells. The Molecular structure of Celosia Cristata was illustrated in Fig. 1.

Much attention has been paid to development in this field for increase dye loading on nanomaterial photoelectrode leading to higher efficiencies. The wavelength of maximum absorption (λ_{max}) for the natural dye in solution are presented in Table I, together with the λ_{max} of the corresponding dyes adsorbed on a ZnO and TiO_2 film in the absence and presence of anti-aggregation agents. Upon dye adsorption onto a ZnO and TiO_2 surface, the λ_{max} is bathochromically shifted as compared to the corresponding spectra in solution, implying that

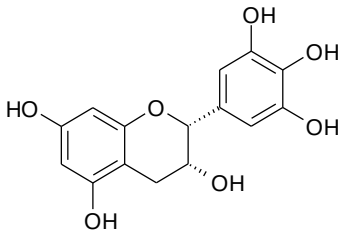

Figure 1. Molecular structure of Celosia Cristata.

TABLE I. ABSORPTION OF THE NATURAL EXTRACT.

Source	λ_{max} (nm)[a]	λ_{max} (nm)[b]	λ_{max} (nm)[c]
Celosia Cristata	510	521	526
With anti-aggregation agent	510	514	516

a. Maximum Absorption of dye measured in solution; b. Absorption maximum of dye adsorbed on the surface of TiO_2; c. Absorption maximum of dye adsorbed on the surface of ZnO

natural dye adsorbed onto ZnO and TiO_2 surface contain partial J-type aggregates. The results showed that bathochromic shifts in the wavelength of maximum adsorption were reduced due to the presence of the anti-aggregation agents moreover [5].

FT-IR spectra of the powders obtained from the dried natural dye and pre-dye treated TiO_2 nanoparticles were carefully analyzed to assess chemical interactions. The intense peak of the dried natural dyes around 3400 cm^{-1} is indicative of the OH stretching modes, while two peaks appeared at around 2900 and 2800 cm^{-1} were attributed to C-H stretching. The peak around 1700 cm^{-1} is a signature of the C=O stretching [6, 7]. The FT-IR spectra of the pre-dye treated TiO_2 depicts the peak of Ti-O band at 450-1000 cm^{-1}, resulting from the reaction between dye molecules and photoelectrode. To make a comparative view, confirming the presence of hydroxyl and carbonyl groups in the molecular structure of natural dye and bonding between dye molecules and TiO_2 nanoparticles. The FTIR spectra of Celosia Cristata was illustrated in Fig. 2.

Inspired by previous studies, the cyclic voltammetry method was applied in evaluating the possibility of the charge transfer from dried natural dyes to the photoelectrode [8]. The

oxidation peal potential (E_{ox}) in solution Celosia Cristata was estimated to be +0.83. The excited

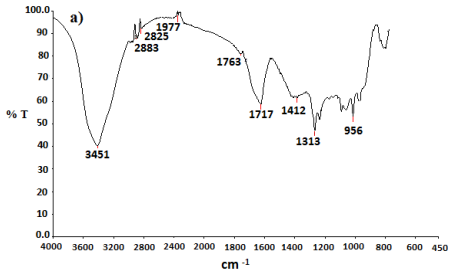

Figure 2. FTIR spectra of Celosia Cristata extraction.

TABLE II. PHOTOVOLTAIC PARAMETERS OF DSSCS BASED ON THE NATURAL DYE EXTRACTION.

Dye	J_{SC} (mA.cm^{-2})	V_{OC} (V)	FF (%)	η (%)
Celosia Cristata (TiO_2)	4.82	0.52	0.55	1.38
Celosia Cristata (TiO_2 and anti-agregation agent)	5.52	0.55	0.59	1.79
Celosia Cristata (ZnO)	3.66	0.50	0.54	0.99
Celosia Cristata (ZnO and anti-agregation agent)	4.22	0.52	0.51	1.12
N719	13.55	0.88	0.71	8.47

state oxidation potentials (LUMO) in the same order were –1.34. The conduction band (CB) for TiO2, redox level of electrolyte [9] and the energy level of dye molecules are compared in Fig. 3. The results suggest that the LUMO state lies above the conduction band of TiO2, and makes possible the electron injection from each excited dye molecule to photoelectrode conduction band. This means that all natural dyes can accept electron from electrolyte due to the HOMO dye molecules being more positive of than the level of energy in the electrolyte. Thus, they can be all considered in DSSC fabrication as sensitizer.

The photovoltaic properties of DSSCs based on natural dye was studied by measuring the J-V curve under the standard global AM 1.5 solar irradiation [10]. The photovoltaic parameters are also presented in Table II and Fig. 3. It is also abundant that photocurrent value depends on the binding affinity and previous study suggest that the amounts of adsorbed extractions (natural dye) are sometimes different under the same concentration and thickness of TiO_2 film [11]. Therefore, the low photocurrent can be attributed to the weak bonding between dye molecules and the surface of semiconductors as photoelectrode [10]. Natural dyes mostly have –OH and –O ligands, instead they lack acid substituents. On the other hand, the majority of organic and organometallic dyes are bonded to photoelectrode via their anchoring groups such as acrylic acid, cyanoacrylic acid and etc. Lower efficiencies and open circuit voltage values of natural dyes in DSSCs structures compared to organic dyes and organometallic pigments is due to such bonding and slow rate of electron transfer. The stability of dye-sensitized solar cells based on natural dyes were tested by monitoring the photovoltaic properties under solar light simulation. Remarkably, no significant alteration was followed after 50 h.

The results presented here in stability state are similar to data reported by other authors. The DSSCs based on N719 was prepared using standard method to compare with the performance of the DSSCs sensitized by natural dye. However, the DSSCs sensitized by N719 as standard dye shows better performance that the DSSCs based on natural dyes. The DSSCs based on N719 as standard dye, due to reduces the charge recombination at the dye molecules and photoelectrode interface, shows higher conversion efficiency. On the other hand, the N719 dye standard contains the expensive

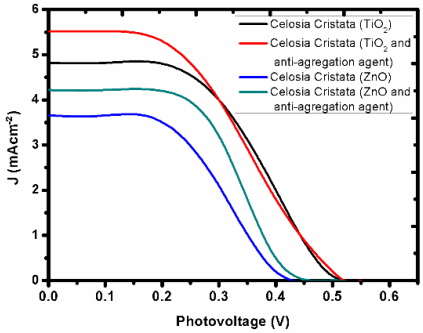

Figure 3. J-V curve of DSSCs based on Celosia Cristata extraction.

ruthenium metal which economically limits its general use.

Dye loading onto ZnO substrate is a critical step for fabrication of dye-sensitized solar cells based on ZnO. The carboxylic acid group of organic dyes lead to some dissolution of ZnO in the dye bath and formation of a Zn^{2+}-organic dye precipitate, but this precipitate does not cause ineffective organic dye on the ZnO electrode. Thus we selected 3h for immersion time for dye adsorption onto ZnO substrate. Our V_{oc}, FF and η values are smaller than those of TiO_2 films in the previous study. Electron injection for ZnO from the sensitizer contains slow (~ ten to hundreds of picoseconds) whereas for TiO_2, the electron injection is found to be near unity. The conversion efficiency depends on the ratio of charge injection rate to the charge recombination rate. So, slow electron injection for ZnO lead to reduce conversion efficiency compared to TiO_2 [12, 13].

IV. CONCLUSION

Natural extraction as photosensitizer show the highest solar to electricity conversion efficiency (η) among natural dyes. Natural extraction prepared and the spectrophotometric properties of the extraction in solution and on ZnO and TiO_2 films in the absence and presence of anti-aggregation agents were also examined. In all cases, the absorption maxima of natural dye applied on the surface of a nanoanatase ZnO and TiO_2 substrate gave bathochromic shifts compared to the corresponding dye spectra in solution. The results mentioned that the natural dye from J-type aggregated on the ZnO and TiO_2 substrate but, the amounts of aggregation were reduced in the presence of anti-aggregation agents because of the decreased of bathochromic shifts in the presence of cheno as anti-aggregation agent. Thus, the electron transfer process is reduced due to aggregation of molecular dyes and anti-aggregation agent was used in preparation of dye-sensitized solar cells. The reduction potential level of natural dye was negative compared with the conduction band level of ZnO and TiO_2. Thus, dye-sensitized solar cells based on ZnO and TiO_2 can be fabricated with this dye. The results showed that the conversion efficiencies were improved with the reduction of aggregation. For example natural dye indicated 1.38 and 1.79 % for conversion efficiency in the absence of anti-aggregation agent and in the presence of cheno and TiO_2, respectively. Thus conversion efficiency of dye sensitized solar cells directly correlated with larger conformational flexibility and diffusion values of organic dye molecules.

REFERENCES

[1] Richhariya, G., Kumar, A., Tekasakul, P., & Gupta, B. (2017). Natural dyes for dye sensitized solar cell: A review. *Renewable and Sustainable Energy Review*, *69*, 705-718.

[2] Hosseinnezhad, M., Gharanjig, K., & Moradian, S. (2020). New D–A–π–A organic photo‐sensitizer with thioindoxyl group for efficient dye‐sensitized solar cells. *Chemical Paper*, *74*, 1487.

[3] Kumara, N. T. R. N., Ekanayake, P., Lim, A., Liew, L. Y. C., Iskandar, M., Ming, L. C., Senadeera, G. K. R. (2013). Layered co-sensitization for enhancement of conversion efficiency of natural dye sensitized solar cells. *Journal of Alloys and Compounds*, *581*, 186.

[4] Hosseinnezhad, M., et al. (2020). Dye-sensitized solar cells based on natural photosensitizers: A green view from Iran. *Journal of Alloys and Compounds*, *828*, 154329.

[5] Hosseinnezhad, M., Moradian, S., & Gharanjig, K. (2015). Investigation of effect of anti-aggregation agent on the performance of nanostructure dye-sensitized solar cells. *Opto-Electronic Review*, *23*, 126.

[6] Teoli, F., Lucioli, S., Nota, P., Frattarelli, A., Matteocci, F., Carlo, A. D., Caboni, E., & Forni, C. (2016). Role of pH and pigment concentration for natural dye-sensitized solar cells treated with anthocyanin extracts of common fruits. *Journal of Photochemistry and Photobiology A: Chemistry*, *316*, 24-30.

[7] Yamazaki, E., Murayama, M., Nishikawa, N., Hashimoto, N., Shoyama, M., & Kurita, O. (2007). Utilization of natural carotenoids as photosensitizers for dye-sensitized solar cells. *Solar Energy*, *81*, 512.

[8] Hosseinnezhad, M., Nasiri, S., Movahedi, J., & Ghahari, M. (2020). Improving the efficiency of organic sensitizers with various anchoring groups for solar energy applications. *Solar Energy*, *211*, 228.

[9] Ananth, S., Vivek, P., Arumanayagam, T., & Murugakoothan, P. (2014). Natural dye extract of lowsoniainermis seed as photo sensitizer for titanium dioxide based dye sensitized solar cells. *Spectrochimica Acta Part A: Molecular and Biomolecular Spectroscopy*, *128*, 420.

[10] Hosseinnezhad, M., Movahedi, J., Nasiri, S. (2020). High stability photosensitizers for dye-sensitized solar cells: Synthesis, characterization and optical performance. *Optical Materilas*, *109*, 110198.

[11] Naik, P., Su, R., Elmorsy, M. R., El-Shafei, A., & Adhikari, A. V. (2018). New carbazole based dyes as effective co-sensitizers for DSSCs sensitized with ruthenium (II) complex (NCSU-10). *Journal of Energy Chemistry*, *27*, 351-360.

[12] Hosseinnezhad, M. (2016). Investigation of photocurrent generation in dye sensitised solar cells based on nanostructured ZnO electrodes. *Materials Technology*, *31*(1), 24.

[13] Zhang, H., et al. (2016). Cyanine tandem and triple-junction solar cells. *Organic Electronic*, *30*,

Theoretical Analysis of Vertical Micro Wind Turbines

Emilyn Barbosa da Silva Cabral[1], Gabriella Pedreira Albuquerque[2], Paulo César Mioralli[3], Pablo Sampaio Gomes Natividade[4], Paulo Henrique Palota[5], Jonas Rafael Antonio[6], José Ferreira da Costa[7], Sílvio Aparecido Verdério Junior[8], Elson Avallone[9]

[1]Student-Federal Institute of Education, Science and Technology of Sao Paulo, Catanduva-SP, Brazil, emilyn.cabral@aluno.ifsp.edu.br,
[2]Student of civil engineering-Faculdades Integradas de Bauru-SP, Brazil, gab.ped.alb@gmail.com
[3,4,5,6,7,8,9]Docent-Federal Institute of Education, Science and Technology of Sao Paulo, Catanduva-SP, Brazil, mioralli@ifsp.edu.br[3], pablo.sgn@ifsp.edu.br[4], palota@ifsp.edu.br[5], jonas.antonio@ifsp.edu.br[6], joseferreira@ifsp.edu.br[7], elson.avallone@ifsp.edu.br[9]

Abstract— **Currently, the energy sector is the main responsible for the emission of carbon dioxide into the atmosphere. Therefore, to reverse this scenario, it is necessary to expand the use of renewable energy sources, such as wind energy. This study aims to theoretically analyze 6 models of vertical axis wind microturbines using the artificial wind from the output of an air conditioner. Using the mathematical models, it was found that, among the Savonius turbines, the most efficient is the one with 2 stages, helical blades and without a central axis.**

Keywords - wind energy, mini wind turbines, Savonius

Nomenclature

Symbol	Name	Units
A_p	Rotor projected area	[m^2]
C_p	Aerodynamic power coefficient	[adimensional]
C_m	Torque coefficient	[adimensional]
D_f	End plate diameter	[m]
I_g	Generator current	[A]
P_A	Aerodynamic power	[W]
P_V	Wind power	[W]
V_{air}	Air speed	[m/s]
V_{perif}	Peripheral speed	[m/s]
V_{tang}	Tangential speed	[m/s]
α_1	Aspect ratio	[adimensional]
D	Rotor diameter	[m]
H	Rotor height	[m]
M	Torsion moment	[m/s]
R_e	Reynolds number	[adimensional]
V	Air speed	[m/s]
d	Diameter of rotor half cylinder	[m]
e	Spacing between the two half cylinders	[m]
n	Rotation	[rpm]
β	Overlap ratio	[adimensional]
λ	Speed coefficient	[adimensional]
ρ	Air density	[kg/m^3]
ω	Angular speed	[rad/s]

I. INTRODUCTION

The world energy sector is the main responsible for the increase of carbon dioxide in the Earth's atmosphere, and in 2007 25% of the total greenhouse gases were emitted, due to the burning of coal, natural gas and oil. Thus, in order to favor economic growth, it is necessary to invest in alternative energy sources aimed at sustainable development [1].

For the generation of energy through the wind, wind turbines are used connected to an electric generator and when the system is rotated, the mechanical power can be converted into electrical power. [2]. Wind turbines are divided into horizontal axis wind turbines (HAWTs) and vertical axis wind turbines (VAWTs) [3, 4].

The HAWTs are more used nowadays because they are more efficient when compared to vertical axis turbines. However, the VAWTs have proven to be viable options due to their low production cost, independence from wind direction and wide applicability. The two main models of vertical axis turbines are Savonius and Darrieus [4].

ISBN: 978-86-80593-73-9

The Savonius turbine was developed after the 1929 crisis, with the increasing demand for new ways of producing electricity. It works by the aerodynamic principle of drag, having no airfoils, being formed by two opposite half channels, supported by a vertical axis [4].

In the 1930s, the Darrieus turbine was developed, operating on the principle of lift and drag from a wing. Its efficiency is similar to horizontal turbines, due to the presence of airfoils. When the moving air hits the blades, fixed to the ends of the deflector plates, a low pressure zone is generated. As the blade is fixed, the force of the wind causes the rotational movement of the set. [4].

Mechanical systems produce constant and artificial exhaust winds, thus producing a constant rotation in the VAWTs, which provides a uniform generation of electrical energy. [5].

Therefore, seeking to expand this approach, the aim of this work is to theoretically analyze the models of Savonius microturbines for a future application in small equipment.

II. SAVONIUS

The sizing of the wind turbines was based on a prototype developed at the Federal Institute of Science and Technology of São Paulo Campus Catanduva, Brazil, which was reduced to a 1:10 scale compared with an existing project that have the followings rotor dimensions: 186 mm high and 55 mm in diameter.

Prototypes printed on a 3D printer have 2 stages, each 90 mm high, as the increase in the number of these stages increases inertia and reduces dependence on the wind direction for the start of rotation. On the other hand, the excess of stages would decrease the aspect ratio and static torques [6].

Three “end plates” were used, or deflector plates with a diameter of 55 mm and 2 mm thick. Wind tunnel tests using 5 models of Savonius turbines found that the "end plates", which form an angle with the shells, provide improvements in efficiency [7]. Thus, the greater the number of deflector plates, the greater the number of fins, which detain the air, increasing the total drag force by up to 36% [8].

All 2-blade turbines were used, which increases the rotational speed, but also generates a reduction in efficiency [4]. Two models use conventional (straight) blades, which have an efficiency of approximately 10% if installed in a single stage. However, when the stages are overlapped the efficiency increases to 13%. Two other models used have helical-shaped blades that have an efficiency close to 18% in a single stage [9].

Savonius wind turbines are designed with the central axis completely blocking the air passage through the cavity of thickness "e" (Fig. 1). This generates better efficiency, while the turbine without the central shaft produces greater stability [10].

In the theoretical analysis of the Savonius rotor (Fig. 1), the equations of aerodynamic power $(\mathrm{P_A})$ and mechanical torque (M) are used [11]. The smallest value of $\mathrm{D_f}$ is 10% greater than the value of D [12].

A. *Aerodynamic Power* (P_A)

The aerodynamic power $(\mathrm{P_A})$ is determined using (1), derived from the Bernoulli Equation, where C_p corresponds to the aerodynamic power coefficient, ρ the air density, $\mathrm{A_p}$ the projected area of the rotor and V the air speed [11].

$$P_A = C_P \cdot \frac{1}{2} \cdot \rho \cdot A_P \cdot V^3 \ . \qquad (1)$$

The projected area (A_P) refers to the product of the diameter (D) by the height of the rotor (H), that is, $\mathrm{A_p = D \cdot H}$ . .

The values of the aerodynamic power coefficient C_p and the torque coefficient (C_m) are obtained graphically through Fig. 2.

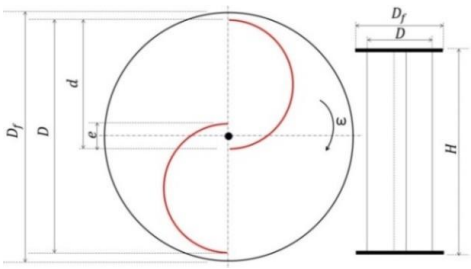

Figure 1. Built characteristics of the Savonius rotor.

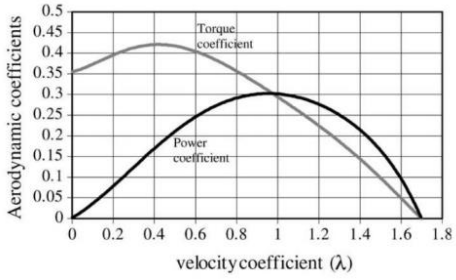

Figure 2. Value of C_p and C_m, as a function of λ [11].

The value of λ is obtained through the relation $\lambda = V_{tang} / V$, where $V_{tang} = \omega \cdot D / 2$. The power coefficient has its maximum value when $\lambda = 1$.

B. Torsion Torque (M)

Torsion torque is defined by the (2) [11].

$$M = C_m \cdot \frac{1}{4} \cdot \rho \cdot D \cdot A_P \cdot V^2 \ . \qquad (2)$$

Aspect ratio is an important characteristic of rotor efficiency and is defined as $\alpha_1 = H / D$. The best rotor power coefficient has a value of $\alpha_1 \approx 4,0$ [12].

The overlapping ratio [1] is calculated by $\beta = e / d$, where the best efficiency is between 20 and 30% [12, 14].

The aerodynamic power coefficient relates the aerodynamic power with the power available in the wind, expressed by the expression of $C_P = P_A / P_V$ [15].

The generator's theoretical electric current (I_g), for a voltage of 12V is defined by (3). where ω corresponds to angular velocity [16].

$$I_g = -0,0024 \cdot \omega^2 + 0,4138 \cdot \omega + 7,6 \ . \ (3)$$

III. RESULTS

The turbines were designed in Autodesk Inventor software and printed on a 400 x 400 x 400 mm 3D printer. The stages, were built

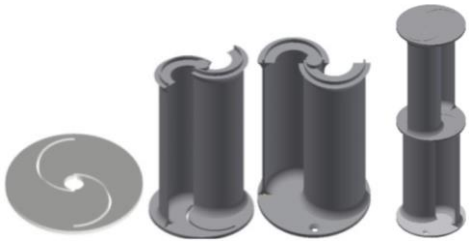

Figure 3. Assembly of the structure of the Savonius turbine with its 2 stages, straight blades and shaft.

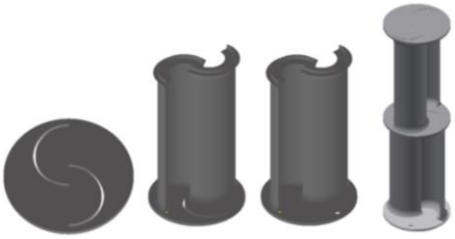

Figure 4. Assembly of the structure of the Savonius turbine with its 2 stages, straight blades and no shaft.

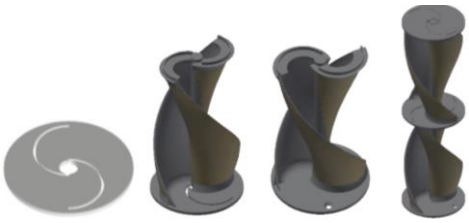

Figure 5. Assembly of the structure of the Savonius turbine with its 2 stages, helical blades and shaft.

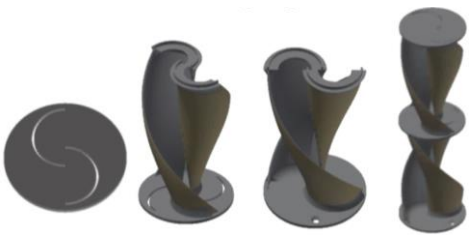

Figure 6. Assembly of the structure of the Savonius turbine with its 2 stages, helical blades and no shaft.

[1] The overlap ratio β in Savonius turbines is the ratio between the overlap of the blades "e" and their chord length (d). Thus, this is beneficial for the wind turbine due to the increase in pressure caused in the concave region of the return blade. However, it also generates pressure reduction in the concave region of the advance blade [13].

separately and fitted with fittings to enable coupling.

The Figs. 3-6 were based on the characteristics of the Fig. 1 with dimensions, $D_f = 55mm$, $D = 48,890\,mm$, $d = 30mm$ and $e = 9,9978\,mm$. The calculations were performed expressed in (1), (2) and (3).

The theoretical results for the two-stage Savonius rotors applied to this work, obtained through (1), (2) and (3) are presented in Table I.

It should be noted that due to the differences between one model and another, with the presence or absence of a central axis and the shape of the blades, the data obtained for the standard model of the Savonius turbine undergo minor changes, which cannot be measured theoretically. However, for comparison purposes, the most efficient blades are of the helical type [10] while turbines that do not have a central axis have a higher power coefficient [11].

IV. CONCLUSION

The present work sought to expand the application of vertical rotor wind turbines with the use of artificial winds from the development and analysis of computer-assisted designs of 6 models of micro aero generators.

TABLE I. THEORETICAL RESULTS FOR THE SAVONIUS ROTOR.

Re	20788,22
V_{air} [m/s]	5
V_{periph} [m/s]	5
ω [rad/s]	23.47
λ	0.12
Cp	0.043
Cm	0.378
P_E [W]	0.031
P_E (x2) [W]	0.063
M [N.m]	0.001
n [rpm]	224.11
β	30
I_g [A]	0.79

Through literature review and theoretical results of torque and mechanical power obtained, the different models of proposed Savonius turbines were analyzed. Thus, it was concluded that the Savonius model with greater efficiency is the one with 2 stages, helical blades and without a central axis.

The analysis carried out in this work is fundamentally theoretical, and to determine the viability of these types of turbines, other analyzes are needed, such as the applicability and economic analysis made from experimental models.

There are several lines of research that need further deeply study. It is suggested, therefore, the 3D printing and testing of the presented turbines, which must be coupled to a single-phase electric generator and the set installed at the outlet of a "split" model air conditioner. In this way, it will be possible to compare theoretical results with experimental data through electronic measurements using a Datalogger system.

ACKNOWLEDGMENENT

To the Federal Institute of Education, Science and Technology of São Paulo for the constant encouragement.

REFERENCES

[1] Arruda, H. B. O. (2018). Mapeamento das emissões de gases de efeito estufa em uma empresa do setor energético. *Conexões Ciência e Tecnologia, 12*(3), 108 – 118. [In Portuguese]

[2] Barros, M., & Varella, V. Fontes de Energia Renováveis: Geração Eólica [web page]. Available at: http://www.solar.coppe.ufrj.br/eolica/eol_txt.htm. [In Portuguese]

[3] Machado, C. F. F (2014). Projeto de uma turbina eólica de eixo horizontal. (Projeto de Graduação em Engenharia Mecânica não editada). Escola Politécnica, Universidade Federal do Rio de Janeiro, Rio de Janeiro. [In Portuguese]

[4] Silva, Neto, D. M. V. (2020). Princípios aerodinâmicos de uma turbina eólica de eixo vertical: características básicas das turbinas Savonius e Darrieus. (Monografia de Bacharelado em Ciência e Tecnologia). Universidade Federal Rural do Semi-Árido, Rio Grande do Norte. [In Portuguese]

[5] Fazlizan, A., Chong, W. T., Yip, S. Y., Hew, W. P., & Poh, S. C. (2015). Design and Experimental Analysis of an Exhaust Air Energy Recovery Wind Turbine Generator. Energies, *8*(7), 6566–6584.

[6] Bianchi, L. S., Beck, D., & Seidel, D. J. (2020). Influência do número de estágios no torque estático da turbina eólica Savonius. *Revista Thema, 17*(2), 309-317. [In Portuguese]

[7] Ogawa, T., & Yoshida, H. (1986). The Effects of a Deflecting Plate and Rotor End Plates on Performances of Savonius-type Wind Turbine. *Bulletin of JSME, 29*(253), 2115–2121.

[8] Utomo, I. S., Tjahjana, D. D. D. P., & Hadi, S. (2018). Experimental studies of Savonius wind turbines with variations sizes and fin numbers towards performance. *AIP Conference Proceedings, 1931*(1).

[9] Caser, E. S., & Paiva, G. M. (2016). Projeto aerodinâmico de uma turbina eólica de eixo vertical (TEEV) para ambientes urbanos. (Projeto de Graduação em

[10] Kothe, L. B. (2016). Estudo comparativo e numérico sobre o desempenho de turbinas Savonius helicoedal e de duplo-estágio. (Dissertação de Pós-graduação em Engenharia Mecânica). Universidade Federal do Rio Grande do Sul, Porto Alegre. [In Portuguese]

[11] Menet, J. L. (2004). A double-step Savonius rotor for local production of electricity: a design study. *Renewable Energy, 29* (11), 1843–1862.

[12] Purificação, L. S., & Fonte, R. B. D. (2012). Estudo de turbinas eólicas verticais com exemplo de dimensionamento de uma turbina eólica darrieus para aplicação em edifícios (Monografia de Bacharelado em Engenharia Mecânica). Universidade Federal do Espírito Santo,Vitória. [In Portuguese]

[13] Ushiyama, I., & Nagai, H. (1988). Optimum design configuration and performance of Savonius rotor. *Wind Engineering, 12* (1), 59–75.

[14] Bianchi, L. S., Beck, D., Seidel, & D. J. (2020). Influência da razão de sobreposição no torque estático da turbina eólica Savonius. *Holos, 36*(6), 1-13. [In Portuguese]

[15] Newman, B. G. (1974). Measurement on a Savonius rotor with variable gap. Proc Sherbrook University Symposium on wind energy, Sherbrook, Canada.

[16] Schetz, J. A., & Fuhs, A. E. (1996). Handbook of Fluid Dynamics and Fluid Machinery. Vol 3. New York: Wiley-Interscience.

Active and Reactive Powers Transmition Capacity of the Electrical Circuits with Uniform Distribution Parameters (long lines)

Mihail Chiorsac[1], Valentin Rimskii[2], Lilia Turcuman[3]

[1]Technical University of Moldova, Kishinev, Republic of Moldova, mkiorsak@mail.ru
[2,3]Institute of Power Engineering of Moldova, Kishinev, Republic of Moldova

Abstract—**Using the equivalent transformations of the telegraph equations, explicit formulas relating transmission capacity of the active and reactive powers from the source to receiver for long transmission electrical lines (electrical circuits with uniform distributed parameters) with sinusoidal and non-sinusoidal currents and voltages are obtained. The examples of the calculation of energy performance in not loaded and loaded modes of operation are given.**

Keywords – long transmission line, the telegraph equations

I. INTRODUCTION

In the educational and professional literature there is no single and strictly based approach for definition of the concept of reactive power transmission capacity, even for sinusoidal steady-state regimes, not to mention the transient processes.

According to the symbolic (vectors) method or Complex Amplitudes Method (CAM), full (apparent) power of the electrical power line S, can be decomposed into two orthogonal components and obtain their distribution along the entire line. However, it remains unclear what is meant by reactive power across a line, without resorting to its simplified representation in the form of lumped RLC – circuit [1-3].

Meanwhile, from the standpoint of mathematical physics, uncertainty in the interpretation of reactive power is easily removable. It is necessary, to take into account the fact, that the basic equations of the theory of linear circuits are of the hyperbolic type. For them, long ago the integral law of conservation of full electromagnetic energy are introduced. [4].

II. TRANSMISSION CAPACITY OF LINE IN SINUSOIDAL MODE

The transmission of electromagnetic energy on a long line by the well-known the telegraph Eqs. is described:

$$L\frac{\partial i}{\partial t}+\frac{\partial u}{\partial x}+Ri=0;\ C\frac{\partial u}{\partial t}+\frac{\partial i}{\partial x}+Gu=0, \quad (1)$$

where L, R, G and C – the specific passive parameters per unit of the line length. System (1) should be supplemented by the boundary and initial conditions. Let, the electric line at the initial time t=0 is connected to an external source of sinusoidal voltage, and to the receiving end is connected the load:

$Z_S = R_S + jX_S$ and $u = U_0 \cdot e^{j\omega t}$ at the beginning of line $(x=0)$. At the end of the line $u = Z_S i\ (x=l)$. By using the equivalent transformations in the complex function, the following integral identities are obtained.

Multiplying the first (1) by a conjugate to the function of current $i*$, and the second equation replacing by conjugate and multiply by u. If add up these two Eqs., will have

$$L\frac{\partial i}{\partial t}i^* + C\frac{\partial u^*}{\partial t}u + \frac{\partial}{\partial x}\left(ui^*\right) + Rii^* + Guu^* = 0$$

$$or\ L\frac{\partial i}{\partial t}i^* + C\frac{\partial u^*}{\partial t}u + \frac{\partial}{\partial x}\left(ui^*\right) + \quad (2)$$
$$+R|i|^2 + G|u|^2 = 0$$

Let to write one more expression conjugate to (2) and summer them:

$$L\frac{\partial i^*}{\partial t}i + C\frac{\partial u}{\partial t}u^* + \frac{\partial}{\partial x}\left(u^*i\right) + \quad . \quad (3)$$
$$+R|i|^2 + G|u|^2 = 0$$

Now, adding and subtract the relations (2) and (3). After simple transformations obtain two identities:

$$\frac{1}{2}\frac{\partial}{\partial t}\left(L|i|^2 + C|u|^2\right) + \frac{\partial}{\partial x}\left[\mathrm{Re}(ui^*\right] + \quad , \quad (4)$$
$$+R|i|^2 + G|u|^2 = 0$$

$$L\left(\frac{\partial i}{\partial t}i^* - \frac{\partial i^*}{\partial t}i\right) + C\left(\frac{\partial u^*}{\partial t}u - \frac{\partial u}{\partial t}u^*\right) + \quad . \quad (5)$$
$$+2j\frac{\partial}{\partial x}\left[\mathrm{Im}(ui^*\right] = 0$$

Assume, that in steady state mode at $t \to \infty$ the solution like as the input voltage, is a complex functions is represented:

$$u(x,t) = U(x)e^{j\omega t} \text{ and } i(x,t) = I(x)e^{j\omega t}.$$

If the effective values of voltages and currents given as $U(x) = |U(x)|e^{j\varphi_u(x)}$; and $I(x) = |I(x)|e^{j\varphi_i(x)}$, it is easy to see, that in this case

$$|u(x,t)| = |U(x)| \text{ and } |i(x,t)| = |I(x)|.$$

Then $Re(ui^*)$ from (4) and $Im(ui^*)$ from (5) may be expressed by active P and reactive Q power in the sense, as defined in [1-3]:

$$ui^* = |U(x)||I(x)|e^{j\varphi_u(x)}e^{-j\varphi_i(x)} = \quad ,$$
$$= |U(x)||I(x)|e^{j\varphi(x)}$$

$$\varphi(x) = \varphi_u(x) - \varphi_i(x),$$

$$\mathrm{Re}\left(ui^*\right) = |U(x)||I(x)|\cos\varphi(x) = P(x),$$

$$\mathrm{Im}\left(ui^*\right) = |U(x)||I(x)|\sin\varphi(x) = Q(x).$$

By substitute the expression $u(x,t) = U(x)e^{j\omega t}$ and $i(x,t) = I(x)e^{j\omega t}$ in (4) and (5) and integrate over x on the interval $0 \le x \le l$, after some transformations, can obtain the following Eq. of balance of active and reactive powers:

$$\int_0^l \left(R|I(x)|^2 + G|U(x)|^2\right)dx = P(0) - P(l). \quad (6)$$

and

$$\omega\int_0^1 \left(L|I(x)|^2 - C|U(x)|^2\right)dx = Q(0) - Q(l). \quad (7)$$

Thus, the left side in (6) and (7) determine respectively the active and reactive power of the long line. The calculations can continue using the calculated ratios of the complex amplitude method:

$$Z_0 = \sqrt{(R + j\omega L)/(G + j\omega C)},$$

$$\delta = \alpha + j\beta = \sqrt{(R + j\omega L)(G + j\omega C)},$$

$$Z_S = R_S + j\left(\omega L_S - 1/\omega C_S\right),$$

$$Z_{INP} = Z_0\frac{Z_S + Z_0 th(\delta l)}{Z_0 + Z_S th(\delta l)},$$

$$U_0 = Z_I I_0; \quad U_1 = Z_S I_1;$$

$$U_1 = U_0 ch(\delta l) - Z_0 I_0 sh(\delta l),$$

$$S = UI^* = P + jQ =$$
$$= |U||I|\cos\varphi + j|U||I|\sin\varphi.$$

Here, $\omega = 2\pi f$ – angular frequency; Z_0 – the complex wave (characteristic) resistance; δ, α, β – factors of distribution, attenuation and

phase; $Z_S.Z_{INP}$ – load and input impedances of circuit; U_0, I_0, U_1, I_1 – complexes effective values of voltages and currents at the beginning and end of the line length l; S – complex power with active P and reactive Q components.

The solution for every point x of the interval [0, l] is represented as:

$$\begin{aligned} U(x) &= U_0 \operatorname{ch}(\delta x) - Z_0 I_0 sh(\delta x); \\ Z_0 I(x) &= -U_0 sh(\delta x) + Z_0 I_0 ch(\delta x) \end{aligned}. \quad (8)$$

Substitute (8) into (6) and (7), integrate on x. After elementary transformations, we obtain explicit formulas, linking the power source, the receiver and long line:

$$\begin{aligned} 2|Z_0|^2 \left[P(0) - P(l)\right] &= \left(R + G|Z_0|^2\right) \frac{sh(\alpha l)}{\alpha} \text{x} \\ \text{x}\, &[\left(|U_0|^2 + |I_0 Z_0|^2\right) ch(\alpha l) - \\ &-2\text{Re}\left(U_0 I_0^* Z_0^*\right) sh(\alpha l)] + \\ &+\left(R - G|Z_0|^2\right) \frac{\sin(\beta l)}{\beta} \text{x} \\ \text{x}[&\left(|I_0 Z_0|^2 - |U_0|^2\right) \cos(\beta l) + \\ &+2\text{Im}\left(U_0 I_0^* Z_0^*\right) \sin(\beta l)]; \end{aligned}$$

$$\begin{aligned} \frac{2|Z_0|^2}{\omega} \left[Q(0) - Q(l)\right] &= \left(L - C|Z_0|^2\right) \text{x} \\ \text{x}\, &\frac{sh(\alpha l)}{\alpha} [\left(|U_0|^2 + |I_0 Z_0|^2\right) ch(\alpha l) - \\ -2\text{Re}&\left(U_0 I_0^* Z_0^*\right) sh(\alpha l)] + \left(L + C|Z_0|^2\right) \text{x} \\ \text{x}\, &\frac{\sin(\beta l)}{\beta} \text{x} \left(|I_0 Z_0|^2 - |U_0|^2\right) \cos(\beta l) + \\ &+2\text{Im}\left(U_0 I_0^* Z_0^*\right) \sin(\beta l)]. \end{aligned} \quad (9)$$

In the case of undistorted line

$$\begin{aligned} Z_0 &= Z_B = \sqrt{L/C}, \\ \delta &= (\gamma + j\omega)/a, \quad a = 1/\sqrt{LC}, \\ \gamma &= R/L = G/C \end{aligned}$$

and dependence (9) greatly are simplified

$$\begin{aligned} P(0) - P(l) &= sh(\gamma\Delta) \text{x} \\ \text{x}\Big[&(Z_B |I_0|^2 + |U_0|^2 / Z_B) \operatorname{ch}(\gamma\Delta) - \\ &-2\text{Re}\left(U_0 I_0^*\right) sh(\gamma\Delta)]; \\ Q(0) - Q(l) &= \sin(\omega\Delta) \text{x} \\ \text{x}\Big[&(Z_B |I_0|^2 - |U_0|^2 / Z_B) \cos(\omega\Delta) + \\ &+2\text{Im}\left(U_0 I_0^*\right) \sin(\omega\Delta)]. \end{aligned}$$

If the load consists only of active resistance, it is easy show that the reactive power at the receiving end of the line is zero and balance equation can be presented as:

$$\begin{aligned} P(0) - P(l) &= U_0^2 / Z_B \text{x} \\ \text{x}\, &\frac{\left(1 - e^{-2\gamma\Delta}\right)\left(1 + z^2 e^{-2\gamma\Delta}\right)}{1 + 2z_\gamma \cos(2\omega\Delta) + z_\gamma^2}, \\ Q(0) &= \frac{U_0^2}{Z_B} \text{x} \frac{z_\gamma \sin(2\omega\Delta)}{1 + 2z_\gamma \cos(2\omega\Delta) + z_\gamma^2}. \end{aligned}$$

$$z_\gamma = z e^{-2\gamma\Delta}; \quad z = \frac{R_S - Z_B}{R_S + Z_B}.$$

In case, when distortion-free line is connected to matched load $R_S = Z_B$, the reactive power at the beginning of line $Q(0) = 0$. The losses in the line are zero $(\gamma = 0)$, generated and transmitted active powers are coincided $P(1) = P(0)$.

For the presented transformations is difficult give a real physical meaning, but the important fact of getting the balance equation of power for the steady sinusoidal mode as a consequence of the initial system of equations (1). The concluding end formulas, even for the simplest special cases, also do not allow to clarify the nature of reactive power and give it to clear physical interpretation.

In [3] and other papers, physically is justified and only recognized the instantaneous power $p = iu$ and its average value as active power P. The reactive Q and apparent S powers are considers comfortable calculated values, that can in some way to characterize the energetic processes in the electrical circuits with sinusoidal currents and voltages. Therefore, let examine in a linear circuits with distributed and lumped

parameters the instantaneous voltages and currents, tracking them from the beginning of connecting switching time, i.e. with a zero initial state until the steady stage of electromagnetic waves. Such approach is justified and logical, since any steady state is always preceded non-stationary wave process. For this transient process from instantaneous power definitely, with physically meaning, can not be obtain one or more allocate reactive components.

Even for non-sinusoidal periodic mode, this problem is far from being resolved, although such attempts repeatedly been made by many authors [5-11].

III. Power Capacity of Line at Non-Sinusoidal Mode

For steady sinusoidal modes the active component of instantaneous power capacity is defined as its average value during the oscillation period. The reactive component can be calculated, for example, by the formula [3]:

$$Q = \frac{1}{\omega T}\int_0^T u\left(\frac{di}{dt}\right)dt = -\left(\frac{1}{\omega T}\right)\int_0^T i\left(\frac{du}{dt}\right)dt \ . \quad (10)$$

However, these and other similar formulas are apply only for the circuits with concentrated parameters and do not allow further generalizations for circuits with distributed parameters and in case of non sinusoidal currents and voltages. Therefore will use generally accepted approach in the theory of linear hyperbolic equations for obtain the integral of energy [4], which is valid for any kind of functions in condition that they are solutions of the original system (1). Using the standard procedure, let multiply the first (1) to *i*, the second − to *u* and add up the results:

$$Li\frac{\partial i}{\partial t} + i\frac{\partial u}{\partial x} + Ri^2 + Cu\frac{\partial u}{\partial t} + u\frac{\partial i}{\partial x} + Gu^2 = 0$$

or

$$\frac{1}{2}\frac{\partial}{\partial t}\left(Li^2 + Cu^2\right) + Ri^2 + Gu^2 + \frac{\partial}{\partial x}(iu) = 0.$$

Integrating this expression in the interval $0 \le x \le l, \quad 0 \le \tau \le t$ taking into account the zero initial conditions, have the following integral Eq.:

$$\int_0^T\int_0^l\left(Ri^2 + Gu^2\right)dxd\tau + \frac{1}{2}\int_0^l\left(Li^2 + Cu^2\right)dx = \\ = \int_0^T\left[i(0,\tau)u(0,\tau) - i(l,\tau)u(l,\tau)\right]d\tau \quad (11)$$

The left side of the equation of energy balance is the sum of its active (irreversibly transforming into heat) and reactive (reversible) components and the right side − the difference of energy between the source and the receiver. It is easy to verify, that all components in (11) have the dimension of J.

Thus, if the instantaneous currents and voltages are solutions of the system (1), then they also satisfy to conservation law (11).

With zero initial and boundary conditions, integral Eq. (11) only for the trivial solution $i \equiv u \equiv 0$ is satisfied. From that and Fredholm alternative, follow the proof of uniqueness the solution of the Eq. (11) if assumes its existence. If is knowing the spatial-temporal distribution of the voltages and currents on the line, from (11) irreversible losses of active power in the line is defined:

$$P(t) = \int_0^l\left(Ri^2 + Gu^2\right)dx \ , \quad (12)$$

the current total energy at time t > 0, storage in distributed reactive parameters of line is calculated by the formula:

$$W(t) = W_M(t) + W_E(t) = \\ = \frac{1}{2}\int_0^l\left(Li^2 + Cu^2\right)dx \quad . \quad (13)$$

After differentiation of relation (11) on time, obtain

$$\int_0^l\left(Ri^2 + Gu^2\right)dx + \frac{1}{2}\frac{d}{dt}\int_0^l\left(Li^2 + Cu^2\right)dx = \\ = i(0,t)u(0,t) - i(l,t)u(l,t)$$

or taking into account (12) and (13):

$$P(t) + \frac{d}{dt}W(t) = \\ = i(0,t)u(0,t) - i(l,t)u(l,t).$$

If now assume, that all the components here are periodic functions, then calculating the average values on interval [0, T] obtain

$$\frac{1}{T}\int_0^T P(t)\,dt+\frac{1}{T}\left[W(T)-W(0)\right]= \\ =\frac{1}{T}\int_0^T i(0,t)u(0,t)\,dt-\frac{1}{T}\int_0^T i(l,t)u(0,t)\,dt \quad . \tag{14}$$

If considering, $W(T)=W(0)$ obtain the equation of balance of active powers of generator, of load and long line

$$P_a=P(0)-P(l)=\frac{1}{T}\int_0^T P(t)\,dt \quad . \tag{15}$$

In particular, at steady sinusoidal mode with a period of $T=2\pi/\omega$:

$$(x,t)=U(x)\sin\left(\omega t+\varphi_u(x)\right),$$
$$i(x,t)=I(x)\sin\left(\omega t+\varphi_i(x)\right).$$

Here, $U(x)$ and $I(x)$ – effective values of amplitudes of voltage and current. The direct calculation of the integrals in (14) leads to the Eqs.:

$$P_a=\int_0^l\left[RI^2(x)+GU^2(x)\right]dx,$$
$$P(0)=I(0)U(0)\cos\varphi(0);$$
$$P(l)=I(l)U(l)\cos\varphi(l);$$
$$\varphi(x)=\varphi_u(x)-\varphi_i(x),$$

those coinciding with (6).

In order to obtain similar expressions for the reactive power to arbitrary periodic functions, let to differentiating on time the first equation (1) and multiply by *i*. Then the second expression let multiply by $\partial u/\partial t$ and summing up the results will obtain:

$$Li\frac{\partial^2 i}{\partial t^2}+i\frac{\partial}{\partial x}\left(\frac{\partial u}{\partial t}\right)+Ri\frac{\partial i}{\partial t}+ \\ +Cu\left(\frac{\partial u}{\partial t}\right)^2+\frac{\partial u}{\partial t}\cdot\frac{\partial i}{\partial x}+Gu\frac{\partial u}{\partial t}=0$$
$$or\ \ \frac{1}{2}\frac{\partial}{\partial t}\left(Ri^2+Gu^2\right)+Li\frac{\partial^2 i}{\partial t^2}+ \\ +C\left(\frac{\partial u}{\partial t}\right)^2+\frac{\partial}{\partial x}\left(i\frac{\partial u}{\partial t}\right)=0$$

Integrating this expression on interval: $0\le x\le l$:

$$\frac{1}{2}\frac{\partial}{\partial t}\int_0^l\left(Ri^2+Gu^2\right)dx+ \\ +\int_0^l\left[Li\frac{\partial^2 i}{\partial t^2}+C\left(\frac{\partial u}{\partial t}\right)^2\right]dx= \quad . \\ =i(0,t)\frac{du(0,t)}{dt}-i(l,t)\frac{du(l,t)}{dt}$$

The average values on interval [0, T]:

$$\frac{1}{T}\left[P(0)-P(l)\right]+ \\ +\frac{1}{T}\int_0^T\int_0^l\left[Li\frac{\partial^2 i}{\partial t^2}+C\left(\frac{\partial u}{\partial t}\right)^2\right]dxdt= \\ =\frac{1}{T}\int_0^T Li(0,t)\frac{du(0,t)}{dt}dt- \\ -\frac{1}{T}\int_0^T Li(l,t)\frac{du(l,t)}{dt}dt.$$

When $P(T)=P(0)$, differentiating those expression and using (10), will obtain the following equation of balance of reactive powers:

$$\frac{1}{T}\int_0^T\int_0^l\left[Li\frac{\partial^2 i}{\partial t^2}+C\left(\frac{\partial u}{\partial t}\right)^2\right]dxdt= \\ =-\omega\left[Q(0)-Q(l)\right]. \tag{16}$$

Applying in left side of (16) the formula for integration by parts, transform the double integral to the form:

$$\frac{1}{T}\int_0^T\int_0^l\left[Li\frac{\partial^2 i}{\partial t^2}+C\left(\frac{\partial u}{\partial t}\right)^2\right]dxdt=$$
$$\frac{1}{T}\int_0^T i\frac{\partial i}{\partial t}\Big|_{t=0}^{T}dx-$$
$$-\frac{1}{T}\int_0^T\int_0^l\left[L\left(\frac{\partial i}{\partial t}\right)^2-C\left(\frac{\partial u}{\partial t}\right)^2\right]dxdt.$$

Note, that for a periodic solution with period T $i\frac{\partial i}{\partial t}\Big|_{t=0}^{T}$ is equal to zero. Therefore, when the active load on the receiving end get zero, reactive power $Q(l)=0$.

Then from (16) get the right correlation of periodic solutions for any problems, linked the reactive power source, the receiver and the long line:

$$\frac{1}{\omega T}\int_0^T\int_0^l\left[L\left(\frac{\partial i}{\partial t}\right)^2-C\left(\frac{\partial u}{\partial t}\right)^2\right]dxdt=Q(0)-Q(l). \quad (17)$$

In the case of sinusoidal mode, get formula:

$$\omega\int_0^l\left[LI^2(x)-CU^2(x)\right]dx=Q(0)-Q(l), \quad (18)$$

coinciding with (7).

IV. Numerical Examples.

Let us consider numerical examples of the analysis of the energy characteristics of a long power transmission line in a constant mode with sinusoidal and non-sinusoidal currents and voltages. For simplicity and clarity, used dimensionless variables

$$L=C=Z_B=\lambda=a=T=f=1,$$

where λ is waver length of the line, and consider the line as undistorted line, for which it is easy to construct an exact solution, both in the transient and in the steady state with arbitrary voltage or current waveforms [12, 13]. Homogeneous line with the parameters $l=3\lambda/8; R=G=0,48$ l=3λ/8; R=G=0,48 instantly connected to source of sinusoidal voltage: $u=sin(2\pi ft)$, and the receiving end $x=l$ is closed on active resistance: $u=R_S i$. In this mode, reactive power of generator and transmission line coincide.

The lines with wave length $\lambda/8,\ 3\lambda/8,\ 5\lambda/8,\ldots$ are remarkable in that the active losses of idling mode calculated by the method of complex amplitude coincide with those in the case of a short circuit, and the reactive powers of the source (generator) in these degenerate modes are also equal to each other in absolute value, but opposite in sign. In the mode of natural power (traveling waves), realized at R_S=1, the reactive power is zero. It is generally accepted that in this case the line is balanced in terms of reactive power [10, 11].

As noted earlier, for any steady state mode is preceded by transient wave process, and therefore their calculation will be carried out in the same sequence, as is the case in reality. Fig. 1 shows the time variation of full power of source $S_0(t)=i(0,t)u(0,t)$ and instantaneous losses of active power in the line $P(t)$ (curves 1, 2) from the switching time at variations load resistance $R_S=\infty(a);\ 0(b);\ 1(c)$. Constant, marked as number 3 corresponds active component as difference in power source and the receiver calculated by CAM, which is exactly the same as the mean steady-state value calculated by (15): $P_a=0{,}1726(a);\ 0{,}1726\ (b);\ 0{,}1512\ (c)$.

For a numerical analysis of exchange electromagnetic processes between a sinusoidal voltage source and a line with distributed reactive resistances. In fig. 2 (curves 1, 2), the instantaneous powers $Q_M(t)$ and $Q_E(t)$ of the magnetic and electric field of the line for the variations in load are presented. They were calculated as the time derivatives from the energy functions $W_M(t)$ and $W_E(t)$ (curves 1, 2). By number 3 marked the reactive power of source, defined by the CAM, which exactly coincides with the value obtained by the formula (18) for sinusoidal currents and voltages.

Noticeable full match, i.e. zero imbalance between the instantaneous power of electric and magnetic field at work of distorting lines on a coherent load is R_S=1. More difficult is the case when the amplitudes and phases of the instantaneous powers does not match not only

the transient mode but also the steady state. For example, the reactive power at beginning of the line in mode $Q_0 = 0,4693$ (curve 3, Fig 2a) and $Q_0 = -0,4693$ 0in short circuit (s.c.) mode (curve 3, Fig. 2b), means that in the first case the power of the magnetic field prevails the electric field of the power line, whereas in the second embodiment, the situation is opposite. The graphs on the marked illustrations show confirmation, that the corresponding periodic functions changed the signee of their amplitudes.

Fig. 3 shows the dynamic of the total power of source and losses of active power for the mode of short-circuit line (curves 1, 2) when $R = 0; G = 0,48\,(a);\ 0\ (b)$. Constant, marked by number 3, correspond to $P_a = 0,1082\ (a); 0,0\,(b)$.

On the Fig. 4, the instantaneous powers of electric and magnetic fields at the short circuit mode of the line are given. Constants $Q_0 = -0,4606\ (a); Q_0 = -0,5\ (b)$ marked as 3, correspond defined by (18). Solutions for the listed variants in steady state mode of the line are periodic piece-wise sinusoidal functions (see Fig. 5) and CAM is not already applicable in principle.

If the irreversible losses of active power in line still can be characterized by its mean value, the imbalance between the instantaneous capacity of magnetic and electric fields of electrical line defined by (18) as a single real number , is unlikely to provide comprehensive information about of the transient processes in the electromagnetic circuit.

When comparing the curves in Fig. 2b and Fig. 4, it is easy to see, that character of variation in time of magnetic and electric fields of shorted line in qualitative and quantitative terms, quite differently, while the integral characteristics those as the value of reactive power (18) differ only in the second or in the third significant part of the digits.

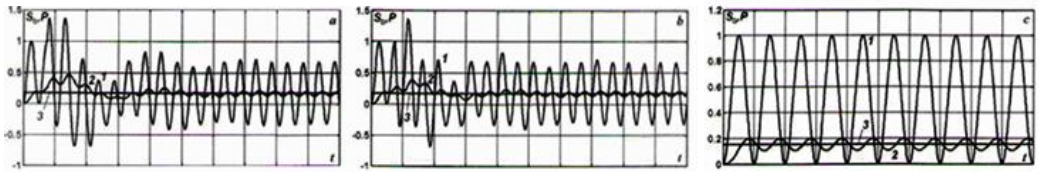

Figure 1. The dynamics of the full power of the source and loss of the active power in the line (curves 1.2) at $R = G = 0,48$ and variations of the load resistance $R_S = \infty$ (a);0 (b); 1 (c).

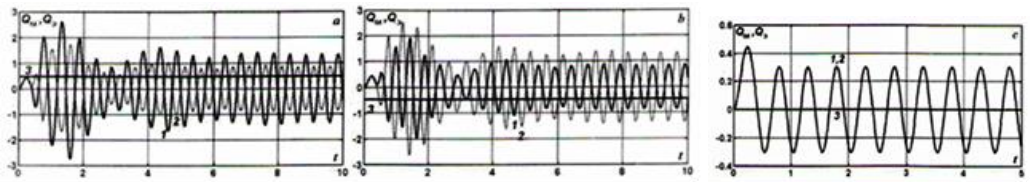

Figure 2. The instantaneous powers of the magnetic and electric field of the line for the variations in load resistance: $R_S = \propto$; 0 (b); 1 (c)

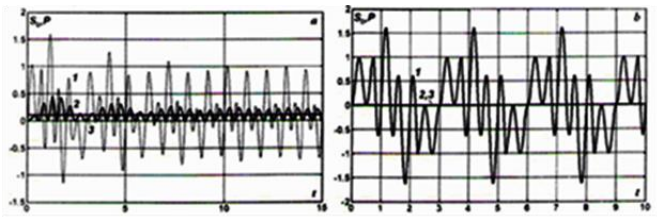

Figure 3. Dynamics of the full power of the source and the active power losses of the short-circuited line (curves 1: 2) at: $R = 0; G = 0,48\ (a); 0\ (b)$.

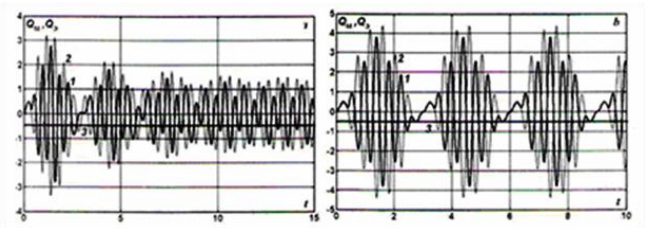

Figure 4. The instantaneous powers of the magnetic and electric field of short-circuited line (curves 1 and 2) when $R = 0; G = 0{,}48\ (a); 0\ (b)$.

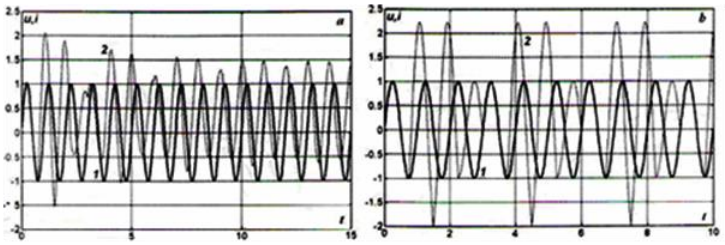

Figure 5. The instantaneous voltages and currents (curves 1, 2) it the input of shorted line when: $R = 0; G = 0{,}48\ (a); 0\ (b)$.

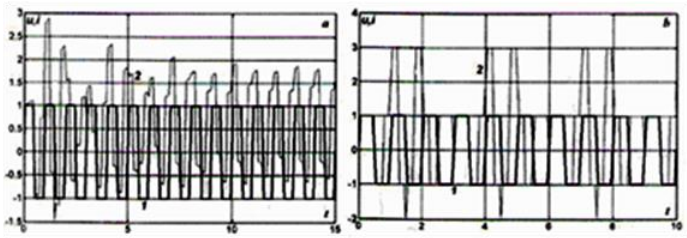

Figure 6. The instantaneous voltages and currents (curves 1, 2) at the input short-circuited line when: $R = 0; G = 0{,}48\ (a); 0\ (b)$.

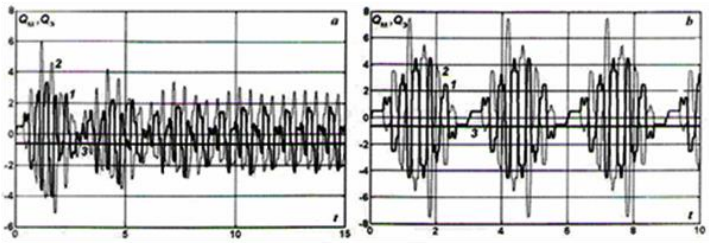

Figure 7. The instantaneous powers of the magnetic and electric fields of shorted line (curves 1, 2) when: *R*=0; *G*=0,48 (a); 0 (b).

If set the input voltage in the form of trapezoid, pretty close to a rectangular shape (Fig. 6), the corresponding values of reactive power somewhat increase: $Q_0 = -0{,}626\ (a)$; $Q_0 = -0{,}636\ (b)$ but the differences between them, as can see, is still quite small (Fig. 7). For periodic input voltages triangular form, the reactive power in these cases halved twice: $Q_0 = -0{,}314\ (a)$; $Q_0 = -0{,}318\ (b)$.

When the generation and transport of large flows of energy in multiphase electrical transmission line the situation of reactive power is much more complicated, than in the above simple examples. Even more difficult to properly assess not stationary balance between the

capacity of magnetic and electric fields in the transition process during such events as short circuit or the sudden off out of the load or her increasing etc. It is obvious that for an adequate description of electromagnetic processes and phenomena in real electrical long lines, must still use the instantaneous capacity of magnetic and electric fields of line.

V. CONCLUSION

1. In this work, on the basis of the law of conservation of energy, strict and adequate expressions for the definition and interpretation of the physical meaning of active and especially reactive power for a long power transmission line were obtained. both in stationary and in transient modes with various forms of periodic changes in the applied voltage

2. It is shown, then the energy characteristics of the unsteady mode and stationary transmission of energy along a long electric line should be analyzed on the basis of the exact spatial and temporal distribution of currents and voltages along the entire line

3. The above expressions and the results of a numerical example of determining the instantaneous power of the magnetic and electric fields of a long electric line give a mathematically accurate and physically reasoned idea of the processes of continuous two-way exchange of electromagnetic energy between the source and the distributed parameters of the line and load.

REFERENCES

[1] Krut, K.A. (1936). Osnovy electritehniki. L: OHTI,

[2] Bessonov, L. A. (1984). Teoreticheskie osnovy electritehniki. Electricheskie tsepi, Uchebnic dlea VTUZov. Vysshaia shkola. M.

[3] Krogheris, A.F., Rannimi, K.K., Treimanis, E.P. et al., (1993). Moschnosti peremennogo toka. Fiz.energ. inst. Latv. AN, Riga.

[4] Samarskii, A.A., (1974). Vvedenie v teoriu raznostnyh shem. Nauka, Moskva.

[5] Demircean, K. S., (1984). Reaktivnaia ili obmennaia moschnosti *Izvestia Akademii nauk SSSR, Energhetika i transport, 2*, 66-72.

[6] Zharkov, F.P., (1984). Ob odnom sposobe opredelenia reactivnoi moschnost. *Izvestia Akademii nauk SSSR, Energhetika i transport, 2*, 73-81.

[7] Demnrchean, K.S., (1992). Reaktivnaia moschnosti na sluchai nesinusoidalinyh funktsii. *Izvestia Akademii nauk RF Energhetika, 1*, 3-18.

[8] Demnrchean, K.K., (1994). Razlojenie mgnovennoi moschnosti na sostavleaiuschie. *Izvestia Akademii nauk РФ Энергетика, 5*, 73-79.

[9] Agunov, M.V., & Agunov, A.V., (2005). Ob energheticheschih sootnosheniah v electricheskih tsepeah s nesinusoidalinymi rejimami. *Elektrichestvo, 4*, 53-56.

[10] Aleksandrov, G. N., (2006). Priroda reaktivnoi moschnosti liniy elektroperedachi. *Trudy SPbGTU, Elektroenergheticheskoe oborudovanie: nadejnosti i bezopasnosti, 501*, 100-109.

[11] Aleksandrov, G. N., (2007). Peredacha electricheskoi energhii. Izd-vo Politehnicheskogo universiteta, Sankt Peterburg.

[12] Patsiuc, V.I., (2008). The no sinusoidal voltages under the sinusoidal current at the entry of the open–ended line with real loss. *Problems of the reghional energhetics, 3*(8), 52-67.

[13] Rimskii, V.S., Berzan, V.P., Patsiuc, V.I. et al. (2008). Volnivye iavlenia v neodnorodnyh strukturah. T.5. In *Teoria i metody raschiota elektricheskih penei, electromagnitnyh polei i zaschitnyh obolochek AES*. Tipografia ANM, Kishinev.

Optimal Decentralized Adaptive Under Frequency Load Shedding Based on RoCoF and Voltage Deviation

Souheil Saboune[1], Ahmed Tiguercha[2], Ahmed Amine Lajdici[3]

[1,2,3]Dept. of electrical engineering University of Houari Boumedien, Algiers, Algeria, ssaboune@usthb.dz[1], ahmed.tiguercha@usthb.edu.dz[2], medamine.ladjici@usthb.edu.dz[3]

Abstract—**the main objective of the electricity supplier is to provide this energy, in high quality, continuously 24 hours a day, 7 days a week in order to satisfy customer demand. To ensure this, two parameters, voltage and frequency, must be constant and maintained within acceptable levels. Under frequency load-shedding still remains the last issue to allow the system to operate within its security limits. The current paper investigates the use of fuzzy logic method for optimal adaptive decentralized under frequency load shedding (UFLS) using Rate of Change of Frequency (RoCoF), Voltage deviation to calculate the optimal amount and location of load shedding, then ROCOF and Rate of Change of Voltage (ROCOV) are used to determine the load shedding thresholds and load amount to be shed. To test the effectiveness of the proposed UFLS scheme, different simulations scenarios have been successfully performed in the IEEE 39-bus system. Simulation results show that the proposed approach can shed optimal adaptive loads, comparing with the conventional load shedding.**

Keywords - under frequency load shedding (UFLS), adaptive decentralize scheme, fuzzy logic algorithm, under voltage angel deviation, RoCoF

I. INTRODUCTION

In the context of stable operation of the electricity grid, the system is maintained in equilibrium by providing a generated power that meets the load demand, under this balanced condition, the system will operate at the synchronization frequency of 50 or 60 Hz.

In the event that the equilibrium is disrupted, for example, the loss of a generator or a line, the production capacity decreases while the load demand remains constant. If the other generators in the system are not able to supply the necessary power from the rotating reserve, the frequency begins to decrease and may lead to grid crashes [1, 2]. Major of disturbance which cause the blackout are complex and combinations of frequency and voltage instability from a deficit in active and reactive power. Consequently, the improvement of protection schemes has become a very important issue for the safety of the power system. Under frequency Load shedding UFLS is the last resort to preserve the frequency stability of the power system following major disturbances [3–5].

The major failing of the conventional UFLS is fail to protect the power system against combination disturbance causing frequency drop and sever voltage decline [6]. To improve the adaptability of the UFLS schemes, various algorithms have been proposed in the literature. Several of these algorithm use the rate of change of frequency (RoCoF) to estimate the amount of load to be shed [4-8].

The work carried out in [9] advocates to determine the frequency sensitive (FS) and frequency droop (FD) relays off line using frequency and rate of change of frequency (ROCOF) information under an abnormal condition. Other research considered the voltage magnitude information in the UFLS algorithms [5, 10–12]. Authors in [10], proposed a scheme use frequency and voltage together to select appropriate amount of load to be shed to preserve power system instability. Reference [13] concentrates to find the location of load shedding based on voltage stability risk index which is

ISBN: 978-86-80593-73-9

calculated for each load using real time data of voltage assumed to be available from the synchrophasor.

This work investigate the use of fuzzy logic controller for adaptive decentralized under frequency load shedding using the rate of change of frequency and voltage deviation index. The proposed scheme benefits from locally measured of frequency and voltage:

a) Does not require a communication system like centralized load shedding methods [5].

b) Calculate the optimal load shedding thresholds and load amount to be shed.

Performance of the proposed load shedding is tested on the simulated model for various disturbances. The obtained results are compared with the conventional scheme.

The paper is organized as follows: the conventional under frequency load shedding (UFLS) and proposed scheme using voltage deviation and ROCOF procedure are described in Section II. The simulation results are discussed in Sections III. Finally, the paper is concluded in Section IV

II. UNDERFREQUENCY LOAD SHEDDING

Load shedding is the temporary shutdown of electricity supply (power outage) to some end customers in certain parts of the grid. This action restores the balance between electricity supply and demand, which would avoid a collapse of the system (blackout). If load shedding is to be carried out, several parameters must be taken into consideration, the most important ones are:

- frequency and Voltage assured in permissible range,
- load quantities and placement to be shed,
- Various frequency thresholds and the number of load shedding levels.

The weaknesses of the conventional under frequency load shedding are the adaptability for combinations disturbance, such frequency droop and voltage declines (generator and transmission line outages, over load). These disturbances can eventually drive the power system to blackout through a voltage and frequency instability process.

According to [14], the voltage instability is a local phenomenon, and if it is not stopped in time by control actions, it can spread to the rest of the network. Since the frequency is measured locally at the load buses is the same throughout the network, the area of voltage instability can be detected only by the voltage value.

A. Proposed Under Frequency Load Shedding

In the proposed decentralized UFLS, the bus voltage, frequency and rate of change of frequency ROCOF are associated in the UFLS process by implementation the load shedding decision based of measured frequency, ROCOF and voltage at the relay location. In this way, the amount and location of load shedding are influenced by the ROCOF and voltage magnitude at each bus of the power system. Hence, the voltage decline side of the combination disturbance are involved in determining the amount and location of load shedding besides the frequency droop side [15].

The ROCOF is an instantaneous indicator of the deficit between production and consumption, it brings speed to the load shedding scheme to stop the drop in frequency [16]. Due to the complex dynamics of the power grid, the frequency profile during faults is non-linear and does not follow regular patterns. To solve this problem, some relays provide the function of monitoring the average rate of frequency change [17].

$$\frac{df}{dt} \approx \frac{f_i(t) - f_i(t-\Delta t)}{\Delta t} , \qquad (1)$$

where f_i is the frequency in bus i , Δt is the step of integration.

The voltage instability is a local phenomenon; it can spread to the rest of the electrical system if it is not stopped by control actions in time. They can be detected on the basis of local voltage measurement [14]. The voltage deviation is calculated as in (2), separately for each bus where the load shedding relay is installed:

$$VD_i = V_i - 1 , \qquad (2)$$

where VD_i and V_i , are the voltage deviation and voltage at bus i .

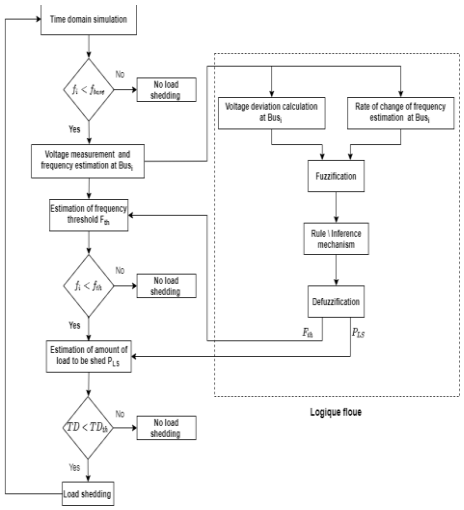

Figure 1. Adaptive fuzzy logic controller organization chart.

The schemes proposed uses fuzzy logic control approach to shed the amount of load. The controller measures the frequency, ROCOF and the voltage locally in each bus where the load is located. The frequency measurement is used to activate the load shedding thresholds, if the frequency is less than a predetermined threshold, the load shedding process activates Fig. 1. The fuzzy logic controller shed an adaptive amount of load for each threshold using the ROCOF and voltage deviation.

The Takagi Sugeno model is used in this work, see [18]. It consists of three main components, fuzzification, rule, inference mechanism and defuzzification. Fuzzification is the process of converting digital input into a fuzzy set using the membership function which determines how much a certain variable belongs to a predefined class. The rules are defined by the designer experience and the nature of the application. The rules in the fuzzy inference system mechanism proposed by Takagi and Sugeno as:

$$\begin{cases} if & x_1 = A_{1i} \\ and & x_2 = A_{2i} \end{cases}, then \quad y = f(x_1, x_2)\ . \quad (3)$$

Finally, defuzzification is carried out by which the rules applied are transformed into net consequences Fig. 2.

The proposed fuzzy logic controller for adaptive under frequency load shedding, has two inputs and two output. The rate of change of frequency (ROCOF) and voltage deviation (VD) are considered as inputs, the load shedding thresholds and the amount of load to be shed are considered as the outputs. Here, the input is fuzzified according to the membership functions as show in Fig. 3. For each input, five linguistic variables are defined as more vulnerable to invulnerable. However, for the outputs variable, the membership functions are constant.

The proposed decentralized load shedding scheme has two objectives.

1) The first is to adapt the load shedding frequency thresholds of the busses according to the disturbance importance. The closed bus to the fault area shed before the farther away by [0.1-0.3Hz].

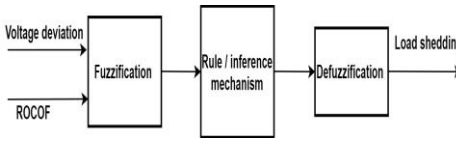

Figure 2. Fuzzy load shedding controller block diagram.

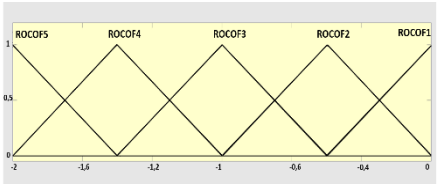

a) Rate of change of frequency ROCOF

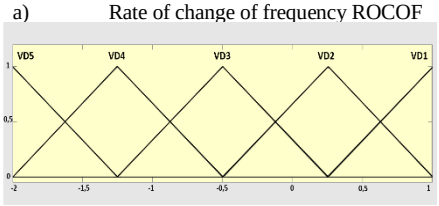

b) Voltage deviation.

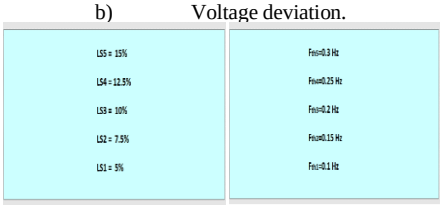

c) Load shedding and threshold.

Figure 3. Membership function input and output of FLC.

2) The second one is to adapt the power to be shed according to the degree and location of the disturbance.

III. SIMULATION RESULTS

For this study, the test network used is the IEEE-39 bus as show in Fig. 4. For the time domain simulation, the fourth order model of the synchronous machine is used for all generators. The machines are equipped with standard regulators IEEE, AVR-1IEEEX1 for the automatic voltage regulator and GOV-IEEESGO for the governor.

The frequency and voltage dependency of active and reactive load characteristics in term of different type of loads is represented by the exponential model in (4) and (5), see [17]:

$$P_L = P_{L0}\left(\frac{V}{V_0}\right)^{pv}\left(\frac{f}{f_n}\right)^{pf}, \qquad (4)$$

$$Q_L = Q_{L0}\left(\frac{V}{V_0}\right)^{qv}\left(\frac{f}{f_n}\right)^{qf}, \qquad (5)$$

where PL and QL are the active and reactive power of load.

Moreover, the appropriate parameters and the divide of different types of load are given in Table I.

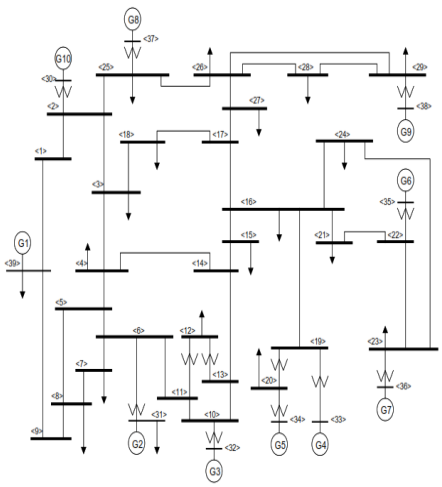

Figure 4. The 39-bus IEEE standard test system.

TABLE I. VOLTAGE AND FREQUENCY LOADS DEPENDENCY.

Load type	***Share (%)***	***pv***	***pf***	***qv***	***qf***
Light bulb	10	1.6	0.0	0.0	0.1
Fluorescent bulb	20	1.2	-1	3	-2.8
Asynchronous motor	70	0.1	2.8	0.6	1.8

TABLE II. FREQUENCY SETTINGS OF THE CONVENTIONAL AND SEMI-ADAPTIVE UFLS SCHEME.

Step	***F* setting (Hz)**	**Amount of load shedding (%)**			**delay(s)**
		Conventional	***Semi-adaptive***		
1	59.5	7.5	ROCOF < 0.2	7.5	0.3
			0.2 < ROCOF < 0.4	8.5	0.3
			0.4 < ROCOF < 0.6	9.5	0.3
			ROCOF > 0.6	10.5	0.3
2	59.2	7.5	7.5		0.3
3	58.9	7.5	7.5		0.3
4	58.6	7.5	7.5		0.3

To assess the effectiveness of the proposed schemes, two scenarios are applied with severe contingencies such as, the cascades of events (overload, loss of transmission line, and loss of a multiple generator) and the results are compared to conventional and semi adaptive UFLS scheme.

In the conventional scheme, for each threshold a fixed load is shed, but in the case of the semi-adaptive scheme, by locally measuring the ROCOF, adapts the amount of load to be shed according to the severity of the event only in the first threshold. The thresholds and the amount of load to be shed for the conventional and semi-adaptive UFLS schemes are shown in Table II. The permissible voltage and frequency ranges in steady state are [0.95 - 1.05] (*pu)* for voltage and [59.8- 60.2] Hz for frequency.

A. Scenario 1 :

In the first scenario, at *t=2s*, a loss of generator G3 (650 MW) with the disconnection of lines 3-4 and 4-15 was simulated.

After the disconnection of the G3, the first load shedding threshold is activated for the three schemes, after which the frequency returns to the safety margin by shedding an amount of 460MW

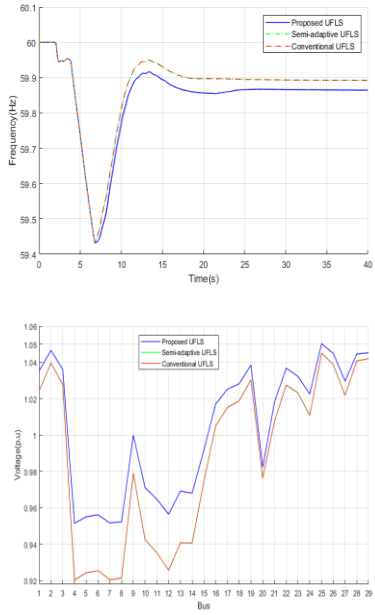

Figure 5. Frequency and voltage comparison for scenario 1.

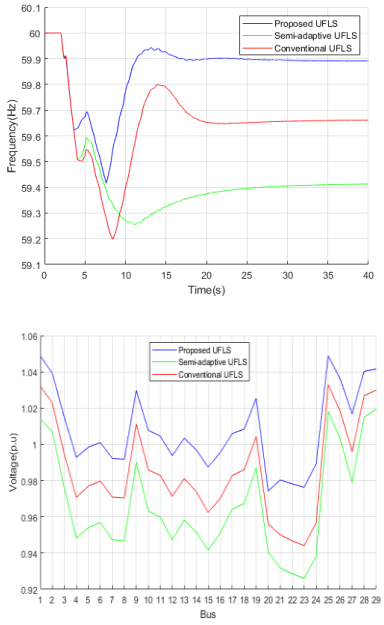

Figure 6. Frequency and voltage comparison for scenario 2.

for the conventional and semi-adaptive scheme and 452MW for the proposed scheme, see Fig. 5.

Fig. 5 shows the comparison between the frequency and voltage simulation results during 40s of time simulation, for the three schemes. For this scenario, one load shedding thresholds are activated; note that for the proposed load shedding, the frequency returns the acceptable range same than conventional load shedding has a greater load, but with a lesser quantity.

Following the disconnection of the generator G3 and lines 3-4 and 4-15, we saw the appearance of a significant voltage drop in nodes 4-8, which is due to the reactive energy deficit, see Table III.

B. Scenario 2

The second scenario consists of the cascade of two events. Loss of generator G6 and line 16-24, at *t=2s* followed by the loss of generator G5 and line 16-21, at *t=5s*.

After the loss of Gen6 and Gen7, an active power deficit of 1158MW is created. Two load shedding thresholds are triggered for the conventional scheme by shedding a load quantity of 886MW, while for the semi-adaptive scheme only one threshold is triggered by shedding a load quantity of 595MW. Both schemes fail to stabilize the frequency within the permissible range, however in the proposed scheme two load shedding thresholds are activated by shedding an 1105MW with triggering thresholds higher than the conventional scheme between 59.73Hz and 59.61Hz, see Fig. 6 and Table III. Proposed scheme, make quickly decision to bring frequency into safe limits.

When comparing the bus voltages near the fault areas, the conventional and semi-adaptive load shedding schemes fail to stabilize the voltages within their allowable limits. In contrast, the proposed load shedding scheme stabilizes these voltages by shedding a sufficient amount of load at these nodes, see Table IV.

By comparing the different scenarios, we can see that, the fuzzy adaptive load shedding controller, offers a better performance in terms of power system security compared to conventional one, because the proposed scheme adapts to each event, and sheds a sufficient amount of load based on the rate of change of frequency (ROCOF) which is an instantaneous indicator of the deficit between the power generated and consumed, and the voltage deviation of each node which indicates the security level of the voltage, therefore the load to be shed is different for each bus of the system.

TABLE III. FREQUENCY SETTINGS OF THE CONVENTIONAL AND SEMI-ADAPTIVE UFLS SCHEME.

Bus	Scenario 1		Scenario 2			
	Fth1 (Hz)	*LS (%)*	*Fth1 (Hz)*	*Fth2 (Hz)*	*LS(%)*	*LS(%)*
3	59.5	5,8	59.69	59.39	10.23	9.23
4	59.65	15.0	59.64	59.39	8.28	9.13
7	59.65	14.0	59.64	59.39	8.31	9.37
8	59.65	14.0	59.64	59.39	8.31	9.32
15	59.5	6.0	59.64	59.41	8.25	8.27
16	59.5	5.7	59.64	59.42	9.03	8.44
18	59.5	5.7	59.70	59.40	10.42	8.98
20	59.5	5.2	59.62	59.38	8.83	9.70
21	59.5	5.2	59.73	59.45	15	15
23	59.5	5.2	59.64	59.44	15	15
24	59.5	5.6	59.67	59.47	15	15
25	59.5	5.7	59.65	59.38	9.40	10.70
26	59.5	5.9	59.67	59.41	9.79	10.92
27	59.5	5.8	59.69	59.38	10.17	8.83
28	59.5	5.8	59.63	59.37	9.38	10.42
29	59.5	5.7	59.61	59.37	9.20	10.12
39	59.5	5.1	59.64	59.37	8.89	9.86

TABLE IV. FREQUENCY SETTINGS OF THE CONVENTIONAL AND SEMI-ADAPTIVE UFLS SCHEME.

Scenarios	Method	Load shed (Mw)	V_{min} (p.u)	V_{max} (p.u)	Steady state freq. (Hz)
Scenario 1	*Proposed UFLS*	450	0.952	1.05	59.86
	semi-adaptive UFLS	460	0.92	1.01	59.89
	Conventi-onnal UFLS	460	0.92	1.01	59.89
Scenario 2	*Proposed UFLS*	1105	0.97	1.05	59.89
	semi-adaptive UFLS	595	0.92	1.01	59.41
	Conventi-onnal UFLS	886	0.94	1.032	59.66

IV. CONCLUSION

Several scenarios are tested which affect the voltage and frequency stability simultaneously. The conventional load shedding scheme fails to provide appropriate action against such disturbance. In this paper we used fuzzy logic for an adaptive UFLS using the voltage deviation as an indicator of voltage stability. In addition, the effectiveness of the proposed approach has been shown in preventing total collapse of the power system:

1- by shedding a sufficient amount of load to correct the frequency fluctuation

2- by shedding in the appropriate location for the voltage drop part.

ACKNOWLEDGMENT

This work, was supported by the "Direction Générale de la Recherche Scientifique et du Développement Technologique" (DGRSDT).

REFERENCES

[1] Shekari, T., Aminifar, F., & Sanaye-Pasand, M. (2015). An analytical adaptive load shedding scheme against severe combinational disturbances. *IEEE Transactions on Power Systems*, *31*(5), 4135-4143.

[2] Abedini, M., Sanaye-Pasand, M., & Azizi, S. (2014). Adaptive load shedding scheme to preserve the power system stability following large disturbances. *IET Generation, Transmission & Distribution*, *8*(12), 2124-2133.

[3] Klaric, M., Kuzle, I., & Tomisa, T. (2005, June). Simulation of undervoltage load shedding to prevent voltage collapse. In *2005 IEEE Russia Power Tech (pp. 1-6)*. IEEE.

[4] Terzija, V. V. (2006). Adaptive underfrequency load shedding based on the magnitude of the disturbance estimation. *IEEE Transactions on power Systems*, *21*(3), 1260-1266.

[5] Hoseinzadeh, B., Da Silva, F. M. F., & Bak, C. L. (2014). Adaptive tuning of frequency thresholds using voltage drop data in decentralized load shedding. *IEEE Transactions on Power Systems*, *30*(4), 2055-2062.

[6] Darebaghi, M. G., & Amraee, T. (2017). Dynamic multi-stage under frequency load shedding considering uncertainty of generation loss. *IET Generation, Transmission & Distribution*, *11*(13), 3202-3209.

[7] Rudez, U., & Mihalic, R. (2010). Monitoring the first frequency derivative to improve adaptive underfrequency load-shedding schemes. *IEEE Transactions on Power Systems*, *26*(2), 839-846.

[8] Rudez, U., & Mihalic, R. (2009). Analysis of underfrequency load shedding using a frequency gradient. *IEEE transactions on power delivery*, *26*(2), 565-575.

[9] Ahsan, M. Q., Chowdhury, A. H., Ahmed, S. S., Bhuyan, I. H., Haque, M. A., & Rahman, H. (2011). Technique to develop auto load shedding and islanding scheme to prevent power system blackout. *IEEE transactions on Power Systems*, *27*(1), 198-205.

[10] Seyedi, H., & Sanaye-Pasand, M. (2008). New centralised adaptive load-shedding algorithms to mitigate power system blackouts. *IET generation, transmission & distribution*, *3*(1), 99-114.

[11] Ghaleh, A. P., Sanaye-Pasand, M., & Saffarian, A. (2011). Power system stability enhancement using a new combinational load-shedding algorithm. *IET generation, transmission & distribution*, *5*(5), 551-560.

[12] Saffarian, A., & Sanaye-Pasand, M. (2010). Enhancement of power system stability using adaptive combinational load shedding methods. *IEEE Transactions on Power Systems*, *26*(3), 1010-1020.

[13] Seethalekshmi, K., Singh, S. N., & Srivastava, S. C. (2011). A synchrophasor assisted frequency and voltage stability based load shedding scheme for self-healing of power system. *IEEE Transactions on Smart Grid*, *2*(2), 221-230.

[14] Shankar, R., & Kundur, P. (1994). *Power system stability and control II*. New York, McGraw-Hill Books (p. 581).

[15] Saboune, S., Ladjici, A. A., & Tiguercha, A. (2018). Optimal adaptive under frequency load shedding using Neuro-Evolution Algorithm. In *2018 International Conference on Electrical Sciences and Technologies in Maghreb (CISTEM) (pp. 1-4). IEEE.*

[16] Power, I. (2007). IEEE Guide for the Application of Protective Relays Used for Abnormal Frequency Load Shedding and Restoration.

[17] Saboune, S., Ladjici, A. A, & Tiguercha, A. (2021). Adaptive decentralized fuzzy logic-based underfrequency load shedding to enhance power system stability. *Int Trans ElectrEnerg Syst.*, *31*(11), e13087. doi:10.1002/2050-7038.13087

[18] Haidar, A. M., Mohamed, A., & Hussain, A. (2010). Vulnerability control of large scale interconnected power system using neuro-fuzzy load shedding approach. *Expert Systems with Applications*, *37*(4), 3171-3176.

Characterization of Damghan Desert Sand for Use as Thermal Energy Storage Medium

Sana Ghoreshizadeh[1], Mahmoud Ghazavi[2], Nima Ghoflgari[3,4], Alireza Bazargan[5]

[1]Name Faculty of Civil Engineering, K.N. Toosi University of Technology, Tehran, Iran, ghoreshisana@email.kntu.ac.ir[1], ghazavi_ma@kntu.ac.ir[2]
[3]Datis Robotics and Artificial Intelligence Industries, Tehran, Iran
[4]School of Metallurgy and Materials Engineering, College of Engineering, University of Tehran, Iran, nima.ghoflgari@ut.ac.ir
[5]School of Environment, College of Engineering, University of Tehran, Tehran, Iran, alireza.bazargan@ut.ac.ir

Abstract—**The thermal conductivity of soil and rock is the most important feature for designing geothermal infrastructure, such as geothermal energy foundations. In municipal applications, heat pumps are used to maintain and operate green buildings, for example by transferring emerging to and from hot or cold water. Therefore, knowing the thermal properties of soil such as the thermal conductivity becomes an important issue. For this purpose, in the paper the thermal conductivity of soil at various porosities, degrees of saturation, and water levels in soil layers have been investigated. The results show that the thermal conductivity decreases with increasing porosity. In one sample from the Damghan desert (between sieve 10 and 200), when 2/3 of the testing cylinder is full of soil, the thermal conductivity is between 0.093 and 0.716 (W/m.K). When the cylinder is 1/2 full of soil, the thermal conductivity is between 0.045 and 0.556 (W/m.K). Discussions are provided regarding the applicability of the different samples for energy storage and transfer. At identical porosity and saturation, soil with finer particles has more thermal conductivity. Meanwhile, increasing the saturation increased the thermal conductivity at the same porosity in all the samples investigated.**

Keywords - energy storage, geothermal energy, heat pump, soil properties, thermal conductivity

I. INTRODUCTION

Non-renewable energy sources such as fossil fuels are limited, and fossil fuels pollute the environment, not least by producing greenhouse gases. As the population grows and energy consumption increases, the human need for energy production increases as well [1]. Energy from the ground or geothermal energy is a promising form of renewable energy. People use different geothermal energy systems such as geothermal power plants, horizontal ground collectors, geothermal energy piles (GEP), ground source heat pumps (GSHP), borehole thermal energy storage (BTES), and U-shaped boreholes heat-exchangers (UBHE). The most popular heat extraction method is through horizontal collectors; this continuous loop of pipework is buried at least one meter under the ground. If space is limited, a compact collector is required, or a series of trenches are sought a specialist contractor will be required to bury a pipe up to a depth of 200 meters; this method of heat collection is more suitable for the ground which contains a higher proportion of rock and stone [2]. Thermal conductivity is one of the basic thermal properties of soil [3]. It is the property of a material's ability to conduct heat. In previous studies, Reference [2] investigated silicate sands with different porosities to observe the effect of fine grain size and porosity on thermal conductivity. Tests were based on the transient method. As the porosity decreases, the thermal conductivity increases. When the initial porosity is high, the coordination between the grains has a more significant effect on reducing the porosity than in the surrounding

ISBN: 978-86-80593-73-9

environment. As the porosity decreases, the impact of the contact environment becomes more critical. Reference [3] studied the effect of moisture content and density on thermal conductivity. Clay, fine sand, and silt loam were used in the experiments. The impact of moisture content and density on thermal conductivity was investigated by the heat probe method. The results showed that the thermal conductivity in dry conditions is the same in all three soils; by adding less water, the thermal conductivity in fine-grained sand increases with a greater slope, and with increasing volumetric density in dry soil, thermal conductivity increases. Reference [4] determined the effect of soil density, water content, and organic matter on the thermal conductivity of 4 types of sandy soils, sandy loam, loam, and clay; the results showed that sandy soil has a higher thermal conductivity than other soils. The thermal conductivity increases with increasing density at constant moisture in all soils, but sandy and clay soils showed a slight increase in thermal conductivity. Also, at a constant density, with increasing the moisture content, the thermal conductivity of the soil increases. The thermal conductivity of sandy and clay soils decreases by keeping the moisture content constant and increasing the amount of salt.

The importance of soil thermal conductivity for geothermal energy production has been extensively studied [5-9]. These studies have not been limited to any particular country, and researchers across the world have been involved in the development of the field [10-15]. In this study, we have investigated the thermal conductivity of soil from the Damghan desert in Iran for geothermal energy applications.

II. Materials and Methods

A. Sand

Sandy soil from Damghan in Iran was tested to determine its thermal properties. The soil is divided into three types: fine, medium, and coarse. Soil 1 passes through sieve number 40 and residue on number 200. Soil 2 passes through sieve 10 and residue on number 40. Soil 3 is selected through a sieve of 10 and a residue of 200.

B. Research method and experimental setup

There are two main methods for measuring soil thermal conductivity: transient method and steady-state method. Needle probes usually carry out transient methods. In this study, equipment, and software manufactured at K.N. Toosi University of Technology, Iran, have been used as shown in Fig. 1. A source of linear heating such as thermal probes is used in the field. The effect of the water content and porosity was investigated on thermal conductivity. The test methodology is based on ASTM D5334 standard [1]. For porosity measurement, dry soil weight is measured for each sample and then filled in a PVC mold. For water content measurement, a cylinder is used with a diameter and height of 7 cm and 14 cm, respectively. Dry, wet, saturated, and more saturated tests have been performed in the soils with varying granulation.

III. Results and Discussion

A. Influence of the Porosity

Soils 1, 2, and 3 are used for measuring porosity. The diameter and height of the cylinder are 7 and 14 cm, respectively. Fig. 2 shows the changes in thermal conductivity at different porosities and saturations.

B. Influence of Water

The amount of water in the soil is influential on thermal conductivity. Two soil granulations have been tested based on the information provided in the materials and methods section. When 2/3 of the cylinder volume (359.18 cm^3) is filled, 100 ml of water is needed to moisturize and 150 ml to saturate. For a case where 1/2 of

Figure 1. The equipment used for testing.

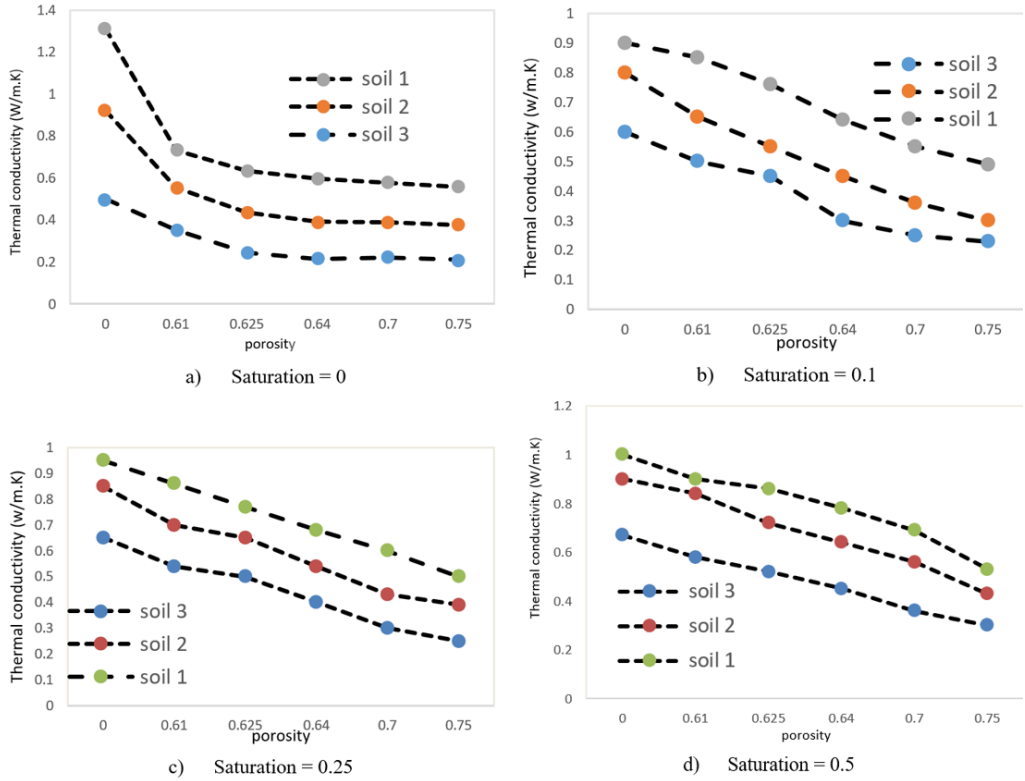

Figure 2. Thermal conductivity versus porosity at different saturation values of Damghan sand.

the cylinder volume (269.39 cm^3) is filled, 60 ml of water is used to moisten, and 130 ml of water is used to saturate the soil. Fig. 3 shows the relationship between saturation and thermal conductivity.

C. Discussion

Fig. 2 indicates the relationships between thermal conductivity and porosity for three sand granulations; it is evident that the thermal conductivity decreases with an increase in porosity at each level. The four figures show four different saturation sandy soils as a function of porosity at a given granule size. At various saturations, thermal conductivity decrease with increasing porosity. Similar results have been reported in the literature [12]. A decrease in thermal conductivity of sandy soil with increased porosity is probably due to reduced contact between soil particles and air resisting the heat flow. At identical porosity and saturation, soil with finer particles has more thermal conductivity. Soil 1 is finer, and the soil particles are closer together; therefore, heat transfer is higher than soils 2 and 3. The closer the particles are to each other, the less space between the particles. So heat transfer speed is enhanced by the particles. Figs. 2a, b, c and d show that increasing the saturation increases the thermal conductivity at the same porosity in all three soils.

Observations show that in soil 3, when 2/3 of the cylinder is full of soil, the thermal conductivity is between 0.093 and 0.716 (W/m.K). When the cylinder is 1/2 full of soil, the thermal conductivity is between 0.045 and 0.556 (W/m.K). In soil 1, when 2/3 of the cylinder is full of soil, the thermal conductivity is between 0.084 and 1.08 (W/m.K). When the cylinder is 1/2 full of soil, the thermal conductivity is between 0.043 and 0.336 (W/m.K). Evidently, in the case of a half-full cylinder, the amount of thermal conductivity is less than in the case of 2/3 of volume. As saturation is reached, the thermal conductivity

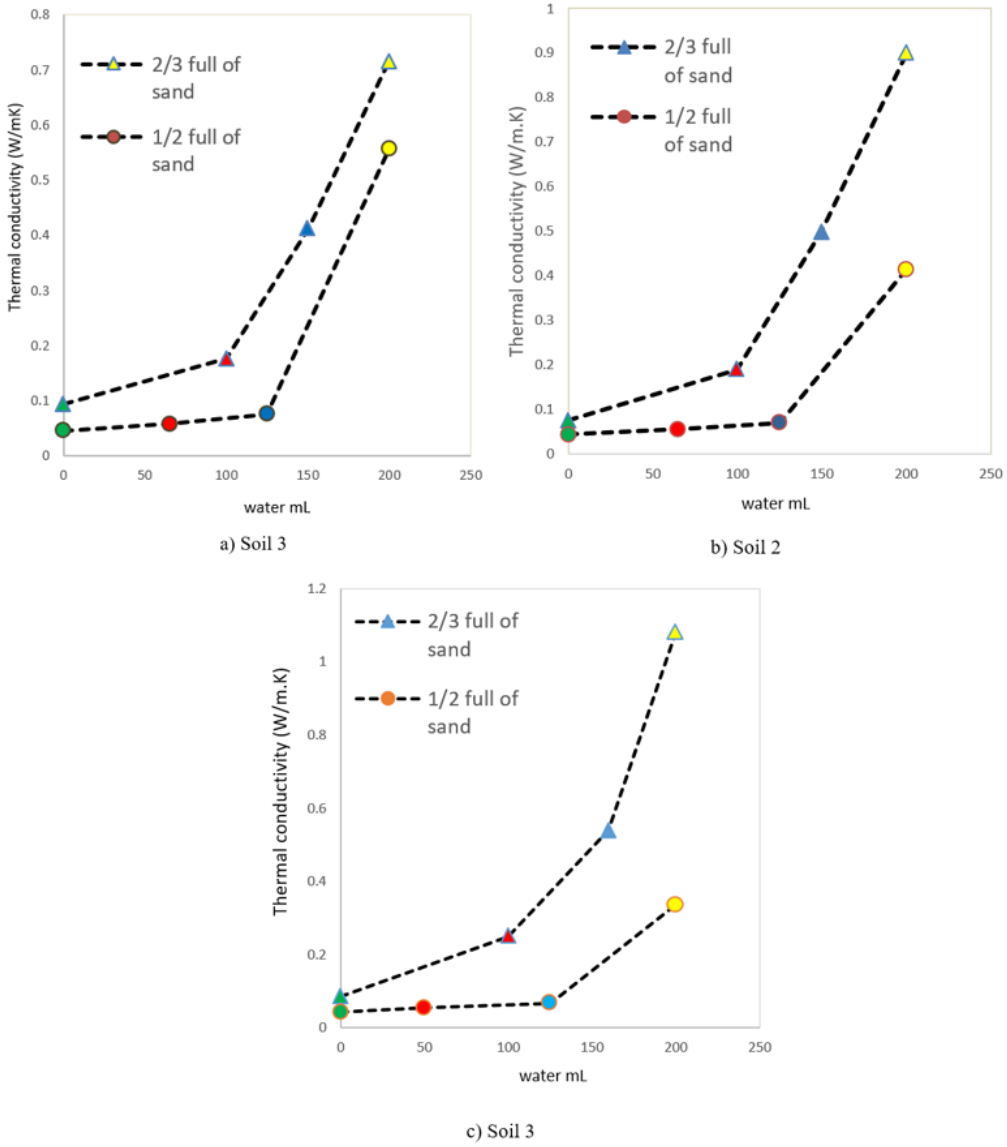

Figure 3. Effect of water content in different volumes of sandy soil on thermal conductivity. The green markers indicate the dry state, the red markers the wet form, the blue markers the saturated state, and the yellow markers the highly saturated state.

increases sharply. It is observed that the finer soil has higher thermal conductivity. When more soil is poured into the mold, more water is needed to achieve the same degree of saturation than when less soil volume is used.

In the case of less soil volume, the amount of water penetrating the soil is more; therefore, it increases the thermal conductivity sharply. In summary, In the dry state, the cylinder with more soil volume has more thermal conductivity. Also, in a wet and saturated state, because a cylinder with more soil requires more water to reach the same degree of saturation, a higher thermal conductivity is expected.

IV. CONCLUSIONS

To understand and use geothermal energy, tests on soil thermal conductivity are essential. This can be the case for industrial scale geothermal infrastructure as well as for use in domestic hot water production. In this research, a thermal conductivity measuring device manufactured in-house has been used to investigate the influence of various physical factors such as porosity and water level on thermal conductivity. This device was designed and built for the first time in Iran for finding the effect of water level on the soil of the Damghan desert region. The main findings are as follows:

1. As the porosity increases, the thermal conductivity decreases.
2. At the same porosity and degree of saturation, finer soil has higher thermal conductivity.
3. With increasing soil volume in the dry state, the thermal conductivity increases.
4. As the amount of moisture increases, the thermal conductivity increases.
5. For the wet state, the soil with a larger volume needs more water and hence will have a higher thermal conductivity.

REFERENCES

[1] ASTM, D. (2008). Standard test method for determination of thermal conductivity of soil and soft rock by thermal needle probe procedure. *ASTM Data Ser. Publ., 5334*, 1-8.

[2] Ahn, J., & Jung, J. (2017). Effects of fine particles on thermal conductivity of mixed silica sands. *Applied Sciences*, *7*(7), 650.

[3] Al Nakshabandi, G., & Kohnke, H. (1965). Thermal conductivity and diffusivity of soils as related to moisture tension and other physical properties. *Agricultural meteorology*, *2*(4), 271-279.

[4] Abu-Hamdeh, N. H., & Reeder, R. C. (2000). Soil thermal conductivity effects of density, moisture, salt concentration, and organic matter. *Soil science society of America Journal*, *64*(4), 1285-1290.

[5] Koçak, B., Fernandez, A. I., & Paksoy, H. (2020). Review on sensible thermal energy storage for industrial solar applications and sustainability aspects. *Solar Energy*, *209*, 135-169.

[6] Sarbu, I., & Sebarchievici, C. (2018). A comprehensive review of thermal energy storage. *Sustainability*, *10*(1), 191.

[7] Malek, K., Malek, K., & Khanmohammadi, F. (2021). Response of soil thermal conductivity to various soil properties. *International Communications in Heat and Mass Transfer*, *127*, 105516.

[8] Urresta, E., Moya, M., Campana, C., & Cruz, C. (2021). Ground thermal conductivity estimation using the thermal response test with a horizontal ground heat exchanger. *Geothermics*, *96*, 102213.

[9] Wang, J., He, H., Li, M., Dyck, M., Si, B., & Lv, J. (2021). A review and evaluation of thermal conductivity models of saturated soils. *Archives of Agronomy and Soil Science*, *67*(7), 974-986.

[10] Vardon, P., Bruhn, D., Steiginga, A., Cox, B., Abels, H., Barnhoorn, A., ... & Wapenaar, K. (2020). A Geothermal Well Doublet for Research and Heat Supply of the TU Delft Campus. *arXiv preprint arXiv:2003.11826*.

[11] He, H., Flerchinger, G. N., Kojima, Y., Dyck, M., & Lv, J. (2021). A review and evaluation of 39 thermal conductivity models for frozen soils. *Geoderma*, *382*, 114694.

[12] Chen, S. X. (2008). Thermal conductivity of sands. *Heat and mass transfer*, *44*(10), 1241-1246.

[13] Wang, J., He, H., Dyck, M., & Lv, J. (2020). A review and evaluation of predictive models for thermal conductivity of sands at full water content range. *Energies*, *13*(5), 1083.

[14] Zhao, X., Zhou, G., & Jiang, X. (2019). Measurement of thermal conductivity for frozen soil at temperatures close to 0° C. *Measurement*, *140*, 504-510.

[15] Xiao, Y., Ma, G., Nan, B., & McCartney, J. S. (2020). Thermal conductivity of granular soil mixtures with contrasting particle shapes. *Journal of Geotechnical and Geoenvironmental Engineering*, *146*(5), 06020004.

Measuring Voltage in Power Electronic Systems Utilizing Transformer Voltage Sensors

Đorđe Lazarević[1], Marko Živković[2], Đorđe Kocić[3], Jovan Ćirić[4]

[1,2,3,4]Faculty of Electronic Engineering, Niš, Serbia, djordje.lazarevic@elfak.ni.ac.rs[1], marko.zivkovic@elfak.ni.ac.rs[2], djordje.kocic@elfak.ni.ac.rs[3], jovan.ciric@elfak.ni.ac.rs[4]

Abstract—**Voltage measurement in power electronic systems e.g. frequency regulators is a standard process that is common for most applications. Usually, in most industrial power systems measurement of AC voltage is done by using different circuitry. One of the most important circuit is the voltage divider. Also in three-phase AC systems voltage measurement is often done by using Hall effect sensors or LEM modules when galvanic isolation is necessary. The output of this circuit is connected to the microprocessor or microcontroller which does AD conversion and voltage measurement. Voltage sensors are part of a bigger system for frequency regulation of AC motor. This paper describes voltage sensor for detection and voltage measurement in three-phase power electronics systems. Also here is presented a simulation of the voltage sensor module, sensor circuit connections, and voltage reading values. Lastly, for full system verification, voltage shapes of the sensor output and inputs are presented, captured by a digital oscilloscope.**

Keywords – hall-effect sensor, LEM module, microcontroller, three-phase AC systems

I. INTRODUCTION

Voltage measurement is an important process in power electronic systems for control and maintenance. There are different ways of measuring voltage. Voltage is often measured by using voltage dividers, Hall-based voltage sensors, LEM sensors, and sensors based on isolation voltage transformers [1]. Two common ways for measuring are by using a voltage divider and voltage transducer. An important fact when using voltage dividers is that values of R1 and R2 must be higher than the values of the impedance of the rest of the circuit and only in that case voltage measurement can be precise enough. Fig. 1 shows a simple voltage divider and Eq. (1) shows a relation between voltage and resistance in a circuit.

$$U2 = U1\frac{R2}{R1+R2}. \qquad (1)$$

Another way of measuring voltage is using sensors that are based on voltage transducers. This type of sensor provides a measurement of AC voltages with galvanic isolation. The voltage transducer utilizes an electrically isolated transformer and two resistors. One resistor is on the primary side and must be dimensioned for high AC voltage and the second resistor is in the secondary circuit. The secondary side is fully isolated from the primary side, so any fault on the primary side of the circuit will not have a damaging effect on the secondary. Fig. 2 shows the working principle of the circuit. Equation 2 shows a relation between voltage, resistance, and current in the equivalent circuit in Fig. 2.

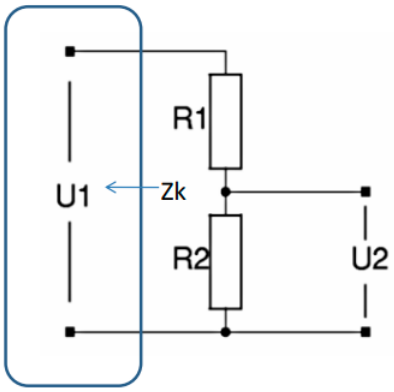

Figure 1. Voltage divider circuit.

ISBN: 978-86-80593-73-9

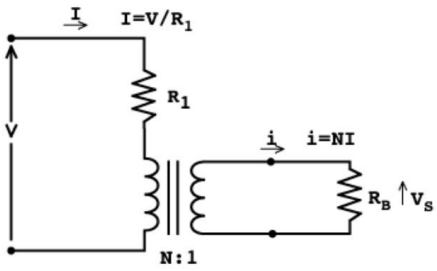

Figure 2. Voltage transducer.

$$Vs = iRB = \frac{NRB}{R1}V \quad . \qquad (2)$$

A similar sensor is used in this work which is also based on a voltage transducer and it is ZMPT101B Current-type voltage transformer. The main idea of this work is to describe the process of detection and voltage measurement in power electronic circuits by using a voltage transducer sensor.

II. VOLTAGE SENSOR ZMPT101B

ZMPT101B AC Voltage Sensor is a good solution, in applications where we need to measure the accurate AC voltage with a voltage transformer. ZMPT101B is an ideal choice to measure the AC voltage using microcontrollers and microprocessor circuits. In many electrical projects, the engineer is confronted with few basic measurement requirements like high galvanic isolation, wide range, high accuracy, and good consistency.

ZMPT101B is a high-precision voltage transformer. This module makes it easy to monitor AC mains voltage up to 1000 volts. It has small dimensions and holds up to 4kV breakdown voltage, the ratio of turns is 1: 1, but this is a current transformer of 2mA: 2mA. The input current is simply set by the resistor in series R1, and a sampling resistor R2 is used in parallel to obtain the output voltage [2]. Fig. 3 shows the ZMPT101B transformer schematic with resistors on its primary and secondary sides. Equation 3 shows the relation between output and input voltage from the voltage divider.

$$Vout = \frac{Vin}{R1}R2 \quad \square\square \qquad (3)$$

Fig. 3 shows the simplest voltage sensor using a voltage transformer. But in practice, it is more often to use a sensor module, which, for example, consists of a ZMPT101B voltage transformer and LM358 [3] operational amplifier circuit which provides active output. The Block diagram of the ZMPT101B sensor module is shown in Fig. 4. The voltage Eq. is shown in (4).

$$U2 = \frac{U1}{R'}R \quad . \qquad (4)$$

This module also has a trimmer potentiometer with which it is possible to adjust output voltage precisely until calibrated with an external multimeter or high precision voltmeter. A physical representation of this type of sensor is shown in Fig. 5.

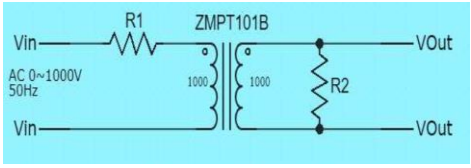

Figure 3. ZMPT101B transformer schematic with resistors.

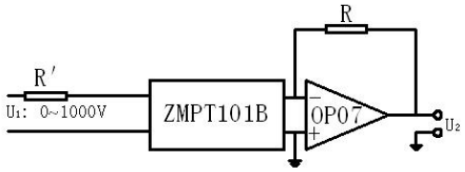

Figure 4. Block diagram of ZMPT101B sensor module.

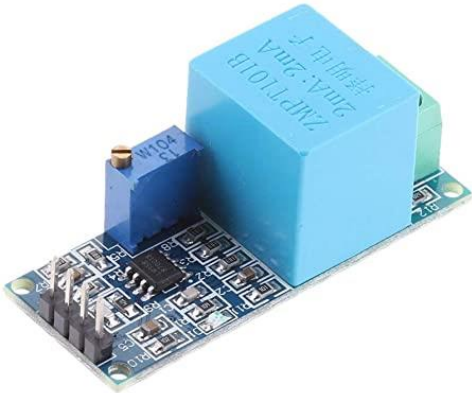

Figure 5. ZMPT101B sensor module.

III. CIRCUIT SIMULATION IN LTSPICE XVII

Simulation of electronic circuits is very useful and a necessary step of design and analysis in all areas of electronics and power electronics also. Test checking of the complete module together with the ZMPT101B voltage transformer was done by using simulation software LTSpice XVII [4]. There is transient analysis with a time of 200ms. Fig. 6 shown a schematics diagram of the complete sensor module.

Trimmer potentiometer R12 is presented like two resistors with different values of resistance which can be changed in time with different number of steps. In this simulation 100K resistor is used whose value can be changed in 5 steps with 20k resistance. An active part of the circuit consists of the two-stage operational amplifier. The first stage has a coupling capacitor on the input with a 1uF value and it is used for filtering DC voltage which is connected to the resistor. The voltage shape on resistor R1 is shown in Fig. 7.

The voltage divider consists of resistors R3 and R4 and the output voltage is used for setting referent voltage because of a single supply for the operational amplifier. Amplification of the first stage is defined by values R5 and R4 and that voltage has a wide range in comparison with voltage on resistor R1 on the input of the

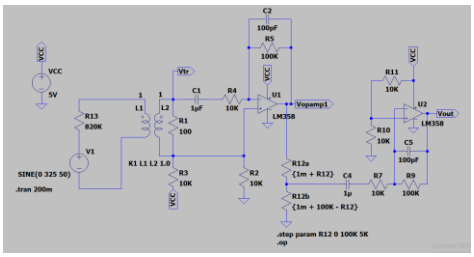

Figure 6. Electrical schematic of ZMPT101B module in LTspice XVII.

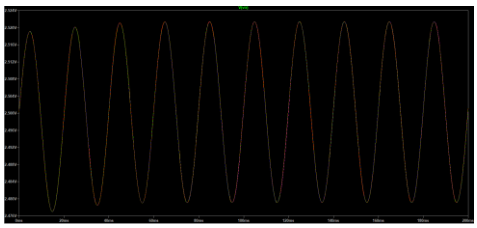

Figure 7. Transformer output voltage.

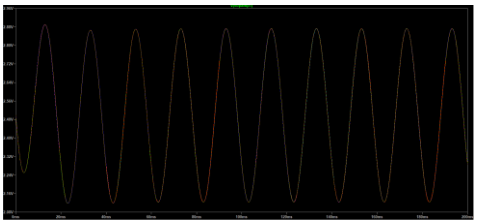

Figure 8. Output voltage on frist operational amplifier circuit stage.

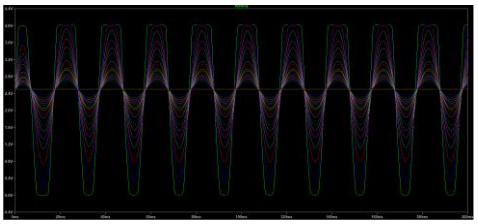

Figure 9. Output voltage on ZMPT101B sensor for different values of resistance R12.

amplifier. The voltage on the output of the first operational amplifier is shown in Fig. 8.

The signal from the first stage amplifier going through the potentiometer on the second stage and the amplitude of output voltage is about Vcc - 1.5V when the operational amplifier is in saturation. In the normal working condition, the output voltage will be defined by changing the value of the potentiometer and its resistance will also be calculated in the final equation of amplification of the second inverting amplifier. Different values of output voltage on the second inverting amplifier as a function of changing values of R12 are shown in Fig. 9.

As it is shown output voltage will change its shape because of the saturation of the operational amplifier and voltage is in the form of the square wave. Changing the value of the potentiometer affects the changing of the voltage amplitude on the output which is used in practical conditions for calculating and measuring in microcontroller circuit. This simulation confirms that the circuit shown in schematics is fully functional and it is working in defined conditions.

IV. PRACTICAL IMPLEMENTATION SENSORS IN THREE-PHASE ELECTRONIC SYSTEM AND CHECKING OF WORK

The voltage transformer sensor module has very small dimensions and because of that, it is very good for implementation in single and three-phase systems. Because of the way it is

implemented on the PCB, it is good for integration in bigger, more complex systems. Fig. 10 shows the implementation of voltage sensors for each phase in power electronic systems with other components on PCB.

Testing the sensor is done by using USB oscilloscope Hantek 6022BE [5] as a form of acquisition card, with the software on the computer. To check a voltage on the output of the transformer and outputs on the operational amplifier and complete module, as in simulation, it was necessary to solder wires which are used for signal sampling which is also shown in Fig. 10. Also, voltage value from the sensor is presented on a screen of an electronic measurement system and that is also part of functionality testing.

After connecting sensors to the system and powering on, the next step is reading the sensor values and calculating voltage on the output. There were used 100 samples of the maximum value of the voltage on the output on the sensors and effective voltage value.

The effective value of AC voltage is calculated as shown in (5).

$$Veff = \frac{V\max}{\sqrt{2}} \ . \tag{5}$$

After that output voltage is calculated by the microcontroller system and it is shown in empirical (6).

$$Veff = \left(\left(\left(\frac{Vmax}{\sqrt{2}} - 420.76\right)\frac{1}{-90.24}\right)(-210.2)\right) + 210.2 \tag{6}$$

Measuring the output voltage and checking voltage on the sensor by using an oscilloscope is shown in Fig. 11.

Figure 10. Implementation of voltage sensors in three-phase electronic system.

When the complete circuit is connected, the output signal on the oscilloscope has a very low amplitude and it is necessary to use the trimmer potentiometer to increase amplification on the operational amplifier and with that to increase the output voltage. Output voltage with low amplification is shown in Fig. 12.

For precise measurement, the amplitude of the voltage on the output of the sensor must be high enough, so that the AD converter in the microcontroller ATmega328P can calculate and present that voltage on a display on the measurement device. For that purpose resistance of the potentiometer is changed and output voltage with higher amplitude is shown in Fig. 13.

With this amplitude of the voltage, it is possible to apply code for the microcontroller which consists of Eq. 6 for calculating the voltage on the input of the sensor. This step is final and after that system can measure the mains voltage of 230V which is earlier shown in Fig. 11.

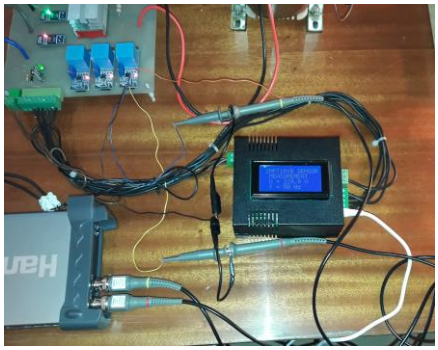

Figure 11. Measuring the output voltage and checking voltage on the sensor by using osciloscope.

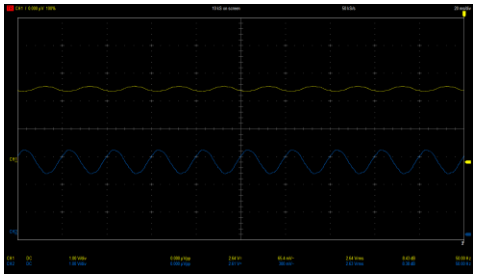

Figure 12. Low output voltage on operational amplifier.

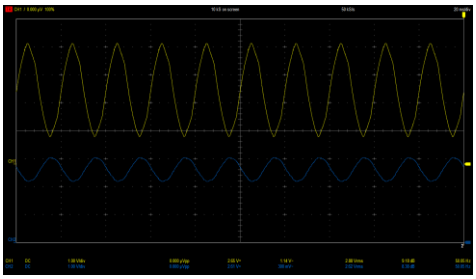

Figure 13. Voltage on the output of the sensor with higher amplitude.

With this amplitude of the voltage, it is possible to apply code for the microcontroller which consists of (6) for calculating the voltage on the input of the sensor. This step is final and after that system can measure the mains voltage of 230V which is earlier shown in Fig. 11.

V. CONCLUSIONS

Voltage sensors are important parts of power electronic systems. Usage, implementation, and simulation of the voltage sensor module is described in this paper. Every step including simulation and practical implementation is introduced. Simulation of the circuit is very useful, through analysis of work of this sensor and later checking signals on the output using oscilloscope provides a better insight of the circuit logic. Also described in this work is one way of integrating voltage sensor module in bigger and more complex systems. This is also one way of measuring voltage in power electronic systems. One more application of this type of circuit is in frequency regulators in three-phase systems, as a phase voltage loss motor protection and by using this type of sensor it is possible to detect which phase is down.

REFERENCES

[1] Despotović, Ž. (2013). *Merenje napona i struje u kolima energetske elektronike*. Available at: https://www.viser.edu.rs/download/681.

[2] *ZMPT101B Micro Precision Voltage Transformers*. Available at: https://innovatorsguru.com/wp-content/uploads/2019/02/ZMPT101B.pdf.

[3] *LMx58 Low power, Dual Operational Amplifiers*. Available at: https://www.ti.com/lit/ds/symlink/lm158-n.pdf.

[4] *LTspice, Analog Devices.* Available at: https://www.analog.com/en/design-center/design-tools-and-calculators/ltspice-simulator.html

[5] *Hantek Oscilloscope 6022BE*. Available at: http://www.hantek.com/products/detail/31

Quantitative Assessment of Safety Culture Within Algerian Powerplant

Ayoub Harfouf[1], Tahar Chorfi[2], Moumene Raid[3], Aboubakr Kertous[4]

[1,2,3,4]Ecole Nationale Polytechnique, Algeria, ayoub.harfouf1@gmail.com[1]

Abstract—**The focus of this work is to improve commitment to the Process Safety Management System (RBPS) in the new Cap-Djinet Power Production Company (SPE). Resilient safety culture (RSC) is a socio-technical safety system that consists of employee capabilities as well as protocols and systems in an organization. The study contributes towards this by adopting a focus on model which manage the major and the frequent accidents caused by the lack of safety culture, which motivated us to conduct this paper to prevent accidents caused by safety culture's lack. In our study, we used a quantitative research approach to assess the resilience of safety culture. Therefore, we designed a questionnaire to collect data to serve as input data of the resilient safety culture model to determine the safety resilience index. after the analysis of all questionnaires, we found Cronbach' α was 0.959, resilient safety culture index, was 0.309.**

Keywords – process, safety culture, resilience, safety

I. INTRODUCTION

For decades, some major accidents have occurred in highly reliable industries. Complex safety management systems and high-level safety culture may possibly help reduce the number of common accidents [1], but these classical methods may not be enough to prevent accidents and extraordinary accidents [2]. Therefore, needs to adopt new standards such as risk-based RBPS to improve the safety of these systems. In a world where being dynamic change and the need to be always ahead of the competition and seek sustainability, the catastrophic losses in major accident pointed the need to go beyond traditional management systems that are more focused on continuous improvement which means that we are always going to be waiting for things to occur. Safety management systems and high-level safety cultures have helped reduce the number of common accidents, but these classic qualitative approaches may not be sufficient to prevent extraordinary accidents [3]. consequently, accidents and their causes can be attributed to organizational factors, variability in performance, and unexpected combinations [4]. We model the safety culture resilience and the data collected using a questionnaire which serves as input to our model, also We analyze goodness of fit of our model using confirmatory factor analysis.

II. MATERIALS AND METHODS

A. Designing Questionnaire

We designed the safety culture questionnaire to assess safety culture resilience based on Arun Garg 42 elements [5], these 42 elements are grouped in three constructs. The first is the Psychological capability (just culture) which has 2 subconstructs: Conceptual orientation, Constructive sense making. The second is the Behavioral capability (reporting culture) which has 4 subconstructs: Learned resourcefulness, Counterintuitive agility, Practical habits, Behavioural preparedness. The third is the Managerial capability divided in 4 subconstructs: Deep social capital, Broad resource network, Psychological safety, Diffused power and accountability [5]. 50 questionnaires were distributed to employees (engineers, operators, managers), Likert scale from 1-5 was used, where 1 on the low side or lower agreement and 5 on the higher side or higher agreement.

B. Method

A Quantitative research approach was used in addressing the objectives of the study. Data was collected using a structured questionnaire designed in two parts. The first part inquired about the demography of the respondents and their position within the organization. The

second part inquired about the safety culture elements [5]. Our study consisted of forty-two (42) Likert-type questions, which were adopted from the Arun Garg elements [5] dealing with different aspects of resilient safety culture. Each question from the survey designed has the corresponding element.

C. Population and Ethical Considerations

The sample for this analysis was derived from workers that completed the safety culture questionnaire as part of the improvement of commitment to process safety management system. The fifty (50) questionnaires distributed clearly stated that the anonymity is a high priority and they answer voluntarily to ensure the reliability and consistency of the results. Participants were fully informed of what will be asked of them and how the data will be used. Thirty-eight questionnaires received after being completed by employees. We analyzed the Cronbach' α using SPSS and it is equal to 0.959.

III. Resilient Safety Culture Model

In order to quantify RSC, we calculated the relative probability of safety culture, the probability of failure and relative importance index. This specific model was never used in a power plant, it should be tested using confirmatory factor analysis process.

The Eq. (1) shows the superior factor's probability which is calculated using the summation of weighted inferior factors:

$$P = \sum_{i=1}^{n} \left(a_i \, p_i \right) \ . \qquad (1)$$

A. Confirmatory Factor Analysis

Before normality tests and starting the analysis collected data was cleaned and inspected by calculating the standard deviation of variables, it shouldn't be close to zero, detecting outliers, then missing data was replaced by the median of nearby variables, the model was identified by determining the chi-square, degrees of freedom and prob-ability level. Structural Equation modelling, however, estimate parameters in the model assess model fit, it relies on several statistical tests to determine the adequacy of the model fit to the data, result is respecifying the model if meaningful.

B. Resilient Safety Culture Index

Once a RSC model is identified, the network needs to be measured through the use of application of qualitative as well as quantitative data or their combination [6]. Complex network theory is used to quantify the resilience and use this new complex relationship between various cultures by calculating the relative probability of safety culture using the three sub-systems which in turn are interrelated using parallel and progressive relationships [5]. More detail afterward. One of the major challenges of quantification of the RSC is that the attributes that determine RSC need to be measured through constructs and indicators which are complex and often interrelated [6]. In our case we applied Weighted probabilities and RII on the model proposed by Arun Garg, to be able to analyze complex and interrelated constructs and indicators. In order to demonstrate the failure path of the weak links in the RSC model [7], we adapted these models to evaluate the RSC of the power plant, results are used for monitoring the progress or comparing it with the resilient levels of other national power plants.

The Eq. (2) shows the RII, and how it is calculated:

$$RII = \frac{\sum W}{\mathbf{A} * N} \ , \qquad (2)$$

where RII = relative importance index, W = weighting given to each factor by respondents (Likert scale range from 1 to 5), A = highest weight (in this case it is 5) and N =total number of respondents.

C. Goodness of Fit Indexes

Using SPSS 24.0 we calculated goodness of fit indexes shown in Table I below:

TABLE I. Goodness of fit indexes.

PCFI=0,559 < 0.7
GFI=0,71 > 0.7
AGFI=0,502 < 0.7
TLI=0,7 = 0.7
CFI=0,787 < 0.7
RMSEA=0,241 > 0.8
PCLOSE=0 < 0.05
CMIN/DF=3.04 < 5

TABLE II. WEIGHTED PROBABILITIES (HOURLY WORKER).

Sub-Constructs	Weighted probabilities	RII
Conceptual orientation (CO)	0.76	2
Constructive sense making (CS)	0.73	5
Learned resourcefulness (LR)	0.708	6
Counterintuitive agility (CA)	0.767	1
Practical habits (PH)	0.743	3
Behavioural preparedness (BP)	0.704	7
Deep social capital (DSC)	0.692	8
Broad resource network (BRN)	0.738	4
Psychological safety (PS)	0.671	9
Diffused power and accountability (DPA)	0.633	10

TABLE III. WEIGHTED PROBABILITIES (FIRST LEVEL SUPERVISOR).

Sub-Constructs	Weighted probabilities	RII
Conceptual orientation (CO)	0.638	1
Constructive sense making (CS)	0.59	3
Learned resourcefulness (LR)	0.475	10
Counterintuitive agility (CA)	0.588	4
Practical habits (PH)	0.62	2
Behavioural preparedness (BP)	0.5	9
Deep social capital (DSC)	0.533	7
Broad resource network (BRN)	0.55	5
Psychological safety (PS)	0.513	8
Diffused power and accountability (DPA)	0.55	5

TABLE IV. WEIGHTED PROBABILITIES (MANAGER).

Sub-Constructs	Weighted probabilities	RII
Conceptual orientation (CO)	0.775	2
Constructive sense making (CS)	0.74	3
Learned resourcefulness (LR)	0.8	4
Counterintuitive agility (CA)	0.675	5
Practical habits (PH)	0.8	1
Behavioural preparedness (BP)	0.5	8
Deep social capital (DSC)	0.517	7
Broad resource network (BRN)	0.525	6
Psychological safety (PS)	0.525	6
Diffused power and accountability (DPA)	0.525	6

D. Weighted Probabilities and Relative Importance Index

The weighted probabilities are calculated for hourly workers, mangers and first level supervisors as shown in Tables II-IV.

IV. DISCUSSION

For the surveyed organization it was found that conceptual orientation sub-construct ranked first among the employees and this can be due to the fact that the site is new and employees have a strong sense of purpose and highly visible morale purpose so company is doing enough in terms of good work environment , psychological safety ranked last among all employees as a result of lack in trust which means that company have communication problems and employees are not able to communicate effectively or without getting negative labels and this is where company's main focus should be. other rank indicators are also displayed. These results show indicators that need to focus on the importance of the organizations surveyed.

A platform for improving commitment to process safety through a safety cultural approach. The result was a list of seven general principles:

A. Organizational transformation is self-transformation. If we accept the premise that cultures are created from the interaction between people, the various groups and professional communities need to be involved in dialogue to define both problems and solutions. [8]

B. Goals should be moderate and relate to everyday realities. Unless improvement measures can be related to the daily tasks and reality of the problem owners, it will not have lasting effects. [8]

C. Change must be viewed as a long-term project. While the boxes and arrows of an organization chart can be moved in a matter of minutes, changing the way people work requires years of persistence. [8]

D. The goal should not be organization-wide consensus, but creating a common language and understanding between groups. Differences between groups can be a vital resource for safety. Multiple perspectives are a source of requisite variety that can

increase the chance of weak danger signals being detected somewhere in the organization. [8]

E. Combine 'push' and 'pull'. Top-down change efforts will fail unless there is a motivation for change at the sharp end of the organization. [8]

F. Management initiates and contributes, but the shop floor must be involved in continuous dialogue. Personnel on the ground have expert knowledge on hazards, work processes and situational demands. This must be acknowledged, respected and utilized. [8]

G. Be sensitive to organizational symbolism. For instance, organizational stories are powerful conveyors of culture and can be emphasized to illustrate the problems to be solved, or the early wins in the change process. [8]

V. CONCLUSION

Selecting the strategy of improvement depends on the problem that needs to be solved, and there is a need to quantify improvement efforts. Safety culture the first element of the process safety management system (RBPS) is the key corn stone toward improving commitment to process safety management system [9]. The study assessed the resilient safety culture by designing the questionnaire using five-point Likert scale with measured reliability and its Cronbach's α is equal to 0.959 using SPSS which is a satisfying result for reliability. This questionnaire will serve as input for the resilient safety culture model. The resilient safety culture model is based on Arun Garg's 42 elements, the calculations were performed using SPSS where different constructs were modeled and confirmatory factor analysis was carried to indicate the model's goodness of fit. The Findings of the analysis show that our model's goodness of fit is acceptable as statisticians' best practice. Once the model's goodness of fit was confirmed, we used weighted relative probabilities to measure the probability of failure of resilient safety culture and then calculate resilient safety culture index, which is equal to 0.309. this is mainly due to the weakness recorded on Psychological safety with Diffused power and accountability subconstruct and Behavioural preparedness subconstruct so there is the need to create awareness on recognized safety concerns, coupled with a dynamic risk response attitude to ensure consistent improvement in safety culture resilience. [10]

ACKNOWLEDGEMENTS

The authors wish to thank the anonymous reviewers for their invaluable comments on an earlier draft of this paper.

REFERENCES

[1] Paul R. (2020). Schulman,Organizational structure and safety culture: Conceptual and practical challenges. *Safety Science*, *126*.

[2] White, A. R. (1926). The Combining of Health and Accident Services by Industry. *The Public Health Journal*, *17*(2), 76–82.

[3] Adolph, L., Lafrenz, B., & Grauel, B. (2012). Safety management systems, safety culture and resilience engineering: comparison of concepts. In *Proceedings of the Human Factors and ergonomics society europe.*

[4] Shirali, G. H. A., Motamedzade, M., Mohammadfam, I., Ebrahimipour, V., & Moghimbeigi, A. (2012). Challenges in building resilience engineering (RE) and adaptive capacity: A field study in a chemical plant. *Process safety and environmental protection*, *90*(2), 83-90.

[5] Garg, A., (2019). Quantitative assessment of resilient safety culture model.

[6] Garg, A., & Mohamed, S. (2018). Resilient safety culture: A modelling perspective. In *Proceedings of ICCPMCE*, Sydney.

[7] Garg, A., Fahim, T., & Sherif, M. (2020). Reliability Evaluation of Resilient Safety Culture Using Fault Tree Analysis. In *Proceedings of ICCEPM 2019 The 8th International Conference on Construction Engineering and Project Management*, Dec. 8-10, 2019, Hong Kong SAR.

[8] Antonsen S. (2018) Key Issues in Understanding and Improving Safety Culture. In Gilbert C., Journé B., Laroche H., Bieder C. (eds) *Safety Cultures, Safety Models. SpringerBriefs in Applied Sciences and Technology*. Springer, Cham. doi:10.1007/978-3-319-95129-4_12

[9] Guidelines for Risk Based Process (2010). (pp. 649-682)

[10] Ranti, A., Olubola, B., Ganiyu, A-Y., Shehu, R., & Theophilus, O. (2020). Effect of Knowledge and Compliance of Health and Safety Information on Construction Sites Workers' Safety in Nigeria. *International Journal of Safety and Security Engineering. 10*, 269-277.

Numerical Study on the Performance of Standing Wave Thermoacoustic Engine Stack Subjected to Various Thermal Profiles

Fawad Ali[1], Wajiha Rehman[2], Muhammad Ali Kamran[3]

[1,3]University of Engineering and Technology Peshawar, Peshawar, Pakistan, alikamran@uetpeshawar.edu.pk[3]

[2]University of Leeds, Leeds, The UK, wajiharehman11@gmail.com

Abstract—**A thermoacoustic engine is a device that converts heat energy into acoustical energy which can be harnessed to generate either electricity or refrigeration effect. It is reliable, eco-friendly and has no moving parts. To generate mechanical waves, it needs a forced temperature gradient employed across the stack region. This paper outlines the effect of different thermal profiles assigned to the stack on the performance of the standing wave thermoacoustic engine (SWTAE) using the computational fluid dynamics (CFD) approach. For this purpose, a 2D computational domain of SWTAE has been generated in Gambit. Air is considered as a fluid medium. The mass, momentum, and energy conservation equations have been solved by using Fluent solver in transient state. To capture the flow turbulences during the oscillatory motion the shear stress transport (SST) k-ω model is considered since it uses the blending function feature. The stack of SWTAE is subjected to five different thermal boundary conditions namely, linear (profile-I), sinusoidal (profile-II), single step (profile-III), double steps (profile-IV) and multiple steps (profile-V) thermal profiles respectively. To analyze the performance of SWTAE, pressure amplitude and output frequency of the standing waves are monitored for each case. Additionally, the vortex shedding phenomena have also been investigated for each thermal profile. The numerical results indicate that single step thermal profile (profile-III) yields the highest-pressure amplitude with minimum frequency among other profiles.**

Keywords - thermoacoustic engine, computational fluid dynamics, temperature gradient, standing waves

I. INTRODUCTION

The worldwide energy demand is increasing exponentially to meet the needs, which is responsible for non-renewable energy resources' depletion and adverse environmental impacts [1]. The energy sector plays a vital role in the country's economic growth and social sustainability; therefore, it is a prime factor to achieve the global sustainability agenda [2]. This situation has compelled humanity to find alternative energy technologies that can address all the issues while meeting the global energy demand. One of these devices is the thermoacoustic engine. The working principle of these engines depends on the thermoacoustic effect which is described by Lord Rayleigh as follows "If heat be given at the moment of greatest condensation or taken from it at the moment of greatest rarefaction the vibration is encouraged" [3]. The conversion of thermal energy into acoustic vibrations, termed as prime mover, can generate electricity; whereas, if the process is reversed and acoustic work is converted into heat then these devices are termed as heat pumps. Fig. 1. shows the thermoacoustic engine working as a heat pump.

The resonance tube or resonator is filled with an inert compressible gas. The acoustic vibrations generate standing waves in the resonator. A standing wave has two regions, i.e., an antinode region where fluid particles have maximum displacement and a node region where fluid particles have zero displacements. At

ISBN: 978-86-80593-73-9

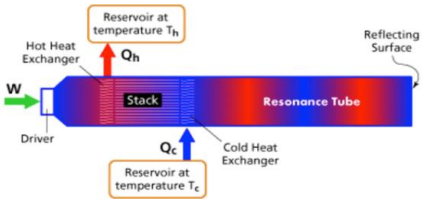

Figure 1. The schematic diagram of thermoacoustic engine as a heat pump [4].

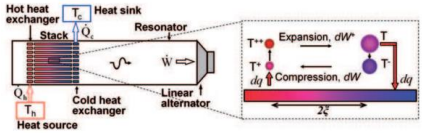

Figure2. The schematic diagram of a thermoacoustic engine [5].

antinode the pressure is high; therefore, the temperature of the fluid rises. Whereas, at the node, the fluid expands, and pressure drops subsequently temperature decreases. A heat exchanger placed at a suitable position can exploit this phenomenon to generate a cooling effect. Fig. 2 describes a thermoacoustic engine working as a prime mover.

The resonator is a gas-filled container that is closed at one end while the other end has a linear alternator. A stack of heat exchangers is placed at a position that can generate standing waves within the resonator when the temperature gradient is created [5]. Timmer *et al*. [6] have provided an overview of current technologies which use thermoacoustic effects for power generation. Fig. 3 presents a brief overview of these technologies.

Thermoacoustic engines have a simple design, as they lack moving parts, and they are easy to manufacture. These traits make this technology appealing, but plenty of work is required to improve efficiency before it can be implemented cost-effectively. This paper is a contribution towards improving the efficiency of these devices by studying the effect of thermal

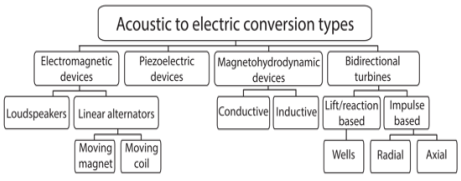

Figure 3. An overview of technologies that deploys thermoacoustic effect for power generation [6].

boundary conditions on the performance of thermoacoustic engines.

II. NUMERICAL MODEL

The model geometry used in the current analysis is based on the Zink et al. [7] standing wave thermoacoustic engine model which is 150 mm long and 12 mm wide. The model dimensions are sufficient to generate resonance conditions in a quarter-wave resonator with one end closed and the other end is opened. The geometrical specifications of this model have been summarized in Table I.

In order to generate the computational domain, the SWTAE model is replicated in Gambit software. To avoid the large computational cost, the mesh is generated in a two-dimensional domain with optimum cell size. This simplification does not affect the analysis accuracy since the geometry of the model is uniform through the z-axis.

Fig. 4 presents the mesh model of SWTAE with a 10 mm stack length and 110 mm resonator length. The triangular pave scheme has been selected to adapt the grid size within the computational domain more easily. Through this

TABLE I. GEOMETRICAL SPECIFICATIONS OF STANDING WAVE THERMOACOUSTIC ENGINE.

Parameters	Symbols	Values
Total Length	L	150 mm
Resonator	R	110 mm
Hot Buffer	L_C	30 mm
Height	H	12 mm
Stack Length	L_S	10 mm
Spacing	s	0.5 mm
Plate Thickness	t	0.5 mm

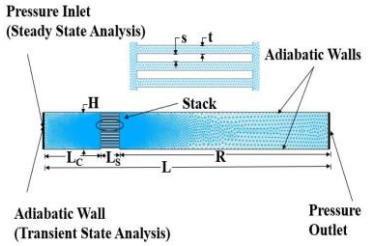

Figure 1 Mesh model of the standing wave thermoacoustic engine.

methodology, the cell size is effectively reduced at the stack region to capture the flow characteristics accurately around the plates. It should be noted that the current model avoids the complexities involving the heat input mechanisms such as heaters and heat exchangers, instead, thermal boundary conditions are specified at the stack walls.

Next, the computational domain is solved by using ANSYS [8] Fluent solver. The following conservation equations are numerically solved.

Continuity Eq.:

$$\frac{\partial \rho}{\partial t} + \nabla \cdot (\rho \mathrm{u}) = 0, \quad . \tag{1}$$

Momentum Eq.:

$$\begin{aligned} &\frac{\partial}{\partial t}(\rho u) + \nabla \cdot (\rho u u) \\ &= -\nabla p + \nabla \cdot (\tau) + pg \end{aligned} \quad . \tag{2}$$

Energy Eq.:

$$\begin{aligned} &\frac{\partial}{\partial t}(\rho E) + \nabla \cdot \left(u(\rho E + p)\right) = \\ &== \nabla \cdot \left(k \nabla \mathrm{T} + (\tau \cdot \mathrm{u})\right) \end{aligned} \quad . \tag{3}$$

Ideal gas Eq.:

$$p = \rho R T \quad . \tag{4}$$

where $\rho, t, u, p, E, k, and\ T$ are the density, time, velocity vector, pressure, stress tensor, acceleration due to gravity, total energy, thermal conductivity, and temperature variables respectively. To include the compressibility effect, the ideal gas equation has been selected by considering the air ideal gas density with R as the ideal gas constant.

To include the Reynolds Averaged Navier-Stokes (RANS) turbulence model for capturing the turbulences, the shear stress transport (SST) k-ω model is considered which is also belongs to the eddy viscosity-based models with the blending function, responsible for activating both k-ε and k-ω models according to the required conditions. For this model the turbulent viscosity can be determined as,

$$\mu_t = \frac{\alpha_1 \rho k}{\max(\alpha_1 \omega, \Omega F_2)} \quad , \tag{5}$$

where k, ρ, α_1 are the turbulent kinetic energy, density and a constant, ω is the specific rate dissipation, F_2 is a function having value ranges from zero to one ($F_2 = 0$, at the free stream and $F_2 = 1$, at the boundary layer), and Ω is absolute vorticity [9].

III. Simulation Setup

To simulate the standing wave thermoacoustic engine in Fluent software, it is necessary to create an initial disturbance in the system which is responsible for the gas oscillations. For this purpose, the simulations are run in a steady state with pressure inlet and pressure outlet boundary conditions. However, the standing waves in the quarter-wave resonator can be achieved with one end closed and the other end open. Thus, in the next stage, the pressure inlet boundary is replaced with adiabatic wall boundary conditions run in a transient state.

A. Boundary Conditions

Initially, a non-zero velocity flow field is obtained by specifying the pressure inlet as 10 Pa and ambient pressure at outlet boundary conditions which acts like an opening. The outer walls are specified with adiabatic and stationary boundary conditions.

In the next part of the simulations, the pressure inlet is replaced by an adiabatic wall while keeping the other boundary conditions the same. It should be noted that the state of the simulation is also changed to the transient state.

To provide heat input, the thermal boundary conditions are defined at the stack walls using different temperature profiles. For each case, the highest and lowest temperatures are specified as 800 K and 300 K respectively. The reason for keeping the large temperature difference is to reach the quasi-steady state (standing waves) condition quickly. Fig. 5 shows different profiles applied to the stack of the thermoacoustic engine. Profile-I and Profile-II present a linear and sinusoidal temperature gradient applied by using a user-defined function (UDF) respectively. Similarly, the temperature profile-III to profile-V represent a stepwise variation in temperature values. These are categorized as single step (profile-III), double steps (profile-IV), and multiple steps (profile-V) temperature variations

respectively. The following Eqs. are utilized for linear and sinusoidal profiles,

$$T(x) = 800 - (50000x) \ , \qquad (6)$$

and:

$$T(x) = 1000 - \left[450 - 250\cos\left(\frac{\pi x}{0.01} \right) \right] . \qquad (7)$$

In the aforementioned equations "x" is the axial distance with origin 30 mm away from the pressure inlet of the thermoacoustic engine. It shows that the maximum temperature can be reached to 800 K whereas the minimum temperature is found 300 K at the right end of the stack. It should be noted that 50 W/m^{2}K convective heat transfer coefficient is also defined at the stack thermal boundary conditions to prevail the thermal interaction between the air and the stack.

To run the simulations, the pressure-based solver is selected. A second-order scheme is used for the discretization of the energy and momentum equations, while a first-order scheme is selected for time discretization. Similarly, the pressure interpolation scheme is achieved by using the pressure staggering option (PRESTO!) scheme. For pressure velocity coupling, the steady-state simulations use SIMPLE algorithm whereas the transient simulations use pressure implicit with split operator (PISO) algorithm. The under-relaxation terms are taken by default and the convergence criteria for the continuity, momentum, and energy is 10^{-4}, $10^{-6,}$ and 10^{-6} respectively. The time step size is taken as 10^{-5} s based on previous studies [10] whereas the number of iterations for each time step is taken by default i.e., 20 iterations.

B. Grid Independence Analysis

To avoid unnecessary computations, an optimal grid size has been chosen for the current simulations by carrying out mesh convergence study. This was achieved by studying different mesh models i.e., course, medium, fine and very fine meshes with 6070, 14392, 19656, and 43744 cells respectively. To analyze the influence of mesh on numerical solutions, pressure magnitude was measured for a selected number of iterations as shown in Fig. 6. The resultant pressure magnitude for the four mesh models was 102322 Pa, 101814 Pa, 101772 Pa, and 101709 Pa respectively. This shows that the

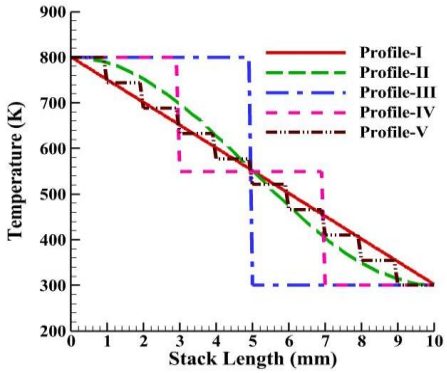

Figure 5. Different thermal boundary conditions defined at the thermoacoustic engine stack.

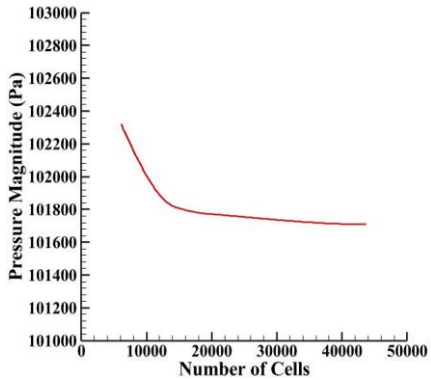

Figure 6. Effect on pressure magnitude by varying the number of cells in different mesh models.

results almost converge when the number of cells is increased from twenty thousand onwards. Thus, in current analysis use a fine mesh model for the simulations of SWTAE.

IV. Result and Discussions

The results were obtained after running the simulations for almost 32 hours using each profile. Fig. 7 shows the temperature distribution across the stack and compliance of the thermoacoustic engine for each temperature gradient profile. A very smooth temperature variation can be observed for profile-I and profile-II since these profiles use linear and sinusoidal functions. On the other hand, profile-III and profile-IV indicate a sudden drop with the constant temperature at the stack. As a result, the gas particles uniformly energize and are experiencing thermal expansion according to the ideal gas law. For this reason, the maximum number of particles are achieving a high-temperature profile at the hot buffer region. Similarly, profile-V shows almost the same

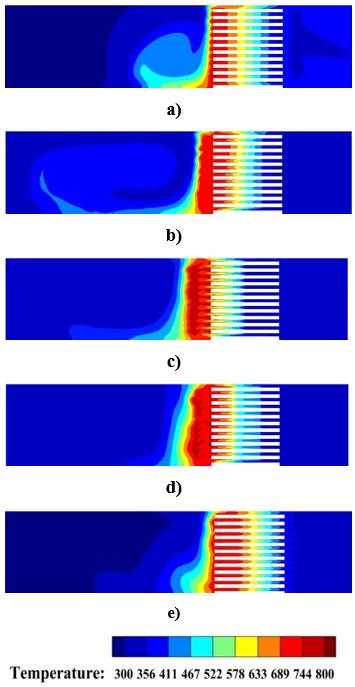

Figure 7. Time-averaged temperature distribution obtained by using (a) Profile-I (b) Profile-II (c) Profile-III (d) Profile-IV (e) Profile-V.

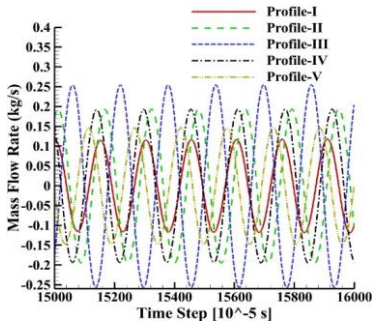

Figure 8. Mass flow rate profiles obtained by using different thermal boundary conditions.

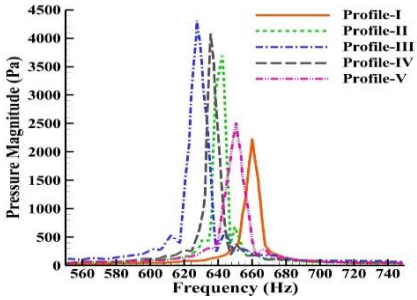

Figure 9. FFT analysis of pressure waves using each profile.

temperature distribution just like linear thermal profile.

In order to confirm the oscillatory flow in SWTAE, the mass flow rate has been monitored at the outlet for each case. Fig. 8 presents the mass flow rate profile for each case. It is observed that the amplitude remains constant throughout the profiles which indicates that the system has reached the quasi-steady state (no appreciable change in amplitude of the waves). It also confirmed that oscillatory motion can be achieved with the mentioned thermal boundary conditions. It should be noted that the negative mass flow rate indicates the flow out of the system whereas the positive mass flow rate indicates flow entering the engine through the opening. Results indicate that the magnitude of mass flow rate is maximum for profile-III. It is expected that the other flow variables magnitudes, such as pressure and velocity magnitudes will also be maximum for the profile-III, discussed in the next section.

The current simulations can be validated by comparing the theoretical frequency with the output frequency of the system. For this purpose, the time-domain pressure waves of the thermoacoustic engine were transformed into the frequency domain by using Fast Fourier Transform (FFT) analysis whereas the theoretical frequency was evaluated by using the following relation.

$$f = \frac{c}{4(L)} = \frac{350\,m/s}{4(150\,mm)} = 583.3\,Hz \quad , \quad (8)$$

where "c" is the speed of sound [7] and "L" is the total length of SWTAE. Fig. 9 shows the output frequency obtained by using each profile i.e., profile-I to profile-V yielded 659.8 Hz, 642.7 Hz, 627.1 Hz, 636.3 Hz, and 651.6 Hz frequency respectively. This indicates that the current results are in good agreement with the theoretical results and shows approximately 10 % deviation. To consider the performance of SWTAE, it is seen that profile-III yields minimum frequency among other profiles, and therefore a single step transition in temperature profile will need less effort to generate a standing wave inside the thermoacoustic engine.

A. Effect on Pressure Amplitude

Another performance indicator in thermoacoustic devices is a pressure magnitude. An engine with high-pressure amplitude is

capable of producing more power and vice versa. In the simulations, the pressure amplitude was monitored at the inlet region where the gas particles experience maximum pressure. Fig. 10 presents the sinusoidal pressure waves obtained for each thermal profile. From the results, it was found that profile-I to profile-V yield 3953 Pa, 6435 Pa, 8274 Pa, 6387 Pa, and 5019 Pa pressure amplitude respectively. This shows that the maximum pressure amplitude is achieved by employing profile-III total pressure of 109599 Pa.

The possible reason for maximum pressure amplitude with profile-III is due to the fact that the gas parcels near the stack are subjected to steeper temperature gradient. In other words, the nearby gas particles are experiencing thermal expansion and compression simultaneously. This results in thermal oscillations in phase which produce an appreciable effect during the formation of standing waves. In the same way, profile-IV is also associated with this effect.

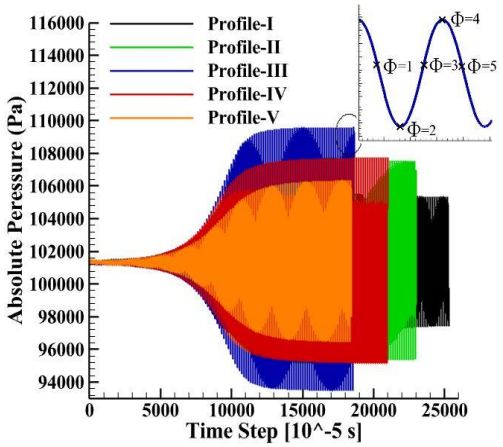

Figure 2. Absolute pressure values against time steps for five different profiles.

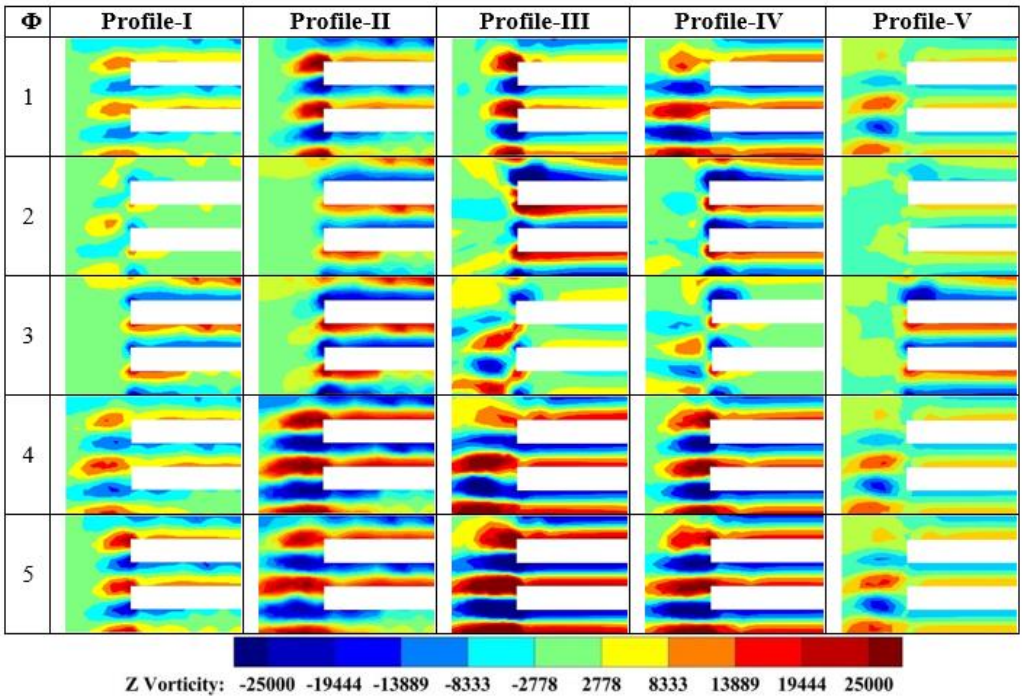

Figure 11. Formation of vortex-blobs in the vorticity contours at the left-hand side of the stack for each thermal profile in different phases.

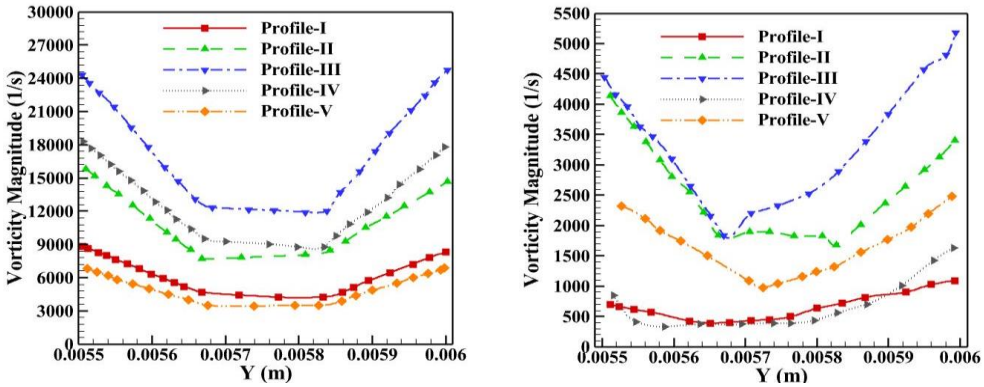

Φ = 1

Φ = 2

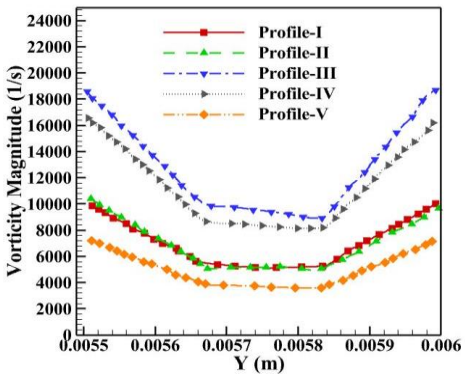

Φ = 3

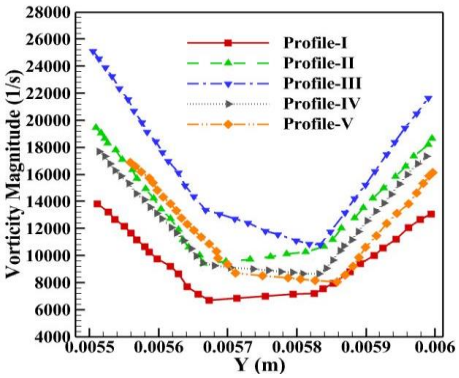

Φ = 4

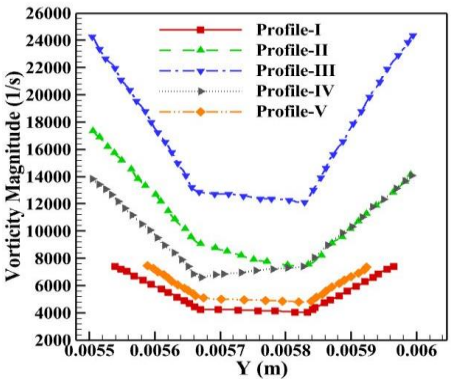

Φ = 5

Figure 12. Vorticity magnitude obtained for five different phases varying across the plate thickness associated with five different thermal profiles.

A. Effect on Vortex Formation

Thermoacoustic devices are mostly suffered from turbulence losses when they are subjected to a high drive ratio (maximum pressure to mean pressure) [11]. The formation of vortices around the stack is one of the major causes for the low performance of thermoacoustic engines. To evaluate the turbulence formation, the vorticity parameter has been considered to indicate the degree of vortices. For this purpose, the vorticity contours have been obtained for different phase angles as depicted in Fig. 11. The visualizations confirmed the presence of vortices formation at the left-hand side of the stack. The formation of vortex-blobs in phase (Φ = 1, 4, 5) indicates the

reverse flow in the engine causing vortex shedding phenomena. On the other hand, phase (Φ = 2, 3) shows small blob formation because the flow direction has been reversed causing the vortices on the right-hand side of the stack.

To quantify the degree of turbulence formation, the vorticity magnitude has been calculated for each thermal profile at the given plate thickness of the stack. Fig. 11 shows the vorticity magnitude plots obtained at region exists in between the walls of the stack. It shows that overall vorticity magnitude increases as moving towards stack walls. By comparison, the results indicate that profile-III achieved maximum vorticity value throughout the phase angles. On the other hand, the minimum vorticity is found by using profile-I (Φ = 2, 4) and profile-V (Φ = 1, 3, 5). The possible reason for the high value of vorticity by using profile-III is due to the high drive ratio. This shows that using profile-I and profile-V will give better results in terms of turbulence loss whereas profile-III offers more turbulences and therefore it will give poor performance.

V. CONCLUSION

In this paper, 2D CFD simulations have been conducted to investigate the effect various thermal boundary conditions on the performance of standing wave thermoacoustic engine. For this purpose, the mesh model was replicated and solved by using Fluent solver. Shear stress transport (SST) k-ω model was employed to model the flow turbulences. The study included five different thermal boundary conditions as, linear and sinusoidal forced temperature gradients (profile-I & profile-II). Similarly, a stepwise temperature gradient as, single step, double steps and multiple steps (profile-III, profile-IV & profile-V) thermal profiles respectively. Based on the simulations, the following results are obtained.

- The minimum output frequency is obtained by using profile-III whereas profile-I shows maximum output frequency.
- The maximum pressure amplitude is achieved by using profile-III whereas profile-I gives minimum pressure amplitude.
- To account for the turbulence losses, profile-V and profile-I yield better results whereas profile-III predicts worst results.

Based on these results, it is concluded that the implementation of single step (profile-III) temperature gradient on the engine stack yields better performance for power applications. However, to include the turbulence losses, the profile-IV is optimal choice for the standing wave thermoacoustic engine.

REFERENCES

[1] Ahmad, T., & Zhang, D. (2020). A critical review of comparative global historical energy consumption and future demand: The story told so far. *Energy Reports*, *6*, 1973-1991.

[2] Pietrosemoli, L., & Rodríguez-Monroy, C. (2019). The Venezuelan energy crisis: Renewable energies in the transition towards sustainability. *Renewable and Sustainable Energy Reviews*, *105*, 415-426.

[3] Rayleigh, J. W. S. B. (1896). *The theory of sound* (Vol. 2). Macmillan.

[4] Babu, K. A., & Sherjin, P. (2017). A Critical Review on Thermoacoustic Refrigeration and its Significance. *Int. J. ChemTech Res.*, *10*, 540-52.

[5] Jaworski, A. J., & Mao, X. (2013). Development of thermoacoustic devices for power generation and refrigeration. *Proceedings of the Institution of Mechanical Engineers, Part A: Journal of Power and Energy*, *227*(7), 762-782.

[6] Timmer, M. A., de Blok, K., & van der Meer, T. H. (2018). Review on the conversion of thermoacoustic power into electricity. *The Journal of the Acoustical Society of America*, *143*(2), 841-857.

[7] Zink, F., Vipperman, J. S., and Schaefer, L. A., (2009). Advancing thermoacoustics through CFD simulation using fluent, *ASME Int. Mech. Eng. Congr. Expo. Proc.*, 8,101-110.

[8] Ansys Fluent Fluid Simulation Software.https://www.ansys.com/products/fluids/ansys-fluent.

[9] Menter, F. R. (1994). Two-equation eddy-viscosity turbulence models for engineering applications," *AIAA J.*, 32, 1598-1605.

[10] Zink, F., Vipperman, J., and Schaefer, L. (2010) CFD simulation of thermoacoustic cooling, *Int. J. Heat Mass Transf.*, 53, 3940-3946.

[11] Swift, G. (2003). Thermoacoustics: A unifying perspective for some engines and refrigerators, *Thermoacoustic engines J. Acoust. Soc. Am.*, *113*(5), 3148.

Investigation of Magnetocaloric Effect Using Theoretical Models in $La_{0.1}Nd_{0.6}Sr_{0.3}MnO_3$

Asme Brahimi[1], Abdelkrim E. Merad[2], Mohammed Benali Kanoun[3]

[1]Automatic Laboratory, A. Belkaid University, Box 119, 13000, Tlemcen, Algeria asmebrahimi@gmail.com

[1,2]Solid State Physics Team, Theoretical Physics Laboratory, Faculty of Sciences, A. Belkaïd University, Box 119, 13000, Tlemcen, Algeria, aemerad@gmail.com[2]

[3]Department of Physics, College of Science, King Faisal University, P.O. Box 400, Al-Ahsa, 31982, Saudi Arabia, mkanoun@kfu.edu.sa

Abstract—**This Advances in magnetic cooling techniques depend on the study of new materials that exhibit significant magnetic effect near magnetic transitions. In this work we examine the phase transitions and magnetocaloric properties of $La_{0.1}Nd_{0.6}Sr_{0.3}MnO_3$ perovskite oxide material. The experimental magnetization of $La_{0.1}Nd_{0.6}Sr_{0.3}MnO_3$ under different magnetic fields 0.5T, 1T, 1.5T is explored using the thermodynamic Maxwell's relation and hence, the magnetic entropy change is determined. In addition, we report the magnetocaloric properties using a phenomenological model. Furthermore, to investigate the nature of the magnetic phase transition, we used a phenomenological universal curve which has confirmed the second-order magnetic phase transition of the sample. The good value of the relative cooling power indicates that the studied material is favorable in the energy resulting from the magnetic cooling technology.**

Keywords - magnetic cooling, magnetization, phenomenological model, universal curve

I. INTRODUCTION

Over recent years, human awareness about energy and the environment has been strongly emphasized. Resulting in a relentless search for environmentally friendly technologies, efficient magnetic refrigeration is one such important technology. It depends on the magnetocaloric effect (MCE), which is related to the magneto thermodynamic phenomenon, that is, the temperature change caused by a substance by the difference of the applied magnetic field [1, 2]. At present, there are several interesting materials of magnetocaloric materials, which are good candidates for used in the room temperature cooling devices [3]. Out of all the materials, perovskite materials of a general chemical formula ABO_3 (A= rare earth metal or alkaline earth, B is the transition metal, O is oxygen), have simple structure with unique physical properties as compared to those of others. Materials having perovskites structure usually behave as good electrical and thermal insulators at room temperature due to the absence of conduction electrons, high melting points, and thus showing different electrical and magnetic properties [4]. The properties of perovskites can also be tailored by suitable substitution i.e. A/B sites, replacement of A/B atoms [5].

In this paper, we are interested in the magnetocaloric effect of the perovskite manganite $La_{0.1}Nd_{0.6}Sr_{0.3}MnO_3$ near paramagnetic (PM)-ferromagnetic (FM) phase transition at different magnetic fields. The calculation by Maxwell relation and phenomenological model, based on the experimental data [6] provides magnetocaloric properties such as the change of magnetic entropy and the relative cooling power.

II. THEORICAL ASPECTS

A. Maxwell Relation

In order to calculate the magnetocaloric effect (MCE) of the $La_{0.1}Nd_{0.6}Sr_{0.3}MnO_3$ material we evaluated the magnetic entropy change $\left(-\Delta S_M\right)$ at several magnetic field values

between 0 and the maximum of the external applied field $\mu_0 H_{max}$. This behaviour can be obtained using the following Maxwell relation [7]:

$$\Delta S_M\left(T,\Delta\mu_0 H\right) = \\ = \mu_0 \int_0^{H_{max}} \left(\frac{\partial M\left(\mu_0 H,T\right)}{\partial T}\right) d\mu_0 H \quad . \qquad (1)$$

B. Phenomenological Model of Hamad

We also used the phenomenological model of Hamad to calculate the magnetocaloric properties [8]. According to this later, the variation of magnetization as a function of temperature is presented by:

$$M = \left(\frac{M_i - M_f}{2}\right)\tanh(A(T_c - T)) + BT + C \text{ , (2)}$$

where M_i and M_f are the initial and the final values of the magnetization, respectively. T_c is the Curie temperature. $A = \frac{2(B - S_c)}{M_i - M_f}$, B is the value of $\frac{dM}{dT}$ at the region before transition T_i , S_c is the value of $\frac{dM}{dT}$ at Curie temperature T_c, and $C = \left(\frac{M_i + M_f}{2}\right) - BT_C$.

The variation of the magnetic entropy is given by the following Eq. (2):

$$\Delta S_M = \int_0^{\mu_0 H_{max}} \left(\frac{\partial M}{\partial T}\right)_H d\mu_0 H = \\ == \left(-A\left(\frac{M_i - M_f}{2}\right) sech^2\left[A(T_c - T)\right] + B\right)\mu_0 H_{max} \qquad (3)$$

The cooling efficiency RCP of a material is defined as the product of ΔS_M^{max} and δT_{FWHM} as follow:

TABLE I. PARAMETERS OF MODEL OF HAMAD FOR $La_{0.1}Nd_{0.6}Sr_{0.3}MnO_3$ AT DIFFERENT APPLIED MAGNETIC FIELD VALUES.

$\mu_0 H$ (T)	M_i (emu/g)	M_f (emu/g)	Tc (K)	B (emu/g.K)	Sc (emu/g.K)
0.5	56.78	15.04	252	-0.48	-3.32
1	56.30	21.9	255	-0.51	-2.56
1.5	59.40	22	258	-0.39	-2.03

$$RCP = -\Delta S_M\left(T,\mu_0 H_{max}\right)\times\delta T_{FWHM} = \\ = \left(M_i - M_f - 2\frac{B}{A}\right)\mu_0 H_{max}\times \qquad . (4) \\ \times cosh^{-1}\left(\sqrt{\frac{2A\left(M_i - M_f\right)}{A\left(M_i - M_f\right) + 2B}}\right)$$

C. Phenomenological Universal Curve

To determine the order of magnetic phase transition, we used universal curve for the field dependence of ΔS_M proposed by Franco et al [9, 10]. Its construction was based on the rescaling the axes for a universal curve, i.e., all ΔS_M curves are normalized with their peak entropy change, respectively, as $\Delta S^{'} = \Delta S_M / \Delta S_M^{max}$, and the temperature axis is rescaled by a new parameter , defined by the expression [11].

$$\theta = \begin{cases} (T_C - T)/(T_{r1} - T_C) & T \le T_c \\ (T - T_C)/(T_{r2} - T_c) & T > T_c \end{cases} \quad , \qquad (5)$$

where T_{r1} and T_{r2} are the temperatures of the two reference points of each curve where ΔS_M . equal $\Delta S_M^{max}/2$.

III. RESULTS AND DISCUSSION

The isothermal magnetization curves of $La_{0.1}Nd_{0.6}Sr_{0.3}MnO_3$ found in [6] were measured over a wide range of temperatures from 227 to 265 K. We extracted the appropriate parameters in order to obtain agreement of magnetization versus temperature under several applied magnetic fields for $La_{0.1}Nd_{0.6}Sr_{0.3}MnO_3$ between the experimental and the modeled results using Eq. 2 of Hamad model. The parameters are listed in Table I. Fig. 1 shows the good agreement that we obtained between the experimental magnetization and the modeled magnetization. The Magnetization (M (T)) curves reveal that the

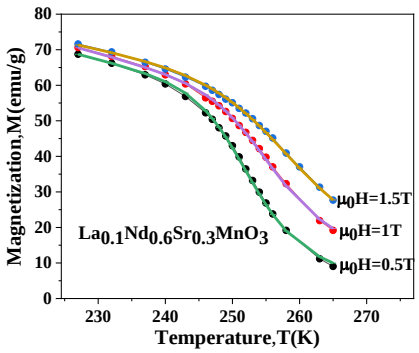

Figure 1. $-\Delta S_M(T,H)$ vs. under 0.5, 1, 1.5 magnetic field. The continuous lines are modeled results by Hamad model and symbols represent results of Maxwell integration.

TABLE II. VALUES OF MAGNETOCALORIC PROPERTIES FOR $La_{0.1}Nd_{0.6}Sr_{0.3}MnO_3$.

Methods	$\Delta\mu_0 H$ **(T)**	$-\Delta S_M^{max}$ $\left(J.Kg^{-1}K^{-1}\right)$	δT_{FWHM} **(K)**	**RCP (J/Kg)**
Hamad model	0. 5	1.66	14.80	24.568
	1	2.560	17.987	46.047
	1.5	3.045	24.235	73.796
Maxwell integration	0. 5	1.7	-	-
	0.1	2.704	-	-
	1.5	3.166	-	-

TABLE III. COMPARISON THE VALUES OF MAGNETOCALORIC PROPERTIES OF $La_{0.1}Nd_{0.6}Sr_{0.3}MnO_3$ WITH OTHER MATERIALS.

Materials	$\Delta\mu_0 H$ **(T)**	$-\Delta S_M^{max}$ $(J/Kg.K)$	**RCP (J/Kg)**	**Ref.**
$La_{0.1}Nd_{0.6}Sr_{0.3}MnO_3$	1.5	3.045	73.796	This work
$Fe_{40}Ni_{38}Mn_4B_{18}$	1.5	0.24	26.05	[12]
$La_{0.67}Ba_{0.33}Mn_{0.99}Sb_{0.01}O_3$	1.5	1.37	69.12	[13]
$Fe_{82}Zr_7Nb_2CuB_8$	1.5	0.3	-	[14]

sample $(0.5 < \mu_0 H < 1.5T)$ exhibits a paramagnetic-ferromagnetic (PM-FM) transition with decreasing temperature, in addition to a significant increase at T_C with increasing magnetic field.

Fig. 2 shows the change of the magnetic entropy $-\Delta S_M(T,\Delta\mu_0 H)$ as a function of temperature under different applied magnetic fields calculated using Maxwell relationship and Hamad model. There is a good agreement between them. Under a magnetic applied field, $\left|\Delta S_M^{max}\right|$ increases with increasing $\Delta\mu_0 H$ and reaches a maximum value of $3.045 J/Kg.K$ for $\Delta\mu_0 H = 1.5T$. The values of maximum

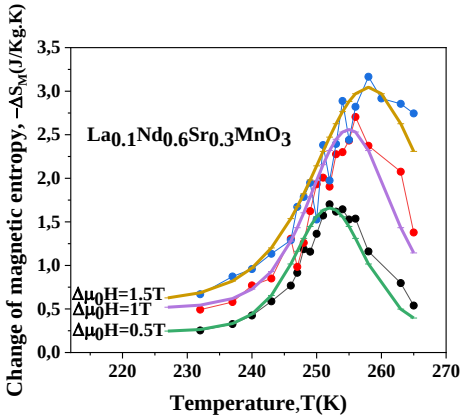

Figure 2. $-\Delta S_M(T,H)$ vs. under 0.5, 1, 1.5 magnetic field. The continuous lines are modeled results by Hamad model and symbols represent results of Maxwell integration.

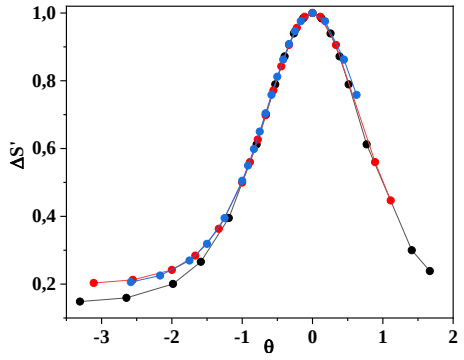

Figure 3. Universal behavior of the scaled entropy change curves of $La_{0.1}Nd_{0.6}Sr_{0.3}MnO_3$ at different fields.

magnetic entropy change $\left|\Delta S_M^{max}\right|$, full width half maximum δT_{FWHM}, and relative cooling power (RCP) are summarized in Table II. A comparison between our obtained results with those of other materials at the same magnetic field change indicate the high value of the RCP. This later make the studied material to be a good candidate in magnetic refrigeration application.

The universal curves of magnetic entropy in Fig. 3 under different maximum magnetic fields change ranging from 0.5 to 1.5 T Data points in the universal curves collapse with each other revealing the universal behavior that confirms the second order transition [10].

IV. Conclussion

In conclusion, we have investigated the magnetocaloric properties of the $La_{0.1}Nd_{0.6}Sr_{0.3}MnO_3$ perovskite material. The phenomenological model has been successfully used to model the change of the magnetic entropy from the magnetization versus temperature. The maximum magnetic entropy values found in this work is 3.045 J/Kg.K for a magnetic field change ($\Delta\mu_0 H$) equal 1.5T. According to the universal curve for the temperature dependence of ΔS_M measured for different maximum fields, the PM–FM phase transition observed for our samples has been classified as a second-order. Moreover, the good value obtained for RCP indicates the potentiality of using this material in magnetic refrigeration technology.

References

[1] Saidi, M., Bessais, L., & Jemmali, M. (2022). Review of the influence of copper and chromium substitution on crystal structure, magnetic properties and magnetocaloric effect of $GdFe_{2-x}$ (Cu, Cr) $_x$ (x= 0, 0.1, 0.15 and 0.2) intermetallic compounds. *Journal of Physics and Chemistry of Solids*, *160*, 110343.

[2] Berkutova, A., Zeleňáková, A., Hrubovčák, P., Kapusta, O., Szűcsová, J., & Tarasenko, R. (2021). Cryogenic magnetocaloric effect in Gd2O3 nanoparticles studied by heat capacity. *Journal of Magnetism and Magnetic Materials*, *540*, 168486.

[3] Kadim, G., Masrour, R., Jabar, A., & Hlil, E. K. (2021, June). First principal calculation and Monte Carlo simulations of the Magnetocaloric effect, Electronic and Magnetic properties in perovskite oxide $Pr_{0.65}Sr_{0.35}MnO_3$. In *IOP Conference Series: Materials Science and Engineering* (Vol. 1160, No. 1, p. 012010). IOP Publishing.

[4] Das, R., Alagarsamy, P., & Choudhary, R. N. P. (2021). Studies of Structural, Electrical, and Magnetic Characteristics of Double Perovskite Ceramic: La_2FeMnO_6. *physica status solidi (b)*, 2100299.

[5] Das, R., Alagarsamy, P., & Choudhary, R. N. P. (2021). Studies of Structural, Electrical, and Magnetic Characteristics of Double Perovskite Ceramic: La_2FeMnO_6. *physica status solidi (b)*, 2100299.

[6] Fan, J., Ling, L., Hong, B., Zhang, L., Pi, L., & Zhang, Y. (2010). Critical properties of the perovskite manganite La 0.1 Nd 0.6 Sr 0.3 MnO 3. *Physical Review B*, *81*(14), 144426.

[7] GschneidnerJr, K. A., Pecharsky, V. K., & Tsokol, A. O. (2005). Recent developments in magnetocaloric materials. *Reports on progress in physics*, *68*(6), 1479.

[8] Hamad, M. A. (2012). Prediction of thermomagnetic properties of La0. 67Ca0. 33MnO3 and La0. 67Sr0. 33MnO3. *Phase Transitions*, *85*(1-2), 106-112.

[9] Franco, V., Blázquez, J. S., & Conde, A. (2006). Field dependence of the magnetocaloric effect in materials with a second order phase transition: A master curve for the magnetic entropy change. *Applied physics letters*, *89*(22), 222512.

[10] Franco, V., Blázquez, J. S., & Conde, A. (2008). Influence of Ge addition on the magnetocaloric effect of a Co-containing Nanoperm-type alloy. *Journal of Applied Physics*, *103*(7), 07B316.

[11] Zheng, T. F., Shi, Y. G., Fan, J. Y., Shi, D. N., Tang, S. L., Lv, L. Y., & Zhong, W. (2013). Critical behavior and the universal curve for magnetocaloric effect in textured Mn5Ge3− x Al x ribbons. *Journal of Applied Physics*, *113*(17), 17A944.

[12] El Ouahbi, S., Charkaoui, A., Moubah, R., Yamkane, Z., Omari, L. H., Derkaoui, S., ... & Lassri, H. (2020). Magnetic, magnetocaloric properties and phenomenological model in amorphous Fe40Ni38Mo4B18 alloy. *Materials Today: Proceedings*, *30*, 951-955.

[13] Hassine, A. B., Dhahri, A., Bouazizi, L., Oumezzine, M., & Hlil, E. K. (2016). Characterization and theoretical investigation of the magnetocaloric effect of $La_{0.67}Ba_{0.33}Mn_{1-x}Sb_xO_3$ compounds. *Solid State Communications*, *233*, 6-10.

[14] Gondroa, J., Bªocha, K., Nabiaªeka, M., & Walltersb, S. Magnetocaloric E ect in Amorphous and Partially Crystallized Fe Zr Nb Cu B Alloy.

Predicting Solar Insolation Using MLR and RBF Based on Metheorological Parameters for Crni vrh and Niš, Serbia

Lazar Z. Velimirović[1], Radmila Janković Babić[2], Petar Vranić[3], Aleksandar Janjić[4]

[1,2,3]Mathematical Institute SANU, Belgrade, Serbia, lazar.velimirovic@mi.sanu.ac.rs[1], lolickaj@gmail.com[2], petarvvv@gmail.com[3]
[4]University of Niš, Faculty of Electronic Engineering, Niš, Serbia, aleksandar.janjic@elfak.ni.ac.rs

Abstract—**This research provided insights into the ability of the multiple linear regression (MLR) and Radial basis function (RBF) neural network to predict insolation using air pressure, air temperature, dew point, humidity, wind speed, cloud cover, and precipitation as independent variables. The study is performed for two meteorological stations Niš and Crni Vrh. Using the MLR and RBF neural network, prediction models have been generated with relative errors of 0.07 (for both Niš and Crni Vrh) and 0.11 (Crni Vrh) and 0.26 (Niš), respectively. Moreover, the sensitivity analysis revealed that the most important independent variables for the RBF neural networks were wind (Crni Vrh) and humidity (Niš), but the other predictors also contributed to the model significantly. The compiled MLR models indicated Crni Vrh might be investigated and included in the projection plans for solar photovoltaic energy generation. The MLR models found solar insolation tends to significantly increase with higher dew point, and lower cloud cover, considering these factors Crni Vrh might have a potential for solar PV generation.**

Keywords – prediction, multiple linear regression, radial basis function, solar energy

I. INTRODUCTION

Serbia falls in the category of energy medium-dependent country, which means that cumulative annual energy consumption outstrips domestic production relying on import of about 40% [1]. Regardless, the energy sector in Serbia is perceived as a vital in supporting sustainable economic growth in the future [2]. Solar energy is the cleanest and most inexhaustible renewable energy source available to us. Contemporary solar technologies allow for its direct exploitation in an environmentally friendly manner providing energy for different use scenarios. In line with the global transition towards an economy based on renewable energy sources (RES), Serbia can count on a significant amount of energy derived from the various types of RES, among which solar is the most abundant one. The average solar radiation in Serbia is about forty percent higher than the EU average, however, the usage of it in the production of electric power lags substantially behind that of EU countries [3]. Instead, it is primarily harvested for heat energy as a cost-effective alternative to conventional energy.

One of the key parameters for the design of a solar power system is available insolation. These values can suggest the expected output of solar panels for a particular location, and thus, inform the spatial analysis of potential power plants. Furthermore, when it comes to the design of the energy cycle within buildings, it is important to understand the relationship between the meteorological parameters and solar insolation. Along these lines, the objective of this research is to investigate the relationship between the key meteorological variables and solar insolation to provide monthly predictions of solar insolation values. For this research two locations in Serbia

ISBN: 978-86-80593-73-9

are selected: the city of Niš, and Crni Vrh mountain. For monthly predictions, multiple linear regression (MLR) and Radial basis function (RBF) neural network are employed.

II. DATA AND METHODOLOGY

A. Data

In this research two datasets were compiled based on the reports provided by the Republic Hydrometeorological Service of Serbia. The datasets comprise seven independent and one dependent variable for two locations in Serbia – Crni vrh and Niš. The independent variables include average air pressure (mb), average air temperature (°C), average dew point (mb), humidity (%), average wind speed (m/s), average cloud cover (in tenths), and the sum of precipitation (mm). The dependent variable is solar insolation measured in hours. The datasets include monthly data for the period January 2008 – December 2019. The Niš meteorological station is located in the city of Niš at 43°20' latitude and 21°54' longitude and the elevation of 202 meters. The Crni vrh meteorological station is located on a mountain in the East of Serbia at 44°08' latitude and 21°58' longitude at the elevation of 1037 meters (Fig. 1).

B. Methodology

The methodology is based on statistical and machine learning techniques, mainly the MLR and RBF.

The MLR is a technique aiming to fit the linear regression line to the data comprising of multiple independent variables as inputs and predict the value of the output variable. The regression Eq. is represented as follows:

$$\gamma = \beta_o + \beta_1 x_1 + \beta_2 x_2 + \beta_3 x_3 + \cdots + \\ + \beta_n x_n + \in \quad , \quad (1)$$

where y is the dependent variable, β_o is the constant term (intercept), $\beta_{1,2,\ldots n}$ are the slope coefficients of each independent variable, and ϵ is the error term. The MLR has several assumptions that need to be met in order to proceed with the analysis. First, the relationship between the dependent and the independent variables needs to be linear. Second, the residuals should be normally distributed. The third assumption is the assumption of homoscedasticity, i.e. the constant variance of errors. Fourth, multicollinearity should not be present in the dataset.

Figure 1. Meteorological stations in Niš and Crni Vrh, Serbia.

The RBF is a feedforward neural network with radially symmetric activation functions [4] and was first introduced by Broomhead and Lowe in [5]. The RBF uses radial basis functions as activations, and has three layers – an input layer, a hidden layer that uses a radial basis function (such as Gaussian), and a linear output layer. All input neurons are connected to each hidden neuron. The network works by first finding the centers and widths using Euclidian distance, and then fitting the model by calculating the weights between the hidden layer and the output layer and minimizing the training error [6]. The output of the activation function ϕ_i in the hidden layer can be represented as in [6]:

$$\phi_i = \left(\left\|x - c_i\right\|\right) = \exp\left(-\frac{\left\|x - c_i\right\|^2}{2\sigma_j^2}\right), \quad (2)$$

where $\left\|x - c_i\right\|$ is the Euclidian norm, c_j is the center of the hidden neuron j, σ_j is the width of the hidden neuron j. The output of the node in the output layer can be found as in [6]:

$$y_k = \sum_{j=1}^{n} w_{jk}\phi_j(x) \ . \quad (3)$$

The main advantage of RBF networks is that they are fast and more compact than other neural networks [7]. These networks are robust to input

TABLE I. DESCRIPTIVE STATISTICS OF THE DATASET.

	Pressure	Temperature	Dew point	Humidity	Wind speed	Cloud cover	Precipitation	Insolation
Crni Vrh								
Valid cases	144	144	144	144	124	144	144	144
Missing	0	0	0	0	20	0	0	0
Mean	897.74	7.615	8.940	78.847	5.110	5.720	69.151	173.99
Std. Deviation	3.5385	7.8312	3.8350	9.0626	0.9854	1.6624	43.6989	90.646
Skewness	-0.586	-0.093	0.319	-0.513	0.639	-0.221	1.036	0.259
Kurtosis	0.592	-1.224	-1.251	-0.223	0.705	-0.759	1.396	-0.989
Minimum	887.4	-9.3	2.9	49.0	2.9	1.7	4.2	26.9
Maximum	908.0	20.8	16.5	95.0	8.6	8.7	246.4	368.2
Niš								
Valid	144	144	144	144	141	144	144	141
Missing	0	0	0	0	3	0	0	3
Mean	992.68	12.976	10.863	68.486	1.028	5.208	53.557	166.12
Std. Deviation	3.7868	8.0240	4.3219	9.8513	0.3101	1.6589	34.3978	86.231
Skewness	0.871	-0.124	0.265	-1.951	0.427	-0.253	1.008	0.065
Kurtosis	1.881	-1.180	-1.228	10.086	-0.298	-0.680	1.252	-1.131
Minimum	984.9	-4.3	3.5	6.0	0.5	1.6	1.7	25.5
Maximum	1007.3	26.6	19.7	84.0	2.0	8.3	177.1	330.0

TABLE II. MULTICOLLINEARITY DIAGNOSTICS.

Multicollinearity diagnostics	**Crni Vrh**		**Niš**	
	Tolerance	***VIF***	***Tolerance***	***VIF***
Pressure	0.462	2.162	0.477	2.095
Temperature	0.016	62.718	0.028	36.070
Dew point	0.023	43.466	0.045	22.416
Humidity	0.070	14.321	0.279	3.589
Cloud_cover	0.101	9.884	0.179	5.587
Precipitation	0.603	1.658	0.603	1.658
SMEAN(Wind)	0.421	2.376	0.682	1.466

noise and have a good generalization ability. The analyses and modellings have been performed in SPSS v.25.

III. RESULTS

A. Descriptive Statistics

First, the descriptive analysis has been performed to inspect variable distribution. The mean, standard deviation, minimum, and maximum values are reported in Table I, as well as skewness and kurtosis for both sets of data. It can be observed that the wind variable has 20 missing values for the Crni Vrh dataset, and 3 missing values for the Niš dataset. Additionally, the Niš dataset also has 3 missing values in the Insolation variable. As it is important to preserve all the data, the missing values were imputed using linear interpolation. The most important descriptive parameters are skewness and kurtosis, as they indicate whether the data is normally distributed. As suggested in [8, 9], the values of skewness and kurtosis should be between -2 and 2 to indicate normal distribution. For both datasets, the values of skewness and kurtosis for the dependent variable are within the limits, confirming normal distribution of data.

B. Multiple Linear Regression

The first MLR trial indicated the existence of collinearity in both datasets. The collinearity statistics for the Crni Vrh dataset indicates VIF

values of above 10 for Temperature, Dew point, and Humidity variables. For Niš, VIF values higher than 10 are observed for Temperature, and Dew point (Table II). Thus, to remove the effects of multicollinearity, the variable Temperature was removed from the MLR model.

The repeated MLR obtained good performance, confirming the model fit. Considering the assumptions of the linear regression, normality of residuals can be confirmed from the P-P plot, while homoscedasticity can be checked using the scatterplot. The residuals are equally distributed hence homoscedasticity assumption can be confirmed (Fig. 2). Lastly, multicollinearity is assessed using VIF values. As all VIF values are below the acceptable value of 10, we can confirm that multicollinearity is not a problem (Table III).

The same can be observed for the Niš dataset. Normality of residuals can be confirmed based on the P-P plot, with small variations in the lower part of the curve (Fig. 3). The residuals are equally distributed hence homoscedasticity assumption can be confirmed. Finally, VIF values are below the acceptable value of 10, thus it can be confirmed that data does not show multicollinearity (Table IV).

The adjusted R^2 of the model for Crni Vrh is 0.951 meaning that the linear regression explains 95.1% of the variance in the data. The F test is significant, confirming that the model explains well the variance in the dependent variable. Based on the p values presented in Table III, it can be observed that only precipitation and wind speed are not significant predictors. Moreover, the highest impact on the prediction has the dew point ($\beta = 0.461$).

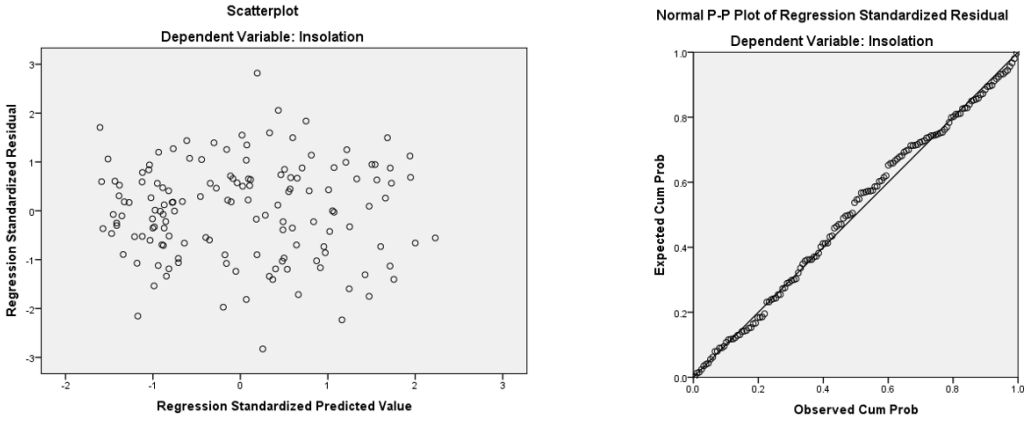

Figure 2. Crni Vrh – scatterplot and normality plot.

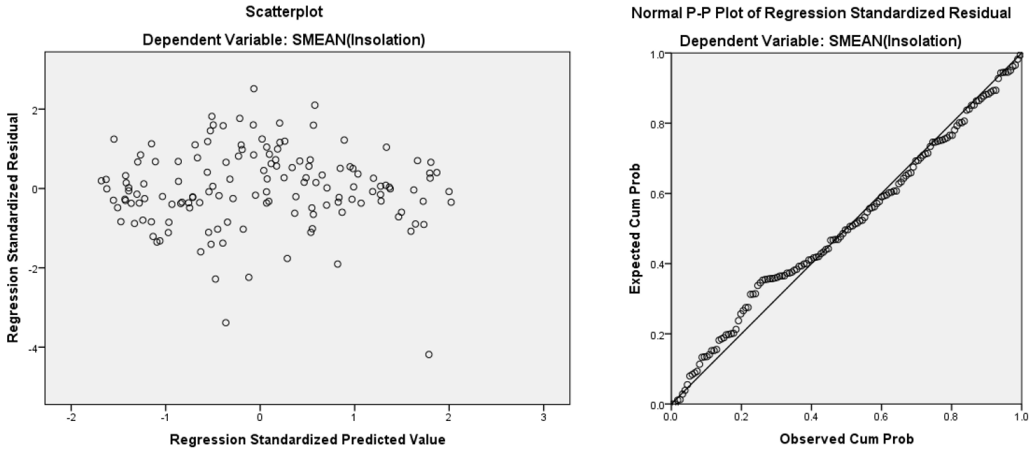

Figure 3. Niš – scatterplot, and the normality plot.

TABLE III. THE RESULTS OF THE MLR FOR CRNI VRH.

Crni Vrh	Unstandardized coefficients		Standardized coefficients			
Variables	B	SE	β	t	p	VIF
Constant	2208.713	601.062		3.675	0.000	
Pressure	-1.978	0.670	-0.077	-2.950	0.004	1.992
Dew point	10.891	0.808	0.461	13.481	0.000	3.398
Humidity	-3.007	0.416	-0.301	-7.223	0.000	5.040
Cloud cover	-22.211	2.976	-0.407	-7.462	0.000	8.666
Precipitation	0.006	0.049	0.003	0.127	0.899	1.634
Wind	1.404	2.739	0.014	0.513	0.609	2.217

F(6, 137) = 461.917, P=0.000; ADJUSTED R2 = 0.951.

TABLE IV. THE RESULTS OF THE MLR FOR NIŠ.

Niš	Unstandardized coefficients		Standardized coefficients			
Variables	B	SE	β	t	p	VIF
Constant	1133.957	708.002		1.602	0.112	
Pressure	-0.806	0.709	-0.036	-1.138	0.257	1.926
Dew point	7.626	0.811	0.386	9.398	0.000	3.286
Humidity	-1.979	0.308	-0.228	-6.434	0.000	2.452
Cloud cover	-26.453	2.469	-0.514	-10.716	0.000	4.481
Precipitation	0.133	0.072	0.054	1.842	0.068	1.653
Wind	15.566	7.616	0.056	2.044	0.043	1.459

F(6, 137)=301.361, p=0.000; Adjusted R2 = 0.926

TABLE V. RBF MODEL PERFORMANCE.

	Model performance	Crni vrh	Niš
Training	Sum of Squares Error	5.334	8.999
	Relative Error	0.112	0.189
	Training Time	0:00:00.10	0:00:00.07
Testing	Sum of Squares Error	4.743[a]	2.814[a]
	Relative Error	0.142	0.092
Dependent Variable: Insolation			
a. The number of hidden units is determined by the testing data criterion: The "best" number of hidden units is the one that yields the smallest error in the testing data.			

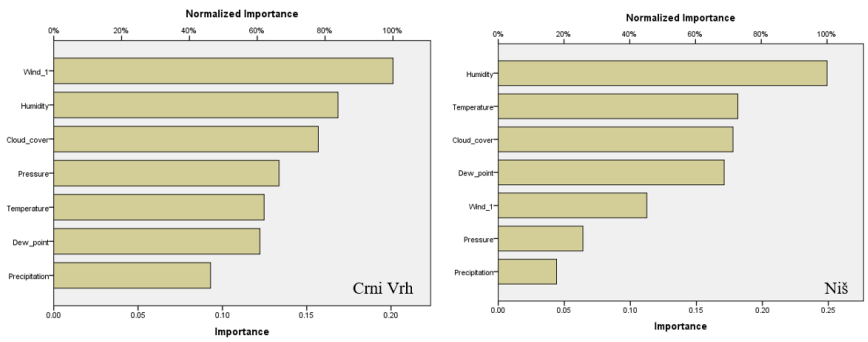

Figure 4. The importance of the independent variables in the RBF model.

For Niš, the adjusted R^2 of the model is 0.926 meaning that the model explains 92.6% of the variance in the data. The F test is significant hence the model explains the variance in the dependent variable adequately. Based on the p values presented in Table IV, it can be observed that pressure and precipitation are not significant predictors. Considering significant predictors, the highest impact on the prediction has the cloud cover (β = -0.514, B = -26.453) indicating that for every 1 unit increase in the cloud cover, the solar insolation decreases by 26.453 hours. For pressure and precipitation, the coefficients of -0.806 and 0.133 are not different from 0.

C. RBF

The datasets were separated into training (96 cases) and testing (48 cases) to prevent overfitting. The RBF for Crni Vrh is composed of an input layer with 7 neurons, one hidden layer with 10 neurons and a softmax activation function, and an output layer with one neuron and the identity activation function. The RBF for Niš has similar architecture, except that it has 3 neurons in the hidden layer. As error function, the sum of squares is used. The data was standardized before RBF modeling.

Considering the network performance for the Crni Vrh dataset, the training sum of squares error is 5.334, while the testing error is 4.743. Additionally, the relative training error is 0.112,

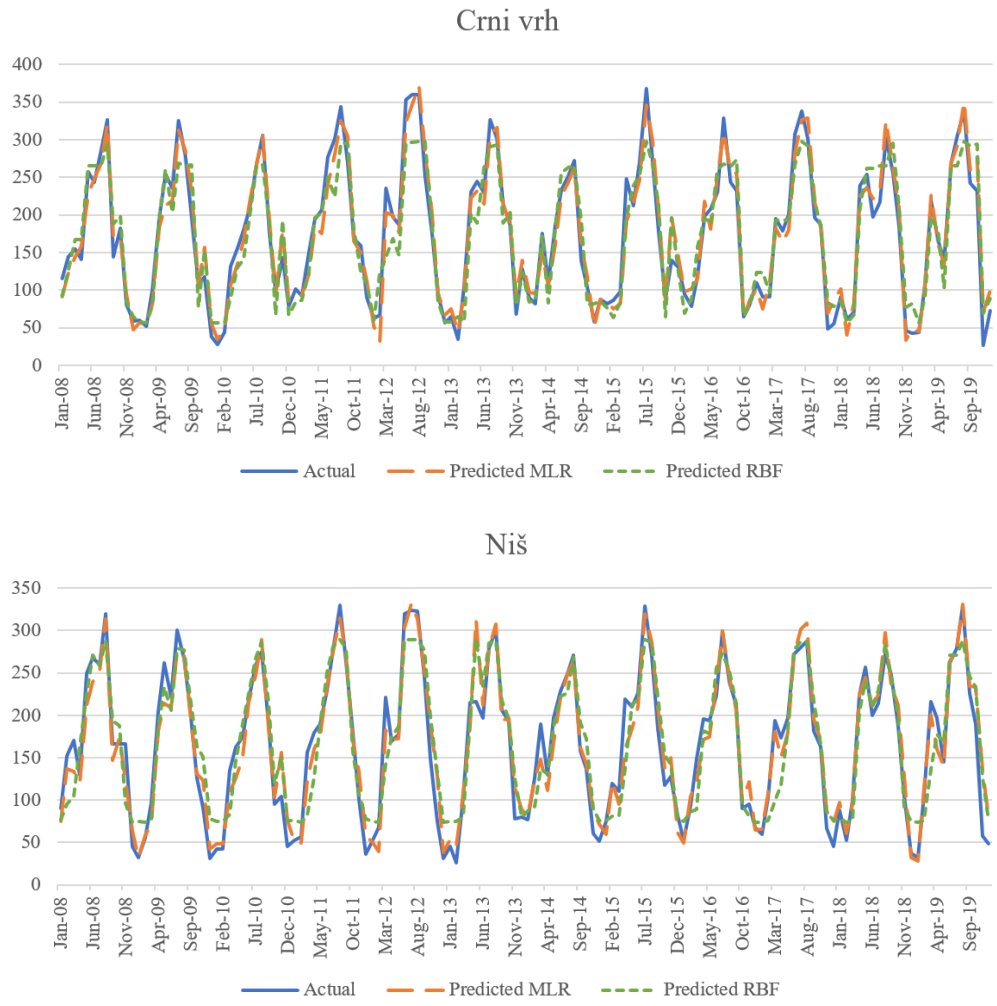

Figure 5. Actual values vs. predicted by the MLR, and predicted by the RBF models.

while the testing error is 0.142. The network performance for the Niš dataset obtained the training sum of squares error of 8.999, while the testing error is 2.814. The relative training error is 0.189, relative testing error is 0.092. These results are shown in Table V.

The sensitivity analysis was used to assess the importance of each independent variable in building the RBF model. For Crni Vrh, every input variable has importance higher than 10%, except precipitation which has importance of 9%. Considering Niš, humidity is the most important variable with an importance of close to 25%, followed by Temperature, cloud cover, and dew point that each have importance of above 15%. The importance plot is shown in Fig. 4.

Lastly, the predicted values from each of the two models were plotted against the actual values, for both locations (Fig. 5). The overall relative errors for the MLR model are almost equal for both locations – 0.074 for Crni Vrh, and 0.075 for Niš. The relative errors for the RBF model are 0.113 for Crni Vrh, and 0.261 for Niš.

IV. Discussion and Conclusion

Insolation values are useful when projecting the solar power systems. These values can suggest the expected output for solar panels and their location where they would be the most effective. Furthermore, when projecting building energy production/consumption, it is important to understand the relationship between the meteorological parameters such as temperature, and solar insolation.

This research aimed to evaluate the relationship of the meteorological variables and solar insolation and make predictions of monthly solar insolation values for two locations in Serbia: a city of Niš, and Crni Vrh mountain. As inputs the monthly values of meteorological parameters were used including air pressure, air temperature, dew point, humidity, wind speed, cloud cover, and precipitation. Using the MLR and RBF neural network, prediction models have been generated with relative errors of 0.07 (for both Niš and Crni Vrh) and 0.11 (Crni Vrh) and 0.26 (Niš), respectively. Furthermore, the sensitivity analysis revealed that the most important independent variables for the RBF neural networks were wind (Crni Vrh) and humidity (Niš), but the other predictors also contributed to the model significantly.

The MLR provided insights on the change and contribution of each of the statistically significant predictors on the model. For Crni Vrh, it was found that for an increase of 1 mb in monthly air pressure, solar insolation decreases by 1.978 hours. Moreover, for every 1 mb increase in monthly dew point, solar insolation increases by 10.891 hours. Considering humidity, for every 1% of increase in humidity, solar insolation decreases by 3.007 hours per month. Lastly, solar insolation decreases by 22.211 hours for every 1 tenth increase in cloud cover. Precipitation and wind speed have found to be insignificant predictors.

Similar relationships have been detected for Niš. Mainly, with every 1 mb increase in monthly dew point, solar insolation increases by 7.626 hours per month. An increase of 1% in humidity decreases solar insolation by 1.979 hours, while an increase in 1 tenth of cloud cover leads to a decrease of solar insolation by 26.453 hours. Lastly, an increase of wind speed of 1 m/s leads to an increase of solar insolation by 15.566 hours, while pressure and precipitation are not significant predictors.

This research provided insights about the ability of MLR model and RBF neural network to predict solar insolation. The compiled MLR models indicated that Crni Vrh might be investigated and included in the projection plans for solar photovoltaic energy generation. Because the MLR models found that solar insolation tends to significantly increase with higher dew point, and lower cloud cover, considering these factors Crni Vrh might have a potential for solar PV generation.

Acknowledgment

This work was supported by the Ministry of Education, Science and Technological Development of the Republic of Serbia through the Mathematical Institute SANU.

References

[1] Tolmaca, J., Prvulovica, S., Nedica, M., & Tolmacb, D. (2019). Analysis of the development opportunities of solar systems in Serbia. *Agricultural Engineering* 23(2), pp. 85-92.

[2] Republic of Serbia Ministry of Mining and Energy (2016). Energy Sector Development Strategy of the Republic of Serbia for the period by 2025 with projections by 2030

[3] Lepotic-Kovacević, B., Lazarević, B. (2016). Construction of plants and electricity generation from photovoltaic plants in the republic of Serbia - Guide for investors. UNEP: Belgrade

[4] Chen, T., & Chen, H. (1995). Approximation capability to functions of several variables, nonlinear functionals, and operators by radial basis function neural networks. *IEEE Transactions on Neural Networks*, 6(4), 904-910.

[5] Broomhead, D. S., & Lowe, D. (1988). Radial basis functions, multi-variable functional interpolation and adaptive networks (No. RSRE-MEMO-4148). Royal Signals and Radar Establishment Malvern (United Kingdom).

[6] Faris, H., Aljarah, I., & Mirjalili, S. (2017). Evolving radial basis function networks using moth–flame optimizer. In *Handbook of neural computation* (pp. 537-550). Academic Press.

[7] Er, M. J., Wu, S., Lu, J., & Toh, H. L. (2002). Face recognition with radial basis function (RBF) neural networks. *IEEE transactions on neural networks*, 13(3), 697-710.

[8] Trochim, W. M., & Donnelly, J. P. (2006). The research methods knowledge base (3rd ed.). Atomic Dog.

[9] Field, A. (2009). Discovering statistics using SPSS. SAGE.

Ultrasonic Mixing Conditions Affect Nanofluids Stability and Physical Properties

Jasim Alenezy[1], Rafet Yapici [2], Amar Hasan Hameed[3]

[1,2]Konya Technical University, Konya, Turkey, iraqi_jas75@yahoo.com[1]
ryapici@ktun.edu.tr[2]
[3]Karatay University, Konya, Turkey, ahasan.hameed@karatay.edu.tr

Abstract—**Nanofluids have attracted the interest of researchers due to their unique thermal and optical characteristics and various potential applications. The stability of nanoparticles in nanofluids is one of the most critical properties of nanofluids. To achieve the optimum homogeneity and stability of the nanoparticles, several factors have to be considered during the preparation processes of nanofluids. These factors include temperature, frequency, location of ultrasound source, and sonication time. This experimental study prepared two nanofluids from two synthetic oils mixed with copper monoxide (CuO) nanoparticles. Different preparation conditions such as frequency, temperature, time, and source location, have been investigated to obtain the optimum stability and physical properties. In addition, Zeta potential analysis (DLS) and Spectral analysis (SPL) observation for possible sedimentation over time have been conducted. The stability results indicated that some prepared samples possess excellent photophysical properties, and they proved long-time stability even after three months of preparation. The best conditions for the mixing process are the longer time of Sonication, higher temperature, direct mixing, higher frequency, and lower base fluid viscosity.**

Keywords - nanofluids, stability, ultrasound source, and sonication time

I. INTRODUCTION

Nanofluid has spread extensively in the last few years in many industrial, renewable energy, and many other various applications. Maintaining the stability of nanoparticles within nanofluids is one of the most crucial challenges facing the practical use of nanofluids and thus takes the interest of many researchers. The strength of a nanofluid is determined by the quality of dispersion and the suspension of nanoparticles in the mixture. Furthermore, these characteristics directly affect the thermophysical and optical properties of nanofluids. The stability of nanofluids is an essential consideration in applications that include heat transfer and solar absorption processes. The sedimentation of nanoparticles decreases the thermal conductivity of nanofluids and changes other optical and thermal properties. Therefore, investigation on stability is necessary, and it is the issue key that influences the properties of nanofluids. Reference [1] used a two-step method to produce alumina nanofluids. Reference [2] prepared TiO2-water nanosuspension in the same way. Xuan et al. used commercially available Cu nanoparticles to formulate water and transformer oil nanofluids. Reference [3] used a two-step method to prepare CuO dispersed ethylene glycol nanofluids by Sonication and without stabilizers. In this work two-step preparation process to prepare nanofluids is selected. It is extensively used to synthesize nanofluids by mixing base fluids with commercially available nanopowders obtained from different mechanical, physical, and chemical routes such as milling, grinding, and sol-gel and vapor-phase methods.

After preparing nanofluids, agglomeration might occur over time, resulting in fast sedimentation of nanoparticles due to the growth of downward body force. The preparation time is one of the essential effective parameters on nanofluid stability, and it differs from one mixture to another. Reference [4] used ultrasonication time eleven hours to prepare CuO (28.6 nm) with distal water at volume fraction (1–4)%. Reference [5] used ultrasonication time

(2–7) hours to preparation CuO (10 nm) with distal water at a volume fraction of 0.003%. Reference [6] used ultrasonication time one hour to prepare CuO (25 nm) with distal water and SDBS at a volume fraction of 0.1%. Reference [7] used 15 minutes to preparer Cu (25 nm) with Distal water and SDBS.

Several methods in the literature have done the stability evaluation. Reference [8] evaluated the dispersion characteristics of alumina and copper suspensions using the conventional sedimentation method with the help of absorbency analysis by using a spectrophotometer after the breaks deposited for 24 h. Reference [9] used UV/Vis spectrophotometric measurements to show the homogeneous dispersion of carbon nanotubes with SDS in the nanofluids. Reference [10] investigated the stability of MWNT nanofluids at different sediment times from the relation between MWNT concentration and its UV/Vis absorbance value, the concentration of the MWNT nanofluids at other sediment times could be obtained. Reference [11] investigated the stability of colloidal FePt nanoparticle systems via spectrophotometer analysis. Reference [12] examined nanofluid's resilience and mixing quality using UV/Vis spectrophotometer. Reference [13] evaluated the dispersion behavior of the aqueous copper Nano suspensions under different pH values, different dispersant types, and concentrations by the method of zeta potential, absorbency, and sedimentation photographs. Reference [14] studied the stability of nanofluids with the UV/Vis spectrophotometer. It is believed that the strength of nanofluids is strongly affected by the characteristics of the suspended particles and the base fluid, such as particle morphology.

In this study, we will discuss the effect of Ultrasonic sonication on the stability of nanofluids, then evaluation of equilibrium will be assessed by Zeta potential analysis (DLS) and Spectral analysis (SPL). This research studies parameters that may affect ultrasonic Sonication, and it will make try to improve stability by optimizing sonication process parameters. Type of ultrasonic sonication equipment, time of preparation of nanofluid, frequency used for practice, and the effect of mixture temperature during preparation period are the factors studied here to investigate the proper role of sonication process instability nanofluid.

II. MATERIAL AND RESULTING

A. Material

Ultrasound sonication remains one of the most critical factors affecting the stability of nanofluids. An ultrasonic vibrator or higher shear mixing device is generally used to stir nanopowders with host fluids. Frequent use of ultrasonication stirring is required to reduce particle agglomeration. According to the user device, there are two types of ultrasound sonication processes: direct Sonication by the vibration of a rod inside the fluid or indirect sonication process, which uses a bath of fluid to transmit sound waves to a container include the mixture of nanofluid, as shown in Fig. 1 In addition, a probe sonication device is used for samples with limited volume.

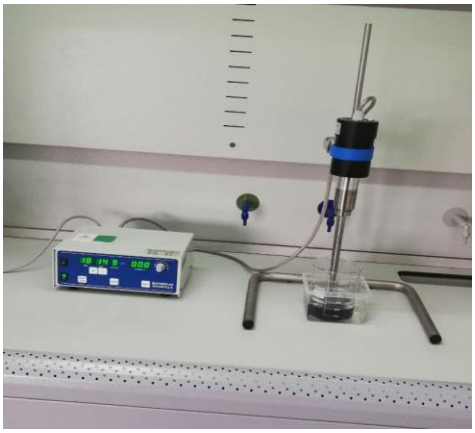

a)

b)

Figure 1. (a) Sonication equipment (Direct (probe sonicator) (b) Indirect sonication device (bath sonicator).

There are many methods to evaluate the stability of nanofluids. This study uses two ways to estimate strength: Zeta potential analysis and Spectral analysis. Zeta potential is the potential difference between the dispersion medium and the stationary layer of fluid attached to the particle. The zeta potential indicates the degree of repulsion between adjacent similarly charged particles in the dispersion. Nanofluids with zeta potential from 40-60 mV are believed to have excellent stability. Reference [15] used zeta potential analysis for Au nanofluids and found outstanding strength. Reference [16] measured Zeta potential to evaluate the stability of water-based nanofluids containing MWNTs with surfactants. The influence of two water-based nanofluids' peace was studied using zeta potential analysis [17]. Spectral analysis via UV/VIS spectrophotometer is another helpful way to evaluate the stability of nanofluids. The change of absorbance is considered a function of the nanofluid's strength. The advantage over other methods is that UV/VIS spectroscopy gives quantitative results corresponding to the concentration of nanofluids. Many researchers used a potential zeta test and UV/VIS spectroscopy to estimate stability. The two pieces of equipment are available in Selcuklu University/Nanotechnology research center, and they are used to test samples, shown in Fig. 2.

a)

b)

Figure 2. Equipment used for testing stability of nanofluid: (a) Zeta Potential, (b) UV/VIS Spectrophotometry.

B. Resulting

To estimating nanofluid's stability consists of (0.075% CuO with 0w20), Zeta potential analysis, and Spectral analysis after preparing nanofluid. To explain the effect of using different mixing instruments, the samples are prepared and mixed using other Sonication devices to compare and investigate the impact of the sonication device on stability. In the first sample, nanofluid is prepared consecutively using the two devices: Ultrasonic bath sonicator for one hour and ultrasonic probe sonicator for one hour. Then, another sample is tested using an ultrasonic bath sonicator only for two hours. This

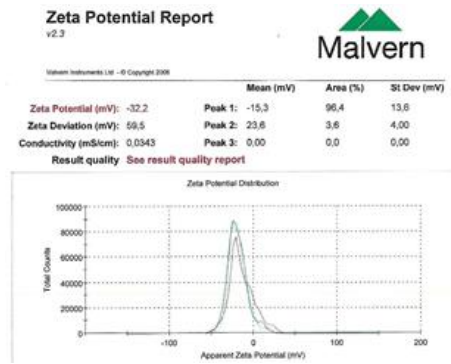

a)

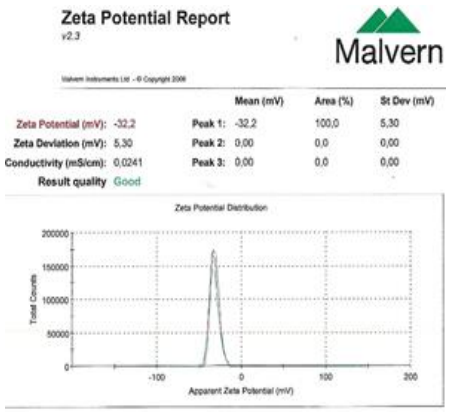

b)

Figure 3. (a) Results of zeta potential for indirect and direct sonication devices, (b) Results of zeta potential for indirect sonication device.

result of zeta potential for the two samples is shown in Fig. 3. Results indicate that the stability in both instances is good, and there is no difference between them in zeta potential.

After three months, the two samples are tested by UV- VIS spectrophotometer for this nanofluid. There is a significant difference in absorption property for the two samples. The first sample shows better absorption properties than the second sample, as shown in Fig. 4. It means that the stability of nanoparticles in the base fluid is higher in the first sample, and sedimentation is less than that of the second sample.

Several experiments are performed under different periods of Sonication to investigate the effect of time of mixing on the stability of nanofluid. In addition, two extra-base liquids with different viscosities are used to examine the relation of mixing time with the base liquid's viscosity. The first synthetic oil used as a base fluid has a lower viscosity value (0W20), and the second synthetic oil used as a base fluid has a higher viscosity (10W60). The nanoparticle used are the same (CuO), and volume fractions for all samples are the same (0.075%). The nanofluid with 0W20 was tested for three periods (2 hours, 3 hours, and 4 hours). The second nanofluid with 10W60 was tested under four time periods (3 hours, 4 hours, 5 hours, and 6 hours). For the first nanofluid, the results of the potential zeta report refer to for this type the best mixing time is 3 hours as shown as in Fig. 5.

The spectrophotometer report for the three samples of the first nanofluid, measured after three months from preparation, refers to the stability for nanofluid improved with a more extended mixing period, as shown in Fig. 6.

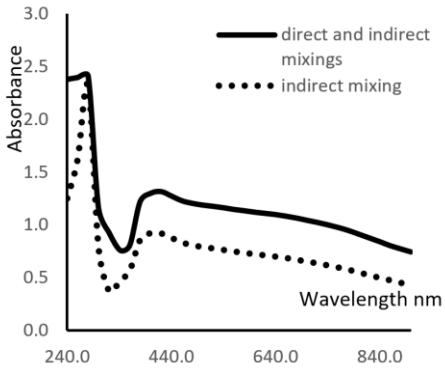

Figure 4. Results of absorbance after three months for two samples prepared by two different devices.

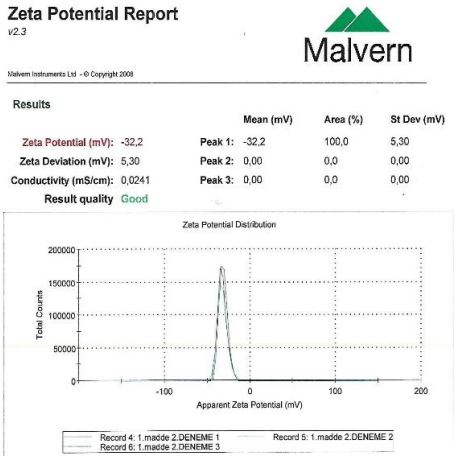

a)

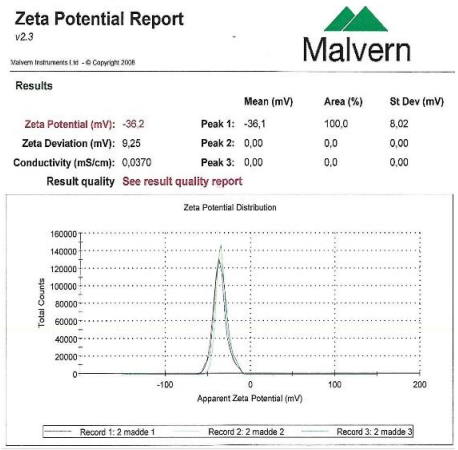

b)

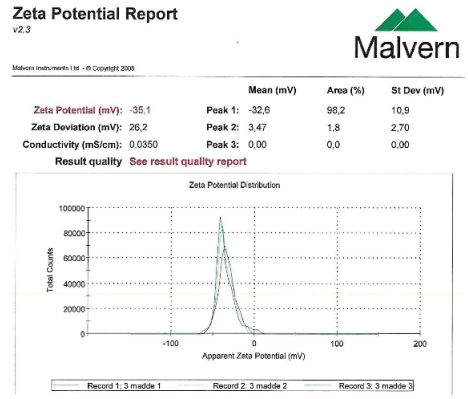

c)

Figure 5. Zeta potential analysis report for nanofluid (0.075% CuO with 0W20) for mixing period (a) 3 hours, (b) 2 hour, (c) 4 hours.

Four different mixing periods are used (3 hours, 4 hours, 5 hours, and 6 hours). For stability analyzing the UV spectrophotometer test is used after samples preparation, and after 40 days, the test is repeated. The first test shows that all absorption values are the same, but after 40 days, the absorption values generally decrease for all the samples, as shown in Fig. 7. However, the piece made under more extended periods (six hours) delivers the best absorption values in Fig. 8.

Fig. 9 and 10 show the effect of ultrasonic selected sonication frequencies on the nanofluid stability. The nanofluid is CuO with motor oil (10W60). Preparing these samples is taken constantly as two hours, and the temperature mixture is constant too. According to the spectrometer report, the models equipped at a

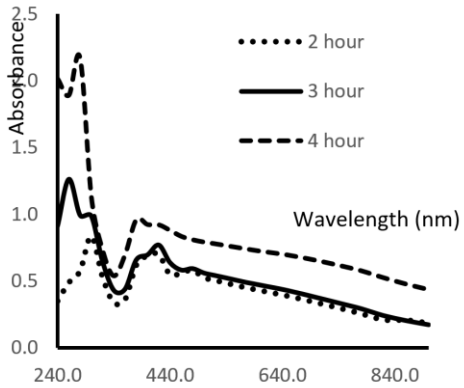

Figure 6. Spectrophotometer report for nanofluid (0.075% CuO with 0W20) at three mixing times.

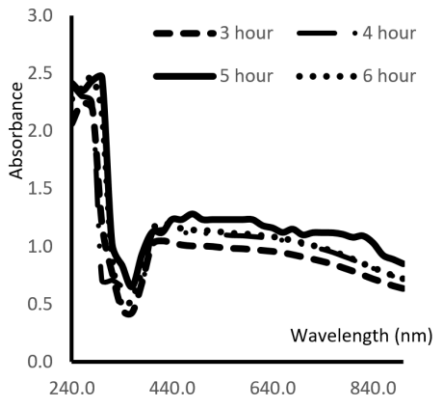

Figure 7. Absorbance values after mixing finish explain the effect of mixing periods for the second nanofluid.

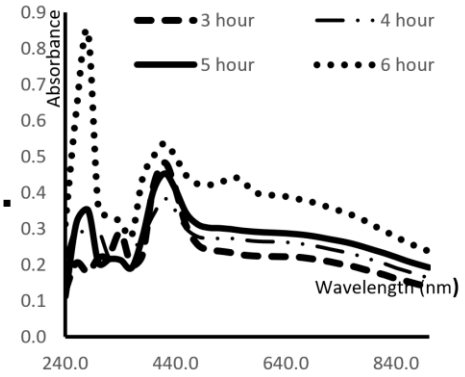

Figure 8. Absorbance values after 40 days explain the effect of the mixing period for the second nanofluid.

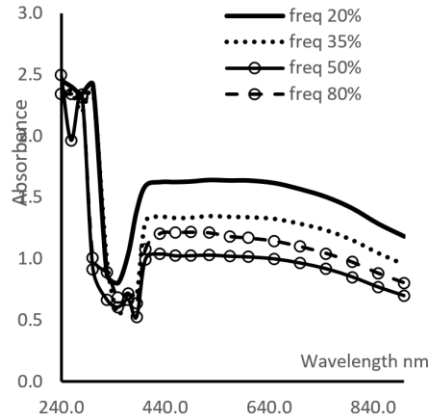

Figure 9. Absorbance values after mixing finish to explain the effect of ultrasonic sonication frequency.

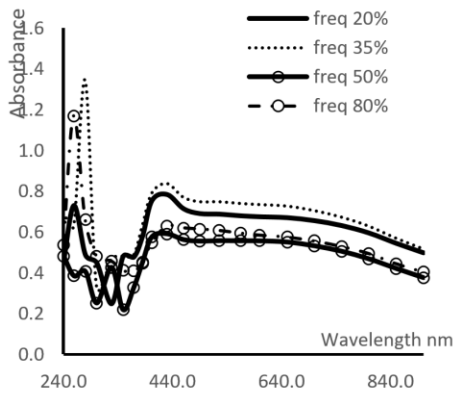

Figure 10. Absorbance values after 40 days to explain the effect of ultrasonic sonication frequency.

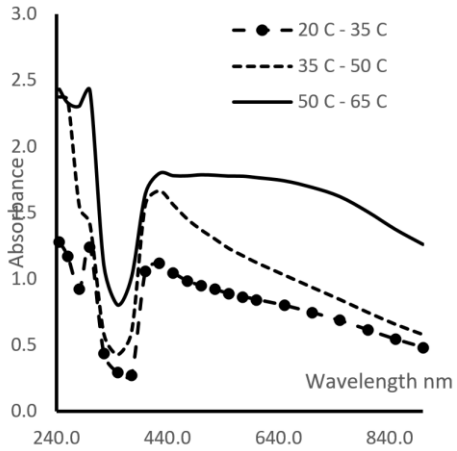

Figure 11. Absorbance values after mixing finish to explain the effect of mixing temperature.

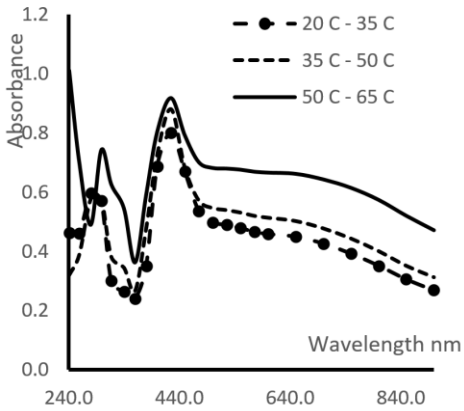

Figure 12. Absorbance values after 50 days to explain the effect of mixing temperature.

higher frequency are better than lower frequencies.

To investigate the effect of temperature mixing, prepare three samples at the same condition, but the temperature mixture at preparation operations is different. The spectrometer report indicates that samples prepared at high temperatures show more stability, but physical properties may change when the mixture temperature is very high.

III. Conclusion

There are several factors may affect the stability of nanofluid related to mixing process. They are investigated here to find the best conditions can be selected for optimization of the preparation process.

- The ultrasonic direct sonication device (probe sonicator) demonstrates nanofluid production with higher stability. However, the mixing for this device is limited by a small amount of fluid, unlike the other device.
- The stability of nanofluid is enhanced by increasing the mixing time.
- The viscosity of base fluid affects nanofluid's mixing time and stability. Lower viscosity fluid requires less time for Sonication and demonstrates higher strength.
- Nanofluid prepared at higher frequency demonstrates higher stability, although, in this situation, increasing mixture temperature may affect nanofluid properties.
- The nanofluid stability is enhanced when prepared at the higher temperature of the mixture.

Acknowledgements

The authors would like to thank the helps of Advanced technology research and application center in selcuk univercity.

Reference

[1] Eastman, J. A., Choi, U. S., Li, S., Thompson, L. J., & Lee, S. (1996). Enhanced thermal conductivity through the development of nanofluids. *MRS Online Proceedings Library (OPL)*, 457.

[2] Murshed, S. M. S., Leong, K. C., & Yang, C. (2005). Enhanced thermal conductivity of TiO2—water-based nanofluids. *International Journal of thermal sciences*, *44*(4), 367-373.

[3] Kwak, K. Y., & Kim, C. Y. (2005). Viscosity and thermal conductivity of copper oxide nanofluid dispersed in ethylene glycol. *Korea-Australia Rheology Journal*, *17*(2), 35-40.

[4] Das, S. K., Putra, N., Thiesen, P., & Roetzel, W. (2003). Temperature dependence of thermal conductivity enhancement for nanofluids. *J. Heat Transfer*, *125*(4), 567-574.

[5] Asirvatham, L. G., Vishal, N., Gangatharan, S. K., & Lal, D. M. (2009). Experimental study on forced convective heat transfer with low volume fraction of CuO/water nanofluid. *Energies*, *2*(1), 97-119.

[6] Li, X. F., Zhu, D. S., Wang, X. J., Wang, N., Gao, J. W., & Li, H. (2008). Thermal conductivity enhancement dependent pH and chemical surfactant for Cu-H2O nanofluids. *Thermochimica Acta*, *469*(1-2), 98-103.

[7] Wang, X. J., & Zhu, D. S. (2009). Investigation of pH and SDBS on enhancement of thermal conductivity in nanofluids. *Chemical Physics Letters*, *470*(1-3), 107-111.

[8] Huang, J., Wang, X., Song, Q., Wen, X., Zhou, Y., & Li, L. (2009, August). Influence of pH on the stability characteristics of nanofluids. In *2009 Symposium on Photonics and Optoelectronics* (pp. 1-4). IEEE.

[9] Jiang, L., Gao, L., & Sun, J. (2003). Production of aqueous colloidal dispersions of carbon nanotubes. *Journal of colloid and interface science*, *260*(1), 89-94.

[10] Chen, L., & Xie, H. (2010). Properties of carbon nanotube nanofluids stabilized by cationic Gemini surfactant. *Thermochimica Acta*, *506*(1-2), 62-66.

[11] Farahmandjou, M., Sebt, S. A., Parhizgar, S. S., Aberomand, P., & Akhavan, M. (2009). Stability investigation of colloidal FePt nanoparticle systems by spectrophotometer analysis. *Chinese Physics Letters*, *26*(2), 027501.

[12] Mukherjee, S., & Paria, S. (2013). Preparation and stability of nanofluids-a review. *IOSR Journal of Mechanical and civil engineering*, *9*(2), 63-69.

[13] Li, X., Zhu, D., & Wang, X. (2007). Evaluation of dispersion behavior of the aqueous copper nano-suspensions. *Journal of colloid and interface science*, *310*(2), 456-463.

[14] Hwang, Y. J., Lee, J. K., Lee, C. H., Jung, Y. M., Cheong, S. I., Lee, C. G., ... & Jang, S. P. (2007). Stability and thermal conductivity characteristics of nanofluids. *Thermochimica Acta*, *455*(1-2), 70-74

[15] Kim, H. J., Bang, I. C., & Onoe, J. (2009). Characteristic stability of bare Au-water nanofluids fabricated by pulsed laser ablation in liquids. *Optics and Lasers in Engineering*, *47*(5), 532-538.

[16] Chen, L., & Xie, H. (2010). Surfactant-free nanofluids containing double-and single-walled carbon nanotubes functionalized by a wet-mechanochemical reaction. *Thermochimica Acta*, *497*(1-2), 67-71.

[17] Wang, X. J., Li, X., & Yang, S. (2009). Influence of pH and SDBS on the stability and thermal conductivity of nanofluids. *Energy & Fuels*, *23*(5), 2684-2689.

Condition Monitoring Systems in Power Plants to Determine the Type of Maintenance Using Multiple Types of Sensors

Muthanna M. Al-Hadeethi[1], Abdulmuttalib A. Muhsen[2], Ruzairi Abdul Rahim[3]

[1,3]School of Electrical Engineering, Faculty of Engineering, Johor, Malaysia
[1,2]Haditha Hydropower Station, Ministry of Electricity, Haditha, Iraq
[2]Faculty of Power and Aeronautical Engineering, Warsaw University of Technology, Warsaw, Poland

Abstract—**Condition monitoring systems play an essential role in operating and maintaining power plants. The impact of such systems is manifested by preserving the different equipment in power plants through monitoring each equipment's operational conditions. This way, the technical staff can establish the appropriate time frame for maintenance, improve equipment reliability, increase production, and reduce unjustified periodic maintenance losses without any real sign of any anticipated failure. The condition monitoring system in the Haditha hydropower plant implemented in the 110 MW Kaplan generation unit will be studied. The work includes investigating the different sensors used for this system, representing the essential part of the system's operational activities.**

Keywords - condition monitoring, power plants, maintenance, sensors

I. INTRODUCTION

The condition monitoring system can be defined as implementing several different modern technologies to monitor various industrial equipment operating conditions. Using such a system is to aid in the detection and early perdition of any technical issues in the kit. Detecting and analyzing errors and faults are the main objectives of such systems to ensure health and safe operation [1]. Within the area of energy generation from various types (hydro, wind, gas... etc.), it is very recommended to take advantage of the different benefits that the condition monitoring systems can provide to maintain the entire operation of the generating units and the auxiliary systems. The priorities of implementing condition monitoring systems rely on the process importance and the type of the machines and equipment within this process. Hence, the system focus is to monitor the condition of the equipment within the process, in addition to any other essential parts of the equipment itself whose stoppage leads to a complete shutdown of the system (unit generation), which could result in a total loss in energy production.

The condition monitoring phrase refers to the different techniques and procedures that can be implemented to monitor the operating condition of machinery and equipment relying on the performance changes. These changes depend on the functional properties of the equipment so that it can be used to determine the equipment's needs. The machine's operational status history line is essential in the condition monitoring process. It plays a crucial role in predicting the different events related to machine performance. Other sensors are usually implemented to monitor the device's status. The sensors will act as data-collecting devices (physical parameters) related to the equipment's physical condition. Next, the collected data are analyzed using special tools to find what type of action is required, like the maintenance or corrective actions that must be done on the equipment to perfume at an optimal level and close to the

ISBN: 978-86-80593-73-9

original design condition [2]. Multiple parameters can be measured and monitored using condition monitoring systems [1, 3]. Such parameters include temperature, vibration, and rotational speed. Also, electrical measurements such as current and voltages, the gap between the stator and rotor, magnetic flux, etc., can be collected. All previous information can be used to estimate the required type of maintenance for the machine. Three types of care [2] can be implemented, which are:

A. Reactive Maintenance

This means to apply maintenance on the equipment only when needed, i.e., when the machine fails and stops working. This is also known as breakdown maintenance. Such maintenance will only include replacing the defective equipment with a new one.

B. Preventive Maintenance

In this type, the equipment is turned off and taken out of service periodically, so it is called periodic maintenance; for example, the generation units in the Haditha power plant are maintained annually according to the manufacturer's recommendations. In this type, the equipment is maintained even if there are no fault indications or defects in the kit—this way, and the equipment is preserved from failure to ensure good performance until the next maintenance date. The equipment will be maintained before it fails and be out of service. However, one of the most important disadvantages of this type of maintenance is that it does not rely on the actual status of the equipment. Hence, the equipment may not even be in for any kind of maintenance, which will mean productivity loss and unjustified maintenance costs.

C. Predictive Maintenance

This maintenance type relies on the previous history and the current operational state of the equipment, i.e., it depends on monitoring the on-time and actual condition of the equipment. This point shows the importance of the condition monitoring system approach, which is based on this type of maintenance. Again, as mentioned earlier, equipment condition is monitored using pre-defined sensor types with additional techniques to analyze the collected data and register any changes in the collected data. Then, based on this information, it is possible to expect the time at which the equipment might fail. Hence maintenance is conducted before the failure occurs. In this way, the maintenance is only performed when an accurate indication is presented, saving time and the cost of maintenance. Finally, the importance of monitoring the condition of equipment in preparing predictive maintenance programs appears as follows [2]:

- Reduce maintenance costs.
- Fewer equipment breakdowns.
- Less repair downtime.
- Lower stock of small parts.
- Longer life of the equipment.
- Increase production.
- Operator safety improvement.

Usually, the condition monitoring system contains four main parts [1, 4]: Sensors, data acquisition system, fault detection, and diagnosis. Sensors of various types convert variables and physical phenomena into electrical signals transferred to the central processing unit, which collects and analyzes these signals, detects errors compared to average values, and diagnoses and displays warnings. The sensors and other parts of the system were linked together using different types of cables (Optical, coaxial, BNC, and signal) according to the type of sensor, and other communication protocols were used [5].

II. SENSORS

The monitoring system in the Haditha dam power plant monitors the following values [3]:

- Relative shaft displacement and axial thrust on guide bearings – 7 sensors
- Generator housing vibrations – 1 sensor
- Rotating speed – 1 sensor
- Air gap – 5 sensors
- Temperature – 15 sensors
- Partial discharge – 3 couplers
- Magnetic induction – 1 sensor
- Cavitation – 2 sensors
- Current – 3 measuring transformers
- Voltage – 3 measuring transformers

A. Vibration Measurements

Vibration is one of the features of mechanical machines. It may cause dangerous operating performance [3]. Therefore, observing the vibration of the parts of the generation units is one of the priorities in the condition monitoring systems. The increase of the vibration beyond the permissible limits leads to significant damage. Vibration can be measured by its displacement, speed, or acceleration [2]. In this system in the Haditha power plant, two types of vibration sensors were used as follows:

1) Radial displacement sensors type proximity eddy current sensors (6 pieces). The shaft displacement relative to the (Bearing housing) is measured in three positions for the unit bearings (upper, lower, and turbine bearing). Two sensors for each class are fixed at a 90-degree angle between the two sensors (X, Y) within the same level to obtain the maximum measurement of the relative displacement vector.

Principle of sensor operation

The sensor types of inductive proximity [6] consist of:

- Sensor coil and ferrite core
- Oscillator circuit
- Detector circuit
- Solid-state output circuit

As shown in Fig. 1

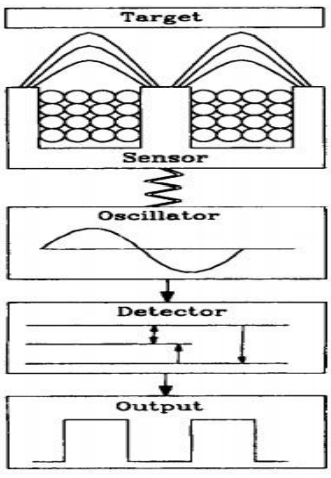

Figure 1. Inductive proximity sensor (Operating principle).

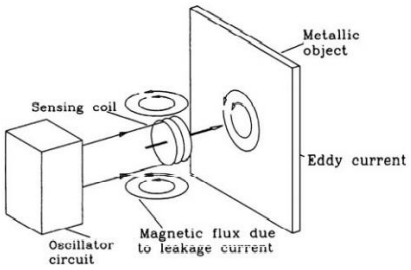

Figure 2. Induced eddy current.

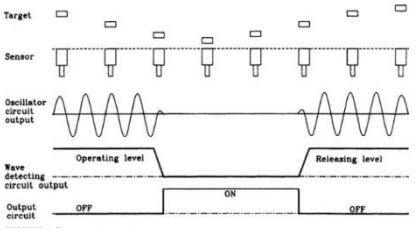

Figure 3. Detection cycle.

When an AC flows through a coil, magnetic flux occurs in the ring. When the magnetic flux passes through a metal object, it creates eddy currents that generate a magnetic field that tends to oppose changes in the wind. As a result, the inductance of the coil changes. The function between the distance from the coil to the object is defined in terms of the variation of the inductance, and the displacement distance can be calculated (Fig. 2). As the distance between the metal object and the Sensor Head decreases, eddy currents increase, and the oscillation amplitude of the oscillation circuit decreases.

Conversely, as the distance between the metal object and the Sensor Head increases, eddy currents decrease, and the oscillation amplitude of the oscillation circuit increases. The oscillation amplitude of the oscillation circuit changes as the position of the metal object changes, so measurements are taken by detecting these changes in oscillation amplitude, Fig. 3 [6].

2) Axial displacement sensor: it is measured by a single sensor fixed vertically concerning the unit shaft (Z) in the upper guide bearing of the unit and its inductive action, such as the displacement sensor above.

3) Stator absolute vibration sensor: Absolute vibration is measured using a single sensor fixed on the outer wall of the generator housing. The type of sensor is (Accelerometer), and this type

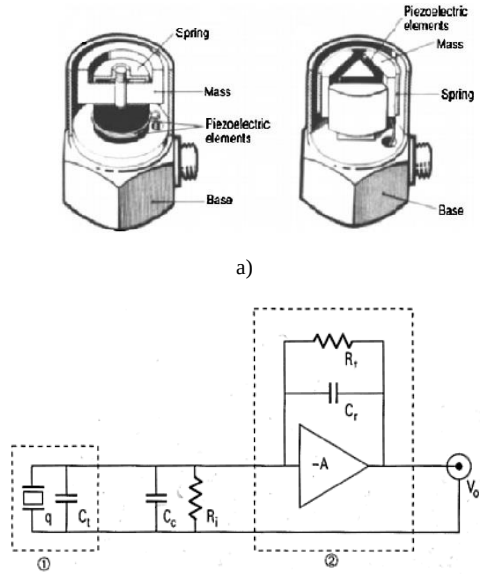

Figure 4. (a) Accelerometer sensor; (b) Accelerometer sensor with measuring circuit.

shown if Fig. 4a. and Fig. 4b. is used Piezoelectric elements which convert mechanical vibration into electric voltage [2], [3]. The Accelerometer measures the pulse of the objects formed in contact with it, unlike the relative displacement sensor, which measures the pulse of an object corresponding to the non-contact sensor. The accelerometer sensor has two main parts: a piezoelectric material such as crystal and a mass of known properties as one of the sides of the piezoelectric material is supported by a column attached to the sensor's base. On the other hand, it is connected to mass with known properties; when the sensor is subjected to vibration, a force will be formed that affects the piezoelectric material, and according to Newton's law of motion F= m*a, the amount of this force will be equal to the product of the acceleration multiplying with the known mass. Therefore, the charge generated inside the sensor will be proportional to the known mass acceleration, and thus the absolute displacement can be calculated [2].

B. Rotational Speed

The rotation speed of the generation unit is measured by using a single sensor type (Tachometer). This type is an inductive sensor [2, 3] that is installed in front of the shaft, a piece of metal (tooth) is placed on the shaft of the turbine, as shown in Fig. 5. When this tooth

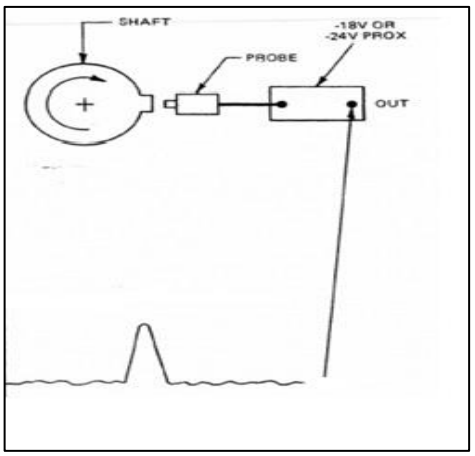

Figure 5. Rotational speed.

passes in front of the sensor, it cuts the magnetic field generated by the sensor, and a pulse is generated every time the tooth is cut. The area represents one rotation for the shaft calculated by the inductive proximity switch.

C. Air Gap Measurement

Measuring the air gap between the stator and the rotor is essential because it provides information about the state of the rotor and stator where the change in the magnetic field leads to the occurrence of vibrations. "This is based on the fact that any change in the normal flux distribution in the motor will cause a change in the vibration spectrum" [1]. Stator and rotor are affected by many factors such as aging, centrifugal force, temperatures, magnetic flux strength, vibrations, expansion of mechanical parts, and expansion of concrete structures. Etc., and accordingly, knowing the condition of the stator and rotor through the monitoring system gives operators and specialists sufficient information to take the unit out of service and perform maintenance before an extensive series of damages occurs due to friction of the parts. The air gap measurement is a measurement of the relative distance or the clearance between the outer circumference of the rotor and the inner bore of the stator. Capacitive type sensors (5 pieces) were used, and they were installed on the inner surface of the stator with equal distances. This sensor is designed to operate in a highly magnetic environment, resistant to dust, moisture, oil, and vibration [5]. The sensor works as a capacitor (the sensor represents the first plate of the capacitor, and the second part of the capacitor is represented by the pole of the

rotating part when it passes in front of the sensor). The insulaelement part between them represents the dielectric. Therefore, any change in the distance between them will lead to a change in the capacitance of the capacitor. This signal is sent to the processing unit that Its transformation into a space between the stator and the rotor. "Air gap sensor consists of the electronic unit for signal processing SZR1, coaxial cable, and measurement probe SZRS50. The air gap is a measure of distance between the rotor and stator in a rotating machine. On the basis of air gap data, information on rotating machine conditions can be obtained. The measurement probe is made from printed circuit board material. The probe is mounted on the inner surface of the generator stator. The change in distance between the probe surface and the rotor shows as a change in the probe's capacity. Coaxial cable connects measurement probe with electronic unit SZR1. The output signal from SZR1 is proportional to the momentary distance between the rotor and stator on the probe location (air gap). The output signal is usually sent to a remote central monitoring unit, located up to 100 meters from the generator" [5] as shown in Fig. 6.

The capacitive sensors have the same component as inductive sensors [6]

- • Sensor (the dielectric plate)
- • Oscillator circuit
- • Detector circuit
- • Solid-state output circuit.

However, the concept of sensitivity differs where the capacitive depends on the capacitor dielectric [6]. "The oscillator circuit in a capacitive switch operates like one in an inductive proximity switch. The oscillator circuit includes feedback capacitance from the external target plate and the internal plate. In a capacitive switch, the oscillator starts oscillating when

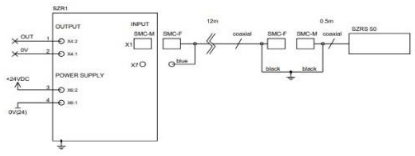

Figure 6. Capacitive sensor SZR50 and an electronic unit for signal processing SZR1.

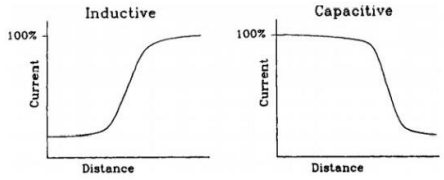

Figure 7. Oscillator damping of inductive and capacitive sensors.

sufficient feedback capacitance is detected. In an inductive proximity switch, the oscillation is damped when the target is present" as shown in Fig. 7.

D. Temperature Measurement

Increasing the temperature of the equipment above the permissible limit is an abnormal condition that leads to rapid aging and damage to the equipment parts. the effect of the temperature on the generation unit is directly on the insulation of the coils as well as on the mechanical parts. Therefore, temperature monitoring by modern methods such as the condition monitoring system is an important priority. At Haditha dam station, two types of sensors were used with a condition monitoring system to measure the temperature, which is a thermocouple and RTD where 15 sensors were installed as follows:

- 6 measurements of stator winding (RTD)
- 1 measurement in the upper guide bearing segment (thermocouple)
- 1 measurement in the lower bearing segment (thermocouple)
- 2 measurements in the lower thrust bearing pad (thermocouple)
- 1 measurement of the temperature of a bearing oil in lower combined bearing (thermocouple)
- 1 measurement of the temperature of a bearing oil in upper bearing (thermocouple)
- •3 measurements on the turbine bearing - one measuring oil temperature, other one segment, and the third one measures turbine oil head temperature (thermocouple)

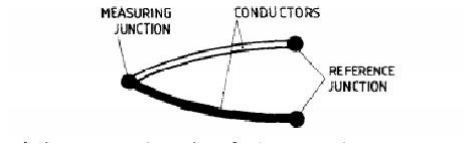

Figure 8 The physical structure of thermocouples.

Principle of Thermocouple Sensor

The connection of two different conductors at one end as in Fig. 8, this connection forms a thermocouple where the connection point represents the measuring junction, and the free end is called the reference junction [7].

When the measuring junction is heated, a current flows through the two conductors, according to T. Seebeck's invention in 1821 [7]. The chart in Fig. 9 is used to find out the temperature values corresponding to the emf produced in the most common thermocouple conductors as a result of being exposed to the heating [7]. Thermocouple sensors are used to measure the range of temperature (-700°C to +2700°C).

Principle of RTD Sensor

The physical principle of RTD sensors [7]. It is based on the fact that the resistance of the metal conductors increases with increasing temperature. RTD's are also called resistance thermometer elements which consist of a resistance conductor wound or deposited on an insulating support. PT-100 made of platinum is the most widely used type. This metal is stable, forgeable, and corrosion-resistant and can be used in Temperatures up to 1000 ° C in neutral atmospheres Fig. 10 shows the structure of the pt-RTD sensor. The Winston bridge is used to measure the voltages resulting from the change of the sensor resistance when the temperature

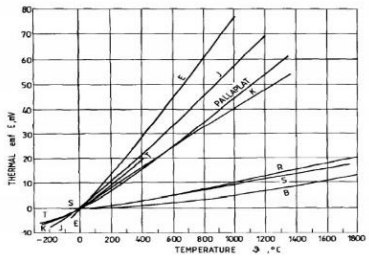

Figure 9. Thermal emf, E, of commonly used thermocouples as a function of temperature.

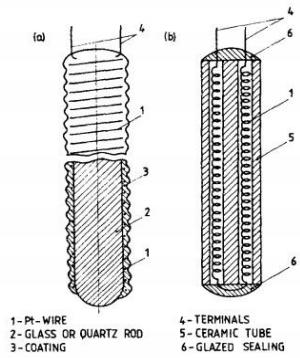

Figure 10. PT- RTD structure.

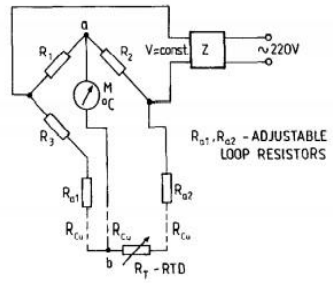

Figure 11. RTD bridge circuit.

changes. A three-wire circuit shown in Fig. 11 is used to avoid the bridge readings being affected by temperature changes in copper conduction wires. This connection also provides some protection against series mode voltages caused by electromagnetic induction [7]. PT- sensors are used to measure the range of temperature (-263ºC to 1545ºC).

E. Partial Discharge

Partial discharge is a localized discharge in a portion of the stator windings that occurs due to the presence of paths (cracks) in the surface of the insulator of the winding's conductors or the presence of a void inside the insulator that leads to the ionization of the insulator due to the strength of the electric field [8] Fig. 12. The high voltage applied to two materials with different permeability coefficients creates an irregular electric field which causes the electrical discharge. The partial discharge causes the coil to overheat, and a spark will cause complete damage to the coil if not detected early.

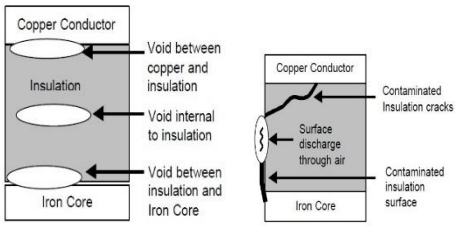

Figure 12. Partial discharge.

In the condition monitoring system, partial discharge is measured using capacitors designated for high voltage (16 KV) EMC type (Epoxy Mica Capacitors). A pair of these capacitors are connected to the end of each phase. These capacitors eliminate electrical noise from the power signal while maintaining sensitivity to the signals received from the electrical generator [9]. The pure signal sends to the PD analyzer, which analyzes the electrical signal. In the case of deformation in the power signal as in Fig 13, the probability of partial discharge is high according to the severity of the distortion and this requires a maintenance procedure before the matter gets worse and the stator windings are completely damaged.

Failure in isolation of the stator windings leads to stopping the unit from working. the procedure of replacing the damaged windings requires long periods of time and large sums of money [9] in addition to the loss of productivity. Therefore, monitoring partial discharge online through the condition monitoring system may avoid such damages and give warning signals before the windings' insulation collapses, so they are maintained at a lower cost and time.

F. Magnetic Flux Measurement

Measurement of the magnetic flux in the gap between the stator and the rotor to find out if there is asymmetry magnetic which caused by the shape deflection of the rotor or short circuit in the pole's windings. In the monitoring system

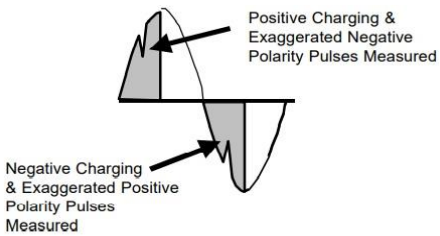

Figure 13. Power signal with partial discharge.

of the Haditha dam station, the magnetic flux is measured using a single Hall sensor, The working principle of the Hall sensor is to measure the voltage resulting from the influence of the magnetic field on the semiconductor, as shown in Fig. 14. "A Hall effect device is a four-terminal solid-state semiconductor material commonly composed of materials like silicon, germanium, indium arsenide, or gallium arsenide. When a Hall device is inserted in a soft iron core around the current-carrying conductor and a current is applied in a direction perpendicular to the magnetic field, a Hall effect voltage is generated proportional to the current flowing in the conductor. Essentially, the Hall effect is another way of detecting the magnetic field around a current-carrying conductor" [2].

G. Cavitation Measurement

Cavitation is one of the dangerous phenomena in hydropower plants that directly affect the turbine blades and it occurs because of air bubbles colliding with the surface of the turbine blades. Its energy will transfer to the surface of turbine blades and cause stress to concentrate on it [2, 4]. With the passage of time, this surface will become brittle and start to crack and pit, the result is a loss in the efficiency of the turbine and a decrease in the life span of the turbine. The cavitation is monitored by two sensors installed on the outer wall of the draft tube at the level of the turbine blades [4, 5, 10, 11]. The measurement of the cavitation is based on the acoustic emission technique that has developed in recent years. The sounds produced by the cavitation phenomenon are transmitted as a result of the bursting of water bubbles on the turbine blades, and these sounds are transmitted through the water to the outer wall, where the sensors transfer the frequencies of these sounds to the central processing units that analyze and compare them with the standard values. These sensors sense the frequencies (1 KHz - 20 MHz), when the frequency exceeds certain limits, this

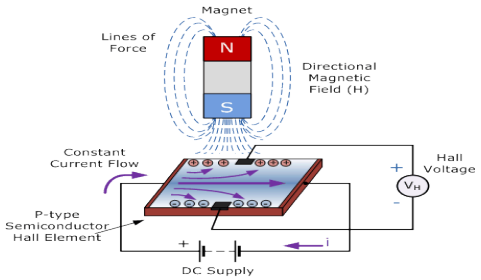

Figure 14. Hall sensors working principle.

means that the operation is within the limits of the cavitation phenomenon, so the condition monitoring system will warn the operators to change the load and work within the safe state of the production unit.

H. Electrical Measurements

Measuring transformers (CT's & VT's) are used to measure the currents and voltages of phases for the generating unit. Thus, active power (Megawatt), reactive power (Mega VAR), and power factor can be calculated and monitored. Fig. 15 shows the method for distributing sensors on the parts of the Kaplan type turbine.

III. CONCLUSION

The influence of some physical phenomena such as cavitation in addition to other factors resulting from the aging of equipment like vibration and partial discharge, which directly affect the turbines and generators in the hydropower plants are usually very crucial for the plant operation. Therefore, measuring and monitoring these factors is very important to maintain this equipment and ensure its high efficiency. The use of the condition monitoring system to collect sufficient information for the equipment by using multiple types of sensors enables the specialists to predict errors before the equipment's condition worsens to conduct maintenance in a timely manner. This helps preserve equipment and increase efficiency and productivity. In a Haditha dam power plant, the condition monitoring system was installed in 2013, where the need to continuously monitor some of the parameters that occur to the unit during work and affect directly on these units. The results of using this system brought many benefits:

1. Avoid operating the units within the cavitation phenomenon, as it is now possible for the operator to know the permissible limits through the Acoustic sensors that send warning signals through the condition monitoring system in the event the operation is within the cavitation phenomenon.
2. Avoid operating in case of vibration higher than the permissible limit, as various types of vibration sensors send warning signals that help the operator to change the load to reduce vibration.
3. The possibility of monitoring the status of stator windings through the partial discharge sensor and this does not need to stop the unit to perform an isolation check in the traditional way (megger test).
4. Monitoring turbine and generator temperatures using different types of sensors.
5. Monitoring the magnetic flux and the air gap between the stator and the rotor by using capacitive sensors gives sufficient information in case of a misalignment of the rotor.
6. The possibility of monitoring the rotational speed of the unit, as well as electrical measurements such as active power (Megawatt), reactive power (Mega VAR), and power factor.
7. The possibility of storing data for very long periods in the database to be used as a reference in future maintenance.

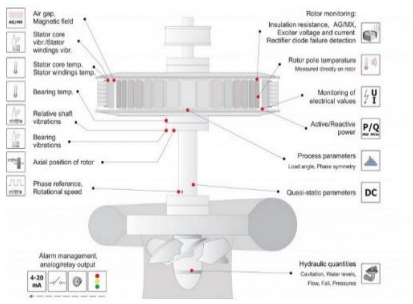

Figure 15. Sensors sites in the generation unit.

The selection of the parameters to be monitored depends on the extent to which these variables affect the equipment. Therefore, the selection of the sensors in terms of accuracy, range, precision, repeatability, sensitivity, and response time is very important to obtain the best measurements that help to indicate the condition of the equipment.

REFERENCES

[1] Han, Y., & Song, Y. H. (2003). Condition monitoring techniques for electrical equipment-a literature survey. *IEEE Transactions on Power delivery*, *18*(1), 4-13.

[2] Mohanty, A. R. (2014). *Machinery condition monitoring: Principles and practices*. CRC Press.

[3] Goyal, D., & Pabla, B. S. (2015). Condition based maintenance of machine tools—A review. *CIRP Journal of Manufacturing Science and Technology*, *10*, 24-35.

[4] Liu, Z., Zou, S., & Zhou, L. (2012, March). Condition monitoring system for hydro turbines based on LabVIEW. In *2012 Asia-Pacific Power and Energy Engineering Conference*. IEEE.

[5] KONCAR, Manufacturer documentation.

[5] Soloman, S. (2009). *Sensors handbook*. McGraw-Hill.

[6] Michalski, L., Eckersdorf, K., Kucharski, J., & McGhee, J. (2002). *Temperature measurement*. IOP Publishing.

[7] Paolitti, G., & Golubev, A. (1999). Partial discharge theory and technologies related to traditional testing methods of large rotating apparatus. In *Conference Record of the 1999 IEEE Industry Applications Conference. Thirty-Forth IAS Annual Meeting* (Cat. No. 99CH36370). IEEE.-

[8] Henriksen, M., Stone, G. C., & Kurtz, M. (1986). Propagation of partial discharge and noise pulses in turbine generators. *IEEE transactions on energy conversion*, (3), 161-166.

[9] Muhsen, A. A., Al-Malik, A. A. R., Attiya, B. H., Al-Hardanee, O. F., & Abdalazize, K. A. (2021, June). Modal analysis of Kaplan turbine in Haditha hydropower plant using ANSYS and SolidWorks. In *IOP Conference Series: Materials Science and Engineering* (Vol. 1105, No. 1, p. 012056). IOP Publishing.

[10] Muhsen, A. A., Szymański, G. M., Mankhi, T. A., & Attiya, B. (2018). Selecting the most efficient maintenance approach using AHP multiple criteria decision making at haditha hydropower plant. *Zeszyty Naukowe Politechniki Poznańskiej. Organizacja i Zarządzanie.*

The Effect of Aging of Surface Non-Metallic Coatings on the Ampacity of Medium Voltage Rectangular Bus Bars

Marko Šućurović[1], Dardan Klimenta[2], Nebojša Raičević[3], Bojan Perović[4]

[1]University of Kragujevac, Faculty of Technical Sciences in Čačak, Serbia, marko.sucurovic@ftn.kg.ac.rs
[2,4]University of Priština in Kosovska Mitrovica, Faculty of Technical Sciences in Kosovska Mitrovica, Serbia, dardan.klimenta@pr.ac.rs[2], bojan.perovic@pr.ac.rs[4]
[3]University of Niš, Faculty of Electronic Engineering, Serbia, nebojsa.raicevic@elfak.ni.ac.rs

Abstract—**There are two major types of non-metallic coatings for bus bars: oil- and epoxy-based coatings. The oil-based coatings have a limited lifespan of a few years, while the epoxy-based ones have a lifespan of over ten years. In contrast to the lifespans of indoor substations and components in them, the lifespans of coatings on bus bars are significantly shorter. Accordingly, it is obvious that the surface coating aging can affect the ampacity of rectangular or other shaped bus bars. The extent to which this effect can reduce the ampacity is analysed in this paper. An indoor substation, in which medium voltage (MV) rectangular bus bars of the same type can be found inside and outside the substation building, is considered as a case study. In order to simulate the aging process of the surface coating, it is assumed that the surface radiation properties (thermal emissivity and solar absorptivity) gradually change in the following manner: a new paint/coating layer, a layer of dirt over oxidised paint/coating, and a layer consisting of heavily-oxidised paint/coating, heavily-oxidised metal and dirt under both indoor and outdoor conditions. The results obtained for indoor and outdoor conditions are compared against one another in order to quantify the effect of solar irradiation. In addition, each non-metallic layer over the bus bars is considered as additional thermal insulation. The aging process is analysed analytically, and then validated numerically by finite element method (FEM) in COMSOL. Finally, the discussion yielded some important conclusions relevant for practice.**

Keywords – aging process, ampacity, rectangular bus bar, non-metallic coating, thermal analysis

I. INTRODUCTION

It is well-known that bus bars can be coated to increase ampacity, provide electrical insulation, inhibit corrosion, identify the phase and neutral conductors (i.e. for cosmetic reasons), and improve joint performance [1]. Metal and non-metallic coatings are used for this purpose. Metal coatings do not affect significantly the ampacity of the bus bars, while non-metallic coatings (such as oil-based coatings and epoxy-based coatings) behave as additional thermal insulation that can reduce the ampacity. In addition to this, aging of any non-metallic coating can contribute to a further reduction in the ampacity. Accordingly, the aging process will also affect the operating temperature of the bus bars [1, 2].

Bus bars coated black are considered in [3], while bus bars coated with various oil paints are analysed or mentioned in [1, 4-6]. There also are studies such as [7] where only bare bus bars are considered. According to [2, 3], when bus bars are installed indoor the thermal emissivity has a low value, and the solar absorptivity equals zero. This provides the most conservative ampacity for indoor conditions. In contrast, when bus bars are installed outdoor a high value of thermal emissivity essentially equal to solar absorptivity can give the most conservative ampacity for

ISBN: 978-86-80593-73-9

outdoor conditions [3]. In connection with this, it should be highlighted that solar heating of any bus bar always reduces its ampacity and can result in outdoor ampacities which are lower than that corresponding to indoor conditions [3]. This is less likely on bus bars with smaller cross-sectional areas for which the coefficients due to forced convection are relatively high. However, for bus bars having large cross-sectional areas and high solar absorptivities, the contribution from solar irradiance can exceed the improvement in heat transfer due to forced convection and the ampacities are decreased accordingly [3]. In addition, as a rule, comparisons of the ampacities of bare and coated bus bars are performed in [2, 5-7]. Furthermore, there are many other studies on bus bars, but they do not need to be reviewed for the purposes of this paper.

Lifespan of non-metallic coatings and its potential effect on the ampacity of bus bars is mentioned in [1]. According to [7], the surface radiation properties of a bus bar are functions of the age, as well as a contamination level of the surface of the bus bar. As a coated bus bar ages, the presence of a layer of dirt over oxidised paint/coating, or a layer consisting of heavily-oxidised paint/coating, heavily-oxidised metal and dirt over its conductor changes both the thermal emissivity and thermal absorptivity. There are a number of papers considering aging of bare bus bars, but there is no paper dealing with aging of coated bus bars. Accordingly, the effect of aging of oil- and epoxy-based coatings on the ampacity of MV rectangular bus bars is analysed in this paper.

The aging process of non-metallic coatings on bus bars is modelled as follows. Firstly, it is assumed that the non-metallic layer consists of two sublayers in different thicknesses, a thicker layer over the conductors of 0.2 mm and a finer layer over the coatings of 0.1 mm. Secondly, it is assumed that the aging process takes place in the following three stages: (i) a 0.3 mm thick new paint/coating layer – the two sublayers have the same values of thermal conductivity, (ii) a 0.1 mm thick dirt layer over a 0.2 mm thick oxidised paint/coating layer – the two sublayers have different values of thermal conductivity, and (iii) a 0.3 mm thick layer consisting of a mixture of heavily-oxidised paint/coating, heavily-oxidised metal and dirt – the two sublayers have the same values of thermal conductivity. In order to identify the effect of solar irradiance, the aging of oil- and epoxy-based coatings is considered for both indoor and outdoor conditions.

Thirdly, it is taken into account that the thermal conductivity of oil-based coatings, epoxy-based coating and dirt is 0.2 W/(m·K) [8], 0.3 W/(m·K) [9] and 0.98 W/(m·K) [10], respectively. In addition to this, the thermal conductivities of the dirt and the mixture of heavily-oxidised paint/coating, heavily-oxidised metal and dirt are assumed to be the same. These assumptions allow each non-metallic layer over the bus bars to be considered as thermal insulation. Fourthly, it is assumed that the thermal emissivity and solar absorptivity of the considered layers gradually change in an appropriate manner [9, 11-16].

Heating of the MV rectangular bus bars installed in and outside the building of an indoor substation is considered as a case study. The aging is analysed using a MATLAB programme entitled BUSBAR.m [2], while the validation is performed by means of FEM in COMSOL. The discussion of the analytical and numerical results yielded a number of important conclusions.

II. GOVERNING EQUATIONS

The steady-state heat conduction equation can be derived from the law of conservation of energy in the volume of a 1-meter length of the coated bus bar. One such volume element having the dimensions W_b, H_b and L_b=1 m is shown in Fig. 1. It is assumed that the materials of the bus bar and two sublayers are homogenous and isotropic, as well as that there is no longitudinal heat conduction in them. In addition, it is assumed that the heat Q_{tg} (in W) is generated within the given volume element and that the values of thermal conductivity k for the materials of the bus bar and two sublayers are constant.

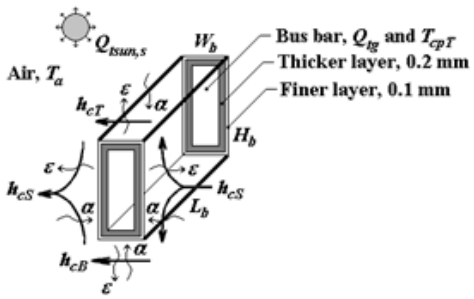

Figure 1. Heat transfer in the volume of a 1-meter length of the coated bus bar for typical outdoor conditions.

Accordingly, for the analytical analysis of heat transfer in a steady-state, the governing Eq. is [2]:

$$\alpha \cdot S_{pM} \cdot Q_{tsun,s} + Q_{tg}(T_{cpT}) = [2 \cdot h_{cS} \cdot S_S + \\ + h_{cT} \cdot S_T + h_{cB} \cdot S_B + h_r(T_{cpT}) \cdot S_{o1}] \cdot (T_{cpT} - T_a) \quad (1)$$

where $\alpha \cdot S_{pM} \cdot Q_{tsun,s}$ is a maximum amount of solar heat that can be absorbed by the outer surface of a 1-meter length of the bus bar in W, α is the solar absorptivity of the outer surface of the bus bar, S_{pM} is the maximum projected area of a 1-meter length of the bus bar in m^2, T_{cpT} is the tabulated continuously permissible temperature of the bus bar in °C (65 or 70°C), h_{cS} is the heat transfer coefficient due to the natural/forced convection between side surfaces of the bus bar and ambient air in W/(m^2·K), S_S is the surface area of one lateral side of the bus bar in m^2, h_{cT} is the heat transfer coefficient due to the natural/forced convection between the top surface of the bus bar and ambient air in W/(m^2·K), S_T is the surface area of the top side of the bus bar in m^2, h_{cB} is the heat transfer coefficient due to the natural/forced convection between the bottom surface of the bus bar and ambient air in W/(m^2·K), S_B is the surface area of the bottom side of the bus bar in m^2, h_r is the heat transfer coefficient due to the radiation heat exchange between the outer surface of the bus bar and ambient air in W/(m^2·K), S_{o1} is the outer surface area of a 1-meter length of the bus bar in m^2, and T_a is the temperature of the surrounding air in °C.

A situation corresponding to typical indoor conditions can be obtained by setting the solar absorptivity to α=0 and the wind velocity to v_w=0 m/s. This means that Fig. 1 and (1) will be simplified accordingly. For instance, the forced convection will be reduced to the natural one, solar radiation will be ignored, and so on. Further details on the analytical modelling of heat transfer in a steady-state can be found in [2].

The ampacities corresponding to central European indoor conditions are determined under the following assumptions [2,5,7]: (i) that the ambient air is still, i.e. v_w=0 m/s; (ii) that the surfaces of conductors are painted/coated giving an emission coefficient of ε=0.94 – for oil-based paint/coating and ε=0.88 – for epoxy-based paint/coating; (iii) that the surfaces of conductors are covered with an oxidised paint/coating layer together with a dirt layer over it giving an emission coefficient of ε=0.5; or (iv) that the surfaces of conductors are covered with a mixture of heavily-oxidised paint/coating, heavily-oxidised metal and dirt giving an emission coefficient of ε=0.7.

The ampacities corresponding to central European outdoor conditions are determined under the following assumptions [2,5,7]: (i) that the ambient air moves slightly, i.e. v_w=0.6 m/s; (ii) that the solar irradiance is $Q_{tsun,s}$=1000 W/m^2; (iii) that the surfaces of conductors are painted/coated giving an emission coefficient of ε=0.94 – for oil-based paint/coating and ε=0.88 – for epoxy-based paint/coating, as well as an absorption coefficient of α=0.7 – for oil-based paint/coating and α=0.94 – for epoxy-based paint/coating; (iv) that the surfaces of conductors are covered with an oxidised paint/coating layer together with a dirt layer over it giving an emission coefficient of ε=0.5 and an absorption coefficient of α=0.9; or (v) that the surfaces of conductors are covered with a mixture of heavily-oxidised paint/coating, heavily-oxidised metal and dirt giving an emission coefficient of ε=0.7 and an absorption coefficient of α=0.9.

In addition to the indoor and outdoor conditions, the scenarios tested in the analytical modelling ignore the effects of thermal conductivities of the two sublayers on the heat transfer processes. This is done for the reason that the potential effects can be identified after performing numerical simulations.

FEM calculations of steady-state temperature distributions over the two-dimensional (2D) domain in Fig. 1 are performed using the following Eq. [17]:

$$\frac{\partial}{\partial x}\left(k\frac{\partial T}{\partial x}\right) + \frac{\partial}{\partial y}\left(k\frac{\partial T}{\partial y}\right) + Q_v = 0 \ , \quad (2)$$

where x, y are Cartesian spatial coordinates in m; k is the thermal conductivity in W/(m·K); T is the temperature in K; and Q_v is the volume power of heat sources in W/m^3.

The volume power of heat sources in the bus bars with a geometric cross-sectional area of approximately $W_b \cdot H_b$ in m^2 is

$$Q_v = \frac{R_{ac}(T_{cpT})}{W_b \cdot H_b} \cdot I_{cp}^2 \ , \quad (3)$$

where $R_{ac}(T_{cpT})$ is the a.c. resistance per unit length of one bus bar at temperature T_{cpT} in Ω/m, and I_{cp} is the ampacity in A. In addition, there are no heat sources in the two sublayers over the conductor.

The numerical validation of the analytical model used for the case of natural or forced convection heat transfer is carried out in COMSOL [2], by performing a thermal FEM-based analysis of rectangular bus bars. The COMSOL Heat Transfer Module uses as input data some of the output data generated by the BUSBAR.m programme. For instance, the effect of the bus bar ampacity (the value of which is obtained by the BUSBAR.m programme) is taken via the volume power of heat sources located in the bus bar material. In addition to this, as boundary conditions, COMSOL also uses heat transfer coefficients due to the natural/forced convection and radiation generated by means of the BUSBAR.m programme.

III. Case Study

The case study 35/10 kV substation considered in this paper is located in the northern part of Bosnia and Herzegovina, in the Brčko District. This case study is presented in Figs. 2 and 3. Fig. 2 provides an actual image of the 35/10 kV substation, while Fig. 3 provides a simplified graphical representation of the outdoor and indoor bus bars used in this substation. In connection with this, the accent on controlling heat transfer along the outdoor and indoor bus bars using the surface radiation properties (i.e. solar absorptivity and thermal emissivity) is very important. For these purposes the oil-based and epoxy-based paints and coating are usually applied to the surfaces of bus bars.

As can be seen from Figs. 2 and 3, after installation the bus bars are usually coated with appropriate paints or coatings. Depending on the phase, the MV bus bars can be coated as follows: phase R – yellow, phase S – green, and phase T – purple. In addition, at the low voltage, neutral conductor N may be white, gray or black. Moreover, a neutral conductor that is not grounded can be coated with black and white stripes, and a neutral conductor that is grounded can be coated with black and purple stripes. Furthermore, plus and minus pole conductors in a dc circuit can be red and gray, respectively. All these paints and coatings are

Figure 2. A 35/10 kV substation in the Brčko District of Bosnia and Herzegovina *(sourcee: https://radiobrcko.ba/vijesti-brcko/u-toku-redovan-godisnji-remont-cvornih-trafo-stanica-u-distriktu/).*

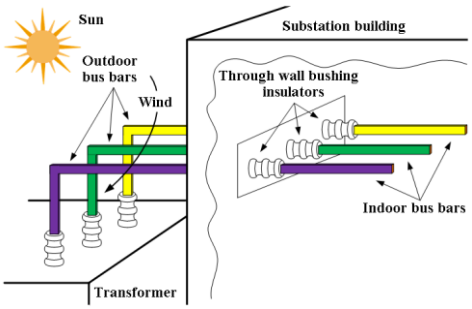

Figure 3. A simplified graphical representation of the outdoor and indoor bus bars used in the 35/10 kV substation from Fig. 2.

standard colors for metal which can withstand temperatures up to 100°C.

IV. Results and Discussion

The results of analytical and numerical simulations carried out for the case of indoor conditions are given in Table I, whilst Table II shows results of analytical and numerical simulations carried out for the case of outdoor conditions. Width W_b, height H_b, assumed current I_{ass}, and skin effect coefficient k_s for the considered bus bars are also given in Tables I and II. In addition, for purposes of comparisons, the ampacities of single bare bus bars with rectangular cross-sections from [2] were utilised. These ampacities are obtained for the same central European indoor and outdoor conditions and are provided in Tables I and II.

According to [2], the dc resistivity of the aluminium alloy 6101-T61 at 20 °C and its temperature coefficient are $2.998 \cdot 10^{-8}$ Ω·m and 0.00383 1/K, respectively. The thermal

conductivity of 218.5 W/(m·K) is taken for the aluminium alloy 6101-T61. Initial values for the heat transfer coefficients due to natural and forced convection corresponding to the turbulent flow in the gases are assumed to be equal to 12 W/(m^2·K) and 300 W/(m^2·K) [2], respectively.

For the indoor installation of single rectangular bus bars, the analytical (using BUSBAR.m) and numerical (using COMSOL) simulations were carried out in accordance with [2], that is, for the following on-site conditions: installations with the vertical and horizontal major axes, T_{cpT}=70 °C, T_a=40 °C, v_w=0 m/s (natural convection), different values for thermal emissivity ε, solar absorptivity α=0, and frequency f=60 Hz. For the outdoor installation of single rectangular bus bars, the analytical and numerical simulations were carried out for the following on-site conditions: installations with the vertical and horizontal major axes, T_{cpT}=70 °C, T_a=40 °C, v_w=0.6 m/s (forced convection), different values for thermal emissivity ε, different values for solar absorptivity α, $Q_{tsun,s}$=1000 W/m^2, and frequency f=60 Hz.

TABLE I. AMPACITIES OF SINGLE BARE AND COATED BUS BARS WITH RECTANGULAR CROSS-SECTIONS OBTAINED FOR CENTRAL EUROPEAN INDOOR CONDITIONS. *

W_b	H_b	k_s at 70 °C / I_{ass} from [2] **	I_{cp} and T_{cp} ***							
			For ε=0.94 and α=0		For ε=0.88 and α=0		For ε=0.5 and α=0		For ε=0.7 and α=0	
			BUSBAR	*COMSOL*	*BUSBAR*	*COMSOL*	*BUSBAR*	*COMSOL*	*BUSBAR*	*COMSOL*
m / in	**m** / in	- / A	**A** / °C	**A** / °C	**A** / °C	**A** / °C	**A** / °C	**A** / °C	**A** / °C	**A** / °C
Bus bars installed with a vertical major axis										
0.00635 / 0.25	**0.0508** / 2	**1.014** / 545	**665** / 69.97	**664.4** / 70.00	**653** / 69.90	**656** / 70.00	**578** / 69.94	**581** / 70.00	**619** / 69.95	**624.8** / 70.00
0.009525 / 0.375	**0.1016** / 4	**1.100** / 1186	**1475** / 69.93	**1468.4** / 70.00	**1448** / 69.93	**1447.1** / 70.00	**1263** / 69.90	**1264.6** / 70.00	**1363** / 69.90	**1370** / 70.00
0.0127 / 0.5	**0.2032** / 8	**1.259** /2376	**3019** / 69.91	**3000** / 70.00	**2959** / 69.90	**2951.2** / 70.00	**2549** / 69.91	**2545.6** / 70.00	**2772** / 69.90	**2778.2** / 70.00
Bus bars installed with a horizontal major axis										
0.0508 / 2	**0.00635** / 0.25	**1.014** / 519	**643** / 69.98	**643.7** / 70.00	**631** / 69.93	**634.9** / 70.00	**553** / 69.98	**556.9** / 70.00	**595** / 69.93	**602.2** / 70.00
0.1016 / 4	**0.009525** / 0.375	**1.100** /1125	**1426** / 69.91	**1421.7** / 70.00	**1398** / 69.91	**1399.2** / 70.00	**1206** / 69.90	**1209.2** / 70.00	**1311** / 69.93	**1318.6** / 70.00
0.2032 / 8	**0.0127** / 0.5	**1.259** /2279	**2950** / 69.90	**2933.1** / 70.00	**2889** / 69.90	**2882.7** / 70.00	**2467** / 69.90	**2465.5** / 70.00	**2697** / 69.90	**2704.4** / 70.00

* For aluminium alloy 6101-T61 horizontally installed bus bars, T_a=40 °C, T_{cpT}=70 °C, v_w=0 m/s and f=60 Hz.
** For bare bus bars, ε=0.35 and α=0.
*** For coated bus bars.

TABLE II. AMPACITIES OF SINGLE BARE AND COATED BUS BARS WITH RECTANGULAR CROSS-SECTIONS OBTAINED FOR CENTRAL EUROPEAN OUTDOOR CONDITIONS. *

W_b	H_b	k_s at 70 °C / I_{ass} from [2] **	I_{cp} and T_{cp} ***							
			For ε=0.94 and α=0.7		For ε=0.88 and α=0.94		For ε=0.5 and α=0.9		For ε=0.7 and α=0.9	
			BUSBAR	*COMSOL*	*BUSBAR*	*COMSOL*	*BUSBAR*	*COMSOL*	*BUSBAR*	*COMSOL*
m / in	**m** / in	- / A	**A** / °C	**A** / °C	**A** / °C	**A** / °C	**A** / °C	**A** / °C	**A** / °C	**A** / °C
Bus bars installed with a vertical major axis										
0.00635 / 0.25	**0.0508** / 2	**1.014** / 675	**638** / 70.09	**632.5** / 70.00	**532** / 70.09	**531.7** / 70.00	**455** / 70.06	**456.4** / 70.00	**506** / 70.05	**512.8** / 70.00
0.009525 / 0.375	**0.1016** / 4	**1.100** /1278	**1163** / 70.09	**1148** / 70.00	**819** / 70.09	**812** / 70.00	**517** / 70.08	**512.4** / 70.00	**730** / 70.09	**732** / 70.00
0.0127 / 0.5	**0.2032** / 8	**1.259** /2190	**1829** / 70.09	**1796** / 70.00	**427** / 70.09	**355.8** / 70.00	**0** / >70.00	**0** / >70.00	**0** / >70.00	**0** / >70.00
Bus bars installed with a horizontal major axis										
0.0508 / 2	**0.00635** / 0.25	**1.014** / 675	**638** / 70.09	**632.5** / 70.00	**532** / 70.09	**531.7** / 70.00	**455** / 70.06	**456.4** / 70.00	**506** / 70.05	**512.8** / 70.00
0.1016 / 4	**0.009525** / 0.375	**1.100** / 1278	**1163** / 70.09	**1148** / 70.00	**819** / 70.09	**812** / 70.00	**517** / 70.08	**512.4** / 70.00	**730** / 70.09	**732** / 70.00
0.2032 / 8	**0.0127** / 0.5	**1.259** /2177	**1829** / 70.09	**1796** / 70.00	**427** / 70.09	**355.8** / 70.00	**0** / >70.00	**0** / >70.00	**0** / >70.00	**0** / >70.00

* For aluminium alloy 6101-T61 horizontally installed bus bars, T_a=40 °C, T_{cpT}=70 °C, v_w=0.6 m/s, wind direction parallel to bus bar axis, $Q_{tsun,s}$=1000 W/m^2 and f=60 Hz.
** For bare bus bars, ε=0.5 and α=0.35.
*** For coated bus bars.

Values of continuously permissible temperature of bus bars obtained in cases of indoor and outdoor conditions using BUSBAR.m and COMSOL differ from the temperature T_{cpT}=70°C by approximately ±0.1°C. Accordingly, the differences are negligible and represent a consequence of the specified accuracies.

According to Table I, it is evident that the coated bus bars, when there is no solar irradiance, have higher ampacities compared to the ampacities of bare bus bars of the same cross-sectional areas. The higher the thermal emissivity, the higher the bus bar ampacity. In addition, and also as expected, the larger the cross-sectional area, the higher the bus bar ampacity. Moreover, the larger the cross-sectional area, the higher the percentage difference between the ampacity of coated bus bars and the ampacity of bare bus bars. Furthermore, the percentage difference between the ampacities of coated and bare bus bars decreases with decreasing the thermal emissivity.

All the previous observations are valid for the results obtained using both BUSBAR.m and COMSOL. Any difference between the results obtained using BUSBAR.m and COMSOL is lower than 1%. This difference is the consequence of not taking thermal conductivity of the materials into account in the BUSBAR.m programme. Accordingly, with physical aging of the paint/coating layer and an increase in the level of contamination on the bus bar surface, it first leads to a decrease in the bus bar ampacity, and then to its increase. Therefore, it can be considered that a 0.3 mm thick layer, consisting of a mixture of heavily-oxidised paint/coating, heavily-oxidised metal and dirt, has a favourable effect on heat dissipation conditions from the surface of any bus bar to the environment.

Based on Table II, when there is solar heating, the coated bus bars have lower ampacities compared to the ampacities of bare bus bars of the same cross-sectional areas. As in the case of indoor conditions, the higher the thermal emissivity, the higher the bus bar ampacity. The bus bar ampacity increases with increasing the cross-sectional area of bus bars in the case only when the thermal emissivity (ε=0.94) is higher than the solar absorptivity (α=0.7). Moreover, the percentage difference between the ampacity of coated bus bars and the ampacity of bare bus bars increases with increasing the cross-sectional area of bus bars. When there is solar radiation, this difference increases with decreasing the thermal emissivity. In this particular case, all the differences between the results obtained using BUSBAR.m and COMSOL are lower than 3.3%. This is due to the fact that thermal conductivity of the materials is not taken into account by the BUSBAR.m programme.

According to Table II, the ampacity is zero for the bus bars having the largest cross-sectional areas and the solar absorptivity α=0.9. This means that the contribution from solar heating exceeds the improvement in heat dissipation due to wind from the surface of the bus bars to the environment. In connection with this, it is found that there is a contribution from solar heating that can heat up the bus bars up to T_{cpT}=70 °C and decrease the ampacity to zero. In the case where ε=0.5 and α=0.9, this would occur for $\alpha \cdot S_{pM} \cdot Q_{tsun,s}$=358.3 W/m^2. In addition, for ε=0.7 and α=0.9, the same would occur for $\alpha \cdot S_{pM} \cdot Q_{tsun,s}$=405.5 W/m^2.

The effect of physical aging of the paint/coating layer covering the bus bar surface on the ampacity has the same trend as in the case of indoor conditions. However, the bus bar ampacities from Table II (outdoor ampacities) are significantly lower than those from Table I (indoor ampacities). Therefore, in the case of outdoor installation, physical aging of the paint/coating layer does not have any favourable effect on heat dissipation from the considered bus bars to the environment.

V. CONCLUSIONS

The main conclusions that can be drawn from the presented results and discussion are as follows:

- It was successfully demonstrated that the physical aging of coated bus bars can be modelled analytically and numerically by the surface radiation properties and thermal conductivity of the layers/materials covering the bus bar conductors. The effectiveness of the proposed model is also ensured.
- The coating of bus burs with oil- and epoxy-based paints/coatings gives the possibility to increase the ampacity of the considered bus bars up to 29.44% for the central European indoor conditions. This applies only for new bus bars.

- The physical aging of coated bus bars, under the central European indoor conditions, can reduce the difference between the ampacities of the coated bus bars and the ampacities of the corresponding bare bus bars to 6.06-8.25%.
- It is found that, during the aging process under the central European outdoor conditions, the contribution from solar heating can exceed the improvement in heat dissipation due to wind from the considered bus bars to the environment.
- The physical aging of the paint/coating layer has a favourable effect on heat dissipation from the considered bus bars to the environment in the case of indoor installation rather than in the case of outdoor installation.
- It is also found that the thermal conductivities of the materials covering the considered bus bars have a negligible effect on the bus bar ampacity.

A priority for future work will be a more in-depth focus on: (i) thermal analysis of bare bus bars together with bus bars coated with oil- or epoxy-based coating, wrapped in mylar insulation, and surrounded by polyolefin shrink tubes, (ii) determination of cooling rate as a function of oil- or epoxy-based coating thickness, and (iii) generalisation of the proposed model for the aging of non-metallic coatings on bus bars.

ACKNOWLEDGMENT

This paper was based on research conducted within the projects Grant No. 451-03-9/2021-14/200132 and Grant No. NIO 200155 supported by the Ministry of Education, Science and Technological Development of the Republic of Serbia.

REFERENCES

[1] Chapman, D., & Norris, T. (2014). *Copper for busbars – Guidance for design and installation*. 15th revision. Copper Development Association Publication No 22. Available at: http://copperalliance.org.uk/uploads/2018/03/copper_for_busbars_book_web_version.pdf

[2] Klimenta, D. O., Perović, B. D., Jevtić, M. D., & Radosavljević, J. N. (2016). An analytical algorithm to determine allowable ampacities of horizontally installed rectangular bus bars. *Thermal Science*, *20*(2), 717-730.

[3] Prager, M., Pemberton, D. L., Craig Jr., A. G. & Bleshman, N. A. (1976). Steady-state and transient ampacity of bus bar. *IEEE Transactions on Power Apparatus and Systems*, *PAS-95*(4), 1361-1368.

[4] Hus, J. (1990). Estimating busbar temperatures. *IEEE Transactions on Industry Applications*, *26*(5), 926-934.

[5] ABB A. G. (2007). Conductor Materials and Accessories for Switchgear Installations, in: *ABB Switchgear Manual*. 12th ed., Chapter 13, pp. 593-724. ABB AG, Mannheim, Germany. Available at: http://at.dii.unipd.it/renato.gobbo/didattica/corsi/Componenti_tecnologie_elettrici/ABB_swithgear_manual_E11/ABB_11_E_13_druck.pdf

[6] Klimenta, D., Perović, B., Anđelković, D., & Todorović, A. (2013). An analytical algorithm to determine the continuously permissible loads of horizontal bus bars with a rectangular cross-section. In *INFOTEH-JAHORINA* (*12*, pp. 148-153).

[7] Coneybeer, R. T., Black, W. Z., & Bush, R. A. (1994). Steady-state and transient ampacity of bus bar. *IEEE Transactions on Power Delivery*, *9*(4), 1822-1829.

[8] OTM Solutions Pte Ltd. (2020). *Thermal conductivity of thin materials (paint, coating, metal sheet)*. Available at: https://www.otm.sg/thermal-conductivity-of-thin-materials-paint-coating-metal-sheet

[9] Akzo Nobel Powder Coatings GmbH. (2018). *Product Datasheet – Resicoat EL201 – Coating for Cores and Busbars by Electrostatic Spray Application Code: HLG03R.*

[10] Abdel-Motaal, M. A. (2014). Improvement of sand fill thermal conductivity using sand-oil mixture (experimental study). *World Applied Sciences Journal*, *32*(5), 807-817.

[11] Moncada, M. L. T., Muñoz, B. C., Yoshida, M. M. & Rodríguez, R. D. (2013). Comparative experimental study of new absorbent surface coatings for flat plate solar collectors. *Energy Procedia*, *00*, 000-000.

[12] Kaminski, D. A., Jensen, M. K. (2017). *Introduction to thermal and fluids engineering*. John Wiley & Sons.

[13] Špes, M., & Márton, M. (2017). The impact of solar radiation for maximum current load of 400 kV power lines. Prague, Czech Republic (pp. 1-4).

[14] TRANSMETRA Messtechnik mit KnowHow. (unknown year) *Table of Emissivity of Various Surfaces*. Available at: https://www.transmetra.ch/component/jifile/download/NjEyOGJhN2M4YTNkZDNmN2ExMzhmODBkOGJiNmI3NmE=/emissivity-table-pdf

[15] Henninger, J. H. (1984). *Solar Absorptance and Thermal Emittance of Some Common Spacecraft Thermal-Control Coatings*. NASA Reference Publication 1121. Available at: https://ntrs.nasa.gov/citations/19840015630

[16] ***. (unknown year). *Table 2.3 Solar Absorptance for Various Exterior Surfaces (Clean)*. Available at: https://simulationresearch.lbl.gov/dirpubs/BASIC/lds2.pdf

[17] Klimenta, D., Perović, B., Anđelković, D., & Todorović, A. (2013). An analytical algorithm to determine the continuously permissible loads of horizontal bus bars with a rectangular cross-section. In *INFOTEH-JAHORINA* (*12*, pp. 148-153).

Physical Design Optimization of Supercritical Carbon Dioxide Reactor Assembly Based on RMC Code

Shanfang Huang[1], Xingyu Zhao[2], Minyun Liu[3]

[1,2,3]Department of Engineering Physics, Tsinghua University, Beijing 100084, China
[3]CNNC Key Laboratory on Nuclear Reactor Thermal Hydraulics Technology, Nuclear Power Institute of China, 610213, China

Abstract—**Existing researches on supercritical carbon dioxide (S-CO_2) direct cycle reactor lack of physical design schemes of the assembly and the core. This paper chooses self-developed RMC code as a tool, and proposes the physical design optimization of S-CO_2 reactor assembly. Based on cross section characteristics analysis, the feasibility of S-CO_2 as core coolant is judged and its moderating performance is evaluated. The results show that S-CO_2 has small neutron absorption cross section, which makes it suitable as core coolant; meanwhile, it has small neutron scattering cross section and weak moderation ability, which results in the hard neutron spectrum and produces large positive coolant void reactivity, thus threatening the reactor safety. Then two kinds of moderating schemes, i.e. coolant hydrogen mixture and dispersion fuel with BeO as diluent, are proposed and verified by establishing single cell model. The results show that when the number of hydrogen nuclei increases, the neutron spectrum softens, and the effective multiplication factor increases; when the volume fraction of BeO increases, the neutron spectrum softens, while the effective multiplication factor decreases. Based od dispersion fuel, the design of introducing YH_2 solid moderating-pin can realize the softening of core energy spectrum and the improvement of critical level at the same time.**

Keywords - Supercritical carbon dioxide reactor; Monte Carlo method; microscopic cross section; neutron spectrum softening

I. INTRODUCTION

Supercritical carbon dioxide direct cycle reactor (S-CO_2 Reactor) is a type of reactor in which supercritical carbon dioxide serves as coolant and power circulation working medium simultaneously. In S-CO_2 Reactor, the coolant directly drives the turbine, and there is no primary or secondary loop which is often applied in traditional light water reactor. The concept of S-CO_2 reactor is a combination of the advanced gas reactor (AGR) with steam indirect Rankine cycle in the secondary loop developed in the United Kingdom in 1965-1982[1-3] and the concept of direct circulation gas cooled fast reactor proposed in the International Forum on Fourth Generation Nuclear Energy Systems (GIF) in 2002 [4]. S-CO_2 reactor has the advantages of safety due to single phase working medium and small neutron loss, which are similar to common gas-cooled reactors. In addition, the study by [5] and [6] et al. showed that the thermophysical properties of S-CO_2 enabled the S-CO_2 reactor to have the highest cycle efficiency at medium core outlet temperature, thus having good economy and less burden on materials. The study of [7] shows that the S-CO_2 reactor power system has a more compact structure and smaller volume compared with other air-cooled reactors. At the same time, CO_2 is abundant in nature and has the characteristics of non-flammable, stable, non-toxic and cheap. Therefore, S-CO_2 reactor is considered as one of the most promising reactor types [8, 9]. At present, the research of S-CO_2 reactor mainly focuses on thermal hydraulic characteristics, while the research on core physical analysis and design direction is scarce. In the study of [10, 11], the tube-in-duct (TID) fuel was deployed using a hexagonal fuel element with round holes inside as a coolant flow channel, and Beryllium Oxide was also used as fuel diluent. This design effectively softened the neutron energy spectrum and reduced the positive vacuolar reactivity coefficient.

ISBN: 978-86-80593-73-9

However, this scheme has not been tested, and the design is infeasible based on current industrial technologies. In this paper, the feasibility of using S-CO_2 as a circulating working medium and its moderating performance are illustrated by comparing the microscopic sections of different working medium based on the analysis of cross section characteristics. Based on practical technologies, the material and geometrical configuration are selected, and the core physical design scheme of S-CO_2 reactor is proposed.

II. COMPUTATIONAL PROGRAM AND MODEL

In the analysis of database and program cross section characteristics, the ENDF/B-VIII database [12] was used. The Monte Carlo neutron transport program RMC has the functions of critical calculation, burnup calculation, gate element counter, etc., and has good parallel calculation efficiency, so it is an ideal tool for core physical analysis [13].

Based on the practical and feasible technology, the hexagonal assembly based on pin-type fuel model is used to verify the core physics scheme. The RMC model is shown in Fig. 1, UO_2 with enrichment degree of 15% is used as fuel, and ODS-MA956 alloy is used as the fuel cladding. Vacuum boundary conditions are applied to the two cylinders of the fuel rod, cladding and coolant boundary, and total reflection boundary conditions are applied to the edges of the hexagonal assembly.

III. ANALYSIS OF CROSS SECTION CHARACTERISTICS OF S-CO_2

In this section, three working substances, H_2O, CO_2 and H_2, are selected for cross-section comparison and analysis. Water is the moderator and coolant used in pressurized water reactor, and is also the most commonly used working medium. The hydrogen cross sections are compared to more intuitively show the source of the difference in cross section characteristics between water and carbon dioxide.

A. Comparison of Microscopic Scattering Cross Sections

For different working medium, the larger the microscopic cross section gives the greater probability that neutron scattering with a single particle of the working medium, which is more conducive to moderating process. Fig. 2 shows the variation curve of the microcosmic scattering cross section in the omnipotent segment of different working medium and the resonance region.

Outside the resonance zone (E<0.2MeV), the scattering microscopic cross sections of the four working substances are H_2O>H_2>CO_2. The scattering microscopic cross sections of water and hydrogen are on average one orders of magnitude higher than that of carbon dioxide, and the scattering cross sections of the three working medium show the same trend with the change of energy. Among them, the water's very close to the cross section of hydrogen, especially in the low energy region, the cross section curve is almost overlap, and water and hydrogen scattering cross section is greater than carbon dioxide, it shows that hydrogen nuclei relative to other kinds of nucleus of scattering contribution is bigger. If the moderator is doped with a certain amount of hydrogen nucleus, the moderating performance will be greatly affected. Within the resonance region (E>0.2MeV), the difference of the microscopic scattering cross sections between carbon dioxide and water is small, and there are a series of formants in the same

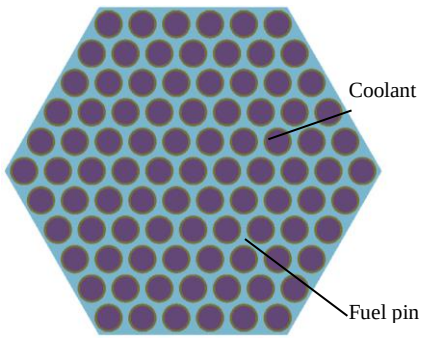

Figure 1. Hexagonal assembly based on pin-type fuel model in RMC.

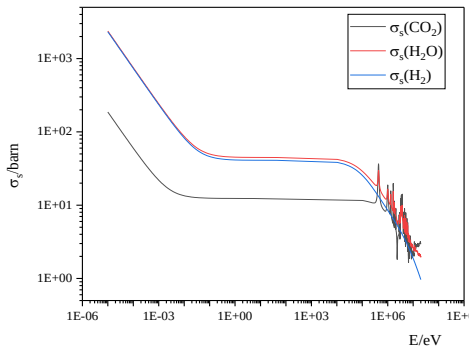

Figure 2. Microscopic Scattering Cross Section of different working medium.

position, and the formant peak value of carbon dioxide is slightly higher. The scattering cross section of hydrogen in the resonance region does not show the shape of the peak, so the probability of its scattering with neutrons is lower than that of water and carbon dioxide in the local energy region.

The microcosmic scattering cross section represents the probability of scattering between neutron and single particle of working medium, and the moderating performance of working medium also depends on its average logarithmic energy drop and density, so a complete analysis of the moderating performance must be carried out under certain working conditions

B. Comparison of Moderating Power and Moderating Ratio

According to the physical property program REFPROP[14], the density of water taken at 15.5MPa and 300℃ is 726.82kg/m^3 ; The density of supercritical carbon dioxide at 20.0MPa and average temperature of 300℃ is 191.9kg/m^3, and the numerical density of water can be calculated as N (H_2O) = 2.43 * 10^{28} m^{-3}, and N(CO_2)=2.22*10^{27}m^{-3}. Fig. 3 shows the curves of moderating power and moderating ratio of water and carbon dioxide with energy.

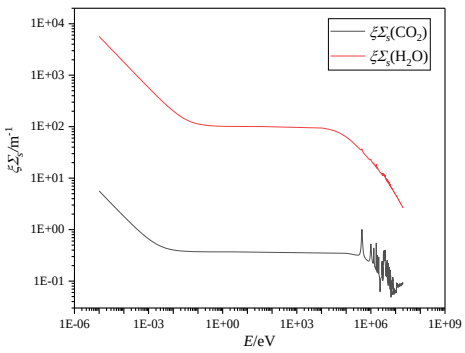

a)

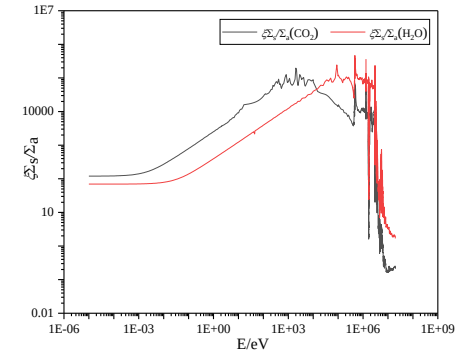

b)

Figure 3. (a) Moderating power and (b) moderating ratio of water and carbon dioxide.

The moderating power of water is two orders of magnitude larger than that of carbon dioxide. For the moderating ratio, in the low energy region, the moderating ratio of carbon dioxide is slightly higher than that of pure water, while in the resonance energy region, both of them have drastic changes, and the slowing down ratio of water is slightly greater than that of carbon dioxide. In general, there is no significant difference in the slowing ratio between water and carbon dioxide, and the advantage of carbon dioxide is not obvious.

Water and carbon dioxide were used as coolants respectively in the RMC infinite length single-rod model, 300 generations of neutron propagation were carried out by using the critical calculation function, in which 50 generations of inactive generation were generated and each generation had 10,000 neutrons. Fig. 4 shows the neutron energy spectrum with two different coolants.

When the coolant was changed from water to carbon dioxide, the energy spectrum hardened significantly, proving that carbon dioxide's moderating performance was insufficient compared with water. The lack of moderating performance makes it more difficult for S-CO_2 reactors of the same size to reach criticality than PWR. Table I shows the k_{eff} in two cases.

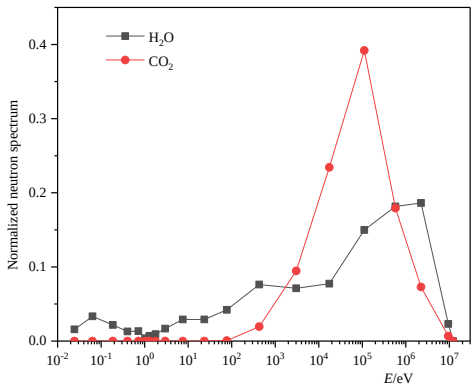

Figure 4. Neutron energy spectrum with different coolants.

TABLE I . THE k_{eff} OF WATER AND CARBON DIOXIDE AS COOLANT.

Collant	k_{eff}	Δk
H_2O	1.4117	0.0003
S-CO_2	0.7402	0.0002

Meanwhile, it has been shown that the harder neutron energy spectrum leads to greater CVR, which is determined by the interfacial properties of the ^{235}U and ^{239}Pu fuel. When the core is not sufficiently moderated, the positive reactivity introduced is an order of magnitude larger than that under the condition of sufficient moderated, which seriously threatens the safety of the reactor. Therefore, in the physical design of S-CO_2 reactor cores, strengthening core moderating is of great significance.

IV. PHYSICAL CORE DESIGN OPTIMIZATION OF S-CO_2 REACTOR ASSEMBLY

According to the above analysis, if the uranium dioxide fuel and pure carbon dioxide coolant are directly used in the S-CO2 reactor, the moderating performance needs to be strengthened. In the following, the coolant and fuel are discussed. The moderating in the core is enhanced by doping lighter nuclei, and the feasibility of the scheme is verified by comparing the neutron energy spectrum.

A. Coolant Doped with Hydrogen Nuclei

The ratio of the number density of doped hydrogen nuclei to carbon dioxide molecules is defined as *x*. Fig. 5 shows the moderating power curve of hydrogen doped carbon dioxide with different value of *x*.

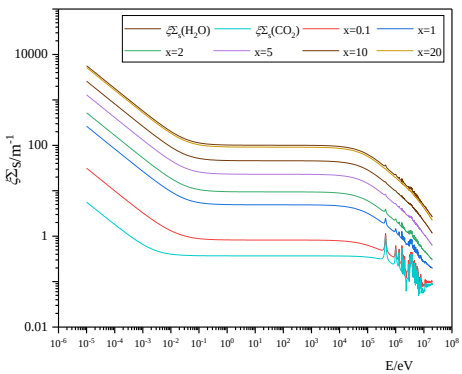

Figure 5. Moderating power of S-CO_2 with different amount of hydrogen nuclei.

When the number of doped hydrogen nuclei gradually increases, the moderating power of carbon dioxide is more and more close to that of pure water. When x=2, the slowing capacity gap between carbon dioxide and water is reduced to one order of magnitude.

Therefore, doping hydrogen nuclei is an effective method to improve the moderating power of the working medium. The RMC assembly model was used for verification, and the doping of hydrogen nuclei in the coolant was realized by mixing supercritical carbon dioxide and methane. Fig. 6 shows the variation of gate element neutron energy spectrum with the amount of mixed methane, and Table II shows the variation of k_{eff}. With the increase of methane, the neutron energy spectrum is obviously softened and k_{eff} is increased. The more the amount of hydrogen doping is, the more favorable it is for the S-CO_2 reactor to reach the criticality and reduce the CVR, so as to improve the safety of the reactor. However, it remains to be further studied how the injection of hydrogen compounds will affect the properties of supercritical carbon dioxide, whether it will bring other adverse factors, or whether it will destroy the advantages of supercritical carbon dioxide

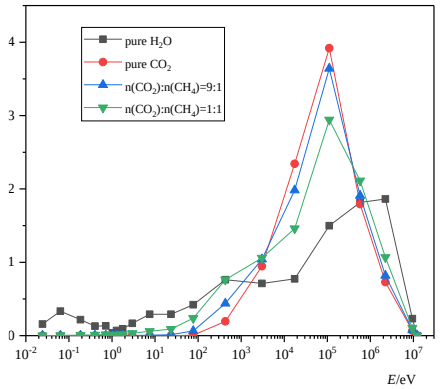

Figure 6. Neutron energy spectrum with different amounts of methane.

TABLE II. k_{eff} WITH DIFFERENT AMOUNTS OF METHANE.

Collant	k_{eff}	Δk
CO_2	0.7402	0.0002
CO_2+CH_4 (9:1)	0.7835	0.0002
CO_2+CH_4 (1:1)	0.8857	0.0003
H_2O	1.4117	0.0003

reactor efficiency in the high and medium temperature region.

B. Dispersion Fuel with BeO as Diluent

Dispersion of nuclear fuel in solid substrates containing light nuclei can also enhance the moderating effect. In the materials composed of light nucleus, BeO meets the characteristics of high melting point, chemically stable, small neutron absorption cross section, and large moderating ratio, which makes it the most capable diluent. Therefore, BeO will be used as the dispersion substrate for discussion. Set the volume fraction of graphite as α, graphite density as 2.9g/cm^3, UO_2 fuel density as 10.3g/cm^3, S-CO_2 as coolant, density as 191.9kg/m^3. Fig. 7 shows the change of neutron energy spectrum when α is changed.

As α increases, the energy spectrum will gradually soften due to the increase of carbon nuclei per unit volume. However, higher volume fraction of BeO doesn't mean better effect. With the increase of graphite volume fraction, both the softening neutron energy spectrum, and the decrease of neutron utilization rate of the fuel tends to decrease the k_{eff}, Fig. 8 shows the k_{eff} with different BeO volume fraction.

The results show that with the increase of graphite volume fraction, the energy spectrum softens gradually while the k_{eff} decreases, which indicates that a compromise may be made between efficiency and safety.

To further strengthen the energy spectrum softening and to make an effort to increase the k_{eff}, the introduction of a hexagonal solid moderating-pin structure inside the assembly is taken into account. The main component of the moderating-pin is metal hydride, and the main materials considered in the S-CO_2 reactor design are ZrH_2 and YH_2, in which ZrH_2 starts to decompose by itself at 300℃ in vacuum. Although the carbon dioxide environment suppresses the decomposition reaction to some extent, ZrH_2 will still start to decompose at 603℃, which greatly limits the design criteria of the reactor core, and the problems of low ZrH_2 melting point and poor thermal stability are difficult to solve. Meanwhile, YH_2 has the characteristics of high melting point and good thermal stability. It can still maintain a high hydrogen content at a high temperature of 1200℃, and is the most suitable material for the moderating-pin of the S-CO_2 core. A schematic diagram of the assembly using both YH_2 moderating-pin and diffusion fuel in RMC is given in Fig. 9.

To verify that this design can achieve the desired effect, 4 different designs, including assembly without diffusion fuel or moderating-pin; only using diffusion fuel; only using moderating-pin; using both diffusion fuel and moderating-pin, are modeled and compared.

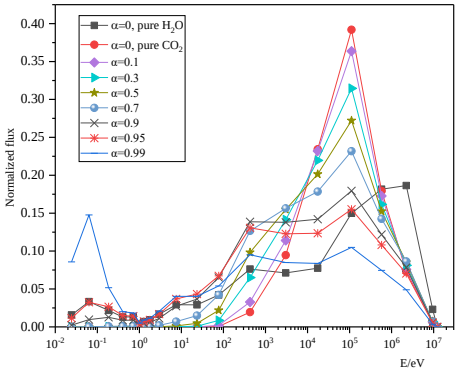

Figure 7. Neutron energy spectrum with different BeO volume fraction.

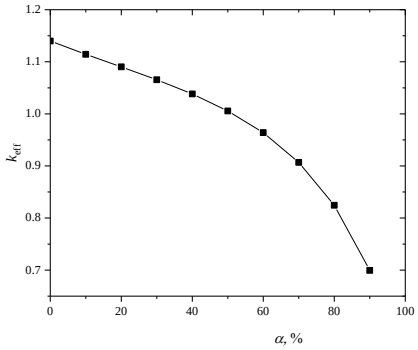

Figure 8. k_{eff} with different BeO volume fraction.

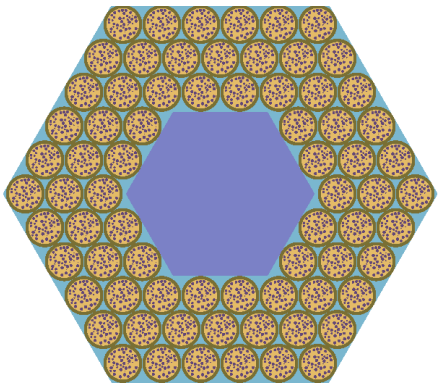

Figure 9. Assembly using both YH_2 moderating-pin and diffusion fuel.

There are six fuel rods on each side of the assembly, with a moderating-pin (if used) occupying 19 fuel rod space, and a diffusion fuel (if used) using a BeO substrate, with a BeO volume fraction of 70%. Each RMC critical calculation used 50 inactive cycles and 250 active cycles, and each cycle included 100,000 neutrons. The results are presented in Fig. 10 and Table III.

The critical calculations show that the design scheme of using both diffusion fuel and moderating-pin in the assembly design has a high level of k_{eff}, while effectively softening the energy spectrum. Therefore, it is recommended to introduce dispersion fuel with BeO as diluent and YH_2 moderating-pin simultaneously in the physical design of S-CO_2 reactor core. At present, however, the heat transfer pattern and the heat resistance limit of the hexagonal structure depend on experimental measurement, and are remained to be further investigated.

V. CONCLUSION

Based on the analysis of cross section characteristics of supercritical carbon dioxide, this paper evaluates the moderating performance of supercritical carbon dioxide. Based on practical and feasible technologies, several core physics design schemes are proposed and verified by RMC program. The main conclusions include:

The supercritical carbon dioxide has a low neutronic absorption cross section, thus it is suitable as a direct circulating coolant. Meanwhile, its neutronic scattering cross section is small, which leads to the insufficient slowing capacity. When pure supercritical carbon dioxide is used as coolant, the moderating power is 2~3 orders of magnitude behind that of water, while there is no obvious advantage in the moderating ratio.

In order to strengthen the core moderating, two kinds of moderating schemes, direct mixture of hydrogen core at the coolant level, and the use of diffusion fuel were proposed. The mixed coolant of carbon dioxide, methane and diffusion fuel using BeO as diluent were taken as examples respectively, and were both verified in the RMC hexagonal assembly model. Both schemes can result in neutron energy spectrum softening, and as the coolant injection hydrogen nuclei number increases, the effective multiplication factor k_{eff} rises, as the fuel in the graphite volume fraction increases, the k_{eff} decreases. Based on the dispersion fuel scheme, the introduction of a hexagonal YH_2 moderating-pin realized a high level of k_{eff} while effectively soften the neutron spectrum.

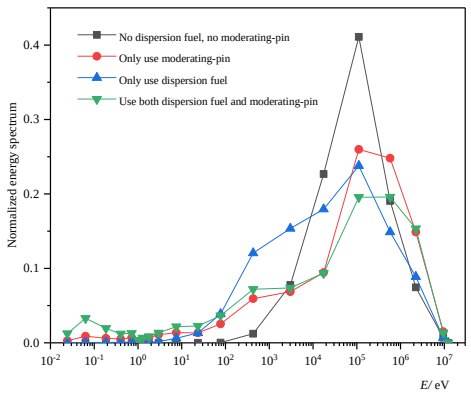

Figure 10. Neutron energy spectrum of the four assembly models.

TABLE III. k_{eff} OF THE FOUR ASSEMBLY MODELS.

Model	k_{eff}	Δk
No dispersion fuel or moderating-pin	0.7029	0.0002
Only use dispersion fuel	1.1417	0.0004
Only use moderaing-pin	0.5946	0.0002
Use both dispersion fuel and moderating-pin	1.1051	0.0004

REFERENCES

[1] Kemmish, W. B. (1982). Gas-cooled fast reactors. *Nucl. Energy, 21*.

[2] Kemmish, W. B., Quick, M. V., Hirst, I. L. (1982). The safety of CO_2 cooled breeder reactors based on existing gas cooled reactor technology. *Progress in Nuclear Energy, 10*(1), 1-17.

[3] Shropshire, D. E. (2004). *Lessons Learned From Gen I Carbon Dioxide Cooled Reactors*. Paper presented at the 12th International Conference on Nuclear Engineering(ICONE12).

[4] Doe. (2002). *A Technology Roadmap for Generation IV Nuclear Energy Systems*. Available at http://gif.inel.gov/roadmap/pdfs/gen_iv_roadmap.pdf

[5] Dostal. V. (2004). *A Supercritical Carbon Dioxide Cycle for Next Generation Nuclear Reactors*. (Doctor), Massachusetts Institute of Technology.

[6] Hejzlar, P., Dostal, V., & Driscoll, M. J. (2006). *A Supercritical CO_2 Cycle- a Promising Power Conversion System for Generation IV Reactors.* Paper presented at the Proceedings of the International Congress on Advanced Nuclear Power Plants 2006, Reno, NV.

[7] Kato, Y., Nitawaki, T., & Muto, Y. (2004). Medium temperature carbon dioxide gas turbine reactor. *Nuclear Engineering and Design*, *230*, 195-207.

[8] Huang, Y. P, Wang. J. F. (2012). Application of supercritical carbon dioxide in nuclear reactor system. *Nuclear power engineering*, *33*(003): 21-27 (in Chinese)

[9] Parma, E. J., Wright, S. A., Vernon, M. E., Fleming, D. D., Rochau, G. E., Suo-Anttila, A. J., et al. (2011). *Supercritical CO_2 direct cycle Gas Fast Reactor (SC-GFR) concept*. Available at https://www.researchgate.net/publication/255240934

[10] Handwerk, C. S. (2007). *Optimized core design of a supercritical carbon dioxide-cooled fast reactor*. (Doctor), Massachusetts Institute of Technology.

[11] POPE M A. Reactor physics design of supercritical CO_2-cooled fast reactors [D]. Massachusetts Institute of Technology, 2004.

[12] Brown, D. A., Chadwick, M. B., Capote, R., Kahler, A. C., Trkov, A., Herman, M. W., et al. (2018). ENDF/B-VIII.0: The 8 th Major Release of the Nuclear Reaction Data Library with CIELO-project Cross Sections, New Standards and Thermal Scattering Data. *Nuclear Data Sheets*, *148*, 1-142

[13] Wang, K., Li, Z., She, D., Liang, J. g., Xu, Q., Qiu, Y.,et al. (2015). RMC – A Monte Carlo code for reactor core analysis. *Annals of Nuclear Energy*, *82*, 121-129.

[14] Lemmon, E. W., Huber, M. L., & Mclinden, M. O. (2010). NIST Standard ReferenceDatabase 23: Reference Fluid Thermodynamic and Transport Properties-REFPROP. 9.0.

Parameter Evaluation of Two Diode Model Based Commercial Photovoltaic Systems with Grey Wolf Optimizer (GWO) and Its Variants: A Performance Study

Souvik Ganguli[1]

[1]Thapar Institute of Engineering and Technology, Patiala, India,
souvik.ganguli@thapar.edu

Abstract—**Mathematical modeling and parameter estimation of PV cells are critical for evaluating the various factors of PV cells. The mathematical modeling of the PV cells can be done in many ways, Double Diode Model (DDM) is one of the methods to do so. In this paper, the seven parameters of the DDM have been determined accurately which consists of seven parameters and with the use of metaheuristic algorithms. Grey Wolf Optimizer (GWO) and some of its popular variants that have proved to give good results for optimization in literature have been used. The square error is optimized generated from the three modeling equations used. Three largely popular solar panels manufactured by Solarex, Kyocera, and Canadian Solar are used along with the information given by the manufacturer in the datasheet. The best values are tabulated and compared and the best algorithm is determined. The results obtained show that the parameter values are within the prescribed limits and the error is less than 0.6% for all panels.**

Keywords - Grey wolf optimizer (GWO), modified grey wolf optimization (mGWO), augmented grey wolf optimization (AGWO), Enhanced leadership based GWO (EGWO), double diode model (DDM)

I. INTRODUCTION

The hastily increasing population and technological advancements have been a great burden for conventional sources of producing electricity because of their limited availability and environmental degradation. The sun has been a source of energy for billions of years and it is an inexhaustive source, unlike fossil fuels. Hence solar energy is known to be the energy of the future due to its availability, accessibility, cost-effectiveness, efficiency, and capacity [1]. It is now being used as a tool for measuring the development index of any country.

The photovoltaic (PV) cells are used for the direct conversion of light from the sun to electricity through the photoelectric effect. Owing to the non-linear (I-V) curve for PV panel, its modeling is essential for understanding and optimizing the system [2]. The modeling of solar cells requires its equivalent electrical network which is chosen based on its simplicity and accuracy. Numerous modeling approaches used are such as a single diode model (SDM), DDM, and three diode model (TDM). Out of these, the SDM offers the lowest computational complexity and thus offers a compromise amongst simplicity and accuracy.

The DDM takes into account the recombination in the space charge and quasi-neutral region using two diodes parallel to each other [3, 4]. Thus, it possesses the advantage of having its accuracy much better than the SDM in which the recombination losses are taken as negligible. DDM has seven parameters in comparison to five in the SDM. The parameters being- photocurrent Ipv, reverse saturation currents of both diodes I01 and I02, series resistance Rs, parallel resistance Rp, ideality

ISBN: 978-86-80593-73-9

factors of both diodes a1 and a2 [6, 7]. The seven parameters calculated help to sketch the different curves pertaining to the cell accurately.

The two major methods used for parameter extraction of parameters are the analytical method and the numerical method. The analytical methods usually require the curve-fitting technique and hence the parameters estimated are dependent on their position on the characteristic curve [8]. The numerical based methods are divided into two sub-categories – deterministic and heuristic methods. The deterministic methods have limitations of introducing some new additional coefficients into the equations and difficulty arises in determining the initial values of the parameters [9]. Metaheuristic algorithms are population-based optimization algorithms that use the positions of the population to reach the optimal point while updating them regularly. They have a good selection procedure and decision-making ability. Hence, metaheuristic techniques are gaining more importance due to their tendency to provide efficient and accurate solutions compared to the other methods. These techniques based on evolutionary algorithms like genetic algorithm, particle swarm optimization (PSO) [10, 11], cuckoo search algorithm [12] has been widely applied in literature for extraction and optimization of these parameters. Many new algorithms have been developed and still works on many of them are going on. The results obtained may enhance when these new algorithms are used on the existing models. Modified Double Diode Model (MDDM) and Three Diode Model (TDM) are the new developments in the field of mathematical modeling of the cells and can also be used for parameter extraction.

The remaining part of the paper is planned in the following approach; in section II the problem equations are defined, in section III the proposed algorithms have been defined which are used for the parameter extraction, in section IV the results obtained from the runs are discussed and in section V the conclusion is written example.

II. PROBLEM DEIFINITION

A typical PV cell is modelled by the Eq. given by

$$I = I_0\left[exp\left(\frac{q(V+IR_S)}{aKT}\right)-1\right]. \qquad (1)$$

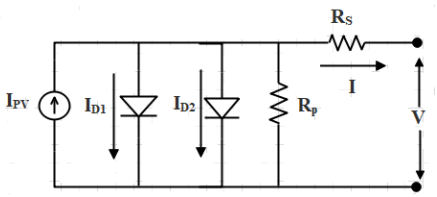

Figure 1. The circuit representation of DDM [2].

I_0 in the above equation denotes the reverse saturation current, while *a* represents the ideality factor. The other terms like R_s is the series resistance of the circuit, whereas K is the Boltzmann constant, T is the temperature of the PV cell in Kelvin (K) and q is the electronic charge.

Fig. 1 shows the schematic model of the DDM. It is represented by a current source denoting the photovoltaic current (I_{pv}). Apart from this the circuit also contains two diodes D_1 and D_2, a series resistance R_s, and a shunt resistance R_p. Applying Kirchhoff's current law to calculate the load current (I) we get,

$$I = I_{pv} - I_{D1} - I_{D2} - \frac{V+IR_s}{R_p}. \qquad (2)$$

Replacing the value of I_{D1} and I_{D2} in Eq. (2) the load current is modified as

$$I = I_{pv} - I_{01}\left[exp\left(\frac{q(V+IR_S)}{a1KT}\right)-1\right] - I_{02}\left[exp\left(\frac{q(V+IR_S)}{a2KT}\right)-1\right] - \frac{V+IR_s}{R_p}. \qquad (3)$$

To develop the constraints with the help of the given data from the specification sheet of the manufacturer, various conditions like open circuit, short circuit and maximum power point are now being substitute in (3).

1. When there is a open circuit, the load current (I) will be zero while the voltage V is represented by V_{oc}. Thus (3) is altered as follows:

$$I_{pv} = I_{01}\left[exp\left(\frac{qV_{oc}}{a1KT}\right)-1\right] + I_{02}\left[exp\left(\frac{qV_{oc}}{a2KT}\right)-1\right] + \frac{V_{oc}}{R_p}. \qquad (4)$$

2. The second case taken up for the investigation is the short circuit condition in which the voltage will be zero while the current I is denoted by I_{sc}. Thus, Eqn. (3) can be modeled as

$$I_{sc} = I_{pv} - I_{01}\left[exp\left(\frac{q(IR_S)}{a1KT}\right)-1\right]- \\ -I_{02}\left[exp\left(\frac{q(IR_S)}{a2KT}\right)-1\right]-\frac{IR_s}{R_p} \quad . \quad (5)$$

3. The third condition considered for the study is the maximum power Point (MPP) condition. Here the voltage V is replaced by Vmp. On the other hand, the current I is represented by Imp Thus the Eqn. (3) can be obtained as:

$$I_{mp} = I_{pv} - \\ -I_{01}\left[exp\left(\frac{q(V_{mp}+I_{mp}R_S)}{a1KT}\right)-1\right]- \\ -I_{02}\left[exp\left(\frac{q(V_{mp}+I_{mp}R_S)}{a2KT}\right)-1\right]- \\ -\frac{V_{mp}+I_{mp}R_S}{R_p} \quad . \quad (6)$$

The errors to constitute the objective function are thus derived from (4), (5) and (6) respectively. The errors may thus be derived as follows:

$$err_{OC} = I_{01}\left[exp\left(\frac{qV_{oc}}{a1KT}\right)-1\right]+ \\ +I_{02}\left[exp\left(\frac{qV_{oc}}{a2KT}\right)-1\right]+\frac{V_{OC}}{R_p}-I_{PV} \quad . \quad (7)$$

$$err_{SC} = I_{SC} + \\ +I_{01}\left[exp\left(\frac{q(IR_S)}{a1KT}\right)-1\right]+ \\ +I_{02}\left[exp\left(\frac{q(IR_S)}{a2KT}\right)-1\right]+ \\ +\frac{I_{SC}R_S}{R_p}-I_{PV} \quad . \quad (8)$$

$$err_{mp} = I_{PV} - \\ -I_{01}\left[exp\left(\frac{q(V_{mp}+I_{mp}R_S)}{a1KT}\right)-1\right]- \\ -I_{02}\left[exp\left(\frac{q(V_{mp}+I_{mp}R_S)}{a2KT}\right)-1\right]- \\ -\frac{V_{mp}+I_{mp}R_S}{R_p}-I_{mp} \quad . \quad (9)$$

The objective function that is to be developed must reduce the above-mentioned errors as much as possible. To achieve this here, the square error has been considered. Therefore, the error Eq. is given as [12].

$$err = err_{OC}^2 + err_{SC}^2 + err_{mp}^2 \quad . \quad (10)$$

III. PROPOSED METHODS

A. *Grey Wolf Optimzer (GWO)*

GWO is a metaheuristic algorithm for the calculation of global maxima where grades of the grey wolves along with the technique used by them for hunting are used. These wolves generally live in chunks of 5-12 wolves where each wolf is assigned a certain rank and they follow that rank very strictly which is depicted in Fig. 2.

There are four categories of grey wolves in the group and those are alpha, beta, delta, and omega. These wolves are hired to mimic the position of the leader and hunt the prey. The alpha (α) is the top rank wolf and also is the most dominating one. The remaining members are beta (β) and delta (δ) which assist in keeping an eye on the rest of the members who

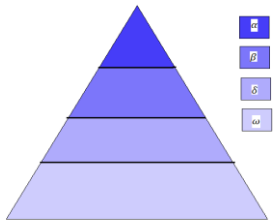

Figure 2. The ranks of the grey wolves in the group.

are considered as omega (ω), who holds the lowest rank in the group. In the GWO algorithm, the hunting down of the prey is done by $\alpha, \beta,$ and δ. The $'\omega'$ follows the steps of the solutions of the first three wolves.

The mathematical model of the encircling of the prey by grey wolves for hunting is given by:

$$\vec{D} = \left| \vec{C}\,\vec{X}_p(t) - \vec{X}(t) \right| , \qquad (11)$$

$$\vec{X}(t+1) = \vec{X}_p(t) - \vec{A}.\vec{D} , \qquad (12)$$

where $\vec{A}$ and $\vec{C}$ are used to represent the coefficient vectors, $\vec{X}_p$ vector is used to determine the position of prey, $\vec{X}$ is used to represent the position of the wolves and t is representing the iteration count. For the calculation of vectors $\vec{A}$ and $\vec{C}$ requires the following Eqs.:

$$\vec{C} = 2.rand_2 , \qquad (13)$$

$$\vec{A} = 2\vec{a}.rand_1 - \vec{a} , \qquad (14)$$

where $\vec{a}$ decreases linearly starting at 2 and ends at 0 during the period of iterations, $rand_1$ and $rand_2$ means random numbers in between $(0,1)$. he hunting process of the wolves is generally directed by the α embers of the chunk. The $'\beta'$ and $'\delta'$ wolves seldom go for hunting. Thus, it is very clear that the α, β, and δ embers of the group have the information of the prey and is reflected in the mathematical s. Therefore, the first three solutions best obtained so far are kept and the others are asked to recondition the location based on the best solutions. The following mathematical Eqs. describe the same:

$$\vec{D}_\alpha = \left| \vec{C}_1 \vec{X}_\alpha - \vec{X} \right| , \qquad (15)$$

$$\vec{D}_\beta = \left| \vec{C}_2 \vec{X}_\beta - \vec{X} \right| , \qquad (16)$$

$$\vec{D}_\delta = \left| \vec{C}_3 \vec{X}_\gamma - \vec{X} \right| , \qquad (17)$$

Thus

$$\vec{X}_1 = \vec{X}_\alpha - \vec{A}_1.\vec{D}_\alpha , \qquad (18)$$

$$\vec{X}_2 = \vec{X}_\beta - \vec{A}_2.\vec{D}_\beta , \qquad (19)$$

$$\vec{X}_3 = \vec{X}_\delta - \vec{A}_3.\vec{D}_\delta , \qquad (20)$$

and finally

$$\vec{X}(t+1) = \frac{\left(\vec{X}_1 + \vec{X}_2 + \vec{X}_3 \right)}{3} . \qquad (21)$$

The grey wolves complete the chase when the prey stops moving by attacking it. The following step includes the reduction in the value of $\vec{a}$ which directly affects the value of $\vec{A}$y reducing the variation in its value. If $\vec{A}$ is between $[-1,1]$ and has random values then the next location of the search agent can be assumed to be between the position of the prey and its current location [13].

B. Modified GWO Algorithm (mGWO)

The GWO algorithm sometimes faces issues related to stagnation to local optima. The reason behind this is the transition from the exploration phase to the exploitation phase of the algorithm. Although these two terms are conflicting in nature, still a balance is required among them particularly for population-based algorithms so that finding global maxima can be guaranteed. The simple deciding criteria used for deciding

the exploration and exploitation in GWO is that if $|A| \geq 1$ then it is the exploration and if $|A| < 1$ then it is exploitation. This parameter is calculated with the help of '*a'*. So by changing the for calculating *'a'* the process can be modified. The decay of the term '*a'* in this algorithm has been described with the help of exponential function over the passage of the iterations and is given as [14]:

$$a = 2\left(1 - \frac{t^2}{T^2}\right) \quad . \tag{22}$$

C. Augmented Grey Wolf Optimizer (AGWO)

GWO algorithm is known for its simplicity and its ability to track the global maxima of any optimization problem. But sometimes when the non-linearity in the problem increases, GWO is not able to perform the task of optimization with much accuracy due to its poor exploration problem. Hence, AGWO augments the exploration ability of the original algorithm by improvising its exploration ability without affecting its simplicity. AGWO considers that the parameter '*a'* varies from 2 to 1 instead of 2 to 0 as it was in the conventional GWO. This helps in obtaining a better exploration phase than the exploitation phase. The value of '*a'* is given as:

$$\vec{a} = 2 - \cos(rand) \cdot \frac{t}{Max\_iter} \quad . \tag{23}$$

Also, in AGWO hunting only depends on α nd βolves. Therefore, considering the (15), (16), (18), and (19) the final Eq. developed is [15]:

$$\vec{X}_1 = \frac{\vec{X}_1 + \vec{X}_2}{2} \quad . \tag{24}$$

D. Enhanced Leadership Based GWO (EGWO)

Based on levy-flight a local search algorithm has been proposed that is called EGWO which solves the problem of the local minima problem of GWO and helps to improvise the hunting quality of the leaders of the hunters. The Levy-flight discovers the favourable areas to find more educated heads in terms of suitability and possibility. A greedy search algorithm is employed which is utilized to create required equality between the exploitation and exploration phase and dodges the wolves from diverging the desirable search place location domains.

In the presented EGWO, the position of i^{th} leading wolf $xi = (xi1, xi2, \ldots..., xin)$ for the j^{th} dimension $(j = 1, 2, 3, \ldots., n)$ is changed in the following manner:

$$xij' = xij + par \times s \quad , \tag{25}$$

where x_{ij}' is the i^{th} changed leading wolf, par is the control parameter which is a linearly decreasing vector and selects the step size. Considering the numerical value of the variable par, it is between par $\in$ (2, 0). The range of par is chosen so that the steadiness amongst exploration and exploitation could be maintained. par is defined as [16]:

$$par = 2 - 2\left(\frac{t}{max\,iter}\right) \quad . \tag{26}$$

IV. Results and Discussions

B The computation was performed with the help of the three widely available and used solar panels and those are manufactured by Kyocera, Solarex, and Canadian Solar. The datasheet used for the computation has been reported in [4]. The computation of parameters was done at STC i.e. irradiance is considered $1000 W/m^2$ the temperature is 298K. The total number of search agents as chosen was 50 and the total number of

TABLE I: Ranges of parameters of DDM.

Parameters	Lower bound	Upper bound
IPV(A) (Photovoltaic current)	0	10
a1, a2, a3 (Ideality Factor)	0.5	2
RS(Ω) (Series Resistance)	0.001	0.5
Rp(Ω) (Parallel Resistance)	0	500
I01, I02 (μA) (Reverse Saturation Currents)	0	1

iterations performed on them was 500. There were seven parameters to be computed and the range of each parameter is listed below (Table I).

Tables II-IV presents the best values of the parameters computed by the GWO variants and compares the errors obtained for each method used. The total number of independent runs considered for each method was 20. The sum of square errors has been considered in the results obtained above. All the estimated values of the parameters and error show that the GWO algorithm and its variants can estimate the results pretty accurately for all kinds of solar panels to be used. The table also tells that the best result has been obtained from the EGWO algorithm and the same has been highlighted in bold for each table. The results obtained for the Kyocera model are presented in two parts as Table II and Table III respectively. A comparison of the best results obtained so far is presented in the form of a graph and Fig. 3 show the same.

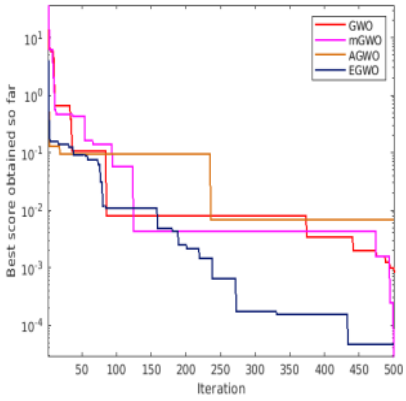

Figure 3. Convergence curve of various GWO algorithms obtained from Kyocera Multi-crystal.

TABLE II. RESULTS OBTAINED FOR KYOCERA KC200GT MULTI-CRYSTAL.

Algorithms	I_{pv}	a_1	a_2	R_s
GWO	8.2361	1.4178	1.8158	0.15314
mGWO	8.2087	1.3397	1.5872	0.18848
AGWO	8.2046	1.5198	1.5511	0.08726
EGWO	8.2157	1.3456	1.5071	0.13269

TABLE III. RESULTS OBTAINED FOR KYOCERA KC200GT MULTI-CRYSTAL.

Algorithms	R_p	I_{01}	I_{02}	***Error***
GWO	254.4104	4.1334e-07	9.4802e-07	8.1152e-04
mGWO	499.7021	1.4257e-07	3.6643e-07	6.9312e-05
AGWO	155.3868	4.2394e-07	1.2292e-06	0.006976
EGWO	201.2547	9.3901e-08	5.5282e-07	**4.8113e-05**

TABLE IV. PARAMETER ESTIMATES OF SOLAREX MSX-60 POLYCRYSTALLINE.

Algorithms	I_{pv}	a_1	a_2	R_s
GWO	3.8056	1.3186	1.9025	0.15488
mGWO	3.7924	1.3995	1.7834	0.06759
AGWO	3.7804	1.5183	2.9420	0.00694
EGWO	3.8064	1.9314	1.4323	0.10207

TABLE V PARAMETER ESTIMATES OF SOLAREX MSX-60 POLYCRYSTALLINE.

Algorithms	R_p	I_{01}	I_{02}	***Error***
GWO	181.851	1.1156e-07	1.0933e-07	9.0975e-05
mGWO	265.8317	2.9802e-07	3.0582e-07	4.527e-04
AGWO	163.123	1.0781e-06	3.816e-07	0.001997
EGWO	268.5272	8.7212e-07	4.337e-07	**4.552e-05**

TABLE VI OUTCOMES OBTAINED FOR CANADIAN SOLAR CS6K-280M MONOCRYSTALLINE.

Algorithms	I_{pv}	a_1	a_2	R_s
GWO	9.4406	1.9068	1.3857	0.00293
mGWO	9.4133	1.5220	1.7784	0.00123
AGWO	9.5216	1.8562	1.4318	0.00317
EGWO	9.4358	1.7583	1.5171	0.00170

Table IV shows that for Kyocera KC200GT Multi-crystal, the algorithms performed nicely and good results were obtained from each of them. Still, the best result was given by EGWO and is closely followed by mGWO. Comparatively the worst result was obtained from AGWO. The results are displayed intwo parts viz. Table IV and V. The same can be verified from the convergence curves of these algorithms for the taken panel. The convergence curve also shows the converging nature of each algorithm. Table VI shows the results obtained from the algorithms for Solarex MSX-60 Polycrystalline and the convergence curves for this panel is depicted in Fig. 4.

The results show that again the algorithms are outperformed by EGWO and this time it is

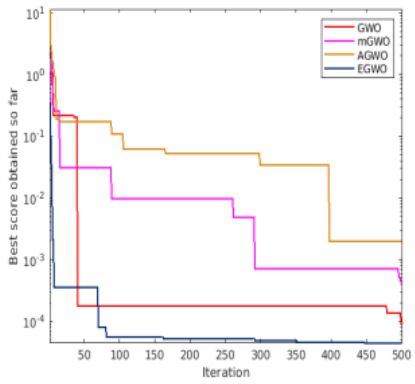

Figure 4. Convergence characteristic of various GWO algorithms obtained from Solarex Polycrystalline.

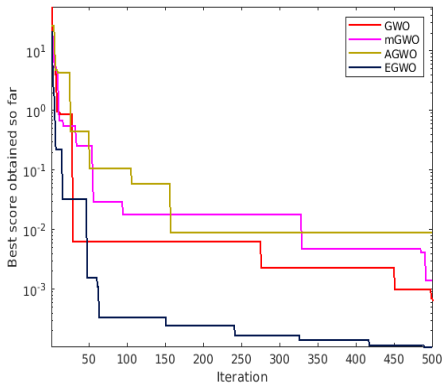

Figure 5. Convergence graph of various GWO algorithms obtained from Canadian Solar.

TABLE VII OUTCOMES OBTAINED FOR CANADIAN SOLAR CS6K-280M MONOCRYSTALLINE.

Algorithms	R_p	I_{01}	I_{02}	***Error***
GWO	152.9559	4.4820e-07	1.3204e-07	6.2702e-04
mGWO	458.1669	6.5734e-07	3.5299-07	0.0014101
AGWO	197.1886	2.4233e-06	2.0038e-07	0.0090371
EGWO	490.1297	4.5335e-07	6.1098e-07	**1.1008e-04**

closely followed by GWO. Others have also shown good values and low errors. In this case, as well the AGWO has shown the worst result among all of them. The same can be correctly verified using the convergence characteristics where the converging power of EGWO can be seen as superior to the others.

Table VII shows the results obtained from Canadian Solar CS6K-280M Monocrystalline and Fig. 5 shows the corresponding convergence curves. The results of Table VII are showcased in two parts as part-a, and b respectively. The minimum error value has been represented with the help of bold letters.

The results again reveal the superiority of EGWO over the other three algorithms and are closely followed by GWO, with good results provided by the others as well. The parameters obtained also have good values where series resistance and reverse saturation current is also very small. The convergence curve also shows the same.

V. CONCLUSIONS

The parameter extraction of PV cells is currently having a lot of interest among all the researchers in the world. Through this paper, the parameter extraction of DDM has been described by using the GWO algorithm and its five variants. The total number of parameters is seven in the case of DDM. Three equations were formed for the extraction of parameters and are based on open circuit, short circuit, and maximum power point condition. The data of three widely panels are used for the extraction of parameters and metaheuristic algorithms are used to minimize the square error. The results obtained are well within the bounds of the variables as specified. Out of all the used methods, the best result was provided by the EGWO algorithm as the error obtained for each type of panel is the lowest. There are other models developed for the diodes and may prove to give better results than these. Also, there may be some new algorithm used in place of the currently used ones for obtaining a better result and this remains in the future scope.

REFERENCES

[1] Kannan, N., & Vakeesan, D. (2016). Solar energy for future world:-A review. *Renewable and Sustainable Energy Reviews, 62*, 1092-1105.

[2] Abbassi, R., Abbassi, A., Jemli, M., & Chebbi, S. (2018). Identification of unknown parameters of solar cell models: A comprehensive overview of available approaches. *Renewable and Sustainable Energy Reviews, 90*, 453-474.

[3] Ishaque, K., Salam, Z., & Taheri, H. (2011). Simple, fast and accurate two-diode model for photovoltaic modules. *Solar energy materials and solar cells, 95*(2), 586-594.

[4] Qais, M. H., Hasanien, H. M., & Alghuwainem, S. (2019). Identification of electrical parameters for three-diode photovoltaic model using analytical and sunflower optimization algorithm. *Applied Energy, 250*, 109-117.

[5] Shannan, N. M. A. A., Yahaya, N. Z., & Singh, B. (2013, November). Single-diode model and two-diode model of PV modules: A comparison. In *2013 IEEE International Conference on Control System, Computing and Engineering* (pp. 210-214). IEEE.

[6] Chin, V. J., Salam, Z., & Ishaque, K. (2015). Cell modelling and model parameters estimation techniques for photovoltaic simulator application: A review. *Applied Energy, 154*, 500-519.

[7] Chin, V. J., & Salam, Z. (2019). A new three-point-based approach for the parameter extraction of photovoltaic cells. *Applied Energy, 237*, 519-533.

[8] Ebrahimi, S. M., Salahshour, E., Malekzadeh, M., & Gordillo, F. (2019). Parameters identification of PV solar cells and modules using flexible particle swarm optimization algorithm. *Energy, 179*, 358-372.

[9] Ye, M., Wang, X., & Xu, Y. (2009). Parameter extraction of solar cells using particle swarm optimization. *Journal of Applied Physics, 105*(9), 094502.

[10] Moldovan, N., Picos, R., & Garcia-Moreno, E. (2009, February). Parameter extraction of a solar cell compact

model using genetic algorithms. In *2009 Spanish Conference on Electron Devices* (pp. 379-382). IEEE.

[11] Ma, J., Ting, T. O., Man, K. L., Zhang, N., Guan, S. U., & Wong, P. W. (2013). Parameter estimation of photovoltaic models via cuckoo search. *Journal of applied mathematics*, 2013.

[12] Biswas, P. P., Suganthan, P. N., Wu, G., & Amaratunga, G. A. (2019). Parameter estimation of solar cells using datasheet information with the application of an adaptive differential evolution algorithm. *Renewable Energy*, *132*, 425-438.

[13] Mirjalili, S., Mirjalili, S. M., & Lewis, A. (2014). Grey wolf optimizer. *Advances in engineering software*, *69*, 46-61.

[14] Mittal, N., Singh, U., & Sohi, B. S. (2016). Modified grey wolf optimizer for global engineering optimization. *Applied Computational Intelligence and Soft Computing*, *2016*.

[15] Qais, M. H., Hasanien, H. M., & Alghuwainem, S. (2018). Augmented grey wolf optimizer for grid-connected PMSG-based wind energy conversion systems. *Applied Soft Computing*, *69*, 504-515.

[16] Gupta, S., & Deep, K. (2019). Enhanced leadership-inspired grey wolf optimizer for global optimization problems. *Engineering with Computers*, 1-24.

The Advanced Cooling System of Generator for Hydropower Plant

Abdulmuttalib A. Muhsen[1], Natalya Kizilova[2]

[1,2]Faculty of Power and Aeronautical Engineering, Warsaw University of Technology, Warsaw

[1]Haditha Hydropower Station, Ministry of Electricity, Haditha, Iraq

Abstract—**This paper documents heat and fluid flow characteristics of the counterflow heat exchangers with line-to-line flow channels embedded fins of a fractal air-water cooler for hydrodynamic power plant generator which was analyzed numerically using AnSys 2021 R1 Fluent software to simultaneously solve the continuity, momentum, and heat equations in a 3D computational domain, and the conformal mesh technique is applied to generate the grid for the conjugate heat flow in the cooling system. At the low Reynolds numbers, the laminar viscous flow model was used, while at higher Re numbers Re~1200 the transitional flow regime was studied on the k-epsilon turbulent model. The governing pressure drop was ~(35-45)x10^5 Pa. Numerical results revealed that the fractal geometry can improve the integrated performance of the cooling system. The pressure drop through the pipe channel of the cooler as decreases obviously when compared with that of conventional parallel channels. The fractal system showed a more uniform temperature distribution and relatively lower maximum surface temperature. Application of the fins could intensify the transfer of heat remarkably and lower the power of the pump in a quick fashion related to the conventional tube system.**

Keywords - fluid dynamics, cooling channel, convection, heat transfer, fractal network

I. INTRODUCTION

Hydropower is a conventional clean renewable source of energy that plays an important role in sustainable energy. Nowadays hydropower plants located in 150 countries generate ~29% of total energy in China, 9% in Brazil, 7% in the US and Canada, and 31% in the rest world [1]. In 2020 global hydropower generation increased 1.5% to reach 4,370 TWh, representing around 16.8% of the world's total electricity generation. It is expected to increase by ~ 3.1% each year for the next 25 years.

Efficient cooling of the hydropower plant is essential to maintain and keep the system in good operational conditions [2]. Hydropower generators' need a cooling system to dissipate heat from some of the heated areas such as the turbine seals, the oil-filled transformers, and lubrication bearings. A close loop circuit in which water supply passes through a tubular heat exchanger directly submerged into draft tube water was proposed in [3]. The hydropower plant must integrate a systematic cooling system such as a heat exchanger (Fig.1) [4]. The efficient design of the cooling system must provide fast uniform heat removal at low-pressure drops and with low acoustic emissions due to flow-induced vibrations of the solid structures [5, 6]. The thermal contact design between the fluid and solid structures has important applications in heat pumps with extraction and release and thermal energy storage [7, 8].

The objective of the paper is to determine the thermal performance of the fluid flow structure of the cooling system. To be precise, we analyze

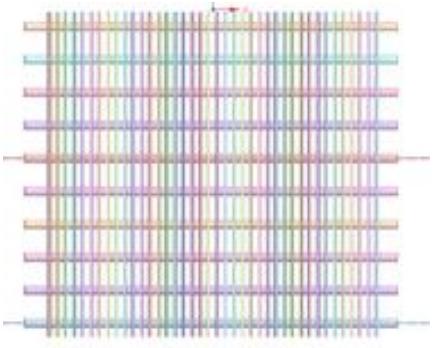

Figure 1. Pipe channel cooling system type.

ISBN: 978-86-80593-73-9

the effect of the flow structure on the overall performance of the system.

II. COOLING SYSTEMS FOR GENERATORS

A hydropower plant like that of Haditha hydropower plant (HPP) is one of the principal hydropower plants in Iraq. The plant has 6 units of Kaplan turbines capable generating of 110 MW of power each which generates a total capacity of 660MW [4]. The most essential part of the hydropower plant is the turbine which is attached to the electric generators that turn the generators by utilizing the energy of water flowing through and impacting on the turbine blades. The friction due to the rotation of the rotary components of the generators causes heat to be generated as well as the fluid friction also causes heat to be generated on the generator components. The occurrence of thermal losses on the generator unit at maximum load is much it is approximately 1000kW. The need for the cooling system in hydropower generators is required. All the generators in the Haditha hydropower plant have 12 radiators located in the stator hub of the generator that is an ideal isolated environment for the radiators to function properly.

In the conventional cooling systems (Fig. 2), the radial fan located at the stator hub makes the airflow which warms the fluid in return. The airflow is constant because the angular velocity of the hydropower unit is fixed. Cold fluid is circulated from the dam into the cooling system through the pipes. Consequently, the temperature data were recorded by the monitoring unit of the plant, as 15˚C to 27˚C of cooling systems inlet changes [8-10].

III. ANALYSIS OF THE COOLING SYSTEM

The cooling system for the hydropower plant generator consists of a series of tubes and fins which are housed on a stainless-steel frame.

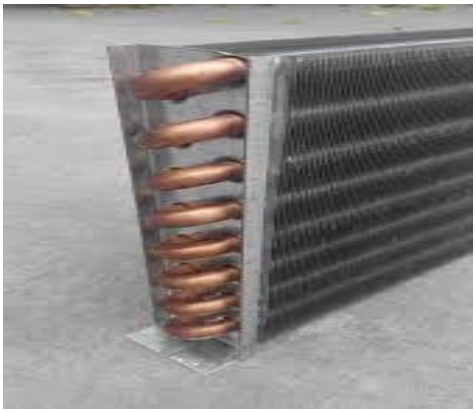

Figure 2. Conventional channel type cooling system.

These tubes contain a heated fluid that needs cooling. The fins are in contact with the walls of the tubes that are used to facilitate air to cool the tube through convection so that it can absorb the heat from the tubes. An engineering simulation software was used to model and design the tubes and fins of the cooling system in ANSYS 2021 R1, Workbench. The analysis was performed using Ansys FLUENT, which was used to compute equations using the Computational Fluid Dynamics (CFD) volumetric control approach (VCA). This VCA simplifies the complex differential equations into simple algebraic equations. The geometric modeling of the cooling system was done using the parametric approach in Solidworks software. Meshing was done using the structured grids as well as unstructured grids using the method and sizing controls to define the meshing properties of the model. The boundary conditions were defined using the name selection tool to indicate the inlet, outlet, walls, etc. in the Ansys modeler for the cooling system model. This file was imported into Fluent software in the Ansys workbench and has given the input values like mass flow rate, pressure, temperature, etc.

TABLE I. DIMENSIONS AND MATERIALS FOR THE COOLING SYSTEM.

Overall Dimension	**Dimension of tube**	**Material details**	**Types of tube pattern**
Length=800mm	Outer diameter=20mm	ANSI1316L Stainless steel	Straight Parallel tubes
Width=140mm	Inner diameter=16mm		
Height=720mm			

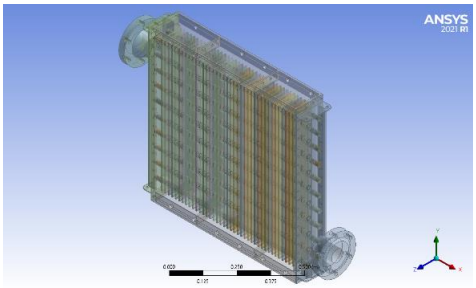

Figure 3. Geometrical model of the cooling system.

Realistic 3D geometry (Fig. 3) was used for the analysis of the heat transfer by the moving fluid in the cooling system sufficient to cool the powerplant generator for solving the mass, momentum, and energy equations. The mean pressure and temperature were defined at the inlet of the cooling system. The laminar flow models were used to solve the convergence of the equations setting the functions as wall standards [11]. The gravitational acceleration of 9.81 m/s2 in the downward flow direction was used. The study was done in a steady state to obtain the results. The inlet of the temperature is 25°C. The material of the pipe is ANSI1316L Stainless steel, and the fins are AlMg3 Aluminum Alloy was used to determine the rate of heat transfer between the two materials using convection [12-14].

After the model is designed, a thermal simulation of the cooling system is to be run. The general conditions played role in the study with the computational domain. Fig. 1 shows the model of the cooling system in Ansys CFD.

IV. Mathematical Model Formulation

The following equations based on the balance of mass, momentum, and energy have been used [15]:

- Mass conservation:

$$\frac{\partial u}{\partial x}+\frac{\partial v}{\partial y}+\frac{\partial w}{\partial z}=0\ , \qquad (1)$$

- Momentum Eq.:

$$\rho\left(\frac{\partial(uu)}{\partial x}+\frac{\partial(uv)}{\partial y}+\frac{\partial(uw)}{\partial z}\right)=-\frac{\partial p}{\partial x}+\begin{pmatrix}\frac{\partial}{\partial x}\left(\mu\frac{\partial u}{\partial x}\right)+\\ +\frac{\partial}{\partial y}\left(\mu\frac{\partial u}{\partial y}\right)+\frac{\partial}{\partial z}\left(\mu\frac{\partial u}{\partial z}\right)\end{pmatrix}, \qquad (2)$$

$$\rho\left(\frac{\partial(uv)}{\partial x}+\frac{\partial(vv)}{\partial y}+\frac{\partial(vw)}{\partial z}\right)=-\frac{\partial p}{\partial x}\begin{pmatrix}\frac{\partial}{\partial x}\left(\mu\frac{\partial v}{\partial x}\right)+\\ +\frac{\partial}{\partial y}\left(\mu\frac{\partial v}{\partial y}\right)+\frac{\partial}{\partial z}\left(\mu\frac{\partial v}{\partial z}\right)\end{pmatrix}, \qquad (3)$$

$$\rho\left(\frac{\partial(uw)}{\partial x}+\frac{\partial(vw)}{\partial y}+\frac{\partial(ww)}{\partial z}\right)=-\frac{\partial p}{\partial x}+\frac{\partial}{\partial x}\left(\mu\frac{\partial w}{\partial x}\right)+\frac{\partial}{\partial y}\left(\mu\frac{\partial w}{\partial y}\right)+\frac{\partial}{\partial z}\left(\mu\frac{\partial w}{\partial z}\right)\ . \qquad (4)$$

- Energy Eq.:

Energy in the fluid domain:

$$\rho_f\left(\frac{\partial\left((c_p)_f\,uT\right)}{\partial x}+\frac{\partial\left((c_p)_f\,vT\right)}{\partial y}+\frac{\partial\left((c_{p)f}\,wT\right)}{\partial z}\right)=\frac{\partial}{\partial x}\left(k_f\frac{\partial T}{\partial x}\right)+\frac{\partial}{\partial y}\left(k_f\frac{\partial T}{\partial y}\right)+\frac{\partial}{\partial z}\left(k_f\frac{\partial T}{\partial z}\right)\ , \qquad (5)$$

Energy in the fluid domain:

$$=\frac{\partial}{\partial x}\left(k_f\frac{\partial T}{\partial x}\right)+\frac{\partial}{\partial y}\left(k_s\frac{\partial T}{\partial y}\right)+\frac{\partial}{\partial z}\left(k_s\frac{\partial T}{\partial z}\right)\ . \qquad (6)$$

The boundary conditions for computations were taken as follows [16, 17]:

TABLE II. BOUNDARY CONDITIONS.

Inlet	Pressure-inlet
Outlet	Zero pressure
Dividers	Convective, no-slip criteria
Liquid	Water (H_2O)
Solid Material	Stainless steel Aluminum Alloy
Energy Condition	ON
Computational model	K-epsilon, feasible, standard wall treatment
Solution Method	Second-order

V. NUMERICAL PROCEDURE

CFD simulations were performed using a finite-volume package with a pressure-based solver, node-based gradient evaluation, the Eqs. (2)-(6) are constant values used in the simulation together with the SIMPLE algorithm for pressure–velocity coupling, and a second-order upwind scheme for momentum and energy equations [18]. In grid generation, tetra grids are adopted for conformal meshing between the fins and the tube. The independence of the solution with respect to the grid size was checked by inspecting the values of the mean pressure, maximum temperature, temperature differences between the inlet and outlet, the coefficient of heat transfer for convection between the wall of the tube and the fins [19-25].

The mesh was carried out on the geometry to ensure there is conformal meshing between the tubes and the fins using the tetrahedral method. The cell grids vary across the model to achieve medium coarse mesh; the smallest number was $6x10^6$.

Convergence is achieved when the residuals for the mass and momentum equation are smaller than 10^{-4}, and the residual of the energy equation is less than 10^{-11}.

TABLE III. RESULT OF THE OUTLET OF THE COOLING SYSTEM ANALYSIS.

Parameters	**Units**
Maximum Velocity	3.5m/s^2
Outlet Maximum pressure	0.9Mpa
Temperature	22.4°C

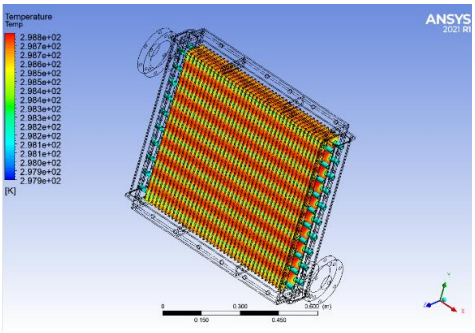

Figure 4. Temperature distribution in the cooling system.

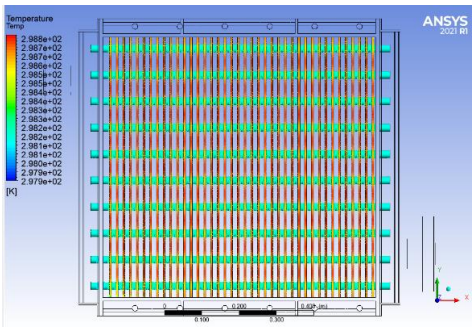

Figure 5. Temperature of the fins and the tubes of the cooling system.

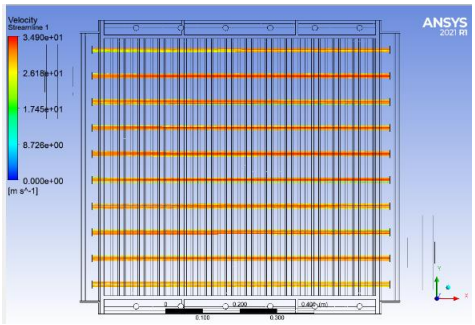

Figure 6. Streamline velocity of the cooling system.

VI. RESULTS AND DISCUSSION

From the CFD analysis of the cooling system of the power plant generator with the variations in tubes, we found the distributions of temperature (Figs. 4, 5), velocity (Fig. 6), and static pressure along the channels and fins.

Numerical simulations revealed the temperature differences. Some numerical results are summarized in Table III. Conclusion

From this study, the flow and heat transfer characteristics in the cooling structure for the system, parallel flow is investigated using CFD in the current study, and the optimization procedure for the leading influencing factors including the level number.

We select Stainless steel material for the tubes and Aluminum Alloy material for fins then analyzed in Ansys and enhance the optimized material temperature value. Assuming that the cooling is system is isolated from the environment and contrasting the results the maximum heat transfer occurred at the parallel flow of the cooling system.

It may be assumed that no heat transfer is taking place in between model and surroundings. It is concluded that tubes and fins need modification to increase the efficiency of the heat transfer flow, water in Parallel flow tubes gives 22°C temps at the outlet which is lowered from 25°C.

REFERENCES

[1] Renewables (2021). *Global status report*. Available at: https://www.ren21.net/wp-content/uploads/2019/05/GSR2021_Full_Report.pdf

[2] Kumar, K., & Saini, R. P. (2022). A review on operation and maintenance of hydropower plants. *Sustainable Energy Technologies and Assessments*, *49*, 101704.

[3] Shah, S. K., & Shrestha, R. (2015). Design Modification of Cooling Water System for Hydropower Plants [A Case Study of Middle Marsyangdi Hydropower Plant in Nepal]. *Global Journal of Research In Engineering*, *15*(6), 090699.

[4] Muhsen, A. A., Szymański, G. M., Mankhi, T. A., & Attiya, B. (2018). Selecting the most efficient maintenance approach using AHP multiple criteria decision making at haditha hydropower plant. *Zeszyty Naukowe Politechniki Poznańskiej. Organizacja i Zarządzanie.*

[5] Hamadiche, M., Kizilova, N., & Gad-el-Hak, M. (2009). Suppression of absolute instabilities in the flow inside a compliant tube. Communications in *Numerical Methods in Engineering*, *25*(5), 505-531.

[6] Kizilova N., Hamadiche M., & Gad-el-Hak M. (2011). Flow stabilization in compliant ducts: from nature-made to human-made. *International Journal Numerical Methods and Applications*, *6*(1), 1-86.

[7] Irshad, M., Kaushar, M., & Rajmohan, G. (2017). Design and CFD analysis of shell and tube heat exchanger. International *Journal of Engineering Science and Computing*, *7*(4), 6453-6457.

[8] Kaliappan, A. S., & Mothilal, T. (2018). Thermal analysis of shell and tube heat exchanger. International *Journal of Pure and Applied Mathematics*, *119*(12), 14299-14306.

[9] Mohanty, S., & Ahmed, S. U. (2018). Performance prediction of Counter flow Heat Exchanger by using CFD technique. *International Journal of Engineering Development and Research*, *6*(2).

[10] Patil, A. S., & Farkade, H. S. (2017). Advances in Design and Development of Heat Exchangers: A Review. *International Research Journal of Engineering and Technology (IRJET)*, *4*(05).

[11] Sethi, C. K. (2017). CFD Analysis on Effectiveness of a Plate Type Heat Exchanger Using Sea Water and Engine Oil. International *Journal of Advanced Mechanical Engineering*, *12*(1), 191-198.

[12] Shrivastava, D., & Mishra, R. (2017). CFD Analysis of Heat Transfer for Tube-In-Tube Heat Exchanger. *International Journal of Recent Trends in Engineering & Research (IJRTER)*, *3*(08).

[13] Kishan, R., Singh, D., & Sharma, A. K. (2020). CFD Analysis of Heat Exchanger Models Design Using Ansys Fluent. *International Journal of Mechanical Engineering and Technology*, *11*(2).

[14] Miao, Q., Wang, Z., & Wang, L. (2017). A Failure Analysis of Air Heat Exchanger Based on Modal Calculation and Thermal-Structural Interaction Simulation. *International Journal of Materials, Mechanics and Manufacturing*, *5*(3).

[15] Miao, Q., Wang, Z., & Wang, L. (2017). A Failure Analysis of Air Heat Exchanger Based on Modal Calculation and Thermal-Structural Interaction Simulation. *International Journal of Materials, Mechanics and Manufacturing*, *5*(3).

[16] Jayachandriah, B., & Rajasekhar, K. (2014). Thermal analysis of tubular heat exchangers using ANSYS. *International Journal of Engineering Research*, *3*(SP 1), 21-25.

[17] Rao, J. B. B., & Raju, V. R. (2016). Numerical and heat transfer analysis of shell and tube heat exchanger with circular and elliptical tubes. *International Journal of Mechanical and Materials Engineering*, *11*(1), 1-18.

[18] *Fluent User's Maual.* (2021). ANSYS, Inc.

[19] Dincer, I., & Rosen, M. A. (2012). *Exergy: energy, environment and sustainable development.* Newnes.

[20] Wu, S. Y., Yuan, X. F., Li, Y. R., & Xiao, L. (2007). Exergy transfer effectiveness on the heat exchanger for finite pressure drop. *Energy*, *32*(11), 2110-2120.

[21] Ujiie, R., Arlitt, R., & Etoh, H. (2006). Application of computational fluid dynamics (CFD) on ventilation-cooling optimization of electrical machines. *Review Energy Technologies Generation, Transmission and Distribution of Electric and Thermal Energy*, 17-22.

[22] Doost, A. K., & Majlessi, R. (2015). Heat transfer analysis in the cooling system of hydropower's generator. *Open Journal of Applied Sciences*, *5*(03), 98.

[23] Doost, A. K., & Majlessi, R. (2015). Heat transfer analysis in the cooling system of hydropower's generator. *Open Journal of Applied Sciences*, *5*(03), 98.

[24] Şahin, A. Ş., Kılıç, B., & Kılıç, U. (2011). Design and economic optimization of shell and tube heat exchangers using Artificial Bee Colony (ABC) algorithm. *Energy Conversion and Management*, *52*(11), 3356-3362.

[25] Cengel, Y. A., & Ghajar, A. J. (2007). *Heat and mass transfer. A practical approach.*

Determining Optimal Sizing of Distributed Generators and Application on "ED Leskovac" Distribution Network

Miloš M. Stevanović[1], Aleksandar Janjić[2], Sreten B. Stojanović[3], Dragan S. Tasić[4]

[1,3]University of Nis, Faculty of Technology, Leskovac, Serbia, smilos@tf.ni.ac.rs[1], sstojanovic@tf.ni.ac.rs[3]

[2,4]University of Nis, Faculty of Electronic Engineering, Nis, Serbia, aleksandar.janjic@elfak.ni.ac.rs[2], dragan.tasic@elfak.ni.ac.rs[4]

Abstract—**In this paper, an algorithm was developed for determining the optimal rated power of the distributed generators (DG), at predetermined locations (nodes) in power system, so that power losses are minimal, using the search method of alternatives. This algorithm requires the calculation of power flow and voltages in the power network, and for these purposes the Newton - Raphson iterative procedure was used. The algorithm was tested on the real 35 kV radial power distribution network.**

Keywords – distributed generation, optimal location, optimal sizing

I. INTRODUCTION

The degree and quality of the influence of DGs on the operation of the system depends on its power, type and location. The purpose of site and power optimization of DGs is to increase the positive and reduce the negative effects that they have on the operation of the power distribution network. Accordingly, the choice of objective function depends of the desired goal. These are usually the following goals:

- Minimization of power and energy losses;
- Improving the power network voltage profile, ie minimizing voltage deviations;
- Increasing the availability of system elements;
- Increased reliability of consumer supply;
- Minimizing the short-circuit current;
- Minimization of harmonic distortions;
- Minimizing total costs associated with power network operation (equipment installation, energy purchase, losses, power outages);
- Minimization of investments, procurement and connection of power distributed generators, etc.

In terms of determining the location and power, DGs can be divided in two groups. In the first group, locations and power are mostly determined by geographical, hydrological and meteorological factors (small hydropower plants, wind generators). In this case, it is possible to talk about optimizing the connection point to the existing power distribution network only if a set of nodes is assigned which a DG can be connected to. It is possible to look for optimal solutions in the planning phase of a completely new or reconstruction of the existing network in the given (geographic and meteorological) tolerable area. In the second group can be classified all DG with predictable output (microturbines, fuel cells, etc.) which can be connected to any point of the distribution network.

II. APPLICATION OF NEWTON RAPHSON'S PROCEDURE FOR THE POWER FLOW

Application of Newton - Raphson's method for the calculation of power flows is based on the equations for active and reactive power injection in hybrid form. With number 1 is marked balance

ISBN: 978-86-80593-73-9

node, numbers from 2 to $N - N_{PQ}$, *PU* (voltage controlled) nodes, and with number from $N - N_{PQ}+1$ to N is marked *PQ* (consumer) nodes. Accordingly, vector of unknown variables is:

$$\vec{X} = \begin{bmatrix} \vec{\theta} \\ \vec{U} \end{bmatrix},$$

where :

$\vec{\theta} = \begin{bmatrix} \theta_2 & \theta_3 & \cdots & \theta_N \end{bmatrix}^T$ – vector of unknown voltage angles

$\vec{U} = \begin{bmatrix} U_{N-N_{PQ}+1} & U_{N-N_{PQ}+2} & \cdots & U_N \end{bmatrix}^T$ - vector of unknown voltage modules.

In order to determine the values of unknown variables, it is necessary to create a system of $N - 1 + N_{PQ}$ equations, which are simultaneously solved. For the creation of this equation, equations for the active and reactive power injection in hybrid form are used:

$$P_i\left(\vec{X}\right) = U_i^2 G_{ii} + \\ + U_i \sum_{\substack{k=1 \\ k \neq i}}^{N} U_k \left(G_{ik} \cos(\theta_i - \theta_k) + B_{ik} \sin(\theta_i - \theta_k)\right) \quad (1)$$

$$Q_i\left(\vec{X}\right) = -U_i^2 B_{ii} + \\ + U_i \sum_{\substack{k=1 \\ k \neq i}}^{N} U_k \left(G_{ik} \sin(\theta_i - \theta_k) - B_{ik} \cos(\theta_i - \theta_k\right) . \quad (2)$$

The symbols $P_i\left(\vec{X}\right)$ and $Q_i\left(\vec{X}\right)$ in relations (1) and (2) indicate that the expressions for the active and reactive power of injection in the nodes and the functions of the vector are variable. In the generator nodes, active power injection are known, and in consumer and active and reactive power injection. These known active and reactive injected powers for the node *i*, will be marked with P_i^{sp} and Q_i^{sp}, respectively. Now, for a node *i*, the following Eqs.can be written:

$$P_i^{sp} - U_i^2 G_{ii} - U_i \sum_{\substack{k=1 \\ k \neq i}}^{N} U_k \left(G_{ik} \cos(\theta_i - \theta_k) + \right. \\ \left. B_{ik} \sin(\theta_i - \theta_k)\right) = 0 \quad (3)$$

$$Q_i^{sp} + U_i^2 B_{ii} - U_i \sum_{\substack{k=1 \\ k \neq i}}^{N} U_k \left(G_{ik} \sin(\theta_i - \theta_k) - \right. \\ \left. - B_{ik} \cos(\theta_i - \theta_k)\right) = 0 \quad . (4)$$

Equation (3) applies to all generating and consumer nodes, and the (4) on the consumer nodes, so that the $N\text{-}1 + N_{PQ}$ equation is obtained. By solving (3) and (4), unknown nodes voltages and unknown angles of the voltage phase are determined.

III. Algorithm for Determining Optimal Location and Power of Distribution Generators

The idea of this algorithm is reduced to a "brute force" variant search that implies the calculation of the active loss power for each combination of DG power and location. By comparing the power loss values for each combination, the optimal solution is determined. Each variant involves one calculation of power flows and voltage nodes. The number of possible combinations can be very large, so certain information about the actual operation of the system can reduce this number. For these purposes among other things, information of potential nodes to which DG can be connected, as well as their available power. Potential nodes in which DGs can be connected are selected based on the energy potential of the place where

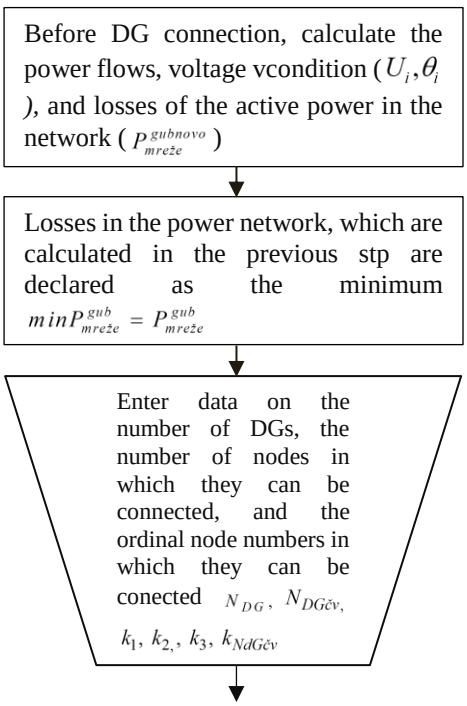

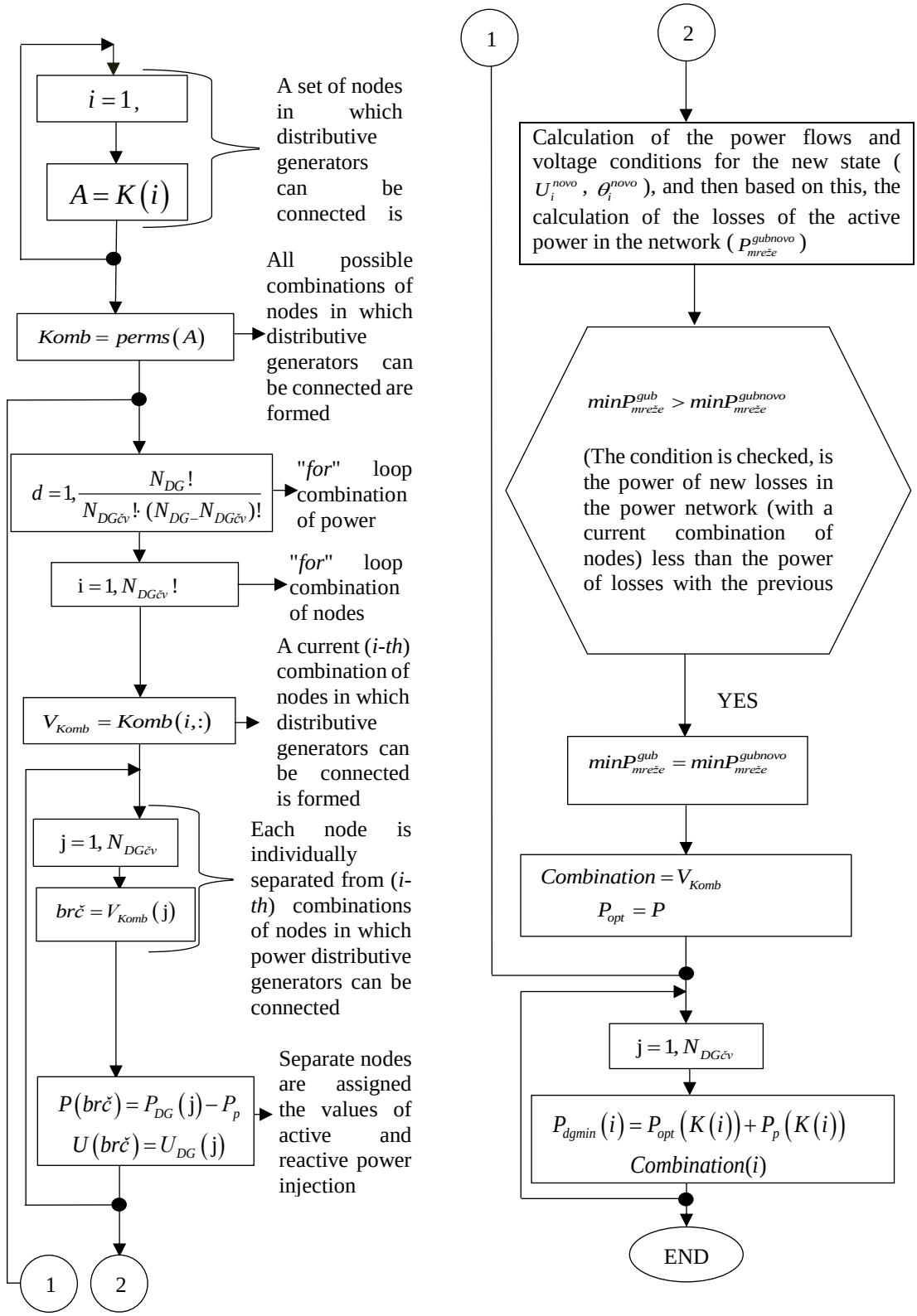
$i = 1,$
$A = K(i)$
A set of nodes in which distributive generators can be connected is
$Komb = perms(A)$
All possible combinations of nodes in which distributive generators can be connected are formed
$d = 1, \frac{N_{DG}!}{N_{DGčv}! \cdot (N_{DG} - N_{DGčv})!}$
"*for*" loop combination of power
$i = 1, N_{DGčv}!$
"*for*" loop combination of nodes
$V_{Komb} = Komb(i,:)$
A current (*i-th*) combination of nodes in which distributive generators can be connected is formed
$j = 1, N_{DGčv}$
$brč = V_{Komb}(j)$
Each node is individually separated from (*i-th*) combinations of nodes in which power distributive generators can be connected
$P(brč) = P_{DG}(j) - P_p$
$U(brč) = U_{DG}(j)$
Separate nodes are assigned the values of active and reactive power injection
1
2
1
2
Calculation of the power flows and voltage conditions for the new state (U_i^{novo} , θ_i^{novo}), and then based on this, the calculation of the losses of the active power in the network ($P_{mreže}^{gubnovo}$)
$minP_{mreže}^{gub} > minP_{mreže}^{gubnovo}$
(The condition is checked, is the power of new losses in the power network (with a current combination of nodes) less than the power of losses with the previous
YES
$minP_{mreže}^{gub} = minP_{mreže}^{gubnovo}$
$Combination = V_{Komb}$
$P_{opt} = P$
$j = 1, N_{DGčv}$
$P_{dgmin}(i) = P_{opt}(K(i)) + P_p(K(i))$
$Combination(i)$
END

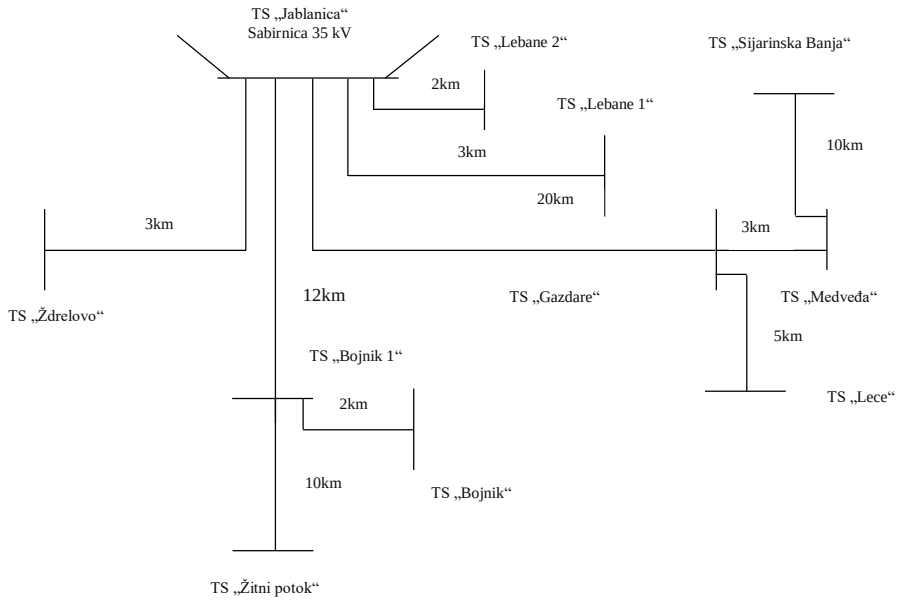

Figure 1. Power distribution network 35 kV ED Leskovac.

they are located. However, nodes that are farther away from the reference node were generally chosen because in this case, in radial power networks losses are reduced and improved voltage conditions. On the basis of the previously presented, an algorithm is given that determines the optimal locations and power of the distribution generator.

IV. TEST POWER DISTRIBUTION NEWVORK "ED LESKOVAC"

The previous algorithm will be applied to the power distribution network 35 kV ED Leskovac. This system includes all 35 kV nodes (total 11), at the substation 110/35 kV/kV „Jablanica“, while all nodes of lower voltage levels are ignored (Table I). The active and reactive power consumption of individual nodes were modeled by constant active and reactive power consumption in these nodes and their average real value occurring in exploitation. The powerlines in the mentioned system are aluminum-steel overhead lines, cross section $3\times \mathrm{Al/Fe}95/15\ mm^2$. For For aluminum-steel ropes $95/15\ mm^2$, longitudinal resistance is $r = 0,31\Omega/km$. For a longitudinal reactance, it is usually assumed in the calculations that it is $x = 0,4\Omega/km$, so the longitudinal impedance will be $\underline{z} = (0,31 + j0,4)\Omega/km$. The lengths of the powerlines are shown in the Fig. 1. Given that the powerlines are relatively short and that it is a medium voltage level, the branches to the ground can be ignored, so that the longitudinal susceptance is approximately equal to zero.

TABLE I. THE DATA ABOUT THE NODES POWER DISTRIBUTION NETWORK.

No	Names substation	$U[kV]$	P_g [MW]	P_p [MW]	Q_p [MW]
1	„Jablanica“	36.75	0	0	0
2	„Lebane 1“	-	0	2.5	1.25
3	„Lebane 2“	-	0	2.5	1.25
4	„Zdeglovo“	-	0	2	1
5	„Bojnik 1“	-	0	2	1
6	**„Gazdare“**	-		1.5	0.75
7	„Bojnik 2“	-	0	2	1
8	**„Zitni Potok“**	-		1	0.5
9	„Medveđa“	-	0	2.5	1.5
10	**„Sijarinska Banja“**	-		1	0.5
11	„Lece“	-	0	1.5	0.75

Data about DGs are given in Table II DGs are disposable with active power change in range $0,5[MW] \le P_{DG} \le 4[MW]$ with a step from $1[MW]$ and reactive power change in the range $0,25[MVAr] \le Q_{DG} \le 2[MVAr]$ with a step from $1[MVAr]$. These generators can be connected to busbars 6 ("Gazdare"), 8 ("Zitni Potok") and 10 ("Sijarinska Banja").

It is necessary to determine which generators need to be connected to the individual nodes of the power network that are available so that the losses in the power network are minimal.

The application of the previously exposed algorithm gives the nodes in which the corresponding generators need to be connected. The result is shown in the Table III.

It can be noted that in the previous algorithm there are needs for the calculation of power flows and voltage conditions. In this paper, Newton-Raphson's iterative procedure was applied for the calculation of voltage conditions. The voltages of nodes with and without power distributed generators are shown in Table IV.

TABLE II. THE DATA ABOUT DISTRIBUTIVE GENERATORS.

Generator	Active power of generator $[MW]$	Reactive power of generator $[MVAr]$
G1	0.5	0.25
G2	1.5	0.75
G3	2.5	1.25
G4	3.5	1.75
G5	4	2

TABLE III. THE DATA ABOUT THE GENERATORS AND POWER DISTRIBUTION NETWORK.

Node	Names substation	G	Active power of generator $[MW]$	Reactive power of generator $[MVAr]$
6	„Gazdare"	G4	3.5	1.75
8	„Zitni Potok"	G3	2.5	1.25
10	„Sijarinska Banja"	G2	1.5	0.75

TABLE IV. THE DATA ABOUT THE GENERATORS AND POWER DISTRIBUTION NETWORK.

No	Names substation	Voltage nodes without generator *U [kV]*	Voltage nodes without generator *U [kV]*	Voltage difference with and without generator *U [kV]*
1	„Jablanica"	36.7500	36.7500	0
2	„Lebane 1"	36.6630	36.6518	0.0112
3	„Lebane 2"	36.6688	36.6583	0.0105
4	„Zdeglovo"	36.6665	36.6557	0.0108
5	„Bojnik 1"	35.8937	36.2261	0.3324
6	**„Gazdare"**	35.4671	35.8530	0.3859
7	„Bojnik 2"	35.8367	36.1624	0.3257
8	**„Zitni Potok"**	35.7510	36.4278	0.6768
9	„Medveđa"	35.4001	35.8043	0.4042
10	**„Sijarinska Banja"**	35.5544	36.0292	0.4748
11	„Lece"	35.2499	35.6382	0.3883

From Table IV it can be noticed that the voltage conditions have improved the most in the nodes in which power distributive generators are connected and in the nodes near the power distribution generators.

V. CONCLUTION

With the proper combination of nodes with connected DGs and their connected power, losses in power network can be minimized. The loss reduction is a logical consequence of the fact that due to the influence of DGs, the power is transmitted locally to a particular peripheral node, while without them the total power is transferred only from one (balancing-reference) feeder node, so the higher power passes through several lines, creating power losses. In the radial network, in order to minimize losses, DGs need to be connected to nodes that are farther away from the feeder node. It is noted that voltage conditions have improved most in nodes with DG connected, and then in nodes that are adjacent to them.

ACKNOWLEDGMENT

This work was supported in part by the Ministry of Science and Technological Development of Republic of Serbia under Grant ON174001.

REFERENCES

[1] Wang, C., & Nehrir, M. H. (2004). Analytical Approaches for Optimal Placement of Distributed Generation Sources in Power Systems. *IEEE Transactions on Power Systems, 19*(4), 2068-2076.

[2] Popović, D. H., Greatbanks, J. A., Begović, M., & Pregelj, A. (2005). Placement of Distributed Generators and Reclosers for Distribution Network Security and Reliability. *Electrical Power and Energy Systems, 27*, 398-408.

[3] Gautam, D., & Mithulananthan, N. (2007). Optimal DG Placement in Deregulated Electricity Market. *Electric Power Systems Research, 77*, 1627-1636.

[4] Keane, A., & O'Malley, M. (2005). Optimal Allocation of Embedded Generation on Distribution Networks. *IEEE Transactions on Power Systems*, *20*(3), 1640-1646

[5] Le, A. D. T., Kashem, M. A., Negnevitsky, M., & Ledwich, G. (2007). Optimal Distributed Generation Parameters for Reducing Losses with Economic Consideration. *IEEE Power Engineering Society General Meeting, Tampa*, FL, (pp. 1-8).

[6] Celli, G., & Pilo, F. (2001). Optimal Distributed Generation Allocation in MV Distribution Networks. In *22nd IEEE Power Engineering Society International Conference* (pp. 81-86).

[7] Borges, C. L. T., & Falcao, D. M. (2006). Optimal Distributed Generation Allocation for Reliability, Losses and Voltage Improvement. *Electrical Power and Energy Systems, 28*, 413-420.

[8] Kim, K. H., Lee, Y. J., Rhee, S. B., Lee, S. K., & You, S. K. (2002). Dispersed Generator Placement using Fuzzy-GA in Distribution Systems. In *Power Engineering Society Summer Meeting, 2002 IEEE*, (vol. 3, pp. 1148 –1153).

[9] Celli, G., Ghiani, E., Mocci, S., & Pilo, F. (2005). A Multiobjective Evolutionary Algorithm for the Sizing and Siting of Distributed Generation. *IEEE Transaction on Power Systems, 20*(2), 750-757.

[10] Harrison, G. P., Piccolo, A., Siano, P., & Wallace, A. R. (2008). Hybrid GA and OPF Evaluation of Network Capacity for Distributed Generation Connections. *Electric Power Systems Research, 78*, 392-398.

Influence of Case Materials on Smartphone Temperatures in Multitasking Operation Modes

Chibuzor Ndubisi[1], Howard O. Njoku[2]

[1,2]Sustainable Energy Engineering Research Group, Department of Mechanical Engineering, University of Nigeria, Nsukka 410001, Nigeria, chibuzor.ndubisi.197845@unn.edu.ng[1]
[2]Department of Mechanical Engineering Science, FEBE, University of Johannesburg, Johannesburg 2006, South Africa, howard.njoku@unn.edu.ng

Abstract—**The capacity of smartphones to execute demanding tasks has improved with advancements in electronic technology, and their user experience has increasingly been shaped by the development of new materials and designs. Moreover, as smartphone prowess and adoption increases, users are more likely to protect their devices from damage using smartphone cases. But smartphones still face the challenge of optimal thermal management. To provide more insight into the problem, then, this work examines the effects of various case materials on smartphones performing multiple tasks simultaneously. The experiments were conducted on two identical smartphones, with one encased (test phone) and the other not encased (control phone). Three sets of tasks—single task set, double task set, and triple task set—were run in order to investigate the impact of the number of tasks on smartphone temperature. The case materials utilized for the study were carbon fiber, silicone, and plastic. The phones' surface temperatures were obtained using an infrared camera, and their battery and processor temperatures were retrieved through their inbuilt thermal sensors. The experiments revealed a significant difference between the use of smartphones with and without cases, and the differences in thermal profiles based on the smartphone case material. The test phones recorded higher temperatures than the control phones, and the plastic case was found to cause the highest smartphone internal temperatures of all three cases. Also, the results indicated a positive correlation between the increase in phone temperatures and the number of tasks being run at the same time.**

Keywords – casings, materials, multitasking, smartphone, temperature.

I. INTRODUCTION

Today, smartphones are more versatile than ever before in history. They have become a significant dimension of human life and a mark of 21st century existence. Among other things, the increased attention to the smartphone industry has resulted in rapid innovations in smartphone technology—including and especially in the areas of processing power, materials engineering, and software. Simultaneously, smartphones have become more compact and portable, and they have enjoyed enhancements in design for optimum user experience.

However, these improvements have been sustained at the cost of other smartphone engineering considerations, resulting in challenges that must be addressed. Among these considerations is the issue of heat generation and transfer in smartphones. This thermal challenge has two major negative effects: first, smartphone internal components deteriorate as they experience repeated fluctuations in temperature; second, the high temperatures diminish the user comfort. Reference [1] notes that heat generation and dissipation are the cause of a significant fraction of smartphone failures.

As smartphone thermal management becomes a major subject of scientific inquiry, it must also be noted that phones generate heat, in the first place, due to the tasks run by their users. Because smartphones are now able to run

ISBN: 978-86-80593-73-9

multiple applications at once, and because different applications impact phone processors at different levels, it is necessary to provide research results on this area of heat generation that is user-based. In addition, as smartphone cases have become a notable accessory, and since these cases are produced with materials of varying thermal properties, their influence on smartphone thermal behavior is also worth investigating.

This work thus aims to evaluate the impact of certain case materials on smartphone temperatures while running more than one task simultaneously. The work entails an analysis of smartphone surface temperatures based on infrared thermal images, a comparison of the processor and battery temperatures of encased and non-encased smartphones, and a comparison of the effects of smartphone case materials on the internal temperatures of encased smartphones.

II. Thermal Behaviour in Mobile Phones

A. Smartphone Heat Generation and Transfer

Within a conventional mobile phone, the major sources of heat are the electronic chips mounted on the printed circuit boards—including transistors, integrated circuits, and resistors—and the phone's battery [2]. Each of these internal components possesses its own thermal conductivity, electrical resistivity, and specific heat capacity among other properties. The electric current flowing through the components when a smartphone is in use is met with resistance, which results in the most basic form of smartphone heat generation as given by (1):

$$P = I^2 R \ , \tag{1}$$

where P is the heat generated, I is the electric current, and R is the resistance to the flow of current. As (2) shows, this generated heat is proportional to the temperature increase in the components:

$$P = mc\Delta t \ , \tag{2}$$

where m is the mass of the component, c is the specific heat capacity, and Δt is the magnitude of temperature increase.

Furthermore, the battery emits its own heat as it discharges during use. Reference [3] carried out experiments on lithium-ion batteries and found that they generate heat due to battery resistance—known as "ohmic heat"—and due to entropy change. Mathematically, this heat generation is represented in (3):

$$\begin{aligned} P_{bat} &= P_{bat,r} + P_{bat,s} = \\ &= I_{bat}(t)^2 \cdot r_{int} - T_{bat} I_{bat}(t) \frac{\partial V^{OC}}{\partial T} \ , \end{aligned} \tag{3}$$

where $P\text{-}_{bat}$ is the heat generated by the battery, $P_{bat,r}$ is the ohmic heat, $P_{bat,s}$ is the heat due to entropy change, $I_{bat}(t)$ is the battery discharge current at time t, r_{int} is the internal resistance of the battery, T_{bat} is battery temperature at *t*, and V^{OC} is the battery open-circuit voltage. The temperature increase due to this heat generation makes it more difficult to maintain a safe operational temperature range for the smartphone internal components, causing them to deteriorate faster. Also, the heat generated might increase the smartphone surface temperature above the healthy threshold of 45°C [4], reducing user comfort in the process, and exposing the user to harmful infrared radiation [5].

In considering the mode of heat transfer from the internal components out of the phone, [2] developed a model based on the electrical analogy of heat transfer. This model specifies a bidirectional pattern of heat transfer, one through the back cover of the smartphone to the surroundings, and another through the smartphone display. Heat travels by conduction within the smartphone and by natural convection from the smartphone surface to the surroundings.

B. Smartphone Thermal Management and Multitasking

Numerous attempts have been made to deepen the understanding of and improve smartphone thermal management. With a focus on determining the relationship between device sizes and heat dissipation, [6] developed a parametric model for heat transfer in handheld electronic devices and applied finite element analysis in understanding heat transfer by

conduction, convection, and radiation. Reference [7] analyzed the energy usage and power consumption in a smartphone and developed a model to estimate the battery life span for varying usage patterns. In addition, [8] performed a detailed thermal analysis for smartphone and tablet systems.

In an attempt to improve heat transfer, [9] integrated a cooling fan into a mobile phone and reported a 60% increase in heat dissipation at a fixed surface temperature. Despite this success, the use of active fans has not been adopted for smartphones, as it would eliminate the advantage of portability. Also, [10] experimented with phase change materials—materials that change phase at constant temperature while absorbing heat—and noted that they would be highly instrumental in thermal management by creating a delay in temperature rise.

A discussion on thermal management would be incomplete without pointing to the effects of multitasking on smartphone performance. When apps are run on a smartphone, more space is occupied in the phone's Random-Access Memory (RAM). This increases the heat generation, as the phone's internal components struggle to maintain high performance. It should be noted that this effect is dependent on the demands of the application itself; for instance, large online games that utilize the phone's Graphic Processing Unit (GPU) in addition to other components would cause more heat generation than a calculator app.

III. Methodology

As shown in Fig. 1, the experiments were conducted in a wooden test chamber, having a glass door and laced internally with aluminum foil to prevent thermal interaction with the surroundings. Placed in the chamber were two identical smartphones, with one encased (test phone) and the other not encased (control phone). An infrared thermal imaging camera was placed at a distance from the smartphones and captured the images through a peephole.

Figure 1. Experimental setup.

Three smartphone cases of different materials—carbon fiber, silicone, and plastic—were used in the experiments. To investigate the effect of the number of running tasks on smartphone temperature, the study involved three sets of tasks: the single task set, the double task set, and the triple task set. Each test was run for 30 minutes, and the infrared camera was utilized in capturing thermal images at the start and end of each test. Also, by connecting with their inbuilt thermal sensors, the CPU Monitor application was used to record the phones' battery and processor temperature variations. To improve the accuracy of the study, the phones' batteries were charged before the experiments and all other background tasks were disabled.

The apps to be run were determined through a survey on the most frequently used apps by people in the local community, and the possibility of using these apps at the same time. The experiments were thus based on the following tasks: the single task set involved **offline music playing** (Muzio Player); the double task set involved **social media** (Instagram) and **video calls** (Google Duo); and the triple task set involved **social media** (Instagram), **internet browsing** (Google Chrome), and **video streaming** (YouTube).

IV. Results and Discussions

A. Smartphone Infrared Thermal Images

The thermograms obtained from the tests are shown in Figs. 2-10. Figs. 2-4 illustrate the smartphone surface thermal profiles for the single task set while switching between the case materials. Figs. 5-7 show the same for the double task set, and Figs 8-10 are the images obtained during the triple task sets.

In each thermal image, the test phone is seen on the left and the control phone on the right. Heat is represented by a spectrum of colors from black to white, with black being the coolest and white the hottest. The thermal images indicate a slight increase in surface temperature after each experiment, with the major heat zones located at the top and bottom of the smartphone. These focal areas of heat generation indicate the

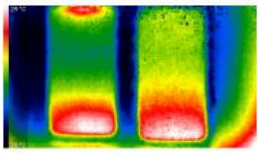

(a) 0 minutes

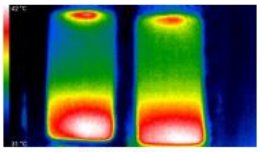

(b) 30 minutes

Figure 2. Single task set – thermograms with silicone case.

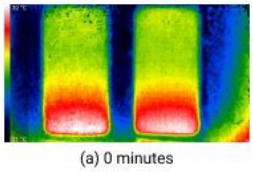

(a) 0 minutes

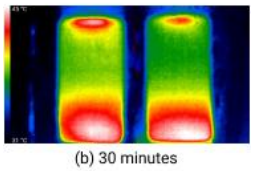

(b) 30 minutes

Figure 3. Single task set – thermograms with plastic case.

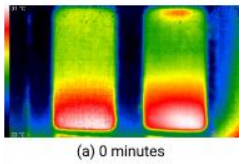

(a) 0 minutes

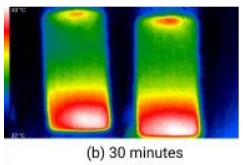

(b) 30 minutes

Figure 4. Single task set – thermograms with carbon fiber -case.

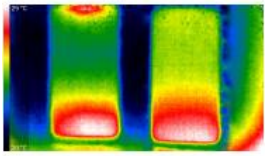

(a) 0 minutes

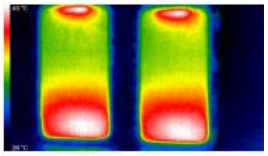

(b) 30 minutes

Figure 5. Double task set – thermograms with plastic case.

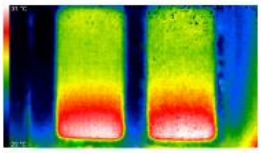

(a) 0 minutes

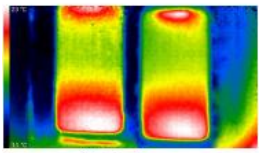

(b) 30 minutes

Figure 6. Double task set – thermograms with silicone case.

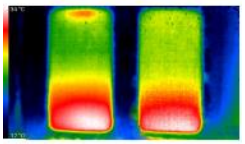

(a) 0 minutes

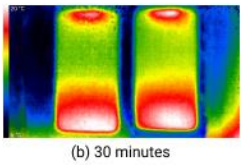

(b) 30 minutes

Figure 7. Double task set – thermograms with silicone case.

location of the internal components responsible for generating the most heat.

B. Smartphone Internal Temperatures

Figs 11-13 plot the temperature variations in the batteries and processors of the test and control phones for each set of tasks. In all cases, the test processor recorded the highest temperatures, and the plastic case resulted in the peak test processor temperatures. For the single task set (Fig. 11), the test processor reached a maximum of 38°C in 12 minutes of running the task, after which it fluctuated between 37°C and 38°C. In the double task set (Fig. 12), a maximum temperature of 41°C was recorded from the test processor, and the test phone

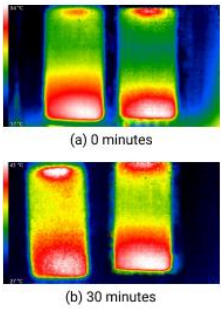

Figure 8. Triple task set – thermograms with plastic case.

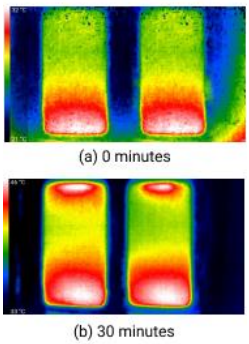

Figure 9. Triple task set – thermograms with silicone case.

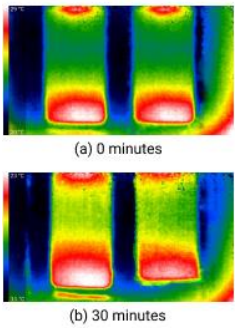

Figure 10. Triple task set – thermograms with carbon fiber case.

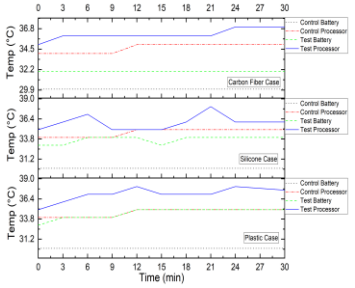

Figure 11. Single task set – internal temperature variations.

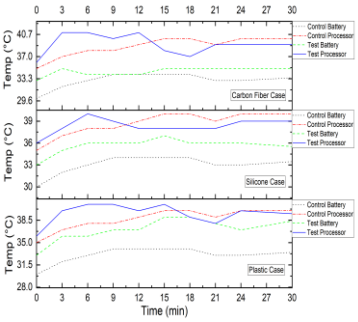

Figure 12. Double task set – internal temperature variations.

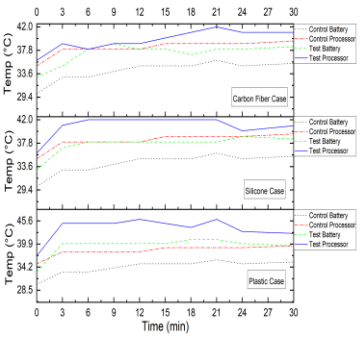

Figure 13. Triple task set – internal temperature variations.

reached this temperature while using both the plastic and carbon fiber case. In the triple task set (Fig. 13), the test processor reached the peak temperature of 46°C while encased in a plastic case; both the carbon fiber and silicone cases gave a maximum temperature of 42°C.

The graphs of temperature variation also point to the significant differences in temperature between the encased and non-encased phones. In the single task set of experiments, the control battery remained at 30°C while the test battery increased to 34°C with the silicone case and 35°C with the plastic case. In the double task set, the control battery reached a maximum temperature of 34°C, while the test battery increased to 35°C for the carbon fiber case, 37°C for the silicone case, and 40°C for the plastic case. And in the triple task set, the control battery recorded a maximum temperature of 36°C while the test battery reached 39°C for the carbon fiber and silicone cases, and 41°C for the plastic case.

V. Conclusion

This study has analyzed the influence of case materials on smartphones performing multiple tasks. It obtained the smartphones' thermal images, identified their major heat zones, and monitored their battery and processor temperatures, while observing the differences in thermal behavior between the test and control phones. The study confirmed the positive relationship between the increase in smartphone temperature and the number of tasks being executed. It also revealed that though the battery and processor both increase in temperature and generate heat in the process, the processor reaches higher temperature levels than the battery and thus generates more heat. In comparing the impact of case materials, it was found that the plastic case caused the highest recorded temperatures—a pointer to the fact that due to its nature as a good thermal insulator, the plastic case inhibits the transfer of heat out of the phone.

It can be inferred from this work that the three focal points of improving smartphone thermal management are materials, design, and usage. Hence, future research should focus on optimizing these areas. Researchers could experiment with new materials for building smartphone components and cases that allow for optimum heat transfer while ensuring smartphone protection. New and improved smartphone internal and external designs should be suggested and studied, so as to strike the right balance between prevention of component damage and a great user experience. And smartphone users could be aided with research-based tips and updates on using their smartphones, to ensure durability and longevity. With all these in place, the landscape of smartphone-user interaction will continue to improve into the future.

References

[1] McPherson, J. W. (2018). *Reliability Physics and Engineering: Time-to-Failure Modeling.* Springer.

[2] Luo, Z., Cho, H., Luo, X., and Cho, K.-i. (2008). System thermal analysis for mobile phone. *Applied Thermal Engineering*, 28(14-15), 1889–1895.

[3] Xie, Q., Kim, J., Wang, Y., Shin, D., Chang, N., and Pedram, M. (2013). Dynamic thermal management in mobile devices considering the thermal coupling between battery and application processor. In *2013 IEEE/ACM International Conference on Computer-Aided Design (ICCAD)*, pages 242–247. IEEE.

[4] Berhe, M. K. (2007). Ergonomic temperature limits for handheld electronic devices. In *International Electronic Packaging Technical Conference and Exhibition*, volume 42789, pages 1041–1047.

[5] International Commission on Non-Ionizing Radiation Protection (2013). Icnirp guidelines on limits of exposure to incoherent visible and infrared radiation. *Health Physics*, 105(1), 74–96.

[6] Lee, J., Gerlach, D. W., and Joshi, Y. K. (2008). Parametric thermal modeling of heat transfer in handheld electronic devices. In *2008 11th Intersociety Conference on Thermal and Thermomechanical Phenomena in Electronic Systems*, pages 604–609. IEEE.

[7] Carroll, A., & Heiser, G. (2010). An analysis of power onsumption in a smartphone. *Proceedings of the 2010 USENIX Annual Technical Conference.*

[8] Gurrum, S. P., Edwards, D. R., Marchand-Golder, T., Akiyama, J., Yokoya, S., Drouard, J.-F., and Dahan, F. (2012). Generic thermal analysis for phone and tablet systems. In *2012 IEEE 62nd Electronic Components and Technology Conference*, pages 1488–1492. IEEE.

[9] Grimes, R., Walsh, E., and Walsh, P. (2010). Active cooling of a mobile phone handset. *Applied Thermal Engineering*, 30(16):2363–2369.

[10] Tomizawa, Y., Sasaki, K., Kuroda, A., Takeda, R., and Kaito, Y. (2016). Experimental and numerical study on phase change material (pcm) for thermal management of mobile devices. *Applied Thermal Engineering*, 98:320–329.

Smart Non-Intrusive Identification and Health Diagnosis of Household Loads

Soumyajit Ghosh[1], Arunava Chatterjee[2]

[1]Electrical Engineering Department, Jadavpur University, Kolkata, India
[2]Electrical Engineering Department, Raghunathpur Govt. Polytechnic, Purulia, India
arunava7.ju@gmail.com

Abstract—**Smart metering technology has been developing at a steady pace in the smart city environment. In this context, control of connected residential loads with smart grid technology has been crucial for energy management. Health monitoring and control of the residential appliances are significant issues for the consumer which are normally done using a sensor installed in every device like a smart plug. Furthermore, it increases the overall cost and complexity of the system. Using the wide availability of the internet and development in computational intelligence techniques, a smart and reliable monitoring system for all residential appliances is required that can be achieved by introduction of the internet-of-things (IoT) technology. For the smart meter's application, knowledge about instantaneous load is also very important. In this paper, household appliance identification is done which requires a minimal sensing system installed in the residential house. Non-intrusive load monitoring (NILM) is a well-known method to assess the power consumption of individual loads as well as their operating behavior. The load health monitoring is also done using load harmonic current spectrum analysis from the aggregated current signal data. Remote monitoring and control are achieved using IoT technology. This technique also provides diagnostic feedback to the consumer in case of electrical appliance's failure. Suitable simulations and experimentally created dataset analysis have been carried out on a residential system to demonstrate the ability of the proposed methodology.**

Keywords - Non-Intrusive load monitoring (NILM), spectrum analysis, Internet-of-things (IoT), smart metering

I. INTRODUCTION

Smart metering technology provides solution for the implementation of energy management systems in a residence. Many power distribution companies around the world are installing smart meter in consumer premises to measure appropriate consumption of electric power and controlling loads [1]. Identification of residential loads is a major challenge in smart metering system as it can help in finding the energy consumption pattern and for energy optimization. Non-intrusive load monitoring (NILM) is a technique used for identification of loads. It is also important to identify different incipient faults in loads in a smart home using the different load sensing techniques which may help in early detection and taking necessary measures to enhance their life.

The subject of energy conservation has increased in recent years due to decrease in conventional fossil fuel assets with increase in development. Concerns on climate change and global warming and reduction of emission of greenhouse gases are of principal interest in the actions of energy efficiency. Available literatures specify that household energy consumption can be abridged using improved energy management systems. Smart grid with household automation has sufficient potential to become a significant way of managing energy for reducing energy consumption. Added to that, smart load fault detection can improve the load energy management and reduce the downtime. Traditional load monitoring methods use electricity meters at electrical installation sites to measure all conceivable load related variables. Various drawbacks are associated when applying

ISBN: 978-86-80593-73-9

this method such as the division of the load circuit, the cost of installing the electricity meters and their installation and the excess space requirement. The NILM work was started by Hart [2] in MIT. This method is applicable for finite state appliances. French researcher Sultanem [3] also proposed almost similar NILM technique but this technique included the transient duration signal and harmonics. Lee et al., planned a NILM technique that displays a correlation between the 5th and 7th harmonics and the real/reactive power expended by variable load appliances [4]. Lately, emphasis is put on research of smart metering techniques, as, it has potential to implement NILM for better smart home energy management. Switching function based variable power estimating technique has also improved NILM research [5]. The waveform-based estimator for NILM technique is used for variable power loads [6]. Recently, optimization [7] and intelligent techniques are also used [8] for NILM. Finally, load feature extraction based NILM is also used for load identification and control [9] and this method can identify loads from aggregated system current data. This technique is helpful as it can be used for load identification from a single-point of entry in a household and thus lower requirement of sensors.

In this paper, a new method of load identification and their health monitoring from smart meter obtained load current data is proposed. Firstly, the load is identified from system aggregated current data [9] and the identified load health monitoring is done using a set of features obtained from the load power spectral density characteristics. For this load health status identification, an intelligent technique is used along with the features extracted from the spectral density waveform. Using the proposed method, the in-grown load faults can be identified with better accuracy and the system downtime and load life can be enhanced. The loads can further be controlled by internet-of-things (IoT) for easy and smart control. The system simulation backed by experiments validate the proposed concept.

II. Proposed Household System

The smart household considered has several loads. These loads are mostly motoring based loads, non-linear loads and constant power loads. The motoring load consists of single-phase induction motor-based pump set, washing machine, air-conditioner, non-linear load is

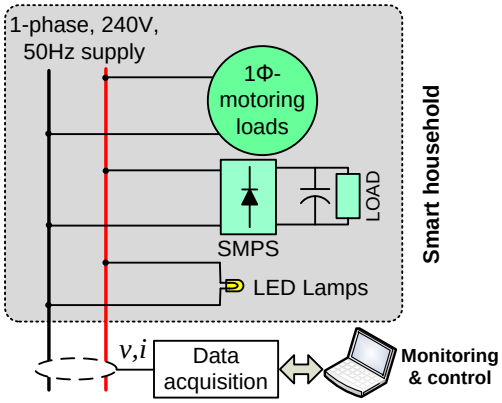

Figure 1. Considered smart household system.

switched mode power supply (SMPS) load in a personal computer. For the constant power load, LED light bulb is considered. The complete smart household system considered with the different loads is shown in Fig. 1.

III. Proposed NILM Technique

For the system considered with different loads, the current data is collected from a single point-preferably at the entry point in the household. The aggregated current signal data is then used for load identification and monitoring. The aggregated current and/or power data may be used for load identification with load transient state detection. This technique can also be used when similar type of loads are used in a household with same energy consumption pattern. The proposed NILM is outlined in Fig. 2.

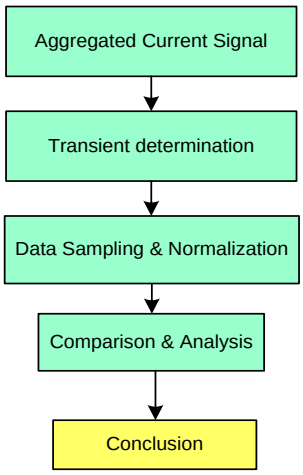

Figure 2. Outline of the proposed NILM.

IV. LOAD MONITORING AND CONTROL

A. *Load Identification and Control*

During operation in the household, the different loads can be changed from one steady state to another steady state. These events are recorded and the system waveforms are analyzed. The normal voltage and current waveforms of the loads are shown in Fig. 3.

From Fig. 3 it can be observed that different loads will have different signatures. Although it is difficult to determine loads from the current signatures, but with different features during transients, such loads can be identified with accuracy. During transients, the load waveforms are shown in Fig. 4.

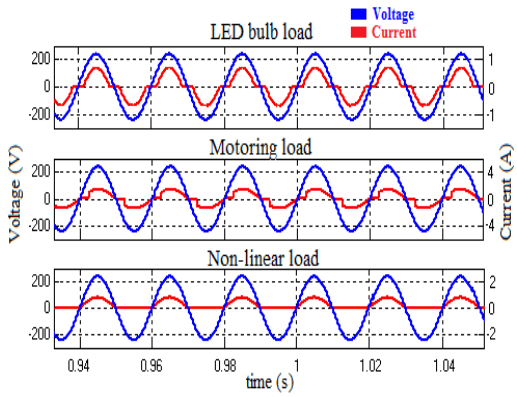

Figure 3. Waveforms of different household loads.

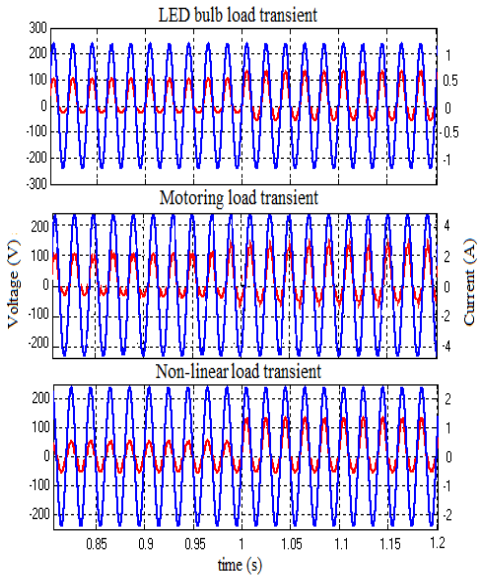

Figure 4. Waveforms during load transients.

In Fig. 4, when the loads are either switched ON or during change of load from one steady state to other at around t = 1s, the different waveforms are shown. Later, a comparison with standard load signatures will identify the different loads with accuracy.

The loads in a smart home setup during these transients may be controlled using internet-of-things (IoT) platform. For this purpose, a Wi-Fi enabled controller may be used and relay modules may be attached to loads for operational purpose. The popular hierarchical message queuing telemetry transport (MQTT) [10] protocol is used for communication during this control of domestic loads.

B. *Load Health Monitoring*

Different loads used in the smart household setup may get faulty with regular use and their analysis will yield features which may be used for this diagnosis. In general, different incipient faults may be noticed and identified for increasing the operating life and reducing the downtime of such loads and appliances.

For motoring based loads, the most common types of faults are the faults occurring in the motor stator, for e.g., inter-turn faults which if unnoticed may lead to phase faults and earth faults. Power electronic based loads may have faults in the firing and control circuits which can also be identified during incipient stage. In general, lighting load faults cannot be identified in an early stage and therefore present research focus is not put on such diagnosis. Moreover, these loads can be easily replaced and used in a household.

For health monitoring of loads, initially the loads have to be identified using the proposed NILM technique. After the loads are identified, the current data for the individual loads are used to determine the harmonic spectrum density plots. From the spectral density waveform, different statistical features are extracted for determination of the different incipient faults present in the domestic loads. The different statistical features used in the study are the mean, median and the rms values that are obtained from the harmonic spectrum density plots. From the plots, the different harmonic frequencies can also be found out to accurately determine the type of the incipient faults in the different household electrical loads. The harmonics are mostly lower order harmonics that are present in the load current during operation and a separate

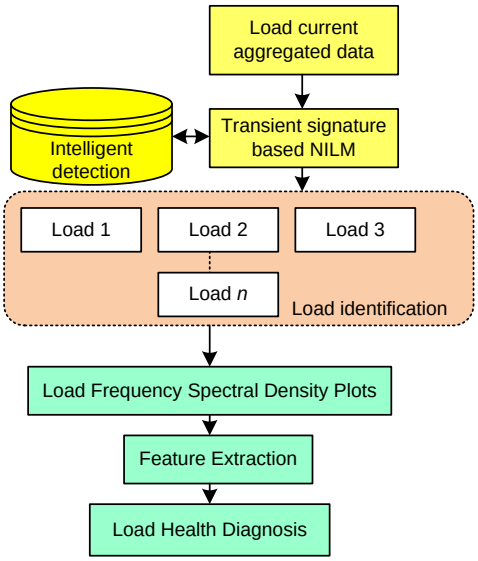

Figure 5. Block diagram of the proposed NILM and health diagnosis method.

segregation of the same are not required. Fig. 5 below shows the block diagram of the proposed NILM and health diagnosis method studied for a smart household.

V. Simulation and Experimental Results

For the domestic system considered, the simulation is done in *MATLAB/Simulink* and later an experimental laboratory prototype is built using real life loads for validation purpose. At first, the loads are modeled in *Simulink* platform and the aggregated current signal data is obtained from the point of common coupling at the entry point of the household. The same is shown in Fig. 6.

The different load waveforms are studied from the simulated system as already shown in Fig. 3. Afterwards from the transient analysis, the different load features are extracted. The load features such as mean, median, standard deviation and variance data are calculated during

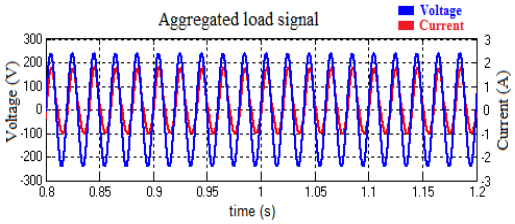

Figure 6. Aggregated load current and voltage signal data for all household loads considered.

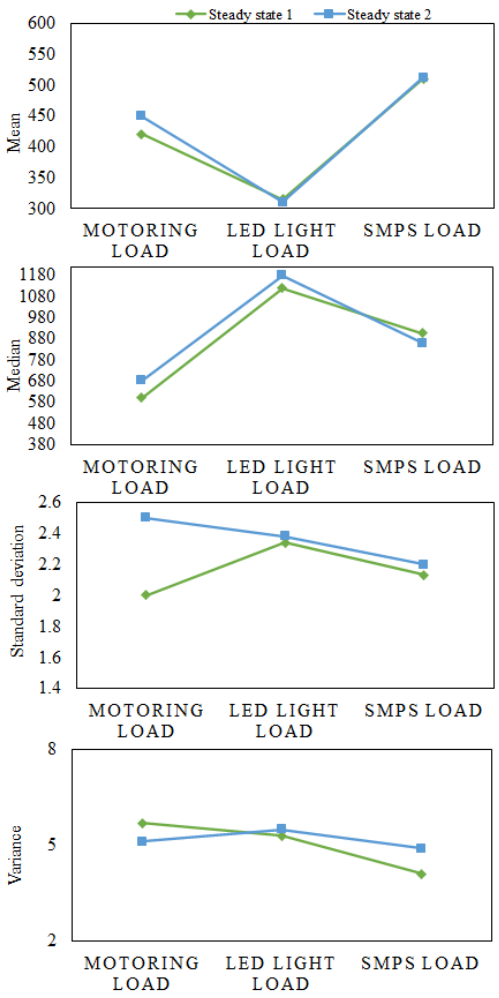

Figure 7. Load transient features when they are changed from one steady state to another steady state.

the transient and afterwards, an intelligent technique is applied for the detection of different loads and comparison with a database. The different features are shown in Fig. 7.

A machine learning technique, *k*-nearest neighbors (*k-NN*) [11] is then applied for identification of load from the transient extracted features of Fig. 7. The role of *k-NN* technique is to teach the extracted features from the transient current waveform for load identification in a non-intrusive manner.

Finally, after identification of loads, the data is then used to health monitoring of the loads. For this purpose, harmonic spectrum density plots are used. Further, some feature extraction techniques are also applied for accurate identification of health condition of the loads.

For the motoring load, the spectrum density plot is shown during 5% inter-turn fault in Fig. 8a. When the motor is operated in this condition for a longer time, the fault is increased to 10% inter-turn fault and the plot for the same is shown in Fig. 8b.

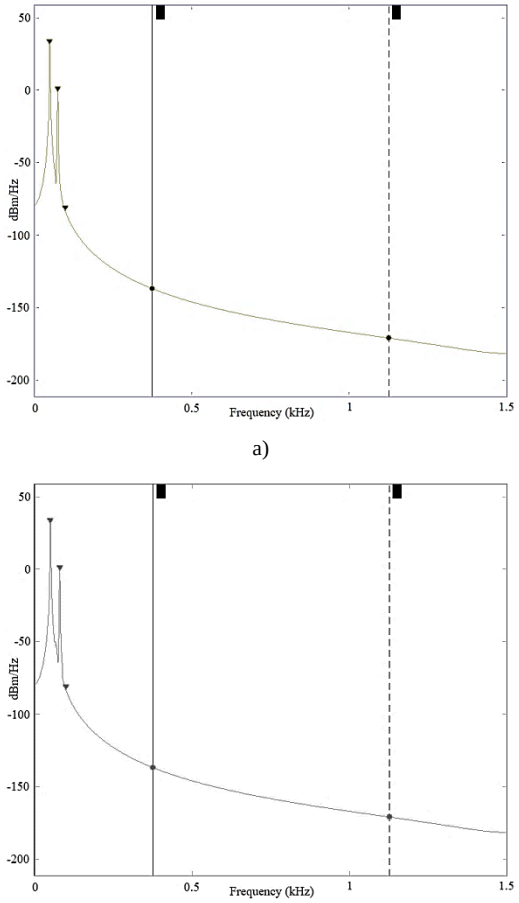

a)

b)

Figure 8. Harmonic spectrum density plot is shown during (a) 5% inter-turn fault and (b) 10% inter-turn fault.

The plots are obtained using spectrum analyzer from the IoT system obtained data, with auto-set resolution bandwidth (RBW) = 1.46Hz, sample rate = 1kHz, by using Hanning window.

Feature from the above plots can be extracted using a simple subroutine and at particular chosen window. The feature extraction is shown in Fig. 9.

Different faults can then be determined from the extracted features using a suitable intelligent technique. In this paper, k-nearest neighbors (*k-NN*) based machine learning technique is applied for accurate estimation of the load health condition. It has advantage of lesser computational and processing time requirement than similar techniques of machine learning. Table I shows the different faults associated with the loads and their experimental determination accuracy using the intelligent technique used.

TABLE I. HOUSEHOLD LOADS WITH FAULT TYPES AND THEIR DETERMINATION ACCURACY.

Household loads	**Fault type**	**Accuracy of determination (%)**
LED lighting load	LED fault, ballast fault	*
Motoring load	Stator inter-turn fault, phase-fault, earth fault	98.9
SMPS load	Arc fault, firing circuit fault	97.2
Battery charging load	Arc fault, firing circuit fault	98.3

*Not considered in this particular study and the fault for such load determination is not particularly important and cost-effective.

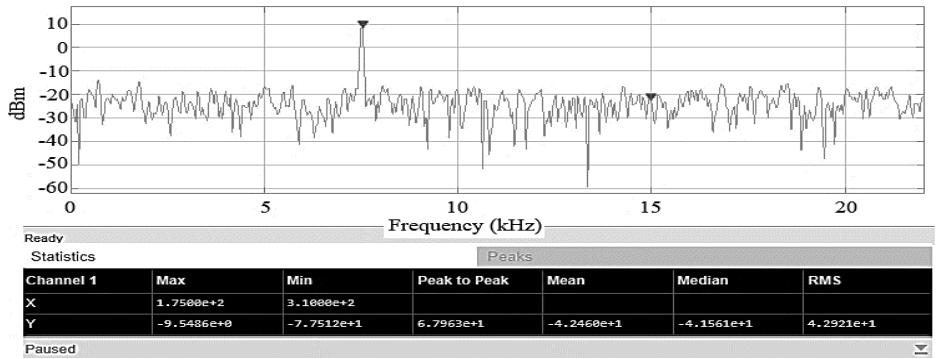

Figure 9. Feature extraction from harmonic spectral density plots for motoring load.

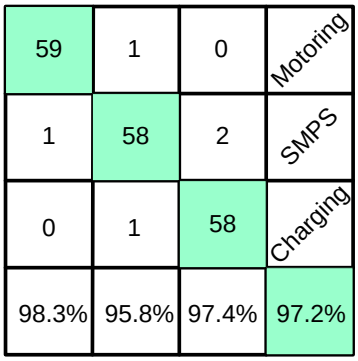

Figure 10. Performance confusion matrix chart of *k-NN* based health identification based on feature selection with *F*1 score.

Fig. 10 shows the performance confusion matrix chart of *k-NN* based health identification based on feature selection with 60 sets of data for each load type. The health identification of each considered appliance can be detected accurately from the laboratory run *F*1 score [8] results. The average *F*1 score which is dependent on precision and recall value for health identification is 97.2% from the laboratory obtained data.

VI. CONCLUSION

This paper presents a technique for non-intrusive load identification, monitoring and control in a smart household. After sucessful identification, the load health is also monitored and incipient faults are found out using harmonic spectral density plot and their feature extraction. The proposed technique aims at reducing energy consumption in a household with IoT based smart control. Using the proposed technique, the load health can be accurately monitored and any incipient fault can be easily detected. Simulation and experimental results validates the proposed methodology.

REFERENCES

[1] Advanced metering infrastructure (2021). *India Smart Grid Week*, 17th March, 2016, (pp. 1–13). Available at: www.indiasmartgrid.org

[2] Hart, G. (1992). Nonintrusive appliance load monitoring. *IEEE Proc.*, *80*(12), 1870–1891.

[3] Sultanem, F. (1991). Using appliance signature for monitoring residential loads at meter panel level. *IEEE Trans. Power Del*., *6*(4), 1380–1385.

[4] Lee, K. D., et.al. (2005). Estimation of variable-speed-drive power consumption from harmonic content. *IEEE Trans. Energy Convers.*, *20*(3), 566–574.

[5] Dong, M., Meira, P., Xu, W., & Freitas, W. (2012). An event window based load monitoring technique for smart meters. *IEEE Trans. Smart Grid.*, *3*(2), 787–796.

[6] Wichakool, W., Remscrim, Z., Orji, U., & Leeb, S.B (2015). Smart metering of variable power loads. *IEEE Trans. Smart Grid*, *6*(1), 189–198.

[7] Ghosh, S., Manna, D., Chatterjee, A., & Chatterjee, D. (2021). Remote appliance load monitoring and identification in a modern residential system with smart meter data. *IEEE Sensors J*., *21*(4), 5082–5090.

[8] Ghosh, S., Chatterjee, A., & Chatterjee, D. (2021). An improved load feature extraction technique for smart homes using fuzzy-based NILM. *IEEE Trans. Instr. Meas*., *70*, 1–9.

[9] Ghosh, S., Chatterjee, A., & Chatterjee, D. (2016). A novel non-intrusive load monitoring technique for domestic applications. In *Proc. 1st Indian Engineering Congress*, Kolkata, India, 1B (pp. 149–153).

[10] Ghosh, S., Chatterjee, A., & Chatterjee, D. (2020). A smart IoT based non-intrusive appliances identification technique in a residential system. In *Proc. 2020 IEEE International Conference on Power Electronics, Smart Grid and Renewable Energy (PESGRE2020)*, Kerala, India (pp. 1–6).

[11] Kelati, A., Gaber, H., Plosila, J., & Tenhunen, H. (2020). Implementation of K-nearest neighbor on field programmable gate arrays for appliance classification. In Proc. *2020 the 8th International Conference on Smart Energy Grid Engineering*, Oshawa, Canada (pp. 51–57).

Spin Orbit Study of Electronic Structural and Elestic Properties of MgO Oxide

Tayeb Halais Wissem[1], Chettibi Sabah[2]

[1,2]Laboratoire de physique des Matériaux, Université 8 Mai 1945 Guelma BP401, Algeria, tayeb.halais782@gmail.com

Abstract—**The objective of this work is to study the effect of spin-orbit on the electronic and structural properties of MgO Oxide using the full-potential linearized augmented plane wave method (FP-LAPW) within the framework of the density functional theory (DFT). The generalized gradient approximation (GGA) is used as an exchange and correlation function with the spin-orbit coupling. The structural parameters such as lattice constant, bulk modulus, and their pressure derivatives are calculated in the rock salt structure. The compound is stable in the non-magnetic phase. Analysis of electronic properties showed that magnesium oxide is a semiconductor with a direct bandgap at the gamma point. The study of the mechanical properties of MgO realized at zero pressure has indicated that it is brittle and mechanically stable. The results are compared with theoretical and experimental measurements.**

Keywords - magnesium oxide, DFT, FP-LAPW, spin orbit, elastic constants

I. INTRODUCTION

Magnesium oxide is a ceramic material belonging to the family of alkaline earth metal oxides. It has undergone intense experimental and theoretical studies with various industrial applications due to its physical properties for this reason we have chosen to study [1]. To this day, various studies have investigated its properties [2-4]. The applications of MgO Oxide have known an accelerated development these last years, in particular in solar cells, catalysis,

Substrate material, optical fibers [5, 6].In this paper, we discussed the structural, electronic, and elastic properties of MgO Oxide.

II. COMPUTATIONAL METHOD

We used the WIEN2K code based on the density functional theory (DFT) [7, 8] to study the effects that occur in the large gap MgO semiconductor when using the generalized gradient approximation [9]. The maximum number of spherical harmonics inside the muffin tin is set to l_{max} = 10. The cut-off plane wave parameter is k_{max} R_{mt} = 7. The Brillouin zone integration is done using 1000 k points with a K-mesh of 10×10×10 [10]. The calculations of the structural and electronic properties have been done relativistically with and without the spin-orbit coupling.

A. Results and Discussions

1) Structural Properties

Magnesium oxide crystallizes in the rock-salt structure (RS) with space group $Fm\bar{3}m$ n° 225. We realized structural optimization in the non-magnetic and ferromagnetic phases to study the structural phase stability. The total energy was calculated as a function of volume and is presented in Fig. 1. The Mg and O atoms are located at positions (0, 0, 0) and (0.5, 0.5, 0.5) respectively. Note that this system is found to be energetically stable in the non-magnetic phase due to the more negative energy. The Murnaghan's equation of state is used to calculate the equilibrium structural parameters. Results are presented in Table I. The calculated MgO lattice constant agrees well with previous experimental and theoretical results.

ISBN: 978-86-80593-73-9

TABLE I. LATTICE PARAMETER A (A) AND BULK MODULUS B (GPA) AND ITS PRESSURE DERIVATIVE (B') AND OTHER THEORETICAL AND EXPERIMENTAL RESULTS.

MgO	Lattice constant a (A)	Bulk modulus B (GPa)	B'
GGA-PBEsol	4.22	156.57	4.15
Spin -Orbit	4.22	160.57	3.89
Experimental	4.213[11]	162	4.08
Theoretical	4.22 [12]	169.1	3.28

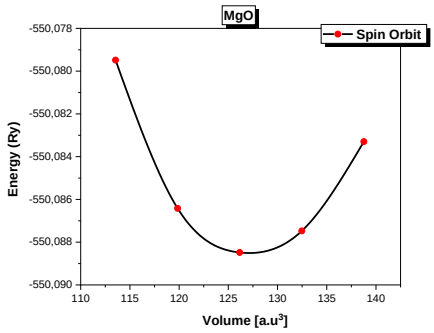

Figure 1. The total energy as function of volume for MgO in the NaCl structure.

2) Electronic Properties

We discuss in this section the electronic properties of MgO oxide in terms of their electronic band structures and total and partial densities of states (DOS) using the GGA-PBEsol and spin-orbit coupling. The energy gap obtained from these approximations is collated in Table II. Respectively, the GGA-PBEsol energy gap is found to be 4.588 eV and with spin-orbit coupling it is 4.586 eV. It is seen in Fig. 2 that MgO is a semiconductor with a direct bandgap at gamma point. Fig. 3 gives the total density of states (DOS). The total and partial densities of states (DOS) show that the conduction bands are mainly dominated by the p states of (O) with a strong contribution from the p states of Mg. The spin-orbit coupling reduces the bandgap.

TABLE II . THE CALCULATED RESULTS OF THE ENERGY GAP.

MgO	Present work	other	Exp
GGA-PBEsol	4.58	4.27	7.8
With Spin-Orbit	4.58 eV		/

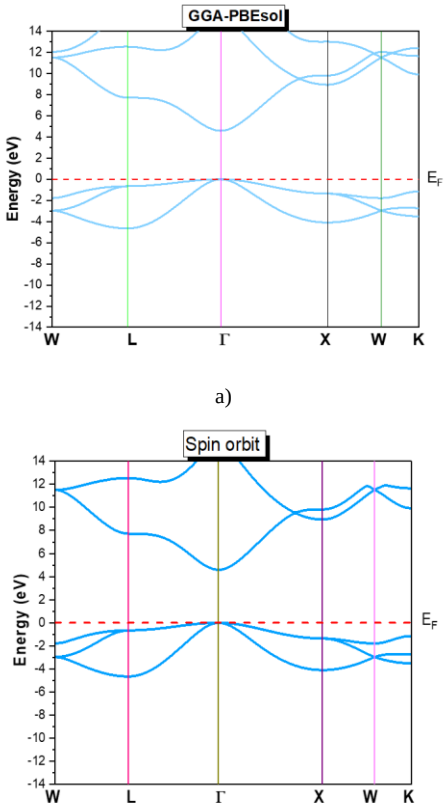

Figure 2. The band structure of binary MgO in the rock-salt non-magnetic phase (a) GGA-PBEsol (b) Spin Orbit.

3) Elastic Properties

Elastic and mechanical properties play a critical role in engineering materials for industrial applications. We calculated the elastic properties at zero pressure using the GGA-PBEsol approximation. We used the method recently developed by M. Jamal and integrated it into a WIEN2K package [13]. The results are shown in Table III. For comparison, the available experimental measurements are also presented. According to the results, the obtained values of elastic anisotropic factor A, shear modulus G(GPa), Young's modulus E(GPa), Poisson's ratio v and B/G ratio show that MgO is an anisotropic material, according to the B / G ratio is a fragile material, also note according to the shear moduli it is an ionic and stable.

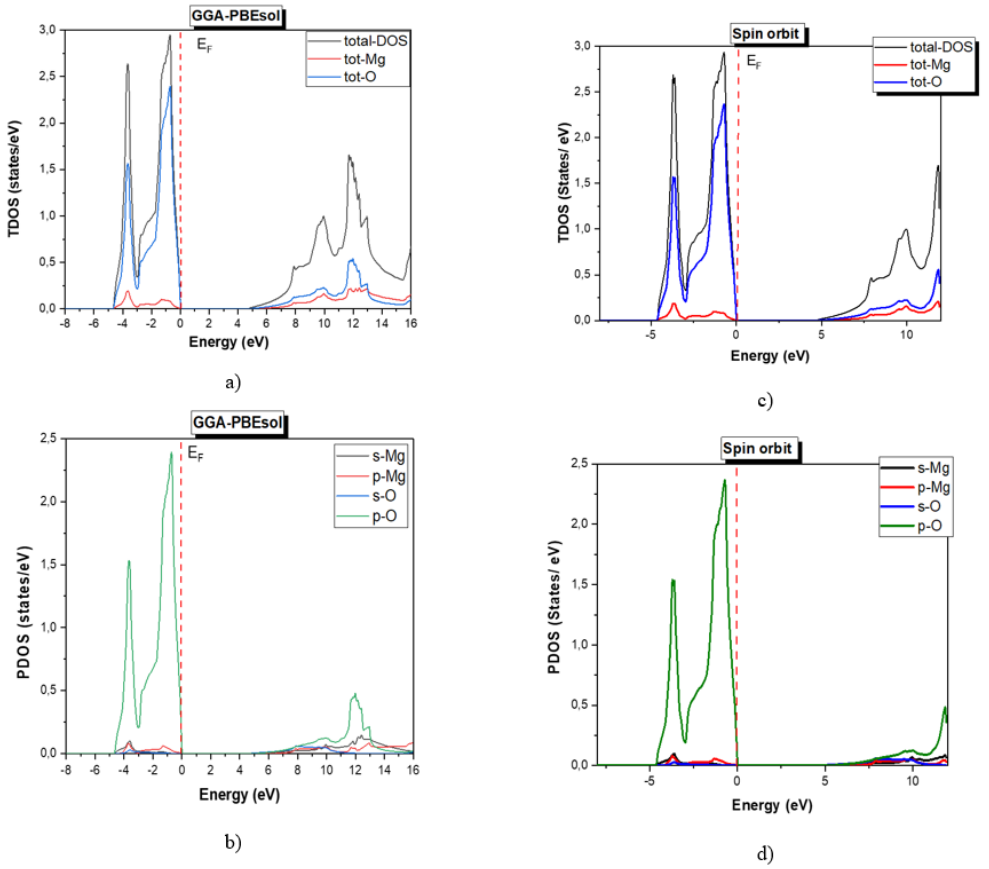

Figure 3. The total and partial density of states for MgO calculated using (a) (b) GGA-PBEsol Spin Orbit.,(c) (d) Spin Orbit.

TABLE III. THE ELASTIC CONSTANTS, VALUES OF ELASTIC ANISOTROPIC FACTOR A, SHEAR MODULUS G(GPA), YOUNG'S MODULUS E(GPA), POISSON'S RATIO V AND B/G OF MGO AT ZERO PRESSURE.

(GPa)	C11	C12	C44	B	E
GGA-PBEsol	295.8	88.9	151.2	157.9	305.8
Exp	297.9	95.8	154.4		

v	G	A	B/G
0.17	129.88	1.46	1.21

III. CONCLUSION

In summary, we have investigated the structural, electronic, and elastic properties of pure MgO with and without spin-orbit coupling. Studied mechanical properties show the stability, brittle, and anisotropic nature of the studied compound. The electronic structure shows the direct bandgap semiconducting nature with an energy gap of 4.588 eV without spin-orbit and 4.586 eV with spin-orbit. The average results show the potential of the compound in optoelectronic, photovoltaic and electronic applications. Our calculations will be an addition from the theoretical side and specific to experimental researchers.

REFERENCES

[1] Julkapli, N. M., & Bagheri, S. (2016). Magnesium oxide as a heterogeneous catalyst support. *Reviews in Inorganic Chemistry*, *36*(1), 1-41.

[2] Baysal, T., Noor, N., & Demir, A. (2020). Nanofibrous MgO composites: structures, properties, and applications. *Polymer-Plastics Technology and Materials*, *59*(14), 1522-1551.

[3] Arani, A. A. A., Alirezaie, A., Kamyab, M. H., & Motallebi, S. M. (2020). Statistical analysis of enriched water heat transfer with various sizes of MgO nanoparticles using artificial neural networks modeling. *Physica A: Statistical Mechanics and its Applications*, *554*, 123950.

[4] Mageshwari, K., & Sathyamoorthy, R. (2012). Studies on photocatalytic performance of MgO nanoparticles

prepared by wet chemical method. *Transactions of the Indian Institute of Metals*, *65*(1), 49-55.

[5] Ramalingam, R. J., et al.. (2021). Facile sonochemical synthesis of silver nanoparticle and graphene oxide deposition on bismuth doped manganese oxide nanotube composites for electro-catalytic sensor and oxygen reduction reaction (ORR) applications. *Intermetallics*, *131*, 107101.

[6] Dutta, P., Seehra, M. S., Zhang, Y., & Wender, I. (2008). Nature of magnetism in copper-doped oxides: ZrO2, TiO2, MgO, SiO2, Al2O3, and ZnO. *Journal of Applied Physics*, *103*(7), 07D104.

[7] Tran, F., Doumont, J., Blaha, P., Marques, M. A., Botti, S., & Bartók, A. P. (2019). On the calculation of the bandgap of periodic solids with MGGA functionals using the total energy. *The Journal of chemical physics*, *151*(16), 161102.

[8] Blaha, P., Schwarz, K., Tran, F., Laskowski, R., Madsen, G. K., & Marks, L. D. (2020). WIEN2k: An APW+lo program for calculating the properties of solids. *The Journal of Chemical Physics*, *152*(7), 074101.

[9] Tran, F., Doumont, J., Kalantari, L., Huran, A. W., Marques, M. A., & Blaha, P. (2019). Semilocal exchange-correlation potentials for solid-state calculations: Current status and future directions. *Journal of Applied Physics*, *126*(11), 110902.

[10] Monkhorst, H. J., & Pack, J. D. (1976). Special points for Brillouin-zone integrations. *Physical review B*, *13*(12), 5188.

[11] Fei, Y. (1999). Effects of temperature and composition on the bulk modulus of (Mg, Fe) O. *American Mineralogist*, *84*(3), 272-276.

[12] Taib, M. F. M., Samat, M. H., Demon, S. Z. N., Hussin, N. H., Hassan, O. H., Yahya, M. Z. A., & Ali, A. M. M. (2020). First-Principles Study on the Doping Effects of La on the Structural, Electronic and Optical Properties of MgO. *International Journal of Nanoelectronics & Materials*, *13*.

[13] Jamal, M., Asadabadi, S. J., Ahmad, I., & Aliabad, H. R. (2014). Elastic constants of cubic crystals. *Computational Materials Science*, *95*, 592-599.

The Impact of Energy Subsidies on Economic Growth in Malaysia

Dzul Hadzwan Husaini[1], Hooi Hooi Lean[2]

[1]Faculty of Economics and Business, Universiti Malaysia Sarawak, Kota Samarahan, Malaysia, hdhadzwan@unimas.my
[2]Economics Program, School of Social Sciences, Universiti Sains Malaysia, Georgetown, Penang, hooilean@usm.com

Abstract—**Energy subsidies are one of the most beneficial strategies that many oil-producing countries have used to boost their economic growth. However, due to the ramifications on economic efficiency, fiscal policy, and other factors, the economic outcome is still contested. This paper uses a dynamic time series analysis, Autoregressive Distributed Lag (ARDL) approach to investigate the influence of energy subsidies on economic output in Malaysia. Our findings imply that energy subsidies have a detrimental impact on economic growth in the long and short run. We recommend that the government sticks to its promise of reducing energy subsidies through subsidy rationalisation.**

Keywords - energy subsidies, oil price, output, time series analysis

I. INTRODUCTION

Malaysia is an oil producer country. It received 2.5% of GDP from oil revenue in 2019. Malaysia's GDP grew at a rate of 4.3 percent in 2019. Since 2000, Malaysia has granted a significant amount of subsidy. In general, as one of oil producer countries in the world, Malaysia spend a lot of money on energy subsidies to boost her macroeconomic performance and raise her people's welfare.

Recently, there have been several debates on the role of subsidies in encouraging economic growth. On one hand, the subsidy is seen to provide a cost advantage to the producer and boost the economic welfare of a market society [1]. As a result, it creates a favourable economic climate for rapid national growth. On the other hand, the subsidy programme is thought not to provide a favourable economic environment due to the market's death weight loss and fiscal pressure problem. As a result, it creates a situation in which the economic system is unproductive in order to promote rapid national growth [2, 3]. In this regard, the government has begun to rationalise its subsidy policy in order to ensure that the subsidy becomes a productive tool for promoting growth while also reducing fiscal pressure. Since 2015, one bold move has been taken: a large reduction in the amount of money allocated for energy subsidies. Because Malaysia is heavily reliant on subsidies, particularly energy subsidies, this policy will undoubtedly have an impact on the country's overall economic activity through a variety of routes.

In this regard, it is critical for current research to determine the influence of economic shocks resulting from the removal of energy subsidies in a country on macroeconomic performance sustainability. Some studies concluded that energy subsidy removal will eventually reflect adverse performance on the macro economy and economic welfare [4-6,]. References [4] and [6] have clearly documented their results which show that GDP is expected to decrease affected by energy subsidy removal in China. It is also supported by [5] where it is expected to have the same experience in the net oil importer and net oil exporter countries. Apart of that, energy subsidy removal also reduces the employment rate [4, 6]. Basically, an absent of energy subsidy will eventually increase the inflation as the price level increase reflect the increase of production cost [7]. This hypothesis is supported by [8] and [9].

The purpose of this research is to investigate the influence of energy subsidies on economic production. Most of the research use a static

ISBN: 978-86-80593-73-9

TABLE I. PHILLIPS-PERRON UNIT ROOT TEST.

	Level		**First Different**	
	Constant	***Trend***	***Constant***	***Trend***
Y	-1.5004	-1.5144	-5.1980***	-5.2884***
EC	-2.8672	-0.9571	-4.6603***	-5.2121***
ES	-1.1651	-3.1737	-12.9335***	-18.0249***
OP	-1.2682	-1.9470	-6.7052***	-6.6817***
K	-1.5751	-2.3114	-5.3069***	-5.3159***
L	-0.7097	-2.4931	-6.2545***	-6.2153***

model analysis to investigate the influence of energy subsidies on economic growth. The objective of this paper is to determine the dynamic impact of energy subsidies on economic growth in both long and short run.

This paper is structured as follows. Section 2 explains the model and data that use in this study. The last two sections discuss the empirical result, conclusion, and policy implication.

II. MODEL

We employ a production function as our baseline model. Hence, our suggested model is as follow:

$$Y = f\left(EC,\ ES,\ OP,\ K,\ L\right), \qquad (1)$$

where,

Y- Gross Domestic Product (MYR)
EC- Energy Consumption (KToe)
ES- Energy Subsidies (MYR)
OP- Brent Oil Price
K- Gross Capital Formation (MYR)
L- Number of Employment

To achieve the objective of the study, we employ the ARDL model to figure out the magnitude impact of exogenous variable on Y in linear perspective.

The data for gross domestic product, gross capital formation and the number of employments are collected form the World Bank Development indicator. Energy subsidies is collected from the ministry of finance. The Brent oil price is collected from BP Statistics. The period of the study covers from 1978-2018.

TABLE II. ARDL BOUNDS TEST.

F-statistic		**28.0573*** **
Critical Value	I(0)	I(1)
10%	2.306	3.353
5%	2.734	3.92
1%	3.657	5.256

III. EMPIRICAL RESULTS

First, we employ the Phillips-Perron unit root test. The result is presented in Table I. We find all variables are stationary at first different. Thus, we proceed to the ARDL bounds test.

The result of the ARDL bounds test is presented in Table II. We find the F-statistic is strongly significant. Hence, we conclude that our suggested model is cointegrated in the long run.

Table III reports the ARDL estimation for long run and short run. All exogenous variables are significant to cause Y at least at 5% critical value. The coefficient of EC, OP, K and L are giving a positive impact on a change of Y. The coefficient of ES is giving a negative impact on a change of Y. EC is the greatest magnitude to influence Y in the long run.

In the short run, all exogenous variables are significant to cause Y at least at 5% critical value except EC. The sign of short-run coefficient for all exogenous variables are consistent with the long-run coefficient. L is the greatest magnitude to influence Y in the short run. The coefficient of ECT is significant with negative sign at 1% critical value. It informs the model takes 2.8 months to translate its effect on a change of Y.

Linear assumption suggests energy consumption and oil price has a positive relationship with economic growth in Malaysia.

TABLE III. ARDL ESTIMATION FOR LONG-RUN AND SHORT-RUN COEFFICIENT. DEPENDENT VARIABLE: Y.

Model	**1,1,2,2,1,0**
EC	0.7097***
ES	-0.0712***
OP	0.0601**
K	0.0772***
L	0.6822***
ECT	-0.2338***
D(EC)	0.0413
D(ES)	-0.009***
D(OP)	0.0232***
D(K)	0.1955***
D(L)	0.2313**
Diagnostic Test	
Jarque-Bera	1.6878
Breusch-Godfrey Serial Correlation LM Test	3.4355
ARCH	0.1119
Ramsey test	0.0032
CUSUM and CUSUM Square	Stable

On the other hand, energy subsidies have a negative relationship with economic growth in Malaysia. This result is consistent with [9].

We also imply that when the oil price interacts with energy subsidies, the oil price has a greater impact on economic growth. Higher oil prices enhance a country's revenue and, as a result, a government's capacity to boost energy subsidy spending [10]. Malaysia is the oil producer country. It is also a country that exports oil in large quantities. As a result, an increase in the price of oil will enhance national revenue.

All diagnostic tests namely Jarque-Bera, Breusch-Godfrey Serial Correlation LM Test, ARCH and Ramsey test suggest all models across all sectors are in good fits.

IV. CONCLUSION AND POLICY IMPLICATIONS

The aim of the study is to identify the magnitude impact of energy subsidies on the economic growth in Malaysia. We use a time series dataset from 1978-2018. Methodologically, we employ Autoregressive Distributed Lag (ARDL) estimation, a dynamic time series analysis. We find energy subsidies is giving an adverse impact to the economic growth. While the rest of the exogenous variables (energy consumption, oil price, capital and labor) are significant to give a positive impact to the economic growth.

For policy recommendation, we recommend that the government continue to rationalize energy subsidies in order to achieve sustainable development. However, the government should provide some countermeasures to compensate for a negative influence that may hurt particular economic sectors. When it comes to energy subsidy rationalization, the government should pay more attention to the issue of energy poverty.

REFERENCES

[1] Van Beers, C., & Van den Berch, J. C. J. M. (2011). Analysis perseverance of pervese subsidies and their impact on trade and environment. *Ecological Economics, 36*, 475-486.

[2] Del Granado, F. J. A., Coady, D., & Gillingham, R. (2012). The unequal benefits of fuel subsidies: A review of evidence for developing countries. *World development, 40*(11), 2234-2248.

[3] Isaak, D., (2015). Oil Security in ASIA and the Pacific. In *Lee, M., Park, D. and Saunders, H., Asia's Energy Challenge: Key Issues and Policy Option* (pp.33-80). Routledge Taylor and Francis Group, London and New York.

[4] Jiang, Z., & Lin, B. (2014). The perverse fossil fuel subsidies in China-the scale and effects. *Energy*. 70; 411-419.

[5] Plate, M. (2014). The long-run macroeconomic mpacts of fuel subsidies. *Journal of Development Economics, 107*, 129-143.

[6] Lin, B., & Jiang, Z. (2011). Estimates of energy subsidies in China and impact of energy subsidy reform. *Energy Economics, 33*, 273-283

[7] The International Institute for Sustainable Development. (2012). A Citizen's Guide to Energy Subsidies in Indonesia. International Institute for Sustainable Development. Manitoba.

[8] Jiang, Z., & Tan, J. (2013). How the removal of energy subsidy affects general price in China: a study based on input-output model. *Energy Policy*. *63*, 599-606.

[9] Solaymani, S. and Kari, F. (2014). Impacts of energy subsidy reform on the Malaysian economy and transportation sector. *Energy Policy, 70*, 115-125.

[10] Husaini, D. H., & Lean, H. H. (2021). Asymmetric impact of oil price and exchange rate on disaggregation price inflation. *Resources Policy, 73*, 102175.

The Influence of Cross-Section Airfoil on the HAWT Efficiency

Bader Somaiday[1], Ireneusz Czajka[2], Muhammad A.R Yass[3]

[1,2]AGH University of Science and Technology, Krakow, Poland, somaiday@agh.edu.pl, iczajka@agh.edu.pl,

[3]University of Technology, Bahgdad, Iraq, 50251@uotechnology.edu.iq

Abstract—**In this paper we study the impact of cross-section airfoil type on the efficiency of horizontal axis wind turbine (HAWT) blades. There were analyzed three different airfoils: symmetric (NACA 4412), asymmetric (NACA 0012), and supercritical (EPLER 417). The carried out analyzes were both theoretical and experimental. Theoretical analyzes were done through Fortran 90 code, and Qblade code based on blade element momentum theory. Solidworks software and 3D-printer were used to design and manufacturing the blade for experimental tests. Results of experimental tests matched theoretical results. Conducted research showed that the blade with supercritical airfoil (Eppler 417) had performance better than other tested objects. The power coefficient of NACA 4412, NACA 0012, and Eppler 417 are 0.516, 0.492, and 0.510 respectively. The experimental results also showed that the Eppler 417 airfoil achieves more power and less speed reduction than other airfoils.**

Keywords - supercritical airfoil, HAWT blade design, optimum power coefficient

a	Axial factor
á	Angular factor
C_d	Drag coefficient
C_l	Lift coefficient
C_p	Power Coefficient
n	Number of revolutions of rotor per minute (rpm)
P	Power (W)
r	Radius (m)
R	Radius of turbine rotor (m)
U	Wind speed (m/s)
α	Angle of attack (degree)
λ	Tip speed ratio
φ	Relative flow angle (degree)
Ω	Angular velocity of the rotor (rad/s)

I. INTRODUCTION

The aerodynamic efficiency of an airfoil is defined by lift-to-drag ratio. It achieves highest values at specific angle of attack, and the value of this angle varies between airfoils. [1]. The lift-to-drag ratio depends on zero-lift drag, aspect ratio, span efficiency and is independent of weight. The use of airfoil in a wind turbine is no more limited than in an aircraft wing because a wind turbine operates at a lower speed than an aircraft [2]. There have been many theoretical and scientific studies on the performance of wind turbine blades. Reference [3] investigated an aerodynamic performance evaluation system using two groups of NACA profiles which were used in a series of five-digit NACA (63-221, 65-415; 23012, 23021) and four-digit NACA (2421, 2412, 4412, 4424) for three HAWT blades. The same airfoils were used along the entire blade. A computer program was developed to automate the entire procedure. Their results show that the elementary power coefficient of NACA 4412 and NACA 23012 was higher than the other profiles. Reference [4] proposed a stable and aerodynamic design using NACA 4412 profile with blade length (800 mm) and power (600 W) with mini HAWT. The length chord and twist angle distributions of the initial blade model were calculated. A reasonable compromise between high efficiency and good starting good starting torque was obtained. The blades were developed using MATLAB software. The optimized blade chord was reduced by 24% and the thickness by 44%. The power level of the optimized blade was significantly increased to 30% compared to the standard blade. Reference [5] explained the design and optimization of a small HAWT blade using custom code. The blades were made using NACA 4412, NACA 2412 and NACA 1812 at a wind speed of 5 m /s,

ISBN: 978-86-80593-73-9

which the most frequent wind speed was prevailing in the Indian peninsula. Based on a self-created code based on BEM (Blade Element Momentum) theory, an optimum blade profile was generated which performs with high efficiency using multiple airfoils. The twist angle distribution, chord distribution and other parameters for different airfoil sections along the blade were determined using the proposed code. For a rotor with a diameter of 4.46 m, a power factor of 0.490 and an output power of 0.56 kW were obtained. The blade analysis result obtained using Q-blade software showed reliable agreement with the proposed code and wind turbine performance analysis. The power factor obtained using the MATLAB code was 0.490, which was very close to that obtained using Q-blade (0.514). In addition, the difference in output power between the two values was only 28.58 W. [6] presented the behaviour and performance of a multi-section HAWT blade with and without fence (Muheisen et al., 2021). The multi-section HAWT blade was designed using supercritical airfoils (SG6043, FX63-137S and FX66-S-196V). The overall performance of the multi-section blade was compared with the single-section NACA4412 blade.

Numerical analyses were performed using the author's code (Fortran 90) and the Qblade package based on BEM theory. The multi-pass vanes show an increase of about 8% in power factor compared to the single-pass vanes. The boundary layer theory was used to design the fences and their position was determined experimentally. An increase in total power factor of about 16% with the use of fences and high flutter stability.

In this study, the behavior and performance for different blade cross-sections, symmetrical, asymmetrical and supercritical airfoils (NACA0012, NACA 4412 and Eppler 417) were investigated theoretically and experimentally. The horizontal axis wind turbine blade design was performed using Fortran 90 code and QBlade software based on BEM theory.

II. THE BLADE CROSS-SECTION

Table I shows the airfoil characteristics in cross sections and the airfoil shapes are shown in Figs. 1-3. The HAWT rotor design parameters are shown in Table II.

TABLE I. CROSS-SECTION AIRFOILS DESCRIBUTION.

Airfoil	Max t/c	Max Cl/Cd
NACA 4412	12% at 30%	129.4 at 5.25°
NACA 0012	12% at 30%	75.6 at 7.5°
EPPLER 417	14.2% at 38.35%	135.9 at 2.25°

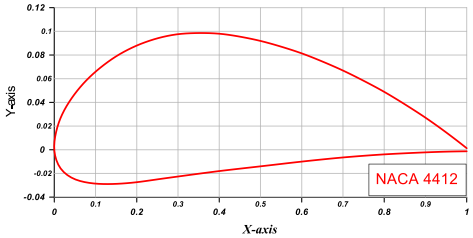

Figure 1. NACA 4412 airfoil geometry.

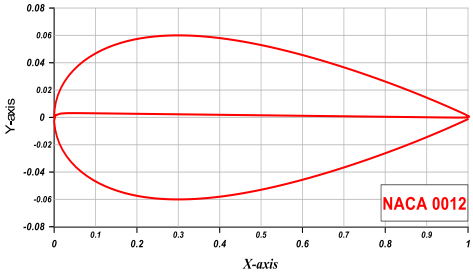

Figure 2. NACA 0012 airfoil geometry

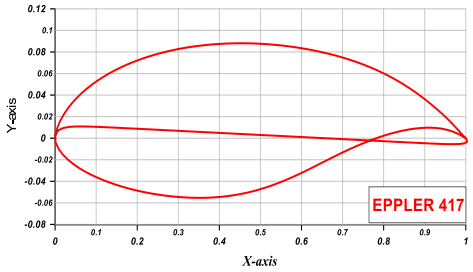

Figure 3. EPLER 417 airfoil geometry

TABLE II. PARAMETERS OF DESIGN.

Rotor Diameter	1.07 m
Hub Diameter	0.20 m
Number of Blades	3
Rated Power	600 W
Cut in Speed	2 m/s^2

III. POWER COEFFICIENT

The maximum power that can be obtained from the wind flow passing inside the ring (Fig. 4) [7]. Upstream and downstream pressures are assumed equal and the velocity around the disk

remains constant ($U_2 = U_3$) . The rotor power coefficient is determined by the Eqs. [6].

$$U_2 = \frac{U_1 + U_4}{2} \ , \tag{1}$$

$$a = \frac{U_1 - U_2}{U_1} \ , \tag{2}$$

$$U_2 = U_1(1-a) \ , \tag{3}$$

$$U_4 = U_1(1-2a) \ , \tag{4}$$

$$P = \int_{r_h}^{R} dP = \int_{r_h}^{R} \Omega dQ \ , \tag{5}$$

$$C_p = \frac{P}{P_{wind}} = \frac{\int_{r_h}^{R} \Omega dQ}{\frac{1}{2}\rho R^2 U_1^{\ 3}} \ , \tag{6}$$

$$C_p = \left(\frac{8}{\lambda^2}\right)\int_{\lambda_h}^{\lambda} \lambda_r^{\ 3} \grave{a}(1-a)\left[1-\left(\frac{C_d}{C_l}\right)cot\varphi\right] d\lambda_r \tag{7}$$

The tip speed ratio:

$$\lambda = \frac{2R\pi N}{60U_1} \ . \tag{8}$$

IV. Design and Manufacturing Blades

A program in FORTRAN (f.90) was written and the Qblade package was used to calculate the aerodynamic data and power factor based on Blade Element Momentum (BEM) theory, as shown in Tables III-V and Figs. 5-7 Solidworks software was used to design the 3D blade shapes (Figs. 8-10). The developed models were fabricated on a 3D printer (Fig. 11). Due to the limited size of the printer's print area, the blades were divided into several sections and then combined. The blades with different profiles in sections (NACA 4412, NACA 0012 and EPPLER 417) were mounted to the wind turbine for testing as shown in Figs. 12-14.

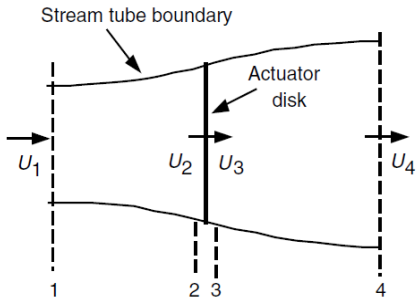

Figure 4. Wind turbine actuator disk model.

TABLE III. NACA 4412 cross-section geometry.

	Position (m)	Chord (m)	Twist (deg)	Foil
1	0.00	0.167	43.42	NACA 4412
2	0.10	0.156	23.14	NACA 4412
3	0.17	0.136	16.72	NACA 4412
4	0.27	0.109	10.91	NACA 4412
5	0.37	0.090	7.42	NACA 4412
6	0.47	0.076	5.11	NACA 4412
7	0.57	0.066	3.47	NACA 4412
8	0.67	0.058	2.25	NACA 4412
9	0.77	0.052	1.30	NACA 4412
10	0.87	0.046	0.56	NACA 4412
11	0.97	0.042	0.05-	NACA 4412
12	1.07	0.038	0.56-	NACA 4412

TABLE IV. NACA 0012 cross-section geometry.

	Position (m)	Chord (m)	Twist (deg)	Foil
1	0.00	0.206	41.43	NACA 0012
2	0.10	0.194	21.14	NACA 0012
3	0.17	0.168	14.72	NACA 0012
4	0.27	0.136	8.91	NACA 0012
5	0.37	0.112	5.42	NACA 0012
6	0.47	0.094	3.11	NACA 0012
7	0.57	0.082	1.47	NACA 0012
8	0.67	0.072	0.25	NACA 0012
9	0.77	0.064	-0.69	NACA 0012
10	0.87	0.057	-1.44	NACA 0012
11	0.97	0.052	-2.05	NACA 0012
12	1.07	0.048	-2.56	NACA 0012

TABLE V. EPPLER 417 CROSS-SECTIONGEOMETRY.

	Position (m)	Chord (m)	Twist (deg)	Foil
1	0.00	0.283	47.42	EPPLER 417
2	0.10	0.266	27.14	EPPLER 417
3	0.17	0.231	20.72	EPPLER 417
4	0.27	0.186	14.90	EPPLER 417
5	0.37	0.153	11.42	EPPLER 417
6	0.47	0.129	9.11	EPPLER 417
7	0.57	0.112	7.47	EPPLER 417
8	0.67	0.098	6.25	EPPLER 417
9	0.77	0.087	5.31	EPPLER 417
10	0.87	0.079	4.55	EPPLER 417
11	0.97	0.072	3.94	EPPLER 417
12	1.07	0.066	3.44	EPPLER 417

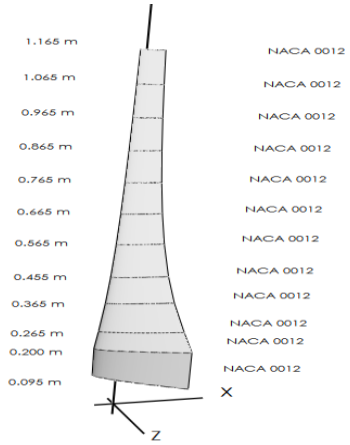

Figure 5. NACA 4412cross-section blade by Qblade package.

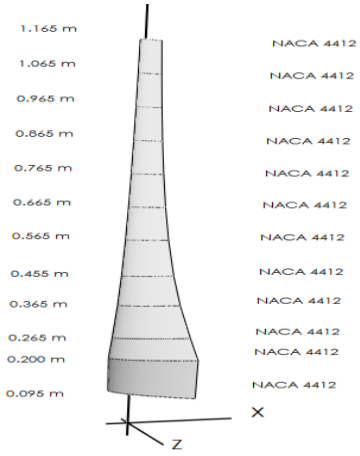

Figure 6. NACA 0012 cross-section blade by Qblade package.

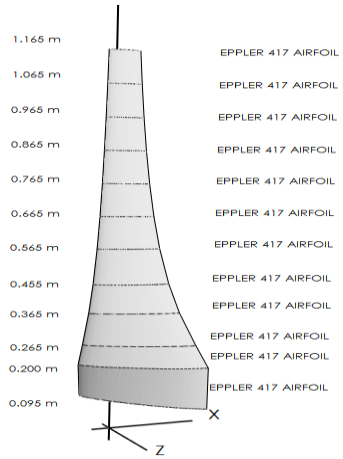

Figure 7. EPPLER 417 cross-section blade by Qblade package

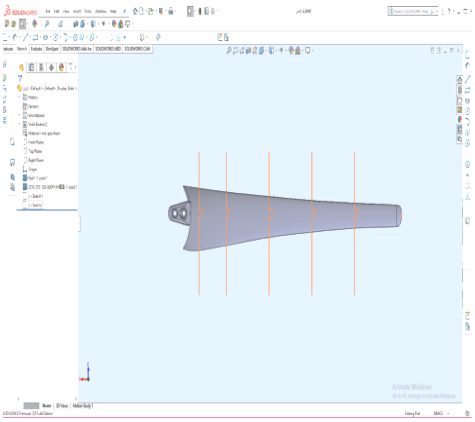

Figure 8. NACA 4412 cross-section blade by Solidworks

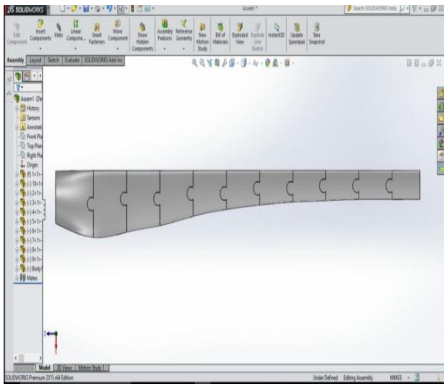

Figure 9. NACA 0012 cross-section blade by Solidworks.

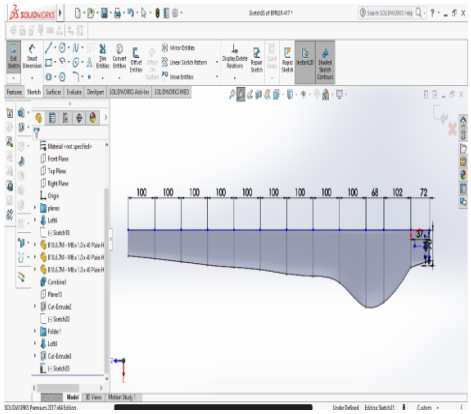

Figure. 10. EPPLER 417 cross-section blade by Solidworks.

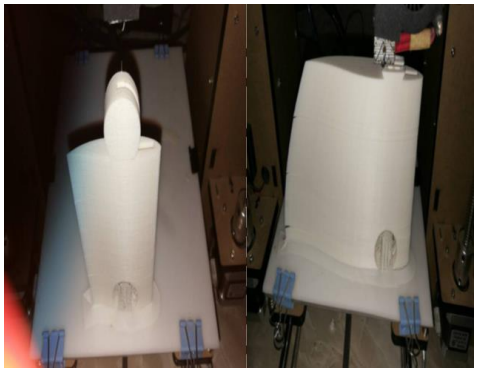

Figure 11. 3D Printer process.

Figure 12. Wind turbine with NACA 4412 cross-section blades.

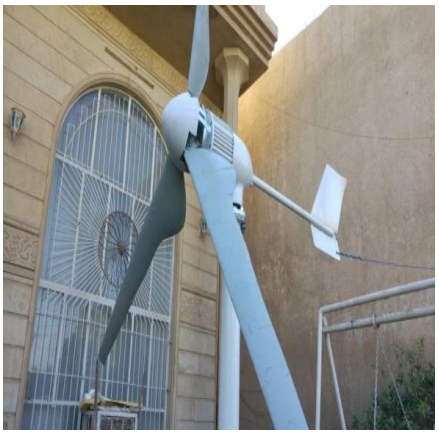

Figure 13. Wind turbine with NACA 0012 cross-section blades.

Figure 14. Wind turbine with EPPLER cross - section blades.

V. RESULTS AND DECISIONS

The cross-sectional area of the airfoil is the main design parameter of a wind turbine blade, which converts the airflow velocity into a pressure distribution along the length of the blade. Different profiles such as symmetrical, asymmetrical and supercritical have been used in this study.

The main characteristics of the profile are the amount of energy absorbed from the free stream, the maximum lift-to-drag ratio and the angle of attack when comparing the performance of the profiles. The overall cross-sectional efficiency of

the airfoil was taken into account, not just the peak point of the power factor.

Fig. 15 shows that the EPPLER 417 profile generated less drag than the other profiles. Furthermore, the Eppler 417 profile generated the largest pressure distribution in the second third of the blade radius, as shown in Fig. 16.

Although the NACA 4412 profile obtained the highest power factor value (Cp =0.516) compared to the NACA 0012 (Cp =1.491) and Eppler 417 (Cp =0.510) profiles, as shown in Fig. 17, the Eppler 417 profile obtained the highest overall efficiency calculated from the area under the power factor curve, see Figs. 18-20.

The experimental results show that Eppler 417 behaves best and generates the highest power among the other profiles, see Table 6.

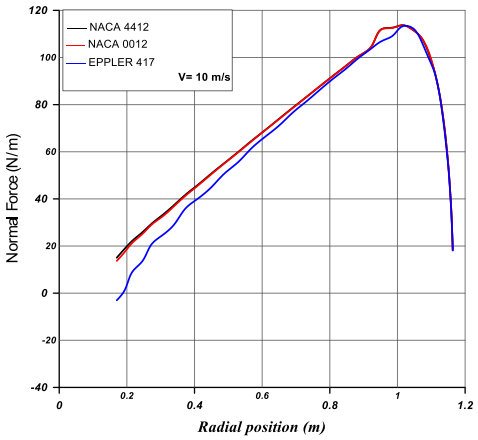

Figure 15. Normal force destribution along the blades radius.

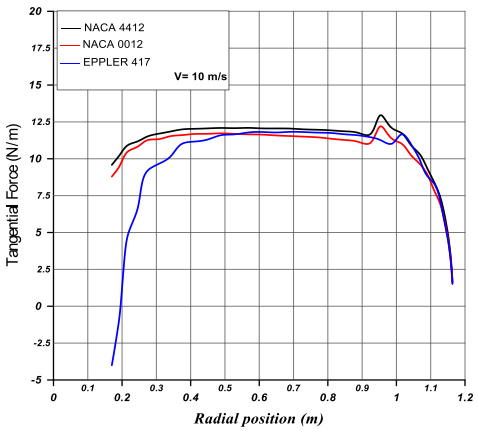

Figure 16. Tangential force destribution along the

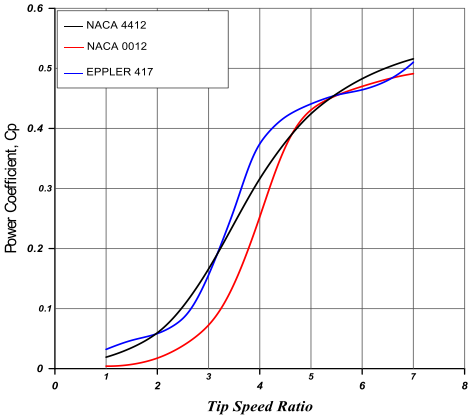

Figure 17. The power coefficient of the cross-sections blades verius tip speed ratio.

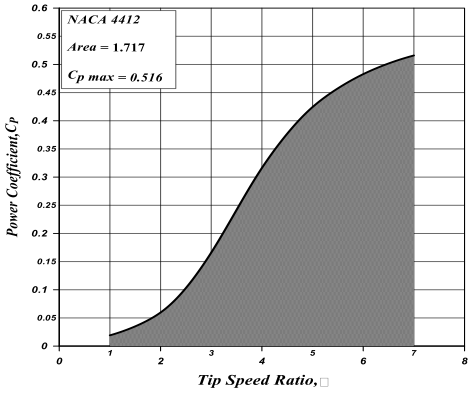

Figure 18. The area under power coefficient curve of NACA 4412 cross-section blade.

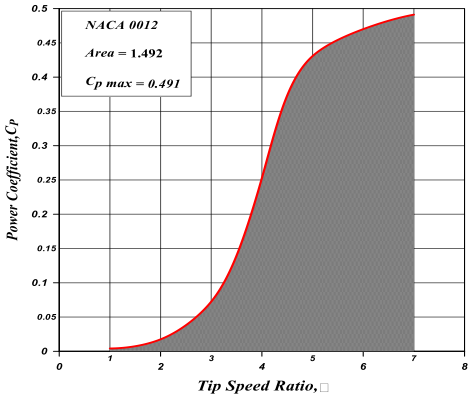

Figure 19. The area under power coefficient curve of NACA 0012 cross-section blade.

TABLE VI. EXPERIMENTAL RESULTS

Wind speed (m/s)	NACA 4412		NACA 0012		EPPLER 417	
	rpm	Power W	rpm	Power W	rpm	Power W
3	62	13	51	10	68	20
4.2	88	93	69	28	95	122
5.4	107	144	96	125	122	173
6.5	125	306	114	285	147	330
7.5	171	506	132	363	178	546

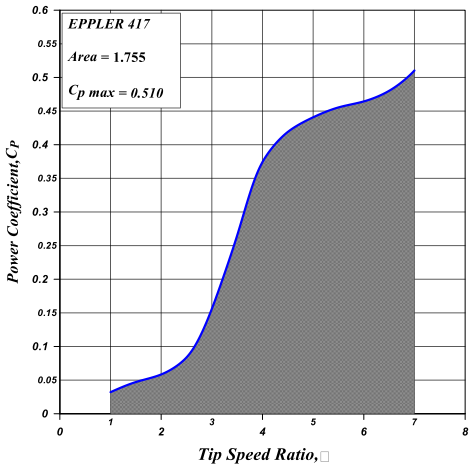

Figure 20. The area under power coefficient curve of EPPLER 417 cross-section blade.

VI. CONCLUSIONS

The impacts of cross-section airfoil types on the efficiency of horizontal axis wind turbine (HAWT) blades were studded. Three different airfoils: symmetric (NACA 4412), asymmetric (NACA 0012), and supercritical (EPLER 417) were analyzed. The carried out analyzes were both theoretical and experimental. Theoretical analyzes were done through Fortran 90 code, and Qblade code based on blade element momentum theory. Results of experimental tests matched theoretical results. Supercritical airfoils always generate the maximum lift-to-drag ratio at a small angle of attack.

Pressure distribution in the second third of the blade radius is important in determining airfoil behavior.

A supercritical airfoil generates more power at a low Reynolds number, so it has a lower operating speed.

Chord length and twist angle depend on the profile characteristics, so EPPLER 417 has high chord length and twist angle, so it generates the highest power.

REFERENCES

[1] Bak, C., Gaunaa, M., Andersen, P., Buhl, T., Hansen, P., Clemmensen, K., & Møller, R. (2007). Wind tunnel test on wind turbine airfoil with adaptive trailing edge geometry. *45th AIAA Aerospace Sciences Meeting and Exhibit*, 1016.

[2] Hull, D. G. (2007). Fundamentals of airplane flight mechanics (Vol. 19). Springer.

[3] Javed, F., Javed, S., Bilal, T., & Rastogi, V. (2016). Design of multiple airfoil HAWT blade using MATLAB programming. In *IEEE International Conference on Renewable Energy Research and Applications (ICRERA)*, (pp. 425–430).

[4] Kale, S. A., & Varma, R. N. (2014). Aerodynamic design of a horizontal axis micro wind turbine blade using NACA 4412 profile. *International Journal of Renewable Energy Research (IJRER)*, *4*(1), 69–72.

[5] Muheisen, A. H., A. R. Yass, M., & Irthiea, I. K. (2021). Enhancement of Horizontal Wind Turbine Blade Performance Using Multiple Airfoils Sections and Fences. *Journal of King Saud University - Engineering Sciences.*

[6] Ragheb, M., & Ragheb, A. M. (2011). Wind turbines theory-the betz equation and optimal rotor tip speed ratio. *Fundamental and Advanced Topics in Wind Power*, *1*(1), 19–38.

[7] Tenguria, N., Mittal, N. D., & Ahmed, S. (2011). Evaluation of performance of horizontal axis wind turbine blades based on optimal rotor theory. *Journal of Urban and Environmental Engineering*, *5*(1), 15–23.

A Design of P-type Iterative Leaning Control for Single Phase Grid-Connected Inverters

Hua Trinh Hoang[1], Nguyen Minh Y[2]

[1,2]Thai Nguyen University of Technology, Thai Nguyen, Vietnam, minhy@tnut.edu.vn

Abstract— **This study proposes a control scheme based on an iterative learning control approach (ILC) for single-phase grid-connected inverters using an LCL filter. The control objective is to regulate the grid current to track the reference current independent of disturbances with a minimum steady-state error. The conventional feedback control methods result in poor steady-state performance in inverter applications. Hence, the hybrid control structure in which ILC is combined with a PD controller to improve the tracking accuracy and disturbance rejection is proposed. Mathematical modeling and the design procedure concerning the stability of the system have been presented. In the proposed control scheme, a low-pass filter is used to prevent the learning at high frequency which may affect the system stability. The design of the control strategy is examined through simulations in MATLAB environment.**

Keywords - Iterative Learning Control (ILC), grid-connected inverters, current controller

I. INTRODUCTION

High performance DC-AC inverters have been widely applied in many applications. Among these application, grid-connected inverters is a one of the most important application. A critical requirement for grid-connected inverters is to provide sinusoidal output current with a lowest harmonic distortion. Various control methods have been investigated to tackle this problem such as deadbeat control, sliding mode control, fuzzy control, or model predictive control [1]. However, they are not capable of dealing with periodic distortions which naturally exist in inverter applications.

In this context. ILC algorithm becomes a suitable candidate to develop the control strategy for inverter applications [2]. ILC has an excellent ability in eliminating the periodic disturbance, but it cannot compensate for the non-repeating disturbance which can randomly present in the operating of inverters and usually results in low performance in transient dynamic.

In this paper, the feedback controller and the use of the ILC algorithm are pro-posed for developing the control strategy for single-phase grid-connected inverters. The feedback control of the grid current is used to stabilize the closed-loop system under non-repeating disturbances and improve the control performance in the transient state. The ILC controller guarantees the low steady-state error of the waveform of the injected current which is required for high-quality power to be injected into the grid. The rest of the paper is organized as follows: Concepts of ILC approach is provided in Section 2. Section 3 presents the control design. The simulation results are provided in Section 5. Finally, the conclusion is given in Section 5.

II. FUNDAMENTALS OF ITERATIVE LEARNING CONTROL

ILC is the intelligent control algorithm that could be able to provide precise control for the system in which the output of the system repeats trial-to-trial. The basic idea of ILC is to use the information of the previous operating cycle to generate the command for the system in the next cycle. The system performance is improved after every learning cycle [3].

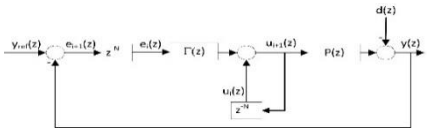

Figure 1. Block diagram of ILC algorithm.

Considering the discrete plant $P(z)$ which is assumed to have the above criteria. Fig. 1 illustrates the ILC control scheme to apply to the plant *P(z)* . The notation denotes the iteration i . The reference,

$$\left|1-P(z)\Gamma(z)\right|_{Z=e^{j\omega T}}<1, \forall \omega \in \left(0, \frac{\pi}{T}\right)$$ and

disturbance $d(z)$ are repetitive within the iteration domain. The block z^{-N} represents the one cycle delay block, where N is the number of samples per one cycle. The zero tracking error is archived as the output is identical to the reference $y_{ref}(z)$. At that time, the error $e_i(z)$ equals zero and the control effort only depends on the signal $u_i(z)$.

The control signal is determined as:

$$u_{i+1}(z)=u_i(z)+\Gamma(z)e_i(z), \qquad (1)$$

where $u_i(z)$ is the control signal at iteration i, $e_i(z)$ is the error signal at iteration *i*, and $\Gamma(z)$ is the learning function.

From (1) and the system dynamic in Fig. 1, the relation between the error signal of two consecutive iterations is expressed as:

$$e_{i+1}(z)=\left(1-P(z)\right)\Gamma(z)e_i(z). \qquad (2)$$

The error signal is decay over subsequent iterations if the following condition fulfills:

$$\left|1-P(z)\Gamma(z)\right|_{Z=e^{j\omega T}}<1, \forall \omega \in \left(0, \frac{\pi}{T}\right), \quad (3)$$

where T is the sampling interval, the value of $\left|1-P(z)\Gamma(z)\right|_{Z=e^{j\omega T}}$ is the decay factor. The error signal would converge to zero faster as the decay factor is smaller. Condition (3) is archived as the Nyquist plot of $P(z)\Gamma(z)$ lies on the right-half plane [4].

The error convergence characteristic can only be obtained if the system holds five assumptions as mentioned above. However, the grid-connected inverter considered in this paper may not ensure these assumptions. The initial conditions at different iteration may not the same, or the measurement noise is high in practical applications. To deal with this problem, the modified ILC scheme with the introduction of the forgetting factor is given. The scheme was verified that it can improve the robustness of the control structure [5]. The modified learning algorithm with the forgetting factor β is expressed as:

$$u_{i+1}(z)=(1-\beta)u_i(z)+\Gamma(z)e_i(z). \quad (4)$$

It is shown in [6] that the introduction of the forgetting factor would increase the robustness, but it also affects the tracking performance of the controller. Therefore, the value of the forgetting factor should be sufficiently small in order to achieve robustness, while keeping the acceptable error bound. The new relation of the error signals in two consecutive iterations becomes:

$$e_{i+1}(z)=\left(1-P(z)\Gamma(z)\right)e_i(z) +\beta P(z)u_i(z). \qquad (5)$$

As the forgetting factor β is sufficiently small, the convergence condition (3) can still be used to ensure the error convergence.

III. ILC Controller for Single Phase Grid-Connected Inverters

A. System Model

The schematic block diagram of a typical grid-connected inverter system is illustrated in Fig. 2 with the inverter side current, grid side current, filter capacitor voltage, inverter output voltage, modulation signal and grid voltage denoted as $i_1, i_2, V_C, V_{inv}, V_M, and V_g$,

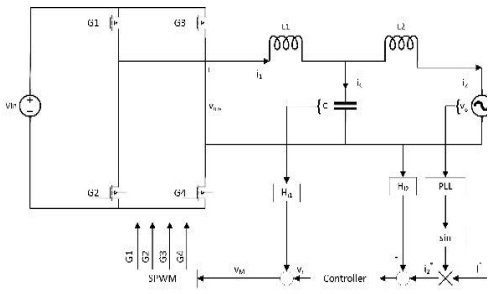

Figure 2. The typical inverter system.

respectively. In this paper, capacitor's current feedback is untilized to damp resonance peak for stability concerns of LCL filter. Applying this method, an inverter system can obtain the same behavior as utilizing passive damping method with a resistor in parallel with a capacitor of LCL filter. The system model of a grid-connected inverter with LCL filter is obtained as:

$$i_2(s) = P(s)V_M(s) - d(s), \qquad (6)$$

where

$$P(s) = \frac{k_{pwm}}{L_1L_2Cs^3 + \frac{L_1L_2Cs2}{R} + (L_1 + L_2)s},$$

and

$$d(s) = \frac{\left(Cs + \frac{1}{R} + 1\right)}{L_1L_2Cs^3 + \frac{L_1L_2Cs^2}{R} + (L_1 + L_2)s} V_g(s),$$

with L_1, L_2, C, are the filter's parameters, R is the value of a resistor parallel to filter's capacitor, and $L_{pwm} = \frac{V_{in}}{V_{carrier}}$.

B. Control Design

In this section, the design of the proposed control algorithm is presented. Considering the inverter system with the value of damping resistor which has the parameters as in Table I.

TABLE I. INVERTER SPECIFICATIONS.

Parameter	***Value***	***Parameter***	***Value***
Grid voltage (RMS)	220 V	Amplitude of triangular wave	3.05 V
Fundamental frequency	50 Hz	Switching frequency	10 kHz
Inverter side inductor	600 μH	Output power	6 kW
Filter Capacitor	10 μF	Injected gird current feedback coefficien	0.15
Grid side inductor	150 μH	Damping resistor	1.5 Ω
Inverter side voltage	360 V	Sampling frequency	40 kHz

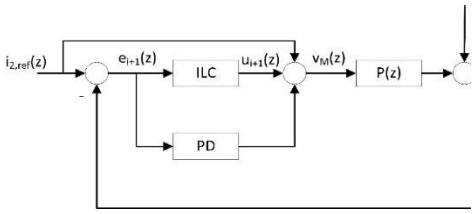

Figure 3. The proposed control structure.

Digitalizing the system (6) with parameters in Table I, we get:

$$i_2(z) = P(z)V_M(z) - d(z), \qquad (7)$$

The proposed control structure is dipicted in Fig. 3, which is digitally implemented. The controller consists of three component which are proportional-derivative feedback, reference current feedforward, and ILC component. The modulation signal is calculated as:

$$V_M(z) = i_2,ref(z) + u_{i+1}(z) + G_{PD}(z)e_{i+1}. \qquad (8)$$

Apllying control mechanism (8) to the system (7) with the learning function $\Gamma(z) = z^x \alpha F(z)$ where α is the learning gain, $F(z)$ is the filter to prevent the high frequency learning, and z^x is the advanced operator to compensate the phase lag caused by the filter. Under the proposed strucuture, the system error at iteration i+1 can be expressed as:

$$e_{i+1} = \left(1 - \frac{\alpha z^x F(z)P(z)}{1 + P(z)G_{PD}(z)}\right)e_i(z) + \\ + P(z)G_{PD}(z)u_i(z) \qquad (9)$$

The error will converge to zero as:

$$\left|1 - \frac{\alpha z^x F(z)P(z)}{1 + P(z)G_{PD}(z)}\right|_{z=e^{j\omega T}} < 1, \forall \omega \in (0,T). \qquad (9)$$

This means that the nyquist plot of $\frac{\alpha z^x F(z)P(z)}{1 + P(z)G_{PD}(z)}$ lies inside a circle of radius 1 with the center at (1,0).

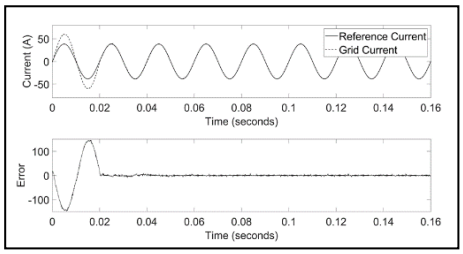

a)

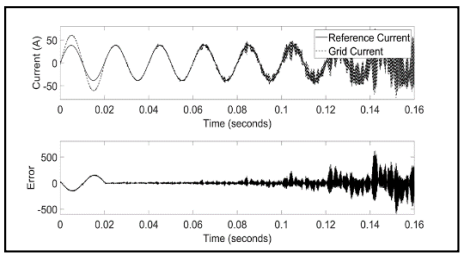

b)

Figure 4. System responses: (a) System response with filter; (b) System response without filter.

The PD controller is obtained as $k_p = 0.98$, and $k_d = 6.59x10^{-5}$ by SISO tool. The parameters of ILC controller are determined as: learning gain $\alpha = 1$, advanced operator z^{10}, and FIR low-pass filter,

$$F(z) = \frac{1}{9}\frac{z^{-8} + z^{-7} + z^{-6} + z^{-5} + z^{-4} + z^{-3} + z^{-2} + z^{-1} + 1}{1}$$

IV. SIMULATION RESUTS

To verify the proposed control design in Section 3, the inverter system has been simulated using Sim Power and Simulink toolboxes in MATLAB environment.

Fig. 4 shows the waveforms of the reference and the grid current when the controller without the FIR filter is applied. The system becomes unstable and the error convergence cannot be archived. As the FIR filter is applied, the grid current gradually tracks the reference and the error almost converges to zero.

Fig. 5 illustrates the current waveform at rated load with different power factor (PF) references. The proposed controller provides good performance in tracking ability with very low harmonic distortions.

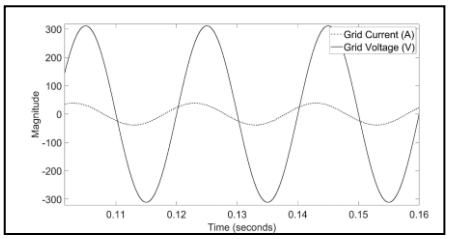

a)

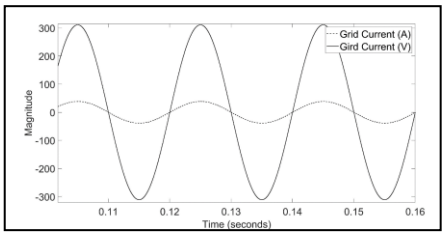

b)

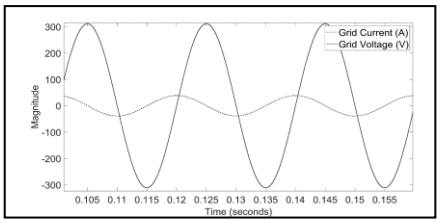

c)

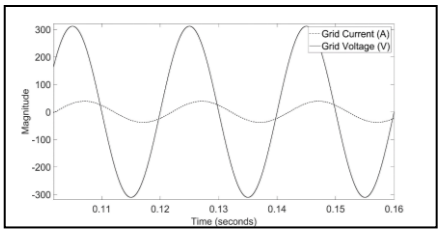

d)

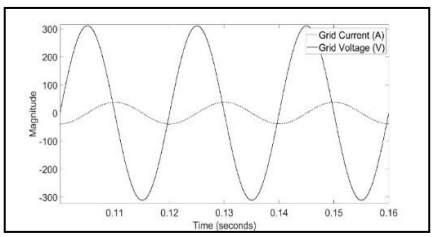

e)

Figure 5. System response with different reference power factors: (a) PF = 1 (Resistive load); (b) PF = 0.8 Lagging (Capacitive load); (c) PF = 0 (Capacitive load); PF = 0.8 (Inductive load); (e) PF = 0 (Inductive load).

V. CONCLUSION

This study proposes a control scheme based on an iterative learning control approach for a single-phase grid-connected inverter with an LCL filter. The capacitor current feedback is exploited to tackle the resonance hazard problem of the LCL filter. As the grid current and the disturbance caused by grid voltage are periodic signals, ILC emerges as the appropriate approach for designing the current controller for the grid current. The design of the controller concerning the convergence condition is presented. The stability of the system is ensured by preventing the learning at the high frequency range. Simulations have proven the effectiveness of the control scheme and design. The control scheme in this paper has achieved a fast convergence rate in which the output tracks the reference signal within one learning iteration after the reference signal changes.

ACKNOWLEDGMENT

This work is supported by Thai Nguyen University of Technology.

REFERENCES

[1] Ciobotaru, M., Teodorescu, R., & Blaabjerg, F. (2006). Control of single-stage single-phase pv inverter. *EPE Journal*, *16*(3), 20–26, 2006.

[2] Kulawinek, R., Galkowski, K., Grzesiak, L., & Kummert, A. (2011). Iterative learning control method for a single-phase inverter with sinusoidal output voltage. In *IECON 2011-37th Annual Conference of the IEEE Industrial Electronics Society*, (pp. 1402–1407). IEEE.

[3] Xu, J.-X., & Tan, Y. (2003). Linear and nonlinear iterative learning control, vol. 291. Springer

[4] Hatonen, J. (2004). Issues of algebra and optimality in iterative learningcontrol.

[5] Arimoto, S., Naniwa, T., & Suzuki, H. (1990). Robustness of p-type learningcontrol with a forgetting factor for robotic motions. In *29th IEEEConference on Decision and Control*, (pp. 2640–2645). IEEE..

.

Purification of Bioethanol Using Inorganic Salts: An Experimental and Modelling Approach

Omar Díaz-López[1], Claudia Gutiérrez-Antonio[2], Salvador Hernández[3]

[1,2]Universidad Autónoma de Querétaro, Facultad de Química Querétaro, México, omardl.iqa@gmail.com[1], claudia.gutierrez@uaq.mx[2]
[3]Universidad de Guanajuato, Departamento de Ingeniería Química, Guanajuato, México, hernasa@ugto.mx

Abstract—**The purpose of this work is to analyze the use of calcium chloride and sodium acetate salts in an extractive distillation process to obtain anhydrous bioethanol. The work is divided into two stages. The first one is the simulation study, in which the extractive distillation process is modeled in a batch distillation column using Aspen Plus software; in this stage, the optimal quantities of the salts to be used in the extractive distillation process are determined to guarantee the breakdown of the ethanol-water azeotrope. The second stage corresponds to the experimental study, where the data obtained from the simulation are used to carry out the runs in a batch distillation column; This allows to validate the modeling as well as the purities achieved in the anhydrous bioethanol. Both simulation and experimental data obtained are compared with those reported in the literature for other solvents. The simulation and experimentation results show that the use of sodium acetate and calcium chloride salts, in the extractive distillation, are an economically viable alternative to obtain high purity bioethanol. This is of great relevance in the development of biofuels with prices competitive to those of their fossil counterpart.**

Keywords – extractive distillation, anhidrous bioethanol, inorganic salts

I. INTRODUCTION

Nowadays, society faces big challenges related with climate change, declining in oil wells production as well as the economic crisis due pandemics. In this context, the International Energy Agency, in collaboration with the World Bank, has developed a sustainable recovery plan [1]; in this plan, it is established that investment in key sectors must be done in order to reach a quick sustainable recovery. Among the sectors included it can be mentioned the renewable energy, energy efficiency, development of low-carbon technologies, and biofuels; the last one is the focus of this work.

Biofuels are defined as those fuels that are generated through the transformation of biomass of the short carbon cycle; in this type of biomass it can be found those material of vegetable, animal or residual origin. Biofuels can be produced in liquid, gaseous and solid states, and they can be used in transport sector and power generation. Among gaseous biofuels it can be listed biogas, syngas, renewable hydrogen, and renewable light gases; these biofuels can be used to produce electrical and/or thermal energy, or as raw materials to produce other biofuels. On the other hand, fuel pellets and briquettes are the most popular solid biofuels; these biofuels can be used to produce electrical and/or thermal energy. Finally, liquid biofuels are developed to be used in transportation mainly; among them it can mentioned renewable aviation fuel, green diesel, biodiesel, biogasoline, biobutanol and bioethanol; excepting renewable aviation fuel, all the previously listed biofuels can be used for the replacement, total or partial, of diesel and gasoline from fossil origin. In particular, bioethanol can be used as an additive, in mixtures with fossil gasoline, and as biofuel, to be used in engines specially design for its combustion. In both cases, bioethanol must be anhydrous (>99.00%wt).

Bioethanol is an alcohol that can be obtained from biomass materials with high contents of sugar and starch. These biomasses must be

ISBN: 978-86-80593-73-9

pretreated in order to release the sugars contained in them; these pretreatments can be physical, chemical, biochemical or biological [2-4]. Once the polysaccharides are released, then they are processed through hydrolysis, which can be realized using concentrated acids, diluted acids, and enzymes [3, 5]. Later, the sugars are fermented with the use of microorganisms, being the most used the yeast *Saccharomyces cerevisiae* [3-6]. In the fermentation process, bioethanol is produced along with other compounds; bioethanol must be purified since it usually is presented in the fermentation broth with concentrations between 5.00 and 12.00%wt [7]. In order to perform the purification of bioethanol, distillation is the most used separation process. For this, first is necessary to separate the water from the ethanol until a composition near to the azeotropic point (95.6 %wt) [5, 8-9]. Then, the azeotropic point must be overpassed to obtain anhydrous bioethanol (99.00% wt); for this, several technologies can be used, such as azeotropic distillation, membranes, pressure swing distillation and extractive distillation; the last technology is one of the most used at industrial scale. In extractive distillation is required the use of a solvent to break the azeotrope, and allows obtaining anhydrous bioethanol. According to the literature, several solvents have been proposed for the bioethanol purification; among them it can be mentioned ethylene-glycol [7, 10], ionic liquids [11], as well as hyperbranched polymers [7, 12]. All the previously listed solvents are effective in breaking the azeotrope to produce anhydrous bioethanol; however, the energy consumption of the purification process is elevated, since the solvent also need to be separated to be recirculated. On the other hand, the use of inorganic salts has been proposed as solvent [7]. In this case, the inorganic salts modify the thermodynamic properties of the mixture bioethanol-water to perform the separation; nevertheless, these salts are dissolved in the mixture, which allows a decreasing in energy consumption during the purification process. According to the literature, calcium chloride, cobalt chloride, cupric chloride, nickel chloride, strontium bromide, sodium and potassium acetates, glucose, mercury and copper chlorides have been effective to break the azeotrope ethanol-water [8, 10, 13-17]. Both experimental and simulation studies have been realized with these inorganic salts. Indeed, calcium chloride and sodium acetate have shown good results in continuous distillation columns (packed and hoods). However, to the authors knowledge these salts have not been analyzed in batch distillation columns through experimental and simulation studies. This study is relevant since its results can be used to boost the production of bioethanol in small scale, which helps to establish local supply chains for this biofuel.

Therefore, in this work is studied the purification of bioethanol through extractive distillation using calcium chloride and sodium acetate as solvents in a batch distillation column. For this, an experimental procedure is established as well as the simulation of the process.

II. METHODOLOGY

The batch distillation column has five stages, condenser, reboiler, two heating blankets of 1200 W, three thermocouples, manual flux valve, distillate tank, feed pump, cooling water rotameter and control panel. This distillation column has a diameter of 60 mm, Fig. 1, and it as located at Guanajuato city (Universidad de Guanajuato), in México.

Figure 1. Experimental batch distillation column considered in this study.

This distillation column was simulated in Aspen Plus software, using the modules Aspen Properties and Aspen Batch modeler. The feed stream was a solution of ethanol (90.00%) and water, as a synthetic mixture to represent the outlet stream of the pre-concentration distillation column. The dimensions of the pot geometry considered were those of the experimental distillation column. The thermodynamic model selected was NRTL-E, which is the most adequate to modelling non ideal mixtures that contains polar compounds and dissolved ions [14, 18].

Moreover, the maximum amount of salt that can be dissolved was determined experimentally. For this, it was considered the mixture bioethanol (90.00%)-water at 604 mm Hg and 22°C (environmental conditions in Guanajuato city). The maximum solubility was 29 g for sodium acetate and 6.5 g for calcium chloride. For both salts, simulations were performed from 0.5 g to the maximum amount of dissolved salt. Also, the reflux ratio was varied from 0.5 to 6, based on the study of [16]. In Aspen Plus, the equilibrium stage model was select to perform the simulations. The simulation time considered was 3 h.

Based on the simulation results, the experimentation tests were carried out in the batch distillation column presented in Fig. 1. For this, the best results obtained in simulation respect to the amount of the inorganic salt were considered. The experimental test was realized by duplicate. The dynamic behavior of bioethanol composition was recorded. The results were compared with the studies presented by [16] and [19].

III. Discussion of Results

In this section, the obtained results from the experimental and simulation results. Fig. 2 shows the bioethanol mass composition with respect to the reflux ratio, for the maximum amount of sodium acetate that can be dissolved. From Fig. 2 it is observed that there are five maximum points of ethanol fraction until having a trough in reflux ratio 1.5, and as the reflux ratio increases, the ethanol fraction remains stable and increases again and remains stable, forming a step; these values, although they rise, continue to remain below the maximum points. However, the variations in the composition of bioethanol are actually very small.

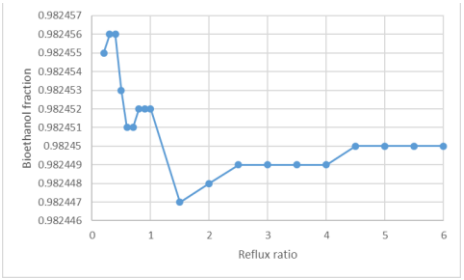

Figure 2. Variation of the mass composition of bioethanol with respect to the reflux ratio, using the maximum amount of sodium acetate that can be solubilized.

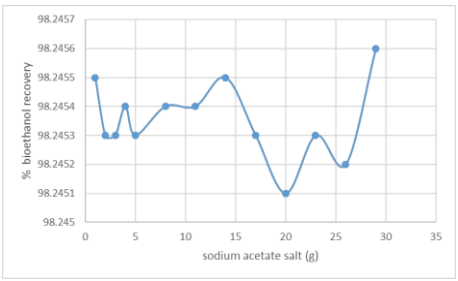

Figure 3. Variation in mass of ethanol with respect to the added amount of sodium acetate.

This process was repeated for different amounts of salt and flow ratios. The maximum mass composition values of bioethanol were selected as a function of the amount of salt. The results are presented in Fig. 3.

In Fig. 3 it can be seen that when using the 29 grams of sodium acetate, which is the saturation point, the best ethanol purification results are obtained (98.24%); however, there are no significant differences in the two first decimal positions using one gram of salt, since 98.24% is obtained, and it is a very small amount, which makes it a very attractive process from an economic point of view. In all cases it is possible to break the azeotrope and obtain high purities for bioethanol. In order to achieve purities of 99.00%, a column with a greater number of stages would undoubtedly be required.

On the other hand, Fig. 4 shows the variation in the mass composition of bioethanol with respect to the reflux ratio, for the maximum amount of calcium chloride that can be dissolved.

From Fig. 4 it can be seen that as the reflux ratio increases, the ethanol fraction continues to increase until it reaches a maximum; after this point the ethanol fraction falls, and, as in sodium acetate salt case, it continues to rise until it forms

a step. However, the variations in the composition of bioethanol are actually very small.

The process was repeated for the different amounts of salt and reflux ratio; this was realized in order to obtain the best results through recursive simulation. Only the best values of these variations are shown in Fig. 5.

In Fig. 5 it is observed that the behavior of the salt is more uniform with respect to sodium acetate salt, being able to obtain the highest purities with very small amounts of salt, 0.5 g. Unlike sodium acetate, when using calcium chloride, it is possible to obtain purities greater than 99.00% without requiring a distillation column with a higher number of stages. An interesting result is observed at high amounts of salt, where there is a decrease in the bioethanol purity. From the economic point of view, this region of the graph is not of interest, since the amounts of salt are greater and the purities are lower; however, it is necessary to validate the results of this zone experimentally, mainly due to the highly non lineal behavior of azeotropic mixtures.

Once that the best conditions were found in the simulation, then the experimental runs were carried out; the experimental run with 29 g of the sodium acetate salt was carried out in duplicate. Fig. 6 shows the dynamic variation of the ethanol composition with respect to time.

Fig. 6 shows that 9 minutes after the column stabilizes, the azeotrope is broken, and as time passes in all the samples taken this behavior continues; after 102 minutes the concentration begins to decline, which is a characteristic behavior of batch distillation. These results allow to validate those obtained in the simulation.

On the other hand, the same procedure was continued for the calcium chloride salt. The experimental run with 6.5 g of the calcium chloride salt was carried out in duplicate. The experimental results are shown in Fig. 7.

It is observed in Fig.7 that at 6.5 g of calcium chloride the azeotrope breaks at 27 minutes, after stabilization of the batch distillation column. After 70 minutes, the concentration begins to decline, which is a characteristic behavior of batch distillation.

Therefore, it is observed that with both salts it is possible to break the ethanol-water azeotrope in the experimental column. However, with

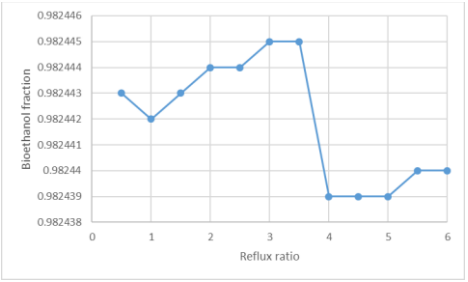

Figure 4. Variation of the mass composition of ethanol with respect to the reflux ratio, using the maximum amount of calcium chloride that can be solubilized.

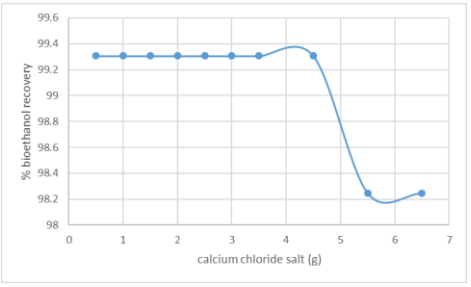

Figure 5. Variation in mass of ethanol with respect to the added amount of calcium chloride.

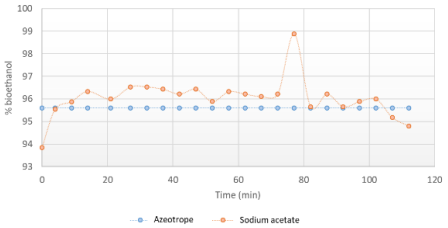

Figure 6. Variation of the composition of bioethanol with respect to time, for a quantity of sodium acetate salt 29 g.

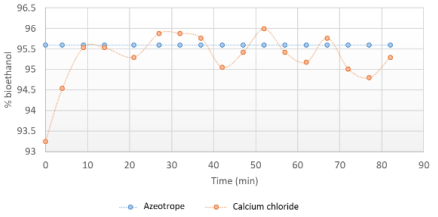

Figure 7. Variation of the composition of bioethanol with respect to time, for a quantity of calcium chloride salt 6.5 g.

sodium acetate, higher purities are achieved in very short times; this will significantly reduce energy costs during the purification of bioethanol. According to the results presented by [16] and [19] it is observed that similar purities

are obtained with a lower amount of extracting agent, and in a significantly shorter time. Moreover, the price of sodium acetate is 27% less than the one of calcium chloride; however, the amount required of calcium chloride is 77.58% less than the one required for sodium acetate. Indeed, it is possible to obtain higher purities with calcium chloride salt. Therefore, the best alternative is calcium chloride salt, due to a minor amount is required and also greater bioethanol purities can be achieved. This result is of great importance, since it is a low-cost alternative for obtaining anhydrous bioethanol.

IV. CONCLUSIONS

Bioethanol with a purity higher than that of the azeotrope was obtained by extractive batch distillation, using salts of sodium acetate and calcium chloride. For this purpose, the process was modeled in the Aspen Plus simulator, and later the results were experimentally validated in a batch distillation column.

The simulation and experimentation results show that the use of sodium acetate and calcium chloride salts, in the extractive distillation, are an economically viable alternative to obtain high purity bioethanol; in addition, the purification has low environmental impact, since it does not use organic solvents or a second recovery column, as is the case with solvent or ionic liquid distillations. In all cases, both in simulation and experimentation with the two salts, the azeotrope is broken and bioethanol is obtained with purities above the azeotropic point. However, the best alternative is calcium chloride salt, due to a minor amount is required and also greater bioethanol purities can be achieved.

In terms of simulation, Aspen Plus represents software with many capabilities for the modeling of processes in chemical engineering, which allows optimizing experimental work. Likewise, it was possible to validate that the NRTL-E thermodynamic model is the most suitable for modeling binary mixtures with salts as extracting agent, since it predicts well the composition of the azeotropic point and, additionally, the convergence of the column is simple.

ACKNOWLEDGMENT

Financial support provided by Universidad Autónoma de Querétaro, through Engineering School, and Universidad de Guanajuato, through Chemical Engineering Department, for the development of this project is gratefully acknowledged.

REFERENCES

[1] IEA. (2020). Sustainable Recovery Plan. Available at: https://www.iea.org/reports/sustainable-recovery

[2] Bayrakci, A. G., & Koçar, G. (2014). Second-generation bioethanol production from water hyacinth and duckweed in Izmir: A case study. *Renewable and Sustainable Energy Reviews*, *30*, 306–316.

[3] Vohra, M., Manwar, J., Manmode, R., Padgilwar, S., & Patil, S. (2014). Bioethanol production: Feedstock and current technologies. *Journal of Environmental Chemical Engineering*, *2*(1), 573–584.

[4] Chen, H., & Fu, X. (2016). Industrial technologies for bioethanol production from lignocellulosic biomass. *Renewable and Sustainable Energy Reviews*, *57*, 468–478.

[5] Limayem, A., & Ricke, S. C. (2012). Lignocellulosic biomass for bioethanol production: Current perspectives, potential issues and future prospects. *Progress in Energy and Combustion Science*, *38*(4), 449–467.

[6] Morales, M., Quintero, J., Conejeros, R., & Aroca, G. (2015). Life cycle assessment of lignocellulosic bioethanol: Environmental impacts and energy balance. *Renewable and Sustainable Energy Reviews*, *42*, 1349–1361.

[7] Huang, H. J., Ramaswamy, S., Tschirner, U. W., & Ramarao, B. V. (2008). A review of separation technologies in current and future biorefineries. *Separation and Purification Technology*, *62*(1), 1–21.

[8] Torres-Ortega, C. E., Segovia-Hernández, J. G., Hernández, S., Hernández, H., Bonilla-Petriciolet, A., & Mayayescas, R. (2009). Design and optimization of thermally coupled Distillation sequences for purification of bioethanol. *Computer Aided Chemical Engineering*, *27*(C), 957–962.

[9] Loy, Y. Y., Lee, X. L., & Rangaiah, G. P. (2015). Bioethanol recovery and purification using extractive dividing-wall column and pressure swing adsorption: An economic comparison after heat integration and optimization. *Separation and Purification Technology*, *149*, 413–427.

[10] Kumar, S., Singh, N., & Prasad, R. (2010). Anhydrous ethanol: A renewable source of energy. *Renewable and Sustainable Energy Reviews*, *14*(7), 1830–1844.

[11] Pereiro, A. B., Araújo, J. M. M., Esperança, J. M. S. S., Marrucho, I. M., & Rebelo, L. P. N. (2012). Ionic liquids in separations of azeotropic systems - A review. *Journal of Chemical Thermodynamics*, *46*, 2–28.

[12] Seiler, M. (2006). Hyperbranched polymers: Phase behavior and new applications in the field of chemical engineering. *Fluid Phase Equilibria*, *241*(1–2), 155–174.

[13] Barba, D., Brandani, V., & di Giacomo, G. (1985). Hyperazeotropic ethanol salted-out by extractive distillation. Theorical evaluation and experimental check. *Chemical Engineering Science*, *40*, 2287-2292.

[14] Pinto, R. T. P., Wolf-Maciel, M. R., & Lintomen, L. (2000). Saline extractive distillation process for ethanol purification. *Computers and Chemical Engineering*, *24*(2–7), 1689–1694.

[15] Llano-Restrepo, M., & Aguilar-Arias, J. (2003). Modeling and simulation of saline extractive distillation columns for the production of absolute ethanol. *Computers and Chemical Engineering*, *27*(4), 527–549.

[16] Pacheco-Basulto, J. Á., Hernández-McConville, D., Barroso-Muñoz, F. O., Hernández, S., Segovia-Hernández, J. G., Castro-Montoya, A. J., & Bonilla-Petriciolet, A. (2012). Purification of bioethanol using extractive batch distillation: Simulation and experimental studies. *Chemical Engineering and Processing: Process Intensification*, *61*, 30–35.

[17] Soares, R. B., Pessoa, F. L. P., & Mendes, M. F. (2014). Dehydration of ethanol with different salts in a packed distillation column. *Process Safety and Environmental Protection*, *93*, 147–153.

[18] Kiss, A. A., & Ignat, R. M. (2013). Optimal Extractive Destilation Process for Bioethanol Dehydration. *Energy Technology*, *1*(2–3), 166–170.

[19] Navarrete-Contreras, S., Sánchez-Ibarra, M., Barroso-Muñoz, F. O., Hernández, S., & Castro-Montoya, A. J. (2014). Use of glycerol as entrainer in the dehydration of bioethanol using extractive batch distillation: Simulation and experimental studies. *Chemical Engineering and Processing: Process Intensification*, *77*, 38–41.

Identifying Mechanical Faults of Wind Turbines with Current Signal Analysis

Abdelkarim Bouras[1], Rabah Boudiaf[2], Issam Harida[3]

[1,2,3]Electromechanical Systems Laboratory, Department of Electromechanical, Badji Mokhtar University, Annaba, Algeria, karim.bouras@hotmail.com

Abstract—**This work presents an experimental study on the identification of mechanical faults in a wind power system based on an induction generator. Several studies have shown that due to mechanical and operational constraints, misalignment and unbalance of the masses of the shaft or coupling of the wind power system are the main causes of bearing failure. Due to their modeling complexity, these single or combined mechanical faults have not received much attention from researchers, and thus, their reliable diagnosis remains a difficult task as they can generate similar frequencies. To do this, we applied the CSA (Current Signal Analysis) technique associated with signal processing techniques in order to detect the various faults of generator wind turbines and analyzed the results obtained. We have demonstrated through this experience the reliability of this technique to identify faults, thus it allows us to plan and apply a maintenance strategy in advance without disrupting operations and production.**

Keywords - wind energy, predictive maintenance, generator, fault detection, CSA.

I. INTRODUCTION

The monitoring of wind systems composed of a generator in the environment of green energy production is a fundamental task in particular, for high caliber ones, where downtime is very critical, given their importance [1]. Following mechanical alterations (unbalance, misalignment, fin degradation, erosion or clogging of the blades...), these systems are often subject to a bearing defect which represents the majority of degradations and which affects other parts of the machine, if these faults are not detected and repaired in time, the effects could be serious and costly.

However, some failures induce couple fluctuations to which the vibratory signature capacities are limited. The sensibility of the couple variations to the current produced by the generator, and consequently to the mechanical faults that induce them, makes the CSA a very efficient complementary investigation tool [2, 3].

Our research was particularly directed towards the CSA (Current Signature Analysis) [4-7]. The subsequent application of the APV (Orbital Signatures of the Park Vector) and the STFC aims to reconcile the advantages of spectral, orbital and time signatures for the benefit of reliable detection and reading of emerging bearing defects affecting a variable speed energy conversion system. In addition, this panoply of signatures has the privilege of recommending simple and low-cost equipment and can be used by maintenance operators [8, 9].

The results obtained can help to establish a perspective of an automatic approach by adding decision-making techniques that would be able to give a reliable diagnosis and improve the maintenance management of the fleet of machines.

II. THEORETICAL BACKGROUND

The analysis of stator current has become one of the most important topics in the field of fault detection. The current signature scan has become popular for detecting and locating many defects.

In the event of mechanical damage, the characteristic frequencies are modulated by the supply frequency up to a predictable frequency [10].

Our experimental investigation focuses on the case of bearings, several research works [11] show that the relation of the bearing vibration to

ISBN: 978-86-80593-73-9

the stator current spectrum can be determined by the following relations [12-14]:

$$f_{ball} = f_s \pm m f_v \ , \quad (1)$$

$$f_{ball} = f_r . \left(0.2 - 1.2 / N_b\right) , \quad (2)$$

$$f_{ball} = / f_s \pm f_{cage} \pm k f_b / \ , \quad (3)$$

$$f_{cage} = f_r . \left(0.5 - 1.2 / N_b\right) . \quad (4)$$

A. *Orbital Signatures of Park Vector*

Usually when the system is operating under ideal conditions, this approach results in a circular representation.

This orbit will serve as a reference for the detection of degradations which can affect the engine quite simply by monitoring the deviations and the degree of deformation of the patterns obtained [15].

$$x_s(t) = \sqrt{x_d^2(t) + x_q^2}(t) \ . \quad (5)$$

B. *Signatures of the Gabor Transform Spectrogram (GT)*

Gabor proposed to use the sliding-window Fourier transform to mitigate FT problems. The GT calculates the FT on a part of the selected signal using a window well localized in time.

Like the FT, the Gabor transform (GT) of a signal contains all the information carried by the signal.

The Gabor spectrogram is used to estimate the frequency content of a signal. It represents, as indicated on (6), a signal of the time domain, s(t), with the linear combination of elementary functions [16]:

$$s(t) = \sum_{m=0}^{m-1} \sum_{n=0}^{n-1} c_{m,n} h_{m,n}(t) \ , \quad (6)$$

where $h_{m,n}$ is the basic function of the time frequency,

$c_{m,n}$ is the weight of $h_{m,n}$. The Gabor transform calculates the coefficients $c_{m,n}$ for the signal s(t).

III. Experimental Context

The experiment required a test bench presented in Fig. 1 composed essentially of a generator of 3-phase rotational machine used as the wind turbine generator whose characteristics are presented in Table I.

The induction generator supply current has been measured and processed in healthy operation and in the presence of the bearing fault. The test campaign involved a deliberate degradation of a bearing ball and the corresponding cage orbit.

IV. Experimental Results And Discussions

A. *Orbital Approaches to the Park Vector (OAPV)*

Fig. 2 shows us that when the wind turbine system operates without the presence of any degradation and under ideal conditions, the pattern will be a perfect circle there $k_a = 1$ and $I_{alpha} = I_{beta}$, according to the report of major and minor axes $k_a = R / r$.

Where I_{alpha} *and* I_{beta} are the current vector components

Figure 1. Test bench.

TABLE I. Nominal characteristics.

Power	Voltage	Speed	cos φ
180 W	220 V	2960 RPM	0.8

Fig. 3 shows us that when the ellipse tends towards a narrowing accompanied by a thickening of its ring, there is a degradation of the bearing.

B. Gabor Transform Spectrogram (GT)

Fig. 4 shows the spectrogram of the healthy engine. Fig. 5 illustrates the spectrogram in the case of degradation of a single ball and the corresponding part of the Bearing cage when the engine is running at 2960 RPM.

We notice a shock with amplitude peaks and unstable oscillations between 18 and 23 dB.

V. CONCLUSION

This experimental work focused on an experimental study for the identification of mechanical faults in a wind power system based on an induction generator known for its wide use in the world of green energy production,

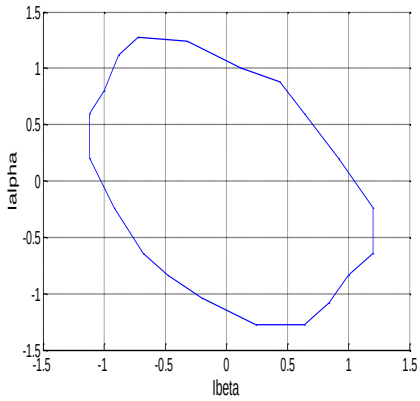

Figure 2. The healthy wind turbine system.

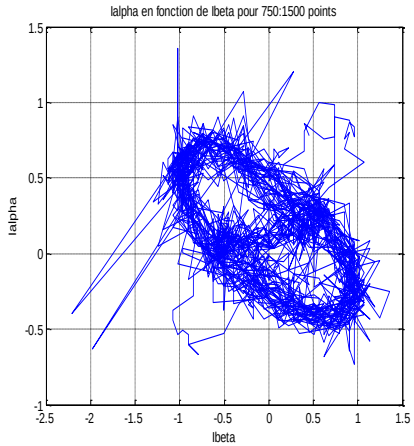

Figure 3. OPVA Bearing fault at speed 2960 RPM.

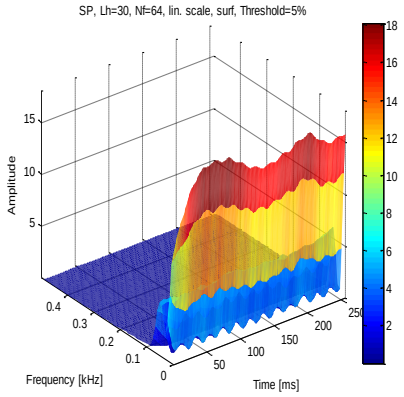

Figure 4. GT healthy wind turbine system.

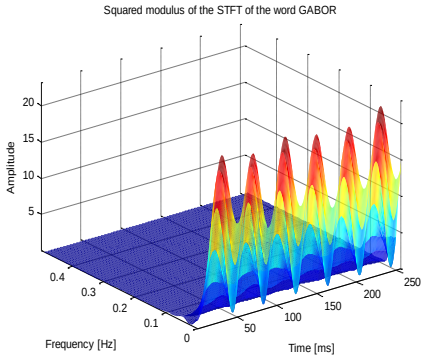

Figure 5. GT bearing fault at speeds: 2960 RPM.

and that by the current analysis for this we started with the simultaneous application of AOPV, Gabor STFC.

The current signatures using this pluralistic approach are more complementary rather than competitive with the performance of classical Fourier analysis for the early detection of ball bearing degradations.

The results obtained by these multiple techniques are easy to use. In addition, our perspective is the implementation of this technique in an automated system able to ensure reliable diagnosis and predictive detection of single and multiple mechanical faults affecting different electrical drives.

REFERENCES

[1] Elshiekh, M. E., Mansour D. A., & Azmy, A. M. (2013). Improving Fault Ride-Through Capability of DFIG-Based Wind Turbine Using Superconducting

Fault Current Limiter. *IEEE Transactions on Applied Superconductivity, 23*(3), 5601204-5601204.

[2] Hsu, M., Tan P. J. B., & Chao, C. (2018, April). Condition monitoring and fault detection of wind turbines generator. ICASI 2018. *IEEE International Conference on Applied System Invention*. Chiba, Japan.

[3] Li, J., Zhang Z., & Chen, J. (2012). Experimental Study on Vibration Control of Offshore Wind Turbines Using a Ball Vibration Absorber. *Energy and Power Engineering, 4*, 153.

[4] Gundewar, S. K., & Kane, P. V. (2020). Condition Monitoring and Fault Diagnosis of Induction Motor. *J. Vib. Eng. Technol*, 1-32.

[5] Irfan, M., Saad, N., Ibrahim, R., et al. (2015). An on-line condition monitoring system for induction motors via instantaneous power analysis. *J Mech Sci Technol, 29*, 1483-1492.

[6] Bouras, A., Bouras, S., & Kerfali, S. (2018). Prediction of the mass unbalance of a variable speed induction motor by stator current multiple approaches. *Turkish Journal of Electrical Engineering & Computer Sciences, 26*, 1056-1068.

[7] Kia, S. H., Henao, H., & Capolino, G. A. (2012, September). A comparative study of acoustic, vibration and stator current signatures for gear tooth fault diagnosis. ICEM 2012. *In 9th International Conference on Electrical Machines*.

[8] Haouem, N. E., Bouras, S., Bouras, A., & Rouabhia, C. E. (2019). Experimental investigation for the detection of high-risk external electrical faults through stator current analysis. *Australian Journal of Electrical and Electronics Engineering, 16*(2), 86-95.

[9] Krishna, M. S. R., & Ravi, K. S. (2013, March) Fault diagnosis of induction motor using motor current signature analysis. *ICCPCT. International conference on circuits, power and computing technologies IEEE*, Nagercoil, India.

[10] Skrimpas G. A., et al. (2015) Detection of generator bearing inner race creep by means of vibration and temperature analysis. *SDEMPED. 10th International Symposium on Diagnostics for Electrical Machines, Power Electronics and Drives*, Guarda, Portugal (pp. 303-309).

[11] Blödt, M., Granjon, P., Raison, B., & Regnier, J. (2010) Mechanical fault detection in induction motor drives through stator current monitoring - Theory and Application examples. *In Wei Zhang, editor. Fault Detection: INTECH*, 2010, (pp.451-488)

[12] Thomson, W. T. (2009) On-Line Motor Current Signature Analysis Prevents Premature Failure of large Induction Motor Drives. *Maintenance & Asset Management, 24*(3), 30-35.

[13] Sonje, D. M., Chowdhury, A., & Kundu, P. (2014, January) Fault diagnosis of induction motor using parks vector approach. ICAEE. *International Conference on Advances in Electrical Engineering*, Vellore, India.

[14] Riera-Guasp, M., Pineda-Sanchez, M., Perez-Cruz, J., Puche-Panadero, R., Roger-Folch, J., Antonino-& Daviu, J. A. (2012) Diagnosis of Induction Motor Faults via Gabor Analysis of the Current in Transient Regime. *IEEE Transaction on Instrumentation and measurement, 61*(6), 1583-1596.

[15] López-Pérez D., & Antonino-Daviu J. (2016, Oct) Detection of mechanical faults in induction machines with infrared thermography: Field cases. *In: 42nd Annual Conference of the IEEE Industrial Electronics Society*, Florence, Italy, (pp.7107–7112).

[16] Fournier E., Picot A., Régnier J., Andrieux C., Saint-Michel J. & Maussion P. (2015), Effects of transmission belt looseness on electrical and mechanical measurements of an induction motor. *In Proc. of the IEEE 10th International Symposium on Diagnostics for Electrical Machines, Power Electronics and Drives*, Guarda, Portugal, (pp. 259–265).

A Digital Twin Approach to PEM Fuel Cell Performance and Efficiency

Abdelhakim Merdjani[1], Natalia Kizilova[2]

[1]Warsaw University of Technology, Warsaw, Poland,
abdelhakim.merdjani.dokt@pw.edu.pl
[2]Warsaw University of Technology, Warsaw, Poland, n.kizilova@gmail.com

Abstract—**Novel "digital twin" approach is discussed in connection to better understanding the multi-physics phenomena in the working proton exchange membrane fuel cells (PEM FC). A brief review of the experimental and theoretical studies is given with a special attention to the flow field optimization aimed at easy and uniform fuel delivery to PEM and preventing the water flooding in the channels. The main strategies of the digital twin based on increasing the FC efficiency as well as the reasons of the discrepancy between the numerical simulations and experiments on the FC prototypes are discussed.**

Keywords – digital twin, proton exchange membrane, fuel cell, efficiency

I. INTRODUCTION

Fuel cells (FC) are efficient energy sources working on clean fuels like hydrogen almost without emissions into the environment. They are more powerful and energy efficient than fossil fuels. During the last decades many efforts have been made for theoretical, experimental and numerical simulations of different regimes of FC function. Lately a promising digital twin (DT) approach is widely used for optimization and increasing the efficiency of different economical, physical, biological and engineered systems including FC [1-3]. The approach is based on a combination of the 3D geometrical and physical model of the FC with experimental data measured on the FC prototype for validation of the model. Variations in the model parameters and operating conditions (fuel flow regimes) can be introduced into the 3D model, and their influence on the FC efficiency can be estimated by numerical simulations. In this paper the main components of the 3D digital twin approach for proton-exchange membrane (PEM) FC and the flow field plate (FFP) optimization are discussed.

II. STRUCTURAL COMPONENTS OF PEM FC

PEMFC are composed of a membrane electrode assembly (MEA) sandwiched between two bipolar plates that serve as current collectors (Fig. 1). MEA consists of a thin porous membrane (polymer electrolyte membrane, or proton-exchange membrane, PEM) placed between two catalyst layers (CL, distributed platinum nanoparticles) and two porous gas diffusion layers (GDL) for the fuel diffusion from the open channels manufactured in the FFP. Each component of the PEM FC can be optimized that is a subject of numerous theoretical, computational and experimental studies [4].

The following components have been studied and modified for the increase of the efficiency of the PEM FC:

1) Material, microstructure, porosity and hydrophobicity (addition of special

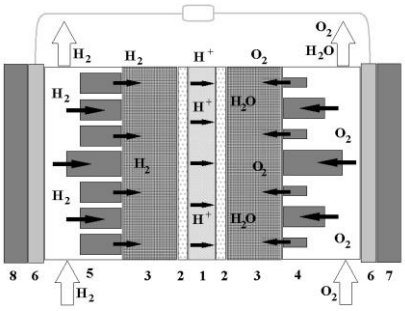

Figure 1. Structure of PEM FC: membrane (1), catalyst (2), GDL (3), anode FFP (4), cathode FFP (5), current collectors (6), end plates (7, 8).

coating) of the GDL;

2) Material, microstructure, porosity of the membrane;
3) Material, size and density of the catalyst;
4) Attaching of additional layers, e.g. microporous layer for the flooding prevention;
5) Material, size and structure of the charge collectors;
6) Design (topology and geometry) of the flow field channels for low cost delivery and uniform fuel distribution over the GDL, water management and flooding prevention at different temperatures;
7) Material, design and operating conditions of the cooling system for the FC stack.

The *efficiency* of the FC is estimated as is electric production versus the energy spent for the FC operation (pre-heating, humidification and pumping of the reactant gases, cooling of the FC, viscous and thermal dissipation, ohmic loss). Therefore, the efficiency of the FC stack depends on the parameters of each of the component (Fig. 1), and their multi-physics behavior and interaction. For instance, wider channels in the FFP design possess lower hydraulic conductivity and energy cost for the flow operation, but they also lead to the less contact area between the current collector and GDL that means higher electric resistivity and ohmic loss in the system [5]. Such complex interconnection can be accounted for in the complete 3D digital twin model of the FC [1-3]. Since the FFP design influences the heat, charge and mass transfer in each of the FC components [6], special attention is paid here to the attempts of the FFP optimization within the digital twin approach. Since the influence of all the applied and dissipated energy can be estimated in a uniform way in the terms of the irreversible entropy production, the minimum entropy production approach is used here for correct estimation of the FC efficiency [5].

III. DT Approach for PEM FC Study

The PEM converts humid gases H_2 and O_2 into water and electric work in two chemical reactions at the anode and cathode surfaces of the FC accordingly

$$H_2 + \frac{1}{2}O_2 \rightarrow H_2O + electricity + heat \quad .(1)$$

The physical phenomena determined the FC work with different fuel regimes include:

1) Pumping of the preliminary heated and humidified gases into the FFP;
2) Delivery of the fuels to the GDL through the channels at a given pressure drop;
3) Movement of the fuels through the porous GDL and microporous sublayer governed by the forced convection, diffusion and coupled thermal and electric processes;
4) Chemical reactions (1) at the PEM accelerated by the Pt nanoparticles in the CL;
5) Electric charge accumulation and conduction through the electrodes accompanied by energy dissipation and heat generation;
6) Water removal from the GDL and cathode FFP with the air flow governed by the pressure drop and accompanied by phase transitions and possible water accumulation in the porous layers and channels;
7) Cooling of the FC stack by the coolant circulating in the channels and governed by the pressure drop.

The basic physical equations for the heat, chemical potential μ_j and electric potential ϕ in each component of the FC are [5].

$$\begin{aligned}
\frac{dT_i}{dx} &= -\frac{1}{\lambda_i}\left[J_i^q - q_i^*\left(J_i^D - \frac{t_i^D J_i^e}{F}\right) - \frac{\pi_i J_i^e}{F}\right], \\
\frac{d\mu_i}{dx} &= -\frac{q_i^*}{T_i}\frac{dT_i}{dx} - \frac{1}{l_{\mu\mu}^i}\left(J_i^D - \frac{t_i^D J_i^e}{F}\right), \\
\frac{dw_i}{dx} &= -\frac{q_i^* w_i}{RT^2}\frac{dT_i}{dx} - \frac{1}{D_{wi}}\left(J_i^D - \frac{t_i^D J_i^e}{F}\right), \\
\frac{d\phi_i}{dx} &= -\frac{\pi_i}{T_i F}\frac{dT_i}{dx} - \frac{t_i}{F}\frac{d\mu_i}{dx} - r_i(J_i^e),
\end{aligned} \quad ,(2)$$

where $i=\{a,c,m\}$ are anode, cathode and membrane layers, J_i^q, J_i^D and J_i^e are the heat, mass and electric charge fluxes, w_i is the mass volume fraction (in moles) of O_2, H_2, and H_2O, F and R are the Faraday and gas constants, λ_i is the thermal conductivity, D_i is the diffusion coefficient, $l_{\mu\mu}^i$ is the mass transfer coefficient, r_i is the electric resistivity, π_i are the ion transport coefficients, t_i are the Peltier heat coefficients.

In the GDL and FFP channels (2) must be coupled with the gas diffusion equations in the porous structures and Navier-Stokes based equations for laminar, turbulent or transition flows along the channels [4, 5].

Due to complex multi-physics processes (fluid flows, heating, phase transitions, thermodiffusion, electrodiffusion, chemical reactions, hydrophobic interactions, etc.) at different scales from nano (chemical reactions at the nanoparticles and nanofibers) to macro (control, cooling, pumping, etc.) scales the *DT approaches based on direct physical modeling* are not always efficient [2]. The entropy production $\dot{S}_{irr}$ due to the irreversible coupled physical phenomena [5]

$$\dot{S}_{irr} = -\frac{\lambda_1 \left(\nabla T_c\right)^2 - \lambda_a \left(\nabla T_a\right)^2}{T} + \\ + \frac{\pi_c - \pi_a}{T}\frac{J^q}{F} - \frac{\hat{\Pi}\hat{v}}{T} - \frac{q_a}{T}\left(J^D - t^D\frac{J}{F}\right) + \\ + \frac{J^e}{4F}\left(2\left(S_w^c - S_{H2}\right) - S_{02}\right) \quad (3)$$

where the terms in the right-hand side correspond to the thermal dissipation, Peltier heat, viscous dissipation, diffusion and electrodiffusion, and entropy excess at the contact lines and fuels accordingly, and dot corresponds to the time derivative, $\hat{v}$ and $\hat{\Pi}$ are the strain rate and viscous stress tensors, can be used as an universal determinant of the completeness of the physical model and its correspondence to the measured data.

The experimental measurements on the prototypes could produce different cell voltage curves V(t) or power density (D_E) on current density (J_q) dependencies due to possible improper arrangement of the layers and poor contact between them due to outer mechanical compression in the stack, Peltier effect, high temperature induced aging of the PEM, performance degradation, etc. [4]. The non-equilibrium thermodynamics of the physical phenomena in the PEM FC (fast heat/mass transfer, high temperatures and importance of the second order effects at the micro/nanoscales) describes additional sources of the discrepancy between the physical model and experimental operating conditions [5].

Therefore, the *data-driven DT approaches* based on the relevance between the physical processes and big data technologies have been proposed. In such approaches the detailed physical model is used for generation of a large dataset of the output V(t), $D_E(J_q)$, temperature $T(t,\vec{r})$ and other output curves at given pumping P(t), fuel temperature T_f and humidity χ_f values. Then the generated dataset can be used to train the artificial intelligence (AI) component, improve the model and update the DT [7]. Recently the data-driven DT based on the machine learning methods has been proposed for establishing a remaining useful life prediction and PEMFC prognostics tools [2]. The data driven DT approaches have also been proposed for the FC health state monitoring, diagnostics and prognostics [8, 9]. DT allows interpretation and integration the collected data by the AI-based expert system constructed in the virtual space [10, 11].

Synthetic DT approaches based on a combination of the detailed 3D physical model and data-driven model have also been proposed for PEMFC [12, 13]. The mean square errors of the multi-physics fields range in the synthetic DT approach have been estimated as ~3.88 - 24.80% [12].

Since the fuel and temperature distributions over the GDL and PEM are determined by the FFP design, and the entropy production (2) can be significantly decreased by the expense of the FFP construction, operating flow regime (lower pressure drop) and efficient water removal mechanisms, the synthetic DT approach could be used based on the collected

data measured on the prototypes with different types of the FFP design.

IV. Design of FFP in PEM FC

The FFP is designed and machined to perform several functions, namely

1) Supply the required amount of the fuels to the GDL and CL according to the operating regime;
2) Provide uniform distribution of the fuels over the PEM;
3) Provide efficient water removal from the PEM and GDL;
4) Serve as a charge collector in the closed circuit (Fig.1) with low electric resistivity at the FFP/GDL interface;
5) Serve as a heat conductor from the PEM to the cooling system providing the uniform constant temperature over the PEM;
6) Provide high mechanical strength to withstand clamping pressure and thermal stress.

In the bipolar plates the flow channels are machined on both sides of the plate, and one side is acting as anode and another side is cathode. Graphite is a preferable material for the FFP due to its high strength, melting point, corrosion resistance, hydrophobicity, and relatively low weight compared to the stainless steel. When the materials for the PEM, GDL and FFP are determined, the design of FFP channels and their interconnections with the GDL remains the mostly studied problem for the CFD-based design optimization and experimental verification of different designs on the prototypes manufactured [4,14].

A continuous serpentine-like single channel design (1SD, Fig. 2a) has been proposed and modified into 2-5 parallel serpentine (Fig. 2b) designs. It remains the golden standard for the comparative study of new designs due to its high efficiency for water removal and flood prevention. The 1SD design has high hydraulic resistivity Z_h and needs significant pressure drop ΔP for flow management. Besides, it produces non-uniform fuel and, therefore, temperature distribution over the PEM. The multiply-channel designs possess lower Z_h and ΔP but worse water removal and still non-uniform fuel distributions.

The parallel (PD), interdigitated, mesh (or pin) type designs (Fig. 2b-e) and their combinations have been proposed for better fuel and water management. Later more sophisticated spiral, radial, tapered and waved channel designs have been studied [4]. During the last decades the biomimetic designs based on the water and gas delivery systems in animals and plants, including the fractal-type distributors (Fig. 2f-h) have been developed and tested. In the case of the bipolar plates,

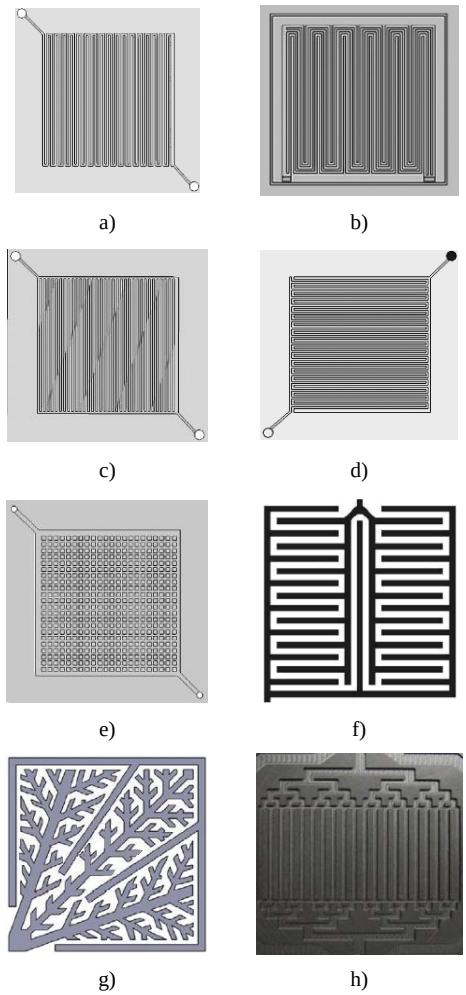

Figure 2. Conventional designs of FFP: 1SD (a); 5SD (b); PD (c); interdigitated (d); mesh (e); lung-type (f); leaf-type (g); fractal-type (h).

different designs have been used for the anode and cathode FFP. The more detailed reviews of the existing types of the FFP have been published in [4, 15].

The synthetic DT approach is based on the similarity between the and between the measured curves. Since the complete CFD model includes the fuel pumping along the anode FFP (i), gas diffusion through the GDL (ii), electrochemical reaction and heat generation in the PEM (iii), water generation, evaporation and multiphase motion outside the FC along the cathode FFP (iv), electric charge transfer through the electrodes (v) and cooling of the system (vi), the FFP designs verified by both corresponding non-isothermal CFD analyses and experimental validations have been selected, the corresponding designs and the results of their theoretical, CFD and experimental studies by different authors are summarized in Table I.

V. Comparison of the CFD and Experimental Results

FFP design optimization aimed at lower hydraulic resistance, energy expense or entropy production is carried out on detailed CFD simulations on different 3D geometries followed by experiments on the corresponding prototypes. The established ability of the SD in good water removal due to high pumping pressure and high energy loss due to the high hydraulic resistance in comparison to the low Zh, pumping pressure and worse water removal at low temperatures stimulated intense research in intermediate designs with better water removal at moderate Zh. The fuel delivery and distribution in SD is also non-uniform in comparison to other conventional designs. The plane fractal-type FFP with n=5 generations and open channels (Fig.2h) demonstrated significantly lower pressure drop in comparison to SD and PD, and quite high voltage [16]. Different fractal designs with open channels revealed higher efficiency and water removal compare to conventional designs but not the SD with different number of the parallel channels [4]. Composition of the of the fractal FFP in several parallel graphite plates allow gas delivery through the closed channels with open outlets only [14, 15, 17]. The relationships between the diameters of the channels in the tree was determined based on the Murray's law [14, 15], constructal law [17], minimum entropy generation [14, 15] and other optimization criteria. The rectangle channels in the open-channel fractal-type FFP

TABLE I. Modern FFP designs; their experimental and CFD estimation.

FFP type	FFP dimensions (cm)	RH (%)	Pressure drop	current density (A/cm2)	Temperature (°C)	Efficiency rise (%)	Compared to	Water flooding	Validation	Reference
1-layer lung type	7x7 (Fig.2f)	50 60	1 bar	<1.5	50^{K*} 60^{A*}	34	3SD	n/a	E^*	[16, 17]
5-layer lung type (n=3,4,5)	5x5	50 75	75% ↓ 50% ↓	> 0.8	70	20 30	1SD	higher at RH=100% and n=5	T^* & E^*	[18-20]
T-type fractal	5x5	50 60 70	0.5 bar	<1.8	80	11	1SD	higher at RH=70%	T^* & CFD & E^*	[15, 21]
1SD	7x7	70	1 bar	<1	50	-	-	high	CFD & E^*	[22]
2 SD	7x7	70	1 bar	<1	50	-10.53	1SD	lower	CFD & E^*	[22]
3 SD	7x7	70	1 bar	<1	50	-19.74	1SD	lower	CFD & E^*	[22]
Waved PD +SD	5x5 10x10	70	2 bar	0.3175	60	7.7-14	1SD	higher at cathode side	CFD & E^*	[23]
wavy 1SD	7.4x7.4	100	1-3 bar	1	50 60 70	3 7 14.5	1SD	lower	AnSys CFD & E^*	[24]
Ribs to channel width r=0.1-0.9	-	-	2 bar	<2.4	80	12.5 17.2 14.9	PD	n/a	T^* & CFD	[25, 26]
Gingko leaf-type	5x5	70	97% ↓ of SD		80	7 ↓ SD 40 ↑ PD	SD, PD	lower PD higher SD	E^*	[27]

A^* - anode, K^* - cathode, E^* - experimental, T^* - theoretical

can be engraved in the graphite plate. The designs with different number of generations (n=5-7) and number of outlets N=16-64 have been tested and compared to the serpentine designs [15, 22-27]. The 3-5 layer lung-type and fractal-type designs are engraved in the inner layers of the graphite or 3D printed plates such as the N outlets are in contact with GDL [19-21]. The latter provides the most uniform fuel distribution over the membrane when the number n and size of the outlets are computed based on the Peclet number Pe~1 that provides the best conditions for the uniform fuel diffusion over the catalyst layer and, therefore, a uniform temperature distribution inside the MEA [21]. When the coupled fluid flow, thermal, electric, a chemical reactions (1)-(3) are accounted in the numerical model, the experimental verification demonstrate appropriate correspondence between theoretical, numerical and experimental studies [18-26]. The main problems in discrepancy between them are the phase transition phenomena, multiphase flow, water accumulation and water flooding of the GDL and FFP which are complex temperature, electric potential and mechanical stress dependent physical processes. Therefore, a combination of the direct physical modeling and data-driven DT approach is a promising synthetic method that needs reasonably short computation time and low complexity of the numerical model.

VI. DATA-DRIVEN DT APPROACH

Experimental studies on the FC stacks working at different operating conditions (OC) like inlet mass flows Q(t) of the fuels, their temperature (T_{in}) and relative humidity (RH) give measures voltage-current density V(J) (Fig. 3a), voltage-current, voltage-power density V(W), voltage-time V(t) (Fig. 3b) curves. During the experiments some rapid drop in the measured signals can be observed (Fig. 3b) that is usually related to local temperature decrease over the membrane due to FFP flooding by the water condensed in the turns of the serpentine FFP, T-junctions and small channels of the fractal FFP, and other designs [4, 14, 15, 19].

The sets of the measured time series V(t), Q(t), and others together with the OC data (T_{in}, RH, etc.) can be filtered, smoothed and normalized for further data treatment (Fig. 4). The smoothed curves can be then differentiated, and the computed time series $V'(t), V''(t)$, and others can later be used for the analysis of the behavior of the dynamical system in the phase planes $V'(V), V''(V'), V''(V)$ for more detailed extraction of useful information on the decision making for the FC modeling by the DT approach. The measured and computed data can be accumulated in the database for further training of the artificial

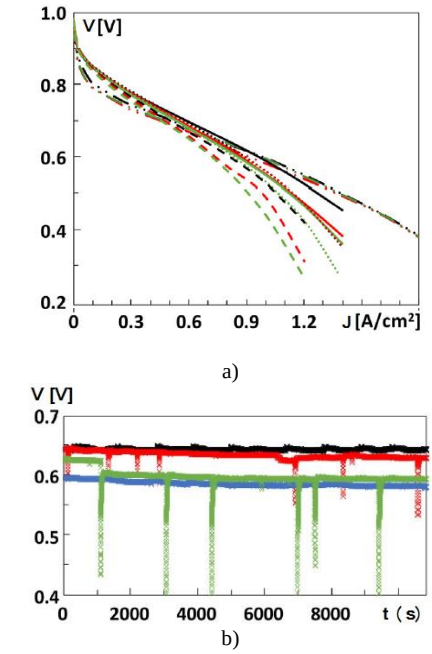

Figure 3. Measured V(J) (a) and V(t) (b) curves (from [2]).

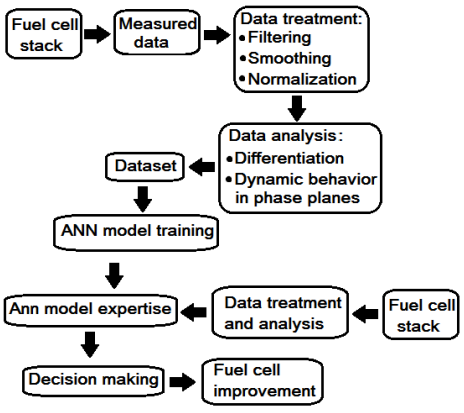

Figure 4. Proposed data-driven DT approach.

neural network (ANN) model. The trained model can be used for the expert estimation of efficiency of new designs of the FFP, GDL, and other components of FCs.

The component 'Data analysis' (Fig. 4) can be extended by novel mathematical methods of Big Data statistics like fractal and wavelet analysis, signal decomposition into the Fourier series (spectral analysis) or other basic functions. An example of the signal decomposition according to the Big Data analysis approach

$$V(t) = V_{mean}(t) + V_{cycl}(t) + V_{fract}(t) + \varepsilon(t), \quad (4)$$

where V_{mean}, V_{cycl}, V_{fract} and $\varepsilon(t)$ are the mean, oscillating (seasonal), irregular (fractal) components and residuals are presented in Fig. 5. Similar approach has been used for prediction of remaining useful life of fuel cells.

The computed spectral, fractal, phase and other time series parameters together with OC and statistical values (mean, dispersion) $\{\chi_j\}_{j=1}^{p}$ have been compared to the corresponding sets from the database $\{\chi_j^{dp}\}_{j=1}^{p}$ (Fig. 4) and the efficiency criteria has been introduced as

$$\Theta_{eff} = \frac{1}{p}\sum_{j=1}^{p}\left|\chi_j - \chi_j^{dp}\right|, \quad (5)$$

where p is the current number of the indexes in the database.

$$\Theta_{eff}(\chi_1, \chi_2, \ldots \chi_p) \to \min, \quad (6)$$

The decision making (Fig. 4) has been carried out by using the multicriteria approach. Preliminary computations have been done based on the open access FC datasets [2]. The relative accuracy RA(t) and precision P(t) curves have been computed for different designs of the FFPs (Fig. 2ab, Table 1). It was shown, the T-junction fractal FFP have similar RA(t) and P(t) curves with $\min(\Theta_{eff}) = 0.362$, 0.353 and 0.348 accordingly, while other convention designs (Fig. 2c-e) have $\min(\Theta_{eff}) = 0.65 - 0.78$, and the biomimetic shapes (Fig. 2f-h) have $\min(\Theta_{eff}) = 0.5 - 0.65$.

VII. Conclusions

Digital twin approach to better understanding the complex multiphysics processes in the FC and CFD-based design optimization of its structure is essential for future technologies. A detailed literature review on the design modification of the anode and cathode flow fields is presented. The main reasons of the discrepancy between the numerical results and experimental measurements on the prototypes are discussed.

The main reasons of the discrepancy between the numerical and experimental data are (1) non-uniform GDL structure; (2) non-plane geometry of GDL and other layers due to their deformation by mechanical compression; (3) imperfect matching of GDL and gaskets that leads to the fuel leakage; (4) non-parallel arrangement of the flow field channels and their wall roughness of the channels wall; (5) ageing of the materials; (6) phase transitions and water flooding of the channels and GDL;

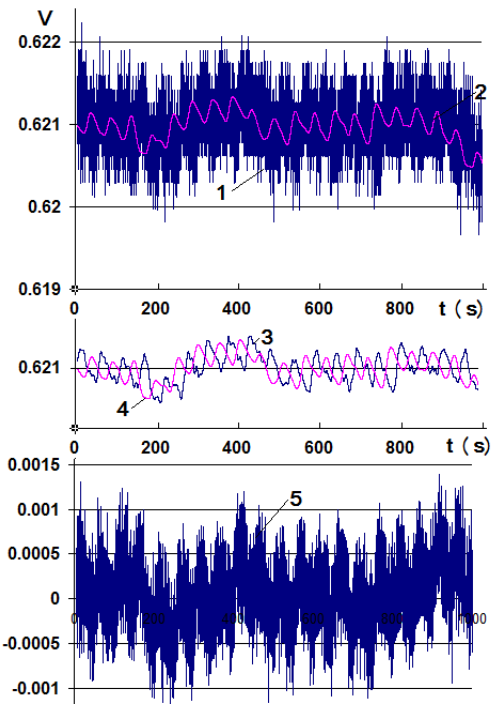

Figure 5. Measured signal V(t) (from [2]) (a); and its decomposition into $V_{mean}(t), V_{cycl}(t), V_{fract}(t)$ (b); signals.

(7) accuracy of the software used for complex multiphysics simulations with chemical reactions in the narrow channels, micro and nanoporous layers. As a result, the difference between the CFD results and experimental studies could reach 5-20%.

The proposed data-driven DT approach allows fast estimation of the most efficient FFP design based on the measured data and the collected datasets obtained on the FC stacks with different FFP designs.

REFERENCES

[1] Wang, B., Zhang, G., Wang, H., et al. (2020) Multi-physics-resolved digital twin of proton exchange membrane fuel cells with a data-driven surrogate model. *Energy & AI*, *1*, 100004.

[2] Meraghni, S., Terrissa, L. S., Yue, M., et al. (2021) A data-driven digital-twin prognostics method for proton exchange membrane fuel cell remaining useful life prediction. *International Journal of Hydrogen Energy*, *46*, 2555-2564.

[3] Mohammadi Moghadam, H., Foroozan, H., Gheisarnejad, M., & Khooban, M. H. (2021). A survey on new trends of digital twin technology for power systems. *Journal of Intelligent & Fuzzy Systems*, *41*(2), 3873-3893.

[4] Sauermoser, M., Kizilova, N., Pollet, B. G., & Kjelstrup, S. (2020). Flow field patterns for proton exchange membrane fuel cells. *Frontiers in Energy Research*, *8*, 13.

[5] Kjelstrup, S., & Bedeaux, D. (2008). Non-equilibrium thermodynamis of heterogenous systems. Series on advances in statistical mechanics. World Scientific.

[6] Marappan, M., Palaniswamy, K., Velumani, T., Chul, K. B., Velayutham, R., Shivakumar, P., & Sundaram, S. (2021). Performance studies of proton exchange membrane fuel cells with different flow field designs–review. *The Chemical Record*, *21*(4), 663-714.

[7] Min, Q., Lua, Y., Liua, Z., Sua, C., & Wang B. (2019). Machine learning based digital twin framework for production optimization in petrochemical industry. *International Journal of Information Management*, *49*, 502–519.

[8] Tao, F., Zhang, M., Liu, Y., & Nee A.Y.C. (2018). Digital twin driven prognostics and health management for complex equipment. *CIRP Annals*, *67*(1), 169-172.

[9] Ma, R , Yang, T , Breaz, E., Li, Z., Briois, P., &Gao F. (2018). Data-driven proton exchange mem- brane fuel cell degradation predication through deep learning method. *Applied Energy*, *231*, 102–115.

[10] Stefan, B., & Roland, R. (2016). Digital twin - the simulation aspect. In: *Mechatronic futures*. Springer. Chapter 5, 59-74.

[11] Wang, B., Xie, B., Xuan, J., & Jiao, K. (2020). AI-based optimization of PEM fuel cell catalyst layers for maximum power density via data-driven surrogate modeling. *Energy Conversion Management*, *205*, 112460.

[12] Wang, B., Zhang, G., Wang, H., Xuan, J., & Jiao, K. (2020). Multi-physics-resolved digital twin of proton exchange membrane fuel cells with a data-driven surrogate model. *Energy and AI*, *1*, 100004.

[13] Tao, F., & Qi, Q. (2019). Make more digital twins. *Nature*, *572*, 490–491.

[14] Sauermoser, M., Kjelstrup, S., Kizilova, N., Pollet, B. G., & Flekkoy, E. G. (2020). Seeking minimum entropy production for a tree-like flow-field in a fuel cell. *Physical Chemistry & Chemical Physics*, *22*(13), 6993-7003.

[15] Kizilova, N., Sauermoser, M., Kjelstrup, S., & Pollet, B.G. (2020). Fractal-like flow-fields with minimum entropy production for polymer electrolyte membrane fuel cells. *Entropy*, *22*, 176.

[16] Tüber, K., Oedegaard, A., Hermann, M., & Hebling, C. (2004) Investigation of fractal flow-fields in portable proton exchange membrane and direct methanol fuel cells. *J Power Sources*, *131*, 175-181.

[17] Badduri, S. R., Srinivasulu, G. N., & Rao, S. S. (2019). Experimental analysis of PEM fuel cell performance using lung channel design bipolar plate. *International Journal of Green Energy*, *16*(15), 1591-1601.

[18] Trogadas, P., Cho, J. I. S., Neville, T. P., et al. (2018). A lung-inspired approach to scalable and robust fuel cell design. *Energy & Environmental Science*, *11*, 136-143.

[19] Cho, J. I. S, Neville, T. P., & Trogadas, P. (2019). Visualization of liquid water in a lung-inspired flow-field based polymer electrolyte membrane fuel cell via neutron radiography. *Energy*, *170*, 14-21.

[20] Cho, J. I. S., Marquis, J., Trogadas, P., et al. (2020) Optimizing the architecture of lung-inspired fuel cells. *Chemical Engineering Science*, *215*, 115375.

[21] Sauermoser, M., Pollet, B. G., Kizilova, N., & Kjelstrup, S. (2021). Scaling factors for channel width variations in tree-like flow field patterns. An experimental study. *International Journal of Hydrogen Energy*, *46*(37), 19554–19568.

[22] Velisala, V., & Srinivasulu, G. N. (2018). Numerical simulation and experimental comparison of single, double and triple serpentine flow channel configuration on performance of a PEM fuel cell. *Arabian Journal for Science and Engineering*, *43*(3), 1225-1234.

[23] Vijayakrishnan, M. K., Palaniswamy, K., Ramasamy, J., et al. (2020). Numerical and experimental investigation on 25 cm^2 and 100 cm^2 PEMFC with novel sinuous flow field for effective water removal and enhanced performance. *International Journal of Hydrogen Energy*, 45(13), 7848-7862.

[24] Seyhan, M., Akansu, Y. E., Murat, M., Korkmaz, Y., &Akansu, S. O. (2017). Performance prediction of PEM fuel cell with wavy serpentine flow channel by using artificial neural network. *International journal of hydrogen energy*, *42*(40), 25619-25629.

[25] Abdulla, S., Seepana, M. M., & Patnaikuni, V. S. (2020). Performance Comparison of PEM Fuel Cell with Enhanced Cross-Flow Split Serpentine and Single Serpentine Flow Field Designs. *Arabian*

Journal for Science and Engineering, *45*(9), 7691-7703.

[26] Pan, W., Chen, X., Wang, F., & Dai, G. (2021). Mass transfer enhancement of PEM fuel cells with optimized flow channel dimensions. *International Journal of Hydrogen Energy*, *46*(57), 29541-29555.

[27] Kang, H. C., Jum, K. M., & Sohn, Y. J. (2019). Performance of unit PEM fuel cells with a leaf-vein-simulating flow field-patterned bipolar plate. *International Journal of Hydrogen Energy*, *44*(43), 24036-24042.

The Design of the Index for Comprehensive Assessment and Ranking of Distribution System Operators in Electricity for the Corresponding RAB-tariff Setting

Serebrennikov Bohdan[1], Petrova Kateryna[2], Serebrennikov Serhii[3]

[1]Institute of Economics and Forecasting of Ukraine's National Academy of Sciences, Kyiv, Ukraine, bs.serebrennikov@gmail.com

[2,3]Central Ukrainian National Technical University, Kropyvnytskyi, Ukraine, [2]kateflash27@gmail.com, [3]sv.serebrennikov@gmail.com

Abstract— **Critical deterioration and obsolescence of network infrastructure in electricity are typical for most member countries of the Energy Community. The situation requires elaboration of an efficient economic mechanism stimulating distribution system operators (DSO) to drastically improve the technical state of the infrastructure to a level acceptable in the EU. For this purpose, it is suggested to set up the profitability margins for DSOs corresponding to their multi-criteria ranking encompassing technical state of networks, efficiency, load, reliability, innovation, and quality of electricity. Currently, there are 32 electricity DSOs in Ukraine, whose distribution tariffs significantly vary within the range of 256.9-982.4 UAH/MWh. The distribution tariffs are radically irrelevant to the operators' ratings. A comprehensive fact-based assessment of the technical state of DSOs' network infrastructure should provide a basis for appropriate tariff setting incentivizing grid modernization. For the calculation of DSOs' ranking scores, the fuzzy logic approach was applied. A method for setting individual distribution tariffs rigidly related to the technical state of the infrastructure has been developed. The economically justified theoretical value of the minimum tariff level was determined individually for each operator considering its break-even point. The maximum tariff level remained equal for all DSOs assessed.**

Keywords - distribution system operator, electricity, tariff setting, ranking criteria, assessment

I. INTRODUCTION

The European Union established the Energy Community to involve neighboring countries in the pan-European energy market by reforming domestic energy markets and bringing their regulatory framework in line with EU legislation. That requires [1]:

- introducing consistent regulatory and market framework capable of attracting investments in electricity generation and the grid infrastructure;
- development of the energy market facilitating cross-border trade and further integration with the EU's market;
- improving the environment and energy efficiency;
- enhancing competition at the regional level, etc.

Integration of Ukraine and the EU's electricity markets is only possible in case of ensuring an appropriate state of market infrastructure, which requires the application of new efficient incentives for DSOs to improve the technical condition of their networks. For the country, which is at the initial stage of competitive market development, the issues of ensuring reliable and efficient electricity systems operation with permanent growth of load on the

excessively worn-out grid have become critical. For instance, in Ukraine, more than 17% of substation equipment and 67% of electricity transmission lines have been operating for more than 40 years [2]. This leads to extra maintenance costs, electricity losses, and low reliability of the electricity supply. Thus, the number and duration of electricity interruptions (SAIDI) in Ukraine substantially exceed European standards. An ordinary Ukrainian consumer has not been supplied with electricity for more than 1100 minutes annually, whereas, in the Netherlands, SAIDI is 27 minutes, in Germany – 23, in Denmark – 19 [2].

International experience demonstrates [3-7] that there is still no unified tariff policy on electricity distribution in European countries. The interaction between regulator and distribution system operators (DSO) is determined by national legislation. This depends on peculiarities of distribution systems in different countries: the difference in the number and composition of end-users, the ownership structure of distribution networks, geographical differences, etc. In European countries, the regulators primarily exploit a combination of two approaches: regulation of the rate of return on capital expenditures (CAPEX) and regulation of the upper margin of income (tariff/price) for operational expenses (OPEX). The regulation of the basic tariff is applied only in Norway and the Netherlands, and the regulation based on performance is adopted in Great Britain [3-6].

The new tariff methodology for distribution companies sets the profitability as a percentage of the value of the regulatory asset base – RAB-regulation (Regulatory Asset Base) [8, 9]. In Great Britain and Australia, the model of RAB appeared after the privatization of major industries with extensive infrastructure (primarily networks); it also safeguarded from the retrospective "withdrawal of assets" [10]. The electricity distribution costs have been halved in 15 years under RAB tariffs in the UK.

The article [11] revealed the main advantages and disadvantages of the RAB and PPP (Public-Private Partnerships) models. In particular, it is emphasized that the RAB approach may lead to excessive capital expenditures to increase the base for the income calculation. At the same time, the RAB is quite flexible in terms of economic regulation.

The German experience of investments, with a massive amount of 109 DSOs, confirms the viability of the RAB method. After the transition to RAB regulation in 2009, investments in electricity networks have increased almost 1.5 times [12].

In pursuance of the provisions of Directive 2009/72/EU, Ukraine has adopted the Law "On the Electricity Market" on 13.04.2017, which envisages the transition to RAB distribution tariffs. The Regulator (NEURC) has developed a regulatory framework for the introduction of RAB regulation with the establishment of equal rates of return on the new asset base (investment in new assets) and the old base (existing assets of companies) – 12.5% per annum. Currently, the issues of dividing the DSOs' asset base into two parts – new and old – are being actively discussed, assigning a certain percentage of profitability to each; however, this approach does not take into account several other important quantitative and qualitative indicators regarding the technical state of the network infrastructure.

The US consulting company IHS Energy claims that in the EU regulatory system, the rate of return on old and new assets is equal or slightly different and that it is not critical whether the asset is new or old because it does not affect commercial risks or maintenance benefits associated with the operation of the asset. However, it should be noted that the EU network infrastructure is characterized by superior condition, while in Energy Community member states, the wear and obsolescence of grid elements reach 60-85%. Therefore, at least in the early stage, while the quality of DSOs' services will improve to an acceptable level, it is necessary to differentiate RAB tariffs considering quantitative and qualitative indicators of DSOs' performance.

The electricity DSOs, unlike producers and suppliers, are natural monopolies. Thus, it requires state regulation of tariffs for electricity distribution provided by independent national energy regulators.

In the regulated segment of Ukraine's electricity market, the price caps are set for peak hours (8…24 h) $C_{MAX.D}$=2.048 UAH/kWh and for off-peak hours (0…8 h) $C_{MAX.H}$=0.959 UAH/kWh. The segment of bilateral agreements remains non-regulated. To cover the costs of "green" (feed-in) tariffs, 85% of Energoatom's electricity output sells to the Guaranteed Buyer by the regulated price of 0.567 UAH/kWh and

50% of Ukrhydroenergo's output by the price of 0.674 UAH/kWh.

The Regulator sets considerably different tariffs for regional DSO: for voltage class 1, tariffs vary in the range of 0.0831-0.2284 UAH/kWh (2.75 times), and for voltage class 2 – 0.5356-0.9824 UAH/kWh (almost two times).

It is essential to objectively determine the asset base of each DSO and differentiated profit set at a level that would stimulate DSOs to improve the technical condition of networks. Ranking the DSO according to the current state of the network infrastructure will provide a basis for the selective allocation of investments and ensure a competitive environment between DSOs.

However, insufficient transparency and data availability on DSOs' performance [13] significantly complicate their appropriate ranking. Therefore, assessment of DSOs is proposed to deliver applying fuzzy logic approach.

The article aims to provide an efficient mechanism of economic incentives in the regulated segment of the electricity market to improve the technical condition of worn-out electricity distribution networks.

II. METHODOLOGY

Differentiation of economic incentives for DSOs aimed at modernization of distribution networks is advisable to set up their profitability following the rating scores of multi-criteria ranking.

For an objective and evidence-based assessment of the current state of the network infrastructure, we chose 20 indicators, which compose a 3-level rating system according to 6 criteria y_i (Fig. 1):

The 1st criterion (y_1) is the efficiency of the distribution system:

$$y_1 = f_1(K_{TC,} K_{CC}) \,, \qquad (1)$$

where $K_{TC} = \Delta W_{TC} \cdot 100\% / W_\Sigma$ – part of technological costs ΔW_{TC} of electricity in the total value of W_Σ of incoming electricity to the grid; K_{CC} , – part of the electricity losses (commercial and non-commercial);

The 2nd criterion (y_2) is the technical condition of distribution network elements, which are functionally related to the degree the overhead electricity lines (OHL) (K_{PL}) and transformation substations (TS) tear and wear (K_{TS}):

$$y_2 = f_2\left(K_{PL}, K_{TS}\right) \,, \qquad (2)$$

where $K_{PL} = \left(L_{REC} + L_{PEP}\right) / L_\Sigma$ – part of the OHL length, which need reconstruction L_{REC} or the replacement L_{PEP} , in the total length L_Σ , coefficient of $K_{PL} = \left\{K_{PL}{}^{110}; K_{PL}{}^{35}; K_{PL}{}^{10}; K_{PL}{}^{0,4}\right\}$ considering the state of distribution OHL with voltage 0,4…110 kV; $K_{TS} = \left(N_{REC} + N_{PEP}\right) / N_\Sigma$ – part of TS, which need reconstruction N_{REC} or replacement N_{PEP} in their total number N_Σ , coefficient $K_{TS} = \left\{K_{TS}{}^{110}; K_{TS}{}^{35}; K_{TS}{}^{10}\right\}$ considering the state of TS 10…110 kV;

The 3rd criterion (y_3) is the level of reliability (continuity) of electricity supply:

$$y_3 = f_3\left(SAIDI, K_{NT}, SAIFI\right), \qquad (3)$$

where *SAIDI*, *SAIFI* are indicators for economic assessment of the reliability of electricity supply, SAIDI is an indicator of average duration of interruptions, $SAIDI = \sum_{i=1}^{k} t_i \cdot n_i \Big/ n$; t_i – time of the i -numbered long term (more than three min.) electricity interruptions; n_i – the number of shutting down electric power outlets; k – the number of long-term electricity interruptions during the reporting period; $i = 1, 2, 3, ..., k; n$ – total number of electric outlets; $SAIDI = \left\{SAIDI_M; SAIDI_C\right\}$ considering the duration of the electric outlets for urban $SAIDIM$ and rural $SAIDIC$ customers; $K_{NT} = W_{ESNT} \cdot 100\% / W_\Sigma$ – part of the electricity, unreleased due to emergency shutdowns, of the

total volume of W_{Σ}; $SAIFI$ – an indicator of the average number (frequency) of interruptions in electricity supply, calculated as the ratio of the number of long breaks due to electricity.

The 4th criterion (y_4) is the load of the distribution system, which is characterized by the coefficient of system load $K_{LOAD.F}$ and the load factor of the installed capacity of transformers $K_{UIC.TR}$:

$$y_4 = f_4(K_{LOAD.F}, K_{UIC.TR}) , \qquad (4)$$

where $K_{LOAD.F} = W_R / \left(T \cdot P^{MAX}\right)$, W_R – the volume of the electricity, transmitted to the network over time T operation of the distribution system in hours per year, P^{MAX} – peak load of the distribution system; $K_{UIC.TR}$ – part of electricity transmitted to consumers at low voltage in the total installed capacity of all transformers in the distribution system.

The 5th criterion is the level of innovation (y_5), which depends mainly on the coefficient of renovation of the equipment K_{RE} , degree of metering systems automation K_{AAS} , and coefficient of distributed generation units introduction $K_{RC.DG}$:

$$y_5 = f_5\left(K_{RE}, K_{AAS}, K_{RC.DG}\right) , \qquad (5)$$

where $K_{RE} = N_{RE} / N_{\Sigma}$ – part of the renovated network equipment in its total number; $K_{AAS} = N_{AU} / N_{\Sigma AS}$ – part of the outlet points of electricity, equipped with automated commercial metering systems (ACMS); $K_{RC.DG} = N_{RC.DG} / N_{\Sigma DG}$ – part of implemented connections of distributed generation sources in the total number of system users' requests.

The 6th criterion is the quality of electricity (compliance of physical parameters of electricity with established standards) (y_6), which primarily depends on the deviation of voltage from nominal value δU_y (normally permissible value $\delta U_{y.н} = \pm 5\%$ and maximum permissible $\delta U_{y.гр} = \pm 10\%$) , Δf – frequency deviation in the electrical network (normally permissible value ±0.2 Hz, maximum permissible ±0.4 Hz):

$$y_6 = f_6(\left|\delta U_y\right|, \Delta f) , \qquad (8)$$

(the crucial criterion y_6 can be considered in case of technical possibility of smart ACMS permanently fixing quality parameters –

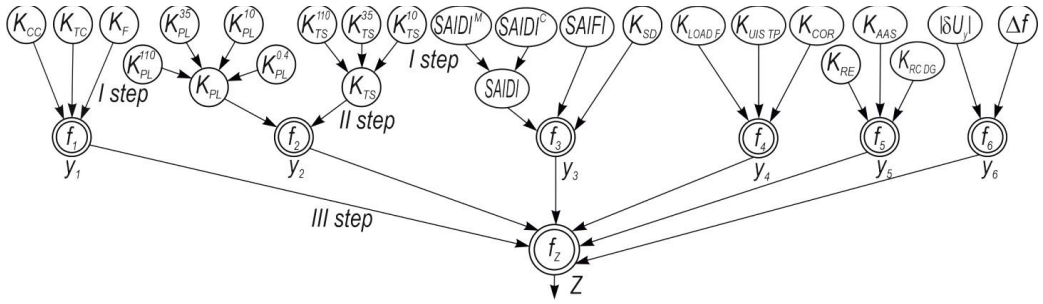

Figure 1. The hierarchical composition of the indicators regarding the state of the network infrastructure and aggregation of partial criteria (y_1-y_6) to the integrated index Z of the DSO rating.

deviations and fluctuations of voltage and frequency, harmonic composition, non-sinusoidality and voltage asymmetry, and other electric energy parameters).

DSOs ranking can be delivered according to a set of partial criteria y1-y6, but more convenient is to apply a single integral index Z (Fig. 1). Correct aggregation of indicators and criteria considering the level of their significance can be carried out by the convolution method, using the OWA-operator Jaeger [13], where Fishburne's coefficients represent the weights in the convolution [14]. Performing successive convolutions of indicators K_i and partial criteria y_j according to Fig. 1, we obtain a single index Z, which integrates all the selected indicators of the distribution systems technical condition.

Among the indicators (7), it is necessary to distinguish the maximization indicators ($K_i \in K^{\max}$), which increase the rating ($K_{RE}; K_{AAS}; K_{RC.DG}) \rightarrow$ max), in contrast to minimization indicators ($K_i \in K^{\min}$), when it is optimal to reduce the indicators values, in particular $(K_{TC}; K_{CC}; K_{PL}; K_{TS}; SAIDI;$

$K_{NT}; SAIFI; K_{LOAD.F}; K_{UIC.TR}) \rightarrow min.$

III. Assessment Results

The data for defining the technical condition of distribution networks elements were received from publicly available statistical reports on DSOs operation. The analysis results were obtained for the sample of three typical DSOs (with maximum, minimum, and average of the 24 regional energy distribution companies Z values) by the criteria y_2 shown in Table I.

Since the limits in which indicators may vary (7) are significantly different and have different physical nature, it is reasonable to perform their normalization before calculating Z. This will allow moving from named to relative units and a standard scale. The transition to the normalized scale [0;1] is carried out by linear transformation of the natural scale of each indicator K_i considering the vector of its change – to a maximum or a minimum.

Then the current values K_i^N are obtained with the aligned vector of their change to the maximum under the following evaluations:

$$K_i^N = \begin{cases} \dfrac{K_i - K_{MIN}}{K_{MAX} - K_{MIN}}, \text{for } K_i \in K^{\max} \\ \dfrac{K_{MAX} - K_i}{K_{MAX} - K_{MIN}}, \text{for } K_i \in K^{\min} \end{cases}, \quad (9)$$

where K_i – the value on a natural scale, K_{MIN} – the starting point of the scale calculation (minimally possible indicator value), K_{MAX} – maximal indicator value.

For instance, let's define the normalized $K^{110\,N}_{PL(\text{DSO}-3)}$ for the DSO-3, which was the minimization indicator ($K_{PL} \in K^{\min}$):

$$K^{110\,N}_{PL(\text{DSO}-3)} = \frac{K^{110}_{PL\,MAX} - K^{110}_{PL(\text{DSO}-3)}}{K^{110}_{PL\,MAX} - K^{110}_{PL\,MIN}} =$$

$$= \frac{52.1 - 5.9}{52.1 - 0} = 0.887$$

Normalization of the values of other indicators is performed following (9).

TABLE I. INITIAL INDICATORS KI FOR THE DEFINITION OF THE TECHNICAL CONDITION OF THE ELEMENTS OF CHARACTERISTIC DISTRIBUTION NETWORKS BY CRITERION Y_2.

№	DSO*	Indicators of technical condition						
		K_{PL}				K_{TS}		
		K_{PL}^{110}	K_{PL}^{35}	K_{PL}^{10}	$K_{PL}^{0,4}$	K_{TS}^{110}	K_{TS}^{35}	K_{TS}^{10}
1	DSO-3	5.9	3.07	2.02	12.19	4.23	0.38	10.71
2	DSO-10	15.48	9.81	6.47	8.76	0.00	0.00	1.54
3	DSO-4	52.10	43.62	15.34	28.42	0.00	0.00	22.52
Maximal value of the indicator (K_{MAX}) for the 24 DSOs		52.10	74.44	21.50	30.34	48.00	29.72	41.77
Minimal value of the indicator (K_{MIN}) for 24 DSOs		0.00	0.00	1.34	0.45	0.00	0.00	0.00

*Number of the DSOs corresponds to the alphabetical list of 24 regional DSOs in Ukraine

TABLE II. RESULTING VALUES OF THE PARTIAL CRITERIA Y_j^*.

№	DSO	Partial criteria y_1-y_5				
		Cost-effectiveness of the distribution system (y_1)	*Technical state of the distribution networks elements (y_2)*	*Reliability of the electricity supply (y_3)*	*Load factor of the system (y_4)*	*Level of innovation (y_5)*
1	DSO-3	1.000	0.877	0.852	0.711	0.852
2	DSO-10	0.306	0.882	0.740	0.357	0.672
3	DSO-4	0.001	0.634	0.379	0.089	0.373

*criteria y_6 can be calculated when automated electricity metering systems (AEMS) fix quality parameters of electricity

Since for the definition of most distribution systems criteria were used $n \geq 2$ indicators, their resulting value is calculated as rounded-off squared average:

$$y_j = \sqrt{\sum_{i=1}^{n} \left(K_i^N\right)^2 \Big/ n}, \quad j = \overline{1,m}, \ . \qquad (10)$$

The results are shown in Table II. yj^*

The rating scores of regional DSOs by criteria $y_1; y_2; y_3; y_4; y_5$ are significantly different. The results of the analysis of the DSOs' ratings within individual partial criteria allow identifying the "weaknesses" and "strengths" of each DSO for designing appropriate managerial decisions and recommendations for targeted investment to upgrade certain network elements or build new assets.

For calculating the integral index *Z*, the fuzzy logic approach can be applied. This approach was used due to the different physical nature of criteria $y_1 - y_5$.

The trapezoidal shape of the membership function, numeral and linguistic borders of the term arrays were chosen accordingly to the physical nature of the criteria $y_1 - y_5$. For the partial criteria y_1, y_3, y_5 term-arrays *"very low"* corresponds the nodal point of fuzzy classifier α_k=0.1; *"low"* – 0.3; *"average"* – 0.5; *"high"* – 0.7; *"very high"* – 0.9.

The aggregation of partial criteria considering the level of their significance is performed by the additive convolution method using the OWA-Jaeger's operator [14]. The weightings were determined by applying expert judgments using the Fishburne principle [15]. Then the generalized integral index Z (rating score) is defined as:

$$Z = \sum_{j=1}^{m} \rho_{yi} \left(\sum_{k=1}^{s} \alpha_k \mu_k \left(y_j \right) \right) . \qquad (11)$$

where ρ_{yj} – the weight of y_j criterion in convolution (its priority rank), *m* – the number of the partial criterion y_j ; *s* – the number of the nodal points accordingly to the number of fuzzy

terms; α_k – k nodal point for j parameter $\left(k=\overline{1,s}\right)$, in which the value of the membership function corresponds to the middle of the intervals; $\mu_k\left(y_j\right)$ – value k-numbered function of criterion.

For identifying the significance of criteria, ρ_{yj} were arranged in order of decreasing their priority $\rho_1 \geq \rho_2 \geq \ldots \geq \rho_{yj}$. The values of ρ_{yj} were evaluated by applying expert judgments using the Fishburne principle. The obtained ratios are shown in Table III.

It needs to notice, that value of ρ_{yj} should be normalized:

$$\sum_{j=1}^{m}\rho_{yj}=\rho_{y1}+\rho_{y2}+\rho_{y3}+\rho_{y4}+\rho_{y5}=1 \ ,$$

Thus, according to the (10), we receive the integral index Z for the DSO-3:

$$Z_{DSO-3}=r_1\cdot a_{VL}\cdot m_{VL}\left(y_1\right)+r_2\times a_{IP}\cdot$$
$$\cdot m_{IP}\left(y_2\right)+r_3\cdot a_{VL}\cdot m_{VL}\left(y_3\right)+r_4\times a_{OL}\cdot$$
$$\cdot m_{OL}\left(y_4\right)+r_5\cdot a_{VL}\times m_{VL}\left(y_5\right)=$$
$$=0.0714\cdot 0.9\cdot 1+0.2857\cdot 0.758\cdot 1+$$
$$+0.21430\cdot 0.9\cdot 1+0.1429\cdot 0.692\cdot 1+$$
$$+0.2857\cdot 0.9\cdot 1=0.83.$$

The respective Z are defined similarly for the DSO-10 and DSO-4 $\left(Z_{DSO-10}=0.632;Z_{DSO-4}=0.421\right)$. The results of the ranking of all regional DSOs according to the integrated index Z are shown in Fig. 2. The Regulator (NEURC) has set current tariffs for the electricity distribution for DSOs, which significantly vary within the range of TMIN.2=0.5356 UAH/kWh to TMAX.2=0.9824 UAH/kWh. And, paradoxically, the highest tariff is assigned to DSO-4 with the lowest rating $ZDSO-4=0.421$, and lesser tariff to DSO-3 with the highest rating $ZDSO-3=0.632$ (Fig. 2). Instead, it should be considered that the existing assets of DSO-4 have already been reimbursed through the tariff, and maintaining them in appropriate condition costs less than creating new ones. Therefore, to avoid price discrimination and adhere to the principle of economic fairness, the regulatory rate of return for old assets should be significantly reduced. The return rate on new DSO-3 assets should be increased to attract investments for building new assets and further modernizing networks.

TABLE III. FISHBURNE'S WEIGHTING SYSTEM.

Weights by Fishburne		Benefits system
ρ_1	0.0714	$\rho_2\left(y_2\right)=\rho_5\left(y_5\right)>>$
ρ_2	0.2857	$>>\rho_3\left(y_3\right)>$
ρ_3	0.2143	$>\rho_4\left(y_4\right)>\rho_1(y_1$
ρ_4	0.1429	
ρ_5	0.2857	

Considering that profitability of the regional DSOs is determined in the range of tariffs set $\left[T_{MIN};T_{MAX.}\right]$ (currently [0.5356; 0.9824]), it is reasonable to choose a classifier for the tariff scale $T\in\left[T_{MIN};T_{MAX}\right]$ (for instance, $T\in\left[0.5;\ 1\right]$). The transition to the 0.5-1 classifier can be delivered by linear transformation (normalization) of the tariff scale $T(Z)$:

$$T_{\mathrm{DSO}}\left(Z_{\mathrm{DSO}}\right)=A\cdot Z_{\mathrm{DSO}}+T_{MIN} \ . \qquad (12)$$

where A – tariff coefficient, UAH/kWh.

The coefficient A could be applied for regulation $\left(A>1;A=1;A<1\right)$ the degree of stimulating impact of the differentiated tariff by change of the progressive step $\Delta T/\Delta Z$ dynamics, depending on the overall technical condition of the network infrastructure and national tariff policy.

An economically justified theoretical value for the minimum differentiated tariff was defined individually $(T_{MIN.BEZ})$ for each DSO considering its break-even point (when the total cost C_Σ will be equal to the income from economic activity, i.e., electricity distribution):

$$T_{MIN.BEZ}=\frac{P+C_\Sigma}{\mathrm{W}_\Sigma}=\frac{C_\Sigma}{\mathrm{W}_\Sigma} \ . \qquad (13)$$

where P – the DSO income (in case of $T=T_{MIN.BEZ}$ DSO shouldn't receive income, namely P=0); W_Σ – the volume of distributed electricity.

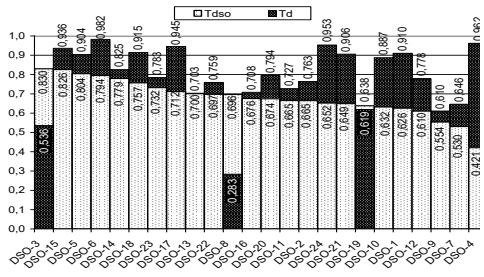

Figure 2. T_D – current tariff for electricity distribution for voltage class 2, T_{DSO} – proposed stimulating tariff for electricity distribution, UAH/kWh.

Values of the T, which are lesser than $T_{MIN.BEZ} \le C_\Sigma / W_\Sigma$ lose the economic meaning.

While calculating T_{MIN} individually for each DSO using (12), the T_{MAX} value should remain unified for all DSOs.

The results of calculating the rating scores by applying a multi-criteria ranking of DSOs were used to implement the approach mentioned above. Therefore, the maximal RAB-tariff should be set for DSO-3, which has the best rating $T_{DSO-3} = A \cdot Z_{DSO-3} = 0.830$ UAH/kWh, while the worst-rated DSO-4 receives twice lower tariff rate $T_{DSO-4} = A \cdot Z_{DSO-4} = 0.421$ UAH/kWh.

Fig. 2 demonstrates that the proposed stimulating tariff rates for electricity distribution are radically different from the current rates set by the Regulator.

IV. Conclusion

To comprehensively assess the DSO assets, a set of 22 indicators characterizing the state of the network infrastructure has been designed. An aggregation of related indicators into six criteria (efficiency, technical condition, load, reliability, innovation, and quality of electricity) allowed us to analyze the DSO ratings, identifying their "strengths" and "weaknesses" for making appropriate managerial influences and decisions on RAB-tariff setting. A convolution of particular criteria into the integrated index allowed to obtain individual rating scores for each DSO, according to which the ranking of energy companies was performed. The developed method of calculating individual RAB-tariffs according to the rating scores of DSO together with the regulated dynamics of the tariff "step" provided a flexible economic mechanism that motivates the modernization of electricity networks and the creation of new grid assets.

Thus, the application of the proposed method for calculating RAB-tariffs as a function of DSOs' rating scores would provide appropriate stimulation and implement an efficient economic mechanism promoting the renovation and upgrade.

References

[1] The Energy Community (2021). Available at: https://energy-community.org/aboutus/whoweare.html

[2] Report on the results of NCCSR activities in 2018 (2021). *Zvit pro rezultaty dijalnosti NKREKP u 2018 roci*. Available at: http://www.nerc.gov.ua/index.php/map_9/data/filearch/Materialy_zasidan/2018/?id=39678

[3] Kuosmanen, T., Saastamoinen, A., & Sipilainen T. (2013). What is the best practice for regulation of electricity distribution? Comparison of DEA, SFA and StoNED methods. *Energy Policy*, *61*, 740-750.

[4] *Electricity distribution investments: what regulatory framework do we need?* [EURELECTRIC report. Brussels, 2014]. Available at: https://cdn.eurelectric.org/media/1870/dso_investment_final-2014-030-0328-01-e-hFFE9D909.pdf

[5] *Distribution and Transmission Network Tariffs and Incentives* [CEER White Paper series on the European Commission's Clean Energy Proposals]. Available at: https://www.ceer.eu/white-papers

[6] Joskow, P. (2014). Incentive regulation in theory and practice: electric transmission and distribution networks. Chapter 5 in Economic regulation and its reform. What have we learned? *National Bureau of Economic Research conference report*. Mit, 291-345.

[7] Migueis, V., Camanho, A., Bjorndal, E., & Bjorndal, M. (2012). Productivity change and innovation in Norwegian electricity distribution companies. *Journal of the Operational Research Society*, *63*, 982-990.

[8] Evans, J., Lester, C. (2009). Hunt International handbook on the economics of energy. Cheltenham, UK, Northampton, VF, USA.

[9] Biggar, D., Hesamzaden, M. (2014). The economics of electricity markets. John Wiley & Sons Ltd. 432 p.

[10] Stern, J. (2013). The Role of the Regulatory Asset Base as an Instrument of Regulatory Commitment. *CCRP Working Paper Series, Working Paper, 22*.

[11] Makovšek, D. (2015). The Regulatory Asset Base Model and the Project Finance Model: A comparative analysis. *International Transport Forum*. Paris.

[12] Cullmann, A. (2016). Nieswand M. Regulation and investment incentives in electricity distribution: an empirical assessment. *Energy Economics*, *57*, 192-203.

[13] 2020 Energy Transparency Index. DiXi Group. Available at: https://index.ua-energy.org/en/assets/indexes/energy_transparency_index_2020_eng.pdf.

[14] Yager, R. (1988). On ordered weighted averaging aggregation operators in multi-criteria decision making. *IEEE Tranmulti-criteria Systems, Man, and Cybernetics*, *18*, 183-190.

[15] Fishburn, P. (1970). Utility Theory for Decision Making. Cheltenham, INC.

Lithium-ion Battery Electro-thermal Model with Peukert Effect in Simulink

Antal Apagyi[1], Flóra Hajdu[2], Csaba Hajdu[3], Rajmund Kuti[4]

[1]Széchenyi István University, Doctoral School of Multidisciplinary Engineering Sciences Győr, Hungary, apagyi.antal@ga.sze.hu

[2]Department of Mechatronics and Machine Design, Faculty of Faculty of Mechanical Engineering, Informatics and Electrical Engineering, Széchenyi István University, Hungary, e-mail: hajdfl@sze.hu

[3]Széchenyi István University, Vehicle Industry Research Center, Győr, Hungary, hajdu.csaba@ga.sze.hu

[4]Department of Mechatronics and Machine Design, Faculty of Faculty of Mechanical Engineering, Informatics and Electrical Engineering, Széchenyi István University, Hungary, e-mail: kuti.rajmund@sze.hu

Abstract—**The mainstream prominence of Lithium-ion batteries started to extend to the propulsion of heavy vehicles besides passenger cars. Freight and passenger transport can be measured mainly on an urban scale as the battery capacity is currently the major limitation for long-distance transport. Therefore, during the development of a fully electric heavy-duty vehicle, the parameters of the Li-ion battery that will drive the vehicle must be known as accurately as possible. Related to this is the battery model we created in Matlab and Simulink. The behavior of a given prismatic $LiFePO_4$ cell can be known as precisely and accurately as possible induced by temperature to create a battery testing and identification system for this purpose.**

Keywords – Lithium-ion, $LiFePO_4$, battery modeling, Simulik, electrothermal model

I. INTRODUCTION

Nowadays battery-powered, fully electric vehicles are being produced in increasing numbers. This growth trend is specific in Asian countries due to the large-scale development and local production of battery technologies. The lithium-ion battery specific energy is about 300 Wh/kg [1]. This value is tripled since 2010. Besides the chemical composition of the battery and the cell management has also improved with the development of faster microprocessors and better state estimation algorithms. In addition to the automotive industry, they also function as hybrid solar systems energy storage.

Regarding energy storage capacity, in both use cases, an essential factor is to examine the loss of capacity due to the change of ambient temperature. During the development of an electric road vehicle, manufacturers usually rely on vehicle simulation models. It can help reduce development costs without the explicit need to build abundant expensive, battery-powered prototypes. However, it is necessary to know the exact behavior of the desired lithium-ion battery cell for a proper realistic simulation. A lot of testing and examination is needed to fit a battery pack into the simulation system. Due to the environmental effects, the thermal behavior inside and around the cells is required for better understanding: further theoretical and practical modeling is required. Different complex modeling methods must be developed for proper design. Nevertheless, an appropriate simulation model is robust, easy to modify, requires little computation, and that a battery pack can be used to verify the simulation results.

In conclusion, it is cheaper to create a simulation model during prototype development than to work with real battery systems. On the other hand, every simulation model has some degree of error, which should be reduced to an appropriate level while keeping the model reasonably simple and easy to use. In our case, the battery cell we tested is one of the safest cell types with iron phosphate cathode material.

ISBN: 978-86-80593-73-9

System-level modeling computer programs such as AVL Cruise [2] or Simulink's built-in battery model are already widespread in industrial use cases. However, the latter is difficult to adjust to the desired battery parameters. Throughout our research, the Matlab software suite was available to implement our contribution. Consequently, the road vehicle and the battery model are both based on Matlab tools.

II. Li-ion Battery Cell Modeling

There are several methods for describing the behavior of battery cells, which can be divided into three large groups. The first two main description techniques are electrochemical, mathematical, and the combination of these two approaches [3]. These methods require complex calculations, and the simulation runs for a long time. The typical error of the chemical model is 1-5% that of the mathematical model is 10-15% [4, 5].

The third main group is based on electrical circuit modeling, including Thevenin-based, impedance-based, or runtime-based modeling [6]. The Thevenin-based simulation works with a relatively low precision error, easily maintained, and its development is typically more straightforward than other methods. This model is composed of a resistor series and connected RC elements, providing transient behavior. On the other hand, the Thevenin model is incapable of examining constant load and operating time. The impedance-based model provides an electrochemical characterization of the battery in the frequency domain. However, this technique only works with specific SOC values. The runtime-based models simulate constant load and operating time through complex circuits. On the other hand, these models tend to be imprecise for variable load.

The combination of Thevenin and the runtime-based model shows better results in [4,6], so our model is also based on a combined model [7,8]. Various measurements determined the relationship between the circuit elements. Our model provides high-precision results but does not consider aging and changes in temperature. Therefore, the model needs to be expanded. The model can handle the battery cells of a fully electric truck connected in series and in parallel to achieve the desired voltage and capacity, so our model supports specifying the number of battery cells, which affects the change in internal resistance.

The performance of the whole battery pack depends on the single performance of each battery cell or module. If the cells in the pack operate at different temperatures, the performance of the whole pack is affected. Due to the different temperatures, the cells will discharge and charge differently. Furthermore, the degradation will be different, which can only be eliminated by appropriately applied balancing. Therefore, it is essential that every cell operates at approximately the same temperature. The battery cell generates heat due to the electrochemical reactions occurring inside [9] and the current flowing through the internal resistor, which depends on the magnitude and intensity of the load. The generated heat is transferred by heat transfer or dissipation to the cell environment or another adjacent cell. However, the amount of heat dissipation depends on the size of the surface. Hence the most significant heat dissipation is the large side surface area of the cell. Although the cell terminals of the associated wires can be considered as heat-dissipating elements [10], but our model omits these two surfaces.

The 40 Ah $LiFePO_4$ battery of our choice depicted in Fig. 1, and the datasheet provides several valuable properties like dimension depicted in Fig. 2, characteristics, and the temperature-dependent SOC characteristic. However, these are static values measured at a

Figure 1. 40 Ah $LiFePO_4$ Thundersky battery cell [11].

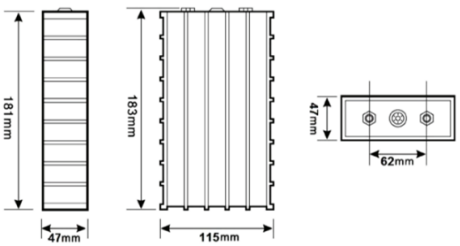

Figure 2. The battery cell dimensions [11].

given temperature [11]. The datasheet does not contain enough data for our circuit model, so further measurements were required. Furthermore, temperature values are constantly changing in the surrounding environment. Consequently, dynamic environmental modeling is needed to predict the SOC change or even degradation caused by temperature changes.

The model in the AVL Cruise software is based on the heat loss in the cell, which is based on the circuit losses and the heat exchange between the environment and the cell. Our model is based on the difference between the open-circuit voltage and the load voltage to determine the heat loss, it is a simplified V_{oc}-V model.

III. Modeling Options

The circuit and the thermal model are not independent of each other, so in Simulink a different one must be made in addition to the previously built circuit subsystem. The relationship between the two is illustrated in Fig 3.

The circuit model was developed empirically. The starting point for the thermal model was [2], and (1) [12]

$$dQ = m_{cell} \cdot C_{heat} \cdot dT_{bat} = P_{th} dt \ . \qquad (1)$$

In this equation, m_{cell} is the cell mass, C_{heat} is the specific heat capacity, T_{bat} is the battery cell temperature. In this case the heat output in the cell consists of $P_{th,el}$ circuit losses and $P_{th,amb}$ heat exchange between the environment and the cell [13] (2)

$$P_{th} = P_{th,el} + P_{th,amb} \ . \qquad (2)$$

The electrical losses are described by (3) [14]

$$P_{th,el} = I^2 \cdot R + I_{trans}^2 \cdot R_{trans} + I_{conc}^2 \cdot T_{act} \cdot R_{conc} + \\ + \left| 0.5 \cdot I_{\text{terminal}} \cdot \left(U_{idle} \cdot I_{\text{terminal,SOC}} - U_{idle} \cdot \left(-I_{\text{terminal,SOC}} \right) \right) \right| \ . \qquad (3)$$

where I is the current, R is internal resistance, U_{idle} is open circuit voltage and $I_{terminal}$ is the current measured at the terminal.

The heat released to the external environment can be determined from [15] (4)

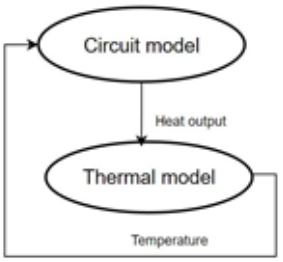

Figure 3. The connection between the circuit and the thermal model

$$P_{th,amb} = \alpha_{trans} \left(T_{bat} - T_{amb} \right), \qquad (4)$$

where α_{trans} is specific heat transfer coefficient, Among the thermal models, it was expedient for us to implement the [16] model based on the principle of energy balance in Simulink. The amount of heat due to circuit losses consists of two parts: the q_{Joule} is Joule heat output [17] (5) and the q_{rev} is reversible heat effect [18] (6)

$$q_{Joule} = i \cdot \left(u - U_0 \right), \qquad (5)$$

$$q_{rev} = i \cdot T_{cell} \cdot \frac{\Delta S}{nF}, \qquad (6)$$

I is the current, u is the instantaneous voltage, U_0 is the open circuit voltage $\left(V_{oc}\right)$, F is the Faraday constant, n is the number of electrons, ΔS is the change in entropy and T_{cell} is the battery cell temperature. The relationship between the environment and the cell temperature consists of heat conduction, heat transfer, and heat radiation. The equation describing the change in cell temperature is illustrated in [19] (3):

$$\frac{dT_{cell}}{dt} = \frac{1}{mc_p} \begin{bmatrix} i \cdot \left(u - U_0 \right) + \frac{T_{cell} \cdot \Delta S}{F} + \\ + A \cdot \left(\alpha \cdot \left(T_{cell} - T_{amb} \right) + \right) \\ + \lambda \cdot \left(T_{cell} - T_{amb} \right) + \\ + \varepsilon \left(T_{cell}^4 - T_{amb}^4 \right) \end{bmatrix} . \qquad (7)$$

In the formula, α is the heat transfer coefficient, λ is the thermal conductivity coefficient, ε is the heat radiation coefficient, A is the cell surface, m is the cell mass, c_p is the heat capacity, and T_{amb} is the ambient temperature.

We need a detailed but easy-to-use model. The AVL Cruise and [16] models that was considered advantageous in our use case is shown in Table I., as while the former describes the electrical losses in detail, it treats the heat exchange processes as a combined parameter. In the case of the latter, the heat exchange processes have been expressed, it is enough to know the value of V_{oc} when calculating the electrical losses, but the treatment of the entropy change describing the irreversible processes complicates the model. Electrical heat output was implemented from the AVL Cruise model, and heat exchange processes were highlighted from [16]. The combination of the two models gives a description of the change in battery temperature [19] (8)

$$\frac{dT_{cell}}{dt} = \frac{1}{mc_p}\begin{pmatrix} I^2 \cdot R + I_{trans}^2 \cdot R_{trans} + I_{conc}^2 \cdot \\ \cdot T_{act} \cdot R_{conc} + 0.5 \cdot I_{\text{terminal}} \cdot \\ \cdot \left(U_{idle} \cdot I_{\text{terminal,SOC}} - U_{idle} \cdot \left(-I_{\text{terminal,SOC}}\right)\right) \\ -A \cdot \begin{pmatrix} \alpha \cdot \left(T_{cell} - T_{amb}\right) + \lambda \left(T_{cell} - T_{amb}\right) \\ + \varepsilon \left(T_{cell}^4 - T_{amb}^4\right) \end{pmatrix} \end{pmatrix}, \quad (8)$$

where I is the current, R is internal resistance, U_{idle} is open circuit voltage, $I_{terminal}$ is the current that flows through the terminal, T_{cell} is the temperature of the battery cell and T_{amb} is the ambient temperature.

IV. Thermal Model in Simulink

The measurement system [8] and the equivalent circuit model have been developed before [7]. Therefore, the thermal model was designed as a separate subsystem. Thermal power was determined in two ways, [2] and [19]. In the case of the former, the polarization voltage is the sum of the voltages at the polarization resistors R_{12} and R_{long} as shown in Fig. 4. In the case of the latter, only the difference between the open circuit voltage and the voltage under load was used, and reversible heat output was not incorporated. Cell and ambient heat exchange [20] (9) were implemented based on [16]

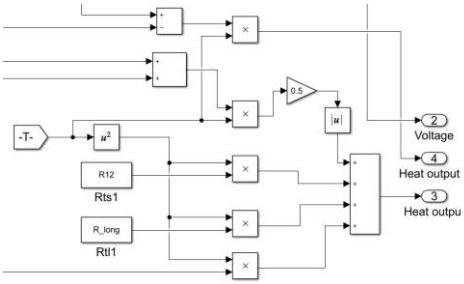

Figure 4. Thermal power model from electrical losses in Simulink

$$q_e = \varepsilon \cdot \left(T_{cell}^4 - T_{amb}^4\right). \quad (9)$$

Simplification can be performed on the model for a temperature difference of less than 20K, so the q_e heat radiation is described below [20] (10)

$$q_e = A \cdot \left(T_{cell} - T_{amb}\right) \cdot 5. \quad (10)$$

The effect of heat conduction was incorporated for the model based on the heat transfer factors determined by [12] and the values found in the data sheet of [11].The total battery surface area (11) was determined from the geometric data:

$$A = 2 \cdot \begin{pmatrix} 0.181 \cdot 0.046 + 0.181 \cdot \\ \cdot 0.11 + 0.046 \cdot 0.116 \end{pmatrix} = 0.07 m^2. \quad (11)$$

TABLE I. Comparison of possible thermal models.

Model Ref.	Advantage	Disadvantage	Unknown parameters
[2]	Detailed electrical loss model	Combined thermal conductivity	Polarization losses, combined heat transfer coefficient, heat capacity
[16]	Detailed heat exchange model parameters and their method of determination are known	Simplified electrical loss model reversible processes are expressed by entropy	Entropy change at reversible heat output, thermal conductivity, heat transfer coefficient, Radiation factor
Combined	The advantages of the previous two models are combined by fewer unknown parameters	The accuracy of the model can be affected by combining two models	Polarization losses, heat transfer coefficient, radiation factor, potential loss

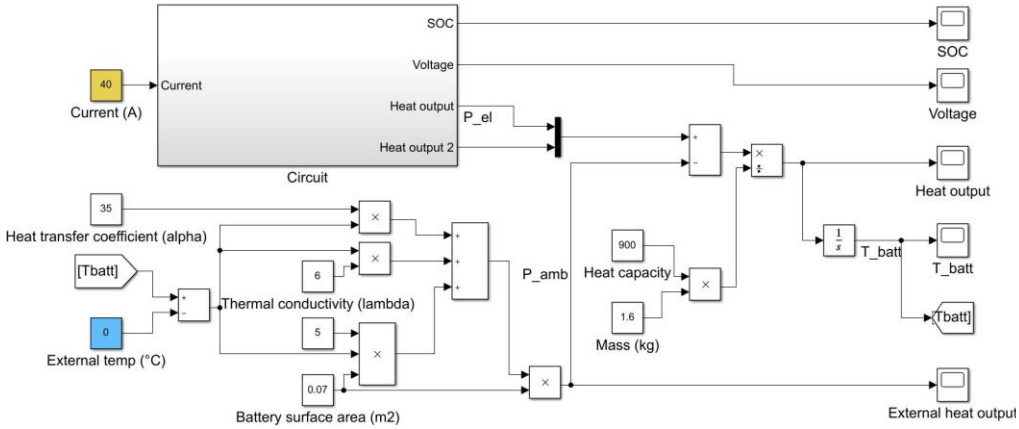

Figure 5. The Simulink model.

Battery weight is 1.6kg, average heat transfer coefficient $\alpha = 6W/mK$ heat capacity $C_p = 900\,J/kgK$ heat transfer coefficient $35W/m^2$. The initial cell temperature was 20°C. The Simulink model thus prepared is shown in Fig. 5. The yellow block parameter can be used to change the load current and the blue one to change the ambient temperature.

V. Simulation Results

The model was evaluated under two conditions. In the first case, the temperature was constant at 20°C, and the load was variable at 0.5C, 1C, and 2C, as depicted in the graphs of Fig. 6. In the second case in Fig. 7, the load values were constant at 1C, but the temperature values were chosen as 0°C, 20°C, and 40°C. The simulation ended in each case when the cell reached a voltage value of 2.5V. It can be observed that with more load, the removable capacity decreases. The blue curve illustrates the output of the AVL Cruise model, and the green curve illustrates the simplified $V_{oc} - V$ electrical loss model.

VI. Conclusion

The difference between the curves is caused by the lack of reversible processes in the simplified model. A more significant discrepancy occurred with the increasing load. We examined degradation with actual validation data and implemented self-discharge with a dynamic temperature test. The combined heat model of the used $LiFePO_4$ battery pack has been

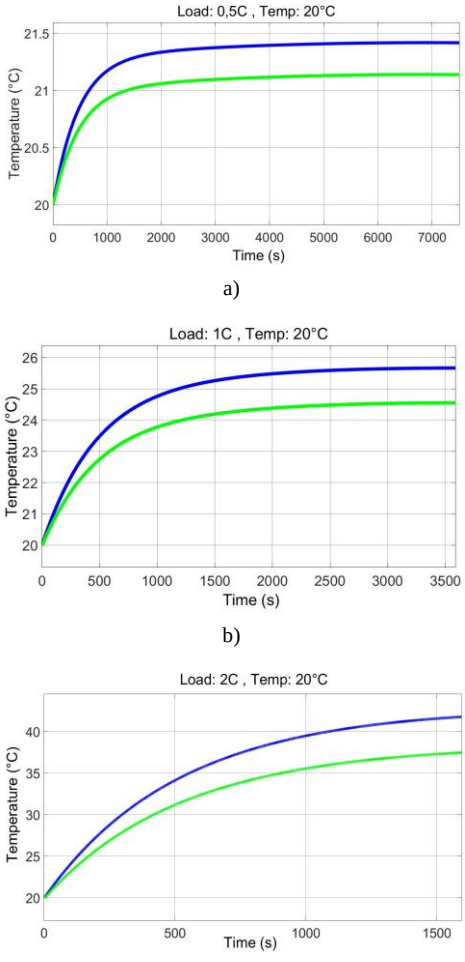

Figure 6. Constant temperature, different load, (a) load is 0.5C, (b) load is 1 C and (c) load is 2C.

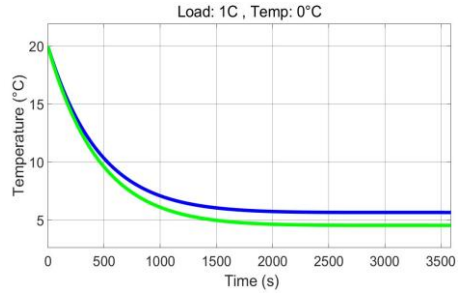

a)

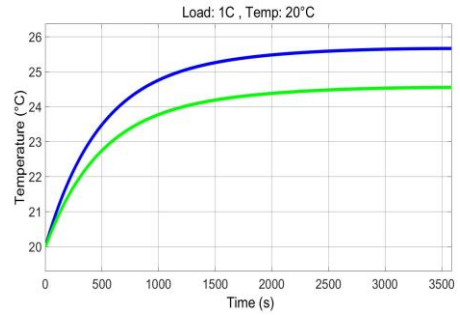

b)

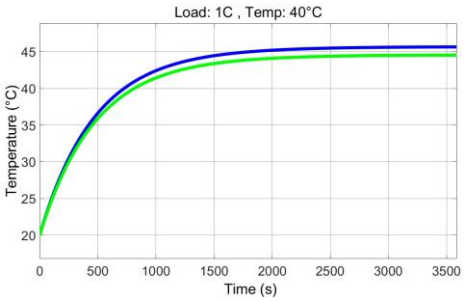

c)

Figure 7. Constant load with different temperature test, a.) temperature is 0°C, b.) 20°C and c.) 40°C.

implemented as a Simulink model during this research. With this model, simulations with primarily smaller constant current load can be carried out considering the Peukert-effect. The battery parameters have been derived from the load-measurement results of a Thundersky 40 Ah with a load rate of 0.5C.

VII. Future Work

The main goal is to create a battery model as shown in Fig 8, which can be further used to model truck vehicles in various load-cycle scenarios considering numerous thermodynamical and aging properties. Our

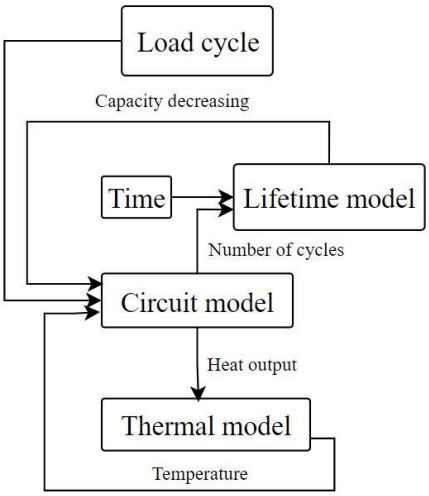

Figure 8. Planned model of the battery.

further work includes additional load measurements that must be carried out with various C rate. Additionally, the temperature range should be extended to a broader spectrum. A promising research direction is the testing of this model with the further examination of Peukert-effects. With this direction, only the Peukert coefficients are required for adjustment, while the change resistance values could be left unchanged. The results of this research shall be compared with measurement data of multi-variable resistor models. We aim to create a simpler, single-variable model if the precision does not decrease significantly with these measurements. As a longer-term goal, the model should be extended with aging properties presumably as a composite function of the charging-discharging count, ambient and cell temperature, and time.

References

[1] Cao, W., Zhang, J., & Li, H. (2020). Batteries with high theoretical energy densities. *Energy Storage Materials, 26*, 46-55. doi:10.1016/j.ensm.2019.12.024

[2] AVL. (2011). AVL Cruise Version 2011 User's guide.

[3] Gomadam, P., Weidner, J., Dougal, R., & White, R. (2002). Mathematical modeling of lithium-ion and nickel battery systems. *Journal of Power Sources, 110*(2), 267-284.doi:10.1016/S0378-7753(02)00190-8

[4] Knauff, M., McLaughlin, J., Dafis, C., Niebur, D., Singh, P., Kwatny, H., & Nwankpa, C. (2007). Simulink Model of a Lithium-Ion Battery for the Hybrid Power System Testbed. *IEEE Electric Ship Technologies Symposium - ESTS*, 421-427.

[5] Jongerden, M., & Haverkort, B. (2008). Battery Modeling. *CTIT Technical Report Series, TR-CTIT-08-01*.

[6] Chen, M., & Rincon-Mora, G. (2006). Accurate electrical battery model capable of predicting runtime and I-V performance. *IEEE Transactions on Energy Conversion, 21*(2), 504-511. doi:10.1109/TEC.2006.874229

[7] Hajdu, F., Lakatos, I., & Kőrös, P. (2013). Lítium akkumulátor modellezése Simulink környezetben. *Innovation and Sustainable Surface Transport (IFFK)*, (old.: 132-140). Budapest.

[8] Kocsis-Szürke, S., Szuromi, C., & Lakatos, I. (2015). Nagy kapacitású lítium-ion akkumulátorok közúti használatát szimuláló rendszer tervezése: Implementation and design of a high-capacity in-vehicle lithium-ion battery simulation system. *XXIII. Nemzetközi Gépészeti Találkozó - OGÉT 2015.*

[9] Damay, N., Forgez, C., Bichat, M.-P., & Friedrich, G. (2015). Thermal modeling of large prismatic LiFePO4/graphite battery. Coupled thermal and heat generation models for characterization and simulation. *Journal of Power Sources, 283*, 37-45. doi:10.1016/j.jpowsour.2015.02.091

[10] Pour, M. (2015). Electro-thermal Modeling of Lithium-ion Batteries. SIMON FRASER UNIVERSITY.

[11] *Technical specification Winston LFP040AHA cell.* (dátum nélk.). Forrás: https://files.gwl.eu/inc/_doc/attach/StoItem/1123/ThunderSky-Winston-LIFEPO4-40Ah-Datasheet.pdf

[12] Pesaran, A., Vlahinos, A., & Burch, S. (1997). Thermal Performance of EV and HEV Battery Modules and Packs. *Proceedings of the 14th International Electric Vehicle Symposium*.

[13] Petrók, J. Lítium-ion akkumulátorok: Áttörés a horizonton? *A jövő járműve*, old.: 72-76.

[14] Gregory L., P. (2004). Extended Kalman filtering for battery management systems of LiPB-based HEV battery packs: Part 3. State and parameter estimation. *Journal of Power Sources, 134*(2), 277-292. doi:10.1016/j.jpowsour.2004.02.033

[15] Rahimi-Eichi, H., & Chow, M.-Y. (2012. 10). Adaptive parameter identification and State-of-Charge estimation of lithium-ion batteries. *IECON 2012 - 38th Annual Conference on IEEE Industrial Electronics Society*, 4012-4017. doi:10.1109/IECON.2012.6389248

[16] Benger, R., Wenzl, H., Beck, H.-P., Jiang, M., Ohms, D., & Schaedlich, G. (2009/6). Electrochemical and thermal modeling of lithium-ion cells for use in HEV or EV application. *World Electric Vehicle Journal*, 342-351. doi:10.3390/wevj3020342

[17] Ranganathan, A. (2004). *The Levenberg-Marquardt Algorithm.* Forrás: Ananth Ranganathan: http://www.ananth.in/Notes_files/lmtut.pdf

[18] Salman, M., Tang, X., & Mao, X.. *Li-Ion Battery State Estimation and Prognosis.* GM Research and Development

[19] Sarasua, A., Molina, M., & Mercado, P. (2013). Dynamic Modelling of Advanced Battery Energy Storage System for Grid-Tied AC Microgrid Applications. *Publication Title: Energy Storage - Technologies and Applications*, 296-320. doi:10.5772/52219

[20] Tremblay, O., Dessaint, L.-A., & Dekkiche, A.-I. (2007). A Generic Battery Model for the Dynamic Simulation of Hybrid Electric Vehicles. *IEEE Vehicle Power and Propulsion Conference*, 284-289.

Modeling and Control of DAB-based Conversion System for Distributed Energy Resources to Support the Grid

Pedro A. N. Neto[1], Camila S. Gehrke[2], Fabiano Salvadori[3], Italo R. F. M. P. Silva[4]

[1]Federal Rural University of Pernambuco, Recife, Brazil, pedrooalvess1@gmail.com
[2,3,4]Federal University of Paraíba, João Pessoa, Brazil, camila@cear.ufpb.br[2], salvadori.fabiano@gmail.com[3], italo@cear.ufpb.br[4]

Abstract—**This paper presents a comprehensive analysis of the model and control of a power conversion system (PCS) as an interface for distributed energy resources (DERs) to support the power grid. In this application, the PCS, by means of the control strategy, has to respond quickly and robustly to adjust the changes and intermittences of the DERs to the grid codes, controlling instantly active and reactive powers. Therefore, the PCS consists of dual active bridge (DAB) converter as an additional stage for regulating the dc-link voltage of the dc-ac converter, which is connected to a three-wire three-phase system. In implementing the control strategy, the contribution of using an integral-proportional controller was evaluated as alternative to the conventional proportional-integral one, whether for the voltage.**

Keywords - power conversion system, distributed energy resource, dual active bridge converter, power grid support

I. INTRODUCTION

In the coming years, the potential for new large hydroelectric plants tend to saturate in Brazil, mainly due to social and environmental impacts. On the other hand, there are growing demand for distributed generation (DG) systems and, for mini and micro generation, DG sources can be placed using the existing grid infrastructure as energy compensation systems, according Brazilian grid codes. Nowadays, the integration of DGs in the power grid has been dispensed energy storage systems (ESSs) because the expensive acquisition of accumulators (e.g., batteries, supercapacitors, flywheel), although the levelized cost of storage (LCOS) has been reducing over the years [1].

However, with the technological development and progress of smart grids, the tendency is to integrate ESSs as distributed energy resources (DERs) into mini and microgeneration plants. From the point of view of the electric power systems, the DER can operate as active nodes to support: 1) intermittent generation sources, complementing the load power demand when needed; 2) power grid (utility companies) operating in peak shaving, and voltage/frequency regulation; 3) end-users (commercial and industrial plants), with management of generated or stored energy on the demand side. Thus, the DER operating at peak shaving allows for supplying the necessary electrical energy during peak hours, reducing or postponing investments by utility companies, for example, in the expansion of transmission and distribution lines. In addition, electricity can be stored during off-peak hours to be used during peak hours in order to reduce costs for end users.

The most efficient and reliable way of integrate DERs to the power grid, for processing the generated/stored energy, is by means of the power converters. In this context, the power conversion system (PCS) allows for controlling instantly active and reactive power, to manage the power flow in the accumulators, to minimize the electric disturbances arising from deviations of wind speed, solar irradiation and so many other features. Generally, PCSs connected to grid employ the use of bulk transformers which operate at the line frequency to obtain galvanic isolation and to adequate the output voltage level to the grid standard. However, line frequency transformers are passive elements that hinder the increase in the power density of the system [2].

ISBN: 978-86-80593-73-9

Over the last decades, several studies have been carried out to employ high-and-medium frequency transformers in solid-state transformers and front-to-front systems as alternative to interface PCS with galvanic isolation to the power grid. The main advantages of these transformers in relation to the line-frequency transformers are distinguished reduction of size, weight and cost of material. In addition, PCS that employs high-frequency transformers can avoid distortion on the voltage/current waveform due to the core saturation and, when the switching frequency is greater than 20 kHz, the audible noise can be mitigated [2]. In Fig. 1 the proposed PCS to integrate the DERs to the grid is illustrated. The dc-dc conversion stage is per- formed from the dual active bridge (DAB). The DAB output supplies the dc-ac converter, which is connected to the power grid.

Considering that the voltage provided by the DER is subject to variations, either due to the availability of energy from intermittent sources or due to the charge and discharge of accumulators, the introduction of an additional dc-dc stage allows for the independent regulation of the dc-link voltage so that the dc-ac converter operates in voltage/current ranges in which it has been designed [3, 4]. For example, the direct connection of the bank of batteries or supercapacitors in the dc bus requires oversized semiconductor devices to safely operate in a high-state-of-charge scenario, additionally, a large variation of the modulation index may be needed to compensate dc-link-voltage oscillations, thus reducing the system efficiency and the output waveform quality [5].

Thus, the PCS is required to be a fast and robust bidirectional interface to adapt the wide range of variation in voltage/current levels

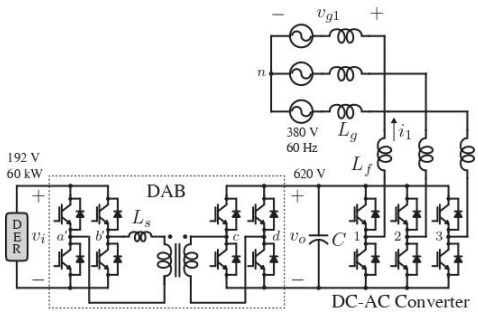

Figure 1. Proposed PCS to interface DERs for supporting the power grid.

between the DERs and the respective converters connected to the grid regardless of the power flow. Besides optimizing the dimensioning of the entire PCS, the use of an additional dc-dc stage makes feasible the creation of a new dc micro-grid from the dc buses (one of low voltage and another of medium voltage), in which new sources and loads can be installed [6]. Therefore, for exploiting the benefits of DERs within the context of smart grids, it is essential that the PCS is able to simultaneously control instantaneous - active and reactive - powers quickly and efficiently, as required in modern power grid applications [7].

The PCS shown Fig. 1 has been extensively investigated over the years for various applications with respect to performance, design, control, and modulation features [8–12]. In [8], the effect of circulation current was evaluated in core saturation of the high-frequency transformer in a ESS application based on low-voltage and high-current batteries. The problem of circulation current can be solved from the variation of phase-shift modulation (PSM) technique of the DAB converter, e.g., from the extended-phase shift (EPS) and dual- phase shift (DPS) methods [2]. With regard to the control strategy, Tian et al. [9] proposed a cascade control strategy with decoupling control between DAB and dc-ac converter. In [10, 11], the effect of bidirectional power flow in the DAB was explored considering deviations of the input and output impedance of the dc-ac converter. It was found that the dc-ac converter can lead the system to instability when acting as a constant power load (presenting negative impedance characteristics), whereas the demanded power rises and the operating frequency is reduced. As solutions, an impedance controller was proposed in [10] for compensating the negative-impedance behavior of the dc-ac converter, and a droop control mode was included for regulating the dc link when the DAB absorbs power at low frequency range (below 10 Hz). Nevertheless, the controllability of the DAB converter can be guaranteed even under constant power disturbance [12], if the limit of dc-link-voltage sag is respected, so that the converter is still capable of processing the required power and does not lose stability.

This paper presents an analysis of the model and control of the PCS shown in Fig. 1, as an interface for DERs to support the power grid. To obtain a fast and smooth dynamic response

(around one fundamental period without overshoot), the use of the integral-proportional (IP) controller is evaluated as an alternative to the conventional proportional-integral (PI) both in the regulation of the dc-link voltage and in the power control. By employing the IP controller, the not-tunable zero included the conventional PI into the closed-loop transfer functions can be eliminated. A comparison between the results employing IP and PI controllers is also presented. For a first evaluation scenario, this paper used the traditional PSM with single-phase shift (SPS) for commanding the DAB converter.

II. System Model and Control Strategy

The dc-dc conversion stage plays an important role in regulating the dc-link voltage by controlling the input and output flow of the active power, besides providing a galvanic isolation and voltage level adjustment between DERs and the power grid. For this, the DAB operation employs the series inductance (L_s) with the high-frequency transformer to transfer energy with bidirectional flow between the input and output full bridges, cf. Fig. 1. A simplified way to analyze the DAB converter is referring the secondary side to the primary side, since transformer turns ratio is given by

$$a = \frac{N_{sec}}{N_{pri}} \ , \qquad (1)$$

in which N_{sec} and N_{pri} are respectively the number of transformer turns on the secondary and primary side. The simplified circuit of the DAB converter referred to primary side is illustrated in Fig. 2. In this case, the power flows through the inductance L that is the sum of inductance L_S and the transformer leakage inductance [13].

For the DAB operation, SPS-PSM technique can be implemented to regulate the dc-link voltage (v_o) (with average value V_o) from the DER voltage (v_i) (with average value V_i) by means of the phase-shift angle (ϕ) between the voltages on the primary and secondary side of the transformer ($v_{a'b'}$ and v_{cd}, respectively). The active power is transferred between the two full bridges depending on the ϕ. Thus, considering an ideal converter, the input power ($P_i = V_i I_i$) is equals the output power ($P_o = V_o I_o$), thus the active power transferred (P) between both bridge is expressed by

$$P_i = P_o = P = \frac{V_i^2 d}{\omega_s L}\phi\left(1 - \frac{|\phi|}{\pi}\right) \ , \qquad (2)$$

in which $d = V_o / aV_i$ is the voltage gain, I_i is average value of the input current (i_i), I_o is average value of the output current (i_o) and $\omega_s = 2\pi f_s$, considering f_s the switching frequency of the DAB converter.

For sizing of dc-dc stage from (2), it is needed to establish the rated value of d and to determine the transformer turns ratio considering the voltages between the full bridges. In addition, the value of d can be determined taking into account the rms current and the input power factor. Thus, the DAB operation is feasible for d values close to unit, so that the adjustment between the input and output-voltage levels is done from ratio a as in (1). Since the active power can be expressed ideally for (2), the average output current I_o is given by

$$I_o = \frac{V_i}{a\omega_s L}\phi\left(1 - \frac{|\phi|}{\pi}\right) \ . \qquad (3)$$

In (3), the average value of $i_o(t)$ is determined during a switching period ($T_s = 1/f_s$) in steady state, i.e., $i_{oT_s} = I_o$ not being possible to evaluate its behavior to load disturbances (from dc-ac converter) and input voltage (from batteries bank for example). For controlling the output voltage $v_o(t)$ against these disturbances, the DAB output stage can be modelled from the small-signal average model, in which $x_{T_s} = X + \delta x$, being x an arbitrary

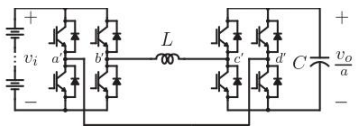

Figure 2. DAB converter referred to the primary side of the high-frequency transformer. Adapted from [13].

variable, X its average value and δx a small deviation around X.

The equivalent circuit presented in [12] was used as the basis, cf. Fig. 3 for development of the DAB-output-stage model. It is noteworthy that the exposed model takes into account the action of the control of voltage v_o by means of current i_ϕ, that depends on ϕ being i_o a disturbance. Therefore, from (3) and analyzing the circuit shown in Fig. 3, $\langle i_\phi \rangle$ can be expressed by

$$\langle i_\phi \rangle = \frac{V_i}{a\omega_s L}\langle \phi \rangle \left(1 - \frac{|\langle \phi \rangle|}{\pi}\right), \quad (4)$$

$$\langle i_\phi \rangle = C\frac{d\langle v_o \rangle}{dt} - \langle i_o \rangle \ , \quad (5)$$

in which C is the dc-link capacitance.

As in (4), there is no a linear relation between $\langle i_\phi \rangle$ and $\langle \phi \rangle$, thus it is not possible obtain a transfer function and the control circuit development. In this case, a quiescence point is defined for the rated DAB phase angle (ϕ_n) and the first-order Taylor polynomial is determined. Applying the Taylor series in (4), $\langle i_\phi \rangle$ can be determined as follows:

$$\langle i_\phi \rangle = \frac{V_i}{a\omega_s L}\left[\phi\left(1 - \frac{2\phi_n}{\pi}\right) + \frac{\phi_n^2}{\pi}\right] \text{ for } \phi > 0 \ , \quad (6)$$

$$\langle i_\phi \rangle = \frac{V_i}{a\omega_s L}\left[\phi\left(1 + \frac{2\phi_n}{\pi}\right) - \frac{\phi_n^2}{\pi}\right] \text{ for } \phi < 0 \ . \quad (7)$$

Then, introducing small variations of the δi_ϕ, δv_o, δi_o and δ_ϕ in (5) to (7), it is possible verify that

$$I_\phi = I_o = \frac{V_i}{a\omega_s L}\phi_n \left(1 - \frac{|\phi_n|}{\pi}\right), \quad (8)$$

$$\frac{d}{dt}\delta v_o = \frac{V_i k_{\phi_n}}{a\omega_s LC}\delta\phi + \frac{1}{C}\delta i_o \ . \quad (9)$$

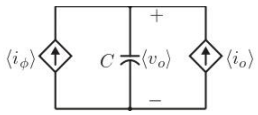

Figure 3. Small-signal average model of the DAB output stage.

in which $k_{\phi_n} = \left(1 - \frac{2|\phi_n|}{\pi}\right)$.

The application of Taylor series in (4) yields a linearized model so that control strategy can be implemented. Therefore, applying the Laplace transform in (9), voltage v_o can be determined in the frequency domain as follows:

$$\delta V_o(s) = \frac{V_i k_{\phi_n}}{a\omega_s LC}\frac{1}{s}\delta\phi(s) + \frac{1}{sC}\delta I_o(s) \ . \quad (10)$$

As can be noticed in (10), a power change caused by i_o from dc-ac converter, naturally causes a variation in the output voltage v_o. For this reason, current i_o should considered as disturbance to the voltage control. Thereby, considering that control action compensates disturbances of i_o, the transfer function of the plant and the load disturbance can be respectively expressed by:

$$\frac{\delta V_o(s)}{\delta\phi(s)} = \frac{V_i k_{\phi_n}}{a\omega_s LC}\frac{1}{s} \ , \quad (11)$$

$$\frac{\delta V_o(s)}{\delta I_o(s)} = \frac{1}{sC} \ . \quad (12)$$

The transfer function in (11) allows that the regulation of v_o may be performed by means of a closed-loop control considering larger variations of ϕ. One of the most traditional controllers is the PI, since its transfer function is first order and has the capability to control plants of higher order. In general, one of the great advantages of the PI controller is response dynamic adjustment of system without steady-state error, even with disturbance acting on the system. The PI controller adds a not-tunable zero into the closed-loop transfer function, which can lead to a high overshoot in the dynamic response. This

overshoot can be mitigated by tuning the controller gains for an over-damped response; however, this reduces the capability of disturbance rejection. As alternative to PI, the IP controller can be employed, which can be tuned to provide a response as fast as PI with an improved disturbance rejection. Moreover, the calculation of IP gains is as simple as that of PI, since the closed-loop transfer function of first-order plant can be compared to the canonical second-order transfer function. In Fig. 4, the block diagram of voltage v_o by means of the IP controller, considering the load disturbance given by i_o is introduced. Thus, for regulating voltage v_o, the reference for phase-shift angle ϕ^* must be determined by associating the reference v_o^* and the controller signal. From (11) and neglecting the sampling delay and time response of the DAB converter (i.e., ideal converter as $\delta\phi \approx \delta\phi^*$), the IP controller can be applied so that

$$\delta\phi^*(s) = -K_1\delta V_o(s) + \\ + \frac{1}{sT_1}\left[\delta V_o^*(s) - \delta V_o(s)\right], \quad (13)$$

Thus

$$\frac{a\omega_s LC}{V_i k_{\phi_n}} = -K_1\delta V_o(s) + \\ + \frac{1}{sT_1}\left[\delta V_o^*(s) - \delta V_o(s)\right]. \quad (14)$$

By solving (14), the closed-loop transfer function for the voltage control is determined as follows:

$$\frac{\delta V_o(s)}{\delta V_o^*(s)} = \\ = \frac{\frac{1}{T_1}\frac{V_i k_{\phi_n}}{a\omega_s LC}}{s^2 + K_1\frac{V_i k_{\phi_n}}{a\omega_s LC}s + \frac{1}{T_1}\frac{V_i k_{\phi_n}}{a\omega_s LC}}. \quad (15)$$

The damping ratio (ζ) was determined in (15) for a critically damped response. Thus,

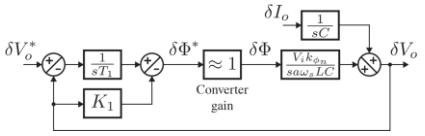

Figure 4. Block diagram of the dc-link voltage control.

assuming $T_1 = 10T_s$, the proportional gain K_1 can be calculated by:

$$K_1 = \sqrt{\frac{4\pi aLC}{5V_i k_{\phi_n} T_s^2}}, \quad (16)$$

considering that time constant T_1 must be slow enough ($\geq 10T_s$,) so that delays of the sensors and converter response can be neglected from the viewpoint of control stability

In the dc-ac conversion stage, the flow of active and reactive power is controlled applying the instantaneous power theory [13]. The development of the model for dc-ac conversion stage is accomplished taking into account the coupling inductance L_f, that connects the dc-ac converter to the grid. Thus, the three-phase converter voltages v_{kn} (v_k in short), considering $k = \{1,2,3\}$, can be expressed by

$$v_k = L_f\frac{di_k}{dt} + v_{gk}, \quad (17)$$

in which i_k denotes the three-phase converter currents and v_{gk} denotes ideal three-phase grid voltages. The vector notation can be adopted so (17) can be rewritten as follows:

$$\mathrm{v}_{123} = L_f\frac{d\mathrm{i}_{123}}{dt} + \mathrm{v}_{g123}. \quad (18)$$

To simplify the model analysis, the invariant-power Clarke and Park transformations were employed. As a three-wire-phase system is considered, the zero-sequence component is null, then (18) can be rewritten as follows:

$$\mathrm{v}_{dq} = L_f\frac{d\mathrm{i}_{dq}}{dt} \mp \left(\omega L_f \mathrm{i}_{qd} - \mathrm{v}_{gdq}\right). \quad (19)$$

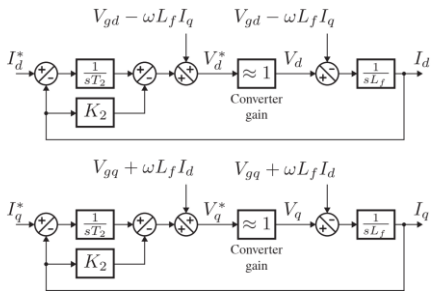

Figure 5. Block diagram of the decoupling dq-current control.

Thus, by applying the instantaneous power theory, the real power (p) and imaginary power (q) are determined from:

$$\begin{bmatrix} p \\ q \end{bmatrix} = \begin{bmatrix} v_{g\alpha} & v_{g\beta} \\ v_{g\beta} & -v_{g\alpha} \end{bmatrix} \begin{bmatrix} i_\alpha \\ i_\beta \end{bmatrix}, \qquad (20)$$

The closed-loop block diagram of the decoupling currents control $\mathbf{i}_{dq}$ employing an IP controller are illustrated in Fig. 5. For controlling the power on the system, the converter current references $\mathbf{i}_{dq}^*$ must be determined for the closed loop with the power references p^* and q^*. By isolating $\mathbf{i}_{\alpha\beta}$ in (20), then applying the Park transformation, references $\mathbf{i}_{dq}^*$ can be determined by

$$\begin{bmatrix} i_d^* \\ i_q^* \end{bmatrix} = \frac{1}{v_{g\alpha}^2 + v_{g\beta}^2} \begin{bmatrix} \cos(\theta) & \sin(\theta) \\ -\sin(\theta) & \cos(\theta) \end{bmatrix} \cdot \cdot \begin{bmatrix} v_{g\alpha} & v_{g\beta} \\ v_{g\beta} & -v_{g\alpha} \end{bmatrix} \begin{bmatrix} p^* \\ q^* \end{bmatrix}. \qquad (21)$$

in which $\theta = \int \omega dt$, being ω the grid angular frequency.

Analyzing (19) in the frequency domain, currents $\mathbf{I}_{dq}$ and voltages $\mathbf{V}_{dq}$ can be associated as follows:

$$sL_f \mathrm{I}_{dq}(s) = \mathrm{V}_{dq}(s) - \left[\mathrm{V}_{gdq}(s) \mp \omega L_f \mathrm{I}_{qd}(s) \right]. \qquad (22)$$

From (22), neglecting the one-sampling delay and considering the converter response a unity gain, i.e., $\mathbf{V}_{dq} \approx \mathbf{V}_{dq}^*$, the IP controller can be applied so that

$$\mathrm{V}_{dq}^*(s) = -K_2 \mathrm{I}_{dq}(s) + \frac{1}{sT_2}\left[\mathrm{I}_{dq}^*(s) - \mathrm{I}_{dq}(s) \right] + \\ + \mathrm{V}_{gdq}(s) \mp \omega L_f \mathrm{I}_{qd}(s), \qquad (23)$$

By solving (23), the closed-loop transfer function for the dq-current control is determined as follows:

$$\frac{\mathrm{I}_{dq}(s)}{\mathrm{I}_{dq}^*(s)} = \frac{\frac{1}{T_2 L_f}}{s^2 + \frac{K_2}{L_f} s + \frac{1}{T_2 L_f}}. \qquad (24)$$

Similarly, to the procedure adopted in the dc-dc stage, the damping factor is defined as $\zeta = 1$ in (24). In addition, assuming $T_2 = 20T_1$, the proportional gain K_2 can be determined by

$$K_2 = \sqrt{\frac{L_f}{50T_s}}. \qquad (25)$$

III. RESULTS

In this section, the simulated results in the software PSIM® are presented for two scenarios: 1) operation under voltage sags on the DER output up to 35% of 192 V; 2) four-quadrant

TABLE I. SYSTEM PARAMETERS USED IN THE SIMULATION.

Description	Parameter	Value
Rated power	P_n/S_n	60 kW/60 kVA
Grid RMS voltage	V_{ef}	380 V
DER voltage	V_i	192 V
DC-link voltage	V_o	620 V
Max. dc-link voltage	$V_{o(max)}$	625 V
Min. dc-link voltage	$V_{o(min)}$	615 V
Grid frequency	f	60 Hz
Switching frequency	f_s	10 kHz
Rated DAB phase angle	ϕ_n	45°
Transformer turns ratio	a	3.4
DC-link capacitance	C	680 μF
Series DAB inductance	L	5 μH
Grid inductance	L_g	100 μH (1.57%)
AC coupling inductance	L_f	500 μH (7.83%)

*Values in ( ) are on a 60-kVA 380-V 60-Hz base.

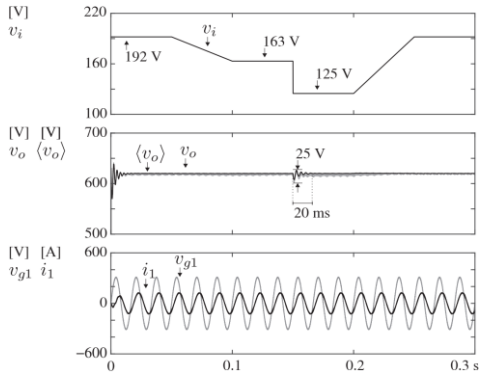

Figure 6. Simulated results of the PCS under disturbances in the voltage supplied by the DER.

operation on the pq plane. The performance comparison of the control system with the IP and PI controllers was also evaluated. The PCS was designed for the connection to the distribution grid with 60 kVA , 380 V and 60 Hz . The parameters used in the simulations are described in Table I. In addition, the sizing of passive elements of the DAB converter was based on the methodology presented in [14], while the coupling inductance L_f was determined taking into account the inductive reactance less than 20% , thus maintaining the power transfer capacity without reducing the power factor. The transformer turns ratio a and the dc-link capacitance C were approximated for standard values.

The PCS behavior in the first scenario, operating with voltage sags in v_i , is shown in Fig. 6. In this scenario, it was considered the power transfer of 40 kW (33.33% less than the rated power for maintaining the system stability) and 40 kvar . As can be seen, voltage v_o presented no significant disturbance in the first voltage sag from 192 V to 163 V (15% of 192 V) in 50 ms. Then, when occurs a sag step on voltage v_i from 163 V to 125 V (35% of 192 V), voltage v_o presented a small peak-to-peak transitory of 4% of 620 V with a settling time around 20 ms.

In Fig. 7, the simulated waveforms of the PCS in the second scenario are illustrated. In this case, the step response of real and imaginary powers is evaluated simultaneously. The power steps of ±40 kW and ±40 kvar were applied, so that the conversion system operated around 94.28% of rated power (i.e., 60 kVA). As expected, voltage v_o suffered greater disturbances in real power transition, while the system provided ±40 kvar to the grid. However,

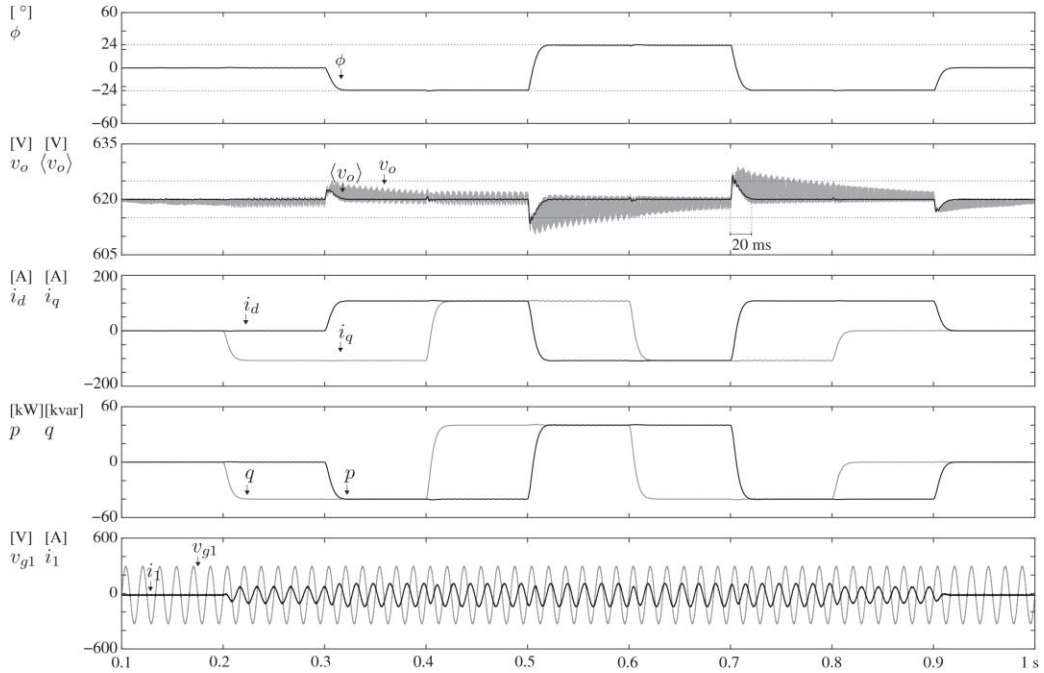

Figure 7. Simulated results of the PCS operating in four quadrants in response to the step of ±40 kW and ±40 kvar every 100 ms.

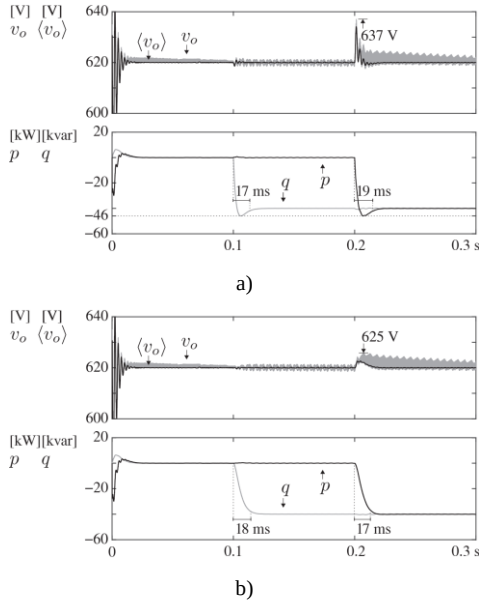

Figure 8. Simulated results of the PCS considering a power step response of -40 kW following a -40 kvar by employing: (a) PI controller in the power control and (b) IP controller in the power control.

it can be considered that the control system had an adequate performance, since the overshoot in v_o was around 0.81% of 620 V with a settling time (for a tolerance less than 1%) around 20 ms .

To compare the control performance of IP controllers over the traditional PI controllers, a power step response of -40 kW following a -40 kvar was simulated as shown in Fig. 8. In this case, the PI controller replaced the IP only in the dq-current control illustrated in Fig. 5 using the same gains for tuning the PI controller. As can be seen in Fig. 8a the use of PI controller led to an overshoot of 15% of 40 kvar / kW , which though can be reduced in exchange for a slower response. On the other hand, in Fig. 8b, a fast response with no overshoot could be obtained by means of the IP controller. In addition, for both cases, the settling time of the power response was similar at around 18 ms , considering a margin ±2% of the steady-state power value. The abrupt change in the real power results in a disturbance in the control of voltage v_o , thus the peak voltage in the PI case was 12 V higher than the IP one. Nevertheless, there was no relevant change in the performance of the dc-link voltage regulation using the PI controller.

IV. CONCLUSION

This paper has presented a comprehensive analysis of the model and control strategy of PCS, composed by DAB and dc-ac converter, which has been proposed to interface DERs and the power grid for providing support services. The employment of IP controllers enabled the development of the closed-loop transfer functions in a simple way, as well as resulted in smooth and fast dynamic responses, even under critical step changes of power, over traditional PI controllers. In addition, the theoretical analyses have been validated by simulation results in several operating scenarios of a three-wire three-phase system, considering both disturbances in the input and output of the PCS. In all simulations, none of the disturbances compromised the correct and stable operation of the PCS, therefore, the output signals from the dc-ac converter did not suffer any degradation on the waveform quality.

REFERENCES

[1] (2019). *Lazard's Levelized Cost of Storage Analysis - Version 5.0*. Lazard.

[2] Zhao, B., Song, Q., Liu, W., & Sun, Y. (2014). Overview of dual-active-bridge isolated bidirectional DC–DC converter for high-frequency-link power-conversion system. *IEEE Transactions on power electronics*, *29*(8), 4091-4106.

[3] Ahmed, M., Abdelrahem, M., Farhan, A., Harbi, I., & Kennel, R. (2021). DC-link sensorless control strategy for grid-connected PV systems. *Electrical Engineering*.

[4] Arunkumar, C. R., Manthati, U. B., & Punna, S. (2021). Supercapacitor-based transient power supply for DC microgrid applications. *Electrical Engineering.*

[5] Wang, G., et al. A review of power electronics for grid connection of utility-scale battery energy storage systems. IEEE *Transactions on Sustainable Energy*, *7*(4), 1778-1790.

[6] Costa, L. F., De Carne, G., Buticchi, G., & Liserre, M. (2017). The smart transformer: A solid-state transformer tailored to provide ancillary services to the distribution grid. *IEEE Power Electronics Magazine, 4(2)*, 56-67.

[7] Molina, M. G. (2017). Energy storage and power electronics technologies: A strong combination to empower the transformation to the smart grid. *Proceedings of the IEEE, 105*(11), 2191-2219.

[8] Tan, N. M. L., Abe, T., & Akagi, H. (2012). Design and performance of a bidirectional isolated DC–DC converter for a battery energy storage system. IEEE *Transactions on Power Electronics*, *27*(3), 1237-1248.

[9] Tian, Y., Chen, Z., Deng, F., Sun, X., & Hu, Y. (2014, September). Coodinative control of active power and DC-link voltage for cascaded dual-active-bridge and inverter in bidirectional applications. In *2014 IEEE Energy Conversion Congress and Exposition (ECCE)* (pp. 2249-2256). IEEE.

[10] Tian, Y., Loh, P. C., Deng, F., Chen, Z., Sun, X., & Hu, Y. (2016). Impedance coordinative control for cascaded converter in bidirectional application. *IEEE Transactions on Industry Applications*, *52*(5), 4084-4095.

[11] Ye, Q., Mo, R., & Li, H. (2019). Impedance modeling and DC bus voltage stability assessment of a solid-state-transformer-enabled hybrid AC–DC grid considering bidirectional power flow. *IEEE Transactions on Industrial Electronics*, *67*(8), 6531-6540.

[12] Vargas, T., Queiroz, S. S., da Silva, G. S., & Rech, C. (2019). Controllability study of dual-active bridge converter in cascaded converter structures. *Eletrônica de Potência*, *24*(1), 18-26.

[13] Akagi, H., Watanabe, E. H., & Aredes, M. (2007). *Instantaneous power theory and applications to power conditionin* (1st ed). John Wiley & Sons, Hoboken, NJ, USA.

[14] Santos, W. M., & Martins, D. C. (2014). *Introduction to single phase Dab converter*. *Eletrônica de Potência*, *19*(1), 36-46.

Thermal Design Aspects of a Rotary Regenerative Air Pre-heater using a Computer Code

Bhupesh Amabadas Parate[1]

[1] Armament Research and Development Establishment (ARDE), Dr. Homi Bhabha Road, Pashan, Pune - 411021, (Maharashtra) India, baparate@gmail.com

Abstract—**This paper explains about the thermal design aspects of a rotary regenerative air pre-heater that are widely used in various industrial domain including gas turbine. Rotary regenerative air pre-heater is the heat exchangers that are commonly used equipment's in the process industries. This heat exchanger extracts the heat from exhaust hot fluid gases. Knowledge of rotary regenerative air pre-heater its working principle and thermal design analysis in every ones concerned. In fact the whole country is interested for efficient and effective utilization of energy from the waste flue gas or fluid. In order to solve this problem, it is highly essential that both industry and academia work on the common platform to achieve the goal. An attempt has been made to analyse the different parameters such as heat transfer areas, heat transfer coefficient, overall heat transfer coefficient, number of transfer unit, modified number of transfer unit, effectiveness and pressure drop. The present design code is developed on the technical specification obtained from KRIBHCO Ammonia plant at Hazira located at Surat. The percentage increase in mass flow is estimated as 5 %. The heat transfer coefficients on air and gas side are estimated 297 W/m2K and 250 W/m2K respectively.**

Keywords - air pre-heater, heat exchanger, heat transfer coefficient, overall heat transfer coefficient, number of transfer unit, rotary regenerative

I. INTRODUCTION

Large fraction of initial capital investment and continuing operating cost of many industries such as oil and gas refinery, petrochemical, chemical, cement, steel, pharmaceutical, paper and pulp can be attributed to the supply and removal of heat from fluids. Heat exchangers are commonly used equipment is of everybody's concern [1]. Waste heat recovery systems usually involve a large volume of gas or air at a pressure around atmospheric and temperature may be as high as 9500C. Heat transfer coefficients for such gases are low and therefore tubular heat transfer equipment becomes large with regard to surface area, space and weight. As heat transfer coefficients of two fluids are of similar magnitude, both internal and external surfaces must be extended to reduce size, which is usually impracticable [2]. Compact light weight heat transfer equipment for such applications is the heat pipe and rotary regenerative heat exchanger or 'heat wheel'. A rotary heat generator was developed primarily to recover heat from the flue gas of large boiler plant, but has since been used in many other applications including the gas turbine and between the two fluids is not large a small quantity of inner-stream leakage can be tolerated, the rotary regenerative heat exchanger is ideally suited to heat interchanged between two gases at a pressure around atmospheric [3, 4]. This paper discusses about the methodology of the thermal design aspects of a rotary regenerative air pre-heater using a computer code.

A. Theoretical Background

The basic requirement of many process chemical and petrochemical industries is energy in the form of heat and power. Today the prices of fuel are increasing day by day and sources of fossil fuels are limited. Therefore industries are paying more attention in what way the fuels can conserve. Further, human brains are putting efforts to utilize the energy in a better and effective way. At present, 80 percent of energy production in the world is from fossil fuels. Hydroelectric, nuclear power and other energy sources such as solar energy, solar cells, geothermal, biomass etc. contributes 20 percent

of energy production. The increasing awareness of exponential growth of energy consumption, the rapid depletion of natural resources, the lagging development of new energy resources and technologies and growing public and institutional demands for energy and material conservation and environmental protection have forced the various countries to look forward towards more rational plan for energy economy. As a result many government and private agencies have initiated broad studies of projected energy consumption and possibility of conserving energy while enhancing the quality of environment. The rotary heat exchanger was invented by [5] a Swedish Engineer, early eighty years ago. It was developed primarily to recover heat from the flue gas of large boiler plant, but has been since used in many other applications including gas turbines and between the two fluids is not large and a small quantity of inner –stream leakage can be tolerated, the rotary regenerative heat exchanger is ideally suited to heat interchanged between two gases at a pressure around atmospheric. From the industrial point of view, the fuel and the power are the most an important item on which national standard of life depends. In the industry a large of heat energy is simply wasted in open atmosphere through the stack from flue gases. If this heat energy is recovered by some devices like heat exchanger and used for various purposes like heating of incoming air from the compressor and supplied to the combustion chamber for power generation. Heat exchangers are extensively in various types of power plants, refrigeration and air conditioning, in automobile of radiator, cryogenics, simply for drying purpose in order to remove the moisture from air, in steel industry of blast furnace, waste heat recovery boiler for steam generation in thermal power plant. The heat energy in the flue gas can be recovered by using heat exchanger of rotary regenerator type.

In the past decades, a considerable interest has been shown in the application of the periodic flow heat exchanger (rotary regenerator) to the gas turbine cycle for exhaust gas thermal energy regeneration. Regeneration by whatever method is applied to the gas turbine cycle obtained, among other improvements, higher thermal efficiency, lower specific fuel consumption, improved part load performance and lower optimum pressure ratio. The advantages to be expected from the application of the periodic flow heat exchanger to be the gas turbine process are discussed by [6], among others. Principle among these is the possibility of a more compact unit than is possible with conventional stationary surface types. This is due to the fact the periodic flow heat exchanger can be finely divided, without structural difficulty resulting in an appreciably reduced heat exchanger volume relative to a stationary type for a given effectiveness and pressure drop

B. Literature Review

The first report appears have to be presented by [7, 8] in 1946 regarding the theory of heat exchange in regenerators. In a direct transfer type heat exchanger, two fluids are separated by a thin wall through which heat flows. Although a simultaneous flow of both fluids are required in the exchanger, there is no mixing of two fluids and there are no moving parts in the exchanger. This type of exchanger is referred as recuperator. [9] proposed that heat exchangers can be used in gas turbine plants and its thermal analysis of contra flow regenerative heat exchanger respectively. Heat exchanger is installed in between compressor and combustion chamber. The temperature of flue gases having high temperature after expansion through turbine is simply given out in free atmosphere. If flue gases passed through heat exchanger the outlet temperature of compressed air is increased and supplied to combustion chamber. The advantage of such plant by regeneration is reduction in specific fuel consumption and part load performance is improved. The use of compact heat transfer surface is proposed [10]. Reference [11] presents the work regarding basic heat transfer and flow friction data on gas turbine plant heat exchangers. A typical installation of compact heat exchanger usually involves a flow contraction at the exchanger core entrance and flow expansion at the core exit. For a particular value of Reynold Number and selected value of porosity friction factor can be found out. Reference [12] proposed a design theory for periodic flow generator. Available special solutions obtained by graphical- numerical method provided by Hausen. Lamberston proposed theory on the performance factor of a periodic flow regenerator. Kayiem & Saunder explained about the performance enhancement of rotary air preheater by the use of pin shaped turbulators [13, 14]. Reference [15] discussed about the parallel flow through rotary heat exchanger. A numerical finite difference method of calculating the effectiveness of periodic flow type heat exchanger is presented by considering the metal ‘stream’ in cross with each of the gas

stream as separate but dependent exchangers. A general purpose digital computer was used to accommodate the large number of sub-divisions necessary for accuracy and extrapolation of data to zero element area such that the values of effectiveness are good to four significant figures. The most questionable of the idealization made is that of zero matrix conductivity particularly in the direction of fluid flow. Although the effect of matrix conductivity would be included in the finite difference equation the additional degree of freedom could make adequate coverage of all the parameters extremely voluminous and time consuming. If for a particular exchanger design the matrix conductivity was considered important then problem could be solved individually on a computer with adequate capacity. A simpler alternative is to neglect conduction and correct the effectiveness for this effect. A depth analysis is presented for understanding of dimensional and dimensionless variables and parameters associated with the thermal design of both rotary and fixed matrix regenerator both $\varepsilon - Nt_{u,o}$ and $\lambda - \pi$ methods are introduced. For the design of 'steady -state' periodic flow performance of regenerators are discussed. Similarity and suitable difference between these methods are outlined. It is shown that both methods are equivalent. In the literature, it is frequently erroneously mentioned that $\varepsilon - Nt_{u,o}$ method is only valid for duration of matrix in cold gas stream is equal to duration of matrix in hot gas stream ($P_h = P_c$). However the solutions are indeed valid for duration of matrix in cold is not equal to duration of matrix in hot gas stream ($P_h \neq P_c$) the rotary regenerator has the following equation.

$$\frac{Disc\,sector\ through\ which\ hot\ gas\ \ flows}{Disc\,sector\ through\ which\ cold\ \ gas\ \ flows} = \frac{Duration\ of\ \ matrix\ in\ hot\ \ gas\ stream}{Duration\ of\ \ matrix\ in\ cold\ \ gas\ stream} = 1.2 \quad . \ (1)$$

Analysis is also presented to account for influence of longitudinal heat conduction, wall thermal resistance, pressure leakage and carry over the leakages on regenerator effectiveness.

The present work is to determine heat transfer area, heat transfer coefficient, effectiveness, number of transfer units and pressure drop of regenerator based on the theoretical and experimental results of previous investigation. A computer code helps in circumventing the investigations problems associated with manual repeated calculations. Thus a computer code in '*C'* language is developed.

II. Thermal Design Consideration

The present work is mainly aimed as a development a comprehensive computer code in 'C' program for thermal design aspects and not to deal with mechanical design. Experience of similar unit operating under process condition is the best guide to exchanger type selection and should always be investigated thoroughly. However if previous operational experience is not available, when heat exchanger is to be designed for a particular application are almost taken into account. Wang and et al brought out about the exergy analysis on the irreversibility of rotary air preheater in thermal power plants [16].

A. Thermal Analysis and Heat Transfer Requirement

The thermal analysis is primarily concerned with the determination of heat transfer surface area required to transfer heat at a specified rate for a given flow rate and temperature of fluids. By forcing the fluids through heat exchanger at a higher velocity, the overall heat transfer coefficient (ho) may be increased but this higher velocity results in larger pressure drop through the heat exchanger is increased, ho and hence pressure drop need not to be so large. However, there are limitations on the physical size, results in a higher cost for the heat exchanger [17].

B. Units

This involves consideration of operating temperature and pressures, corrosive nature of either one or both fluids, relative thermal expansions, accompanying thermal stresses and relation of heat exchanger to other equipment concerned. Heat exchanger operating under relatively low pressure and temperature (15 atmosphere and 150^0C) do not require any detail consideration regarding the stresses developed. The knowledge of surface temperature may also be required for thermal design. In the design of heat transfer equipment for high or sub-zero temperatures, it is sometime necessary to calculate the temperature of heat transfer surface to check that the selected material is suitable for operating conditions. In the case of heat sensitive fluids, it may be necessary to calculate the temperature of adjacent of the adjacent fouling layer or heat transfer surface to check that the safe operating temperature for the fluid is not

exceed [18].

C. Design for Manufacturing

It requires translation of physical characteristics and dimensions into a unit, which can be built at a low cost. Selection of materials, seals, enclosures and optimum mechanical arrangement has to be made and manufacturing procedure must be specified [19].

D. Pressure Drop Consideration

The design of liquid to liquid heat exchangers, accurate knowledge of friction characteristics of heat exchanger surface is relatively unimportant because of low pressure requirement for pumping high density fluid. For gases, however, because of their low density, the friction power per unit mass flow rate is greatly multiplied. Thus, to the designer the friction characteristics of surface assume an importance equal to that of heat transfer characteristics. The friction characteristics needed is the function of flow friction factor and Reynolds number. The friction factor is affected by variations of fluid properties, density and kinetic viscosity over the cross section as well as variations in the flow direction.

E. Speed Influence

For minimum carryover, it could be desirable to operate at low relative speed but results in a lower effectiveness. Another advantage of low speed operation is the reduction of seal wear, if rubbing seals employed. Rotational speed of rotary regenerator lies in the range of 3 to 20 rpm.

F. Fluid Temperature

For the view point of the user, however, one of the most important distinctions in the selection of gas-gas heat recovery equipment is the operating temperature range. Temperature has the adverse effects on the heat exchanger material performance and at both ends of scale. If temperature is too low, the dew point may be reached and condensation can result in corrosive products effecting heat exchanger material. At the end of the temperature scale, material degradation may occur. Another aspect, common to gas-air is fouling. The accumulation of matter on heat exchange surface affects both pressure drop and heat transfer. Therefore periodic cleaning is required as per manufactures recommendation. The temperature of two fluid streams might be either specified for a given inlet temperature or designer must have to fix the outlet temperature based on flow rates and heat transfer considerations. Once inlet and outlet temperature are defined, the ratio of the fluid temperature rise (or drop) to the maximum temperature difference called effectiveness, could give an indication of the type of flow path parallel or cross or counter flow [20].

G. Flow Rates

In establishing flow rates, the restriction on the velocities that can be employed without causing excessive pressure drop or other problems such as erosion, noise and vibration must be considered. The maximum velocity in case of liquids is usually kept below 7.5 ms^{-1} and in the case of gases below 30 ms^{-1}. With this restriction the flow rate of the two fluid streams give a good indication of flow passage cross sectional area required for each of the two fluid streams.

H. Nature of Fluids

If corrosion characteristics of the fluids are especially aggressive, the high corrosion resistant exchanger such as graphite, glass or Teflon should be considered, provided pressure, temperature and capacity are not great. If suitable plate and gasket materials are available, the gasketed plate should also be considered. The Camella and spiral exchangers minimise the possibility of inter stream leakage and for fluids which are highly flowing or suspensions, slurries or fibrous liquids these types merit consideration, if pressure, temperature and size are within their range. If fluids are also corrosive the graphite, glass or teflon types should be considered.

I. Physical Size and Cost

To achieve the maximum economy, the majority of manufactures have adopted standard lines of heat exchangers. Some engineering design is necessary for almost every exchanger, but if service condition permits the use of exchangers, build to standard line saves money. It is also important that requirements of safety codes be met. Cost factor is an important but the exchanger type having the lowest capital cost may provide the serious problem in service and

become expensive to operate. Each case may be treated individually and it may be necessary to design and cost several alternatives before a decision is made. The size range of selected type may be too small to meet the required duty without having a large number of parallel units leading to expensive pipe work and valves, with possibility of flow distribution problem. Typical cost and power consumption of rotary regenerative heat exchanger is based on rotor/heat transfer material combinations.

III. RESULT AND DISCUSSIONS

A computer code was developed to carry out the thermal design of rotary regenerative type of heat exchanger. For thermal design of regenerator technical specifications of rotary regenerator for air preheating to boiler were obtained from KRIBHCO Ammonia plant at Hazira, in Surat. A numerical solution for the performance of rotary regenerative heat exchanger was carried out by [21]. Assuming suitable frontal areas on hot and cold side, considering both air and gases as a perfect gases and noting properties at the mean temperature heat transfer data are obtained using a computer program written in '*C'* language. The program documentation is in '*C'* consist of main program and input output files. The main programme is started with 'Include file' such as input, output files, mathematical files etc. declaration of variables. With the main flower bracket provided the excess for executing the main programme. All the variables used are declared as float which will read the input parameter that is required for the design evaluation. In this design for various input parameters remaining parameters can be calculated from the computer aided design. With the input file, when the program is executed, the input parameters are asked for which have to be entered in the prescribed units. The programme computes the various factors. All the calculation values are transferred to a separate output file. The reason in doing this is to accommodate many values for all elements and a lucid access to adjust the output in any required form. The complete programme is attached herewith at Appendix 'A'.

The various input parameters used in programming of air preheater obtained from KRIBHCO boiler plant is given at Table I.

The principles summarised in this article is widely used in the design of rotary air pre-heater whose primary function is to transfer heat from the hot fluid to cold fluid in a efficient way. Design of heat exchangers involves compromise of various aspects among several design factors. Readers are requested to make a note that one to one comparison is not possible as thermal performance data is not readily available in plant catalogue. Due to insufficient input data, the data required for actual inputs such as frontal areas on cold and hot side, selection matrix material, length of regenerator, area of matrix, heat transfer areas per unit volume are assumed. Further, assuming air and gas as perfect gases in addition to rotor with a infinite heat capacity. Designing a rotary heat exchanger is tedious and laborious process to arrive at the results, diligence and accuracy also matter. To overcome this, a computer programming is one of the ways, which gives the results quickly and efficiently. Some of promising results obtained from '*C*' program are given below:

TABLE I. THE VARIOUS INPUT PARAMETERS OF AIR PREHEATER

Description	**Magnitude with units**
Fuel to air ratio (fa_{rg})	0.04 kg/kg
Air flow rate (w_a)	46.763 kg/s
Inlet cold air pressure (P_{ci})	1.2 bar
Inlet cold air temperature (T_{ci})	30^0 C
Outlet cold air pressure (P_{co})	1.1bar
Outlet cold air temperature (T_{co})	37.6^0 C
Inlet hot gas pressure (P_{hi})	1.3bar
Inlet hot gas temperature (T_h)	290^0 C
Outlet hot gas pressure (P_{ho})	1.2bar
Outlet hot gas temperature (T_{ho})	135^0 C
Frontal area on hot side (af_{rh})	27.391 m^2
Frontal area on cold side (af_{rc})	9.795 m^2
Porosity (P)	0.832
RPM of regenerator	1.76 rpm
Hydraulic radius (r_h)	4.2 m
Heat transfer area pr unit volume (a)	30.94m^2/m^3
Volume of the matrix (v)	100 m^3
Length of regenerator (L)	1.7 m

- The heat transfer areas, on hot and cold side are estimated as 2279 m^2 and 815 m^2 respectively.
- The overall heat transfer coefficient is very high of the order of 1700 w/ m^2k, which shows a high heat transfer performance.
- The numbers of heat transfer units on air and gas side are estimated as 5.134 and 11.568. The modified NT_{uo} is estimated as

3.609

- The effectiveness for counter flow regenerator is estimated as 79.57 %
- The total pressure drop for air pr-heater is estimated as 0.05 % which is below 1 % and is within accepted range. The losses due to transport of gas from hot cold side at a speed are estimated to be less than 1 percent. This is the reason why rotary heat exchangers are not used for liquids.
- The percentage increase in the mass flow is estimated to be 5 percent.
- The flow periods for hot and cold fluids are 37.836 s and 71.941 s respectively. The ratio of hot to cold period worked as 1.90.
- Effectiveness for counter flow (ε) 79.75 percent
- Heat transfer coefficients on air side (h_a) and on gas side (h_g) are worked out as 297 w/m^{2}k and 250 w/m^{2}k
- Effective free flow area on cold and hot side are estimated as 8.15 m^2 and 22.79 m^2
- Total area is calculated as 3094 m^2

IV. CONCLUSIONS

The thermal design aspects of a rotary air pre-heater are addressed in this research article. The main objective of this paper is to describe the thermal design aspects of a rotary air pre-heater using '*C*' program.

ACKNOWLEDGMENTS

The author expresses his heartfelt thanks to his guide Dr. P Prabhakaran, Dept of Mech Engg, Maharaja Sayajirao University, Vadodara for selecting this topic. The views and conclusions contained herein are those of the author and should not be interpreted as necessarily representing the official policies or endorsements, either expressed or implied. The authors also gratefully acknowledge the helpful comments and suggestions of the reviewers, which have improved the presentation.

REFERENCES

[1] Shah, R. A. (1981). Classification of Heat Exchangers. In Bergts, K. A. E. & Scientific Affairs Division Applied Sciencer (E *Two Phase Flow Heat Exchanger thermal and Hydraulic design*. 143, 9-45.

[2] Hilmer, K., & Sven, H., (1943). Heat transfer and fluid resistance in Ljunstrom regenerative-type air preheaters. *Transaction of ASME*, 61-72.

[3] Ghodsipour, N., & Sadrameli, M., (2003). Experimental and sensitivity analysis of a rotary air heater for the flue gas heat recovery. *Applied Thermal Engineering, 23*, 571-580.

[4] Skiepko, T., & Shah, R. K. (2004). A comparison of rotary regenerator theory and experimental results for an air preheater for a thermal power plant. *Experimental thermal and fluid Science, 28*, 257-264.

[5] Lamberston T. J., & Montery, C. (1958). Performance factor of a periodic flow heat exchanger. *ASME Trans. 80*, 586-592.

[6] Sandira, A, Nikola, S., Ahmed, A., & Buljubašiü, I. (2005). Numerical analysis of heat transfer and fluid flow in rotary regenerative air pre-heaters. *Journal of Mechanical Engineering. 517-8*, 411-417.

[7] Hausen H. On the theory of heat exchangers

[8] Hausen, H. (1942). Accomplished calculations of heat exchange in regenerators. *MAP reports and Translatiosn. 9*, 193-200.

[9] Johnson, J. E. (1948). Regenerator heat exchangers for gas turbine and thermal analysis of the contra-flow regenerative heat exchangers. *Royal Aircraft Establishment Report No. Aero 2266*.

[10] Kays, W. M., & London, A. L. (1950). The gas turbine regenerator- The use of compact heat transfer surfaces. *ASME Trans. 72*, 611-621.

[11] London, A. L, Johnson, D. W., & Kays, W. M. Basic heat transfer and flow friction data.

[12] Coppage, J. E., & London, A. L. The periodic-flow regenerator : A summary of design theory.

[13] Al-Kayiem, H. H. & Mahdi. H. A. A. (2010). Performance enhancement of rotary air preheater by the use of pin shaped turbulators. *WIT Transactions on Engineering Sciences, 68*, 35-49.

[14] Saunder O. A., & Smoleniec, S. (1951). Heat transfer in regenerators. *IME-ASME*. 443.

[15] Eckrich, T. L. & Theoclitus G. (1966). Parallel flow through rotary heat exchanger. In *Proceedings of the third international heat transfer conference. 1* (pp. 130-138)

[16] Wang, F. Y., Zhao, L. L., Zhou, Q. T., Xu, Z. G., & Kim, H. T., 2008. Exergy analysis on the irreversibility of rotary air preheater in thermal power plants. *Energy, 33*, 647-656.

[17] American society of Mechanical Engineer, (1956). Miles J. C. & Smoot R. L.

[18] S. A. Al Ghamdi. (2006). *Analysis of air to air rotary wheels.* (Ph.D thesis).

[19] Stasiek, J. A. (1998). Experimental studies of heat transfer and fluid flow across corrugated-undulated heat exchanger surfaces. *Int. J. Heat and Mass Transfer, 41*(6-7), 899-914.

[20] Research Report No. AD 446233, Defence documentation center for scientific and technical information, Alexendria, Verginia

[21] Bae, Y. L. (1987). *A performance of rotary regenerative heat exchanger – A numerical solution.* (Ph. D. thesis).

APPENDIX A

PROGRAM FOR STUDY OF THERMAL DESIGN ASPECTS OF A ROTARY REGENERATIVE AIR PREHEATER
FILE NAME : PRJ_FILE.C
BY : Dr. BHUPESH A PARATE

```
#include<stdo.h>
#include<math.h>
#define pf printf
#define r 287
#define g 9.87
#define sc canf
float wa, pci, tci, vsci, pco, tco, vsco, phi, thi, vshi, pho,
vsho, farv, wg;
float afrh, tmc, afrc, rc, rpm, mpi, d, delta, ros, cps, a, rh,
ac, acc, ach, rhc;
float farg, p, ah, v, ua, npra, cpa, vmc, tmh, nprg, cpg, ga,
gg, nrc, nrh, ug, fa, fg;
float mpl, mpw, mprh, m, n, delpa, vmh, delpg, tpd, ho, cra,
ca, cp, rhoc, q, hon;
int ch;
void main()
{
pf("REGENERATOR INLET AIR SIDE");
pf("\n please enter the parameters:");
pf("\n air humidity ------essentially zero");
pf("\n fuel air ratio in kg/kg");
sc("%f", &farg);
pf("\a\a regenerator inlet air side:");
pf("\n air mass flow rate in kg/s");
sc("%f", &wa);
pf("\n inlet cold air pressure in bar");
sc("%f", &pci);
pf("\n inlet cold air temperature in %cC, 248");
sc("%f", &tci);
/* calculate specific volume of air */
vsci =(r*(tci+273.16))/ (pci*pow(10,5));
pf("\n inlet specific volume of air at inlet is %9.6f:", sci);
pf("\a\a regenerator outlet air side");
pf("\n outlet cold air pressure in bar");
sc("%f", &pco);
pf("\n outlet cold air temperature in %cC", 248);
sc("%f", &tco);
/* calculate outlet specific volume of air */
vsci =(r*(tco+273.16))/ (pco*pow(10,5));
pf("\n specific volume of air at outlet is %9.6f:", vsco);
clrscr();
pf("\a\a regenerator inlet gas side");
wg=wa*(1.0+farg);
pf("\n mass flow rate on gas side is %in kg/s, wg");
pf("\n inlet hot gas pressure in bar", 248);
sc("%f", &phi);
pf("\n inlet hot gas temperature in %cC", 248);
sc("%f", &thi);
/* calculate inlet specific volume of gas */
vshi =(r*(thi+273.16))/ (phi*pow(10,5));
pf("\n specific volume of gas at inlet is %:kg/m^3", vshi);
pf("\n regenerator outlet gas pressure in bar");
sc("%f", &pho);
pf("\n outlet hot gas temperature in %cC", 248);
sc("%f", &tho);
/* calculate outlet specific volume of gas */
2
vsho =(r*(tho+273.16))/ (pho*pow(10,5));
pf("\n specific volume of gas at outlet is %f:" vsho);
getch();
clrscr();
pf("\n please enter the details of matrix");
pf("\n frontal area on hot gas side");
sc("%f", &afrh);
pf("\n frontal area on cold air side");
sc("%f", & afrc);
/* calculate frontal area ratio */
rc =(afrh/afrc);
pf("\n frontal area ration is %f:", rc);
pf("\n rpm of regenerator");
sc("%f", &rpm);
pf("\n the mass of matrix");
sc("%f", &wm);
pf("\n wire diameter inch");
sc("%f", &d);
pf("\n thickness of one screen");
sc("%f", &delta);
pf("\n porosity");
sc("%f", &p);
b:
pf("\n enter the choice of the material of the matrix");
pf("\n\t\ 1.for metal");
pf("\n\t\ 2.for ceramic");
sc("%d", &ch);
switch(ch);
{
case 1:
pf("\n specific heat of metal");
sc("%f", &cps);
pf("\n density of metal");
sc("%f", &rhos);
break;
case 2:
pf("\n specific heat of ceramics");
sc("%f", &cpc);
pf("\n density of ceramics");
sc("%f", &rhoc);
break;
default:
pf("\n wrong choice -enter again");
goto b;
}
pf("\n enter the heat transfer area per unit volume");
sc("%f", &a);
pf("\n hydraulic radius");
sc("%f", &rh);
pf("\n enter the volume of matrix");
sc("%f", &v);
pf("\n length of regenerator");
sc("%f", &l);
/* to calculate area on cold and hot side */
ac=(a*v)/ (1+rc);
pf("\n area on cold side is %f", ac);
ah=(a*v)-ac;
pf("\n area on hot side is %f", ah);
/* to calculate effective free flow area */
acc=p*afrc;
pf("\n effective free flow area on cold side is %f", acc);
3
arh =p*afrh;
pf("\n effective free flow area on hot side is %f", ach);
rhc=1/rh;
pf("\n the ratio of length to hydraulic radius is %f", rhc);
```

```
tmc= (tci+tco)/2.0;
pf("\n kinematic viscosity of air at mean temperature");
sc("%f", &ua);
pf("\n prandtl no air side");
sc("%f", &npra);
pf("\n specific heat of air at mean temperature");
sc("%f", &cpa);
/* to calculate mean specific volume of air */
vmc = (vsci+vsco)/2.0;
pf("\n mean specific volume of air is %f", vmc);
/* to calculate mean specific volume of gas */
vmh =(vshi+vsho)/2.0;
pf("\n mean specific volume of gas is %f", vmh);
pf("\n properties of gas at mean temperature is %f", tmh);
pf("\n kinematic viscosity of gas at mean temperature %f");
sc("%f", &ug);
pf("\n prandtl no gas side");
sc("%f", &nprg);
pf("\n specific heat of gas at mean temperature");
sc("%f", &cpg);
/* to calculate cold gas flow period */
vc = (wa*vmc)/ac;
pf("\n the velocity of air is %f", vc);
tc=1/vc
pf("\n cold gas flow period is %f", tc);
/* to calculate hot gas flow period */
vh=(wg*vmh)/ah;
pf("\n the velocity of gas is %f", vh);
th=1/vh
pf("\n hot gas flow period is %f", th);
/* to determine mass flux */
ga = wa/acc;
pf("\n mass flux on air side is %f", ga);
gg=wg/ach
pf("\n mass flux on gas side is %f", gg);
/* to determine Reynolds numbers */
nrc=(rh*rc)/ua;
pf("\n Reynolds number on air side is %f", nrc);
nrh=(rh*vh)/ug;
pf("\n Reynolds number on gas side is %f", nrh);
/* to determine Nussult numbers */
pf("\n enter the value of friction factor on air side :");
nrc=(rh*rc)/ua;
nrh=(rh*vh)/ug;
pf("\n Reynolds number on gas side is %f", nrh);
pf("\n kinematic viscosity of gas at mean temperature %f");
sc("%f", &fa);
pf("\n enter the value of m at nrc");
sc("%f", &m);
nsta=m/pow(npra, 2.0/3.0);
pf("\n Stantant number on air side is %f:", nsta);
/* to determine the number of transfer units */
ntua=nsta*ac/acc;
nrh=(rh*vh)/ug;
pf("\n no of transfer units on air side is %f", ntua);
ha=nsta*ga*cpa;
pf("\n heat transfer coefficient on air side is %f", ha);
4
pf("\n enter the value of friction factor on gas side is %f",
ha);
sc("%f", &fg);
pf("\n enter the value of n at nrh");
sc("%f", &n);
nstg =n/(pow9nprg, 2.0/3.o);
pf("\n Statant number on gas side is %f:", nstg));
hg=nstg*gg*cpg
pf("\n heat transfer coefficient on gas side is %f:", hg);
/* to calculate the number of transfer units */
ntug=(nstg*ah)/ach;
pf("\n number of transfer units on gas side is %f", ntug);
cag=(wa*cpa)/(wg*cpg);
pf("\n capacity rate ratio is %f", cag);
cr=rpm*60.0*wm*cps;
pf("\n the heat capacity of matrix is %f", cr);
ca=wa*cpa;
pf("\n the heat capacity of air is %f", ca);
cra=cr/ca;
pf("\n the ratio of rotor to heat capacity is %f", cra);
/* to calculate modified number of transfer units */
ntuo=1.0/(1.0/ntua+cag/ntug);
pf("\n modified number of transfer unit is %f", ntuo);
hon=(ha*ac)/(hg*ah);
pf("\n non dimensional ratio is %f", hon);
/* to calculate overall heat transfer coefficient */
ho=1.0/(1.0/(ha*ac)+1.0/(hg*ah));
pf("\n overall heat transfer coefficient is %f", ho);
/* to calculate the effectiveness */
a:
pf("\n enter choice of effectiveness of heat exchanger");
pf("\n\t\t 1. for counter flow");
pf("\n\t\t 2. for parallel flow");
sc("%d", &ch);
switch(ch);
{
case1:
ec=(1.0-exp((-1)*ntuo*(1.0-cag)))/(1.0-cag*exp((-
1)*ntuo*(1.0-cag)));
pf("\n effectiveness for counter flow heat exchanger is
%e:", ec);
break;
case2:
ec=(1.0-exp((-1)*ntuo*(1.0-cag))/(1.0+cag);
pf("\n effectiveness for parallel flow heat exchanger is
%e:", ep);
break;
default:
pf("\n wrong choice-enter again");
goto a;
}
/* to calculate the pressure drop */
delpa=(ga*ga*vsci*((1.0+p*p)*(vsco/vsci-
1.0)+((fa*ac*vmc)/acc*vsci)))/(2.0*g*pci*pow(10,5);
pf("\n the pressure drop on air side is %f:", delpa);
delpg=(gg*gg*vshi*((1.0+p*p)*(vsho/vshi-
1.0)+((fg*ah*vmh)/ach*vshi)))/(2.0*g*phi*pow(10,5);
pf("\n the pressure drop on gas side is %f:", delpg);
tpd=(delpa+delpg)*100;
pf("\n total pressure drop is in percentage %f:", tpd);
}
```

Autor index

www.energetics.cosrec.org

ISBN: 978-86-80593-73-9